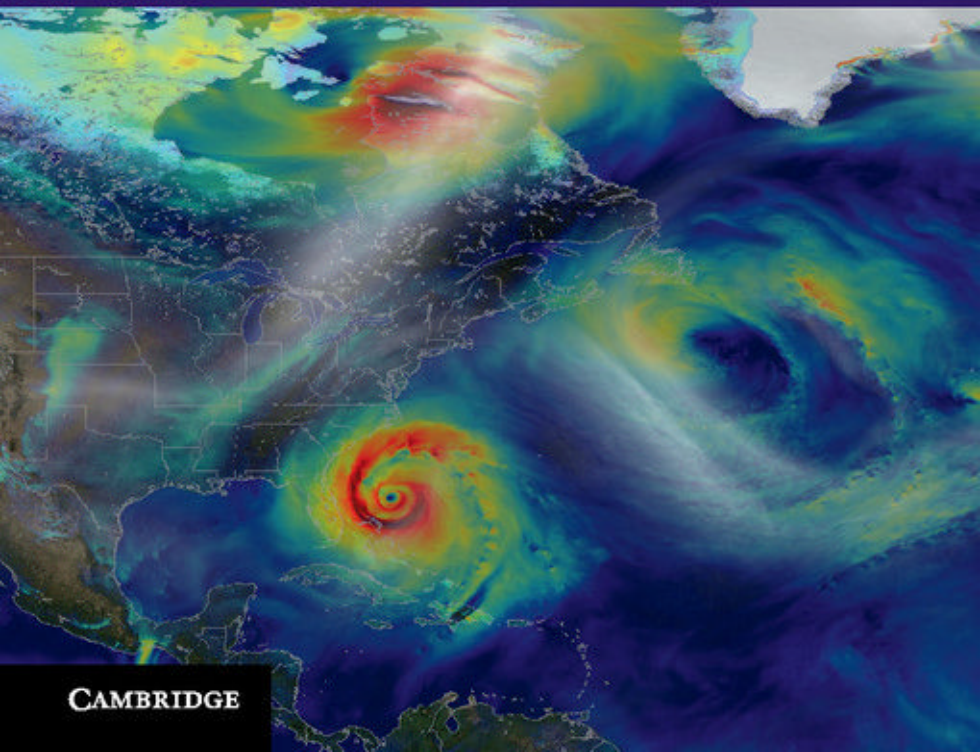


# Dynamics and Predictability of Large-Scale, High-Impact Weather and Climate Events

Edited by Jianping Li, Richard Swinbank,  
Richard Grotjahn, and Hans Volkert





## Dynamics and Predictability of Large-Scale, High-Impact Weather and Climate Events

In recent years, a significant number of high-impact weather and extreme climate events have inflicted catastrophic property damage, and loss of human life, around the world, and hindered socio-economic development. Improving simulation and prediction of these events is an increasingly important requirement of public meteorological services.

Based largely on an International Commission on Dynamical Meteorology (ICDM) workshop, this timely volume covers a range of important research issues related to extreme events. Dynamical linkages between these extremes and various atmospheric and ocean phenomena are examined, including Atlantic Multi-decadal, North Atlantic, and Madden–Julian Oscillations, Annular Modes, tropical cyclones, and Asian monsoons. This book also examines the predictability of high-impact weather and extreme climate events on multiple time scales. Highlighting recent research and new advances in the field, this book enhances understanding of dynamical and physical processes associated with these events, to help managers and policy makers make informed decisions to manage risk and prevent or mitigate disasters. It also provides guidance on future research directions for experts and young scientists.

Written by leading researchers in weather and climate extremes, this comprehensive volume is ideal for professionals and policy makers working in disaster prevention and mitigation, and is a key resource for graduate students and academic researchers in atmospheric science, meteorology, climate science, and weather forecasting.

JIANPING LI is Dean and Professor at the College of Global Change and Earth System Sciences (GCESS), Beijing Normal University, and Director of the Joint Center for Global Change Studies (JCGCS). He is also an affiliated faculty member of the University of Hawaii, a Fellow of the International Union of

Geodesy and Geophysics (IUGG), and a Fellow of the Royal Meteorological Society. His major research interests include climate dynamics and climate change, predictability, monsoons, and annular modes. He is Vice-Chair of the IUGG Commission on Climatic and Environmental Change (CCEC), and Executive Secretary of the International Commission of Climate (ICCL) within IAMAS (International Association of Meteorology and Atmospheric Sciences).

RICHARD SWINBANK is a Scientific Manager in Weather Science at the Met Office in the UK and a Fellow of the Royal Meteorological Society. He is past President of the IAMAS International Commission on Dynamical Meteorology (ICDM) and Co-Chair of the World Weather Research Programme (WWRP) working group on Predictability, Dynamics, and Ensemble Forecasting (PDEF). His research interests include ensemble forecasting, data assimilation, atmospheric dynamics, and predictability of high-impact weather.

RICHARD GROTJAHN is (upper level) Professor of Climate Dynamics at the University of California, Davis, California, USA. He is currently President of the ICDM commission of IAMAS, and is Co-Chair of the US CLIVAR working group on Large Scale Circulation Patterns Associated with Extremes. His research interests include extreme weather, climate model assessment, and large-scale atmospheric synoptic-dynamics.

HANS VOLKERT is Senior Scientist at the Deutsches Zentrum für Luft-und Raumfahrt (DLR), Institut für Physik der Atmosphäre (IPA), Germany, and a Fellow of the Royal Meteorological Society. He served as Secretary-General of IAMAS from 2007 to 2015 and as IUGG liaison officer to the World Meteorological Organization (WMO) from 2011 to 2015, with a focus on atmospheric issues. His main research interests are in mesoscale meteorology, weather forecasting, and the development of meteorology as a branch of physics.

## *Special publications of the International Union of Geodesy and Geophysics Series*

The International Union of Geodesy and Geophysics (IUGG) promotes and co-ordinates international scientific studies of Earth (physical, chemical, and mathematical) and its environment in space, aiming to apply this knowledge to societal needs such as mineral resources, mitigation of natural hazards, and environmental preservation. The series is co-published by the IUGG and Cambridge University Press, providing researchers and graduate students with authoritative insights into major scientific developments and state-of-the-art research.

### SERIES EDITORS

Christophe Cudennec, *Agrocampus Ouest, Rennes, France*  
Hermann Drewes, *Deutsches Geodätisches Forschungsinstitut, Munich, Germany*  
Alik Ismail-Zadeh, (Editor-in-chief), *Karlsruhe Institute of Technology, Germany*  
Andrew Mackintosh, *Victoria University of Wellington, New Zealand*  
Mioara Mandea, *Centre National d'Etudes Spatiale, Paris, France*  
Joan Martí, *Instituto de Ciencias de la Tierra "Jaume Almera", Barcelona, Spain*  
Johan Rodhe, *University of Gothenburg, Sweden*  
Peter Suhadolc, *University of Trieste, Italy*  
Hans Volkert, *Deutsches Zentrum für Luft-und Raumfahrt, Oberpfaffenhofen, Germany*

### ADVISORY BOARD

Ian Allison, *Antarctic Climate & Ecosystems CRC, Hobart, Australia*  
Isabelle Ansorge, *University of Cape Town, South Africa*  
Tom Beer, *Commonwealth Scientific and Industrial Research Organisation, Australia*  
Claudio Brunini, *Universidad Nacional de La Plata, Argentina*  
Jeff Freymueller, *University of Alaska, Fairbanks*  
Harsh Gupta, *National Geophysical Research Institute, Hyderabad, India*  
David Jackson, *University of California, Los Angeles*  
Setsuya Nakada, *University of Tokyo, Japan*  
Guoxiong Wu, *Chinese Academy of Sciences, Beijing, China*  
Gordon Young, *Wilfrid Laurier University, Waterloo, Canada*

### TITLES IN PRINT IN THIS SERIES

A. Ismail-Zadeh, J. Urrutia Fucugauchi, A. Kijko, K. Takeuchi, and I. Zaliapin, *Extreme Natural Hazards, Disaster Risks and Societal Implications*.  
J. Li, R. Swinbank, R. Grotjahn, and H. Volkert, *Dynamics and Predictability of Large-Scale, High-Impact Weather and Climate Events*.

# Dynamics and Predictability of Large-Scale High-Impact Weather and Climate Events

EDITED BY

JIANPING LI

*Beijing Normal University*

RICHARD SWINBANK

*Met Office*

RICHARD GROTJAHN

*University of California, Davis*

HANS VOLKERT

*Deutsche Zentrum für Luft- und Raumfahrt*



CAMBRIDGE  
UNIVERSITY PRESS

# CAMBRIDGE

UNIVERSITY PRESS

University Printing House, Cambridge CB2 8BS, United Kingdom

Cambridge University Press is part of the University of Cambridge.

It furthers the University's mission by disseminating knowledge in the pursuit of education, learning and research at the highest international levels of excellence.

[www.cambridge.org](http://www.cambridge.org)

Information on this title: [www.cambridge.org/9781107071421](http://www.cambridge.org/9781107071421)

© Cambridge University Press 2016

This publication is in copyright. Subject to statutory exception and to the provisions of relevant collective licensing agreements, no reproduction of any part may take place without the written permission of Cambridge University Press.

First published 2016

Printed in the United Kingdom by TJ International Ltd. Padstow Cornwall

*A catalogue record for this publication is available from the British Library*

*Library of Congress Cataloguing in Publication data*

Dynamics and predictability of large-scale high-impact weather and climate events / edited by Jianping Li, Beijing Normal University, Richard Swinbank, Met Office, Richard Grotjahn, University of California, Davis, Hans Volkert, Deutsche Zentrum für Luft- und Raumfahrt eV (DLR).

pages cm

Includes index.

ISBN 978-1-107-07142-1 (Hardback)

1. Severe storms—Forecasting. 2. Weather forecasting. I. Li, Jianping (Meteorology professor), editor. II. Swinbank, Richard, editor. III. Grotjahn, Richard, editor. IV. Volkert, Hans, editor.

QC941.D96 2015

551.55—dc23 2015023762

ISBN 978-1-107-07142-1 Hardback

Cambridge University Press has no responsibility for the persistence or accuracy of URLs for external or third-party internet websites referred to in this publication, and does not guarantee that any content on such websites is, or will remain, accurate or appropriate.

# Contents

<i>Preface</i>	<i>page</i> viii	
<i>Acknowledgments</i>	x	
<i>List of contributors</i>	xii	
<b>Part I. Diagnostics and prediction of high-impact weather</b>		
1. Global prediction of high-impact weather: diagnosis and performance <i>Mark Rodwell and Alan Thorpe</i>	3	
2. Severe weather diagnosis from the perspective of generalized slantwise vorticity development <i>Guoxiong Wu, Yongjun Zheng, and Yimin Liu</i>	16	
3. Probabilistic extreme event attribution <i>Pardeep Pall, Michael Wehner, and Dáithí Stone</i>	37	
4. Observed and projected changes in temperature and precipitation extremes <i>Xuebin Zhang and Francis Zwiers</i>	47	
<b>Part II. High-impact weather in mid latitudes</b>		
5. Rossby wave breaking: climatology, interaction with low-frequency climate variability, and links to extreme weather events <i>Olivia Martius and Gwendal Rivière</i>	69	
6. The influence of jet stream regime on extreme weather events <i>Nili Harnik, Chaim I. Garfinkel, and Orli Lachmy</i>	79	
7. Forecasting high-impact weather using ensemble prediction systems <i>Richard Swinbank, Petra Friederichs, and Sabrina Wahl</i>	95	
8. Storm tracks, blocking, and climate change: a review <i>Tim Woollings</i>	113	
9. The North Atlantic and Arctic Oscillations: climate variability, extremes, and stratosphere–troposphere interaction <i>Adam A. Scaife</i>	122	
<b>Part III. Tropical cyclones</b>		
10. Opportunities and challenges in dynamical and predictability studies of tropical cyclone events <i>Russell L. Elsberry and Hsiao-Chung Tsai</i>	133	
11. Predictability of severe weather and tropical cyclones at the mesoscales <i>Fuqing Zhang, Christopher Melhauser, Dandan Tao, Y. Qiang Sun, Erin B. Munsell, Yonghui Weng, and Jason A. Sippel</i>	141	
12. Dynamics, predictability, and high-impact weather associated with the extratropical transition of tropical cyclones <i>Patrick A. Harr and Heather M. Archambault</i>	153	
13. Secondary eyewall formation in tropical cyclones <i>Chun-Chieh Wu, Yi-Hsuan Huang, and Zhemin Tan</i>	168	
14. Seasonal forecasting of floods and tropical cyclones <i>Tom Beer and Oscar Alves</i>	176	
<b>Part IV. Heat waves and cold-air outbreaks</b>		
15. European heat waves: the effect of soil moisture, vegetation, and land use <i>Fabio D'Andrea, Philippe Drobinski, and Marc Stéfanon</i>	185	
16. Western North American extreme heat, associated large-scale synoptic-dynamics, and performance by a climate model <i>Richard Grotjahn</i>	198	
17. Decadal to interdecadal variations of northern China heat wave frequency: impact of the Tibetan Plateau snow cover <i>Zhiwei Wu and Jianping Li</i>	210	
18. Global warming targets and heat wave risk <i>Robin Clark</i>	220	
19. Cold-air outbreaks over East Asia associated with blocking highs: mechanisms and their interaction with the polar stratosphere <i>Hisashi Nakamura, Kazuaki Nishii, Lin Wang, Yvan J. Orsolini, and Koutarou Takaya</i>	225	
<b>Part V. Ocean connections</b>		
20. Response of the Atlantic Ocean Circulation to North Atlantic freshwater perturbations <i>Henk A. Dijkstra</i>	239	

21. Key role of the Atlantic Multidecadal Oscillation in twentieth century drought and wet periods over the US Great Plains and the Sahel <i>Suman Nigam and Alfredo Ruiz-Barradas</i>	255	<b>Part VI. Asian monsoons</b>
22. Floods and droughts along the Guinea Coast in connection with the South Atlantic Dipole <i>Hyacinth C. Nnamchi and Jianping Li</i>	271	25. Extreme weather and seasonal events during the Indian summer monsoon and prospects of improvement in their prediction skill under India's Monsoon Mission <i>D. R. Sikka</i>
23. The effect of global dynamical factors on the interannual variability of land-based rainfall <i>Peter G. Baines and Benjamin J. Henley</i>	280	26. Interannual variability and predictability of summer climate over the Northwest Pacific and East Asia <i>Shang-Ping Xie and Yu Kosaka</i>
24. MJO and extreme weather/climate events <i>Chidong Zhang</i>	294	27. Impacts of annular modes on extreme climate events over the East Asian monsoon region <i>Jianping Li</i>
		<i>Index</i>
		<i>Color plate section between pages 210 and 211</i>

# Preface

In recent years, a significant number of high-impact weather and climate events have inflicted catastrophic property damage and loss of human life, and hindered socio-economic development. Tropical cyclones are some of the most damaging weather systems; recent examples include hurricane Katrina in the USA in 2005 and hurricane Sandy in the USA in 2012, while multiple typhoons affected China in 2012. Severe flooding occurred in Australia in 2010–11, Europe in 2002, China in 2012, and Pakistan in 2010; there were droughts in China in 2010–2011, the USA in 2012; heat waves swept across the United States in 2012 and freezing rain in China in 2008. “High-impact” events encompass not only severe or extreme weather, but also other weather and climate events that have a major socio-economic impact. Thus, further improving weather forecasting and climate prediction capabilities are not only the topics at the forefront of the atmospheric science community, but also increasingly important requirements of public meteorological services. However, it is undeniable that there is a need for greater scientific knowledge to underpin weather forecasts and climate predictions, especially, for high-impact weather and climate events. The main outcome of this deficiency is a lack of knowledge of the dynamic mechanism and predictability of high-impact weather and climate events.

In view of this, the International Commission on Dynamical Meteorology (ICDM) held a workshop on the subject of “Dynamics and predictability of high-impact weather and climate events” on 6–9 August 2012, in Kunming, China. The ICDM is one of the commissions of the International Association of Meteorology and Atmospheric Sciences (IAMAS), which is in turn a constituent association of the International Union of Geodesy and Geophysics (IUGG). The commission is composed of international scientists who are committed to pursuing and cooperating in the science of dynamical meteorology. In the past, the ICDM has made very valuable contributions to the observation, research, analysis, and simulation of atmospheric dynamics across a range of time and space scales, and coupling of the atmosphere to the ocean. In turn those developments have led to improved skill in weather, climate, and environmental prediction for the benefit of society. The ICDM sponsors symposia that are held during the biennial IUGG General Assemblies and IAMAS Assemblies. The workshop was an additional event, intended to foster further understanding of the

relevant dynamical and physical mechanisms that lead to extreme weather and climate events.

This book is largely based on the invited lectures presented at that workshop. It sets out our current understanding of the critical issues concerning dynamics and predictability of global and regional high-impact weather and climate events. Our aim is to summarize relevant newest advances in this field, and to enhance the understanding of physical processes associated with these events. The book covers a range of important research issues related to extreme events, including tropical cyclones, Asian monsoon, Madden–Julian oscillation, and annular modes, as well as the predictability of high-impact weather and climate events on multiple time scales. The combination of leading scientists and highly topical subject matter makes the book particularly appropriate for inclusion in the IUGG Special Publications series.

There have been a number of recent books describing high-impact or extreme weather and climate events. Many of these books describe extreme events with simple and vivid images to popularize the science, or they focus on the social and economic impacts of extreme events. However, this book focuses on the dynamics and predictability of extreme events, and assumes prior knowledge of the fundamentals of atmospheric dynamics. It may be the first comprehensive book dedicated to almost all key topics of extreme weather and climate events, with the main focus on synoptic and larger-scale phenomena. Our intention is not to create a geographical survey of extreme events, but rather to use specific examples to illustrate broader dynamical causes of such events. We anticipate that the book will become an important reference for these particular areas of atmospheric science.

This book is organized into six parts, comprising 27 peer-reviewed chapters. *Part I, Diagnostics and prediction of high-impact weather*, introduces the numerical prediction of high-impact weather, and discusses projected changes in climate extremes. *Part II, High-impact weather in mid latitudes*, discusses the relationship between variations in mid-latitude jet streams and severe weather events, troposphere–stratosphere interaction, and the use of probabilistic prediction techniques. *Part III, Tropical cyclones*, covers many aspects of the life-cycle of tropical cyclones and prediction of the associated severe weather. *Part IV, Heat waves and cold-air outbreaks*, analyses summer heat and drought and their relationship with both

large-scale dynamics and surface conditions. It also explores related mechanisms linked to cold-air outbreaks over Asia. **Part V**, *Ocean connections*, explores how the ocean contributes to extreme weather and climate events, with a primary focus on extended drought and wet periods. **Part VI**, *Asian monsoons*, surveys the prediction of extreme events associated with the Indian monsoon, and wider connections with East Asia, the Northwest Pacific, and links with annular modes.

The main authors for each chapter are leading scientists in the field of weather and climate extremes. The book comprises the most important content of the ICDM 2012 workshop, including contributions from the invited lecturers and other selected participants. However, in order to

produce a more balanced book, additional contributions were solicited from other leading researchers in the field.

The book is intended for graduate students and post-doctoral and other researchers who are interested in atmospheric dynamics and its relevance to the prediction of extreme events, across a range of time scales, from short-term weather forecasting to climate prediction. The book will provide a theoretical reference for improving researchers' understanding of the critical issues concerning the dynamics and predictability of global and regional high-impact weather and climate events. The improved understanding will also help relevant managers and policy makers to make proper decisions to manage risk and prevent or mitigate disasters.

We hope you enjoy reading this book.



Dynamics and Predictability of High-impact Weather and Climate Events  
An ICDM / IAMAS / IUGG Workshop  
6-9 August 2012, Kunming, Yunnan province, China



01 Dong-Kyun KIM, Korea	19 Yimin MA, Australia	37 Zhitao YU, USA	55 Istvan SZUNYOGH, USA	73 Sehwan YANG, China	90 Xiaofeng LI, China	107 Deqiang LIU, China	124 Jie FENG, China
02 Chengji LIU, China	20 Ryusuke MASUNAGA, Japan	38 Debah NATH, China	56 Mark RODWELL, UK	74 Chidong ZHANG, USA	91 Meng-Kuang TSAI, C.-Taipei	108 Haiyang YU, China	125 Yu DU, China
03 Ruowan YANG, China	21 Bo WU, China	39 C.T. SABEERALI, India	57 Cheng SUN, China	75 Xiaodong TANG, China	92 Chenxing RUAN, China	109 Qingqing LI, China	126 Yangyang ZHAO, China
04 Patrick HARR, USA	22 Chuanxi LIU, China	40 Robin CLARK, UK	58 David RAYMOND, USA	76 Tao LIAN, China	93 Hanlie XU, China	110 Ning SHI, China	127 Thomas SPENGLER, Norway
05 Wei HONG, China	23 Daria IAROVA, Ukraine	41 Russell ELSBERRY, USA	59 Bohua HUANG, USA	77 Haipeng YU, China	94 Sen ZHAO, China	111 Zuowei XIE, China	128 Haigong ZHOU, China
06 Xuzan GU, China	24 Kuranoshin KATO, Japan	42 Kevin CHEUNG, Australia	60 Jie SONG, China	78 Fei ZHENG, China	95 Jiayu ZHENG, China	112 Shan YIN, China	129 Ting LIU, China
07 Yubin LI, Australia	25 Takafumi MIYASAKA, Japan	43 Sarat C. KAR, India	61 Fei XIE, China	79 Cholaw BUEH, China	96 Nan XING, China	113 Xiaofang WANG, China	130 Hongqing ZHANG, China
08 Hyacinth NNAMCHI, Chi./Nigeria	26 Chun LI, China	44 Mio MATSUEDA, Japan	62 Rufus EWANLEN, Nigeria	80 Kazuaki NISHII, Japan	97 Pei-Yu HUANG, C.-Taipei	114 Yanyan KANG, China	131 Panxing LOU, China
09 Jie CAO, China	27 Fabio D'ANDREA, France	45 Tim WOOLLINGS, UK	63 Christoph WELKER, Switzerl.	81 Xu XUE, China	98 Luis RODRIGUES, Spain	115 Qin SU, China	132 Yangyang YONG, China
10 Zheng (Jenny) LIN, China	28 Adam SCAIFE, UK	46 Zhiwei WU, China	64 Xin LIU, China	82 Ruoqi GAO, China	99 Jingwen ZHANG, China	116 Yoon-Jeong HWANG, Korea	133 Chihua TSOU, C.-Taipei
11 Lun LI, China	29 Henk DIJKSTRA, Netherlands	47 Alexandre LAINE, Japan	65 Sang LI, China	83 Hisashi NAKAMURA, Japan	100 Saska GJORGEVSKA, USA	117 Jong-IM PARK, Korea	134 Huiqin HU, China
12 Chao LI, China	30 Satoru OKAJIMA, Japan	48 Thomas KNUTSON, USA	66 Miaoqi GAO, China	84 Chun-Chieh WU, C.-Taipei	101 Feifan ZHOU, China	118 Yang-fan CUI, China	135 Wenling ZHOU, China
13 Heather ARCHAMBAULT, USA	31 Xuejuan REN, China	49 Sumanti NIGAM, USA	67 Shangping XIE, China	85 Jing YANG, China	102 Junmei LU, China	119 Qixia WU, China	136 Miao YU, China
14 Haruko KATO, Japan	32 Petra FRIEDERICHS, Germany	50 Mohan DAS, Bangladesh	68 Xiaokang WANG, China	86 Hongbo LIU, China	103 Liang FENG, China	120 Hui XU, China	137 Chuanyi WANG, China
15 Fuqing ZHANG, USA	33 Nili HARNIK, Israel	51 Suaydh SUAYDHI, Australia	69 Xiaohao QING, China	87 Yali LUO, China	104 Shoujuan SHU, China	121 Yi ZHANG, China	138 Zhiyong MENG, China
16 Chung-Chieh WANG, C.-Taipei	34 Fumiaki OGAWA, Japan	52 Junpeng YUAN, China	70 Kamoru LAWAL, S.Africa	88 Alan THORPE, UK	105 Neil HOLBROOK, Australia	122 Mitchell MONCRIEFF, USA	139 Devraj SIKKA, India
17 Wansuo DUAN, China	35 Zhemin TAN, China	53 Richard SWINBANK, UK	71 Tom BEER, Australia	89 Guoxiong WU, China	106 Peter BAINES, Australia	123 John NIELSEN-GAMMON, USA	140 Ruiqiang DING, China
18 Richard GROTJAHN, USA	36 Jianping LI, China	54 Tetsuo NAKASAWA, WMO	72 Hans VOLKERT, Germany				

Legend: *id number*, First name/initial(s), FAMILY NAME, Country (of work, not necessarily nationality)

Majority of participants at noon, 6 August 2012 (photo: Tao LONG)

Arrangement: Zheng LIN & Hans VOLKERT (IAMAS)

## Acknowledgments

This book could not have been completed without the strong support of the international and national organizations, international and national projects (Fig. P1) as follows:

- The International Union of Geodesy and Geophysics (IUGG);
- The Observing System Research and Predictability Experiment (THORPEX) of the World Weather Research Programme (WWRP);
- The World Climate Research Programme (WCRP);
- The Chinese Association for Science and Technology (CAST);
- The Chinese National Committee for IUGG;
- The Chinese Academy of Sciences (CAS);
- The National Natural-Science Foundation of China (NSFC);
- The State Key Laboratory of Numerical Modelling for Atmospheric Sciences and Geophysical Fluid Dynamics (LASG), Institute of Atmospheric Physics (IAP);

- The National Basic Research Program of China (973 Program): “Air-Land-Sea interactions in Asia and their role in the global change (ALS)” (2010CB950400);
- The NSFC Key Project: “New theory of planetary wave in non-uniform basic flow and interaction between SH and NH atmospheres” (41030961);
- The International Association of Meteorology and Atmospheric Sciences (IAMAS);
- The International Commission of Dynamical Meteorology (ICDM)/IAMAS;
- Nanjing University.

We sincerely thank all authors of the book chapters for their excellent contributions. This comprehensive book could not have been completed without their continued support. We are most grateful to the reviewers of the chapters for their constructive reviews, which helped improve upon the original manuscripts. The chapter reviewers were as follows: Peter G. Baines, Tom Beer,



Figure P1. Logos of the relevant supporting organizations and projects for the book.

Robin Clark, Henk Dijkstra, Russell L. Elsberry, Juan Feng, Petra Friederichs, Richard Grotjahn, Nili Harnik, Patrick Harr, Bohua Huang, Jianping Li, Jian Ling, Yimin Liu, Olivia Martius, Mu Mu, Hisashi Nakamura, Tetsuo Nakazawa, John W. Nielsen-Gammon, Xiaohao Qin, Mark Rodwell, Adam A. Scaife, Richard Swinbank, Zhe-Min Tan, Tim Woollings, Chun-Chieh Wu, Zhiwei Wu, Shang-Ping Xie, and Feifan Zhou.

Special thanks go to Susan Francis, Zoë Pruce, Cassi Roberts, Karyn Bailey, and Rosina Piovani of Cambridge University Press for their guidance throughout the

production of the book. We are very grateful to Zheng Lin, Chuanyi Wang, and Wenling Zhou for their excellent support with the organization of the workshop. We are particularly thankful to Chuanyi Wang for her coordinating efforts in the chapter collecting, language editing and reviewing processes. We also thank Wenling Zhou and Xiaoxi Li for their valuable assistance at the early and late stages of book preparation. We also thank Ruiqiang Ding, Wansuo Duan, Qing Bao, Juan Feng, Xiaofeng Li, Xiaohao Qin, Jie Song, Cheng Sun, Bo Wu, Fei Xie, Feifan Zhou, and Yanjie Li for their helpful assistance.

# Contributors

**Oscar Alves**

Centre for Australian Weather and Climate Research, Australia

**Fabio d'Andrea**

Laboratoire de Meteorologie Dynamique, Ecole Normale Supérieure, France

**Heather Archambault**

National Oceanic and Atmospheric Administration, USA

**Peter Baines**

University of Melbourne, Australia

**Tom Beer**

Centre for Australian Weather and Climate Research, Australia

**Robin Clark**

Met Office Hadley Centre, UK

**Henk Dijkstra**

Utrecht University, Netherlands

**Philippe Drobinski**

Laboratoire de Meteorologie Dynamique, Ecole Normale Supérieure, France

**Russell Elsberry**

Naval Postgraduate School, USA

**Petra Friederichs**

University of Bonn, Germany

**Chaim Garfinkel**

Hebrew University, Jerusalem, Israel

**Richard Grotjahn**

University of California, Davis, USA

**Nili Harnik**

Tel Aviv University, Israel

**Patrick Harr**

National Science Foundation, USA

**Benjamin J. Henley**

University of Melbourne, Australia

**Yi-Hsuan Huang**

National Taiwan University

**Yu Kosaka**

Scripps Institution of Oceanography, USA

**Orli Lachmy**

Tel Aviv University, Israel

**Jianping Li**

Beijing Normal University, China

**Yimin Liu**

Institute of Atmospheric Physics, China

**Olivia Martius**

University of Bern, Switzerland

**Christopher Melhauser**

Pennsylvania State University, USA

**Erin B. Munsell**

Pennsylvania State University, USA

**Hisashi Nakamura**

University of Tokyo, Japan

**Sumant Nigam**

University of Maryland, USA

**Kazuaki Nishii**

University of Tokyo, Japan

**Hyacinth C. Nnamchi**

University of Nigeria, Nigeria

**Yvan J. Orsolini**

Norwegian Institute for Air Research, and University of Bergen, Norway

**Pardeep Pall**

Lawrence Berkeley National Laboratory, USA

**Gwendal Rivière**

Laboratoire de Météorologie Dynamique, Ecole Normale Supérieure, France

**Mark Rodwell**

European Centre for Medium-range Forecasts, UK

**Alfredo Ruiz-Barradas**

University of Maryland, USA

**Adam A. Scaife**

Met Office Hadley Centre, UK

**D. R. Sikka**

Indian Institute of Tropical Meteorology, India

**Jason A. Sippel**

I. M. Systems Group, and National Oceanic and Atmospheric Administration, USA

**Marc Stéfanon**

Laboratoire des Sciences du Climat et de l'Environnement Institut Pierre Simon Laplace, France

**Dáithí Stone**

Lawrence Berkeley National Laboratory, USA

**Y. Qiang Sun**

Pennsylvania State University, USA

**Richard Swinbank**

Met Office, UK

**Koutarou Takaya**

Kyoto Sangyo University, Japan

**Zhe-Min Tan**

Nanjing University, China

**Dandan Tao**

Pennsylvania State University, USA

**Alan Thorpe**

European Centre for Medium-range Forecasts, UK

**Hsiao-Chung Tsai**

Naval Postgraduate School Monterey, USA

**Hans Volkert**

Deutsches Zentrum für Luft-und Raumfahrt, Germany

**Sabrina Wahl**

University of Bonn, Germany

**Lin Wang**

University of Tokyo, Japan and Institute of Atmospheric Physics, China

**Michael Wehner**

Lawrence Berkeley National Laboratory, USA

**Yonghui Weng**

Pennsylvania State University, USA

**Tim Woollings**

University of Oxford, UK

**Chun-Chieh Wu**

National Taiwan University

**Guoxiong Wu**

Institute of Atmospheric Physics, China

**Zhiwei Wu**

Nanjing University of Information Science and Technology, China

**Shang-Ping Xie**

Scripps Institution of Oceanography, USA

**Chidong Zhang**

University of Miami, USA

**Fuqing Zhang**

Pennsylvania State University, USA

**Xuebin Zhang**

Environment Canada, Canada

**Yongjun Zheng**

Chinese Academy of Meteorological Sciences, China

**Francis Zwiers**

University of Victoria, Canada



## PART I

### **Diagnostics and prediction of high-impact weather**



# 1

## Global prediction of high-impact weather: diagnosis and performance

*Mark Rodwell and Alan Thorpe*

### 1.1 Introduction

Weather that has a high impact on society is generally rare, but when it occurs it often has devastating impacts; being rare it lies in the tail of the climatological distribution of weather events. Impacts can be as a result of a short-lived extreme (such as very strong local winds) or a more persistent regime (such as a period of drought). Usually these phenomena are embedded within larger-scale weather systems and owe their existence to patterns of flow and sources of heat and moisture that are associated with the larger-scale circulation. At forecast lead-times beyond a few days, this large-scale flow can only be predicted by global models. It is because of this embedded nature of high-impact weather systems, and the authors' location at the European Centre for Medium-Range Weather Forecasts (ECMWF) that we focus here on global predictability and forecasting aspects. Of course for a more complete picture of high-impact weather, it is necessary to overlay the detailed structures evident in regional forecasting systems.

There has been huge progress in weather science over the past half century and more. This has led to significant advances in our ability to make skilful predictions of weather even as far ahead as two weeks. These advances have been as a result of scientific research, and increasing observational and computational capabilities. Modern numerical weather prediction (NWP) relies on international cooperation to exchange observations made across the globe and to share scientific findings. It also relies on advanced numerical models that allow the laws of physics to be 'solved', starting from an initial description of the current state of the atmosphere (and increasingly of the ocean and land surfaces). These global models require supercomputers of incredible speed – today 200 trillion floating point operations per second is not untypical – to enable high resolution predictions to be made in real time so that society has access to timely forecasts.

As high-impact weather events are relatively unusual, it is important to draw on long observational records. The

past 30 years or more have seen a rapid increase in the availability of satellite observations, and this means we have a much better description of weather phenomena to draw upon. It is now possible, and it is routinely done, to carry out re-analyses of past weather and use today's science and models to re-forecast this weather. Such re-analyses and re-forecasts are an invaluable source of information on the frequency, properties, and our current skill in the prediction of high-impact events.

A key advance has been in the resolution at which these global models can operate. Today at ECMWF, the high resolution global forecast has a grid mesh of around 16 km by 16 km. This means that smaller-scale phenomena can now be explicitly resolved, and even predicted. For example the super-storm Sandy, that affected New York in late October 2012, was predicted relatively well by global forecast models even as far ahead as eight days; see Magnusson *et al.* (2014). Nevertheless, further improvements in resolution continue to be needed if the details of high-impact weather are to be resolved.

As longer and more accurate data records become available, and as model resolution increases, the scientific focus on high-impact weather is accelerating. This chapter explores new diagnostic tools and methods of forecast evaluation that help to reveal how and why predictions of high-impact weather can be improved as part of the overall pursuit of accurate and reliable weather forecasts.

In this chapter, we focus mainly on instantaneous extremes (short-lived weather extremes). We highlight current forecast system performance and demonstrate some useful diagnostic techniques. The chapter is structured as follows. We discuss systematic model errors in Section 1.3, and discuss estimates of uncertainty (observation, background, and model) within the probabilistic (ensemble) context in Section 1.4. A summary is given in Section 1.5 and then, in Section 1.6, we identify future avenues to pursue in order to improve the forecasting of high-impact weather. Firstly, however, it is useful to discuss

how NWP is done today – the framework within which extreme weather is predicted.

## 1.2 Global NWP: how it is done today

Since, as we have noted, high-impact weather is usually embedded within larger-scale weather systems, and these systems can only be predicted beyond a few days with global models, we start with a brief introduction to global NWP.

Numerical weather prediction is largely an initial value problem. As Fig. 1.1 shows schematically, it involves an estimation of the current state (analysis) of the atmosphere, and the integration of a numerical model of the laws of physics from this analysis forward in time (as indicated by the medium-range forecast). Error growth with lead-time (e.g. due to chaos: Lorenz 1963, and biases: e.g. Jung *et al.* 2010) is restrained by the periodic introduction (assimilation) of new observations. The assimilation process combines short-forecast (background) information from a previous analysis with these new observations in a way that is consistent with estimated errors and uncertainties in the observations (Isaksen *et al.* 2010), background

(Bonavita *et al.* 2011), and sometimes the model (Trémolet 2007; Fisher *et al.* 2011). A good data assimilation system is crucial for the success of NWP. Turned on its head, data assimilation also represents fertile ground for the diagnosis of errors and uncertainties – as we will discuss here in the context of severe weather.

One component of ECMWF's Integrated Forecast System (IFS; for a recent listing of further details see, e.g. Jung *et al.* 2012) is a single 'high resolution' forecast, known as the HRES. Figure 1.2 highlights trends in HRES performance, as measured by spatial anomaly correlation of 500 hPa geopotential height. For the Northern Hemisphere, the rate of improvement has been at about one day's lead-time per decade. The relative lack of conventional observations (from Synop, radiosonde, aircraft, etc.) of the Southern Hemisphere, and the increase over the last 30 years in global satellite data coverage, explain the Southern Hemisphere's faster improvement from a lower starting value.

One contributing factor to the improvement in forecast performance over the last 35 years has been the increase in model resolution (see, e.g. Simmons *et al.* 1989) – permitted by the increase in available computing power. HRES horizontal mesh size has roughly halved every eight years. At present, the HRES model stores the state of the

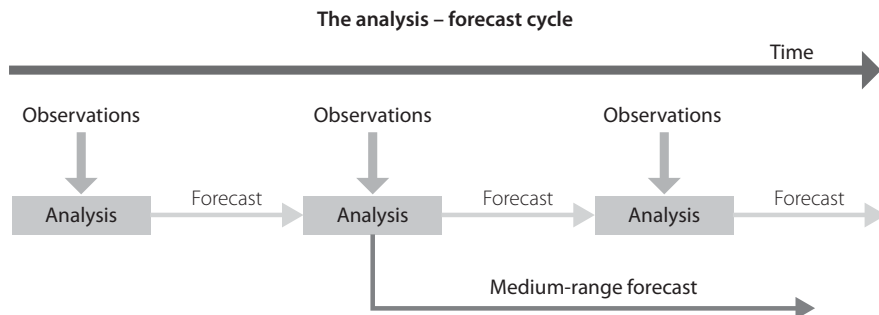


Fig. 1.1 Schematic of the analysis-forecast cycle. See main text for explanation.

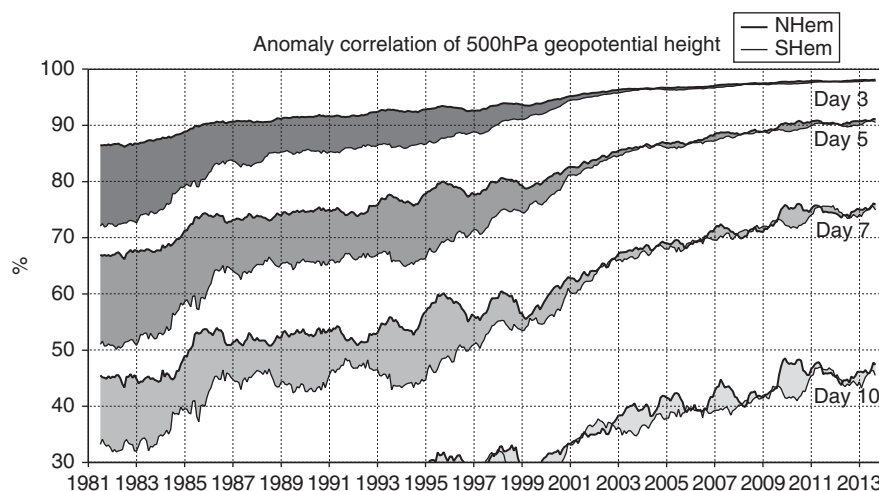


Fig. 1.2 Trends in ECMWF HRES performance, as measured by spatial anomaly correlation of the extratropical 500 hPa geopotential height field. Anomalies are from the climatology of the ECMWF ‘interim’ re-analysis (ERA-Interim, Dee *et al.*, 2011). Scores are shown for the northern and southern extratropics (poleward of 20° latitude) and for four lead-time ranges.

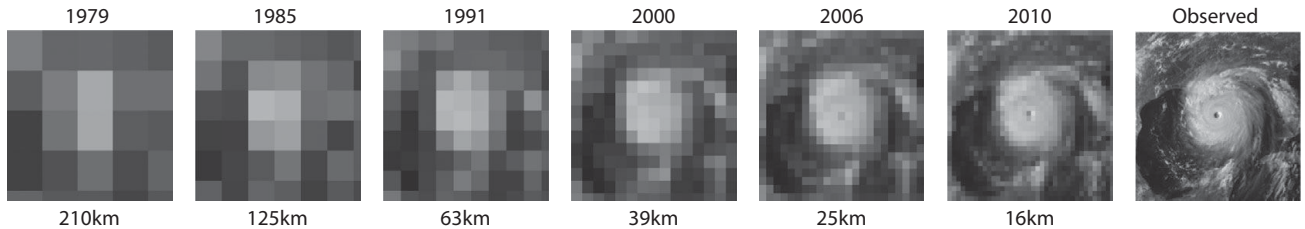


Fig. 1.3 Diagrams showing how well a particular tropical cyclone would have been resolved over the years as HRES model resolution has increased.

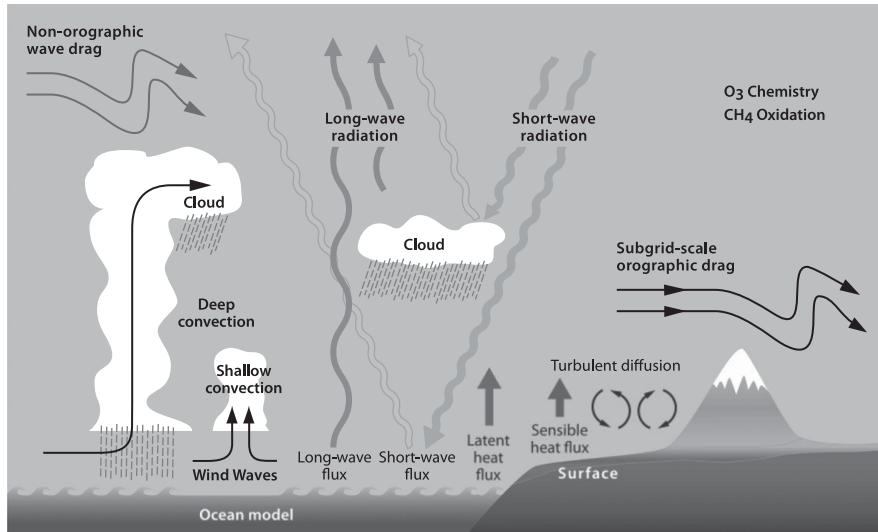


Fig. 1.4 Schematic diagram showing some of the physical aspects represented in the current ECMWF forecast system.

atmosphere in around five billion variables. Figure 1.3 demonstrates the impact of resolution on how well a given tropical cyclone would have been represented in the forecast model. It is only by being able to resolve such severe weather features that we stand any chance of being able to predict them; and it is only relatively recently that we have been in that position.

In addition to resolution effects, fundamental to the increase in forecast skill has been the improvement in observation, assimilation, and model aspects. At ECMWF, the number of assimilated observations has increased greatly over the years, reaching about one million per day by the year 2000, and now exceeding 40 million per day (still orders of magnitude less than the 30 billion state variables). There have also been improvements in quality and usage of observations, for example with the introduction of variational bias correction in 2006 (Dee and Uppala 2009; see also Derber and Wu, 1998) and the direct assimilation of ‘all-sky’ microwave radiances in 2009 (Bauer *et al.* 2010, Geer *et al.* 2010). The ECMWF assimilation system has also improved; for example changing from 3D variational data assimilation (3D-Var) to incremental 4D-Var (which allows interpolation in space and time;

see, e.g. Courtier *et al.* 1994) in 1997, and with the introduction of flow-dependent background errors in 2011 (Isaksen *et al.* 2010). 4D-Var currently takes as much computer power as the ten-day forecast – a sign of the importance attached to the data assimilation process. The ECMWF forecast model has also been extensively developed over the years. The physical aspects currently represented (parameterized) in the model are shown in Fig. 1.4. Improvements to parameterizations have included, for example, the introduction of a prognostic cloud micro-physics scheme in 2010 (Forbes *et al.* 2011). At the heart of model development is a drive to ‘get things right for the right reasons’.

### 1.3 The need for dynamical understanding: getting things right for the right reasons

Statistics of the forecast system are essential for monitoring progress and for assessing the impacts of possible system upgrades. However, if we are to initiate new developments, there is also a need for dynamical understanding; and dynamical paradigms can be helpful in diagnosis. For

example, an understanding of the importance of Rossby waves – their triggering and propagation – motivates the development of diagnostic tools based on the barotropic vorticity equation; the Rossby wave source for example. Sometimes one can think of small-scale weather being forced from the larger scale – perhaps associated with regime behaviour. Potential vorticity (PV), which is essentially the product of the vorticity and the stratification, provides a natural and meaningful way of connecting the dynamical and physical components. ‘PV thinking’ (Hoskins *et al.*, 1985; Thorpe, 1986; Joos and Wernli, 2012) can help us in designing diagnostics to understand such connections in reality and in forecast error.

Figure 1.5 shows the analysed surface pressure and (isentropic) PV on the 330 K isentropic surface for 21 July 2012. These fields highlight a strong extra-tropical cyclone in the North Atlantic. This cyclone was ‘high-impact’ not only from being strong, but also because it occurred shortly before the opening of the London 2012 Olympic Games. Within the cyclone, high PV values are predominantly associated with air from further north and higher up, including from the stratosphere. In general, as such air descends, it can form a ‘tropopause fold’ and sometimes leads to damaging sting jets at the surface, or to the triggering of secondary frontal cyclones. To the east, low PV values are partly associated with air from further south and lower down, and partly as the result of a reduction in upper-tropospheric stratification due to mid-tropospheric latent heat release and upper-tropospheric radiative cooling. Errors in this physics may lead to forecast errors in the developing downstream trough (see, e.g. Madonna, 2013).

We can use the ‘initial tendencies’ method to obtain a better understanding of the salient processes involved in

the development of this cyclone, and possible errors in the parameterization of these processes. Figure 1.6 explains the basis of this method – which is centred on the data assimilation system. As we have noted above, the data assimilation provides the ‘next analysis’ by combining information from a previous short-range first-guess forecast with the new observations. The short forecast provides a complete set of model fields, but these will include forecast errors. The observations are more scattered but are bias-corrected (in general). The data assimilation combines these sources of information in a way that is consistent with the estimated observation and short-forecast errors. The difference between the new and previous analyses is an estimate of the true evolution of the flow over the assimilation window. The analysis increment is the difference between the new analysis and the first-guess forecast, and can be thought of as a correction to the first guess. The fact that the first-guess forecast can be expressed as the sum of the tendencies of each of the processes represented in the model – dynamics, radiation, convection, etc., provides a means of relating increments to model process errors.

Figure 1.7 demonstrates application of the initial tendency method to the case of the strong cyclone shown in Fig. 1.5. Figure 1.7 (a) to (e) show the initial tendencies on temperature at 500 hPa (T500) from the various processes represented in the IFS model, each accumulated over the first 12 hours of the HRES forecast initialized from the 6UTC analysis on 21 July 2012. This is the forecast used as the first guess for the 12UTC analysis depicted in Fig. 1.5. Figure 1.7(g) shows the corresponding analysis increment, and Fig. 1.7(h) shows the analysed evolution of the atmospheric state. The total budget is closed with the

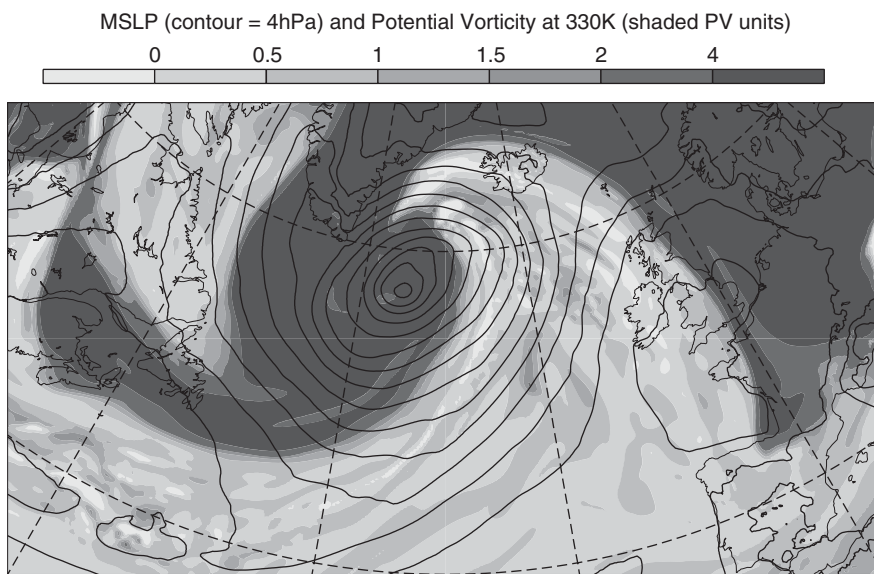


Fig. 1.5 Mean sea-level pressure (contoured) and potential vorticity on the 330 K isentropic surface (shaded) from the HRES analysis at 12UTC on 21 July 2012 (from 12-hour window data assimilation).

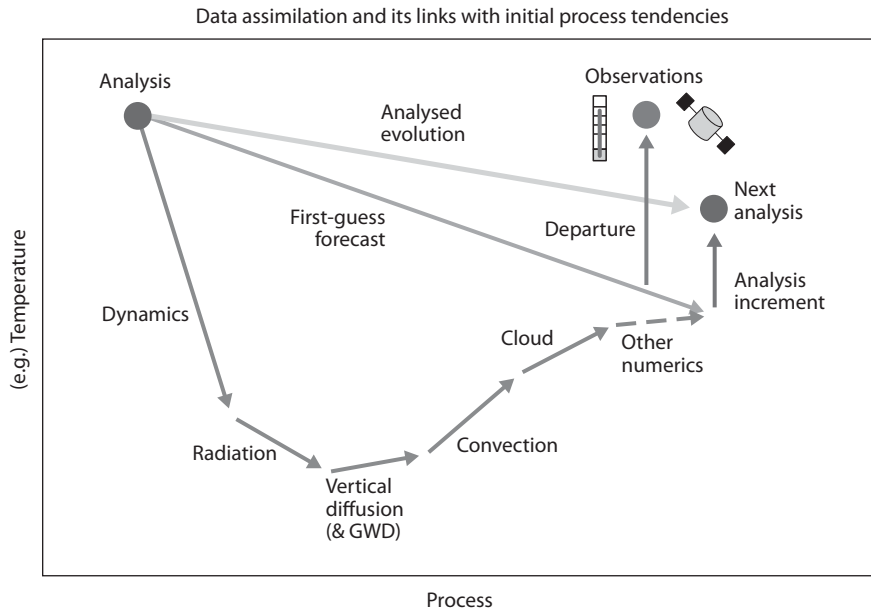


Fig. 1.6 Schematic showing the links between data assimilation and initial process tendencies. Please see the main text for more discussion.

residual term shown in Fig. 1.7(f), which reflects other minor processes and numerical aspects. Hence the sum of terms (a) to (g) is equal to (h). Note that the increment and residual terms are smaller in magnitude and plotted with a smaller shading interval.

Figure 1.7(h) highlights the movement of the cold and warm fronts associated with the cyclone. Much of this evolution is purely dynamical, as shown by Fig. 1.7(a), but other terms are also important. In particular, notice the positive temperature tendencies associated with the convection (Fig. 1.7d) and cloud (Fig. 1.7e) within the cold front, and the strong warming at the cloud-head (Fig. 1.7e). These terms are comparable in magnitude with the dynamical tendencies (Fig. 1.7a), and suggest that moist physics can play an appreciable role in the overall evolution of ‘extreme’ events – via the modification of PV for example. The negative analysis increments around the northern perimeter of the cloud-head (Fig. 1.7g) suggest that this cloud-head warming leaves the first-guess forecast a little too warm. Although further investigation would be needed, this is an identification of a possible model error – and highlights the power of this technique. Figure 1.7(i) shows the ‘departure’ of one observation field (AMSUA channel 5 microwave radiance observations) from the same radiance field obtained from the first-guess forecast. This microwave channel observes mid-tropospheric temperatures. Notice the similarity in patterns between the departures and the analysis increments. It is clear that this is one observation source that is ‘supporting’ the increments. Notice that the departure field in Fig. 1.7(i) is missing (white) in some key areas because it is still difficult to use this data in cloud-affected regions. This is indicative of a key issue

for forecasting – the (moist) instabilities that act to magnify forecast error (including severe cyclones) are often the most difficult to analyse, and can lead to particularly large forecast errors at longer lead-times.

The technique of ‘initial tendencies’ is a refinement of the methodology proposed by Klinker and Sardeshmukh (1992). Recently, it has been applied to averages of several analysis cycles, to highlight more definitively model issues associated with convective momentum transport and upper tropospheric humidity drift (Leroy and Rodwell, 2014), as well as aiding the understanding of the beneficial impacts of a change in model aerosol climatology (Rodwell and Jung, 2008) and for assessing perturbed climate model ensembles (Rodwell and Palmer, 2007). A variation of the approach is discussed by Mapes and Bacmeister (2012). Klocke and Rodwell (2014) show that initial tendencies can identify an introduced model error, when diagnosis at longer lead-times cannot. Indeed, the ability of the method to identify potential errors lies in its application very early on in the forecast – which minimises complications associated with interactions between processes and the resolved flow, the growth of chaos, and variations in predictability.

#### 1.4 The need for uncertainty information: assessing the degree of confidence

Incremental reductions in initial condition and model errors over the years have led to reduction in the growth of error from chaos and bias throughout the forecast. Figure 1.8(a), which shows annual means of the root-mean-square error

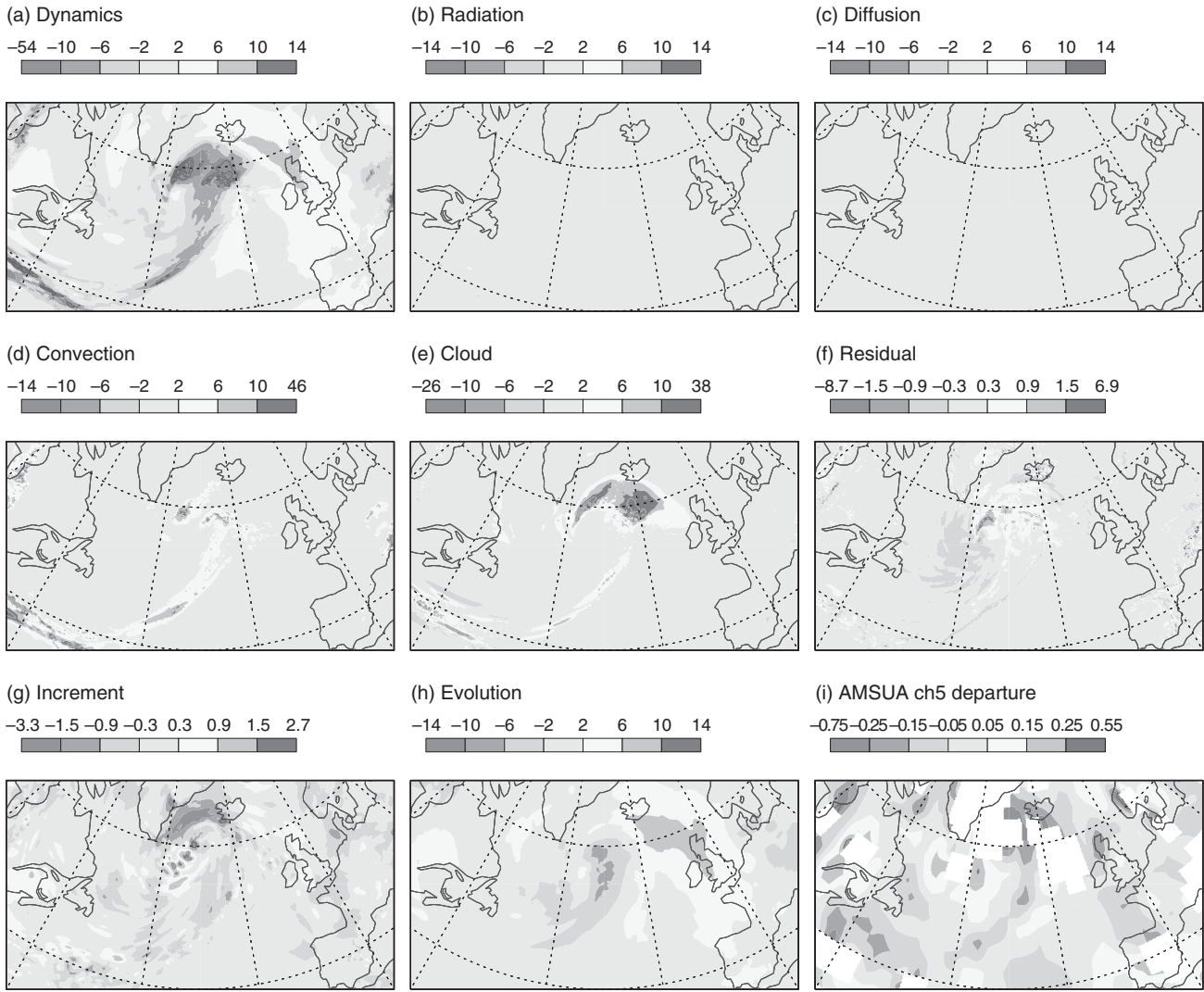


Fig. 1.7 For temperature at 500 hPa, (a) to (f) show initial tendencies from the various processes represented in the IFS model (and a residual term associated with other processes and numerics), each accumulated over the first 12 hours of the HRES forecast initialized from the 6UTC analysis on 21 July 2012. (g) Analysis increment at 18UTC. (h) Analysed evolution of the flow between 6 and 18 UTC. (i) Departure of AMSUA channel 5 microwave radiance observations (which reflect mid-tropospheric temperatures) relative to the same radiance field obtained from the forecast. (Please see the main text for further explanation).

(RMSE) of HRES 500 hPa geopotential heights in the Northern Hemisphere for selected years, highlights the integrated effects of these changes. Note the reduction in 12 hr errors and the (greater) reduction in forecast errors at day 10. Notice also that the shape of the curve at days 1 and 2 is flatter in 2013 (black) than before (light and dark grey).

These days, quantifying uncertainties is mainstream in operational NWP. Another component of the IFS is the 50-member ensemble (ENS; see, e.g., Leutbecher and Palmer, 2008) of perturbed, lower-resolution forecasts. Perturbations (historically singular vectors; Buizza and Palmer, 1995) are applied to the initial conditions to represent our uncertainty in the present state, and stochastic

perturbations are applied to the physics tendencies to represent model uncertainty (Buizza *et al.*, 1999). The fundamental reason for the ENS is the desire to ‘predict the predictability’, which is dependent on the initial state, our uncertainty in this initial state, the lead-time, and what ‘event’ we are interested in predicting.

The lead-time aspect is highlighted in Fig. 1.8(b), which shows annual-means of (solid) the RMSE of the ENS ensemble-mean and (dashed) the ensemble standard deviation (spread). (Note that, because Fig. 1.8b quantifies anomalies from the ensemble-mean, values should typically be about a factor  $\sqrt{2}$  smaller than those in Fig. 1.8a – which effectively quantifies anomalies from

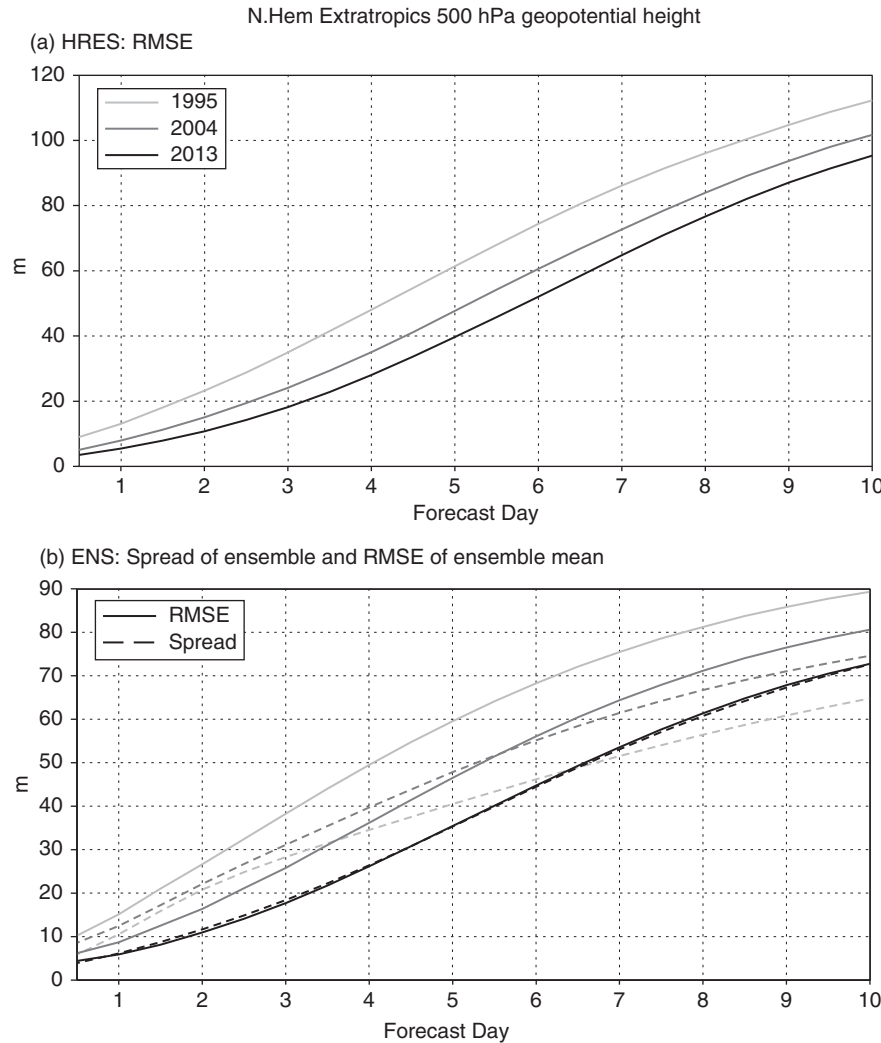


Fig. 1.8 For geopotential height at 500 hPa in the Northern Hemisphere, (a) annual mean of HRES RMSE as a function of forecast lead-time, and (b) annual means of ENS ensemble-mean RMSE (solid) and ENS spread (dashed) as a function of forecast lead-time. Both panels show results for the years 1995, 2004, and 2013.

the analysis.) For a well-balanced ensemble system, the mean spread should equal the mean error (Leutbecher and Palmer, 2008). Figure 1.8(b) shows that the ensemble was very under-spread in 1995 (light grey). In 2004 (dark grey), initial condition uncertainty was unduly large, partly to ensure reasonable spread at longer lead-times. In 2013 (black), the better balance of initial uncertainty and model uncertainty leads to a very good agreement between mean spread and mean error at all lead-times. This agreement ensures that the spread decreases with decreasing lead-time, and hence that the probability of an event occurring should ideally converge to either 0% or 100% as the lead-time decreases.

For example, we might define an event to be extreme precipitation (greater than 50 mm in 24 hours). Figure 1.9 shows the ENS day 1 probability for such an event to occur on 21 July 2012. Very high probabilities ( $\approx 90\%$ ) occur over Beijing at this time and, indeed, extreme precipitation did occur.

It is clearly of interest to know how the longer-range forecasts predicted this extreme precipitation in Beijing. Figure 1.10 shows cumulative distributions of precipitation that can help explain the performance of the ENS over a range of lead-times. The observed climate curve (grey dotted) is the fraction of July days during the period 1980–2009 for which the observed 24 hr precipitation was more than the given threshold on the  $x$ -axis. It starts at the climatological frequency of a wet day (57% of days in Beijing in July have precipitation  $> 0$  mm) and ‘asymptotes’ to the maximum recorded value (1% of days in Beijing in July have precipitation  $> 63$  mm). This curve represents the distribution of a baseline probability forecast using only climatological information. The model climate curve (grey dashed) is derived from 100 ensemble reforecasts, with five members each, initiated from analyses spanning the previous 20 years and within two calendar-weeks of the real-time forecast. The (minor) differences between the observed and model climate distributions

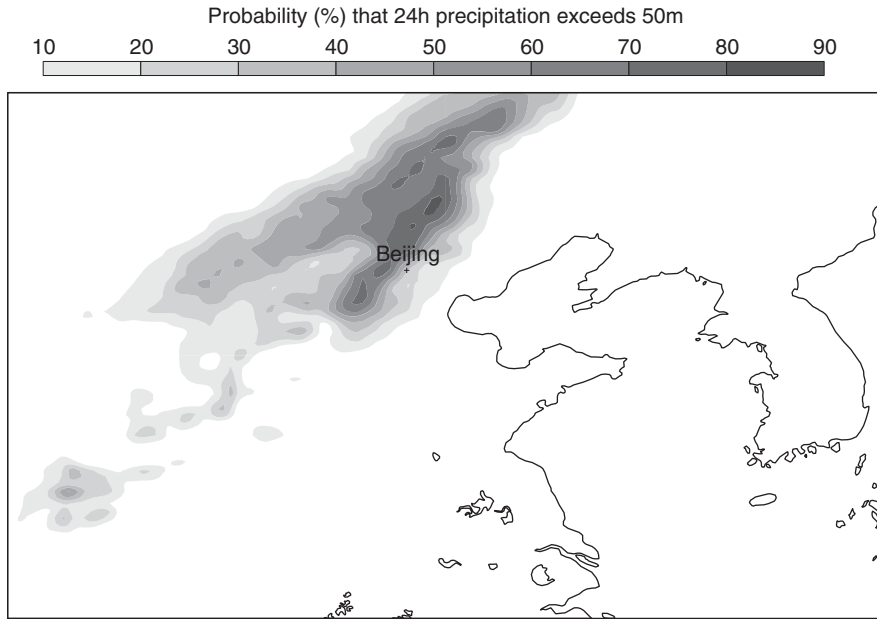


Fig. 1.9 Probability that precipitation would exceed 50 mm on 21 July 2012, based on ENS accumulations over lead-times 0–24 h ('day 1 precipitation').

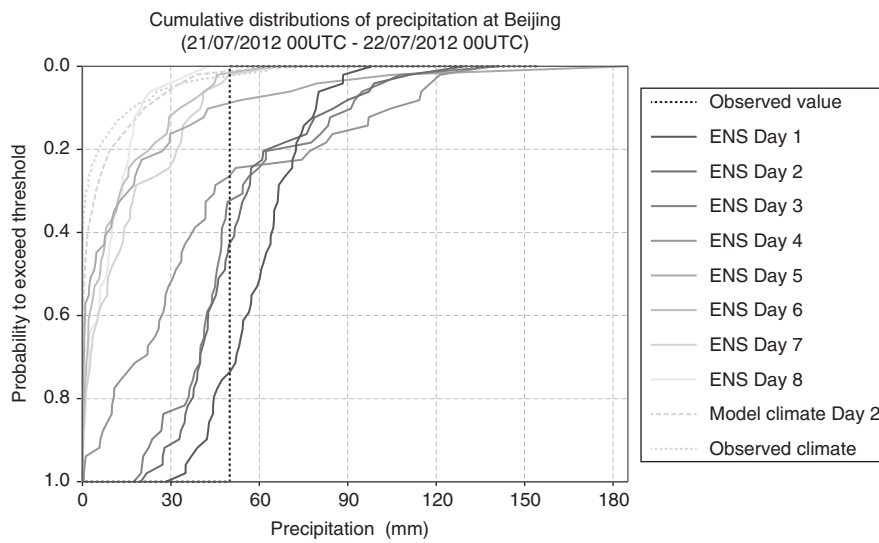


Fig. 1.10 Cumulative distributions of precipitation at Beijing based on the observed climate (from Synop observations), the model climate at Day 2, the operational ENS at lead-times 1–8 days, and the observed outcome. Please see the main text for more explanation of these curves.

reflect forecast system deficiencies (for diagnostic purposes, the forecasts are not calibrated here), along with discrepancies between the periods used to derive these climatologies. The cumulative distribution for the observed value (black dotted) is a step-function centred at the observed outcome. This curve represents the distribution of a perfect probability forecast (the vertical line at the observed outcome reflects a delta-function in the probability density function). Each ENS curve (solid) shows, for the indicated lead-time, the fraction of 50 real-time ensemble members that predict more than a given threshold on the x-axis (the darker the shade of grey, the shorter the lead-time). The main point to emphasize is the gradual

progression from curves at long lead-times (e.g. day 8) that are close to the observed climatology towards curves at short lead-times (days 3–1) that are close to the step-function of the observed value. Such convergence is not only desirable from a meteorological modelling point of view, but also from a user perspective. A smooth ramping up (or down) of probabilities as the possible extreme event approaches is much more desirable for emergency planning than contradictory information from one day to the next.

Having mean-spread equal to mean-error is clearly a desirable property for an ensemble prediction system, but this is not sufficient for it to be a perfect ensemble

system. We know that there are state-dependent variations in predictability – some initial states are easier to predict from than others. Getting the mean-spread right does not necessarily imply that we capture these variations correctly. Could it have been, for example, that the probabilities for the extreme precipitation over Beijing could have converged more quickly than they did? One measure of the ability of the ENS to predict such variations in uncertainty is to plot the observed frequency of an event against its forecast probability. Figure 1.11 shows such a ‘reliability diagram’ for European day 6 precipitation over the period 1 December 2013–28 February 2014. Three events are shown (24 hr precipitation exceeds >1 mm, >5 mm, and >20 mm). Ideally these curves would lie on the diagonal (grey) so that, for example, if we predict an event with  $x\%$  probability, it should occur  $x\%$  of the time. For the event that precipitation is greater than 1 mm (black dotted), the curve lies below the diagonal. This indicates that the ENS is too confident that there will be light precipitation. It highlights the well-known ‘drizzle problem’ whereby many operational models tend to produce too much light rain. The ENS probabilities are more reliable for the event that precipitation exceeds 5 mm (black dashed). For the event that precipitation exceeds 20 mm (black solid), the curve is reasonably close to the diagonal, but less smooth. This highlights an important issue for the prediction of extreme weather – such weather tends to be rare, and this

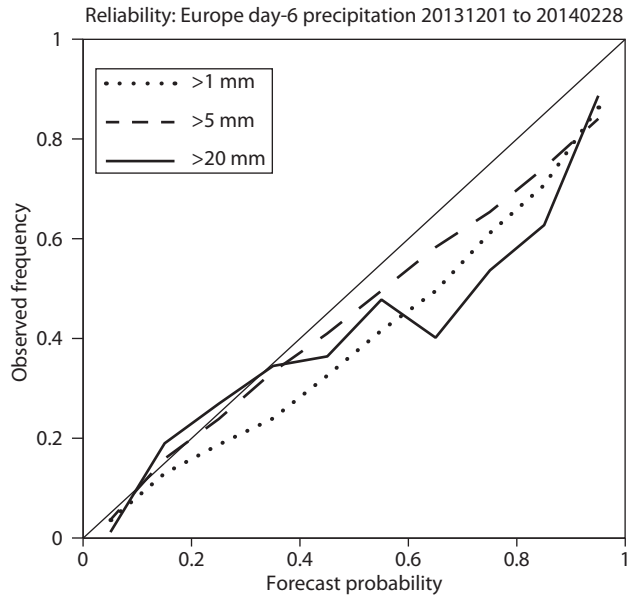


Fig. 1.11 Reliability diagram for European precipitation based on the ENS at day 6 and Synop observations, for the period 1 December 2013 to 28 February 2014. Curves are shown for the events that 24 hr precipitation exceeds 1 mm (dotted), 5 mm (dashed), and 20 mm (solid).

increases uncertainty in sample estimates of expected system performance.

Reliability (at all lead-times) is a desirable condition for a good ensemble prediction system, but again, it is not a sufficient condition for the ensemble system to be perfect. For example, a forecast based on climatological probabilities is completely reliable but only represents a baseline forecast, which operational systems must aim to beat. The Brier skill score (BSS) measures the ENS performance in the prediction of a given event, over and above that of a climatological forecast. Figure 1.12(a) shows the BSS for the prediction of extreme low geopotential heights at 500 hPa in the Northern Extratropics. Since climatological distributions vary with location and time of year, the event

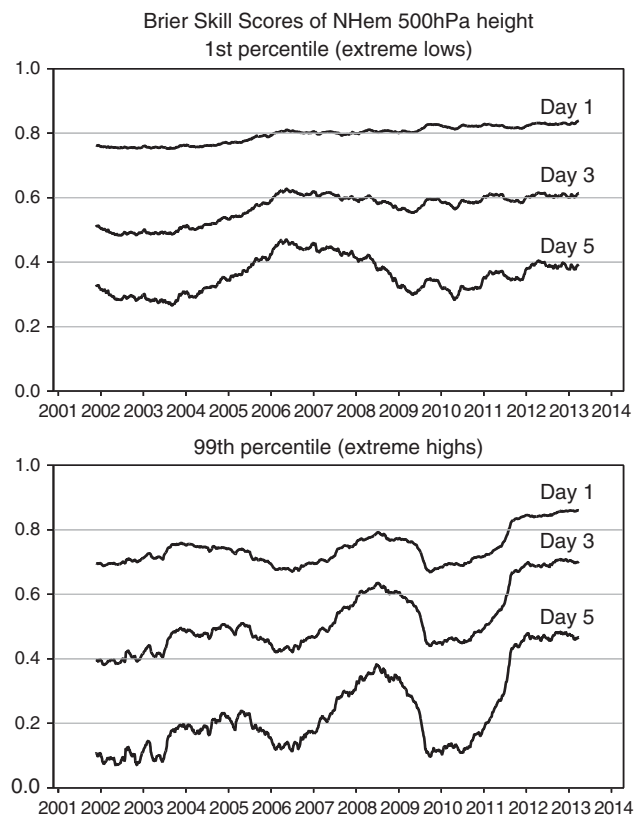


Fig. 1.12 Performance of the operational ENS in the prediction of extreme weather, as measured by the Brier skill score. Results are based on geopotential height at 500 hPa in the Northern Extratropics (north of 20°N) at three forecast lead-times (days 1, 3, and 5), and a two-year running-mean has been applied. (a) Extreme lows (height below the first percentile). (b) Extreme highs (height above the 99th percentile). The area-integrated Brier skill score is calculated here as  $BSS = 1 - \overline{BS}/\overline{BS}_{clim}$ , where  $BS = (p - v)^2$  is the Brier score (with  $p$  the fraction of ensemble members predicting an event and  $v = 0$  or 1 depending on whether the event occurs or not) and  $BS_{clim} = (p_{clim} - v)^2$  (with  $p_{clim}$  the climatological frequency of the event).

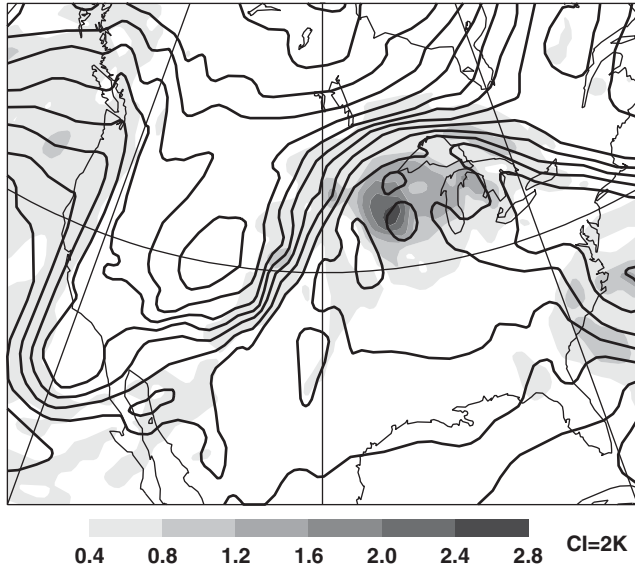
is defined here as the first percentile of the climatology at each location and time of year, based on ERA interim re-analyses. Results are smoothed with a two-year running-mean (for further details on our calculation of BSS, please see the caption to Fig. 1.12). There are upward trends in performance – perhaps a little less than one day per decade. Notice, however, that by day 5, even a two-year running-mean seems insufficient to remove all of the interannual variability. Fig. 1.12(b) shows the corresponding results for extreme highs (above the 99th percentile). These scores appear to show a better overall trend, but with more interannual variability. This variability requires further investigation. It is possible that it is associated with sampling deficiencies – the period of poor scores in around 2010 corresponds to a prolonged period of increased activity in the Northern Hemisphere. However, similar score variations for the Southern Hemisphere (not shown) suggest that part of the variability may reflect true fluctuations in performance; associated with forecast system changes, before this performance was being routinely monitored.

As noted for the HRES, such statistics on the ENS are important for monitoring performance and assessing system developments but, to initiate new developments, a more dynamical understanding of the flow-dependence of spread and error, and of reliability in general, can aid diagnosis. Such diagnosis has been greatly facilitated by the recent introduction of an ensemble of data assimilations (EDA, Isaksen *et al.*, 2010). The EDA better represents the balance of uncertainties in the background, the observations, and the

model. In particular, observation uncertainty is included by applying different perturbations to the observation set, assimilated by each EDA member. Figure 1.13 shows an example of the EDA in action for a particular initial state. The temperature field at 200 hPa averaged over all EDA first-guess forecasts (contours in Fig. 1.13a) shows a trough over the Rockies. Warm moist advection ahead leads to the development of a meso-scale convective system (MCS) near the Great Lakes. The shading shows the standard deviation of the EDA first-guess forecasts – indicating considerable uncertainty in temperatures associated with the details of this MCS. Figure 1.13(b) shows the result after the new observations have been assimilated. The gross structure of the trough is unchanged, but the uncertainty within the MCS is reduced. This is what one would hope to see – the error growth with lead-time being reduced by the introduction of the new observations.

MCS events can interact strongly with the upper-level jet, and uncertainties in the MCS therefore lead to uncertainties in the subsequent evolution of the jet. A composite of many similar trough situations shows enhanced day 6 RMSE within the North Atlantic stormtrack compared to background levels (compare Fig. 1.14c and Fig. 1.14d). Indeed, such cases (including that presented in Fig. 1.13) occasionally lead to severe HRES ‘busts’ over Europe, where the anomaly correlation can even become negative (Rodwell *et al.*, 2013). Comparison of the ENS spread from the composite with the background spread (compare Fig. 1.14a and Fig. 1.14b) suggests that the ENS predicts, to some extent, the increased error.

(a) Forecast mean & stdev at T+12



(b) Analysis mean & stdev

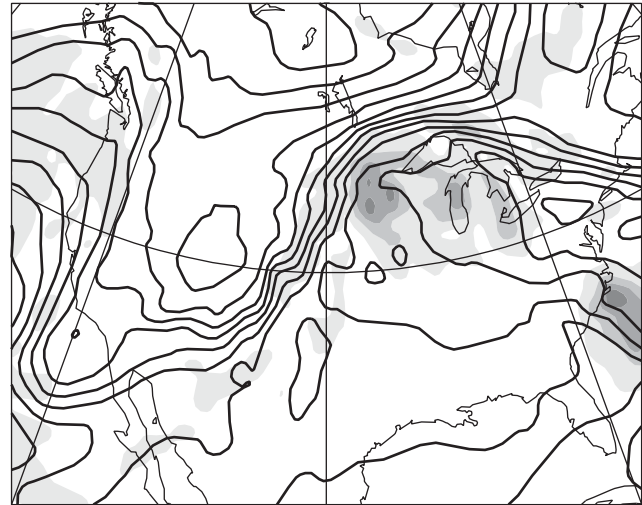


Fig. 1.13 Mean (contours) and standard deviation (shaded) of 200 hPa temperature from (a) EDA forecasts at a lead time of 12 h valid at 0600 UTC 10 Apr 2011, and (b) EDA analyses valid at the same time.

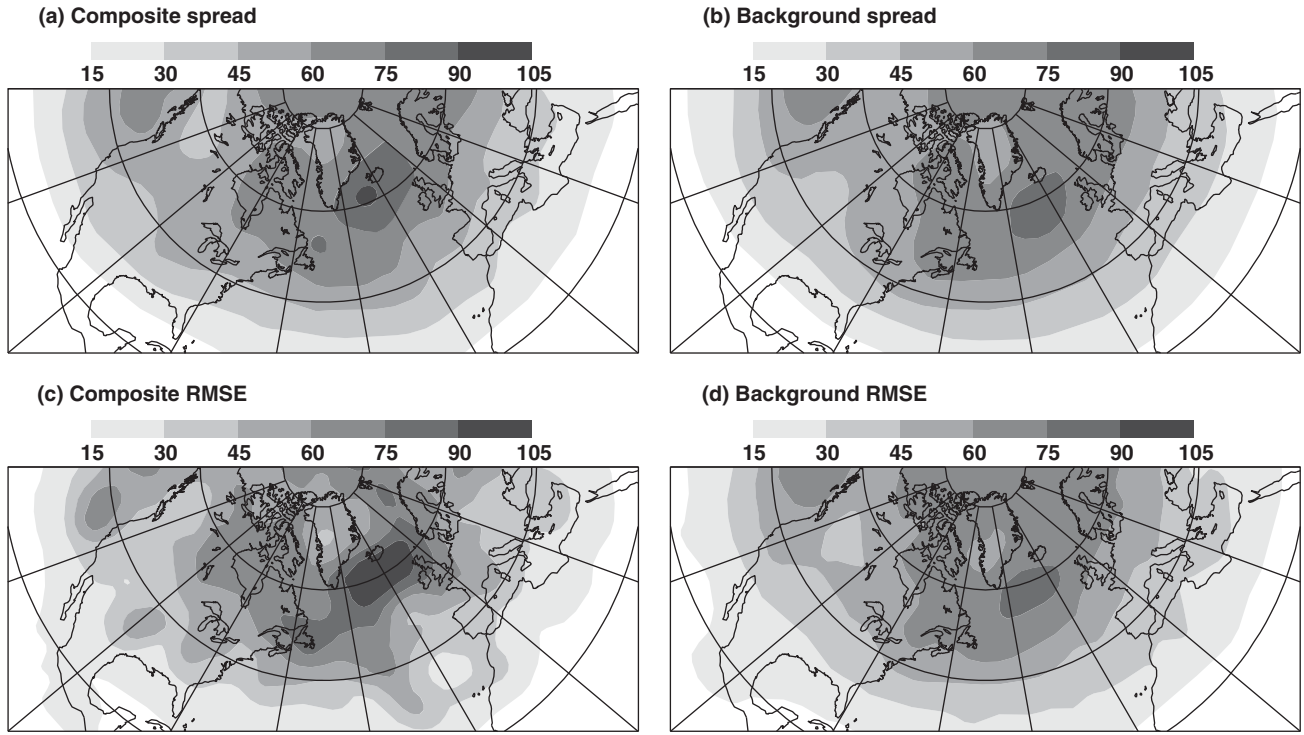


Fig. 1.14 ENS spread and error in 500 hPa geopotential height at day 6. (a) ENS spread for the composite of 84 cases where the initial state includes a trough over the Rockies and high CAPE to its east. (b) Background spread. (c) RMSE of the ensemble-mean for the trough/CAPE composite. (d) Background RMSE. Results are based on all 0000 and 1200 UTC forecasts from 10 Nov 2010 to 20 Mar 2012.

The case highlighted in Fig. 1.13 illustrates that it is not just the prediction of severe weather itself that is important. The fact that severe weather is often associated with instabilities of the flow means that such events can act to greatly magnify forecast uncertainty, particularly if they occur close to the initial time of the forecast. Our diagnostics need to be able to inform us about whether the ENS is magnifying uncertainty by the correct amount. This raises questions about the model's representation of physics within severe weather events; including linear physics (Janisková and Lopez, 2012) and stochastic physics (Shutts *et al.*, 2011; Berner *et al.*, 2009), and also about observation availability, accuracy, and usage.

## 1.5 Summary

With the advent of ensemble systems, the dual aims of NWP research can perhaps be summarized as a drive to reduce forecast error and to improve our prediction of the uncertainty (sometimes metaphorically referred to as ‘predicting the predictability’).

Until recently, the skill in our probabilistic predictions of extreme weather has not been monitored to the same extent

as our deterministic skill in predicting the large-scale circulation, and has consequently not had such a direct impact on system development. In spite of this, retrospective Brier skill scores of extreme weather, computed here, demonstrate overall improvement trends of the order of one day per decade in the extratropics – albeit with some interannual or inter-model-cycle variations. To some extent, it would appear that what improves the forecast system in general also improves its ability to predict extremes, but more routine monitoring of extreme weather prediction could prevent the occasional drops in skill with the introduction of some new cycles.

We have highlighted the ‘initial tendency’ approach as a means of understanding errors in a model’s representation of extreme weather. More general investigation of the deterministic data assimilation system highlights the reduced availability and/or use of observational data during such extreme events – due to large departures or cloud contamination, for example. Future work should include consideration of more cases and, if feasible, compositing over these cases.

Desirable attributes of a probabilistic (ensemble) forecasting system include a good agreement between ensemble spread and error (throughout the forecast range, including the ensemble of data assimilations), and reliability in

general. A smooth transition of probabilities, for a given event-definition, from the climatological probability at long lead-times to either 0 or 1 at short lead-times is also desirable. The ECMWF ENS is increasingly capable of achieving these aspects – in the mean at least. Diagnostic studies need to investigate how well these attributes are attained for composites over given initial flow regimes that involve an extreme event – particularly where there is strong coupling between the dynamics and moist physics – as in the case of diabatic Rossby waves, MCSs, warm conveyor belts, and tropical cyclones, etc. A key challenge here is how best to work with the limited number of available events (in reality and in the forecast).

This chapter has not focused on weather that is high-impact because it is extreme in duration (blocking and droughts, or extended periods of rainfall, for example). For such events, we are interested in regimes, regime transitions, the predictability of these transitions, and the meteorological pathways involved in these transitions. This is currently an area of active investigation.

## 1.6 Opportunities for further progress

Current circumstances are such that there are many opportunities for making progress in the prediction of high-impact weather, and the use of such forecasts.

- Further decreases in model mesh size to enable ‘forecasts on the human scale’ (particularly through the nesting of ultra-high-resolution regional models within high-resolution global models). This means that the NWP community can begin to focus much more on the user and their needs, of which high-impact weather is necessarily a key aspect.
- Ongoing improvements in model physics (including in uncertainty), observations, and ensemble data assimilation, and increased monitoring, should improve our performance (scores, reliability, flow-dependent uncertainty, etc.) in the prediction of high-impact weather over the medium range, and allow greater use of these forecasts.
- Promotion of more seamless integration of forecasting processes, such as the integration of flood and air-pollution forecasting, should improve the prediction of a wider range of high-impact events.
- Gain a better understanding of what high-impact aspects of the weather have predictability at longer lead-times – weeks 2, 3, 4, and also months 2, 3, 4. Where does this predictability arise – from larger-scale regimes, sea-surface temperature, sea-ice anomalies, teleconnections? What key aspects of our models need to be improved to exploit this predictability?

- Promotion of more seamless integration of time scales, including weather and climate services – putting extreme weather events into the climate context, learning more about what we can say with confidence about individual extreme events.
- Encourage more use of probabilistic forecasts, by extolling the virtues of the ensemble – particularly for rare and extreme weather.
- The importance of re-analysis and ensemble re-forecasts in IFS diagnosis, and the growing significance of the EDA, suggest the potential benefits of combined ensemble re-analyses/re-forecasts. While computationally expensive, the benefits to NWP (in particular for high-impact events), and the synergistic provision of uncertainty estimates in climate time series, make this worth investigating.
- International cooperation, e.g., through THORPEX and post-THORPEX programmes such as the Subseasonal-to-Seasonal, Polar-Prediction, and High-Impact-Weather-Prediction projects. An example (out of many) of the utility of these programmes are the observational campaigns focused on key physical processes, such as extreme weather events, warm conveyor belts, the Madden–Julian Oscillation, etc. These should help us to diagnose key model errors, where there tend to be gaps in the operational satellite coverage.

It should be anticipated that significant progress will be made in the coming years – in the prediction of high-impact weather, and in the use of these forecasts.

## References

- Bauer, P., A. J. Geer, P. Lopez, and D. Salmond (2010). Direct 4D-Var assimilation of all-sky radiances. Part I: Implementation. *Q. J. R. Meteorol. Soc.*, **136**, 1868–1885, doi: 10.1002/qj.659.
- Berner, J., G. J. Shutts, M. Leutbecher, and T. N. Palmer (2009). A spectral stochastic kinetic energy backscatter scheme and its impact on flow-dependent predictability in the ECMWF ensemble prediction system. *J. Atmos. Sci.*, **66**, 603–626, doi: 10.1175/2008JAS2677.1.
- Bonavita, M., L. Raynaud, and L. Isaksen (2011). Estimating background-error variances with the ECMWF Ensemble of Data Assimilations system: Some effects of ensemble size and day-to-day variability. *Q. J. R. Meteorol. Soc.*, **137**, 423–434, doi: 10.1002/qj.756.
- Buizza, R., M. Miller, and T. N. Palmer (1999). Stochastic representation of model uncertainties in the ECMWF ensemble prediction system. *Q. J. R. Meteorol. Soc.*, **125**, 2887–2908, doi: 10.1002/qj.49712556006.
- Buizza, R. and T. N. Palmer (1995). The singular-vector structure of the atmospheric global circulation. *J. Atmos. Sci.*, **52**, 1434–1456, doi: 10.1175/1520-0469(1995)052<1434:TSVSOT>2.0.CO;2.

- Courtier, P., J.-N. Thépaut, and A. Hollingsworth (1994). A strategy for operational implementation of 4D-Var, using an incremental approach. *Q. J. R. Meteorol. Soc.*, **120**, 1367–1387, doi: 10.1002/qj.49712051912.
- Dee, D. P., and Co-authors, 2011: The ERA-Interim reanalysis: Configuration and performance of the data assimilation system. *Q. J. R. Meteorol. Soc.*, **137**, 553–597, doi: 10.1002/qj.828.
- Dee, D. P. and S. Uppala (2009). Variational bias correction of satellite radiance data in the ERA-Interim reanalysis. *Q. J. R. Meteorol. Soc.*, **135**, 1830–1841, doi: 10.1002/qj.493.
- Derber J. C. and W.-S. Wu (1998). The use of TOVS cloud-cleared radiances in the NCEP SSI analysis system. *Mon. Wea. Rev.*, **126**, 2287–2299, doi: 10.1175/1520-0493(1998)126<2287:TUOTCC>2.0.CO;2.
- Fisher, M., Y. Trémolet, H. Auvinen, D. Tan, and P. Poli, 2011: Weak-constraint and long window 4D-Var. *ECMWF Tech. Memo.*, **655**, ECMWF, Reading, United Kingdom, 47 pp.
- Forbes, R. M., A. M. Tompkins, and A. Untch (2011). A new prognostic bulk microphysics scheme for the IFS. *ECMWF Tech. Memo.*, **649**, ECMWF, Reading, United Kingdom, 30 pp.
- Geer, A. J., P. Bauer, and P. Lopez (2010). Direct 4D-Var assimilation of all-sky radiances. Part II: Assessment. *Q. J. R. Meteorol. Soc.*, **136**, 1886–1905, doi: 10.1002/qj.681.
- Isaksen, L., M. Bonavita, R. Buizza, et al. (2010). Ensemble of Data Assimilations at ECMWF. *ECMWF Tech. Memo.*, **636**, ECMWF, Reading, United Kingdom, 48 pp.
- Hoskins, B. J., M. E. McIntyre, and A. W. Robertson (1985). On the use and significance of isentropic potential vorticity maps. *Q. J. R. Meteorol. Soc.*, **111**, 877–946, doi: 10.1002/qj.49711147002.
- Janisková, M., and P. Lopez (2012). Linearized physics for data assimilation at ECMWF. *ECMWF Tech. Memo.*, **666**, ECMWF, Reading, United Kingdom, 26 pp.
- Joos, H. and H. Wernli (2012). Influence of microphysical processes on the potential vorticity development in a warm conveyor belt: a case-study with the limited-area model COSMO. *Q. J. R. Meteorol. Soc.*, **138**, 407–418, doi: 10.1002/qj.934.
- Jung, T., G. Balsamo, P. Bechtold, et al. (2010). The ECMWF model climate: Recent progress through improved physical parametrizations. *Q. J. R. Meteorol. Soc.*, **136**, 1145–1160, doi: 10.1002/qj.634.
- Jung, T., and Co-authors (2012). High-resolution global climate simulations with the ECMWF model in project Athena: Experimental design, model climate, and seasonal forecast skill. *J. Climate*, **25**, 3155–3172, doi:10.1175/JCLI-D-11-00265.1.
- Klinker, E., and P. D. Sardeshmukh (1992). The diagnosis of mechanical dissipation in the atmosphere from large-scale balance requirements. *J. Atmos. Sci.*, **49**, 608–627, doi:10.1175/1520-0469(1992)049<0608:TDOMDI>2.0.CO;2.
- Klocke, D. and M. J. Rodwell (2014). A comparison of two numerical weather prediction methods for diagnosing fast-physics errors in climate models. *Q. J. R. Meteorol. Soc.*, **140**, 517–524, doi: 10.1002/qj.2172.
- Leroy, S. S., and M. J. Rodwell (2014). Leveraging highly accurate data in diagnosing errors in atmospheric models, *Bull. Am. Meteorol. Soc.*, doi: 10.1175/BAMS-D-12-00143.1.
- Leutbecher, M., and T. Palmer (2008). Ensemble forecasting. *J. Comp. Phys.*, **227**, 3515–3539, doi: 10.1016/j.jcp.2007.02.014.
- Lorenz, E. N. (1963). Deterministic non-periodic flow. *J. Atmos. Sci.*, **20**, 130–141, doi:10.1175/1520-0469(1963)020<0130:DNF>2.0.CO;2.
- Magnusson, L., J.-R. Bidlot, S. Lang, A. Thorpe, and N. Wedi (2014). Evaluation of medium-range forecasts for hurricane Sandy. *Mon. Wea. Rev.*, **142**, 1962–1981, doi:10.1175/MWR-D-13-00228.1.
- Mapes, B. E. and J. T. Bacmeister (2012). Diagnosis of tropical biases and the MJO from patterns in the MERRA analysis tendency fields. *J. Climate*, **25**, 6202–6214, doi: 10.1175/JCLI-D-11-00424.1.
- Madonna, E. (2013). Warm conveyor belts: Climatology and forecast performance. *PhD thesis. Diss.*, **21315**, ETH, Zurich, Switzerland, 143 pp.
- Rodwell, M. J. and T. Jung (2008). Understanding the local and global impacts of model physics changes: an aerosol example. *Q. J. R. Meteorol. Soc.*, **134**, 1479–1497. doi: 10.1002/qj.298.
- Rodwell M. J., L. Magnusson, P. Bauer, et al. (2013). Characteristics of occasional poor medium-range weather forecasts for Europe. *Bull. Am. Meteorol. Soc.*, **94**, 1393–1405, doi: 10.1175/BAMS-D-12-00099.1.
- Rodwell, M. J. and T. N. Palmer (2007). Using numerical weather prediction to assess climate models. *Q. J. R. Meteorol. Soc.*, **133**, 129–146, doi: 10.1002/qj.23.
- Shutts, G., M. Leutbecher, A. Weisheimer, et al. (2011). Representing model uncertainty: Stochastic parametrization at ECMWF. *ECMWF Newsletter*, **129**, ECMWF, Reading, United Kingdom, 19–24.
- Simmons, A. J., D. M. Burridge, M. Jarraud, C. Girard, and W. Wergen (1989). The ECMWF medium-range prediction models development of the numerical formulations and the impact of increased resolution. *Meteor. Atmos. Phys.*, **40**, 28–60, doi: 10.1007/BF01027467.
- Thorpe, A. J. (1986). Synoptic scale disturbances with circular symmetry. *Mon. Wea. Rev.*, **114**, 1384–1389, doi: 10.1175/1520-0493(1986)114<1384:SSDWCS>2.0.CO;2.
- Trémolet, Y. (2007). Model-error estimation in 4DVar. *Q. J. R. Meteorol. Soc.*, **133**, 1267–1280, doi:10.1002/qj.94.

# 2

## Severe weather diagnosis from the perspective of generalized slantwise vorticity development

Guoxiong Wu, Yongjun Zheng, and Yimin Liu

### 2.1 Introduction

In a frictionless and adiabatic dry atmosphere, the Ertel potential vorticity ( $PV_e$ ) is conserved (Ertel, 1942). Many applications of the Ertel potential vorticity to the diagnosis of atmospheric motion were summarized by Hoskins *et al.* (1985). Based on the conservation of Ertel potential vorticity, Wu and Liu (1997) proposed a theory of slantwise vorticity development (SVD) to interpret the development of the vertical vorticity of a Lagrangian particle sliding down a slantwise isentropic surface. Many applications of the SVD theory have obtained reasonable results and demonstrated the development of vertical vorticity on the slope of an isentropic surface (Cui *et al.*, 2002, Ma *et al.*, 2002, Chen *et al.*, 2004, Jiang *et al.*, 2004, Wang *et al.*, 2007). However, vertical vorticity development depends not only on the horizontal component of the  $PV_e$ , but also on the static stability  $\theta_z$  under the conservation of  $PV_e$ . More importantly, the latent heat release associated with precipitation plays a significant role in vertical vorticity development (Shen *et al.*, 1986, Ding and Lu, 1990, Chen *et al.*, 1996). Therefore, understanding how diabatic heating contributes to vertical vorticity development from the viewpoint of potential vorticity and diabatic heating ( $PV-Q$ ) is important, and is one of the objectives of this study.

On the other hand, during some stages of vortex development, the adiabatic processes that are associated with the internal thermal structure of the atmosphere, and can be interpreted by SVD, can play comparable roles to diabatic heating during vortex development. Actually, SVD usually occurs during the initial stage of vortex development and before precipitation begins. After vortex development begins, vertical rising is generated within the vortex and precipitation appears, leading to condensation diabatic heating, and thereby enhancing the development of the vortex. In this regard, it is important and useful to understand how SVD occurs in a more

general sense from the  $PV-\theta$  perspective, and this is another objective of this study.

The Tibetan Plateau (TP) vortex (TPV) is a shallow low-level cyclonic system that develops near 500 hPa, over the TP and in the lower troposphere over the plain areas. The TPV occurs during the boreal summer. In general, it originates over the central western TP, then moves eastward before dying out over the eastern TP. Its horizontal and vertical scales are typically about 500 and 2–3 km, respectively. Sometimes, the TPV persists and moves eastward out of the TP, and this often results in severe weather over eastern China, especially in the Sichuan Basin (Ye and Gao, 1979, Tao and Ding, 1981, Qiao and Zhang 1994, Li, 2002). Previous studies have shown that the formation of the TPV is driven by surface sensible heating, topography, static stability, boundary layer friction, and large-scale circulation of the mid-latitude trough or cyclone (Group of Tibetan Plateau Low System, 1978, Tao, 1980, Zhang *et al.*, 1988, Ding, 1993, Chen *et al.*, 1996, Ding, 2005). It is generally believed that the development of the TPV is closely related to diabatic heating, especially condensation heat release (Shen *et al.*, 1986, Ding and Lu, 1990, Chen *et al.*, 1996). The movement of the TPV depends on the difference in divergence between 200 and 500 hPa (Liu and Fu, 1985) and the steering flow of the southwesterly jet at 300 hPa (Qiao, 1987, Sun and Chen, 1988). However, there are still questions regarding TPV development. For example, how does the 3D heterogeneous distribution of the diabatic heating affect the development and movement of the TPV? What is the relationship between diabatic heating and circulation configuration during the development of the TPV? What role do adiabatic processes play in the development and movement of the TPV? These questions remain unanswered and need to be investigated. An attempt to address these points using the theory of generalized slantwise vorticity development from both  $PV-Q$  and  $PV-\theta$  perspectives is the main aim of this study.

## 2.2 Generalized slantwise vorticity development

By definition,  $PV_e$  (Ertel, 1942) is expressed as

$$PV_e = \alpha(2\Omega + \nabla \times \mathbf{V}) \cdot \nabla \theta = \boldsymbol{\eta}_a \cdot \nabla \theta, \quad (2.1)$$

where  $\boldsymbol{\eta}_a = \eta_x \mathbf{i} + \eta_y \mathbf{j} + \eta_z \mathbf{k}$  is the absolute vorticity per unit mass, and  $\nabla = \frac{\partial}{\partial x} \mathbf{i} + \frac{\partial}{\partial y} \mathbf{j} + \frac{\partial}{\partial z} \mathbf{k}$  is the 3D gradient operator. Defining the horizontal component of  $PV_e$  as

$$PV_2 = \eta_x \theta_x + \eta_y \theta_y = \boldsymbol{\eta}_s \cdot \boldsymbol{\theta}_s, \quad (2.2)$$

where  $\boldsymbol{\eta}_s = \eta_x \mathbf{i} + \eta_y \mathbf{j}$  is the horizontal vorticity,  $\boldsymbol{\theta}_s = \theta_x \mathbf{i} + \theta_y \mathbf{j} = \nabla_s \theta$  is the horizontal gradient of the potential temperature, and  $\nabla_s = \frac{\partial}{\partial x} \mathbf{i} + \frac{\partial}{\partial y} \mathbf{j}$  is a horizontal gradient operator, then

$$\eta_z = \frac{PV_e - PV_2}{\theta_z} = \frac{PV_e}{\theta_z} - C_D, \quad \theta_z \neq 0, \quad (2.3)$$

where

$$C_D = \frac{PV_2}{\theta_z} = \frac{\boldsymbol{\eta}_s \cdot \boldsymbol{\theta}_s}{\theta_z}, \quad \theta_z \neq 0. \quad (2.4)$$

The notations used here are as follows:  $\eta_x = \alpha(\frac{\partial w}{\partial y} - \frac{\partial v}{\partial z})$ ,  $\eta_y = \alpha(e + \frac{\partial u}{\partial z} - \frac{\partial w}{\partial x})$ ,  $\eta_z = \alpha(f + \frac{\partial v}{\partial x} - \frac{\partial u}{\partial y})$ ,  $\theta_x = \frac{\partial \theta}{\partial x}$ ,  $\theta_y = \frac{\partial \theta}{\partial y}$ ,  $\theta_z = \frac{\partial \theta}{\partial z}$ ,  $e = 2\Omega \cos \phi$ , and  $f = 2\Omega \sin \phi$ .  $\Omega = 7.292 \times 10^{-5} \text{ s}^{-1}$  is the rotation rate of the Earth,  $\phi$  is latitude,  $\theta$  is potential temperature, and  $\alpha$  is specific volume.

To evaluate the development of vertical vorticity, taking the operator  $\frac{D}{Dt}$  in Eq. (2.1) leads to

$$\begin{aligned} \frac{D\eta_z}{Dt} &= \frac{D}{Dt} \left( \frac{PV_e - PV_2}{\theta_z} \right) \\ &= \frac{1}{\theta_z} \frac{DPV_e}{Dt} - \frac{1}{\theta_z} \frac{DPV_2}{Dt} - \frac{\eta_z}{\theta_z} \frac{D\theta_z}{Dt}, \end{aligned} \quad (2.5)$$

where  $\frac{D}{Dt} = \frac{\partial}{\partial t} + \mathbf{V} \cdot \nabla$ . This demonstrates that the change in  $PV_e$ ,  $PV_2$ , and  $\theta_z$  along a Lagrangian particle track can influence the individual change in vertical vorticity of the particle.

### 2.2.1 Revisiting slantwise vorticity development

Based on the conservation of Ertel potential vorticity, Wu and Liu (1997) proposed the SVD theory to interpret the intense vertical vorticity development of a Lagrangian particle sliding down a slantwise isentropic surface. The condition for the SVD is also given in Wu and Liu (1997) and is duplicated here:

$$C_D(t + \Delta t) = C_D(t) < PV_e \left[ \frac{1}{\theta(t + \Delta t)} - \frac{1}{\theta_z(t)} \right]. \quad (2.6)$$

The SVD for a statically stable atmosphere was explained schematically by Wu and Liu (1997) for a down-sliding case, and by Cui *et al.* (2003) for an up-sliding case.

Many applications of the SVD theory used to diagnose the occurrence of torrential rain and severe weather obtained reasonable results and demonstrated that vertical vorticity can develop dramatically along the sharply sloping isentropic surface, and the condition  $C_D < 0$  was diagnosed in some cases (Cui *et al.*, 2002, Ma *et al.*, 2002, Chen *et al.*, 2004, Jiang *et al.*, 2004, Wang *et al.*, 2007). However, as shown in Eq. (2.3), the vertical vorticity development depends not only on  $C_D$ , but also on the static stability  $\theta_z$  under the conservation of  $PV_e$ . From the definition of  $C_D$  in Eq. (2.4), a negative  $C_D$  under stable stratification implies a negative  $PV_2$ . Hoskins *et al.* (1985) proved that in pressure coordinates,  $PV_2^p$  is negative for geostrophic balance. In height coordinates, the hydrostatic balance yields

$$\begin{cases} \frac{1}{\rho} \nabla_s p = \theta \nabla_s \Pi \\ \frac{\partial \Pi}{\partial z} = -\frac{g}{\theta} \end{cases}, \quad (2.7)$$

where  $\Pi = C_p \left( \frac{p}{p_0} \right)^{R/C_p}$  is the Exner function. Then, the geostrophic wind in the height coordinates is

$$\mathbf{V}_g = \frac{\mathbf{k}}{\rho f} \times \nabla_s p = \theta \frac{\mathbf{k}}{f} \times \nabla_s \Pi. \quad (2.8)$$

Taking  $\frac{\partial}{\partial z}$  upon Eq. (2.8) yields the thermal wind,

$$\begin{aligned} \frac{\partial \mathbf{V}_g}{\partial z} &= \frac{\partial \theta}{\partial z} \frac{\mathbf{k}}{f} \times \nabla_s \Pi + \theta \frac{\mathbf{k}}{f} \times \nabla_s \frac{\partial \Pi}{\partial z} \\ &= \theta_z \frac{\mathbf{k}}{f} \times \nabla_s \Pi + \frac{g}{\theta} \frac{\mathbf{k}}{f} \times \nabla_s \theta. \end{aligned} \quad (2.9)$$

Therefore,

$$\begin{aligned} PV_2 &\simeq \alpha \left( \mathbf{k} \times \frac{\partial \mathbf{V}_g}{\partial z} \right) \cdot \nabla_s \theta \\ &= -\frac{\alpha}{f} \left( \theta_z \nabla_s \Pi \cdot \nabla_s \theta + \frac{g}{\theta} |\nabla_s \theta|^2 \right) \end{aligned} \quad (2.10)$$

and

$$C_D = \frac{PV_2}{\theta_z} = -\frac{\alpha}{f} \left( \nabla_s \Pi \cdot \nabla_s \theta + \frac{g}{\theta_z} |\nabla_s \theta|^2 \right). \quad (2.11)$$

In the Northern Hemisphere,  $f$  is positive, and the second term  $PV_2^2 (= -\frac{\alpha g}{f \theta} |\nabla_s \theta|^2)$  on the right-hand side of Eq. (2.10) is negative. Although, the first term,  $PV_2^1 (= -\frac{\alpha}{f} \theta_z \nabla_s \Pi \cdot \nabla_s \theta)$ , is not necessarily negative, its magnitude is usually smaller than the second term,  $PV_2^2$ , so  $PV_2$  is almost negative in the troposphere under the geostrophic balance. Figure 2.1 contains the 3D distributions of  $C_D$  and  $PV_2$  under real weather conditions at 0600 UTC 22 July 2008. The distributions for other time slices are similar. Figure 2.1 demonstrates that both  $C_D$  and

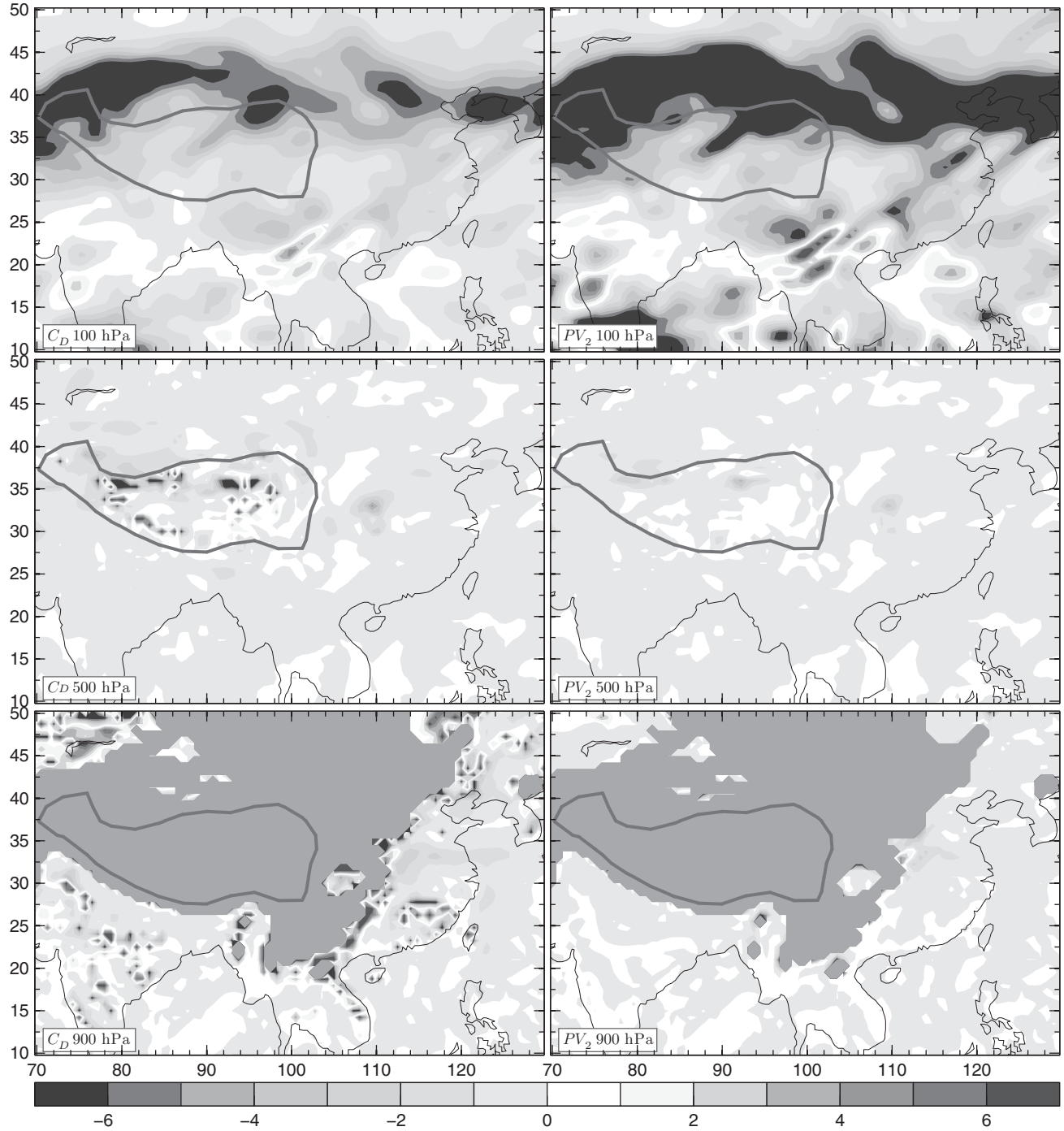


Fig. 2.1: Distributions at 100 (top), 500 (middle), and 900 hPa (bottom) of  $C_D$  ( $10^{-5} \text{m}^{-3}(\text{kg s})^{-1}$ ; left) and  $PV_e$  ( $10^{-1} \text{PVU}$ ,  $1 \text{PVU} = 10^{-6} \text{m}^2(\text{kg s})^{-1}$ ; right) at 0600 UTC 22 July 2008. In this figure, and those that follow, the yellow shading indicates the region below the ground surface. The thick gray line indicates the 3000 m contour of surface elevation. A black and white version of this figure will appear in some formats. [For the colour version, please refer to Plate 1.](#)

$PV_2$  are usually negative throughout the troposphere. Therefore, using  $C_D < 0$  alone as the criterion for SVD is inappropriate. For more general cases, the influence of the change in static stability needs to be considered. The SVD

theory (Wu and Liu, 1997) is based on the conservation of Ertel potential vorticity, so it did not explicitly consider the impacts of diabatic heating. Recently, Wu *et al.* (2013) and Zheng *et al.* (2013) have proposed an approach to severe

weather diagnosis in eastern China based on generalized slantwise vorticity development. In the following two sections, generalized slantwise vorticity development (GSVD), as an extension of SVD, is used to consider both diabatic and adiabatic processes from a Lagrangian perspective.

### 2.2.2 Diabatic vorticity development

The first term on the right-hand side of Eq. (2.5) associated with diabatic heating is determined by the static stability  $\theta_z$  and the change in  $PV_e$ :

$$\left(\frac{D\eta_z}{Dt}\right)_Q = \frac{1}{\theta_z} \frac{DPV_e}{Dt}, \quad \theta_z \neq 0. \quad (2.12)$$

Based on the potential vorticity equation (Ertel, 1942; Hoskins *et al.*, 1985)

$$\frac{DPV_e}{Dt} = \boldsymbol{\eta}_a \cdot \nabla Q + (\alpha \nabla \times \mathbf{F}) \cdot \nabla \theta, \quad (2.13)$$

where  $Q = \frac{D\theta}{Dt}$  denotes diabatic heating. In the free atmosphere, friction  $\mathbf{F}$  can be neglected, so

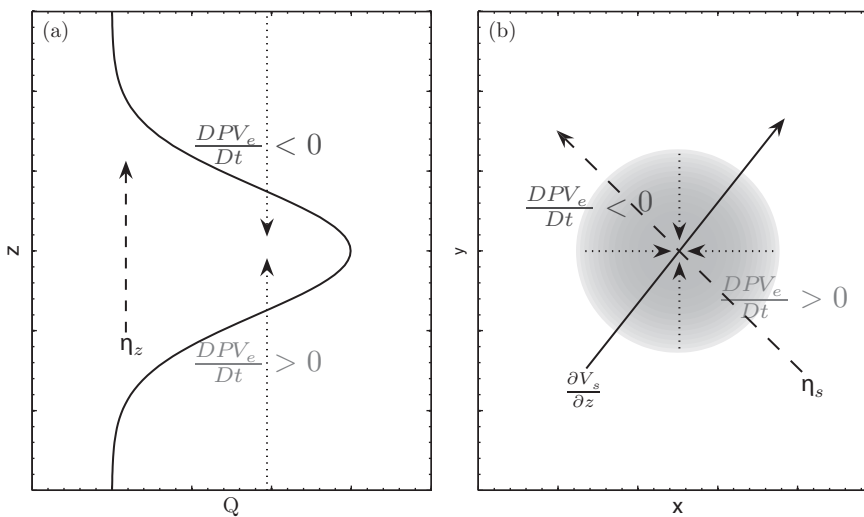
$$\frac{DPV_e}{Dt} = \boldsymbol{\eta}_a \cdot \nabla Q = \eta_z \frac{\partial Q}{\partial z} + \boldsymbol{\eta}_s \cdot \nabla_s Q = \left(\frac{DPV_e}{Dt}\right)_z + \left(\frac{DPV_e}{Dt}\right)_s \quad (2.14)$$

where

$$\left(\frac{DPV_e}{Dt}\right)_z = \eta_z \frac{\partial Q}{\partial z} \quad (2.15)$$

and

$$\left(\frac{DPV_e}{Dt}\right)_s = \boldsymbol{\eta}_s \cdot \nabla_s Q \quad (2.16)$$



represent contributions to the  $PV_e$  changes due to the non-uniformity of diabatic heating in the vertical and horizontal directions, respectively.

#### Impacts on vertical vorticity development of the vertical non-uniformity of diabatic heating

In the case of the non-uniformity of diabatic heating in the vertical direction, according to Eq. (2.15),  $PV_e$  increases (decreases) where the vertical gradient of diabatic heating is positive (negative: Wu and Liu, 2000). This is illustrated schematically in Fig. 2.2a. In such circumstances, the vertical gradient of diabatic heating leads to positive (negative)  $PV_e$  generation below (above) the maximum of the diabatic heating. According to Eq. (2.12), for a stable stratified atmosphere, the low-level positive  $PV_e$  generation corresponds to an increasing cyclonic circulation that can strengthen the low-level vortex; and the upper-level negative  $PV_e$  generation corresponds to an increasing anticyclone circulation that can weaken the upper-level vortex, causing the vortex to be confined in a lower vertical extension.

It should be noted that the condensation diabatic heating in a vortex usually occurs on its eastern side. This is because the horizontal advection of vorticity is negligible across the center of the vortex. Consequently, the vorticity equation at a steady state can be approximated as  $\beta v \approx f \frac{\partial w}{\partial z}$ , and the vertical velocity becomes  $w \propto -\frac{\beta}{f} \frac{\partial v}{\partial z}$ . As on the eastern (western) side of a vortex,  $\frac{\partial v}{\partial z} < 0$  ( $\frac{\partial v}{\partial z} > 0$ ), air rising (sinking) occurs normally on the eastern (western) side of the vortex. This implies that condensation diabatic heating usually occurs on the eastern side of a vortex. Consequently, the generation of positive vorticity in the lower troposphere on the east of a vortex associated with the vertical non-uniformity of condensation diabatic heating will contribute to the eastward movement of the vortex.

Fig. 2.2: Lagrangian  $PV_e$  generation associated with (a) the vertical profile of diabatic heating  $Q$  (thick solid line) and (b) the horizontal distribution of diabatic heating  $Q$  (shading). Long solid arrow in (b) is the vertical shear  $(\frac{\partial V_s}{\partial z})$  of horizontal wind, long dash arrow in (a) is the vertical vorticity  $\eta_z$  and in (b) is the horizontal vorticity  $\boldsymbol{\eta}_s$ , and short dot arrows are the vertical gradient  $(\frac{\partial Q}{\partial z})$  of diabatic heating in (a) and  $\nabla_s Q$  in (b), which is the horizontal gradient of diabatic heating. A black and white version of this figure will appear in some formats. For the colour version, please refer to Plate 6.

### Impacts on vertical vorticity development of the horizontal non-uniformity of diabatic heating

According to Eq. (2.16), the horizontal gradient of diabatic heating may contribute to the development of the vertical vorticity of a vortex, as indicated by Liu *et al.* (2001). There is a positive (negative) potential vorticity generation when the horizontal vorticity  $\boldsymbol{\eta}_s$  and the horizontal gradient of diabatic heating are in the same (opposite) direction; i.e. the potential vorticity generation is the largest (smallest or negative) when two vectors are parallel (orthogonal). As the horizontal variation of vertical velocity  $w$  is several orders of magnitude less than the vertical shear of horizontal wind  $\mathbf{V}_s$ , Eq. (2.16) can be approximated as

$$\left(\frac{DPV_e}{Dt}\right)_s = \boldsymbol{\eta}_s \cdot \nabla_s Q \approx \alpha \left( \mathbf{k} \times \frac{\partial \mathbf{V}_s}{\partial z} \right) \cdot \nabla_s Q. \quad (2.17)$$

This means that the sign of the change in  $PV_e$  depends on the disposition between the atmospheric circulation and diabatic heating. As illustrated schematically in Fig. 2.2b, the horizontal vorticity  $\boldsymbol{\eta}_s$  due to the vertical shear ( $\frac{\partial \mathbf{V}_s}{\partial z}$ ) is perpendicular to, and pointing to the left of, the shear vector in the Northern Hemisphere, while the horizontal gradient of diabatic heating ( $\nabla_s Q$ ) points toward the center of the diabatic heating. Consequently, on the right (left) side of the shear vector, the scalar product of the horizontal vorticity  $\boldsymbol{\eta}_s$  associated with the vertical shear ( $\frac{\partial \mathbf{V}_s}{\partial z}$ ) of horizontal wind and the horizontal gradient of diabatic heating ( $\nabla_s Q$ ); i.e.  $\boldsymbol{\eta}_s \cdot \nabla_s Q$ , is positive (negative), corresponding to positive (negative)  $PV_e$  generation. According to Eq. (2.12), in a stable stratified atmosphere, positive and negative vorticities will be generated on the right and left sides, respectively, of the vertical shear of horizontal wind. In such circumstances, the horizontal gradient of diabatic heating can not only strengthen the vertical vorticity on the right side of the shear vector and weaken the vertical vorticity on the left side of the shear vector, but also further influence the movement of the vortex as the tendency of vertical vorticity generation is asymmetrically distributed on the two sides of the shear vector that pass through the center of diabatic heating, which is usually on the eastern side of the vortex.

### 2.2.3 Adiabatic vorticity development

#### Slantwise vorticity development on a sloping isentropic surface

Defining  $\beta \in [0, \frac{\pi}{2}]$  as the acute angle between  $\nabla\theta$  and the vertical direction; i.e.  $\tan\beta = \frac{\theta_z}{|\theta_s|}$ , and defining  $\Lambda \in [0, \pi]$  as the angle between horizontal vorticity  $\boldsymbol{\eta}_s$  and baroclinity  $\boldsymbol{\theta}_s$ , then

$$\begin{cases} C_D = \frac{\eta_s \theta_s \cos \Lambda}{\theta_z} = +\eta_s \cos \Lambda \tan \beta, & \text{if } \theta_z > 0 \\ C_D = \frac{\eta_s \theta_s \cos \Lambda}{\theta_z} = -\eta_s \cos \Lambda \tan \beta & \text{if } \theta_z < 0 \end{cases}, \quad (2.18)$$

where  $\eta_s = |\boldsymbol{\eta}_s|$  and  $\theta_s = |\boldsymbol{\theta}_s|$ . As

$$\nabla\theta = \theta_x \mathbf{i} + \theta_y \mathbf{j} + \theta_z \mathbf{k} = \theta_s \mathbf{s} + \theta_z \mathbf{k} = \theta_n \mathbf{n}, \quad (2.19)$$

where  $\theta_n = |\nabla\theta|$ , the unit vector  $\mathbf{n}$  is the direction of  $\nabla\theta$ , and the unit vector  $\mathbf{s}$  is the direction of  $\nabla_s \theta$ , then

$$\begin{cases} PV_e = \boldsymbol{\eta}_a \cdot \nabla\theta = \eta_n \theta_n > 0, \Rightarrow \eta_n > 0, & \text{if } \theta_z > 0 \\ PV_e = \boldsymbol{\eta}_a \cdot \nabla\theta = \eta_n \theta_n < 0, \Rightarrow \eta_n < 0, & \text{if } \theta_z < 0, \end{cases} \quad (2.20)$$

where  $\eta_n = \boldsymbol{\eta}_a \cdot \mathbf{n}$  is the projection of absolute vorticity  $\boldsymbol{\eta}_a$  on the direction of  $\mathbf{n}$ .

Therefore, Eq. (2.3) can be rewritten as

$$\begin{cases} \eta_z = +\frac{\eta_n}{\cos \beta} - \eta_s \cos \Lambda \tan \beta, & \text{if } \theta_z > 0 \\ \eta_z = -\frac{\eta_n}{\cos \beta} + \eta_s \cos \Lambda \tan \beta, & \text{if } \theta_z < 0 \end{cases}. \quad (2.21)$$

if  $C_D < 0$ , Eq. (2.18) yields

$$\begin{cases} \cos \Lambda < 0, \Rightarrow \Lambda \in \left(\frac{\pi}{2}, \pi\right], & \text{if } \theta_z > 0 \\ \cos \Lambda > 0, \Rightarrow \Lambda \in \left[0, \frac{\pi}{2}\right), & \text{if } \theta_z < 0 \end{cases}. \quad (2.22)$$

As both  $\eta_s$  and  $\theta_s$  are positive, using Eqs. (2.22) and (2.20), Eq. (2.21) can be rewritten as

$$\eta_z = \frac{|\eta_n|}{\cos \beta} + \eta_s |\cos \Lambda| \tan \beta. \quad (2.23)$$

Under the constraint of  $C_D < 0$ , taking the derivative of Eq. (2.23) with respect to  $\beta$  leads to

$$\begin{aligned} \frac{D\eta_z}{D\beta} = & \left( \frac{|\eta_n| \sin \beta}{\cos^2 \beta} + \frac{\eta_s |\cos \Lambda|}{\cos^2 \beta} \right) + \left( \frac{D|\eta_n|}{D\beta} \frac{1}{\cos \beta} \right. \\ & \left. + \frac{D\eta_s}{D\beta} |\cos \Lambda| \tan \beta + \eta_s \frac{D|\cos \Lambda|}{D\beta} \tan \beta \right). \end{aligned} \quad (2.24)$$

The terms in the first parentheses on the right side of Eq. (2.24) are second-order positive infinite, but the terms in the second parentheses are first-order positive or negative infinite when  $\beta$  approaches  $\frac{\pi}{2}$ , thus

$$\frac{D\eta_z}{D\beta} \rightarrow \infty, \quad \text{if } \beta \rightarrow \frac{\pi}{2}, \quad (2.25)$$

which demonstrates that when an air particle is sliding down the concave slope or up the convex slope of an isentropic surface and  $C_D < 0$ , its vertical vorticity will increase rapidly.

Assuming the directions of horizontal vorticity  $\eta_s$  and baroclinity  $\theta_s$  are strictly opposite (identical) for a stable (unstable) atmosphere; i.e.  $\Lambda = \pi(\Lambda = 0)$  for  $\theta_z > 0$  ( $\theta_z < 0$ ), then  $C_D < 0$ ; and assuming  $\theta_n$  is constant, then  $\eta_n$  is constant as  $PV_e = \eta_n \theta_n$  is conserved. Thus, Eq. (2.23) becomes

$$\eta_z = \frac{|\eta_n|}{\cos \beta} + \eta_s \tan \beta \Rightarrow \eta_z \rightarrow \infty, \text{ if } \beta \rightarrow \pi/2, \quad (2.26)$$

which is illustrated schematically in Fig. 2.3 (Fig. 2.4) for the down-sliding SVD in the stable (unstable) atmosphere. The up-sliding SVD in the stable or unstable atmosphere is explained by Eq. (2.26). As there is no essential difference between the down-sliding and up-sliding SVD, the schematic diagram for the up-sliding SVD is not shown here. An air particle at the initial position  $A^0$  possesses zero  $C_D$  because the isentropic surface is horizontal. During the adiabatic movement of the particle, because the directions of horizontal vorticity  $\eta_s$  and baroclinity  $\theta_s$  are strictly opposite (identical) for a stable (unstable) atmosphere, when the particle moves from  $A^0$  to  $A$  on the same isentropic surface, its vertical absolute vorticity  $\eta_z$  is increased under the conservation of  $PV_e$ .

It is worth noting that the above analysis is just a qualitative demonstration of the SVD concept. Under the premise  $C_D < 0$ , vertical vorticity will increase dramatically when a particle is moving along a sharply tilted isentropic surface; i.e.  $\beta$  increases rapidly.

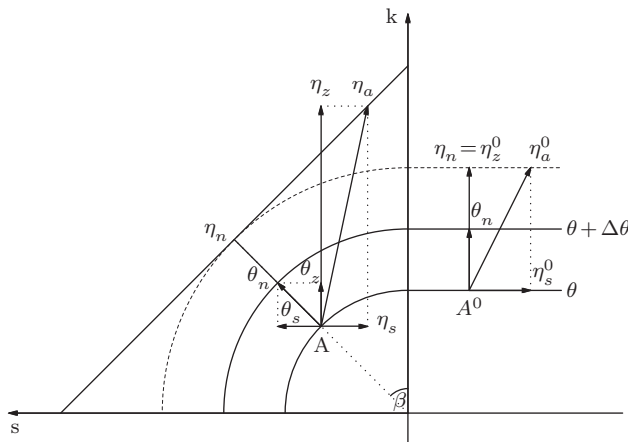


Fig. 2.3: Schematic diagram showing the development of vertical vorticity in a stable atmosphere caused by the slantwise sloping of the isentropic surface when the directions of horizontal vorticity  $\eta_s$  and baroclinity  $\theta_s$  are opposite. Initially, a particle is at position  $A^0$  on the horizontal part of a  $\theta$  surface, and  $PV_e (= \eta_n \theta_n)$  is conserved. When it slides down the  $\theta$  surface at angle  $\beta$  to position  $A$ , due to  $\eta_z = \frac{|\eta_n|}{\cos \beta} + \eta_s$ , the increase in  $\beta$  can result in the development of  $\eta_z$ .

### Slantwise vorticity development from a Lagrangian perspective

The above SVD theory is based on isentropic coordinates with a priori assumption that the sloping angle  $\beta$  of the isentropic surface increases with time. However, as  $\frac{D\eta_z}{Dt} = \frac{D\eta_z}{D\beta} \frac{D\beta}{Dt}$ , the change in the tilting angle  $\beta$  of the isentropic surface must also be analyzed. This is inconvenient and usually ignored in the application of SVD. For practical reasons, and to generalize the analysis, the SVD will be studied from a Lagrangian perspective.

#### Vorticity development (VD)

Taking the derivative of Eq. (2.3) with respect to time under the constraint of the conservation of Ertel potential vorticity leads to

$$\left( \frac{D\eta_z}{Dt} \right)_A = - \frac{PV_e}{\theta_z^2} \frac{D\theta_z}{Dt} - \frac{DC_D}{Dt}, \quad \theta_z \neq 0, \quad (2.27)$$

where  $\left( \frac{D\eta_z}{Dt} \right)_A$  denotes the adiabatic development of vertical vorticity. Thus, the necessary and sufficient condition for vorticity development (VD) is

$$\frac{DC_D}{Dt} < - \frac{PV_e}{\theta_z^2} \frac{D\theta_z}{Dt}, \quad \theta_z \neq 0. \quad (2.28)$$

This is the condition given in Eq. (2.6) by Wu and Liu (1997), but in a different form.

#### Slantwise vorticity development (SVD)

If

$$\frac{DC_D}{Dt} < 0, \quad (2.29)$$

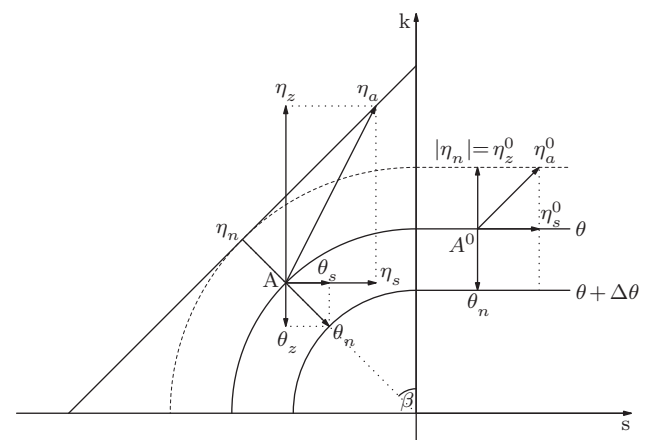


Fig. 2.4: As Fig. 2.3, but for the unstable atmosphere case when the directions of horizontal vorticity  $\eta_s$  and baroclinity  $\theta_s$  are strictly parallel.

Eq. (2.27) can be written as

$$\left(\frac{D\eta_z}{Dt}\right)_A = -\frac{PV_e}{\theta_z^2} \frac{D\theta_z}{Dt} + \left|\frac{DC_D}{Dt}\right|, \quad \theta_z \neq 0. \quad (2.30)$$

If

$$\frac{DC_D}{Dt} < 0 < -\frac{PV_e}{\theta_z^2} \frac{D\theta_z}{Dt}, \quad \theta_z \neq 0, \quad (2.31)$$

Eq. (2.30) yields

$$\left(\frac{D\theta_z}{Dt}\right)_A \rightarrow \infty, \quad \text{if } |\theta_z| \rightarrow 0. \quad (2.32)$$

This implies that when Eq. (2.31) is satisfied, the vertical vorticity of an air particle can develop rapidly if the atmosphere's static stability approaches neutral.

In general, in an inertial stable atmosphere, the signs of  $PV_e$  and  $\theta_z$  are identical. In such circumstances, Eq. (2.31) can be interpreted as

$$\begin{cases} \frac{D\theta_z}{Dt} < 0 \quad \text{and} \quad \frac{DC_D}{Dt} < 0, \quad \text{if } \theta_z > 0 \\ \frac{D\theta_z}{Dt} > 0 \quad \text{and} \quad \frac{DC_D}{Dt} < 0, \quad \text{if } \theta_z < 0 \end{cases}. \quad (2.33)$$

Therefore, the SVD can be stated as: when an air particle is sliding down the concave slope or up the convex slope of an isentropic surface in a stable stratified atmosphere with its static stability decreasing, or in an unstable atmosphere with its static stability increasing, its vertical vorticity can develop rapidly if its  $C_D$  is decreasing. That is, the vertical vorticity of an air particle will intensify rapidly when its stability approaches zero; i.e. the particle is inclined to neutral stability if its  $C_D$  decreases.

#### *Relationship between $PV_2$ and SVD*

The necessary and sufficient condition of Eq. (2.31) for SVD can be written as

$$\frac{1}{\theta_z} \frac{DPV_2}{Dt} - \frac{PV_2}{\theta_z^2} \frac{D\theta_z}{Dt} < 0 < -\frac{PV_e}{\theta_z^2} \frac{D\theta_z}{Dt}, \quad \theta_z \neq 0. \quad (2.34)$$

Adding a negative term  $\frac{PV_e}{\theta_z^2} \frac{D\theta_z}{Dt}$  to the inequality in Eq. (2.34) leads to

$$-\frac{1}{\theta_z} \frac{DPV_2}{Dt} - \frac{\eta_z}{\theta_z} \frac{D\theta_z}{Dt} > -\frac{PV_e}{\theta_z^2} \frac{D\theta_z}{Dt} > 0, \quad \theta_z \neq 0. \quad (2.35)$$

For  $PV_e$  conservation, Eq. (2.5) becomes

$$\left(\frac{D\eta_z}{Dt}\right)_A = -\frac{1}{\theta_z} \frac{DPV_2}{Dt} - \frac{\eta_z}{\theta_z} \frac{D\theta_z}{Dt} > -\frac{PV_e}{\theta_z^2} \frac{D\theta_z}{Dt} > 0, \quad \theta_z \neq 0. \quad (2.36)$$

This provides the relationship between SVD and the change in  $PV_2$ , and indicates that in a stable (unstable) atmosphere, a decrease (increase) of  $PV_2$  will result in vertical vorticity development. The intensity of SVD depends on the change of atmosphere static stability:

$$\left(\frac{D\eta_z}{Dt}\right)_A > PV_e \frac{D}{D} \left(\frac{1}{\theta_z}\right), \quad \theta_z \neq 0, \quad (2.37)$$

which indicates that only when  $PV_e \frac{D}{D} \frac{1}{\theta_z} > 0$  and the adiabatic development  $\left(\frac{D\eta_z}{Dt}\right)_A$  of vertical vorticity development exceeds  $PV_e \frac{D}{D} \frac{1}{\theta_z}$ , can such SVD actually be defined as SVD. For a symmetric stable atmosphere with  $PV_e > 0$ , when the static stability decreases to approach neutral stratification, SVD will occur, leading to the occurrence of severe weather.

## 2.3 Application of generalized slantwise vorticity development

### 2.3.1 Data and computational method

#### *Data*

The data used in this study are the ERA-Interim reanalysis data with a horizontal resolution of  $0.75^\circ$  (Dee et al., 2011) and the TRMM 3B42 precipitation data with a three-hour interval and a  $0.25^\circ$  horizontal resolution (Huffman et al., 2007). The ERA-Interim reanalysis data have 60 hybrid levels in the vertical with the top level at 0.1 hPa, and have been archived at six-hourly intervals since 0000 UTC 1 January 1979.

#### *Computational method*

All of the computations in this study were performed at the model level, with vertical coordinates transforming so that the vertical and horizontal components of vorticity and gradient were strictly perpendicular and acclinic, respectively. In addition, the results were interpolated onto the isobaric or isentropic surface to simplify the plotting of the figures.

The GSVD theory presented above is based on a Lagrangian perspective. For application to the corresponding diagnosis using the ERA-Interim reanalysis data with a time span of 6 h, we perform a Lagrangian conversion to calculate the material derivative. The Lagrangian change of any quantity  $q$  can be evaluated as

$$\frac{Dq}{Dt} = \frac{q(\mathbf{r}(t)) - q(\mathbf{r}(t - \Delta t))}{\Delta t}, \quad (2.38)$$

where  $\mathbf{r}(t)$  and  $\mathbf{r}(t - \Delta t)$  are the arrival position and departure position of a particle, respectively. The standard

iterative algorithm for backward trajectory in a semi-Lagrangian transport scheme is not accurate enough for a very large time step. Here, the large time step is divided into multiple smaller intervals, and in each small interval  $\delta\tau$ , the departure  $\mathbf{r}(\tau - \delta\tau)$ , can be obtained by Taylor series expansion of  $\mathbf{r}(\tau - \delta\tau)$  about the arrival position  $\mathbf{r}(\tau)$  following the idea of McGregor (1993),

$$\mathbf{r}(\tau - \delta\tau) = \mathbf{r}(\tau) + \sum_{n=1}^N \frac{(-\delta\tau)^n}{n!} \frac{D^n \mathbf{r}(\tau)}{D\tau^n} + O(\delta\tau^{N+1}). \quad (2.39)$$

In Cartesian coordinates,  $\mathbf{r} = r \cos \lambda \cos \phi \mathbf{i} + r \sin \lambda \cos \phi \mathbf{j} + r \sin \phi \mathbf{k}$ , so the first derivative  $\frac{D\mathbf{r}(\tau)}{D\tau}$  required in Eq. (2.39) can be calculated analytically as

$$\begin{aligned} \frac{D\mathbf{r}(\tau)}{D\tau} &= [-u \sin \lambda - v \cos \lambda \sin \phi + w \cos \lambda \cos \phi] \mathbf{i} \\ &\quad + [u \cos \lambda - v \sin \lambda \sin \phi + w \sin \lambda \cos \phi] \mathbf{j} \\ &\quad + [v \cos \phi + w \sin \phi] \mathbf{k}. \end{aligned} \quad (2.40)$$

By taking  $\frac{D}{D\tau}$  in Eq. (2.40) and dropping the higher-order terms  $\frac{D^2 u}{D\tau^2}$ ,  $\frac{D^2 v}{D\tau^2}$ , and  $\frac{D^2 w}{D\tau^2}$ , the second derivative  $\frac{D^2 \mathbf{r}(\tau)}{D\tau^2}$  required in Eq. (2.39) can be approximated as

$$\begin{aligned} \frac{D^2 \mathbf{r}(\tau)}{D\tau^2} &\simeq \left[ -2 \frac{uw}{r} \sin \lambda - 2 \frac{vw}{r} \cos \lambda \sin \phi + 2 \frac{uv}{r} \sin \lambda \tan \phi \right. \\ &\quad \left. - \frac{u^2}{r \cos \phi} \cos \lambda - \frac{v^2}{r} \cos \lambda \cos \phi \right] \mathbf{i} \\ &\quad + \left[ 2 \frac{uw}{r} \cos \lambda - 2 \frac{vw}{r} \sin \lambda \sin \phi - 2 \frac{uv}{r} \cos \lambda \tan \phi \right. \\ &\quad \left. - \frac{u^2}{r \cos \phi} \sin \lambda - \frac{v^2}{r} \sin \lambda \cos \phi \right] \mathbf{j} \\ &\quad + \left[ 2 \frac{vw}{r} \cos \phi - \frac{v^2}{r} \sin \phi \right] \mathbf{k} \end{aligned} \quad (2.41)$$

As the derivatives  $\frac{D\mathbf{r}(\tau)}{D\tau}$  and  $\frac{D^2 \mathbf{r}(\tau)}{D\tau^2}$  are obtained analytically, the algorithm of Eq. (2.39) is at a third-order precision and is more accurate than the numerical iterative algorithm. Therefore, Eq. (2.38) was used to calculate the Lagrangian change of various variables below.

### 2.3.2 Description of the TPV in 2008

#### *Track of the TPV and associated precipitation*

On 20 July 2008, a TPV moved eastward over the eastern TP (Fig. 2.5). It moved out of the TP after 1800 UTC 20 July 2008 before shifting suddenly southwards at 1200 UTC 21 July 2008. Finally, it moved east-northeastwards from 22 July 2008 and died out over the Yellow Sea on 23 July 2008. The track of the TPV and the horizontal pattern of associated 6-hour accumulated precipitation are shown in Fig. 2.5, and the time series of the central

maximum vertical relative vorticity and the  $3^\circ \times 3^\circ$  area-average of every 6-hour precipitation around the center of the TPV are shown in Fig. 2.6. As the TPV moved eastward from 1800 UTC 20 July 2008 onwards, it generated heavy rainfall over eastern China to its east, especially over the Sichuan Basin, and Hubei, Anhui, Henan, and Shandong provinces. As shown in Fig. 2.6, the central vertical relative vorticity intensified at 1800 UTC 20 July 2008 as the TPV began to move down the TP. On 21 July 2008, the TPV was located over the Sichuan Basin, and while the vertical relative vorticity decreased, precipitation over the center and east of the Sichuan Basin increased tremendously. The period from 0000 UTC 20 to 1800 UTC 21 July 2008 is defined as the first stage of the TPV development, during which it slid down from the TP into the Sichuan Basin and triggered severe rainfall over Sichuan Province. The second stage of the TPV is from 0000 UTC 22 to 1800 UTC 23 July 2008, during which the TPV moved northeastward and produced heavy rainfall over Hubei, Anhui, Henan, and Shandong provinces. At this stage, the vertical vorticity strengthened again at 0600 UTC 22 July 2008, then weakened gradually. However, the intensification of precipitation occurred at 0000 UTC 22 July 2008, ahead of the intensification of vertical vorticity (Fig. 2.6). This phenomenon implies that the vertical vorticity intensification may be due to the diabatic heating associated with precipitation, which will be discussed further in Section 3.3.

#### *Large-scale circulation associated with the TPV*

The distribution of the 300 and 500 hPa horizontal wind, geopotential height, and vertical relative vorticity at 0600 and 1800 UTC 20 July 2008 are presented in Fig. 2.7a and 2.7b, respectively. This figure demonstrates the circulation associated with the TPV before it moved down off the TP. At 0600 UTC 20 July 2008 (Fig. 2.7a) at 300 hPa in mid latitudes, a weak geopotential height ridge was located near  $100^\circ\text{E}$ , and a trough was located over northern China. Along the subtropics, westerly prevailed with a weak trough over the northeastern TP. At 500 hPa, the trough was near the TP surface and the circulation pattern was similar to that at 300 hPa; however, the trough over the northeastern TP was strong. A strong closed cyclone with vorticity of more than  $10^{-4}\text{s}^{-1}$ , which we defined as the TPV in the current study, was embedded in the trough. By 1800 UTC (Fig. 2.7b), the general features of the circulation had changed little, except for a shift to the east. Consequently, the eastern portion of the TPV had slid down the eastern slope of the TP, while the vorticity center was still over the eastern TP. Figure 2.7c and 2.7d are the same as Fig. 2.7a and 2.7b, but for 500 and 700 hPa at 0600 and 1200 UTC 22 July 2008, respectively, which

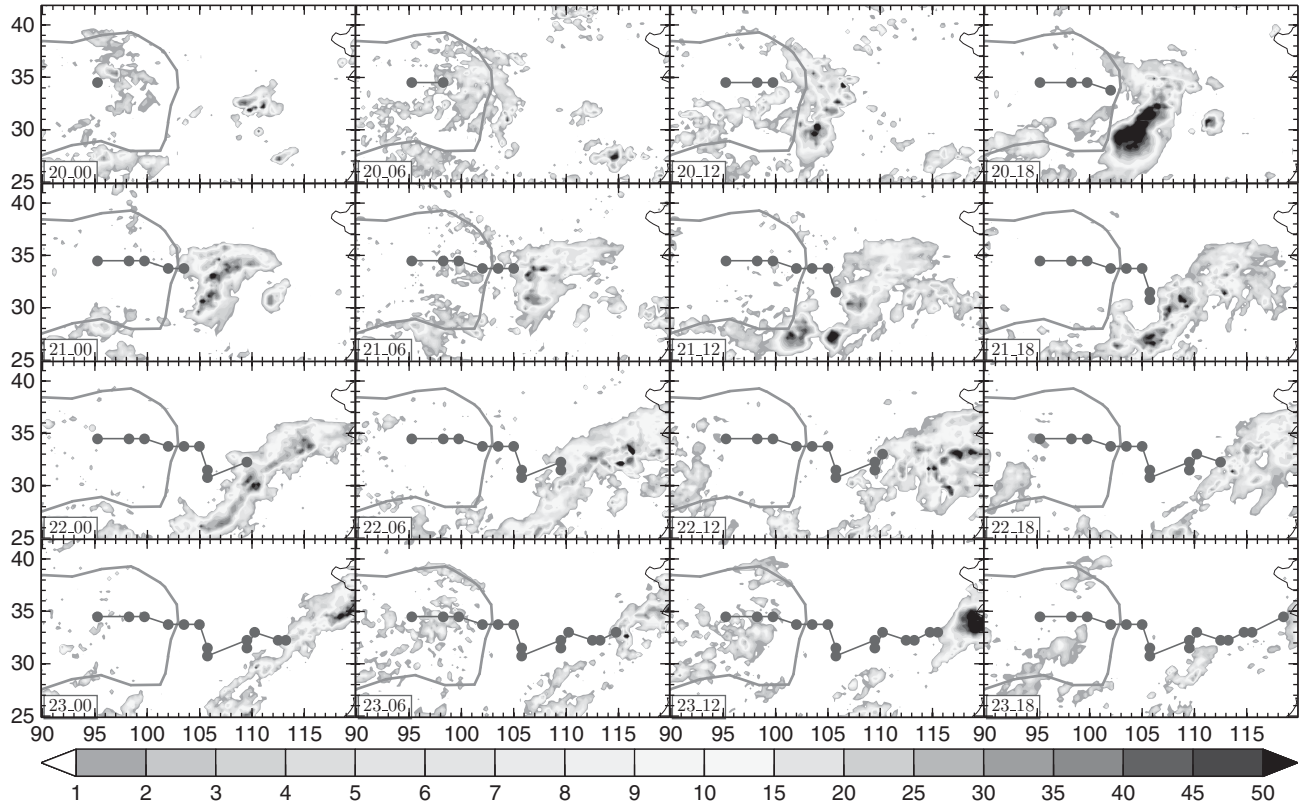


Fig. 2.5: Track of the TPV from 0000 UTC 20 to 1800 UTC 23 July 2008 and the associated 6-hour precipitation. Shading represents the TRMM 3B42 precipitation ( $\text{mm}(6\text{h})^{-1}$ ) and the blue line with solid circles indicates the track of the TPV. A black and white version of this figure will appear in some formats. [For the colour version, please refer to Plate 2.](#)

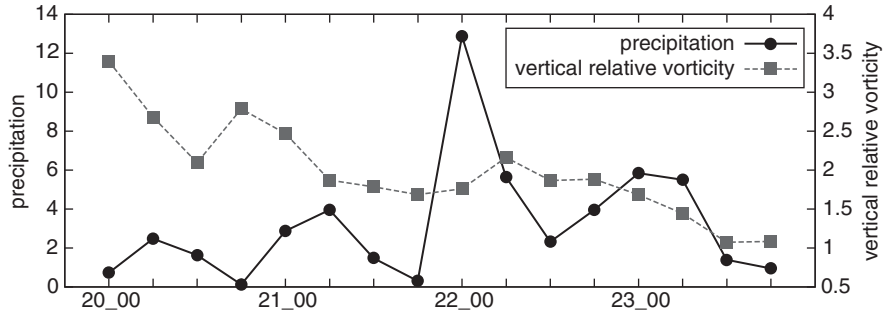


Fig. 2.6: Time series of the central maximum vertical relative vorticity ( $10^{-4}\text{s}^{-1}$ ; dashed line) of the TPV and the  $3^\circ \times 3^\circ$  area-average of precipitation ( $\text{mm}(6\text{h})^{-1}$ ; solid line) around the center of the TPV from 0000 UTC 20 to 1800 UTC 23 July 2008. A black and white version of this figure will appear in some formats. [For the colour version, please refer to Plate 9.](#)

show the circulations associated with the vortex during its second stage. The circulation showed high geopotential to the west of  $100^\circ\text{E}$  and low geopotential to its east. As the TPV moved eastward, the closed cyclone slid down to the lower troposphere, and evolved into a developing vortex at 700 hPa and an eastward moving mid-latitude trough at 500 hPa. As described above, the TPV re-intensified at 0600 UTC 22 July 2008 (Fig. 2.7c), and reached 500 hPa where the closed contour of 580 dgpm was re-established at 1200 UTC 22 July 2008 (Fig. 2.7d).

### 2.3.3 Diabatic vorticity development due to inhomogeneous heating

#### Relative contributions to vertical vorticity development of the changes in $PV_e$ , $PV_2$ , and $\theta_z$

By applying Eq. (2.38) to each term in Eq. (2.5), the change in vertical vorticity can be calculated for every time step. Figure 2.8 shows these relative contributions when the vortex slid down the TP; i.e. the relative contribution to the development of vertical vorticity due to the changes in  $PV_e$ ,  $PV_2$ , and  $\theta_z$ . It demonstrates that the contribution

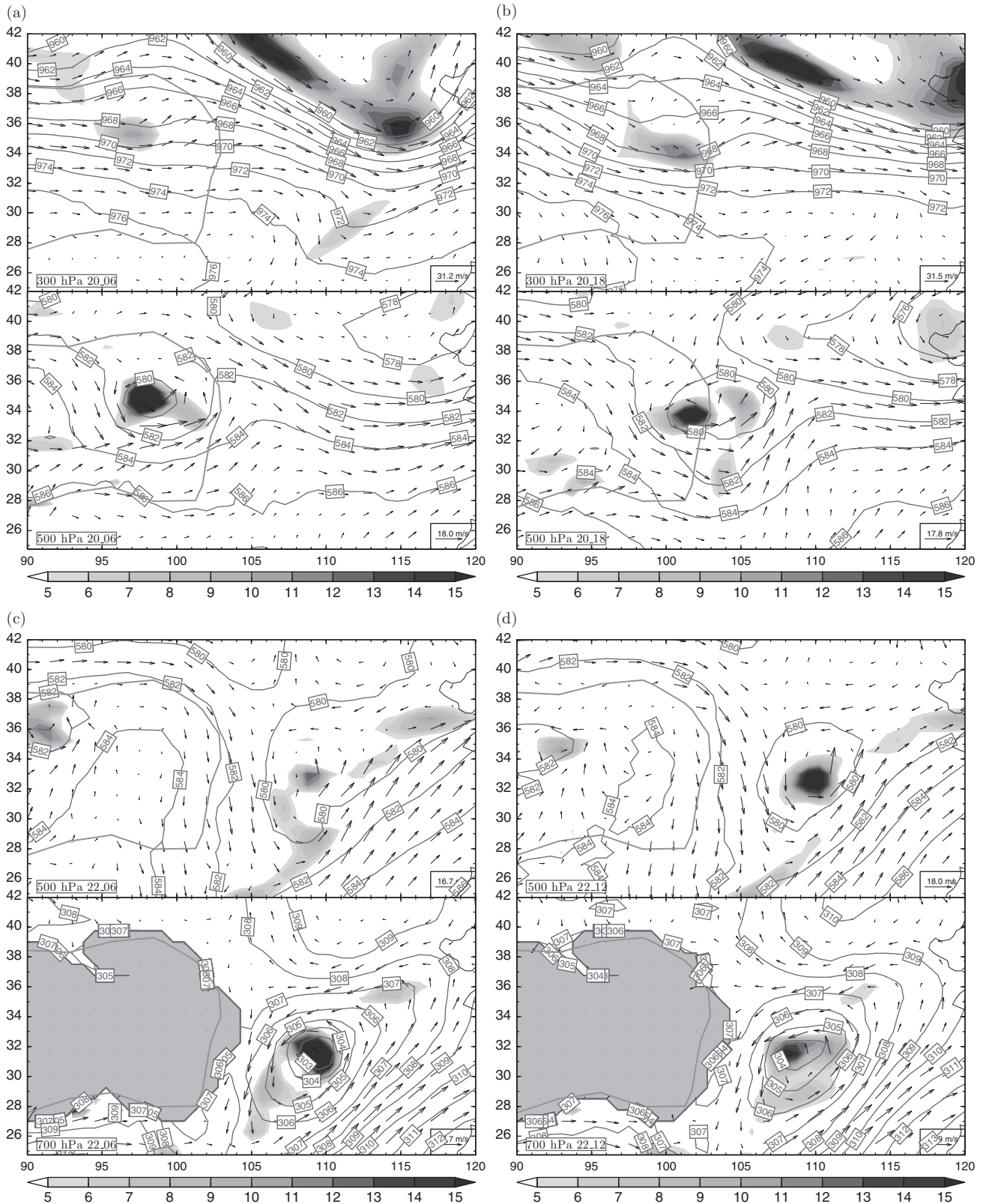


Fig. 2.7: Distributions of wind (vector), geopotential height (dgpm; contour), and vertical relative vorticity ( $10^{-5} \text{ s}^{-1}$ ; shading) at (a) 300 and 500 hPa at 0600 UTC 20, (b) 300 and 500 hPa at 1800 UTC 20, (c) 500 and 700 hPa at 0600 UTC 22, and (d) 500 and 700 hPa at 1200 UTC 22 July 2008. A black and white version of this figure will appear in some formats. For the colour version, please refer to Plate 3.

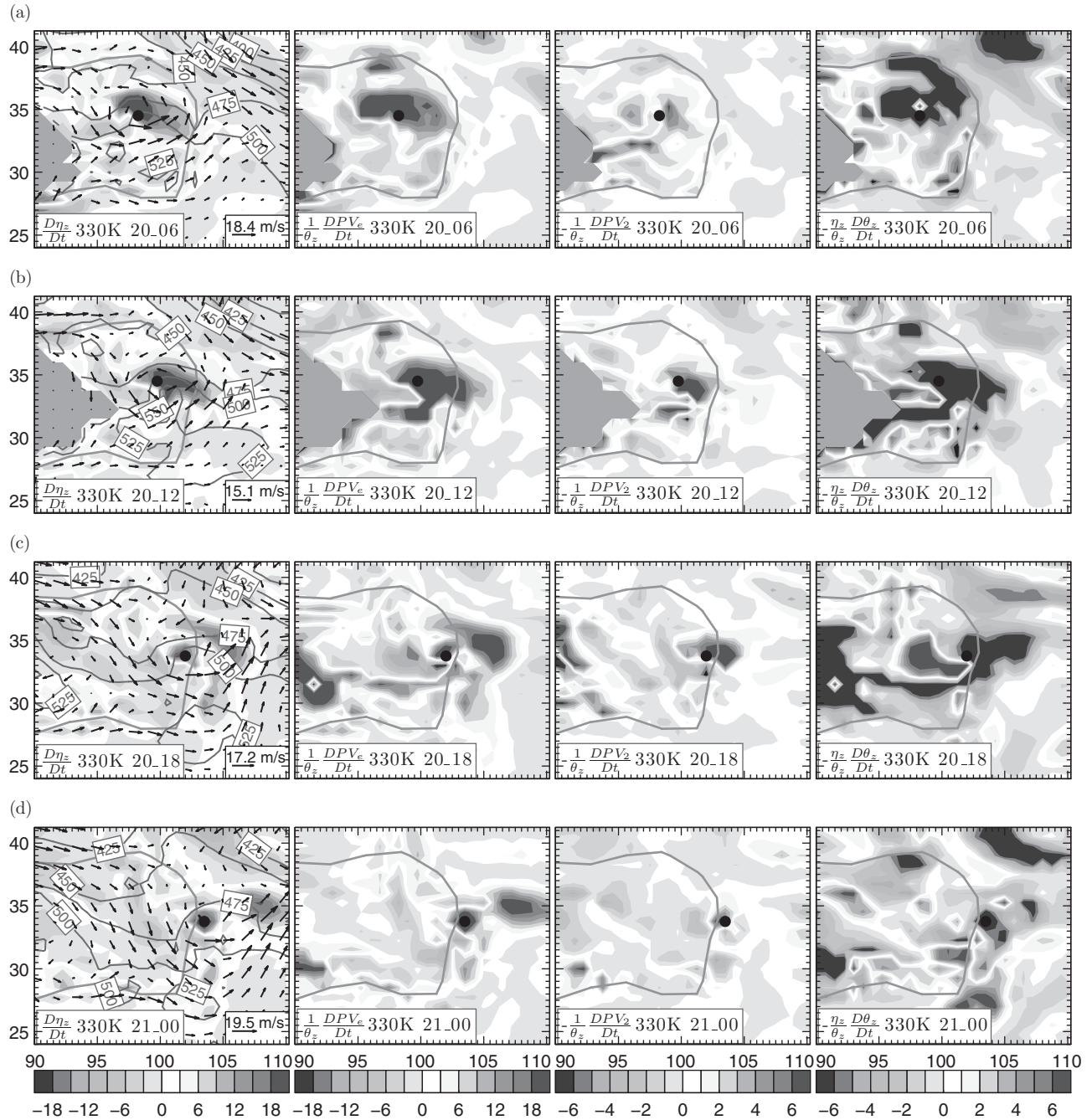


Fig. 2.8: Relative contributions to the development of vertical vorticity on the 330 K isentropic surface (first column) due to the change in  $PV_e$  (second column),  $PV_2$  (third column), and  $\theta_z$  (fourth column) at (a) 0600 UTC 20, (b) 1200 UTC 20, (c) 1800 UTC 20, and (d) 0000 UTC 21 July 2008. The vector is horizontal wind, the contour line is pressure in hPa, and the shading is in  $10^{-5} \text{m}^3(\text{kg s } 6\text{h})^{-1}$ . In this figure and following, the black solid circles indicate the location of the TPV. A black and white version of this figure will appear in some formats. [For the colour version, please refer to Plate 4.](#)

$\left(\frac{1}{\theta_z} \frac{DPV_e}{Dt}\right)$  due to the change of  $PV_e$  is analogous to the total change  $\left(\frac{D\eta_z}{Dt}\right)$  of vertical vorticity and with the same order of magnitude. The positive center of the contribution  $\left(\frac{1}{\theta_z} \frac{DPV_2}{Dt}\right)$  due to the change in  $PV_2$  is coincident with the

development center of vertical vorticity of the TPV, though weaker in magnitude compared with the impact of diabatic heating. On the other hand, the contribution  $\left(-\frac{\eta_z}{\theta_z} \frac{D\theta_z}{Dt}\right)$  due to the change in static stability  $\theta_z$  to the development of vertical vorticity is usually negative and is weaker in

magnitude; i.e. the vertical vorticity decreases when the static stability  $\theta_z$  increases. In other words, in a stable atmosphere, when the atmosphere becomes more stable, it does not favor vortex development. This differs from the linear model of flow over a mountain (on the lee side, the air column is stretched and static stability  $\theta_z$  decreases, so vertical vorticity develops). The increase in  $\theta_z$  is due to the nonlinear effect of the flow around the TP and the diabatic heating, that is, decreases in elevation and nocturnal surface cooling weaken the low-level potential temperature while the mid-level condensation latent heating associated with precipitation increases potential temperature aloft, so the Lagrangian change of  $\theta_z$  increases. The above analysis indicates that the Lagrangian change of  $PV_e$  associated with diabatic heating plays a leading role in the development of vertical vorticity during the intense development of the TPV.

During the second stage of the TPV, at 0000 UTC 22 July 2008 (Fig. 2.9a), the vertical vorticity developed at low levels near 700 hPa, and weakened at middle levels near 500 hPa. At 0600 UTC (Fig. 2.9b), the vertical vorticity intensified at both low and middle levels, and the TPV extended above 500 hPa. At 1200 UTC (Fig. 2.9c), the development of vertical vorticity near 500 hPa was maintained, but that at 700 hPa began to weaken. Afterwards, the vertical vorticity at both low and middle levels weakened and moved gradually northeastward (figure omitted). The same pattern can be seen more clearly from the contribution due to the change in  $PV_e$  (second column in Fig. 2.9). In addition, the contribution due to the change in the horizontal component  $PV_2$  of  $PV_e$  was also significant near 500 hPa at 0600 UTC (Fig. 2.9b). As during the first stage, the contribution due to the change in static stability  $\theta_z$  was negative at 0000 UTC 22 July 2008 (Fig. 2.9a). However, Fig. 2.9b and 2.9c show that the contribution due to the change in static stability  $\theta_z$  was positive surrounding the center of the vortex at the 330 K level. This indicates that in such circumstances, the static stability  $\theta_z$  contributes positively to the development of vertical vorticity; i.e. when the static stability  $\theta_z$  decreases (increases) in a stable (unstable) atmosphere, vertical vorticity will develop.

#### **Effect of the vertical gradient of diabatic heating**

The above results demonstrate that the change in  $PV_e$  plays a leading role in the development of vertical vorticity. The change of  $PV_e$  is due to friction and diabatic heating. According to Eq. (2.15), in the free atmosphere, the change in  $PV_e$  is due to diabatic heating. To understand its impact, the total change in vertical vorticity ( $\eta_z$ ), the change in  $PV_e$ , the diabatic heating ( $Q$ ), and the effect of vertical gradient of diabatic heating ( $\eta_z \frac{\partial Q}{\partial z}$ ) for the second stage are demonstrated in Fig. 2.10.

At 1800 UTC 21 July 2008, there was no significant diabatic heating at middle levels, and the low-level positive  $PV_e$  generation by the vertical gradient of diabatic heating was weak, so the development of the low-level vortex was weak and the TPV was concentrated at low levels (figure omitted). Subsequently, when the TPV arrived at the up-slope of the northeastern edge of the Sichuan Basin, the diabatic heating strengthened and uplifted gradually from 0000 to 1200 UTC 22 July 2008 (Fig. 2.10). Correspondingly, the vertical vorticity in the lower troposphere near the center of the vortex was intensified, and the TPV developed vertically above 500 hPa, which is consistent with the intensification above 500 hPa presented in Figs. 2.7c, 2.7d, and 2.9. Figure 2.10 shows that there was positive  $PV_e$  generation below the maximum of diabatic heating to strengthen the low-level vortex, and negative  $PV_e$  generation above it to weaken the upper-level vortex.

#### **Effect of the horizontal gradient of diabatic heating**

It is worthwhile noting that in Fig. 2.10, there are distinct differences between  $\frac{D PV_e}{Dt}$  and  $\eta_z \frac{\partial Q}{\partial z}$ . This implies that other factors, such as the horizontal gradient of diabatic heating, also contribute to the development of vertical vorticity under certain circumstances.

During different development stages of the TPV, the distribution of the  $PV_e$  generation ( $\eta_s \cdot \nabla_s Q$ ) due to the horizontal gradient of diabatic heating, the diabatic heating ( $Q$ ), and the vertical shear ( $\frac{\partial V_x}{\partial z}$ ) of horizontal wind are shown in Figs. 2.10 and 2.11. According to Eq. (2.16), the positive  $PV_e$  generation in association with the intensification of vertical vorticity; i.e.  $(\frac{D PV_e}{Dt})_s = \eta_s \cdot \nabla_s Q$ , is mostly located on the right side of the vertical shear ( $\frac{\partial V_x}{\partial z}$ ) of horizontal wind across the center of diabatic heating. Although the magnitude of  $PV_e$  generation due to the horizontal gradient of diabatic heating is commonly one order of magnitude less than that due to the vertical gradient of diabatic heating, sometimes it can reach the same order. Such a case developed after the vortex slid down the TP at 0600 UTC 21 July 2008 (Fig. 2.11c), and also when it was climbing up the hillside over the northeastern Sichuan Basin at 0600 UTC 22 July 2008 (Fig. 2.12b). It is evident from Figs. 2.11 and 2.12 that, in most cases, the movement of the vortex was toward positive  $PV_e$  generation on the right side of the vertical shear of horizontal wind at 400 hPa due to the horizontal gradient of diabatic heating. For example, the sudden southward shifting of the track of the vortex at 1200 UTC 21 July 2008 (Fig. 2.11d) is well correlated with the fact that the positive  $PV_e$  generation associated with the horizontal gradient of diabatic heating was located to its south. There was an exception at 1200 UTC 22 July (Fig. 2.12c) when the vortex had climbed up the hill and became weaker and stagnant above

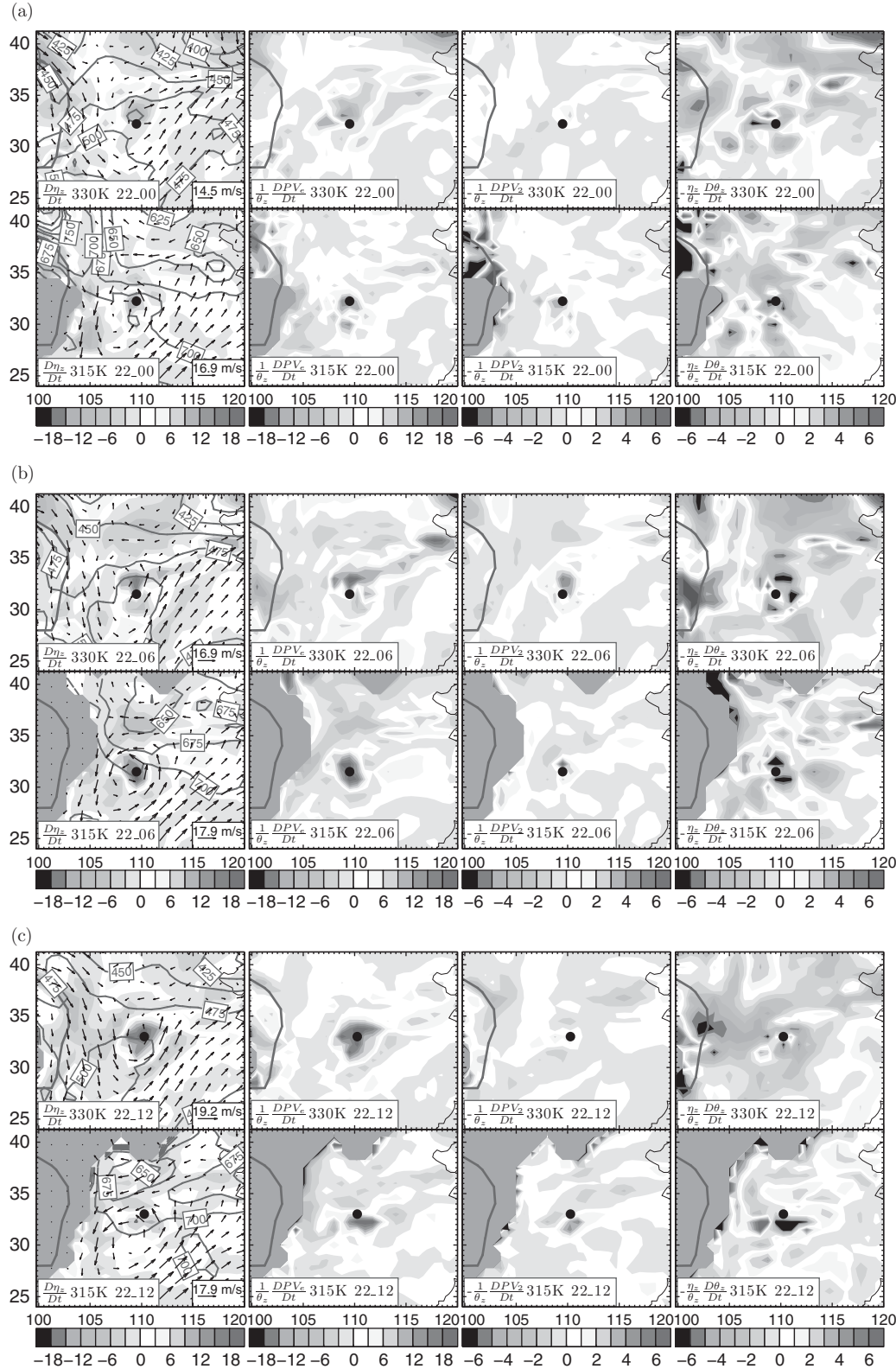


Fig. 2.9: As Fig. 2.8, but on the 330 and 315 K isentropic surfaces at (a) 0000, (b) 0600, and (c) 1200 UTC 22 July 2008. A black and white version of this figure will appear in some formats. For the colour version, please refer to Plate 5.

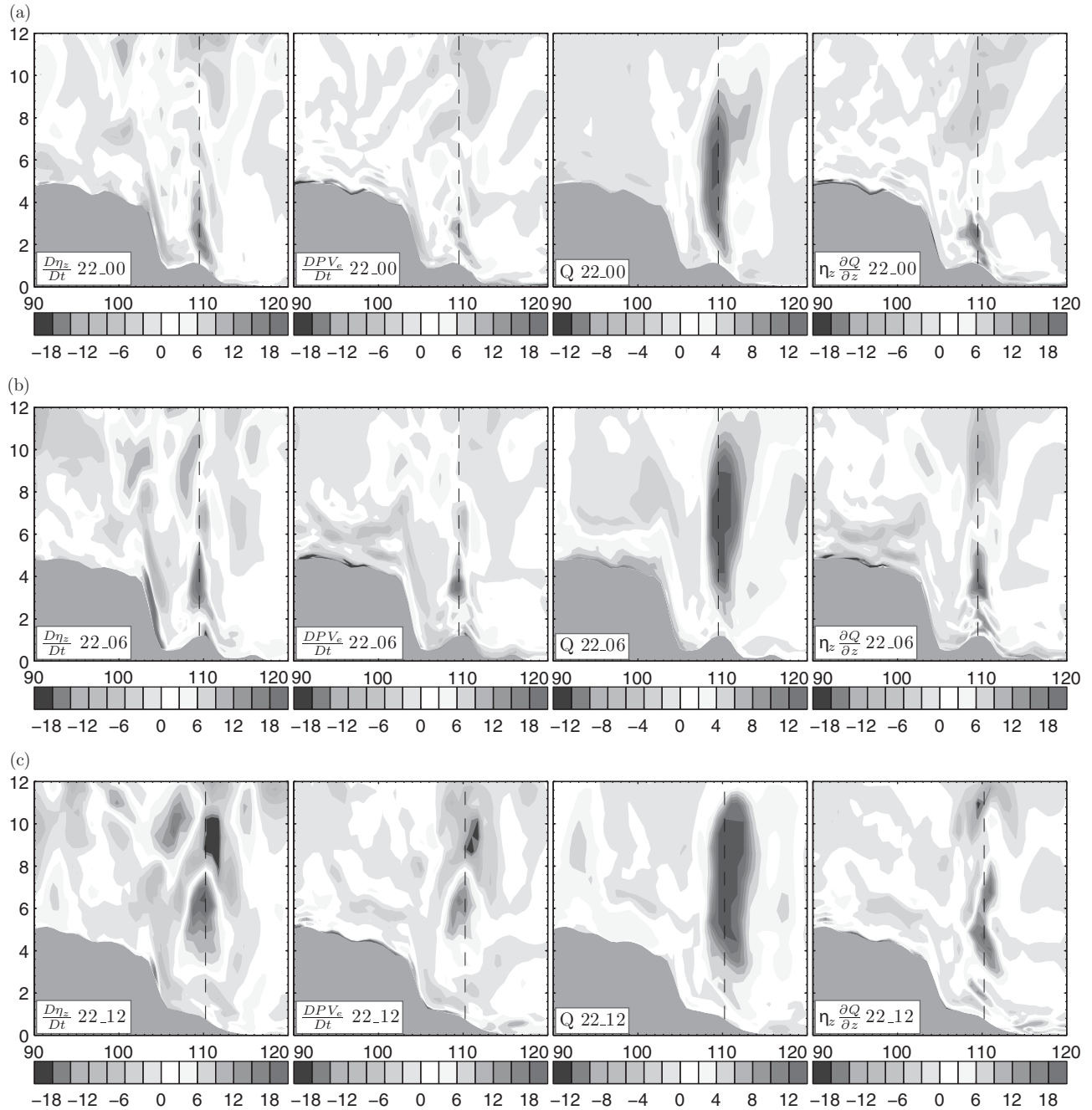


Fig. 2.10: Vertical cross-sections at (a) 0000 UTC, (b) 0600 UTC, and (c) 1200 UTC 22 July 2008 of the total change in vertical vorticity (first column;  $\frac{D\eta_z}{Dt}$ ;  $10^{-5} \text{ m}^3 (\text{kg s } 6\text{h})^{-1}$ ), the change in  $PV_e$  (second column;  $\frac{DPV_e}{Dt}$ ;  $10^{-1} \text{ PVU } (6\text{h})^{-1}$ ), the diabatic heating  $Q$  (third column; K  $(6\text{h})^{-1}$ ), and the change in  $PV_e$  due to the vertical gradient of diabatic heating (fourth column;  $10^{-1} \text{ PVU } (6\text{h})^{-1}$ ). A black and white version of this figure will appear in some formats. [For the colour version, please refer to Plate 6.](#)

it (Fig. 2.6). Even so, the maximum of  $PV_e$  generation ( $\eta_s \cdot \nabla_s Q$ ) due to the horizontal gradient of diabatic heating at that moment was still on the eastern side of the TPV, which subsequently led to the eastward movement of

the vortex. The relationship between the movement of the TPV and positive  $PV_e$  generation due to the horizontal gradient of diabatic heating was more obvious at 400 hPa than at other levels (figure omitted).

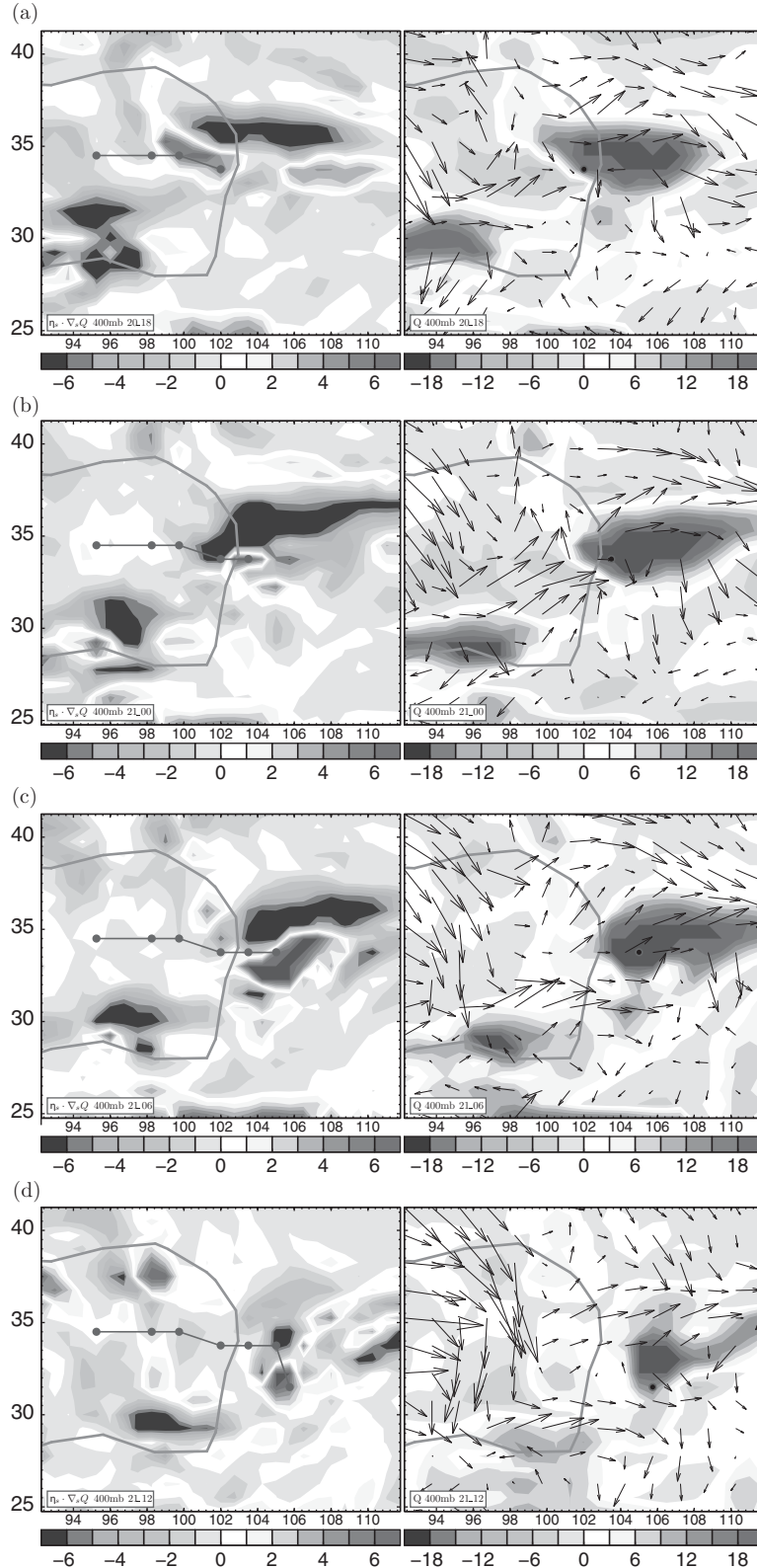


Fig. 2.11: The change at 400 hPa of  $PV_e$  (first column;  $5 \times 10^{-2}$  PVU ( $6h$ ) $^{-1}$ ) due to the horizontal gradient of diabatic heating (second column;  $5 \times 10^{-1}$  K ( $6h$ ) $^{-1}$ ) at (a) 1800 UTC 20, (b) 0000 UTC 21, (c) 0600 UTC 21, and (d) 1200 UTC 21 July 2008. The vector denotes vertical shear of horizontal wind. A black and white version of this figure will appear in some formats. For the colour version, please refer to Plate 7.

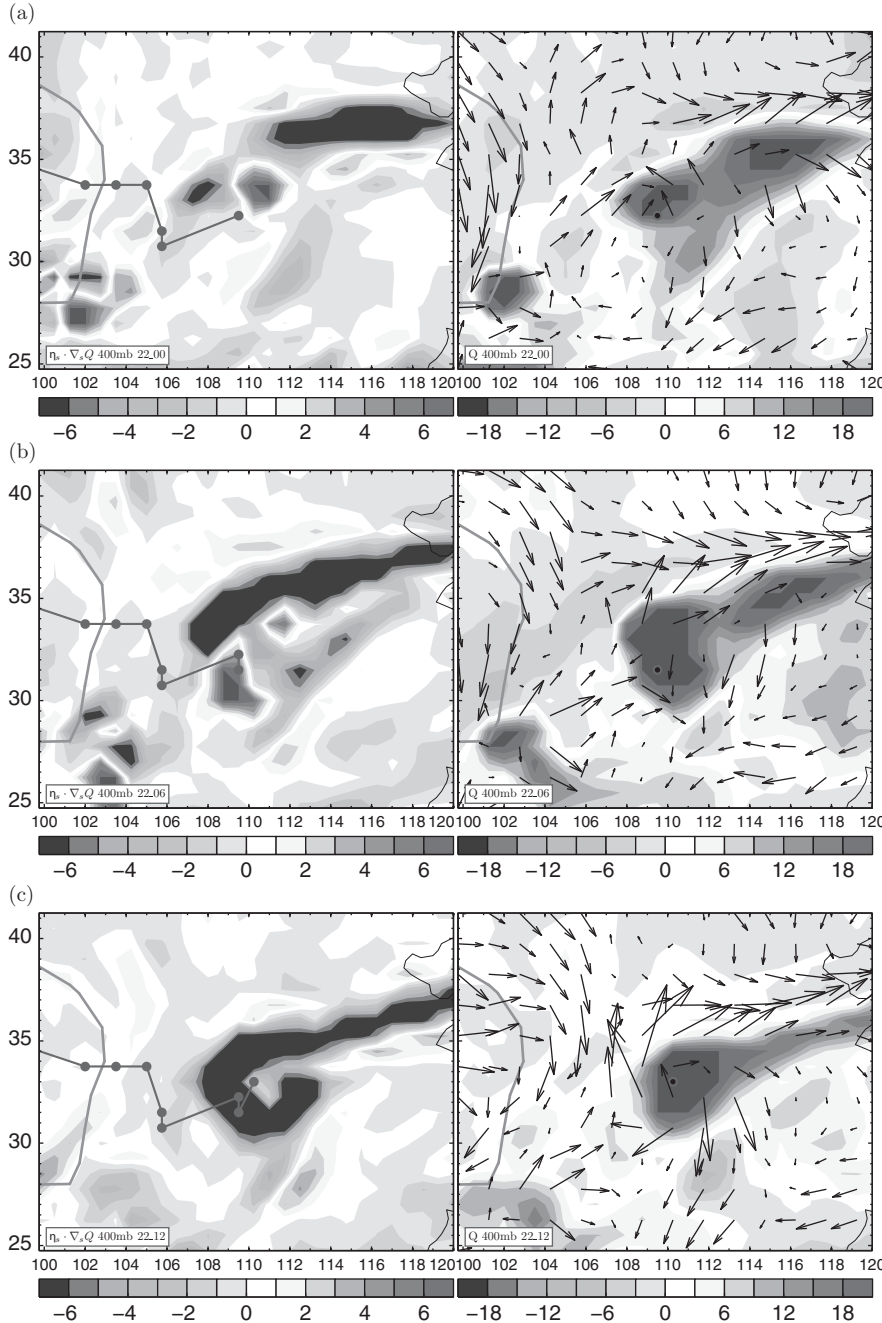


Fig. 2.12: As Fig. 2.11, but at (a) 0000, (b) 0600, and (c) 1200 UTC 22 July 2008. A black and white version of this figure will appear in some formats. For the colour version, please refer to Plate 8.

### 2.3.4 Adiabatic vorticity development due to slantwise vorticity development

The above analysis demonstrates that diabatic heating plays a leading role in the development and movement of the TPV. However, at some stage in the evolution of the vortex, the adiabatic term  $\left(-\frac{1}{\theta_z} \frac{D PV_2}{Dt}\right)$  plays a significant role in its development, which is comparable with the role of diabatic heating. An example of this situation occurred

on 22 July 2008 when the vortex was climbing the upslope of the mountain range over northeastern Sichuan Province. As shown in Fig. 2.6, the area-average precipitation associated with the TPV reached a maximum of 13 mm in 6 h at 0000 UTC 22 July 2008, and the vertical relative vorticity of the TPV was intensified to a maximum  $2 \times 10^{-4} \text{ s}^{-1}$  at 0600 UTC 22 July 2008. The evolutions of vertical vorticity development (first column in Fig. 2.10) and

diabatic heating (third column in Fig. 2.10) of the TPV indicate that its intensity and precipitation developed rapidly during this 12-hour interval. More importantly, the contribution to this development from the diabatic heating ( $\left(\frac{1}{\theta_z} \frac{DPV_e}{Dt}\right)$ , second column in Fig. 2.10) was significant, with its intensity at each time step being close to the total change ( $\left(\frac{D\eta_z}{Dt}\right)$ ) in vertical vorticity. Besides, the height of

its maximum center also increased from 2 km at 1800 UTC 21 July 2008 to 3 km at 0000 UTC 22 July 2008, and reached 4 km 6 hours later, so contributing to the vertical extension of the vortex.

Figure 2.13 shows the distribution on the 330 and 315 K isentropic surfaces of the terms  $\frac{DC_D}{Dt} = \frac{1}{\theta_z} \frac{DPV_2}{Dt} - \frac{PV_2}{\theta_z^2} \frac{D\theta_z}{Dt}$ ,  $\gamma = -\frac{PV_e}{\theta_z^2} \frac{D\theta_z}{Dt}$ , and  $\left(\frac{D\eta_z}{Dt}\right)_A = \gamma - \frac{DC_D}{Dt}$  at 0000 and 0600

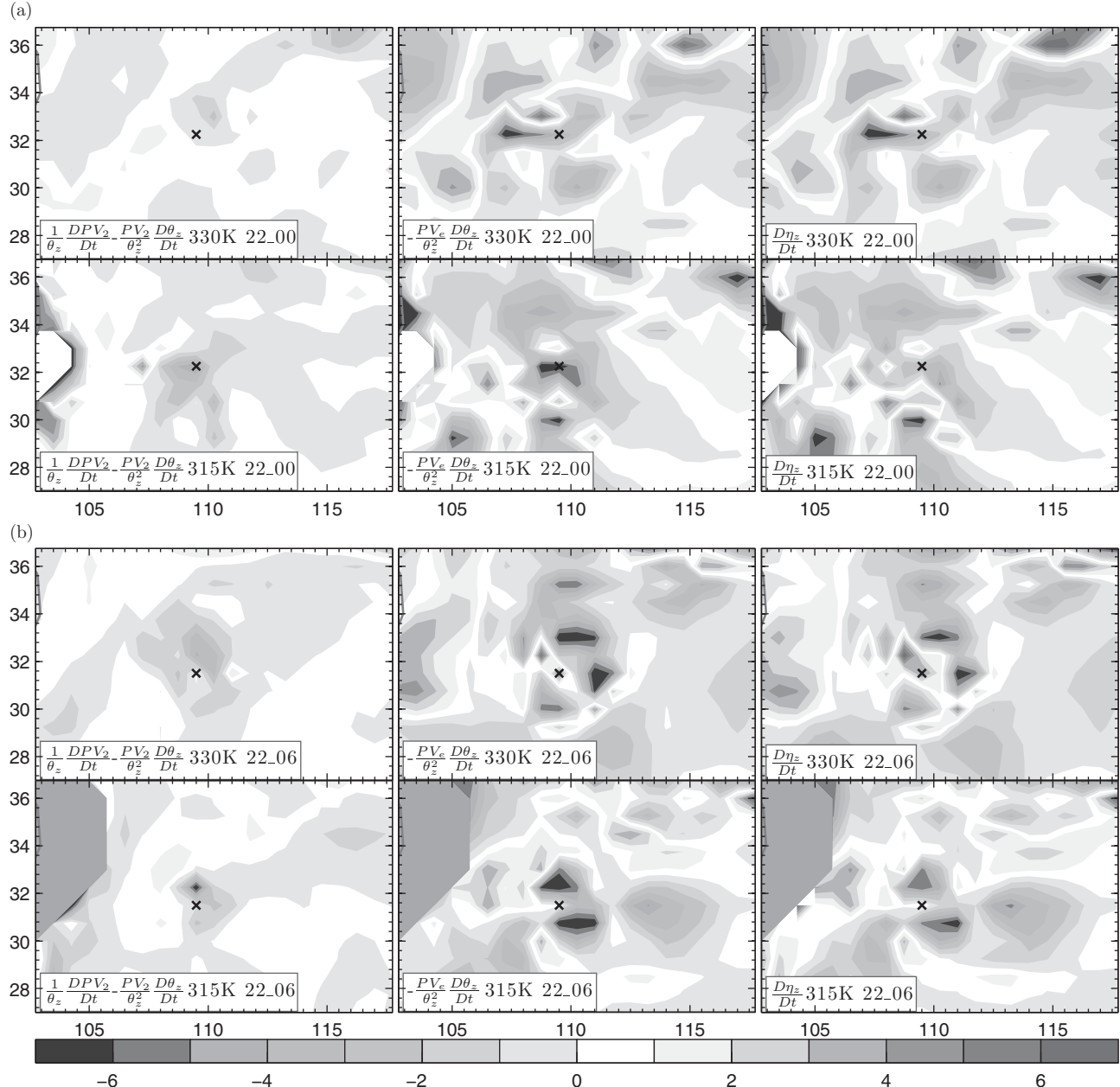


Fig. 2.13: Distributions on the 330 and 315 K isentropic surfaces of  $\left(\frac{D\eta_z}{Dt}\right)_A$  (first column);  $10^{-5} \text{ m}^3(\text{kg s } 6\text{h})^{-1}$ ,  $\gamma$  (second column;  $10^{-5} \text{ m}^3(\text{kg s } 6\text{h})^{-1}$ ), and  $\left(\frac{D\eta_z}{Dt}\right)_A$  (third column;  $10^{-5} \text{ m}^3(\text{kg s } 6\text{h})^{-1}$ ). The cross indicates the location of the TPV. (a) 0000 UTC and (b) 0600 UTC on July 22, 2008. A black and white version of this figure will appear in some formats. For the colour version, please refer to Plate 9.

UTC 22 July 2008. At 0000 UTC, in the region surrounding the vortex center on both the 330 and 315 K isentropic surfaces,  $\frac{DC_D}{Dt} > \gamma$  and  $\left(\frac{D\eta_z}{Dt}\right)_A < 0$ , implying that the criteria in Eq. (2.28) for VD were not satisfied, and the vortex development at 0000 UTC was basically due to the diabatic heating. At 0600 UTC on the 315 K isentropic surface at the center of the vortex,  $\frac{DC_D}{Dt} < \gamma$  and  $\left(\frac{D\eta_z}{Dt}\right)_A > 0$ , implying that the criteria in Eq. (2.28) for VD were satisfied, and the development of the vortex in the lower layer was at least partly due to the adiabatic contribution. However, as  $\gamma > 0$  at this level, the SVD criteria in Eq. (2.31) are violated, so the adiabatic development of the vortex should be rather limited. On the 330 K isentropic surface at the center of the vortex, not only was  $\frac{DC_D}{Dt} < \gamma$ , but also  $\frac{DC_D}{Dt} < 0 < \gamma$ . This indicates that the criteria in Eqs. (2.28) and (2.31) were satisfied, thus both VD and SVD occurred. This is consistent with the upward intensification of the TPV at 0600 UTC 22 July 2008, as presented in Fig. 2.7.

As shown in Eq. (2.36), the vertical vorticity development  $\left(\frac{D\eta_z}{Dt}\right)_A$  under adiabatic conditions is composed of two parts: the part  $\left(-\frac{1}{\theta_z} \frac{DPV_2}{Dt}\right)$  due to the change in the horizontal component ( $PV_2$ ) of potential vorticity, and the part  $\left(-\frac{\eta_z}{\theta_z} \frac{D\theta_z}{Dt}\right)$  due to the change in static stability. The part of the adiabatic development of vertical vorticity due to the change in  $PV_2$  can be expressed as

$$\begin{aligned} \left(\frac{D\eta_z}{Dt}\right)_{PV_2} &= -\frac{1}{\theta_z} \frac{DPV_2}{Dt} = -\frac{1}{\theta_z} \frac{D(\boldsymbol{\eta}_s \cdot \boldsymbol{\theta}_s)}{Dt} \\ &= -D \frac{\boldsymbol{\eta}_s \cdot \boldsymbol{\theta}_s}{Dt} - \frac{\boldsymbol{\eta}_s}{\theta_z} \cdot D \frac{\boldsymbol{\theta}_s}{Dt}. \end{aligned} \quad (2.42)$$

The second, third, and fourth columns in Fig. 2.14 demonstrate the spatial distributions of these three terms in Eq. (2.42) on the 330 and 315 K isentropic surfaces on 22 July 2008. It is evident that both of the contributions to the development of vertical vorticity due to the changes in horizontal vorticity  $\boldsymbol{\eta}_s$  and baroclinity  $\boldsymbol{\theta}_s$ , are positive. As shown in Fig. 2.1,  $PV_2 = \boldsymbol{\eta}_s \cdot \boldsymbol{\theta}_s$  is commonly negative; that is, the directions of  $\boldsymbol{\eta}_s$  and  $\boldsymbol{\theta}_s$  are opposite. The positive contributions of the two terms on the right-hand side of Eq. (2.42) imply that the change in  $\boldsymbol{\eta}_s$  is opposite to the direction of  $\boldsymbol{\theta}_s$ , and the change in  $\boldsymbol{\theta}_s$  is opposite to the direction of  $\boldsymbol{\eta}_s$ , during the development of vertical vorticity. Thus, either the component of horizontal vorticity or that of baroclinity along the projected direction is increasing when vertical vorticity develops. This confirms the conclusion of Wu and Liu (1997) that the development of vertical vorticity is not necessarily associated with conversion of the vorticity from its horizontal to vertical component caused by the uneven lifting of a vortex. In other

words, an increase in vertical vorticity may not require a decrease in horizontal vorticity, and can also be achieved by an increase in either horizontal vorticity or baroclinity along the projected direction. In summary, both the dynamical effect of horizontal vorticity, and the thermal effect of baroclinity, make positive contributions to the development of vertical vorticity.

## 2.4 Discussion and conclusions

Based on the Lagrangian change equation of vertical vorticity deduced from the equation of the three-dimensional  $PV_e$ , the development and movement of a vortex due to diabatic and adiabatic processes were studied, from both a PV-Q and a PV- $\theta$  perspective. This GVSD theory was used to diagnose the development and movement of a TPV that occurred in July 2008.

In most cases, the atmosphere below the tropopause is statically stable and under geostrophic balance,  $C_D$  and  $PV_2$  are usually negative. Thus, merely using  $C_D < 0$  as a condition for SVD on an isentropic surface is incomplete, and although an increase in the tilting angle  $\beta$  of an isentropic surface is required, it is inconvenient for operational and practical purposes. A generalized slantwise vorticity development was introduced to consider both diabatic and adiabatic processes from a Lagrangian perspective, and can be used in any coordinate system. This GSVD indicates that the non-uniformity of diabatic heating contributes not only to the intensification of vertical vorticity, but also to the movement of the vortex. The criteria for VD and SVD were developed to distinguish between the two: VD requires  $\frac{DC_D}{Dt} < \gamma$ , in which  $\gamma = -\frac{PV_2}{\theta_z^2} \frac{D\theta_z}{Dt}$ ,  $\theta_z \neq 0$ ,

whereas SVD requires  $\frac{DC_D}{Dt} < 0 < \gamma$ . This demonstrates that the demand for SVD is much more restricted than that for VD; correspondingly,  $\frac{D\eta_z}{Dt} > 0$  under VD, whereas  $\frac{D\eta_z}{Dt} > PV_e \frac{D}{Dt} \left(\frac{1}{\theta_z}\right)$  under SVD. This accounts for the frequent occurrences of frontal and cyclonic systems, and the scarcity of severe weather. When an air particle is sliding down the concave slope or up the convex slope of an isentropic surface in the stable (unstable) atmosphere with its static stability decreasing (increasing), its vertical vorticity can develop rapidly if  $C_D$  is decreasing. That is, the vertical vorticity of an air particle will intensify rapidly when its static stability approaches zero; i.e. the particle is inclined to neutral stratification, if  $C_D$  decreases. The intensity of vertical vorticity development due to SVD can be estimated as  $\frac{D\eta_z}{Dt} > PV_e \frac{D}{Dt} \left(\frac{1}{\theta_z}\right)$ , which indicates that when the atmosphere approaches neutral stratification, the development of vertical vorticity approaches infinity.

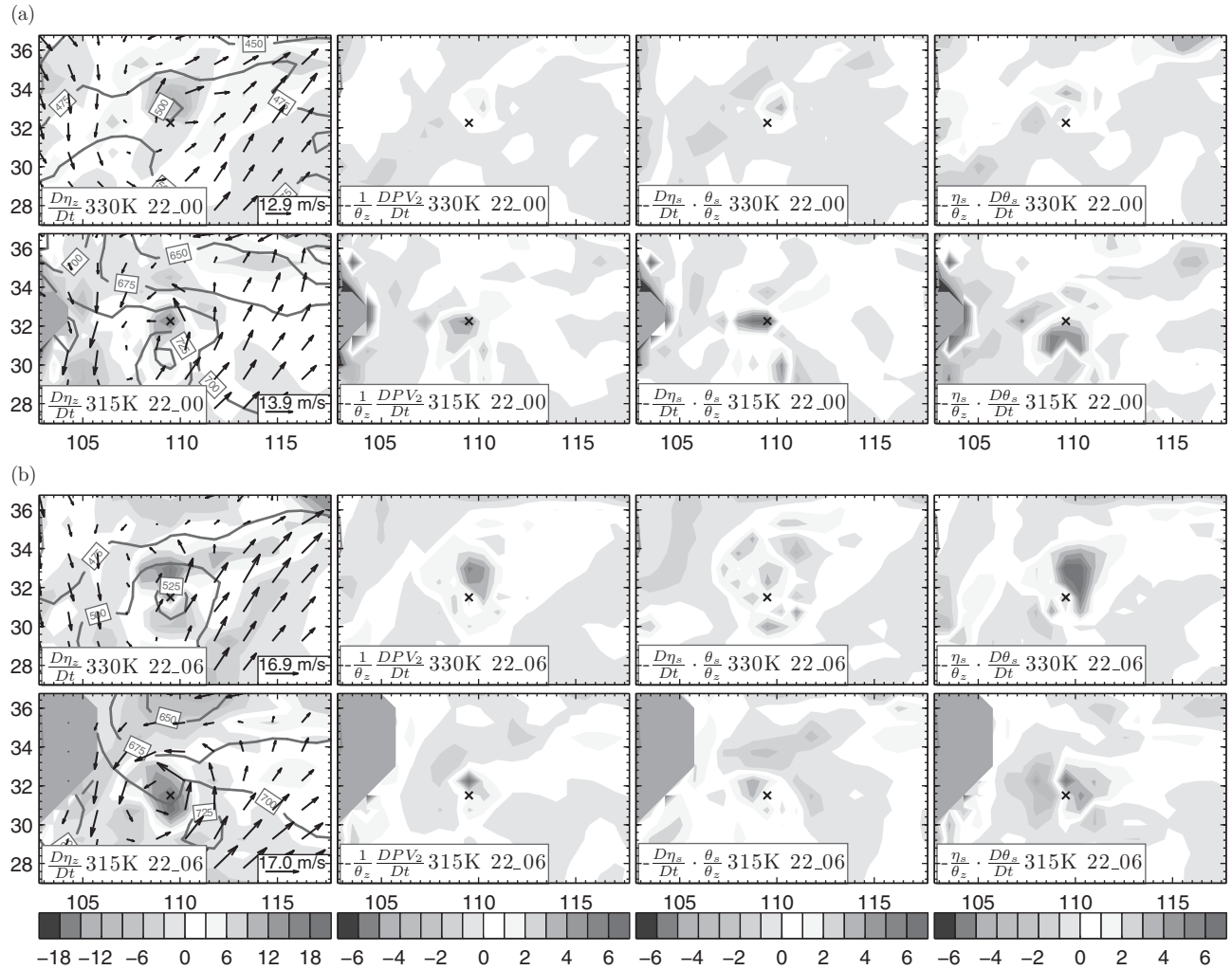


Fig. 2.14: Contribution to the development of vertical vorticity (first column;  $10^{-5} \text{ m}^3(\text{kg s } 6\text{h})^{-1}$ ) due to the change in  $PV_2$  (second column;  $0.5 \times 10^{-5} \text{ m}^3(\text{kg s } 6\text{h})^{-1}$ ), the change in  $\eta_s$  (third column;  $0.5 \times 10^{-5} \text{ m}^3(\text{kg s } 6\text{h})^{-1}$ ), and the change in  $\theta_s$  (fourth column;  $0.5 \times 10^{-5} \text{ m}^3(\text{kg s } 6\text{h})^{-1}$ ). A black and white version of this figure will appear in some formats. [For the colour version, please refer to Plate 10.](#)

The relative contribution to the development of vertical vorticity due to the change in  $PV_e$ ,  $PV_2$ , and  $\theta_z$  demonstrates that in a static stable atmosphere, the Lagrangian change of  $PV_e$  associated with diabatic heating plays a leading role; the change of  $PV_2$  has a positive, but less significant contribution; and the change of  $\theta_z$  usually has a negative effect in a stable environment as the atmosphere becomes more stable. However, in some cases surrounding the center of the vortex, the vertical vorticity develops rapidly as the static stability decreases (increases) in the stable (unstable) atmosphere. These observations indicate that strong stable and unstable conditions alone are not indicative for the development of a vortex, while near neutral stratification is favorable for the development of a vortex; i.e. the vertical vorticity will develop rapidly when  $\theta_z \rightarrow 0$ . The vertical gradient of the diabatic heating

creates positive (negative)  $PV_e$  generation that strengthens (weakens) the vertical vorticity below (above) the maximum of diabatic heating. The re-intensification of the TPV, the vertical extent of which extends above 500 hPa during its second stage, is mainly due to the re-strengthening and the vertical uplifting of the diabatic heating. As condensation heating usually occurs on the eastern side of a vortex, the effect of the vertical non-uniform heating is to move the vortex eastwards, as well as to intensify the local vertical vorticity. The horizontal gradient of diabatic heating causes positive (negative)  $PV_e$  generation on the right (left) side of the vertical shear of horizontal wind. The horizontal non-uniform heating not only intensifies the vertical vorticity on the right side of the vertical shear of horizontal wind, but also leads to the movement of the vortex towards the positive  $PV_e$  generation site.

At some stages of the TPV, the VD criteria are violated, implying that the vortex development depends solely on the diabatic heating. At other stages, the VD criteria are satisfied while the SVD criteria are violated, and the adiabatic development of the vortex is limited. At one point; i.e. 0600 UTC 22 July, on the 330 K isentropic surface, both the VD and SVD criteria were satisfied, and the adiabatic intensification of vertical vorticity contributed to the upward development of the vortex. It was further demonstrated that the change in  $PV_2$  contributed to the intensification of the TPV from 0000 TO 0600 UTC 22 July 2008, when it slid up the up-slope of the north-eastern mountain in the Sichuan Basin, because the changes in both horizontal vorticity and baroclinicity had a positive effect on the development of vertical vorticity.

The appearance of the strong signals concerning VD and SVD in the region surrounding the vortex compared with other parts of the troposphere indicates that GSVD can serve as a useful tool for diagnosing the development of severe weather systems. As the SVD has been extended to a saturated moist atmosphere (Wu *et al.*, 1995) and can be extended to an unsaturated moist atmosphere (Gao *et al.*, 2004), GSVD should be extended to a moist atmosphere in future to investigate the mechanisms that drive the formation and development of severe weather, such as the torrential rain in summer.

Diabatic heating plays a leading role in the development of vertical vorticity on most occasions, and static stability plays a significant role in the adiabatic development of vertical vorticity under the constraint of conservation of  $PV_e$ . In the real atmosphere, diabatic heating and static stability can interact in a complex feedback manner. It will be both important and challenging to further investigate the effect of this feedback on the development of severe weather systems. In addition, ongoing study of the relationship between the horizontal movement and horizontal gradient of diabatic heating, and its robustness, is required for verification. Also, the formation of the TPV, which was not considered in this study, is an interesting topic that is worthy of thorough investigation.

## References

- Chen, B., Z. Qian, and L. Zhang (1996). Numerical simulation of the formation and development of vortices over Qinghai-Xizang Plateau in summer. *Scientia Atmosferica Sinica*, **20**, 491–502. (in Chinese)
- Chen, Z., W. Min, and M. Xu (2004). Mesoscale characteristics of the unbalanced force of atmospheric motion and environmental fields of rain storm on 20–21 July 1998. *Acta Meteor. Sinica*, **62**, 375–383. (in Chinese)
- Cui, X., G. Wu, and S. Gao (2002). Numerical simulation and isentropic analysis of frontal cyclone over the western Atlantic Ocean. *Acta Meteor. Sinica*, **60**, 385–399. (in Chinese)
- Cui X., S. Goa, and G. Wu, (2003). Up-sliding slantwise vorticity development and the complete vorticity equation with mass forcing. *Adv. Atmos. Sci.*, **20**(5), 825–836.
- Dee, D.P., S.M. Uppala, A.J. Simmons, *et al.* (2011). The ERA-Interim reanalysis: Configuration and performance of the data assimilation system. *Quart. J. Roy. Meteo. Soc.*, **137**, 533–597.
- Ding, Y. (1993). *Monsoons over China*. Beijing: Springer.
- Ding, Y. (2005). *Advanced Synoptic Meteorology*. Beijing: China Meteorological Press. (in Chinese)
- Ding, Z. and J. Lu (1990). A numerical experiment on the eastward movement of a Qinghai-Xizang Plateau vortex. *J. Nanjing Institute of Meteorology*, **13**, 426–433. (in Chinese)
- Ertel, H. (1942). Ein neuer hydrodynamischer Wirbelsatz. *Meteorology Z.* **59**, 33–49.
- Gao, S., X. Wang, and Y. Zhou (2004). Generation of generalized moist potential vorticity in a frictionless and moist adiabatic flow. *Geophys. Res. Lett.*, **31**, L12113.
- Group of Tibetan Plateau Low System (1978). The preliminary research on the formation and development of the Tibetan Plateau vortex in boreal summer. *Sci. China (Ser. A)*, **3**, 341–350. (in Chinese)
- Hoskins, B., M. McIntyre, and A. Robertson (1985). On the use and significance of isentropic potential vorticity maps. *Quart. J. Roy. Meteor. Soc.*, **111**, 877–946.
- Huffman, G., R. Adler, D. Bolvin, *et al.* (2007). The TRMM multi-satellite precipitation analysis: Quasi-global, multi-year, combined-sensor precipitation estimates at fine scale. *J. Hydrometeorol.*, **8**, 38–55.
- Jiang, Y., Z. Chen, and Z. Zhou (2004). Slantwise vorticity development and meso- $\beta$  scale low vortex. *Journal of PLA University of Science and Technology*, **5**, 81–87. (in Chinese)
- Li, G. (2002). *The Tibetan Plateau Dynamic Meteorology*. Beijing: China Meteorology Press. (in Chinese)
- Liu, F. and M. Fu (1985). A study on the eastward moving lows over Qinghai-Xizang Plateau. *Plateau Meteorology*, **5**, 125–134. (in Chinese)
- Liu, Y.M., G.X. Wu, H. Liu, and P. Liu (2001). Condensation heating of the Asian summer monsoon and the subtropical anticyclone in Eastern Hemisphere. *Clim. Dyn.*, **17**(4), 327–338.
- Ma, L., Z. Qin, and Y. Duan (2002). Case study on the impact of atmospheric baroclinicity to the initial development of Jian-ghuai cyclones. *Acta Oceanologica Sinica*, **24**, 95–104.
- McGregor, J. (1993). Economical determination of the departure points from the Semi-Lagrangian models. *Mon. Wea. Rev.*, **121**, 221–230.
- Qiao, Q. (1987). The environment analysis on 500 hPa vortexes moving eastward out of Tibetan Plateau in summer. *Plateau Meteorology*, **6**, 45–55. (in Chinese)
- Qiao, Q. and Y. Zhang (1994). *Synoptic Meteorology of the Tibetan Plateau*. Beijing: China Meteorology Press. (in Chinese)
- Shen, R., E. Reiter, and J. Bresch (1986). Numerical simulation of the development of vortices over the Qinghai-Xizang (Tibet) Plateau. *Meteor. Atmos. Phys.*, **35**, 70–95.
- Sun, G. and B. Chen (1988). Dynamic processes of the moving and development low over Qinghai-Xizang Plateau during

- the early summer. *Journal of Chinese Academy of Meteorological Sciences*, **3**, 56–63. (in Chinese)
- Tao, S. (1980). *Chinese Rainstorms*. Beijing: Science Press. (in Chinese)
- Tao, S. and Y. Ding (1981). Observational evidence of the influence of the Qinghai-Xizang (Tibet) Plateau on the occurrence of heavy rain and severe convective storms in China. *Bull. Amer. Meteor. Soc.*, **62**, 23–30.
- Wang, Y., Y. Wang, and L. Zhang (2007). The development of slantwise vorticity near a weakened tropical cyclone. *Journal of Tropical Meteorology*, **23**, 47–52. (in Chinese)
- Wu, G., Y. Cai, and X. Tang (1995). Moist potential vorticity and slantwise vorticity development. *Acta Meteor. Sinica*, **53**, 387–405. (in Chinese)
- Wu, G. and H. Liu (1997). Vertical vorticity development owing to down-sliding at slantwise isentropic surface. *Dyn. Atmos. Ocean.*, **27**, 715–743.
- Wu, G. and Y. Liu (2000). Thermal adaptation, overshooting, dispersion, and subtropical anticyclone. Part I: Thermal adaptation and overshooting. *Chinese J. Atmos. Sci.*, **24**, 433–446. (in Chinese)
- Wu, G., Y. Zheng, and Y. Liu (2013). Dynamical and thermal problems in vortex development and movement. Part II: Generalized slantwise vorticity development. *Acta Meteor. Sinica*, **27**(1), 15–25, doi: 10.1007/s13351-013-0102-2
- Ye, D. and Y. Gao (1979). *The Tibetan Plateau Meteorology*. Beijing: Science Press. (in Chinese)
- Zhang, J., B. Zhu, and F. Zhu (1988). *Progresses in Tibetan Plateau Meteorology*. Beijing: Science Press. (in Chinese)
- Zheng, Y., G. Wu, and Y. Liu (2013). Dynamical and thermal problems in vortex development and movement. Part I: A PV-Q View. *Acta Meteor. Sinica*, **27**(1), 1–14, doi: 10.1007/s13351-013-0101-3.

# 3

## Probabilistic extreme event attribution

Pardeep Pall, Michael Wehner, and Dáithí Stone

### 3.1 Introduction

Extreme weather often has direct and immediate impacts on the public. Whenever a particularly serious weather-related event occurs, many people want to know if it was caused, in some deterministic sense, by human-induced climate change. While this is a legitimate question, it is ill-posed because of the chaotic nature of weather in the climate system and uncertainty in the event's antecedent conditions, so that many untraceable drivers, anthropogenic or natural, may have contributed to the occurrence of an individual event. Thus, as well as occurring in reality, the event could also have occurred at that time, by chance, in a counterfactual 'natural' world in which human drivers had never existed. Instead, any treatment of the question has to be formulated in probabilistic terms. By defining climate as encompassing all possible weather that might have materialized at the time of the event, as consistent with the antecedent uncertainty, we can ask a better-posed question: to what extent have human drivers affected the probability of the weather-related event occurring between real and natural world climates?

This is the central idea behind Probabilistic extreme event attribution (PEEA). As we will further elaborate in this chapter, the PEEA framework can allow one to distinguish the influence of human (or other) climate drivers on the probability of an event occurring, from that of natural drivers, and thus arrive at attribution statements that address the above question in terms of changes in probability of the event. Along the way we will describe how the event itself might be defined in terms of a given magnitude or percentile of some metric, and how, in the absence of observations of all possible weather realizations, a modelling-based approach may be used, as well as limitations of and future research on PEEA.

The first PEEA-type study, following the approach initially proposed by Allen (2003) and formalized by Stone and Allen (2005), was by Stott *et al.* (2004), who analysed the hot European summer of 2003. This unprecedented

event included a two-week heat wave associated with 70,000 excess deaths in France, Italy, Spain, and Germany (Robine *et al.*, 2008). Near the centre of the action, the average Swiss summer temperature exceeded the long-term seasonal average by as much as  $\sim 5$  °C (Schär *et al.*, 2004). Stott *et al.* (2004) compared, observed, and simulated summer temperatures and found that the odds of a hot summer over a large region of southern Europe were at least doubled by human-induced climate change. Their methodology, focusing on a specific event, was a significant step forward from conventional 'detection and attribution' studies (Bindoff *et al.*, 2013) that use an established multiple linear regression-based technique to optimally detect the fingerprint of large-scale (sub-continental to global) long-term (decadal to centennial) changes in relatively well observed variables (e.g. mean and, more recently, extreme temperature and precipitation – e.g. Min *et al.* 2009, Min *et al.* 2011, Min *et al.* 2013) and attribute these (or not) to human or other external climate drivers. However, it is important to note that an intermediate step in Stott *et al.* (2004) nevertheless relied critically on results from such 'optimal fingerprinting' studies that provided the large-scale human-induced mean surface warming signal, according to which modelled European summer temperature variability was scaled. More recent PEEA studies have progressed from temperature-related events to more complex hydrometeorological events such as floods (Pall *et al.*, 2011, Wolski *et al.*, 2014), but still incorporate optimal fingerprinting results in a similar manner (see Section 2.4).

In fact, a wide variety of extreme weather-related events can be subjected to a PEEA-type framework, and whilst the above studies, and this chapter, focus on approaches within that framework that use both observations and climate model simulations to estimate changes in event probability, it is not the only attribution framework under development. For instance, as applied to the 2010 Russian heat wave, a related approach used an empirical model of

the probability of a record event, based on observations, to estimate the trend in probability of record events (Rahmstorf and Coumou, 2011; see also Wergen *et al.*, 2014); in concert with evidence that the average regional warming is due to human-induced emissions, one thus infers a human influence on record events. Another alternative, but complimentary, approach decomposed the anomalous magnitude of the heat wave into various components attributed to be related to, for example, predictability from the anomalous ocean state, atmospheric dynamics, and the regional mean trend (Dole *et al.*, 2011). Thus this latter more process-based approach determines the change in magnitude of an event having a given occurrence probability, as opposed to the change in occurrence probability of a given magnitude of event. This contrast leads to the curious situation for most contemporary extreme events that emissions may have substantially altered the probability of an event, while providing only a minor perturbation to the anomalous magnitude – a direct consequence of the generally exponential-shaped tail of the temperature-based probability distributions used to characterize the heat wave (Otto *et al.*, 2012).

The numbers of PEEA and other types of attribution studies are increasing at a rapid pace, and advances in climate model sophistication and resolution and in observational systems suggest that the variety of events studied could also increase. This has motivated the attribution community to produce an attribution-focused supplement accompanying the Bulletin of the American Meteorological Society's annual State of the Climate Report. The 2011 supplement (Peterson *et al.*, 2012) featured analyses of six events. The same annual supplement issued the following year (Peterson *et al.*, 2013), featured analyses of 12 events by 18 teams. These analyses cover a range of significant events from seasonal heat waves to anomalously wet seasons, at a variety of locations worldwide. Some of these events have clearly identifiable human drivers, which may either increase or decrease the impact. As human changes to the climate system continue to increase, the fraction of overall event probability attributable to those changes will continue to change as well.

Finally, while all the above studies are reactive to extreme events that have already occurred some months or years in the past, the growing public demand for attribution statements in the immediate aftermath of damaging events has motivated work towards a more proactive, near-real-time, response. This effort was pioneered by the Weather Risk Attribution Forecast project (<http://www.csag.uct.ac.za/~daithi/forecast/index.html>), which implements the PEEA framework in a seasonal forecast mode – making a climate model-based forecast of change in event probabilities between real and natural climates about a month ahead of time, where the events are predefined based on temperature

and precipitation indices (e.g. fifth hottest month in the historical record) in predefined regions spanning the globe. Several issues have been uncovered along the way in this essentially proof-of-concept project, including those of model reliability, conditionality of results on climate model boundary conditions, and of event definition. Indeed, developing near-real-time attribution products is currently one of the most active research areas in the attribution field, as evidenced for example by the subsequent C20C+ project (Kinter and Folland, 2011; see Section 2.4) that is generating multi-model estimates of attributable changes in event probabilities over both of the latter decades of the twentieth century, in order to better understand historical behaviour, through to the present time and beyond, in order to better understand near-future behaviour.

## 3.2 Concepts

### 3.2.1 Weather versus climate

As outlined in our opening, we define the climate as the statistics (mean, variability, etc.) of all possible weather that might have materialized at the time of the event, given the uncertainty in our knowledge of the event's initial conditions (Lorenz, 1982, Allen, 2003); typically, estimated over the initial state of the preceding few weeks', months', or season's weather. This conceptual definition is in contrast to more traditional empirical definitions of climate as the statistics of weather over some long time period, typically a few decades (Baede, 2001), which we prefer not to use as this does not account for the fact that the statistics of the weather may not have remained stationary over that period.

Adopting this definition of climate, however, presents two challenges when estimating event probabilities in 'real' and 'natural world' climates: (1) we only have a single observed materialization of the weather at the time of the event, which is problematic for determining all possible weather in the real world and associated uncertainty; (2) we have no observed materializations whatsoever of the possible 'natural world' weather that might have occurred at the time of the event. Thus we must resort to modelling of some form to generate samples of real and natural world event probabilities. Typically, efforts centre on using computer climate models to generate ensembles of weather simulations consistent with observational records, and possibly the use of statistical techniques to then make inference about extreme values (Stott *et al.*, 2013).

### 3.2.2 Risk versus probability

It is important, at this point, to note the distinction between event probability and event risk. To decision makers, *risk = probability of occurrence x damage*. So whilst a weather event (e.g. a hurricane) may have a certain probability of

occurrence, damage may not arise from the meteorological event itself but rather through a mediating weather-related event (e.g. a flood), which itself may be affected by a number of drivers, such as land cover change and water resource management changes. The amount of damage also depends on what is vulnerable to that event (e.g. communities, infrastructure, communications, transport, and businesses). Depending on the nature of the event, this damage function may vary widely in its complexity – reflecting sensitivity to magnitude and time scale of the weather event, the area affected in terms of administrative jurisdictions, and the influence of antecedent conditions (e.g. recent forest fires or logging increasing vulnerability to mudslides during a heavy rainfall event) or a lagged response (e.g. a heavy winter snowfall event contributing later to spring floods). This distinction between probability and risk is critical in, for example, the field of insurance when considering whether a potential portfolio is sufficiently at risk to provide cover, even in the presence of a high event probability (Reichenmiller *et al.*, 2010). To date, PEEA studies, while referring to risk, use this term erroneously only as a shorthand – as we will encounter in the next section – and have actually in strict terms focused on event probability with no treatment of damage; instead typically assuming other drivers including changes in vulnerability to be unchanging (Huggel *et al.* 2013).

### 3.2.3 Metrics of attributable risk

The concept of PEEA can be formalized in a few alternative, but related, metrics that have been used in a variety of attribution studies (Bindoff *et al.*, 2013). We present them here as a guide and to highlight some of the issues that arise when attempting to formalize a quantitative answer to the event attribution question. Central to all of the metrics is the notion of a threshold above which the extreme event is deemed to have occurred, and so a risk of threshold exceedance. Typically, this threshold is based on the observed magnitude of the event, or on observations of the previous highest magnitude of similar events in the preceding record.

#### Risk ratio (RR)

This is the most straightforward metric. It is defined as

$$RR = R_{real}/R_{nat}, \quad (3.1)$$

where  $R_{real}$  is the risk of the event occurring in a ‘real world’ climate, including the influence of human-induced climate change; and  $R_{nat}$  is the corresponding risk in a hypothetical ‘natural world’ climate for that same period, not including the influence of human-induced climate change (Stone and Allen, 2005). Thus if, e.g.  $R_{real}$  is 30%

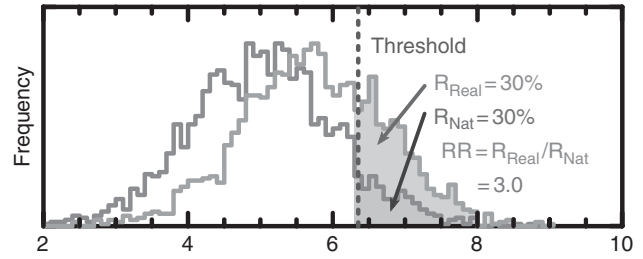


Fig. 3.1: Schematic example of a risk ratio calculation for an extreme event.

and  $R_{nat}$  is 10%, then event risk has trebled due to human-induced climate change (Fig. 3.1). That is to say, the risk of the event occurring when it did was, on average, three times higher than it would have been in the absence of human-induced climate change. Note however, that, in itself, reporting  $RR$  provides no information on how rare the event was, and thus how concerned one should be with the event occurring in the first place (compare, e.g.  $R_{real}/R_{nat} = 30\%/10\%$  to  $R_{real}/R_{nat} = 0.3\%/0.1\%$ ).

Frequency distributions are generated for an event’s magnitude (e.g. summer temperature anomaly; bottom axis) in a ‘real world’ (top distribution) and ‘natural world’ (bottom distribution) climate. The frequency of exceedance of some threshold representing an extreme realization of that event (vertical dashed line; usually based on observations) then gives real world and natural world event occurrence probabilities (shaded areas) that are multiplied by respective damage functions to arrive at respective event risks. In this schematic, the event risk is 30% in the real world and 10% in the natural world, giving a risk ratio,  $RR$ , of 3.0.

#### Fraction of attributable risk (FAR)

This metric has its roots in epidemiology and environmental law (Stone and Allen, 2005) as a more intuitive way of expressing how much of the current risk is due to a particular agent. It is defined as

$$FAR = 1 - R_{nat}/R_{real}, \quad (3.2)$$

with  $R_{real}$  and  $R_{nat}$  as defined above. Thus if, e.g.  $R_{real}$  is 30% and  $R_{nat}$  is 10%, then two-thirds of event risk in the current climate is attributable to human-induced climate change. That is to say, on average, in two-thirds of instances, the risk of the event occurring when it did is due to human-induced climate change.

#### Fraction of attributable increase and decrease in risk (FAIR and FADR)

The notion of FAR is straightforward to grasp in cases where there is an increase in risk, as it then falls in the

range  $0 < FAR \leq 1$  (with  $FAR = 1$  indicating that all of the current risk is attributable to human-induced climate factors alone). So in this regime FAR may alternatively be termed fraction of attributable increase in risk, FAIR. However, in cases where there is a decrease in risk, FAR falls in the range  $-\infty \leq FAR < 0$ , and these negative values are less straightforward to grasp (note also the asymmetry of an unbounded lower value, with the consequence that any estimation of a distribution on FAR will have an ill-defined mean; typically in such cases one instead refers to the median; Stott *et al.*, 2004). So in this regime we may alternatively re-formulate FAR as the Fraction of Attributable Decrease in Risk,

$$FADR = 1 - R_{real}/R_{nat}, \quad (3.3)$$

whereby the risk terms have been switched so that FADR falls in the range  $0 < FADR \leq 1$ , and the interpretation is then analogous to FAIR (with  $FADR = 1$  indicating that all of the current risk is attributable to natural climate factors alone; Wolski *et al.*, 2014).

Note, however, that not all of the metrics require knowledge of the absolute values of the risks – only their ratios. This can be useful in negating the effect of systematic bias in the estimation of risk, which can typically arise due to risk being inferred from too short an observational record from which to reliably estimate extremes, and/or from the use of climate models with insufficient spatio-temporal resolution and physical parameterization to reliably simulate extremes (Bindoff *et al.*, 2013).

Furthermore, when drawing conclusions one can to some extent acknowledge uncertainty in the modelling system by focusing on the more robust features of estimated metric values. For example, if a distribution calculated on RR lies significantly (e.g. at the 10% level) above unity, then we can confidently say that the risk of the event has ‘very likely’ (to use the language of the Intergovernmental Panel on Climate Change; Mastrandrea *et al.*, 2010) increased due to human-induced climate change. Moreover, statements regarding the degree of confidence in an increase of risk (if any), or e.g. a doubling in risk, are generally a more effective communication tool than focusing on a precise change, as decision makers generally wish to know whether such types of critical threshold have been passed.

In the next section we present some of the current modelling approaches for estimating attributable risk in a PEEA framework.

### 3.2.4 Atmosphere-only modelling approaches

In cases where an event is not deemed to be critically dependent on the state of the ocean, one can expedite the task of modelling the weather at the time by using a climate

model of the atmosphere and land alone, and prescribing ocean surface conditions – specifically, sea surface temperature (SST) and sea-ice coverage – as lower boundary conditions to the model. This eliminates the relatively computationally expensive task of modelling a full dynamical ocean and ‘spinning it up’ into equilibrium with the atmosphere, which can take several model decades. Instead, atmosphere-only simulations need only to start typically a few model months or weeks before the event (depending on the importance of also capturing antecedent conditions to the event, such as e.g. heavy winter snowfall preceding spring snowmelt-driven floods). These are accordingly termed ‘time slice’ experiments, whereby relatively short duration simulations are performed, targeted specifically at capturing an observed event of interest and its attributable risk (Pall *et al.*, 2011). Ensembles of independent and identically distributed (i.i.d.) simulations for each case are generated to produce enough results to generate meaningful statistics of extreme events. The experiment can be set up by generating ‘real world’ and ‘natural’ climates as described below.

#### Targeted probabilistic extreme event attribution

The real world climate can be generated by performing weather simulations with an atmosphere-only climate model under the following boundary conditions for the period of interest (and see Section 3.1 for examples):

- observed concentrations of atmospheric greenhouse gases, sulphate aerosols, ozone, and other atmospheric pollutants,
- observed SSTs; typically weekly or monthly varying,
- observed sea-ice coverage; typically varying weekly or monthly.

Additionally, each weather simulation is first given a unique perturbation to its start state (i.e. to the prognostic variables in the model) to reflect uncertainty in our knowledge of the event’s initial conditions; the consequent spread of simulations reflecting all possible ‘real world’ weather that could have materialized at the time of the event. This technique is used to generate the i.i.d. ensemble. We note that real world climate simulations essentially follow the specifications of the Atmospheric Model Intercomparison Project (AMIP) (Gates *et al.* 1999).

The natural world climate is generated in a similar manner, but with boundary conditions to the atmosphere-only model adjusted as follows.

- The concentrations of greenhouse gases, sulphate aerosols, ozone, and other atmospheric pollutants are reduced to pre-industrial levels.
- The observed SSTs are cooled accordingly – by removing an estimate of the industrial warming that

occurred due to human-induced climate change. This can be done in various ways. For example, one approach is simply to remove the long-term observed trend. Strictly speaking, however, observations contain the signal of both human-induced and natural drivers, as well as internal variability. So another more defensible approach is to deduce the human-induced warming in the observations using the established method of optimal fingerprinting (Allen and Stott, 2003) that we outlined in the introduction (Section 3.1). This warming can then be removed from those observations to produce an estimate of natural world SSTs during the time of the event. Since optimal fingerprinting also returns an uncertainty distribution on the amplitude of human-induced warming, one can in theory remove a range of warming, consistent with this uncertainty, to produce a range of possible natural world SSTs (Pall *et al.*, 2011; Wolski *et al.*, 2014).

- The observed sea-ice coverage is adjusted according to the SST cooling. Again, this can be done in various ways, with the most defensible being via the same optimal fingerprinting based procedure as above. However, optimal fingerprinting analysis is limited in its ability to detect changes in variables having relatively small spatial coverage and sharp gradients, and both coupled model simulations and early industrial period observations of sea ice are unreliable. In practice, one may instead make the adjustment via a simple empirical SST–sea ice relationship, determined from observations, to scale the observed sea-ice coverage down according to the spatial-temporal pattern of the SST cooling, while ensuring that it remains consistent with the characteristics of sea-ice coverage (Pall *et al.*, 2011).

This method of adjusting SST and sea ice is the most comprehensive to date, albeit it relies to some extent on the fidelity of the coupled atmosphere–ocean models used to simulate SST response to climate drivers. It also becomes less justifiable the greater the dependence of the event on ocean and atmosphere–ocean interactions, and thus any study using it should make clear that results are conditional on the state of the prescribed real world SSTs and sea ice.

Risk ratios and attributable risk fractions for meteorological events can be calculated directly from such ensembles of weather simulations (e.g. Christidis *et al.*, 2010). Furthermore, the climate model output may also be fed into an impact model – such as a hydrological model for floods, or a forest model for fires – to determine the change in risk of the impacting event. In both cases, the event attribution is deemed ‘multi-step’ (Stone *et al.*, 2009; Stott *et al.*, 2013) because information is lost at the interface between the initial attribution analysis linking ocean surface

warming to human-induced emissions, and the subsequent attribution analysis linking the change in event risk to the real world versus natural world difference. Likewise, if it is not possible to perform large numbers of weather simulations (e.g. due to computational constraints) and feed them into an impact model to capture what are, by definition, rare extreme events, then statistical models may alternatively be employed to extrapolate to the extremes of the impact variable from a limited number of the weather simulations.

Critical to this time-slice approach is the ability of the complete modelling system to reliably simulate the event type under consideration: from the large-scale weather patterns through to the small-scale impact variable. This means evaluation of both the atmospheric climate model (including any embedded higher-resolution regional models over the area of interest) through to any associated physically based or statistically based impact model. This can be achieved by performing lengthy (multi-year or multi-decadal) simulations with the modelling system and comparing and correcting against observations of the event type under consideration, but for a range of magnitudes (e.g. for a range of peak stream flow as a proxy for a range of flood severities). This also lays the foundations for more systematic PEEA studies.

### **Systematic probabilistic extreme event attribution**

Thus far, atmospheric simulations for PEEA studies have only been conducted for a few short periods, designed to specifically capture a particular event using a single model (e.g. Pall *et al.* 2011, Christidis *et al.*, 2013, Shiogama, *et al.*, 2013, Wolski *et al.*, 2014). This means that possible strong sensitivity to the underlying assumptions of the approach have not been tested and that a full estimate of the uncertainty of results has never been made. To start to address both of these issues, a number of climate modelling groups around the world are conducting the Climate of the Twentieth Century (C20C+) Detection and Attribution Project, a large coordinated project that is running large ensembles of attribution simulations over a modelling period of at least a decade, using multiple climate models and model setups, and multiple estimates of attributable ocean warming and associated sea-ice retreat (Kinter and Folland, 2011; <http://portal.nersc.gov/c20c>).

A related project, known as weather@home (<http://www.weatherathome.org>) uses distributed computing to produce uniquely large ensembles of simulations through the use of distributed computing. The climate model simulations are performed on desktop computers volunteered by thousands of individuals around the world, permitting the timely generation of several-thousand-member ensembles (Massey *et al.*, 2006). The focus is on a variety of assessments of the attributable trend, over recent decades,

for a range of event types in selected regions worldwide, via regional climate modelling. With these and other projects, understanding of the atmospheric modelling approach and attribution estimates using that approach should develop significantly over the coming years.

### 3.2.5 Coupled atmosphere–ocean modelling approaches

The fifth phase of the international Coupled Model Intercomparison Project (CMIP5) includes simulations specifically designed for detection and attribution analysis. These multi-model ensembles provide another source of information for estimating the risk of extreme events. Although the simulations are not specifically targeted to extreme event risk, as they can be in atmosphere-only simulations as described above, the wider variety of participating modelling groups permits extensive analysis of the uncertainties in past and future extreme event risk. Well over a dozen CMIP5 models include submitted simulations following the *historical* scenario (driven with human and natural forcing changes) and the *historical\_NAT* scenario (driven with natural forcing changes only). Seven models from the earlier CMIP3 exercise have also been informally integrated in these configurations.

The early study of Stott *et al.* (2004) used one of these CMIP3 models, HadCM3, to find that the risk of the 2003 European summer heat wave had at least doubled. Although large numbers of i.i.d. realizations of fully coupled model integrations are not generally available to directly extract sufficient numbers of simulated events of the appropriate magnitude, time-dependent extreme value statistics (Coles, 2001) can be used to fit distributions of extreme events. Under the constraints of these distributions, risk ratios and attributable risk fractions can be determined from the existing CMIP database.

The doubling of the risk of the 2003 European summer heat wave was reconfirmed in a pending study by Smith and Wehner (in prep.), which used multiple CMIP3 model simulations. Such multi-model studies permit assessment of the structural uncertainties in risk ratios and attributable risk fractions. Furthermore, using CMIP3/5 model simulations of future scenarios in a similar manner can provide estimates of future risk ratios. For instance, Smith and Wehner (in prep.) calculate that the median estimate of the risk of a summer in 2040, as hot in Europe as it was in 2003, is 150 times more than it was in the pre-industrial era.

## 3.3 Examples: seasonal-mean extremes

Here we outline how PEEA has been applied to seasonal extreme events. Studies thus far have tended to be for

seasonal, or at the very least a few weeks long, events (Stott *et al.*, 2013) because the large-scale weather features that persist can be reasonably captured by the resolution of climate models and computational resources usually available to the climate community (e.g. persistent weather-blocking pressure systems, as opposed to transient sub-gridscale features such as tornadoes).

### 3.3.1 Hot season

Hot events are those most obviously related to global warming and are thus strong candidates for the easiest detection of a contribution of human-induced emissions. In part, for this reason, the first PEEA study examined the hot summer of 2003 over southern Europe (Stott *et al.*, 2004). This summer was the hottest on record and was probably the hottest since at least 1500 (Luterbacher *et al.*, 2004; Schär *et al.*, 2004). A centrepiece of the summer was the intense heat wave that occurred during the first two weeks of August, including record temperatures over much of southern Europe. In spite of the fact that the heat wave was the more iconic event, for instance associated with 15,000 excess deaths in France (Hémon and Jouglard, 2003; Fouillet *et al.*, 2006), and was focused on France, Italy, and Switzerland, Stott *et al.* (2004) examined the chance of a June–August summer over a region encompassing southern Europe and Mediterranean Africa being warmer than the previous record (2001). The main reason for this was that the authors wanted to ask a question they might have asked before 2003 (using a standard seasonal and regional definition), in part to reduce selection bias (see Section 3.4.1) and in part to allow a more general interpretation of results.

Using a multiple regression analysis, they compared observations against a small set of simulations of an atmosphere–ocean climate model representing the actual ('real world') climate of the past century, and a similar set of simulations representing what the ('natural') climate might have been in the absence of human-induced emissions. This comparison produced probabilistic estimates of what the expected average temperature for 2003 actually is and what it would have been in the absence of emissions. Adding the variability from 1000 years of a constant-forced simulation (i.e. no changes in human-induced or natural drivers) to these estimates, and fitting extreme value distributions to the tails, they were able to make probabilistic estimates ( $R_{real}$  and  $R_{nat}$ ) of the chance of a record hot 2003 summer for both climates. With these they could then calculate a likelihood distribution for the FAR resulting from emissions. While the median estimate was for a quadrupling of the chance as a result of emissions, the authors chose to emphasize a result that could be stated with confidence; hence the headline result was that there

was high statistical confidence that human-induced emissions had at least doubled the chance ( $RR > 2$ ) of a record hot summer.

Other studies have revisited the 2003 event, making it the most widely studied for event attribution. For instance, Chrisitidis *et al.* (2012) performed a similar study for the full European continent with two different climate models for the Stott *et al.* (2004) study, finding similar (in fact stronger) attribution results. A major contribution from human-induced emissions is also consistent with the recent rise in frequency of hot summers (Stone *et al.*, 2013).

### 3.3.2 Flood

Floods are more complex events to treat with PEEA than hot (or cold) spells, because they are at least one further step removed from global warming and so require a multi-step approach (Section 3.2.2), and usually have smaller spatio-temporal characteristics so are more challenging to model. Pall *et al.* (2011) performed a PEEA study for the England and Wales floods that occurred during the record wet autumn of 2000 and damaged nearly 10,000 properties nationwide, disrupted services severely, and resulted in insured losses estimated at £1.3 billion (Environment Agency, 2001). The floods were associated with a commonplace but unusually strong large-scale ‘Scandinavia’ atmospheric weather pattern, which was not related to the state of the ocean in any obvious manner, and featured a persistent low pressure centre over the UK throughout the autumn (Blackburn and Hoskins, 2001). That low pressure resulted in repeated frontal precipitation systems passing over the UK, causing the ground to saturate and flood (Marsh and Dale, 2002).

Thus Pall *et al.* (2011) used a multi-step modelling system consisting of: (1) a seasonal-forecast-resolution (~100 km horizontal resolution) global atmospheric climate model capable of capturing the Scandinavia pattern; (2) a large-scale England and Wales flood model into which weather simulations from the climate model were fed – in fact, it was a statistical precipitation–river runoff model with parameters tuned from a more comprehensive physical flood model, with large peak daily river runoff values serving as a proxy for flood occurrence. The climate model boundary conditions used followed the targeted approach of Section 3.2.2 in terms of imposing real and natural world atmospheric pollutant concentrations, SSTs, and sea ice (albeit, for simplicity, only removing the major greenhouse gas influence when adjusting to the natural world, and not also e.g. the sulphate aerosol influence). In particular, when adjusting observed SSTs to the natural climate, optimal fingerprinting was applied to industrial SST simulations from four coupled atmosphere–ocean climate models to get a range of estimates for the adjustment.

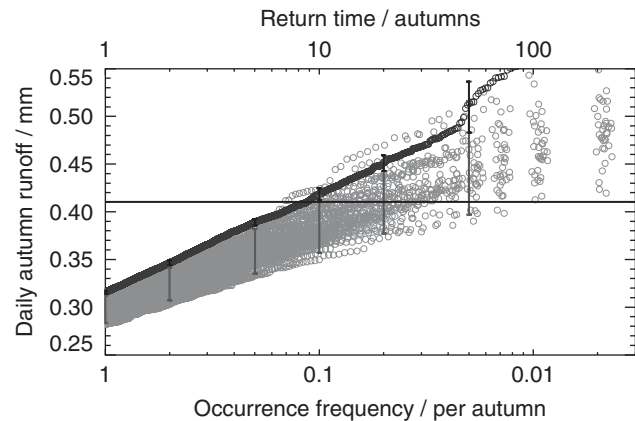


Fig. 3.2. Distributions of England and Wales autumn 2000 daily river runoff simulated for real and natural worlds.

With this setup, Pall *et al.* (2011) generated real and natural world weather simulations for a one-year time slice centred on autumn 2000. Because the event was so rare and relatively unpredictable, several thousand simulations were performed to confidently estimate its occurrence frequency in both worlds – and this was only possible at the time via the novel approach of public distributed computing with [climateprediction.net](#) (see Section 3.4.2). This is reflected in the range of simulated England and Wales runoff values in Fig. 3.2, such that even 1-in-100 year occurrences can be found directly from the data, without the need for statistical extrapolation.

Several thousand climate model simulations of global weather for the ‘real’ autumn 2000 climate are fed into an England and Wales precipitation–runoff model to simulate a range of daily river runoff values (dark grey circles (blue circles in colour version)), with occurrence frequency in autumn on the bottom axis; the top axis is equivalent return time; bars represent 5–95% confidence intervals). This is repeated for a ‘natural’ autumn 2000 climate (grey circles (green circles in colour version)), with the larger spread reflecting uncertainty in estimating SSTs for that hypothetical climate (see text). The horizontal black line marks the highest observation-based autumn 2000 runoff – found by feeding the ERA-40 re-analysis (Uppala *et al.*, 2005) of autumn 2000 weather into the precipitation–runoff model. After Pall *et al.* (2011).

The horizontal black line in Fig. 3.2 constitutes the observation-based runoff threshold above which floods are deemed to have occurred in autumn 2000. Thus by comparing the frequency at which this threshold was exceeded by the real and natural world runoff simulations ( $R_{real}$  and  $R_{nat}$ , assuming an unchanging damage function), Pall *et al.* (2011) calculated a risk ratio for autumn 2000 flood occurrence. By repeating this calculation several times via monte-carlo bootstrapping, they estimated a

distribution on the risk ratio, and concluded that the risk of floods occurring in England and Wales in autumn 2000 was likely nearly doubled (*RR* nearly 2) due to human-induced greenhouse gas emissions. They also found that this increase was broadly consistent with basic thermodynamic arguments for increased atmospheric moisture availability in a warmer world; and though it should be noted that the dynamical situation – in this case the Scandinavia pattern and associated storms – also played an important role in determining precisely where and when this moisture-fed flood risk occurred in the real climate (see also e.g. Allan *et al.*, 2014), Pall *et al.* further found that their main result of increased flood risk was not, to first order, influenced by dynamical changes in going from a natural to a real world climate.

It should be noted, though, that any increase becomes less confident when extending the study to the sub-England and Wales catchment scale using a more detailed flood model, and this to some extent reflects the limits of the resolution of the climate model used in Pall *et al.* (2011), as well as the increased importance of individual catchment characteristics such as permeability. Furthermore, the same climate model simulations indicated a decreased risk of any snowmelt-driven floods in the following spring of 2001, because of the warmer industrial temperatures inhibiting antecedent snowfall (Kay *et al.*, 2011).

### 3.4 Current issues

#### 3.4.1 Selection bias

There is a sharp xkcd (<http://xkcd.com>) comic in which a researcher searches through studies using 20 different colours of jelly beans and finds that the green ones are associated with an increased risk of acne at the 5% significance level; the news headline duly reports a discovery that green jelly beans cause acne. The event attribution discipline faces a major challenge in dealing with such selection bias (Chase *et al.*, 2006, Stott *et al.*, 2013). One element of this, prevalent in science, is publication bias: that null results are not considered worthy of publications by authors, reviewers, or journals. Thus far, event attribution studies have tended to be reactive, in that they only examine events that have occurred. This puts events that are occurring more often than they used to because of emissions (such as heat waves) in the spotlight, while neglecting those that are becoming less frequent (such as cold snaps).

But event attribution faces further complications, in that the definition of an event is ill-defined and thus open to tuning. For instance, for the Stott *et al.* (2004) study of the 2003 European summer, the researchers could have studied the heat wave of the first two weeks of August rather than the three-month summer, or focused on France or Paris

instead of the region they chose. They could have used a different threshold, a different climate model, a different analysis approach, or a different concept of causation (e.g. whether the anomalous magnitude of the event was substantially changed, rather than whether the likelihood was changed). Standards have not been established for any of these aspects (Stott *et al.*, 2013), but the flexibility provides a major challenge in preventing the conscious or unconscious selection of experimental parameters that provide a more desired attribution conclusion (whatever that may be). One way to reduce this risk of tuning is to set the experimental parameters to standard values that could plausibly have been asked in advance of the event (Stott *et al.*, 2004, Pall *et al.*, 2011). There are still multiple options (e.g. a country's borders versus some frequently used climate box region), but at least they are more restricted.

In the end the only way to truly tackle selection bias is to perform analyses on a pre-defined list of events before they occur, examine whether there is a collective signal (e.g. that not just 10% of events are showing a significant attribution signal at the 10% significance level), and then refer to this existing analysis if/when an event occurs. The Weather Risk Attribution Forecast (WRAF, <http://www.csag.uct.ac.za/~daithi/forecast>), for instance, has been producing monthly attribution estimates in advance in parallel with an existing seasonal forecast service, and other systematic event attribution services are under development (e.g. Christidis *et al.*, 2013). The main challenges for these services will be relevance: the WRAF produces 232 estimates each month (for 58 regions for four types of monthly events), but is still ignoring non-monthly events and events that take place on spatial scales greater than or less than  $\sim 2 \text{ Mm}^2$ .

#### 3.4.2 Computational constraints

The computational demands of PEEA are large but not insurmountable with current high performance computing technologies (as well as with creative usage of the public's interest in climate change – for example, the weather@-home project (see Section 3.2.2), under the umbrella of the climate prediction.net project, makes use of publicly volunteered computing time on tens of thousands of computers worldwide to generate several terabytes worth of climate model simulations).

Under the C20C+ project (see Section 3.2.4), multiple modelling groups are integrating 50-member real and natural ensembles of atmosphere-only climate models for multiple decades on various platforms available to them. At the Lawrence Berkeley National Laboratory, the Community Atmospheric Model version 5 (CAM5) (Neale *et al.*, 2010, Ghan *et al.*, 2012), has been integrated in a  $1^\circ$  configuration from 1950 to 2012. This exercise used

roughly 9 million processor hours on hopper, a Cray XE-6 at the National Energy Research Supercomputing Center. Several hundreds of terabytes of model output were also saved, although this could be reduced substantially if only monthly and daily output were saved. This resolution is adequate for analysis of large-scale events such as heat waves and seasonal floods. Finer-scale precipitation events require higher resolutions to realistically simulate short duration extreme precipitation (Wehner *et al.*, 2010). Use of high-resolution regional models, particularly for short periods, is entirely feasible with present day technologies. However, this is the reason why the Berkeley CAM5 output data volume is so large. The vast majority of it consists of the sub-daily fields to drive regional models. High-resolution global atmosphere-only models will soon be viable tools for PEEA analyses, as advances in high performance computing are expected to continue. Estimates of the resources to use a 0.25° version of CAM5 for these purposes are in the several-hundred-million processor hour allocation and the production of a few petabytes of model output. This class of model is appealing for this work as it permits realistic tropical cyclogenesis and other extreme weather phenomena. While these numbers are large, they are obtainable today at the largest institutions and will become more routine as supercomputers surpass the million-processor-core mark.

### 3.5 Summary

The aftermath of damaging weather-related events often motivates the public and decision makers to ask whether the weather event was caused by human-induced climate change. This question is challenging to answer because the event could also have occurred, by chance, at that time in a natural climate that we can never observe. In light of this, the climate science community has formulated probabilistic answers to this question, attempting to separate human-induced and natural influences on the event by modelling ‘real’ and ‘natural’ climates from which to estimate changes in the risk (or probability) of the type of events in question – for example, quantifying probabilities of changes in the occurrence frequency of similar magnitude events.

As interest and capacity in PEEA increases within the climate science community, we have gained a greater appreciation of the various issues and limitations, including those related to event definition and selection/publication bias. The computational resources (including data storage and mining) needed to rigorously quantify attributable risk with the latest generation of modelling systems are great, but becoming feasible – indeed, it is no coincidence that recent advances have accompanied recent developments in computing hardware and software. With these

developments, we anticipate major developments in this relatively new branch of climate science over the coming years.

## References

- Allan, R. P. *et al.* (2014). Physically consistent responses of the global atmospheric hydrological cycle in models and observations. *Surv. Geophys.*, **35**, 533–552.
- Allen, M. R. (2003). Liability for climate change. *Nature*, **421**, 891–892.
- Allen, M. R. and Stott, P. A. (2003). Estimating signal amplitudes in optimal fingerprinting, part I: theory. *Clim. Dyn.*, **21**, 477–491.
- Baede, A. P. M. (2001). The climate system: an overview. In *Climate Change 2001, The Scientific Basis*, eds. J. T. Houghton *et al.* Cambridge University Press, pp. 85–98.
- Bindoff, N. L. *et al.* (2013). Detection and attribution of climate change: from global to regional. In *Climate Change 2013: The Physical Science Basis*, eds. T. F. Stocker *et al.* Cambridge University Press, pp. 867–952.
- Blackburn, M. and Hoskins, B. J. (2001). Atmospheric variability and extreme autumn rainfall in the UK. Available at <<http://www.met.reading.ac.uk/mike/autumn2000.html>>.
- Chase, T. N., Wolter, K., Pielke, R. A. Sr., and Rasool, I. (2006). Was the 2003 European summer heat wave unusual in a global context? *Geophys. Res. Lett.*, **33**, L23709.
- Christidis N., Stott, P. A., Zwiers F. W., Shiogama, H., and Nozawa, T. (2010). Probabilistic estimates of recent changes in temperature: a multi-scale attribution analysis. *Clim. Dyn.*, **34**, 1139–1156.
- Christidis, N. *et al.* (2012). Human activity and anomalously warm seasons in Europe. *International Journal of Climatology*, **32**, 225–239.
- Christidis, N. *et al.* (2013). A new HadGEM3-A-based system for attribution of weather- and climate-related extreme events. *J. Climate*, **26**, 2756–2783.
- Coles, S. (2001). *An Introduction to Statistical Modeling of Extreme Values*. London: Springer.
- Dole, R. *et al.* (2011). Was there a basis for anticipating the 2010 Russian heat wave? *Geophysical Research Letters*, **38**, L06702.
- Environment Agency (2001). *Lessons Learned: Autumn 2000 Floods*. Bristol, UK.
- Fouillet, A. *et al.* (2006). Excess mortality related to the August 2003 heat wave in France. *International Archives of Occupational and Environmental Health*, **80**, 16–24.
- Gates, W. L. *et al.* (1999). An overview of the results of the Atmospheric Model Intercomparison Project (AMIP I). *Bull. Amer. Meteor. Soc.*, **80**, 29–55.
- Ghan, S. J. *et al.* (2012). Toward a minimal representation of aerosols in climate models: comparative decomposition of aerosol direct, semidirect, and indirect radiative forcing. *Journal of Climate*, **25**, 6461–6476.
- Hémon, D. and Jouglard, E. (2003). Sur mortalité liée à la canicule d'août 2003: rapport d'étape. *Rapport Remis Au Ministre De La Santé, De La Famille Et Des Personnes Handicapées Le 25 Septembre 2003*, 59 pp.

- Huggel, C., Stone, D. A., Auffhammer, M., and Hansen, G. (2013). Loss and damage attribution. *Nature Climate Change*, **3**, 694–696.
- Kay, A. L., Crooks, S. M., Pall, P., and Stone, D. A. (2011). Attribution of Autumn/Winter 2000 flood risk in England to anthropogenic climate change: a catchment-based study. *J. Hydrology*, **406**, 97–112.
- Kinter, J. and Folland, C. (2011). The International CLIVAR Climate of the 20th Century Project: Report of the Fifth Workshop. *CLIVAR Exchanges*, **16**, 39–42.
- Lorenz, E. N. (1982). Atmospheric predictability experiments with a large numerical-model. *Tellus*, **34**, 505–513.
- Luterbacher, J., Dietrich, D., Xoplaki, E., Grosjean, M., and Wanner, H (2004). European seasonal and annual temperature variability, trends, and extremes since 1500. *Science*, **303**, 1499–1503.
- Marsh, T. J. and Dale, M. (2002). The UK floods of 2000–2001: a hydrometeorological appraisal. *J. Chart. Inst. Wat. Environ. Mgmt.*, **16**, 180–188.
- Massey, N. *et al.* (2006). Data access and analysis with distributed federated data servers in climateprediction.net. *Adv. Geosci.*, **8**, 49–56.
- Mastrandrea, M. D. *et al.* (2010). Guidance note for lead authors of the IPCC Fifth Assessment Report on consistent treatment of uncertainties. Intergovernmental Panel on Climate Change (IPCC). Available at <<http://www.ipcc.ch>>.
- Min, S.-K., Zhang, X. B., Zwiers, F. W., Friederichs, P., and Hense, A. (2009). Signal detectability in extreme precipitation changes assessed from twentieth century climate simulations. *Climate Dyn.*, **32**, 95–111.
- Min, S.-K., Zhang, X. B., Zwiers, F. W., and Hegerl G. C. (2011). Human contribution to more-intense precipitation extremes. *Nature*, **470**, 378–381.
- Min, S.-K., Zhang, X. B., Zwiers, F. W., Shiogama, H., Tung, Y.-S., and Wehner, M. F. (2013). Multi-model detection and attribution of extreme temperature changes. *J. Clim.*, **26**, 7430–7451.
- Neale, R. B. *et al.* (2010). *Description of the NCAR Community Atmosphere Model (CAM 4.0)*. NCAR Technical Note, National Center of Atmospheric Research, TN-485+STR.
- Otto, F. E. L., Massey, N., van Oldenborgh, G. J., Jones, R. G., and Allen, M. R. (2012). Reconciling two approaches to attribution of the 2010 Russian heat wave. *Geophysical Research Letters*, **39**, L04702.
- Pall, P., *et al.* (2011). Anthropogenic greenhouse gas contribution to UK autumn flood risk. *Nature*, **470**, 382–385.
- Peterson, T. C., Stott, P. A., and Herring, S., eds. (2012). Explaining extreme events of 2011 from a climate perspective. *Bull. Amer. Meteor. Soc.*, **93**, 1041–1067.
- Peterson, T. C., Hoerling, M. P., Stott, P. A., and Herring, S., eds. (2013). Explaining extreme events of 2012 from a climate perspective. *Bull. Amer. Meteor. Soc.*, **94**(9), S1–S74.
- Rahmstorf, S., and Coumou, D. (2011). Increase of extreme events in a warming world. *Proceedings of the National Academy of Sciences of the United States of America*, **108**, 17905–17909.
- Reichenmiller, P., Spiegel, A., Bresch, D., and Schnarwiler, R. (2010). *Weathering Climate Change: Insurance Solutions for More Resilient Communities*, ed. E. Baur. Swiss Reinsurance Company Ltd., Zurich.
- Robine, J.-M., Cheung, S. L. K., Le Roy, S. *et al.* (2008). Death toll exceeded 70,000 in Europe during the summer of 2003. *Comptes Rendus Biologies*, **331**, 171–178.
- Schär, C. *et al.* (2004). The role of increasing temperature variability in European summer heatwaves. *Nature*, **427**, 332–336.
- Shiogama, H. *et al.* (2013). An event attribution of the 2010 drought in the South Amazon region using the MIROC5 model. *Atmospheric Science Letters*, **14**, 170–175.
- Stone, D. A. and Allen, M. R. (2005). The end-to-end attribution problem: from emissions to impacts. *Clim. Change*, **71**, 303–318.
- Stone, D. A. *et al.* (2009). The detection and attribution of human influence on climate. *Annu. Rev. Env. Resour.*, **34**, 1–16.
- Stone, D. A., Paciorek, C. J., Prabhat, Pall, P., and Wehner, M. F. (2013). Inferring the anthropogenic contribution to local temperature extremes. *Proceedings of the National Academy of Sciences*, **110**, E1543.
- Stott, P. A., Stone, D. A., and Allen, M. R. (2004). Human contribution to the European heatwave of 2003. *Nature*, **432**, 610–614.
- Stott, P. A. *et al.* (2013). Attribution of weather and climate-related events. In *Climate Science for Serving Society: Research, Modeling and Prediction Priorities*, eds. G. R. Asrar and J. W. Hurrell. Springer, pp. 307–337.
- Uppala, S. M. *et al.* (2005). The ERA-40 re-analysis. *Q. J. R. Meteorol. Soc.*, **131**, 2961–3012.
- Wehner, M. F., Smith, R. L., Bala, G., and Duffy, P. (2010). The effect of horizontal resolution on simulation of very extreme US precipitation events in a global atmosphere model. *Climate Dynamics*, **34**, 241–247.
- Wergen, G., Hense, A., and Krug, J. (2014). Record occurrence and record values in daily and monthly temperatures. *Clim. Dyn.*, **42**, 1275–1289.
- Wolski, P., Stone, D. A., Tadross, M., Wehner M. F., and Hewitson, B. (2014). Attribution of floods in the Okavango Basin, Southern Africa. *Journal of Hydrology*, **511**, 350–358.

# 4

## Observed and projected changes in temperature and precipitation extremes

Xuebin Zhang and Francis Zwiers

### 4.1 Introduction

This chapter reviews aspects of the current status of research on changes in temperature and precipitation extremes. The aim of this chapter is to provide some accessible entry points for readers interested in the subject. We are not attempting to provide a comprehensive review or assessment, for which there is already a large body of literature, including the Intergovernmental Panel on Climate Change Assessments (Bindoff *et al.*, 2013; Hartmann *et al.*, 2013; Seneviratne *et al.*, 2012). For this reason, we first describe in some detail the relevant statistical methods and tools that have been used in the literature. We then focus on three related aspects: (1) changes in the historical instrumental period, (2) the extent to which detection and attribution research has linked observed changes to external forcing of the climate system, and (3) some aspects of projections for the twenty-first century, as simulated by climate models under various emission scenarios. We hope that our discussion of these topics will give a sense of the nature of the results to date and the challenges that arise from observational, methodological, and climate modelling uncertainties.

We examine extremes that, in general, can be characterized by using daily temperature and precipitation data, including for example, the hottest or coldest daily temperatures annually or the annual maximum amount of precipitation falling in one day. These extremes have been and continue to be the most comprehensively and directly observed, and are thus better studied and understood than some other types of extremes. Moreover, they are also well linked to impacts such as heat waves and flash flooding in an urban setting. While this chapter is limited to the modern instrumental era, it is also very important to understand changes in extremes over longer periods of history, particularly where proxy data indicate larger extremes than those observed during the instrumental period. Such is the case for regional drought (e.g. Woodhouse and Overpeck, 1998; Woodhouse *et al.*, 2010) and

changes in other extremes such as those related to tornadoes and tropical cyclones.

Before beginning our review, it is worth taking a few minutes to think about the terminology that is used to describe extremes in climate science (see also Seneviratne *et al.*, 2012, Box 3-1). The Intergovernmental Panel on Climate Change in its special report, *Managing the Risks of Extreme Events and Disasters to Advance Climate Change Adaptation*, defined a climate extreme as, ‘The occurrence of a value of a weather or climate variable above (or below) a threshold value near the upper (or lower) ends of the range of observed values of the variable’ (IPCC, 2012). While helpful, this definition does not provide a precise criterion for what is considered to be extreme. A great deal of climate research on ‘extremes’ deals with indicators of the frequency or intensity of events that, in fact, describe parts of the distribution that are not very extreme, such as warm events that occur beyond the 90th percentile of daily maximum temperature. Such events lie well within the observations that are collected each season, and they are typically studied by determining whether there are trends in their rates of occurrence. They are often referred to as ‘moderate extremes’ (Zhang *et al.*, 2011). However, the term ‘moderate extremes’ is not used in statistical science to describe the tail of a distribution, since the 90th percentile of daily values, for example, while in the upper tail does not necessarily have the statistical properties of extreme values considered in the statistical literature. Nevertheless, the mechanisms involved in the occurrence of these ‘moderate extremes’ would often be similar to those involved in truly extreme events, and we might also expect them to be affected by different model biases from those for mean values (Hanlon *et al.*, 2012).

In addition to the literature on indices, or ‘moderate extremes’ of climate variables, there is also a body of work that deals with rare values of climate variables that are generally not expected to recur each year. In this case the concept corresponds well to that used in the statistical

sciences, and thus powerful statistical tools based on extreme value theory are available to aid in the analysis of historical and future extremes (e.g. Bernard *et al.*, 2013, Coles, 2001, Katz *et al.*, 2002). Such tools were originally developed to make statements about what might happen outside the range of the observed sample, such as the problem of estimating the 100-year return value on the basis of a 30- or 40-year sample. Hence, the notion of ‘extremes’ in that context is defined as very high quantiles, such as the 95th, 99<sup>th</sup>, or 99.9th percentiles of annual maximum values. An important aspect of this theory is to quantify the uncertainty of such extrapolations through the computation of suitably constructed confidence intervals. Increasingly, these tools are being used in the evaluation of extreme events simulated in climate models (e.g. Kharin *et al.*, 2007, 2013, Wehner, 2013, Wehner *et al.*, 2010). These tools are being further developed in the statistical sciences and there is currently a high level of interaction between that community and the climate science community on the development and application of methods that can be used in the climate sciences, such as the ExtREmes toolkit (see <http://cran.r-project.org/web/packages/extRemes/>).

A schematic illustration of how simple changes in the probability distribution of a climate variable such as temperature can affect extremes is given in Fig. 4.1. This figure has been frequently used, including in IPCC (2012) and it clearly shows how changes in extremes can be caused by various factors. In particular, a shift in the mean of a given climate variable without a change of variance can cause a change in the frequency of extreme events (Fig. 4.1a). Similarly, changes in extremes may come about because of a change in variance of the particular climate variable (Fig. 4.1b), even in the absence of a change in the mean. Changes to the frequency of extreme events could also be brought about by a combination of these two factors (i.e. a shift in mean and variance; Fig. 4.1c), which can cause a change in the shape of the distribution.

Extreme phenomena such as droughts, heat waves, tornadoes, and tropical cyclones, which have an impact on a region during a certain time period, are often ‘tracked’ over a given space. Monitoring changes in such events therefore requires scanning across space, since they evolve over time in terms of size, structure, and location. In addition, monitoring these phenomena also requires measuring fixed quantities at fixed locations (in the case of heat waves and droughts). Because these phenomena are characterized in multiple ways, they are more difficult to quantify than simple temperature and precipitation extremes, and as a result their long-term change is also difficult to assess. They are not reviewed in this chapter.

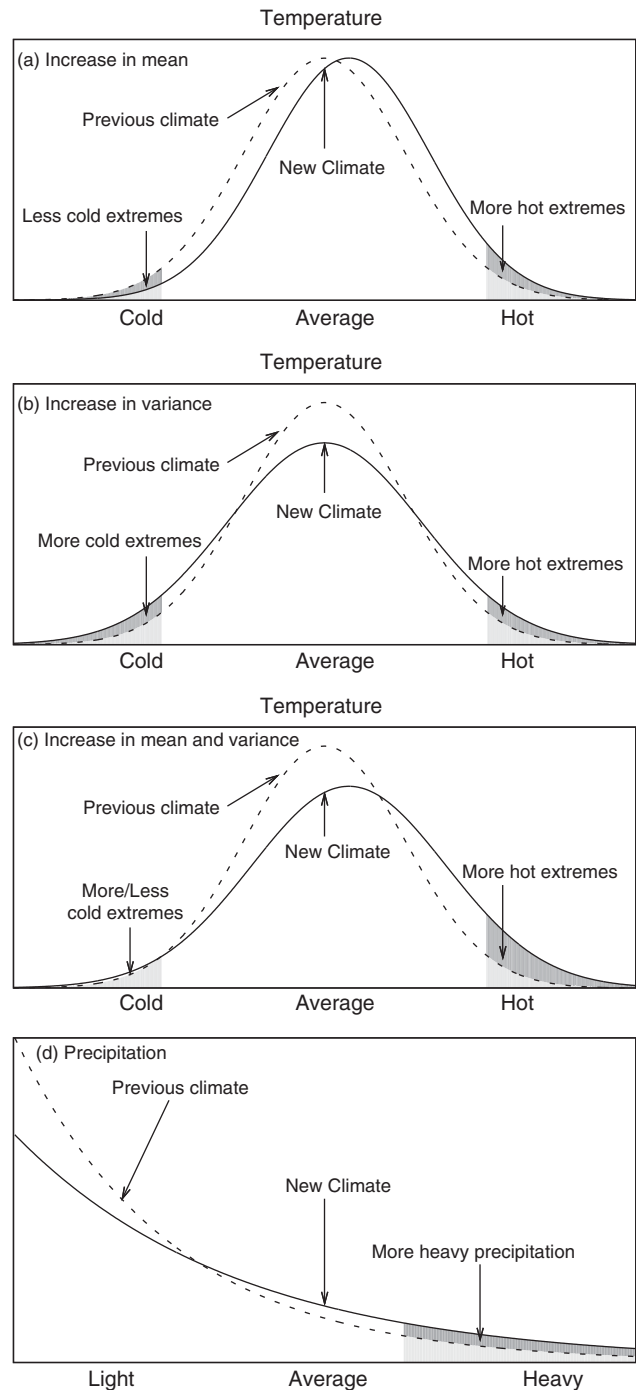


Fig. 4.1. Schematic representations of the probability distributions of daily temperature (a, b, c), which tend to be approximately Gaussian (exceptions can be caused by soil freezing, feedbacks, or energy balance constraints, see text), and daily precipitation (d), which has a skewed distribution. Reproduced from Zhang and Zwiers (2013).

The word *extreme* has also been used to describe impacts caused by weather and climate events. In this case, the concept of what constitutes an extreme event is often less well defined. This is because impacts are always linked with vulnerability and exposure (IPCC, 2012) and various adaptations alter the impacts of extreme events. Therefore, similar climate events may cause different impacts if they occur (a) in different places (due to differences in vulnerability) or (b) at different times at the same place (due to adaptation action). For example, a heat wave of similar severity may cause less damage after cooling equipment has been installed. These aspects of extremes are also not reviewed in this chapter.

In this chapter, we will mainly consider two types of extremes: those that lie in the tail of the distribution of a climate variable, including the annual maxima of one-day or five-day precipitation amounts or the annual maxima (and minima) of daily temperatures, and some ‘moderate extremes’ of daily temperatures. For the purpose of understanding long-term changes in the extremes and their causes, as well as their projected future changes, we will very briefly introduce, in the following section, some statistical tools that have been used in the detection and attribution of changes in extremes, including the identification of trends. We will also provide some examples to demonstrate the utility of those tools. We then present past and projected future changes in temperature and precipitation extremes in Sections 4.3 and 4.4, respectively. We conclude the chapter with some discussion in Section 4.5.

## 4.2 Statistical characterization of extremes

### 4.2.1 Extreme value analysis

Extreme value analysis of hydrometeorological data has been developed for the interpretation of past records and to make inferences about the future probabilities of occurrence of extreme events such as floods and extreme rainfall. The analysis is typically based on extreme value theory (e.g. Coles, 2001) which describes the probability distribution of extreme values that are either represented by the maximum values of a given variable over a certain period of time (such as a year), or by the exceedance of a high threshold. While statisticians tend to prefer the latter ‘peaks over threshold’ approach, its use remains relatively difficult to automate due to a lack of generally accepted objective methods for determining the ‘threshold’, and thus analyses of extremes at thousands of locations are very frequently performed using the former (i.e. ‘block maximum’) approach. Also, observational data from some parts of the world are only available in a form that can be analysed with block maximum approaches (e.g. monthly maxima of daily maximum surface air temperature).

Under fairly general conditions, the probability distribution of the maximum of a sample of variables from the same distribution (i.e. identically distributed variables in statistical terminology) converges to one of three types of extreme value (EV) distribution as the length of the sample goes to infinity. This result, which is known as the “three types theorem”, was originally demonstrated by Fisher and Tippett (1928) and later presented in a more general setting by Gnedenko (1943). The generalized extreme value (GEV) distribution (Smith, 1989) has the following probability density function:

$$G(y) = \begin{cases} \frac{1}{\sigma} \left(1 + \xi \frac{y - \mu}{\sigma}\right)^{-1-1/\xi} \exp\left[-\left(1 + \xi \frac{y - \mu}{\sigma}\right)^{-1/\xi}\right], & \xi > 0, y > \mu - \sigma/\xi, \\ \frac{1}{\sigma} \exp\left[-\frac{y - \mu}{\sigma} - \exp\left(-\frac{y - \mu}{\sigma}\right)\right], & \xi = 0, \\ \frac{1}{\sigma} \left(1 + \xi \frac{y - \mu}{\sigma}\right)^{-1-1/\xi} \exp\left[-\left(1 + \xi \frac{y - \mu}{\sigma}\right)^{-1/\xi}\right], & \xi < 0, y < \mu - \sigma/\xi \end{cases} \quad (4.1)$$

Parameters  $\mu$ ,  $\sigma$  ( $>0$ ), and  $\xi$  are termed the location, the scale, and the shape parameters, respectively. The three types are the Gumbel ( $\xi = 0$ , Gumbel, 1958), the Frechet ( $\xi > 0$ ), and the Weibull ( $\xi < 0$ ) distributions, respectively.

The GEV is the most widely used distribution for extreme value analysis in hydrology and climatology (Katz *et al.*, 2002), particularly when an analysis needs to be repeated a large number of times at different locations in a network of climate stations and at individual locations in a large grid. A classical application of extreme value analysis is to derive engineering design values such as the magnitude of the once in 100 years one-day rainfall accumulation. In such an application, a series of annual maximum one-day precipitation amounts is first collected. These data are then fitted to a GEV distribution, resulting in estimates of the location, scale, and shape parameters. With these parameter estimates, the magnitude of the once in 100-year event can be inferred by evaluating the 99th percentile of the fitted GEV distribution. An estimate of the uncertainty of such a 100-year ‘return-value’ can generally also be obtained in the form of a confidence interval. Depending upon the engineering objectives, return values based on other return periods (either shorter or longer than 100 years), or maxima over different periods of observation (ranging from minutes to several days) may also be required. When fitting the GEV distribution to a collection of extreme values, one important assumption that has to be made is that these extreme values are independent and identically distributed (i.i.d.). Various methods, including the method of maximum likelihood (e.g. Coles, 2001) and L-moments (Hosking, 1990) have been used to estimate the parameters. For small samples, the method of L-moments provides more robust estimates. On the other hand, the method of maximum likelihood provides greater flexibility

since it allows extension of the GEV to situations where extremes have properties that are conditional on other variables such as indices of the state of the large-scale atmospheric circulation (e.g. see Sillmann *et al.*, 2011, Zhang *et al.*, 2010) or vary in time, for example, as a consequence of global warming (e.g. see Kharin *et al.*, 2013 or Zwiers *et al.*, 2011 for examples). The use of L-moments implicitly assumes that the shape parameter is not greater than  $-0.5$  (Katz *et al.*, 2002). Kharin and Zwiers (2000) provide details on implementation of this method in a climate study.

Zwiers and Kharin (1998), Kharin and Zwiers (2000), and Kharin *et al.* (2005, 2007, 2013) used the GEV distribution to analyse changes in extreme temperature and precipitation simulated by climate models. In these studies, climate extremes were expressed in terms of 20-year return values of annual extremes of near-surface daily temperatures and daily precipitation amounts. Model simulated extremes over 20-year periods for the present climate and those projected for the middle and the end of the twenty-first century were compared to assess projected future changes. The GEV distribution was fitted using the method of L-moments, assuming there is no change of distribution (stationarity in statistical terms) within each 20-year period. Because changes in extreme temperature and precipitation are relatively small within each of the 20-year time slices, this assumption was found to be reasonable (Kharin and Zwiers, 2005).

Climate is changing and will continue to change due to anthropogenic influence. As an integral part of the climate system, climate extremes are also changing. This means that the stationary assumption underlying classic frequency analysis using the GEV distribution may not be met in many analyses, especially when an analysis spans a relatively long period of time. Smith (1989) introduced the concept of covariates to the GEV distribution, such that one or more of the parameters of the GEV distribution may be treated as a function of covariates that alter the characteristics of extremes. This non-stationary GEV distribution allows the examination of statistically significant changes in extreme values (Katz *et al.*, 2002, Kharin *et al.*, 2013, Wang and Swail, 2004, Zhang *et al.*, 2004) or to identify the linkage of local extreme values with larger-scale phenomena (Sillmann *et al.*, 2011, Wang and Zhang, 2008, Westra *et al.*, 2013, Zhang *et al.*, 2010) or with external forcings to the climate system (Zwiers *et al.*, 2011). Different methods have been used to estimate the parameters (e.g. Coles, 2001, El Adlouni *et al.*, 2007).

An example is Zhang *et al.* (2010) who examine the influence of large-scale variability represented by the Southern Oscillation Index (SOI) and the Pacific Decadal Oscillation Index (PDOI) on winter maximum daily precipitation over North America. The underlying level of

extremal behaviour of precipitation conditional on the states of these oscillations is assessed by introducing those variables as covariates into the GEV model. Here, the location parameter and logarithm of the scale parameter are considered to be linearly associated with large-scale fields, such that

$$\mu = \mu_0 + \sum_{i=1}^k \beta_i x_i, \quad (4.2)$$

and

$$\log(\sigma) = \theta + \sum_{i=1}^k \delta_i x_i, \quad (4.3)$$

where  $x_1, x_2, \dots, x_k$  are  $k$  covariates, which could be indices such as the SOI, PDOI, etc., and  $\beta_1, \beta_2, \dots, \beta_k$  and  $\delta_1, \delta_2, \dots, \delta_k$  are the corresponding regression coefficients for the location and scale parameters, respectively. The indices considered by Zhang *et al.* (2010) reflect the main large-scale modes of climate variability affecting North America – the Southern Oscillation, Pacific Decadal Oscillation, and North Atlantic Oscillation. These modes alter circulation and storm tracks (and those, moisture advection onto and across the continent, and moisture convergence), as well as air mass temperature (altering moisture holding capacity), and thus they should be indicative of the influence of large-scale circulation variations on local precipitation extremes. Note that Eq. (4.3) ensures that the scale parameter remains positive. The shape parameter  $\xi$  is held constant to avoid the complications that arise from allowing all three parameters to vary with covariates. Essentially, this assumes that the factors considered do not affect the shape of the tail in extreme precipitation distributions. A modestly lengthened or shortened tail relative to the main body of the distribution can be dealt with approximately by varying the scale parameter.

Covariates are assessed to have a significant influence on the extreme precipitation at a given station if their inclusion significantly improves the model's fit, as determined by a likelihood ratio test. Specifically, let  $l^0$  be the negative log likelihood of the model  $M_0$  without covariates (i.e.  $\beta_i = \delta_i = 0$  in Eqs. (4.2 and 4.3)), and let  $l^1$  be the log likelihood of the model  $M_1$  with covariates. The log of the likelihood ratio statistic,

$$T = 2(l^1 - l^0), \quad (4.4)$$

is asymptotically  $\chi_q^2$  distributed (Cox and Hinkley, 1974) with  $q$  degrees of freedom if the covariates have no influence on the distribution of extreme daily precipitation. Here,  $q$  is the difference in the number of free parameters in the two models. The hypothesis  $M_0$  (i.e. there is no influence) is rejected at significance level  $\alpha$  if  $T$  is larger than the  $1-\alpha$  quantile of the  $\chi_q^2$  distribution.

Most applications of the GEV distribution only consider the maxima of data blocks (e.g. the maximum value of every year). This may not make the best use of information concerning extremes that is available within daily precipitation amount station records. To make better use of the available information while still retaining the essence of the block maximum approach, the  $r$ -largest method (e.g. Katz *et al.*, 2002) has also been used in some studies. The idea is that under suitable assumptions it is possible to write down the likelihood function for the sample of  $r$  largest-order-statistics (i.e. the largest  $r$  values from a block of data) that is obtained from  $n$  blocks of observations, with parameters that correspond to those of the GEV model (Coles, 2001). The advantage is that fitting such a model allows improved use of the available data by incorporating more of the observed extremes data. The model parameters can be estimated using the method of maximum likelihood, where the likelihood function is given by

$$L = \prod_{i=1}^n \left\{ \exp \left[ - \left( 1 + \xi \frac{y_i^{(r)} - \mu}{\sigma} \right)^{-1/\xi} \right] \prod_{j=1}^r \sigma^{-1} \left( 1 + \xi \frac{y_i^{(j)} - \mu}{\sigma} \right)^{-1/\xi-1} \right\}, \quad (4.5)$$

and  $y_i^{(j)}$  is the  $j$ th order-statistic in season  $i$ . In the case of nonstationary extremes, the regression coefficients can be estimated by replacing  $\mu$  and  $\sigma$  with Eqs. (4.2) and (4.3) respectively, and by minimizing the negative log-likelihood,  $-\log(L)$ , of the  $r$ -largest model given by

$$l = n \log \sigma + \sum_{i=1}^n \left\{ (1 + 1/\xi) \sum_{j=1}^r \log \left[ 1 + \xi \frac{y_i^{(j)} - \mu}{\sigma} \right] + \left[ 1 + \xi \frac{y_i^{(r)} - \mu}{\sigma} \right]^{-1/\xi} \right\}. \quad (4.6)$$

Relative to a standard GEV modelling approach, the interpretation of the parameters is unaltered.

By using the  $r$ -largest method to fit the GEV distribution to winter season extreme daily precipitation over North America, with indices representing the El Niño Southern Oscillation (ENSO), the Pacific Decadal Oscillation (PDO), and the North Atlantic Oscillation (NAO) as covariates, it was found that ENSO and PDO have spatially consistent and statistically significant influences on extreme precipitation, while the influence of NAO on precipitation extremes in North America is regional and is not field significant. The spatial pattern of extreme precipitation response to large-scale climate variability is similar to that of total precipitation, but somewhat weaker in terms of statistical significance. An El Niño condition or high phase of the PDO corresponds to a substantially

increased likelihood of extreme precipitation over a vast region of southern North America, but a decreased likelihood of extreme precipitation in the north; especially in the Great Plains and Canadian Prairies and the Great Lakes/Ohio River valley (Zhang *et al.*, 2010).

#### 4.2.2 Estimation of trends

Changes in extreme values can be assessed by identifying changes in either frequency or intensity. Keim and Cruise (1998) describe a method for estimating a trend in the frequency of extreme events that is based on a simplified test introduced by Cox and Lewis (1966). Their method includes testing to see whether the occurrence of extremes follows a Poisson process (meaning that the waiting time since the occurrence of the previous event is not predictive of the additional amount of waiting time until the next event; one of the criteria used in statistics to characterize extremes in stochastic processes). If this test of stationarity fails, it then prepares and tests time series of inter-arrival times for trend analysis through linear regression. Frei and Schär (2001) describe a closely related technique that uses a binomial distribution to model the counts of rare events and a logistic regression to estimate trend in the counts. Many other studies have investigated changes in the magnitude of the extremes by comparing return values for different time periods (e.g. Kharin *et al.*, 2007; see also Section 4.2.1) or by estimating linear trends in the extreme values (Kunkel *et al.*, 1999, Zhang *et al.*, 2001).

A statistical method may sometimes fail to detect a trend that is present in a time series. The reliability with which a trend can be detected is affected by multiple factors, including the magnitude of trend in relation to noise (or variability), the size of data sample, and the statistical method. Different methods for detecting trends have different levels of reliability, often depending on the extensiveness of the strength of the statistical assumptions that are implicitly made when applying the method. In statistical parlance, a method that detects a trend more frequently when trend is present is said to have higher *power* (*power* is defined as the probability of detection) and is obviously preferred. Zhang *et al.* (2004) investigated the power of detecting a significant trend in extreme values. They compared four different methods, including (1) the ordinary least squares method that fits a linear trend to an extreme value series, based on minimizing the sum of squared differences between the extremes and the trend line, (2) a Kendall rank correlation-based method, (3) a generalized linear regression method, and (4) the  $r$ -largest method. They used Monte Carlo simulations with simulated extreme values containing trends of different magnitudes in both location and scale parameters. They found that the least squares method, which requires the

residual time series to be normally distributed, has very poor trend detection power because of the violation of the distributional assumption. A Kendall rank correlation-based method, which does not require a distributional assumption, has been frequently used as an alternative to ordinary least squares in the literature; its use improves performance relative to ordinary least squares only when the sample size is large. A generalization of the linear regression method, which explicitly incorporates trend into the parameters of the generalized extreme value (GEV) distribution, has better detection power than the ordinary least squares and Kendall methods. The GEV method that considers trend only in the location parameter was shown in Monte Carlo testing to do a better job than a method that considers trends in both location and scale parameters, suggesting the advantage of using a more parsimonious model. The  $r$ -largest method that uses more than one extreme per (annual) block was shown to significantly improve trend detection performance but at the cost of underestimation of the magnitude of trends.

#### 4.2.3 Detection and attribution

Understanding the causes of changes in extremes, and especially identifying causes external to the climate system, is important. For example, confidence in the projected changes in extremes would be improved if the underlying causes of similar changes in current observations were well understood. This would in turn help the development of better climate adaptation strategies, since it is generally accepted that extremes are responsible for much of the impact of climate (IPCC, 2012). In the climate literature, identification of changes and attribution to possible causes is usually termed detection and attribution. An identified change is detected in observations if its likelihood of occurrence by chance due to natural internal climate system variability is determined to be small, for example, less than 10%. Identification of a statistically significant trend in a time series of climate observations is a simple example of detection. Attribution is defined as the process of evaluating the relative contributions of multiple causal factors to a change or event with an assignment of statistical confidence.

Hegerl *et al.* (2010) outline standard procedures for detection and attribution. As reviewed in great detail in Hegerl and Zwiers (2011), most detection and attribution studies use climate models to determine both the expected ‘fingerprint’ of climate change and the uncertainty in the estimated magnitude of this fingerprint in observations, given the natural background climate variability. Different statistical approaches have been used. The most popular approach is perhaps the optimal fingerprinting method (e.g. Allen and Stott 2003, Hasselmann, 1979, Hegerl *et al.*,

1996, 1997, Ribes *et al.*, 2013). This method is essentially a generalized multiple regression, in which observed climate variations are regressed onto model simulated signals with the residual compared with model simulated variability. A typical application of this method assumes that the residuals are Gaussian distributed, which makes direct application to extreme values difficult. Approaches that have been used include application of the standard optimal fingerprinting method to estimates of changes in extreme value distribution parameters, or to data that have been pre-processed with some kind of transform so that they more closely conform to the Gaussian assumption. Also, attempts have been made to explicitly consider the distributional properties of the extremes being analyzed. Christidis *et al.* (2011) used a marked point process model for extremes, with different location parameters for different decades, and then applied the standard fingerprinting method to understand the causes of the decade-to-decade changes in the location parameter estimates. Min *et al.* (2011, 2013) and Zhang *et al.* (2013) converted the extreme values into an index based on probability that is more suitable for the application of the standard ‘fingerprint’ technique and then conducted detection analysis on the probability indices. Zwiers *et al.* (2011), which is briefly described below, used a method that conducts the detection analysis directly within the framework of extreme value theory. Some studies, such as Zwiers *et al.* (2011) and Zhang *et al.* (2013), were able to estimate the contribution from external forcing to observed changes in the likelihood or magnitude of extremes.

The main idea in the Zwiers *et al.* (2011) method is to fit a non-stationary GEV distribution to observed extreme temperatures, assuming that the climate change signal only appears in the location parameters. Thus, for each grid point  $k$  in the study domain of  $K$  points, they assume that the parameters for the GEV distribution of (4.1) have the form

$$\left\{ \begin{array}{l} \mu = \mu_k + \beta \Delta \hat{\mu}_{jk} \\ \xi = \xi_k \\ \sigma = \sigma_k \end{array} \right. , \quad (4.7)$$

where  $\Delta \hat{\mu}_{jk}$  is the estimated externally forced signal at grid point  $k$  in year  $j$ , and  $\beta$  is a scaling factor common for the whole region under consideration that adjusts the amplitude of the signal so that the GEV model best fits the observed extremes over the domain and time period considered. The externally forced signal is estimated from historical climate change simulations after making the assumption that the location parameter  $\mu$  changes only slowly over time due to forcing. Zwiers *et al.* assume that at each grid point,  $\mu$  remains roughly constant within decades, which means that for each location, an ensemble

of  $M$  forced climate simulations would provide a sample of  $10M$  annual extremes with which to estimate  $\mu$ . Consequently,  $\Delta\hat{\mu}_{jk}$  is obtained by considering increments between estimates of  $\mu$  for different decades. Zwiers *et al.* used ensembles of 25 simulations providing samples of 250 annual extremes for each decade. Because a common scaling factor is used for all  $K$  grid boxes, the parameters for all grid boxes in the region must be estimated jointly. Assuming independence between grid boxes, the joint negative log-likelihood for the GEV density function at  $K$  grid boxes is given by

$$nllh = \sum_{k=1, \dots, K} nllh_k, \quad (4.8)$$

where  $nllh_k$  is the negative log-likelihood function at grid box  $k$ :

$$\begin{aligned} nllh_k = & 10N \log(\sigma_k) + \left(1 + \frac{1}{\xi_k}\right) \sum_{j=1, \dots, 10N} \\ & \log\left(1 + \xi_k \left(\frac{X_{jk} - \mu_k - \beta\Delta\hat{\mu}_{jk}}{\sigma_k}\right)\right) \\ & + \sum_{j=1, \dots, 10N} \left[1 + \xi_k \left(\frac{X_{jk} - \mu_k - \beta\Delta\hat{\mu}_{jk}}{\sigma_k}\right)\right]^{-1/\xi_k}. \end{aligned} \quad (4.9)$$

Maximum likelihood estimates of parameters,  $\beta$ ,  $\mu_k$ ,  $\xi_k$ ,  $\sigma_k$ , where  $k = 1, 2, \dots, K$ , are obtained by minimizing  $nllh$  using the profile-likelihood method. A block bootstrap resampling procedure is used to estimate the uncertainty in the scaling factor; this also takes into account the spatial and temporal structures of extreme temperature in the estimation. Once the parameters are estimated, the GEV distributions at individual grid boxes are then determined, allowing estimation of the changes in the likelihood of events due to external forcing. This method is similar to the standard optimal fingerprint method, in that a single scaling factor is used to modify the space-time pattern of change in model simulated location parameters. However, it is not considered to be an optimized method because the likelihood function does not represent dependence between extremes at different locations. Unlike the standard method, this method also does not account for low-frequency internal variability beyond the time scales that correspond to the length of blocks used in the block bootstrap procedure.

### 4.3 Temperature extremes

Next we show explicit examples of the application of the methods described above to study changes in temperature extremes.

#### 4.3.1 Observed changes

Many studies on changes in extreme temperatures have been focused on temperature indices, which include (1) absolute quantities such as annual maximum and minimum temperatures; (2) the frequency of exceedance above a fixed absolute threshold, such as 0 °C; and (3) the frequency of exceedance above or below fixed relative thresholds, such as the 90th percentile of daily maximum temperature or the 10th percentile of daily minimum temperature where the threshold is determined from a climatological base period such as 1961–1990. The latter also considers the length of spells within which exceedance occurs on several consecutive days, such as the length of heat waves. The indices of category (2) do not necessarily represent extremes per se and thus they are not discussed in this chapter. The indices of categories (1) and (3) are complementary. The former has many applications in planning and societal and ecological impact studies for winter and summer seasons, while the latter also allows changes within seasons to be monitored.

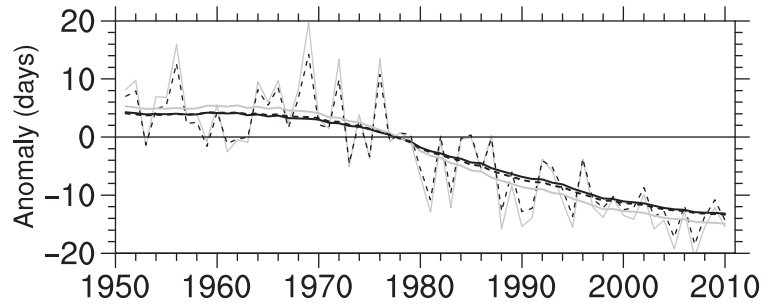
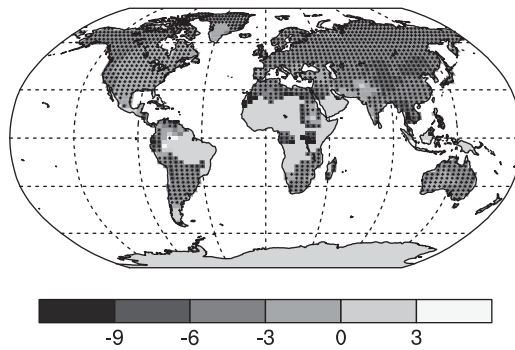
Frich *et al.* (2002) provided an initial global analysis of long-term changes in these temperature indices. International coordination of the development of suites of climate indices with a primary focus on extremes made it possible for Alexander *et al.* (2006) to produce a gridded indices data set (named HadEX) with greatly improved spatial and temporal coverage at the time. The analyses of Alexander *et al.* (2006), as well as other studies based on HadEX, were the principal studies on temperature extremes that were assessed by the IPCC AR4 (Trenberth *et al.*, 2007) and SREX reports (Seneviratne *et al.*, 2012). Recently, Donat *et al.* (2013) released HadEX2, which updates HadEX with many more stations as well as more recent observations to improve spatial and temporal coverage. This analysis and many other studies based on temperature indices constitute the majority of studies that were assessed by the IPCC AR5 with regard to long-term changes in temperature extremes (Hartmann *et al.*, 2013). Below, we summarize the main findings of Donat *et al.* (2013) with regard to long-term trends in temperature extremes.

Donat *et al.* (2013) computed 17 temperature indices, based on over 7000 stations, and analysed long-term trends in those indices. They interpolated the station indices data to a regular  $3.75^\circ \times 2.5^\circ$  longitude–latitude grid over the period 1901–2010 using a modified version of Shepard's angular distance weighting (ADW) interpolation algorithm (Shepard, 1968). Gridding the observations helps to solve several issues. For example, gridding station data prior to area averaging weights individual stations appropriately, accounting for their uneven spatial distribution. It also reduces the impact of data quality issues at individual stations due to averaging.

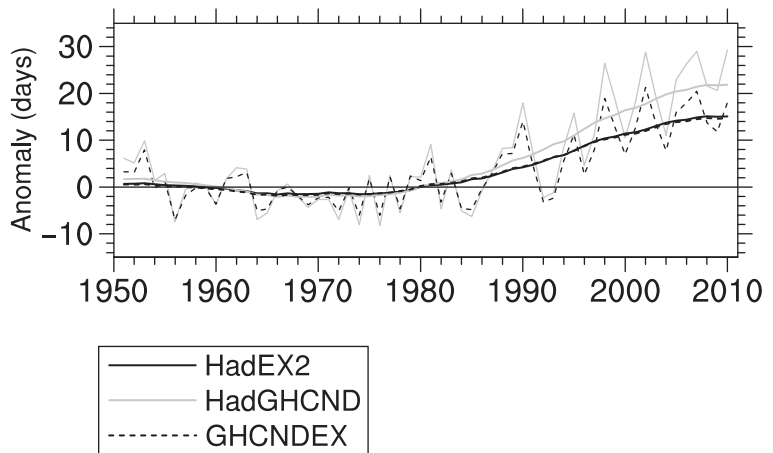
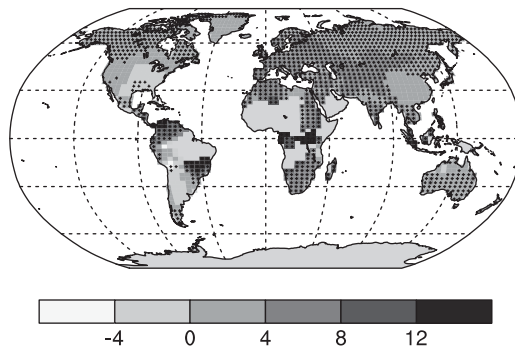
The HadEX2 temperature-related indices generally show long-term trends consistent with warming, with stronger trends in the indices computed from daily minimum temperatures than in those computed from daily maximum temperatures. Figure 4.2 shows long-term changes in the number of cold nights and warm days. The change in temperature indices indicates a reduction in the frequency or severity of cold events, such as a decrease in the number of cold nights (Fig. 4.2a) or cold days (not shown), or correspondingly, increases in the annual minimum of daily maximum and daily minimum temperatures. We also see the effects of warming on hot events through increases in their frequency (Fig. 4.2d) or

magnitude. The number of hot nights and hot days has increased while the magnitudes of the annual maximum of daily maximum and daily minimum temperatures have both increased. However, the increase in the annual maximum of daily maximum temperature is much smaller than that in the annual maximum of daily minimum temperature. Trends in the temperature indices that are consistent with cooling only occur in small regions over eastern North America and a small portion of South America. Evidently, a pause in the warming of temperature extremes is not seen except regionally for annual cold extremes, despite the pause in the warming of global mean temperature (Sillmann *et al.*, 2014).

(a) cold nights



(b) warm days



— HadEX2  
— HadGHCND  
- - - GHCNDEX

Fig. 4.2. Trends in annual frequency of extreme temperatures over the period 1951–2010, for (a) cold nights (TN10p), and (b) warm days (TX90p). Trends were calculated only for grid boxes that had at least 40 years' of data during this period and where data ended no earlier than 2003. Lightest grey areas indicate incomplete or missing data. Black plus signs (+) indicate grid boxes where trends are significant (i.e. a trend of zero lies outside the 90% confidence interval). The data source for trend maps is HadEX2 (Donat *et al.*, 2013) updated to include the latest version of the European Climate Assessment data set (Klok and Tank, 2009). Beside each map are the near-global time series of annual anomalies of these indices with respect to 1961–1990 for three global indices data sets: HadEX2 (black); HadGHCND (Caesar *et al.*, 2006; solid grey) and updated to 2010 and GHCNDEX (Donat *et al.*, 2013; dotted). Global averages are only calculated using grid boxes where all three data sets have at least 90% of data over the time period. Trends are significant (i.e. a trend of zero lies outside the 90% confidence interval) for all the global indices shown. Reproduced from Fig. 4.2.32 of Hartmann *et al.* (2013) by Markus Donat to grey scale.

### 4.3.2 Understanding the causes

Both qualitative and quantitative comparisons between observed data and climate model simulations point to human influence as the main contributing factor for the observed changes in extreme temperature indices. Alexander and Arblaster (2009) and Meehl *et al.* (2007) compared observed trends in several extreme temperature indices with those simulated by climate models participating in the Coupled Model Inter-comparison Project Phase 3 (CMIP3) over Australia and the USA, respectively. They found that the observed changes are consistent with simulations that included anthropogenic forcing but not with simulations that included natural forcing alone. Morak *et al.* (2011, 2013) compared observed and model simulated changes in the number of warm nights, warm days, cold nights, and cold days at both global and sub-continental regional scales using optimal fingerprinting techniques. They found detectable anthropogenic influence in these indicators of change in the frequency of moderate temperature extremes at both scales.

Changes in observed annual maximum and minimum daily temperatures have also been compared with climate model simulations in a number of different ways. The results are similar across the different approaches, with the result being that long-term changes in those extreme temperatures can be attributed to human influence. Christidis *et al.* (2011) estimated time-varying location parameters of extreme value distributions for extreme daily maximum temperatures and then compared changes in location parameters estimated from observations with corresponding changes from model simulations using an optimal fingerprint method. They detected anthropogenic influence in extreme daily maximum temperatures at the global scale. Min *et al.* (2013) transformed extreme temperatures at individual grid boxes into probability-based indices and calculated regional means of their probability indices at continental and sub-continental scales. They compared the resulting regional series from observations with those from CMIP3 model simulations using the optimal fingerprint method and found human influence on extreme minimum and maximum temperatures at the continental and sub-continental scales. Wen *et al.* (2013) averaged station observations of extreme temperatures across seven large regions in China and compared the evolution of these averages with corresponding averages from simulations of the CanESM2 climate model (Arora *et al.*, 2011) also using an optimal fingerprinting method. They found that anthropogenic influence was distinctly detectable from that of natural forcing in Chinese extreme temperatures. Overall, these quantitative analyses show very clearly that much of the observed change in the annual extremes of daily temperature is attributable to human influence.

Zwiers *et al.* (2011) took a different approach towards the comparison of observations and model simulations. Based on a powerful extreme value theory, they assumed that annual maximum and minimum daily maximum and daily minimum temperatures have generalized extreme value (GEV) distributions, which, as described previously, are characterized by location, shape, and scale parameters. They fitted GEV distributions to the observed extreme temperatures with location parameters represented as linear functions of signals ( $\Delta\hat{\mu}_{jk}$  in Eq. 4.7) obtained from multi-model ensemble simulations under different external forcings, as briefly described in Section 4.2.3 and detailed in the paper. They found that both anthropogenic influence and the combined influence of anthropogenic and natural forcing can be detected in extreme temperatures at the global scale over the land, and also regionally over many large land areas. They estimated that the external influence has caused large changes in the likelihood of extreme annual maximum and minimum daily temperatures (Fig. 4.3). Globally, waiting times for extreme annual minimum daily minimum and daily maximum temperature events that were expected to recur once every 20 years in the 1960s are now estimated to exceed 35 and 30 years, respectively. In contrast, waiting times for c. 1960s 20-year extremes of annual maximum daily minimum and daily maximum temperatures are estimated to have decreased to less than 10 and 15 years, respectively.

### 4.3.3 Future changes

Observed changes in temperature indices are projected to continue into the future, according to simulations conducted by multiple climate models participating in the Coupled Model Intercomparison Project Phase 3 and Phase 5 (Sillmann *et al.*, 2013). The projected changes include further decreases in the frequency of cold events and increases in warm events, with larger changes projected for the indices based on daily minimum temperatures than those based on maximum temperatures. At the global scale, cold nights and cold days that occurred 10% of the time in 1961–1990 are projected to decline substantially in frequency by the end of the twenty-first century to 3%, 1.5%, and 0.3% for cold nights and to 4%, 2%, and 0.7% for cold days, under the RCP2.6, RCP4.5, and RCP8.5 emissions scenarios, respectively (Fig. 4.4). That is, there will be virtually no cold nights or days as defined for the 1961–1990 base period by the year 2100 under the highest emissions scenario. While there are uncertainties, the inter-quartile model spread becomes smaller as the projected exceedance rate frequency approaches zero, as more and more models simulate fewer and fewer cold nights and cold days. At the global scale, warm nights and warm days that occurred with a frequency of 10% in 1961–1990 are

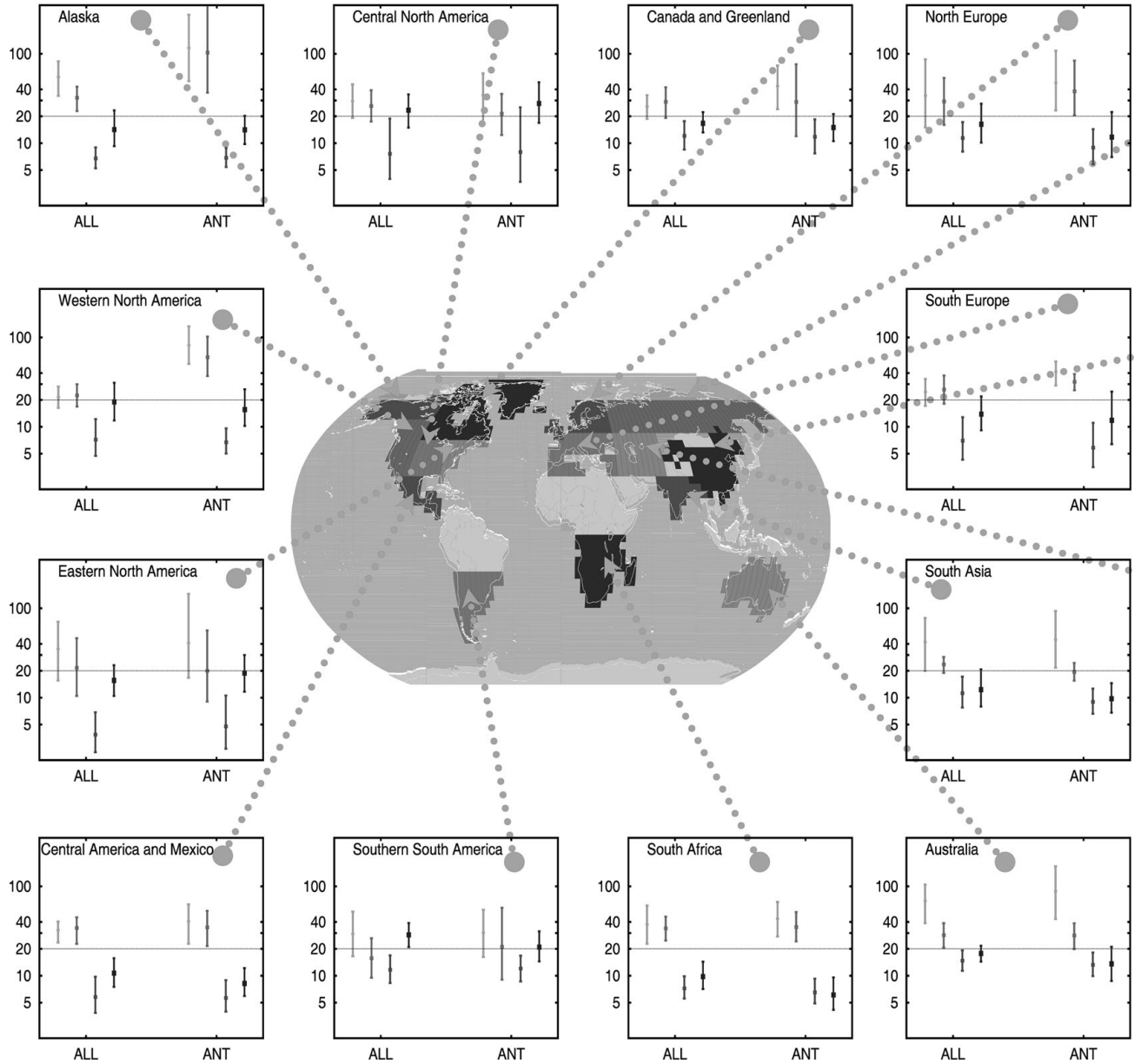


Fig. 4.3. Estimated waiting times (yr) and their 5% and 95% uncertainty limits for 1960s 20-yr return values of annual extreme daily temperatures in the 1990s climate, based on extreme value analyses of observed extreme temperatures fitted to GEV distributions whose location parameters vary with simulated extreme temperature responses to ALL or ANT forcings. The light, medium, and dark grey bars and black bars correspond to TN<sub>n</sub>, TX<sub>n</sub>, TN<sub>x</sub>, and TX<sub>x</sub>, respectively.

projected to become much more frequent by the end of the twenty-first century, with frequencies reaching 34%, 44%, and 69% for warm nights and 29%, 39%, and 62% for warm days, under the RCP2.6, RCP4.5, and RCP8.5 emissions scenarios, respectively (Fig. 4.5). This means that a warm day/night extreme that formerly occurred once in ten days is projected to recur more frequently (i.e. at a rate exceeding once every other day) in the future under the highest emissions scenario. The largest changes in

recurrence frequency are projected in the tropical regions, where day-to-day temperature variability is the smallest.

Climate model simulations project similar changes for the annual maximum and annual minimum daily maximum and daily minimum temperatures (Kharin *et al.*, 2007, 2013). Kharin *et al.* (2013) estimated changes in 20-year return values of these annual extreme temperatures using two different methods. They fitted the GEV distribution using a method based on L-moments (Hosking, 1990) to

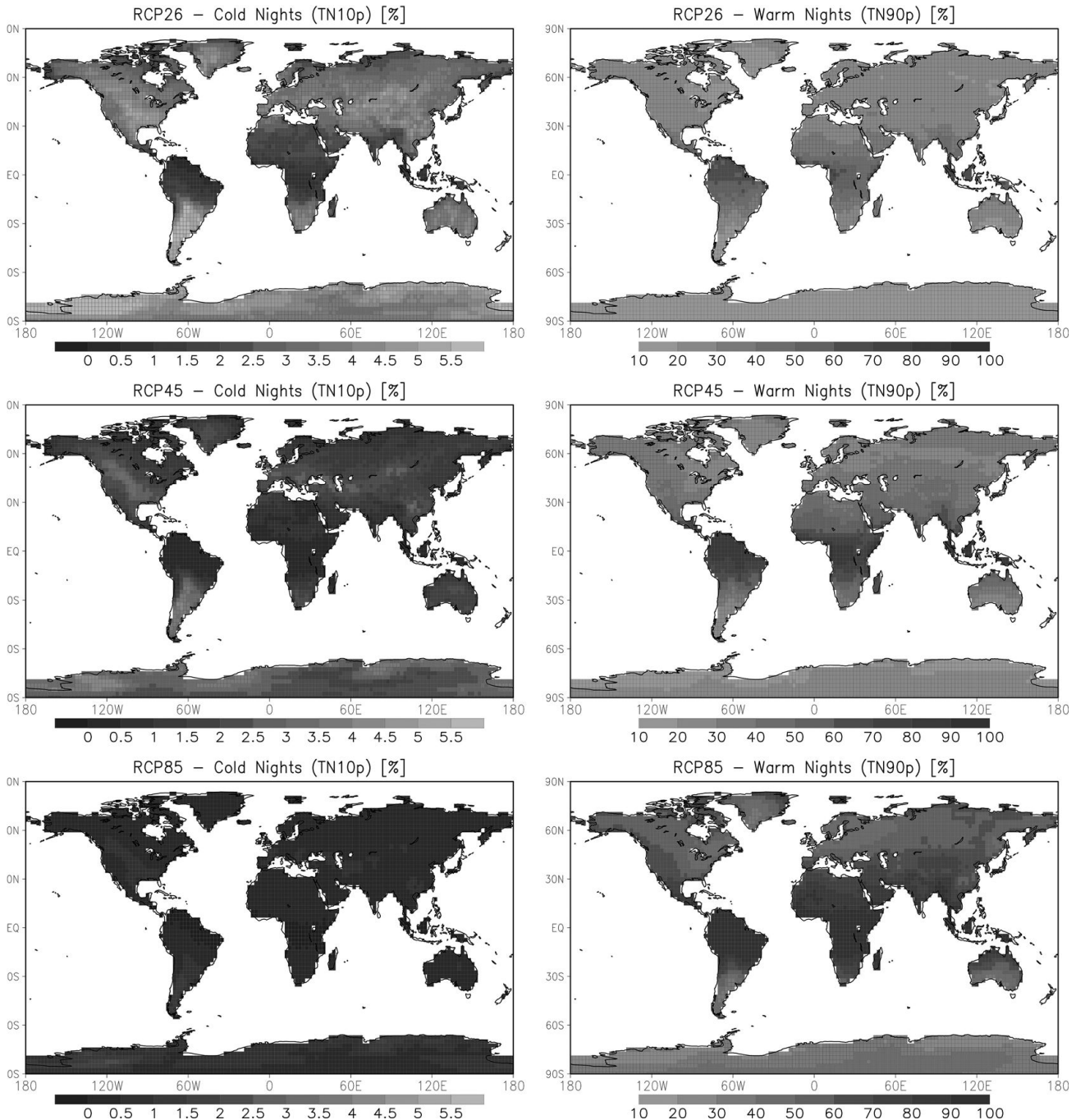


Fig. 4.4. The multimodel median of the annual frequency of cold nights (TN10p, left) and warm nights (TN90p, right) temporally averaged over the period 2081–2100 as absolute values of the exceedance rate (in %). By construction, the exceedance rate averages to about 10% over the base period 1961–1990. All changes are significant at the 5% significance level. Reproduced from Fig. 4.9 of Sillmann *et al.* 2013 to grey scale.

estimate return values in several 20-year time slices, including 1986–2005 (for the current climate), 2016–2035 (for the near future), 2046–2065 for the mid twenty-first century, and 2081–2100 (for the late twenty-first

century), to estimate projected future changes. They also used the method of maximum likelihood for estimating the parameters of a GEV distribution that depend on time as a covariate. The parameters are estimated for each year

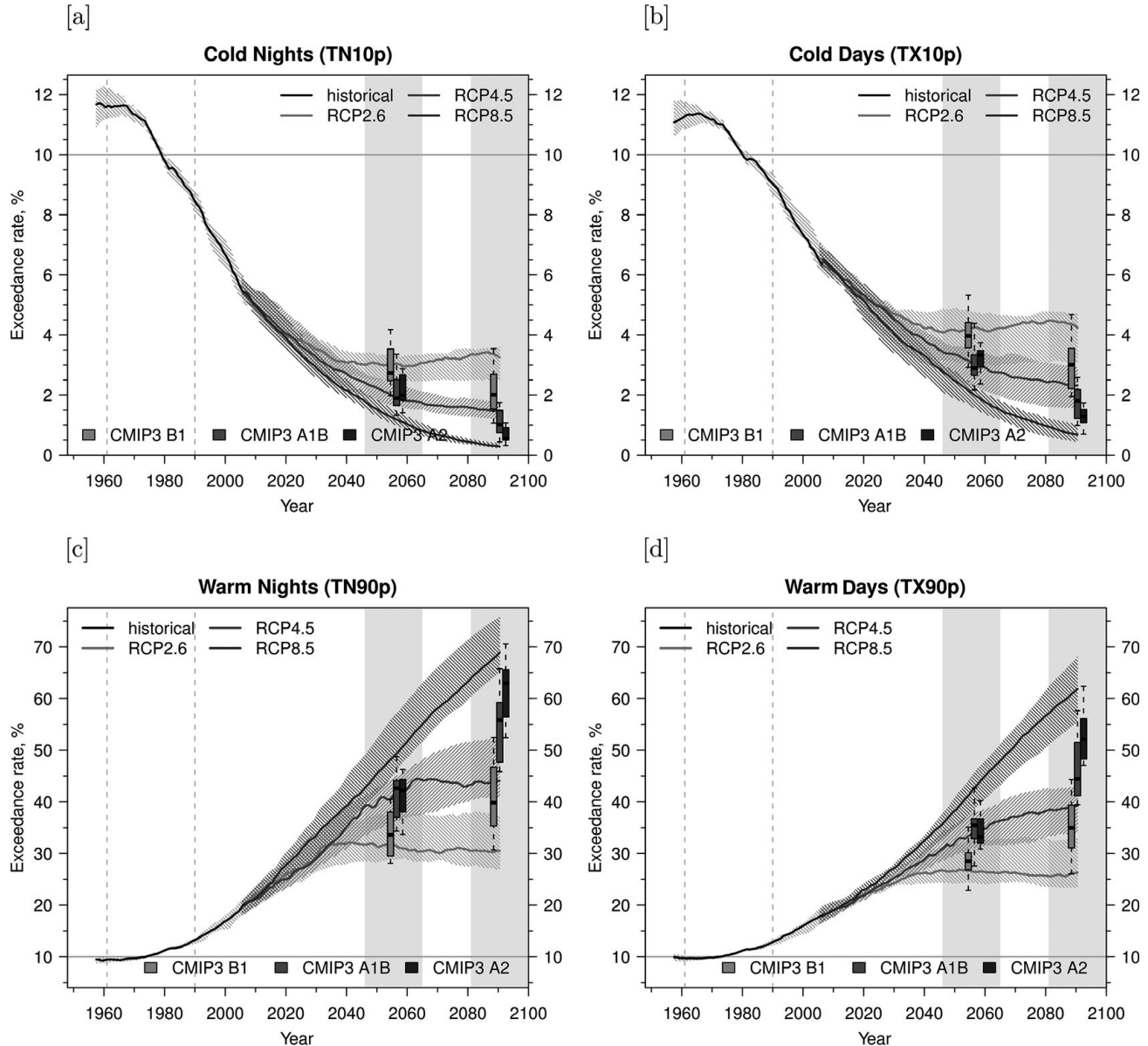


Fig. 4.5. Global averages of temperature percentile indices including (a) cold nights (TN10p), (b) cold days (TX10p), (c) warm nights (TN90p), and (d) warm days (TX90p) over land as simulated by the CMIP5 ensemble for the RCP2.6 (light grey), RCP4.5 (medium grey), and RCP8.5 (dark grey) displayed as anomalies from the reference period 1981–2000. Solid lines indicate the ensemble median and the shading indicates the interquartile ensemble spread (25th and 75th quantiles). Time series are smoothed with a 20-year running mean filter. The box-and-whisker plots show the interquartile ensemble spread (box) and outliers (whiskers) for 11 CMIP3 model simulations of the SRES scenarios A2 (black), A1B (medium grey), and B1 (light grey) globally averaged over the respective future time periods (2046–2065 and 2081–2100) as anomalies from the CMIP3 reference period 1981–2000. Reproduced from Fig. 4.9 of Sillmann *et al.* 2013 to grey scale.

(as functions of time) from overlapping 51-year time windows. The location and log scale parameters are assumed to depend linearly on time while the shape parameter is assumed to be constant. Both methods result in very similar estimates of return value changes.

The land-averaged multi-model median change in the 20-year return value of annual maximum daily maximum temperature by the end of the twenty-first century is 1.2 °C, 2.4 °C, and 5.4 °C in the RCP2.6, RCP4.5, and RCP8.5 experiments, respectively, compared to the corresponding

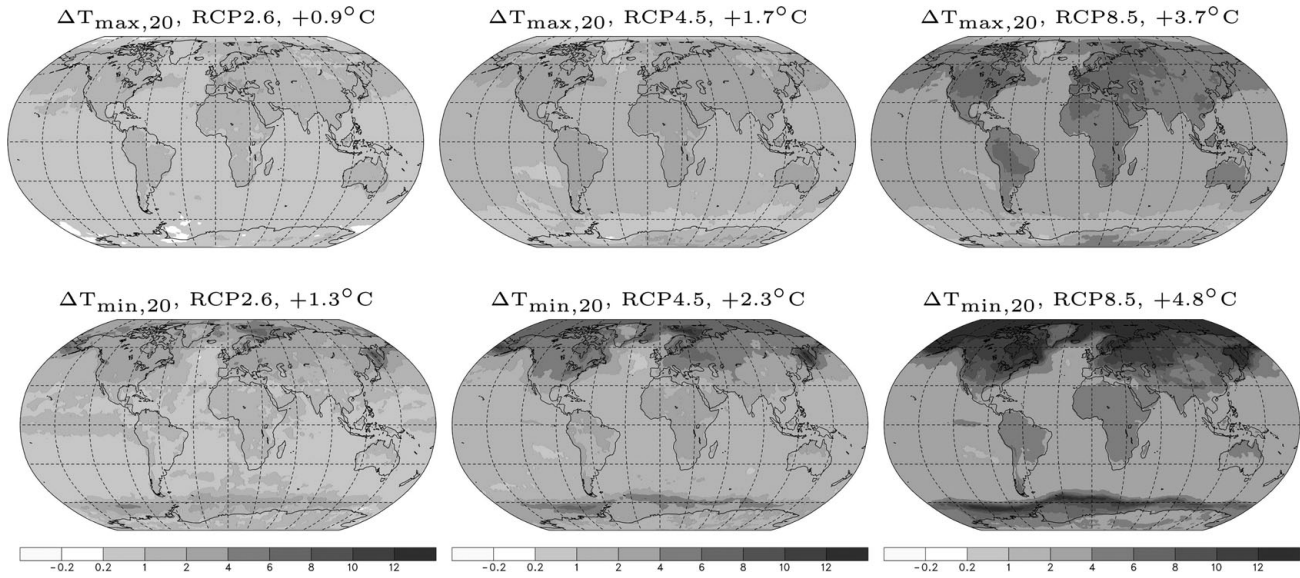


Fig. 4.6. Top row: The CMIP5 multi-model median change in 20-year return values of annual warm temperature extremes  $T_{\text{max},20}$  simulated in 2081–2100 relative to 1986–2005 in the RCP2.6 (left), RCP4.5 (middle), and RCP8.5 (right) experiments. Global averages of changes are indicated in the titles. Middle row: The same as above but for 20-year return values of annual cold temperature extremes  $T_{\text{min},20}$ . Reproduced from Fig. 4.3 of Kharin *et al.* (2013) to grey scale.

changes of 1.7 °C, 3.2 °C, and 6.2 °C for annual minimum daily temperature. There is appreciable inter-model uncertainty in the magnitude of the projected future changes over global land for a particular forcing scenario, which becomes the dominant component in the overall uncertainty by about 2050. The projected changes in extreme temperature are not uniform across space. Figure 4.6 displays multi-model median changes in 20-year return values of annual warm and cold extremes projected for 2081–2100, relative to 1986–2005, as simulated by the CMIP5 models in the RCP2.6, RCP4.5, and RCP8.5 experiments. Changes in warm and cold extremes are comparable over ice-free oceans. Cold extremes warm considerably faster over extratropical land masses and over high latitude oceans, likely due to snow and sea-ice related feedbacks in these and adjacent regions. The models tend to simulate larger increases in warm extremes than in cold extremes over subtropical land regions, most notably over the Iberian Peninsula, northern and southern Africa, southern Asia, central and south America, and south Australia. These are regions that become generally drier and the larger increases in warm extremes are presumably at least partially due to reduced moderation by evaporative cooling from the land surface (e.g. Mueller and Seneviratne, 2012). Changes in warm extremes generally follow changes in the mean summertime temperature. Changes in cold extremes substantially exceed changes in the mean wintertime temperature in regions where snow and sea-ice retreat with global warming.

## 4.4 Precipitation extremes

### 4.4.1 Observed changes

Westra *et al.* (2013) investigated the presence of trends in annual maximum one-day precipitation amount over the globe. They examined trends at over 8000 land-based observing stations with more than 30 years of records from 1900 to 2009 using two different methods: the Mann-Kendall nonparametric trend test and a non-stationary generalized extreme value analysis. They found statistically significant increasing trends in this quantity at the global scale. Their results showed that 8.6% of stations had significant increasing trends while 2.2% had significant decreasing trends (Fig. 4.7). The number of stations showing a significant decreasing trend is consistent with expectations from random chance under a no-trend hypothesis, while the number of stations with significant increasing trends is not consistent with such expectations. The location of stations with significant trends does not exhibit a clear spatial pattern, suggesting the possibility of a broad upward influence from warming on precipitation extremes. This is consistent with their analysis of annual maximum one-day precipitation using a non-stationary generalized extreme value distribution, in which they found a positive association between the intensity of extreme precipitation and the annual global mean temperature anomaly at about two-thirds of the stations they analysed. Donat *et al.* (2013) also analysed trends in precipitation indices. They found that most precipitation indices show changes toward more

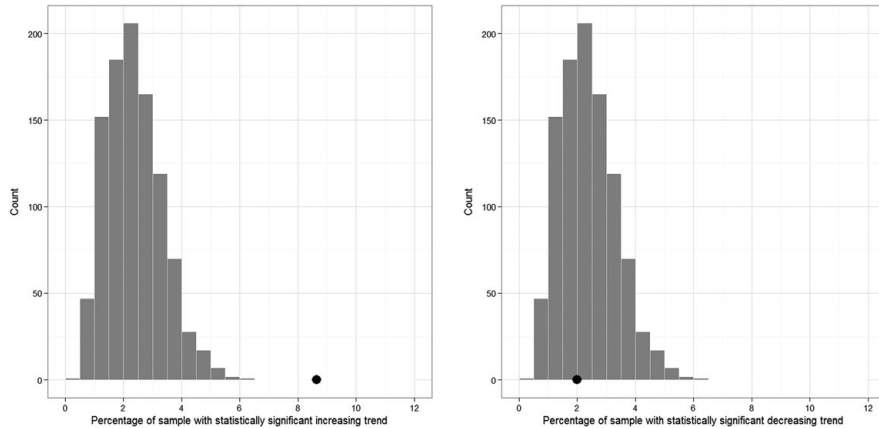


Fig. 4.7. Percentage of stations showing statistically significant (left) increasing and (right) decreasing trends based on the Mann–Kendall test. The histogram represents the distribution of results from 1000 bootstrap realizations of the global annual maximum rainfall data, and the black dot represents the value from the observed data.  
Reproduced from Westra *et al.* (2013) to grey scale.

intense precipitation over the eastern half of North America as well as over large parts of Eastern Europe, Asia, and South America, and a tendency toward less frequent and intense precipitation around the Mediterranean, in Southern Asia, and the northwestern part of North America. Overall, while there is clear evidence of intensification in extreme precipitation at the global scale over land, regional patterns of statistically significant increase or decrease in extreme precipitation are not well defined.

#### 4.4.2 Understanding the causes

Atmospheric saturation vapour pressure increases as temperature increases according to the Clausius–Clapeyron relationship. As relative humidity is expected to change little (Allen and Ingram, 2002), global warming should result in increased atmospheric moisture content. Extreme precipitation typically scales with total column moisture if circulation does not change. An observational analysis shows that winter maximum daily precipitation in North America has statistically significant positive correlations with local atmospheric moisture (Wang and Zhang, 2008). It follows that warming would also generally lead to stronger extreme precipitation, as is expected based on CMIP3 and CMIP5 projections (e.g. Kharin *et al.*, 2007, 2013). In observational analysis, Westra *et al.* (2013) suggested that this is indeed the case. The percentage increase in annual maximum one-day precipitation per kelvin of global surface temperature is estimated to be approximately 7.1% if a non-stationary GEV is fitted to the extreme precipitation with global surface temperature as a co-variate to the location parameter. CMIP3 and CMIP5 simulations project an increase in the globally averaged 20-year return values of annual maximum 24-hour precipitation amounts of about 6 to 7% per kelvin global mean warming, with the bulk of models simulating values in the range 4 to 10% per kelvin (Kharin *et al.*, 2007, 2013).

Quantitative comparison between observed annual maximum one-day or five-day precipitation amounts and those simulated by coupled climate models also suggests human influence on extreme precipitation. Min *et al.* (2011) conducted a detection and attribution analysis on annual maximum one-day and five-day precipitation amounts using simulations from a limited set of coupled climate models participating in CMIP3 and observations with limited spatial coverage ending in the year 2000. They first independently transformed annual precipitation extremes in CMIP3 simulations and observations into a probability based index that replaces the extremes at a grid location with a measure of relative intensity (on the scale 0–1) at that location. They then compared those indices from observations and model simulations using an optimal fingerprinting method and detected the response to anthropogenic influence. Detection of all external forcings including both anthropogenic and natural forcings was less robust than detection of the response to anthropogenic forcing alone. Furthermore, the climate models used showed substantially smaller changes compared to the observations.

Zhang *et al.* (2013) improved the Min *et al.* (2011) study by using an updated observational data set and a new multi-model ensemble of CMIP5 climate simulations. Their observational data set is based on gridded annual maximum one-day and five-day precipitation amounts from the HadEX2 data set (Donat *et al.*, 2013), which was augmented with station observations of Russian data ([http://www.meteo.ru/English/climate/d\\_temp.php](http://www.meteo.ru/English/climate/d_temp.php)) that have very recently become available. They used a method similar to that used by Min *et al.* (2011) to convert observed and model simulated extreme precipitation into dimensionless probability-based indices. Considering the annual maxima of daily (RX1day) and five-day consecutive (RX5day) precipitation amounts over the Northern Hemisphere land area for 1951–2005, they found good correspondence between observed and simulated extreme precipitation changes, and detected the effect of anthropogenic forcings

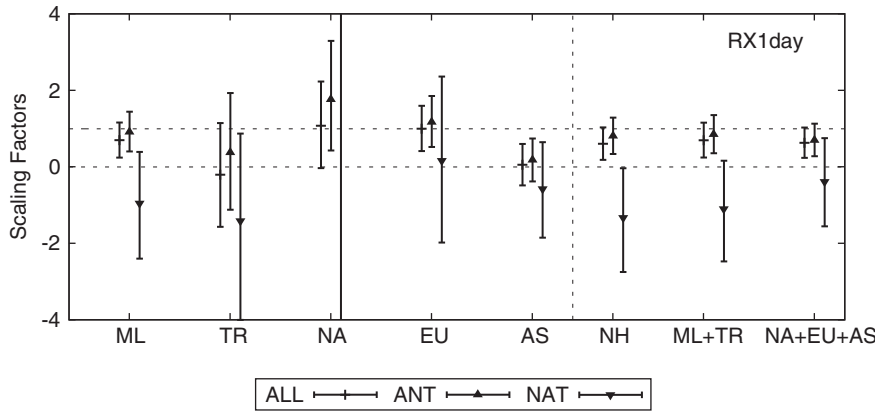


Fig. 4.8. Best estimates (data points) and 5–95% confidence intervals (error bars) of the scaling factors by which the model-simulated responses to ALL, ANT, and NAT forcing best match observed changes for annual maximum one-day precipitation, when using a five-year mean probability index averaged over midlatitude (ML), northern tropics (TR), Western Hemisphere land (NA), western East Hemisphere land (EU), and eastern East Hemisphere land (AS), Northern Hemisphere (NH), and when using two regional averages (ML + TR) or three regional averages (NA + EU + AS). Reproduced from Fig. 4.2 of Zhang *et al.* (2013) to grey scale.

in observations, both individually and when simultaneously estimating anthropogenic and naturally forced changes (Fig. 4.8). By converting changes in the probability indices back to physical units, Zhang *et al.* (2013) estimated that human influence had intensified annual maximum one-day precipitation in sampled Northern Hemisphere locations by 3.3% [1.1% to 5.8%, >90% confidence interval] on average. This corresponds to an average intensification in maximum one-day precipitation of 5.2% [1.3%, 9.3%] per kelvin increase in observed global mean surface temperature, consistent with the increase in atmospheric moisture with temperature that is predicted by the Clausius–Clapeyron relationship. Detection of anthropogenic influence on smaller spatial scales is more difficult due to the increased level of noise and uncertainties and confounding factors on local scales. Fowler and Wilby (2010) suggested that there may have only been a 50% likelihood of detecting anthropogenic influence on UK extreme precipitation in winter at that time, and a very small likelihood of detecting it in other seasons.

#### 4.4.3 Future changes

Sillmann *et al.* (2013) estimated projected changes in several precipitation indices as simulated by CMIP5 models and showed general trends toward further intensification of precipitation extremes in the future. Global land averaged total precipitation and precipitation intensity (average precipitation rate during days with precipitation) are projected to increase by 9% and 12%, respectively, by the end of the twenty-first century under the RCP8.5 emissions scenario. The increases are smaller under more moderate emissions

scenarios, at 3.5% and 6% under RCP2.6 and RCP4.5, respectively. Annual maximum five-day precipitation averaged over the global land area is projected to increase at 6%, 10%, and 20% corresponding to the RCP2.6, RCP4.5, and RCP8.5 emissions scenarios, respectively. These increases are of similar magnitude when compared with projected future changes for annual maximum one-day precipitation (Kharin *et al.*, 2013), as discussed below.

Kharin *et al.* (2013) reported projected changes in more extreme aspects of precipitation, considering annual maximum one-day and five-day precipitation amounts with 20-year recurrence times. In the following, we provide more details from Kharin *et al.* (2013). The CMIP5 multi-model ensemble median changes in annual mean and extreme precipitation are displayed in Fig. 4.9, as simulated in 2046–2065 and 2081–2100, relative to 1986–2005 in the RCP4.5 experiment. Globally, relative changes in 20-year return values of annual maximum daily precipitation generally exceed changes in annual mean precipitation. For example, the global average of multi-model median change in extreme precipitation is about 11% by the end of the twenty-first century in the RCP4.5 scenario, compared to about 5% for mean precipitation. There are regions where annual mean precipitation is projected to decrease (e.g. Central America, parts of Africa, Australia), but the intensity of precipitation extremes increases. The corresponding return periods for late twentieth-century 20-year extreme precipitation events are reduced, except for drying subtropical regions. Averaged over the global land areas, the multi-model median increase in the magnitude of the 20-year return values is about 6%, 12%, and 30% in the RCP2.6, RCP4.5 and RCP8.5 experiments, respectively,

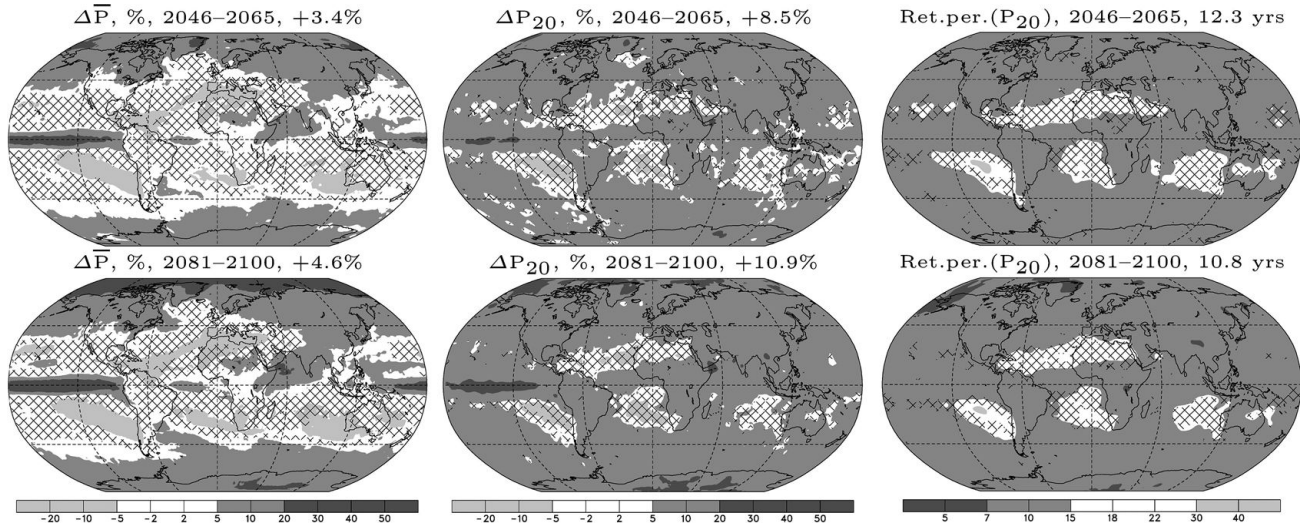


Fig. 4.9. Top row: The CMIP5 multi-model median relative change (%) in the annual mean precipitation rate (left) and in 20-year return values of annual extremes of daily precipitation (middle) simulated in 2046–2065 relative to 1986–2005 in the RCP4.5 experiment. The corresponding median of return periods, in years, for 1986–2005 20-year events is shown in the right panel. Bottom row: The same as above but for the 2081–2100 period. Global averages, or global medians for the return periods, are indicated in the titles. Changes that are not significant at the 5% level are indicated by cross-hatching. Reproduced from Fig. 4.4 of Kharin *et al.* (2013).

by the year 2100. Correspondingly, return periods for 1986–2005 20-year events are reduced to about 14, 11, and 6 years, respectively.

The percentage change in globally averaged 20-year return values as a function of global annual mean temperature changes as simulated by the CMIP5 models in 2046–2065 and 2081–2100 in the three emissions scenarios is about 6% per kelvin. However, there is considerable inter-model spread with the majority of the models simulating values in the 4–10% per kelvin range. In contrast, the simulated sensitivity to warming for annual mean precipitation is much smaller, with the bulk of models simulating values in the 1.5–2.5% per kelvin range. Relative changes in extreme precipitation per unit of warming are not uniformly distributed over the globe. Over global land or land in the Northern extra-tropics, the CMIP5 multi-model median estimate of 20-year return value change is about 4% per kelvin in local temperature increase. In the generally wetter tropical land regions, the sensitivity to warming can be much greater than that predicted by the Clausius–Clapeyron relation.

#### 4.5 Summary and discussion

In this chapter we have reviewed some, but not all, aspects of the current status of research on changes in temperature and precipitation extremes in the hope of providing readers with an introduction to this field. We have described tools and methods, especially some of the more recent

applications of extreme value theory to the identification of long-term changes in extremes and in attributing those changes to causes. For both temperature and precipitation, we started from observed changes in the historical instrumental record, then discussed literature that attempts to attribute the changes to causes, and finally gave an overview of projected future changes as simulated by climate models forced with various future emissions scenarios.

Extreme temperatures of daily scale (e.g. annual maximum daily minimum temperature) have changed significantly in the historical record, consistent with warming of the mean climate. The changes can be attributed to human influence (due to emission of greenhouse gases) and are projected to continue into the future under all emissions scenarios. Extreme precipitation, as represented by annual maximum one-day and five-day accumulations, has also increased at the global scale. Over the global land areas where there are sufficient long-term observations, far more stations show increases in extreme precipitation than decreases. Existing studies suggest that these observed changes in extreme precipitation are attributable to human influence as well at the global scale, but evidence to date remains insufficient to confidently attribute change in precipitation extremes at regional scales. The observed intensification of extreme precipitation is projected to continue into the future, with extreme precipitation that currently has a 20-year recurrence period to become more frequent in the future, possibly becoming a six-year event by the end of the twenty-first century.

We have not reviewed new developments in the statistical literature that consider multi-variate extremes or the spatial modelling of extremes. We have also not reviewed changes in extreme precipitation and temperature over larger time scales, such as are associated with prolonged drought, etc. These are all important aspects of the research on changes in extremes, but it is difficult to discuss them in sufficient detail within the limited space of this chapter.

## References

- Alexander, L. V. and J. M. Arblaster (2009). Assessing trends in observed and modelled climate extremes over Australia in relation to future projections. *Int. J. Climatol.*, **29**, 417–435.
- Alexander, L. V., et al., (2006). Global observed changes in daily climate extremes of temperature and precipitation. *J. Geophys. Res.*, **111**, D05109, doi:10.1029/2005JD006290.
- Allen, M. R. and W. J. Ingram (2002). Constraints on future changes in climate and the hydrologic cycle. *Nature*, **419**, 224–232.
- Allen, M. R. and P. A. Stott (2003). Estimating signal amplitudes in optimal fingerprinting, Part I: Theory. *Clim. Dyn.*, **21**, 477–491.
- Arora, V. K., J. F. Scinocca, G. J. Boer, et al. (2011). Carbon emission limits required to satisfy future representative concentration pathways of greenhouse gases. *Geophys. Res. Lett.*, **38**, L05805, doi:10.1029/2010GL046270.
- Bernard, E., P. Naveau, M. Vrac, and O. Mestre (2013). Clustering of maxima: spatial dependencies among heavy rainfall in France. *J. Climate*, **26**, 7929–7937. doi: <http://dx.doi.org/10.1175/JCLI-D-12-00836.1>
- Bindoff, N.L., P.A. Stott, K.M. AchutaRao, et al., (2013). Detection and attribution of climate change: from global to regional. In *Climate Change 2013: The Physical Science Basis. Contribution of Working Group I to the Fifth Assessment Report of the Intergovernmental Panel on Climate Change* [Stocker, T.F., D. Qin, G.-K. Plattner, et al. (eds.)]. Cambridge University Press, Cambridge, United Kingdom and New York, NY, USA, pp. 867–952.
- Caesar, J., L. Alexander, and R. Vose, 2006. Large-scale changes in observed daily maximum and minimum temperatures: Creation and analysis of a new gridded data set. *J. Geophys. Res. Atmos.*, **111**, D05101.
- Christidis N., P. A. Stott, and S. J. Brown (2011). The role of human activity in the recent warming of extremely warm daytime temperatures. *J. Climate*, **24**, 1922–1930.
- Coles, S. (2001). *An Introduction to the Statistical Modeling of Extreme Values*. Springer, London, 208 pp. ISBN ISBN 1-85233-459-2.
- Cox, D. R. and D. V. Hinkley (1974): *Theoretical Statistics*. Chapman and Hall, 511 pp.
- Cox, D. R. and P. A. W. Lewis (1966): *The Statistical Analysis of Series of Events*. John Wiley and Sons, 285 pp.
- Donat, M. G., et al., (2013). Updated analyses of temperature and precipitation extreme indices since the beginning of the twentieth century: The HadEX2 dataset. *Journal of Geophysical Research: Atmospheres*, doi:10.1002/jgrd.50150.
- El Adlouni, S., T. B. M. J. Ouarda, X. Zhang, R. Roy, and B. Bobe'e (2007). Generalized maximum likelihood estimators for the nonstationary generalized extreme value model. *Water Resour. Res.*, **43**, W03410, doi:10.1029/2005WR004545.
- Fisher, R. A. and L. H. C. Tippett (1928). Limiting forms of the frequency distribution of the largest or smallest member of a sample. *Proc. Cambridge Philos. Soc.*, **24**, 180–190.
- Frei, C. and C. Schär (2001). Detection probability of trends in rare events: theory and application to heavy precipitation in the Alpine region. *J. Climate*, **14**, 1568–1584.
- Fröhlich, P., L. V. Alexander, P. Della-Marta, et al. (2002). Observed coherent changes in climatic extremes during the second half of the 20th century. *Climate Research*, **19**, 193–212.
- Fowler, H. J. and R. L. Wilby (2010). Detecting changes in seasonal precipitation extremes using regional climate model projections: Implications for managing fluvial flood risk. *Water Resour. Res.*, **46**, W03525.
- Gnedenko, B. V. (1943). Sur la distribution limite du terme maximum d'une série aleatoire (Limiting distribution of maximum values of random series). *Ann. Math.*, **44**, 423–453.
- Gumbel, E. J. (1958): *Statistics of Extremes*. Columbia University Press, 375 pp.
- Hanlon H., G. C. Hegerl, S. F. B. Tett, and D. M. Smith (2012). Can a decadal forecasting system predict temperature extreme indices? *J. Climate*, doi 10.1175/JCLI-D-12-00512.1
- Hartmann, D.L., A.M.G. Klein Tank, M. Rusticucci, et al., (2013). Observations: atmosphere and surface. In *Climate Change 2013: The Physical Science Basis. Contribution of Working Group I to the Fifth Assessment Report of the Intergovernmental Panel on Climate Change* [Stocker, T.F., D. Qin, G.-K. Plattner, et al. (eds.)]. Cambridge University Press, Cambridge, United Kingdom and New York, NY, USA, pp 158–254.
- Hasselmann, K. (1979). On the signal-to-noise problem in atmospheric response studies. In *Meteorology of Tropical Oceans* [Shaw, D. B. (ed.)]. Royal Meteorological Society, Bracknell, UK, pp. 251–259.
- Hegerl, G. C., H. v. Storch, K. Hasselmann, et al. (1996). Detecting greenhouse gas induced Climate Change with an optimal fingerprint method. *J. Climate*, **9**, 2281–2306.
- Hegerl, G.C., K. Hasselmann, U. Cubasch, et al. (1997). Multi-fingerprint detection and attribution of greenhouse-gas and aerosol-forced climate change. *Clim. Dyn.*, **13**, 613–634.
- Hegerl, G. C., O. Hoegh-Guldberg, G. Casassa, et al. (2010). Good practice guidance paper on detection and attribution related to anthropogenic climate change. In *Meeting Report of the Intergovernmental Panel on Climate Change Expert Meeting on Detection and Attribution of Anthropogenic Climate Change*, T. F. Stocker, et al., eds., IPCC Working Group I Technical Support Unit, University of Bern, Bern, Switzerland.
- Hegerl, G. C. and F. W. Zwiers (2011). Use of models in detection and attribution of climate change. *WIREs: Climate Change*, **2**, 570–591.
- Hosking, J. R. M. (1990). L-moments: analysis and estimation of distributions using linear combinations of order statistics. *J. R. Stat. Soc.*, **52**, 105–12.

- IPCC (2012). Summary for policymakers. In *Managing the Risks of Extreme Events and Disasters to Advance Climate Change Adaptation* [Field, C.B., V. Barros, T.F. Stocker, et al. (eds.)]. A Special Report of Working Groups I and II of the Intergovernmental Panel on Climate Change. Cambridge University Press, Cambridge, UK, and New York, NY, USA, pp. 1–19.
- Katz, R., M. Parlange, and P. Naveau (2002). Extremes in hydrology. *Adv. Water Resour.*, **25**, 1287–1304.
- Keim, B. D. and J. F. Cruise (1998). A technique to measure trends in the frequency of discrete random events. *J. Climate*, **11**, 848–854.
- Klok, E. J. and A. Tank, 2009. Updated and extended European dataset of daily climate observations. *Int. J. Climatol.*, **29**, 1182–1191.
- Kunkel, K. E., K. Andsager, and D. R. Easterling (1999). Long-term trends in extreme precipitation events over coterminous United States and Canada. *J. Climate*, **12**, 2515–2527.
- Kharin, V. V. and F. W. Zwiers (2000). Changes in the extremes in an ensemble of transient climate simulation with a coupled atmosphere–ocean GCM. *J. Climate*, **13**, 3760–3788.
- Kharin, V. V. and F. W. Zwiers (2005). Estimating extremes in transient climate change simulations. *J. Climate*, **18**, 1156–1173.
- Kharin, V. V., F. W. Zwiers, X. Zhang, and G. C. Hegerl (2007). Changes in temperature and precipitation extremes in the IPCC ensemble of global coupled model simulations. *J. Climate*, **20**, 1419–1444.
- Kharin, V. V., F. W. Zwiers, X. Zhang, and M. Wehner (2013). Changes in temperature and precipitation extremes in the CMIP5 ensemble. *Clim. Change*, doi:10.1007/s10584-013-0705-8.
- Meehl, G. A., J. M. Arblaster, and C. Tebaldi (2007). Contributions of natural and anthropogenic forcing to changes in temperature extremes over the U.S. *Geophys. Res. Lett.*, **34**, L19709.
- Min, S.-K., X. Zhang, F. W. Zwiers, and G. C. Hegerl (2011). Human contribution to more-intense precipitation extremes. *Nature*, **470**, 378–381. doi: 10.1038/nature09763
- Min, S.-K., X. Zhang, F. Zwiers, et al. (2013). Multi-model detection and attribution of extreme temperature changes. *Journal of Climate*, doi:10.1175/JCLI-D-12-00551.w.
- Morak, S., G. C. Hegerl, and N. Christidis (2013). Detectable changes in the frequency of temperature extremes. *Journal of Climate*, **26**, 1561–1574.
- Morak, S., G. C. Hegerl, and J. Kenyon (2011). Detectable regional changes in the number of warm nights. *Geophysical Research Letters*, **38**, L17703.
- Mueller B and S. I. Seneviratne (2012). Hot days induced by precipitation deficits at the global scale. *Proc Natl Acad Sci USA*, **109**, 12398–12403, doi: 10.1073/pnas.1204330109.
- Ribes A, S. Planton, and L. Terray (2013). Application of regularized optimal fingerprinting to attribution. Part I: method, properties and idealized analysis. *Clim Dyn*, doi:10.1007/s00382-013-1735-7
- Seneviratne, S.I., N. Nicholls, D. Easterling, et al., (2012). Changes in climate extremes and their impacts on the natural physical environment. In *Managing the Risks of Extreme Events and Disasters to Advance Climate Change Adaptation* [Field, C.B., V. Barros, T.F. Stocker, et al. (eds.)]. A Special Report of Working Groups I and II of the Intergovernmental Panel on Climate Change (IPCC). Cambridge University Press, Cambridge, UK, and New York, NY, USA, pp. 109–230.
- Shepard, D. (1968). A two-dimensional interpolation function for irregularly spaced data, paper presented at 23rd National Conference, Assoc. for Comput. Mach, New York.
- Sillmann, J., M. Kallache, M. Croci-Maspoli, and R. W. Katz, (2011). Extreme cold winter temperatures in Europe under the influence of North Atlantic atmospheric blocking. *Journal of Climate*, **24**, 5899–5913.
- Sillmann, J., V. V. Kharin, F. W. Zwiers, X. Zhang, and D. Bronaugh (2013). Climate extremes indices in the CMIP5 multimodel ensemble: Part 2. Future climate projections. *J. Geophys. Res. Atmos.*, **118**, 2473–2493, doi:10.1002/jgrd.50188
- Sillmann, J., M. Donat, J. C. Fyfe, and F. W. Zwiers (2014). Observed and simulated temperature extremes during the recent warming hiatus. *Environmental Research Letters*, **9**(6), 8 pp.
- Smith, R. L. (1989). Extreme value analysis of environmental time series: an application to trend detection in ground-level ozone (with discussion). *Stat. Sci.*, **4**, 367–393.
- Trenberth, K. E., P. D. Jones, P. Ambenje, et al. (2007). Observations: surface and atmospheric climate change. In *Climate Change 2007: The Physical Science Basis*. Contribution of Working Group I to the Fourth Assessment Report of the Intergovernmental Panel on Climate Change [Solomon, S., D. Qin, M. Manning, et al. (eds.)]. Cambridge University Press, Cambridge, United Kingdom and New York, NY, USA.
- Wang, X. L. and V. R. Swail (2004). Historical and possible future changes of wave heights in northern hemisphere oceans. In: *Atmosphere Ocean Interactions*, **2**, W. Perrie (ed.). Wessex Institute of Technology Press, Southampton, UK.
- Wang, J. and X. Zhang (2008). Downscaling and projection of winter extreme daily precipitation over North America. *J. Climate*, **21**, 923–937.
- Wehner, M. F. (2013). Very extreme seasonal precipitation in the NARCCAP ensemble: model performance and projections. *Clim Dyn*, **40**, 59–80. doi: 10.1007/s00382-012-1393-1.
- Wehner M. F., R. L. Smith, and T. L. Pala Duffy (2010). The effect of horizontal resolution on simulation of very extreme precipitation events in a global atmospheric model. *Clim Dyn* **34**, 241–247. doi: 10.1007/s00382-009-0656-y
- Wen, H. Q., X. Zhang, Y. Xu, and B. Wang (2013). Detecting human influence on temperature extremes in China. *Geographical Research Letter*, doi: 10.1002/grl.50285
- Westra, S., L. V. Alexander, and F. W. Zwiers (2013). Global increasing trends in annual maximum daily precipitation. *J. Climate*, doi:10.1175/JCLI-D-12-00502.1.
- Woodhouse C. A., D. M. Meko, G. M. MacDonald, D. W. Stahle, and E. R. Cook (2010). A 1200-year perspective on 21st century drought in southwestern North America. *Proc Natl Acad Sci USA*, **107**, 21283–21288.

- Woodhouse C.A. and J. T. Overpeck (1998.: 2000 years of drought variability in the central United States. *Bull Am Meteorol Soc*, **79**, 2693–2714.
- Zhang X., L. V. Alexander, G. C. Hegerl, *et al.* (2011). Indices for monitoring changes in extremes based on daily temperature and precipitation data. *Wiley Interdiscip Rev Clim Change*, 851–870. doi: 10.1002/wcc.147
- Zhang, X., W. D. Hogg, and E. Mekis (2001). Spatial and temporal characteristics of heavy precipitation events over Canada. *J. Climate*, **14**, 1923–1936.
- Zhang, X., H. Wan, F. W. Zwiers, G. C. Hegerl, and S.-K. Min, (2013). Attributing intensification of precipitation extremes to human influence, *Geophys. Res. Lett.*, **40**, 5252–5257, doi:10.1002/grl.51010.
- Zhang, X., J. Wang, F. W. Zwiers, and P. Y. Groisman (2010). The influence of large scale climate variability on winter maximum daily precipitation over North America. *J. Climate*, **23**, 2902–2915.
- Zhang, X. and F. W. Zwiers (2013). Statistical indices for diagnosing and detecting changes in extremes. In *Hydrologic Extremes in a Changing Climate: Detection, Analysis & Uncertainty* (Eds. Sorooshian *et al.*), Springer-Verlag.
- Zhang X., F. W., Zwiers, and G. Li (2004). Monte Carlo experiments on the detection of trends in extreme values. *J. Climate*, **17**, 1945–1952.
- Zwiers, F. W. and V. V. Kharin (1998). Changes in the extremes of climate simulated by CCC GCM2 under CO<sub>2</sub> doubling. *J. Climate*, **11**, 2200–2222.
- Zwiers, F. W., X. Zhang, and Y. Feng (2011). Anthropogenic influence on long return period daily temperature extremes at regional scales. *J. Climate*, **24**, 881–892.



## PART II

### **High-impact weather in mid latitudes**



# 5

## Rossby wave breaking: climatology, interaction with low-frequency climate variability, and links to extreme weather events

*Olivia Martius and Gwendal Rivière*

### 5.1 Introduction

Breaking Rossby waves (RWB) are an integral feature of the atmospheric flow and play a key role in the meridional transport of momentum and the meridional exchange of ozone and moisture. Furthermore, and importantly in the context of this book, they are closely linked to the surface weather evolution and the formation of high-impact weather events. This chapter is organized as follows. Firstly, a definition and description of RWB are given ([Section 5.2](#)), then the climatological occurrence of RWB and links to low-frequency patterns of variability are illustrated ([Section 5.3](#)). Finally, the relationship between RWB and surface weather is discussed in [Section 5.4](#), with particular emphasis on extreme and high-impact weather events.

### 5.2 Rossby wave breaking: definition and upper-level signature

RWB is defined in a very general way as ‘a process in which material contours are rapidly and irreversibly deformed’ (McIntyre and Palmer, 1984). This general definition applies to both planetary-scale RWB in the stratosphere and to synoptic-scale RWB at the tropopause. The focus of this chapter is on synoptic-scale RWB events. On isentropic surfaces, RWB adopts the shape of meridionally elongated and narrow tongues of potential vorticity (PV), which can overturn and thereby result in an inversion of the meridional PV gradient (McIntyre and Palmer (1984); see [Fig. 5.1](#) for an example). The inverted meridional PV gradient is often used to detect RWB in automated RWB identification algorithms.

In the extratropics, synoptic-scale RWB forms during the final, nonlinear, part of the life cycle of baroclinic waves. Some of these baroclinic RWB events reach as far equatorward as the subtropics. However, in the subtropics and the deep tropics, RWB can also form independently of extratropical baroclinic waves, downstream and to the

south of subtropical anticyclones (Postel and Hitchman, 1999). Hitchman and Huesman (2007) refer to these RWB events as Monsoon RWB.

The temporal evolution of extratropical RWB typically follows one of two distinctive life cycles (Thorncroft *et al.*, 1993). These two life cycles were first identified in idealized numerical simulations of baroclinic waves, and are known as LC1 (anticyclonic type) and LC2 (cyclonic type). The two life cycles emerge from adding a barotropic anticyclonic or cyclonic shear to a basic state flow in these idealized simulations. The upper-level flow evolution of the two life cycles diverges strongly during the nonlinear phase of the life cycle when the waves break. The cyclonic type (LC2) corresponds to a cyclonic overturning of isentropic PV isolines along the cyclonically sheared, poleward edge of the jet, and to a broadening of the wave trough in the zonal direction ([Fig. 5.1a](#)). The anticyclonic type (LC1) corresponds to an anticyclonic overturning of PV isolines on the anticyclonically sheared, equatorward edge of the jet, and to a progressive thinning of the wave trough ([Fig. 5.1b](#)). During the final stage of the anticyclonic life cycle, the trough can eventually decay into one, or several, cut-off cyclones.

Appenzeller and Davies (1992) provide a detailed description of synoptic-scale RWB structures and their temporal evolution based on upper-tropospheric water vapour imagery. This imagery beautifully illustrates the irreversible decay of the LC1 RWB structures through stretching, thinning, and their eventual breakup into individual vortices. The two different life cycles are linked to distinct surface weather patterns such as cyclones and frontal features (Davies *et al.*, 1991). This link will be discussed in [Section 5.4](#).

Breaking waves exert an important forcing on the upper-level circulation through the associated westerly momentum fluxes. The momentum flux is directed poleward for LC1 RWB, but equatorward for LC2 RWB. As a consequence, the jet in the vicinity of the breaking wave is shifted northwards after completion of an LC1 RWB, but

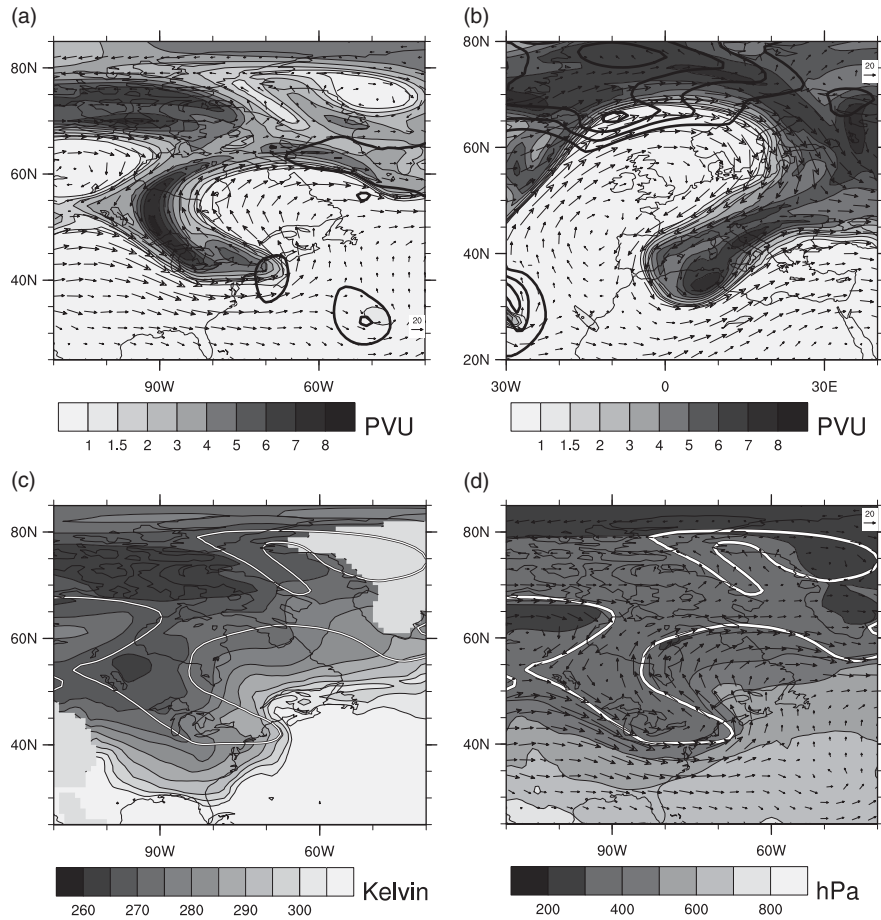


Fig. 5.1. (a) 1200 UTC 2 December 2005, PV (colour shading) and wind vectors (arrows) on the 310 K isentrope and sea-level pressure (SLP) (black contours; 990, 995, 1000, 1005, and 1010 hPa). (b) 0000 UTC 11 December 2005, PV (colour shading) and wind vectors (arrows) on the 330 K isentrope and SLP (black contours; 990, 995, 1000, 1005, and 1010 hPa). (c) 1200 UTC 2 December 2005, equivalent potential temperature at 850 hPa (colour shading) and the 2 PVU contour on the 310 K isentrope (white contour). (d) 1200 UTC 2 December 2005, height of the 310 K isentrope (colour shading) and wind vectors (arrows) and the 2 PVU contour on the 310 K isentrope (white contour)

southwards after completion of an LC2 RWB. This interaction between the jet and RWB is discussed in more detail in the [next chapter](#).

### 5.3 Climatological occurrence of RWB and link to patterns of low-frequency variability

In the extratropics, the spatial distribution of RWB is governed by the topography and location of the main baroclinic zones (Gerber and Vallis, 2009). RWB frequency maxima are located in areas where the time mean wind speeds and time mean horizontal PV gradients are weak. In the climatological mean LC2, RWB is located at the poleward edge of the extratropical jet, while the LC1 RWB is located equatorward of the extratropical jet (Figs. 5.2 and 5.3). The climatological occurrence of equatorward LC1 and LC2 RWB is described in the next paragraph. For more detailed information on poleward RWB, the reader is referred to Wernli and Sprenger (2007).

#### 5.3.1 Climatological occurrence of RWB

The RWB climatologies presented here were obtained using an object-based RWB detection algorithm developed by Wernli and Sprenger (2007) (Fig. 5.2) and a PV-contour reversal-based RWB detection algorithm (Rivière *et al.*, 2010) (Fig. 5.3). Both were applied to the ERA-interim data set (Dee *et al.*, 2011). These RWB climatologies were generally in good agreement with climatologies based on slightly different detection methods and other data sets.

In winter, extratropical LC2 RWB frequency maxima are located on the poleward flank of each core region of storm tracks, while LC1 RWB frequency maxima are located downstream of the storm tracks (Fig. 5.3). This is a consequence of the life cycle of baroclinic waves. They form in regions of strong thermal contrasts (hereafter called baroclinicity) on the western side of the oceanic basins and reach their maximum amplitude in the middle of the basins, where they lose their energy to the background state while breaking. During this process, the waves accelerate the upper-level westerlies at mid latitudes by depositing westerly momentum there and forming the so-called

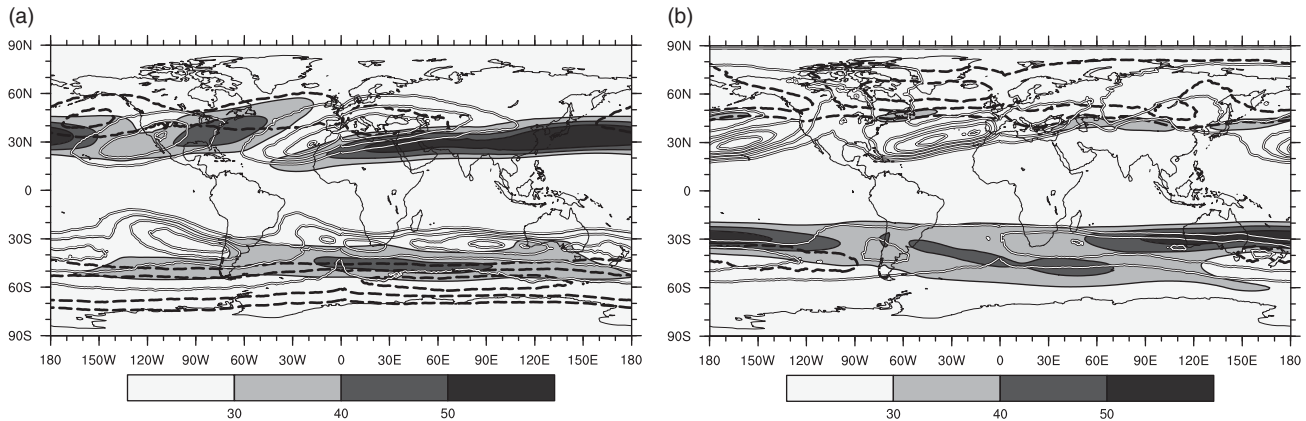


Fig. 5.2. (a) DJF frequency of LC1 RWB (solid lines) and LC2 RWB (dashed lines). The contours start at 5%, increasing in 5% steps and indicate a vertically aggregated (300–360 K) RWB frequency using the detection algorithm of Wernli and Sprenger (2007). The grey shading is the DJF mean wind velocity at 200 hPa. (b), as (a), but for JJA.

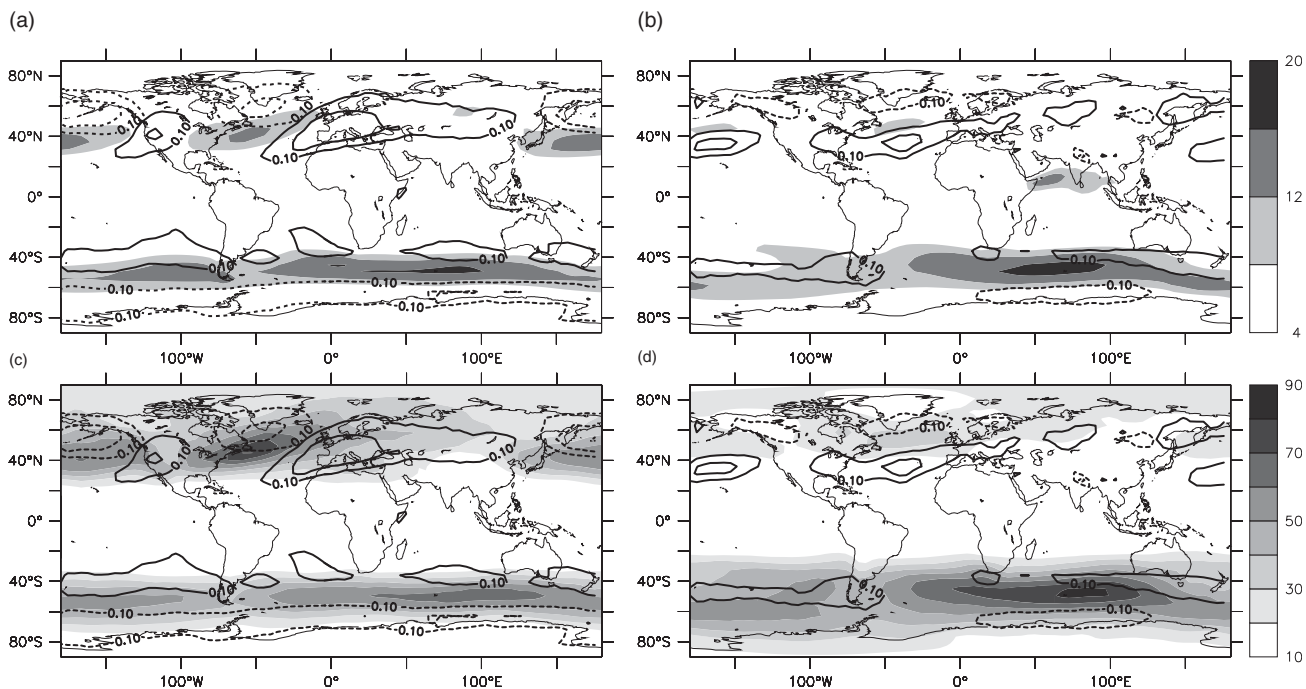


Fig. 5.3. (a) and (c) DJF frequency of LC1 RWB (solid lines) and LC2 RWB (dashed lines). The contours start at 10%, increasing in 5% steps and indicate a vertically aggregated RWB frequency based on PV contour overturnings at 300, 315, 330, and 350 K. The grey shading is in (a) the DJF mean zonal wind at 800 hPa and in (c) the DJF high-frequency (periods less than one week) eddy kinetic energy at 500 hPa. (b) and (d), as (a) and (c), respectively, but for JJA.

eddy-driven jet (Fig. 5.3a–b). LC1 and LC2 RWB events occur on the equatorward and poleward sides, respectively, of the eddy-driven jets on the eastern side of the North Pacific and North Atlantic basins (Figs. 5.2 and 5.3). Peak densities of LC1 RWB events are found on the poleward side of the subtropical jets (e.g. the African subtropical jet during December–January–February (DJF) or the Australian

subtropical jet during June–July–August (JJA) in Fig. 5.2). In other words, LC1 maximum densities are found between the subtropical and eddy-driven jets when both jets coexist at the same longitude, while LC2 densities always peak on the poleward side of the eddy-driven jets. In the subtropics during the Northern Hemisphere winter, RWB frequency maxima are located over the eastern Atlantic and the eastern

Pacific oceans. During the Southern Hemisphere winter, fewer RWB events occur in the subtropical regions, which is consistent with the more poleward position of the eddy-driven jets (50S) compared with the Northern Hemisphere (about 40N; Fig. 5.3a and b).

In the Northern Hemisphere summer (JJA), extratropical frequency maxima are located in the extratropics over the Atlantic, the Asian continent, and the Pacific (primarily LC2 RWB), while in the subtropics, LCI frequency maxima extend across the entire Atlantic and Pacific basins. LC1 RWB frequency maxima lie in the middle of the oceans during JJA, whereas they are located on the eastern side of the ocean basins during DJF. During the Southern Hemisphere summer (DJF), more LC2 RWB events occur on the poleward side of the eddy-driven jets compared with the Southern Hemisphere winter. In the subtropics, LC1 RWB densities have local maxima over the eastern Pacific, the Atlantic, and the central Indian Ocean (Fig. 5.2). Breaking events that reach the deep tropics (10°S to 10°N) are more frequent during the Northern Hemisphere winter and are typically located in the longitudinal bands of the westerly ducts (Waugh and Polvani, 2000).

For more detailed information on the climatology of Northern Hemisphere RWB, the reader is referred to Postel and Hitchman (1999), Wernli and Sprenger (2007), Martius *et al.* (2007), Hitchman and Huesmann (2007), and Woollings *et al.* (2008). For more information on the climatology of Southern Hemisphere RWB, the reader is referred to Postel and Hitchman (1999), Hitchman and Huesmann (2007), Berrisford *et al.* (2007), and Ndarama and Waugh (2011).

The frequency of RWB is not constant over time (Isotta *et al.*, 2008) and it is expected to change in a warmer climate. Model projections indicate that in a warmer climate a poleward shift of the extratropical jet will be accompanied by a reduction in LC2 RWB and an increase in LC1 RWB (Riviere, 2011, Barnes and Hartmann, 2012).

### 5.3.2 RWB and patterns of low-frequency variability

The relation between low-frequency patterns of variability and synoptic-scale RWB is bi-directional. Low-frequency patterns of variability modify the background state and thereby the type and frequency of RWB. RWB, on the other hand, can extend the lifetime of extratropical and potentially even tropical patterns of variability. An example of the first type of interaction is the tropical patterns of variability, which modulate subtropical and extratropical RWB through the interaction of the upper-level outflow of tropical convection with the subtropical and extratropical jets. For example, the El Niño Southern Oscillation (ENSO) and associated changes in the jet structure affect the frequency of LC1 RWB and LC2 RWB in the Pacific Basin in both hemispheres (Fig. 5.4). There is an increase in LC2 RWB during the warm phase of ENSO, when a zonally extended jet is present over the North Pacific, and a reduction in LC2 RWB during the cold phase of ENSO; and during the cold phase of ENSO the subtropical LC1 RWB increases (Shapiro *et al.* (2001); Fig. 5.4) in areas where the jets are more diffluent. This signal of increased LC1 RWB carries forward into the deep tropics where more tropical RWB events are found in the Pacific Basin during the cold phase (Waugh and Polvani, 2000). In contrast, more RWB events occur in the Southern Hemisphere Atlantic Basin during the warm phase (Berrisford *et al.*, 2007). The increase in LC1 RWB in the tropics during the cold phase goes in tandem with stronger equatorial westerlies, i.e. “active” westerly ducts, and changes in the tropospheric moisture availability (Waugh and Polvani, 2000). Further on, Riviere and Orlanski (2007) suggest that enhanced moisture availability in the Caribbean region during the warm phase could be linked to increased LC2 RWB over the extratropical Atlantic during the warm phase.

Similarly to ENSO, the Madden–Julian Oscillation (MJO) also modulates the frequency of LC1- and LC2-type RWB

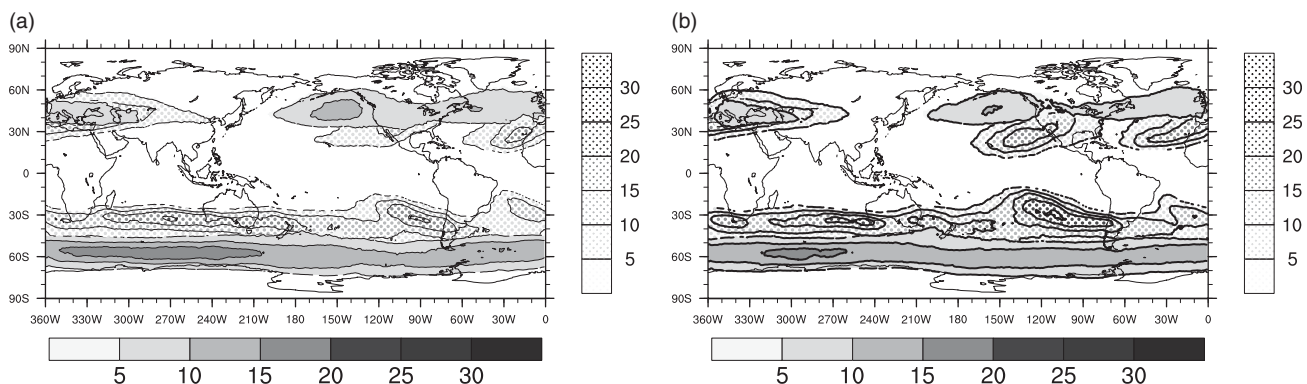


Fig. 5.4. (a) DJF frequency of LC1 RWB (dotted contours) and LC2 RWB (filled contours) during El Niño seasons. Contours start at 5% and increase in 5% steps. (b) As (a), but for La Niña seasons.

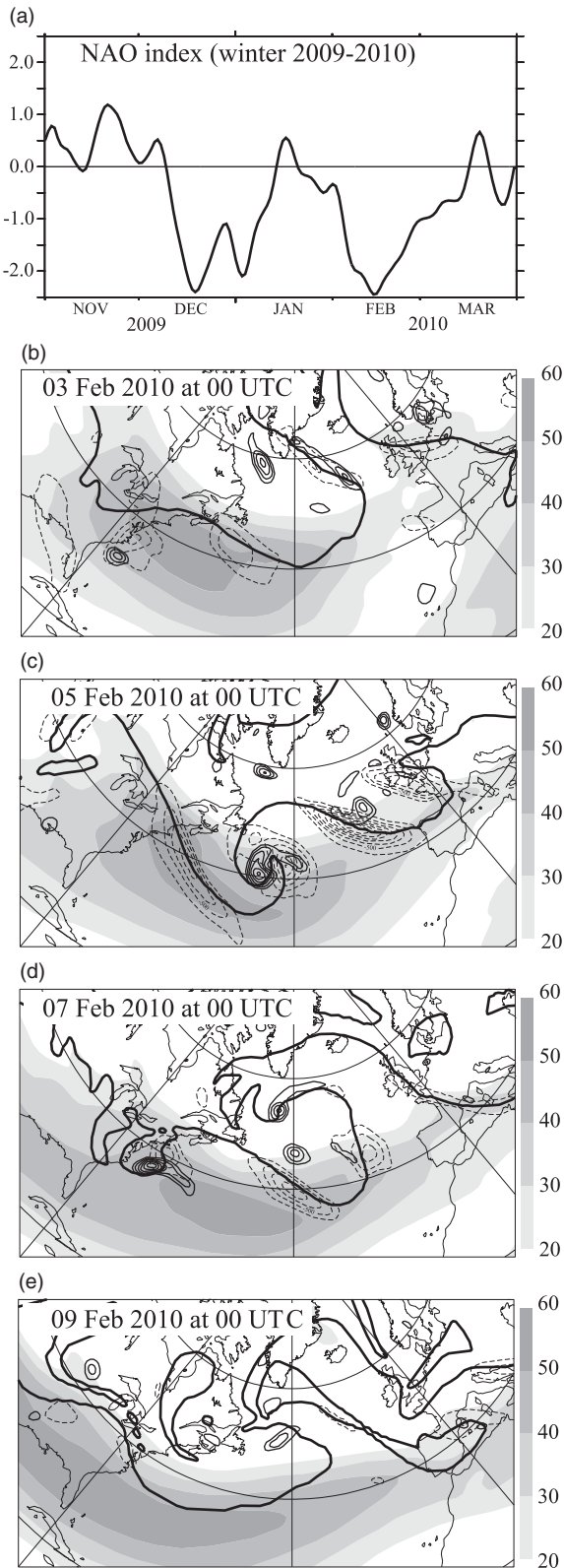


Fig. 5.5. Example of LC2 RWB events leading to the formation of the negative NAO phase in early February 2010. (a) Daily

in the Pacific (Moore *et al.*, 2010) and Atlantic basins (Cassou, 2008).

RWB is also closely related to extratropical variability. Over recent years, a new paradigm has emerged that links extratropical variability such as the North Atlantic Oscillation (NAO) directly to RWB (e.g. Franzke *et al.*, 2004, Benedict *et al.*, 2004). The dynamics of the NAO can be interpreted as variations in the frequency of occurrence of LC1- and LC2-type RWB. The presence or absence of breaking waves is reflected in variations in the surface pressure signal, surface temperature signal, storm track, and upper-level flow, and these flow anomalies project onto the NAO pattern.

More specifically, the negative phase of the NAO corresponds to periods with enhanced LC2 RWB over Greenland and the western North Atlantic, and a southward shifted extratropical jet. This is illustrated in Fig. 5.5a, which shows the NAO index for the winter of 2009–2010. In early February, the NAO index was almost zero (Fig. 5.5a) and the Atlantic jet was located at 40°N, and was well separated from the African subtropical jet (Fig. 5.5b). Between 3 February and 9 February, a succession of LC2 RWB events occurred over the western Atlantic that resulted in equatorward oriented momentum fluxes at upper-tropospheric levels. These momentum fluxes pushed the Atlantic jet successively equatorward. The result was that a zonally oriented jet merged with the African subtropical jet (Fig. 5.5e), while at the same time, the NAO index became strongly negative. The positive phase of the NAO is characterized by the absence of LC2 RWB over the western North Atlantic, enhanced LC1 RWB over the eastern subtropical Atlantic, and a double jet structure over the Atlantic with a northward shifted extratropical jet.

A positive feedback exists between the latitudinal position of the jet and the momentum fluxes associated with the breaking waves. There is a preference for cyclonic wave breaking if the jet is located farther south (Rivière, 2009) and the momentum fluxes associated with the cyclonically breaking waves keep the jet in its southerly position. Similarly, anticyclonic wave breaking occurs preferentially when the jet is located farther north (Rivière, 2009) and the associated momentum fluxes keep the jet in its northerly position. This feedback links the dynamics at the synoptic

---

Caption for Fig. 5.5. (cont.) NAO index from November 2009 to March 2010. (b)–(e) Snapshots from 3 February to 9 February 2010 of low frequency (periods longer than eight days) zonal wind (grey colour bar; units:  $\text{ms}^{-1}$ ), high-frequency eddy momentum fluxes (dashed contours for negative values only; interval:  $250 \text{ m}^2 \text{ s}^{-2}$ ), positive relative vorticity at 850 hPa (black contours; interval:  $5 \cdot 10^{-5} \text{ s}^{-1}$ ), and the 2 PVU contour at the 315 K isentropic surface (thick black contour). Data from ERA-interim reanalysis.

timescale to the lower frequency intraseasonal variability of the NAO. For instance, the intense storm in the mid Atlantic on 5 February (Fig. 5.5c) followed an LC2 life cycle and resulted in an equatorward acceleration of the low-frequency jet. The subsequent LC2 RWB events reinforced the equatorward shift of the jet, and in that sense provides an example of the positive eddy feedback. However, the positive feedback can be interrupted by one, or several, successive strong storms associated with intense RWB events over the western Atlantic (Rivière and Orlanski, 2007).

In the context of low-frequency variability, it is important to briefly discuss the link between RWB and blocking events. From an upper-level PV perspective, the majority of blocking episodes are associated with, or essentially correspond to, RWB because the blocks encompass areas of meridionally overturning PV contours and hence RWB (Pelly and Hoskins, 2003, Masato *et al.*, 2012). Conversely, not all RWB events correspond to blocking anticyclones. Blocking events are typically located at the latitudes of the main storm tracks, and they persist for an extended time period. Consequently, Berrisford *et al.* (2007) and Woollings *et al.* (2008) classify wave-breaking events as blocks if they have a significant vertical extent and occur in a region where the time mean westerly flow exceeds a defined threshold.

The RWB events located upstream (mainly LC2 RWB) and downstream (mainly LC1 RWB) of a block can be important for blocking maintenance (Hoskins *et al.*, 1983) and for blocking stationarity (Altenhoff *et al.*, 2008). European blockings are usually triggered by quasi-stationary Rossby wave trains initiated in the subtropical western Atlantic (Nakamura *et al.*, 1997, Michel and Rivière, 2011). The breaking of a ridge associated with a quasi-stationary Rossby wave train can also contribute to the blocking amplification and persistence (Nakamura *et al.*, 1997) together with synoptic RWB events (Michel and Rivière, 2011). RWB can also be responsible for the displacement of a block. Scandinavian blocking, for instance, can be displaced from Scandinavia towards Greenland by an intensified LC2 RWB on its western edge, which results in a negative NAO phase (Michel and Rivière, 2011, Michel *et al.* 2012).

In summary numerous studies over past decades have shown that RWB reinforces low-frequency anomalies and maintains them as they are. However, there is also some evidence that RWB events disrupt existing low-frequency anomalies and assist the formation of new ones.

#### 5.4 RWB and surface weather

Breaking Rossby waves in the extratropics are typically linked to a distinct surface synoptic development. This link

between upper-level breaking waves and the strength, temporal evolution, and spatial configuration of surface frontal systems has been examined in idealized dry life cycle experiments (Davies *et al.*, 1991, Thorncroft *et al.*, 1993, Davies, 1999). In these simulations, the weather evolution differs between the two life cycles, with the surface low located farther south during the cyclonic life cycle compared with the anticyclonic life cycle. In the cyclonic case, a bent-back warm front is present, and the cold front is disrupted to the southeast of the cyclone. In the anticyclonic case, the cold front is connected to the surface low and the warm front is weaker.

RWB events are upper-level PV anomalies, and hence their effects on tropospheric flow and surface weather evolution can be significant. The following summary is based on the concepts presented in Hoskins *et al.* (1985). The effects are described for the positive upper-level PV anomalies within a tropopause-level breaking wave. These positive PV anomalies are associated with a cyclonic wind field that extends from the tropopause down into the troposphere, and in some cases all the way to the surface (see Fig. 5.6 for an example). The vertical depth of the wind field associated with the upper-level positive PV anomaly depends on the horizontal scale of the upper-level anomaly and the stratification of the atmosphere, i.e. the Rossby depth (Hoskins *et al.* 1985). Larger-scale anomalies and an

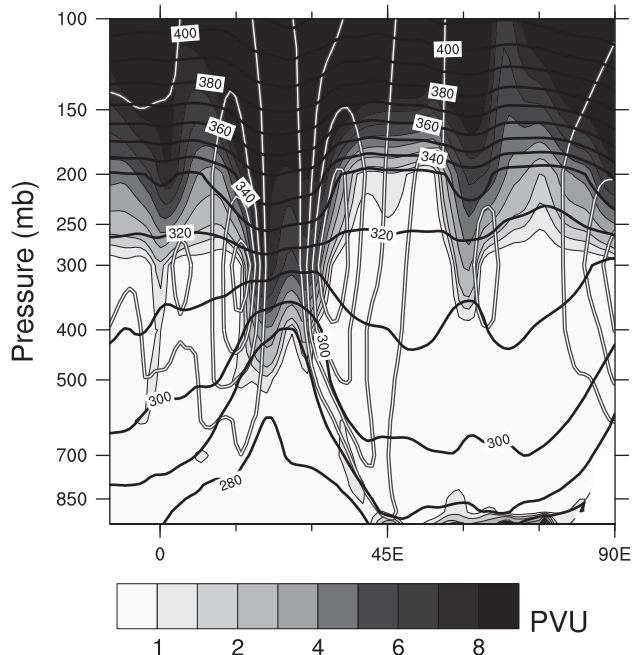


Fig. 5.6. 1200 UTC 2 December 2005 vertical cross-section taken at 45°N showing PV (colour shading), isentropes (solid black lines), and the wind velocity (white lines; interval: 10 ms<sup>-1</sup> starting at 20 m s<sup>-1</sup>).

unstable stratification favour a deeper vertical extent. Positive upper-level PV anomalies are further associated with a reduction in the static stability and cold temperature anomalies underneath in the troposphere (Figs. 5.1 and 5.6). If the temperature anomalies extend down to the surface, then surface frontal structures form (Fig. 5.1).

The propagation of the upper-level positive PV anomaly can result in a lifting motion along the upward sloping isentropes on the downstream flank, and in isentropic descent along the upstream flank; i.e. the so-called vacuum cleaner effect. In the example presented in Fig. 5.1, the 300 K isentrope directly underneath the breaking wave is approximately 200 hPa higher than its elevation to the east of the breaking wave. If the upper-level anomaly is oriented in the meridional direction, the combination of north–south sloping isentropes and the southerly flow field along the downstream edge of the breaking wave will result in additional lifting (Fig. 5.1). This adiabatic lifting can be enhanced by diabatic heating along the downstream edge of the RWB; for example, when a warm conveyor belt is present.

Both the tropospheric wind field and the effects on tropospheric stability are important for the evolution of surface weather. For example, the effect of the upper-level anomalies on the low-level flow field is very important for the formation and intensification of precipitation in mountainous terrain in the extratropics and subtropics (Doswell *et al.*, 1998). The forced ascending motion along the downstream edge of the breaking wave can further assist the formation and intensification of precipitation (e.g. Masato *et al.*, 2012).

In the subtropics and tropics the lower static stability underneath the upper-level trough can play an important role in triggering convection (Funatsu and Waugh, 2008). This process is important, not only over synoptic time scales, where intensive storms can be triggered by the upper-level breaking waves (see Section 5.4.1), but also over seasonal time scales. A feedback between the tropics and the extratropical dynamics can arise, where strong and organized tropical convection affects the propagation and breaking of Rossby waves in the subtropics. RWB in return affects the frequency and location of tropical convection (Slingo, 1998). For example Matthews and Kiladis (1999) show that the reduction of the upper-level wave activity during the ENSO warm phase occurs in tandem with a statistically significant decrease in tropical convection just downstream of the area where these waves typically break. The forcing of tropical convection by upper-level troughs, i.e. breaking waves in the subtropics, is particularly relevant in the tropical eastern Pacific in the area of the westerly ducts (Kiladis and Weickmann, 1992, Slingo, 1998), and in the tropical eastern Atlantic and over West Africa (Kiladis and Weickmann, 1992, Knippertz, 2007). Individual cases of

tropical–extratropical–subtropical interactions that involve wave breaking are discussed in the next section.

## 5.5 Link to high-impact weather events

Breaking waves have been linked to a myriad of extreme and high-impact weather events in various parts of the world, and a limited and subjective selection is presented here. The effects of the upper-level RWB on the lower tropospheric wind field and stratification, as discussed in the previous section, are very important for the formation of extreme weather events. A first important point is the transport of moisture by the tropospheric wind field associated with breaking waves. Substantial amounts of moisture can be transported (amounts similar to the discharge of the Amazon River, e.g. Schlemmer *et al.* (2010)) and this moisture contributes to extreme precipitation events.

This process is especially effective, and will often result in extreme precipitation events, if the flow is directed perpendicular to an orographic obstacle. Examples of extreme precipitation events driven by RWB have been documented in the Alps (Massacand *et al.*, 1998, see also Fig. 5.7), in Pakistan (Martius *et al.*, 2013), and in North Africa (Knippertz, 2005), but the process also plays an important role in forcing extreme over other mountainous areas in middle latitudes. The interaction of synoptic-scale wave-breaking with the orography can also be responsible for the channeling of low-level moisture fluxes that favour convection in some regions of the western Mediterranean (Nuissier *et al.*, 2008).

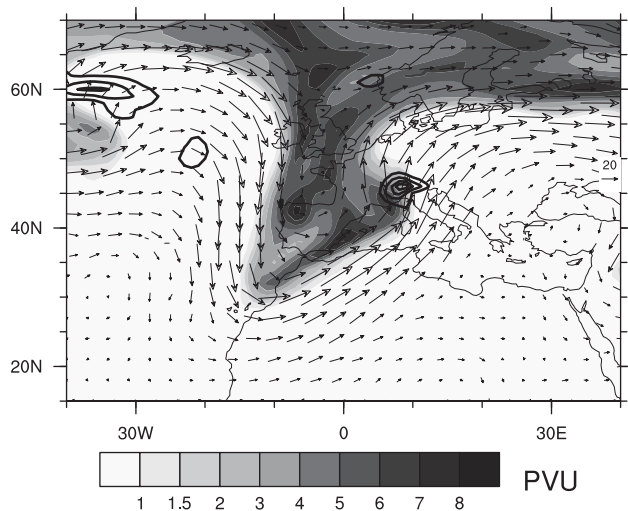


Fig. 5.7. 1200 UTC 16 November 2002 PV on the 320 K isentrope (shading), wind vectors on the same isentrope (arrows), and 6 h accumulated ERA-interim precipitation (9 UTC to 15 UTC, solid black lines; interval: 5 mm starting at 5 mm).

The advection of anomalously cold or warm air by upper-level breaking waves can lead to extreme temperature events. Heat waves and bushfires in southeastern Australia, for example, have been linked to anticyclonically breaking waves that advect very warm air from the interior of the continent to the coasts (Engel *et al.*, 2013). An example of cold extremes is given by the cold surges that affect the coffee growing areas of Brazil. Strong southerly flows associated with an upper-level blocking located upstream of South America, accompanied by a breaking wave downstream of the block, advect very cold air equatorwards into Brazil (Sprenger *et al.*, 2013). Similarly, cool spells in East Asia in summer can be driven by strong surface flow associated with anticyclonic RWB and blocking (Nakamura and Fukamachi, 2004). Wintertime cold spells over East Asia can also be linked to cyclonic RWB (Takaya and Nakamura, 2005).

Climatologically, extreme cold events occur more frequently during periods when wave breaking is more prevalent (Cai, 2003). Snowstorms and blizzards over North America are often closely related to RWB events over the western Atlantic; e.g. in February 2010, a series of cyclonic wave-breaking events occurred over the northeast coast of the USA and downstream in the mid Atlantic. Those RWB events over the USA were related to intense blizzards at the surface, such as that shown in Fig. 5.5d. Two of these events led to very significant snowfall accumulation in early February. However, this link between North American blizzards, LC2 events, and negative NAO cannot be considered to be systematic. For example, the superstorm of March 1993, referred to as the storm of the century, led to an exceptional anticyclonic wave-breaking event in the mid Atlantic and an abrupt transition towards the positive phase of the NAO (Riviere and Orlanski, 2007).

Finally, we note that the momentum fluxes associated with North American and Atlantic storms and RWB affect the storm tracks downstream. At the end of February 2010, and because of the unusually negative NAO index and southward displaced jet, the European wind storm Xynthia was initiated very far south, and followed a very unusual trajectory, as it moved rapidly from the subtropics towards Spain and France. Generally, the concomitant occurrence of cyclonic and anticyclonic RWB over the eastern Atlantic leads to an eastward extension of the eddy-driven jet. This flow configuration is favourable for the formation and intensification of extreme winter storms affecting central Europe (Hanley and Caballero, 2012).

Anticyclonically breaking waves often result in the formation of upper-level cut-off structures, which can then affect the surface weather. One example of this process is given by the lee cyclones that form over the Gulf of Genoa, which can trigger, locally, high-impact weather, ranging

from intense precipitation (e.g. Porcu *et al.*, 2007) to severe hurricane-like storms (e.g. Fita *et al.*, 2007). In rare and extreme cases, these cut-off lows move northeastward and trigger heavy precipitation in central Europe (e.g. Ulbrich *et al.*, 2003, Enomoto *et al.*, 2007).

The upper-level high PV signature of anticyclonic wave breaking that reaches far into the subtropics can trigger convection through forced vertical motion and a destabilization of the atmosphere. In a moisture-rich environment, these high PV intrusions can initiate tropical cyclogenesis (e.g. Davis and Bosart, 2006).

This process, known as tropical transition, is most relevant in the tropical eastern Atlantic, where 60% of all storms are influenced by baroclinic systems during their formation phase (McTaggart-Cowan *et al.*, 2008), but is also relevant in all other ocean basins where tropical cyclones form (McTaggart-Cowan *et al.*, 2013). A more benign form of this interaction is the triggering of so-called Kona lows, which are subtropical cyclones that affect the islands of Hawaii, by breaking Rossby waves in the central Pacific (Moore *et al.*, 2008). However, wave breaking is not only relevant for tropical cyclone formation: the interaction of an upper-level breaking wave with a tropical cyclone can also result in the intensification of the tropical cyclone (Leroux *et al.*, 2013).

The interaction between tropical cyclones and breaking waves is not unidirectional. Tropical cyclones that transition poleward can interact with the extratropical waveguide and thereby modify the mid-latitude Rossby wave trains and RWB linked with extreme events farther downstream. Several examples where transitioning hurricanes in the Atlantic Basin resulted in an amplification of the mid-latitude Rossby wave trains and subsequent RWB, triggering high-impact weather events in the Mediterranean, have been described (e.g. Grams *et al.*, 2011).

## References

- Altenhoff, A., O. Martius, and M. Croci-Maspoli (2008). Linkage of atmospheric blocks and synoptic-scale Rossby waves: A climatological analysis. *Tellus* **60**, 1053–1063.
- Appenzeller, C. and H. C. Davies (1992). Structure of stratospheric intrusions into the troposphere. *Nature* **358**, 570–572.
- Barnes, E. A. and D. L. Hartmann (2012). Detection of Rossby wave breaking and its response to shifts of the midlatitude jet with climate change. *J. Geophys. Res.* **117**, D09117, doi:10.1029/2012JD017469.
- Benedict, J. J., S. Lee, and S. B. Feldstein (2004). Synoptic view of the North Atlantic Oscillation. *J. Atmos. Sci.* **61**, 121–144.
- Berrisford, P., B. J. Hoskins, and E. Tyrlis (2007). Blocking and Rossby wave breaking on the dynamical tropopause in the Southern Hemisphere. *J. Atmos. Sci.* **64**, 2881–2898.

- Cai, M. (2003). Potential vorticity intrusion index and climate variability of surface temperature. *Geophys. Res. Lett.* **30**, doi:10.1029/2002GL015926.
- Cassou, C. (2008). Intraseasonal interaction between the Madden-Julian Oscillation and the North Atlantic Oscillation. *Nature* **455**, doi:10.1038/nature07286.
- Davies, H. C. (1999). Theories of frontogenesis, pp. 215–238. In *The Life Cycles of Extratropical Cyclones*. M. A. Shapiro and S. Groenens (eds.). American Meteorological Society.
- Davies, H. C., C. Schaer, and H. Wernli (1991). The palette of fronts and cyclones within a baroclinic wave development. *J. Atmos. Sci.* **48**, 1666–1689.
- Davis, C. A. and L. F. Bosart (2006). The formation of hurricane Humberto (2001): The importance of extra-tropical precursors. *Quart. J. Roy. Meteor. Soc.* **132**, 2055–2085.
- Dee, D. P., S. M. Uppala, A. J. Simmons, et al. (2011). The Era-interim reanalysis: configuration and performance of the data assimilation system. *Quart. J. Roy. Meteor. Soc.* **137**, 553–597.
- Doswell, C. A., C. Ramis, R. Romero, and S. Alonso (1998). A diagnostic study of three heavy precipitation episodes in the western mediterranean region. *Weather Forecast* **13**, 102–124.
- Engel, C. B., T. P. Lane, M. J. Reeder, and M. Rezny (2013). The meteorology of black saturday. *Quart. J. Roy. Meteor. Soc.* **139**, 585–599.
- Enomoto, T., W. Ohfuchi, H. Nakamura, and M. A. Shapiro (2007). Remote effects of tropical storm Cristobal upon a cut-off cyclone over Europe in August 2002. *Met. Atmos. Phys.* **96**, 29 – 42.
- Fita, L., R. Romero, and C. Ramis (2007). Objective quantification of perturbations produced with a piecewise pv inversion technique. *Ann. Geophys.* **25**, 2335–2349.
- Franzke, C., S. Lee, and S. B. Feldstein (2004). Is the North Atlantic Oscillation a breaking wave? *J. Atmos. Sci.* **61**, 145–160.
- Funatsu, B. M. and D.W. Waugh (2008). Connections between potential vorticity intrusions and convection in the eastern tropical Pacific. *J. Atmos. Sci.* **65**, 987–1002.
- Gerber, E. P. and G. K. Vallis (2009). On the zonal structure of the North Atlantic Oscillation and annular modes. *J. Atmos. Sci.* **66**, 332–352.
- Grams, C. M., H. Wernli, M. Boettcher, et al. (2011). The key role of diabatic processes in modifying the upper-tropospheric wave guide: a North Atlantic case-study. *Quart. J. Roy. Meteor. Soc.* **137**, 2174–2193.
- Hanley, J. and R. Caballero (2012). The role of large-scale atmospheric flow and Rossby wave breaking in the evolution of extreme windstorms over Europe. *Geophys. Res. Lett.* **39**, L21708, doi:10.1029/2012GL053408.
- Hitchman, M. H. and A. S. Huesmann (2007). A seasonal climatology of Rossby wave breaking in the 320-2000-K layer. *J. Atmos. Sci.* **64**, 1922–1940.
- Hoskins, B. J., I. N. James, and G. H. White (1983). The shape, propagation and mean-flow interaction of large-scale weather systems. *J. Atmos. Sci.* **40**, 1595–1612.
- Hoskins, B. J., M. E. McIntyre, and A. W. Robertson (1985). On the use and significance of isentropic potential vorticity maps. *Quart. J. Roy. Meteor. Soc.* **111**, 877–946.
- Isotta, F., O. Martius, M. Sprenger, and C. Schwierz (2008). Long-term trends of synoptic-scale breaking Rossby waves in the northern hemisphere between 1958 and 2001. *Int. J. Clim.* **28**, 1551–1562.
- Kiladis, G. N. and K. M. Weickmann (1992). Circulation anomalies associated with tropical convection during northern winter. *Mon. Wea. Rev.* **120**, 1900–1923.
- Knippertz, P. (2005). Tropical-extratropical interactions associated with an Atlantic tropical plume and subtropical jet streak. *Mon. Wea. Rev.* **133**, 2759–2776.
- Knippertz, P. (2007). Tropical-extratropical interactions related to upper-level troughs at low latitudes. *Dynam. Atmos. Oceans* **43**, 36–62.
- Leroux, M. D., M. Plu, D. Barbary, F. Roux, and P. Arbogast (2013). Dynamical and physical processes leading to tropical cyclone intensification under upper-level trough forcing. *J. Atmos. Sci.* **70**, 2547–2565.
- Martius, O., C. Schwierz, and H. C. Davies (2007). Breaking waves at the Tropopause in the wintertime Northern Hemisphere: Climatological analyses of the orientation and the theoretical LC1/2 classification. *J. Atmos. Sci.* **64**, 2576–2592.
- Martius, O., H. Sodemann, H. Joos, et al. (2013). The role of upper-level dynamics and surface processes for the Pakistan flood of July 2010. *Quart. J. Roy. Meteor. Soc.* **139**, 1780–1797.
- Masato, G., B. Hoskins, and T. Woollings (2012). Wave-breaking characteristics of mid-latitude blocking. *Quart. J. Roy. Meteor. Soc.* **138**, 1285–1296, doi: 10.1002/qj.990
- Massacand, A., H. Wernli, and H. Davies (1998). Heavy precipitation on the Alpine southside: An upper-level precursor. *Geophys. Res. Lett.* **25**, 1435–1438.
- Matthews, A. J. and G. N. Kiladis (1999). Interaction between ENSO, transient circulation, and tropical convection over the Pacific. *J. Clim.* **12**, 3062–3086.
- McIntyre, M. E. and T. N. Palmer (1984). The 'surf zone' in the stratosphere. *Atmos. Terr. Phys.* **46**, 825–849.
- McTaggart-Cowan, R., G. D. Deane, L. F. Bosart, C. A. Davis, and T. J. Galarneau (2008). Climatology of tropical cyclogenesis in the North Atlantic (1948–2004). *Mon. Wea. Rev.* **136**, 1284–1304.
- McTaggart-Cowan, R., T. J. Galarneau, L. F. Bosart, R. W. Moore, and O. Martius (2013). A global climatology of baroclinically influenced tropical cyclogenesis. *Mon. Wea. Rev.* **141**, 1963–1989.
- Michel, C. and G. Riviere (2011). The link between Rossby wave breakings and weather regime transitions. *J. Atmos. Sci.* **68**, 1730–1748.
- Michel, C., G. Riviere, L. Terray, and B. Joly (2012). The dynamical link between surface cyclones, upper-tropospheric Rossby wave breaking and the life cycle of the Scandinavian blocking. *Geophys. Res. Lett.* **39**, L10806.
- Moore, R. W., O. Martius, and H. C. Davies (2008). Downstream development and Kona low genesis. *Geophys. Res. Lett.* **L20814**.
- Moore, R. W., O. Martius, and T. Spengler (2010). The modulation of the subtropical and extratropical atmosphere in the pacific basin in response to the Madden-Julian Oscillation. *Mon. Wea. Rev.* **138**, 2761–2779.

- Nakamura, H., M. Nakamura, and J. L. Andreason (1997). The role of high- and low-frequency dynamics in blocking formation. *Mon. Wea. Rev.*, **125**, 2074–2093, DOI: 10.1175/1520-0493
- Nakamura, H. and T. Fukamachi (2004). Evolution and dynamics of summertime blocking over the Far East and the associated surface Okhotsk high. *Quart. J. Roy. Meteor. Soc.* **130**, 1213–1233.
- Nadarana, T. and D. Waugh (2011). A climatology of Rossby wave breaking on the Southern Hemisphere tropopause. *J. Atmos. Sci.* **68**, 798–811.
- Nuissier, O., V. Ducrocq, D. Ricard, C. Lebeaupin, and S. Anquetin (2008). A numerical study of three catastrophic precipitating events over southern France. I: Numerical framework and synoptic ingredients. *Quart. J. Roy. Meteor. Soc.* **134**, 111–130.
- Pelly, J. L. and B. J. Hoskins (2003). A new perspective on blocking. *J. Atmos. Sci.* **60**, 743–755.
- Porcu, F., A. Carrassi, C. M. Medaglia, F. Prodi, and A. Mugnai (2007). A study on cut-off low vertical structure and precipitation in the Mediterranean region. *Meteorol. Atmos. Phys.* **96**, 121–140.
- Postel, G. A. and M. H. Hitchman (1999). A climatology of Rossby wave breaking along the subtropical tropopause. *J. Atmos. Sci.* **56**, 359–373.
- Rivi  re, G. (2009). Effect of latitudinal variations in low-level baroclinicity on eddy life cycles and upper-tropospheric wave-breaking processes. *J. Atmos. Sci.*, **66**, 1569–1592. doi: <http://dx.doi.org/10.1175/2008JAS2919.1>
- Rivi  re, G. (2011). A dynamical interpretation of the poleward shift of the jet streams in global warming scenarios. *J. Atmos. Sci.* **68**, 1253–1266.
- Rivi  re, G., A. Laine, G. Lapeyre, D. Salas-Melia, and M. Kageyama (2010). Links between Rossby wave breaking and the North Atlantic Oscillation-Arctic Oscillation in present-day and last glacial maximum climate simulations. *J. Clim.* **23**, 2987–3008.
- Rivi  re, G. and I. Orlanski (2007). Characteristics of the Atlantic storm-track eddy activity and its relation with the North Atlantic Oscillation. *J. Atmos. Sci.* **64**, 241–266.
- Schlemmer, L., O. Martius, M. Sprenger, C. Schwierz, and A. Twitchett (2010). Disentangling the forcing mechanisms of a heavy precipitation event along the alpine south side using potential vorticity. *Mon. Wea. Rev.* **138**, 2336–2353.
- Shapiro, M. A., H. Wernli, N. A. Bond, and R. Langland (2001). The influence of the 1997–99 El Ni  o Southern Oscillation on extratropical baroclinic life cycles over the eastern North Pacific. *Quart. J. Roy. Meteor. Soc.* **127**, 331–342.
- Slingo, J. M. (1998). Extratropical forcing of tropical convection in a northern winter simulation with the UGAMP GCM. *Quart. J. Roy. Meteor. Soc.* **124**, 27–51.
- Sprenger, M., O. Martius, and J. Arnold (2013). Cold surge episodes over southeastern Brazil – a potential vorticity perspective. *Int. J. Climatol.* **33**, 2758–2767.
- Takaya, K. and H. Nakamura (2005). Mechanisms of intraseasonal amplification of the cold Siberian high. *J. Atmos. Sci.*, **62**, 4423–4440. doi: <http://dx.doi.org/10.1175/JAS3629.1>
- Thornicroft, C. D., B. J. Hoskins, and M. F. McIntyre (1993). Two paradigms of baroclinic-wave life-cycle behavior. *Quart. J. Roy. Meteor. Soc.* **119**, 17–55.
- Ulbrich, U., T. Bruecher, A. Fink, et al. (2003). The central European floods of August 2002: Part 2 Synoptic causes and considerations with respect to climatic change. *Weather* **58**, 434–442.
- Waugh, D. W. and L. M. Polvani (2000). Climatology of intrusions into the tropical upper troposphere. *Geophys. Res. Lett.* **27**, 3857–3860.
- Wernli, H. and M. Sprenger (2007). Identification and ERA-15 climatology of potential vorticity streamers and cutoffs near the extratropical tropopause. *J. Atmos. Sci.* **64**, 1569–1586.
- Woollings, T., B. Hoskins, M. Blackburn, and P. Berrisford (2008). A new Rossby wave-breaking interpretation of the North Atlantic Oscillation. *J. Atmos. Sci.* **65**, 609–626.

# 6

## The influence of jet stream regime on extreme weather events

Nili Harnik, Chaim I. Garfinkel, and Orli Lachmy

### 6.1 Introduction

This chapter discusses the relation between extreme events and the large-scale circulation in the subtropics and extratropics as represented by the type of jet stream. While extreme events often depend strongly on local physical conditions and small-scale processes such as convection and interaction with the Earth's surface (i.e. topography, surface moisture, and land-sea contrast), they are also often strongly influenced by the large-scale flow. Extreme weather events, in particular in the extratropics, are often associated with synoptic weather systems (e.g. Romero *et al.*, 1999, Martius *et al.*, 2006), or with anomalous large-scale undulations of the atmospheric jet stream (Rossby waves) which cause large masses of air to be displaced latitudinally (as for example during the boreal winter of 2013–14, Wallace *et al.*, 2014; see also Schubert *et al.*, 2011). Both of these phenomena – synoptic weather systems and larger scale Rossby waves – depend quite strongly on the large-scale circulation and in particular on the structure and location of the atmospheric jet streams. At a more basic level, we expect the extreme values of a quantity to be related to its statistical properties like the mean, variance, and skewness. For flow variables like wind and vorticity, these statistical properties are inherently tied to the large-scale circulation.

A relation between extreme events and the jet streams has been suggested before but has not been studied very systematically. Schubert *et al.* (2011, see also review by Schubert *et al.*, 2014) suggested that observed extreme summer weather (heat waves, droughts, and floods) is often associated with amplifying or stationary Rossby waves developing on the zonal jet stream, though their studies concentrated on understanding the effect of variations in wave forcing. Petoukhov *et al.* (2013) examined the possibility of extreme summer weather resulting from resonant amplification of waves when the jet is strong enough to form a well-defined isolated wave guide. Mahlein *et al.* (2012) found a significant relation between the

distribution of extreme events and the latitude of the Atlantic jet stream, while Ashcroft *et al.* (2009) found extreme Australian cold events to be associated with a temporary merging of the subtropical and mid-latitude jet streams. Recently, Harnik (2014) examined the seasonal variations in the occurrence and evolution of extreme upper level cyclonic vorticity in the Southern Hemisphere, where the jet undergoes a clear seasonal transition in type, as a first step in understanding the influence of jet stream type on extreme events. Upper level cyclonic vorticity was chosen because it is more directly affected by the large-scale circulation than are quantities like surface temperature and precipitation. At the same time, upper level vorticity is related to Rossby wave breaking and potential vorticity (PV) streamers and to deep upper level troughs, all of which have been shown to be related to extreme surface weather (see Chapter 5 this book and references therein). Indeed, Harnik (2014) found a strong relation between jet stream type and both the distribution and the synoptic evolution of extreme upper level cyclonic vorticity.

In this chapter, we extend the analysis further, and apply it to two idealized models. The first model is the two-level global circulation model of Lachmy and Harnik (2014), which captures the three main jet regimes discussed in the next section, but is very idealized. The second model is the dry general circulation model (GCM) used by Garfinkel and Waugh (2014) to examine the influence of changes in jet latitude on wave breaking. This combination of observational analysis and studies of idealized models is a first step towards isolating the role of large-scale dynamics, and specifically the jet stream, in the formation and evolution of extreme weather events.

### 6.2 Dynamical regimes of the large-scale circulation

One of the main characteristics of the mid-latitude atmospheric flow is its organization into zonally oriented jet

streams, identified as primarily zonal flows that are strongest at a particular latitude. Meteorologists have long distinguished between two types of jets based on their latitudinal location: subtropical jets at the edge of the Hadley cells, and polar front jets. Another distinction is in terms of the momentum source of the jet: meridional advection of angular momentum into the subtropics by the thermally driven Hadley circulation (e.g. Schneider, 1977, Held and Hou, 1980), or the convergence of zonal momentum by synoptic eddies (e.g. Held, 1975, 2000, Rhines, 1975, Panetta, 1993). While thermal driving forces a jet at the subtropical edge of the Hadley cell, eddy forcing occurs farther poleward and is much more variable in its location. Lee and Kim (2003) noted that both forcing mechanisms are always present to some degree, and depending on their relative strength and positions, both a subtropical thermally driven jet and a mid-latitude eddy driven jet may exist simultaneously in a double jet state, or when the eddy forcing is close enough to the thermally driven jet, a single merged jet evolves.

The two dynamical processes that force a jet stream – Hadley circulation and mid-latitude synoptic eddies – are not independent. Moreover, the jet stream structure affects the growth and evolution of synoptic eddies. The resulting global circulation is the outcome of the mutual interactions of the three components – the zonal jets, the mean meridional circulation, and synoptic eddies – in the presence of diabatic forcing and dissipation. The jet stream state is one way to characterize this global circulation.

The influence of jet forcing type on the location and variability of the jets and associated storm tracks, and the causes and evolution of the transitions between different jet states, have been the subject of many studies, both observational and modeling (e.g. Son and Lee, 2005, Eichelberger and Hartmann, 2007, Barnes and Hartmann, 2011, Michel and Riviere, 2014, and references therein). For our discussion on extreme events, it suffices to briefly discuss the three main types of jet stream:

- A *subtropical jet* is thermally driven, located at the subtropical edge of the Hadley cell, and is strongly baroclinic (strong vertical shear with very weak surface winds). The jet's location at the edge of the Hadley cell, where the upper level mean meridional wind is zero, also implies that it is located at the latitude where eddy momentum flux convergence is zero (Dima et al, 2005). Thus, this jet can only exist when baroclinic eddies are sufficiently weak so as not to shift the jet poleward into the Ferrel cell (Lachmy and Harnik, 2014).
- An *eddy driven jet* is forced by eddy momentum flux convergence, typically in mid and high latitudes in the Ferrel cell. It is characterized by a relatively barotropic structure (weak vertical shear and strong surface

westerlies) and strong latitudinal meandering. It often exists alongside a weak subtropical jet. This jet regime is the most nonlinear (turbulent), and is characterized by strong eddies.

- A *merged jet* occurs when both jet forcing mechanisms are important and are close enough to influence each other. This type of jet forms in the Ferrel cell, at relatively low latitudes, which are sometimes even subtropical. It has a relatively strong vertical shear and strong surface westerlies. Its latitude is relatively constant with time, with most of the variability due to pulsation of the winds (Eichelberger and Hartmann, 2007). This type of jet behaves as a distinct wave guide, and is typically characterized by a sharper zonal wavenumber spectrum, implying relatively coherent and persistent wave packets (Lachmy and Harnik, 2014).

Recently, Lachmy and Harnik (2014) studied the maintenance and evolution of these three jet regimes in a very idealized model of the general circulation and showed that, for a given external forcing, the circulation regime changes from a subtropical jet, to a merged jet, to an eddy driven jet, as the eddies become stronger. Moreover, they showed that each of the three regimes is characterized by very different eddy morphology (also referred to as waves). In the subtropical jet regime, slowly propagating, planetary scale, high latitude waves dominate, alongside weak, slowly propagating, subtropical, medium-scale waves. In the merged jet regime, highly coherent medium scale waves of a single dominant wavenumber (zonal wave 5) emerge, which maintain the jet at its latitude in a quasi-linear balance (Lachmy et al, 2015, in preparation). In the eddy driven jet regime, a range of zonal wavenumbers (of larger scale than the merged jet waves) dominates the flow, with relatively large variability in the latitudinal structure of the waves and strongly nonlinear dynamics. While these features were found in an idealized model, they also seem to be relevant to the observations (see discussion in Lachmy and Harnik, 2014, of the observational analysis of Randel and Held, 1991 and Lee and Kim, 2003).

Looking at the observations, it is quite easy to distinguish between the subtropical jet and the other two kinds of jets (eddy driven and merged). While the subtropical jet is located at the edge of the Hadley cell where the upper level meridional wind is zero (and the vertical velocity is downwards), the eddy driven and merged jets are located in the Ferrel cell, where the upper level meridional wind is directed equatorward (and the vertical velocity changes from downward to upward moving poleward). Moreover, while the subtropical jet is strongly baroclinic so that the upper level winds peak above the equatorward flank of the surface westerly jet, in the other two jet types the upper and lower level jets coincide in latitude. The eddy driven and

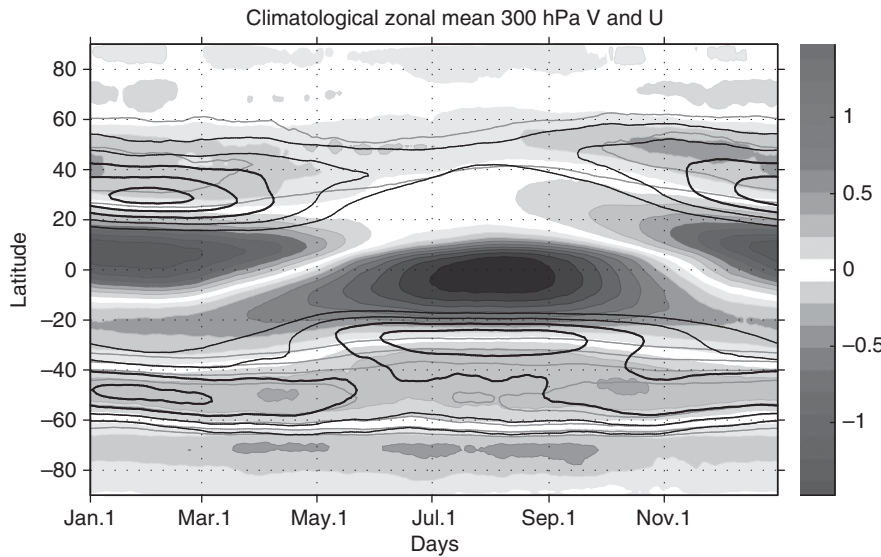


Fig. 6.1. Zonally averaged climatological seasonal cycle of: 300 hPa meridional wind (shading,  $\text{ms}^{-1}$ ), 300 hPa zonal wind (black contours, contour interval  $5 \text{ ms}^{-1}$ , thick contours for  $25 \text{ ms}^{-1}$  and above, only positive values are plotted) and 925–700 hPa zonal wind (green contours, contour interval  $3 \text{ ms}^{-1}$ , thick contours for  $12 \text{ ms}^{-1}$  and higher, only positive values are shown). The meridional wind is colored blue for southward and red for northward flow and white for zero. The dipole in meridional wind between  $30^\circ\text{S}$ – $20^\circ\text{N}$  during Nov–May (boreal winter) and between  $25^\circ\text{S}$ – $40^\circ\text{N}$  during May–Nov (boreal summer) represents the two Hadley circulation cells, with the winter cell being much stronger and the summer cell extending more poleward. Note the upper level Southern Hemisphere winter jet is at the edge of the Hadley cell, with weak surface winds, while the Southern Hemisphere summer jet at both levels is in the Ferrel cell. A black and white version of this figure will appear in some formats. For the colour version, please refer to Plate 10.

merged jets are more similar in structure and both are located within the Ferrel cell. A main distinguishing characteristic is the temporal variability – the thermally driven jet is relatively fixed in latitude, while the eddy driven jet meanders much more (e.g. Eichelberger and Hartmann, 2007). However, under some conditions, for example when tropical thermal forcing is weak (e.g. in summer), other processes like surface thermal forcing at oceanic fronts (e.g. Nakamura *et al.*, 2004; see also Michel and Riviere, 2014 for later references) may also act to keep the jet in place, giving rise to a different kind of mixed thermally and eddy driven jet.

Figure 6.1 shows the zonally averaged climatological seasonal cycle of the upper and lower level zonal winds (300 hPa and 925–750 hPa), relative to the mean overturning circulation cells, represented by the upper level (300 hPa) zonally averaged meridional wind. Figure 6.2 shows the corresponding seasonal maps for Jan–Mar and Jun–Aug, respectively, with the mean overturning circulation represented by the mid-tropospheric (400–600 hPa mean) vertical pressure velocity. Examining the two figures, we see that the type of jet stream varies both seasonally and meridionally, with the clearest variation found in the Southern Hemisphere. The figures provide the following clear jet categorization.

A subtropical jet is found during austral winter. This is very clear in the zonal mean fields (Fig. 6.1) during Jun–Oct, and in the Jun–Aug map over the Indian Ocean, Australia, and part of the Pacific Ocean (Fig. 6.2b), where a strong jet extends eastwards from  $70^\circ\text{E}$  to around  $250^\circ\text{E}$  in the subtropics, although it lies over a region of mean descent only between  $70^\circ\text{E}$  and  $180^\circ\text{E}$ . A subtropical jet also exists in the Northern Hemisphere during boreal winter over North Africa and South Asia (Fig. 6.2), lying between  $20$ – $30^\circ\text{N}$  and  $5^\circ\text{W}$ – $150^\circ\text{E}$ , where there is mean descent, ignoring small scale topographic features in the vertical velocity.

The upper and lower level jets are collocated in the Ferrel cell during austral summer, and over both the North Atlantic and North Pacific oceans during boreal winter and summer, suggesting these jets are either eddy driven or merged. Similar characteristics are also found during austral winter at around  $50^\circ\text{S}$  over the South Atlantic and Indian Ocean, and around  $60^\circ\text{S}$  alongside the subtropical jet in the South Pacific. Examination of the temporal variability of these jets indicates clearly that the North Pacific winter jet is a merged jet, while the North Atlantic jet is eddy driven (see Figure 3 of Harnik *et al.*, 2014). The summer Southern Hemisphere jet, however, is harder to categorize since its variability

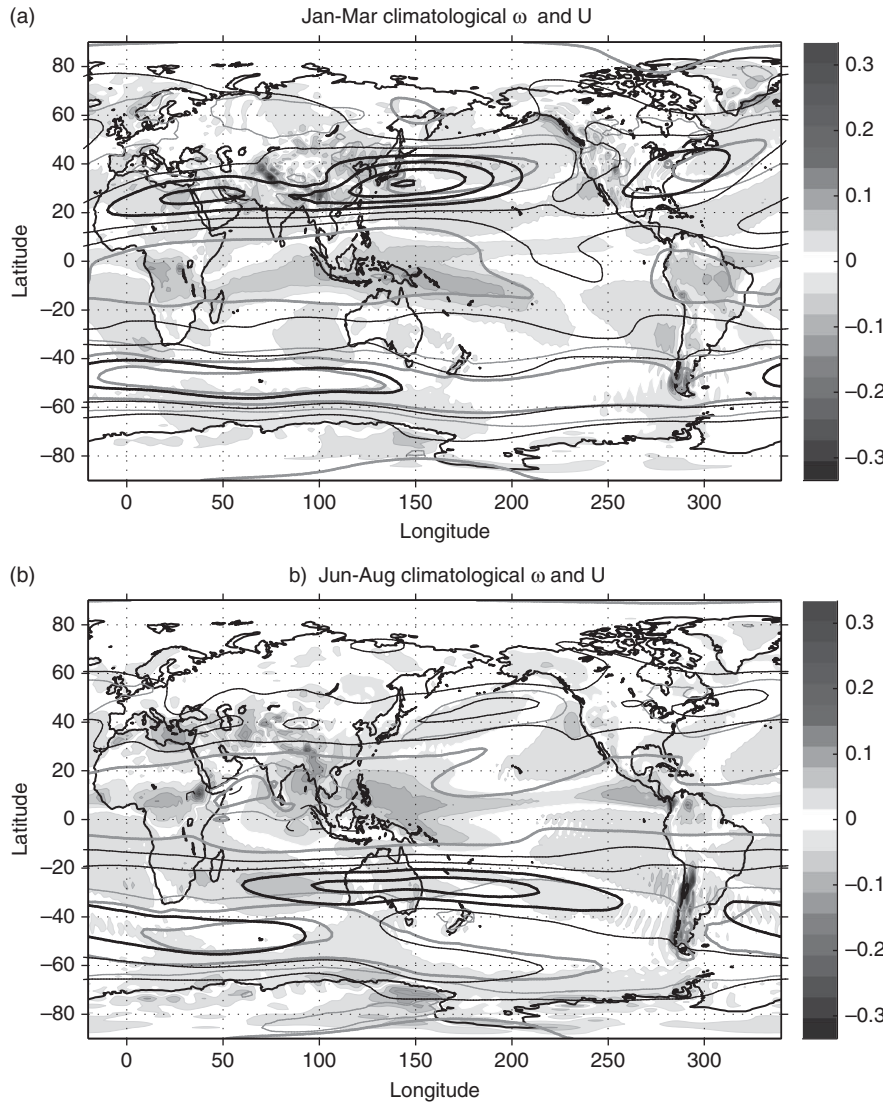


Fig. 6.2. Seasonal mean distribution of: 400–600 hPa  $\omega$  ( $\text{hPa s}^{-1}$ , shading), 300 hPa zonal wind (black contours, contour interval  $10 \text{ ms}^{-1}$ ,  $30 \text{ ms}^{-1}$  and above thick, zero contour gray, and negative values dashed) and 925–700 hPa zonal wind (green contours, contour interval  $5 \text{ ms}^{-1}$ ,  $10 \text{ ms}^{-1}$  and higher thick, only positive values are shown), for (a) Jan–Mar, (b) Jun–Aug. A black and white version of this figure will appear in some formats. [For the colour version, please refer to Plate 11.](#)

changes interannually between strong and weak meandering (not shown), suggesting it can be of both types. For simplicity, however, we will refer to the Southern Hemisphere summer jet as eddy driven. The Northern Hemisphere summer jets, which are very weak, will only be discussed briefly.

To summarize, the observed jet streams vary seasonally and longitudinally between the different jet types, with the clearest transition between a subtropical and an eddy driven jet found as part of the seasonal cycle in the Southern Hemisphere. In what follows, we will examine how the distribution and evolution of extreme events varies seasonally in relation to the jet stream, both in observations (mostly of the Southern Hemisphere), and in two idealized models of varying complexity.

### 6.3 Methods

In what follows we examine the spatial and temporal distribution of extreme events, as well as their characteristic mean synoptic variability, in observations and two idealized models. In this section we briefly present these diagnostics and models.

#### 6.3.1 Diagnostics of extreme events

The extreme event diagnostics were used in Harnik (2014), and are briefly described here, including their explicit application to the models. We will present observational analysis using daily mean fields from ERA Interim (Dee *et al.*, 2011) for the years 1979–2012. The results presented

were also reproduced using NCEP re-analysis (Kalnay *et al.*, 1996) for the years 1959–2012. Vorticity  $\zeta$  is calculated from the daily horizontal winds ( $u$  in the longitudinal direction  $\lambda$ , and  $v$  in the latitudinal direction  $\phi$ ):

$$\zeta = \frac{1}{a_e \cos \phi} \left( \frac{\partial v}{\partial \lambda} - \frac{\partial (u \cos \phi)}{\partial \phi} \right), \quad (6.1)$$

where  $a_e$  is the Earth's radius. For the observations, we define an extreme cyclonic vorticity event as when the full  $\zeta$  field (including its seasonal variations) assumes a value within the strongest 1% of vorticity values, for all days and all grid points within the hemisphere. This entails performing separate calculations for each hemisphere, with Southern Hemisphere cyclonic events having vorticity values within the lowest one percent (e.g. 1% most negative vorticity values), and Northern Hemisphere cyclonic events having vorticity values within the highest one percent of all vorticity values. We then calculate the frequency of occurrence of extreme events as a function of spatial location or day of the year. We will present both the climatological seasonal cycle of events and seasonal mean spatial distributions. The seasonal cycle plot is created by counting the number of extreme events that occur at each latitude for each calendar date (excluding Feb 29), while the spatial distributions are calculated by counting the number of days with extreme values at each grid point. To get a frequency of occurrence, we divide the seasonal cycle by the number of years times the number of longitude grid points, and divide the spatial fields by the total number of days. Thus a value of 0.015 (which is the minimum shading value) at a given point on the plots means that, on average, at that latitude and day of the year (seasonal cycle) or at the latitude and longitude (fields), events occur 1.5% of the time (i.e. more frequently than the extreme event threshold of 1%). For the models, we examine the Southern Hemisphere only, and find the lowest 1% based on all hemispheric grid points, all model output times, and all model experiments in the given run set. Thus, while in the observations the seasonal cycle includes different jet regimes, in the model, runs which are for fixed baroclinic forcing, a change in jet regime is included by using all runs of an external parameter sweep.

We use composite analysis to obtain a characteristic evolution of the extreme events in different seasons, at the latitude of most frequent occurrence. For extreme vorticity events that last for two or more consecutive days, we choose only the day with the most extreme value. We also isolate the events spatially and temporally by discounting extreme values that occur within a certain longitudinal and temporal range of the event peak. For observations we choose ranges of  $30^\circ$  longitude and five days, for the idealized two-level model we choose  $28.125^\circ$  longitude (ten grid points) and 6.3 days (20 time steps), and for the

GCM we choose  $28.125^\circ$  longitude (ten grid points) and five days. We then centre the events on the peak longitude. While the vorticity composite fields are by construction statistically significant around the composite centre, the spatial extent of the significant vorticity anomalies, as well as the significance of the composited patterns of other atmospheric fields, needs to be determined objectively using a common significance test. For this we use a two-sided t-test method, with the null hypothesis of the t-test being the daily fields within the composite season (e.g. 1 January–31 March of all years), with the field on each day centered on a randomly chosen longitude. This random longitude centring is done since the composites are also centered on the extreme event. We choose to show points which are significant at the 99% level. The composites are calculated both for full fields and for the anomalies, defined as the deviation from the climatological seasonal cycle. The statistical significance, however, is determined purely from the anomaly fields. The climatological seasonal cycle is calculated by averaging the given field for each calendar day over all years, and smoothing with a 21 day running mean.

### 6.3.2 The idealized models

The location and synoptic evolution of extreme events in observations will be compared with those simulated by two different models of varying complexity. The first is the Modified quasi-geostrophic (MQG) model of Lachmy and Harnik (2014) which resolves the main components of the global circulation: the overturning circulation cells (Hadley, Ferrel, and polar), the zonal jet streams, and baroclinically unstable mid-latitude Rossby waves. The model is a modified two-level spherical quasi-geostrophic model. It is written as separate but coupled equations for the zonal mean (representing the jet streams) and the deviations from zonal mean (the baroclinically unstable waves). To capture the ageostrophic mean meridional circulation cells, in particular, the tropical Hadley cells, the ageostrophic advection terms, are added to the equation for the zonal mean circulation. This has the main effect of strengthening the ageostrophic meridional overturning in the tropics, where it is strongest as a response to thermal heating (the Hadley cell). This increases the Coriolis force acting on the meridional flow – a major source of zonal momentum for the subtropical jet. By capturing the basic dry Hadley cell dynamics, the model is able to crudely represent the thermal forcing of the subtropical jet, and also captures the essential coupling to the midlatitude wave-mean flow dynamics. The model is run to equilibrium over a range of external parameter values. Lachmy and Harnik (2014) found that the eddy amplitude is a key parameter controlling the type of jet stream. Here we present results

from a set of runs in which wave damping is increased between the runs, and the jet transitions from being eddy driven, to merged, to subtropical. We note that similar behavior is found when varying other parameters controlling wave amplitudes, for example the width of the model levels (which affects the static stability and vertical wind shear). We use 1000 days from each run to obtain extreme event statistics, and use extended 2500 day runs for the composite analysis.

The second model is a primitive equation dry dynamical core run at T42 with 40 levels in the vertical parameterized as in Held and Suarez (1994), but with modifications to the structure of the tropospheric baroclinicity. The experiments are described in detail in Garfinkel et al. (2013). Briefly, Garfinkel et al. (2013) modified the tropospheric baroclinicity in order to change the location of the eddy driven jet stream. In all of their experiments, the equator-to-pole temperature difference does not change, and therefore heat fluxes and maximum jet speeds are nearly equal in strength among all the integrations. Thus, these factors cannot be modulating the distribution of extreme events in these simulations. Note that unlike in Garfinkel et al. (2013) and Garfinkel and Waugh (2014), we focus on the hemisphere in which there is no topography, as topography can influence the distribution of extreme events. Note that an eddy driven jet is present in all of the experiments. However, the precise location of the eddy driven jet relative to the Hadley cell edge does change systematically in these experiments. Specifically, the center of the most equatorward jets at 700 hPa lies close to the  $\bar{v} = 0$  isotach. Furthermore, the principal mode of variability is no longer dominated by meridional meandering of the jet; while meandering of the jet explains more than five times as much of the total variance of the jet as jet pulsing for jets

near  $40^\circ$ , meandering only explains twice as much of the total variance compared with pulsing for the most equatorward jets (computed as in the appendix of Garfinkel et al., 2013, but for the hemisphere without topography), and thus approaches the merged jet regime.

## 6.4 The relation between jet stream type and the distribution and evolution of extreme weather events

Taking into account the differences in the characteristics of the jet stream and dominant waves, we expect the different circulation regimes to give rise to different distributions and evolutions of extreme events. The relation between the jet stream and extreme events also varies between different atmospheric diagnostics. For brevity, we will focus on cyclonic extremes of upper level vorticity before discussing temperature extremes.

### 6.4.1 Observed extreme upper level cyclonic vorticity events

Figures 6.3 and 6.4 show the daily seasonal evolution and seasonal mean maps, respectively, of the frequency of occurrence of extreme 300 hPa cyclonic vorticity values. Also shown on all plots are the climatological zonal mean winds at 300 hPa and at 925–700 hPa, representing the upper and the lower level jet streams, respectively. The figures reveal a strong relation between the distribution of extreme events and the jet stream, but this relation varies seasonally, geographically, and between the different jet types. Overall we see three different relations. (a) Extreme events peak at the jet center for the Southern Hemisphere

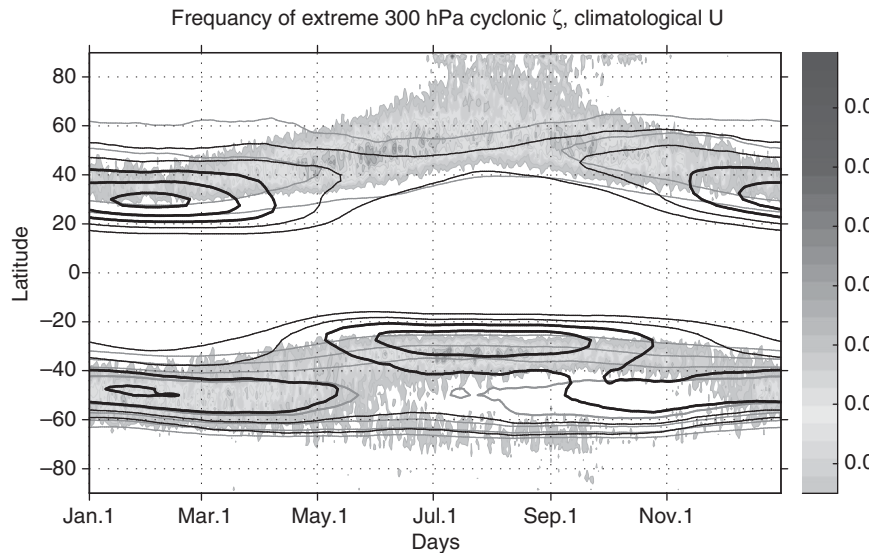


Fig. 6.3. Frequency of extremely strong cyclonic 300 hPa vorticity values on a given day and latitude, counting over all years and longitudes (color shading), with extreme cyclonic vorticity values defined as the lowest (highest) 1% for the Southern (Northern) hemisphere. Also shown in contours on all plots are the daily climatological zonal mean 300 hPa (black) and 925–700 hPa (green) zonal winds, with contour levels and line widths as in Fig. 6.6. The Southern Hemisphere results were presented in Harnik (2014). A black and white version of this figure will appear in some formats. For the colour version, please refer to Plate 11.

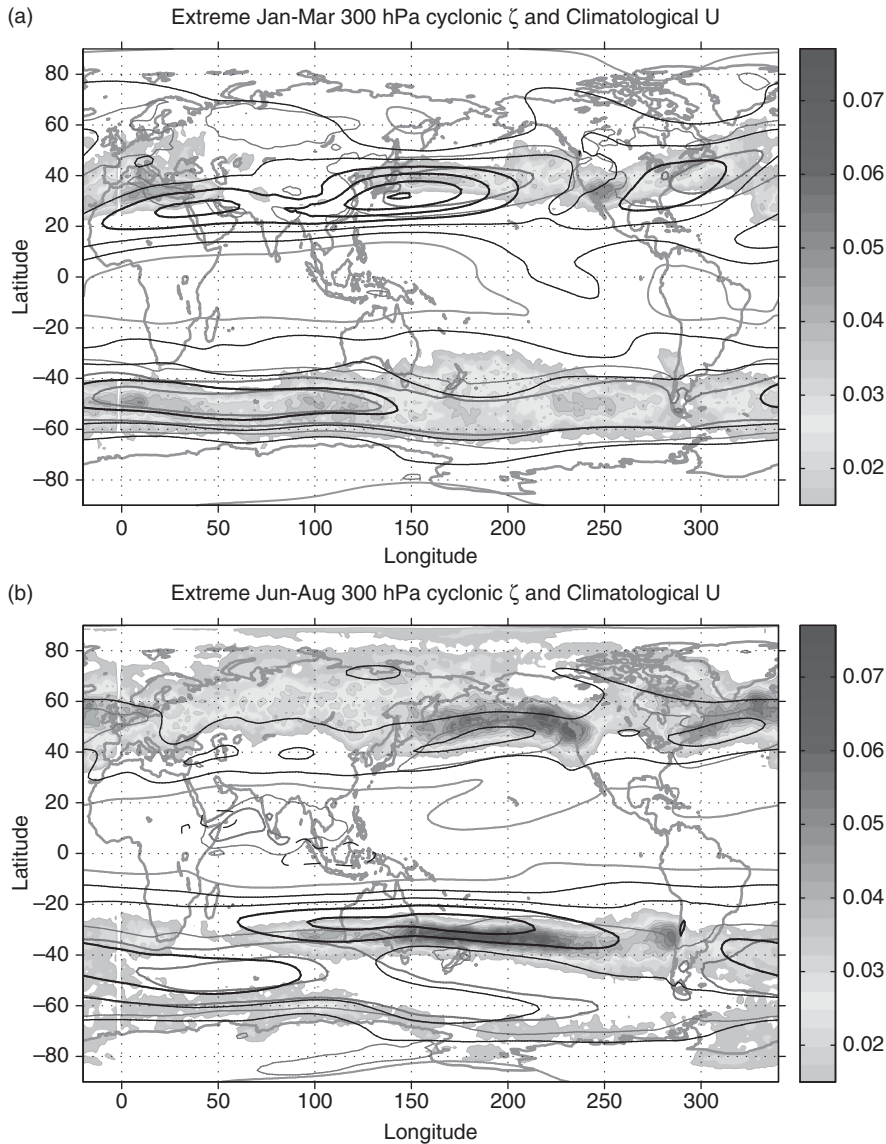


Fig. 6.4. Seasonal mean maps of the frequency of extreme 300 hPa cyclonic vorticity values at a given grid point (color shading) counting over all seasons for 1979–2012 for the periods: (a) Jan–Mar, (b) Jun–Aug. Also shown in contours on both graphs are the corresponding climatological seasonal mean zonal winds at 300 hPa and 925–700 hPa (black and green contours respectively, with values and line thicknesses as in Fig. 6.2. The Southern Hemisphere results were presented in Harnik (2014). A black and white version of this figure will appear in some formats. For the colour version, please refer to Plate 12.

summer eddy driven jet. (b) Extreme events occur in two peaks during Southern Hemisphere winter: a main peak on the poleward flanks of the subtropical jet and a secondary peak on the poleward flanks of the mid–high latitude eddy driven jet. (c) Extreme events occur on the poleward flanks of the Northern Hemisphere jets, with more extremes during summer, but the distribution being more tightly concentrated during winter. This could be indicative of a weaker relation between the weak Northern Hemisphere summer jet streams and extreme upper level cyclonic vorticity. We note that the distribution of extreme vorticity events is quite different at 500 hPa. This suggests the upper level vorticity extremes are associated with tropopause dynamics, consistent with the results of composite analysis (Harnik, 2014 and Fig. 6.5) that the extremes form during wave breaking.

Harnik (2014) examined the Southern Hemisphere cases and showed that while extreme events in both winter and summer jet regimes occur when waves break and a tongue of upper level vorticity deepens strongly due to stretching, the temporal evolution leading to this wave breaking is quite different.

To examine the characteristic temporal evolution of the extreme events, Harnik (2014) composited various fields around the extreme events at the peak latitude of the distribution, for the different winter and summer jet types. For completeness, we present the main findings here, before comparing with model results. Figure 6.5 shows the –3 days (a,d) and 0 day (b,e) centred composites of 300 hPa absolute vorticity, a quantity which nicely tracks the overturning of vorticity contours during Rossby wave breaking events (Barnes and Hartmann, 2012), along with

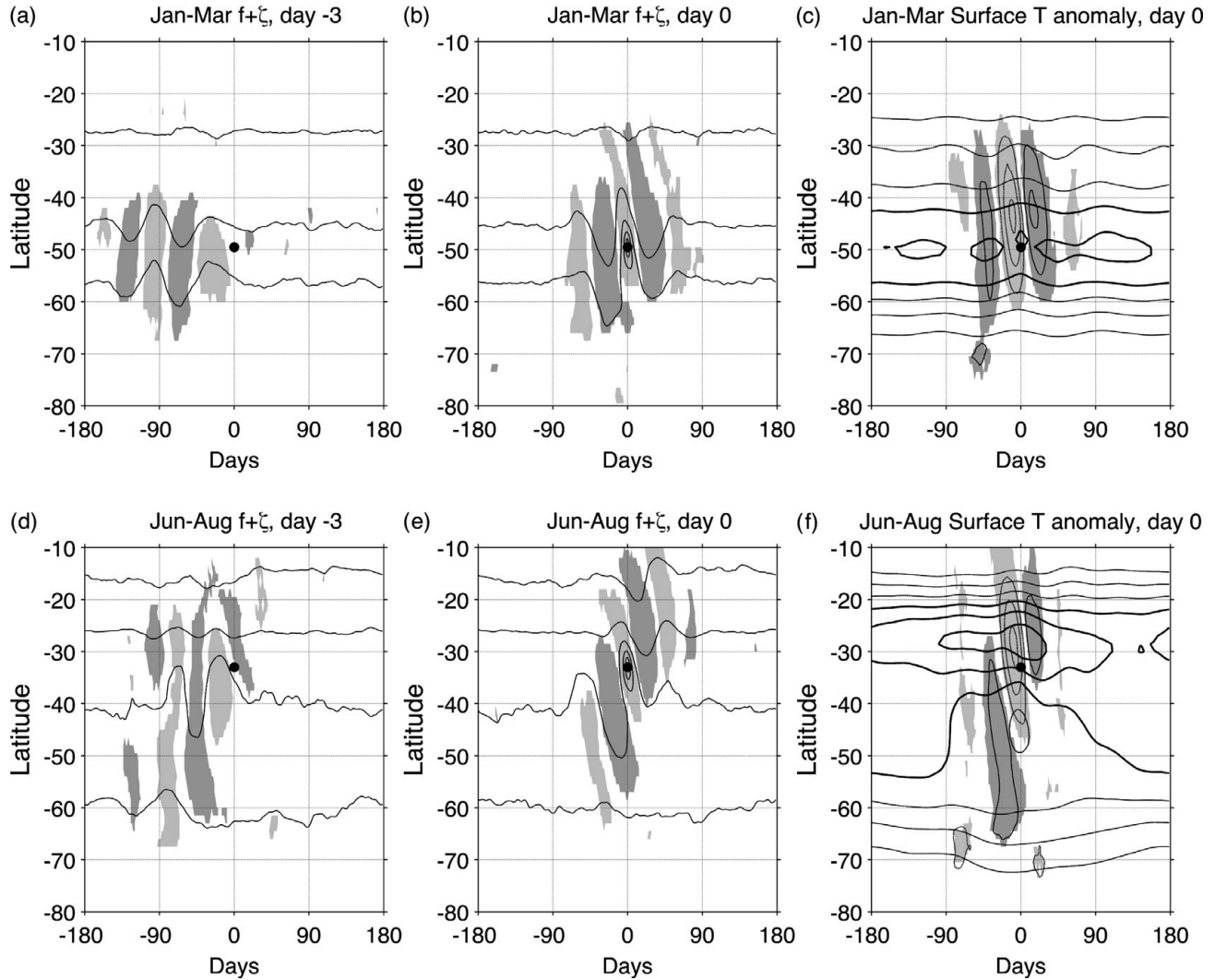


Fig. 6.5. Longitudinally centered composites of different fields for the most extreme negative vorticity events occurring at latitude 49.5°S during Jan–Mar (a–c) and along the subtropical jet at latitude 33°S between 50°E–250°E during Jun–Aug (d–f). Left and middle columns: Composites of absolute vorticity ( $f+\zeta$ , a wavy relative vorticity field on top of a northward increasing negative planetary vorticity field) on day  $-3$  (plots a,d) and day  $0$  (plots b,e). Right column: Composites of surface temperature anomaly on day  $0$ , plotted on top of the zonal wind composite averaged over days  $-6:6$  (plots c,f). The shading marks the significant regions for absolute vorticity (left and middle columns) and surface temperature (right column), with dark (light) gray representing regions of significant positive (negative) anomalies based on a 99% significance level. The Jan–Mar and Jun–Aug composites are based on 1521 and 1287 events respectively. Wind contours are  $25, 30, 35 \text{ ms}^{-1}$  in black. The center of the composites is marked by a magenta dot. Absolute vorticity contours are  $(-1.4:0.4:-0.4) \times 10^{-4} \text{ s}^{-1}$ . The surface temperature contour interval is  $0.5^\circ\text{C}$ , with negative values dashed and the zero contour omitted. Figure modified from Harnik (2014)

(c,f) the day  $0$  composite of surface temperature overlain on the centred composite of 300 hPa zonal winds, averaged over days  $-6$  to  $6$ . The composites for Jun–Aug include 1521 extreme cyclonic vorticity events which peak at 33°S, between 50°E and 250°E (the peak along the subtropical jet), while the Jan–Mar composites include 1287 events at 49.5°S at all longitudes (the peak along the eddy driven jet). Looking at the absolute vorticity composites, we see

different flow evolution between the two seasons. During Jan–Mar we see an upper level wave packet that grows in amplitude and breaks, leading to the formation of an elongated tongue of low vorticity which deepens at the event centre due to stretching (seen in composites of potential temperature, not shown). During Jun–Aug, on the other hand, we see two wave trains, on the eddy driven and subtropical jets, which interact during wave breaking

to form a similar deepening vorticity tongue. While this two-wave interaction could be apparent, as a result of compositing over two main wave propagation routes which occur during different times, a preliminary examination of individual cases, as well as compositing only the strongest subset of these events, indicate that waves coexist on both wave paths simultaneously. We note also that the evolution of these events involves an upper level geopotential height evolution (e.g. Figure 3 of Harnik, 2014) similar to that observed by Marengo *et al.* (2002), in relation to extreme winter cold events in Brazil. The extreme events in both seasons affect surface temperature (Fig. 6.5c,f) with significant localized negative and positive anomalies associated with northward and southward temperature advection to the north-west and east of the extreme cyclonic vorticity centre. Harnik (2014) also showed evidence of significant precipitation anomalies for both cases. These surface anomalies are consistent with the dynamical evolution around PV streamers (as summarized in Schlemmer *et al.*, 2010).

One question which these results raise is whether the 1% extreme vorticity values generally occur at some point during most typical wave breaking events, or whether they represent anomalously extreme wave breaking events. Given, however, the ambiguity in defining the spatial extent and duration of a wave breaking event, it is not simple to answer this question with a simple objective algorithm, and we leave it for a future study.

#### 6.4.2 Extreme events in the idealized models

In the observations, other processes besides dynamic eddy–jet stream interactions can affect extreme events. We thus further examine the relations between the jets and extreme events in the idealized MQG model which isolates the relevant dynamical processes behind the three jet regimes.

Figure 6.6a shows the frequency of occurrence of extreme events for the MQG model, as a function of latitude and of the wave damping parameter, which varies

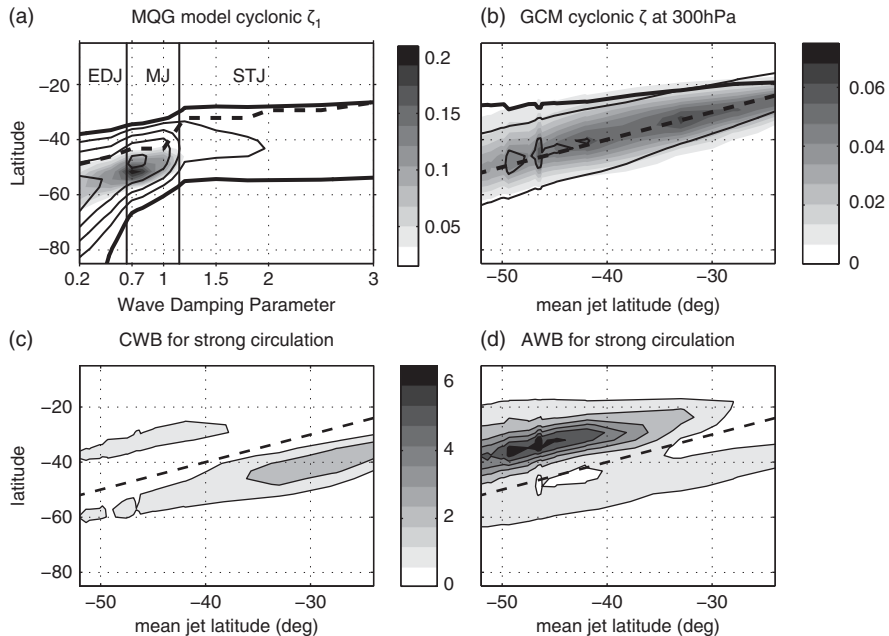


Fig. 6.6. Zonally averaged plots of: (a) Frequency of occurrence of extreme upper level cyclonic vorticity for the MQG model (defined as the lowest 1% of all vorticity values using all grid points in the Southern Hemisphere and all time steps, of all the model runs for all values of the wave damping parameter, shading) and lower level zonal winds (thin black contours, contour interval is  $3 \text{ ms}^{-1}$ , only positive values shown). Also shown is the latitude of upper level jet maximum (thick black dashed line) and the lines of zero  $V_T = V_{top} - V_{bot}$  as an indication of the poleward edges of the Hadley and Ferrel cells (thick solid black lines). Vertical gray lines mark the transition between the eddy driven (EDJ), merged (MJ), and subtropical (STJ) regimes. The horizontal axis denotes the wave-damping parameter of each model run. (b) As in (a) but for 300 hPa cyclonic vorticity in the GCM. Thin black contours denote the  $3 \text{ ms}^{-1}$  and  $10 \text{ ms}^{-1}$  isotachs at 700 hPa. The dashed black line shows the latitude of maximum zonal winds at 300 hPa, while the thick black line shows the edge of the Hadley cell (zero meridional wind at 300 hPa). The horizontal axis now denotes the mean jet latitude of the run. (c–d) Gray shading denotes the frequency (per day) of Rossby wave breaking for the different model runs for wave breaking events with an average absolute vorticity anomaly exceeding  $1.75 \times 10^{-5} \text{ s}^{-1}$  for (c) cyclonic wave breaking (CWB) and (d) anti-cyclonic wave breaking (AWB). The dashed line in (c–d) shows the jet core at 300 hPa.

with model run. The upper and lower level zonal winds are also shown, as well as the line of zero meridional thermal wind ( $V_T = V_{top} - V_{bot}$ ), which indicates the edges of the meridional circulation cells. Looking first at the zonal mean zonal winds, in relation to the Hadley and Ferrel cells, we see three dynamical regimes as wave damping increases from weak to strong: an eddy driven jet (marked EDJ), a merged jet (marked MJ), and a subtropical jet (marked STJ). The lower level jet and Ferrel cell, which are driven by the eddy momentum flux convergence and are thus co-located, shift equatorward and narrow as wave damping is strengthened. The upper level jet lies equatorward of the surface jet, and while it lies within the Ferrel cell for the eddy driven and merged jets, it shifts to the edge of the Hadley cell in the subtropical jet regime. We note that in observations, the upper level eddy driven and merged jets tend to peak at the same latitude as their respective surface jets (c.f. Fig. 6.2).

The distribution of extreme events also changes with jet type: in the eddy driven jet regime, extremes peak at the poleward flank of the upper level jet along the axis of the lower level jet. Thus the relation between extreme events and the jet is similar to the Southern Hemisphere summer lower level eddy driven jet, and to the Northern Hemisphere upper and lower level eddy driven jets. The merged jet is the regime with the most frequent occurrence of extreme events (even though eddies are stronger in the eddy driven jet regime), with the peak occurring on the poleward flanks of both the upper level and surface jets. The spatial relation to the jet is similar to the Northern Hemisphere jets, but if we assume that the North Pacific jet undergoes a seasonal transition from a winter merged jet to a summer eddy driven jet, extreme events in the observations are more frequent in the eddy driven rather than merged jet regime. This again supports the notion that other factors influence observed summer extreme events. In the subtropical jet regime we see a sharp decline in the frequency of extreme events, and they peak at the poleward flank of the surface jet, away from the upper level jet. Compared with the observations, the MQG model captures the secondary peak at the poleward flank of the eddy driven jet, though the modelled jet and the extremes' peak are more equatorwards, and the extremes are closer to the jet center. The model completely misses the strong primary peak on the flank of the subtropical jet. As the subsequent composite analysis will show, part of this difference is due to the lack of zonal asymmetry in the MQG model, while the observed austral winter subtropical jet spans a finite longitude sector. In addition, an examination of the vertical structure of extreme fields suggests a possible strong role for tropopause dynamics, which is clearly not captured in the MQG model.

Figure 6.7 shows centred composites similar to those shown for observations (Fig. 6.5, with temperature

anomalies shown for the model mid-level), for three runs, one from each of the three jet regimes. We see that in all regimes, extreme  $\zeta_{top}$  involves the formation of an absolute vorticity tongue which deepens, as in the observations, but the dynamic evolution leading to this tongue differs between the runs. In the eddy driven jet regime (Fig. 6.7 top row) a high latitude positive vorticity anomaly forms first, and subsequently interacts with a mid-latitude wave packet, to form a vorticity tongue. The day 0 composite patterns appear to resemble the observed day 0 composites of the subtropical jet, because the evolution involves an interaction of mid- and high-latitude modes; however, the dynamics of the modes differ and in observations they are more latitudinally separated. In the merged jet regime (Fig. 6.7 middle row), the dominant waves are highly coherent circumglobal waves, which break on the jet flanks near their critical surface. Extreme cyclonic vorticity forms when high latitude vorticity is pulled and also deepened by stretching, as part of this wave breaking process. In the sense that the extremes form as part of the nonlinear life cycle of waves propagating on the jet, this regime is most similar to the observed Jan–Mar events, but the model waves are much more coherent than in the observations. We note that coherent wave packets which traverse the globe have been observed in some years (e.g. Randel and Stanford, 1985). In fact, the observed Jan–Mar Southern Hemisphere jet varies interannually, in some years showing strong latitudinal jet meandering (an eddy driven jet), and in others the jet is fixed in latitude (a merged jet). In the subtropical jet regime (Fig. 6.7 bottom row), extreme events involve breaking of the highly nonlinear high latitude waves. This differs from the observed Jun–Aug Southern Hemisphere composites (Fig. 6.5); however, as the model does not have the strong eddy driven jet found upstream of the subtropical jet in the observations, this difference is not surprising. In fact, in both the MQG model and observations, the local growth of waves on the subtropical jet is weak. This weak growth might explain why extreme events on the subtropical jet cannot result from dynamics local to that jet, and must involve waves propagating on another jet. Similarly to the observations, in all regimes the extreme events have significant temperature anomalies, which are consistent with the pattern of meridional temperature advection implied by the absolute vorticity composites.

The differences between the MQG model and observations prompt us to examine these relations in a more realistic GCM. Recently Garfinkel and Waugh (2014) examined the influence of changes in jet latitude on wave breaking. Here we choose to analyze this same set of runs (see also Garfinkel *et al.*, 2013) to examine the effect of jet latitude and wave breaking changes on extreme events. We note that the jet in this set of runs is eddy driven, and

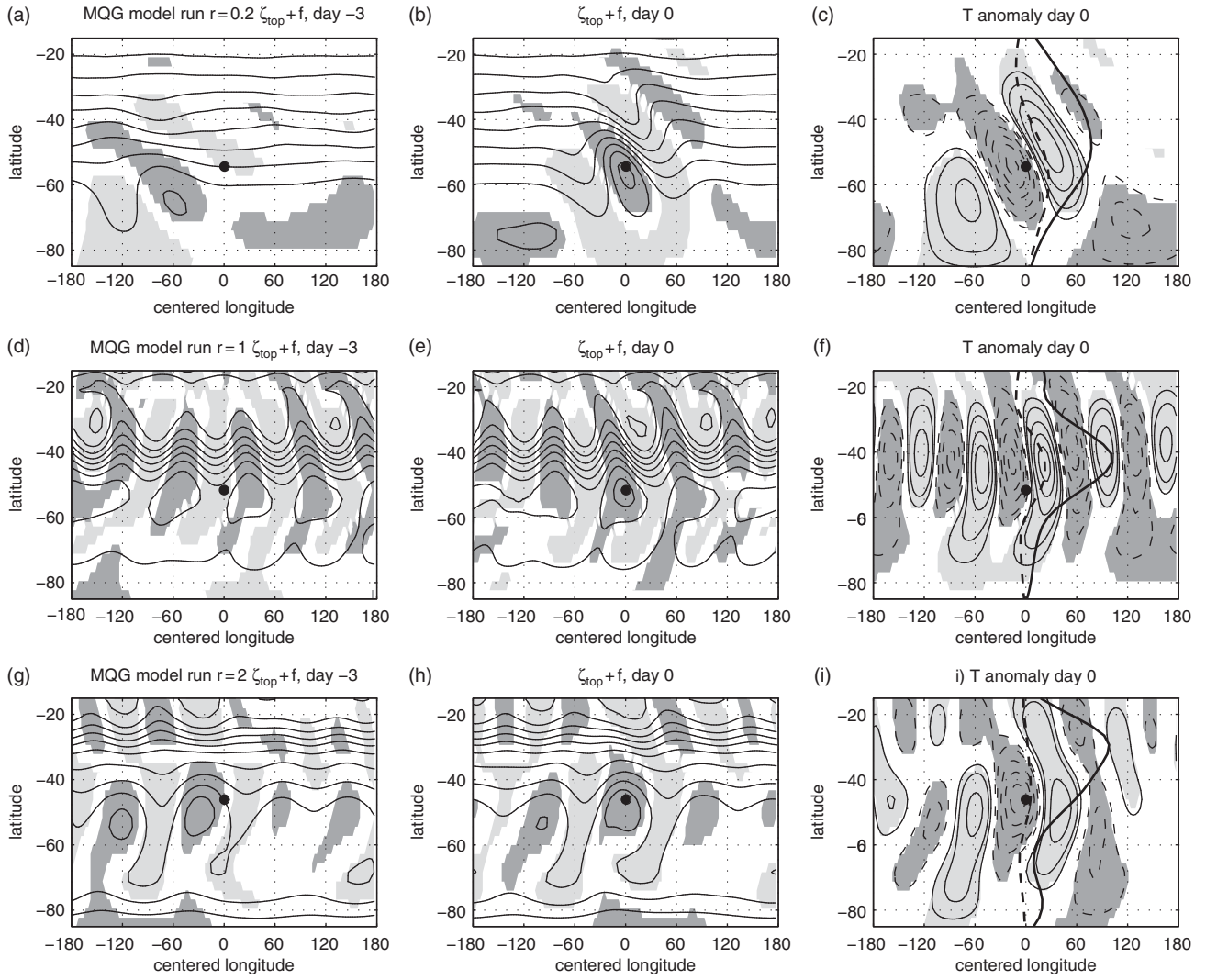


Fig. 6.7. As in Fig. 6.5 but for integrations of the MQG model, for an eddy driven jet run (wave damping value  $r = 0.2$ , plots a–c), a merged jet run ( $r = 1$ , plots d–f), and a subtropical jet run ( $r = 2$ , plots g–i). Left and middle columns: the upper level absolute vorticity ( $f+\zeta$ ) on days -3 (left) and day 0 (middle). Right column: the model mid-level temperature anomaly on day 0. Also shown in the right-hand column are the time mean upper and lower level zonal mean wind (solid and dashed lines, respectively). To better see the weak lower level wind structure in the subtropical jet regime, the zonal wind is plotted in units of  $0.5 \text{ m s}^{-1}$  (e.g. upper level winds reach  $40\text{--}50 \text{ m s}^{-1}$  depending on the model run). Absolute vorticity contours (left and middle) are  $(-1.6:0.15:-0.1) \times 10^{-4} \text{ s}^{-1}$ . The mid-level temperature contours (right) are  $\pm(0.5, 1.5) \text{ }^{\circ}\text{C}$ , with negative values dashed. Composites are produced for extreme events centered at latitudes of  $52.4^{\circ}\text{S}$ ,  $51.6^{\circ}\text{S}$ , and  $46^{\circ}\text{S}$ , and include 1542, 1496, and 273 composite members, respectively, corresponding to the eddy driven, merged, and subtropical jets.

thus leave the examination of these relations for the other jet regimes for future studies. Figure 6.6b shows the latitude-model run distribution of the frequency of occurrence of extreme events. In this model, the upper and lower level jets coincide, as in the observed eddy driven jets (and unlike the MQG model). Consistent with the observations, the distribution of extreme events peaks at the jet center, and as the jet shifts equatorward, the extreme events shift slightly to the poleward flank of the

jet. An examination of the distribution of wave breaking associated with strong upper level vorticity (Fig. 6.6 c,d) suggests that this shift to the poleward flank of the jet is associated with a change in the morphology of wave breaking as the jet shifts in latitude – from having more anticyclonic wave breaking on the equatorward flank of the more poleward jets (Fig. 6.6d), to more cyclonic wave breaking on the poleward flank of the more equatorward jets (Fig. 6.6c).

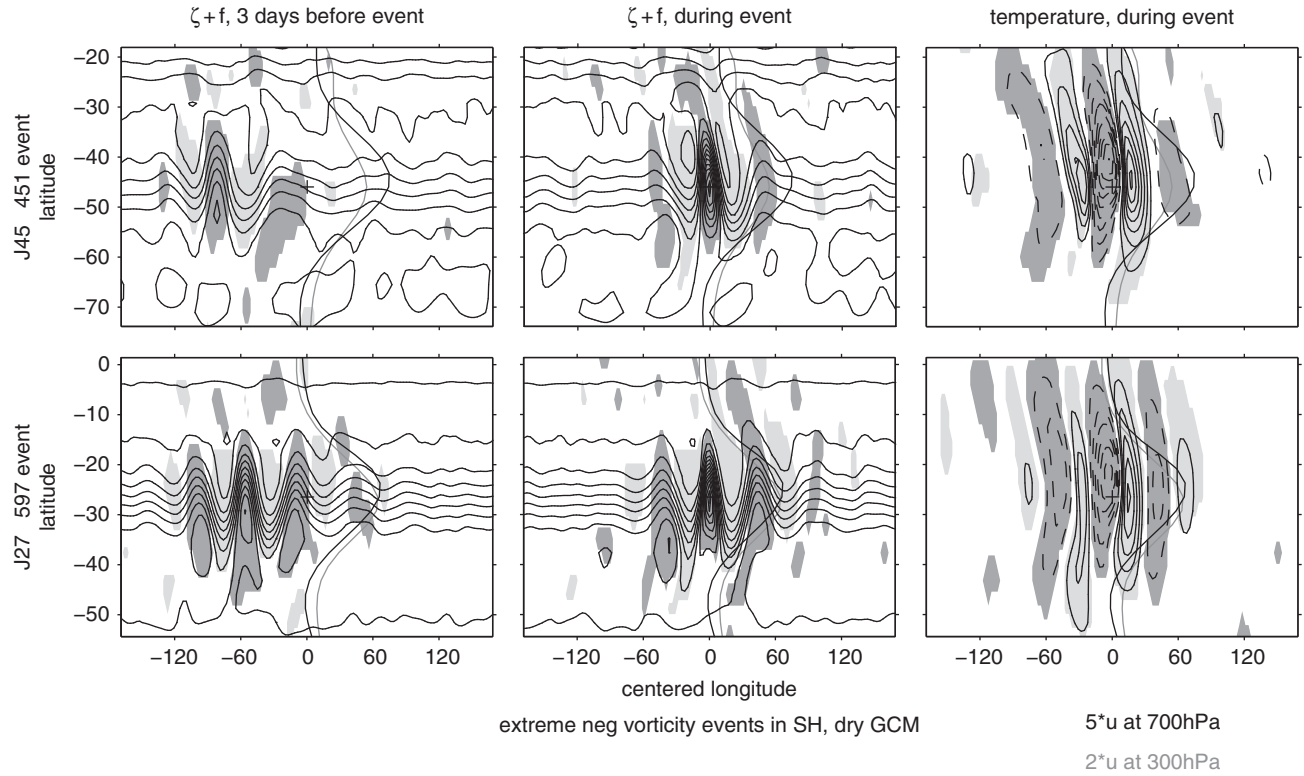


Fig. 6.8. As in Fig. 6.5 but for integrations of the dry primitive equation GCM in which the jet latitude is near 45°S (upper) and near 27°S (lower). Composites are produced for extreme events which peak at the jet core, for the jet at 45°S (top row) and at 27°S (bottom row). The contour interval for the left and middle columns is  $1.333 \times 10^{-5} \text{ s}^{-1}$  and for the right column 0.666K. A black plus marker indicates the center of the extreme event. Black and gray lines indicate the zonal wind profile of a control run at 700 hPa and 300 hPa multiplied by a constant scaling for clarity.

The synoptic evolution of the extreme events (Fig. 6.8) also shows similarities to the observed eddy driven jet composites (Fig. 6.5, top row): extremes are formed during the breaking of a wave packet propagating on the jet, by the deepening of an elongated vorticity tongue pulled equatorward from high latitudes. This pattern is quite robust between the different GCM runs, with the differences being mostly in the zonal wavelength and the degree of coherence of the preceding regular wave packet. This increased coherence in the merged jet regime as compared to the eddy driven jet regime, which is even stronger in the MQG model, deserves more attention since it could be important for the predictability or persistence of the extreme events.

#### 6.4.3 The distribution of observed extreme temperature anomalies

The previous sections have examined the distribution of extreme upper level cyclonic vorticity events. While these events are associated with significant surface temperature anomalies (e.g. Fig. 6.5c,f), it is not clear how their

occurrence is related to *extreme* surface temperature anomalies, or even to extreme upper level temperature anomalies. To get a better sense of the influence of the jet stream on extreme temperature anomalies, we examine their statistical distribution, as was done for vorticity extremes in Fig. 6.3. Figure 6.9 shows the seasonal distribution of the zonally averaged frequency of occurrence of extreme temperature anomalies calculated as the hemispheric highest and lowest one percent of temperature anomaly values, for the surface and for three pressure levels representing the lower, middle, and upper tropospheric regions. As in Fig. 6.3, we also show the upper and lower tropospheric jet streams. We see a large difference in the seasonal evolution of anomalies at the different levels, with polar regions dominating the surface and lower tropospheric anomalies (plots a–d). At higher levels there is a large difference between the hemispheres. Starting with the mid troposphere (Fig. 6.9e,f), in the Southern Hemisphere, the maximum number of extreme events occurs during fall, with negative anomalies peaking at the jet core (with a spreading of the anomalies toward the subtropics during winter, Fig. 6.9e) and positive anomalies peaking on the

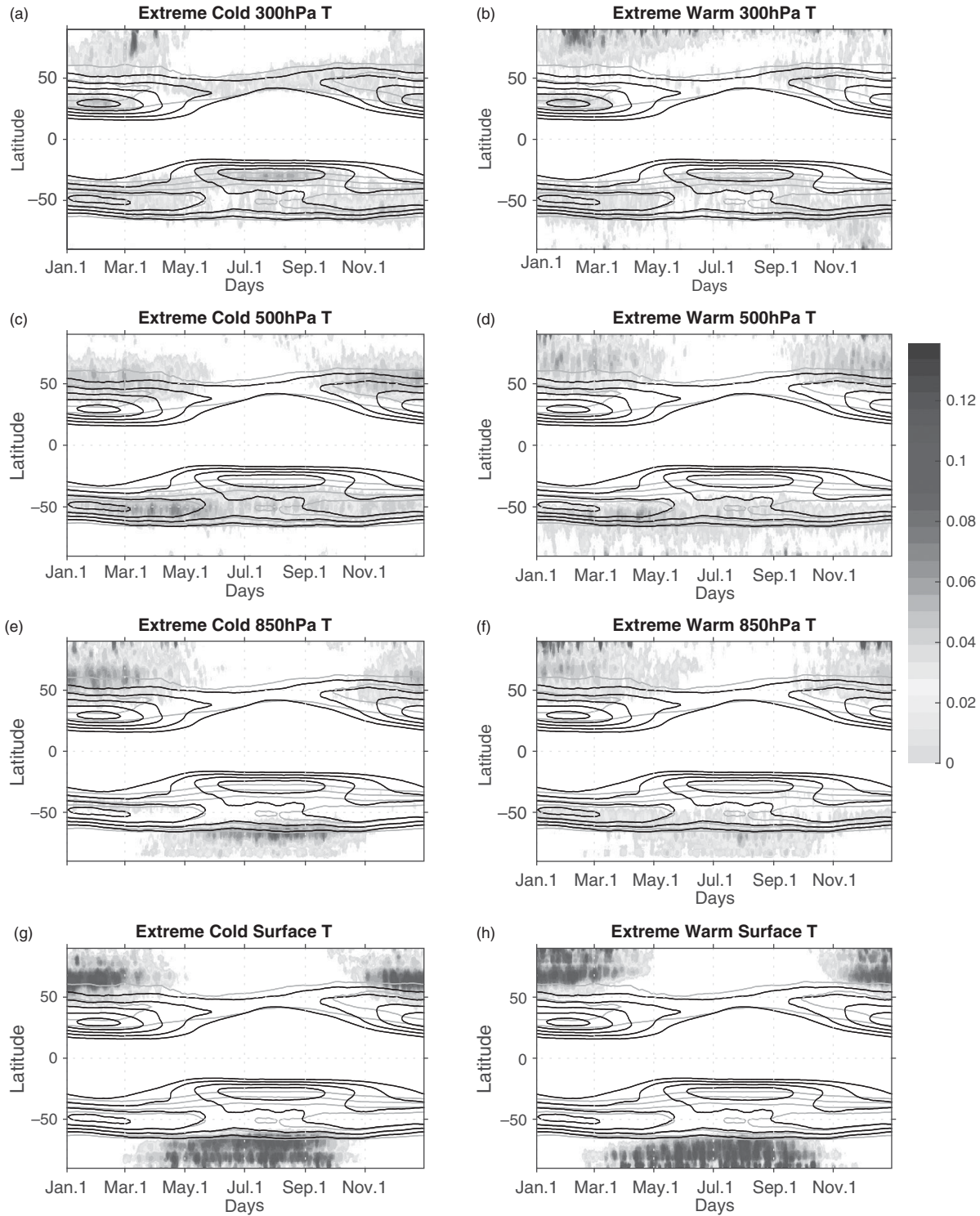


Fig. 6.9. As in Fig. 6.3, but for extreme temperature anomalies defined using the highest and lowest percentiles for each hemisphere. The left and right columns show extreme negative and positive anomalies respectively, at (a–b) the surface, (c,d) 850 hPa, (e,f) 500 hPa, (g,h) 300 hPa. The black and green contours show the upper and lower level jets as in Fig. 6.3. A black and white version of this figure will appear in some formats. For the colour version, please refer to Plate 13.

poleward jet flank and at high latitudes (Fig. 6.9f). This asymmetry between negative and positive anomalies, which is larger in observations than in the two idealized models (not shown), is an inherent feature of temperature advection when the flow is highly undulated, and the advection occurs over a few days, so that the strongest warm anomalies are created polewards of the jet center and the strongest cold anomalies occur equatorwards of it (Garfinkel and Harnik, 2015, to be submitted). In the Northern Hemisphere, mid tropospheric temperature extremes occur most frequently at high latitudes during fall, winter, and spring, with a very sharp decline during summer. Thus the examination of Northern Hemisphere summer extremes requires an analysis based on summer-only statistics.

At upper levels (Fig. 6.9g,h) we see a stronger influence of the jet on the distribution of extreme events. In particular, in the Southern Hemisphere, extreme summer events peak at the eddy driven jet, while extreme winter events peak at the subtropical jet (with a secondary peak at the mid-latitude eddy driven jet). In the Northern Hemisphere, we see a peak in extreme events at the winter jet and along the summer eddy driven jet (in particular for cold extremes, Fig. 6.9g Apr–Oct), although the majority of extreme events occur at very high latitudes during winter. An examination of the spatial distribution of these extremes (not shown) indicates that most of the mid-latitude extremes occur along the South Asian subtropical jet and along the Pacific merged jet during both seasons, and also over the Western Atlantic jet during summer. In addition, at high latitudes we find frequent extreme events mostly over the North Pacific, North America, and Greenland, but essentially no extremes during summer (except for some polar positive anomalies poleward of  $80^\circ$ , Fig. 6.9h). These results indicate a possible involvement of the stratosphere in the occurrence of extreme high latitude 300 hPa temperature anomalies. Figure 6.9 suggests that the large-scale circulation does affect the distribution of tropospheric temperature extremes quite strongly. However, in order to examine its possible influence on the surface, the effect of local surface processes must first be filtered out. This can be done by examining extremes based on more local threshold statistics and will be the subject of future research.

## 6.5 Discussion

In this chapter we have examined how the distribution and characteristic temporal evolution of extreme weather events varies with the type of jet stream, which we associate with different global scale circulation regimes. This was examined in observations and using experiments conducted with two different idealized models in which

systematic changes in the global circulation and jet stream type were studied in response to different changes in model parameters and forcing. We discuss three main types of jet streams: eddy driven, subtropical, and merged jets. An eddy driven jet forms when there are strong eddies or very weak thermal jet forcing. In observations, the summer jets as well as the North Atlantic winter jet and the high latitude austral winter jet (in particular over the South Atlantic) are eddy driven. A subtropical jet forms at the subtropical edge of the Hadley cell, at times when the mid-latitude eddies are either too far polewards or not strong enough to shift the jet. In observations, the main Southern Hemisphere winter jet is subtropical, as is the winter Northern Hemisphere jet over Africa and South Asia. A merged thermally and eddy driven jet forms when both processes are strong and close enough to each other. It is quite hard to distinguish between the merged and eddy driven jets in observations, although the North Pacific winter jet clearly has characteristics of a merged jet, and it is possible that during some of the years the Southern Hemisphere summer jet was also a merged jet.

As well as analyzing observations, we used two idealized models of the global circulation. The first is a two-level modified quasi-geostrophic (MQG) model in which eddy damping is varied gradually, and the circulation differs for all three jet regimes. We also examine a set of runs of the GCM of Garfinkel and Waugh (2014), in which an eddy driven jet is shifted gradually in latitude. In all these runs the jet is most characteristic of an eddy driven jet, although as it shifts equatorward the jet variability changes to resemble that of a merged jet.

We start by examining extremes of upper level cyclonic vorticity, which on the one hand is more directly affected by the large-scale circulation than quantities like surface temperature and precipitation, but is also related to Rossby wave breaking and the formation of PV streamers which are associated with extreme surface weather (Chapter 5, this book). Extreme upper tropospheric cyclonic vorticity events are found to occur in all three jet regimes, both in observations and in the models, but their frequency, spatial location, and temporal evolution differ. In observations, for the eddy driven and merged jet regimes, the extremes occur most frequently at the jet center in the Southern Hemisphere, and on the poleward flanks of the jet in the Northern Hemisphere. For the subtropical jets, the extreme events occur on their poleward flanks, while in Southern Hemisphere winter there is another secondary high latitude peak on the poleward flanks of the relatively weak surface eddy driven jet. In the MQG model, the upper level extreme cyclonic events follow the surface jet more closely, and thus occur on the poleward flanks of the upper level jet for all jet types. The peak of extreme event distribution for the subtropical jet is much weaker and

more poleward relative to the jet axis than for the other two regimes, suggestive more of the secondary peak found in observations in the subtropical jet regime. The GCM, on the other hand, reproduces the observed peak of extreme cyclonic events at the center of the eddy driven jet.

Composite studies of the observed and modeled Southern Hemisphere extremes show, for all jet types, that extreme upper level cyclonic vorticity forms during wave breaking, when an equatorward tongue of absolute vorticity deepens substantially (via stretching). At the same time, temperature is advected on both sides of this tongue, leading to a pattern of alternating significant positive and negative surface temperature anomalies. While these features are typical of all the composites, the synoptic evolution leading to the formation of this vorticity tongue differs with jet type, with two main types of evolution. The first, which is characteristic of the eddy driven jets that we examined in observations and in the GCM, and of the merged jet regime in the MQG model, is the formation of a vorticity tongue as part of the nonlinear life cycle of a wave packet propagating along the jet stream. The second kind of evolution occurs when perturbations, which form outside the jet, interact with the anomalies on the jet stream to form the extreme cyclonic vorticity event. This kind of evolution is unsurprisingly characteristic of the subtropical jet, both in observations and in the MQG model, since this jet is inherently associated with weak baroclinic growth. The observations and MQG model differ however. In observations (examined so far only for the Southern Hemisphere subtropical jet), extremes form when waves propagating on the upstream mid latitude eddy driven jet reach the subtropical jet region and interact with the subtropical waves to form the extreme event. In the subtropical jet of the MQG model, extremes form distinctly poleward of the subtropical jet, due to the breaking of high latitude large-scale waves, and the association with the upper level jet is not clear. A different kind of evolution is found in the eddy driven regime of the MQG model, where high latitude large-scale anomalies interact with mid-latitude waves to form the extreme anomalies.

The central role of wave breaking in the formation of upper level cyclonic vorticity extremes deserves further investigation. In particular, we need to understand what features in the evolution of wave breaking are important for extremes to form. We are currently examining these questions in more detail using further observational analysis and the GCM runs of Garfinkel and Waugh (2014).

Our composites show that extreme cyclonic vorticity events influence surface temperature, and while the composited temperature anomalies are not very large, other studies have shown that the upper level flow patterns are related to the formation of extreme negative surface temperature anomalies in the Southern Hemisphere. In particular, Sprenger *et al.* (2012) and Marengo *et al.* (2002) found

cold events in Brazil to be associated with wave breaking and PV streamer formation, and with upper level patterns similar to our extreme events. Here we also examined how the distribution of extreme temperature anomalies varies seasonally and spatially with the jet stream, at a range of tropospheric levels. Not surprisingly, we find a clear influence of the jet streams on the anomaly distribution at upper levels, although other processes also seem to play a role; however, at low levels, polar regions dominate the global percentile statistics, indicating the necessity for a more local approach to defining extreme temperature anomalies. This is particularly important for studying summer temperature extremes, which are completely masked by the winter, fall, and spring anomalies, except in the upper troposphere.

The study presented here is a first step in understanding how large-scale dynamics can influence extreme weather. Our results indicate a strong direct influence on upper tropospheric flow fields, and at least an indirect influence on temperature all the way down to the surface. By expanding the analysis to other flow features, and lower levels, we hope to gain a more complete understanding of the degree to which the large-scale circulation regime influences extreme events. Of particular importance is the possibility of a transition in the type of jet stream (e.g. Harnik *et al.*, 2014, Woollings *et al.*, 2010), which can change the distribution and statistics of extreme events (Franzke, 2013).

## 6.6 Acknowledgments

We acknowledge support provided by the Israeli Science Foundation grant 1537/12 and by the USA-Israel Binational Science Foundation grant number 2008436. C. Garfinkel acknowledges support from the Israeli Science Foundation grant 1558/14. All calculations presented here were performed using GOAT (Geophysical Observation Analysis Tool), a freely available MATLAB based data analysis and visualization program, written by Ori Adam (<http://www.goat-geo.org/>). ECMWF ERA-Interim data used in this study were obtained from the ECMWF Data Server <http://data-portal.ecmwf.int/data/d/interim/daily/>.

## References

- Ashcroft, L. C., A. B. Pezza, and I. Simmonds (2009). Cold events over Southern Australia: Synoptic climatology and hemispheric structure, *J. Clim.*, **22**, 6679–6698.
- Barnes, E. A. and D. L. Hartmann (2011). Rossby wave scales, propagation and the variability of eddy-driven jets, *J. Atmos. Sci.*, **68**, 2893–2908.
- Barnes, E. A. and D. L. Hartmann (2012). Detection of Rossby wave breaking and its response to shifts of the midlatitude jet with climate change, *J. Geophys. Res.* D09117, doi: 10.1029/2012JD017469

- Dee, D. P. *et al.* (2011). The ERA-Interim reanalysis: configuration and performance of the data assimilation system. *Q. J. R. Meteorol. Soc.*, **137**, 553–597.
- Dima, I. M., J. M. Wallace, and I. Kraucunas (2005). Tropical zonal momentum balance in the NCEP reanalyses, *J. Atmos. Sci.*, **62**, 2499–2513.
- Eichelberger, S. J. and D. L. Hartmann (2007). Zonal jet structure and the leading mode of variability, *J. Clim.*, **20**, 5149–5163.
- Franzke, C. (2013). Persistent regimes and extreme events of the North Atlantic atmospheric circulation, *Phil. Trans. R. Soc. A*, **371**, 20110471.
- Garfinkel, C. I. and D. W. Waugh (2014). Tropospheric Rossby wave breaking and variability of the latitude of the eddy-driven jets\*, *J. Climate*, **27**, 7069–7085.
- Garfinkel, C. I., D. W. Waugh, and E. P. Gerber (2013). The effect of tropospheric jet latitude on coupling between the stratospheric polar vortex and the troposphere, *Journal of Climate*, **26**, 2077–2097.
- Garfinkel, C. I. and N. Harnik (2015). The non-Gaussianity and spatial asymmetry of temperature extremes relative to the jet: the role of horizontal advection. To be submitted.
- Harnik, N. (2014). Extreme upper level cyclonic vorticity events in relation to the southern hemisphere jet stream. *Geophys. Res. Lett.*, **41**, 4373–4380.
- Harnik, N., E. Galanti, O. Martius, and O. Adam (2014). The Anomalous Merging of the African and North Atlantic Jet Streams during Northern Hemisphere Winter of 2010. *J. Climate*, **27**, 7319–7334.
- Held, I. M. (1975). Momentum transport by quasi-geostrophic eddies. *J. Atmos. Sci.*, **32**, 1494–1497.
- Held, I. M. (2000). The general circulation of the atmosphere. Introduction to general circulation theories. *Proc. Prog. Geophys. Fluid Dyn.* Woods Hole Oceanogr. Inst., <http://gfd.whoi.edu/proceedings/2000/PDFvol2000.html>.
- Held, I. M. and A. Y. Hou (1980). Nonlinear axially symmetric circulations in a nearly inviscid atmosphere, *J. Atmos. Sci.*, **37**(3), 515–533.
- Held, I. M. and M. J. Suarez (1994). A proposal for the intercomparison of the dynamical cores of atmospheric general-circulation models, *B. Am. Meteorol. Soc.*, **75**, 1825–1830.
- Kalnay, E. *et al.* (1996). The NCEP/NCAR 40-year reanalysis project, *B. Am. Meteorol. Soc.*, **77** 434–471.
- Lachmy, O. and N. Harnik (2014). The transition to a subtropical jet regime and its maintenance, *J. Atmos. Sci.*, **71**, 1389–1409.
- Lee, S. and H. K. Kim (2003). The dynamical relationship between subtropical and eddy-driven jets, *J. Atmos. Sci.*, **60**, 1490–1503.
- Mahlstein, I., O. Martius, C. Chevalier, and D. Ginsbourger (2012). Changes in the odds of extreme events in the Atlantic basin depending on the position of the extratropical jet, *Geophys. Res. Lett.*, **39**, L22805.
- Marengo, J. A., T. Ambrizzi, G. Kiladis, and B. Liebmann (2002). Upper-air wave trains over the Pacific Ocean and wintertime cold surges in tropical-subtropical South America leading to freezes in southern and southeastern Brazil, *Theor. Appl. Clim.*, **73**, 223–242.
- Martius, O., E. Zenklusen, C. Schwierz, and H. C. Davies (2006). Episodes of alpine heavy precipitation with an overlying elongated stratospheric intrusion: A climatology, *Int. J. Climatol.*, **26**, 1149–1164.
- Michel, C. and G. Riviere (2014). Sensitivity of the position and variability of the eddy-driven jet to different SST profiles in an aquaplanet general circulation model, *J. Atmos. Sci.*, **71**, 349–371.
- Nakamura, H., T. Sampe, Y. Tanimoto, and A. Shimpo (2004). Observed associations among storm tracks, jet streams and midlatitude oceanic fronts, *Geophysical Monograph Series*, **147**, 329–345.
- Panetta, R. L. (1993). Zonal jets in wide baroclinically unstable regions: Persistence and scale selection, *J. Atmos. Sci.*, **50**, 2073–2106.
- Petoukhov, V., S. Rahmstorf, S. Petri, and H. J. Schellnhuber (2013). Quasi resonant amplification of planetary waves and recent northern hemisphere weather extremes, *Proc. Natl. Acad. Sci. U.S.A.*, **110**, 5336–5341.
- Randel, W. J. and I. M. Held (1991). Phase speed spectra of transient eddy fluxes and critical layer absorption, *J. Atmos. Sci.*, **48**, 688–697.
- Randel, W. J. and J. L. Stanford (1985). An observational study of medium scale wave dynamics in the southern hemisphere summer. Part I: Wave structure and energetics. *J. Atmos. Sci.*, **42**, 1172–1188.
- Rhines, P. B. (1975). Waves and turbulence on a beta-plane, *J. Fluid Mech.*, **69**, 417–443.
- Romero, R., G. Sumner, C. Ramis, and A. Genoves (1999). A classification of the atmospheric circulation patterns producing significant daily rainfall in the Spanish Mediterranean area. *Int. J. Climatol.*, **19**, 765–785.
- Schlemmer, L., O. Martius, M. Sprenger, C. Schwierz, and A. Twitchett (2010). Disentangling the forcing mechanisms of a heavy precipitation event along the alpine south side using potential vorticity inversion. *Mon. Wea. Rev.*, **138**, 2336–2353, doi: 10.1175/2009MWR3202.1.
- Schneider, E. K. (1977). Axially symmetric steady-state models of the basic state for instability and climate studies. Part II. Nonlinear circulations, *J. Atmos. Sci.*, **34**, 280–296.
- Schubert, S., H. Wang, and M. Suarez (2011). Warm season subseasonal variability and climate extremes in the northern hemisphere: The role of stationary Rossby waves, *J. Clim.*, **24**, 4773–4792.
- Schubert, S. D., H. Wang, R. Koster, M. Suarez, and P. Y. Groisman (2014). Northern Eurasian heat waves and droughts. *J. Clim.*, **27**, 3169–3207.
- Son, S. W. and S. Lee (2005). The response of westerly jets to thermal driving in a primitive equation model, *J. Atmos. Sci.*, **62**, 3741–3757.
- Sprenger, M., O. Martius, and J. Arnold (2012). Cold surge episodes over Southeastern Brazil – a potential vorticity perspective, *Int. J. Climatol.*, **33**, 2758–2767.
- Wallace, J. M., I. M. Held, D. W. J. Thompson, K. E. Trenberth, and J. E. Walsh (2014). Global warming and winter weather, *Science*, **343**.
- Woollings, T., A. Hannachi, B. Hoskins, and A. Turner (2010). A regime view of the North Atlantic oscillation and its response to anthropogenic forcing, *J. Clim.*, **23**(6), 1291–1307.

# Forecasting high-impact weather using ensemble prediction systems

*Richard Swinbank, Petra Friederichs, and Sabrina Wahl*

## 7.1 Introduction

Improving forecasts and warnings of hazardous weather events is the top priority for operational weather forecasting services. Severe weather can have a wide range of serious impacts, potentially causing loss of life, damage to property, and impact on the general public and economic activity. Improving the forecasts of severe weather events helps people and businesses to be better prepared and so mitigate those potential losses. The time horizon for warnings ranges from early warnings several days ahead, for larger-scale events affecting countries or states, to very short range (minutes and hours), for severe thunderstorms and accompanying wind gusts and heavy rain or hail. In this chapter we focus on severe weather that is related to synoptic scale storm systems, as well as mesoscale systems dominated by moist deep convection. Several chapters in Part IV of this book discuss severe heat waves and cold spells, and their prediction.

Over recent decades, major progress has been made in improving the skill of numerical weather prediction; in the medium range (5 to 15 days ahead) forecasting skill has improved by around a day per decade (see, e.g. Chapter 1). Conventionally, weather forecasting has been based on carrying out a single numerical model integration, starting from the best available estimate of the atmospheric initial conditions. Subsequent evolution of the atmosphere is predicted using the numerical model to simulate the most important dynamical and physical processes. This approach is often referred to as deterministic prediction – which has the aim of producing a single best estimate of the future weather.

However, from everyday experience it is clear that weather forecasts are not perfect. At all scales, predictions of extreme events can never be precise nor certain, so predictions need to be probabilistic in nature. Many weather forecasting agencies now use ensemble forecasting techniques to quantify uncertainties in the forecast, and enable the probabilistic prediction of high impact events.

Rather than running a single model prediction, a number of predictions (typically 20 to 50 ensemble members) are run in such a way as to sample the uncertainties in the forecast. So, in principle, the probability of a forecast event can be estimated from the proportion of ensemble members in which that event is predicted. End users can use this uncertainty information to make decisions in order to balance the risk of losses due to severe weather against the cost of taking action to mitigate the losses, i.e. to optimize their individual cost–loss ratio. The value at risk has two components, the amount of the potential loss and the probability that the loss will occur.

## 7.2 Quantifying uncertainty

### 7.2.1 An ideal ensemble prediction system

An ideal ensemble prediction system (EPS) will represent uncertainties in the atmospheric state at all forecast ranges – including both the uncertainties in the forecast initial conditions and how those uncertainties evolve during the forecast. At any time and location, the values predicted by a particular member of an ensemble should correspond to a random draw from a statistical distribution representing the possible range of forecast values. In other words, the set of ensemble members should be a good, unbiased, representation of the forecast probability distribution.

This ideal EPS is illustrated in Fig. 7.1. A set of perturbations is added to the initial conditions, to represent the uncertainties in the analysis – represented by the small grey circle. A set of ensemble members, i.e. individual model predictions, is initiated from each of the perturbed initial conditions. Small differences between the initial conditions of the different ensemble members may grow quite slowly – in this case the state can be said to be predictable. On the other hand, as first demonstrated by Lorenz (1969) in a simple three parameter model, it is possible that small differences may soon lead to large differences between the

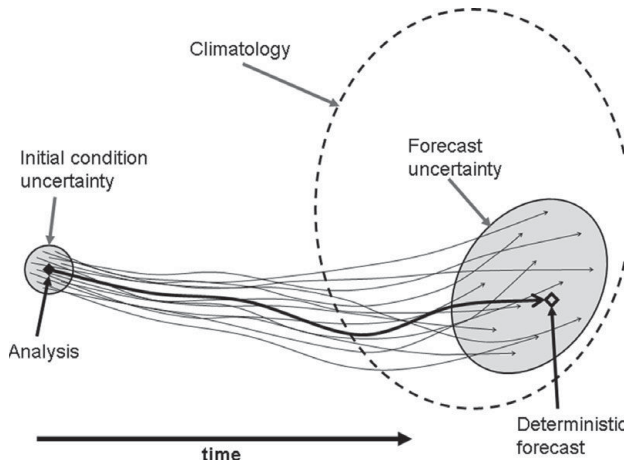


Fig. 7.1. Illustration of an idealized ensemble forecast, and the corresponding deterministic forecast.

ensemble members. These differences result from the chaotic nature of the atmospheric dynamics.

At the end of the forecast period, the spread of the ensemble (illustrated by the grey oval) should represent the uncertainties in the forecast values. In general, the forecast uncertainties will be smaller than the climatological range of values, shown by the large dashed oval. By contrast, a single deterministic prediction (shown with the thicker line) just gives one forecast state, and no measure of the uncertainty. In many EPS implementations, one of the ensemble members is a ‘control run’, with no initial condition or model error perturbations – that is equivalent to a deterministic forecast.

In practice, real ensemble prediction systems may not capture the full range of uncertainties (i.e. the grey oval is too small). In these circumstances, the ensemble is over-confident and is likely to underestimate the risks of hazardous weather events. This highlights a key aspect of ensemble evaluation, which we will return to in Section 7.4.

### 7.2.2 Initial condition uncertainty

As described in Chapter 1, initial conditions for numerical weather predictions are created using an analysis–forecast cycle. At each cycle (typically every six hours), a wide range of data, including observations from surface stations, aircraft, and satellites are assimilated into a numerical model. Quantifying the uncertainty in the initial conditions is intimately linked with data assimilation methods used to create those initial conditions. To see this, it helps to consider equations showing how the analysis ( $\mathbf{x}_a$ ) is derived by combining a previous (background) state  $\mathbf{x}_b$ , plus observation values ( $\mathbf{y}_o$ ),

$$\mathbf{x}_a = \mathbf{x}_b + \mathbf{K}(\mathbf{y}_o - H\mathbf{x}_b). \quad (7.1)$$

Thus, the analysis value is given by the background value plus a weighting ( $\mathbf{K}$ ) times the difference between the observed value and the background value (transformed to observation space using the observation operator  $H$ ). The weighting matrix  $\mathbf{K}$  is derived from error covariance matrices. Data assimilation embodies the basic statistical relationships underlying optimal interpolation, variational data assimilation, and the Kalman filter (see, e.g. Kalnay, 2003). So, adding information from the observations reduces the uncertainty that was in the background data (and the corresponding ensemble spread). However, in practice, it is not feasible to represent the covariances as matrices in model space, because the matrix would be far too big to store. We need to use approximate methods for practical construction of ensemble initial condition perturbations.

An obvious approach to generate a set of initial conditions for ensemble forecasting is to use ensemble data assimilation methods. In an ensemble Kalman filter (e.g. Evensen, 1994, Houtekamer and Mitchell, 2005), an ensemble is used to carry the error covariance information, with an analysis step carried out in the full model space. A practical variation on this approach, currently used at the Met Office (Bowler *et al.*, 2008), is to employ the ensemble transform Kalman filter (ETKF; Wang and Bishop, 2003), which solves the analysis equations in the subspace represented by an ensemble. Because of the limited way in which error covariances can be represented by a small number of ensemble members, this tends to over-estimate the reduction in uncertainties due to the observations, so an additional inflation term is used to boost the magnitude of the perturbations.

Other ensemble prediction systems use different methods to generate the initial condition perturbations, generally aiming to identify the fastest growing perturbations. A simple approach pioneered by Toth and Kalnay (1993) is known as error breeding. First an ensemble is set up with small random differences between ensemble members; these then grow and are periodically rescaled to a magnitude consistent with the analysis errors. An ‘ensemble transform’ step has more recently been included to ensure that the error modes are mutually orthogonal (Wei *et al.*, 2008). An alternative is to utilize singular vectors; while error breeding generates modes that have grown most rapidly in the recent past, the singular vector method generates perturbations that will grow rapidly in the near future. The original implementation of the ECMWF EPS used singular vectors to generate initial condition perturbations (Molteni *et al.*, 1996). More recently, the ECMWF EPS has been enhanced to use a combination of the singular vector approach and an

ensemble of data assimilation systems to generate the initial condition perturbations.

### 7.2.3 Uncertainty due to model error

A practical ensemble prediction system not only needs to take into account the growth in uncertainties resulting from the potentially chaotic nature of atmospheric dynamics, but also the way in which model errors and approximations contribute to forecast uncertainty.

One approach for taking account of model errors is to employ different combinations of physical parameterization schemes in different ensemble members (e.g. different convective parameterizations). If each of the parameterizations includes different representation of the relevant physical processes, this is a plausible way to represent that aspect of model uncertainties. This approach has some disadvantages, including additional cost to maintain different parameterization schemes, known systematic differences between ensemble members, and not sampling the full range of model uncertainties. A variation on this approach is to use the same parameterization scheme in each ensemble member, but with different values for some key parameters – varying them within the range of values that are consistent with measurements.

Buizza *et al.* (1999) introduced the approach of using stochastic physics schemes to represent the effect of model uncertainties. They introduced a method known as ‘stochastic perturbed physical tendencies’ in which the standard physical parameterizations calculate tendencies (i.e. increments to temperature, wind, humidity, etc.), but they are multiplied by a stochastic scaling factor before being added to the model fields. The scaling factor averages out to 1 and has a spatial and temporally coherent structure. Another method is a kinetic backscatter scheme (Shutts, 2005, Tennant *et al.*, 2011); the physical rationale is that dissipative processes remove excessive energy at small scales, but a proportion of this is replaced with stochastic wind increments in the regions where the dissipation is most active.

## 7.3 Practical ensemble prediction systems

### 7.3.1 Global EPS

The initial motivation for ensemble forecasting in operational weather forecasting centres came from the desire to extend the range of useful forecasts beyond the limit of deterministic predictive skill, by considering probabilistic predictions. The approach was pioneered at the Met Office by Murphy and Palmer (1986) for monthly predictions. In 1992, ECMWF introduced the first medium-range ensemble prediction system. This was soon followed by other

medium-range ensembles from NCEP, CMC and other centres, and ensemble forecasting became well established as a way of dealing with uncertainties inherent to weather forecasts at the medium range and longer.

In 2003, the World Meteorological Organization agreed to establish a decade-long programme to accelerate improvements in forecasting high impact weather. This programme, known as THORPEX (The Observing System Research and Predictability Experiment – WMO, 2005), had a major emphasis on developing the use of ensemble forecasting techniques via the TIGGE (THORPEX Interactive Grand Global Ensemble) project. Starting in October 2006, ten of the leading weather forecast centres have provided regular global ensemble predictions and made them available for research via three TIGGE archive centres. Each of the ensemble prediction systems that contribute to TIGGE are based on the principles described in Section 7.2 – although there are many differences in the details of their implementation. The TIGGE data have been used for a range of studies, including research on ensemble prediction methods, calibration and combination of ensemble predictions, development of products to support forecasts of high-impact weather, and research on dynamical processes and predictability.

Part of the original THORPEX vision was to develop a prototype Global Interactive Forecast System (GIFS), including the use of ensemble predictions from several models to produce probabilistic forecasts for high-impact weather events. The first priority was agreed to be the forecasting of tropical cyclones, so the TIGGE data providers set up an exchange of ensemble tropical cyclone prediction data. This data exchange was first started in conjunction with the THORPEX Pacific Asian Regional Campaign (T-PARC) that took place in 2008, and it has been continued to support several forecast demonstration projects. Figure 7.2 shows an example forecast of strike probability for a tropical cyclone, calculated from the track forecasts from the Met Office global EPS. The strike probability (Van der Grijn *et al.*, 2004) shows the estimated probability that the cyclone will pass within 120 km of a point, and has proved a useful way to display the uncertainties in tropical cyclone track forecasts. Similar products have been developed by other leading global NWP centres and are supplied to specialist tropical cyclone forecast centres.

Over recent decades there has been a considerable increase in the skill of tropical cyclone track forecasts. Yamaguchi *et al.* (2012) evaluated the skill of the tropical cyclone track forecasts of the TIGGE ensembles. There are significant variations between the different ensembles, but they showed that a grand ensemble gives improved predictions, compared with any single-model ensemble. The biggest benefit is obtained by combining the most

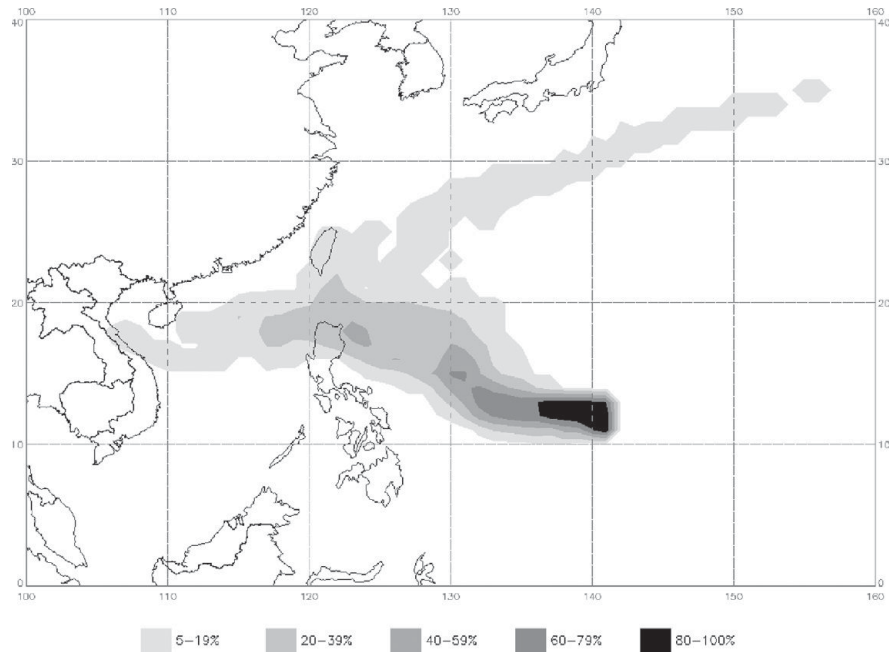


Fig. 7.2. The ‘strike probability’ for the Met Office ensemble forecast of typhoon Lupit with an initial time of 12UTC on 15 October 2009. This is defined as the probability of the centre of the storm passing within 75 miles (120 km) of any point.

skilful ensembles, but even adding in some of the less skilful ensembles improves the statistical reliability because the ensemble track predictions tend to be over-confident.

Figure 7.3 shows an example of a gridded forecast product that has been developed using TIGGE data to highlight the risk of strong winds (Matsuura and Nakazawa, 2014). This example shows a five-day forecast of the ‘St Jude’ storm of late October 2013 which brought very strong winds to England, Denmark, and neighbouring countries. This storm was well forecast by the TIGGE ensembles even though the storm had not yet formed at the initial time of the forecast.

Similar products are also used to highlight the risk of heavy rainfall and extreme temperatures. These products are calculated by comparing each ensemble forecast with the forecast climatology from the same ensemble system. For each ensemble system, at each grid point and for each date, the forecast climatology is calculated in terms of percentiles. (Some averaging over time is included to ensure that the climatology varies smoothly from day to day). The maps display the probability of the forecast wind speed exceeding the 95th climatological percentile. The probability is calculated from the number of ensemble members exceeding the relevant threshold for each EPS. The plot also shows the probability of exceeding the 95th percentile calculated across the grand ensemble using all four contributing single-model ensembles. Since these percentiles are calculated relative to the relevant ensemble forecast climatologies, these products are calibrated to take into account systematic errors in the ensembles, insofar as

is feasible. More general ensemble postprocessing methods to take into account systematic errors are discussed in Section 7.5.

Both the tropical cyclone track forecasts and the gridded products are now starting to be introduced into the WMO Severe Weather Forecast Demonstration Project (SWFDP). The SWFDP is a project designed to bring some of the benefits of modern numerical weather prediction (NWP) systems to developing and less developed countries. The SWFDP is organized on a regional basis, each region has one or more coordinating centres. Some of the major global NWP centres provide graphical products to the regional centres, based on both their deterministic and ensemble prediction systems. Forecasters at the regional centre interpret those products and provide guidance which is then cascaded to neighbouring countries. For example, the first regional project was established in southern Africa with a lead regional centre in Pretoria provided by the South African Weather Service (SAWS). To supplement single-model ensemble products, multi-model ensemble tropical cyclone forecasts and the gridded severe weather products are being made available for use in the SWFDP.

### 7.3.2 Convective-scale EPS

With the increasing availability of high performance computers, numerical weather prediction models can resolve much more detailed features and processes. A new generation of high-resolution atmospheric models has been developed to provide detailed predictions of convective systems and wind storms. A particular objective is to

## Occurrence probability of extreme surface wind speed

Initial: 2013.10.23.12UTC, Valid: 2013.10.28.12UTC

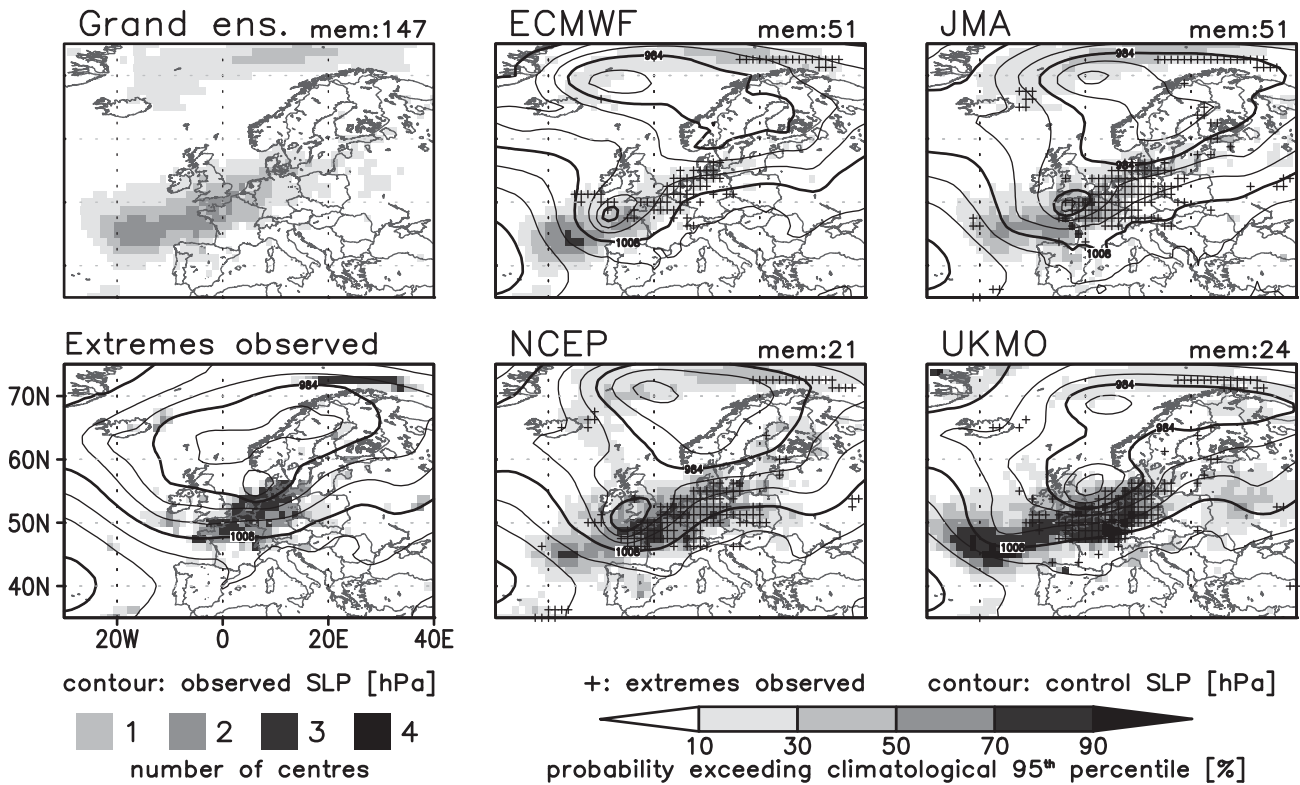


Fig. 7.3. Example of product showing the risk of high wind speed (above the 95th climatological percentile), calculated from four of the TIGGE ensembles (right-hand panels), a multi-centre grand ensemble combination (upper left), and the corresponding observed extremes (number of centres for which the analysed wind speed exceeded the threshold, lower left).

improve forecasts of deep moist convection, which can produce high impacts through severe precipitation, hail, and wind gusts. Using grid lengths of about 2 km or better, these models are starting to be able to represent large-scale convection, rather than relying on parameterizations of sub-grid-scale convection – so they are often referred to as convection-permitting models. However, convective processes are highly nonlinear and characterized by short time scales. As a consequence, forecasts are strongly impacted by uncertainties in the initial conditions and in the model formulation. So, ensemble techniques are now starting to be deployed to quantify uncertainties in these convective-scale forecasts, too. In this section we focus on examples of predictions from the UK and the German convective-scale ensembles. Convective-scale ensembles are also being implemented in France (Bouttier *et al.*, 2012, Nussier *et al.*, 2012), with other groups developing systems in other countries across the world.

The German COSMO-DE-EPS is developed as a multi-physics and multi-analysis ensemble (Baldauf *et al.*, 2011,

Gebhardt *et al.*, 2011, Peralta *et al.*, 2012). Its 20 members differ in both initial and boundary conditions and physical parameterizations, as shown in Fig. 7.4. Boundary conditions are provided by four global models (IFS, GME, GFS, GSM) which drive a boundary conditions EPS (BCEPS) using COSMO-EU with a grid spacing of 7 km. Five COSMO-DE simulations are nested into one member of COSMO-BCEPS, respectively, where the model physics are changed by parameter variation of the parameterizations for microphysics, turbulence, and shallow convection. COSMO-DE-EPS uses data assimilation including a latent heat nudging for precipitation rates (Stephan *et al.*, 2008). In order to preserve the benefit of the assimilation, the initial conditions are slightly perturbed by adding the differences between the respective COSMO-BCEPS member and a 3 h forecast of the COSMO-EU deterministic systems. COSMO-DE-EPS is initialized every three hours with a lead time of 21 hours. It was first implemented in December 2010, and operational forecasts are available since May 2012. Figure 7.5 shows quantitative

COSMO-DE-EPS	IFS	GME	GFS	GSM
mean entrainment rate for shallow convection	1	6	11	16
critical value for normalized over-saturation	2	7	12	17
scaling factor boundary layer for heat (min)	3	8	13	18
scaling factor boundary layer for heat (max)	4	9	14	19
maximal turbulent length scale	5	10	15	20

Fig. 7.4. Setup of the multi-physics and multi-analysis COSMO-DE-EPS.

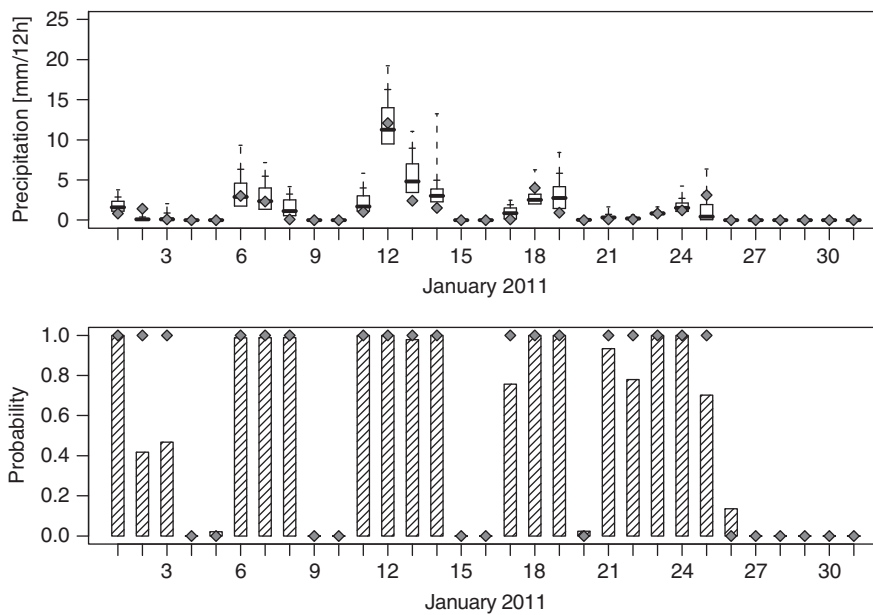


Fig. 7.5. Quantitative precipitation forecasts of COSMO-DE-TLEPS for Bonn station. The upper panel shows the median, the lower and upper quartiles (boxes), and the 0.9- and 0.99-quantiles (whiskers). The lower panel shows the probability of precipitation. The dots represent the observed rain rate in mm/12 h (upper panel) and as zero and one for precipitation below and above 0.1 mm.

precipitation forecasts for the next 12 hours in terms of the probability of precipitation and the quantiles based on the time-lagged COSMO-DE-EPS, which will be discussed in Section 7.4. The probabilistic forecasts are mainly designated to forecasters issuing weather warnings on the shortest range for heavy precipitation and severe winds.

A convective scale variable-resolution model, designated UKV, was introduced in the UK in 2010 (Lean *et al.*, 2008; Tang *et al.*, 2012). The UK ensemble (known as MOGREPS-UK), uses a 2.2 km version of the UKV model, in which a 12-member ensemble is run four times a day. It has a stretching zone around the lateral boundaries where the resolution decreases to facilitate nesting directly in global models. For its initial implementation in June 2012, MOGREPS-UK was nested in a regional ensemble (MOGREPS-R) covering Europe and the North Atlantic. In January 2013, the global (MOGREPS-G) ensemble was upgraded to a 33 km grid, enabling the global ensemble to drive MOGREPS-UK directly. Currently MOGREPS-UK

is a downscaling ensemble, with both initial conditions for each member and the boundary conditions, derived from the equivalent global ensemble members. Since no high-resolution initial conditions or boundary data are used, the fine-scale detail has to spin up in the first few hours of each forecast.

Shortly after its initial implementation, MOGREPS-UK was used to provide products as part of the Met Office Olympic showcase (Golding *et al.*, 2014) to support the London 2012 games. The products included a set of maps showing the likelihood of rainfall, high temperatures, or strong wind; the maps were presented for a range of time periods and thresholds. Site-specific forecasts were presented for each of the main Olympic venues. Figure 7.6 shows an example product for the sailing venue at Weymouth, showing the hourly wind forecasts. The main graph shows the range of forecast surface wind speeds, both in terms of miles per hour and the Beaufort scale. The range of speeds is shown in box and whisker style, with the box

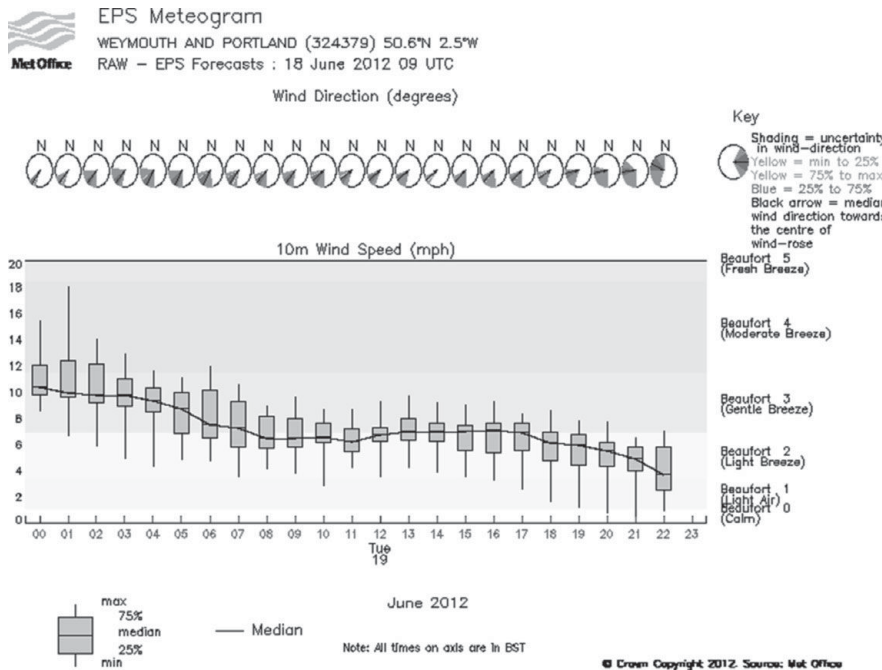


Fig. 7.6. Example of site-specific forecast from the Met Office Olympic showcase website, showing wind forecasts for the sailing event at Weymouth and Portland. The main graph depicts the hourly wind speeds (using both mph and the Beaufort scale), with the range of likely values shown using box and whisker plots. The ranges of likely wind directions are shown in the upper part of the diagram.

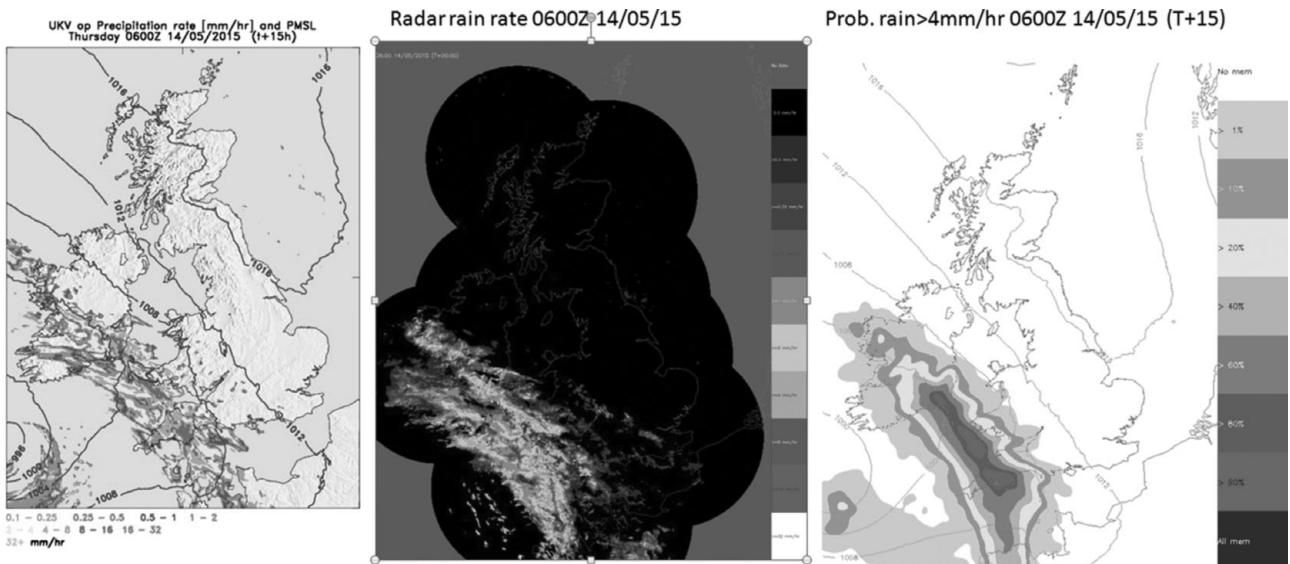


Fig. 7.7. Example of precipitation forecast products from the deterministic UKV model (left) and MOGREPS-UK ensemble (right), along with the verifying radar image (centre). The UKV and radar products show instantaneous rain rates, while the MOGREPS-UK chart illustrates the ‘Chance of Heavy Rain in the Hour’ which is defined as 4 mm/hr. A black and white version of this figure will appear in some formats. For the colour version, please refer to Plate 14.

showing the range between the 25th and 75th percentile, and the whiskers showing the full range of ensemble values. The range of forecast wind directions is shown by the circular wind roses, again presented probabilistically.

Figure 7.7 illustrates the presentation of rainfall forecast information. Three plots are shown: the left hand map

shows the rainfall forecast from the 1.5 km deterministic UKV model, the centre plot shows the corresponding radar rainfall observations, and the right-hand plot shows the chance of heavy rain (over 4 mm/hour) calculated from MOGREPS-UK. The normal way of calculating probabilities for a particular forecast event is from the fraction of an

ensemble in which that event is forecast to occur. For MOGREPS-UK there are only 12 members in each six-hourly ensemble, and that ensemble size is insufficient to provide smooth probabilities for local weather.

For both global and regional ensembles, a lagged ensemble is often used for generating probabilistic products; this also reduces unrealistic run to run variations. A lagged ensemble merges the forecasts from different initialization times into a time-lagged ensemble (TLE). For a highly variable field like precipitation, the lagged ensemble technique is not sufficient to provide smooth probabilities. So, for convective-scale ensembles we employ a ‘neighbourhood processing’ technique (Theis *et al.*, 2005, Roberts and Lean, 2008, Ben Bouallègue *et al.*, 2013). Since the spatial uncertainty in local detail is larger than the scale of the weather phenomena themselves, nearby grid squares are used to give plausible alternative outcomes, i.e. increasing the effective ensemble size. As shown in Fig. 7.7, the effect of the neighbourhood processing is to fill in gaps between convective cells and provide more realistic probability fields. At present, fixed neighbourhood sizes are used for each product, but the optimal size will vary from forecast to forecast and across the domain, depending on the predictability of the situation and the impact of local effects. To address this issue, work is in progress to trial an adaptive method to determine the neighbourhood size.

#### 7.4 Probabilistic forecast verification

The notion of an ideal/perfect ensemble prediction system is that the ensemble members represent mutually independent draws from the distribution of the observations under a given forecast uncertainty that represents the forecaster’s lack of knowledge. In this case, the ensemble members and the observations are interpreted as samples from the same distribution. Several forecast strategies are applied to an EPS. The forecasts of an EPS may be evaluated on its individual members, as done, e.g. when looking at the rank histogram (see Fig. 7.8). Ferro (2013) discusses this strategy and formalizes the definition of fair scoring rules (Fricker *et al.*, 2013). Another way is to derive a probability distribution from the ensemble, or estimate statistical moments, probabilities, or quantiles thereof. If the predictive distribution is Gaussian, the estimation of the two statistical moments mean and variance is sufficient. However, for largely non-Gaussian variables or for extremes, other forecast strategies may be more informative. Quantiles of a predictive distribution for instance may be portrayed in a box-plot and are an intuitive way to communicate uncertainty to users (see Figs. 7.5 and 7.6).

Any EPS is subject to systematic biases and dispersion errors. Probabilistic forecast verification assesses and

quantifies these deficiencies, but also measures the information content of an EPS. A comprehensive overview of forecast verification is given in Wilks (2011) and Jolliffe and Stephenson (2010). Murphy and Winkler (1987) provide a basic concept of forecast verification that is based on the joint distribution of forecasts and observations. Although rigorous mathematics would require the definition of a prediction space (Gneiting and Ranjan, 2013), the concept of Murphy and Winkler (1987) is in principle applicable to probabilistic forecasts (i.e. forecasts issued in terms of probabilities, quantiles, distribution, or probability density functions). The reader is also referred to Gneiting and Katzfuss (2014) and Broecker (2012) for a review on probabilistic forecasting.

We show in the following how a forecaster may gather a broad picture of the capacity of an EPS. We concentrate on

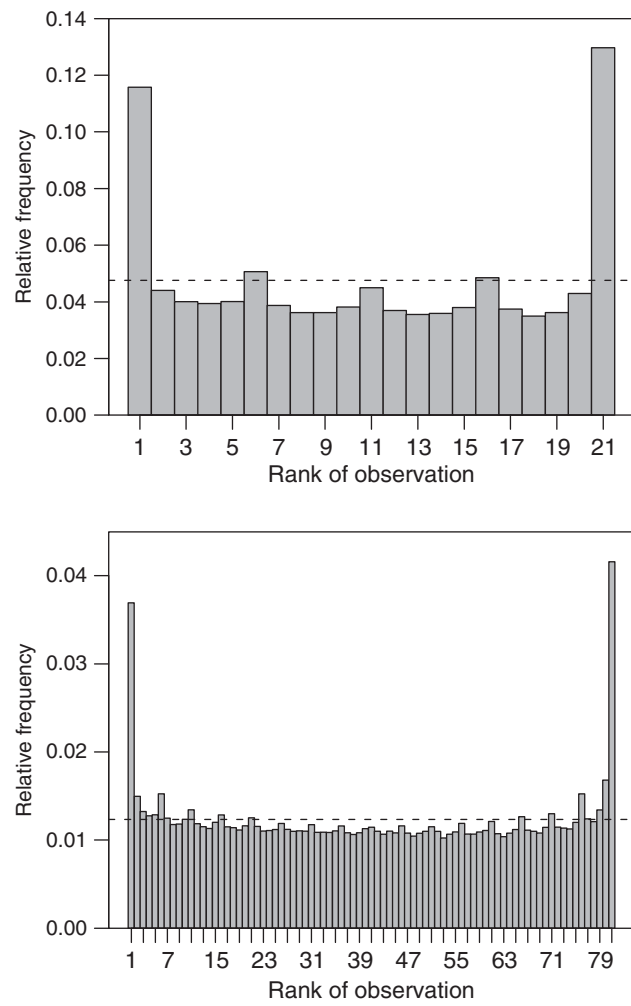


Fig. 7.8. Rank histogram of observed precipitation with respect to precipitation predicted by COSMO-DE-EPS (upper) and time-lagged COSMO-DE-TLEPS (lower). The dotted line indicates the value of a uniform distribution.

forecasts issued as continuous predictive distributions. There are essentially two ways to look at a predictive distribution, namely as a distribution function over threshold levels or a quantile function over probability levels. Both perspectives are equivalent, and although it is more popular to work with probabilities of threshold exceedances, a quantile view reveals other characteristics of the predictive distribution, and may be more useful, particularly for extremal levels. We further introduce the decomposition of proper scoring rules into uncertainty, reliability, and resolution. The methods are illustrated and discussed for quantitative precipitation forecasts based on COSMO-DE-EPS.

Statistical consistency between the ensemble forecasts and the observations is commonly assessed graphically by the analysis rank histogram (e.g. Anderson, 1996, Hamill and Colucci, 1997) or by a histogram of probability integral transforms (PIT; Gneiting *et al.*, 2007), i.e. the predictive distribution(s) evaluated at the observed values. In the case of a perfect EPS without biases or dispersion errors, the ranks or PIT values of the observations are uniformly distributed. A flat histogram thus gives evidence for statistical consistency between the ensemble of forecasts and the observations, although deficiencies might be averaged out for means over space or other inhomogeneities (Hamill, 2001). A skewed distribution in turn indicates a systematic bias in the ensemble mean, and if the histogram exhibits a bulbous (or conversely U-shaped) form, then the probabilistic forecasts are over- (under-) dispersive, i.e. if evaluated on an EPS the observations are too frequently in the centre (outside) of the spread of the ensemble.

**Figure 7.8** (upper panel) shows rank histograms for daily 12 h precipitation forecasts from COSMO-DE-EPS, evaluated at about 1000 observational sites located in Germany during the year 2011. The rank histogram is U-shaped and shows that the observations fall more frequently between groups of ensemble members, namely those that have equal boundary forcing. Because of the three-hour rapid update cycle, it is possible to construct a time-lagged COSMO-DE-TLEPS, in which a 12 h period is covered by four forecast simulations for each of the 20 configurations of COSMO-DE-EPS. The ensemble spread of the 80-member COSMO-DE-TLEPS is increased. However, the rank histogram (**Fig. 7.8**, lower panel) still shows extreme outer ranks, although less extreme than without time lagging.

#### 7.4.1 Proper scoring rules

A rank histogram assesses statistical consistency, but does not evaluate the information content of a forecast system. A scoring rule is a summary measure which allows for a ranking of competitive forecasting systems. We define a scoring rule as a cost function that a forecaster aims at

minimizing. An important requisite of objective forecast verification is the propriety of the scoring rule (Murphy, 1973, Gneiting and Raftery, 2007). A scoring rule is (strictly) proper if the expected score is minimized if (and only if) the forecaster's best judgement is issued as forecast. If the score is improper, then hedging is encouraged and a minimal score may be achieved for forecast other than the best possible forecast.

The choice of an adequate scoring rule depends on the measure that is issued as a forecast. The most complete forecast is given in terms of a predictive probability density function  $f$  or distribution  $F$ . The monotone character of a distribution function enables the definition of its inverse, the quantile function  $F^{-1}(\tau) = \inf\{x \in \mathfrak{R}, \tau \leq F(x)\}$ . Instead of a point forecast, both issue a function, i.e. give exceedance probabilities  $F(u)$  at all possible thresholds  $u$  or quantiles  $F^{-1}(\tau)$  at all probability levels  $\tau$ . **Figure 7.9** illustrates the various ways to display a distribution. Both distribution and quantile function give identical probabilistic information.

A widely used proper scoring rule to evaluate a continuous predictive distribution function  $F$  is the continuous ranked probability score (CRPS, Matheson and Winkler, 1976),

$$S_{CRP}(F, y) = \int (F(t) - H(t - y))^2 dt. \quad (7.2)$$

Here,  $H(t - y)$  denotes the Heaviside step function and  $y$  the observed value. For a deterministic forecast, the CRPS reduces to the mean absolute error (MAE). Thus the CRPS may also be used to assess the relative gain of a probabilistic over a deterministic forecast. Another proper scoring rule is the logarithmic score, which evaluates a predictive density function. Since the logarithmic score evaluates the expected log-likelihood of the observations given the forecasts, it is closely related to information theory (Roulston and Smith, 2002).

The CRPS averages over the complete range of the predictive distribution, and deficiencies at certain probability levels might remain undetected. An additional evaluation of the predictive distribution with respect to selected thresholds or probability levels is thus highly recommended. In this sense, we further focus on two other proper scoring rules which are widely used in probabilistic forecast verification and related to the CRPS, namely the Brier score (BS) and the quantile score (QS).

The BS (Brier, 1950) is used to assess the predictive performance of probability forecasts  $p_u$  for a dichotomous event. In our case,  $p_u = 1 - F(u)$  is the predictive probability for the observation to exceed a threshold  $u$ . It would be used to evaluate a set of probability forecasts, e.g. as displayed in **Fig. 7.3**, where the 95th climatological percentile takes the role of the threshold  $u$ . The BS for an

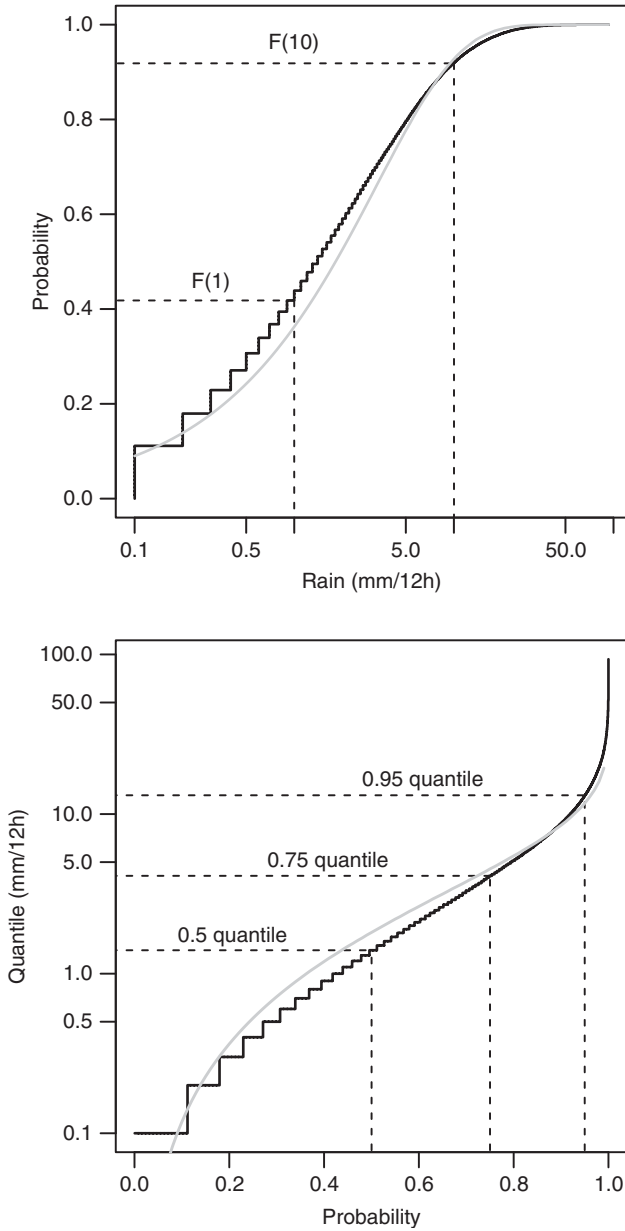


Fig. 7.9. Illustration of a distribution function (upper) and a quantile function (lower). The black lines show the empirical distribution/quantile function, and the grey lines its continuous approximation. The 1 mm and 10 mm exceedance probabilities, as well as 0.5-, 0.9-, and 0.95-quantiles are indicated as dashed lines.

observation  $y$  is given by the squared difference between the forecast  $p_u$  and an indicator function  $I_{y>u}$ ,

$$S_B(f, y, u) = (p_u - I_{y>u})^2, \quad (7.3)$$

where  $I_{y>u}$  is 1 if  $y > u$  and zero otherwise. A small average BS indicates good predictive performance at the threshold  $u$ . Alternatively, the QS assesses forecasts in

terms of quantiles/percentiles at an a priori selected probability level  $\tau$ , as displayed by box-plots in Figs. 7.5 and 7.6. If  $F$  represents the predictive distribution, then  $q_\tau = F^{-1}(\tau)$  is the respective quantile forecast. The QS (Koenker and Machado, 1999, Gneiting and Raftery, 2007, Friederichs and Hense, 2007) is defined as

$$S_Q(F, y, \tau) = \tau(y - q_\tau)I_{y>q_\tau} + (\tau - 1)(y - q_\tau)I_{y\leq q_\tau}, \quad (7.4)$$

which is a weighted absolute difference between forecasts and observations. For more information on this formula and its relation to quantile regression, the reader is referred to Koenker (2005). BS and QS are strictly proper scoring rules. The integrals of both the BS over all thresholds  $u$  and the QS over all probability levels  $\tau$  are proportional to the CRPS. An advantage of the quantile view is that no prior knowledge of the data is needed to define the probability level at which the predictive quantile is to be evaluated, whereas the definition of a meaningful threshold to evaluate probability forecasts requires some knowledge of the range of the data, i.e. the 99.9th percentile always lies in the tail of the distribution, but 10 mm precipitation in one hour is extreme in some regions and very normal in others.

#### 7.4.2 Proper score decomposition

Every proper score can be decomposed into components related to uncertainty, reliability, and resolution. The decomposition is related to the calibration-refinement factorization of Murphy and Winkler (1987). Reliability describes the statistical consistency between the predictive distribution and the observations. A forecast system is reliable (i.e. well calibrated) if, for all times, the observations are statistically consistent with the predictive distribution. Resolution assesses the discriminative power of a forecast system, and is closely related to the sharpness of a predictive distribution subject to calibration.

In general, scores are calculated statistically from a set of forecast–observation pairs  $(F_i, y_i)$ , where  $i = 1, \dots, N$ . The average score is given by

$$S = \frac{1}{N} \sum_{i=1}^N S(F_i, y_i), \quad (7.5)$$

and is an estimate of the mean expected score, where the expectation is taken over the joint distribution of both forecasts and observations. Likewise, an estimate of the expected score  $S(F, G) = E_Y[S(F, y)]$  is obtained by averaging the score function of fixed forecasts of  $F$  over an ensemble of observations. Unfortunately, we generally dispose only of one observation  $y_i$  per forecast  $F_i$ . In order to estimate the score decomposition which relies on a conditioning of the forecasts, the data have to be grouped into

clusters of similar forecasts. Estimates of the score decomposition and their bias sensitively depend on this clustering. For meaningful estimates and small biases each cluster should be sufficiently sampled. Score decompositions have been derived for the CRPS (Hersbach, 2000, Candille and Talagrand, 2005), the BS (Murphy, 1973), and most recently for the QS (Bentzien and Friederichs, 2014). Software routines for the calculation and decomposition of the CRPS, BS, and QS are freely available for the R statistical programming language (R Core Team, 2013) within the ‘verification’ package (NCAR – Research Applications Laboratory, 2013).

In order to illustrate the verification of an EPS and the score decomposition, we derive first guess (fg) probabilities and quantiles from the COSMO-DE-EPS and the COSMO-DE-TLEPS. The measures are estimated at each location of a weather station using locally a neighbourhood of  $5 \times 5$  grid points. For example, the probability of precipitation is estimated as the relative frequency of precipitating grid points, whereas quantiles are estimated by ordering the precipitation values. Reliability can be displayed graphically in a reliability diagram, where the empirical probability/quantile is plotted against the predicted probability/quantile. If the forecasting system is reliable, then the empirical estimates and the forecasts should lie on a diagonal. Figure 7.10 shows a reliability diagram for the probability of precipitation (fgPoP) and the 0.9-quantile (fgQ0.9). The reliability is estimated as an average over the forecast–observation pairs at all stations during the year 2011. Confidence intervals are estimated by the method of bootstrapping (see below).

The reliability diagram for fgPoP (Fig. 7.10, upper panel) shows significant deviations from the diagonal. fgPoP underpredicts the occurrence probability in the case that lower fgPoP ( $< 0.6$ ) are predicted, and overpredicts the occurrence probability otherwise. The histogram in Fig. 7.10 (upper panel) represents the distribution of the forecasts. It shows that using fgPoP gives relatively sharp predictions of values either close to zero or close to one. This sharpness, however, may be misleading for poorly calibrated forecasts, as seems to be the case here.

Figure 7.10 (lower panel) shows a quantile reliability diagram for fgQ0.9. A double logarithmic scale is used for a better representation. The clusters of fgQ0.9 on which the empirical quantiles are estimated are such that each cluster contains an equal number of forecast–observation pairs. The quantile reliability diagram for fgQ0.9 shows large deviations from the diagonal. fgQ0.9 generally underestimates the conditional 0.9-quantile of the observations, indicating that either the ensemble spread of the time-lagged COSMO-DE-EPS is too small, or fgQ0.9 is biased due to a too small ensemble size. Although time lagging improves the reliability of the first guess estimates for PoP

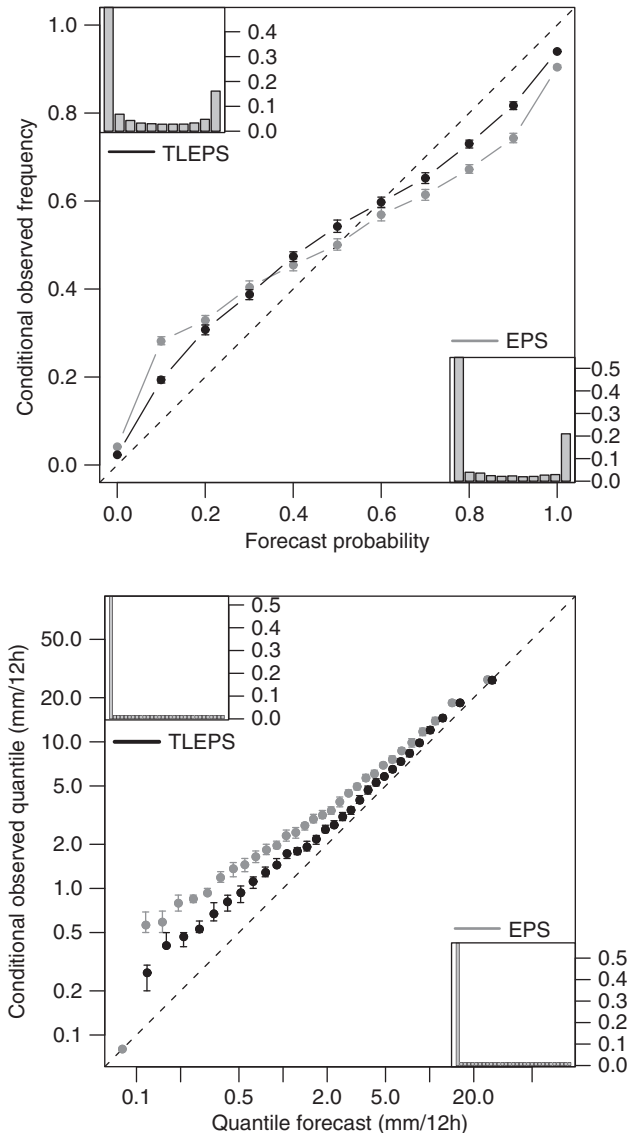


Fig. 7.10. Reliability diagram for fgPoP (upper panel) and fgQ0.9 (lower panel) for COSMO-DE-EPS (grey) and COSMO-DE-TLEPS (black). The whiskers indicate the sampling uncertainty. The grey bars within the inner plots show the histogram of forecasts.

and Q0.9, postprocessing is needed to account for these deficiencies and to obtain a better calibration of the forecasts. This is particularly important for rare events (i.e. large quantile probabilities or high thresholds).

In order to quantify the benefit of time lagging we show QS and BS, as well as its decompositions in Figure 7.11. Both BS for fgPoP and QS for fgQ0.9 are significantly improved. Most of it is due to a better reliability component of about 0.003 for the BS and 0.02 for the QS. However, time lagging likewise increases the discriminative power of the EPS. For fgPoP, the resolution increases by

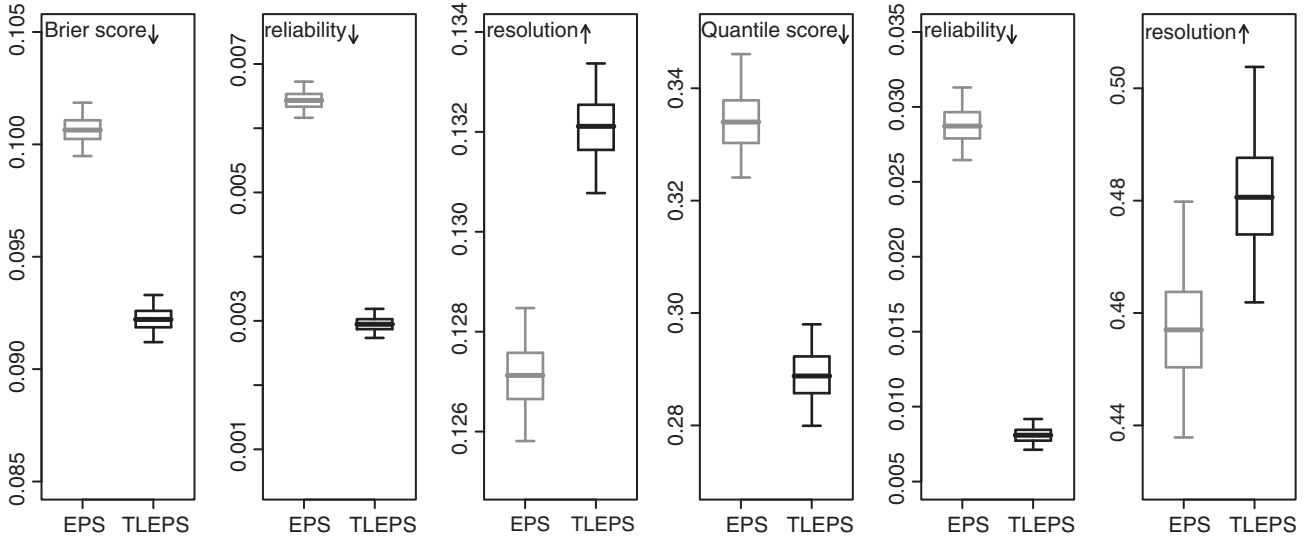


Fig. 7.11. BS for fgPoP with its decomposition into reliability and resolution (left) and QS for fgQ0.9 with its decomposition into reliability and resolution (right) for COSMO-DE-EPS (grey) and COSMO-DE-TLEPS (black). The boxes show median, inner quartile range, and 95% confidence of bootstrap sample.

about 0.004 and for fgQ0.9 by about 0.02. Thus the benefit from an improved reliability and a larger resolution is of the same order of magnitude.

Each average score is an estimate and comes with a sampling uncertainty that a forecaster should be aware of. Most notably it has to be assessed if different forecast systems are to be rated. A general procedure to estimate sampling uncertainty is the bootstrap method (Efron and Tibshirani, 1993). In our case we estimate confidence intervals by resampling the forecast–observations pairs in time. We keep seven days worth of spatially distributed data together while resampling, thereby preserving temporal and spatial dependencies. The 1000-member bootstrap sample is then used to estimate the 95% confidence interval, as displayed in Figs. 7.10 and 7.11.

## 7.5 Calibration and postprocessing

‘For the same reasons that data assimilation is required to feed observed information into numerical prediction models, an analogous process of forecast assimilation is required to convert model predictions into well-calibrated forecasts of observable variables’ (Stephenson *et al.*, 2005). Although ideally, an ensemble forecast should represent independent realizations of the predictive distribution, any EPS is subject to systematic bias and dispersion errors (Gneiting and Katzfuss, 2014). We argue that postprocessing should be an integral part of an EPS, and will demonstrate how simple regression techniques significantly improve the probabilistic forecasts.

Following Gneiting *et al.* (2007), postprocessing aims at maximizing the sharpness of the predictive distribution subject to calibration. Although sharpness is a characteristic of the forecast, it is closely related to the resolution, as defined in the previous section, since only a sharp predictive distribution provides discriminative power. A large variety of methods exist for ensemble postprocessing, and only a few of them are mentioned here. Very common techniques are ensemble model output statistics (EMOS, Gneiting *et al.*, 2005), Bayesian model averaging (BMA, Raftery *et al.*, 2005), and extended logistic regression (Wilks, 2009, Schmeits and Kok, 2010). All of these techniques provide full predictive distributions. EMOS relies on an a priori specification of the parametric form of the predictive distribution, and links the parameters of the distribution to the ensemble forecasts via a linear regression. BMA attributes a distribution to the predicted variable of each ensemble member, and provides as predictive distribution a weighted mixture thereof. Other approaches apply postprocessing directly to probability or quantile forecasts of the EPS (i.e. first guess estimates or other moments of the EPS) via logistic regression (LR, Fahrmeir and Tutz, 1994) and quantile regression (QR, Bremnes, 2004, Bentzien and Friederichs, 2012). EMOS, as well as LR and QR, may include a large amount of information from the ensemble, and not necessarily the variable that is to be predicted.

Ensemble postprocessing represents a statistical model between the EPS output and the observable. The parameters of the statistical model are inferred from a historic data set and are estimated such that they minimize a cost

function. For probabilistic forecasting this cost function should rely on a strictly proper scoring rule, thence the alliance between verification and postprocessing. The negative log-likelihood which is minimized with maximum likelihood techniques represents a strictly proper scoring rule, as does the CRPS or the QS. While reliability may easily be improved by postprocessing, the resolution depends on the intrinsic information content of the ensemble. The ability to choose very different variables out of the EPS and optimally combine them is crucial to improving upon the resolution. However, including too many covariates may result in overfitting, and comes with large computational costs. Predictor selection may be achieved with penalized regression, which puts a constraint on the regression coefficients and forces them to be close to zero unless there is a significant improvement of the score function. Examples for penalized regression are the least absolute shrinkage and selection operator (LASSO; Tibshirani, 1996) or ridge regression. LASSO pulls the regression coefficients faster towards zero than ridge regression, and sets some of the regression coefficients exactly to zero.

We illustrate the benefit of postprocessing for quantitative precipitation forecasts using COSMO-DE-TLEPS, in terms of predictive quantiles at probability levels between 0.25 and 0.99. The postprocessing uses quantile regression with ensemble mean precipitation, the respective fgQ, and the phase of the annual cycle as covariate (for more details, see Bentzien and Friederichs, 2012, 2014). Figure 7.12 shows the quantile skill score (QSS), which is defined as the percentage gain in QS with respect to a climatological forecast. It further shows the decomposition of the QS in reliability and resolution. Note that a smaller reliability represents a better agreement between forecasts and observations, whereas the resolution is better the larger it is. The

benefit of postprocessing for the 0.75-quantile is small. However, at lower and higher probability levels (i.e. less frequent events) the improvement of the quantile forecast is significant. The decomposition in reliability and resolution shows that the improvements are mainly due to a much better reliability, whereas the resolution is not significantly improved.

### 7.5.1 Postprocessing for extremes

Postprocessing is particularly beneficial for quantiles at large probability levels (Figure 7.12), or for probabilities at high thresholds (not shown). However, when the probability level or the threshold becomes large (i.e. extreme), then only very few observations if any are available. Extreme value theory (EVT; cf. Coles, 2001) uses a limit law for the behaviour of extremes, which provides very general universal distributions for extremes. More concretely, EVT provides asymptotic distributions for maxima and threshold exceedances over high thresholds.

Post-processing for extremes is hampered by the brevity of historic forecast and observation data. This is all the more true for mesoscale ensemble prediction. Not only is training of the postprocessing impeded, but also the verification of models for rare events, since only few extremes occur during a few years. Although EVT aims at the estimation of return levels for periods (e.g. quantiles) which exceed the record length of the observations, verification and model inter-comparisons are impossible due to large uncertainties (few events). This is why many studies only work with intermediate extremes. The 0.99-quantile of 12-hourly precipitation corresponds to a return period of only 50 days. In the January 2011 example shown in Fig. 7.5, the estimated 0.99 quantile varies between 0 and

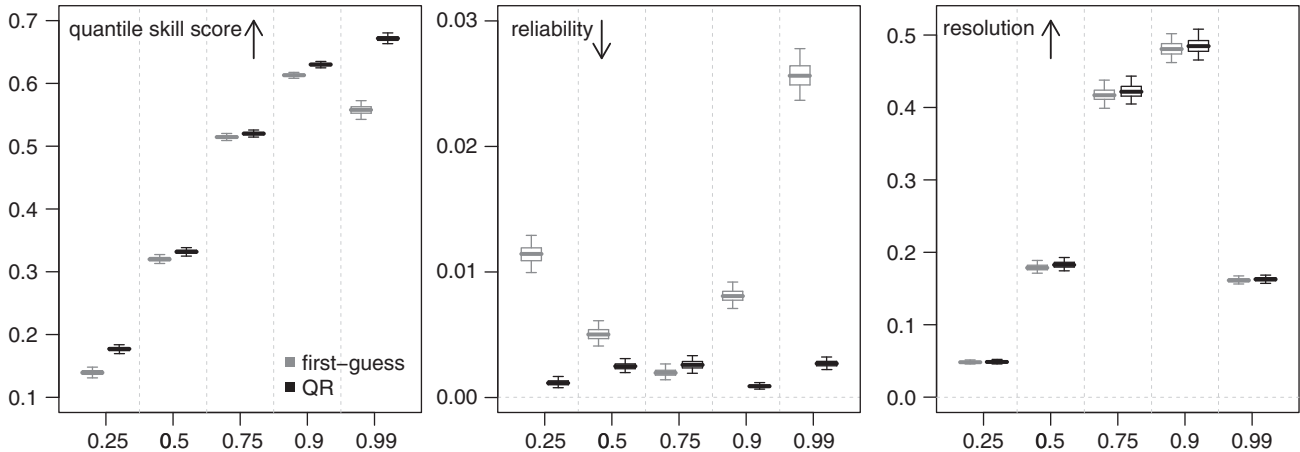


Fig. 7.12. QSS, reliability, and resolution of QS for COSMO-DE-TLEPS for 0.25-, 0.5-, 0.75-, 0.9-, and 0.99-quantiles before (fg in grey) and after (QR in black) postprocessing. The box-whiskers represent the bootstrap uncertainty (Figure 5 in Bentzien and Friederichs, 2014).

20 mm/12 h, and is thus neither extreme in the sense of EVT nor of high impact. Reforecasts are a well-known approach to provide long and homogeneous training data sets for postprocessing (cf. Hagedorn *et al.*, 2008, Hamill *et al.*, 2008), and are indispensable for a probabilistic prediction of extremes.

Only few studies employ EVT in postprocessing of ensemble forecasts. One approach to employ EVT in postprocessing is the EMOS, where the parameters of the non-stationary distribution linearly depend on predictors from the ensemble forecasts (e.g. Friederichs, 2010). One may also use a mixture of distributions for the occurrence of precipitation, for moderate and for extreme precipitation. The tail of such a mixture model may be represented by a non-stationary generalized Pareto distribution, as proposed by Frigessi *et al.* (2003). In a recent study, Oesting *et al.* (2013) jointly model observed and forecasted maximal wind gusts by a bivariate Brown–Resnick process. The study combines the joint modelling of forecasts and observations with spatial random fields for extremes. Another approach worth exploring for ensemble postprocessing is Bayesian hierarchical modelling (BHM, Cooley *et al.*, 2007) for weather variables, and in particular for extremes. Such a model would allow spatial interpolation of the postprocessing to locations without any observations. BHMs have found application in climate studies (e.g. Cooley and Sain, 2010, Sang and Gelfand, 2009), and only recently in ensemble prediction (Di Narzo and Cocchi, 2010).

## 7.6 Communicating uncertainty

This chapter has explored the use of ensemble prediction for producing risk-based forecasts of high-impact weather. As noted at the start, probabilistic forecasting can be very useful to businesses and other expert users to help them manage risk and mitigate losses due to hazardous weather events. In this section, we will briefly explore how probabilistic forecasts can be communicated more widely.

Conventionally, weather forecasts are presented to the public and customers in a deterministic way. For example, the forecast for Heathrow airport at 12 UTC could be for a temperature of 20°C with a SW wind at 5 m/s. While people are used to hearing this kind of information, there is an implicit understanding that the temperature and wind won't be precisely the forecast values, but there is a degree of uncertainty in the forecast values. However, communicating information about uncertainties in the forecast, as well as information about the ‘best estimate’ forecast presents a challenge. In weather forecasts presented on television, or other media, the forecaster often gives a verbal indication of the uncertainties in the predictions.

But in many cases it is helpful if uncertainties can be presented in a more quantified manner.

How best to communicate uncertainty information in a way that people can readily understand is a live topic for research. There have been several research studies on the public understanding of uncertainties and probabilistic forecasts, showing experimental evidence that decision-making with uncertainty information is improved (Joslyn and Savelli, 2010), but also that people may misunderstand probability forecasts (Joslyn *et al.*, 2009). In summer 2011 the Met Office ran a ‘weather game’ on its website to trial different approaches to presenting probabilistic weather forecast information – see <http://www.metoffice.gov.uk/news/releases/archive/2011/weather-game>. As a result, there have been some changes in the way information is presented on the website.

The weather warnings issued by the Met Office for the UK National Severe Weather Warning Service (NSWWS) are based on a probabilistic risk-based approach. A simple three-colour system is used: yellow indicates ‘be aware’ of severe weather, amber ‘be prepared’, and red ‘take action’, where the colours reflect a combination of likelihood and impact. For example, yellow could mean either high probability of a low-impact event or a very low probability of a high-impact event – see the impact matrix illustrated in Fig. 7.13. So, if the probability of a high-impact event is increased as the forecast is updated, the warning level may be increased from yellow to amber or red.

Forecasters take account of a range of raw and post-processed NWP output when making decisions over which warning is issued. This information includes the Ensemble Prediction System Warning system (EPS-W, referred to as “MOGREPS-W” in Neal *et al.* 2014) which generates ‘first guess’ warnings from both global and UK ensemble prediction systems. The first guess warnings use low, medium, and high impact thresholds for each parameter. These thresholds vary geographically, taking account of varying levels of impact of severe weather for different parts of the UK. For example, wind gusts of 60 mph may have little impact in north-west Scotland, where strong winds are common, but have a much higher impact in south-east England, where they are rarer and population density is much higher. Wind gust thresholds are reduced during the summer as lower wind gusts can still cause an impact since, for example, trees are more vulnerable to wind damage with their leaves on. Two sets of rainfall thresholds are available, with first guess warning maps created for both sets. One set is for use when the ground is saturated and one set for use during and soon after dry conditions, when relatively high rainfall totals are less likely to cause much flooding.

Figure 7.13 illustrates how the EPS-W system may be used to support the NSWWS, for a case of strong winds during December 2013. As well as causing severe damage,

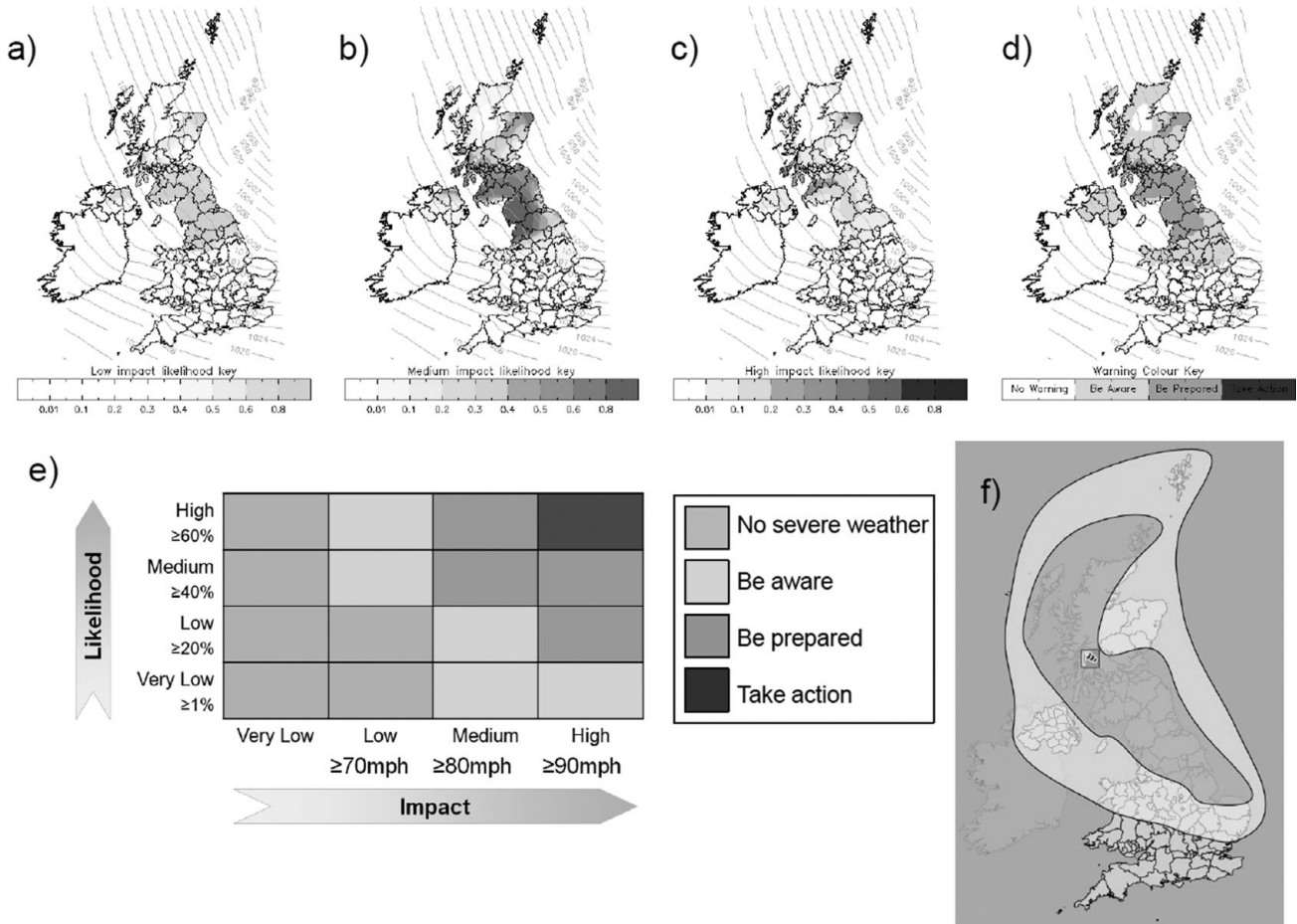


Fig. 7.13. Example of how the automatic probabilistic EPS-W system can be used to support the production of weather warnings, for a case of strong winds on 5 December 2013. (a), (b), and (c) show 24-hour forecasts (valid at 12 UTC on the 5th) of the probabilities of wind speed exceeding low, medium, and high impact thresholds, respectively. These data are combined to generate an overall warning colour (d), with impact taking precedence over likelihood. (e), the impact matrix, shows how the warning level depends on both likelihood and impact. Example wind speed impact thresholds are shown for the Scottish Highlands and Islands in winter; the thresholds for other regions will generally be different. (f) shows the warning map issued on 4 December. A black and white version of this figure will appear in some formats. For the colour version, please refer to Plate 15.

the winds also led to a storm surge that caused severe flooding along the east coast of England. The upper set of maps show the calculated probability of wind speed exceeding the pre-defined thresholds for a low, medium, or high impact event, based on the proportion of the ensemble members in which the event is predicted to occur. The three impact levels are combined to give an overall warning status at each point. Here, the impact colour takes precedence over the likelihood, giving emphasis to 'low probability high impact' events. For example (using the weather impact matrix), a 25% high impact warning (amber) would take priority over a 75% low impact warning (yellow), even though the yellow warning has a higher likelihood. The warning map is produced by the forecaster, taking into account both the information from the EPS-W system and

from other sources. Note that the warning map is valid for the whole day on 5 December, so the area covered by the warning is more extensive than that shown in the maps generated by the EPS-W system, which are only valid for a single time

## 7.7 Conclusion

This chapter has demonstrated how ensemble techniques are applied to risk-based forecasting of high-impact weather events – taking operational weather forecasting beyond the conventional deterministic approach. Ensemble prediction was initially applied to gain information about weather related risks beyond the limit of deterministic

predictability for medium and longer range forecasts. It has proved very useful in providing warnings for tropical cyclones and other major large-scale weather phenomena. More recently, ensemble techniques have been applied to short-range predictions at convective scales, where it is not possible to predict the details of (for example) convective storms. In those circumstances, ensemble predictions can give valuable indications of the risk of high-impact events.

While EPS increases useful forecasting skill, evaluation of the forecasts can be a challenge, because probabilistic forecasts introduce an extra dimension over and above the conventional deterministic approach. We have described a number of complementary approaches for evaluating ensemble forecasts, and have discussed proper scoring rules and their decompositions. We have also demonstrated that post-processing is indispensable for reliable probabilistic forecast products – approaches can include the use of a time-lagged forecast or the application of neighbourhood methods. However, bias and dispersion errors in ensemble prediction system need to be amended by statistical post-processing methods, which are furthermore qualified to extract the maximal amount of predictive information.

In the future, the challenge is to extend the use of ensembles to even higher scales, for example to focus on very high resolution predictions for urban areas and to improve warnings of small-scale hazards such as tornadoes. To address these issues the WMO is planning a WWRP project on high-impact weather, focusing on five hazard areas: urban flood, localized extreme wind, wildfire, urban heat and air quality, and disruptive winter weather. As well as covering atmospheric prediction and processes at a range of scales, the project will also cover forecast evaluation, vulnerability and risk, and communication. Verification and postprocessing should move from a univariate perspective, which only assesses predictive distributions for one variable at one location, towards a multivariate treatment of multi-variable spatio-temporal fields. In addition to improving forecasting methods, it is critical that forecast information is communicated well to users, including non-experts – especially for hazardous weather events.

## 7.8 Acknowledgements

We would like to thank Mio Matsueda, Piers Buchanan, and Rob Neal for assistance in the preparation of some of the figures.

## References

- Anderson, J. L. (1996). A method for producing and evaluating probabilistic forecasts from ensemble model integrations. *J. Climate*, **9**, 1518–1530.
- Baldauf, M., Seifert, A., Förstner, J., et al. (2011). Operational convective-scale numerical weather prediction with the COSMO model: description and sensitivities. *Mon. Wea. Rev.*, **139**, 3887–3905.
- Ben Bouallègue, Z., Theis, S. E., and Gebhardt, C. (2013). Enhancing COSMO-DE ensemble forecasts by inexpensive techniques. *Meteor. Z.*, **22**, 49–59..
- Bentzien, S. and Friederichs, P. (2012). Generating and calibrating probabilistic quantitative precipitation forecasts from the high-resolution NWP model COSMO-DE. *Wea. Forecasting*, **27**, 988–1002.
- Bentzien, S. and Friederichs, P. (2014). Decomposition and graphical portrayal of the quantile score. *Quart. J. Roy. Meteor. Soc.*, **40**, 1924–1934.
- Bouttier, F., Vie, B., Nussier, O., and Raynaud, L. (2012). Impact of stochastic physics in a convection-permitting ensemble. *Mon. Wea. Rev.*, **140**, 3706–3721.
- Bowler, N. E., Arribas, A., Mylne, K. R., Robertson, K. B., and Beare, S. E. (2008). The MOGREPS short-range ensemble prediction system. *Quart. J. Roy. Meteor. Soc.*, **134**, 703–722,
- Bremnes, J. B. (2004). Probabilistic forecasts of precipitation in terms of quantiles using NWP model output. *Mon. Wea. Rev.*, **132**, 338–347.
- Brier, G. W. (1950). Verification of forecasts expressed in terms of probability. *Mon. Wea. Rev.*, **78**, 1–3.
- Broecker, J. (2012). Probability forecasts. In *Forecast Verification: A Practitioner's Guide in Atmospheric Science*, eds. I. T. Jolliffe and D. B. Stephenson, 2nd edn., Wiley.
- Buizza, R., Miller, M., and Palmer, T. N. (1999). Stochastic representation of model uncertainties in the ECMWF ensemble prediction system. *Quart. J. R. Meteorol. Soc.*, **125**, 2887–2908.
- Candille, G. and Talagrand, O. (2005). Evaluation of probabilistic prediction systems for a scalar variable, *Quart. J. Roy. Meteor. Soc.*, **131**, 2131–2150.
- Coles, S. (2001). *An Introduction to Statistical Modeling of Extreme Values*. Springer.
- Cooley, D., Nychka, D., and Naveau, P. (2007). Bayesian spatial modeling of extreme precipitation return levels. *J. Amer. Stat. Assoc.*, **102**, 824–840.
- Cooley, D. and Sain, S. R. (2010). Spatial hierarchical modeling of precipitation extremes from a regional climate model. *Journal of Agricultural, Biological, and Environmental Statistics*, **15**, 381–402.
- Di Narzo, A. F. and Cocchi, D. (2010). A Bayesian hierarchical approach to ensemble weather forecasting. *J. Roy. Stat. Soc. Ser. C*, **59**, 405–422.
- Efron, B. and Tibshirani, R. J. (1993). *An Introduction to the Bootstrap*. Chapman & Hall/CRC.
- Evensen, G. (1994). Sequential data assimilation with a nonlinear quasi-geostrophic model using Monte Carlo methods to forecast error statistics. *J. Geophys. Res.*, **99**(C5), 10143–10162.
- Fahrmeir, L. and Tutz, G. (1994). *Multivariate Statistical Modeling Based on Generalized Linear Models*. Springer.
- Ferro, C. A. T. (2013). Fair scores for ensemble forecasts. *Quart. J. Roy. Meteor. Soc.*, doi: 10.1002/qj.2270, 2013

- Fricker, T.E., Ferro, C. A. T., and Stephenson, D. B. (2013). Three recommendations for evaluating climate predictions, *Meteorol. Appl.*, **20**, 246–255.
- Friederichs, P. and Hense, A. (2007). Statistical downscaling of extreme precipitation events using censored quantile regression. *Mon. Wea. Rev.*, **135**, 2365–2378.
- Friederichs, P. (2010). Statistical downscaling of extreme precipitation using extreme value theory. *Extremes*, **13**, 109–132.
- Frigessi, A., Haug, O., and Rue, H. (2003). A dynamic mixture model for unsupervised tail estimation without threshold selection. *Extremes*, **5**, 219–236.
- Gebhardt, C., Theis, S. E., Paulat, M., and Ben Bouallègue, Z. (2011). Uncertainties in COSMO-DE precipitation forecasts introduced by model perturbations and variations of lateral boundaries. *Atmospheric Research*, **100**, 168–177.
- Gneiting, T., Balabdaoui, F., and Raftery, A. E. (2007). Probabilistic forecasts, calibration and sharpness. *Journal of the Royal Statistical Society. Series B (Methodological)*, **69**, 243–268.
- Gneiting, T. and Katzfuss, M. (2014). Probabilistic forecasting. *Annual Review of Statistics and its Application*, **1**, 125151.
- Gneiting, T. and Raftery, A. E. (2007). Strictly proper scoring rules, prediction, and estimation. *J. Amer. Stat. Assoc.*, **102**, 359–378.
- Gneiting, T., Raftery, A. E., Westveld, A. H., and Goldman, T. (2005). Calibrated probabilistic forecasting using ensemble model output statistics and minimum CRPS Estimation. *Mon. Wea. Rev.*, **133**, 1098–1118.
- Gneiting, T. and Ranjan, R. (2013). Combining predictive distributions. *Electronic Journal of Statistics*, **7**, 1747–1782.
- Golding, B. W., Ballard, S. P., Mylne, K., et al. (2014). Forecasting capabilities for the London 2012 Olympics. *Bull. Amer. Meteor. Soc.*, **95**, 883–896.
- Hagedorn, R., Hamill, T. M., and Whitaker, J. S. (2008). Probabilistic forecast calibration using ECMWF and GFS ensemble forecasts. Part I: 2-meter temperature. *Mon. Wea. Rev.*, **136**, 2608–2619.
- Hamill, T. M. (2001). Interpretation of rank histograms for verifying ensemble forecasts. *Mon. Wea. Rev.*, **129**, 550–560.
- Hamill, T. M., Hagedorn, R., and Whitaker, J. S. (2008). Probabilistic forecast calibration using ECMWF and GFS ensemble reforecasts. Part II: precipitation. *Mon. Wea. Rev.*, **136**, 2620–2632.
- Hamill, T. M. and Colucci, S. J. (1997). Verification of Eta-RSM short-range ensemble forecasts. *Mon. Wea. Rev.*, **125**, 1312–1327.
- Hersbach, H. (2000). Decomposition of the continuous ranked probability score for ensemble prediction systems. *Wea. Forecasting*, **15**, 559–570.
- Houtekamer, P. L. and Mitchell, H. L. (2005). Ensemble Kalman filtering. *Quart. J. Roy. Meteor. Soc.*, **131**, 3269–3289.
- Jolliffe, I. T. and Stephenson, D. B. (eds.) (2010). *Forecast Verification: A Practitioner's Guide in Atmospheric Science*. 2nd edn. Wiley.
- Joslyn, S. and Savelli, S. (2010). Communicating forecast uncertainty: Public perception of weather forecast uncertainty. *Meteor. Appl.*, **17**, 180–195.
- Joslyn, S., Nadav-Greenberg, L., and Nichols, R. M. (2009). Probability of precipitation: Assessment and enhancement of end-user understanding. *Bull. Amer. Meteor. Soc.*, **90**, 185–193.
- Kalnay, E. (2003). *Atmospheric Modeling, Data Assimilation and Predictability*. Cambridge University Press, Cambridge.
- Koenker, R. (2005). Quantile regression. *Econometric Society Monographs*, **38**, Cambridge University Press.
- Koenker, R. and Machado, J. A. F. (1999). Goodness of fit and related inference processes for quantile regression. *J. Amer. Stat. Assoc.*, **94**, 1296–1310.
- Lean, H. W., Clark, P. A., Dixon, M., et al. (2008). Characteristics of high-resolution versions of the Met Office unified model for forecasting convection over the United Kingdom. *Mon. Wea. Rev.*, **136**, 3408–3424.
- Lorenz, E. N. (1969). The predictability of a flow which possesses many scales of motion. *Tellus*, **21**, 289–307.
- Matheson, J. E. and Winkler, R. L. (1976). Scoring rules for continuous probability distributions. *Management Science*, **22**, 1087–1096.
- Matsueda, M. and Nakazawa, T. (2014). Early warning products for severe weather events derived from operational medium-range ensemble forecasts. *Meteor. Appl.*, doi: 10.1002/met.1444
- Molteni, F., Buizza, R., Palmer, T. N., and Petroliagis, T. (1996). The ECMWF ensemble prediction system: methodology and validation. *Quart. J. Roy. Meteor. Soc.*, **122**, 73–119.
- Murphy, A. H. (1973). A new vector partition of the probability score. *Journal of Applied Meteorology*, **12**, 595–600.
- Murphy, A. H. and Winkler, R. L. (1987). A general framework for forecast verification. *Mon. Wea. Rev.*, **115**, 1330–1338.
- Murphy, J. M. and Palmer, T. N. (1986). Experimental monthly long-range forecasts for the United Kingdom. 2. A Real-time long-range forecast by an ensemble of numerical integrations. *Meteorol. Mag.*, **115**, 337–349.
- Neal, R., Boyle, P., Grahame, N., Mylne, K., and Sharpe, M. (2014). Ensemble based first guess support towards a risk based national severe weather warning service. *Meteorol. Apps.*, **21**, 563–577.
- NCAR – Research Applications Laboratory (2013). *Verification: Weather Forecast Verification Utilities*. R package version 1.36.
- Nussier, O., Joly, B., Vie, B., and Ducrocq, V. (2012). Uncertainty of lateral boundary conditions in a convective-permitting ensemble: a strategy of selection for Mediterranean heavy precipitation events. *Nat. Hazards Earth Syst. Sci.*, **12**, 2993–3011.
- Oesting, M., Schlather, M., and Friederichs, P. (2013). Conditional modelling of extreme wind gusts by bivariate Brown-Resnick processes. arXiv:1312.4584 [stat.ME].
- Peralta, C., Ben Bouallègue, Z., Theis, S. E., Gebhardt, C., and Buchhold, M. (2012). Accounting for initial condition uncertainties in COSMO-DE-EPS. *J. Geophys. Res.*, **117**, D07108.
- R Core Team, R (2013). *A Language and Environment for Statistical Computing*. R Foundation for Statistical Computing, Vienna, Austria.
- Raftery, A. E., Gneiting, T., Balabdaoui, F., and Polakowski, M. (2005). Using Bayesian model averaging to calibrate forecast ensembles. *Mon. Wea. Rev.*, **133**, 1155–1174.

- Roberts, N. M. and Lean, H. W. (2008). Scale-selective verification of rainfall accumulations from high-resolution forecasts of convective events. *Mon. Wea. Rev.*, **136**, 78–97.
- Roulston, M. S. and Smith, L. A. (2002). Evaluating probabilistic forecasts using information theory. *Mon. Wea. Rev.*, **130**, 1653–1660.
- Sang, H. and Gelfand, A. E. (2009). Hierarchical modeling for extreme values observed over space and time. *Environmental and Ecological Statistics*, **16**, 407–426.
- Schmeits, M. J. and Kok, K. J. (2010). A comparison between raw ensemble output, (modified) Bayesian model averaging, and extended logistic regression using ECMWF ensemble precipitation reforecasts. *Mon. Wea. Rev.*, **138**, 4199–4211.
- Shutts, G. (2005). A kinetic energy backscatter algorithm for use in ensemble prediction systems. *Quart. J. Roy. Meteor. Soc.*, **131**, 3079–3102.
- Stephan, K., Klink, S., and Schramm, C. (2008). Assimilation of radar-derived rain rates into the convective-scale model COSMO-DE at DWD. *Quart. J. Roy. Meteor. Soc.*, **134**, 1315–1326.
- Stephenson, D. B., Coelho, C. A. S., Doblas-Reyes, F. J., and Balmaseda, M. (2005). Forecast assimilation: a unified framework for the combination of multi-model weather and climate predictions. *Tellus A*, **57**, 253–264.
- Tang, Y., Lean, H. W., and Bornemann, J., (2012). The benefits of the Met Office variable resolution NWP model for forecasting convection. *Meteor. Appl.*, **20**, 417–426.
- Tennant, W. J., Shutts, G. J., Arribas, A., and Thompson, S. A. (2011). Using a stochastic kinetic energy backscatter scheme to improve MOGREPS probabilistic forecast skill. *Mon. Wea. Rev.*, **139**, 1190–1206.
- Theis, S. E., Hense, A., and Damrath, U. (2005). Probabilistic precipitation forecasts from a deterministic model: A pragmatic approach. *Meteor. Appl.*, **12**, 257–268.
- Tibshirani, R. J. (1996). Regression shrinkage and selection via the Lasso. *Journal of the Royal Statistical Society. Series B (Methodological)*, **58**, 267–288.
- Toth, Z., and Kalnay, E. (1993). Ensemble forecasting at NMC – the generation of perturbations. *Bull. Amer. Meteorol. Soc.*, **74**, 2317–2330.
- Van der Grijn, G., Paulsen, J. E., Lalurette, F., and Leutbecher, M. (2004). Early medium-range forecasts of tropical cyclones. *ECMWF newsletter*, **102**, 7–14.
- WMO (2005). THORPEX International Research Implementation Plan, World Meteorological Organization WMO/TD no 1258, WWRP/THORPEX no. 4.
- Wang, X. and Bishop, C. H. (2003). A comparison of breeding and Ensemble Transform Kalman Filter ensemble forecast schemes. *J. Atmos. Sci.*, **60**, 1140–1158.
- Wei, M., Toth, Z., Wobus, R., and Zhu, Y. (2008). Initial perturbations based on the ensemble transform (ET) technique in the NCEP global operational forecast system. *Tellus A*, **60**(1).
- Wilks, D. S. (2009). Extending logistic regression to provide full-probability-distribution MOS forecasts, *Meteor. Appl.*, **16**, 361–368.
- Wilks, D. S. (2011). *Statistical Methods in the Atmospheric Sciences*, 3rd edn. Elsevier.
- Yamaguchi, M., Nakazawa, T., and Hoshino, S. (2012). On the relative benefits of a multi-centre grand ensemble for tropical cyclone track prediction in the western North Pacific. *Q. J. Roy. Meteorol. Soc.*, **138**, 2019–2029.

# Storm tracks, blocking, and climate change: a review

Tim Woollings

## 8.1 Introduction

Storm tracks and their associated jet streams lie at the heart of weather and climate in the mid latitudes. Any changes in these systems under climate change will have considerable impact on society as well as on the general circulation of the atmosphere. This chapter provides a general introduction to the science of storm tracks and how they are expected to respond to anthropogenic forcing. Another recent review, particularly focused on cyclone characteristics, is provided by Ulbrich *et al.* (2009).

Much of the high-impact weather experienced in the mid latitudes is associated with storm tracks. The most direct impacts occur through the high winds and precipitation associated with intense cyclones. Single cyclones can cause considerable damage, but the most serious events comprise a series of cyclones over the same region. A recent example occurred in January/February 2014, when several successive storms followed the same path across the Atlantic and over the British Isles, causing widespread flooding and coastal damage. Conversely, when the storm track is persistently shifted away from one region the resulting loss of precipitation can ultimately lead to drought conditions.

Storm tracks ultimately owe their existence to the meridional contrast in solar heating, which necessitates a poleward transport of heat by the atmosphere and oceans. In the mid latitudes this is accomplished largely by transient baroclinic eddies with typical lifetimes of a few days. The eddies form preferentially over the oceans leading to well-defined ‘storm tracks’ of strong wind variability (Blackmon *et al.*, 1977). So-called ‘dry’ dynamics can account for much of the structure and behaviour of storm track eddies (Simmons and Hoskins, 1978), but moist processes can also play a role and the poleward moisture transport associated with the systems is a significant part of the total energy transport.

There are two general approaches used to diagnose storm tracks in gridded atmospheric data. Many methods

have been developed to identify and track cyclonic systems, using features such as the sea level pressure (minimum or Laplacian) or the vorticity maximum. This approach provides detailed information on characteristics such as the intensities and growth rates of cyclonic storms. The alternative approach is to filter the data to retain only fast timescales (periods typically shorter than 10 days) and then calculate the variance of the filtered data. This can be performed on winds, pressure-related fields, or fluxes, such as the meridional heat flux  $v'T'$ . The two approaches generally compare well and are thought of as describing complementary aspects of the flow (Hoskins and Hodges, 2002, Chang, 2009). The recent IMILAST project compared many different cyclone tracking methods and found that, while there is considerable spread between methods in the resulting cyclone climatologies, strong storms are generally identified by all methods (Neu *et al.*, 2013). Furthermore, the storm track response to forcing shows reasonable agreement between the methods (Ulbrich *et al.*, 2013).

The storm tracks are closely related to the mid-latitude jets. Jets can be conceptually separated into subtropical jets embedded in the Hadley cell circulation and eddy-driven jets which are distinct in extending down to the surface (Li and Wettstein, 2012). As the name suggests, the westerly momentum in the eddy-driven jets is derived from forcing by the transient (largely storm track) eddies. The jets themselves act to steer and shape the evolution of the eddies, resulting in a strongly coupled system of eddies and mean westerly flow (e.g. Lorenz and Hartmann, 2003, Vallis and Gerber, 2008). As a consequence of this strong two-way coupling the variability and response of this system to forcing can be complex, and clear chains of cause and effect are often hard to determine.

Blocking systems are persistent, quasi-stationary weather patterns which disrupt the jets and the usual eastward progression of cyclones. Several different paradigms exist for blocking; some see it simply as a persistent anticyclonic anomaly (Altenhoff *et al.*, 2008) while others

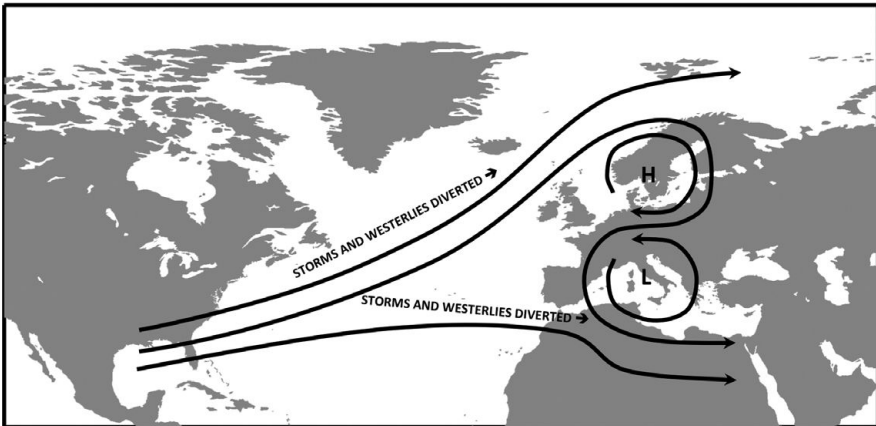


Fig. 8.1. Flow pattern for a typical European blocking dipole, with high pressure (H) to the north and low pressure (L) to the south. The westerlies and storm track are split around the block. The flow contours overturn in an anticyclonic wave breaking over Europe.

relate it to the breaking of Rossby waves which leads to a local reversal of the usual meridional height gradient, and associated easterly winds (Pelly and Hoskins, 2003; see also Fig. 8.1). There are also strong interactions between blocking and the other mid-latitude features, with blocks often deriving a positive feedback from a strong storm track located upstream (Shutts, 1983). Blocking patterns have considerable impact on surface weather due to their persistence, generally leading to heatwaves in summer and ‘coldwaves’ in winter (Buehler *et al.*, 2011, Pfahl and Wernli, 2012). Particular recent examples of blocking impact are the Russian heatwave of 2010 (Matsueda, 2011) and the cold European winter of 2010 (Cattiaux *et al.*, 2010).

The natural variability of this system largely reflects meridional shifts of the jet and storm track and changes in their intensity. This variability is often described in terms of patterns such as the North Atlantic Oscillation (NAO), and again reflects coupling between the mean westerlies, the storm tracks, and the occurrence of blocking (Thompson *et al.*, 2003, Woollings *et al.*, 2008). The variability from week to week can be large, and it is not clear how much of the variability on interannual and longer timescales is forced by any factors external to the atmosphere (Feldstein, 2000, Franzke and Woollings, 2011). Recent trends in the storm tracks/jets are weak and not clearly linked to anthropogenic forcing, with the noticeable exception of the Southern Hemisphere response to stratospheric ozone loss (Gillett and Thompson, 2003).

## 8.2 Climate models and a historical perspective

Because of the complexity of the problem, investigations of the storm track response to climate change are focused on the use of fully coupled ocean–atmosphere general circulation models (GCMs). These models have improved

considerably over the last couple of decades, though many still suffer from weaker versions of the bias that has plagued them in the past. Of particular relevance for the storm tracks is the tendency for models to be too ‘zonal’; i.e. to have mid-latitude westerly winds which are too strong and generally lie too far equatorward (Woollings, 2010, Barnes and Polvani, 2013). As shown by Zappa *et al.* (2014), this goes hand in hand with a tendency for too weak stationary waves (e.g. with little SW–NE tilt in the Atlantic storm track) and an underestimate of blocking, particularly over Europe (Scaife *et al.*, 2010). A (potentially related) persistent bias is for extratropical cyclones to be too weak in both weather (Froude, 2010) and climate models (Zappa *et al.*, 2013a).

The improvement in these features over time has largely arisen through gravity wave drag parameterization (e.g. Palmer *et al.*, 1986) and increases in model resolution (Shaffrey *et al.*, 2009, Matsueda *et al.*, 2009). Increased horizontal resolution has been shown to improve the representation of atmospheric dynamics, but also simply leads to higher orography and hence stronger stationary waves (Jung *et al.*, 2012, Berckmans *et al.*, 2013). There is potential for increased vertical resolution to give further improvements (Anstey *et al.*, 2013). Improvements to physical parameterizations have also been found to influence features such as blocking (Jung *et al.*, 2010).

Scaife *et al.* (2010) showed that the indices often used to identify blocking in models can be very sensitive to the mean state of the flow, and hence diagnostics of blocking bias often reflect a climatological bias rather than a problem with the synoptic variability. Hence model skill can be improved by the reduction of error in sea surface temperatures (SSTs) for example (Scaife *et al.*, 2011). Many models in CMIP3 (Barnes *et al.*, 2012) and CMIP5 (Masato *et al.*, 2013) still strongly underestimate European blocking (with some models having hardly any blocking at all), and it seems likely that SST errors contribute to this. While these biases could largely be reduced by improving

the ocean models, it seems unlikely that very accurate blocking frequencies can be achieved without a good representation of the orography, as achieved through high atmospheric resolution.

Prior to the Fourth Assessment Report of the IPCC, there was little agreement between models on how the storm tracks might respond to climate change, though the theoretical ideas were discussed in Held (1993). However, in the CMIP3 set of models some consistent signals appeared to emerge. Yin (2005) demonstrated a poleward shift of the storm tracks, as measured by eddy kinetic energy, which was particularly clear in the upper troposphere. Lambert and Fyfe (2006) also showed a consistent change in cyclone intensities across CMIP3, with an increase in strong cyclones despite an overall reduction in cyclone numbers. While it is tempting to place high confidence on these seemingly consistent signals, the following sections show that we should generally treat them with caution.

Finally in this section, we note that for both storm tracks (Chang *et al.*, 2012, Zappa *et al.*, 2013b) and blocking (Anstey *et al.*, 2013) there are at best weak correlations between the bias of a model and its response to climate change, at least in the Northern Hemisphere. While systematic biases are clearly a problem in climate models it is not clear what the quantitative effect of model bias is for projections.

### 8.3 Mechanisms causing storm track change

The leading mechanisms by which climate change is expected to influence the storm tracks are essentially global in character (Fig. 8.2), comprising changes in the thermal

structure of the atmosphere, which can be interpreted as changes in the potential energy available for storm growth (O’Gorman, 2010). In the zonal mean, the pattern of warming is dominated by regions of enhanced warming: (1) at upper tropospheric levels in the tropics due to latent heat release, and (2) at lower tropospheric levels over the poles (especially over the Arctic in winter) due to a combination of local feedbacks (Hwang *et al.*, 2011). At the same time the stratosphere cools due to changes in the local radiative balance, making an increase in the equator-to-pole temperature gradient at upper levels a particularly robust response. This upper level change was initially suggested by Yin (2005) to be the cause of the poleward shift of storm tracks.

However, the polar warming implies a decrease in the temperature gradient at lower levels, and the relative importance of these two competing effects is one of the central issues in predicting storm track change (Rind, 2008). When the polar warming is applied in isolation, models generally respond with an equatorward shift of the storm tracks (Bader *et al.*, 2011). The fact that a poleward shift of the storm tracks is seen, to some extent suggests that the upper level changes often dominate, although the more recent CMIP5 models appear to be more sensitive to Arctic warming than the earlier models (Cattiaux and Cassou, 2013). The results of Harvey *et al.*, (2013) suggest that, while model spread in the lower temperature gradient is a key source of uncertainty in the storm track response, the large increase in the upper gradient is common to all models and is hence the dominant factor shaping the ensemble mean response in many regions/seasons. In the experiments of Hernandez-Deckers and von Storch (2010), the upper and lower level forcings result in opposite changes in eddy kinetic energy at these levels. However, this is not seen in

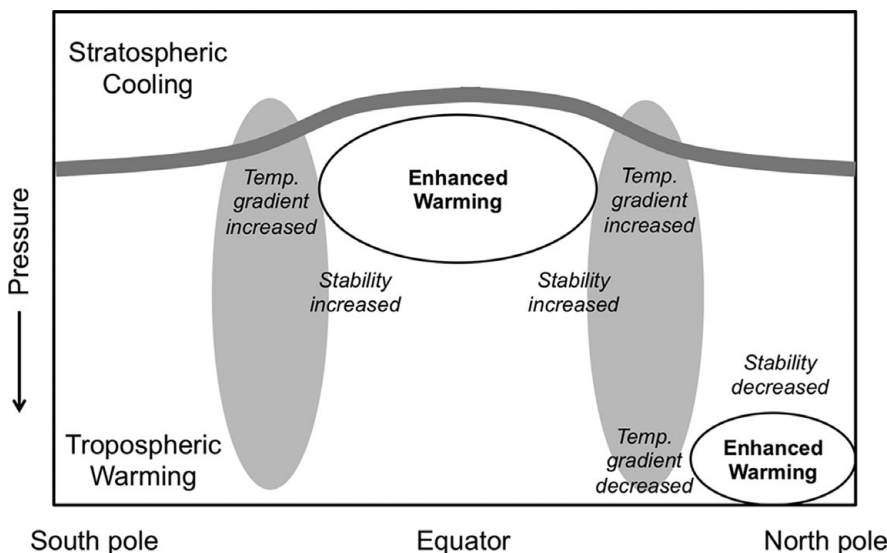


Fig. 8.2. Zonal mean schematic illustrating some global drivers of storm track change. The storm tracks are marked in grey shading with the tropopause as a thick dark line.

all models; often the upper and lower level storm track changes are similar (Mizuta *et al.*, 2011, Wu *et al.*, 2011).

Several idealized model studies have investigated the relative roles of tropical and polar heating (Son and Lee, 2005). These show considerable robustness in a poleward shift in response to tropical heating and an equatorward shift due to polar heating. In general, the response to equivalent heating is strongest when placed in the tropics (Lorenz and DeWeaver, 2007, Butler *et al.*, 2010), although baroclinic life-cycles are particularly sensitive to lower tropospheric shear (Hartmann, 2000). There is no clear agreement on whether the responses to individual forcings combine linearly or not (Butler *et al.*, 2010, Simpson *et al.*, 2010). While these zonally symmetric experiments are useful, the full three-dimensional temperature change may be needed to reconstruct the storm track response using such models (Lunkeit *et al.*, 1998).

While the focus has often been on the horizontal temperature gradients, the tropical and polar temperature anomalies also imply changes in the vertical gradients and hence in the static stability, and these have been suggested to play an important role (Lim and Simmonds, 2009, Kodama and Iwasaki, 2009). In particular, the increased stability in the subtropics is one possible mechanism by which the storm track is damped on its equatorward side (Lu *et al.*, 2008), although this may only be the dominant factor for regions on the very equatorward edge of the storm track (Harvey *et al.*, 2013).

These discussions implicitly assume that tropical and polar warming act as forcings on the storm tracks. In principle the reverse is also possible, in that the storm track may change the temperature structure by altering the heat transport. However, in practice it seems that the atmospheric heat transports can be well reproduced from the assumption that the tropical and polar temperatures are set by local feedbacks (Hwang and Frierson, 2010), so it seems reasonable to consider the temperatures as forcings on the storm track.

The effects of changing temperatures are often described, as has been done here, in terms of the changing baroclinicity of the atmosphere. This suggests an emphasis on the baroclinic growth of eddies in understanding the storm track response. It may indeed be the sources of baroclinic eddies which are key to the response (Butler *et al.*, 2011). However, it may also be other consequences of the temperature changes which are most important, such as refractive effects (Simpson *et al.*, 2009), wave breaking behaviour (Riviere, 2011), or altered eddy characteristics (Chen *et al.*, 2008, Kidston *et al.*, 2011).

The final global change of relevance to the storm tracks is the increase in moisture content in a warmer atmosphere. Somewhat counter-intuitively, this is generally expected to lead to a weakening of storm track activity. This arises

because latent heat transport increases, and so weaker eddies can achieve the same poleward heat transport (Branscome and Gutowski, 1992, Boer, 1996, Frierson *et al.*, 2007, Lucarini and Ragonne, 2011). While the eddies are growing in a moister environment, they also experience weaker baroclinicity and stronger dry stability than before (Schneider *et al.*, 2010). It seems likely that this effect is at least partly responsible for the small decrease in cyclone numbers generally predicted by models. This is also consistent with the finding that cyclone intensities don't increase even though the precipitation associated with cyclones does (Bengtsson *et al.*, 2009, Zappa *et al.*, 2013b). In idealized experiments, Booth *et al.* (2013) found the direct intensification of cyclones by moisture increase to be small for realistic moisture changes. In spite of this picture, there remains speculation that some types of storm, particularly those with a strong diabatically forced element, may intensify due to the increased moisture content (Fink *et al.*, 2009, 2012, Dacre and Gray, 2013, Ludwig *et al.*, 2014).

In addition, there are several regional factors which may have important influences on the storm tracks. The pattern of SST change is one such factor (Graff and LaCasce, 2012), with the structure of the tropical Pacific changes being particularly important (Delambre *et al.*, 2013). The land-sea contrast in warming will act to perturb surface temperature gradients in the storm track genesis regions, though it is not clear whether this is a very important effect (Long *et al.*, 2009, McDonald, 2011, Colle *et al.*, 2013). The Atlantic storm track may be influenced by the changing ocean circulation, in particular by the weakening of the Atlantic Meridional Overturning Circulation (AMOC). The AMOC transports warm water northward in the Atlantic, so its weakening leads to a clear region of reduced warming in the northern North Atlantic (Fig. 8.3). This strengthens the meridional SST gradient to the south, which increases the baroclinic instability from which cyclones grow. The result is a strengthening of the storm track (Woollings *et al.*, 2012a), which is in agreement with the results of idealized experiments.

Finally, stratospheric circulation has been shown to influence the storm track response, particularly in the Atlantic (Morgenstern *et al.*, 2010, Scaife *et al.*, 2012, Karpechko and Manzini, 2012). Since some CMIP5 models still have a poor representation of the stratosphere, this influence may be underestimated in current projections. A clear example of the stratospheric importance is the strong influence of ozone changes on the Southern Hemisphere circulation. The recovery of ozone over the coming century is expected to shift the jet and storm track equatorward there, although the projected poleward shift from greenhouse gas forcing appears to dominate (Son *et al.*, 2008, Arblaster *et al.*, 2011).

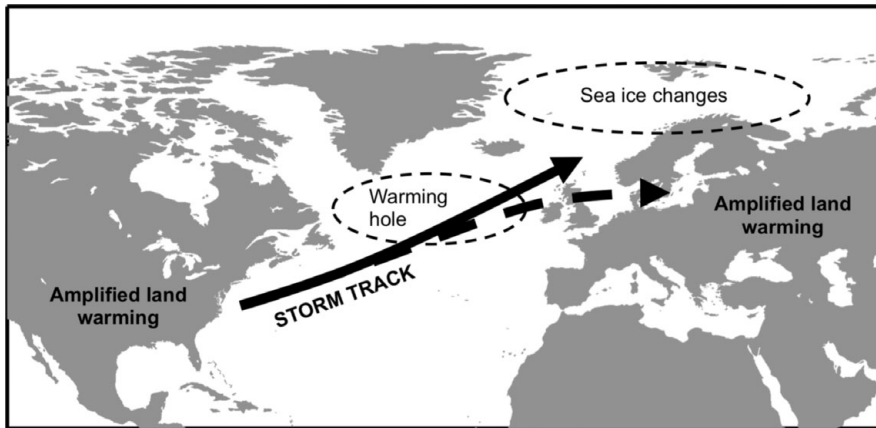


Fig. 8.3. Regional factors influencing the North Atlantic storm track, with a typical projected future storm track position dashed.

#### 8.4 Storm track projections

In this section we briefly summarize the storm track response projected by current climate models. An overall decrease in cyclone numbers remains a robust feature of projections, although the change is small (Zappa *et al.*, 2013b) and sometimes only clear in the Northern Hemisphere (Chang *et al.*, 2012). The increase in intense cyclones suggested by Lambert and Fyfe (2006) has proved to be sensitive to the method used to define the intensity (Ulbrich *et al.*, 2009). Using the absolute pressure minimum in particular can be misleading as large-scale background pressure changes are included. When other metrics such as wind speed are used, there is no consistent sign of an increase in severe storms (e.g. Bengtsson *et al.*, 2009, Catto *et al.*, 2011).

In a general sense, the response of the storm tracks and associated eddy-driven jets does resemble a poleward shift. This is especially true at upper levels and in the Southern Hemisphere. The Northern Hemisphere response is largely a weakening on the equatorward side of the storm track only (Chang *et al.*, 2012), so that the storm track *contracts* polewards rather than shifts. The response can still be quite sensitive to the variable used, with sea level pressure variance for example showing few obvious regions of poleward shift (Harvey *et al.*, 2012). An upwards shift of storm track activity is quite robust (Yin, 2005, Lorenz and DeWeaver, 2007, Chang *et al.*, 2012). Projected changes are weaker and less consistent between models in summer, compared to winter (Lang and Waugh, 2011).

Regionally, the response can differ strongly from the picture of a poleward shift (Chang *et al.*, 2012). A clear example is the North Atlantic in winter. Here there is little model agreement on a shift of the jet (Woollings and Blackburn, 2012, Barnes and Polvani, 2013), and the response is instead best characterized as a strengthening and extension of the jet and storm track into western Europe (Delcambre *et al.*, 2013, Haarsma *et al.*, 2013a),

with tripolar cyclone track anomalies (Zappa *et al.*, 2013b). This difference could arise from the AMOC forcing which is particular to this region (Woollings *et al.*, 2012a). The Mediterranean storm track shows a robust weakening, likely due to the increased static stability there (Raible *et al.*, 2010).

#### 8.5 Blocking changes

Our understanding of how blocking may change in the future is driven by climate models, despite the long-standing problems with European blocking in particular. There are no theoretical arguments for how blocking may change, in contrast to the storm tracks. As in CMIP3 (Barnes *et al.*, 2012), CMIP5 models predict a general reduction in blocking occurrence in the future (Masato *et al.*, 2013, Anstey *et al.*, 2013, Dunn-Sigouin and Son, 2013). Experimental high resolution models predict a similar decline (Matsueda *et al.*, 2009). This decrease is well explained by the change in the mean state and variance of the westerly winds in the blocking regions (de Vries *et al.*, 2013), such as the extension of the jet into Europe. This suggests that the blocking itself is not ‘actively’ changing in the future, rather that it is responding passively to the mean flow changes. However, Masato *et al.* (2014) show that even though changes in blocking occurrence can be modest, the impacts of blocking can change more strongly, in particular due to the changing land–sea temperature contrast which affects the temperature anomalies that can be achieved through thermal advection.

There has been much interest in recent suggestions that blocking occurrence has already been influenced by sea ice loss and associated rapid warming of the Arctic (Petoukhov and Semenov, 2010, Liu *et al.*, 2012, Francis and Vavrus, 2012). However, the observed correlations are only seen in a short recent period, and the suggested

changes are very sensitive to the methods used (Screen and Simmonds, 2013, Barnes, 2013). Yang and Christensen (2012) suggested a strong link between cold European winters and Arctic warming emerging in the CMIP5 models. However, this signal is not retained after the data is detrended (Woollings *et al.*, 2014), raising doubts over whether the two are physically linked.

## 8.6 Outlook

Climate models have improved to the point where several, in particular high-resolution, models provide generally good simulations of the storm track, jet, and blocking system. Some aspects of the response are quite robust between models, which adds confidence to the projections. In particular, there is considerable agreement on an overall decrease in cyclone numbers, and a poleward shift of storm tracks in the southern hemisphere.

The projected storm track changes are a relatively small perturbation relative to the climatology, but relative to the natural variability they are in many cases large enough to be noticed by society (Pinto *et al.*, 2007, Woollings *et al.*, 2012a, Harvey *et al.*, 2012). While storm track changes are relatively small on the global scale, regional changes can be much more significant. It must also be remembered that the storm track response is a balance between several competing factors. If any of these factors is systematically misrepresented in current models then the storm track response could be significantly larger. For example, the storm track response is sensitive to both the stratospheric and oceanic circulation. Both of these, but especially the ocean, are poorly represented in models.

It also remains possible that there are some missing factors which may emerge as being important for storm track change. A prime candidate is small-scale circulation features, and Haarsma *et al.* (2013b) recently showed an example of this in the form of increased tropical to extratropical cyclone transitions in a high resolution climate model. Little can currently be said on how mesoscale convective systems may change in the future, although the large-scale changes in stability can provide a guide for this (Zahn and von Storch, 2010, Woollings *et al.*, 2012b).

Finally, it is unclear whether blocking systems have the potential to change in any way other than passively in response to mean state changes. Blocking is not subject to clear energetic arguments in the way that storm tracks are, although changes in the level of wave activity in the atmosphere may provide a guide to its behaviour. Croci-Maspoli and Davies (2009) suggested that diabatic processes can be important for blocking. This previously overlooked aspect opens up another pathway by which

climate change may influence blocking. Any change in summer blocking would have a particularly strong influence due to its link to heat waves (Matsueda, 2011), yet the summertime events have been much less studied than their winter counterparts. This suggests summer blocking as a particular focus in future work.

## References

- Altenhoff, A. M., Martius, O., Croci-Maspoli, M., Schwierz, C., and Davies, H. C. (2008). Linkage of atmospheric blocks and synoptic-scale Rossby waves: a climatological analysis. *Tellus A*, **60**(5), 1053–1063.
- Anstey, J. A., P. Davini, L. J. Gray, *et al.* (2013). Multi-model analysis of Northern Hemisphere winter blocking: Model biases and the role of resolution. *J. Geophys. Res. Atmos.*, **118**, 3956–3971.
- Arblaster, J. M., G. A. Meehl, and D. J. Karoly (2011). Future climate change in the Southern Hemisphere: Competing effects of ozone and greenhouse gases. *Geophys. Res. Lett.*, **38**, L02701,
- Bader, J., Mesquita, M. D., Hodges, K. I., *et al.* (2011). A review on Northern Hemisphere sea-ice, storminess and the North Atlantic Oscillation: Observations and projected changes. *Atmospheric Research*, **101**(4), 809–834.
- Barnes, E. A. (2013). Revisiting the evidence linking Arctic amplification to extreme weather in midlatitudes, *Geophys. Res. Lett.*, **40**, 4728–4733.
- Barnes, E. A., Slingo, J., and Woollings, T. (2012). A methodology for the comparison of blocking climatologies across indices, models and climate scenarios. *Climate Dynamics*, **38**(11–12), 2467–2481.
- Barnes, E. A. and Polvani, L. M. (2013). Response of the mid-latitude jets and of their variability to increased greenhouse gases in the CMIP5 models. *Journal of Climate*, **26**, doi:10.1175/JCLI-D-12-00536.1.
- Bengtsson, L., K. I. Hodges, and N. Keenlyside (2009). Will extratropical storms intensify in a warmer climate? *Journal of Climate*, **22**, 2276–2301.
- Berckmans, J., Woollings, T., Demory, M. E., Vidale, P. L., and Roberts, M. (2013). Atmospheric blocking in a high resolution climate model: influences of mean state, orography and eddy forcing. *Atmospheric Science Letters*, **14**, 34–40.
- Blackmon, M. L., Wallace, J. M., Lau, N. C., and Mullen, S. L. (1977). An observational study of the Northern Hemisphere wintertime circulation. *Journal of the Atmospheric Sciences*, **34**, 1040–1053.
- Boer, G. J., (1996). Some dynamical consequences of greenhouse gas warming. *Atmosphere-Ocean*, **33**, 731–751.
- Booth, J. F., Wang, S., and Polvani, L. (2013). Midlatitude storms in a moister world: lessons from idealized baroclinic life cycle experiments. *Climate Dynamics*, **41**, 787–802.
- Branscome, L. E. and Gutowski Jr, W. J. (1992). The impact of doubled CO<sub>2</sub> on the energetics and hydrologic processes of mid-latitude transient eddies. *Climate Dynamics*, **8**, 29–37.

- Buehler, T., Raible, C. C., and Stocker, T. F. (2011). The relationship of winter season North Atlantic blocking frequencies to extreme cold or dry spells in the ERA-40. *Tellus A*, **63**, 212–222.
- Butler, A. H., Thompson, D. W., and Heikes, R. (2010). The steady-state atmospheric circulation response to climate change-like thermal forcings in a simple general circulation model. *Journal of Climate*, **23**, 3474–3496.
- Butler, A. H., Thompson, D. W., and Birner, T. (2011). Isentropic slopes, downgradient eddy fluxes, and the extratropical atmospheric circulation response to tropical tropospheric heating. *Journal of the Atmospheric Sciences*, **68**, 2292–2305.
- Cattiaux, J., R. Vautard, C. Cassou, et al. (2010), Winter 2010 in Europe: A cold extreme in a warming climate, *Geophys. Res. Lett.*, **37**, L20704, doi:10.1029/2010GL044613.
- Cattiaux, J. and C. Cassou (2013). Opposite CMIP3/CMIP5 trends in the wintertime Northern Annular Mode explained by combined local sea ice and remote tropical influences, *Geophys. Res. Lett.*, **40**, 3682–3687, doi:10.1002/grl.50643.
- Catto, J. L., L. C. Shaffrey, and K. I. Hodges (2011). Northern Hemisphere extratropical cyclones in a warming climate in the HiGEM high-resolution climate model. *J. Climate*, **24**, 5336–5352.
- Chang, E. K. (2009). Are band-pass variance statistics useful measures of storm track activity? Re-examining storm track variability associated with the NAO using multiple storm track measures. *Climate dynamics*, **33**, 277–296.
- Chang, E. K., Guo, Y., and Xia, X. (2012). CMIP5 multimodel ensemble projection of storm track change under global warming. *Journal of Geophysical Research: Atmospheres*, **117**(D23).
- Chen, G., J. Lu, and D. M. W. Frierson (2008). Phase speed spectra and the latitude of surface westerlies: interannual variability and global warming trend. *Journal of Climate*, **21**, 5942–5959.
- Colle, B. A., Z. Zhang, K. A. Lombardo, et al. (2013). Historical evaluation and future prediction of eastern North American and western Atlantic extratropical cyclones in the CMIP5 models during the cool season. *J. Climate*, **26**, 6882–6903.
- Croci-Maspoli, M. and Davies, H. C. (2009). Key dynamical features of the 2005/06 European winter. *Monthly Weather Review*, **137**, 664–678.
- Dacre, H. F. and S. L. Gray (2013). Quantifying the climatological relationship between extratropical cyclone intensity and atmospheric precursors, *Geophys. Res. Lett.*, **40**, 2322–2327.
- Delcambre, S. C., D. J. Lorenz, D. J. Vimont, and J. E. Martin (2013). Diagnosing Northern Hemisphere jet portrayal in 17 CMIP3 global climate models: twenty-first-century projections. *J. Climate*, **26**, 4930–4946.
- de Vries, H., Woollings, T., Anstey, J., Haarsma, R. J., and Hazeleger, W. (2013). Atmospheric blocking and its relation to jet changes in a future climate. *Climate Dynamics*, **41**, 2643–2654.
- Dunn-Sigouin, E. and S.-W. Son (2013). Northern Hemisphere blocking frequency and duration in the CMIP5 models, *J. Geophys. Res. Atmos.*, **118**, 1179–1188.
- Feldstein, S. B. (2000). The timescale, power spectra, and climate noise properties of teleconnection patterns. *Journal of Climate*, **13**, 4430–4440.
- Fink, A. H., T. Bruecher, V. Ermert, A. Krueger, and J. G. Pinto (2009). The European storm Kyrill in January 2007: synoptic evolution, meteorological impacts and some considerations with respect to climate change. *Natural Hazards and Earth System Sciences*, **9**, 405–423.
- Fink, A., S. Pohle, J. Pinto, and P. Knippertz (2012). Diagnosing the influence of diabatic processes on the explosive deepening of extratropical cyclones. *Geophysical Research Letters*, **39**.
- Francis, J. A. and Vavrus, S. J. (2012). Evidence linking arctic amplification to extreme weather in mid-latitudes, *Geophys. Res. Lett.*, **39**, L06801.
- Franzke, C. and Woollings, T. (2011). On the persistence and predictability properties of North Atlantic climate variability. *Journal of Climate*, **24**, 466–472.
- Frierson, D. M. W., I. M. Held, and P. Zurita-Gotor (2007). A gray-radiation aquaplanet moist GCM. Part II: energy transports in altered climates. *J. Atmos. Sci.*, **64**, 1680–1693.
- Froude, L. S. (2010). TIGGE: Comparison of the prediction of Northern Hemisphere extratropical cyclones by different ensemble prediction systems. *Weather and Forecasting*, **25**, 819–836.
- Gillett, N. P. and Thompson, D. W. (2003). Simulation of recent Southern Hemisphere climate change. *Science*, **302**, 273–275.
- Held, I. M. (1993). Large-scale dynamics and global warming. *Bulletin of the American Meteorological Society*, **74**, 228–241.
- Graff, L. and J. LaCasce (2012). Changes in the extratropical storm tracks in response to changes in SST in an AGCM. *Journal of Climate*, **25**, 1854–1870.
- Haarsma, R. J., Selten, F., and van Oldenborgh, G. J. (2013a). Anthropogenic changes of the thermal and zonal flow structure over Western Europe and Eastern North Atlantic in CMIP3 and CMIP5 models. *Climate Dynamics*, **41**, 2577–2588.
- Haarsma, R. J., W. Hazeleger, C. Severijns, et al. (2013b). More hurricanes to hit western Europe due to global warming, *Geophys. Res. Lett.*, **40**, 1783–1788.
- Hartmann, D. L. (2000). The key role of lower-level meridional shear in baroclinic wave life cycles. *Journal of the Atmospheric Sciences*, **57**, 389–401.
- Harvey, B. J., L. C. Shaffrey, T. J. Woollings, G. Zappa, and K. I. Hodges (2012). How large are projected 21st century storm track changes? *Geophys. Res. Lett.*, **39**, L18707.
- Harvey, B., Shaffrey, L., and Woollings, T. (2013). Equator-to-pole temperature differences and the extra-tropical storm track responses of the cmip5 climate models. *Climate Dynam.* doi: 10.1007/s00382-013-1883-9.
- Hernández-Deckers, D. and von Storch, J. S. (2010). Energetics responses to increases in greenhouse gas concentration. *Journal of Climate*, **23**, 3874–3887.
- Hoskins, B. J. and Hodges, K. I. (2002). New perspectives on the Northern Hemisphere winter storm tracks. *Journal of the Atmospheric Sciences*, **59**, 1041–1061.

- Hwang, Y.-T. and Frierson, D. M. W. (2010). Increasing atmospheric poleward energy transport with global warming. *Geophysical Research Letters*, **37**, L24807.
- Hwang, Y. T., Frierson, D. M., and Kay, J. E. (2011). Coupling between Arctic feedbacks and changes in poleward energy transport. *Geophysical Research Letters*, **38**, L17704.
- Jung, T., Balsamo, G., Bechtold, P., et al. (2010). The ECMWF model climate: Recent progress through improved physical parametrizations, *Q. J. Roy. Meteorol. Soc.*, **136**, 1145–1160.
- Jung, T. and Coauthors (2012). High-resolution global climate simulations with the ECMWF model in Project Athena: experimental design, model climate, and seasonal forecast skill. *J. Climate*, **25**, 3155–3172.
- Karpeckho, A. Y. and E. Manzini (2012). Stratospheric influence on tropospheric climate change in the Northern Hemisphere, *J. Geophys. Res.*, **117**, D05133.
- Kidston, J., G. K. Vallis, S. M. Dean, and J. A. Renwick (2011). Can the increase in the eddy length scale under global warming cause the poleward shift of the jet streams? *Journal of Climate*, **24**, 3764–3780.
- Kodama, C., and Iwasaki, T. (2009). Influence of the SST Rise on Baroclinic Instability Wave Activity under an Aquaplanet Condition. *Journal of the Atmospheric Sciences*, **66**, 2272–2287.
- Lambert, S. J. and Fyfe, J. C. (2006). Changes in winter cyclone frequencies and strengths simulated in enhanced greenhouse warming experiments: results from the models participating in the IPCC diagnostic exercise. *Climate Dynam.*, **26**, 713–728.
- Lang, C. and D. W. Waugh (2011). Impact of climate change on the frequency of Northern Hemisphere summer cyclones, *J. Geophys. Res.*, **116**, D04103.
- Li, C. and Wettstein, J. J. (2012). Thermally driven and eddy-driven jet variability in reanalysis. *Journal of Climate*, **25**, 1587–1596.
- Lim, E. P. and Simmonds, I. (2009). Effect of tropospheric temperature change on the zonal mean circulation and SH winter extratropical cyclones. *Climate Dynamics*, **33**, 19–32.
- Liu, J., Curry, J. A., Wang, H., Song, M., and Horton, R. M. (2012). Impact of declining arctic sea ice on winter snowfall. *P. Natl. Acad. Sci. USA*, **109**, 4074–4079.
- Long, Z., W. Perrie, J. Gyakum, R. Laprise, and D. Caya (2009). Scenario changes in the climatology of winter midlatitude cyclone activity over eastern North America and the Northwest Atlantic. *Journal of Geophysical Research-Atmospheres*, **114**.
- Lorenz, D. J. and Hartmann, D. L. (2003). Eddy-zonal flow feedback in the Northern Hemisphere winter. *Journal of Climate*, **16**, 1212–1227.
- Lorenz, D. J. and DeWeaver, E. T. (2007). Tropopause height and zonal wind response to global warming in the IPCC scenario integrations. *Journal of Geophysical Research: Atmospheres*, **112**, D10.
- Lu, J., G. Chen, and D. M. W. Frierson (2008). Response of the zonal mean atmospheric circulation to El Nino versus global warming. *Journal of Climate*, **21**, 5835–5851.
- Lucarini, V. and F. Ragone (2011). Energetics of climate models: net energy balance and meridional enthalpy transport. *Reviews of Geophysics*, **49**.
- Ludwig, P., Pinto, J. G., Reyers, M., and Gray, S. L. (2014). The role of anomalous SST and surface fluxes over the southeastern North Atlantic in the explosive development of windstorm Xynthia. *Q.J.R. Meteorol. Soc.*, **140**, 1729–1741.
- Lunkeit, F., Fraedrich, K., and Bauer, S. E. (1998). Storm tracks in a warmer climate: sensitivity studies with a simplified global circulation model. *Climate Dynamics*, **14**, 813–826.
- Masato, G., B. J. Hoskins, and T. Woollings (2013). Winter and summer Northern Hemisphere blocking in CMIP5 models. *J. Climate*, **26**, 7044–7059.
- Masato, G., Woollings, T., and Hoskins, B. J. (2014). Structure and impact of atmospheric blocking over the Euro-Atlantic region in present day and future simulations. *Geophys. Res. Lett.*, **41**, 1051–1058.
- Matsueda, M. (2011). Predictability of Euro-Russian blocking in summer of 2010, *Geophys. Res. Lett.*, **38**, L06801.
- Matsueda, M., Mizuta, R., and Kusunoki, S. (2009). Future change in wintertime atmospheric blocking simulated using a 20-km-mesh atmospheric global circulation model. *Journal of Geophysical Research: Atmospheres*, **114**, D12.
- McDonald, R. E. (2011). Understanding the impact of climate change on Northern Hemisphere extra-tropical cyclones. *Climate Dynamics*, **37**, 1399–1425.
- Mizuta, R., Matsueda, M., Endo, H., and Yukimoto, S. (2011). Future change in extratropical cyclones associated with change in the upper troposphere. *Journal of Climate*, **24**, 6456–6470.
- Morgenstern, O. and Coauthors (2010). Anthropogenic forcing of the Northern Annular Mode in CCMVal-2 models. *Journal of Geophysical Research-Atmospheres*, **115**.
- Neu U. et al. (2013). IMILAST – a community effort to inter-compare extratropical cyclone detection and tracking algorithms. *Bull. Amer. Meteor. Soc.*, **94**, 529–547.
- O’Gorman, P. A. (2010). Understanding the varied response of the extratropical storm tracks to climate change. *Proceedings of the National Academy of Sciences*, **107**, 19176–19180.
- Palmer, T. N., Shutts, G. J., and Swinbank, R. (1986). Alleviation of a systematic westerly bias in general circulation and numerical weather prediction models through an orographic gravity wave drag parametrization. *Quarterly Journal of the Royal Meteorological Society*, **112**(474), 1001–1039.
- Pelly, J. L. and Hoskins, B. J. (2003). A new perspective on blocking. *Journal of the Atmospheric Sciences*, **60**, 743–755.
- Petoukhov, V. and Semenov, V. A. (2010). A link between reduced Barents-Kara sea ice and cold winter extremes over northern continents. *J. Geophys. Res.*, **115**, D21.
- Pfahl, S. and Wernli, H. (2012). Quantifying the relevance of atmospheric blocking for co-located temperature extremes in the Northern Hemisphere on (sub-) daily time scales. *Geophysical Research Letters*, **39**.
- Pinto, J. G., U. Ulbrich, G. C. Leckebusch, et al. (2007). Changes in storm track and cyclone activity in three SRES ensemble experiments with the ECHAM5/MPI-OM1 GCM. *Climate Dynamics*, **29**, 195–210.
- Raible, C. C., B. Ziv, H. Saaroni, and M. Wild (2010). Winter synoptic-scale variability over the Mediterranean Basin under future climate conditions as simulated by the ECHAM5. *Climate Dynamics*, **35**, 473–488.

- Rind, D. (2008). The consequences of not knowing low- and high-latitude climate sensitivity. *Bulletin of the American Meteorological Society*, **89**, 855–864.
- Riviere, G. (2011). A dynamical interpretation of the poleward shift of the jet streams in global warming scenarios. *Journal of the Atmospheric Sciences*, **68**, 1253–1272.
- Scaife, A. A., Woollings, T., Knight, J., Martin, G., and Hinton, T. (2010). Atmospheric blocking and mean biases in climate models. *Journal of Climate*, **23**, 6143–6152.
- Scaife, A. A., Copsey, D., Gordon, C., et al. (2011). Improved Atlantic winter blocking in a climate model. *Geophysical Research Letters*, **38**(23).
- Scaife, A. A., Spanghell, T., Fereday, D. R., et al. (2012). Climate change projections and stratosphere–troposphere interaction. *Climate Dynamics*, **38**, 2089–2097.
- Schneider, T., P. A. O’Gorman, and X. J. Levine (2010). Water vapor and the dynamics of climate changes. *Reviews of Geophysics*, **48**.
- Screen, J. A., and I. Simmonds (2013). Exploring links between Arctic amplification and mid-latitude weather, *Geophys. Res. Lett.*, **40**, 959–964.
- Shaffrey, L. C., Stevens, I., Norton, W. A., et al. (2009). UK HiGEM: The new UK high-resolution global environment model-model description and basic evaluation. *Journal of Climate*, **22**, 1861–1896.
- Shutts, G. J. (1983). The propagation of eddies in diffluent jet-streams: Eddy vorticity forcing of ‘blocking’ flow fields. *Quarterly Journal of the Royal Meteorological Society*, **109**, 737–761.
- Simmons, A. J. and Hoskins, B. J. (1978). The life cycles of some nonlinear baroclinic waves. *Journal of the Atmospheric Sciences*, **35**, 414–432.
- Simpson, I. R., Blackburn, M., and Haigh, J. D. (2009). The role of eddies in driving the tropospheric response to stratospheric heating perturbations. *Journal of the Atmospheric Sciences*, **66**, 1347–1365.
- Simpson, I. R., Blackburn, M., Haigh, J. D., and Sparrow, S. N. (2010). The impact of the state of the troposphere on the response to stratospheric heating in a simplified GCM. *Journal of Climate*, **23**, 6166–6185.
- Son, S. W. and Lee, S. (2005). The response of westerly jets to thermal driving in a primitive equation model. *Journal of the Atmospheric Sciences*, **62**(10), 3741–3757.
- Son, S. W., Polvani, L. M., Waugh, D. W., et al. (2008). The impact of stratospheric ozone recovery on the Southern Hemisphere westerly jet. *Science*, **320**, 1486–1489.
- Thompson, D. W., Lee, S., and Baldwin, M. P. (2003). Atmospheric processes governing the northern hemisphere annular mode/North Atlantic oscillation. *Geophysical Monograph–American Geophysical Union*, **134**, 81–112.
- Ulbrich, U., Leckebusch, G. C., and Pinto, J. G. (2009). Extratropical cyclones in the present and future climate: a review. *Theoretical and Applied Climatology*, **96**, 117–131.
- Ulbrich, U. et al. (2013). Are greenhouse gas signals of Northern Hemisphere winter extra-tropical cyclone activity dependent on the identification and tracking methodology? *Meteorol Z.* **22**, 61–68 doi:10.1127/0941–2948/2013/0420.
- Vallis, G. K. and Gerber, E. P. (2008). Local and hemispheric dynamics of the North Atlantic Oscillation, annular patterns and the zonal index. *Dynamics of Atmospheres and Oceans*, **44**, 184–212.
- Woollings, T. (2010). Dynamical influences on European climate: an uncertain future. *Philosophical Transactions of the Royal Society A*, **368**, 3733–3756.
- Woollings, T. and Blackburn, M. (2012). The North Atlantic jet stream under climate change and its relation to the NAO and EA patterns. *Journal of Climate*, **25**, 886–902.
- Woollings, T., Hoskins, B., Blackburn, M., and Berrisford, P. (2008). A new Rossby wave-breaking interpretation of the North Atlantic Oscillation. *Journal of the Atmospheric Sciences*, **65**, 609–626.
- Woollings, T., J. Gregory, J. Pinto, M. Reyers, and D. Brayshaw (2012a). Response of the North Atlantic storm track to climate change shaped by ocean-atmosphere coupling. *Nature Geoscience*, **5**, 313–317.
- Woollings, T., B. Harvey, M. Zahn, and L. Shaffrey (2012b). On the role of the ocean in projected atmospheric stability changes in the Atlantic polar low region, *Geophys. Res. Lett.*, **39**, L24802.
- Woollings, T., B. Harvey, and G. Masato (2014). Arctic warming, atmospheric blocking and cold European winters in CMIP5 models. *Env. Res. Lett.*, **9**, 014002.
- Wu, Y., Ting, M., Seager, R., Huang, H. P., and Cane, M. A. (2011). Changes in storm tracks and energy transports in a warmer climate simulated by the GFDL CM2. 1 model. *Climate Dynamics*, **37**, 53–72.
- Yang, S. and Christensen, J. H. (2012). Arctic sea ice reduction and European cold winters in cmip5 climate change experiments. *Geophys. Res. Lett.* **39**(20).
- Yin, J. H. (2005). A consistent poleward shift of the storm tracks in simulations of 21st century climate. *Geophys. Res. Lett.*, **32**, L18701. doi:10.1029/2005GL023684.
- Zahn, M. and von Storch, H. (2010). Decreased frequency of North Atlantic polar lows associated with future climate warming. *Nature*, **467**, 309–312.
- Zappa, G., Shaffrey, L. C., and Hodges, K. I. (2013a). The ability of CMIP5 models to simulate North Atlantic extratropical cyclones. *Journal of Climate*, **26**, 5379–5396.
- Zappa, G., Shaffrey, L. C., Hodges, K. I., Sansom, P. G., and Stephenson, D. B. (2013b). A multi-model assessment of future projections of North Atlantic and European extratropical cyclones in the CMIP5 climate models. *Journal of Climate*, **26**, 5846–5862.
- Zappa, G., Masato, G., Shaffrey, L., Woollings, T., and Hodges, K. (2014). Linking Northern Hemisphere blocking and storm track biases in the CMIP5 climate models. *Geophysical Research Letters*. **41**, 135–139.

# The North Atlantic and Arctic Oscillations: climate variability, extremes, and stratosphere–troposphere interaction

*Adam A. Scaife*

## 9.1 What is the North Atlantic Oscillation and how is it related to the Arctic Oscillation?

The North Atlantic Oscillation (NAO; Walker and Bliss, 1932, Hurrell *et al.*, 2003) and its hemispheric equivalent the Arctic Oscillation (AO; Thompson and Wallace, 1998) are single circulation patterns that explain the largest fractions of climate variability over the Atlantic and the Northern Hemisphere respectively. They occur throughout the year, albeit with shifting centres of action (Barnston and Livezey, 1987), but here we will focus mainly on the winter season. The NAO and AO are often defined by the first empirical orthogonal function of sea level pressure, or 500 hPa geopotential height, or simply as the sea level pressure difference between Iceland and the Azores or between high and low latitudes (Jones *et al.*, 1997, Li and Wang, 2003). Whichever index is used, the NAO and AO are highly correlated from year to year ( $r > 0.7$ ) and their extreme phases often coincide (Thompson and Wallace, 1998). The AO and NAO involve the same process of transient eddy fluxes strengthening the large-scale circulation (Vallis and Gerber, 2008) and extreme phases coincide with changes in the frequency and intensity of atmospheric blocking (Shabbar *et al.*, 2001, Scaife *et al.*, 2008) and large-scale wave breaking (Franzke *et al.*, 2004). The large concentration of transient baroclinic wave activity over the ocean basins allows the strongest variability to occur over the North Atlantic, where it is separately identified as the NAO (Hurrell *et al.*, 2003).

Through its effect on the large-scale winds, changes in the winter NAO (and AO) produce a change in advection and hence temperature over land. As the NAO becomes negative/positive, anomalous advection results in colder/milder winter conditions in Europe and the eastern USA (Figure 9.1), with opposite anomalies in the Mediterranean and eastern Canada. The NAO pressure gradient is also related to the strength and position of the Atlantic storm track and associated jet stream, both of which weaken/strengthen and move equatorward/poleward as the NAO

decreases/increases. Cyclonic weather systems are preferentially directed towards southern or northern Europe in association with the NAO phase (Hurrell *et al.*, 2003, Riviere and Orlanski, 2007).

## 9.2 The NAO as a governor of extreme weather

Given that fluctuations in the NAO correspond to changes in the large-scale structure of the atmospheric circulation and cyclonic weather systems over the Atlantic, it is not surprising that the risk of extreme weather events is also governed by the NAO. Winter mean temperature signals associated with anomalous advection are large enough to create large shifts in the regional frequency of very cold winter days, the frequency of floods, and the number of winter storms around the Atlantic basin (Scaife *et al.*, 2008, Renggli *et al.*, 2011). All of these change systematically with the NAO index over time scales ranging from months to decades. In some cases, the effects of the NAO can outweigh many years of climate change. An example is shown in Fig. 9.2, where a large multi-decadal decrease in the frequency of winter frosts is reproduced in a climate model simulation, but this reduction in frost days occurs only if the NAO increases, irrespective of ocean surface conditions and increasing greenhouse gases (Scaife *et al.*, 2008).

Reliable historical records of the NAO are available back to the nineteenth century and perhaps longer (Jones *et al.*, 1997), but recent years have seen unprecedented extremes in the NAO (Hanna *et al.*, 2014). The winter of 2009/10, for example, showed the lowest average NAO value for over a century (Fereday *et al.*, 2012). Although it was not the coldest winter, even in regions strongly affected by the NAO, due to the accumulated effects of general climate warming (Ouzeau *et al.*, 2011), there were severe impacts on European and US transport networks and an increased incidence of weather related deaths (Ilkka *et al.*, 2012). In this case, the Arctic Oscillation was also

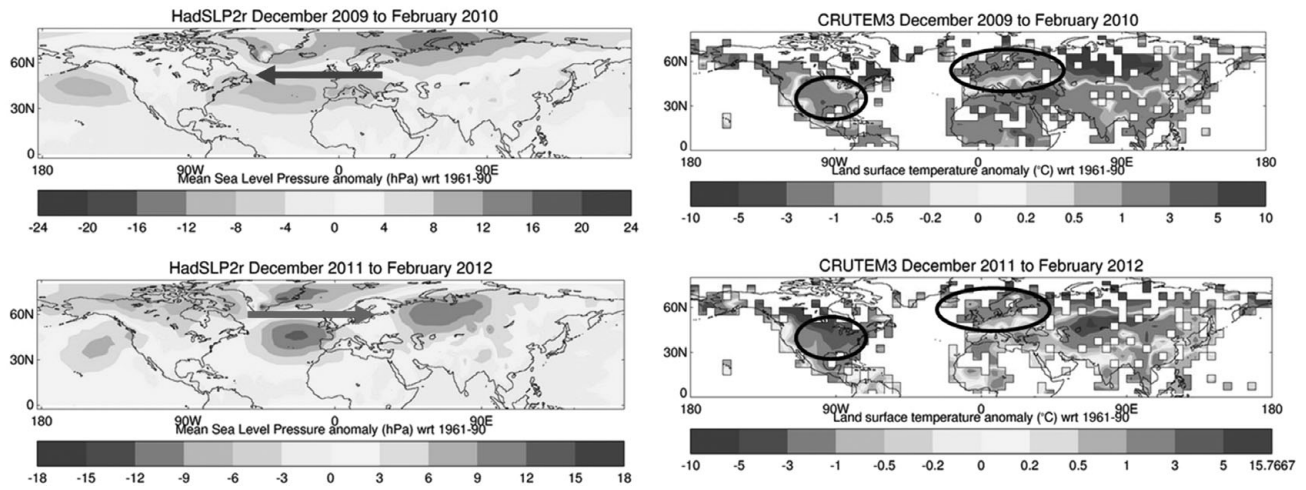


Fig. 9.1. Recent extreme phases of the winter North Atlantic and Arctic Oscillations. Winter mean sea level pressure anomalies (left) and winter mean land surface temperature anomalies (right) for the extreme negative NAO winter of 2009/10 (upper) and extreme positive NAO winter of 2011/12 (lower). Blue and red arrows show the sense of anomalous advection across the Atlantic due to anomalous mean winds. Data are from Hadley Centre observational analyses ([www.hadobs.org](http://www.hadobs.org)). A black and white version of this figure will appear in some formats. For the colour version, please refer to Plate 14.

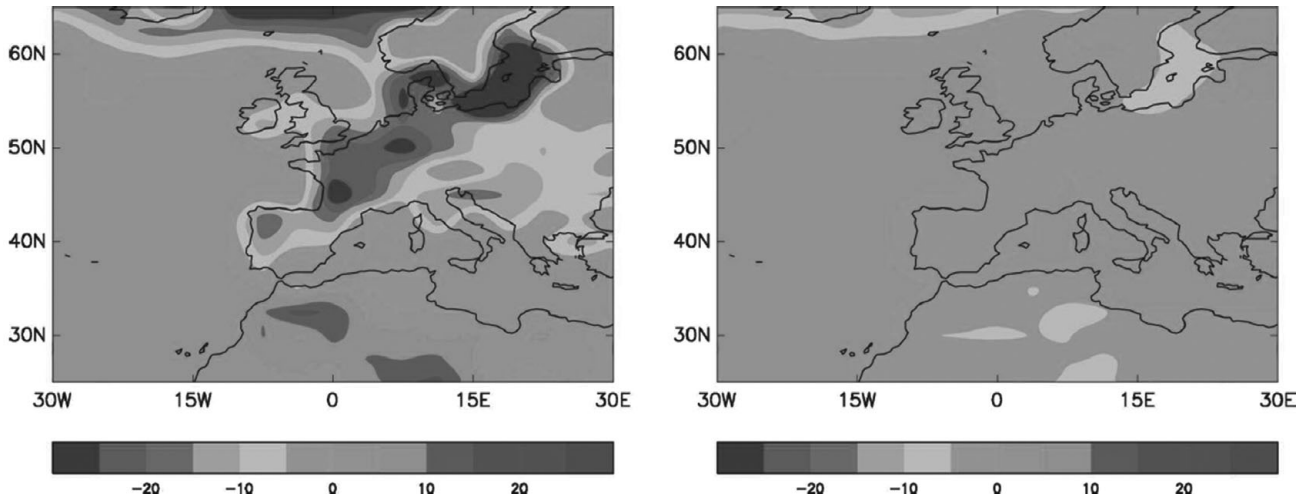


Fig. 9.2. Modelled changes in the frequency of winter frost days between 1960–65 and 1990–95. The left-hand panel shows a large reduction in the number of frosts per winter in a global climate model which includes known climate forcings, such as greenhouse gases and observed changes in sea surface conditions. The right-hand panel shows the change in the number of frosts in a similar climate model simulation but without the change in the North Atlantic Oscillation. Units are frost days per winter. Figure from Scaife *et al.* (2008). A black and white version of this figure will appear in some formats. For the colour version, please refer to Plate 16.

extremely low and the cold anomaly stretched across the whole of Northern Eurasia (Figure 9.1, upper right), with intense snowstorms as far east as China and Korea (see Chapter 4). Pressure gradient anomalies in the Atlantic in 2009/10 (Figure 9.1, upper left) were so large that the mean winter pressure gradient was eliminated and the mean winter flow was reversed from westerly to easterly. In

addition to these immediate impacts, later in the season, the spring NAO may even affect the subsequent behaviour of the East Asian summer monsoon (Wu *et al.*, 2009). These examples illustrate the profound extent to which the NAO therefore also governs extreme seasonal and even decadal climate events, as well as the frequency of daily extremes.

### 9.3 Degeneracy in the response to different drivers

The power spectra of the NAO and AO show few, if any, statistically significant peaks at particular frequencies and so the term oscillation is perhaps a misnomer in this case. In spite of this, recent studies have started to overturn the null hypothesis that the NAO and AO are purely the result of unpredictable chaotic climate variability. Instead, a picture is emerging of systematic changes in the NAO and AO in response to a number of climatic factors, many of which are external to the Atlantic.

The El Niño-Southern Oscillation (ENSO) is well known as a source of year to year variability in the tropics where the quasi-periodic warming of the tropical Pacific produces large impacts on regional climate throughout the tropics. Perhaps less well recognized until recently is that ENSO also affects the North Atlantic and the NAO. Historical data suggest that the NAO is often negative during El Niño events (Brönnimann, 2007) and this is now reproduced in state of the art numerical models. Figure 9.3 shows the striking agreement between modelled and observed pressure anomalies during El Niño winters. The negative AO and NAO are clearly seen in Fig. 9.3, and

although this effect only amounts to a few hPa over a three-month period, this represents a substantial fraction of the interannual standard deviation of the variability. It can therefore significantly alter the probability of cold or warm conditions on regional scales.

Perhaps the most striking source of climate variability in the atmosphere is the Quasi-Biennial Oscillation (Graystone, 1959). The tropical lower stratospheric winds oscillate between easterly and westerly phases with a period of around 28 months. Although it is situated deep in the tropical stratosphere, it too shows a clear connection to the NAO and AO in winter (Fig. 9.4). During easterly phases, the NAO tends to be more negative than during westerly phases (Ebdon, 1975, Pascoe *et al.*, 2006, Boer and Hamilton, 2008, Marshall and Scaife, 2009) with associated changes in jet stream winds, temperatures, and storminess.

Other factors, external to the Atlantic act to drive the AO and NAO on longer time scales. It has long been debated whether variations in solar irradiance due to the 11-year solar activity cycle has a significant effect on surface climate (Labitzke, 1987, Gray *et al.*, 2010). Recent model simulations appear to be finally demonstrating a reproducible link to the atmospheric circulation (Matthes *et al.*, 2006, Ineson *et al.*, 2011, Schmidt *et al.*, 2013) and again,

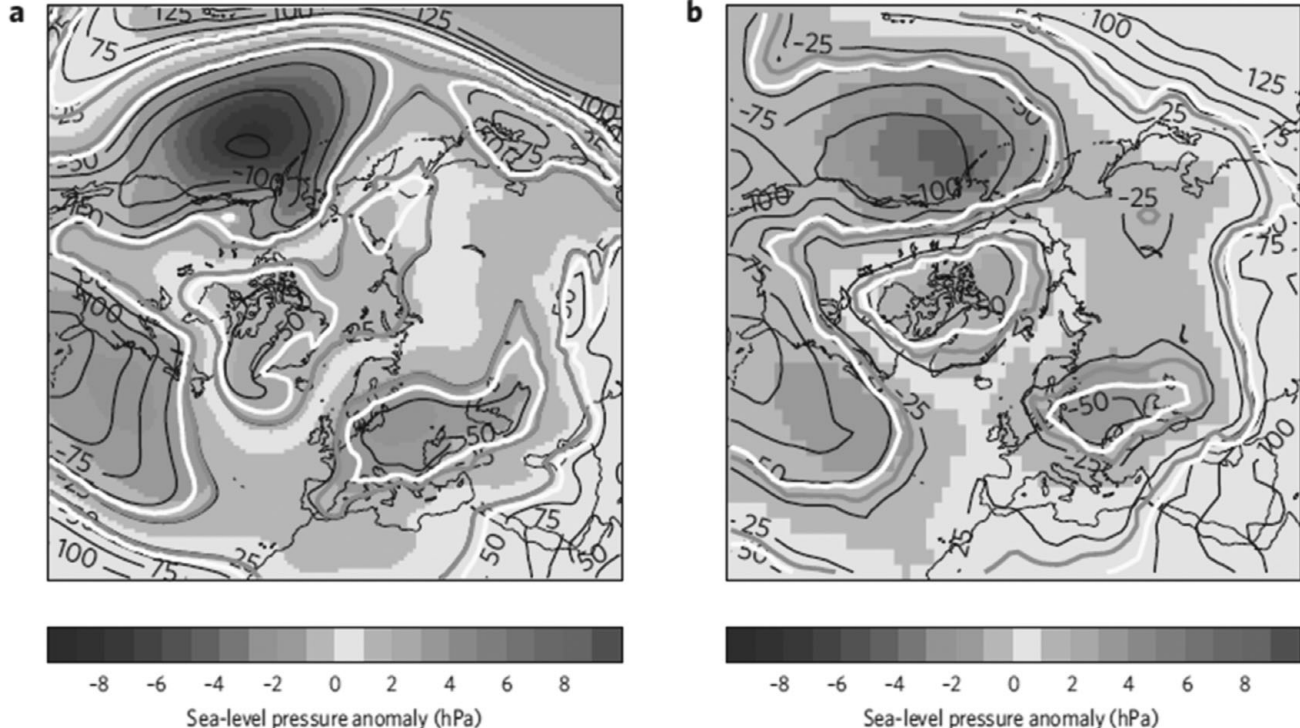


Fig. 9.3. The effect of El Niño on extratropical sea level pressure in late winter (Jan–Mar). Note the high pressure over the Arctic and low pressure in a surrounding annulus in both model simulation (left) and observations (right). Solid contours show the anomaly as a proportion of the year-to-year standard deviation. See Ineson and Scaife (2009) for further details. A black and white version of this figure will appear in some formats. [For the colour version, please refer to Plate 16.](#)

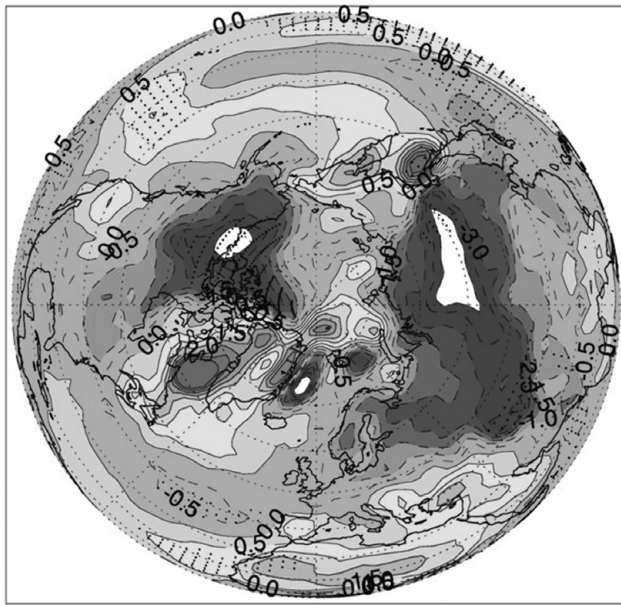


Fig. 9.4. Near surface temperature impact of the Quasi-Biennial Oscillation in winter. Note the characteristic quadrupole pattern of cold–warm–cold–warm across northern Europe, Mediterranean, eastern USA, and eastern Canada. This change results from a shift in the surface NAO towards negative phase during the easterly phase of the QBO. A black and white version of this figure will appear in some formats. [For the colour version, please refer to Plate 17.](#)

the pattern of response is the AO/NAO, with low solar variability driving negative NAO and AO conditions across the Northern Hemisphere (Fig. 9.5).

Needless to say, solar minimum conditions are therefore associated with cold European and US winters and mild conditions in eastern Canada and the Mediterranean.

On longer time scales, there is even evidence that components of the climate change signal will project onto the NAO and the AO. Climate projections with models containing improved representation of the atmospheric circulation in the stratosphere show an adjustment to the future surface climate that strongly resembles the negative phase of the AO and NAO (Morgenstern *et al.*, 2010, Scaife *et al.*, 2012, Karpechko and Manzini, 2012). A key point here is that the change in the NAO/AO produces a signal in sea level pressure of comparable amplitude but opposite sign to the original climate change signal (Fig. 9.6). As expected, this results in a large additional change in the frequency of associated extreme events such as heavy rainfall (Scaife *et al.*, 2012).

In this section we have seen how several independent factors can drive a shift in the NAO and AO. There are others that we have not discussed explicitly, such as volcanic eruptions (Stenchikov *et al.*, 2002), snow cover

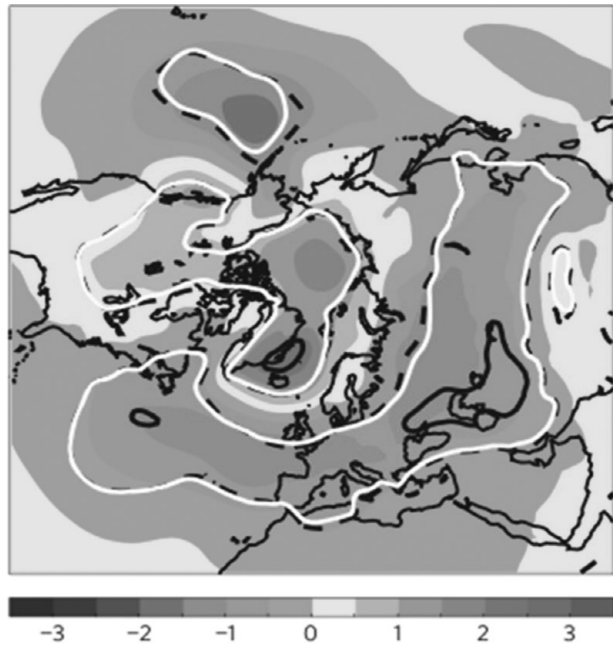


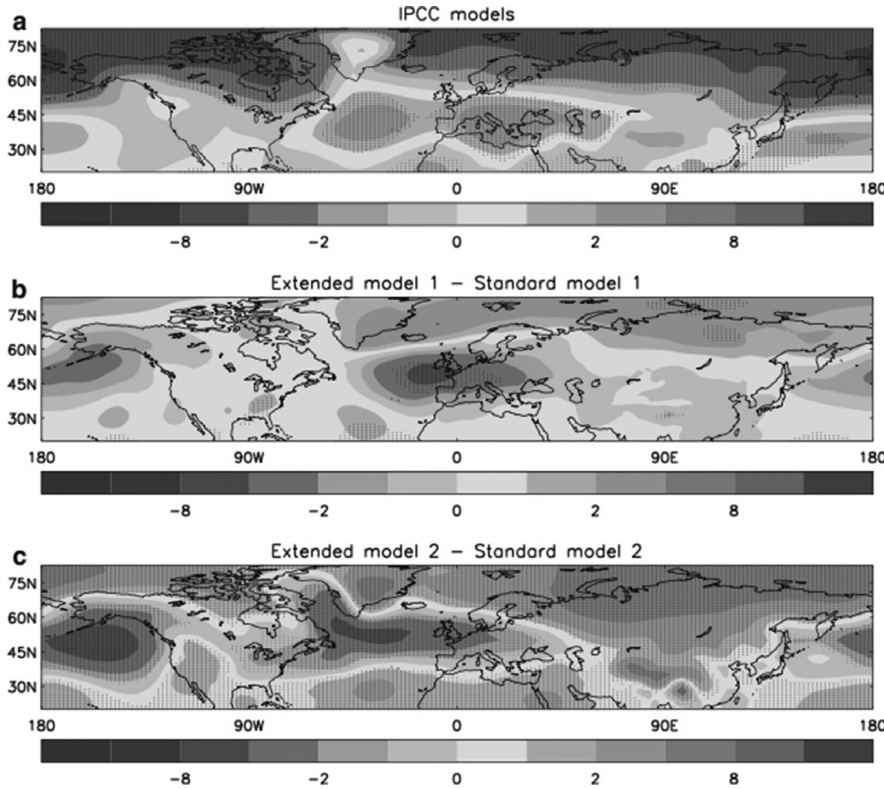
Fig. 9.5. Impact of low solar activity on winter sea level pressure in the Northern Hemisphere. Note the high pressure signal over the Arctic and the low pressure signal in a surrounding annulus. White contours show statistical significance at the 95% level using a t-test. Units are hPa. See Ineson *et al.* 2011 for further details. A black and white version of this figure will appear in some formats. [For the colour version, please refer to Plate 17.](#)

(Cohen and Entekhabi, 1999), and the Madden Julian Oscillation (Cassou, 2008). In many cases, observations and numerical models are also beginning to agree on the pattern and size of response. In summary, there is degeneracy in the response to these different climatic drivers, all of which project onto essentially the same NAO/AO-like patterns.

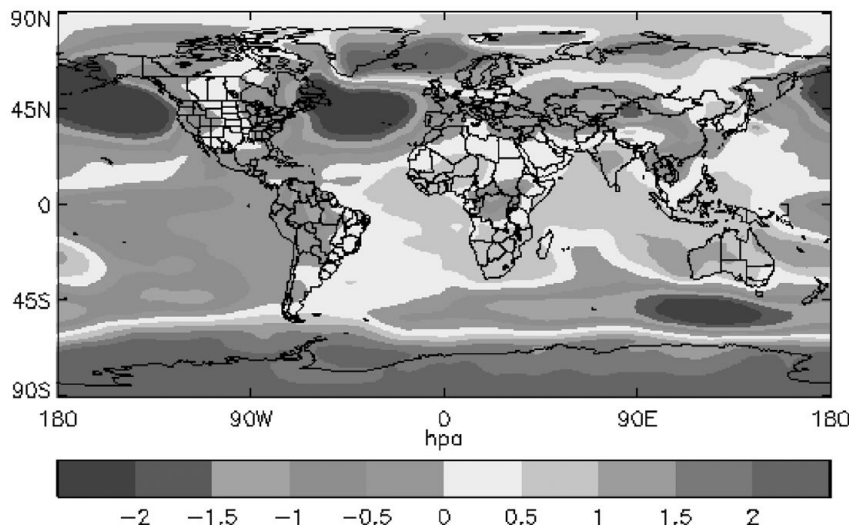
#### 9.4 Chaotic ‘noise’ or predictable signal?

Skilful predictions of the NAO and AO have been sought for many years but have generally proved elusive beyond weather forecast time scales (Johansson, 2007). In spite of occasional fluctuations in forecast skill scores above the level required for significance, such results have not proved robust in subsequent versions of operational forecast models (Kim *et al.*, 2012, Arribas *et al.*, 2011).

However, there have been occasional windows of opportunity where at least some models appear to convert activity in the climatic factors discussed above into a forecast NAO signal. Figure 9.7 gives one example where a seasonal forecast issued in November 2009 produced a signal



Ensemble mean anomaly : mean sea level pressure : Dec/Jan/Feb  
Issued November 2009



indicative of the extreme negative NAO which followed in the winter of 2009/10, as discussed above (Fig. 9.1). This forecast signal arose in part from the response to an El Niño and easterly QBO conditions in that winter (Fereday *et al.*, 2012) but it was not predicted by all operational forecast systems.

Very recently, however, exciting new evidence has emerged for predictability of the NAO and AO. At least two current operational forecast systems report significant and potentially useful levels of predictability of the winter NAO/AO on seasonal time scales (Riddle *et al.*, 2013, Scaife *et al.*, 2014). Given the control of the NAO over

Fig. 9.6. Changes in winter sea level pressure under conditions of quadrupled CO<sub>2</sub>. The upper panel shows sea level pressure changes in standard climate model projections. The lower two panels show the additional change in two independent climate models when the representation of stratospheric circulation is improved. Note that the scales are the same in all cases so that the additional NAO/AO-like signal cancels much of the original change. Figure from Scaife *et al.*, 2012. A black and white version of this figure will appear in some formats. For the colour version, please refer to Plate 19.

Fig. 9.7. Real time seasonal prediction of mean sea level pressure anomalies prior to the extreme negative NAO in the winter of 2009/10. Sea level pressure anomalies are plotted for the ensemble mean forecast for winter (December–February). Forecasts were issued in real time before the start of winter in November from the Met Office. Units are hPa. The observed sea level pressure anomalies for this extreme winter are shown in Fig. 9.1 (upper left panel). A black and white version of this figure will appear in some formats. For the colour version, please refer to Plate 18.

extreme weather and climate events, this leads to the possibility for seasonal length predictions of the risk of weather related impacts across the northern extratropics.

## 9.5 Summary

The North Atlantic and Arctic Oscillations are not really *oscillations* in any clear sense at all as they fluctuate on all time scales, but these fluctuations are still crucial to explain variability from year to year and decade to decade in the seasonal climate of the extratropical Northern Hemisphere. Changes in the winter NAO (or AO) govern changes in advection and hence temperature over land. Similarly, the NAO is also related to the strength and position of the Atlantic jet stream; the associated Atlantic storm track and hence the risk of extreme weather events around the Atlantic basin is also governed by the NAO and AO.

Predictability of the NAO and the AO will always be limited to some degree by inherently unpredictable chaotic fluctuations in the atmosphere. Some model based studies suggest that there may be little else at work in NAO and AO variability (e.g. Koenigk and Mikolajewicz, 2009). However, theoretical computer models do not properly represent all of the observed factors which can drive the NAO and AO, and model based estimates of the predictability can easily be misleading (Eade *et al.*, 2014). Similarly, in the presence of low frequency climate variability, estimates of predictability based on average skill estimates over long multi-decadal periods may not be representative of contemporary levels of predictability, nor will they represent conditional predictability when key predictable climate phenomena are active. Recent studies suggest that much of the winter NAO variability is not simply explained as a residual of weather noise (Keeley *et al.*, 2009) and a number of potentially predictable mechanisms for NAO variability have now been identified, several of which involve stratosphere–troposphere interaction, and some of which are only just beginning to be properly represented in contemporary forecast models. Much more encouraging levels of predictability for the winter NAO are therefore now beginning to emerge in long range prediction systems (Riddle *et al.*, 2013, Scaife *et al.*, 2014, Kang *et al.*, 2014). The potential for making risk based predictions of extreme events out to months ahead is therefore evolving quickly.

A key message of this overview is that the same NAO-like pattern appears in response to a variety of different climatic drivers. We have shown examples ranging from the Pacific Ocean (El Niño – Southern Oscillation) to the tropical stratosphere (Quasi-Biennial Oscillation). Although these remote drivers are quite different and independent phenomena, they all trigger the same degenerate

pattern of response in the North Atlantic. This can present a problem for linear methods of detecting and attributing extreme events to different causes, as these methods often rely on distinguishing different patterns of response. In contrast, it may actually help to simplify the approach to improving long-range prediction of weather and climate extremes around the Atlantic basin. A large fraction of observed Atlantic climate variability is known to be attributable to the NAO and given that many of the predictable drivers identified so far also project onto the NAO, it may be that an even larger fraction of the *predictable* variability occurs via the NAO.

This raises some interesting questions about forecast methods for those extreme events that are strongly governed by the NAO or AO. The summary schematic given in Fig. 9.8 illustrates the relationship between an ensemble forecast of the chance of an extreme weather or climatic event (upper right) and the observed event (lower right). These are related by the modelled link (1) between the NAO and the extreme event. The forecast NAO is then hopefully skilfully related to the observed NAO (2), which is in turn related (3) to the chance of an extreme event actually occurring (lower right).

There are a number of places where the forecast can go awry. Of course we are always limited by the strength of link 3 for events that are only partly governed by the NAO

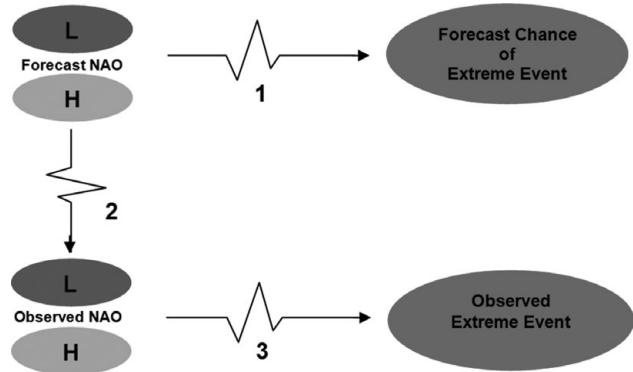


Fig. 9.8. Relationship between forecasts and observations of extreme events that are governed by the NAO. The relationship between the forecast chance of extreme events (upper right) and the observed occurrence of an event (lower right) is limited by imperfect links (broken arrows) between: (1) the forecast number of extreme events and the forecast NAO, (2) the forecast NAO and the observed NAO, and (3) the observed NAO and the observed occurrence of extreme events. Using the forecast NAO as a direct predictor of the observed events (an example of statistical downscaling) can therefore improve forecast skill by eliminating link 1 which is both noisy and imperfectly represented in global circulation models. A black and white version of this figure will appear in some formats. For the colour version, please refer to Plate 18.

and otherwise occur by chaotic, unpredictable fluctuations. Limitations in forecast skill due to link 3 are therefore irreducible. In addition, the skill of NAO forecasts themselves is limited (e.g. Johansson, 2007) and although increasing in skill (Riddle *et al.*, 2013, Scaife *et al.*, 2014, Kang *et al.*, 2014), forecasts will of course never be perfectly skilful. Link 2 is therefore a weakness for all events except those downstream impacts that can be predicted from the recently observed state of the NAO (e.g. Wu *et al.*, 2009). Interestingly, the link between the NAO and extreme weather and climate events in forecasts (1) may be avoidable by using the prediction of the NAO itself as a proxy for the forecast chance of an extreme event. In this case, the forecast NAO is the most skilful indicator of the likelihood of impending weather or climate extremes.

## References

- Arribas A., M. Glover, A. Maidens, *et al.* (2011). The GloSea4 ensemble prediction system for seasonal forecasting. *Mon. Wea. Rev.*, **139**, 1891–1910.
- Barnston, A. G. and R. E. Livezey (1987). Classification, seasonality and persistence of low-frequency atmospheric circulation patterns. *Mon. Wea. Rev.*, **115**, 1083–1126.
- Boer, G. and K. Hamilton (2008). QBO influence on extratropical predictive skill, *Clim. Dyn.*, **31**, 987–1000.
- Brönnimann, S. (2007). Impact of El Niño–Southern Oscillation on European climate. *Rev. Geophys.*, **45**, doi: 10.1029/2006RG000199
- Cassou C. (2008). Intraseasonal interaction between the Madden Julian Oscillation and the North Atlantic Oscillation. *Nature*, **455**, 523–527.
- Cohen, J. and D. Entekhabi (1999). Eurasian snow cover variability and Northern Hemisphere climate predictability, *GRL*, **26**, 345–348.
- Eade R., D. Smith, A.A. Scaife, and E. Wallace (2014). Do seasonal to decadal climate predictions underestimate the predictability of the real world? *Geophys. Res. Lett.*, DOI: 10.1002/2014GL061146.
- Ebdon, R. A. (1975). The quasi-biennial oscillation and its association with tropospheric circulation patterns. *Meteorol. Mag.*, **104**, 282–297.
- Fereday D., A. Maidens, A. Arribas, A. A. Scaife, and J. R. Knight (2012). Seasonal forecasts of Northern Hemisphere Winter 2009/10. *Env. Res. Lett.*, **7**, doi:10.1088/1748-9326/7/3/034031.
- Franzke, C., S. Lee, and S. B. Feldstein (2004). Is the North Atlantic Oscillation a breaking wave?. *J. Atmos. Sci.*, **61**, 145–160.
- Gray, L. J. *et al.* (2010). Solar influences on climate. *Rev. Geophys.* **48**, RG4001.
- Graystone, P., (1959). Meteorological office discussion on tropical meteorology. *Met. Magazine*, **88**, 117.
- Hanna E., T. E. Cropper, P. D. Jones, A. A. Scaife, and R. Allan (2014). Recent seasonal asymmetric changes in the NAO: a marked summer decline and increased winter variability. *Int. J. Clim.*, DOI: 10.1002/joc.4157.
- Hurrell, J. W., Y. Kushnir, G. Ottersen, and M. Visbeck (eds.) (2003). *The North Atlantic Oscillation: Climatic Significance and Environmental Impact*, American Geophysical Union, Washington, DC, 279 pp.
- Ilkka, J., Heikki, T., and Väinö, N. (2012). The variability of winter temperature, its impacts on society, and the potential use of seasonal forecasts in Finland. *Weather* **67**, 328–332.
- Ineson S. and Scaife A. A. (2009). The role of the stratosphere in the European climate response to El Nino. *Nat. Geosci.*, **2**, 32–36.
- Ineson S., A. A. Scaife, J. R. Knight, *et al.* (2011), Solar forcing of winter climate variability in the Northern Hemisphere, *Nat. Geosci.*, **4**, 753–757, doi:10.1038/GEO1282.
- Johansson, Å. (2007): Prediction skill of the NAO and PNA from daily to seasonal time scales. *J. Climate*, **20**, 1957–1975. doi:10.1175/JCLI4072.1
- Jones, P. D., T Jónsson, and D. Wheeler (1997). Extension to the North Atlantic Oscillation using early instrumental pressure observations from Gibraltar and south-west Iceland. *Int. J. Climatol.* **17**, 1433–1450.
- Kang, D., M. I. Lee, J. Im, *et al.* (2014). Prediction of the Arctic Oscillation in boreal winter by dynamical seasonal forecasting systems. *Geophys. Res. Lett.*, **10**, 3577–3585, doi:10.1002/2014GL060011.
- Karpechko, A. Y. and E. Manzini (2012). Stratospheric influence on tropospheric climate change in the Northern Hemisphere, *J. Geophys. Res.*, **117**, D05133, doi:10.1029/2011JD017036.
- Keeley, S. P. E., R.T. Sutton, and L. C. Shaffrey (2009). Does the North Atlantic Oscillation show unusual persistence on intraseasonal timescales? *Geophys. Res. Lett.*, **36**, L22706, doi:10.1029/2009GL040367.
- Kim, H-M., P. Webster, and J. Curry (2012). Seasonal prediction skill of ECMWF System 4 and NCEP CFSv2 retrospective forecast for the Northern Hemisphere Winter. *Clim. Dyn.*, **23**, doi:10.1007/s00382-012-1364-6.
- Koenigk, T. and U. Mikolajewicz (2009). Seasonal to interannual climate predictability in mid and high northern latitudes in a global coupled model. *Clim. Dyn.* **32**, 783–798, doi:10.1007/s00382-008-0419-1
- Labitzke, K. (1987). Sunspots, the QBO, and the stratospheric temperature in the north polar region. *Geophys. Res. Lett.* **14**, 535–537.
- Li, J. and J. X. L. Wang (2003). A modified zonal index and its physical sense. *Geophys. Res. Lett.*, **30**(12), 1632, doi: 10.1029/2003GL017441.
- Marshall, A. and A.A. Scaife (2009). Impact of the Quasi-Biennial Oscillation on 321 seasonal forecasts. *J. Geophys. Res.*, **114**, D18110, doi:10.1029/2009JD011737.
- Marshall A. and A.A. Scaife (2010). Improved predictability of stratospheric sudden warming events in an AGCM with enhanced stratospheric resolution. *J. Geophys. Res.*, vol.**115**, D16114, doi:10.1029/2009JD012643.

- Matthes, K., Kuroda, Y., Kodera, K., and Langematz, U. (2006). Transfer of the solar signal from the stratosphere to the troposphere: Northern winter. *J. Geophys. Res.*, **111**, D06108.
- Morgenstern O. *et al.* (2010). Review of the formulation of present generation stratospheric chemistry-climate models and associated external forcing. *J. Geophys. Res.*, **115**, D00M02. doi: 10.1029/2009JD013728
- Ouzaeu, G., J. Cattiaux, H. Douville, A. Ribes, and D. Saint-Martin (2011). European cold winter 2009–2010: How unusual in the instrumental record and how reproducible in the ARPEGE-Climat model? *Geophys. Res. Lett.*, **38**, L11706, doi:10.1029/2011GL047667.
- Pascoe, C. L., L. J. Gray, and A. A. Scaife (2006). A GCM study of the influence of equatorial winds on the timing of sudden stratospheric warmings, *Geophys. Res. Lett.*, **33**, L06825, doi:10.1029/2005GL024715.
- Renggli, D., G. C. Leckebusch, U. Ulbrich, S. N. Gleixner, and E. Faust (2011). The skill of seasonal ensemble prediction systems to forecast wintertime windstorm frequency over the North Atlantic and Europe. *Mon. Wea. Rev.*, **139**, 3052–3068.
- Riddle, E. E., A. H. Butler, J. C. Furtado, J. L. Cohen, and A. Kumar, (2013). CFSv2 ensemble prediction of the wintertime Arctic Oscillation. *Climate Dyn.*, **41**, 1099–1116, doi:10.1007/s00382-013-1850-5.
- Riviere, G. and I. Orlanski (2007). Characteristics of the Atlantic storm-track eddy activity and its relation with the North Atlantic Oscillation, *J. Atm. Sci.*, **64**, 241–266.
- Scaife, A. A., C. K. Folland, L. Alexander, A. Moberg, and J. R. Knight (2008). European climate extremes and the North Atlantic Oscillation. *J. Clim.*, **21**, 72–83.
- Scaife, A. A., T. Spangenhil, D. Fereday, *et al.* (2012). Climate change and stratosphere-troposphere interaction. *Clim. Dyn.*, **38**, 2089–2097, doi:10.1007/s00382-011-1080-7.
- Scaife, A. A., A. Arribas, E. Blockley, *et al.* (2014). Skilful long range prediction of European and North American winters. *Geophys. Res. Lett.*, **41**, 2514–2519, doi:10.1002/2014GL059637.
- Schmidt, H., J. Kieser, S. Misios, and A. N. Gruzdev (2013). The atmospheric response to solar variability: Simulations with a general circulation and chemistry model for the entire atmosphere, in: F.-J. Luebken (ed.): *Climate And Weather of the Sun-Earth System (CAWSES): Highlights from a priority program*, Springer, Dordrecht, the Netherlands.
- Shabbar, A., Huang, J., and Higuchi, K. (2001). The relationship between the wintertime north Atlantic oscillation and blocking episodes in the north Atlantic. *Int. J. Climatol.*, **21**, 355–369. doi: 10.1002/joc.612
- Stenchikov, G., A. Robock, V. Ramaswamy, *et al.* (2002). Arctic Oscillation response to the 1991 Mount Pinatubo eruption: effects of volcanic aerosols and ozone depletion. *J. Geophys. Res.*, **107** (D24), 4803, doi:10.1029/2002JD002090.
- Thompson, D. W. J. and J. M. Wallace (1998). The Arctic oscillation signature in the wintertime geopotential height and temperature fields. *Geophys. Res. Lett.*, **25**, 1297–1300.
- Vallis, G. and E. Gerber (2008). Local and hemispheric dynamics of the North Atlantic Oscillation, annular patterns and the zonal index. *Dyn. Atmos. Oceans*, **44**, 184–212.
- Walker G. T. and Bliss E. W. (1932). World weather V. *Mem. Roy. Meteor. Soc.*, **4**, 53–84.
- Wu, Z., B. Wang, J. Li, and F. Jin (2009). An empirical seasonal prediction model of the East Asian summer monsoon using ENSO and NAO. *J. Geophys. Res.*, **114**, D18120, doi:10.1029/2009JD011733.



## PART III

### **Tropical cyclones**



# 10

## Opportunities and challenges in dynamical and predictability studies of tropical cyclone events

Russell L. Elsberry and Hsiao-Chung Tsai

### 10.1 Introduction

Tropical cyclones are one of the most important high-impact weather events in terms of loss of life and damage. As recently as 1970, the Bhola cyclone killed more than 300,000 people in Bangladesh. However, many tropical islands and countries depend on tropical cyclone precipitation for their domestic and agricultural water supplies. Thus, one of the great meteorological challenges is to provide timely and highly accurate forecasts of tropical cyclones, to allow the longest possible warnings so that people can seek safe shelter and disaster preparedness activities can be completed.

The primary focus in this chapter is on tropical cyclone track forecasting, because the track is by far the most important factor in determining where and when the high winds and extreme precipitation may be expected. Fortunately, it is in the understanding of the dynamic processes in tropical cyclone motion and in numerical model predictions of the track that the greatest advances have been made since the mid 1990s (Elsberry, 2007). As summarized in Section 1.1, great progress has been achieved in numerical predictions, and the improved numerical model guidance for tropical cyclone tracks, plus the use of consensus forecasting, have allowed five-day track forecasts that are as accurate as the three-day forecasts of a decade earlier. Consensus forecasting is the average of multiple skillful track forecasts to reduce the impact of random errors that arise from limited observations and uncertainty in the model physics.

The combined Tropical Cyclone Structure (TCS-08)/THORPEX Pacific Asia Regional Campaign (T-PARC) field experiment studies have advanced understanding of the dynamics and thermodynamics of western North Pacific tropical cyclone formation (see Elsberry and Harr, 2008). However, prediction of the transition from a pre-tropical cyclone seedling to a self-sustaining, warm-core circulation is difficult because both large-scale environmental factors and the convective-scale and mesoscale processes must be

accurately resolved. The limit of predictability of these convective-scale and mesoscale processes in tropical cyclones is further discussed in Chapter 11. The formation of the eyewall of the tropical cyclone, which is the region of maximum winds and heavy precipitation, is examined in Chapter 13. Since much less progress has been achieved in intensity forecasting, this topic will not be discussed.

As indicated above, several numerical weather prediction centers have been producing five-day forecasts of the tracks of *existing* tropical cyclones, and the European Centre for Medium-range Weather Forecasts (ECMWF) began in January 2012 to issue forecasts of up to 10 days (Vitart *et al.*, 2012). In this chapter, the opportunities and challenges to produce extended-range (5–30 day) forecasts by the ECMWF of tropical cyclone events (both formation and subsequent track through its life cycle) will be described for the western North Pacific and for the Atlantic. A second objective is to examine the ECMWF seasonal forecasts in both of these basins to determine the predictability of these tropical cyclone events, and specifically whether these seasonal forecasts will be able to predict the critical question of the number of landfalling events (rather than just the number of tropical cyclones in the basin).

### 10.2 Extended-range predictions of western North Pacific tropical cyclone events

Experimental 51-member ECMWF 32-day ensemble forecasts of tropical cyclone-like vortices in the western North Pacific were made available once a week for mission planning support during TCS-08/T-PARC. Elsberry *et al.* (2010) combined the ensemble member vortices with similar tracks into “ensemble storm” tracks with a weighted-mean vector motion technique in which the weighting factor was inversely proportional to the distance from the endpoint of the previous 12-hour motion vector. These ECMWF 32-day ensemble forecasts indicated a dry period

of no formations late in August 2008, and then an active period of formations, which was indeed the case. Thus, an expanded sample of 30 weekly forecasts beginning 5 June through 25 December 2008 was compared with the Joint Typhoon Warning Center (JTWC) tracks (Elsberry *et al.* 2010). The ensemble storms identified in the ECMWF 32-day forecasts provided guidance on extended-range (5–30 day) time scales of the formations and tracks of the three strongest typhoons and two other typhoons, but not for two early season typhoons and the late season Dolphin. Four strong and one weak tropical storm events were consistently predicted to form in the first week (Week 1) forecast prior to formation, and in the Week 2, Week 3, and Week 4 forecasts prior to formation. Two other weak tropical storms, three tropical cyclones that developed from precursor baroclinic systems, and three other tropical depressions, were not predicted on these extended-range time scales. The Elsberry *et al.* (2010) study was the first demonstration that the ECMWF 32-day ensemble may provide guidance of western North Pacific formations and specific tracks on 5–30 day time scales, as opposed to tropical cyclone activity forecasts as in Vitart (2009).

Elsberry *et al.* (2011) then evaluated the performance of the ECMWF 32-day ensemble predictions of western North Pacific tropical cyclone events (formation plus track), made once a week during the 2009 season with the same procedures as for the 2008 season. Seventeen of the 23 tropical cyclones during the 2009 season occurred during multiple storm scenarios that are more difficult to predict, and many of the deficient track predictions involved unusual and rapidly changing tracks that typically involve interactions with adjacent synoptic circulations that are not predictable on extended-range time scales (5–30 days). Such incorrect predictions of the duration and tracks of these multiple cyclones were found to degrade the performance in predicting subsequent tropical cyclone formations and tracks during the 32-day integration. Predominantly northward tracks throughout the life-cycle tended to be less predictable on extended-range time scales. Given these caveats, the overall performance of the ECMWF ensemble for the 12 typhoons was more successful than during the 2008 season. However, the performance for three tropical storms during the 2009 season was less successful due to the difficult track forecast scenarios. A surprisingly good performance was also found in predicting over these extended-range time scales the formation, location, and early track segments of eight minimal tropical storms or tropical depressions. The less satisfactory aspect for many of the late season tropical depressions was that the ECMWF ensemble continued to predict member vortices for extended periods after the system had actually dissipated.

Tsai *et al.* (2013) developed an objective track analog verification technique to select all ensemble storm tracks

predicted by the ECMWF 32-day ensemble during the 2009 and 2010 seasons that match the overall JTWC tracks. In the Tsai *et al.* (2013) verification technique, ensemble storms within specified time and space differences of the JTWC track are first extracted as potential analogs, and four metrics of shortest distance, average distance, distance at formation time, and distance at ending time are calculated. An objective quality measure (i.e. likelihood value – LHV) that assesses the overall track similarity between the potential analogs and the JTWC storm is calculated in terms of membership functions for the four track metrics. Weighting factors multiplying these membership functions are adjusted to match the quality measures for the ECMWF ensemble storm forecasts in Elsberry *et al.* (2011).

An example of the verification technique is given in Fig. 10.1 for Supertyphoon Megi (2010). The 0000 UTC 7 October 2010 forecast (Fig. 10.1a) is designated as Week 1 since Megi did not form until 12 October. Four ensemble storms labeled 4, 7, 9, and 12 were potential analogs with the Megi track and were assigned quality measures with LHVs of 0.30, 0.70, 0.26, and 0.51. The Week 2 forecast (Fig. 10.1b) initiated on 30 September is somewhat better than the Week 1 forecast in that ensemble storm 11 begins close to where Megi formed and has a track (LHV = 0.78) that crosses northern Luzon. Ensemble storm 18 is also assigned a quality measure of “Above Average” (LHV = 0.76) as it has a somewhat similar track as ensemble storm 11. The Week 3 forecast (Fig. 10.1c) from 23 September includes ensemble storm 20 with an exceptional track (LHV = 1.0) that begins close to where Megi would form more than three weeks later, and it also predicts a sharp turn to the north and overlays Megi’s track to landfall on the China coast. Ensemble storm 19 begins very near where Megi formed and has a track almost as good as that of ensemble 20, except that it terminates in the middle of the South China Sea. Finally, ensemble storm 23 in the Week 4 forecast (Fig. 10.1d) is also exceptional (LHV = 1.0) considering the agreement in initial positions, a period of overlapping tracks between 135°E and 125°E, and a turn toward the northwest late in the track.

Objective verifications for the 2009 and 2010 seasons have been summarized in terms of hits, misses, false alarms, and correct negatives that no tropical cyclone would be present throughout the western North Pacific (Table 10.1). The most important result is that the ECMWF ensemble was able to predict nearly all of the tropical cyclones in both seasons, and thus with only a small number of Misses that were generally short-lived tropical depressions. Good performance in terms of correct negatives was achieved during the 2010 season.

A challenging forecasting issue associated with the ECMWF ensemble is the false alarms, which were defined by Tsai *et al.* (2013) to be all ensemble storms that could

Table 10.1. Contingency table of the performance of the weekly ECMWF 32-day ensemble forecasts in predicting the formations and subsequent tracks of the western North Pacific tropical cyclones 05W through 28W during the 2009 season (2 July to 31 December 2009) and 01W through 19W during 2010. The definition of hits is  $LHV \geq 0.2$  (FAs: false alarms; CNs: correct negatives).

	Hits	FAs	Misses	CNs
<b>Week 1</b>	41	103	3	15
<b>Week 2</b>	41	44	2	35
<b>Week 3</b>	38	93	1	20
<b>Week 4</b>	35	132	4	20

not be matched with JTWC storms within the specified thresholds. Evaluation of the characteristics of the false alarms indicate seasonal and geographic biases and that about 50% of the false alarms originate from the initial conditions in the model. A relative minimum of false alarms being created in Week-2 forecasts was attributed to the decrease in horizontal resolution in the model from about 32 km to about 63 km that occurs at day 10 (model cycle 36rl). A steady and nearly uniform increase in false alarms in the Week-3 and Week-4 forecasts may be attributed to net convective heating in response to persistent environmental forcing in the tropics. Research is in progress to objectively identify these false alarms in the ECMWF 32-day ensemble forecasts.

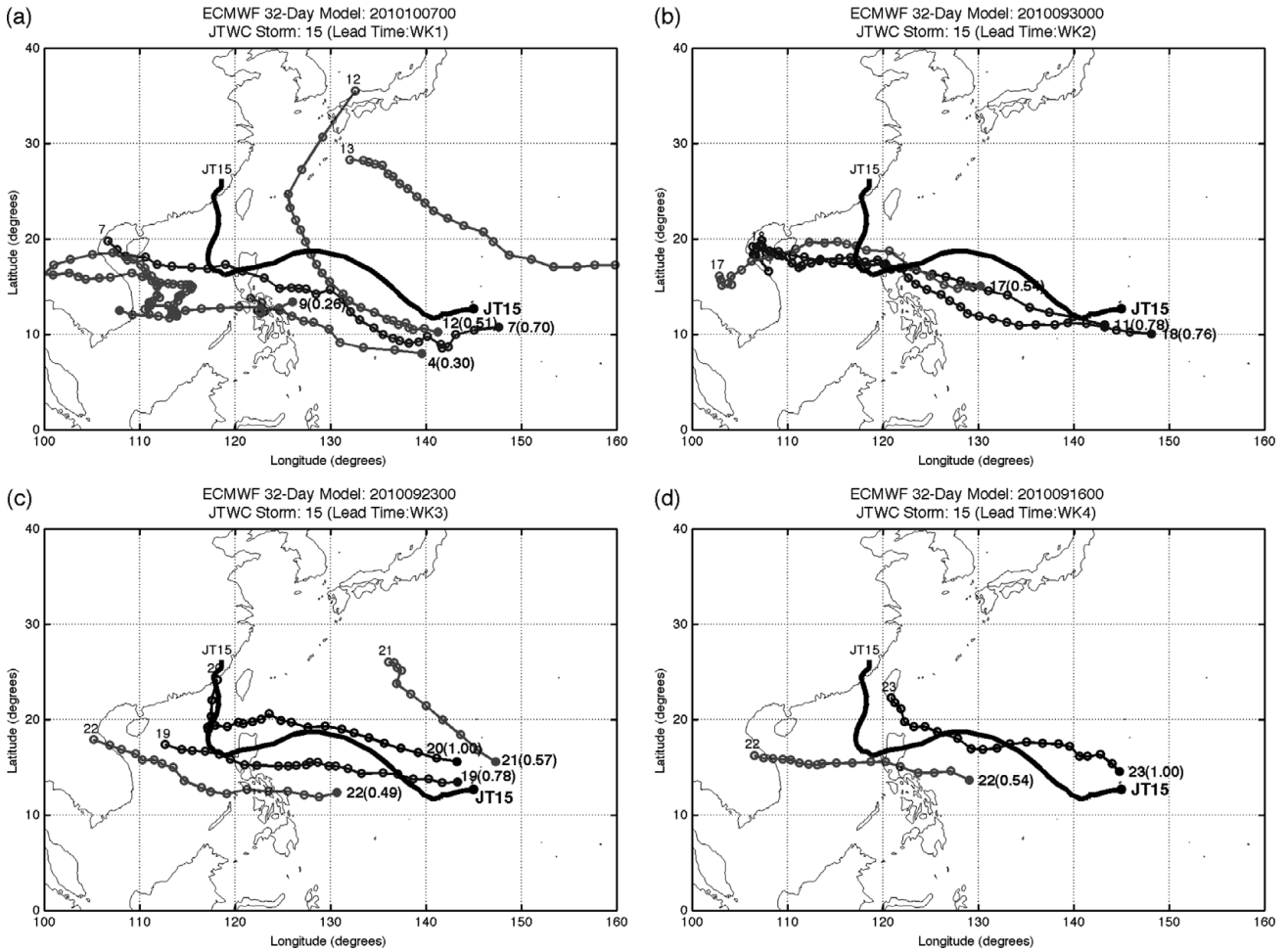


Fig. 10.1. Ensemble storm tracks (gray lines with 12-h positions indicated by dots) that the typhoon analog technique matched with the track of Typhoon Megi (solid line, labeled JT15) for the ECMWF 32-day forecasts initiated (a) Week 1, (b) Week 2, (c) Week 3, and (d) Week 4 prior to the actual formation of Megi. That is, the initial times are at 0000 UTC on 7 October, 30 September, 23 September, and 16 September, respectively. Note that the lengths of the ensemble storm tracks are generally longer than that of Typhoon Megi. The matched ensemble storm numbers and the overall track likelihood value (LHV) that is used as a quality measure are given at the beginning of each track (Tsai *et al.* 2013).

A capability to predict a gap period of no tropical cyclones was important during the Impact of Typhoons on the Ocean in the Pacific (ITOP) field experiment during August–October 2010. That is, the weekly ECMWF 32-day ensemble forecasts were able to predict no tropical storms or greater intensity would exist within 1000 km of the ITOP aircraft operations center in Guam during a critical three-week period following TY Malakas and before the formation of TY Megi (Tsai and Elsberry 2013). The situation was that the final oceanographic instrument deployment was awaiting the occurrence of a typhoon with at least 100 kt intensity before the aircraft had to depart on 20 October. A three-week gap with no TCs in the western North Pacific during late September and early October is relatively rare, so it is quite significant that the ECMWF 32-day ensemble could predict this gap. Tsai and Elsberry (2013) propose that an opportunity exists to extend support to the decision-making processes of water resource management and hydrological operations on 5–30 day time scales for countries and islands that depend on tropical cyclone-related rainfall, and these decision makers will also benefit from reliable information as to extended-range periods with no tropical cyclones in their region.

### 10.3 Extended-range predictions of Atlantic tropical cyclone events

The ECMWF also provided twice-weekly 32-day ensemble forecasts from 31 May to 17 December 2012 in support of the NASA Hurricane and Severe Storm Sentinel (HS3) field experiment in the Atlantic region. The performance of the ECMWF 32-day ensemble forecasts is summarized in Fig. 10.2 in terms of the quality measure LHV for the ensemble storm that matched a National Hurricane Center (NHC) storm (Elsberry *et al.* 2014). For example, the summary for Ernesto (AL05) in Fig. 10.2 is LHV = 0.58 (0, 0.94, 0.29) for Week 1 (2, 3, 4), which would be designated as good (miss, excellent, below average) in Tsai *et al.* (2013).

An immediate conclusion from comparing the 2012 Atlantic summary of LHV in Fig. 10.2 with the western North Pacific summary for the 2009 and 2010 seasons (Tsai *et al.* 2013) was that the ECMWF ensemble performance on extended-range time scales was more limited in the Atlantic. Since a small sample of 17 Atlantic storms during 2012 cannot be used to assess *predictability*, this evaluation of the ECMWF ensemble performance will be characterized in terms of a “*forecastable*” metric for certain types of tropical cyclone events. That is, the objective is to inform the NHC forecaster that some Atlantic tropical cyclone events may be forecastable in the extended range, but other types of Atlantic tropical cyclones are not. Indeed, the variation of forecastability is from four weeks to no forecastability even one week before the storm has appeared in the NHC Working Best-Track (WBT). Four groupings of the storms will be described that are characterized as: (1) highly forecastable (EF4), which is defined as all four weeks’ (1, 2, 3, and 4) forecasts had a match; (2) somewhat forecastable (EF3), which will be for ensemble storm forecasts that had  $LHV \geq 0.2$  in only three of the four weeks; (3) limited forecastable (EF2), which were ensemble storm forecasts that had  $LHV \geq 0.2$  in only the first two weeks; and (4) not forecastable (EF0) storms for which the ECMWF 32-day ensemble forecasts failed to have a match in all four weeks.

Only two hurricanes (AL11 and AL12) and two tropical storms (AL10 and AL15) in Fig. 10.2 were successfully forecast in all four weeks, which is a strong contrast with Tsai *et al.* (2013) who found that nearly all of the typhoons and even many of the tropical depressions in the western North Pacific during 2009 and 2010 were successfully forecast out to four weeks in advance of the actual formation time. While these four highly forecastable storms were forecast by the ECMWF on extended-range time scales (5–30 days), it should be noted that these four EF4 storms generally occurred in the mid season and all developed from African systems. Although the forecast tracks were frequently too long (and thus resulted in a LHV deduction of 0.22), they are considered to be highly

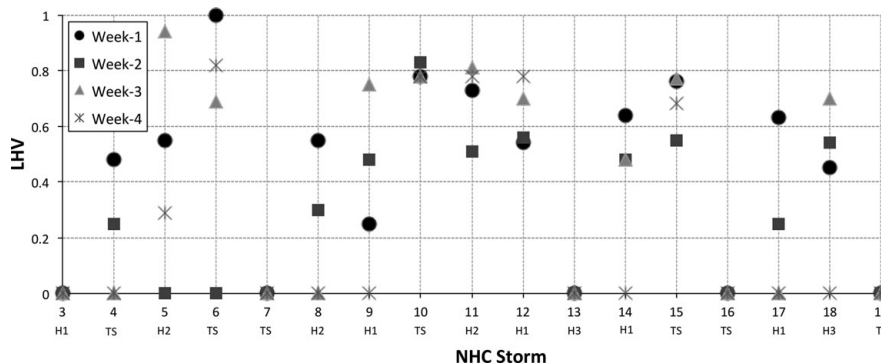


Fig. 10.2. Quality measure likelihood values (LHV, ordinate) for Week 1, 2, 3, and 4 (symbols in inset) for the AL03 through AL19 tropical storms (TS) and Hurricane categories one, two, and three (H1, H2, H3) during the 2012 Atlantic hurricane season (Elsberry *et al.* 2014). A  $LHV \geq 0.2$  is considered a hit and  $LHV < 0.2$  is considered a miss. Note that  $LHV = 0$  for all four weeks for AL03, AL07, AL13, AL16, and AL19.

forecastable, and potentially useful outlooks of specific TC events in the Atlantic.

Four hurricanes and one tropical storm were classified as EF3 storms, as the ECMWF 32-day ensemble was able to successfully forecast these storms in three of the four weeks (Fig. 10.2). For Hurricanes Isaac (AL09), Nadine (AL14), and Sandy (AL18), the unsuccessful forecast was in Week 4 (as might be expected), but for Hurricane Ernesto (AL05) and TS Florence (AL06), the unsuccessful forecast was in Week 2. The inability of the ECMWF ensemble to forecast the formations and tracks in Week 4 for Hurricanes Sandy, Isaac, and Nadine indicates that these are only somewhat forecastable EF3 storms. The late-season Sandy was strongly impacted by interactions with deep mid-latitude troughs. Similarly, the extremely sharp recurvature and subsequent complex track indicate that Nadine was also strongly impacted by mid-latitude circulations, and these interactions are not forecastable on four week time scales. In the case of Isaac, it is only the LHV deductions for the forecast starting and ending points that make the Week 2 and Week 3 forecasts appear less desirable. No explanation for the absence of a Week 4 forecast of Isaac is available at this time.

Two hurricanes and one tropical storm were classified as EF2 storms, as the ECMWF 32-day ensemble was able to successfully forecast these storms in only the first two weeks (Fig. 10.2). Hurricane Rafael (AL17) was a late season storm that seemed to have its origins at low latitudes, but moved poleward after reaching tropical storm stage near 14.7°N, 62.7°W at 1800 UTC 12 October. Both TS Debby (AL04) and Hurricane Gordon (AL08) had their origin near 20°N and had short poleward tracks before recurving to the northeast. These three EF2 storms represent limited forecastability of the ECMWF ensemble for somewhat different reasons. The low-latitude origin and poleward track of the late season Rafael has some of the same difficulties as Sandy due to interactions with a deep mid-latitude trough. The importance of interaction with the mid latitudes for the formation, track, and intensification of Hurricane Gordon can account for its limited forecastability. Finally, Debby's formation adjacent to the Yucatan Peninsula and its short poleward track before recurving may indicate limited predictability due to land and ocean interaction as well as mid-latitude interaction.

The most surprising result of this evaluation of the 2012 Atlantic season was that the ECMWF 32-day ensemble forecasts on Mondays or Thursdays did not predict even in Week 1 the formations and tracks of five TCs (Fig. 10.3). That is, the LHV of three tropical storms (Helene-AL07, Patty-AL16, and Tony-AL19) and two hurricanes (Chris-AL03 and Michael-AL13) were equal to zero for all four weeks (Fig. 10.2). The tentative conclusion from four of these five EF0 storms that began in the

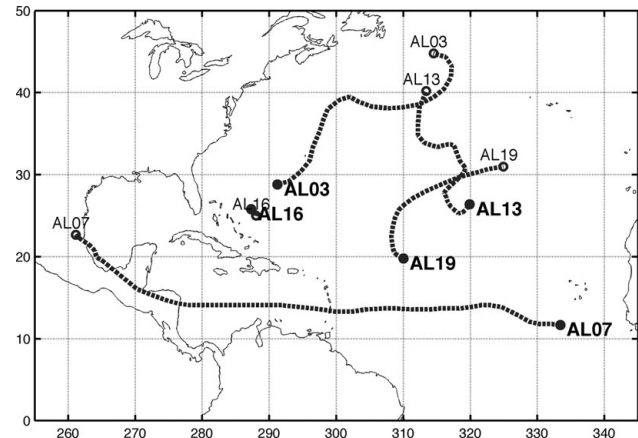


Fig. 10.3. Working best tracks for five Atlantic tropical storms and hurricanes in the not forecastable (EF0) category of Elsberry *et al.* (2014) (see text for names and characteristics).

central Atlantic is that strong mid-latitude influences make their formation locations and timing, and subsequent tracks, not forecastable by the twice-weekly ECMWF 32-day ensemble. Diagnostic studies to demonstrate the types and magnitudes of the interactions of the mid-latitude circulations with the pre-tropical cyclones in the ECMWF ensemble fields are needed.

While a larger sample of Atlantic tropical cyclone events needs to be studied, the implication from this 2012 season is that tropical cyclone events in the Atlantic are much less predictable on extended-range time scales than in the western North Pacific. In particular, those Atlantic tropical cyclones that have their origin in the subtropics and then have poleward tracks, and those forming in the tropics during the early season or late season due to baroclinic effects associated with deep mid-latitude troughs, may have limited to no predictability even one week in advance. Because the dynamics of these tropical cyclone events are strongly affected by baroclinic processes during the interaction of the eastward-moving mid-latitude troughs with the westward-moving pre-tropical cyclone seedlings, and such interactions are inherently difficult to predict, extended-range predictability of a considerable fraction of Atlantic tropical cyclone events is quite limited.

#### 10.4 Seasonal prediction of Atlantic tropical cyclone events

Camargo *et al.* (2007) reviewed the progress in seasonal forecasts of tropical cyclone activity (total number in each region) and indicated that the skill of the better dynamical models was comparable to that of the statistical models in some ocean basins. The ECMWF, which has one of the

more skillful dynamic seasonal prediction models, provided their 51-member ensemble forecasts in the Atlantic (and western North Pacific) for seven-month periods beginning 1 May, 1 June, and 1 July during 2012. The seasonal model horizontal and vertical resolution are  $\sim 80$  km and 91 levels, respectively. The same ensemble storm generation code and validation code (except for permitting larger time intervals for matching) as for the extended-range ensemble forecasts were applied to these seasonal forecasts and verified for the same 17 storms, as in Fig. 10.2.

Note that this verification of the Atlantic seasonal forecast is not just for the number of tropical cyclones – rather the *events* (formations and subsequent tracks) are being matched with the NHC tracks. A summary of the seasonal forecasts beginning from the first of May, June, and July 2012 is given in Table 10.2 in terms of a hit ( $LHV \geq 0.2$ ) or a miss ( $LHV < 0.2$ ) for four categories of storm types and tracks. For this 2012 Atlantic season, the ECMWF seasonal forecasts from May, June, and July do have some useful information on the African Easterly Wave (AEW) type of storms [Table 10.2(b)]. In addition to the four mid-season AEW storms that recurred in the central Atlantic, five other AEW storms that had westward tracks that might lead to landfalls in the Caribbean or the United States were also judged to be hits. In agreement with the evaluation of the extended-range forecasts for the Atlantic in Section 10.3, the ECMWF seasonal forecasts beginning in May, June, or July had limited (tracks matched NHC track only in first few days of the forecast) or no skill for the baroclinic-influenced formations [Table 10.2(a)]. Specifically, the baroclinically influenced Hurricanes Chris (AL03) and Michael (AL13) and Tropical Storm Tony (AL19), and the mesoscale Tropical Storm Patty (AL16), for which tracks are indicated in Fig. 10.3, were not predicted in any of the ECMWF seasonal forecasts from 1 May, 1 June, and 1 July, 2012.

Since these four storms were not predicted even one week in advance by the ECMWF 32-day ensemble forecasts (see Chapter 10.3), it is not surprising that they would also not be predicted by the ECMWF seasonal forecast model. However, a total of ten of the 19 Atlantic tropical cyclone events during 2012 that have baroclinic-influenced formations and tracks [Table 10.2(a)] have limited or no predictability in these three ECMWF seasonal forecasts. The reason that the Atlantic seasonal tropical cyclone *activity* forecasts by the ECMWF have been successful (Camargo *et al.*, 2007) must be due to a calibration technique that relates the total number of all forecast tracks during each seven-month integration to the observed number based on re-forecasts over many prior seasons. If the goal is to predict the number of *landfalling* tropical

Table 10.2. Summary of the matching of ensemble storms in the ECMWF seasonal forecasts beginning 1 May, 1 June, and 1 July 2012 with National Hurricane Center storm tracks in terms of hits ( $LHV \geq 0.2$ ) or misses ( $LHV < 0.2$ ) for (a) baroclinic-influenced formations and subsequent tracks either in the subtropics or in low latitudes, and (b) African Easterly Wave origins with either predominantly westward tracks toward North America or recurver tracks in the central Atlantic.

(a) Baroclinic-influenced formations

*Subtropical formation locations*

Storm	May	June	July
Alberto (AL01)	Miss	–	–
Beryl (AL02)	Miss	–	–
Chris (AL03)	Miss	Miss	Miss
Debby (AL04)	Hit*	Miss	Miss
Gordon (AL08)	Hit*	Miss	Miss
Michael (AL13)	Miss	Miss	Miss
Patty (AL16)	Miss	Miss	Miss

*Low-latitude formation locations*

Storm	May	June	July
Rafael (AL17)	Miss	Miss	Miss
Sandy (AL18)	Miss	Hit*	Hit*
Tony (AL19)	Miss	Miss	Miss

\*Only first few days

(b) African Easterly Wave origins

*Predominantly westward tracks*

Storm	May	June	July
Ernesto (AL05)	Hit	Hit	Miss
Florence (AL06)	Hit	Hit	Hit
Helene (AL07)	Hit	Hit	Hit
Isaac (AL09)	Hit	Hit	Hit
Joyce (AL10)	Hit	Hit	Hit

*Recurvature tracks central Atlantic*

Storm	May	June	July
Kirk (AL11)	Hit	Hit	Hit
Leslie (AL12)	Hit	Hit	Hit
Nadine (AL14)	Hit	Hit	Hit
Oscar (AL15)	Hit	Hit	Hit

cyclones in the Atlantic, the track types associated with the baroclinic-influenced storms [ten of 19, Table 10.2(a)] must also be predicted. This failure in prediction for both the extended-range (Fig. 10.2) and the seasonal (Table 10.2) forecasts by the ECMWF illustrates a

fundamental dynamical challenge for predicting Atlantic tropical cyclone events.

## 10.5 Seasonal forecasts for western North Pacific tropical cyclone events

A similar evaluation was made of the ECMWF ensemble seasonal forecasts from 1 May, 1 June, and 1 July for the western North Pacific storms according to the JTWC (Fig. 10.4). With three exceptions, the performance in the western North Pacific is far superior to the Atlantic in terms of the LHV for all three forecasts. Indeed, these LHV are of the same magnitude as the LHV for the extended-range forecasts in Tsai *et al.* (2013), which indicates that nearly all of the JTWC storms can be matched with an ECMWF ensemble storm track within the time thresholds. While this is in part due to the ECMWF ensemble model being over-active in predicting tropical cyclone-like vortices, it does mean that formations and subsequent tracks are being predicted close in time and space to actual storms, which is quite different from the seasonal forecasts in the Atlantic (Chapter 10.4).

The exceptions to this excellent result were: (i) WP03, which was an early season storm that started near 10°N, 147°E and, although it had a classical recurver track, dissipated at 30°N, 150°E; (ii) Tropical Storm Kirogi (WP13), which was a baroclinic-influenced system that began near 23°N, 163°E and moved northward; and (iii) WP25, which was a late season Tropical Depression in the South China Sea that lasted about one day. Thus, these three storms had some of the same characteristics (early or late season, baroclinic-influenced) as in the Atlantic, but were generally weak and thus not a serious limitation.

While this analysis was for a single season, the similarity of the ECMWF ensemble forecast performance for the extended range and the seasonal range in the western North Pacific is very encouraging. That is, even the distribution

of numbers among the three basic track types (westward, northwestward, and recurving) of tropical cyclone events may be predictable in the western North Pacific with an appropriate calibration procedure.

## 10.6 Concluding remarks

While there are many challenges in tropical cyclone forecasting, this chapter has focused on the opportunities for extended-range and dynamical model predictions using the ECMWF ensembles as examples. Both the ECMWF 32-day ensemble and seasonal forecasts provide useful information of the western North Pacific tropical cyclone events, which are defined here to be both the formations and the subsequent tracks. Because the large-scale environmental conditions must be favorable over a relatively large area for a circulation to have the space and the time to become a typhoon, the ECMWF models must have skill in predicting the favorable environmental conditions for tropical cyclone formation. If these anomalous conditions do exist over large areas, it follows that the tracks of the pre-tropical cyclone seedlings that become strong tropical storms or typhoons may also be predicted, since the first-order effect in tropical cyclone motion is the environmental flow. Especially in the western North Pacific, the tropical cyclone activity is strongly modulated by the Madden–Julian Oscillation (MJO), and Vitart *et al.* (2009) has demonstrated that the ECMWF ensemble has skill in predicting the MJO. While the actual formation time and location may have limited predictability due to the critical role of convective-scale processes, the tracks in the tropics may be quite predictable until significant interactions with mid-latitude troughs and ridges become important. For western North Pacific tropical cyclone events, the ECMWF ensemble models must be correctly resolving the large-scale components of the Asian monsoon that extend eastward over

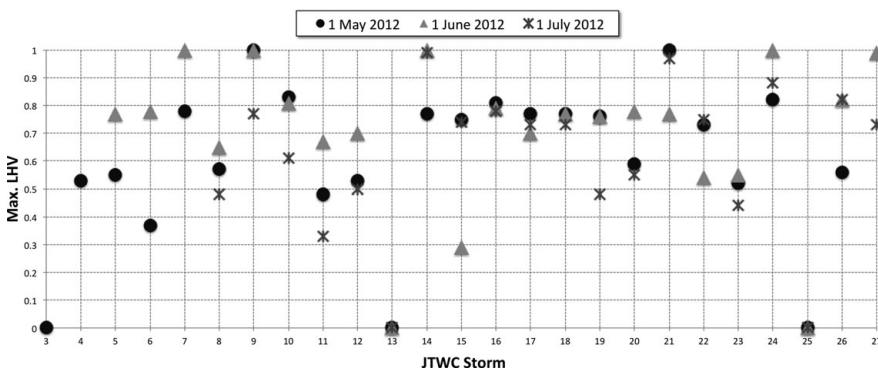


Fig. 10.4. Quality measure likelihood values (LHV) as in Fig. 10.2, except for the performance by the ECMWF seasonal tropical cyclone forecasts in the western North Pacific from 1 May, 1 June, and 1 July 2012. Note that Tropical Storm Kirogi (WP13) and Tropical Depression 25 are not predicted in any of the 1 May, 1 June, and 1 July ECMWF seasonal forecasts.

the formation areas. In addition, the intraseasonal and seasonal variations of the monsoon circulation must also be predicted by the ECMWF ensemble model, because the shifts in the monsoon trough (e.g. westward shift during La Niña; Tsai and Elsberry 2013) are critical for tropical cyclone formation. Another important factor is the large areal extent of warm water over which formation is possible in the western North Pacific.

As diagnosed from the analyses of the ECMWF ensemble model performance in the Atlantic during 2012, the critical reason for the limited predictability on both the extended range and the seasonal range is the considerable fraction of tropical cyclone events that are baroclinic influenced. Belanger *et al.* (2010) have demonstrated the ECMWF 32-day ensemble has skill relative to climatology in predicting levels of tropical cyclone activity in the main development region and Gulf of Mexico, with some sensitivity to the phase and amplitude of the MJO. While this activity forecast success in the main development region is related to the AEW cases in Table 10.2(b), the implication is that they also did not find skill for the baroclinic-influenced events such as in Table 10.2(a). With the different dynamics and characteristics of the formations and tracks of these baroclinic-influenced events versus the AEW-type events [Table 10.2(b)], the predictability is more limited in the Atlantic because of the important role of the mid-latitude troughs and ridges interacting with the tropical cyclones. By contrast, the fraction of baroclinic-influenced tropical cyclones is much smaller in the western North Pacific.

## 10.7 Acknowledgments

The contributions of colleague Mary Jordan are gratefully acknowledged. Long-term support from the Office of Naval Research has been critical for this research. The ECMWF, with special acknowledgment to Dr. Frederic Vitart, has been most helpful in providing their forecasts. Mrs. Penny Jones provided excellent support in preparing the manuscript.

## References

- Belanger, J. I., Curry, J. A., and Webster, P. J. (2010). Predictability of North Atlantic tropical cyclone activity on intraseasonal timescales. *Monthly Weather Review*, **138**, 4362–4374.
- Camargo, S. J., Barnston, A. G., Klotzbach, P. J., and Landsea, C. W. (2007). Seasonal tropical cyclone forecasts. *WMO Bull.*, **56**, 297–309.
- Elsberry, R. L. (2007). Advances in tropical cyclone motion prediction and recommendations for the future. *World Meteorological Organization Bulletin*, **56**, 131–135.
- Elsberry, R. L., and P. A. Harr, 2008: Tropical Cyclone Structure (TCS08) field experiment: Science basis, observational platforms, and strategy. *Asian Pacific Journal of Atmospheric Science*, **44**, 209–231.
- Elsberry, R. L., Jordan, M. S., and Vitart, F. (2010). Predictability of tropical cyclone events on intraseasonal timescales with the ECMWF monthly forecast model. *Asia-Pacific Journal of Atmospheric Sciences*, **46**, 135–153.
- Elsberry, R. L., Jordan, M. S., and Vitart, F. (2011). Evaluation of the ECMWF 32-day ensemble predictions during 2009 season of western North Pacific tropical cyclone events on intraseasonal timescales. *Asia-Pacific Journal of Atmospheric Sciences*, **47**, 305–318.
- Elsberry, R. L., Tsai, H.-C., and Jordan, M. S. (2014). Extended-range forecasts of Atlantic tropical cyclone events during 2012 using the ECMWF 32-day ensemble predictions. *Weather and Forecasting*, **29**, 271–288.
- Tsai, H.-C. and Elsberry, R. L. (2013). Opportunities and challenges for extended-range predictions of tropical cyclone impacts on hydrological predictions. *Journal Hydrology*, **506**, 42–54, doi:10.1016/j.jhydrol.2012.12.025.
- Tsai, H.-C., Elsberry, R. L., and Jordan, M. S. (2013). Objective verifications and false alarm analyses of western North Pacific tropical cyclone event forecasts by the ECMWF 32-day ensemble. *Asia-Pacific Journal of Atmospheric Sciences*, **49**, doi:10.1007/s13143-013-0038-6.
- Vitart, F., (2009). Impact of the Madden-Julian Oscillation on tropical storms and risk of landfall in the ECMWF 32-day ensemble. *Geophysical Research Letters*, **36**, L15802, doi: 10:1029/2009GL035089.
- Vitart, F., Prates, F., Bonet, A., and Sahin, C. (2012). New tropical cyclone products on the web. *European Centre Medium-range Weather Forecasts Newsletter*, No. 130, 17–23.

# 11

## Predictability of severe weather and tropical cyclones at the mesoscales

Fuqing Zhang, Christopher Melhauser, Dandan Tao,  
Y. Qiang Sun, Erin B. Munsell, Yonghui Weng,  
and Jason A. Sippel

### 11.1 Introduction

Atmospheric predictability may be loosely defined as the limited length of time when a meaningful prediction of a future atmospheric state becomes indistinguishable from an educated random guess or climatology. There are two types of predictability problems: (1) intrinsic predictability refers to the limit of prediction if the initial state is known nearly perfectly with a nearly perfect forecast model (Lorenz, 1969), and (2) practical predictability refers to the limit on atmospheric prediction using the current optimal analysis procedures to derive the initial state with the best available atmospheric forecast model (Lorenz, 1982, 1996). Practical predictability is limited by realistic uncertainties in the forecast model and initial conditions. These uncertainties can include the adequacy of observations (i.e. accuracy, spatial and temporal coverage, and usability), data assimilation procedures, and deficiencies in the forecast models (Lorenz, 1996, Zhang *et al.*, 2006, Melhauser and Zhang, 2012). Given the chaotic nature of the atmosphere, there will be a finite intrinsic limit of predictability (as in any chaotic dynamic system) even if the initial condition and forecast model are nearly perfect.

Using an idealized toy model to represent atmospheric convection, Edward Lorenz set the foundation for chaos theory and the study of atmospheric predictability, discovering that small errors in the initial states grow rapidly causing the modeled solutions to diverge (Lorenz, 1963, 1969). In his pioneering 1963 publication *Deterministic Nonperiodic Flow*, Lorenz concluded that the atmosphere may have an inevitable limit to predictability, stating: *...prediction of the sufficiently distant future is impossible by any method, unless the present conditions are known exactly. In view of the inevitable inaccuracy and incompleteness of weather observations, precise very-long range forecasting would seem to be non-existent* (Lorenz, 1963). Furthermore, in his subsequent 1969 paper, he conjectured: *'An error in observing a thunderstorm, after doubling perhaps every fifteen minutes until it becomes large, may subsequently lead*

*to an error in a larger scale of motion, which may then proceed to double every five days. If this is the case, cutting the original error in half would increase the range of predictability of the larger scale not by five days but by only fifteen minutes'* (Lorenz, 1969).

Although the synoptic-scale evolution of the typical mid-latitude weather system is relatively well forecasted, numerical weather-prediction models still have difficulties in forecasting the ‘mesoscale details’, often in the form of severe and convective weathers, which are of most concern to the typical user of the forecast. It is of great interest to assess the predictability of these mesoscale severe weather systems, whether the predictability limit is a few tens of hours or several days, particularly with respect to the amount and spatial distribution of the associated precipitation (Zhang *et al.*, 2007). This chapter summarizes some of our recent research on the flow-dependent predictability of severe weather phenomena at the mesoscales which include (1) a winter snowstorm and mid-latitude moist baroclinic waves, (2) warm-season mesoscale convective systems and heavy precipitation, and (3) tropical cyclones. Special attention will be given to the dynamical processes that control the different mesoscale predictability behaviour, through examination of how different background time-mean flows modulate the error-growth characteristics in idealized and/or actual numerical forecasts.

### 11.2 Mesoscale predictability of mid-latitude winter snowstorms and moist baroclinic waves

The mesoscale predictability of precipitation forecasts of cold season weather events with strong baroclinic instability has been the focus of many recent studies (e.g. Langland *et al.*, 2002, Zhang *et al.*, 2002, 2003, Zhang, 2005). These studies are exemplified by the surprise snowstorm of 24–25 January 2000, which brought heavy

snowfalls from the Carolinas through the Washington D.C. area and up into New England, which was poorly predicted by the then-operational forecast models, even within 1–2 days' lead-time. The forecasts of the surface cyclone that developed off the southeastern seaboard had small position and sea-level pressure errors, but had large precipitation forecast errors in both spatial coverage and accumulation.

With regard to the practical predictability of this storm, Zhang *et al.* (2002) showed that there is large sensitivity of precipitation forecasts to model grid resolution and initial conditions used to generate the deterministic forecasts. Insufficient model grid resolution and inaccurate physics parameterizations (both are model errors), and uncertainties in the initial conditions may have contributed significantly to the poor precipitation forecasts by operational prediction models. The precipitation forecast quality is systematically degraded with decreasing model grid resolution; moist processes are explicitly modeled with microphysical parameterizations at finer grid resolution. Errors in the initial conditions of the operational analysis significantly impact precipitation forecasts; omitting even a single sounding when generating the analysis can greatly impact the mesoscale distribution of precipitation. In the meantime, it is also shown that lateral boundary conditions may also be a significant source of forecast uncertainty for limited area numerical weather prediction models, which could have contributed to the limited practical predictability of this snowstorm (Zhang *et al.*, 2002, Zhang, 2005).

Nevertheless, prediction of this winter snowstorm with regard to exact location and intensity of the precipitation is further found to be hard, even within 1–2 days' lead-time and with a nearly perfect model and nearly perfect initial conditions; a clear indication that prediction of this event may be approaching the limit of intrinsic predictability (Zhang *et al.* 2003). In spite of a reasonable control simulation (Cnlt-30km) of the winter cyclone and associated precipitation by a deterministic convection-permitting limited-area NWP model, a perturbed forecast (Pert-30km), by adding small-scale small amplitude initial condition errors, may quickly diverge from the control simulations due to rapid error growth in the presence of moist convection. At finer resolution (Cnlt-3.3km and Pert-3.3km), the small-scale errors start as differences in the timing and position of individual convective cells in the first few hours. These errors grow quickly in scale and amplitude and begin to change the mesoscale organization of the convective rainbands in 12 hours or so. By 30–36 hours, the centres of the sub-synoptic scale cyclones in these two 'identical twin' simulations can be dislocated by as much as 150 km, while the locations and organization of some precipitation bands differ greatly (Fig. 11.1). It is evident that moist processes are the key drivers of the initial rapid small-scale error growth, that may ultimately limit the

predictability of the winter snowstorm at the mesoscales. The upper-scale error growth dynamics through a moist process is evident in the power spectrum of difference total energy (DTE) between the control and perturbed simulations (Fig. 11.2). The small-scale initial error quickly saturated at scales below 100 km within 3–6 h. By 12–18 h, the spectral peak of error shifts to around 300–500 km in near saturation, while by 36 h, the largest error amplitude is at scales greater than 1000 km (in the range of meso-alpha or sub-synoptic scales).

Zhang *et al.* (2003) found that similar error growth also occurs in coarser resolution simulations with parameterized convection. However, the error growth in finer resolution experiments grows more rapidly and increases in maximum amplitude (saturates) more quickly than their coarser resolution simulation. As the amplitude of small-scale errors decreases, the rate of error growth increases, thus saturating the convective scale more rapidly, implying a diminishing return for reducing the error in the initial forecast analysis. At coarser resolution, initial error growth is associated with nonlinearities in the convective parameterization; while for convection permitting simulations, it is the explicit microphysics scheme, since cumulus parameterization is not included.

The structure and evolution of mesoscale error covariance for the winter snowstorm show initial small-scale uncorrelated, unbalanced errors imposed on the initial conditions grow rapidly into quasi-balanced, structured disturbances within 12–24 h; a spatial correlation between the same (auto covariance) and different variables (cross-covariance) is found across all vertical levels and at horizontal distances up to 1000 km (Zhang 2005). Moist processes modify both the mean dynamics and underlying forecast uncertainty of winter snowstorm. Both the underlying balanced dynamics and moist processes govern the error structure of the error covariance. The spatial regions of largest error growth and reduced predictability are found in the vicinity of upper-level, surface fronts and areas of moist convection.

Findings on the impact of moist convection on mesoscale predictability of this winter snowstorm were generalized through understanding the error growth in an idealized baroclinic wave amplifying in a conditionally unstable atmosphere (Tan *et al.*, 2004, Zhang *et al.*, 2007, Sun and Zhang, 2014). Initial perturbations of different scales and amplitudes are added to the idealized model and their growth dynamics are studied. Our results show that, for large-scale baroclinically unstable initial perturbations, the error growth is dictated by the growth rate of the large-scale background baroclinic instability, with a strong sensitivity to the amplitude of the large-scale initial perturbation. This type of error can grow without the help of moisture. Whereas for small-scale random initial perturbations, there is little error growth in the short term (0–36 h, starting from

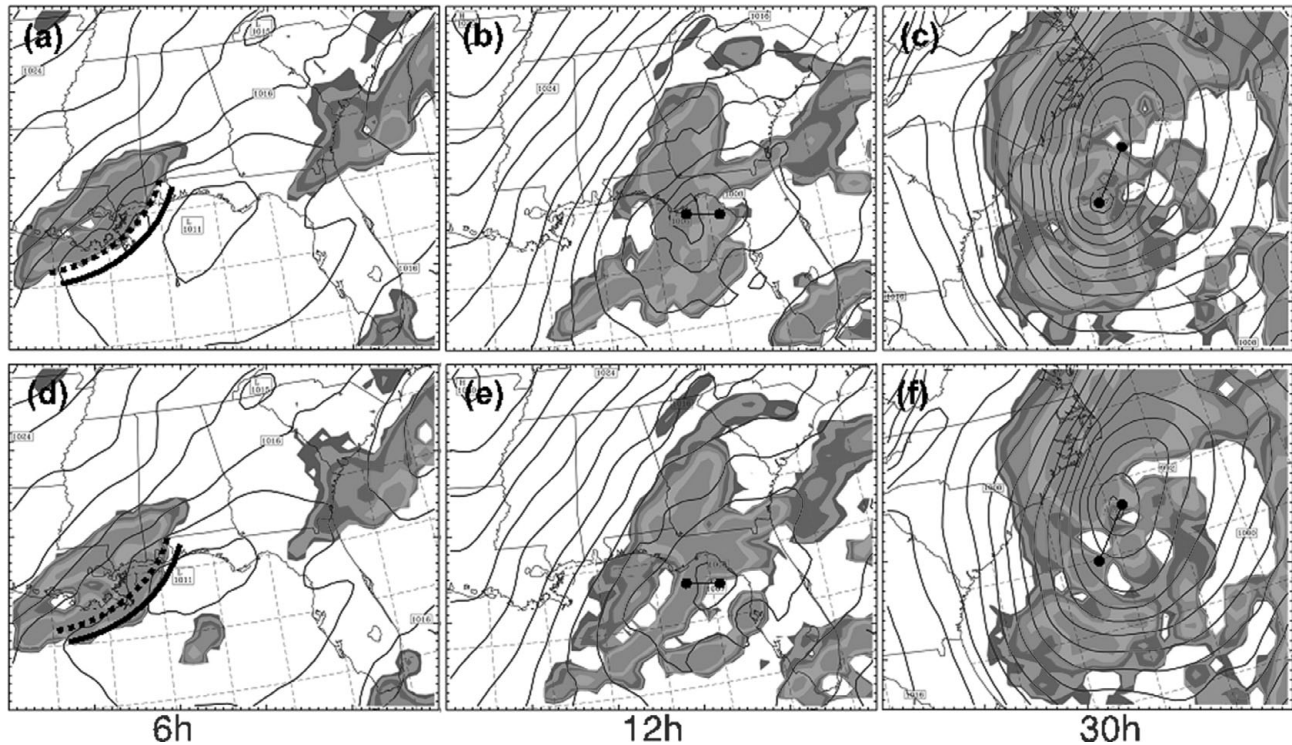


Fig. 11.1. Comparison of mean sea level pressure (contour interval 4 hPa) and simulated reflectivity (dBZ, coloured) on the 30 km grid for Cntl-3.3km and Pert-3.3km. Simulations are shown at (a), (d) 6 h, (b), (e) 12 h, and (c), (f) 30 h. Thick curves in (a) and (b) denote the relative locations of the convective outflow boundary in Cntl-3.3km (dashed) and Pert-3.3km (solid). The dots in (b), (c), (e), and (f) denote the locations of the primarily surface cyclone centres in Cntl-3.3km and Pert-3.3km. Adapted from Figure 12 of Zhang *et al.* (2003). A black and white version of this figure will appear in some formats. [For the colour version, please refer to Plate 20.](#)

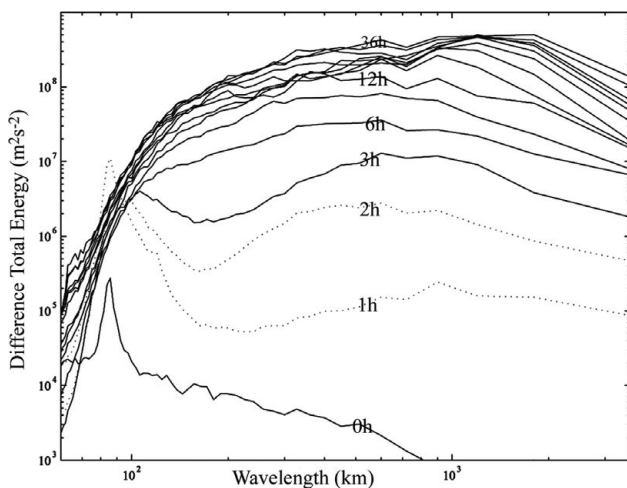


Fig. 11.2. Power spectra of the DTE (in  $m^2 s^{-2}$ ) between Cntl-3.3km and Pert-3.3km on the 30 km grid, and showing spectra after 1 and 2 h of simulation (dotted lines). Adapted from Figure 10 of Zhang *et al.* (2003).

minute amplitude random noise) without moisture, even though the basic jet used here produces a rapidly growing synoptic-scale disturbance. With the effect of moisture, the small-scale initial error is characterized by upscale growth, similar to that found in the study of the numerical prediction of the winter snowstorm.

Through analysing error growth between convection-permitting ‘identical-twin’ experiments with model grid increments down to 3.3 km, Zhang *et al.* (2007) proposed a three-stage error growth conceptual model: (1) *the initial convective growth stage*, which begins with convective instability followed by rapid error saturation, (2) *the intermediate adjustment stage* during which small-scale error projects to balanced field, and (3) *the large-scale growth stage* where error grows with larger-scale baroclinic instability (Fig. 11.3). The *initial convective growth stage* occurs 0–6 h after initialization, with errors growing from small-scale convective instabilities, quickly saturating the convective scales. In the *intermediate adjustment stage*, 3–18 h after initialization, the errors change from the

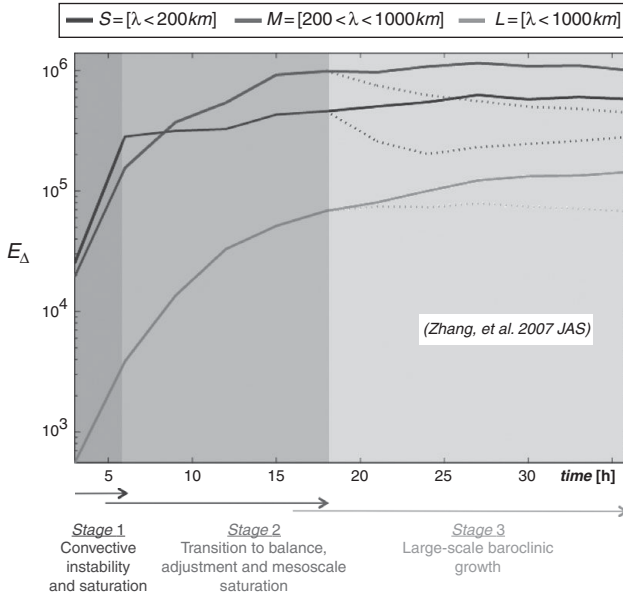


Fig. 11.3. Evolution of the domain-integrated difference total energy ( $E_\Delta, m^2 s^{-2}$ ) at three different characteristics scales (S: smaller scale  $L < 200$  km; M: intermediate scale  $200 < L < 1000$  km; and L: larger scale  $L > 1000$  km), between CNTL-D3 and CNTL-D3P (solid curves) and between CNTLfd-D3 and CNTLfd-D3P (dotted curves). Adapted from Figure 7 of Zhang *et al.* (2007). A black and white version of this figure will appear in some formats. For the colour version, please refer to Plate 19.

unbalanced convective-scale motions to more large-scale, balanced motions through differences in diabatic heating from moist processes. These errors grow upscale through geostrophic adjustment and/or cold pool dynamics. In the *large-scale growth stage*, beyond 12 h, errors from the intermediate stage retained in the balanced motion subsequently grow with the large-scale baroclinic instability. Through examination of the error-energy (difference kinetic energy, DKE) budget in the two control experiments (results from domain 3 of the original initial condition (CNTL-D3) and perturbed initial condition (CNTL-D3P)), it is found that buoyancy production due mostly to moist convection is comparable to shear production (nonlinear velocity advection, Fig. 11.4). While turning off latent heating (CNTLfd-D3 and CNTLfd-D3P respectively) will not only dramatically decrease buoyancy production, but also reduces shear production to less than 20% of its original amplitude (Fig. 11.4).

### 11.3 Mesoscale predictability of warm season severe weather events

Generally, warm season precipitation forecasts remain the element with the largest error at all scales. In contrast to

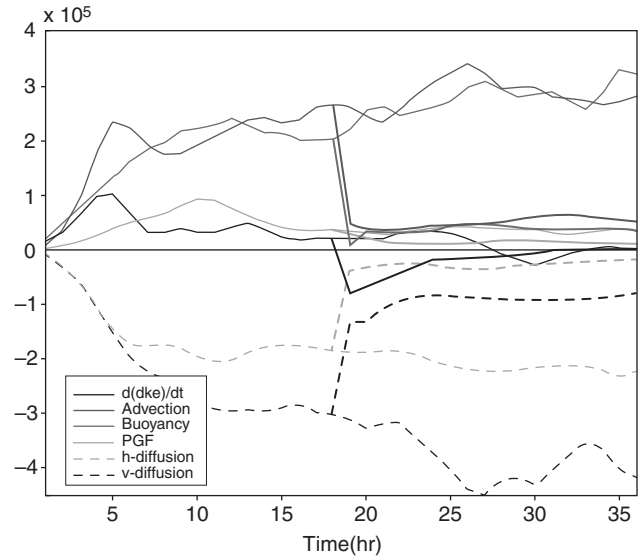


Fig. 11.4. Time evolution of the DKE tendency and each of the source/sink terms ( $J m^{-2} s^{-1}$ ) estimated with the 10 km grid hourly outputs from CNTL-D3 and CNTL-D3P (solid) and from CNTLfd-D3 and CNTLfd-D3P (dashed). Adapted from Figure 14 of Zhang *et al.* (2007). A black and white version of this figure will appear in some formats. For the colour version, please refer to Plate 20.

cold season weather events, which have much stronger baroclinic instability, warm season weather is typically dominated by strong convective instability with much weaker baroclinic instability. Convective instability drives error growth at smaller scales through moist processes, while baroclinic instability may better facilitate the upscale error growth from smaller to larger scales. Here we summarize some of our recent studies on the mesoscale predictability of several warm season severe weather events over both China and North America.

In China, heavy warm season precipitation along the Mei-Yu front can cause extreme flooding along the Yangtze River basin. The Mei-Yu front is generally characterized by strong gradients of moisture, weak gradients of temperature, and is typically very shallow compared to their mid-latitude frontal system counterparts. Examining a heavy precipitation event along this front, Bei and Zhang (2007) found a strong sensitivity in precipitation forecasts using realistic and idealized initial condition uncertainties with different scales and amplitudes. Errors in the initial conditions with different scales and decreasing amplitude by scale (large scale  $> 1200$  km (T106L); small scale  $< 300$  km (T106S); medium scale in between (T106M)) cause systematic differences in accumulated precipitation; Fig. 11.5 highlights the dislocation and magnitude (differences) of forecast rainfall. Their spectral analysis,

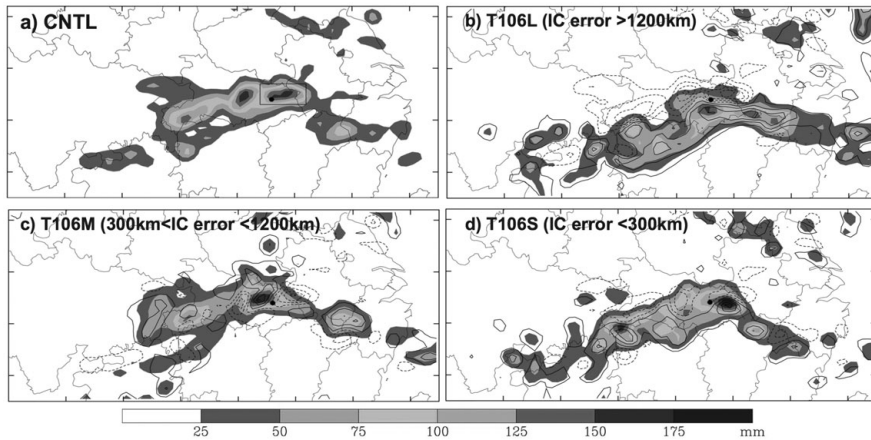


Fig. 11.5. The simulated 24 h accumulated precipitation (mm, shaded) from 12:00 UTC 20 to 12:00 UTC 21 July 1998 by experiments (a) control (CNTL), (b) large-scale error (T106L), (c) medium-scale error (T106M), and (d) small-scale error (T106S) plotted on the 30 km domain (D1) and the corresponding difference from CNTL (contoured every 30 mm). Adapted from Figure 5 of Bei and Zhang (2007). A black and white version of this figure will appear in some formats. For the colour version, please refer to Plate 21.

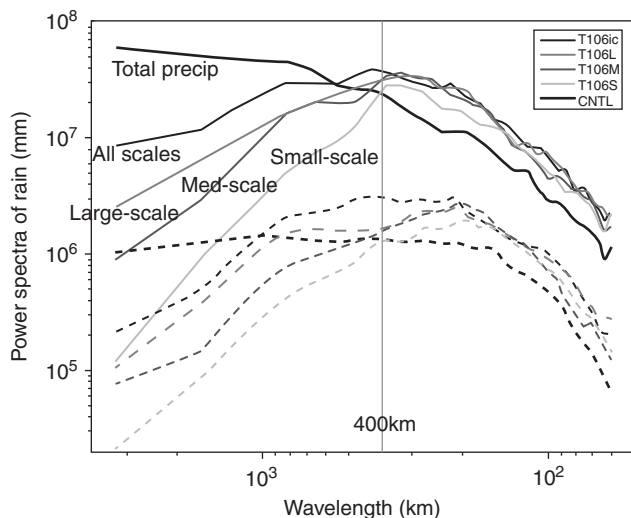


Fig. 11.6. Power spectra of the 3 h (dash) and 24 h (solid) accumulated precipitation difference ( $\text{mm}^2$ ) between control experiment (CNTL) and the four experiments of different initial data source (T106ic), large-scale error (T106L), medium-scale error (T106M), and small-scale error (T106S), valid at the 24 h and 36 h forecast times, respectively. Adapted from Figure 9(c) of Bei and Zhang (2007). A black and white version of this figure will appear in some formats. For the colour version, please refer to Plate 21.

reproduced in Fig. 11.6, of the 3 h (24 h) accumulated precipitation difference between the control and the scale perturbation experiments valid at a 24 h (36 h) lead-time both peak at  $\sim 400$  km and saturate at smaller scales. In terms of daily accumulated precipitation forecasts, the error energy of the 24 h accumulated precipitation differences valid at 36 h were larger than the total precipitation spectrum of CNTL at scales  $< 400$  km, indicating a complete loss of predictability at smaller scales. A clear

separation in sensitivity experiments can be seen between those at larger scales and the difference energy is less than the total precipitation spectrum of CNTL, implying prediction is still possible. Overall, if initial uncertainties in a model analysis are large, a reduction of initial errors at the larger errors can improve warm season precipitation forecasts, predominantly at the larger scales; but reducing the initial errors at the smaller scales does not significantly impact precipitation forecasts at any scale.

In the study of mesoscale predictability of a warm season extreme rainfall event over central Texas of the United States, Zhang *et al.* (2006) found that the accuracy of precipitation forecasts can be heavily impacted by both initial condition and model error. In particular, small-scale, small amplitude errors in the initial analysis combined with model error generated by varying model physical parameterizations resulted in large precipitation forecast errors. In contrast with cold season events, fine resolution forecasts did not perform better than coarse resolution forecasts of precipitation. Increased error growth at smaller scales is found in the fine resolution forecasts, spreading to a much broader area by 12 h compared with coarse simulations. Additionally, the substantial differences in precipitation forecasts by varying parameterization schemes indicate that there is room to improve precipitation forecasting through better resolved or better parameterized physical processes.

Another case study, by Hawblitzel *et al.* (2007), examining the predictability and dynamics of a mesoscale convective vortex (MCV) that developed over the southwest United States, found that moist processes played a critical role in the development, evolution, and predictability of the MCV. Applying small amplitude, large-scale balanced initial perturbations to an ensemble of coarse (30 km) and convection-permitting model grid resolutions (10 km), a wide variety of solutions ensued, ranging from ensemble members that developed a strong MCV to no MCV

development. Moist convection near the centre of the MCV occurred a day after formation and produced a stronger mid-level vortex, which is more conducive for subsequent convective development and moist processes. The slight perturbations in the initial conditions and spread of the ensuing simulations highlights the extreme sensitivity of warm season MCV formation to preceding moist convective events.

Most recently, Melhauser and Zhang (2012) examined a warm season mesoscale convective system (MCS) through ensemble sensitivity analysis, which found extreme forecast sensitivity to the initial condition uncertainties. The spread in the initial conditions of the ensemble was representative of the realistic uncertainty in the then-operational analysis. A strong divergence of solutions was found with some members developing bowing MCSs, while others did not produce organized systems. The divergence in solutions was traced to the evolution of cold pools from convection that propagated into a favourable environment for MCS development. The developing members had stronger cold pools, triggering strong convective development and upscale storm growth, while non-developing members had weaker cold pools that dissipated before triggering additional convection. The differences in upstream moist processes caused evolutionary strength and spatial displacements of cold pools, which impacted the subsequent convective development of the MCS system.

Focusing on the intrinsic predictability, the study created a set of reduced initial uncertainty simulations by linearly averaging the initial conditions between averages of members that produced an MCS and those that did not produce an MCS, effectively isolating the flow regimes inherent in the ensemble (Fig. 11.7). The reduced uncertainty of initial condition differences between the simulations were up to an order of magnitude smaller than the then-operational analysis error. The resulting analysis of the simulations showed a clear bifurcation between the two flow regimes by 12–18 h, as denoted by the red circles in Fig. 11.7; a bifurcation point exists when development (no development) occurred for simulations when slightly greater weight was given to the ‘developing’ (‘non-developing’) initial conditions. This alludes to the concept that no matter how much the initial condition error is reduced, the prediction of this type of weather event may be intrinsically limited.

#### 11.4 Mesoscale predictability of tropical cyclones

Although some aspects of tropical cyclone forecasts have improved considerably over the past decade, they are still plagued by significant errors, especially in terms of intensity changes. In addition, forecasting genesis remains a

challenge, and predictions of rapid intensification (RI) and decay remain particularly problematic. Fortunately, increasing computational power allows more simulations for tropical cyclone cases as an ensemble, which is better for both operational forecasting and scientific research.

A recent study by Sippel and Zhang (2008) showed that the rate of intensification of a 2004 Gulf of Mexico disturbance in an ensemble MM5 forecast depended on the amount of initial convective instability (MUCAPE) and deep moisture in the ensemble. MUCAPE was related to the strength of surrounding quasi-geostrophic lift, and along with mid-level moisture it modulated convective intensity during the first 6–12 h. Differences in convection resulted in quicker genesis in some ensemble members than others. Thus, these factors were the primary source for ensemble spread by 12 h, and spread was thereafter amplified by differences in convection related to oceanic heat fluxes. Eventually the wind-induced surface heat exchange (WISHE) mechanism resulted in even larger ensemble spread.

A follow-up investigation in Zhang and Sippel (2009) used several of the above ensemble members to examine the sensitivity of genesis to minute changes in initial conditions, as highlighted in Fig. 11.8 for simulations with convection-permitting grid spacing (3.3 km) or coarse resolution (30 km). Much of the extreme forecast uncertainty was the result of how initial convection responded to differences in the environment. The amount of convection early in the simulations, which was modulated by the initial convective instability, was instrumental in forming a deep vortex. Also, widespread cold convective down-drafts that formed during the convection subsequently damped convective activity, in a period that neither growth nor decay of the storm-scale vortices was seen. After the boundary layer recovered, convection reigned and stronger storm-scale vortices strengthened more quickly. Randomness in the details of small-scale convection may lead to differences in inner core organization and subsequent organization/growth to larger scales. Thus, the route to cyclogenesis can depend significantly on the same small initial condition differences. This result is due to chaotic interactions of convective and mesoscale features, whose timing and placement vary significantly with slight initial differences. Initial differences can therefore more easily explain differences in simulated area-average quantities (such as average wind speed) than absolute quantities (such as maximum wind speed), implying that often-used absolute metrics of hurricane intensity have much more limited predictability.

A more recent study of Sippel and Zhang (2010) investigated Hurricane Humberto (2007), which is known for its extreme unpredictability. As with the Gulf of Mexico low, deep moisture and MUCAPE again modulated the intensity of convection, which governed the rate of

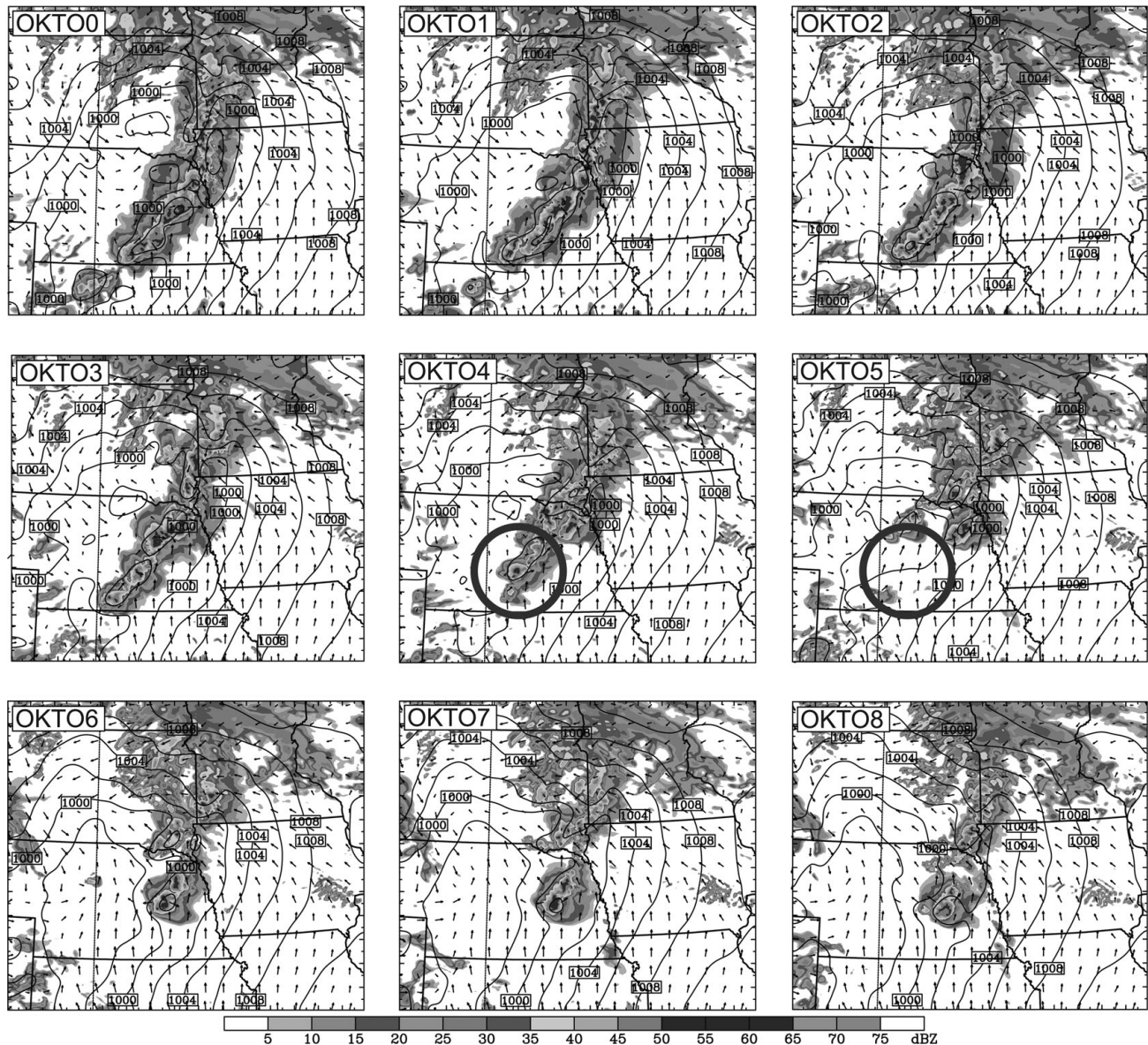


Fig. 11.7. Simulated radar reflectivity (shaded every 5 dBZ), sea level pressure (contoured every 2 hPa), and surface wind vectors for linearly averaged sensitivity forecasts (OKTO0 is the simulation with the developing initial condition, while OKTO8 is the simulation with the non-developing initial condition. OKTO1–OKTO7 are in between.) at 0400 UTC 10 Jun. The red circles denote the area of strong forecast divergence. Adapted from Figure 11 of Melhauser and Zhang (2012). A black and white version of this figure will appear in some formats. For the colour version, please refer to Plate 22.

intensification. With Humberto, much of the moisture and MUCAPE variance were related to the proximity and strength of a nearby surface front, and thus varying degrees of interaction between the developing cyclone and the front ultimately caused much of the ensemble spread. Once again, strength-dependent heat fluxes and WISHE also acted to increase existing ensemble spread. In addition, ensemble members made landfall at different times, which drove spread even higher.

Munsell *et al.* (2013) examined the predictability of Tropical Storm Erika (2009) by analysing a 60-member convection-permitting ensemble initialized with perturbations from a real-time ensemble Kalman filter (EnKF) system. Erika was forecast to intensify into a hurricane by most operational numerical models, but in reality its intensity never exceeded 50 kts. There is a fairly large spread in the final intensities of the 60 ensemble members, indicating large uncertainty in the deterministic prediction of Erika's

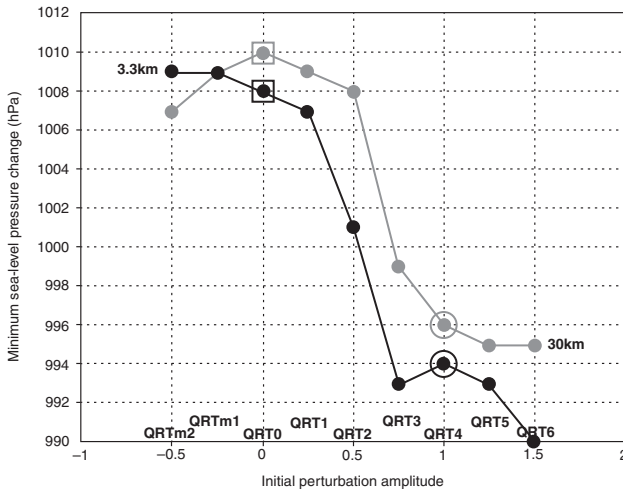


Fig. 11.8. Sensitivity of the 36 h minimum sea-level pressure to the initial-perturbation amplitude for the 30 km (grey) and 3.3 km (black) simulations, respectively. The x-axis depicts the initial perturbation magnitude scaled by the difference vector, which is the initial difference for all prognostic variables between QRT4 (circle) and QRT0 (square). Adapted from Figure 4 of Zhang and Sippel (2009).

intensity at 36–48 h lead-times. Through ensemble sensitivity and correlation analysis, it is found that the mid-level relative humidity, absolute vorticity, and the distribution of convection relative to the storm centre all play a role in determining whether or not a given ensemble member intensifies. In addition, although differences in deep-layer shear among ensemble members are difficult to discern, many of the ensemble members that do not intensify fail to do so because of apparent dry air intrusions that wrap around the centres of the storms, particularly in the 700–500 hPa layer. In the presence of moderate shear, this dry air is able to penetrate the core of the cyclone, thereby preventing further development.

Munsell and Zhang (2014) further utilized the Pennsylvania State University (PSU) real-time convection-permitting hurricane analysis and forecasting system (WRF-EnKF) that assimilates airborne Doppler radar observations to examine the predictability of Hurricane Sandy (2012), one of the costliest storms on record. The performance of the track and intensity forecasts of both the deterministic and ensemble forecasts by the PSU WRF-EnKF system show significant skill and are comparable to or better than forecasts produced by operational dynamical models, even at lead-times of 4–5 days prior to landfall (Fig. 11.9). Many of the ensemble members correctly capture the interaction of Sandy with an approaching mid-latitude trough, which precedes Sandy's forecasted landfall in the Mid-Atlantic region of the United States. However, the ensemble reveals considerable forecast uncertainties in the prediction of

Sandy. For example, in the ensemble forecast initialized four days prior to landfall, ten of the 60 members do not predict a United States landfall. Using ensemble composite and sensitivity analyses, the essential dynamics and initial condition uncertainties that lead to forecast divergence among the members in tracks and precipitation are examined. It is observed that uncertainties in the environmental steering flow are the most impactful factor on the divergence of Sandy's track forecasts, and its subsequent interaction with the approaching mid-latitude trough. Although the mid-latitude system does not strongly influence the final position of Sandy, differences in the timing and location of its interactions with Sandy lead to considerable differences in rainfall forecasts, especially with respect to heavy precipitation over land.

As stated in several of the above case studies and by others in literature, vertical wind shear can also have profound impacts on the predictability of tropical cyclones. The forecast of a TC is particularly problematic under shear conditions, not only because of the low predictability of the TC itself, but also the error from the environmental wind (Zhang and Tao, 2013, Tao and Zhang, 2014a,b). In idealized ensemble simulations, the simplified condition excludes the error from the environment in order to study the predictability of the TC vortex itself. The findings from the ensemble simulations using initial conditions with only very tiny initial moisture perturbations in the boundary layer, and the predictability of tropical cyclone intensity can be significantly influenced by the environmental vertical wind shear; in general, the larger the vertical wind shear, the larger the forecast uncertainty, especially during the rapid intensification stage (Fig. 11.10). In the presence of vertical wind shear, small-scale, small amplitude random initial noise may lead to changes in the onset and ending of rapid intensification by as much as 1–2 days.

It is the randomness of the convection that accumulates over time, leading to deviations in both the vortex tilt and strength, that contributes to further discrepancies in the development cycles of the different members. Before these systematic differences form, the random convection influences the TC circulation in such a way that small differences in the location and amount of the diabatic heating slightly alter the precessions of different members. The interruption of moist convection by the hostile shear during the precession brings in the possibility of further evolution, especially at downshear left quadrant where the tilt is the largest. The influence of the adverse environment can only happen when the TC is vulnerable (e.g. large tilt) and the TC could be near the point of bifurcation. Larger magnitudes of vertical wind shear lower the predictability of rapid intensification onset. From another aspect of combining the ensemble sets of small shear differences (e.g. 2 m/s), which can represent the possible shear error,

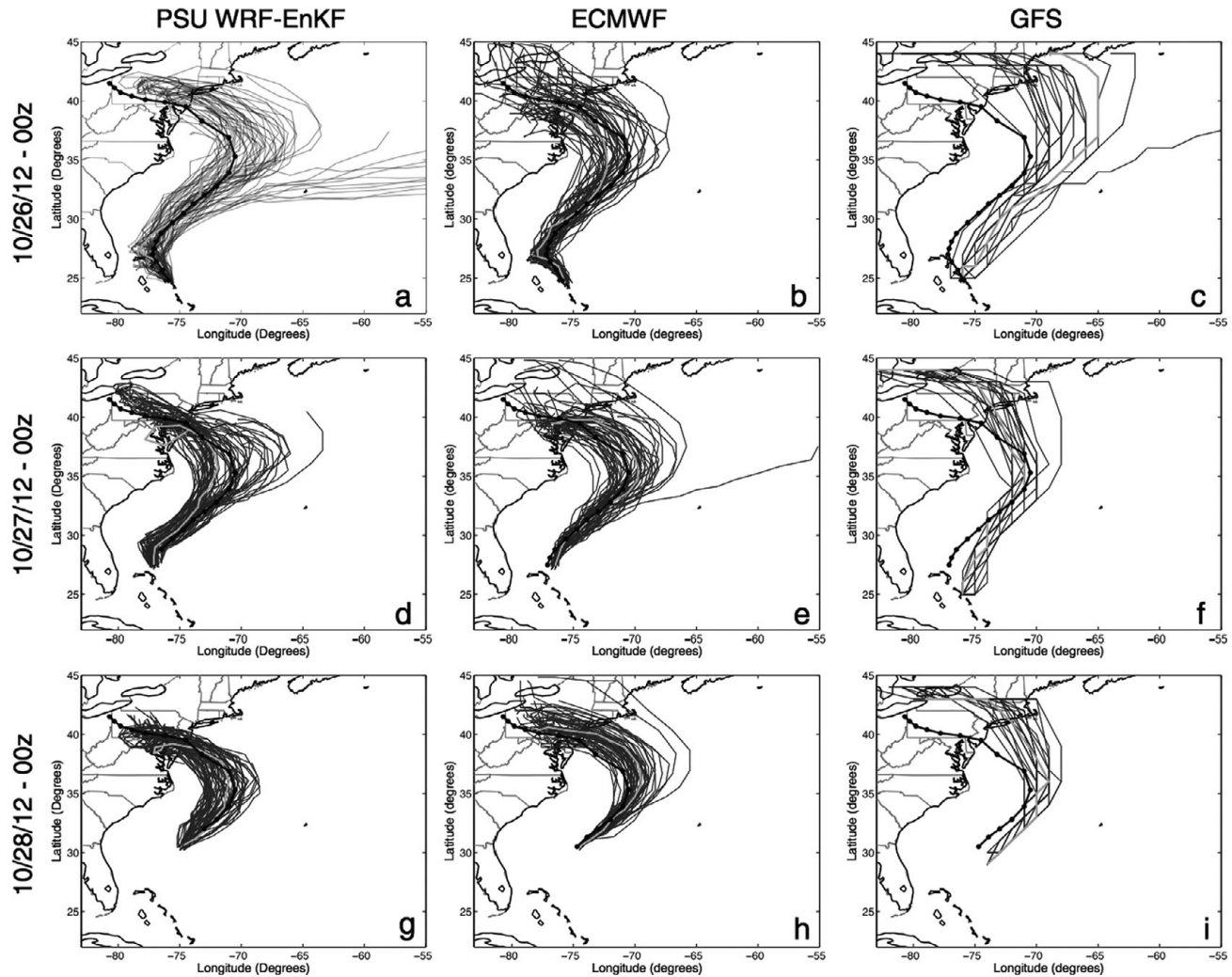


Fig. 11.9. Ensemble tracks (blue lines) for the PSU WRF-EnKF (first column), ECMWF (second column), and GFS (third column) forecasting systems for Hurricane Sandy initialized at (a–c) 0000 UTC 26 October 2012, (d–f) 0000 UTC 27 October 2012, and (g–i) 0000 UTC 28 October 2012. The three forecasting systems utilize 60, 50, and 20 ensemble members, respectively. The NHC best track for Hurricane Sandy is overlaid in black, with positions marked every 6 h and the deterministic runs are plotted in cyan. Adapted from Figure 1 of Munsell and Zhang (2014). A black and white version of this figure will appear in some formats. [For the colour version, please refer to Plate 23.](#)

the large uncertainty of the RI onset displays a big challenge for improving the TC predictability under the presence of vertical wind shear.

More sensitivity ensembles are done with increased SST. The higher SST condition leads to smaller tilt magnitudes and shortens RI onset times, under the same vertical wind shear conditions (Tao and Zhang, 2014a,b). This randomness is also present under this higher SST condition. However, the sea surface is the moisture and heat reservoir for the TC; higher SST conditions can produce a higher diabatic heating rate, which strengthens the vortex quickly enough to resist the effects of vertical wind shear. Because of the positive feedback between the diabatic

heating and the vortex mean circulation, much stronger heat forcing will shorten the precession process and reduce the impact that the randomness of the convection has on the RI onset time. This subsequently increases the predictability of RI onset under this higher SST condition. It is also observed that when environmental dry air is introduced into the simulation, whether or not the timing of RI of the TC is impacted is dependent on the shear magnitude. The spread of TC RI onset time under smaller shear magnitudes is not greatly influenced by a drier environment, while the predictability of TC RI onset under larger shear magnitude decreases significantly. Under the critical shear magnitude condition, the drier environment prevents

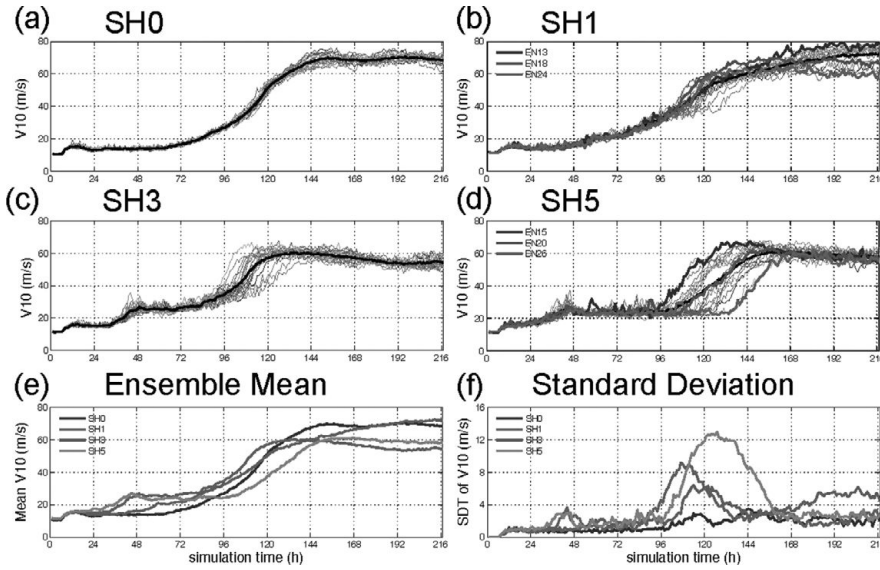


Fig. 11.10. Time evolution of the tropical cyclone intensity in terms of the 10 m maximum wind speed for all ensemble members of (a) SH0 (no background flow), (b) SH1 (1 m/s shear), (c) SH3 (3 m/s shear), (d) SH5 (5 m/s shear), along with (e) the ensemble mean and (f) the standard deviation (ensemble spread) from all ensemble experiments. The thick black lines in (a)–(d) denote the ensemble mean, while members EN13, EN18, and EN24 of SH1 in (b) and members EN15, EN20, and EN26 of SH5 in (d) are denoted as thick coloured lines. Adapted from Figure 2 of Zhang and Tao (2013). A black and white version of this figure will appear in some formats. For the colour version, please refer to Plate 23.

all of the members from developing. These environmental moisture sensitivity experiments reveal that the ensembles under larger shear conditions ingest more dry air into the updrafts and therefore need more time to precess as a result of a weaker secondary circulation, which suppresses the convergence of angular momentum and reduces the vortex strength. The ensembles under smaller shear conditions, that ingest less dry air into the updraft, experience a shorter precession process and therefore have higher predictability.

The strong sensitivity to initial condition differences in both real and ideal cases exemplifies the inherent uncertainties in hurricane intensity prediction, where moist convection is the key that limits predictability, a result similar to findings regarding extratropical winter snowstorms. These studies imply that the predictability of tropical cyclones may be strongly limited at all time scales, ranging from day 1 to long-term projections. This remains true regardless of whether one uses statistical methods or numerical weather/climate prediction models. The limit of intensity predictability, given realistic initial condition and model errors (which are still large at present), in numerical weather prediction models may be alleviated through improving our understanding of dynamics and physics, development of better numerical models, and improved data coverage and assimilation techniques, as seen in recent studies of Zhang *et al.* (2009, 2011), Munsell *et al.* (2014), Poterjoy and Zhang (2014a,b) and Zhang and Weng (2015).

For example, Zhang and Weng (2015) presented the performance in the prediction of hurricane intensity with a convection-permitting forecast system that uses ensemble data assimilation techniques to ingest high-resolution airborne radar observations from the inner core. This system performed well for three of the 10 costliest Atlantic

hurricanes: Ike (2008), Irene (2011), and Sandy (2012). Four to five days before these storms made landfall, the system produced good deterministic and probabilistic forecasts of not only track and intensity, but also the spatial distributions of surface wind and rainfall. Averaged over all 102 applicable cases that have inner-core airborne Doppler radar observations during 2008–2012, the system reduced the day 2-to-day 4 intensity forecast errors by 25–28% compared to the corresponding National Hurricane Center’s official forecasts (which have seen little or no decrease in intensity forecast errors over the past two decades) (Fig. 11.11). Empowered by sufficient computing resources, advances in both deterministic and probabilistic hurricane prediction will enable emergency management officials, the private sector, and the general public to make more informed decisions that minimize loss of life and property. Nevertheless, there will always be forecast errors due to the inherent limit of predictability arising from initial errors with amplitudes far smaller than any observation and analysis system.

## 11.5 Concluding remarks

In summary, from both real data and idealized case studies, we have demonstrated that predictability of severe weathers and TCs can be intrinsically limited at the mesoscale through the chaotic nature of moist convection. We also showed that convection-permitting numerical weather prediction brings apparent benefits, but with faster error growth due to finer-scale instability. However, for most severe and convective weather, most of the current forecast error likely still comes from large environmental condition

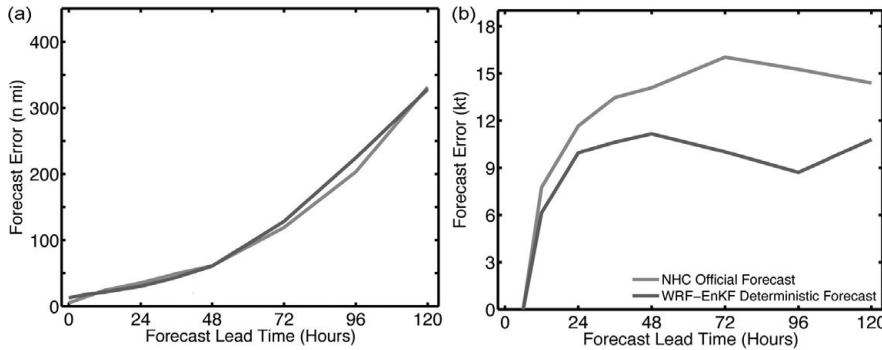


Fig. 11.11. The mean absolute forecast errors of (a) track and (b) intensity at different forecast lead times (verified 346 against post-storm best track observations estimated by NHC) for the PSU WRF-EnKF system (red) and the 347 NHC official forecasts (cyan), averaged over all applicable P3 Doppler missions during 2008–2012. Adapted from Figure 2a–b of Zhang and Weng (2015). A black and white version of this figure will appear in some formats. For the colour version, please refer to Plate 22.

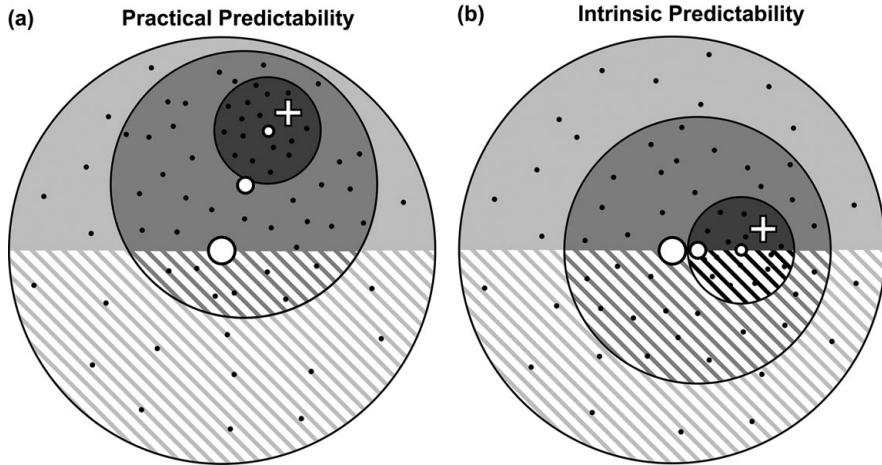


Fig. 11.12. Idealized schematic illustrating the reduction of initial condition error by reducing the ensemble spread, highlighting (a) the practical predictability representative of the 9–10 Jun 2003 squall line and bow echo and (b) the intrinsic predictability representative of a theoretical ensemble forecast with the ensemble forecast having equally favourable solutions. Solid shading – flow regime 1; striped pattern – flow regime 2; black dots – ensemble members; white dots – ensemble mean; white cross – forecast truth. Adapted from Figure 18 of Melhauser and Zhang (2012).

and model deficiencies that can be reduced through advanced data assimilation techniques with high-resolution observations and improved cloud-resolving numerical weather prediction models. An understanding of the limit of flow-dependent mesoscale predictability, the associated error growth dynamics, and the distance and difference in the limits of practical versus intrinsic predictabilities is essential for setting up expectations and priorities for advancing deterministic mesoscale forecasting and for providing guidance on the design, implementation, and application of short-range ensemble prediction systems.

To further differentiate practical versus intrinsic predictability, Fig. 11.12, adapted from Melhauser and Zhang (2012), gives an idealized schematic illustrating how the predictability of severe weather can be improved through reduction of initial condition error by reducing the ensemble spread, which may improve practical predictability but may be ultimately limited given the inherent nonlinearities in the underlying dynamics, especially in the presence of moist convection or other hydrodynamic instabilities. Both practical predictability and intrinsic predictability are flow dependent and are likely more limited during regime transition; a weather regime can be loosely thought of as

a particular dominant synoptic flow pattern. Most of the loss of predictability in simulation forecasts arises from chaotic behaviour near a regime transition or bifurcations due to nonlinearities, such as those induced by hydrodynamic instability. If a simulation's initial conditions, that represent the correct flow regime of the weather phenomenon of interest, are known, improvements in the initial conditions will cause the ensemble to converge towards the truth and the practical predictability can be improved. Conversely, if the truth were to straddle the flow regimes, no matter how well the initial conditions of the simulation are known, the prediction will straddle two flow regimes, and the predictability cannot be improved; thus the predictability is intrinsically limited by the system.

## References

- Bei, N. and Zhang, F. (2007). Impacts of initial condition errors on mesoscale predictability of heavy precipitation along the Mei-Yu front of China. *Quarterly Journal of the Royal Meteorological Society*, **133**, 83–99.
- Hawblitzel, D. P., Zhang, F., Meng, Z., and Davis, C. (2007). Probabilistic evaluation of the dynamics and predictability

- of the mesoscale convective vortex of 10–13 June 2003. *Monthly Weather Review*, **135**, 1544–1562.
- Langland, R. H., Shapiro, M. A., and Gelaro, R. (2002). Initial condition sensitivity and error growth in forecasts of the 25 January 2000 east coast snowstorm. *Monthly Weather Review*, **130**, 957–974.
- Lorenz, E. N. (1963). Deterministic nonperiodic flow. *Journal of the Atmospheric Sciences*, **20**, 130–141.
- Lorenz, E. N. (1969). The predictability of a flow which possesses many scales of motion. *Tellus*, **21**, 289–307.
- Lorenz, E. N. (1982). Atmospheric predictability experiments with a large numerical model. *Tellus*, **34**, 505–513.
- Lorenz, E. N. (1996). Predictability—A problem partly solved. *Proc. Seminar on Predictability*, Reading, United Kingdom, ECMWF, 1–18.
- Melhauser, C. and Zhang, F. (2012). Practical and intrinsic predictability of severe convective weather at the mesoscales. *Journal of the Atmospheric Sciences*, **69**, 3350–3371.
- Munsell, E. B. and Zhang, F. (2014). Prediction and uncertainty of Hurricane Sandy (2012) explored through a real-time cloud-permitting ensemble analysis and forecast system assimilating airborne Doppler observations. *Journal of Advanced Modeling in Earth Sciences*, **6**, 1–20.
- Munsell, E. B., Zhang, F., and Stern, D. P. (2013). Predictability and dynamics of a non-intensifying tropical storm: Erika (2009). *Journal of the Atmospheric Sciences*, **70**, 2505–2524.
- Poterjoy, J. and Zhang, F. (2014a). Predictability and genesis of Hurricane Karl (2010) examined through the EnKF assimilation of field observations collected during PRE-DICT. *Journal of the Atmospheric Sciences*, **71**, 1260–1275.
- Poterjoy, J. and Zhang, F. (2014b). Inter-comparison and coupling of ensemble and variational data assimilation approaches for the analysis and forecasting of Hurricane Karl (2010). *Monthly Weather Review*, **142**, 3347–3364.
- Sippel, J. A. and Zhang, F. (2008). A probabilistic analysis of the dynamics and predictability of tropical cyclogenesis. *Journal of the Atmospheric Sciences*, **65**, 3440–3459.
- Sippel, J. A. and Zhang, F. (2010). Factors affecting the predictability of hurricane Humberto (2007). *Journal of the Atmospheric Sciences*, **67**, 1759–1778.
- Sun, Y. Q. and Zhang, F. (2014). Predictability and error growth dynamics of moist baroclinic waves under varying baroclinic and convective instabilities. WMO Weather Open Science Conference (WWOSC), Montreal, Canada, August 2014 (Abstract # 56057).
- Tan, Z. M., Zhang, F., Rotunno, R., and Snyder, C. (2004). Mesoscale predictability of moist baroclinic waves: Experiments with parameterized convection. *Journal of the Atmospheric Sciences*, **61**, 1794–1804.
- Tao, D. and Zhang, F. (2014). Effect of environmental shear, sea-surface temperature and ambient moisture on the formation and predictability of tropical cyclones: an ensemble-mean perspective. *Journal of Advanced Modeling in Earth Sciences*, **6**, 384–404.
- Tao, D. and Zhang, F. (2014b). Predictability and dynamics of tropical cyclones: sensitivity to environmental shear, sea-surface temperature and moisture. AMS 31st Conference on Hurricanes and Tropical Meteorology, San Diego, California, April 2014 (oral presentation #4A.1).
- Zhang, F. (2005). Dynamics and structure of mesoscale error covariance of a winter cyclone estimated through short-range ensemble forecasts. *Monthly Weather Review*, **133**, 2876–2893.
- Zhang, F. and Sippel, J. A. (2009). Effects of moist convection on hurricane predictability. *Journal of the Atmospheric Sciences*, **66**, 1944–1961.
- Zhang, F. and Tao, D. (2013). Effects of vertical wind shear on the predictability of tropical cyclones. *Journal of the Atmospheric Sciences*, **70**, 975–983.
- Zhang, F. and Weng, Y. (2015). Modernizing the prediction of hurricane intensity and associated hazards: a five-year real-time forecast experiment concluded by Superstorm Sandy (2012). *Bulletin of the American Meteorological Society*, **96**, 25–32.
- Zhang, F., Odins, A., and Nielsen-Gammon, J. (2006). Mesoscale predictability of an extreme warm-season precipitation event. *Weather and Forecasting*, **21**, 149–166.
- Zhang, F., Snyder, C., and Rotunno, R. (2002). Mesoscale predictability of the "surprise" snowstorm of 24–25 January 2000. *Monthly Weather Review*, **130**, 1617–1632.
- Zhang, F., Snyder, C., and Rotunno, R. (2003). Effects of moist convection on mesoscale predictability. *Journal of the Atmospheric Sciences*, **60**, 1173–1185.
- Zhang, F., Weng, Y., Gamache, J. F., and Marks, F. D. (2011). Performance of convection-permitting hurricane initialization and prediction during 2008–2010 with ensemble data assimilation of inner-core airborne Doppler radar observations. *Geophysical Research Letters*, **38**, L15810, doi:10.1029/2011GL048469.
- Zhang, F., Bei, N., Rotunno, R., Snyder, C., and Epifanio, C. C. (2007). Mesoscale predictability of moist baroclinic waves: convection-permitting experiments and multistage error growth dynamics. *Journal of the Atmospheric Sciences*, **64**, 3579–3594.
- Zhang, F., Weng, Y., Sippel, J. A., Meng, Z., and Bishop, C. H. (2009). Cloud-resolving hurricane initialization and prediction through assimilation of Doppler radar observations with an ensemble Kalman filter. *Monthly Weather Review*, **137**, 2105–2125.

# 12

## Dynamics, predictability, and high-impact weather associated with the extratropical transition of tropical cyclones

Patrick A. Harr and Heather M. Archambault

### 12.1 Introduction

Although significant improvement has been made in the forecasting skill of operational numerical weather prediction models, systematic errors continue to exist and instances of extreme forecast failures do occur (Rodwell *et al.*, 2013). Extreme errors often occur in forecasts of Rossby wave breaking and high-impact weather downstream of the primary mid-latitude waveguide. The waveguide, which generally defines the quasi-horizontal (on an isentropic surface) boundary of tropospheric and stratospheric air, is the location of the jet stream.

Diabatic processes associated with the interactions among synoptic-scale disturbances and the primary mid-latitude waveguide are often significant sources of reduced predictability of downstream weather. A primary source of such diabatic forcing is the poleward movement of a tropical cyclone into the mid-latitudes, but then the process of extratropical transition (ET) (Jones *et al.*, 2003) often results in significant modifications to both the tropical cyclone and the mid-latitude circulation into which it is moving (e.g. Harr *et al.*, 2000). The downstream evolution of the mid-latitude flow pattern is determined by various factors that include: (i) the structure and amplitude of the original tropical cyclone disturbance; (ii) the shape and intensity of the mid-latitude flow (including the intensity of the jet stream and lower-tropospheric baroclinicity); and (iii) the diabatic forcing. The downstream flow may be impacted in ways that are unique to individual characteristics of each perturbation source.

Because of the potential impacts of extreme weather, it is important to increase understanding of the downstream response to upstream forcing due to the ET process. Concentrated effort is required to evaluate predictability in terms of impacts to data assimilation, initial condition sensitivities, utility of ensemble prediction systems, and improved model strategies and parameterizations.

In this chapter, impacts of the movement of a tropical cyclone into the mid latitudes are addressed by defining the

role of the ET process in modifying the tropical cyclone and the environment into which it is moving. Included is the excitation of Rossby wave packets that may propagate downstream and lead to high-impact weather over regions quite remote from the ET event. Additionally, predictability of such impacts is examined using various operational and research deterministic and ensemble forecast systems.

### 12.2 Physical processes

#### 12.2.1 Extratropical transition

Matano and Sekioka (1971) introduced two *conceptual* modes of ET. In a *complex* transition, a pre-existing mid-latitude front or trough interacts with a tropical cyclone to produce a new extratropical cyclone on the front. The interactions between a mid-latitude trough and a tropical cyclone have been examined via a variety of fundamental processes that involve quasi-geostrophic forcing (Sinclair, 1993, Foley and Hanstrum, 1994, Harr and Elsberry 2000, Harr *et al.*, 2000, Hart *et al.*, 2006, Evans and Hart, 2003), a potential vorticity (PV) framework (Browning *et al.*, 1998, Thorncroft and Jones, 2000, McTaggart-Cowan *et al.*, 2001, Agusti-Panareda *et al.*, 2004), and the kinematics associated with upper-level trough interactions (Molinari and Vollaro, 1989, Molinari *et al.*, 1995, Kitabatake, 2002). A common aspect of these characterizations is that the ET process may result in the re-intensification of the tropical cyclone as an extratropical cyclone in a manner similar to Petterssen–Smebye Type-B cyclogenesis (Petterssen and Smebye, 1971). In this framework, the transformation occurs as the lower-level tropical cyclone remnants interact with an upper-level jet and its associated tropospheric baroclinic zone.

In a *compound* transition, a mid-latitude cyclone approaches and appears to merge with a decaying tropical cyclone such that the original tropical cyclone is transformed into an extratropical cyclone (Sekioka, 1956, Matano and Sekioka, 1971, Brand and Guard, 1979). A third

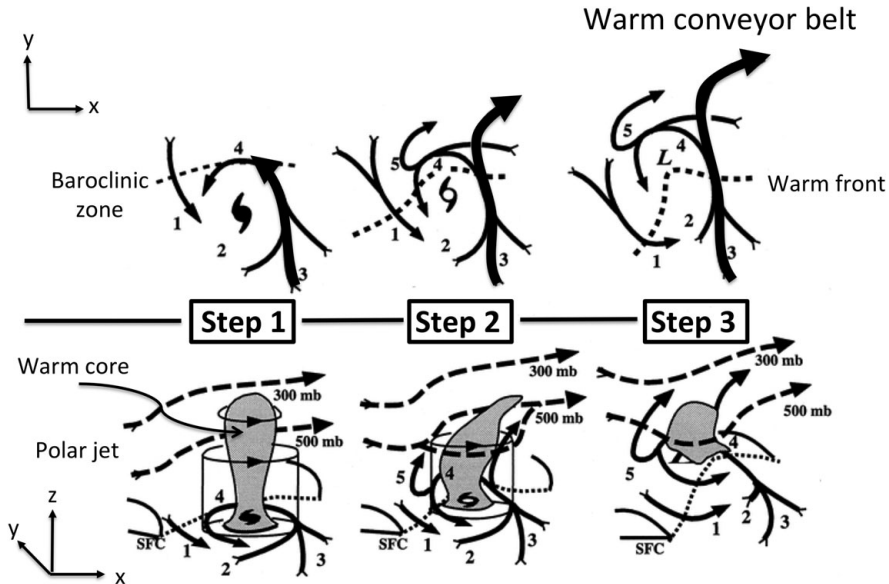


Fig. 12.1. Conceptual model of the transformation stage of ET. Labeled arrows define environmental flow as follows: (1) environmental equatorward flow of cooler, drier air (with corresponding open cell cumulus); (2) decreased tropical cyclone-related convection in the equatorward and westward quadrant in step 1 and extends throughout the equatorward quadrant in steps 2 and 3; (3) poleward flow of warm, moist air that is ingested into the tropical cyclone and maintains convection in the eastern quadrant; in steps 2 and 3, airflow 3 evolves into a southerly jet that ascends tilted isentropic surfaces; (4) ascending warm, moist inflow over tilted isentropic surfaces that define the baroclinic zone; (5) ascent that is undercut by dry-adiabatic descent to produce cloudbands that wrap westward and equatorward around the storm center. Modified from Klein et al. (2002).

classification is based on unfavorable conditions (i.e. strong vertical wind shear) such that the tropical cyclone remnants dissipate while moving into the mid latitudes (Kitabatake, 2002).

The interaction between the poleward-moving tropical cyclone and mid-latitude environment results in characteristic structural changes to the original tropical disturbance. Klein *et al.* (2000) defined the transformation stage of ET as the change from a warm-core vortex to a baroclinic extratropical cyclone (Fig. 12.1). Step 1 of the transformation process is initiated as the tropical cyclone encounters lower sea-surface temperatures (SSTs) and a lower-tropospheric baroclinic zone. Structural changes begin with erosion of the central region of deep convection in the equatorward portion (labeled 2 in Fig. 12.1) of the tropical cyclone due to entrainment of cool, dry air from the mid latitudes (air stream 1 in Fig. 12.1). The poleward movement of subtropical air (air streams 3 and 4 in Fig. 12.1) up tilted isentropic surfaces that define the mid-latitude baroclinic zone brings warm, moist air to higher latitudes. This air stream is a developing warm conveyor belt (WCB) (Carlson, 1980), which can contribute to diabatic forcing for downstream ridge amplification and strengthening of the downstream upper-level jet stream (Bosart and Lackmann, 1995, Agusti-Panareda *et al.*, 2004, Archambault *et al.*, 2013, 2015, Grams *et al.*, 2013a,b).

During Step 2 (Fig. 12.1), the decaying tropical cyclone becomes influenced by westerly vertical wind shear and the WCB turns anticyclonically to become part of the upper-level outflow and merges with the mid-latitude jet stream. Additionally, a cold conveyor belt-like air stream (air stream 5 in Fig. 12.1) lies beneath the WCB and ascends tilted isentropic surfaces on the poleward side of the remaining low-level center. A portion of air stream 5 contributes with air stream 4 to produce convection and banded clouds along the poleward portion of the decaying center. A second portion of air stream 5 turns anticyclonically and ascends as part of the upper-level outflow and merges with the mid-latitude jet stream.

During Step 3 (Fig. 12.1), the decaying tropical cyclone becomes fully embedded in the mid-latitude baroclinic environment characterized by high westerly vertical wind shear and low SSTs. At this time, the transformation stage is complete and the process may continue into a re-intensification stage (Klein *et al.*, 2000, 2002) during which a significant extratropical, cold-core cyclone may result. For re-intensification to occur in the Petterssen–Smebye Type-B framework, the remnant tropical cyclone, which defines the low-level thermodynamic conditions, must be favorably aligned with a region of dynamic forcing for cyclone development. Using numerical simulations in which tropical cyclone remnants were either

removed or displaced relative to the mid-latitude circulation, Klein *et al.* (2002) examined the sensitivity of the re-intensification stage to the phasing between the low-level remnants of the tropical cyclone and the mid-latitude environment in which there were varying degrees of support for Petterssen Type-B cyclogenesis. A key result was that the re-intensification stage was not dependent solely on the mid-latitude circulation. The tropical cyclone outflow interaction with the jet streak and the modification of the low-level baroclinic zone by the poleward-moving tropical cyclone combined to define the degree of support for re-intensification of the tropical cyclone as an extratropical cyclone.

### 12.2.2 Impacts on the mid-latitude circulation

Many studies have documented amplification of the mid-latitude flow pattern in association with the ET process (Agusti-Panareda *et al.*, 2004, 2005, Harr and Dea, 2009, Anwender *et al.*, 2010, Grams *et al.*, 2011, Pantillon *et al.*, 2013, Archambault *et al.*, 2013, 2015). The poleward movement of a tropical cyclone and associated air streams (e.g. air stream 3 in Fig. 12.1) can result in adjacent ridge amplification and an intensification of the mid-latitude jet streak. In the tropics (Fig. 12.2a), convection in the tropical cyclone may lead to preferred outflow channels toward the equator or toward the mid latitudes. As the tropical cyclone moves poleward, a poleward-directed outflow channel (Fig. 12.2b) may form and interact with the mid-latitude jet stream during the transformation stage of ET with a subsequent strengthening and extension of the jet downstream (Fig. 12.2c). Initiation of a Rossby wave packet may then result in further amplification of the downstream mid-latitude flow pattern.

Archambault *et al.* (2013, 2015) related upper-level flow amplification sensitivity to the strength of the interaction between the decaying tropical cyclone and the mid-latitude

circulation, which is defined by the magnitude of the negative PV advection by the divergent upper-level outflow from the tropical cyclone. The sensitivity of the downstream response to ET with respect to the intensity of the mid-latitude jet and moist processes was examined by Riemer *et al.* (2008) with a full physics of simulations from idealized initial conditions. In their simulations, a weak jet is related to meridional-oriented downstream flow amplification, while a strong jet is related to a more zonal-oriented development. In each case, the impact of moist processes was to increase the amplitude of the downstream pattern.

As occurred during the recurvature of TY Saola in September 2005 (Fig. 12.4a,c), the poleward movement of a tropical cyclone does not always result in downstream flow amplification. Harr and Elsberry (2000) suggested that downstream flow amplification may be related to the location of the primary mid-latitude PV center relative to the position of the recurring tropical cyclone. A position that is poleward and upstream of the recurring tropical cyclone may be more favorable for flow amplification than a position that is poleward and downstream of the tropical cyclone. Grams *et al.* (2013a,b) examined the case of TY Jangmi in 2008, during which outflow from the decaying tropical cyclone strengthened the mid-latitude jet without subsequent amplification of the downstream flow pattern. Therefore, a significant amount of variability exists in relation to ET and impacts on mid-latitude flow characteristics, which also relates to the difficulty in predicting such events (Harr *et al.*, 2008, Anwender *et al.*, 2008).

### 12.2.3 Downstream development

Harr and Dea (2009) placed the amplification of the mid-latitude flow pattern related to an ET event (Fig. 12.3) into the context of downstream baroclinic development (Orlanski and Sheldon, 1995). The local budget of eddy

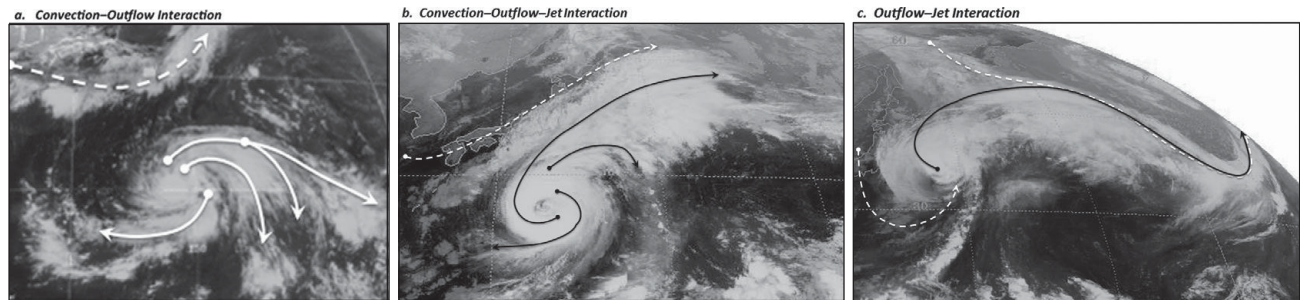


Fig. 12.2. Three types of tropical cyclone outflow – related characteristics as defined during the occurrence of TY Choi-Wan during September 2009 as the storm moves through (a) tropical latitudes at 0600 UTC 14 September; (b) subtropical latitudes on 1800 UTC 18 September; and (c) extratropical latitudes at 0000 UTC 20 September. Solid arrows define outflow patterns into the subtropical region and dashed arrows define extratropical air streams.

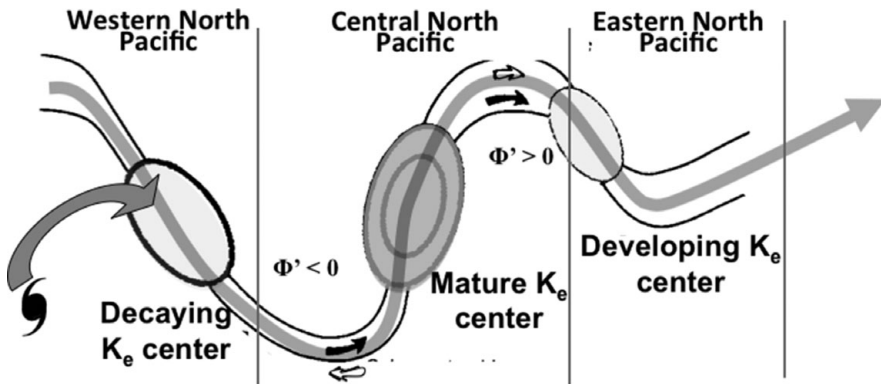


Fig. 12.3. Schematic depicting relationships among the outflow from a tropical cyclone, eddy kinetic energy, and components of a mid-latitude baroclinic wave. The upper-level geopotential field is indicated by the two nearly parallel solid lines. The geopotential anomaly,  $\Phi'$ , relative to the time mean is positive (negative) in the ridge (trough). Airflow relative to the wave is indicated by the heavy solid arrows and the ageostrophic wind is indicated by the open arrows. Upper-level outflow from the tropical cyclone is defined by the gray arrow. Centers of maximum vertically integrated eddy kinetic energy are shown as ellipses. Modified from Orlanski and Sheldon (1995).

kinetic energy ( $K_e$ ) was used to examine the production of  $K_e$  by baroclinic processes during the ET process, the transport of  $K_e$  to the mid-latitude flow via ageostrophic geopotential fluxes, and the transport downstream by the mean flow. In this context, the transport by ageostrophic geopotential fluxes is similar to the negative potential PV advection, described by Archambault *et al.* (2013, 2015) as a mechanism for the generation of a wave packet. The downstream development process is then manifest as extra-tropical cyclogenesis in the poleward exit region of the downstream jet streak, and subsequent ridge building occurs farther downstream.

An overarching aspect to downstream development in association with ET is the importance of adjacent ridge amplification, which has been related to negative PV advection (Archambault *et al.*, 2013), divergent outflow from the tropical cyclone (Davis *et al.*, 2008; Riemer and Jones, 2010, and Grams *et al.*, 2013a,b), or ageostrophic geopotential fluxes (Harr and Dea 2009). Furthermore, adjacent ridge modification has been examined by Harr *et al.* (2008) and Anwender *et al.* (2008) as a primary factor related to the reduction in skill of forecasts produced by operational numerical prediction models during periods of ET and downstream flow amplification.

Downstream development following the ET process is often manifested as generation of a Rossby wave packet. Rossby wave breaking is characterized by the irreversible deformation of PV surfaces along the primary mid-latitude wave guide. Anticyclonic wave breaking on the equatorward side of the wave guide tends to produce PV streamers, which have been implicated as precursors to a variety of extreme weather events downstream (Chabourneau *et al.*, 2012). Cyclonic wave breaking on the poleward

side of the wave guide, which is associated with explosive cyclogenesis, may result in high-latitude ridge amplification or a blocking type of pattern (Altenhoff *et al.*, 2008). Although significant improvement has been made in forecast skill of operational numerical weather prediction models during periods of downstream development, systematic errors continue to exist and instances of extreme forecast failure do occur. Rodwell *et al.* (2013) related these periods of reduced skill to forcing by divergent flow that is diabatically forced, such as occurs during ET.

### 12.3 Predictability

Jones *et al.* (2003) provided examples of reduced forecast skill over regions downstream of recurring tropical cyclones. Errors in downstream conditions were related to errors in the forecasts of the tropical cyclone track, mid-latitude circulation characteristics, and mesoscale features that are key aspects of the transformation stage of ET. While Jones *et al.* (2003) provided evidence that skill, as measured by reduced values of forecast anomaly correlations in 500 hPa geopotential heights over hemispheric scales, was reduced in operational global forecast models used in the mid 1990s, Harr (2010) provided additional evidence of reduced forecast skill over hemispheric scales in global prediction models that were operational in 2005. Given that Rodwell *et al.* (2013) related periods of reduced forecast skill in current operational global prediction systems to features that exhibit intense diabatic heating as typical of tropical cyclones undergoing ET, current forecast systems likely continue to exhibit reduced forecast skill during ET.

Harr and Wu (2011) and references therein provide evidence that forecast skill of the transformation stage of the ET process may be increased with improved representation of tropical cyclone and mid-latitude characteristics using targeted aircraft observations obtained during field programs over the western North Pacific. However, forecast skill of downstream flow amplification does not always increase with improved initial conditions. Harnisch and Weissmann (2010) used the operational global model from the European Centre for Medium-Range Weather Forecasts (ECMWF) to show that selected aircraft observations obtained in the tropics prior to recurvature of TY Sinlaku in September 2008 improved model initial conditions and the forecasts of the typhoon track through recurvature. However, aircraft observations over the mid latitudes during the transformation stage of the ET of TY

Sinlaku did not lead to improved forecasts as the aircraft data did not seem to alter initial conditions because of the abundance of operational observations over mid latitudes.

Harr (2010) showed that two then-operational global forecast systems had reduced skill (based on low five-day forecast 500 hPa geopotential height anomaly correlations over the Northern Hemisphere) during the recurvature of TY Nabi and TY Saola in September 2005 (Fig. 12.4). These errors were related to the presence of an observed downstream wave packet following the ET of TY Nabi that was not forecast (Fig. 12.4a) and the lack of an observed wave packet following TY Saola (Fig. 12.4b).

To investigate whether forecast skill of current global prediction systems is reduced during periods of recurring tropical cyclones that undergo ET, the recently produced National Oceanic and Atmospheric Administration (NOAA)

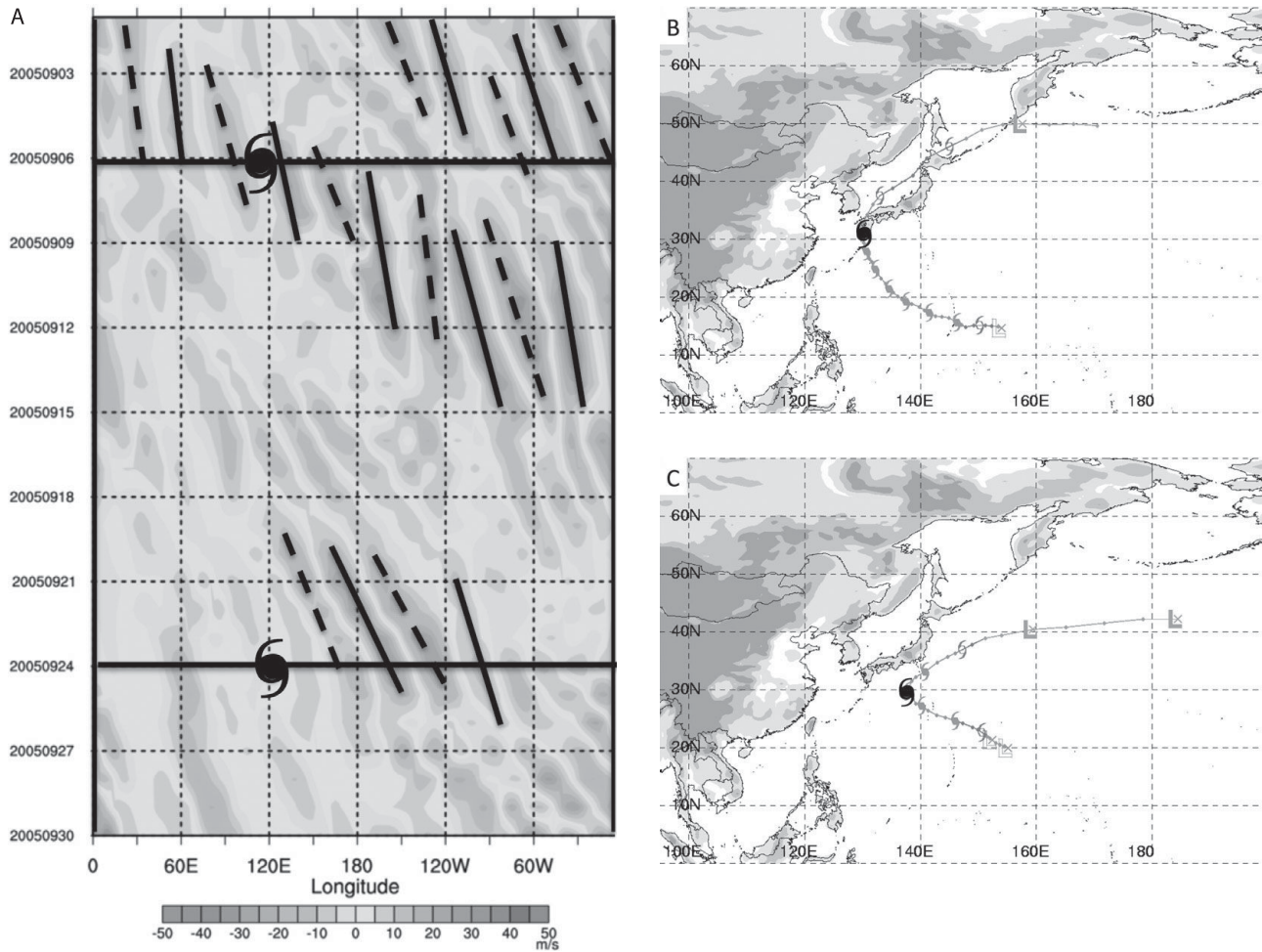


Fig. 12.4. (a) Time-longitude diagram of 200 hPa meridional winds ( $\text{m s}^{-1}$ ) averaged between  $40^\circ\text{N}$  and  $60^\circ\text{N}$  for September 2005. The recurvature times and longitudes for (b) TY Nabi and (c) TY Saola are marked by the thin horizontal lines and tropical cyclone symbols. Times and regions of southerly winds are marked by thin time-oriented solid lines and northerly winds are marked by thin time-oriented dashed lines.

second generation reforecast data set (Hamill *et al.*, 2013) can be used. The Reforecast-2 data set is made up of 27 years of once-daily, 11-member ensemble forecasts using the same model version as used during 2012 at the NOAA National Centers for Environmental Prediction (NCEP) as part of the Global Ensemble Forecast System (GEFS). Model initial conditions are generated from the NOAA Climate Forecast System Reanalysis (CSFR) (Saha *et al.*, 2010). The Reforecast-2 data set is a proxy for current operational model forecast guidance that can be applied to historical cases of ET to systematically assess forecast skill during ET and subsequent downstream flow amplification.

Based on Reforecast-2 ensemble mean seven-day forecast 500 hPa height anomaly correlations (Fig. 12.5), forecast skill was significantly reduced over the western North Pacific and entire North Pacific during the recurvature of TY Nabi. Forecast anomaly correlations were reduced to below 0.6 for the North Pacific following the recurvature of TY Saola. The reduced forecast skill suggests the negative impact of the forced wave packet on forecast skill increased downstream with increasing forecast range (not shown). Following the recurvature of TY Saola, the seven-day forecast skill (Fig. 12.5) was

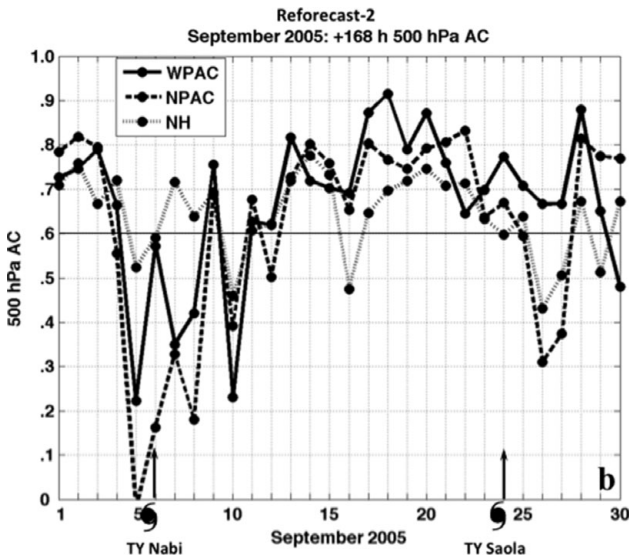


Fig. 12.5. Anomaly correlations of 500 hPa geopotential heights seven-day ensemble mean forecasts of the Reforecast-2 system that verify during September 2005. The recurvature times of TY Nabi and TY Saola are marked by the tropical cyclone symbols. The anomaly correlations are computed over three regions averaged between  $40^{\circ}$  and  $60^{\circ}\text{N}$  over the western North Pacific ( $100^{\circ}\text{E}$ – $180^{\circ}\text{E}$ ), the North Pacific ( $100^{\circ}\text{E}$ – $120^{\circ}\text{W}$ ), and the Northern Hemisphere. The anomaly correlation value of 0.6 is marked by the thin horizontal line as representative of useful forecast skill.

much reduced over the entire North Pacific and Northern Hemisphere, which may be attributed to the lack of a high-amplitude wave packet and the observed strengthening of a zonal-oriented jet stream that extended across the entire North Pacific downstream of Saola.

Similar error characteristics were defined by the progression of 500 hPa geopotential height root mean square errors (not shown) that occurred after the recurvature of TY Nabi and TY Saola, which means that the errors were not just due to a pattern mismatch, but the overall height distribution was in error. The errors in these ensemble mean forecasts suggest that current operational forecast systems continue to experience reduced skill during the movement of a tropical cyclone into the mid latitudes.

In 2008, The Observing Research and Predictability Experiment (THORPEX) Pacific Asian Regional Campaign (T-PARC) (Harr and Wu, 2011) was conducted to gather observations during recurring tropical cyclones undergoing ET over the western North Pacific. Forecasts of the track of Typhoon Sinlaku and its subsequent ET from multiple operational deterministic and ensemble prediction systems varied, from indicating no recurvature, rapid recurvature, ET and re-intensification as a major extratropical cyclone, or dissipation (Harnish and Weissmann, 2010, Chou *et al.*, 2011). As defined above, downstream impacts on the remote large-scale flow pattern following ET are related to the distribution of  $K_e$  and the downstream development process.

The predictability associated with downstream development following the recurvature of TY Sinlaku during T-PARC is investigated using forecasts of  $K_e$  and the transport of  $K_e$  across the North Pacific. Sinlaku recurved on 14 September 2008 and weakened under strong vertical wind shear. However, Sinlaku re-intensified at 1200 UTC 18 September then underwent ET farther downstream east of Japan by 0000 UTC 21 September.

Forecasts from the ECMWF that were initiated near the time of recurvature and before re-intensification significantly overpredicted the magnitude and spatial distribution of  $K_e$  downstream over the central North Pacific. Examination of the vertically integrated  $K_e$  and the total flux of  $K_e$  (Fig. 12.6) indicates that five-day forecasts initiated at 1200 UTC 15 September (Fig. 12.6a) significantly overpredicted the flux of  $K_e$  from Sinlaku compared to the analysis (Fig. 12.6c), which contributed to a significant amount of  $K_e$  and a large cyclone over the central North Pacific. The downstream development process in the forecast sequence (not shown) contributed to continued evolution with strong ridging over the eastern North Pacific and cyclone development over North America.

Forecasts initialized 24 h later at 1200 UTC 16 September (Fig. 12.6b) also overpredicted the flux of  $K_e$  from Sinlaku, but the magnitude of the flux, distribution of  $K_e$ ,

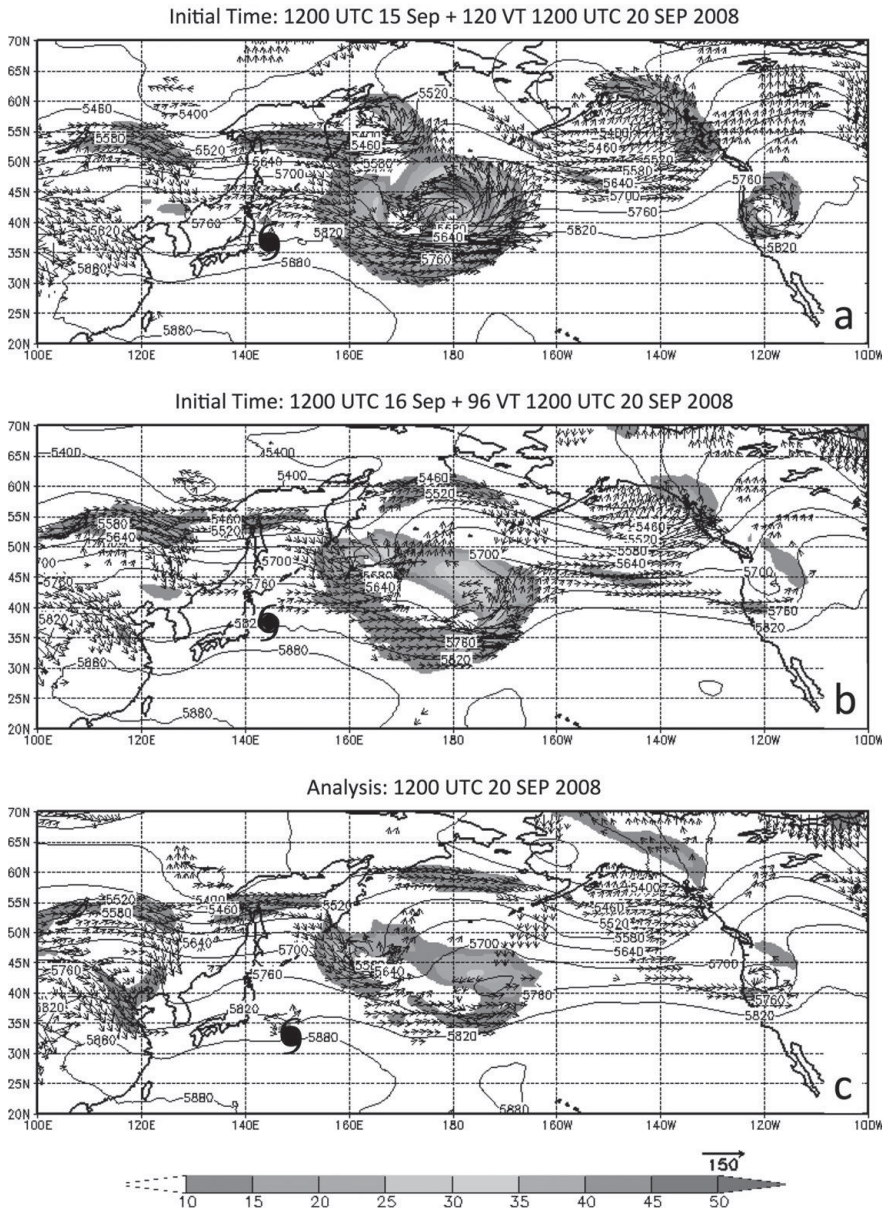


Fig. 12.6. Vertically averaged  $K_e$  (shaded,  $10^5 \text{ J m}^{-2}$ ) and total energy flux vectors (reference vector in lower right,  $10^5 \text{ W m}^{-1}$ ) from (a) five-day forecasts produced by the ECMWF global Integrated Forecast System with an initial time of 1200 UTC 15 September 2008, and (b) four-day forecasts initialized at 1200 UTC 16 September 2008, and analyzed at 1200 UTC 20 September 2008. The tropical cyclone symbol marks the location of TY Sinlaku at each forecast and analysis time. A black and white version of this figure will appear in some formats. For the colour version, please refer to Plate 24.

and cyclone development over the central North Pacific were all reduced. As the forecast initial time drew closer to the ET time, the overprediction of the downstream development process was reduced. Therefore, forecasts that do not accurately represent the ET process may misrepresent the processes associated with downstream development and wave packet formation, propagation, and possible high-impact weather impacts far downstream from the ET event.

Even when numerical forecasts of the ET process are accurate, there is often considerable variability in the forecasts of the downstream flow amplification and in association with downstream development of severe mid-latitude

weather conditions. Harr *et al.* (2008) and Anwender *et al.* (2008) diagnosed the predictability of downstream impacts following recurvature of typhoons over the western North Pacific and hurricanes over the western North Atlantic respectively. In their analyses, the spread among ensemble members from operational forecast systems and from lagged deterministic forecasts increased over mid latitudes downstream from tropical cyclone recurvature. However, the number of possible solutions based on a fuzzy clustering technique decreased as the lead time to the ET time of a recurring tropical cyclone decreased.

Whereas deterministic forecasts of the downstream development process in the case of Sinlaku (Fig. 12.6)

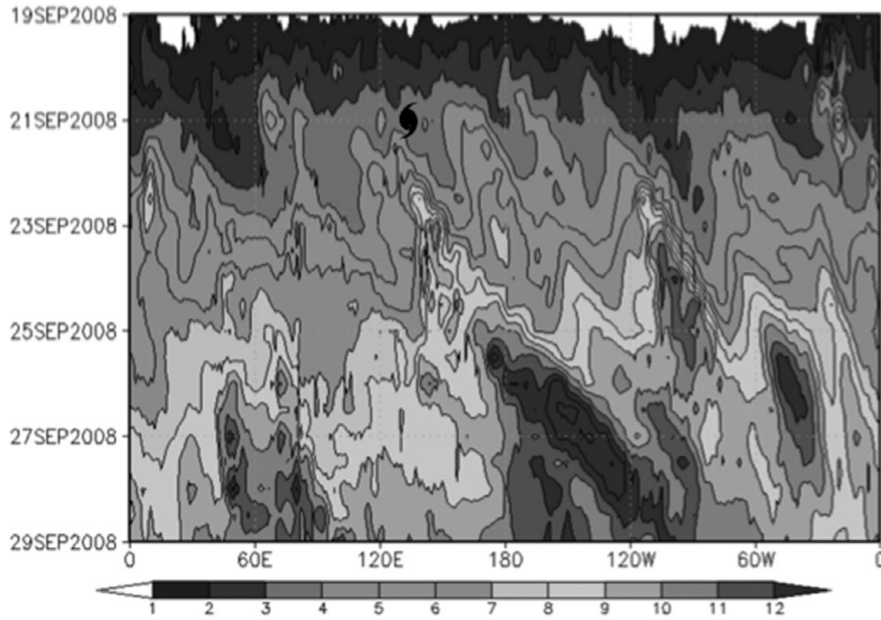


Fig. 12.7 Time–longitude diagram of the standard deviation averaged between  $30^{\circ}\text{N}$  and  $60^{\circ}\text{N}$  in potential temperature (K) on the 2 potential vorticity unit surface among 51 ensemble members from the ECMWF ensemble prediction system forecasts initialized at 0000 UTC 19 September. The longitude of TY Sinlaku at 0000 UTC 21 September 2008 is marked by the tropical cyclone symbol.

became more accurate nearer the ET time, considerable variability still existed in the ensemble forecasts of the large-scale conditions downstream of the ET of TY Sinlaku (Fig. 12.7). The standard deviation among forecasts of potential temperature on the 2 potential vorticity unit (PVU) surface, which is used to represent the large-scale flow pattern across mid latitudes, increased systematically downstream from Sinlaku and extended as far downstream as North America.

## 12.4 Recurving TC Oscar and extreme weather downstream over North America

### 12.4.1 Overview and life cycle

The case of recurring western North Pacific TY Oscar in September 1995 provides an excellent example of how recurring tropical cyclones can serve as precursors to large-scale flow reconfigurations and extreme weather far downstream. According to the Japan Meteorological Agency (JMA) best track data set, the pre-Oscar disturbance formed at 0000 UTC 12 September 1995 and rapidly strengthened to a typhoon within 48 h. Oscar recurved on 0000 UTC 16 September and accelerated northeastward while undergoing ET (Fig. 12.1). Oscar became extratropical by 1800 UTC 17 September and began re-intensification (e.g. Klein *et al.*, 2002) as an extratropical storm at 0000 UTC 18 September. The system was still deepening while moving rapidly eastward at 0600 UTC 19 September, when it was last tracked by the JMA.

### 12.4.2 Tropical cyclone–extratropical flow interaction

As Oscar recurved into the mid latitudes, an extensive cirrus plume emanated poleward and eastward from the storm as is characteristic of ET (Fig. 12.2). This cirrus shield indicated an ongoing interaction between the tropical cyclone outflow and the extratropical jet stream. As in Archambault *et al.* (2013), the strength of the tropical cyclone–extratropical flow interaction was determined by calculating spatial and temporal ( $15^{\circ} \times 15^{\circ}$  and 48 h, respectively) averages of upper-level (250–150 hPa) PV advection by the divergent outflow centered on the point and time of the maximum interaction.

Archambault *et al.* (2013, Fig. 5) examined the evolution of the tropical cyclone–extratropical flow interaction associated with Oscar in 12 h intervals (Fig. 12.8). At 1800 UTC 15 September (Fig. 12.8a), diabatically driven divergent outflow emanated from an area of mid-level ascent to the northeast of the TC center and impinged upon a meridional upper-level PV gradient (i.e. wave guide). At this time, weak negative PV advection by the divergent wind (approximately  $-3 \text{ PVU day}^{-1}$ ) was occurring along the PV wave guide near the entrance region of a mid-latitude jet stream. However, only 12 h later, at 0600 UTC 16 September (Fig. 12.8b), the divergent outflow intensified greatly and was associated with the maximum negative PV advection (and maximum tropical cyclone–extratropical flow interaction) by the divergent wind (less than  $-9 \text{ PVU day}^{-1}$ ). Of 292 recurring western North Pacific TCs from 1979 to 2009, recurring TC Oscar ranks as the second strongest tropical cyclone–extratropical flow

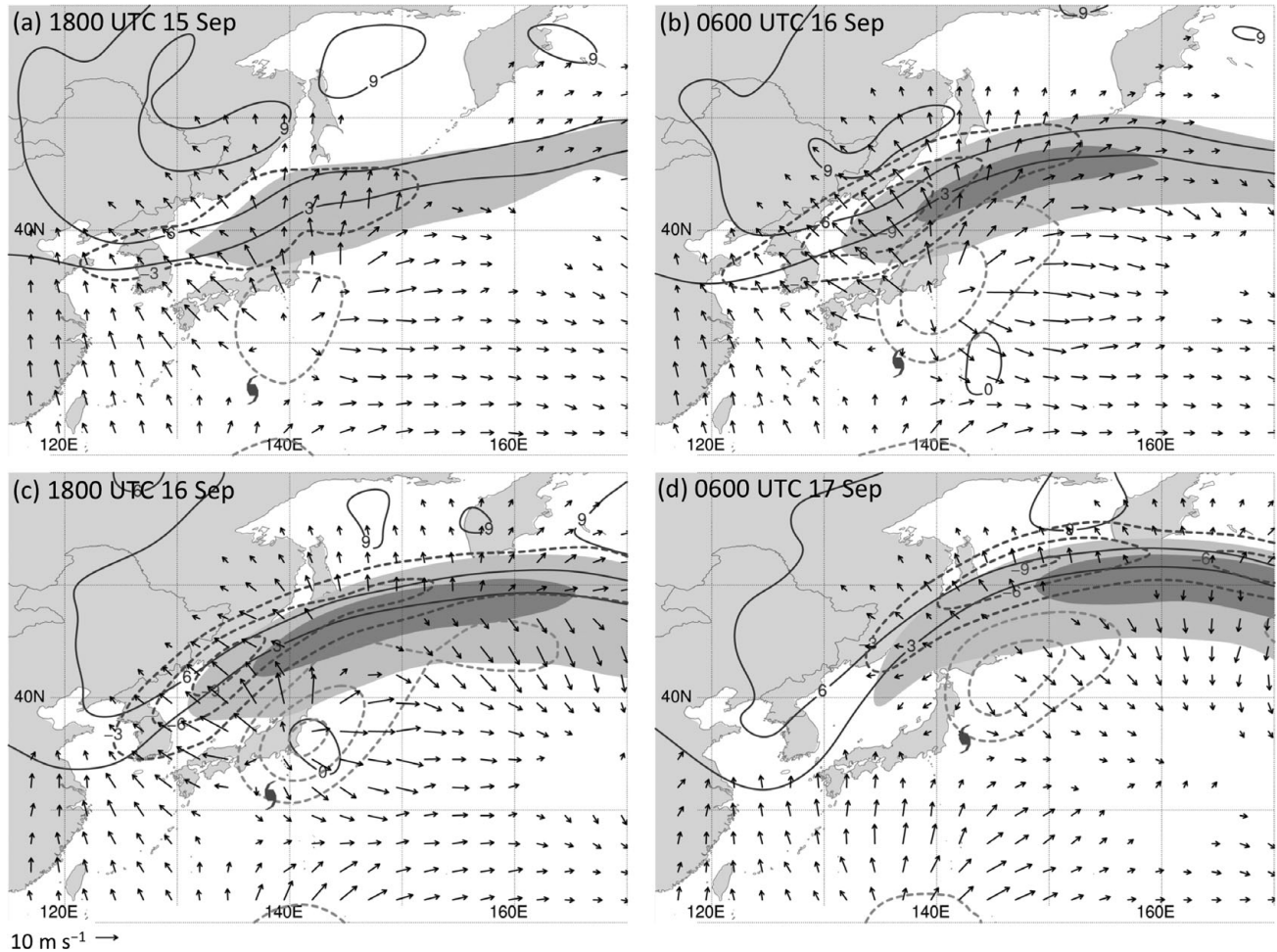


Fig. 12.8 Sequence of 12 h 0.5°CFSR analyses spanning (a–d) 12 h prior to 24 h after the time of maximum TC–extratropical flow interaction associated with recurring TC Oscar (0600 UTC 16 Sep 1995) for the same times and approximately the same domain as in Fig. 12.12. The fields plotted are 500 hPa ascent (dashed light gray, every  $2 \times 10^{-3}$  hPa s $^{-1}$ ), and 250–150 hPa layer-averaged wind speed (light gray shading denotes 50 m s $^{-1}$ ; dark gray shading denotes 70 m s $^{-1}$ ), PV (solid, every 3 PVU), irrotational wind (vectors,  $>3$  m s $^{-1}$  only), and negative PV advection by the irrotational wind (dashed dark gray, every 3 PVU day $^{-1}$ ). The TC symbol indicates the best-track position of TC Oscar.

interaction (Archambault *et al.*, 2013). By this time, signatures of an extratropical response to the tropical cyclone forcing were evident: (i) a sharp edge of the cirrus shield was just south of the curved band of strongest negative PV advection; (ii) the jet intensified over 20 m s $^{-1}$  in 12 h, with a wind speed maximum greater than 70 m s $^{-1}$  located just downstream of the strongest negative PV advection; and (iii) a signature of downstream ridge amplification was apparent in the upper-level PV field.

At 1800 UTC 16 September (Fig. 12.8c), the jet stream had further intensified and the ridge had become more amplified. Strong divergent outflow from Oscar continued to impinge upon the PV waveguide in the same location as 12 h earlier, with the maximum negative PV advection by

the divergent wind still below  $-9$  PVU day $^{-1}$ . This northwestward-directed divergent outflow had impeded the eastward progression of the upstream PV trough, as indicated by the nearly stationary position of the trough axis over 12 h (c.f. Figs. 12.8b and c).

At 0600 UTC 17 September (Fig. 12.8d), the TC–extratropical flow interaction had diminished even though TY Oscar had moved northeastward in concert with the eastward migrating downstream jet. Nevertheless, divergent outflow was still impinging upon the PV waveguide and the flow pattern further amplified based on the upper-level PV field (Fig. 12.8d) and the increase in curvature of the outflow plume compared to the previous 12 h (c.f. Figs. 12.8c and d).

### 12.4.3. Downstream flow reconfiguration

The tropical cyclone–extratropical flow interaction accompanying the recurvature of TY Oscar contributed to a large-scale flow reconfiguration that was associated with downstream baroclinic development over the North Pacific and North America between 16 and 22 September (Fig. 12.9). At 1200 UTC 16 September (Fig. 12.9a), TY Oscar recurved ahead of a 1000–500 hPa thickness trough over eastern Asia. Such that low-level southerly flow on the eastern side of Oscar impinged upon a baroclinic zone to the northeast that was intensifying (not shown). The presence of warm air advection and frontogenesis indicated that Oscar had entered the transformation stage of ET (Klein *et al.*, 2000). Slantwise ascent associated with the warm air advection and frontogenesis northeast of the TC center, in addition to the deep vertical ascent within the TC core, was likely contributing to the extensive cirrus shield and signature of divergent outflow (Figs. 12.8b and c).

By 1200 UTC 18 September (Fig. 12.9b), the jet stream had intensified and a large-scale thickness ridge had formed over the western–central North Pacific in response to the TC–extratropical flow interaction. The remnants of Oscar were now embedded within the jet stream and associated baroclinic zone and a surface low had developed downstream at the tip of the jet stream. On the poleward side of the jet stream, a second, higher latitude surface low was moving northwestward in association with cyclonic

wave breaking, that was evident in the thickness field as a negatively tilted trough. Ahead of this second surface low, a strong thickness ridge had developed over Alaska, as is indicated in Fig. 12.9b by the 540 dam 1000–500 hPa thickness contour that reached as far poleward as the Beaufort Sea.

By 1200 UTC 20 September (Fig. 12.9c), the remnants of Oscar had merged with the low previously located at the tip of the jet stream to form an intense cyclone over the Gulf of Alaska. Ahead of the cyclone, warm air advection tended to reinforce the downstream thickness ridge that had developed over northwestern North America. Downstream of this thickness ridge, an amplifying thickness trough marked the onset of a cold air surge across central Canada. This trough was associated with an unseasonably strong (greater than 1040 hPa) surface high. Based on the positively tilted thickness ridge upstream, this strong surface high had developed in response to strong dynamical forcing via upper-level anticyclonic vorticity advection.

By 1200 UTC 22 September (Fig. 12.9d), the surface high had moved equatorward to the US Southern Plains, while a large-scale high-latitude thickness ridge remained in place over northwestern North America. This cold air surge was associated with numerous daily record low temperatures and widespread freezing conditions that brought an early end to the growing season over the Great Plains (Archambault *et al.*, 2013).

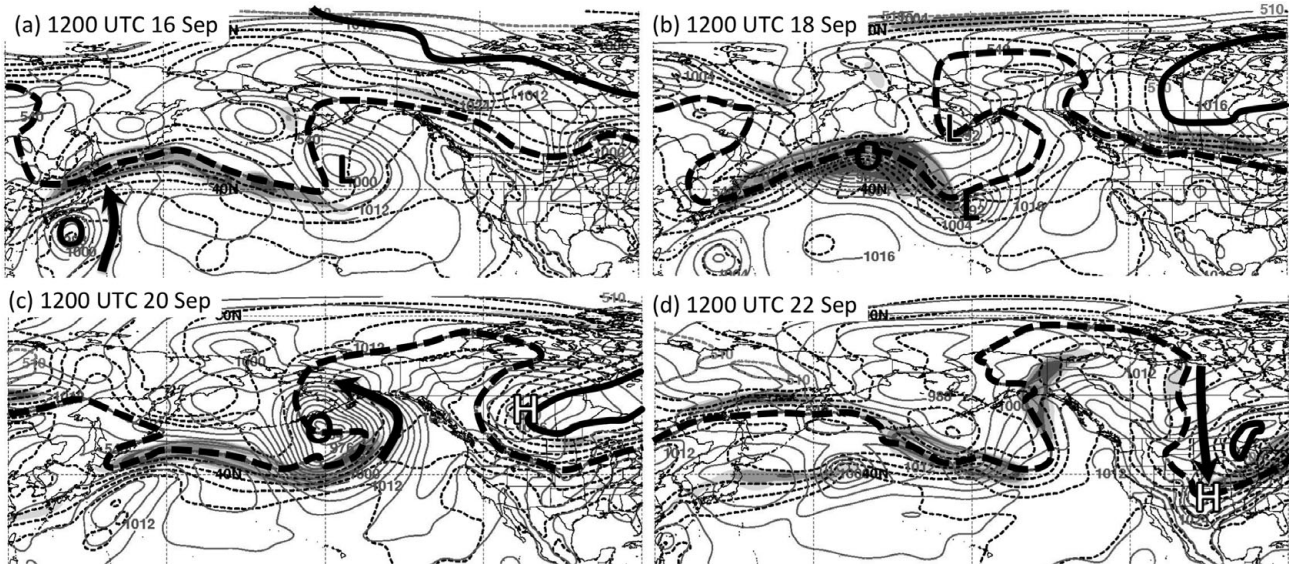


Fig. 12.9. Analyses of 300 hPa wind speed (shaded according to the color bar,  $\text{ms}^{-1}$ ), 1000–500 hPa thickness [dashed every 6 dam, except thick dashed (solid) denoting 540-(510-) dam], and sea level pressure (thin solid, every 4 hPa) computed from the 1.125° ECMWF ERA-40 reanalysis for (a) 1200 UTC 16 Sep, (b) 1200 UTC 18 Sep, (c), 1200 UTC 20 Sep, and (d), 1200 UTC 22 Sep 1995. The “O” and “P” symbols denote the locations of TCs Oscar and Polly, respectively. The “L”’s and “H”’s indicate key surface low and high pressure systems, respectively. The arrows in (a) and (c) denote the transport of warm air with Oscar. The arrow in (d) indicates a cold air surge.

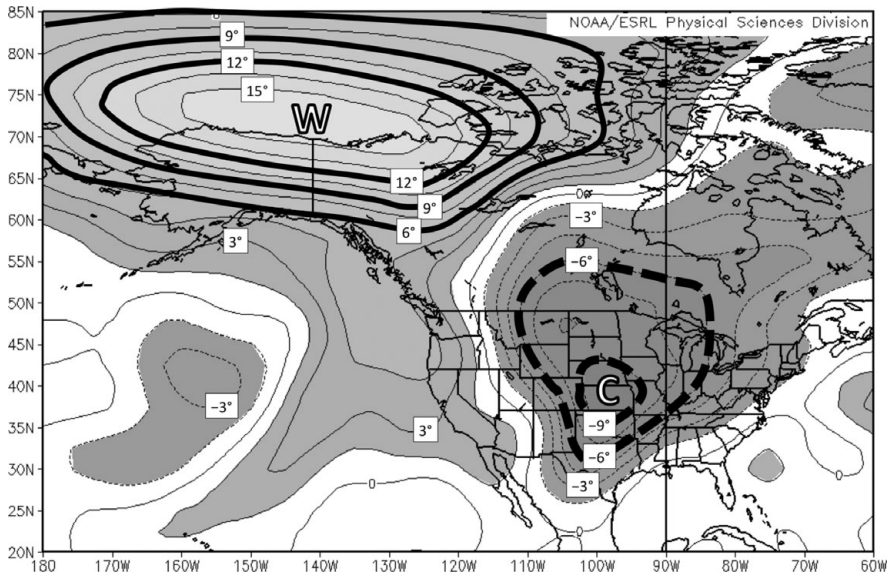


Fig. 12.10. Five-day (19–23 Sep 1995) mean 925 hPa temperature departure ( $^{\circ}\text{C}$ ) from a long-term (1981–2010) climatology computed from the 2.5° NCEP–NCAR reanalysis. Source image provided by the NOAA/ESRL Physical Sciences Division, Boulder Colorado from their website at <http://www.esrl.noaa.gov/psd/>.

In summary, the extreme weather associated with the flow reconfiguration following the recurvature of TY Oscar manifested as centers of strong positive and negative 925 hPa temperature anomalies over Alaska and the Beaufort Sea, and over the central USA, respectively (Fig. 12.10). The maximum positive temperature anomaly exceeded  $+15^{\circ}\text{C}$  averaged over 19–23 September, whereas the minimum negative temperature anomaly was below  $-9^{\circ}\text{C}$  for the same five-day period. The dynamical processes linking the recurvature of TCY Oscar to the cold air outbreak over the USA are summarized in a schematic in Archambault *et al.* (2013; their Fig. 1).

#### 12.4.4 Possible role of low-frequency tropical forcing

In addition to recurring TCs, lower frequency tropical forcing such as that associated with the Madden–Julian Oscillation (MJO, Madden and Julian, 1994) and the El Niño Southern Oscillation (ENSO, Rasmusson and Carpenter, 1982) may induce extratropical flow anomalies. These extratropical flow anomalies often comprise an arcing Rossby wave pattern that emanates poleward along a Great Circle from heating associated with strong convection tied to particular phases of the MJO and ENSO.

It is therefore of interest to consider whether the ENSO and MJO may be factors in the large-scale flow reconfiguration that occurred following the recurvature of TY Oscar. To explore this possibility, the Multivariate ENSO Index (MEI; Wolter and Timlin, 1993, 1998; indices available at <http://www.esrl.noaa.gov/psd/enso/mei/table.html>) and the Multivariate MJO index (Wheeler and Hendon, 2004; indices available at <http://cawcr.gov.au/staff/mwheeler/>

[maproom/RMM/phasediag.list.htm](http://maproom/RMM/phasediag.list.htm)) were examined for September 1995.

Based on the September–October  $-0.49$  standard deviation MEI during 1995, ENSO was in a weak (cool) phase. Thus, ENSO is not likely important to understanding the extratropical flow response to the recurvature of TY Oscar. On the other hand, based on the MJO index, a moderate convectively active MJO event was ongoing during this period. Coinciding with the formation and recurvature of Oscar, an MJO signal was over the Maritime Continent (Phase 5) during 8–18 September. The MJO signal then migrated eastward to the western North Pacific (Phase 6) during 19–22 September, which was the period of the mid-latitude flow reconfiguration and onset of extreme weather over North America.

Therefore, it is possible that the MJO played a role in the extratropical flow evolution (in particular the onset of the high-latitude ridge over northwestern North America) following the recurvature of TY Oscar. The extent to which lower-frequency tropical forcing may influence the extratropical flow response to TY Oscar, and to recurring western North Pacific TCs more generally, are topics of ongoing investigation.

#### 12.4.5 Predictability associated with TY Oscar

The impact of TY Oscar on predictability of mid-latitude weather patterns can be examined using the reforecast-2 data set. The skill in seven-day forecasts measured by 500 hPa height anomaly correlations (Fig. 12.11) that verify during the time period Oscar impacted the mid latitudes following 18 September was dramatically reduced

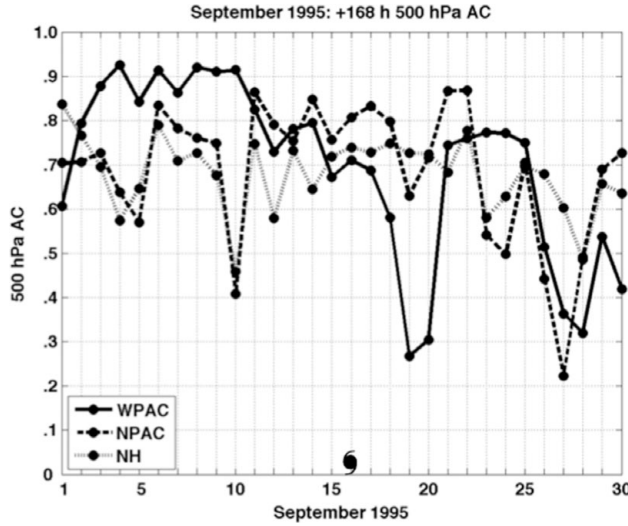


Fig. 12.11. As in Fig. 12.5, except for 500 hPa geopotential height (a) anomaly correlation and (b) root mean square error for the reforecast-2 system for September 1995. The tropical cyclone symbol marks the date of the recurvature of TY Oscar.

to well below 0.3. Interestingly, at the time of maximum downstream wave amplification after 20 September, the verifying seven-day 500 hPa height anomaly correlations became higher over the western North Pacific (Fig. 12.11) but much lower over the North Pacific and Northern Hemisphere as the impact of Oscar propagated downstream. Therefore, the impact on reduced predictability of the large-scale mid-latitude flow based on current forecast system capability was very large following the recurvature of TY Oscar.

The impact of TY Oscar on the predictability of mid-latitude flow patterns was also evident in the spread among the 11 ensemble members (Fig. 12.12) of the reforecast-2 system. The seven-day ensemble forecast spread increased dramatically for all regions and all forecasts verifying after 16 September, which was the time of the recurvature of TY Oscar. The increase in ensemble spread is diagnosed to be related to the recurvature of Oscar as plumes of increased standard deviation in 500 hPa heights averaging between  $40^{\circ}\text{N}$  and  $60^{\circ}\text{N}$  (Fig. 12.13) clearly extend downstream in space and time from the location of the recurvature of TY Oscar. The increased uncertainty extends to North America in association with the high-impact weather that occurred there, as defined in Section 12.4.

## 12.5 Summary and future directions

The extratropical transition of a tropical cyclone often has far reaching effects on the mid-latitude circulation. Furthermore, there is a large amount of variability in the

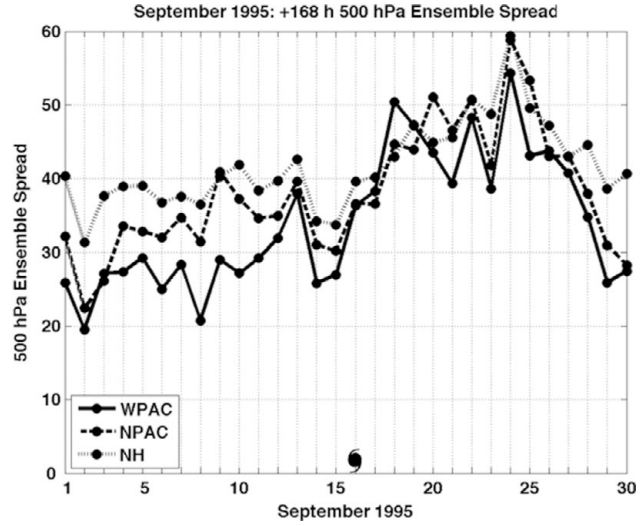


Fig. 12.12. As in Fig. 12.5, except for 500 hPa geopotential height ensemble spread for the reforecast-2 system for September 1995. The tropical cyclone symbol marks the date of the recurvature of TY Oscar.

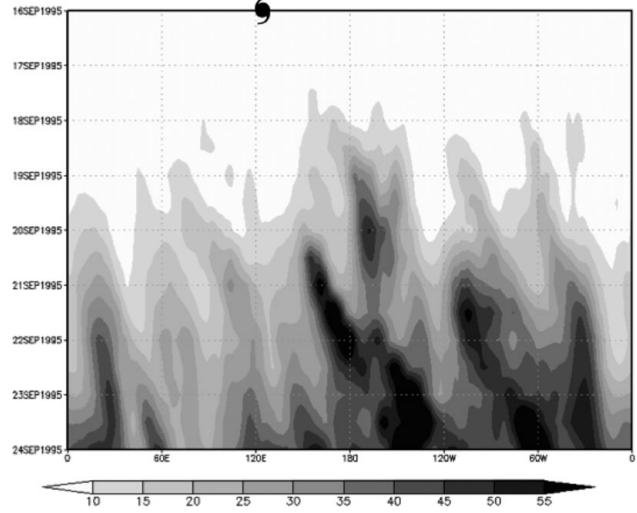


Fig. 12.13. Time-longitude diagram of the standard deviation averaged between  $40^{\circ}\text{N}$  and  $60^{\circ}\text{N}$  in 500 hPa geopotential height among 11 ensemble members from the reforecast-2 system forecasts initialized at 0000 UTC 16 September. The longitude of TY Oscar at 0000 UTC 16 September 1995 is marked by the tropical cyclone symbol.

occurrence and amplitude of the downstream impacts. Forecasts of the downstream circulations tend to have reduced skill (Jones *et al.*, 2003) and the variability among ensemble members during ET events suggests that the predictability associated with these cases is low (Harr *et al.*, 2008, Anwender *et al.* 2008). The process of downstream development (Orlanski and Sheldon, 1995) has

often been found to occur in association with the ET of tropical cyclones over the western North Pacific. Harr and Dea (2009) examined the sequence of downstream development forecasts from the ECMWF forecast system in relation to TY Sinlaku, that occurred during the T-PARC field program. Forecasts of the  $K_e$  distribution over the central North Pacific were quite accurate until the time of ET drew near. After this time, the forecast distribution of central North Pacific  $K_e$  spreads considerably, with the error increasing with increasing forecast range. Forecasts of downstream development are sensitive to characteristics of the tropical cyclone, the mid-latitude circulation into which the tropical cyclone is moving, or the interaction between the tropical cyclone and mid-latitude flow.

While forecast accuracy with respect to large-scale flow patterns has increased over recent years, the movement of a tropical cyclone into the mid-latitudes and associated diabatic forcing often contribute to extreme forecast errors. Furthermore, these errors propagate downstream from the ET event to impact forecasts of high-impact weather over North America and Europe. While research has concentrated on identifying key aspects of tropical cyclone-extratropical interactions, there has been little progress on identifying the role of specific factors that increase uncertainty and reduce the predictability of mid-latitude weather patterns. Although studies of targeted observations seem to indicate improved predictions of tropical cyclone track, these improvements in tropical regions do not translate to similar improvements over mid latitudes.

Key aspects regarding mechanisms, observations, and modeling need to be studied so that an increased understanding of the role(s) of ET on impacts over mid-latitude regions can be realized. Specific goals are:

- Document the contributions and temporal evolution of various physical processes that impact the development of the deep tropospheric anticyclone immediately downstream of an ET event. Physical mechanisms such as the poleward movement of heat and moisture along the eastern side of the decaying tropical cyclone, warm frontogenesis, and interaction of the tropical cyclone outflow and the mid-latitude jet stream need to be examined.
- Define the relative roles of a variety of tropical cyclone and mid-latitude circulation characteristics as they influence the variability of downstream impacts during ET.
- Examine the utility of satellite data in defining the important physical characteristics of an ET event.
- Examine the occurrence of the re-intensification of the decaying tropical cyclone as an extratropical cyclone on maintaining the downstream transport of energy.

- Examine the impact on forecast accuracy due to improved analysis of key structural characteristics during the ET of a decaying tropical cyclone.
- Establish the missing elements or the environmental conditions that are absent when a poleward-moving tropical cyclone does not produce an ET and subsequent downstream impacts.

The downstream impacts of the ET process and downstream flow amplification can have significant societal implications due to extreme conditions related to high winds, significant wave heights, and heavy precipitation. Therefore, a continuing need exists for improved predictability of such events over temporal and spatial scales that range from mesoscale to synopticscales.

## 12.6 Acknowledgments

This review is based in part on material presented at the International Commission of Dynamic Meteorology Workshop on Dynamics and Predictability of High-Impact Weather and Climate Events. Support for the preparation of this review came from the Office of Naval Research, Marine Meteorology Program Grant N0001414WX20029 and National Science Foundation Grant ATM-0736003.

## References

- Altenhoff, A. M., O. Martius, M. Croci-Maspoli, C. Schwierz, and H. C. Davies (2008). Linkage of atmospheric blocks and synoptic-scale Rossby waves: a climatological analysis. *Tellus*, **60**, 1053–1063.
- Archambault, H. M., L. F. Bosart, D. Keyser, and J. M. Cordeira (2013). A climatological analysis of the extratropical flow response to recurring western North Pacific tropical cyclones. *Mon. Wea. Rev.*, **141**, 2325–2346.
- Archambault, H. M., D. Keyser, L. F. Bosart, C. A. Davis, and J. M. Cordeira (2015). A composite perspective of the extratropical flow response to recurring western North Pacific tropical cyclones. *Mon. Wea. Rev.*, **143**, 1122–1141. Doi: <http://dx.doi.org/10.1175/MWR-D-14-00270.1>
- Agusti-Panareda, A., C. D. Thorncroft, G. C. Craig, and S. L. Gray (2004). The extratropical transition of hurricane Irene (1999): A potential vorticity perspective. *Quart. J. Roy. Meteor. Soc.*, **130**, 1047–1074.
- Agusti-Panareda, A., S. L. Gray, G. C. Craig, and C. Thorncroft (2005). The extratropical transition of Tropical Cyclone Lili (1996) and its crucial contribution to a moderate extratropical development. *Mon. Wea. Rev.*, **133**, 1562–1573.
- Anwender, D., P. A. Harr, and S. C. Jones (2008). Predictability associated with the downstream impacts of the extratropical transition of tropical cyclones: Case studies. *Mon. Wea. Rev.*, **136**, 3205–3225.

- Anwender, D., S. C. Jones, M. Leutbecher, and P. A. Harr (2010). Sensitivity experiments for ensemble forecasts of the extratropical transition of Typhoon Tokage (2004). *Quart. J. Roy. Meteor. Soc.*, **136**, 183–200.
- Bosart, L. F. and G. M. Lackmann (1995). Postlandfall tropical cyclone reintensification in a weakly baroclinic environment: A case study of Hurricane David (September 1979). *Mon. Wea. Rev.*, **123**, 3205–3225.
- Brand, S. and C. P. Guard (1979). An observational study of extratropical storms that evolved from tropical cyclones in the western North Pacific. *J. Meteor. Soc. Japan*, **57**, 479–482.
- Browning, K. A., G. Vaughan, and P. Panagi (1998). Analysis of an ex-tropical cyclone after reintensifying as a warm-core extratropical cyclone. *Quart. J. Roy. Meteor. Soc.*, **124**, 2329–2356.
- Carlson, T. N. (1980). Airflow through midlatitude cyclones and the comma cloud pattern. *Mon. Wea. Rev.*, **108**, 1498–1509.
- Chaboureau, J.-P., F. Pantillon, D. Lambert, R. Richard, and C. Claud (2012). Tropical transition of a Mediterranean storm by jet crossing. *Quart. J. Roy. Meteor. Soc.*, **138**, 596–611, doi: 10.1002/qj.960.
- Chou, K.-H., C.-C Wu, P.-H. Lin, et al. (2011). The impact of dropwindsonde observations on typhoon track forecasts in DOTSTAR and T-PARC. *Mon. Wea. Rev.*, **139**, 1728–1743.
- Davis, C. A., S. C. Jones, and M. Riemer (2008). Hurricane vortex dynamics during Atlantic extratropical transition. *J. Atmos. Sci.*, **65**, 714–736.
- Evans, J. L. and R. E. Hart (2003). Objective indicators of the life cycle evolution of extratropical transition for Atlantic tropical cyclones. *Mon. Wea. Rev.*, **131**, 909–925.
- Foley, G. R. and B. N. Hanstrum (1994). The capture of tropical cyclones by cold fronts off the west coast of Australia. *Wea. Forecasting*, **9**, 577–592.
- Grams, C. M. and Coauthors (2011). The key role of diabatic processes in modifying the upper-tropospheric wave guide: A North Atlantic case study. *Quart. J. Roy. Meteor. Soc.*, **137**, 2174–2193.
- Grams, C. M., S. C. Jones, C. A. Davis, P. A. Harr, and M. Weissmann (2013a). The impact of Typhoon Jangmi (2008) on the midlatitude flow. Part I: Upper-level ridge building and modification of the jet. *Quart. J. Roy. Meteor. Soc.*, **139**, 2148–2164, doi: 10.1002/qj.2091.
- Grams, C. M., S. C. Jones, and C. A. Davis (2013b). The impact of Typhoon Jangmi (2008) on the midlatitude flow. Part II: Downstream evolution. *Quart. J. Roy. Meteor. Soc.*, **139**, 2165–2180, doi: 10.1002/qj.2119.
- Hamill, T. M., G. T. Bates, J. S., Whitaker, et al. (2013). NOAA's Second-generation global medium-range ensemble reforecast dataset. *Bull. Amer. Meteor. Soc.*, **94**, 1553–1565.
- Harnisch, F. and M. Weissmann (2010). Sensitivity of typhoon forecasts to different subsets of targeted dropsonde observations. *Mon. Wea. Rev.*, **138**, 2664–2680.
- Harr, P. A. (2010). The extratropical transition of tropical cyclones: Structural characteristics, downstream impacts, and forecast challenges. *Global Perspectives on Tropical Cyclones*, World Scientific Series on Asia-Pacific Weather and Climate, Vol. 4, J. C. L. Chan and J. D. Kepert, Eds. World Scientific Press, pp. 149–177.
- Harr, P. A. and R. L. Elsberry (2000). Extratropical transition of tropical cyclones over the western North Pacific. Part I: Evolution of structural characteristics during the transition process. *Mon. Wea. Rev.*, **128**, 2613–2633.
- Harr, P. A., R. L. Elsberry, and T. F. Hogan (2000). Extratropical transition of tropical cyclones over the western North Pacific. Part II: The impact of midlatitude circulation characteristics. *Mon. Wea. Rev.*, **128**, 2634–2653.
- Harr, P. A., D. Anwender, and S. C. Jones (2008). Predictability associated with the downstream impacts of the extratropical transition of tropical cyclones: Methodology and a case study of Typhoon Nabi (2005). *Mon. Wea. Rev.*, **136**, 3205–3225.
- Harr, P. A. and J. M. Dea (2009). Downstream development associated with the extratropical transition of tropical cyclones over the western North Pacific. *Mon. Wea. Rev.*, **137**, 1295–1319.
- Harr, P. A. and C.-C. Wu (2011). Tropical cyclone characteristics and monsoon circulations. *The Global Monsoon System: Research and Forecast*, 2nd Edition, World Scientific Series on Asia-Pacific Weather and Climate, Vol. 5, C. –P. Chang, Y. Ding, N.-C. Lau, R. H. Johnson, B. Wang, and T. Yasunari, Eds., World Scientific Press, 357–372, 634–652.
- Hart, R. E., J. L. Evans, and C. Evans (2006). Synoptic composites of the extratropical transition lifecycle of North Atlantic tropical cyclones: Factors determining post-transition evolution. *Mon. Wea. Rev.*, **134**, 553–578.
- Jones, S. C. and Coauthors (2003). The extratropical transition of tropical cyclones: Forecast challenges, current understanding, and future directions. *Wea. Forecasting*, **18**, 16–56.
- Kitabatake, N. (2002). Extratropical transition of Typhoon Vicki (9807): Structural changes and the role of upper-tropospheric disturbances. *J. Meteor. Soc. Japan*, **80**, 229–247.
- Klein, P. M., P. A. Harr, and R. L. Elsberry (2000). Extratropical transition of western North Pacific tropical cyclones: An overview and conceptual model of the transformation stage. *Wea. Forecasting*, **15**, 373–395.
- Klein, P. M., P. A. Harr, and R. L. Elsberry (2002). Extratropical transition of western North Pacific tropical cyclones: Midlatitude and tropical cyclone contributions to reintensification. *Mon. Wea. Rev.*, **132**, 2240–2259.
- Madden, R. A. and P. R. Julian (1994). Observations of the 40–50 day tropical oscillation – A review. *Mon. Wea. Rev.*, **122**, 814–837.
- Matano, H. and M. Sekioka (1971). Some aspects of extratropical transformation of a tropical cyclone. *J. Meteor. Soc. Japan*, **49**, 282–295.
- McTaggart-Cowan, R., J. R. Gyakum, and M. K. Yau (2001). Sensitivity testing of extratropical transitions using potential vorticity inversions to modify initial conditions. Hurricane Earl case study. *Mon. Wea. Rev.*, **129**, 1617–1636.
- Molinari, J. and D. Vollaro (1989). External influences on hurricane intensity. Part I: Outflow-layer eddy angular momentum fluxes. *J. Atmos. Sci.*, **46**, 1093–1105.
- Molinari, J., S. Skubis, and D. Vollaro (1995). External influences on hurricane intensity. Part III: Potential vorticity structure. *J. Atmos. Sci.*, **52**, 3593–3606.

- Orlanski, I. and J. P. Sheldon (1995). Stages in the energetics of baroclinic systems. *Tellus*, **47**, 605–628.
- Pantillon, F. J., J.-P. Chaboureau, C. Lac, and P. Mascart (2013). On the role of a Rossby wave train during the extratropical transition of Hurricane Helene (2006). *Quart. J. Roy. Meteor. Soc.*, **139**, 370–386.
- Petterssen, S. and S. J. Smebye (1971). On the development of extratropical storms. *Quart. J. Meteor. Soc.*, **97**, 457–482.
- Rasmusson, E. M. and T. H. Carpenter (1982). Variations in tropical sea surface temperature and surface wind fields associated with the Southern Oscillation/El Niño. *Mon. Wea. Rev.*, **110**, 354–384.
- Riemer, M. and S. C. Jones (2010). The downstream impact of tropical cyclones on a developing baroclinic wave in idealized scenarios of extratropical transition. *Quart. J. Roy. Meteor. Soc.*, **136**, 617–637.
- Riemer, M., S. C. Jones, and C. A. Davis (2008). The impact of extratropical transition on the downstream flow: An idealized modeling study with a straight jet. *Quart. J. Roy. Meteor. Soc.*, **134**, 69–91.
- Rodwell, M. and Coauthors (2013). Characteristics of occasional poor medium-range weather forecasts for Europe. *Bull. Amer. Meteor. Soc.*, **94**, 1393–1405.
- Saha, S. and Coauthors (2010). The NCEP climate forecast system reanalysis. *Bull. Amer. Meteor. Soc.*, **91**, 1015–1057.
- Sekioka, M. (1956). A hypothesis on complex of tropical and extratropical cyclones for typhoon in middle latitudes. I. Synoptic structure of typhoon Marie over the Japan Sea. *J. Meteor. Soc. Japan*, **34**, 52–53.
- Sinclair, M. (1993). Synoptic-scale diagnosis of the extratropical transition of a southwest Pacific tropical cyclone. *Mon. Wea. Rev.*, **111**, 941–960.
- Thorncroft, C. D. and S. C. Jones (2000). The extratropical transition of Hurricane Felix and Iris in 1995. *Mon. Wea. Rev.*, **128**, 947–972.
- Wheeler, M. C. and H. H. Hendon (2004). An all-season real-time multivariate MJO index: Development of an index for monitoring and prediction. *Mon. Wea. Rev.*, **132**, 1917–1932.
- Wolter, K. and M. S. Timlin (1993). Monitoring ENSO in COADS with a seasonally adjusted principal component index. *Proc. of the 17th Climate Diagnostics Workshop*, Norman, OK, NOAA/NMC/CAC, NSSL, Oklahoma Clim. Survey, CIMMS and the School of Meteor., Univ. of Oklahoma, 52–57.
- Wolter, K. and M. S. Timlin (1998). Measuring the strength of ENSO events – how does 1997/98 rank? *Weather*, **53**, 315–324.

# 13

## Secondary eyewall formation in tropical cyclones

Chun-Chieh Wu, Yi-Hsuan Huang, and Zhemin Tan

### 13.1 Introduction

Secondary eyewall formation (SEF), and the subsequent eyewall replacement cycle, are often observed in intense tropical cyclones (TCs), and its association with short-term changes in TC intensity and structure has been widely documented from aircraft observations and satellite imagery (Willoughby *et al.*, 1982, Black and Willoughby, 1992, Willoughby and Black, 1996, Houze *et al.*, 2006, 2007, Hawkins and Helveston, 2008, Kossin and Sitkowski, 2009, Kuo *et al.*, 2009, Didlake and Houze, 2011, Sitkowski *et al.*, 2011, Bell *et al.*, 2012, Hence and Houze, 2012). A double-eyewall TC contains two concentric quasi-circular deep convective rings (inner and outer TC eyewalls) with a nearly cloud-free region (moat) between them. In most such cases, the outer eyewall is established later, with characteristics similar to the inner eyewall. A localized maximum swirling wind is often present in the outer eyewall, with its scope confined to the lower troposphere. Taking the example of a model simulation of Typhoon Sinlaku (2008), constructed by Wu *et al.* (2012), Fig. 13.1 demonstrates such flow characteristics in a concentric eyewall TC. For cases undergoing an eyewall replacement cycle, during which a TC usually weakens and enlarges, the inner eyewall gradually dissipates, while the outer eyewall later becomes the new primary eyewall. More recently, it has been shown that SEF is preceded by a broadening tangential wind field with small radial gradients in the storm's outer-core region, serving as a precursory flow characteristic for SEF (Wu *et al.*, 2012, Huang *et al.*, 2012; hereafter WH12). Considering such temporary, but pronounced, changes in storm intensity and structure, and the lack of skill in predicting concentric-eyewall events, SEF remains an important research issue and forecast priority for the understanding of TC intensity/structure evolution.

This review provides an updated summary and discussion of the literature concerned with our current understanding of the favorable conditions for, and potential mechanisms of,

SEF. Because of limited or discontinuous spatial/temporal coverage of observations, studies of SEF mechanisms have mostly been based on numerical simulations. The remainder of this article is organized as follows. Section 13.2 describes the possible roles of various environmental conditions in SEF. Having considered the environmental factors that are conducive to SEF, Section 13.3 introduces a variety of internal dynamical processes suggested for SEF, such as the axisymmetrization process, energy accumulation through vortex Rossby wave activities, beta-skirt-induced energy cascade, unbalanced responses to boundary layer dynamics, and balanced response to convective heating. Finally, in Section 13.4, the merits and caveats of the various dynamical interpretations are discussed, and the remaining unresolved issues are addressed to provide guidance for future SEF research.

### 13.2 Environmental conditions

Numerical models of various designs have been used to study the impact of ambient relative humidity on SEF. In the axisymmetric model framework of Nong and Emanuel (2003), high relative humidity is critical to SEF only if the hydrostatic assumption is applied. In contrast, full-physics model simulations have shown that high environmental relative humidity is crucial to the formation of an outer eyewall in a TC (e.g. Hill and Lackmann, 2009, Wang, 2009). Sitkowski *et al.* (2011) presented supporting results for the important role of higher relative humidity in SEF based on observational data. A plausible explanation for this finding is that high ambient humidity provides more moisture and so enhances latent heat release in the vortex's outer-core region. Therefore, the development of convection outside the primary eyewall is enhanced, and, subsequently, the formation/intensification of rainbands and even SEF. Another pathway for environmental influence on SEF, described by Nong and Emanuel (2003), is the

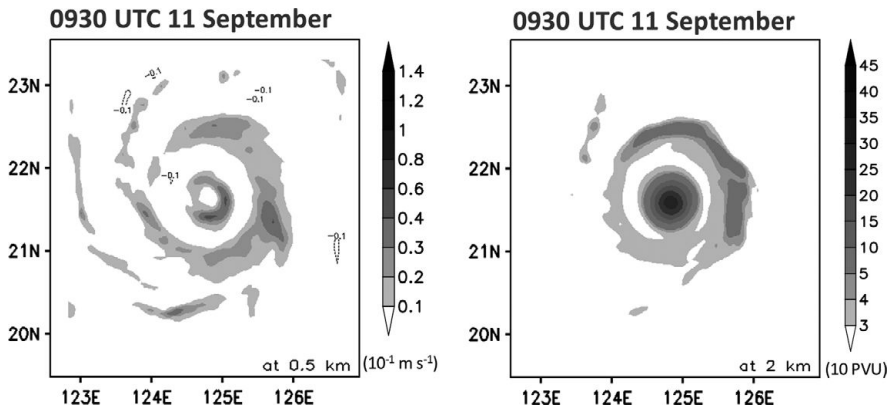


Fig. 13.1. Plan view of vertical velocity ( $10^{-1} \text{ ms}^{-1}$ ; left) at 0.5 km and potential vorticity (10 PVU; right) at 2 km at 0930 UTC 11 September when the simulated storm underwent a concentric-eyewall episode.

sustained eddy angular momentum fluxes raised by interactions between a mature TC and its environment. This TC–environment interaction, if sufficiently influential in strength and space, can generate the WISHE (wind-induced surface [air–sea] heat exchange; Yano and Emanuel, 1991) process, which may serve as a promising dynamical means for the establishment of a secondary eyewall outside the primary eyewall.

### 13.3 Internal mechanisms of SEF

Five internal mechanisms frequently discussed in previous SEF studies are considered in this subsection, namely, vortex Rossby waves, the axisymmetrization process, the beta-skirt axisymmetrization formation hypothesis, unbalanced boundary layer dynamics near the top of the TC boundary layer, and the balanced response to diabatic heating in a region of enhanced inertial stability.

#### 13.3.1 Vortex Rossby waves

Based on radar and satellite images, Macdonald (1968) found that disturbances with similar characteristics to Rossby waves are often associated with TC rainbands, and the term vortex Rossby waves (VRWs) was coined for these eddy activities in TCs. Similarly to Rossby waves in the planetary system, the dispersion relationship for VRWs is closely related to the vorticity gradient. In a dry and barotropic framework, Montgomery and Kallenbach (1997) obtained an analytic solution for the stagnation radius of VRWs that propagate radially outwards from the eyewall. It has since been proposed that the accumulation of energy near that stagnation radius of VRWs contributes to the outer rainbands, and perhaps to SEF (Montgomery and Kallenbach, 1997, Chen and Yau, 2001, Wang, 2002a, b, Chen *et al.*, 2003, Corbosiero *et al.*, 2006, Martinez *et al.*, 2010, 2011, Qiu *et al.*, 2010, Abarca and Corbosiero,

2011, Menelaou *et al.*, 2012, 2013). While the role of VRWs in TC rainbands has been clarified, the role of VRWs in SEF remains unclear. Recent studies with high-resolution models and more sophisticated physical processes have suggested that VRW activities may not directly contribute to SEF, which is different from results obtained from simple model configurations. Judt and Chen (2010) indicated that the near-zero potential vorticity (PV) gradient, subsidence, and straining effect that are already present prior to SEF are not conducive to the outward propagation of VRWs, suggesting reasonable doubt regarding the essential role of VRWs in SEF. Noting the ambiguous role of the eddy fluxes associated with VRWs in speeding up the tangential wind in the SEF region, Corbosiero *et al.* (2012) inferred that the outward propagation of the convectively coupled VRWs from the inner eyewall may act to redistribute PV and so allow moisture to accumulate at the stagnation radius. This suggests that VRWs make the active convection more prominent, but not to the extent that would directly cause SEF. Sun *et al.* (2013) showed only limited contribution from VRWs to SEF in their simulation of Typhoon Sinlaku.

#### 13.3.2 Axisymmetrization process

The axisymmetrization process, which has been articulated in previous studies on fundamental vortex dynamics (Melander *et al.*, 1987, McWilliams, 1990, Dritschel and Waugh, 1992, Fuentes, 2004), has also been used to interpret the formation of a vorticity ring outside the parent vortex in 2D barotropic models. It is suggested that the primary vortex can axisymmetrize weak vorticity patches into a vorticity ring, provided that the primary vortex is strong enough and the two vortices are sufficiently close to each other (Kuo *et al.*, 2004, 2008). Kuo *et al.* (2008) indicated that a vorticity skirt (where the radial gradient of vorticity is small) in the vortex's outer-core region

provides an additional flow background that is conducive to the formation of an outer vorticity ring enhanced by the binary-vortex interaction. Nevertheless, recent studies noted that PV patches outside the eyewall, either in the real TC environment or in a simulated TC that considers more realistic physical processes (such as moist convection), can be of comparable magnitude to that in the eyewall region and have dipole structures. Moon *et al.* (2010) demonstrated that the interaction between the TC core vortex and the convection-induced small vorticity dipoles of considerable strength in 2D flows does not lead to the formation of a coherent concentric vorticity ring. Consequently, the axisymmetrization process under a simplified 2D incompressible flow appears insufficient for describing SEF in the real atmosphere. The critical role of the 3D moist process in the maintenance of a vorticity ring has also been demonstrated (e.g. Wu *et al.*, 2009).

### 13.3.3 Beta-skirt axisymmetrization formation hypothesis

Terwey and Montgomery (2008) presented a new moist-based beta-skirt axisymmetrization (BSA) formation hypothesis for SEF. This hypothesis requires a region with a sufficiently long filamentation time (Rozoff *et al.*, 2006) and moist convective potential, together with a sufficient low-level radial potential vorticity gradient (i.e. a beta skirt) associated with the primary swirling flow and the follow-up WISHE process. The long filamentation time and sufficient moist convective potential establish a convectively favorable environment. The beta-skirt structure and WISHE process provide a dynamical pathway to SEF. Applying the 2D turbulence theory (Huang and Robinson, 1998) to the problem of SEF in a rotating TC environment, the theme of the BSA hypothesis is that the upscale energy cascade tends to occur on the beta skirt. Following this pathway, eddy kinetic energy associated with the sporadic convective cells outside the primary eyewall may be injected into the tangential direction and enhance local low-level jets (axisymmetrized into the mean tangential flow) on the skirt of the vortex's PV profile. Once the low-level jet strengthens substantially, it can be further intensified by coupling with the boundary layer through a wind-induced moisture feedback process such as WISHE, and may ultimately lead to SEF. The time scale of this energy cascade process, and the width of the corresponding jet, can be evaluated from the values of its PV gradient. Although relevant studies have shown consistency between the evaluated and simulated jet width in Terwey and Montgomery (2008) and Qiu *et al.* (2010), direct supporting evidence for the energy upscale process described above remains to be found.

### 13.3.4 Unbalanced boundary layer dynamics near the top of the TC boundary layer

A deeper understanding of the boundary layer dynamics associated with SEF has been provided by two recent companion studies (WH12), based on the two mechanisms for the spin-up of azimuthal-mean tangential winds in single-eyewall TCs, highlighted in Smith *et al.* (2009). Both mechanisms are associated with the radial advection of absolute angular momentum ( $M = fr^2/2 + rv$ ). The first mechanism applies to the spin-up above the boundary layer where  $M$  is materially conserved. The convergence of  $M$  is enhanced by the negative radial gradient of a diabatic heating rate associated with convective structures in a TC. This mechanism is the balanced dynamics (closely approximated by gradient wind and hydrostatic balance) addressed in many extant studies (cf. Section 13.3.5), and explains why the vortex expands in size. The second mechanism is related to the spin-up process within the boundary layer, and is considered to be important in the inner-core region of the storm. Although  $M$  is not materially conserved in the boundary layer, tangential winds can still be enhanced if the boundary layer inflow is sufficiently large to bring the air parcels to the small radii with minimal loss of  $M$  to friction. The boundary layer flow is coupled to the interior flow via the radial pressure gradient at the top of the boundary layer, but the spin-up of a vortex is ultimately tied to the dynamics of the boundary layer where inflow is prevailing, and the swirling wind is not in gradient wind balance over a substantial radial span.

By assimilating T-PARC (THORPEX Pacific Asian Regional Campaign; Elsberry and Harr, 2008) data (in particular, the aircraft observations) into the WRF (Weather Research and Forecasting; Skamarock *et al.*, 2005) model using an ensemble Kalman filter data assimilation (as in Wu *et al.* 2010), Wu *et al.* (2012) constructed a model/observation-consistent and high-resolution spatial/temporal data set for Typhoon Sinlaku (Fig. 13.2). The following features were robustly identified in the storm's outer-core region around one day before SEF: (1) the horizontal broadening of low-level tropospheric swirling flow; and (2) intensification of boundary layer inflow over the outer region. These two important features are consistent with flow characteristics indicated in the two mechanisms, one related to balance dynamics and the other connected with unbalanced dynamics, suggested to be responsible for the spin-up of single-eyewall TCs, and to set the scene for a progressive boundary layer control pathway to SEF.

In the second of the two companion papers, Huang *et al.* (2012) addressed the association between increases in storm size and SEF from the axisymmetric viewpoint. Their findings point to collective structure changes in the outer-core region of a mature TC (Fig. 13.3), which

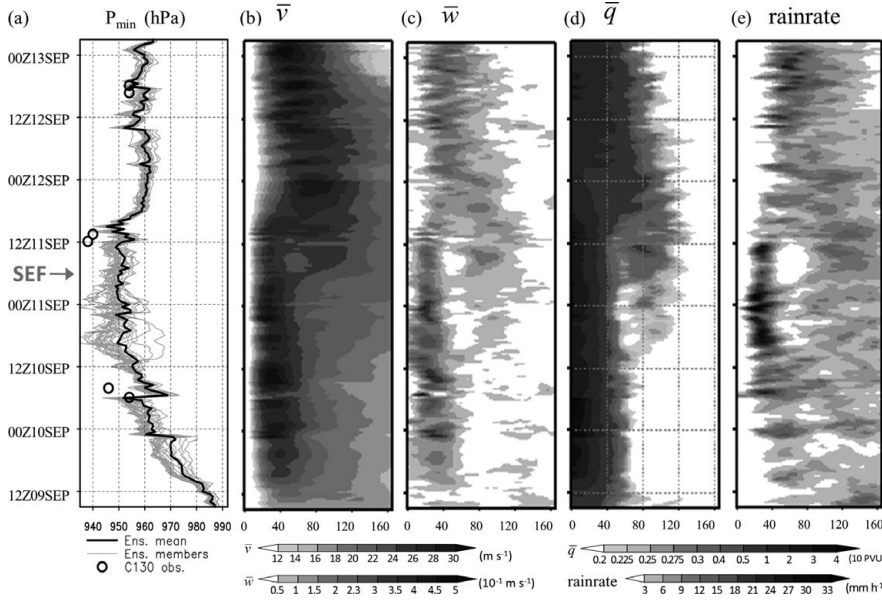


Fig. 13.2. (a) Temporal evolution of minimum sea level pressure in the control simulation of Typhoon Sinlaku (ensemble mean: black; ensemble members: gray) and C-130 flight observations (circles). Time–radius diagrams of the azimuthally mean (b) tangential wind ( $\text{ms}^{-1}$ ) at the lowest model level, (c) vertical velocity ( $10^{-1} \text{ ms}^{-1}$ ) at a height of 0.5 km, (d) potential vorticity ( $10 \text{ PVU}$ ) at a height of 2 km, and (e) total column rain rate ( $\text{mmh}^{-1}$ ) for the ensemble mean (average of 28 ensemble members). SEF time (0700 UTC 11 September) is indicated by an arrow on the  $y$ -axis (modified after Wu *et al.*, 2012, their Figures 4d and 5; ©American Meteorological Society. Used with permission.)

ultimately culminates in the formation of a secondary eyewall. The sequence begins with broadening of the low-level tangential wind field associated with the intensification of the eyewall that can be demonstrated by the balanced response above the boundary layer (the first spin-up mechanism). As a result of the presence of surface friction, boundary layer inflow increases underneath the broadened swirling wind, and becomes large enough to enhance the swirling circulation within the boundary layer (the second spin-up mechanism). This rapid increase in tangential winds near the top of the boundary layer results in the local development of supergradient winds, which causes deceleration of the inflow air that is moving inward. This process leads to the transition outside the primary eyewall from sporadic and/or weak convergence in the lower troposphere to a well-defined convergence zone concentrated within, and just above, the boundary layer. This progressive increase in supergradient forces continuously provides a mechanical means for high-enthalpy air to erupt from the boundary layer. Given the dynamically and thermodynamically favorable environment for convective activity, the progressive responses of the unbalanced boundary layer flow to an expanding swirling-wind field appear to be an important mechanism for concentrating and sustaining deep convection in a narrow supergradient wind zone collocated with the SEF region. While understanding the importance of the balanced response, this study particularly noted the critical role of unbalanced dynamics in SEF. The presented progressive boundary layer control on SEF also implies that the boundary layer scheme, and its coupling to the atmosphere above, need to be adequately represented in numerical models to improve

our understanding of SEF, as well as the accuracy of SEF forecasts, including the timing and preferred radial intervals.

The dynamical pathway to SEF advanced in WH12 is attractive on physical grounds, and its simplicity means that it is easy to examine. A number of recently published studies have revisited the impact of boundary layer dynamics on SEF from different perspectives. Concerning the asymmetry associated with rainbands that prevail prior to SEF, Qiu and Tan (2013) extended this SEF mechanism to include both axisymmetric and asymmetric components. The sequence of structural changes within, and just above, the boundary layer preceding SEF, and the corresponding dynamical pathway to SEF found in their simulation provided support to findings of WH12. Qiu and Tan (2013) further indicated the important role of the pre-existing outer rainbands in SEF. Wang *et al.* (2013) investigated the depth-integrated boundary layer flow, and demonstrated results that generally agree with the SEF pathway proposed in WH12. Sun *et al.* (2013) also found such an unbalanced dynamical pathway to SEF, while emphasizing how the axisymmetrization of outer rainbands and the balanced response contributed to peripheral heating in the rainbands. Forcing a slab boundary layer with a flat tangential wind profile, Abarca and Montgomery (2013) were able to generate a double-eyewall structure consistent with results from a full-physics model simulation. Taking a different point of view, Kepert (2013) indicated that the updraft in the secondary eyewall could be reasonably predicted from the gradient wind balance approximation alone. Applying a family of diagnostic boundary layer models, Kepert (2013) demonstrated that Ekman-like

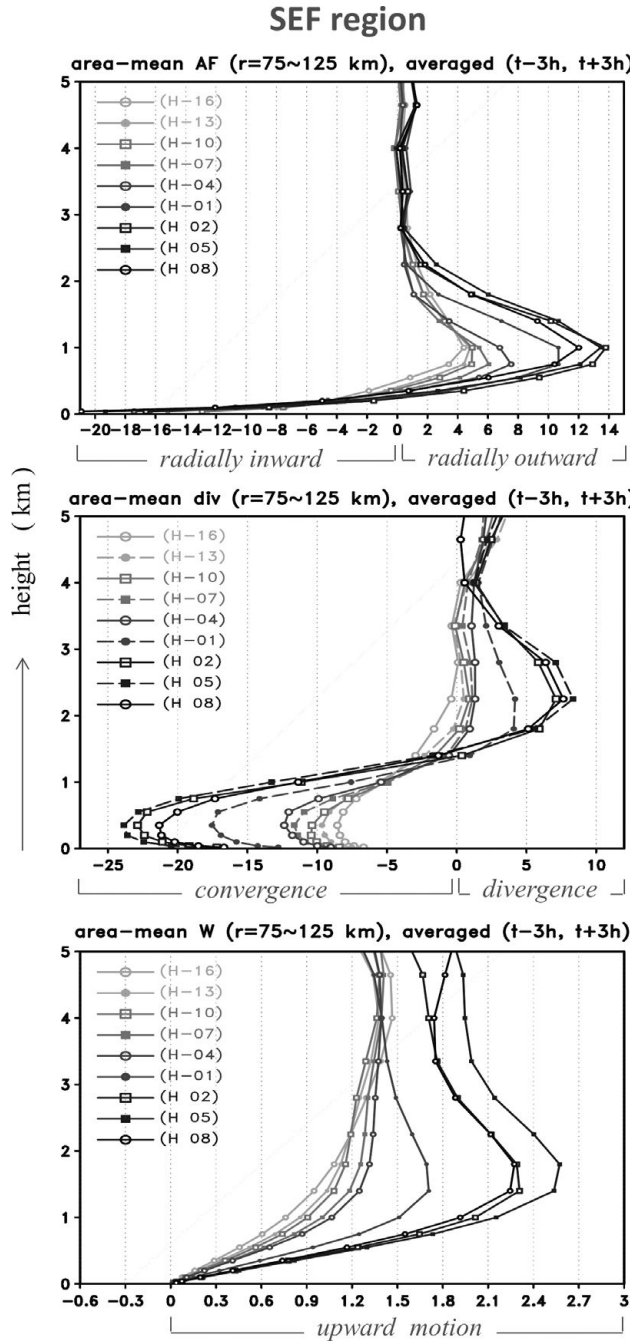


Fig. 13.3. Vertical profiles of the azimuthally, area-, and temporally averaged gradient wind ( $\text{ms}^{-1}$ ; top), divergence ( $10^{-5} \text{s}^{-1}$ ; middle), and vertical velocity ( $10^{-1} \text{ms}^{-1}$ ; bottom) in the SEF region over  $(t - 3 \text{ h}, t + 3 \text{ h})$ . Results are shown from 16 h before SEF (H - 16) to 8 h after SEF (H08) (modified after Huang *et al.*, 2012, their Figures 6a,c and 7a; ©American Meteorological Society. Used with permission.)

updraft in response to a small radial gradient of vorticity at the outer radii of a vortex, and the feedback between this frictionally forced updraft and the subsequent convectively generated vorticity contributes to SEF. More recently, Wu

*et al.* (2014) and Kepert and Nolan (2014) re-examined the mechanism proposed by Kepert (2013) using numerical simulations with sophisticated model physical processes. Some discrepancies have been shown between these analyses. Further studies are ongoing that aim to develop a better understanding of the role of boundary layer dynamics in SEF.

### 13.3.5 Balanced response to diabatic heating in a region of enhanced inertial stability

Regarding balanced dynamics, the response of transverse circulation to a heating/momentu source/sink to satisfy the gradient wind and hydrostatic balance relationship (known as the Sawyer–Eliassen equation; Eliassen, 1951) has been applied to the evolution of the mean swirling circulation in idealized vortices in many previous studies (e.g. Schubert and Hack, 1982, Shapiro and Willoughby, 1982, Hack and Schubert, 1986). Rozoff *et al.* (2012) revisited the balanced dynamics of SEF from the axisymmetric viewpoint using results from cloud-resolving models. An expansion of kinetic energy (or enhanced inertial stability) had been found to occur prior to SEF in their WRF model simulation, a feature consistent with the presence of beta-skirt structure and the expansion of tangential winds mentioned in other studies. The impact of this enhanced kinetic energy and diabatic heating on SEF was further investigated with a symmetric linearized non-hydrostatic model (a balanced vortex model similar to the Sawyer–Eliassen model). Given the axisymmetric tangential wind and temperature profiles from the WRF model output, this simple model depicts how the transverse circulation responds to diabatic heating and surface friction, which are forcings prescribed by the WRF simulation. The diagnosed results are similar to the mean vortex structure in the WRF simulation in a number of ways, and suggest that the sustained diabatic heating, along with the broadening wind outside the primary eyewall, contribute most to the enhancement of tangential winds in the SEF region. Conducting the same analysis, Sun *et al.* (2013) demonstrated supporting results based on a WRF simulation of Typhoon Sinlaku.

## 13.4 Concluding remarks

In addition to the above discussion, other perspectives exist that are not categorized as environmental conditions or internal dynamics for SEF, but are still worth noting. Houze *et al.* (2007) indicated that their model simulation failed to capture the eyewall replacement cycle of Hurricane Rita (2005) when the horizontal resolution was reduced from 1.67 to 5 km. Meanwhile, it was speculated that the small-scale features shown in the radar data during

Rita's eyewall replacement cycle may be related to the VRW dynamics. The importance of increasing model resolution, and the value of targeting small-scale structures in TCs, are suggested as likely factors in the future improvement of our understanding of SEF and the subsequent eyewall replacement cycle. Details of the microphysical processes used in the models have shown that they affect the timing and locations of SEF, the intensity of eyewalls, and the duration of an eyewall replacement cycle (Willoughby *et al.*, 1984, Terwey and Montgomery, 2008, Zhou and Wang, 2011, Fang and Zhang, 2012).

The environmental conditions and internal mechanisms suggested as being responsible for SEF in existing studies are briefly summarized below. Regarding the environmental control of SEF, model initial relative humidity has been shown to be critical to the increase of storm size and the subsequent SEF in recent studies using sophisticated numerical models. In contrast, a variety of different approaches have been proposed as the internal mechanisms of SEF, including: (1) axisymmetrization of prescribed/present outer vorticity patches; (2) the accumulation of eddy kinetic energy associated with VRWs near their stagnation radii; (3) the energy cascade process over the beta skirt of the TC vortex in a convectively favorable condition and subsequent positive feedback provided by WISHE (BSA hypothesis); (4) the unbalanced response (i.e. the generation of supergradient wind, and its impact on the transverse circulation) to the expanding winds; and (5) the balanced response of transverse circulation to diabatic heating over the area with enhanced inertial stability. Particularly noteworthy is that the broadening tangential wind (the beta-skirt structure and enhanced kinetic energy basically indicate a similar structure as well) furnishing the pathway to SEF is a consistently vital process among the various internal dynamical interpretations of SEF. Several conditions and mechanisms have been suggested for the establishment of such a skirted vortex structure, including higher environmental relative humidity or diabatic heating associated with outer rainbands, the initial vortex size/shape, concurrent storm intensity, convective heating in an intensifying storm, and radially outward-propagating VRWs.

Although recent advances in the unbalanced and balanced dynamics of TCs with double eyewalls appear promising for the interpretation of SEF from the axisymmetric perspective, the quantitative impacts of these factors on SEF and their mutual feedback require further investigation. While axisymmetric dynamics have been shown to play a critical role in SEF, the question of how the asymmetric components (e.g. spiral rainbands and sporadic convective cells in the vortex's outer-core region) influence SEF also requires further study if we are to develop a more comprehensive understanding of SEF. While the environmental conditions are relatively well understood and better

presented in the observations and numerical models, discoveries are also being made of more uncertainties associated with the evolution of a TC vortex and the accompanying convective-scale features. More TC observations and further investigation of internal vortex dynamics are required if we are to better present the corresponding physical processes (e.g. microphysics, boundary layer dynamics) in numerical simulations of SEF, as well as the whole TC life-cycle.

### 13.5 Acknowledgment

Chun-Chieh and Yi-Hsuan were supported by the National Science Council of Taiwan under Grant NSC102-2628-M-002-008.

### References

- Abarca, S. F. and Corbosiero, K. L. (2011). Secondary eyewall formation in WRF simulations of hurricanes Rita and Katrina (2005). *Geophys. Res. Lett.*, **38**, L07802, doi:10.1029/2011 GL047015.
- Abarca, S. F. and Montgomery, M. T. (2013). Essential dynamics of secondary eyewall formation. *J. Atmos. Sci.*, **70**, 3216–3230.
- Black, M. L. and Willoughby, H. E. (1992). The concentric eyewall cycle of Hurricane Gilbert. *Mon. Wea. Rev.*, **120**, 947–957.
- Bell, M. M., Montgomery, M. T., and Lee, W.-C. (2012). An axisymmetric view of eyewall evolution in Hurricane Rita (2005). *J. Atmos. Sci.*, **8**, 2414–2432.
- Chen, Y. and Yau, M. K. (2001). Spiral bands in a simulated hurricane. Part I: Vortex Rossby wave verification, *J. Atmos. Sci.*, **58**, 2128–2145.
- Chen, Y., Brunet, G., and Yau, M. K. (2003). Spiral bands in a simulated hurricane. Part II: Wave activity diagnostics, *J. Atmos. Sci.*, **60**, 1239–1256.
- Corbosiero, K. L., Molinari, J., Aiyyer, A. R., and Black, M. L. (2006). The structure and evolution of Hurricane Elena (1985). Part II: Convective asymmetries and evidence for vortex Rossby waves. *Mon. Wea. Rev.*, **134**, 3073–3091.
- Corbosiero, K. L., Abarca, S., and Montgomery, M. T. (2012). Vortex Rossby waves and secondary eyewall formation in a high-resolution simulation of Hurricane Katrina (2005). 30th Conference on Hurricanes and Tropical Meteorology. Amer. Meteor. Soc., Jacksonville, FL. 1A.6.
- Didlake, A. C. and Houze, R. A., Jr. (2011). Kinematics of the secondary eyewall observed in Hurricane Rita (2005). *J. Atmos. Sci.*, **68**, 1620–1636.
- Dritschel, D. G. and Waugh, D. (1992). Quantification of the inelastic interaction of unequal vortices in two-dimensional vortex dynamics. *Phys. Fluids*, **4A**, 1737–1744.
- Eliassen, A. (1951). Slow thermally or frictionally controlled meridional circulation in a circular vortex. *Astrophys. Norv.*, **5**, 19–60.

- Elsberry R. L. and Harr, P. A. (2008). Tropical cyclone structure (TCS08) field experiment science basis, observational platforms, and strategy. *Asia-Pacific J. Atmos. Sci.*, **44**, 3, 209–231.
- Fang, J. and Zhang, F. (2012). Effect of beta shear on simulated tropical cyclones. *Mon. Wea. Rev.*, **140**, 3327–3346.
- Fuentes, O. U. V. (2004). Vortex filamentation its onset and its role on axisymmetrization and merger. *Dyn. Atmos. Oceans*, **40**, 23–42.
- Hack, J. J. and Schubert, W. H. (1986). Nonlinear response of atmospheric vortices to heating by organized cumulus convection. *J. Atmos. Sci.*, **43**, 1559–1573.
- Hawkins, J. D. and Helveston, M. (2008). Tropical cyclone multiple eyewall characteristics. 28th Conf. on Hurricanes and Tropical Meteorology, Orlando, FL. *Amer. Meteor. Soc.*, 14B.1.
- Hence, D. A. and Houze, R. A., Jr. (2012). Vertical structure of tropical cyclones with concentric eyewalls as seen by the TRMM precipitation radar. *J. Atmos. Sci.*, **69**, 1021–1036.
- Hill, K. A. and Lackmann, G. M. (2009). Influence of environmental humidity on tropical cyclone size. *Mon. Wea. Rev.*, **137**, 3294–3315.
- Houze, R. A., Jr., Chen, S. S., Lee, W.-C., et al. (2006). The Hurricane Rainband and Intensity Change Experiment: Observations and modeling of Hurricanes Katrina, Ophelia, and Rita. *Bull. Am. Meteor. Soc.*, **87**, 1503–1521.
- Houze, R. A., Jr., Chen, S. S., Smull, B. F., Lee, W.-C., and Bell, M. M. (2007). Hurricane intensity and eyewall replacement, *Science*, **315**, 1235–1239.
- Huang, H.-P. and Robinson, W. A. (1998). Two-dimensional turbulence and persistent zonal jets in a global barotropic model, *J. Atmos. Sci.*, **55**, 611–632.
- Huang, Y.-H., Montgomery, M. T., and Wu, C.-C. (2012). Concentric eyewall formation in Typhoon Sinlaku (2008). Part II: Axisymmetric dynamical processes. *J. Atmos. Sci.*, **69**, 662–674.
- Kepert, J. D. (2013). How does the boundary layer contribute to eyewall replacement cycles in axisymmetric tropical cyclones? *J. Atmos. Sci.*, **70**, 2808–2830.
- Kepert, J. D. and Nolan, D. S. (2014). Analysis of a simulated tropical cyclone eyewall replacement cycle. 31st Conference on Hurricanes and Tropical Meteorology. *Amer. Meteor. Soc.*, San Diego, CA. 11C.3.
- Kossin, J. P. and Sitkowski, M. (2009). An objective model for identifying secondary eyewall formation in hurricanes. *Mon. Weather Rev.*, **137**, 876–892.
- Kuo, H.-C., Lin, L.-Y., Chang, C.-P., and Williams, R. T. (2004). The formation of concentric vorticity structures in typhoons. *J. Atmos. Sci.*, **61**, 2722–2734.
- Kuo, H.-C., Schubert, W. H., Tsai, C.-L., and Kuo, Y.-F. (2008). Vortex interaction and barotropic aspects of concentric eyewall formation. *Weather Rev.*, **137**, 5182–5198.
- Kuo, H.-C., Chang, C.-P., Yang, Y.-T. and Jiang, H.-J. (2009). Western North Pacific typhoons with concentric Eyewalls. *Mon. Weather Rev.*, **137**, 3758–3770.
- Judit, F. and Chen, S. S. (2010). Convectively generated potential vorticity in rainbands and formation of the secondary eyewall in Hurricane Katrina of 2005. *J. Atmos. Sci.*, **67**, 3581–3599.
- MacDonald, N. J. (1968). The evidence for the existence of Rossby type waves in the hurricane vortex. *Tellus*, **20**, 138–150.
- Martinez, Y., Brunet, G., and Yau, M. K. (2010). On the dynamics of two-dimensional hurricane-like concentric rings vortex formation. *J. Atmos. Sci.*, **67**, 3253–3268.
- Martinez, Y., Brunet, G., Yau, M. K., and Wang, X. (2011). On the dynamics of concentric eyewall genesis: Space-time empirical normal modes diagnosis. *J. Atmos. Sci.*, **68**, 457–476.
- McWilliams, J. C. (1990). The vortices of two-dimensional turbulence. *J. Fluid. Mech.*, **219**, 361–385.
- Melander, M. V., McWilliams, J. C., and Zabusky, N. J. (1987). Axisymmetrization and vorticity-gradient intensification of an isolated two-dimensional vortex through filamentation. *J. Fluid Mech.*, **178**, 137–159.
- Menelaou, K., Yau, M. K., and Martinez, Y. (2012). On the dynamics of the secondary eyewall genesis in Hurricane Wilma (2005). *Geophys. Res. Lett.*, **39**, L04801, doi:10.1029/2011GL050699.
- Menelaou, K., Yau, M. K., and Martinez, Y. (2013). Impacts of asymmetric dynamical processes on the structure and intensity change of two-dimensional hurricane-like annular vortices. *J. Atmos. Sci.*, **70**, 559–582.
- Montgomery, M. T. and Kallenbach, R. J. (1997). A theory for vortex Rossby waves and its application to spiral bands and intensity changes in hurricanes, *Q. J. R. Meteorol. Soc.*, **123**, 435–465.
- Moon, Y., Nolan, D. S., and Iskandarani, M. (2010). On the use of two-dimensional incompressible flow to study secondary eyewall formation in tropical cyclones. *J. Atmos. Sci.*, **67**, 3765–3773.
- Nong, S. and Emanuel, K. A. (2003). A numerical study of the genesis of concentric eyewalls in hurricane. *Quart. J. Roy. Meteor. Soc.*, **129**, 3323–3338.
- Qiu, X., Tan, Z.-M., and Xiao, Q. (2010). The roles of vortex Rossby waves in Hurricane secondary eyewall formation. *Mon. Wea. Rev.*, **138**, 2092–2019.
- Qiu, X. and Tan, Z.-M. (2013). The roles of asymmetric inflow forcing induced by outer rainbands in tropical cyclone secondary eyewall formation. *J. Atmos. Sci.*, **70**, 953–974.
- Rozoff, C. M., Schubert, W. H., McNoldy, B. D., and Kossin, J. P. (2006). Rapid filamentation zones in intense tropical cyclones. *J. Atmos. Sci.*, **63**, 325–340.
- Rozoff, C. M., Nolan, D. S., Kossin, J. P., Zhang, F., and Fang, J. (2012). The roles of an expanding wind field and inertial stability in tropical cyclone secondary eyewall formation. *J. Atmos. Sci.*, **69**, 2621–2643.
- Schubert, W. H. and Hack, J. J. (1982). Inertial stability and tropical cyclone development. *J. Atmos. Sci.*, **39**, 1687–1697.
- Shapiro, L. J. and Willoughby, H. E. (1982). The response of balanced hurricanes to local sources of heat and momentum. *J. Atmos. Sci.*, **39**, 378–394.
- Sikowstki, M., Kossin, J. P., and Rozoff, C. M. (2011). Intensity and structure changes during hurricane eyewall replacement cycles. *Mon. Wea. Rev.*, **139**, 3829–3847.

- Skamarock, W. C., Klemp, J. B., Dudhia, J., et al. (2005). A description of the Advanced Research WRF Version 2. NCAR Tech. NoteNCAR/TN-4681ST, 88 pp.
- Smith, R. K., Montgomery, M. T., and Nguyen, S. V. (2009). Tropical cyclone spin-up revisited. *Q. J. R. Meteorol. Soc.*, **135**, 1321–1335.
- Sun, Y. Q., Jiang, Y., Tan, B., and Zhang, F. (2013). The governing dynamics of the secondary eyewall formation of Typhoon Sinlaku (2008). *J. Atmos. Sci.*, **70**, 3818–3837.
- Terwey, W. D. and Montgomery, M. T. (2008). Secondary eyewall formation in two idealized, full-physics modeled hurricanes. *J. Geophys. Res.*, **113**, D12112.
- Wang, Y. (2002a). Vortex Rossby waves in a numerically simulated tropical cyclone. Part I: Overall structure, potential vorticity, and kinetic energy budgets. *J. Atmos. Sci.*, **59**, 1213–1238.
- Wang, Y. (2002b). Vortex Rossby waves in a numerically simulated tropical cyclone. Part II: The role in tropical cyclone structure and intensity changes. *J. Atmos. Sci.*, **59**, 1239–1262.
- Wang, Y. (2009). How do outer spiral rainbands affect tropical cyclone structure and intensity? *J. Atmos. Sci.*, **66**, 1250–1273.
- Wang, X., Ma, Y., and Davidson, N. E. (2013). Secondary eyewall formation and eyewall replacement cycles in a simulated hurricane: effect of the net radial force in the hurricane boundary layer. *J. Atmos. Sci.*, **70**, 1317–1341.
- Willoughby, H. E., Clos, J. A., and Shoreibah, M. G. (1982). Concentric eyewalls, secondary wind maxima, and the evolution of the hurricane vortex, *J. Atmos. Sci.*, **39**, 395–411.
- Willoughby, H. E., Jin, H.-L., Lord, S. J., and Piotrowicz, J. M. (1984). Hurricane structure and evolution as simulated by an axisymmetric, nonhydrostatic numerical model, *J. Atmos. Sci.*, **41**, 1169–1186.
- Willoughby, H. E. and Black, P. G. (1996). Hurricane Andrew in Florida: Dynamics of a disaster, *Bull. Am. Meteorol. Soc.*, **77**, 543–549.
- Wu, C.-C., Cheng, H.-J., Wang, Y., and Chou, K.-H. (2009). A numerical investigation of the eyewall evolution in a landfalling typhoon. *Mon. Wea. Rev.*, **137**, 21–40.
- Wu, C.-C., Lien, G.-Y., Chen, J.-H., and Zhang, F. (2010). Assimilation of tropical cyclone track and structure based on the Ensemble Kalman Filter (EnKF). *J. Atmos. Sci.*, **67**, 3806–3822.
- Wu, C.-C., Huang, Y.-H., and Lien, G.-Y. (2012). Concentric eyewall formation in Typhoon Sinlaku (2008). Part I: Assimilation of T-PARC data based on the ensemble Kalman filter (EnKF). *Mon. Wea. Rev.*, **140**, 506–527.
- Wu, C.-C., Kuan, S.-P., Cheng, Y.-M., and Huang, Y.-H. (2014). Unbalanced dynamics of secondary eyewall formation in tropical cyclones- Part II: Analyses from higher-resolution simulations. 31st Conference on Hurricanes and Tropical Meteorology. Amer. Meteor. Soc., San Diego, CA. 11C.2.
- Yano, J.-I. and Emanuel, K. A. (1991). An improved model of the equatorial troposphere and its coupling with the stratosphere, *J. Atmos. Sci.*, **48**, 377–389.
- Zhou, X. and Wang, B. (2011). Mechanism of concentric eyewall replacement cycles and associated intensity change. *J. Atmos. Sci.*, **68**, 972–988.

# 14

## Seasonal forecasting of floods and tropical cyclones

*Tom Beer and Oscar Alves*

### 14.1 Introduction

The Centre for Australian Weather and Climate Research (CAWCR) is a partnership between the Australian Bureau of Meteorology and the CSIRO Division of Marine and Atmospheric Research. CSIRO (Commonwealth Scientific and Industrial Research Organisation) is the Australian Federal Government's major research agency which means that the partnership offers the possibility of bringing both research and operational expertise to bear on issues related to weather and climate.

One of the areas in which this partnership has borne fruit is in the treatment of floods and tropical cyclones in which the research base of CSIRO has combined with the forecasting arm of the Bureau of Meteorology to improve the service offered to the Australian public.

The Australian public is concerned both with the occurrence of tropical cyclones in the immediate future, and in the longer term future, when it is possible that climatic change may affect the distribution, landfall location, and intensity of tropical cyclones. CAWCR, through its Climate Variability and Change Research Program has the largest group of climate scientists in Australia, working together to look at seasonal prediction, climate change and climate variability.

The rainfall in the Australian tropics is due to the effects of the monsoonal wet season, augmented by extra rainfall from the occasional tropical cyclone. Although tropical cyclones themselves can produce strong winds, storm surges, and floods – the combination of a particularly wet wet-season and a tropical cyclone can intensify the disaster and amplify the consequences.

This was the situation on 3 February 2011, when Cyclone Yasi made landfall in North Queensland, following on from a December–January period that had seen extensive flooding in Queensland as a result of a strong La Niña.

The predictive ocean–atmosphere model of the Centre for Australian Weather and Climate Research (POAMA) indicated in May 2010 that the wet season in Queensland would be extensive, with large amounts of rainfall.

Tropical cyclone Yasi, though intense, had a well-behaved track and from 30 January was forecast to make landfall in Northern Queensland.

Model results indicate that the effects of climate change will be to decrease the numbers of tropical cyclones affecting Northern Australia and to increase the proportion of severe tropical cyclones affecting the region.

### 14.2 Seasonal forecasting

The Bureau of Meteorology has developed a seasonal prediction model known as POAMA, which is an acronym for the Predictive Ocean Atmosphere Model for Australia. It is a dynamic computer model of the climate system run on the operational supercomputer that is used to generate weather forecasts. Because the weather and climate of the eastern part of Australia is strongly influenced by El Niño (McBride and Nicholls, 1983), a significant product generated by POAMA consists of model forecasts of the El Niño – Southern Oscillation. They are provided as an operational product on the website of the Bureau of Meteorology and are included in the monthly model summary of predictions from POAMA and other models operated by international organizations. Because the south-eastern Australian climate is also influenced by the Indian Ocean Dipole (IOD), forecasts of the IOD are provided in addition.

The latest operational version of POAMA is POAMA-2 (version 2.4). A 30-member ensemble of POAMA-2 forecasts is run twice per month and gives forecasts out to nine months ahead. Probabilities are based on a 30-member ensemble from POAMA-2 starting on the first and the fifteenth of the month. The results, which are forecast out to nine months' lead-time, show all the runs so that the probability distributions that result provide a range of possible developments in sea surface temperature (SST) in the equatorial Pacific Ocean and for the Indian Ocean.

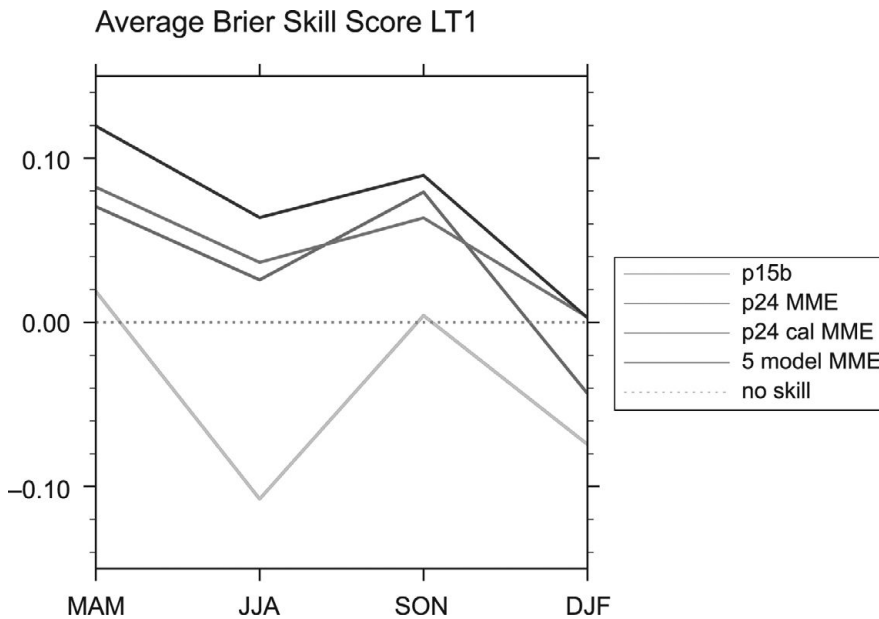


Fig. 14.1. Australian rainfall Brier skill score for POAMA1.5 (p15b), POAMA 2.4 (P24 MME), a re-calibrated version of POAMA2.4 (P24 cal MME), and a five member multi-model ensemble that incorporates POAMA 2.4a, POAMA 2.4b, POAMA 2.4c plus ECSys3 and the UKMO HadGEM2 seasonal forecast (5 model MME). A black and white version of this figure will appear in some formats. For the colour version, please refer to Plate 25.

More detailed information about the model is available on the experimental POAMA page: <<http://poama.bom.gov.au/>>. Further details on POAMA-2 SST skill can be found in Wang *et al.* (2011).

A separate system (POAMA-2 Multiweek) is now run every week in experimental mode to produce an ensemble of 33 members also out to nine months. This system is tailored to forecasting on multi-week/monthly time scales and includes a new coupled breeding method.

The performance of the POAMA model is illustrated in Fig. 14.1, which depicts the Brier skill score for POAMA1.5, POAMA 2.4, a re-calibrated version of POAMA2.4, and a five-member multi-model ensemble that incorporates POAMA 2.4a, POAMA 2.4b, POAMA 2.4c, plus ECSys3 (Stockdale *et al.*, 2011), and the UKMO HadGEM2 seasonal forecast (Arribas *et al.*, 2011). Details of skill over Australia, including a comparison with other international models can be found in Langford and Hendon (2011)

### 14.3 POAMA and the Beijing floods of 21 July 2012

On Saturday 21 July 2012, Beijing suffered its heaviest rainfall for over 60 years, with average precipitation reaching 170 mm, while a town in the suburban district of Fangshan received 460 mm of rain. The storm was widespread. In Hebei province, as at 26 July 2012, 32 people were confirmed dead and another 20 missing after the storm over the weekend. More than 2.66 million people had been directly affected by the storm that flooded 59 counties in Hebei province. The official death toll until

27 July was reported as 37 people, after which it was raised to 77. Direct economic losses totalled more than 12.28 billion yuan (\$1.92 billion).

Using archived POAMA output, we have examined the performance of POAMA in its ability to forecast high rainfall in the Beijing area. POAMA consistently provided forecasts of high rainfall (exceeding 10 mm/day) for the Beijing region as from 28 June 2012 (Fig. 14.2), indicating that there was approximately three-week predictability for this event from a seasonal prediction model. The Bureau of Meteorology numerical weather prediction model, known as ACCESS, was able to provide high resolution analysis 48 hours before the storm that indicated that localized precipitation in excess of 100 mm/day was to be expected.

### 14.4 May 2010 POAMA forecast

Fig. 14.3 depicts the observed (green curve) and the ensemble of POAMA2.4 forecasts (thin blue and violet curves, with ensemble indicated by dark green curve) for the Niño34 SST index during 2010 and early 2011. The forecasts were initialized on 1 May 2010. The strong La Niña during 2010, which contributed to extreme rainfall in eastern Australia during spring and early summer, was not predictable prior to May 2010, but by May 2010 the POAMA2.4 forecasts were clearly indicating the development of a strong cold event that would extend for at least the next nine months.

POAMA also provides information on the spatial distribution of expected rainfall. Figure 14.4 shows the observed (Fig. 14.4a) and forecast (Fig. 14.4b) rainfall anomaly for October–December 2011 for Australia. The forecast is the 30-member ensemble mean from the POAMA2.4 seasonal

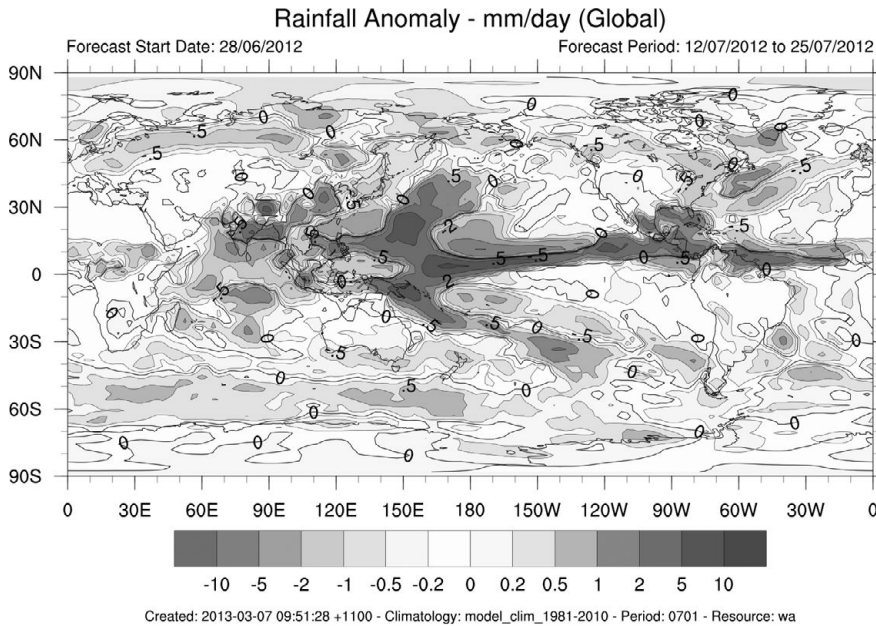


Fig. 14.2. POAMA forecast made on 28 June 2012 predicted heavy rainfall in the Beijing area for the 12 July to 25 July 2012 period.

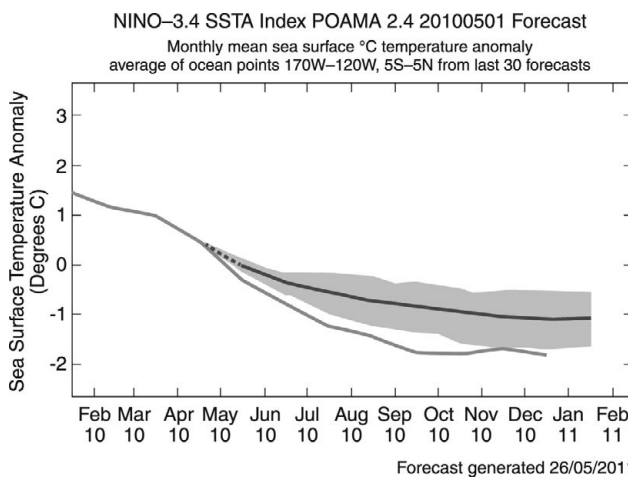


Fig. 14.3. May 2010 forecasts of the El Niño index from POAMA indicating that strong La Niña conditions were to be expected at least the next nine months. La Niña conditions are indicative of above normal rainfall in Eastern Australia.

forecast that was initialized on 1 May 2010. The colour bars are the same for Figs. 14.4a and b. Extreme wet conditions in eastern Australia for October–December 2011 were well forecast from at least 1 May 2010 due to the development of a strong La Niña event that was well predicted by the POAMA2.4 model, as shown in Fig. 14.3.

In fact this forecast was very accurate with extreme rainfall occurring over much of eastern Australia. The dramatic effects of localized severe storms and flash flooding on topography that had been previously moistened was graphically illustrated in January 2011, when the continuation of heavy rainfall that had started over

much of Queensland in December 2010 caused severe flash flooding in the centre of the City of Toowoomba.

The record rainfalls and flooding experienced across much of the region, and throughout Australia, in the 2010/11 and 2011/12 summers highlighted that the tropical Pacific ocean temperatures are not the only sea surface temperatures of importance, but one needs to consider the status of all three oceans surrounding Australia – Pacific, Indian, and Southern – in influencing seasonal and inter-annual rainfall variability. The spring/summer of 2010/11 saw one of the strongest La Niña events on record, combined with a negative IOD event and a positive SAM – i.e. all three key influences were in their wet phases in terms of expected rainfall impacts on south-eastern Australia.

SAM describes the north–south movement of the westerly wind belt that circles Antarctica, dominating the middle to higher latitudes of the Southern Hemisphere. The changing position of this westerly wind belt influences the strength and position of cold fronts and mid-latitude storm systems, and is an important driver of rainfall variability in southern Australia. In a positive SAM event, the belt of strong westerly winds contracts towards Antarctica. This results in weaker than normal westerly winds and higher pressures over southern Australia, restricting the penetration of cold fronts inland. The positive phase of SAM is typically associated with wetter and cooler conditions over much of Australia during spring and summer, but with drier and cooler conditions over the south-west and south-east coasts of the continent during winter (Hendon *et al.*, 2007).

These conditions, coupled with the warmest sea-surface temperatures on record to the north of the Australian continent, contributed to making 2010–11 Australia's wettest

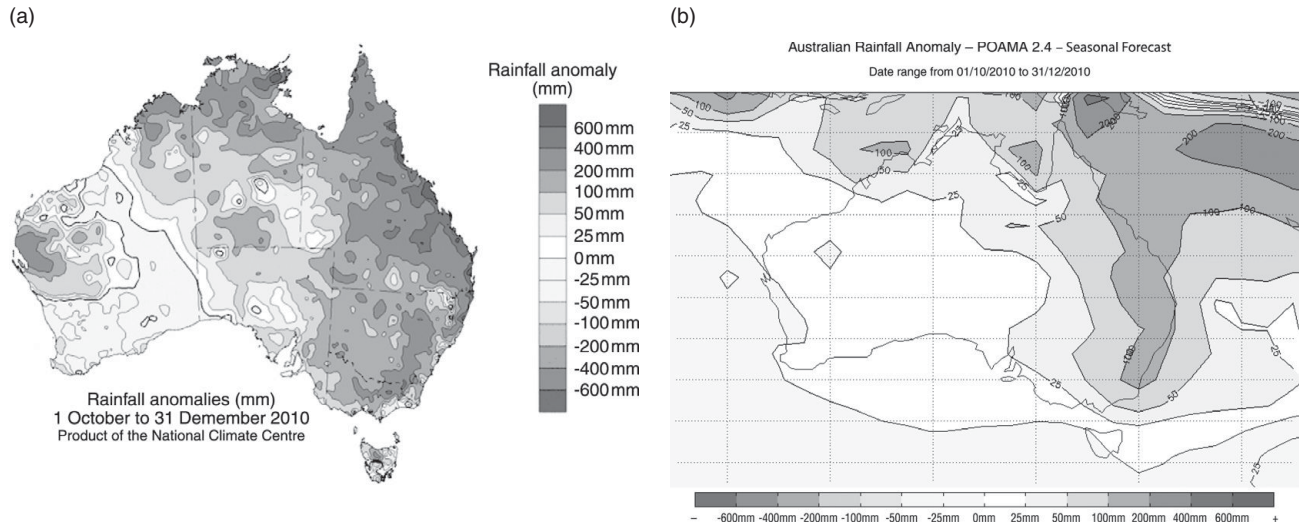


Fig. 14.4. (a) Observed rainfall anomalies for October to December 2011. (b) POAMA Forecast of rainfall anomalies for October to December 2011.

two-year period on record. While the extensive flooding of 2010/11 was, by and large, consistent with natural variability, it is possible that ongoing global warming contributed to the magnitude of the event through its impact on ocean temperatures. The spring and summer of 2011/12 saw the re-emergence of another (weaker) La Niña event, combined with a positive SAM during early summer, but this time the Indian Ocean played a lesser role.

#### 14.5 Tropical cyclones during the 2010/2011 rainy season

There are, on average, approximately 12 tropical cyclones per year that are identified as occurring within the Australian region. Of these about 40% (~5) make landfall over the Australian continent. Tropical cyclones and tropical storms provide a large proportion of rainfall in tropical Australia, that ranges from 40% in tropical Queensland to 60% in tropical western Australia (Lavender and Abbs, 2013). Tropical cyclone climatologies for Australia have been used to determine the tropical cyclone hazard.

Numerical weather prediction models have not, as yet, reached sufficiently fine resolution that they can predict the formation and subsequent strengthening and motion of a tropical cyclone. They are, however, able to identify tropical lows so that a sufficiently skilled forecaster is able to use such numerical weather prediction models, along with satellite photographs of tropical cyclone clouds that position the tropical cyclone, and thus use the two items of information to assist with forecasts of tropical cyclone tracks.

Once the tropical cyclone has made landfall, there are four particular impacts that need to be considered: strong winds, extreme rainfall, the flooding associated with the

cumulative rainfall, and the short-term rise of sea level (known as storm surge).

During the severe wet season of January–February 2011 the eastern coast of Australia was affected by three tropical cyclones. Severe Tropical Cyclone Zelia, from 14–18 January 2011, Tropical Cyclone Anthony, from 22–31 January 2011, and Severe Tropical Cyclone Yasi from 30 January to 3 February 2011.

#### 14.6 Cyclone Yasi

Figure 14.5 depicts the track of Severe Tropical Cyclone Yasi. The scale shows very destructive winds in red, destructive winds in pink, and gale force winds are shaded. The forecast indicates the areas that may be impacted from landfall. Orange is used to indicate the Tropical Cyclone Warning Zone, whereas Yellow is used to denote the Tropical Cyclone Watch Zone.

Severe Tropical Cyclone Yasi is remembered in Australia because a major portion of the Australian banana crop was wiped out causing extreme spikes in the banana price – repeating the situation of 2006 when Tropical Cyclone Larry made landfall on 20 March 2006 and also destroyed 80–90% of Australia’s banana crop. Australia is relatively free of banana pests and diseases, and therefore does not allow bananas to be imported. Bananas were in short supply throughout Australia for the remainder of both 2011 and 2006, which increased prices across the country by 400–500%.

#### 14.7 Downscaling

A question of continuing relevance relates to the influence of climate change on tropical cyclone numbers, intensity,

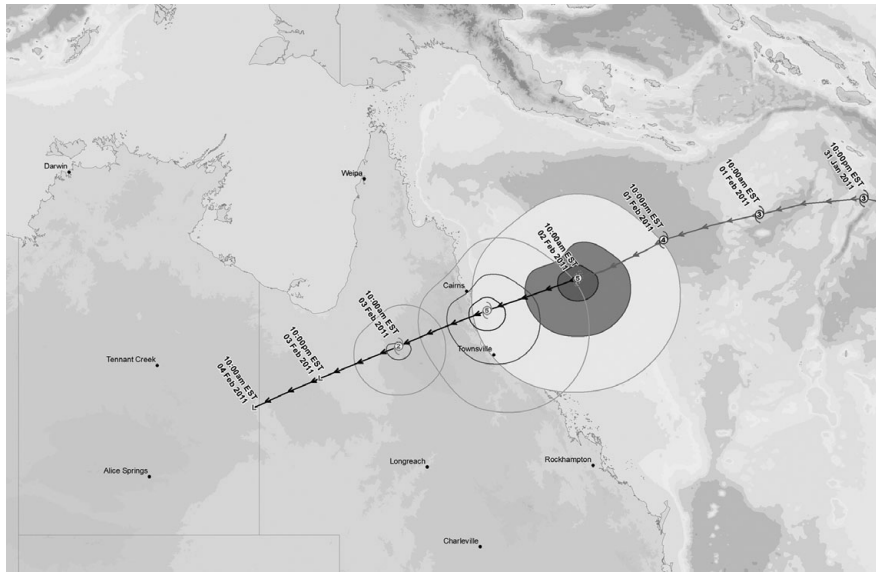


Fig. 14.5. Forecast track of TC Yasi as at 4am on 2 February 2011. An animated version of this is available at: <http://www.bom.gov.au/cyclone/history/yasi.shtml#loops>

and landfall location. Callaghan and Power (2011) examined the statistics of past Queensland tropical cyclones and found that the number of tropical cyclones making landfall over eastern Australia declined from about 0.45 TCs/year in the early 1870s to about 0.17 TCs/year in recent times. They noted that this decline can be partially explained by a weakening of the Walker Circulation, and a natural shift towards a more El Niño-dominated era. The extent to which global warming might also be partially responsible for the decline in landfalls—if it is at all—is unknown.

This question has been examined by using dynamical downscaling of computer models (Daloz *et al.*, 2012). In particular, the output from the 200 km resolution CSIRO Mark 3.6 general circulation model has been nested into the 65 km output of CCAM in which tropical cyclone-like vortices are detected. The details of these vortices are then elucidated using mesoscale models such as RAMS and WRF that have 5 km resolution. Using this method, simulations were undertaken for the present climate and for the end of the twenty-first century using the SRES A2 scenario. Based on 11 simulations there is a strong signal confirming a decrease in tropical cyclone numbers in the Australasian region – both north-eastern and north-western Australia.

The maximum wind speed of tropical cyclones increases from about 32 m/s to about 37 m/s and associated with this increase in maximum wind speed there is a marked increase in the maximum integrated kinetic energy of tropical cyclones. At the moment, the probability distribution of maximum integrated kinetic energy has a mode (consisting of 16% of tropical cyclones) at 55 TJ. This mode lies at 75 TJ in the simulations for 2070. The radius of maximum winds is also increased from 90 km at present to 130 km in 2070.

Table 14.1 *Projected changes in precipitation over the most intense 12 hours of the tropical cyclone.*

Distance from tropical cyclone centre (km)	Change in average rainfall intensity (%)	Change in maximum rainfall intensity (%)
100	-9	28
200	23	30
300	33	35
400	30	44

Table 14.1 depicts the changes in precipitation between the situation in 2010 and the situation in 2070 at various distances from the centre of the tropical cyclone. In all cases except one, both the average rainfall intensity and the maximum rainfall intensity increases. The exception is the average rainfall at 100 km from the centre of the tropical cyclone, which decreases by 9%. These results are all consistent with the concept that under climate change tropical cyclones will increase in size and be stronger (Beer *et al.*, 2014).

The projected changes between 2010 and 2070 in the number, duration, and location of Australian tropical cyclones obtained by downscaling seven general circulation models are shown in Table 14.2.

The models are all consistent in indicating that the number of tropical cyclones will decrease. Although the occasional model may produce different results there is also an overwhelming consensus that the duration of tropical cyclones will decrease – though all models appear to indicate overly short duration times. There is also a consensus that tropical cyclones move equatorward – both in

Table 14.2 Projected changes between 2010 and 2070 in the number, duration, and location of Australian tropical cyclones obtained by downscaling seven general circulation models.

Model	South West Pacific region					Southern Indian Ocean region				
	Number (%)	Days (%)	Duration (Days)	Genesis (°Lat)	Decay (°Lat)	Number (%)	Days (%)	Duration (Days)	Genesis (°Lat)	Decay (°Lat)
ECHAM5	-58	-53	0.0	-2.5	-1.5	-57	-62	-0.6	-0.1	1.0
GFDL CM2.0	-51	-48	0.2	-1.3	-1.9	-54	-62	-1.0	-0.2	-0.2
GFDL CM2.1	-50	-62	-1.2	-1.7	-0.7	-37	-39	-0.9	-1.4	-1.8
MIROC3.2	-87	-90	-1.3	-0.9	-0.8	-58	-64	-0.8	-1.6	-2.5
CSIRO MK3.5	-40	-31	0.5	-0.2	0.0	-39	-49	-0.7	-0.6	-0.2
UK HADCM3	-54	-55	-0.1	-1.7	-1.4	-47	-43	0.4	-0.1	-1.9
CSIRO MK3.0	-9	11	0.7	-0.5	-2.9	-44	-49	-0.3	-0.5	-0.2
<b>Ensemble average</b>	<b>-50</b>	<b>-40</b>	<b>-0.2</b>	<b>-1.3</b>	<b>-1.3</b>	<b>-48</b>	<b>-53</b>	<b>-0.6</b>	<b>-0.6</b>	<b>-0.8</b>

terms of the location of their genesis, and the location of their decay (which, presumably, approximates to their landfall). These results apply both to tropical cyclones in the south-western Pacific Ocean, which are the ones that affect Queensland on the east coast of Australia, and to tropical cyclones in the southern Indian Ocean, which are the ones that affect western Australia.

#### 14.8 Summary and conclusion

Advances in numerical weather prediction, combined with information on the drivers of Australian climate, have led to the production of a seasonal forecasting model, known as POAMA, that has displayed considerable skill in the production of multi-week and seasonal forecasts. POAMA could have been used to provide about three weeks' warning of the 21 July 2012 heavy precipitation in Beijing.

POAMA was also successful in its May 2010 predictions of the La Niña that led to extreme rainfall in eastern Australia during the last quarter of 2010 and the first quarter of 2011. Both the magnitude and spatial extent of the rainfall were accurately reproduced. This time period corresponded to extreme flash flooding in parts of Queensland, and flooding in Brisbane, the capital of Queensland. During a La Niña event, there is a tendency for tropical cyclone numbers to increase – and there were three tropical cyclones that made landfall in Queensland over this period. Cyclone Yasi, the most memorable, destroyed the Queensland banana crop.

By using dynamical downscaling techniques, it is possible to use general circulation models to investigate the impact of climate change on the likely changes in tropical cyclone numbers, intensity, duration, and location.

Climate change models are consistent in indicating that the number of tropical cyclones will not increase. The IPCC AR5 report (Christensen *et al.*, 2013) states:

The assessment provided by Knutson *et al.* (2010) of projections based on the SRES A1B scenario concluded that it is *likely* that the global frequency of tropical cyclones will either decrease or remain essentially unchanged while mean intensity (as measured by maximum wind speed) increases by +2 to +11% and tropical cyclone rainfall rates increase by about 20% within 100 km of the cyclone centre. However, inter-model differences in regional projections lead to lower confidence in basin-specific projections, and confidence is particularly low for projections of frequency within individual basins.

There is also an overwhelming consensus that the duration of Australian tropical cyclones will decrease – though all models appear to indicate overly short duration times. There is also a consensus that Australian tropical cyclones move equatorward – both in terms of the location of their genesis, and the location of their decay (which, presumably, approximates to their landfall).

#### References

- Arribas, Alberto, and coauthors (2011). The GloSea4 Ensemble Prediction System for Seasonal Forecasting. *Monthly Weather Review*, **139**, 1891–1910.
- Beer, T., Abbs, D., and Alves, O. (2014) Concatenated hazards: tsunamis, climate change, tropical cyclones and floods, In Y. A. Kontar *et al.* (eds.), *Tsunami Events and Lessons Learned: Environmental and Societal Significance*, Advances in Natural and Technological Hazards Research **35**, 255–270.
- Callaghan, J. and S. B. Power (2011). Variability and decline in the number of severe tropical cyclones making land-fall over eastern Australia since the late nineteenth century, *Clim. Dyn.*, **37**, 647–662.
- Christensen, J. H. *et al.* (2013) Climate phenomena and their relevance for future regional climate change, Chapter 14 of Working Group I Contribution to the IPCC Fifth Assessment Report Climate Change 2013: The Physical Science Basis.

- Daloz, A. S., Chauvin, F., Walsh, K., *et al.* (2012). The ability of general circulation models to simulate tropical cyclones and their precursors over the North Atlantic main development region. *Clim. Dyn.*, **39**, 1559–1576.
- Hendon, H., Thompson, D. W. J. and M. C. Wheeler (2007). Australian rainfall and surface temperature variations associated with the Southern Hemisphere annular mode. *J. Climate*, **20**, 2452–2467.
- Knutson, T. R. *et al.* (2010). Tropical cyclones and climate change. *Nature Geosci.*, **3**, 157–163.
- Langford, S. and Hendon, H. 2011. Assessment of international seasonal rainfall forecasts for Australia and the benefit of multi-model ensembles for improving reliability. *CAWCR Technical Report No. 039*.
- Lavender, S. L and D. J. Abbs (2013). Trends in Australian rainfall: contribution of tropical cyclones and closed lows, *Clim. Dyn.*, **40**, 317–326.
- McBride, J.L. and Nicholls, N. (1983). Seasonal relationships between Australian rainfall and the Southern Oscillation. *Monthly Weather Review*, **111**, 1998–2004.
- Stockdale, T.N., Anderson, D.L.T., Balmaseda, M.A., *et al.* (2011). ECMWF seasonal forecast system 3 and its prediction of sea surface temperature. *Clim. Dyn.*, **37**, 317–326.
- Wang, G., D. Hudson, Y. Ying, *et al.* (2011). POAMA-2 SST Skill Assessment and Beyond. *CAWCR Research Letters*, **6**, 40–46.

## PART IV

### **Heat waves and cold-air outbreaks**



# 15

## European heat waves: the effect of soil moisture, vegetation, and land use

*Fabio D'Andrea, Philippe Drobinski, and Marc Stéfanon*

### 15.1 Introduction

There has been considerable alarm about the occurrence of extremely high temperature events in the past decade, mainly due to a number of exceptional events during continental mid-latitude summers. Some of the most notable events are the heat waves of 2003 and 2005 in western Europe (Schär *et al.*, 2004), 2010 in Russia (Barriopedro *et al.*, 2011), and 2011 and 2012 in Texas and the midwest of the USA (Hoerling *et al.*, 2013).

These events are of concern due to their wide range of impacts on society. Public health is a primary concern, since extreme heat has been shown to dramatically increase morbidity and mortality rates, especially among the elderly (e.g. Fouillet *et al.*, 2006, 2008). The increase in morbidity and mortality occurs when high minimal temperatures persist, preventing the human body from recovering from daytime heat exposure (Laaidi *et al.*, 2012), and becomes particularly pronounced when temperature exceeds a threshold, typically depending on the local climate of a city or a region (García-Herrera *et al.*, 2010). Mortality and morbidity may also be linked to a deterioration in air quality during such events (Vautard *et al.*, 2005).

The economic sector is subject to diverse impacts from high-temperature events. The most obvious impacts are linked to energy consumption (Fink *et al.*, 2004), but the forestry and agricultural sectors may also experience huge losses as a result of factors such as forest fires that regularly accompany heatwaves (García-Herrera *et al.*, 2010). In 2003, a heatwave in western Europe resulted in a severe reduction in agricultural production (COPA–COGECA 2003). The sum of these impacts can amount to very high compound damages, with estimates reaching tens of billions of US dollars (De Bono *et al.*, 2004; see also NCDC and references therein, available online: <http://www.ncdc.noaa.gov/billions/events>).

The frequency of extreme heat events has increased in recent decades (Della-Marta *et al.*, 2007), and there are reasons to believe that the frequency and magnitude of

these events will increase in the future due to climate change (Meehl and Tebaldi, 2004, Seneviratne *et al.*, 2006, Fischer and Schär 2010). Further, it is remarkable that the increase of extreme events has continued in the past decade, while the mean temperature increase has slowed (Rahmstorf and Coumou, 2011, Lovejoy, 2014, Seneviratne *et al.*, 2014). This behavior is more generally consistent with that of simple dynamical systems, in which extremes can be more sensitive to an external forcing (Khatiwala *et al.*, 2001).

The scientific community has responded to this increasing trend in extreme temperature events, and many studies have sought to reconstruct the climatology of heat and drought events, analyze their physical mechanisms, and assess the capacity of current numerical systems to predict these events on short to seasonal time scales.

In this chapter, we review some key articles on this subject, and present some recent results obtained by the authors. Section 15.2 presents the characteristics of typical heat waves in Europe, including the prominent examples of 2003 and 2010. Section 15.3 examines the dynamical mechanisms associated with heat wave formation, while Section 15.4 describes the important influence of soil hydrological conditions on the amplification of extreme hot temperatures. Section 15.5 provides a short summary of the state of knowledge of the complex interactions between land surfaces and temperature and precipitation, and Section 15.6 shows how this complexity affects the European climate, with particular reference to heat waves. Section 15.7 briefly discusses the first studies on the effect of vegetation physiology on climatic extremes.

### 15.2 Climatology of European heat waves

The intensity of recent European heatwaves is illustrated in Fig. 15.1. The figure shows two remarkably similar maps, extracted from two different articles that refer to the

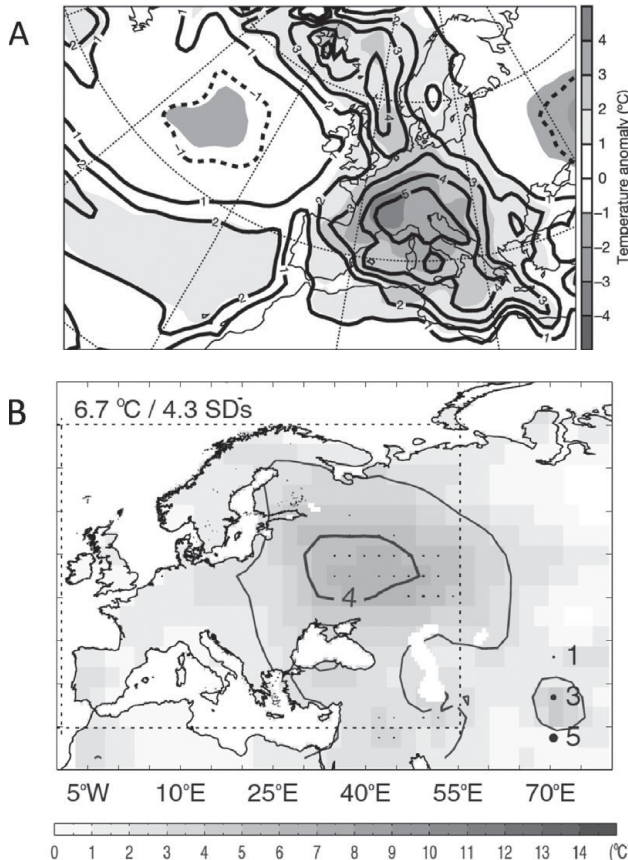


Fig. 15.1. Summer mean temperature anomalies (grayscale) and standard deviation contours (black lines) for (a) the western Europe heatwave of 2003 (adapted from Schar *et al.* 2004), and (b) the Russian heatwave of 2010 (adapted from Barriopedro *et al.* 2011).

2003 and 2010 heatwaves (Schär *et al.*, 2004, Barriopedro *et al.*, 2011). In the two panels, standard deviation contours are plotted alongside temperature anomalies. The temperature anomalies associated with these – measured in units of standard deviation of a probability density function (PDF) of temperature estimated from historical data – are 5 and 4, respectively. If the PDF has a Gaussian distribution, summers like these have a probability of occurrence of less than  $10^{-4}$  or  $10^{-5}$ . However, as the temperature distributions have ‘fatter tails’ than Gaussian distributions (Rahmstorf and Coumou, 2011 and references therein; Lovejoy, 2014), the probability of these events is higher.

The two events shown in Fig. 15.1a and b have similar amplitude and comparable spatial extent, and, as discussed below, the physical mechanisms associated with these events have similar characteristics. This similarity can be framed by an analysis of heat wave types for the region. Stéfanon *et al.* (2012a), for example, applied a cluster analysis algorithm to the ECAD database, which compiles

station temperature data for Europe in the period 1950–2009 (Klein Tank *et al.*, 2002). The cluster analysis was applied after filtering the data to extract only days that exceed the 95th percentile of the local temperature probability distribution. Criteria were also applied to the duration and spatial extent of the anomaly. In this way, only the periods of strong, extended, and persistent heat were retained for clustering (Fig. 15.2). The heat wave events are classified into six ‘typical’ classes in this study: Russian (RU), West European (WE), East European (EE), Iberian (IB), and Scandinavian (SC) patterns, and one additional pattern centered over the North Sea (NS). Comparison of Fig. 15.1 and 15.2 reveals that the two patterns in Fig. 15.1 can be attributed to the West European and Russian classes respectively. Of note, the data set used in the cluster analysis does not contain the year 2010, but the pattern associated with the Russian heatwave is nevertheless present.

The classes in Fig. 15.2 are defined using temperature anomaly data, but the composite maps of 500 hPa geopotential height are also shown for each class. With the exception of the IB class, areas of high temperature are accompanied by a strong anticyclonic anomaly. This is consistent with many climatological studies of heat waves that identify synoptic weather anomalies as the primary cause of these events. The next section contains a short review of the dynamical processes leading to heat waves.

### 15.3 Dynamical processes

Extreme values of surface variables, such as temperature and rainfall, are primarily the result of persistent and intense large-scale circulation patterns. The first large-scale pattern to be identified, atmospheric blocking (Rex, 1950), consists of a persistent positive pressure anomaly that ‘blocks’ the mid-latitude jet. Atmospheric blocking tends to appear with higher frequency in some regions, namely the Euro-Atlantic region over and east of the British Isles, and over the North Pacific Ocean (D’Andrea *et al.*, 1998). Subsequent analysis has identified other persistent and recurrent patterns that were given the name of weather regimes (see Michelangeli *et al.*, 1995 and references therein). Extensive research has been conducted into these regimes in different seasons (especially winter), and has found that regime patterns are relatively stable across seasons.

Cassou *et al.* (2005) reported the summer weather regimes of Western Europe (Fig. 15.3), defined by cluster analysis on 500 hPa geopotential height data. Blocking can be seen in Fig. 15.3a, and the other regimes are: (i) a low-pressure anomaly in the center of the north Atlantic (Fig. 15.3b); (ii) an enhanced high-pressure center over Greenland or the

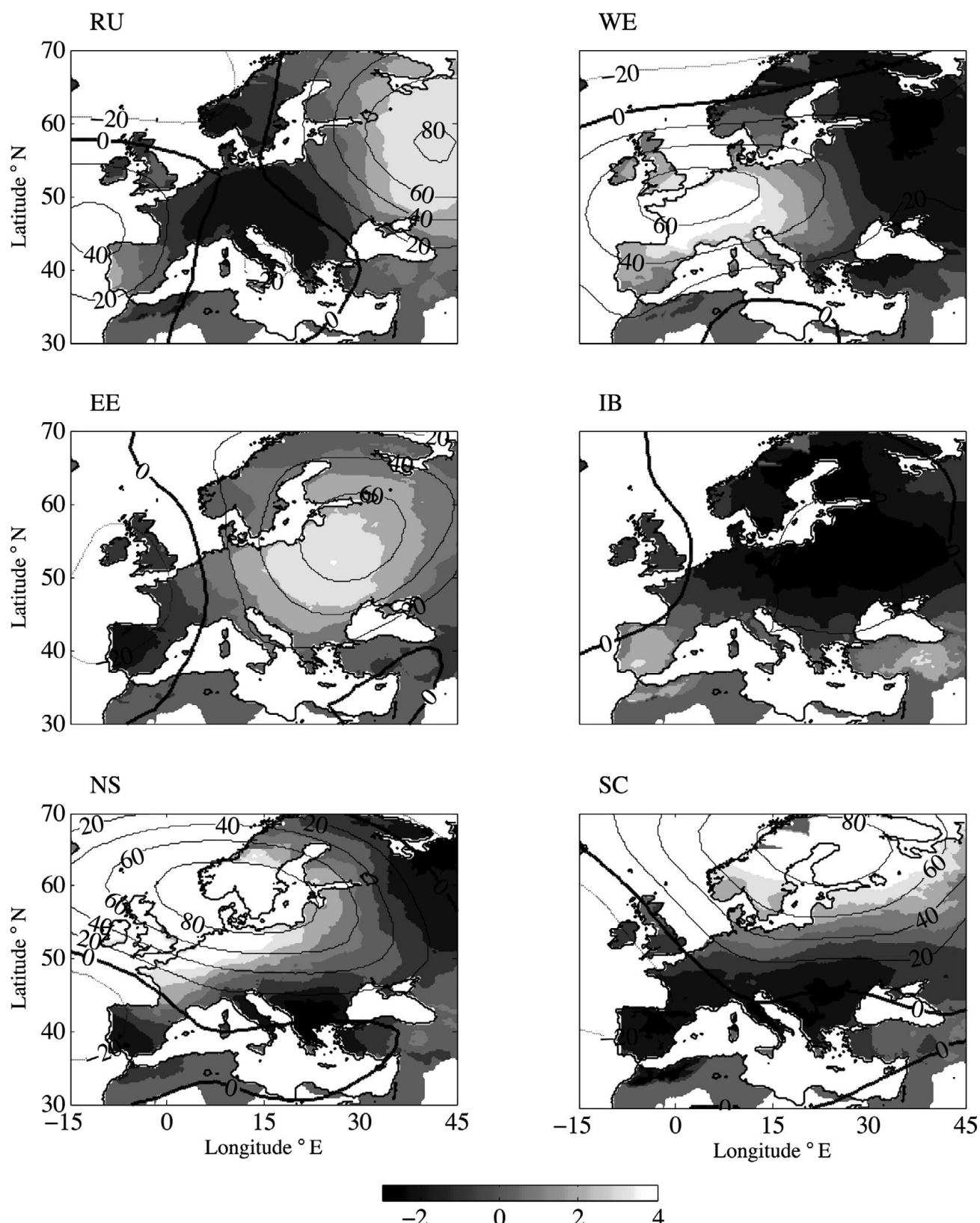


Fig. 15.2. Six heat wave classes from the cluster analysis of Stéfanon *et al.* (2012a) for the Euro-Mediterranean region: (a) the ‘Russian’ class (RU), (b) the ‘Western Europe’ class (WE), (c) the ‘Eastern Europe’ class (EE), (d) the ‘Iberian’ class (IB), (e) the ‘North Sea’ class (NS), and (f) the ‘Scandinavian’ class (SC). Daily maximum temperature anomalies (grayscale) are expressed in K and isolines are the 500 hPa geopotential height anomaly.

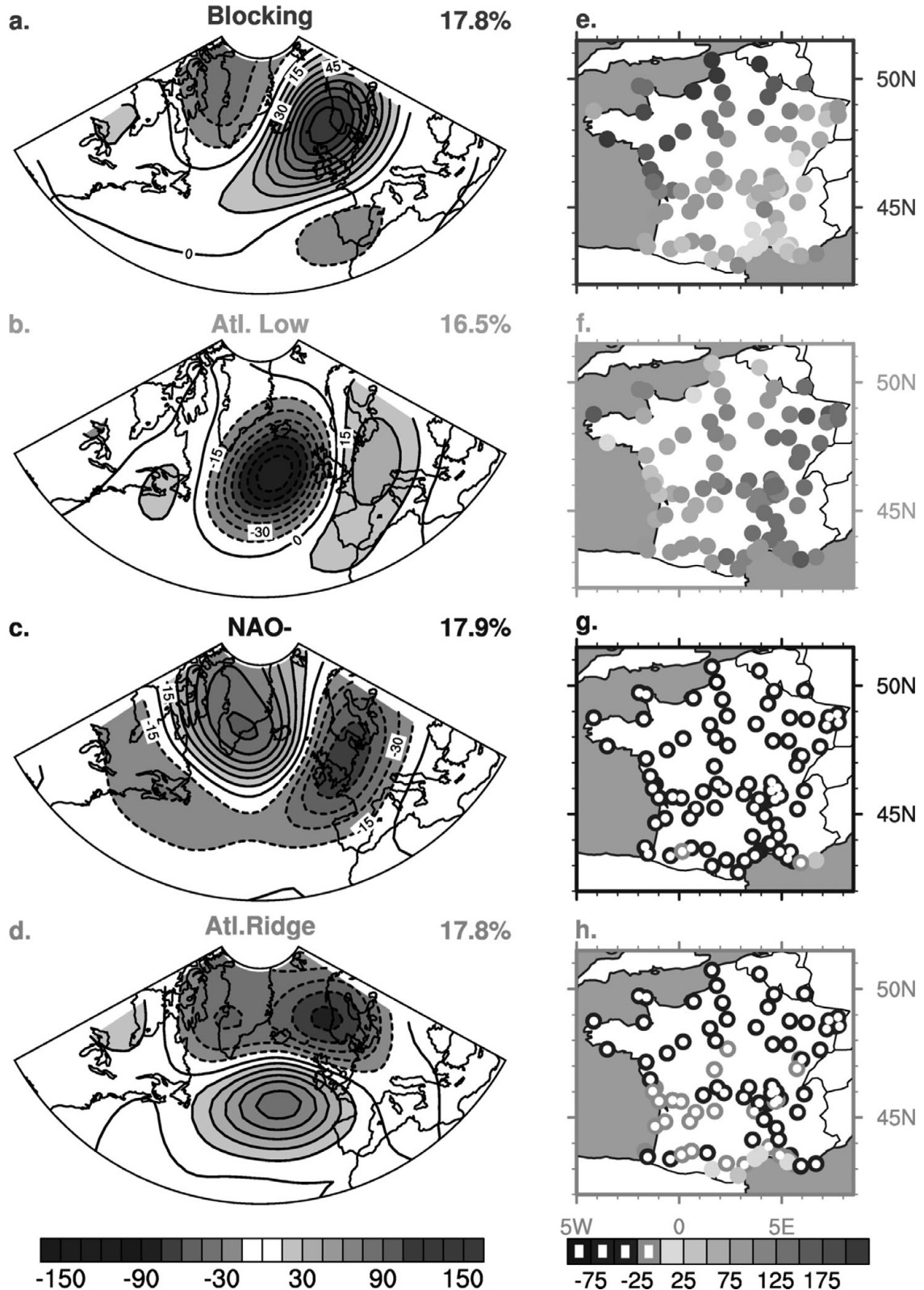


Fig. 15.3. (a)–(d) Summer 500 hPa geopotential height weather regimes of the North Atlantic–European sector. The contour interval is 15 m, and the dashed lines indicate negative contours. (e)–(h) Relative changes (%) in the frequency of extreme warm days for each individual regime. The interval is 25% and white bullets indicate negative values (adapted from Cassou *et al.*, 2005).

Greenland ridge (Fig. 15.3c); and (iii) a high-pressure center in the central North Atlantic, accompanied by a low pressure center to the north (Fig. 15.3d). While these patterns are of interest in terms of regional climatology and weather predictability, they are also important in the context of heat waves. In fact, Cassou *et al.* (2005) found that two of these regimes are linked to hot temperatures in France (and western Europe). These regimes are visible in Fig. 15.3, which shows the change in the probability of extreme temperatures in France, linked to the different regimes.

Cassou *et al.* (2005) noted that large seasonal excursions from climatological mean surface values could be explained by an anomalous frequency of a given weather regime occurrence. They verified that heat waves in Europe are linked to such changes in regime frequency. Therefore, the problem of predicting the occurrence of a heat wave, or of predicting a change in its probability, becomes a problem of predicting changes in the frequency of regimes.

The succession of persistent circulation anomalies is primarily due to the nonlinear dynamics of the synoptic-scale flow, which consists of Rossby wave dynamics, the life-cycle of baroclinic perturbations, and topographic effects. However, the probability of occurrence of the regimes is influenced, in a measurable though small amount of its total variance, by a number of external forcing mechanisms (Ghil and Robertson, 2002 and references therein).

Oceanic forcing, typically via sea surface temperature (SST), is the main forcing mechanism for large-scale pressure patterns. The SST effect in summer 2003 was the focus of studies by Feudale and Shukla (2007), Black and Sutton (2006), and Jung *et al.* (2006). In these studies, a GCM simulation was forced with observed SST in different oceanic basins and compared with control integrations using climatological SSTs. Forced SST integrations showed a pressure anomaly closely resembling the Atlantic low regime of Cassou *et al.* (2005) (Fig. 15.3b), who also showed that atmospheric convective activity over the Indian Ocean (representing the effect of a high SST anomaly) led to the anticyclonic regimes shown in Fig. 15.3.

## 15.4 Surface hydrology

Bieli *et al.* (2014), using a Lagrangian approach, showed that over the decades 1989–2009 hot events were associated with a strong adiabatic warming, consistent with the presence of a positive pressure anomaly, but were also enhanced by radiative and surface sensible heat fluxes. In fact, the above-cited works agree in that, while the response to an external forcing such as SST has the correct pattern, it is insufficient to explain the amplitude of heat wave temperature anomalies (Yiou *et al.*, 2007). Indeed,

another physical process that generates temperature extremes must be considered.

Heat waves in the central plains of the USA are accompanied and preceded by a drought (Chang and Wallace, 1987). Fischer *et al.*, (2007) provide a good illustration of the effect of hydrology on heat waves, as reproduced in Fig. 15.4. The figure shows regional model integrations for four recent major European heat wave events (1976, 1994, 2003, and 2005). Two sets of integrations were produced: one with an interactive hydrology, and a control with prescribed climatological soil moisture. Furthermore, the initial conditions in soil moisture differed between the two integrations. Boundary conditions in the regional model are imposed by large-scale synoptic atmospheric conditions, so that a heat wave is indeed observed in all integrations. The amplitude of the reproduced heat wave is, however, much larger in the integration with interactive hydrology than in the control, and much more in agreement with the observations. The interactive hydrology integration is capable of reproducing the drought associated with the heat waves, and the soil moisture depletion is responsible for the amplification of the temperature anomaly created by synoptic conditions (Fischer *et al.*, 2007). Imposing climatological soil moisture reduces the summer temperature anomaly by 40% over certain regions. Furthermore, the land–atmosphere coupling accounted for 50%–80% of the total number of hot days during the heat waves considered here.

Many other studies have reported the importance of soil hydrology in explaining the large amplitude of summer heat waves. Observational studies include Black *et al.* (2004), Zaitchik *et al.* (2006), Hirschi *et al.* (2006a,b); and modeling studies include Zampieri *et al.* (2010) and Seneviratne *et al.* (2006). See also the commentary by Alexander (2010) and references therein.

It appears that drying and preconditioning of the soil due to a decrease of precipitation precedes the occurrence of heat waves. While heat waves rapidly develop on a time scale of 2–3 days, soil moisture varies on the time scale of weeks to months and carries a long-term memory of the climate (Shukla and Mintz, 1982, Huang and van den Dool, 1992, D’Andrea *et al.*, 2006). This suggests the possibility of using the hydrological state of the soil as a precursor of heat waves. A number of studies have analyzed the potential of using soil moisture as a forecasting tool, but while a more correct initialization of soil moisture has been shown to improve the prediction of the 2003 heat wave by the ECMWF operational model (Ferranti and Viterbo, 2006), the overall predictability of these events is still problematic, due mainly to deficiencies in model physics, in terms of land-surface hydrology and in relation to radiation, clouds and moist convection (Weisheimer *et al.*, 2011). Quesada *et al.* (2012) found that excess

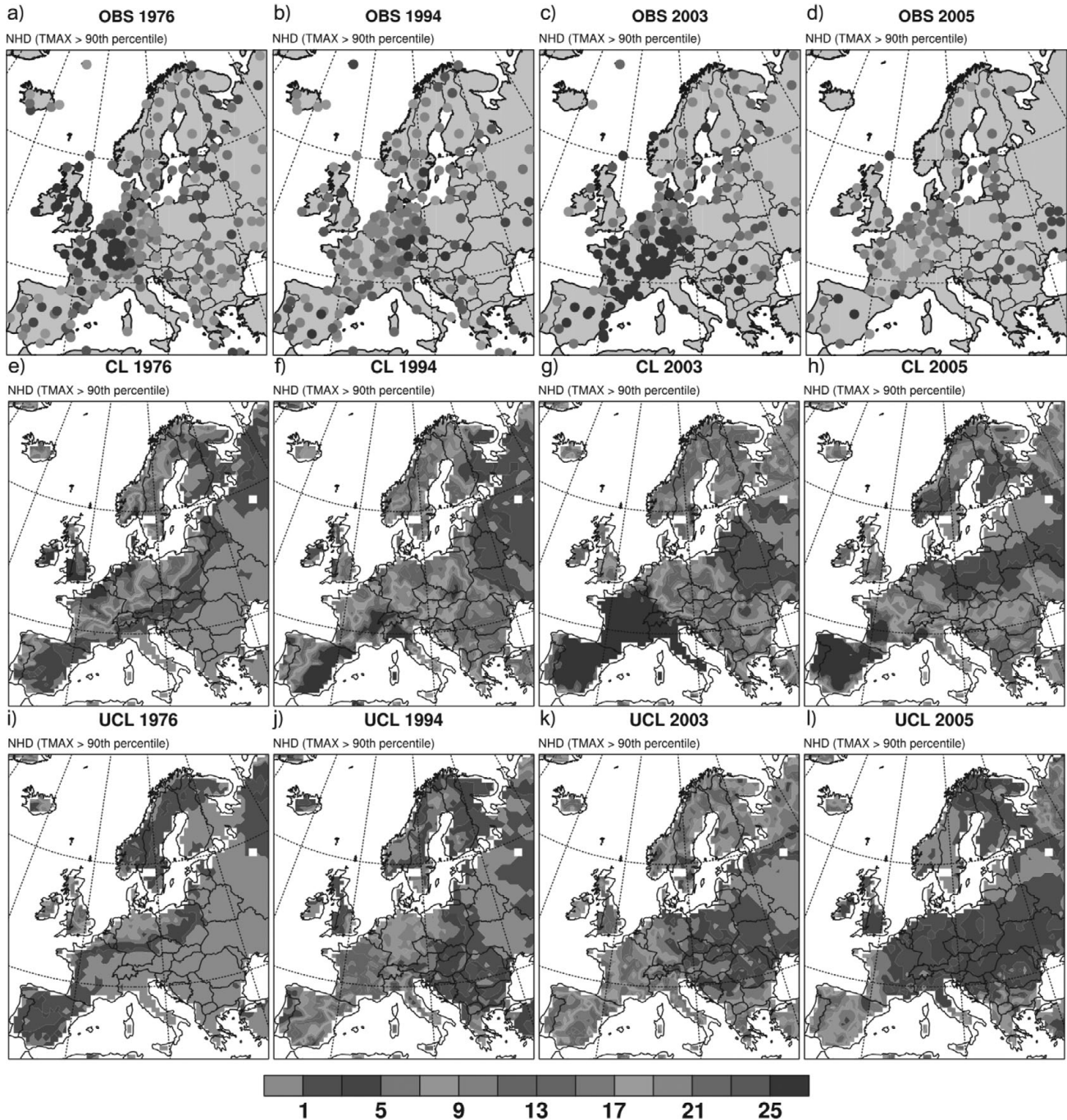


Fig. 15.4. Number of hot days (NHD) during the summers (JJA) of 1976, 1994, 2003, and 2005 derived from: (a–d) observed ECAD daily maximum temperature series, (e–h) simulations with (CL), and (i–l) without land–atmosphere coupling (UCL). From Fischer *et al.* (2007). A black and white version of this figure will appear in some formats. [For the colour version, please refer to Plate 26.](#)

precipitation in the preceding months, and hence moist soil conditions, has a higher prediction skill for the non-occurrence of summer heat waves than the opposite scenario; i.e. the prediction of heat waves by preceding dry conditions.

Comparing the heat wave classes of Stéfanon *et al.* (2012a) (Figure 2) and the maps in Fig. 15.4, it can be seen that the 1976 episode belongs to the NS class, the 1994 episode to the EEclass, and the 2003 and 2005 episodes to the WE class. Stéfanon *et al.* (2012a) showed

that each of these clusters is systematically preceded by a reduction in precipitation frequency. This precipitation anomaly is located to the south of the subsequent heat wave (Vautard *et al.*, 2007, Zampieri *et al.*, 2010). According to the cluster analysis of Stéfanon *et al.* (2012a), not all types of heat wave are preceded by a drought or a precipitation anomaly (see e.g. Grotjahn and Faure, 2008). Notably, the more northern classes (the Russian and Scandinavian heat waves) do not appear to be preceded by a precipitation anomaly, which is in agreement with the work of Hirshi *et al.* (2006a,b). Recent studies suggest, however, that the 2010 Russian heat wave was preceded by a drought (Barriopedro *et al.*, 2011, Schubert *et al.*, 2014). For an extensive analysis of the global link between heat waves and preceding droughts, see also Mueller and Seneviratne (2012).

### 15.5 Soil moisture – climate feedback

As demonstrated above, soil hydrology has a major effect on heat waves. In general, the land surface acts on surface temperatures and on precipitation by controlling heat flux partitioning, albedo, evapotranspiration, planetary boundary layer (PBL) dynamics, and convective stability. As a number of comprehensive reviews have been published on this subject (e.g. Pielke *et al.*, 1998, Seneviratne *et al.*, 2010), the present section provides only a brief overview. Gaining an understanding of all of the physical mechanisms involved is a field of active research.

The land surface interacts with the atmosphere through complex feedback loops that couple energy and the water cycle. The main difficulty in studying these feedbacks is that these processes have a high spatial heterogeneity and a wide spectrum of time variability. Short-term interactions include the response of PBL turbulence to the partitioning of energy into sensible and latent heat fluxes, which is mainly determined by soil characteristics. The partitioning of energy responds to variations in incoming radiations in a matter of hours (due to the passage of a cloud, for instance). On longer time scales (days to months), soil hydrology responds to soil moisture depletion or replenishing. If vegetation is present, the change in stomatal conductance in leaves will produce most of the response.

On seasonal to interannual time scales, the physiological state of vegetation and its dynamics acquire greater importance. Albedo and evapotranspiration changes are caused by the dynamics and phenology of vegetation, which in turn reflect the natural behavior of vegetal ecosystems under different types of forcing. This forcing also includes human-induced changes, both direct (e.g. changes in land use) and indirect (e.g. climate change).

In the specific context of droughts and heat waves in the mid latitudes, many studies (cited in the preceding section) have suggested that a positive feedback between soil moisture and precipitation could be at the origin of the amplitude and persistence of extreme conditions. While the effects on temperature, via sensible heat flux, can be easily understood as a direct heating effect, the effect on precipitation is more indirect, involving complex interactions between PBL dynamics, moist convection, and clouds. Two kinds of processes have been hypothesized as leading to feedbacks of opposing sign (see Findell and Eltahir, 2003 and references therein). First, a positive soil moisture anomaly leads to an increase in latent heat (and decrease in sensible heat), thereby reducing PBL height, increasing moist static energy, and leading to convective instability. This results in a positive soil moisture–precipitation feedback. Second, an increase in sensible heat and PBL height over a dry surface raises the PBL towards the level of free convection, thereby triggering precipitation. This mechanism would correspond to a negative feedback loop between soil moisture and precipitation.

The feedbacks between soil hydrologic conditions and precipitation can consequently have different amplitudes and a different sign. The prevalence of one or the other mechanism depends on large-scale conditions. Another negative feedback is a mesoscale mechanism observed in subtropical semiarid environments. The heterogeneity of the land surface (i.e. the existence of soil-moisture gradients and wet and dry patches) creates differential heating and the formation of mesoscale circulations, analogous to sea breezes. These circulations result in the convergence of moisture and heat towards dry patches, producing increased convective activity and correspondingly strong gradients in soil moisture, with the rain falling mainly over dry patches (Taylor *et al.*, 2012 and references therein). The following section considers how this complexity affects the regional climate of Europe in the context of heat waves.

### 15.6 Mesoscale effects

Stéfanon *et al.* (2013) investigated the role of mesoscale boundary layer dynamics, generally produced by land-surface heterogeneity (e.g. mountainous or coastal regions) on the sign of the soil moisture–precipitation feedback, and thus on the magnitude of temperature anomalies during recent heat waves that occurred over France. The study compared two simulations of the WRF (weather research and forecasting) regional model (Skamarock *et al.*, 2008) that use two different land-surface modules. One land-surface module, the *rapid update cycle* (RUC) model (Smirnova *et al.*, 1997, 2000), resolves the hydrology and is able to simulate summer dryness, while the other, the

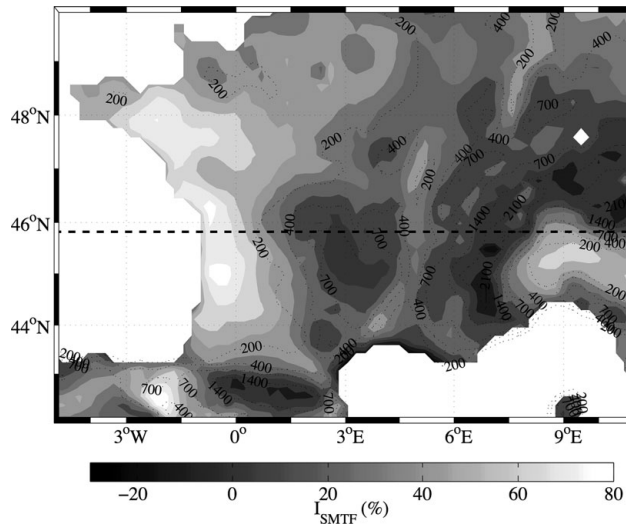


Fig. 15.5. The  $I_{SMTF}$ index (see text for definition) averaged over the 1989–2008 heat wave period. The thick dashed line indicates the cross-section at  $45.8^{\circ}\text{N}$ , shown in Fig. 15.6. Thin dashed lines are topographic contours. Adapted from Stéfanon *et al.* (2013).

*thermal diffusion* (Slab) scheme (Skamarock *et al.*, 2008), prescribes constant and high soil moisture and hence no soil moisture deficit. The two integrations use the ERA-interim reanalysis (Simons *et al.*, 2007) for the boundary conditions, and are run for 20 years from 1989 to 2008 with a horizontal resolution of 20 km.

The results of this sensitivity analysis are summarized by Fig. 15.5. The figure shows, for all heat wave episodes, the average value of an index of the soil moisture–temperature feedback,  $I_{SMTF}$ , defined as the normalized difference of the heat wave temperature anomaly of the two integrations,  $I_{SMTF} = \frac{\Delta T_{RUC} - \Delta T_{Slab}}{\Delta T_{Slab}}$ , where the suffix *RUC* represents interactive hydrology integration and the suffix *Slab* represents the constant soil moisture integration.

Figure 15.5 highlights different soil moisture–temperature responses: over low-elevation plains, drought leads to increased temperature anomalies during heat waves, while over mountains and coastal regions the opposite effect is visible. In the plains, the soil moisture deficit results in reduced evapotranspiration and a higher sensible heat flux. This has the effect of heating the PBL and, at the same time, creating higher convective instability (discussed further below), thereby creating a positive feedback.

Figure 15.6 contains an explanation for the opposite negative feedback effect observed in mountainous regions. This figure shows potential temperature contours with relative humidity (RH; panels a and b) and vertical velocity (panels c and d) for a cross-section at  $45.8^{\circ}\text{N}$  (marked by the dashed line in Fig. 15.5) for the two integrations. The variables are averaged for all heat wave days. In the RUC

integration, high RH values appear at 700–650 mb, which corresponds to the top of the PBL. Conversely, in the Slab, RH is lower and confined within a much lower PBL (Fig. 15.6b). Higher RH over drier soil has been previously observed, indicating increased shallow cloud cover (Westra *et al.*, 2012). This behavior results from the interplay between different physical mechanisms: the effect of reduced evapotranspiration that tends to reduce RH, and entrainment of cold air from the top of the PBL that increases RH by lowering the saturation threshold. Under conditions of low instability, the second effect prevails, in which case the air column is in a so-called “dry advantage” regime (Ek and Holtslag, 2004, Gentine *et al.*, 2013).

The dry advantage condition is present everywhere in the domain, and in fact a slightly higher cloud cover is observed in the drier RUC integration (see Stéfanon *et al.*, 2013). However, the RH is highest above mountain areas. Vertical velocity due to upslope anabatic winds is visible over mountains in the RUC, with a maximum on the eastern flank of the Alps. The anabatic wind mechanical forcing with the dry advantage regime described above, and the dry conditions of the RUC simulation, combine to trigger shallow convection over the mountains. This explains the increased cloud cover and precipitation over mountains in the RUC, as well as the somewhat counter-intuitive result that under heat wave conditions and dry soil, temperature can sometimes be locally reduced. Conversely, in Slab, the conditions for the dry advantage regime are not met, meaning that no convection is triggered.

Finally, the response observed in coastal regions is also explained by Stéfanon *et al.* (2013) by a mesoscale dynamical effect. The land–sea thermal contrast is enhanced in the case of dry soil, strengthening sea-breeze circulation and the advection of moist cold marine air over land. This dampens the magnitude of the heat wave temperature anomaly over a narrow land band near the Atlantic coast, and even decreases it near the Mediterranean coast.

## 15.7 Vegetation and land-use change effects

As mentioned in Section 15.4, vegetation plays a major role in land surface–climate coupling. Plants mediate between soil hydrology and biogeochemistry, and the overlying atmosphere. Their roots extract water and nutrients from the ground and their leaves exchange  $\text{CO}_2$  and water with the atmosphere through respiration and photosynthesis. These exchanges are regulated by soil moisture, air humidity and temperature, solar radiation, and the chemical composition of the atmosphere (e.g. Sellers *et al.*, 1997). Plants also affect the albedo and aerodynamic properties of the land surface, which are also relevant to land surface–climate feedbacks.

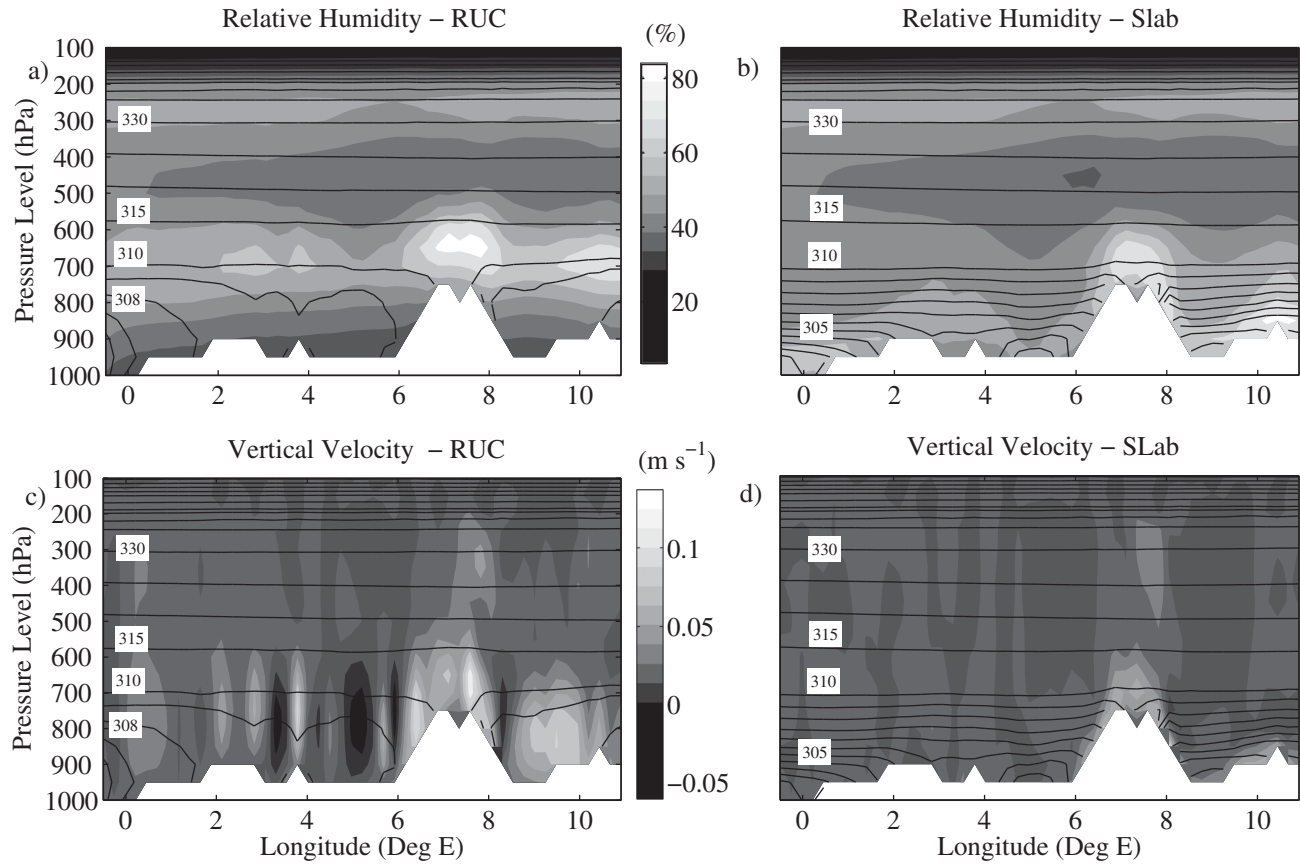


Fig. 15.6. Cross-section of relative humidity (a, b) and vertical velocity (c, d) in grayscale at 45.8°N with superimposed isentropes (isocontours of potential temperature) at 1500 UTC averaged over all heat wave days for the RUC (right column a, c) and SLab (left column; b, d) simulations. Adapted from Stéfanon *et al.* (2013).

Some modeling studies have investigated the coupling of vegetation physiology and climate in the context of extreme temperature or precipitation events, but until very recently only one-way interactions have been analyzed; i.e. forcing a vegetation model with heat wave conditions, or conversely prescribing vegetation states at the surface and assessing the climate response. The European vegetal ecosystem suffered from the 2003 heat wave, and the slump in primary productivity could offset many years of biomass carbon sink (Ciais *et al.*, 2005). Conversely, historical changes in land use and land cover have been found to impact temperature extremes with responses as large as those from GHG forcing (Pitman *et al.*, 2012).

To our knowledge, Stéfanon *et al.* (2012b) were the first to conduct a fully coupled modeling study of the interaction between vegetation physiology and climate. The authors performed two high-resolution simulations over France: one with prescribed vegetation phenology set to the 2002 behavior, and one with interactive phenology. The integrations were for one year and used the ERA-interim reanalysis as the boundary condition for the year

2003. They found that vegetation dampened the temperature anomaly in June 2003, and amplified the temperature anomaly in August 2003. In June, the excess agricultural vegetation, caused by high springtime insolation, contributes to the increase in evapotranspiration, and thus greater surface cooling and damping of the temperature anomaly during the heat wave. In August, the critical soil-moisture stress on plants suppresses evapotranspiration and enhances the sensible heat flux, thereby amplifying the temperature anomaly. They estimated the influence of the vegetation on the total heat wave temperature anomaly to be as high as 20% of the total, which is smaller but comparable to the direct contribution of soil-moisture depletion. A comparison of the evolution of the leaf-area index in the two simulations suggests an early start of the phenological cycle in spring 2003, which lasted until late July, when the plants started dying. These results are in agreement with the observations of Zaitchik *et al.* (2006). Subsequent work confirmed this result and extended it to the heat wave that occurred in southeastern Europe during the summer of 2007 (Lorenz *et al.*, 2013). This work also

highlights the fact that today's European mean spring and summer climate is not strongly affected by vegetation phenology, although the response becomes important for climate extremes.

Stéfanon *et al.* (2014) reported similar results to Stéfanon *et al.* (2012b). This time, the response was obtained in a fully coupled regional model by comparing an afforestation scenario to an agricultural scenario. Under the hot 2003 conditions, agricultural vegetation developed much more quickly than the tree phenology in the afforestation scenario. This dampened the extreme temperatures from April to the end of June 2003. From early July to October, crops become senescent and were limited by soil moisture, while trees in the afforestation scenario were still able to exploit water with their deeper roots. Evapotranspiration was consequently smaller in the agricultural scenario, which amplified the July–August extreme temperatures. The land-cover change (i.e. trees versus crop extent) was hence found to dampen or amplify extreme temperature events.

These previous studies did not include the effects of chemical composition changes (e.g. ozone concentration) in the lower atmosphere, or the effect of carbon fluxes during heat waves and droughts in the phenology. Plants might be highly sensitive to carbon fluxes, given the fact that carbon uptake and evapotranspiration reinforce each other. The nature of carbon-cycle changes in the context of droughts and heat waves requires additional research.

## 15.8 Concluding remarks

Extreme temperature and precipitation events in Europe and elsewhere are strongly dependent on interactions and feedbacks with soil hydrological conditions and land surface cover. Clarifying and quantifying these feedbacks is therefore necessary when devising prevention and adaptation strategies to combat increases in extreme hydrometeorological events due to climate change. Indeed, typical prevention and adaptation strategies would probably encompass changes in land use and land management, possibly including agricultural practices.

Widening the perspective slightly, it should be mentioned that the link between land surface hydrology and vegetation, and extreme hydrometeorological events is also important in areas of high climate sensitivity like the Sahel (Hulme, 2001, Held *et al.*, 2005) and in southeast Asia, as highlighted by recent floods in Bangladesh in 2010 and Thailand in 2011.

Quantitative assessment of the impacts of large-scale deforestation and land-use modification on climate change and variability requires a thorough mechanistic understanding of soil moisture–precipitation feedbacks (Eltahir, 1998, Avissar and Werth, 2005, Chagnon and Bras, 2005).

The same quantitative knowledge is necessary to understand, in a systemic way, water resource problems in sensitive regions.

Studies of the interaction between the land surface and meteorological processes are hampered by two of the main sources of uncertainty in current modeling systems:(i) the representation of deep moist convection and cloud formation, and (ii) the simulation of surface–atmosphere energy exchanges, surface hydrology, and vegetation dynamics, including their relation to the carbon cycle. These problems seriously limit the skill of weather forecasts from the weekly to the seasonal scale (Koster *et al.*, 2010, Conil *et al.*, 2006, Kanae *et al.*, 2006, Sutton *et al.*, 2006, Guo *et al.*, 2011) as well as the confidence in climate projections (Dufresne and Bony, 2008, Sherwood *et al.*, 2014). Consequently, there is a need to reconsider model parameterizations, bearing in mind that ongoing increase in the spatial resolution of models may make many obsolete in the near future.

To address these model deficiencies, there is still a need for physical understanding and process-based studies that nourish the development of new parameterizations. The key tools for this work should include simplified theoretical models. In fact, there is no unified theoretical approach encompassing the land surface, PBL turbulence, and moist convection. Complex tools can also be used, such as regional models, spanning spatial resolutions from tens of kilometers down to cloud-resolving and large-eddy simulations. Regional models have the advantage of allowing the prescription of the synoptic atmospheric state via boundary conditions. This permits the selection of favorable situations for the occurrence of a heatwave, imposing, for example, a well-chosen large-scale weather regime. The research can then concentrate on understanding the physical feedbacks that take place in that case.

Since the response to surface forcing appears to be enhanced in the case of extreme climatic events, heat waves can also become a testbed for our physical understanding of land–climate coupling.

## References

- Alexander, L. (2010). Extreme heat rooted in dry soils. *Nature Geosciences*, **4**(1), 12–13. Available at: <http://dx.doi.org/10.1038/ngeo1045>.
- Avissar, R. and Werth, D. (2005). Global hydroclimatological teleconnections resulting from tropical deforestation. *Journal of Hydrometeorology*, **6**, 134–145.
- Barriopedro, D. *et al.* (2011). The hot summer of 2010: redrawing the temperature record map of Europe. *Science (New York, N.Y.)*, **332**(6026), 220–224. Available at: <http://www.ncbi.nlm.nih.gov/pubmed/21415316> [Accessed July 27, 2012].

- Bieli, M., Pfahl, S., and Wernli, H. (2014). A Lagrangian investigation of hot and cold temperature extremes in Europe. *Q. J. R. Meteorol. Soc.*. doi: 10.1002/qj.2339
- Black, E., M. Blackburn, G. Harrison, B. Hoskins, and J. Methven (2004). Factors contributing to the summer 2003 European heatwave. *Weather*, **59**(8), 217–223.
- Black, E. and Sutton, R. T. (2006). The influence of oceanic conditions on the hot European summer of 2003. *Climate Dynamics*, **28**, 53–66.
- Cassou, C., Terray, L., and Phillips, A. (2005). Tropical Atlantic influence on European heat waves. *Journal of Climate*, **18**, 2805–2811.
- Chagnon, F. J. F. and Bras, R. L. (2005). Contemporary climate change in the Amazon. *Geophysical Research Letters*, **32**(13), 1–4. Available at: <http://www.agu.org/pubs/crossref/2005/2005GL022722.shtml> [Accessed August 21, 2012].
- Chang, F.-C. and Wallace, J. M. (1987). Meteorological conditions during heat waves and droughts in the United States Great Plains. *Monthly Weather Review*, **115**, 1253–1269.
- Ciais, P. et al. (2005). Europe-wide reduction in primary productivity caused by the heat and drought in 2003. *Nature*, **437** (7058), 529–533. Available at: <http://www.ncbi.nlm.nih.gov/pubmed/16177786> [Accessed July 25, 2012].
- Conil, S., Douville, H. and Tyteca, S. (2006). The relative influence of soil moisture and SST in climate predictability explored within ensembles of AMIP type experiments. *Climate Dynamics*, **28**(2–3), 125–145. Available at: <http://link.springer.com/10.1007/s00382-006-0172-2> [Accessed July 6, 2013].
- COPA COGECA. (2003). Assessment of the impact of the heat wave and drought of the summer 2003 on agriculture and forestry. Fact sheets of the Committee of Agricultural Organisations in the European Union and the General Committee for Agricultural Cooperation in the European Union. Available at: [http://www.copa-cogeca.com/pdf/pocc\\_03\\_78i4\\_1e.pdf](http://www.copa-cogeca.com/pdf/pocc_03_78i4_1e.pdf).
- D'Andrea, F. et al. (2006). Hot and cool summers: Multiple equilibria of the continental water cycle. *Geophysical Research Letters*, **33**(24). Available at: <http://www.agu.org/pubs/crossref/2006/2006GL027972.shtml> [Accessed September 14, 2012].
- D'Andrea, F. et al. (1998). Northern Hemisphere atmospheric blocking as simulated by 15 atmospheric general circulation models in the period 1979–1988. *Climate Dynamics*, **14**(6), 385–407. Available at: <http://www.springerlink.com/openurl.asp?genre=article&id=doi:10.1007/s003820050230>.
- De Bono, A., Peduzzi, P., Kluser, S., and Giuliani, G. (2004). *Impacts of Summer 003 Heat Wave in Europe*. (333.7–333.9). United Nations Environment Programme. Retrieved from <http://archive-ouverte.unige.ch/unige:32255>
- Della-Marta, P.M. et al. (2007). Doubled length of western European summer heat waves since 1880. *Journal of Geophysical Research*, **112**(D15), p.D15103. Available at: <http://doi.wiley.com/10.1029/2007JD008510> [Accessed May 23, 2014].
- Dufresne, J.-L. and Bony, S. (2008). An assessment of the primary sources of spread of global warming estimates from coupled atmosphere–ocean models. *Journal of Climate*, **21**(19), 5135–5144. Available at: <http://journals.ametsoc.org/doi/abs/10.1175/2008JCLI2239.1> [Accessed February 10, 2014].
- Ek, M. B. and Holtslag, A. a. M. (2004). Influence of soil moisture on boundary layer cloud development. *Journal of Hydrometeorology*, **5**, 86–99.
- Eltahir, E. A. B. (1998). A soil moisture–rainfall feedback mechanism: 1. Theory and observations. *Water Resources Research*, **34**(4), 765–776. Available at: <http://doi.wiley.com/10.1029/97WR03499>.
- Ferranti, L. and Viterbo, P. (2006). The European summer of 2003: Sensitivity to soil water initial conditions. *Journal of Climate*, **20****5**, 3659–3680.
- Feudale, L. and Shukla, J. (2007). Role of Mediterranean SST in enhancing the European heat wave of summer 2003. *Geophysical Research Letters*, **34**(3), 2–5. Available at: <http://www.agu.org/pubs/crossref/2007/2006GL027991.shtml> [Accessed March 14, 2012].
- Findell, K. L. and Eltahir, E. A. B. (2003). Atmospheric controls on soil moisture – boundary layer interactions. Part I: Framework development. *Journal of Hydrometeorology*, **4**(3), 552–569.
- Fink, A. H., Leckebusch, G. C., and Pinto, J. G. (2004). The 2003 European summer heatwaves and drought – synoptic diagnosis and impacts. *Weather*, **59**, 209–216.
- Fischer, E. M. et al. (2007). Contribution of land–atmosphere coupling to recent European summer heat waves. *Geophysical Research Letters*, **34**(6), 1–6. Available at: <http://www.agu.org/pubs/crossref/2007/2006GL029068.shtml> [Accessed March 27, 2012].
- Fischer, E. M. and Schär, C. (2010). Consistent geographical patterns of changes in high-impact European heatwaves. *Nature Geoscience*, **3**(6), 398–403. Available at: <http://www.nature.com/doifinder/10.1038/ngeo866> [Accessed May 23, 2014].
- Fouillet, a et al. (2006). Excess mortality related to the August 2003 heat wave in France. *International Archives of Occupational and Environmental Health*, **80**(1), 16–24. Available at: <http://www.ncbi.nlm.nih.gov/pmc/articles/PMC1450003/> [Accessed May 6, 2014].
- Fouillet, a et al. (2008). Has the impact of heat waves on mortality changed in France since the European heat wave of summer 2003? A study of the 2006 heat wave. *International Journal of Epidemiology*, **37**(2), 309–317. Available at: <http://www.ncbi.nlm.nih.gov/pmc/articles/PMC2475264/> [Accessed May 6, 2014].
- García-Herrera, R. et al. (2010). A review of the European summer heat wave of 2003. *Critical Reviews in Environmental Science and Technology*, **40**(4), 267–306. Available at: <http://www.tandfonline.com/doi/abs/10.1080/10643380802238137> [Accessed July 27, 2012].
- Gentine, P. et al. (2013). Surface and atmospheric controls on the onset of moist convection over land. *Journal of Hydrometeorology*, p.130211131121003. Available at: <http://journals.ametsoc.org/doi/abs/10.1175/JHM-D-12-0137.1> [Accessed June 24, 2013].

- Ghil, M. and Robertson, A. W. (2002). "Waves" vs. "particles" in the atmosphere's phase space: A pathway to long-range forecasting? *Proceedings of the National Academy of Sciences of the United States of America*, **99**, 2493–2500.
- Grotjahn, R. and Faure, G. (2008). Composite predictor maps of extraordinary weather events in the Sacramento California region. *Weather and Forecasting*, **23**, 313–335.
- Guo, Z., Dirmeyer, P. a., and DelSole, T. (2011). Land surface impacts on subseasonal and seasonal predictability. *Geophysical Research Letters*, **38**(24), p.n/a–n/a. Available at: <http://doi.wiley.com/10.1029/2011GL049945> [Accessed June 17, 2013].
- Held, I. M. et al. (2005). Simulation of Sahel drought in the 20th and 21st centuries. *Proceedings of the National Academy of Sciences of the United States of America*, **102**(50), 17891–17896.
- Hirschi, M., Seneviratne, S. I., and Schär, C. (2006a). Seasonal variations in terrestrial water storage for major mid-latitude river basins. *J. Hydrometeorol.*, **7**, 39–60.
- Hirschi, M., Viterbo, P., and Seneviratne, S. I. (2006b). Basin-scale water-balance estimates of terrestrial water storage variations from ECMWF operational forecast analysis data. *Geophys. Res. Lett.*, **33**, L21401.
- Hoerling, M. et al. (2013). Anatomy of an extreme event. *Journal of Climate*, **26**(9), 2811–2832. Available at: <http://journals.ametsoc.org/doi/abs/10.1175/JCLI-D-12-00270.1> [Accessed December 14, 2013].
- Huang, J. and H. M. van den Dool (1992). Monthly precipitation–temperature prediction over the United States, *J. Clim.*, **13**, 1111–1132.
- Hulme, M. (2001). Climatic perspectives on Sahelian dessication: 1973–1998. *Global Environmental Change*, **11**, 19–29.
- Jung, T., Ferranti, L., and Tompkins, A. M. (2006). Response to the summer of 2003 Mediterranean SST anomalies over Europe and Africa. *Journal of Climate*, **3**, 5439–5455.
- Kanae, S. et al. (2006). Influence of "realistic" land surface wetness on predictability of seasonal precipitation in boreal summer. *Journal of Climate*, **19**, 1450–1460.
- Khatiwala, S., Shaw, B. E., and Cane, M. a. (2001). Enhanced sensitivity of persistent events to weak forcing in dynamical and stochastic systems: Implications for climate change. *Geophysical Research Letters*, **28**(13), 2633–2636. Available at: <http://doi.wiley.com/10.1029/2000GL012773>.
- Klein Tank, A. M. G. et al. (2002). Daily dataset of 20th-century surface air temperature and precipitation series for the European climate assessment. *Int. J. Climatol.*, **22**, 1441–1453.
- Koster, R. D. et al. (2010). Contribution of land surface initialization to subseasonal forecast skill: First results from a multi-model experiment. *Geophysical Research Letters*, **37**(2), p.n/a–n/a. Available at: <http://doi.wiley.com/10.1029/2009GL041677> [Accessed July 21, 2013].
- Laaidi, K., Zeghnoun, A., Dousset, B., et al. (2012). The impact of heat islands on mortality in Paris during the August 2003 heat wave. *Environmental Health Perspectives*, **120**(2), 254.
- Lorenz, R. et al. (2013). How important is vegetation phenology for European climate and heat waves? *Journal of Climate*, **26**(24), 10077–10100. Available at: <http://journals.ametsoc.org/doi/abs/10.1175/JCLI-D-13-00040.1> [Accessed May 27, 2014].
- Lovejoy, S. (2014). Scaling fluctuation analysis and statistical hypothesis testing of anthropogenic warming. *Clim. Dyn.*, **42**, 2339–2351.
- Meehl, G. a and Tebaldi, C. (2004). More intense, more frequent, and longer lasting heat waves in the 21st century. *Science (New York, N.Y.)*, **305**(5686), 994–997. Available at: <http://www.ncbi.nlm.nih.gov/pubmed/15310900> [Accessed May 23, 2014].
- Michelangeli, P.-A., Vautard, R., and Legras, B. (1995). Weather regimes: recurrence and quasi stationarity. *Journal of the Atmospheric Sciences*, **52**(8), 1237–1256.
- Mueller, B. and Seneviratne, S. I. (2012). Hot days induced by precipitation deficits at the global scale. *Proceedings of the National Academy of Sciences of the United States of America*, **109**(31), 12398–12403. Available at: <http://www.ncbi.nlm.nih.gov/articlerender.fcgi?artid=3411978&tool=pmcentrez&rendertype=abstract> [Accessed May 28, 2014].
- Pielke, R. A. et al. (1998). Interactions between the atmosphere and terrestrial ecosystems : influence on weather and climate. *Global Change Biology*, **4**, 461–475.
- Pitman, A. J. et al. (2012). Effects of land cover change on temperature and rainfall extremes in multi-model ensemble simulations. *Earth System Dynamics Discussions*, **3**(2), 597–641. Available at: <http://www.earth-syst-dynam-discuss.net/3/597/2012/> [Accessed May 28, 2014].
- Quesada, B. et al. (2012). Asymmetric European summer heat predictability from wet and dry southern winters and springs. *Nature Climate Change*, **2**(10), 736–741. Available at: <http://www.nature.com/doifinder/10.1038/nclimate1536> [Accessed December 16, 2013].
- Rahmstorf, S. and Coumou, D. (2011). Increase of extreme events in a warming world. *Proceedings of the National Academy of Sciences of the United States of America*, **108**(44), 17905–17909. Available at: <http://www.ncbi.nlm.nih.gov/articlerender.fcgi?artid=3207670&tool=pmcentrez&rendertype=abstract> [Accessed May 23, 2014].
- Rex, D. R. (1950). Blocking action in the middle troposphere and its effect upon regional climate. I. An aerological study of blocking action. *Tellus*, **2**, 169–211.
- Schär, C. et al. (2004). The role of increasing temperature variability in European summer heatwaves. *Nature*, **427** (January), 3926–3928.
- Schubert, S. D. et al. (2014). Northern Eurasian heat waves and droughts. *Journal of Climate*, **27**(9), 3169–3207. Available at: <http://journals.ametsoc.org/doi/abs/10.1175/JCLI-D-13-00360.1> [Accessed May 7, 2014].
- Sellers, P. J. et al. (1997). Modeling the exchanges of energy, water, and carbon between continents and the atmosphere. *Science*, **275**(5299), 502–509. Available at: <http://www.sciencemag.org/cgi/doi/10.1126/science.275.5299.502> [Accessed May 23, 2014].
- Seneviratne, S. I. et al. (2010). Investigating soil moisture–climate interactions in a changing climate: A review. *Earth-Science Reviews*, **99**(3–4), 125–161. Available at:

- <http://linkinghub.elsevier.com/retrieve/pii/S0012825210000139> [Accessed March 2, 2012].
- Seneviratne, S. I. *et al.* (2006). Land-atmosphere coupling and climate change in Europe. *Nature*, **443**(7108), 205–209. Available at: <http://www.ncbi.nlm.nih.gov/pubmed/16971947> [Accessed May 22, 2013].
- Seneviratne, S. I., Donat, M. G., Mueller, B., and Alexander, L. V. (2014). No pause in the increase of hot temperature extremes. *Nature*, **4**(March), 161–164.
- Sherwood, S. C., Bony, S., and Dufresne, J.-L. (2014). Spread in model climate sensitivity traced to atmospheric convective mixing. *Nature*, **505**(7481), 37–42. Available at: <http://www.ncbi.nlm.nih.gov/pubmed/24380952> [Accessed January 20, 2014].
- Shukla, J. and Y. Mintz (1982). Influence of land–surface evapotranspiration on the Earth's climate. *Science*, **215**, 1498–1501.
- Skamarock, W. C., Klemp, J. B., Dudhia, J., *et al.* (2008). A description of the advanced research WRF version 3. Technical Report, NCAR.
- Simons, A., Uppala, S., Dee, D., and Kobayashi, S. (2007). ERA-interim: new ecmwf reanalysis products from 1989 onwards. *ECMWF Newslett.* **110**, 25–35.
- Smirnova, T. G., Brown, J. M., and Benjamin, S. G. (1997). Performance of different soil model configurations in simulating ground surface temperature and surface fluxes. *Mon. Wea. Rev.* **125**, 1870–1884.
- Smirnova, T. G., Brown, J. M., Benjamin, S. G., and Kim, D. (2000). Parameter-ization of cold season processes in the maps land-surface scheme. *J. Geophys. Res.* **105**, 4077–4086.
- Stéfanon, M., D'Andrea, F., and Drobinski, P. (2012a). Heatwave classification over Europe and the Mediterranean region. *Environmental Research Letters*, **7**.
- Stéfanon, M., F. D'Andrea, Ph. Drobinski, and N. de Noblet-Ducoudré (2012b). Effects of interactive vegetation phenology on the 2003 summer heat waves. *Journal of Geophysical Research*, **117**(October), 1–15.
- Stéfanon, M. *et al.* (2013). Soil moisture–temperature feedbacks at meso-scale during summer heat waves over Western Europe. *Climate Dynamics*. Available at: <http://link.springer.com/10.1007/s00382-013-1794-9> [Accessed June 12, 2013].
- Stéfanon, M., Schindler, S., Drobinski, P., de Noblet-Ducoudré, N., and D'Andrea, F. (2014). Simulating the impact of anthropogenic vegetation land cover on temperature over central France in summer 2003 heatwaves. *Climate Research*, **Lmd**. doi:10.3354/cr01230
- Sutton, C., Hamill, T. M. and Warner, T. T. (2006). Will perturbing soil moisture improve warm-season ensemble forecasts? A proof of concept. *Monthly Weather Review* **134**, 3174–3189.
- Taylor, C. M. *et al.* (2012). Afternoon rain more likely over drier soils. *Nature*, **489**(7416), 423–426. Available at: <http://www.ncbi.nlm.nih.gov/pubmed/22972193> [Accessed August 15, 2013].
- Vautard, R. *et al.* (2007). Summertime European heat and drought waves induced by wintertime Mediterranean rainfall deficit. *Geophysical Research Letters*, **34**(7), p.L07711. Available at: <http://doi.wiley.com/10.1029/2006GL028001> [Accessed November 19, 2013].
- Vautard, R., Honore, C., Beekmann, M., and Rouil, L. (2005). Simulation of ozone during the August 2003 heat wave and emission control scenarios. *Atmospheric Environment*, **39**, 2957–2967.
- Weisheimer, A. *et al.* (2011). On the predictability of the extreme summer 2003 over Europe. *Geophysical Research Letters*, **38**(5), p.n/a–n/a. Available at: <http://doi.wiley.com/10.1029/2010GL046455> [Accessed May 28, 2014].
- Westra, D., Steeneveld, G. J. and Holtslag, A. a. M. (2012). Some observational evidence for dry soils supporting enhanced relative humidity at the convective boundary layer top. *Journal of Hydrometeorology*, **13**(4), 1347–1358. Available at: <http://journals.ametsoc.org/doi/abs/10.1175/JHM-D-11-0136.1> [Accessed November 30, 2012].
- Yiou, P. *et al.* (2007). Inconsistency between atmospheric dynamics and temperatures during the exceptional 2006/2007 fall/winter and recent warming in Europe. *Geophysical Research Letters*, **34**(21), 1–7. Available at: <http://www.agu.org/pubs/crossref/2007/2007GL031981.shtml> [Accessed March 14, 2012].
- Zaitchik, B. F., A. K. Macalady, L. R. Bonneau, and R. B. Smith (2006). Europe's 2003 heat wave: A satellite view of impacts and land–atmosphere feedbacks. *Int. J. Climatol.*, **26**, 743–769, doi:10.1002/joc.1280.
- Zampieri, M. *et al.* (2010). Hot European summers and the role of soil moisture in the propagation of Mediterranean drought, *Journal of Climate*, **22**, 1–35.

# 16

## Western North American extreme heat, associated large-scale synoptic-dynamics, and performance by a climate model

Richard Grotjahn

### 16.1 Introduction

How well do we understand the dynamics and predictability of extreme heat events? This chapter will not answer such a broad question, but instead will focus on a context in which one can begin to address the question. Illustrative examples of some aspects of the dynamics and predictability will be shown for hot spells affecting much of western North America.

Various definitions and criteria abound for ‘heat waves’ (Table 3 in Grotjahn *et al.*, 2015). In this report the more general term ‘hot spells’ is used to describe unusually hot maximum temperatures persisting a day or longer.

Generally speaking, North American extreme hot spells are associated with large-scale displacements of air masses, placing unusually warm air where it is not normally found. Examples are numerous and occur over a wide range of time scales. A lengthy heat wave affected the central United States from June–August during the summer of 1980 (Karl and Quayle, 1981, Namias, 1982). An intermediate time-scale event, 16–26 July 2006, affected California (and subsequently other regions of North America to the east and north; Gershunov *et al.*, 2009) Events shorter than three days, more properly called hot spells, are also of interest though three days is a commonly used minimum period (Grotjahn and Faure, 2008, Bumbaco *et al.*, 2013). In each case, the displacement of the hot air mass is reflected in the geopotential height fields and hence the winds. So the displacement results in a large-scale pattern for several primary meteorological variables. These large-scale meteorological patterns (LSMPs) will be a focus of this chapter.

Monthly mean data are not adequate to resolve heat waves nor the associated LSMPs. As an illustration, one of the largest temperature anomalies in the past 60 years at California Central Valley (CV) stations occurred in early July, 1991. Temperature anomalies at the stations were more than 1.6 standard deviations above normal for four successive days. Most of the rest of the month was below

average, so that the monthly mean for July 1991 was –0.2 standard deviations (i.e. below normal). Hence, a daily time scale is needed to resolve the LSMPs.

The remaining sections of this chapter discuss the synoptics and dynamics of the LSMPs associated with California extreme hot spells. Then the predictive ability of the LSMPs is shown in an illustrative pilot study. Finally, LSMPs are used in a simple assessment of both a model skill and future prediction of hot spells by the model.

### 16.2 California heat waves: upper air large-scale meteorological patterns (LSMPs) synoptics and dynamics

A hot spells synoptic description of the regional weather conducive to hot conditions affecting much of central and northern California is shown in Fig. 16.1. The figure shows composite averages of several representative variables, combining the times that 14 different extreme hot spells started. The hottest days occur when these conditions are met. First, temperatures need to be elevated in the upper atmosphere. The elevated temperatures (Fig. 16.1a) result in part from air advected from the Desert Southwest. Those elevated temperatures occur in part due to the parched source region and with strong sinking (Fig. 16.1b). Sinking is the normal state during summer over California and a subsidence inversion is a common occurrence. During the hottest days, the subsidence is stronger and the inversion lower, resulting in a thinner layer of near surface air for solar radiation to heat up. The geographic location of the anomalously high temperature values is crucial, with the hotter temperatures being at or off shore, causing the ‘thermal low’ in sea level pressure to migrate to the coast (Fig. 16.1a,c). The result is a near-surface pressure gradient that opposes the formation of a sea breeze (Fig. 16.1d). In addition, the flow has a downslope component above the western slope of the Sierra Nevada Mountains. (A shallow

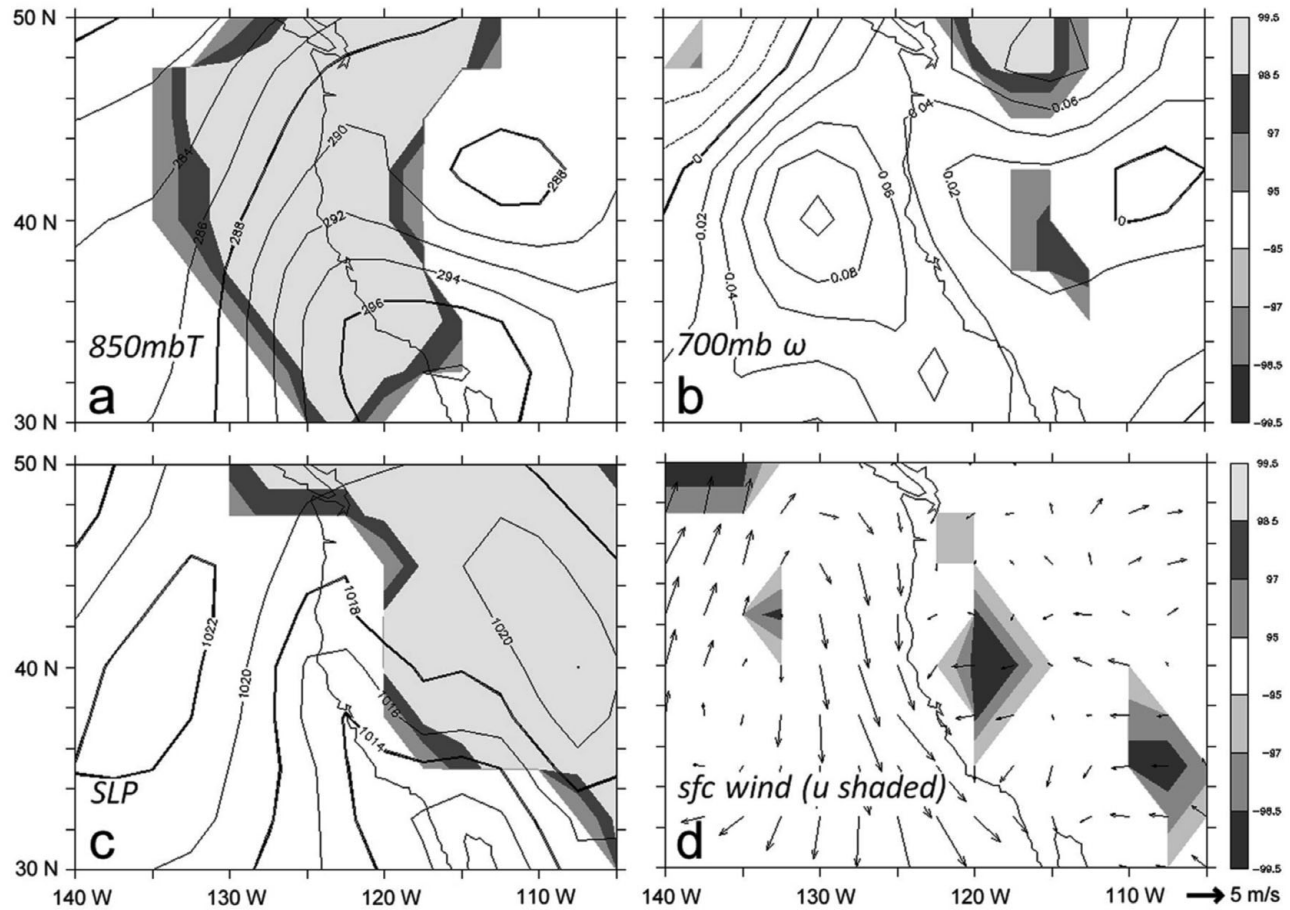


Fig. 16.1. Synoptic conditions at the onset of a hot spell affecting the California Central Valley. Shown are ensemble averages of (a) temperature at 850 hPa, (b) pressure velocity at 700 hPa, (c) sea level pressure, and (d) surface wind vectors, where the shading applies to the zonal component. Shading indicates unusual values for the variables. Light shading surrounded by darker shading indicates composite values of the ensemble of extreme hot spell in the top 1.5% of a distribution of randomly drawn composites. Darker shading surrounded by lighter indicates composite values in the lowest 1.5% of randomly drawn composites.

upslope flow can be created by solar radiative heating, but above the boundary layer the topography accentuates the sinking, adiabatic warming, and intensification downstream of the subsidence inversion over the Central Valley.) There is further discussion of this figure in Grotjahn (2011).

A major contributing factor to an extreme heat wave can be drought. For example, the extreme European heat wave of 2003 was preceded by drought over a region including most of France and portions of adjacent countries. Heat wave and drought combined during March 2012 over the northern central part of the USA. The heat was amplified by extensive drought over the region since evaporation was reduced in the surface energy balance. Daily weather maps all show that the greatest heat anomaly occurred as hot air was drawn northward just east of the Rocky Mountains. Drought has less importance for California hot spells since the state experiences an annual drought during the summer

months. Also, even when drought is ongoing, there are cooler and hotter periods but the latter still occur with the hot spell LSMPs.

Identification of the LSMPs begins with identification of relevant ‘target’ dates. Two different criteria are used to identify hot spell target dates. When discussing the onset and patterns leading up to the onset, the dates are the first day of a period lasting at least three days with maximum temperatures exceeding 38 °C and with at least one day greater than 40.5 °C at Sacramento California station KSAC. When discussing and using an ‘LSMP index value’, the target dates are defined as when three CV stations are all exceeding their own normalized maximum temperature anomaly threshold of 1.6 standard deviations. The three stations are: KRBL, KFAT, KBFL. The value of 1.6 was exceeded by all three stations simultaneously for about 1% of the time during the recent 30-year period (1979–2008).

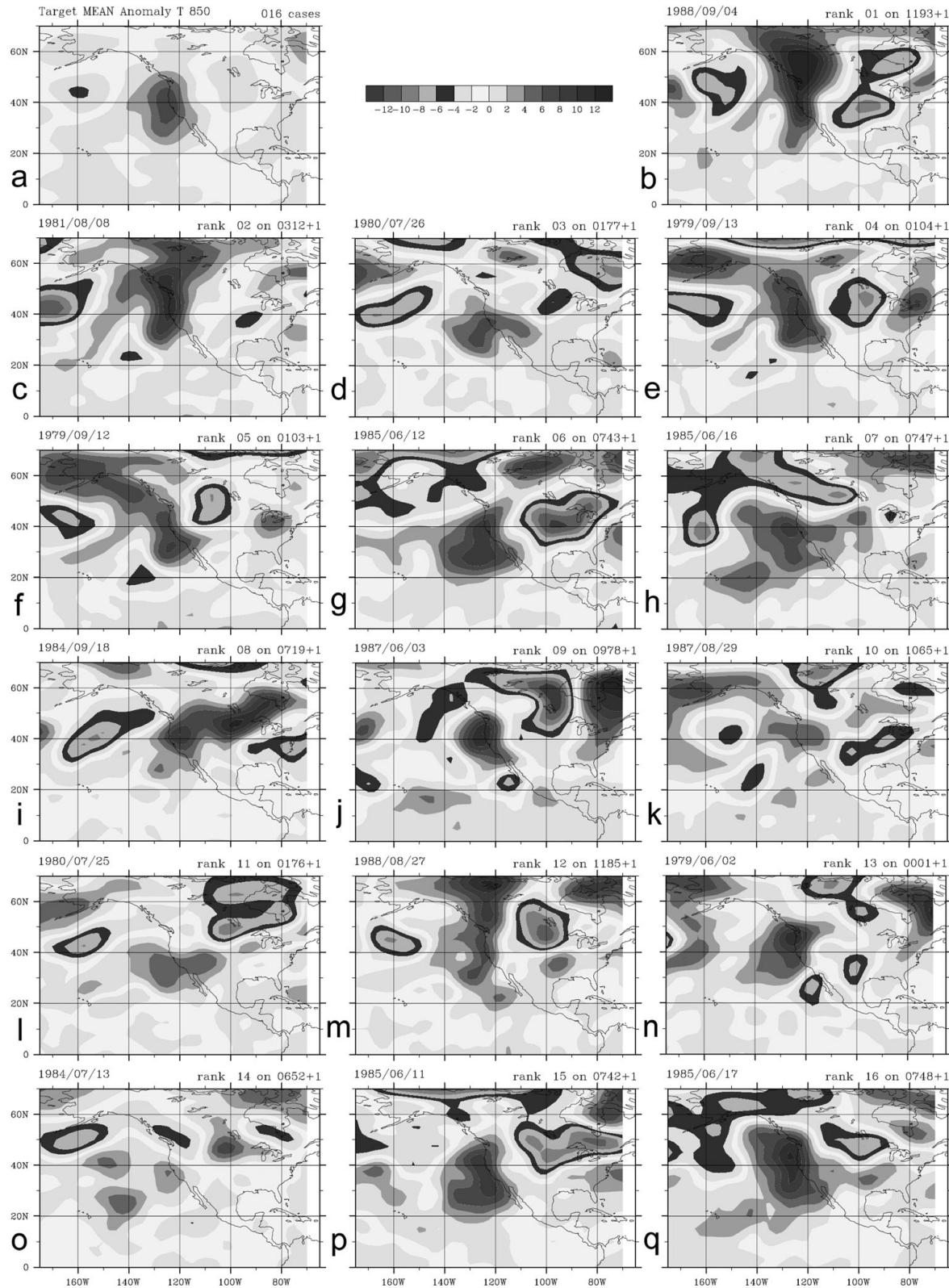


Fig. 16.2. Daily temperature anomalies at 850 hPa for the (a) target ensemble mean and (b–q) members of the ensemble, one for each target date. The hottest event in the ensemble is (b) and the least hot is (q). There is a consistent location of strong, positive anomaly (light shading that becomes darker for higher anomaly values) at and just off shore of northern California. Negative anomalies are shaded in a way surrounded by a dark black ring.

Meteorological fields on the target dates are composited to form the LSMPs, when either set of criteria is applied. The fields may be total fields or anomaly (with respect to long-term means) fields. The LSMPs are thus a ‘target’ ensemble mean constructed from a specified number of target dates. For example, the LSMP index is constructed based on the target ensemble mean of 16 dates that occurred during 1979–88. The target ensemble mean is further evaluated by comparing it against a large number of ‘random’ ensemble means, using the same number of dates each time, but where the dates are selected randomly, with replacement, from the historical record. The number of random ensemble means drawn is 1000. When the value at a grid point in the target ensemble mean equals or exceeds the highest ten values at that grid point among the random ensemble means, then the target ensemble is in the highest 1% of values at that point. This procedure, referred to as ‘bootstrap resampling’ provides a means to identify parts of the LSMP that are statistically significant and hence warrant attention. In Fig. 16.1, shading indicates the highest and lowest 1.5% of the values of the variable based on this methodology. In addition to significance, consistency among the target ensemble members must be assessed. Consistency tests include: low values of the variance between ensemble members (compared with members in each random ensemble) and simple sign

counts at each grid point. The sign count is the number of ensemble members having the same sign anomaly with respect to the long-term daily mean, minus those ensemble members having the opposite sign.

Figure 16.2a shows the hot spells target ensemble mean 850 hPa temperature anomaly field; this field can be compared with the total field (for a smaller region) shown in Fig. 16.1a. The other parts of Fig. 16.2 show the 16 individual target ensemble members. The upper air data used are from the National Centers for Environmental Prediction / Department of Energy reanalysis (hereafter, NDRA2), described in Kanamitsu *et al.* (2002). Shading in Fig. 16.2 indicates the anomaly value (not significance). Darker shading indicates higher anomaly value while lighter shading surrounded by a very dark ring indicates the lowest (largest negative) values. The figure is discussed further in Grotjahn (2011). The progressively darker shading indicates progressively higher (positive) values. The pattern is very consistent in having a strong positive anomaly at and just off the northern California coast. While there are often negative extrema west and east of the positive anomaly, the location and intensity of those negative extrema are inconsistent between the ensemble members.

Figure 16.3 shows the ensemble average 500 hPa geopotential height daily anomaly field at the onset and at several times prior to the onset. This time evolution shows that the

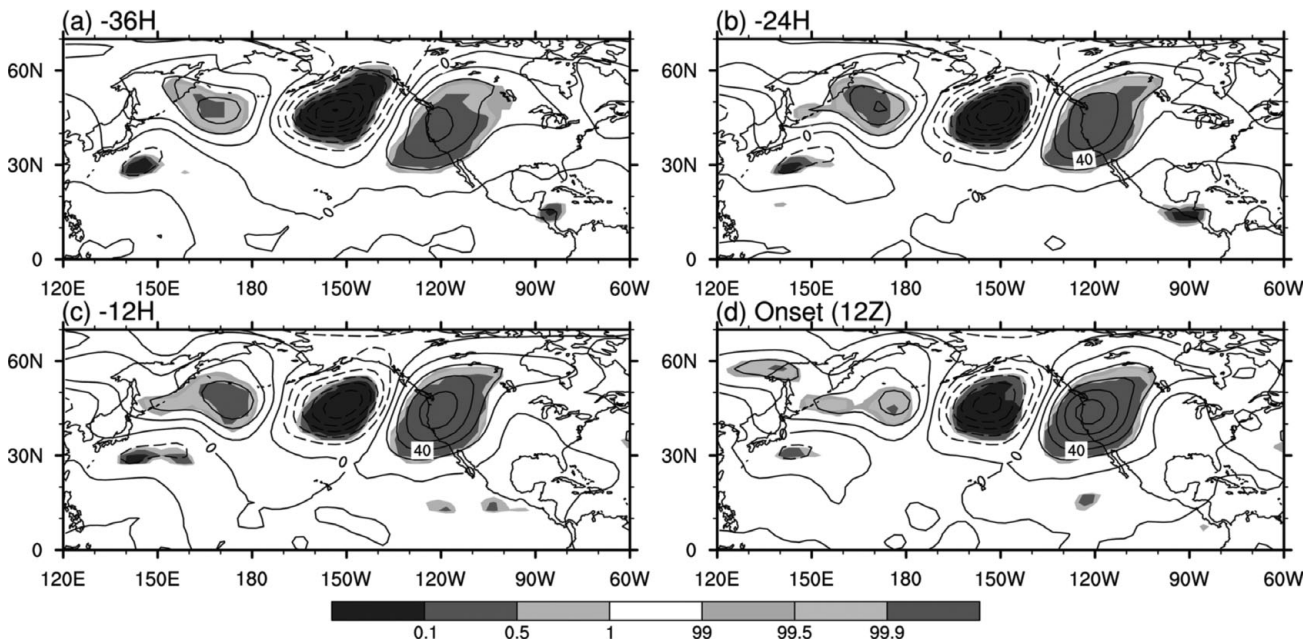


Fig. 16.3. LSMP in geopotential height (in m) anomalies at 500 hPa, composites for 49 hot spell target dates from 1951–2010. The target ensemble average from the 12 GMT map immediately prior to each hot spell onset is shown in (d). Other panels are at earlier times prior to hot spell onset: (a) 36 hours, (b) 24 hours, and (c) 12 hours. Light shading is used for significant positive anomalies while darker shading is for significant negative anomalies. Scale at the bottom indicates the level of significance in percent compared with 1000 random ensembles.

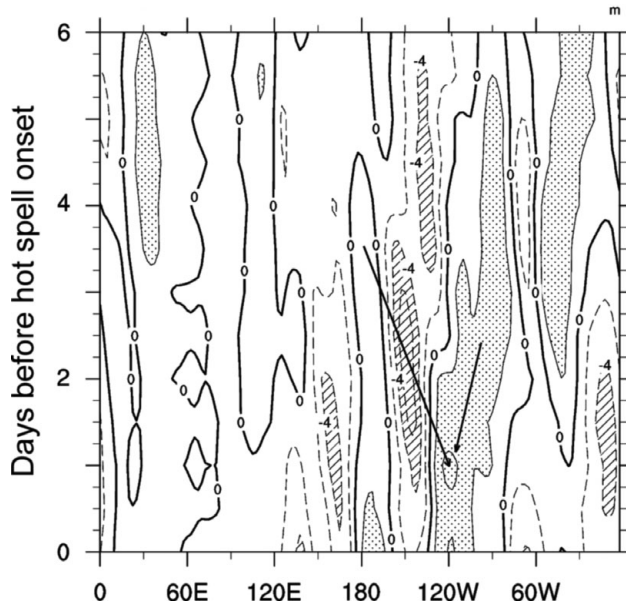


Fig. 16.4. Hovmöller diagram of 500 hPa level geopotential height anomaly (in dam) composite for 23 hot spells that occur from 1979–2006. The height anomaly plotted at each longitude is a meridional average from 30N to 50N. The dotted shaded regions are positive (ridge) values and the hatched shaded regions are negative (trough) values. The ridge–trough–ridge structure across the Pacific is visible from the Dateline to 120W. The ridge near the Dateline precedes the downstream trough and ridge over California (left arrow). To the East is some evidence for a positive (ridge) migrating westward (right arrow).

expected strong ridge centered near the west coast of North America is preceded by unusually high geopotential height values in the southeastern United States and northwestern Pacific. The strong ridge in the northwest Pacific precedes a trough in the east-central Pacific that in turn builds the ridge along the North American west coast. While that occurs, the ridge in the southeastern USA diminishes or possibly migrates westward. This chain of events can be seen in a simple Hovmöller diagram (Fig. 16.4). Bumbaco *et al.* (2013) also find an upstream trough for heat waves affecting latitudes north of the CV (western Washington and Oregon).

Figure 16.5 shows some dynamical analysis of the LSMPs using ensemble mean data. In Fig. 16.5a, contours of low frequency (periods longer than 14 days) 850 hPa temperature are shown with vectors of high frequency (periods less than 7 days) heat flux one day prior to the onset of 23 different hot spells. The heat flux by transients is advecting a ‘bubble’ of higher temperature air in a direction northwestward, along and just offshore of Northern California and Oregon.

The large ridge along the west coast present during hot spells suggests drawing a parallel to the dynamics of

blocking studies, though the season is summer, not winter. In Fig. 16.5b, the horizontal components of  $E_u = \{ \frac{1}{2} [(v')^2 - (u')^2], -u'v' \}$  are plotted along with the low frequency zonal wind component at 300 hPa. In  $E_u$  the high frequency (periods less than 7 days) zonal wind is  $u'$  while  $v'$  is the corresponding meridional component. The figure shows the composite of 23 events at their onset. Trenberth (1986) shows that the divergence of  $E_u$  is proportional to the total derivative of the zonal wind component. The figure shows convergence of the vectors off the west coast, indicative of slowing of the zonal wind thereby building the ridge. In a related analysis, the dot product of the high frequency  $E$  vector with the gradient of the low frequency zonal wind is proportional to the barotropic energy conversion for a mass of the atmosphere. (See further discussion in Dole and Black, 1990, Black and Evans, 1998.) In this analysis,  $E = \{ [(v')^2 - (u')^2], -u'v' \}$ . On the north side of the jet stream axis, that dot product is negative, implying that the high frequency eddy loses energy to the low frequency flow. On the west side of the ridge, the low frequency flow also gains energy, but the prior analysis showed the zonal component to be diminishing, hence the meridional component must be increasing. In short, the ridge is being amplified.

### 16.3 LSMPs as a predictor of surface extreme heat

A simple index can be formulated to measure how similar a particular day is to days when extreme hot spells occur. This index is a combination of un-normalized projections: one for each given daily anomaly field projected onto the corresponding field from the target ensemble of hottest days. Each projection is only calculated for one or more regions of the LSMP where that variable has significant amplitude and high consistency in the LSMP. The combination results in one number for each day, which is called the ‘LSMP index value’ in this document. Further details are found in Grotjahn (2011, who calls this a ‘circulation index’). Grotjahn (2011) has an illustrative pilot calculation using only two variables: temperature at 850 hPa and meridional wind at 700 hPa. Those choices are not ideal but were dictated by available data for a climate model application at that time. The relative weighting of the two projections to form the LSMP index was based on best capturing of the extreme events during the 1979–88 training period.

The properties of this LSMP index are discussed at length in Grotjahn (2011). A brief summary is presented here to provide a context for applying this approach to analyzing climate model output in the next section.

Higher LSMP index values imply hotter surface temperatures. The LSMP index is intended to capture the

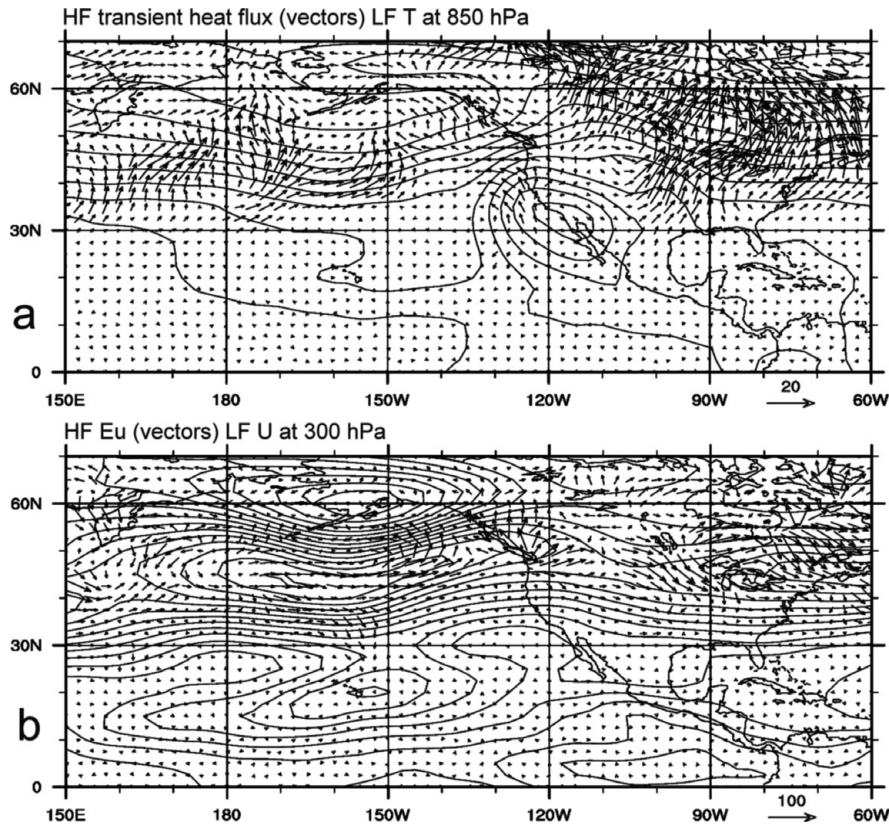


Fig. 16.5. Simplified dynamical analysis. (a) Horizontal, high frequency (<7 day period), heat flux vectors ( $\text{mK/s}$  units) superimposed on contours of low frequency temperature (2 K interval) at 850 hPa. These composites are ensemble averages constructed at the onset of 23 hot spell events from 1979–2006. A mass of hot air is migrating out of the southwestern desert region in a direction that keeps the hotter temperatures centered along or off shore of the California coast. (b) Horizontal vectors of high frequency  $E_u$  (see text;  $\text{m}^2\text{s}^{-2}$  units) and contours of low frequency zonal wind component (2.5 m/s interval). The convergence of  $E_u$  reduces the zonal component, consistent with building a ridge along the west coast.

extreme hottest days. Almost half of the dates match when comparing the highest 1% of the index values versus the hottest 1% of the Central Valley surface temperatures. Most of the other highest values of the index occur on days that are among the hottest 2% of the observed surface temperatures. The index also has a few of its highest 1% values during days that are merely above normal. The index has considerable skill in capturing extreme events compared to chance using various measures of skill in forecasting rare events. Since the LSMP index is based on large-scale patterns and correlates with smaller-scale regional hot spells, that makes the LSMP useful for downscaling extreme events.

The LSMP index also does a good job of identifying days that are near normal and even below normal. (The meteorological patterns for unusually cool days enhance the sea breeze with an upper level trough, essentially the inverse of hot spell LSMPs.) So the observed upper air LSMP index and surface max temperatures are highly correlated. (Correlation equals 0.83 during verification period: 1989–2006) (To illustrate, Figure 4 in Grotjahn, 2011, compares the LSMP index and the observed maximum surface temperature anomalies for the ten-year training period and the subsequent 18-year testing period.) Given the high correlation, one might expect the simulation

of the LSMP index distribution to be a good indicator of how well the model could simulate surface temperatures.

Of course the LSMP index is just an approximation to how conducive the large-scale conditions are to a hot spell. The index does not incorporate other relevant factors like those that reduce the heat (irrigation) and those that enhance the heat (drought and urbanization). With those caveats, distributions of the circulation indices for reanalysis, corresponding model data, and for two future scenarios are shown next.

#### 16.4 How well are LSMPs captured by a climate model?

This section makes an analysis of the LSMPs present in the fourth generation NCAR Community Climate model (CCSM4). The specific version uses 1.1 degree finite volume resolution. See Gent *et al.* (2011). One reason for examining the model LSMPs is because surface maximum temperatures can be poorly simulated in the climate model due to insufficient topographic resolution, poor surface and boundary layer simulation during the extremes, incorrect soil moisture, and inadequate surface type (vegetation/urban). Another reason is that the LSMPs are essentially

the boundary conditions needed by a regional climate model that is better able to simulate regional climate. Hence, if the global model does not produce the LSMPs adequately, then even a superb regional model cannot properly simulate the hot spell.

The topography of California is very complex. CCSM4 at  $\sim 1.1$  degree resolution cannot capture this complexity. Instead of a rather flat, low elevation CV ringed by higher mountain ranges with a few low passes accessing the ocean, the model has a broad gentle slope. (See Figure 1 in Grotjahn, 2013.) One consequence is the CCSM4 grid points near the CV stations are several hundred meters higher than the actual stations.

When maximum observed daily surface temperatures (an average of three stations that span the CV) are compared with the corresponding average of CCSM4 grid points close to those station locations, the model values

are  $\sim 6$  K cooler than the observed maxima. (The averages are over a 55-year period.) One might assume this bias is due to the higher elevations of the CCSM4 surface, but that would require a super-adiabatic lapse rate. Furthermore, the actual CV stations are placed in a heavily irrigated domain (which lowers the observed temperatures on the order of 3 K), and the climate model knows nothing about that irrigation. The standard deviation in the observed data versus the model data ( $4.38$  °C versus  $4.7$  K) and the skew ( $-0.31$  versus  $-0.27$ ) do match well. However, the distribution of model maximum surface temperature cannot be simply fixed by a simple shift of the whole distribution.

A trivial addition of 6 K to the model temperatures is inadequate as a bias correction procedure because the model hot spells LSMP is flawed. Figure 16.6 compares ensemble mean daily anomaly fields, where the ensemble is constructed from the hottest 1% of observed days

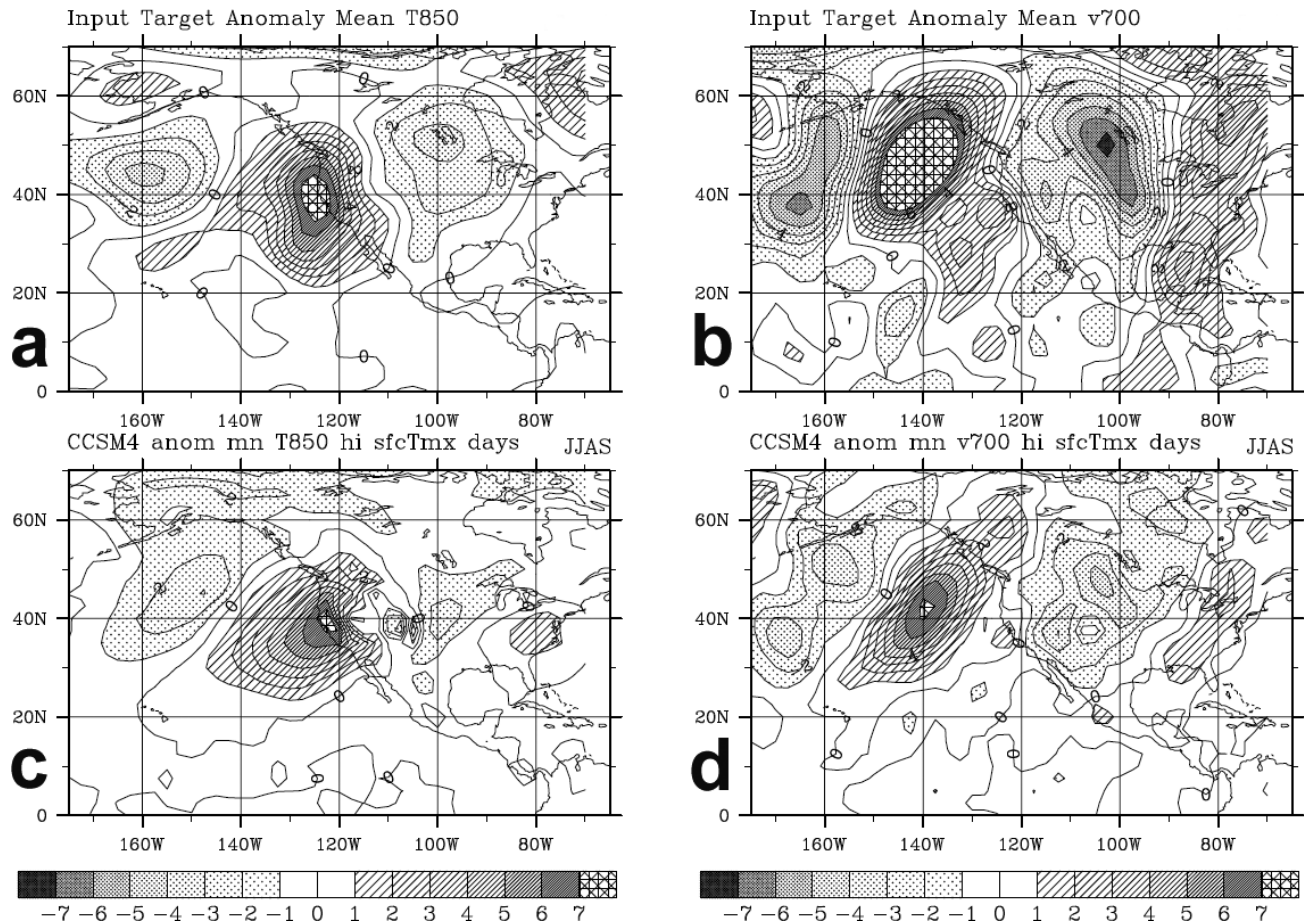


Fig. 16.6. Comparison of the reanalysis and climate model LSMPs. Shown are 850 hPa temperature anomaly (K units; left column) and 700 hPa meridional wind (m/s units; right column) in the NDRA2 reanalysis (top row) and in CCSM4 (bottom row) data. The CCSM4 target dates are when values are in the highest 1% average of three low elevation, near shore, grid points over land in CCSM4. The model LSMP has a broadly similar LSMP as observed, but some key flaws are: the magnitude is too weak and the 850 hPa maximum temperature anomaly location is onshore instead of offshore.

(LSMP in reanalysis data on top row) and hottest 1% of simulated surface temperatures near the California Central Valley (CCSM4 data on bottom row). The general structures look similar, but that is hardly surprising. In both ensembles the model and observations have high temperatures through a depth of the lower troposphere and the mid-tropospheric winds are mainly geostrophic. More interesting is that the model has weaker amplitude in its LSMP. Hence, this model, even as a driver of a regional model, will not produce extreme hot spells. And it will not produce extremes often enough (Grotjahn, 2013). Even more interesting is that the model data have the maximum thermal anomaly over the CV grid points, but the observation based reanalysis data have that maximum offshore (primarily to suppress the sea breeze). Hence, the model is completely missing this regional process.

If scatter plots are made of the LSMP index versus the surface maximum temperatures, then the general skill of the LSMP index as a predictor of surface maximum temperatures can be visualized. Such plots are found in Grotjahn (2013) but not reproduced here. The higher elevation of the CCSM4 surface makes the LSMP index less independent of the surface values, even though the fields used in the LSMP index occur 12 hours before the maximum temperature.

CCSM4 bias is evident in the LSMP index. The LSMP index varies less in CCSM4 data than it does in reanalysis data, as can be seen in Fig. 16.7. The standard deviation is 0.9 in the reanalysis data, but less than 0.8 in the model data. The skew is too little in the model ( $-0.11$ ) versus the reanalysis data ( $-0.16$ ). Even so, the CCSM4 data have fewer events above a given threshold that occurs rarely in the observations (reanalysis data). For example, using a the threshold of 2.0 corresponds to the top  $\sim 2\%$  of the LSMP

index for the reanalysis data (1951–2005), but the corresponding index for CCSM4 data have fewer than half as many members (50 instead of 111). These model biases hold for sub periods as well, with one exception, the model has a slight trend of increasing values that is *not* seen in the reanalysis LSMP index values. Grotjahn (2013) found a similar under-prediction of events though the average duration ( $\sim 2.5$  days) agreed well with reanalysis data.

Keeping in mind these biases, one can consider how the model simulates California hot spell LSMPs in future climate. Figure 16.8 shows how the LSMP index distribution in CCSM4 evolves for two representative concentration pathways (RCPs). The RCPs are defined in Moss *et al.* (2008). Both RCP scenarios show a shift to higher LSMP index values: about half a standard deviation for RCP4.5 and nearly a full standard deviation higher for RCP8.5. The magnitude of the skew is generally larger than in the historical simulations by this model. Hence, the mean and median are shifting more than the extreme values. Curiously, in the lower emission scenario, the distributions are shifted but, the interdecadal variation does not show a continuing shift, and possibly shows a decline in the bulk of the index values. In contrast, for the higher emission scenario, each later distribution has a clear shift of the whole pattern to a higher value. These changes have implications for the durations of extremes and raise some questions.

The shift in future scenarios of the distributions relative to the recent historical period (Fig. 16.8) makes it more likely that more days will be above one standard deviation. Consequently, durations above some threshold are much more common and last much longer. For example, durations above one standard deviation are shown in Fig. 16.9. In the historical period, only four periods last longer than

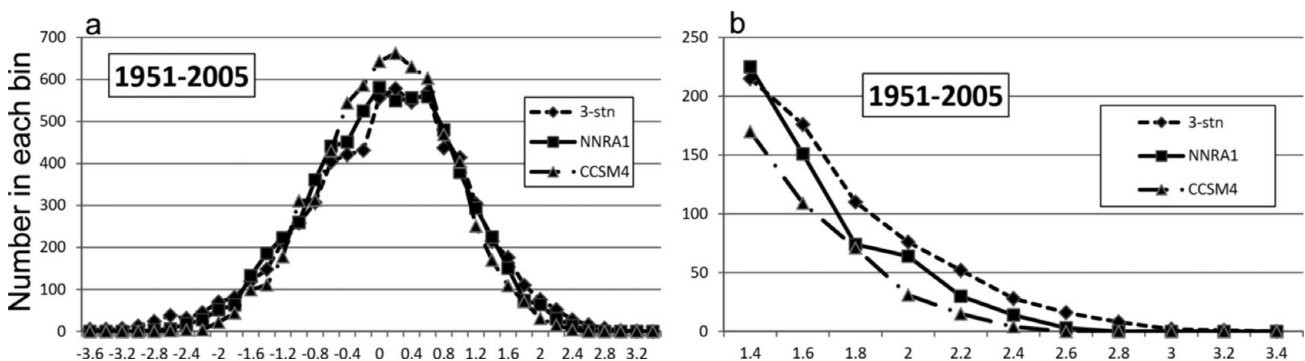


Fig. 16.7: (a) Distribution of LSMP index for NCEP/NCAR reanalysis and CCSM4 data over the period 1951–2005. Also shown are the normalized anomaly average daily values of surface maximum temperature at three CV stations over the corresponding period. The overall distributions of reanalysis and surface values match well, even though the index is based on only a few extremely hot events. The distribution of corresponding CCSM4 index values has notably smaller standard deviation. In terms of values above a high threshold, (b) the model produces about half as many as occur in the reanalysis data, though the highest index value in the model is comparable to the highest value in the reanalysis. Hence, the model can produce an extreme hot spell, but does so at a rate about half as often as is observed. The horizontal axes are bins of LSMP index values, where the value shown is the lower value of the 0.2 unit range.

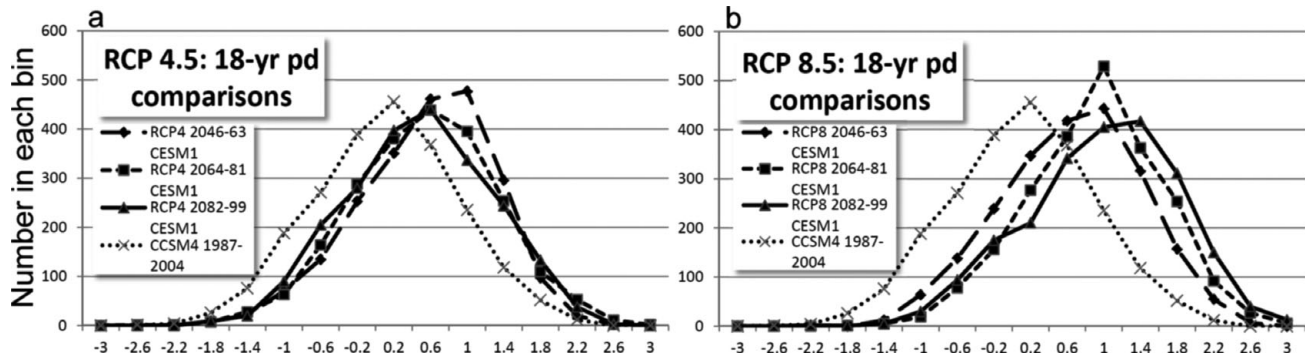


Fig. 16.8. Similar to Fig. 16.7a, except for two representative concentration pathways (RCP) scenarios. CCSM4 LSMP index in 18-year periods (a) for RCP 4.5 and (b) for RCP 8.5. For reference, the distribution in the model simulation for an 18-year period late in historical simulation is plotted as a dotted line.

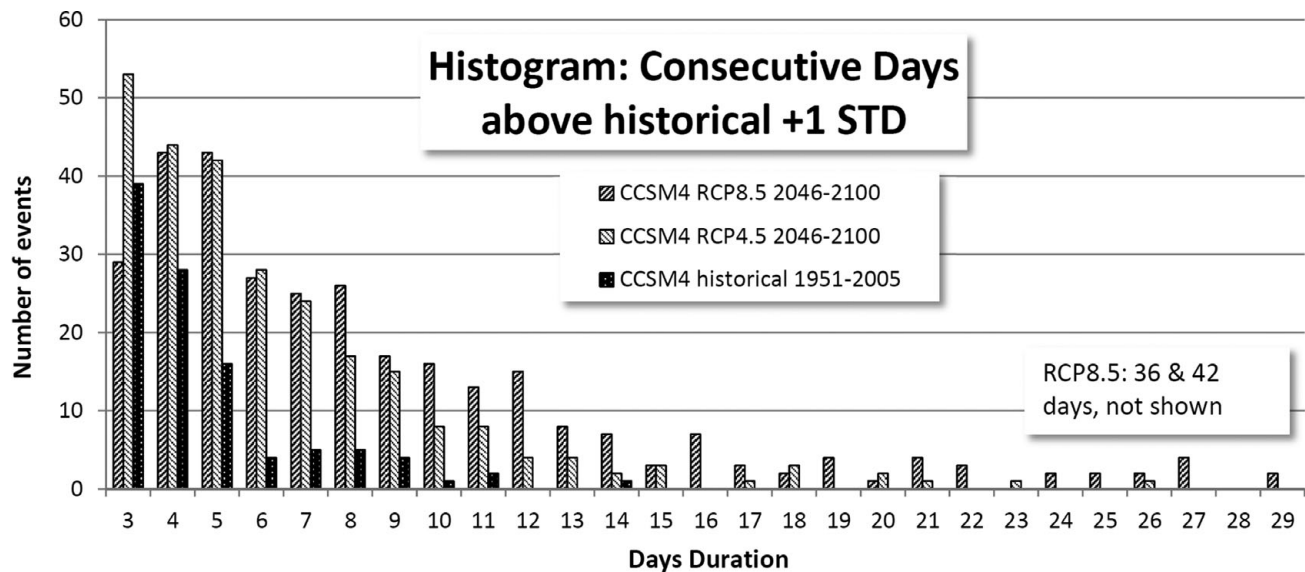


Fig. 16.9. Plot of the number of events that CCSM4 LSMP index values exceed one standard deviation (based on the historical LSMP distribution) organized by the number of consecutive days the threshold is exceeded during each event. Future climate, RCP scenarios simulated by CCSM4 have more and longer durations above the threshold.

nine days. For the lower emission case (RCP4.5), there are around ten times as many (38) periods lasting longer than nine days. A couple of periods each last more than three weeks. For the higher emission case (RCP8.5), there are 25 times as many (100) periods lasting longer than nine days (1569 out of 6710 days). Indeed, the number of periods peaks at four to five days for RCP 8.5, confirming that this is the new normal implied by this scenario. Two of the periods are above one standard deviation for more than a month!

There are commensurate changes in the LSMP index value corresponding to a 20-year return value. During 1951–2005, the 20-year return value is 2.2. The corresponding return value for 2046–2100 increases to: 2.8 for the RCP 4.5 and 3.1 for the RCP 8.5 scenarios. These are 25% and 40%

increases. The RCP 8.5 return value is outside the range of values estimated for the historical period.

It is unclear how much to trust CCSM4 future hot spells as visualized by the LSMP index. One can see some problems by visualizing all the LSMP index data as in Fig. 16.10. First, the smaller standard deviation of the CCSM4 data is quite apparent from the scatter of values during the 55 year historical period (Fig. 16.10 a,b). When these data are fitted to a regression line, another problem mentioned before is apparent: there is a trend in the CCSM4 data but it is much smaller in the reanalysis data. Since both sets of data are based on upper air quantities and the portions of those quantities used are located primarily over the Pacific Ocean, then neither the CCSM4

bias: the model has a trend, nor the lack of a trend in the reanalysis data, can be explained by a lack (or presence) of Central Valley irrigation. There must be a dynamical difference between model and observations (reanalysis).

The future climate scenarios (Figs. 16.8 and 16.10 c,d) are a mixture of expected and unexpected results. There is a strong trend (increasing values over time) in the RCP8.5 data as one might expect. Oddly, for the RCP4.5 values

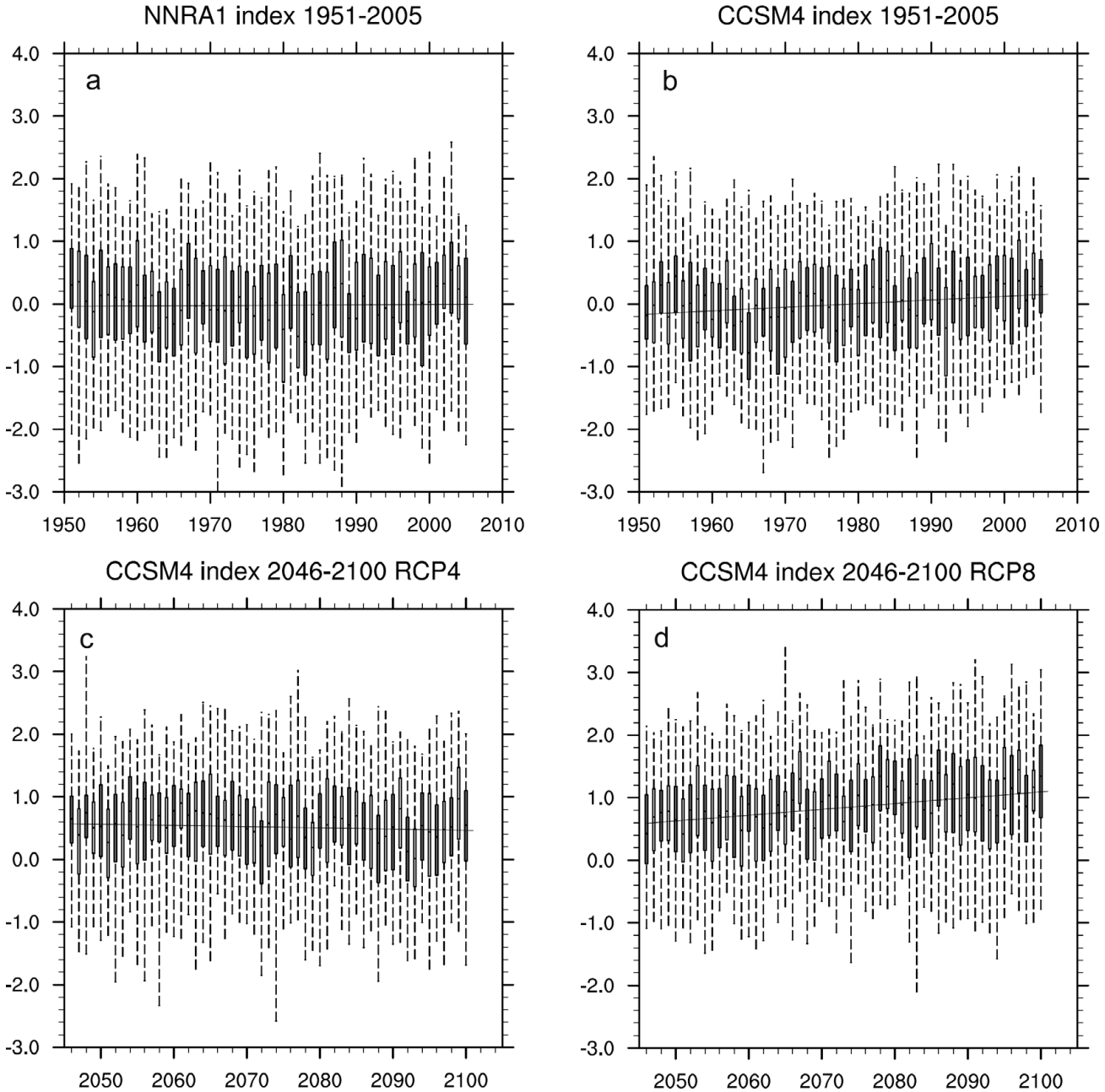


Fig. 16.10. LSMP index values from (a) NCEP/NCAR reanalysis data (NNRA1) and (b) corresponding CCSM4 data from 1951–2005. CCSM4 predictions for 2046–2100 under the (c) RCP 4.5 and (d) RCP 8.5 emission scenarios. Each box indicates first and third quartiles and the whiskers indicate the extremes in each warm season. Each trend line is calculated using all 55 years of data. In the historical period the model has smaller standard deviation (0.757) than the reanalysis (0.872); also, the model has a larger trend than the reanalysis data. In the two future scenarios, the extreme values are slightly decreasing in the lower emission but strongly increasing in the higher emission scenario. Notably, the standard deviation is essentially unchanged: 0.747 in RCP 4.5 and 0.749 in RCP 8.5. All standard deviations are computed separately for each year, then the annual values are averaged together over each 55-year period.

there is a slight decreasing trend. The extreme values have corresponding trends: increasing for RCP8.5, decreasing for RCP4.5 during 2046–2099. Given that the model has a positive trend where none existed historically, does the decreasing trend of RCP4.5 imply a strongly decreasing trend of future LSMP index values? Such a question is beyond the scope of this chapter. Instead, these results raise deeper issues about the model's simulation skill in handling the dynamics of extreme hot spells.

## 16.5 Conclusions

This chapter examined California Central Valley (CV) hot spells from the perspective of the large-scale meteorological patterns (LSMPs) associated with those events. The LSMPs are large in scale and magnitude, and hence potentially well resolved by climate models. Such LSMPs form the basis for statistical and dynamical downscaling.

The LSMPs are found by compositing the data on target days, where the target days are dates of hot spells on their onset. Bootstrap re-sampling, which compares the target ensemble mean to a large number of randomly drawn ensemble means, is used to identify significant areas. In addition to significance, areas of consistent behavior among the target ensemble members are also needed. Some other statistical issues were described. Areas that are both significant and consistent in upper air data were used in an unnormalized projection scheme to obtain an index of how similar a given day is to the target ensemble mean. This upper air 'LSMP index value' is generally positive and larger the hotter the daily maximum surface temperatures are. Although intended just for the positive extremes, the LSMP index also models well the whole distribution of daily maximum surface temperatures. CV cooler days have a somewhat opposite LSMP to the hot spells during summer. Hence, the LSMP index is highly correlated with all the daily summer maximum temperatures in the CV. Some simple dynamical and synoptic interpretations were applied to understand better the LSMPs.

An LSMP-based index was used to assess hot spells created by the NCAR climate model CCSM4. The LSMP index is used because: (a) the model has no Central Valley in its topography, (b) the model does not simulate surface temperatures adequately, and (c) the index has relevance to downscaling methods. The model does resolve and capture the large-scale patterns associated with hot spells. While similar, the model patterns during hot spells are not as strong as observed and have key differences, partly related to the smooth model topography.

An LSMP index is useful to provide a compact description of a complex pattern associated with hot spells. As such, other analyses can be done using that index. Properties

of the index were examined and implications for the future climate were drawn along with concerns about how well the model can capture extreme events. For historical periods CCSM4 bias: (a) has notably less variability in LSMP index than is observed, (b) underestimates the extremes by about half, and (c) has an increasing trend in LSMP index that was not observed. In future climate scenarios for the last half of this century, CCSM4: (a) has a strong increasing trend in LSMP index for the higher emission (RCP8.5) scenario, but a peculiar, slight decreasing trend in the lower emission (RCP4.5) scenario; (b) extreme values have corresponding trends, such that 20-year return values (not shown) exceed the historical asymptote, i.e. are unprecedented for RCP8.5; and (c) extreme events have much longer duration than historically, becoming commonplace.

The biases and curious results of the CCSM4 LSMP index need some additional quantification. Dynamical tools can be applied to understand why these biases and curious results are occurring in the model. Given daily, instantaneous, upper air and surface data, this LSMP approach can be applied to other models and potentially to investigate hot spells occurring in other regions of the Earth. Finally, the LSMP approach is potentially applicable to other extreme events, particularly cold air outbreaks and heavy frontal cyclone precipitation (Grotjahn and Faure, 2008).

## 16.6 Acknowledgments

This research was supported in part by the United States National Science Foundation under Grant No. 1236681. Dr. Yun-Young Lee prepared the figure of 500 hPa height anomalies. This work was supported by the USDA National Institute of Food and Agriculture, Hatch project CA-D-LAW-4264-H.

## References

- Black, R. X. and Evans, K. J. (1998). The statistics and horizontal structure of anomalous weather regimes in the Community Climate Model. *Monthly Weather Review*, **126**, 841–859.
- Bumbaco, K. A., Dello, K. D., and Bond, N. A. (2013). History of Pacific Northwest heat waves: synoptic pattern and trends. *Journal of Applied Meteorology and Climatology*, **52**, 1618–1631. doi: <http://dx.doi.org/10.1175/JAMC-D-12-094.1>
- Dole, R. M. and Black, R. X. (1990). Life cycles of persistent anomalies. Part II: The development of persistent negative height anomalies over the North Pacific Ocean. *Monthly Weather Review*, **118**, 824–846.
- Gent, P. R., Danabasoglu, G., Donner, L. J., et al. (2011). The Community Climate System Model Version 4. *Journal of Climate*, **24**, 4973–4991. doi: <http://dx.doi.org/10.1175/2011JCLI4083.1>

- Gershunov, A., Cayan, D. R., and Iacobellis, S. F. (2009). The great 2006 heat wave over California and Nevada: Signal of an increasing trend. *Journal of Climate* **22**, 6181–6203.
- Grotjahn, R. (2011). Identifying extreme hottest days from large scale upper air data: a pilot scheme to find California Central Valley summertime maximum surface temperatures. *Climate Dynamics* **37**, 587–604. DOI 10.1007/s00382-011-0999-z
- Grotjahn, R. and Faure, G. (2008). Composite predictor maps of extraordinary weather events in the Sacramento, California, region. *Weather and Forecasting*, **23**, 313–335. doi: <http://dx.doi.org/10.1175/2007WAF2006055.1>
- Grotjahn, R. (2013). Ability of CCSM4 to simulate California extreme heat conditions from evaluating simulations of the associated large scale upper air pattern. *Climate Dynamics* **41**, 1187–1197. doi:10.1007/s00382-013-1668-1
- Grotjahn, R., Black, R., Leung, R., et al. (2015). North American extreme temperature events and related large scale meteorological patterns: a review of statistical methods, dynamics, modeling, and trends. *Climate Dynamics* doi:10.1007/s00382-015-2638-6.
- Kanamitsu M., Ebisuzaki, W., Woollen, J., et al. (2002). NCEP-DOE AMIP-II reanalysis (R-2). *Bulletin of the American Meteorological Society*, **83**, 1631–1643.
- Karl, T. R. and Quayle, R. G. (1981). The 1980 summer heat wave and drought in historical perspective. *Monthly Weather Review*, **109**, 2055–2073. doi: [http://dx.doi.org/10.1175/1520-0493\(1981\)109<2055:TSHWAD>2.0.CO;2](http://dx.doi.org/10.1175/1520-0493(1981)109<2055:TSHWAD>2.0.CO;2)
- Moss, R., Babiker, M., Brinkman, S., et al. (2008). *Towards New Scenarios for Analysis of Emissions, Climate Change, Impacts, and Response Strategies*. Intergovernmental Panel on Climate Change, Geneva, 132 pp.
- Namias, J. (1982). Anatomy of Great Plains protracted heat waves (especially the 1980 U.S. summer drought). *Monthly Weather Review*, **110**, 824–838. doi: [http://dx.doi.org/10.1175/1520-0493\(1982\)110<0824:AOGPPH>2.0.CO;2](http://dx.doi.org/10.1175/1520-0493(1982)110<0824:AOGPPH>2.0.CO;2)
- Trenberth, K. E. (1986). An assessment of the impact of transient eddies on the zonal flow during a blocking episode using localized Eliassen–Palm flux diagnostics. *Journal of the Atmospheric Sciences*, **43**, 2070–2087.

# Decadal to interdecadal variations of northern China heat wave frequency: impact of the Tibetan Plateau snow cover

Zhiwei Wu and Jianping Li

## 17.1 Introduction

Under the global warming background, heat waves have become a major meteorological disaster on the Earth (Trenberth *et al.*, 2007). For example, over 25,000 deaths were attributable to the 2003 heat wave in Europe (Garcia-Herrera *et al.*, 2010). In the summer of 2010, Moscow experienced 33 consecutive days with maximum temperatures exceeding 30 °C. This unprecedented heat wave took 15,000 lives and cost the economy \$15 billion as fires and drought ravaged the country (Alexander, 2010).

Northern China has also undergone frequent heat waves, associated with a severe drought and desertification trend during summer in past decades (e.g. Zhai *et al.*, 1999, Fu, 2003, Wang and Ding, 2006, Trenberth *et al.*, 2007, Ding *et al.*, 2007). More than half a billion people are facing drinking water shortages, which has triggered the South–North Water Transfer Project, to better utilize water resources available to China (<http://www.nsbd.gov.cn/>). Therefore, understanding the origins of the northern China heatwaves is obviously of great societal as well as scientific value. This has motivated the present study.

Reasons for the northern China heat waves are far from being clarified. Most previous studies have primarily focused on northern China rainfall variations rather than on heatwaves. For example, Fu (2003) proposed that human-induced land cover change may impact on the northern China drought tendency. Based on observational and theoretical evidence, Li *et al.* (2010) suggested that regionally meridional asymmetric warming, with the most prominent surface warming center in northeastern Asia, can induce a southward shift of the Meiyu–Baiu–Changma rain belt and in turn lead to drought over northern China.

The reason why the northern rainfall receives more research interest than surface air temperature is partly due to the fact that the rainfall has a more direct impact on local droughts and partly due to the assumption that surface air temperature usually exhibits coherent variations with rainfall. However, the relationship between summer

precipitation and surface air temperature is rather complicated. For instance, in eastern China, significant negative correlations between summer precipitation and air temperature are mainly along the middle and lower reaches of the Yangtze River valley, while correlations may be less significant in other regions (Nitta and Hu, 1996). Hirschi *et al.* (2010) used observations of surface air temperature and precipitation in Europe and found that soil-moisture deficits are likely to have enhanced the frequency and duration of extreme summer heat in southeastern Europe. However, they also noted that for wetter climates, such as that in central Europe, observations indicate only a weak relationship between heat waves and precipitation variations.

Northern China is dominated by transitional climate, from monsoon to desert (e.g. Ding, 1992). The subtropical front of the East Asian summer monsoon can bring notable precipitation to northern China in some strong monsoon years, and vice versa in some weak monsoon years (e.g. Wang *et al.*, 2008b, Wu *et al.*, 2009). Coupling between heat waves and precipitation varies considerably year to year in this region. Therefore, it is necessary to re-investigate heat wave origins over northern China, in spite of many studies having been conducted on local rainfall variations. In this study, we focus on the potential association of the Tibetan Plateau (TP) snow cover (TPSC) with heat wave frequency (HWF) over China.

TPSC anomalies were found to have a close connection with the Asian climate, especially the East Asian summer monsoon (e.g. Qian *et al.*, 2003, Yu *et al.*, 2004, Massimo and Benedict, 2004, Zhang *et al.*, 2004, Li *et al.*, 2005, Wu *et al.*, 2007, Wu and Kirtman, 2007, Zhao *et al.*, 2007, Wang *et al.*, 2008a, Seol and Hong, 2009, Duan *et al.*, 2011, Liu and Chen, 2011, Wu *et al.*, 2012a, and many others). With the highest mountains in the world, the TPSC can persist through the warm seasons over high-altitude areas (Pu *et al.*, 2007; Wu *et al.*, 2012a,b), making it a potential predictability source for summer climate. During summer (June–August, JJA), the most persistent snow

**Plate 1**

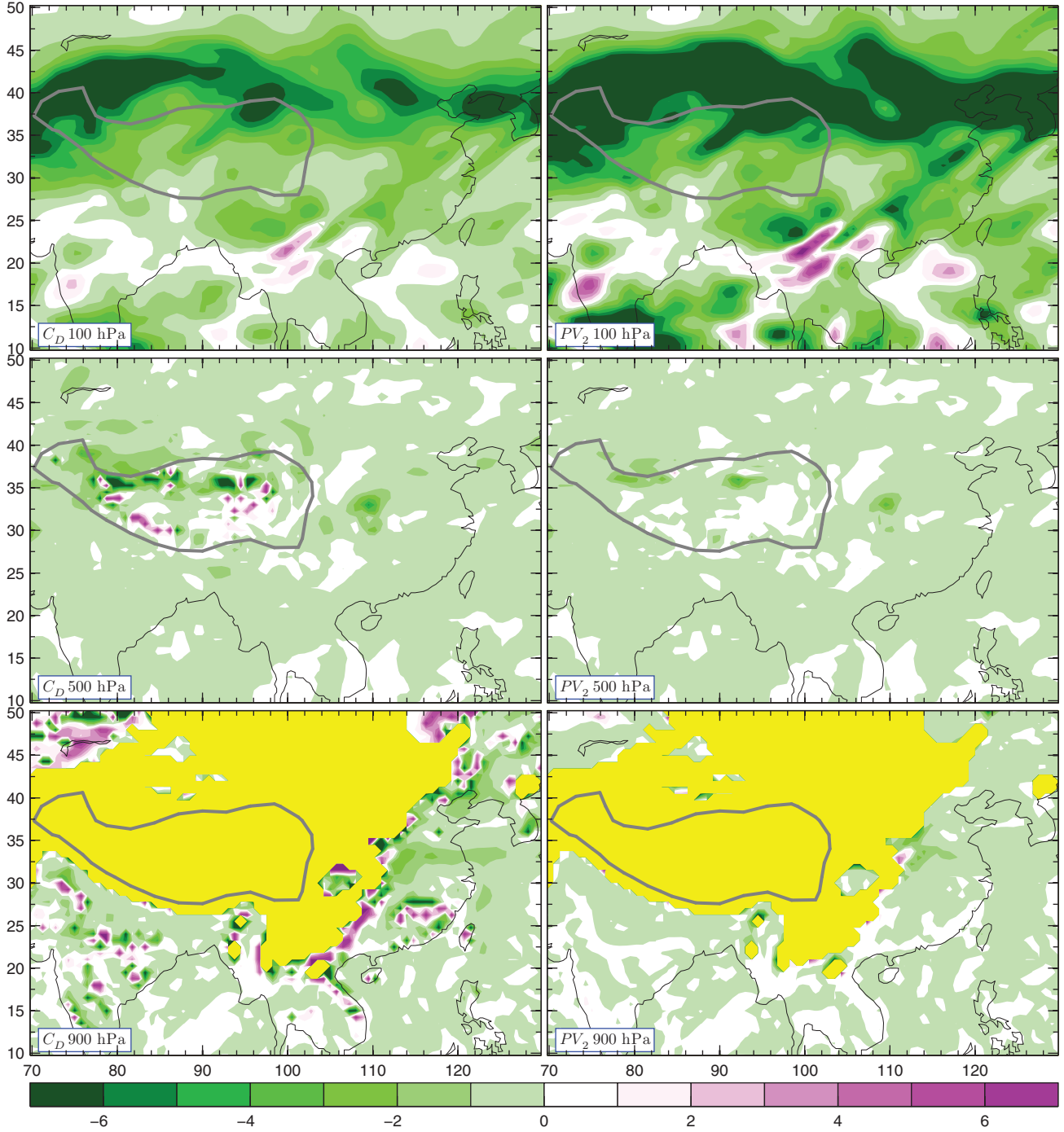


Fig. 2.1: Distributions at 100 (top), 500 (middle), and 900 hPa (bottom) of  $C_n$  ( $10^{-5} \text{m}^{-3}(\text{kg s})^{-1}$ ; left) and  $PV_e$  ( $10^{-1} \text{PVU}$ ,  $1 \text{PVU} = 10^{-6} \text{m}^2(\text{kg s})^{-1}$ ; right) at 0600 UTC 22 July 2008. In this figure, and those that follow, the yellow shading indicates the region below the ground surface. The thick gray line indicates the 3000 m contour of surface elevation.

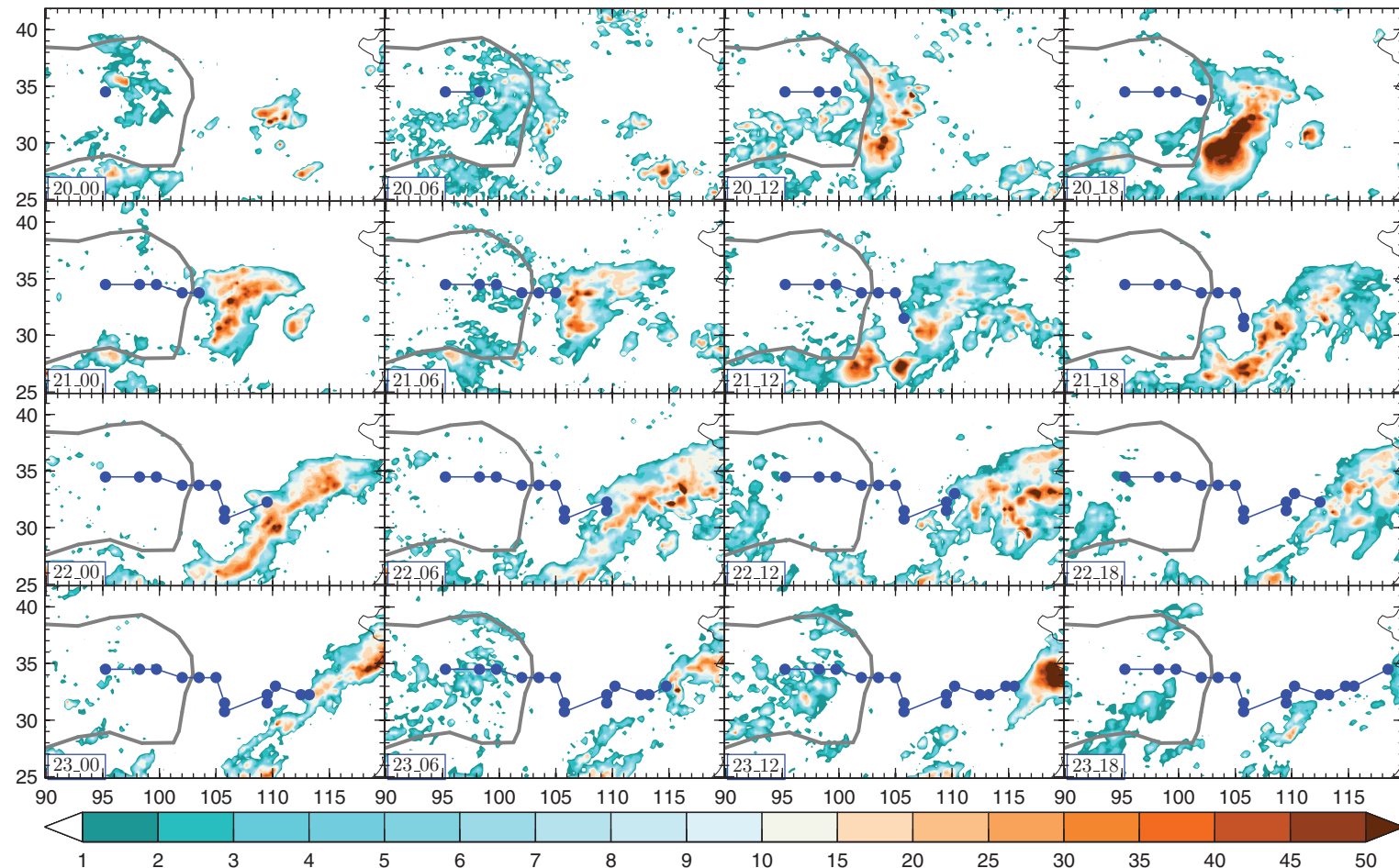


Fig. 2.5: Track of the TPV from 0000 UTC 20 to 1800 UTC 23 July 2008 and the associated 6-hour precipitation. Shading represents the TRMM 3B42 precipitation ( $\text{mm}(6\text{h})^{-1}$ ) and the blue line with solid circles indicates the track of the TPV.

### Plate 3

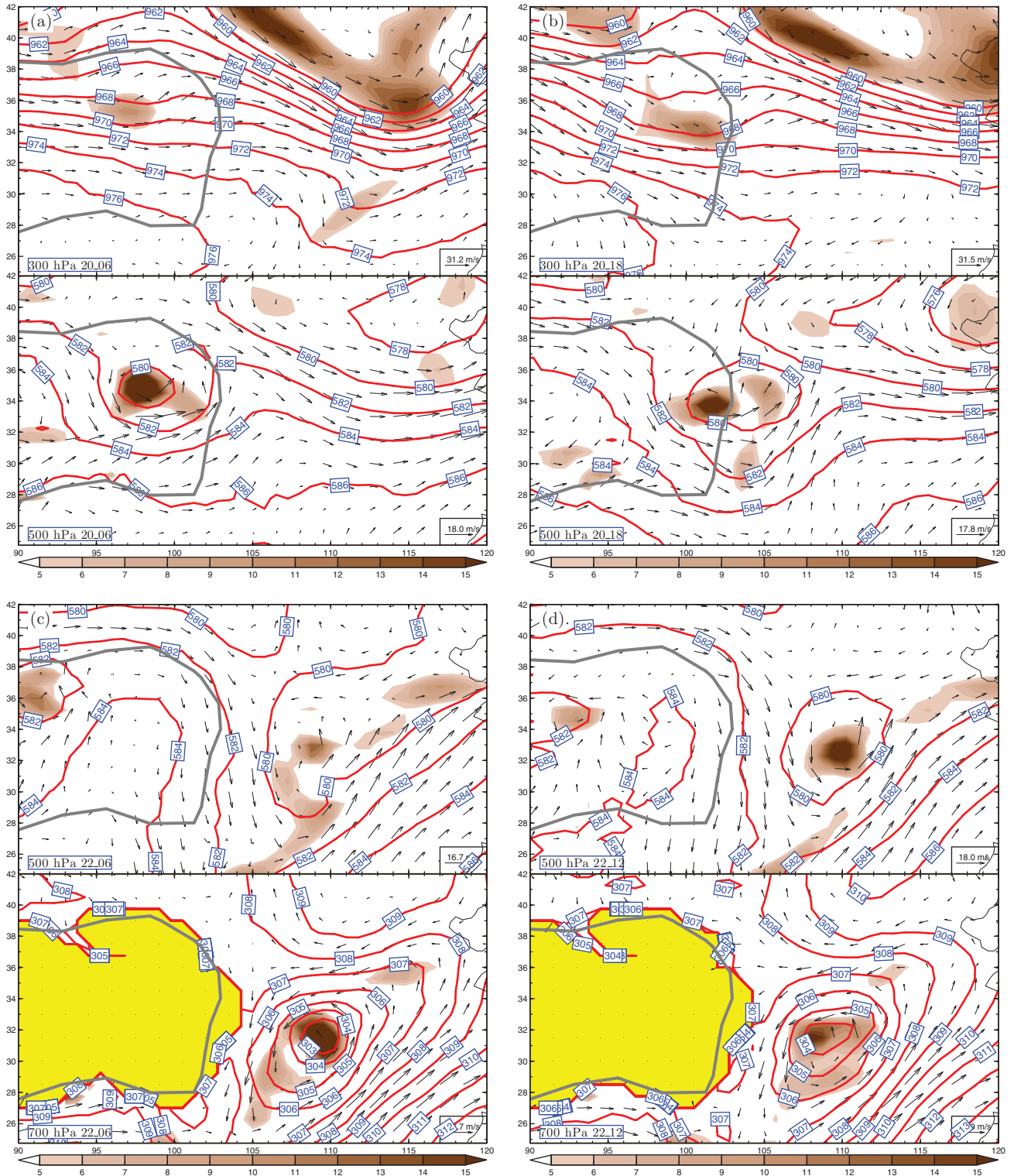


Fig. 2.7: Distributions of wind (vector), geopotential height (dgm; contour), and vertical relative vorticity ( $10^{-5} s^{-1}$ ; shading) at (a) 300 and 500 hPa at 0600 UTC 20, (b) 300 and 500 hPa at 1800 UTC 20, (c) 500 and 700 hPa at 0600 UTC 22, and (d) 500 and 700 hPa at 1200 UTC 22 July 2008.

**Plate 4**

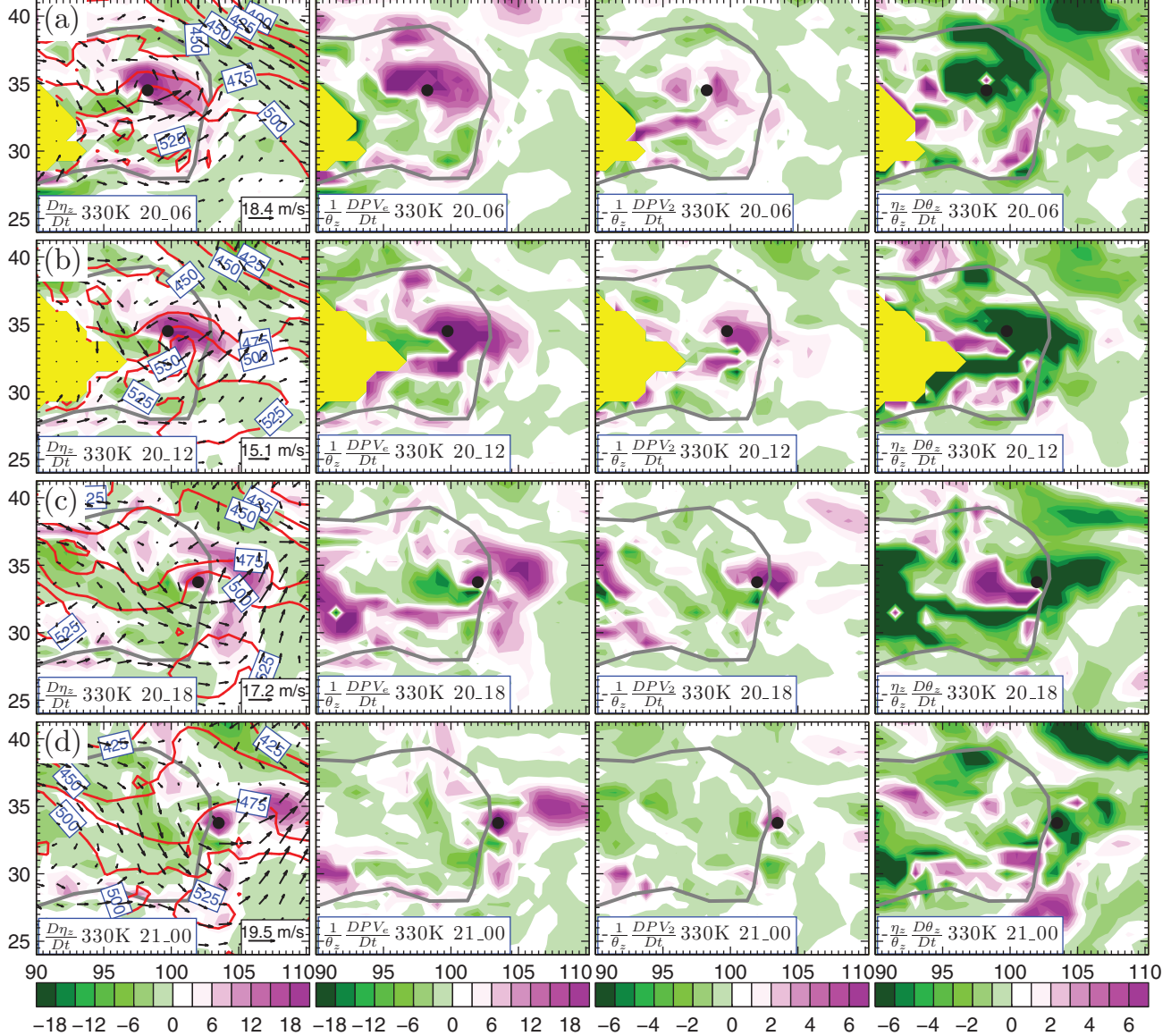


Fig. 2.8: Relative contributions to the development of vertical vorticity on the 330 K isentropic surface (first column) due to the change in  $PV_e$  (second column),  $PV_2$  (third column), and  $\theta_z$  (fourth column) at (a) 0600 UTC 20, (b) 1200 UTC 20, (c) 1800 UTC, and (d) 0000 UTC 21 July 2008. The vector is horizontal wind, the contour line is pressure in hPa, and the shading is in  $10^{-5} \text{ m}^3 (\text{kg s } 6\text{h})^{-1}$ . In this figure and following, the black solid circles indicate the location of the TPV.

**Plate 5**

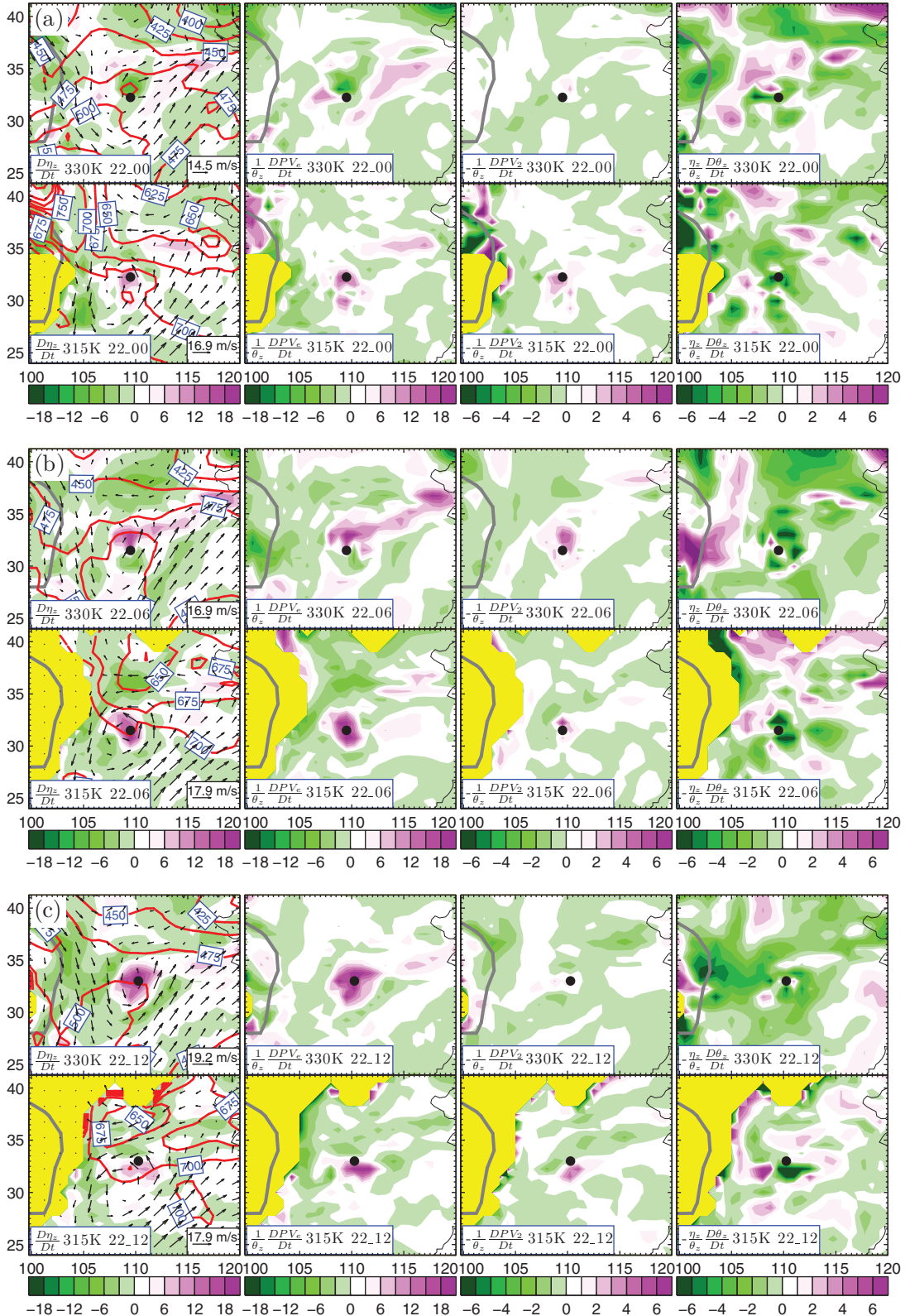


Fig. 2.9: As Fig. 2.8, but on the 330 and 315 K isentropic surfaces at (a) 0000, (b) 0600, and (c) 1200 UTC 22 July 2008.

## Plate 6

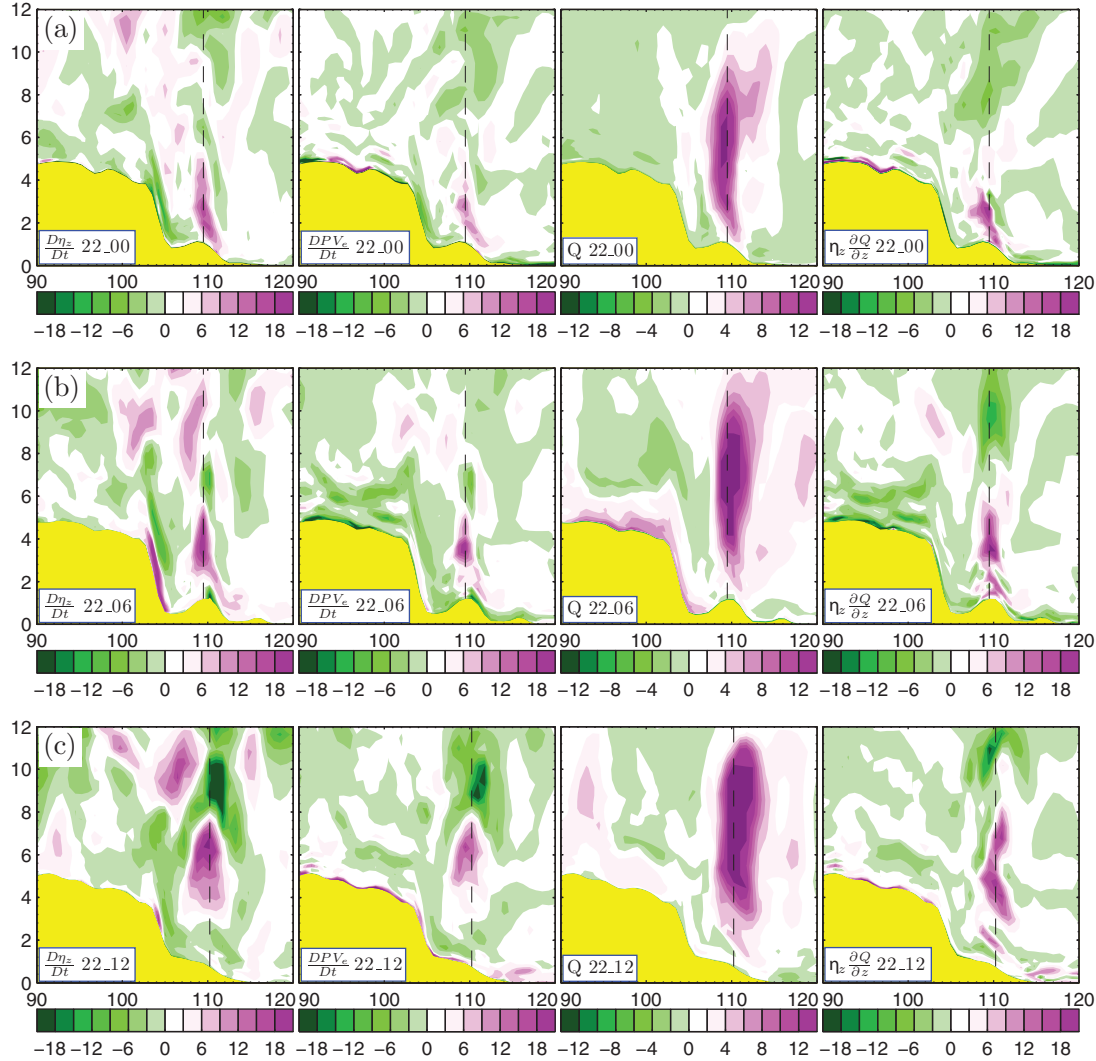


Fig. 2.10: Vertical cross-sections at (a) 0000 UTC, (b) 0600 UTC, and (c) 1200 UTC 22 July 2008 of the total change in vertical vorticity (first column;  $\frac{D\eta_z}{Dt}$ ;  $10^{-5} \text{ m}^3 (\text{kg s } 6\text{h})^{-1}$ ), the change in  $PV_e$  (second column;  $\frac{DPV_e}{Dt}$ ;  $10^{-1} \text{ PVU (6h)}^{-1}$ ), the diabatic heating  $Q$  (third column;  $\text{K (6h)}^{-1}$ ), and the change in  $PV_e$  due to the vertical gradient of diabatic heating (fourth column;  $10^{-1} \text{ PVU (6h)}^{-1}$ ).

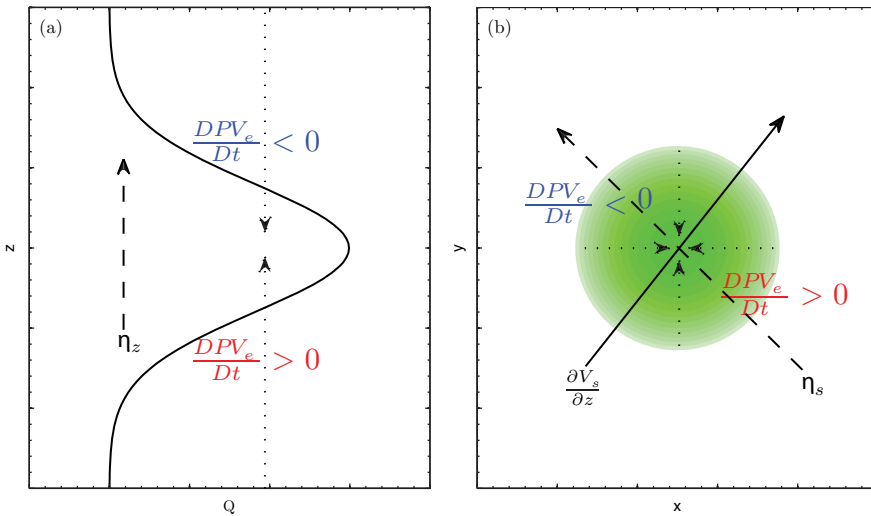


Fig. 2.2: Lagrangian  $PV_e$  generation associated with (a) the vertical profile of diabatic heating  $Q$  (thick solid line) and (b) the horizontal distribution of diabatic heating  $Q$  (shading). Long solid arrow in (b) is the vertical shear ( $\frac{\partial V_s}{\partial z}$ ) of horizontal wind, long dash arrow in (a) is the vertical vorticity  $\eta_z$  and in (b) is the horizontal vorticity  $\eta_s$ , and short dot arrows are the vertical gradient ( $\frac{\partial Q}{\partial z}$ ) of diabatic heating in (a) and  $\nabla_s Q$  in (b), which is the horizontal gradient of diabatic heating.

**Plate 7**

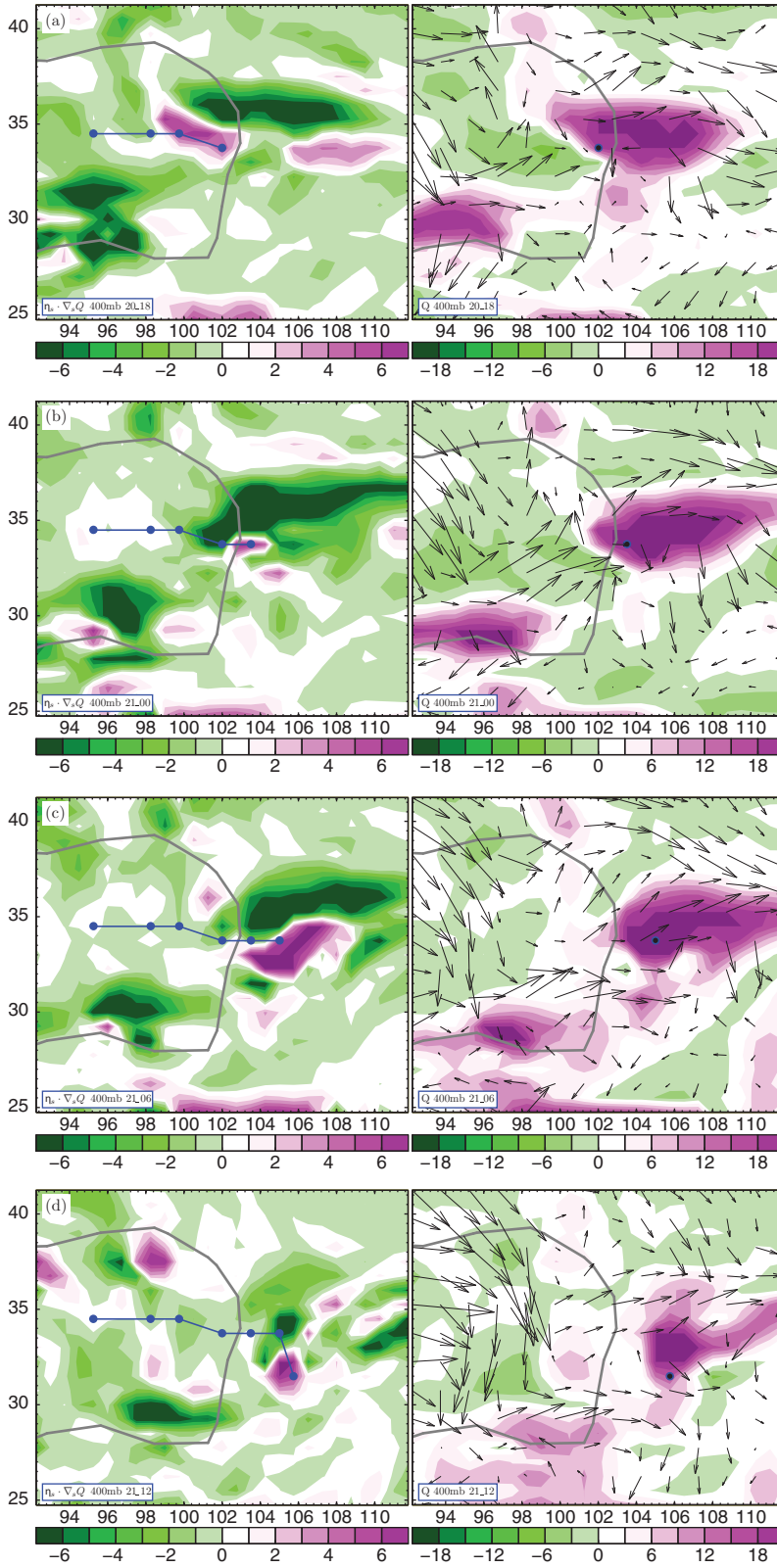


Fig. 2.11: The change at 400 hPa of  $PV_e$  (first column;  $5 \times 10^{-2}$  PVU  $(6h)^{-1}$ ) due to the horizontal gradient of diabatic heating (second column;  $5 \times 10^{-1}$  K  $(6h)^{-1}$ ) at (a) 1800 UTC 20, (b) 0000 UTC 21, (c) 0600 UTC 21, and (d) 1200 UTC 21 July 2008. The vector denotes vertical shear of horizontal wind.

**Plate 8**

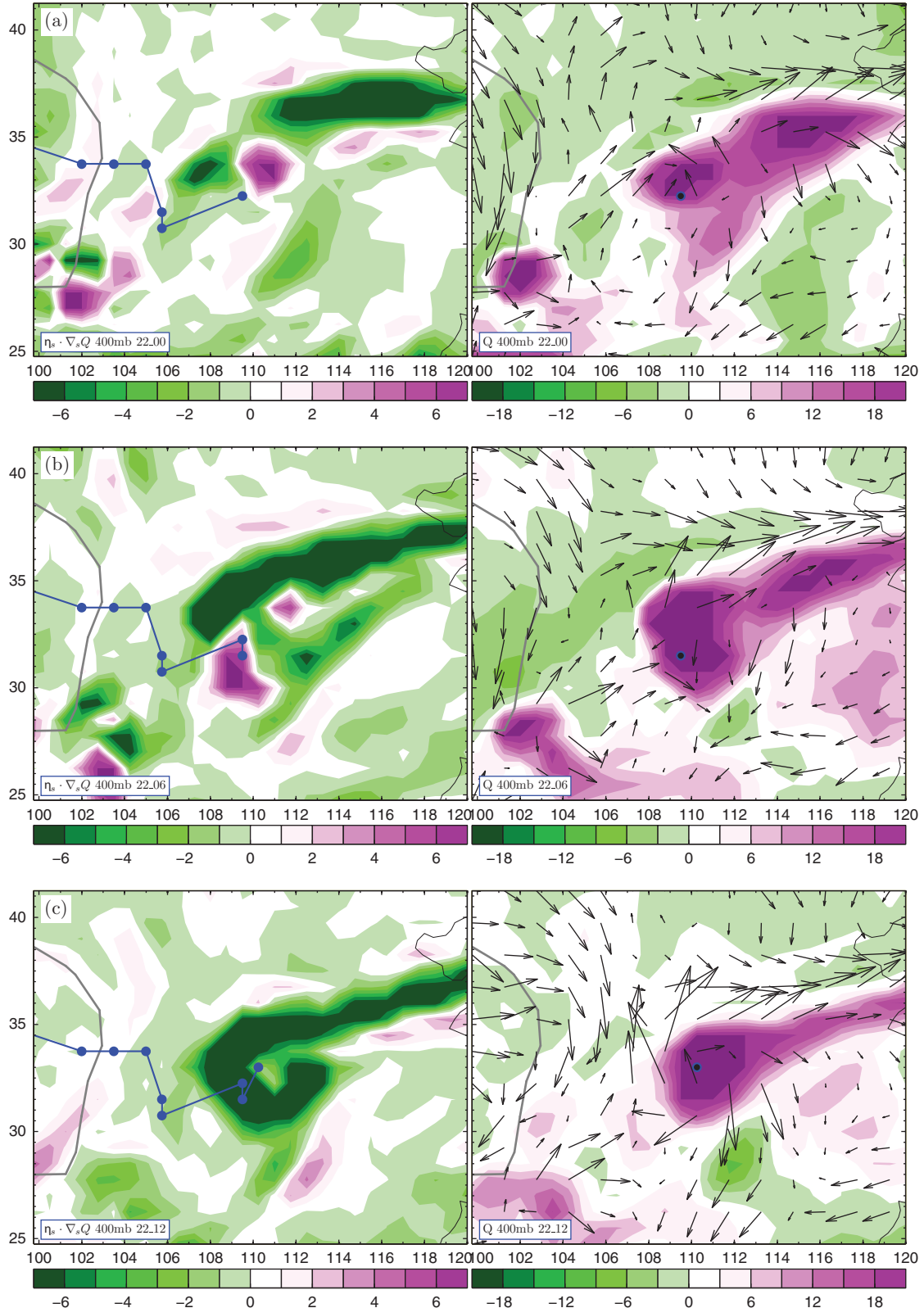


Fig. 2.12: As Fig. 2.11, but at (a) 0000, (b) 0600, and (c) 1200 UTC 22 July 2008.

## Plate 9

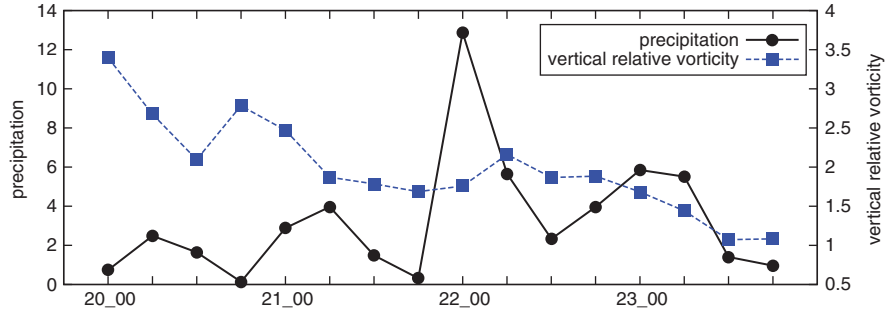


Fig. 2.6: Time series of the central maximum vertical relative vorticity ( $10^{-4}s^{-1}$ ; dashed line) of the TPV and the  $3^\circ \times 3^\circ$  area-average of precipitation ( $mm(6h)^{-1}$ ; solid line) around the center of the TPV from 0000 UTC 20 to 1800 UTC 23 July 2008.

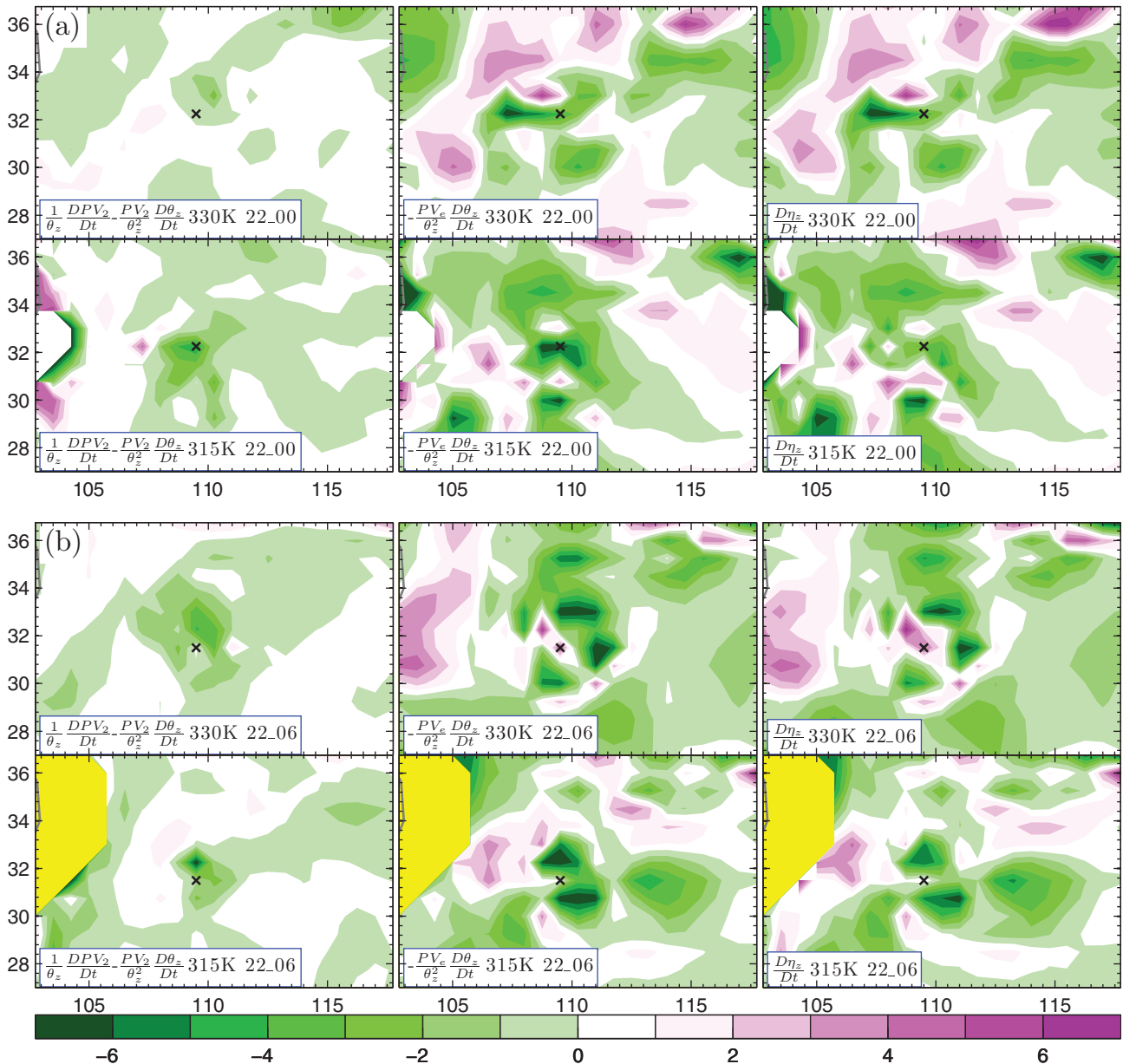


Fig. 2.13: Distributions on the 330 and 315 K isentropic surfaces of  $\left(\frac{D\eta_z}{Dt}\right)_A$  (first column);  $10^{-5} m^3(kg s 6h)^{-1}$ ,  $\gamma$  (second column;  $10^{-5} m^3(kg s 6h)^{-1}$ ), and  $\left(\frac{D\eta_z}{Dt}\right)_A$  (third column;  $10^{-5} m^3(kg s 6h)^{-1}$ ). The cross indicates the location of the TPV. (a) 0000 UTC and (b) 0600 UTC on July 22, 2008.

**Plate 10**

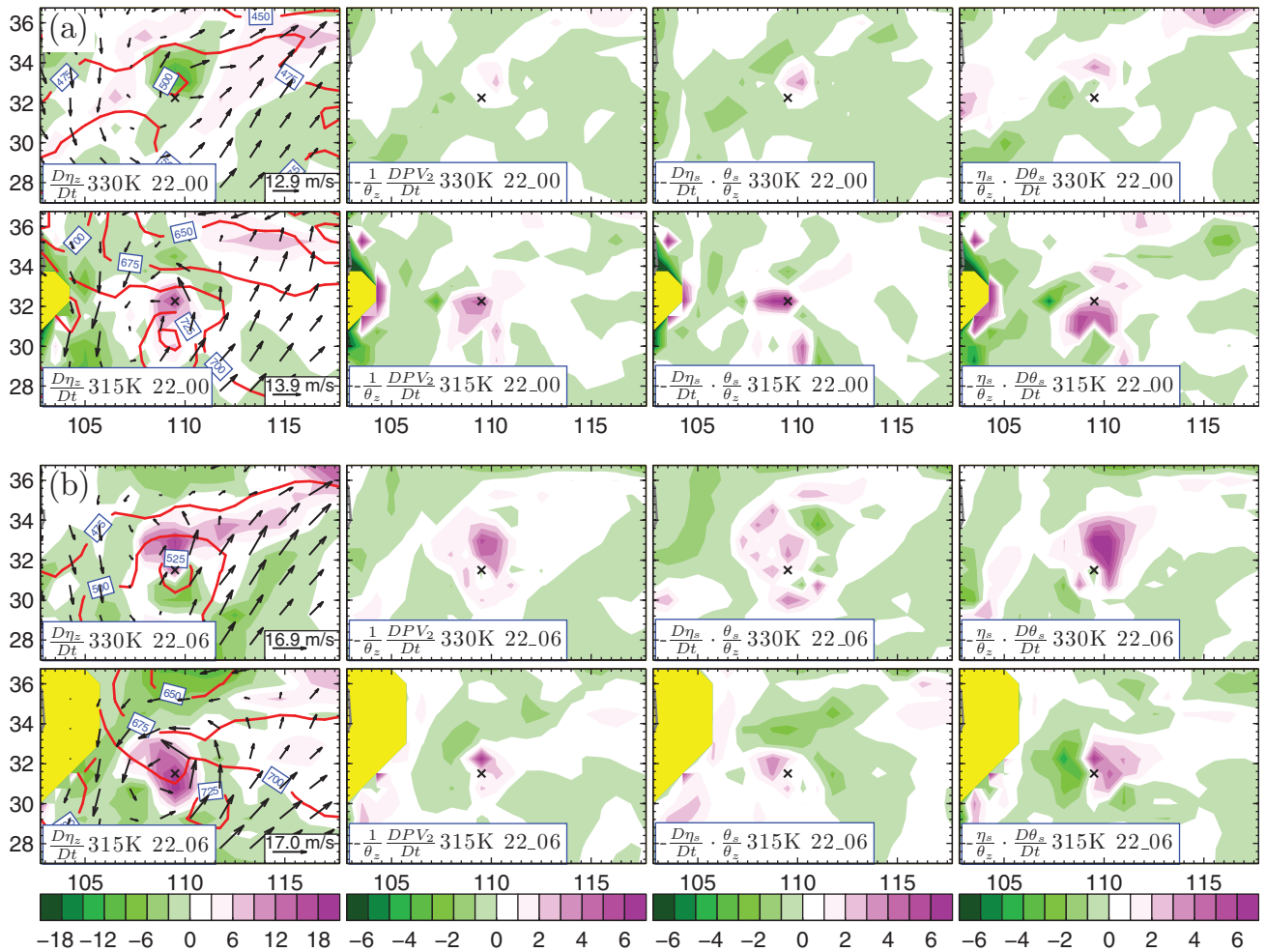


Fig. 2.14: Contribution to the development of vertical vorticity (first column;  $10^{-5} \text{ m}^3(\text{kg s } 6\text{h})^{-1}$ ) due to the change in  $PV_2$  (second column;  $0.5 \times 10^{-5} \text{ m}^3(\text{kg s } 6\text{h})^{-1}$ ), the change in  $\eta_s$  (third column;  $0.5 \times 10^{-5} \text{ m}^3(\text{kg s } 6\text{h})^{-1}$ ), and the change in  $\theta_s$  (fourth column;  $0.5 \times 10^{-5} \text{ m}^3(\text{kg s } 6\text{h})^{-1}$ ).

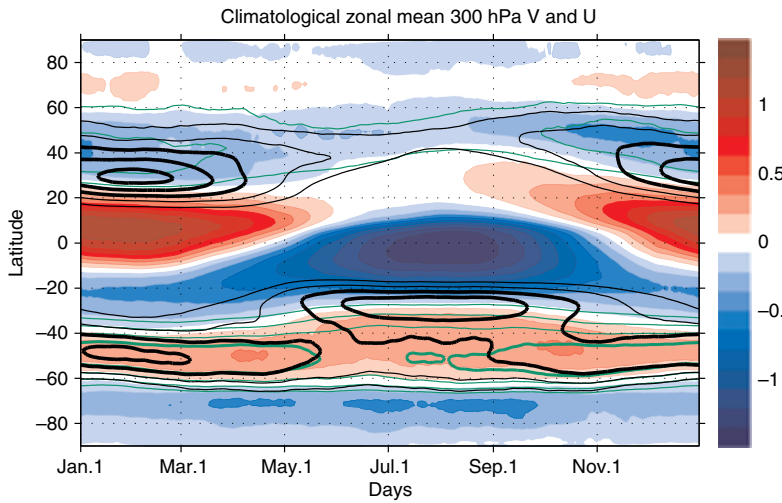


Fig. 6.1. Zonally averaged climatological seasonal cycle of: 300 hPa meridional wind (shading,  $\text{ms}^{-1}$ ), 300 hPa zonal wind (black contours, contour interval  $5 \text{ ms}^{-1}$ , thick contours for  $25 \text{ ms}^{-1}$  and above, only positive values are plotted) and 925–700 hPa zonal wind (green contours, contour interval  $3 \text{ ms}^{-1}$ , thick contours for  $12 \text{ ms}^{-1}$  and higher, only positive values are shown). The meridional wind is colored blue for southward and red for northward flow and white for zero. The dipole in meridional wind between  $30^\circ\text{S}$ – $20^\circ\text{N}$  during Nov–May (boreal winter) and between  $25^\circ\text{S}$ – $40^\circ\text{N}$  during May–Nov (boreal summer) represents the two Hadley circulation cells, with the winter cell being much stronger and the summer cell extending more poleward. Note the upper level Southern Hemisphere winter jet is at the edge of the Hadley cell, with weak surface winds, while the Southern Hemisphere summer jet at both levels is in the Ferrel cell.

**Plate 11**

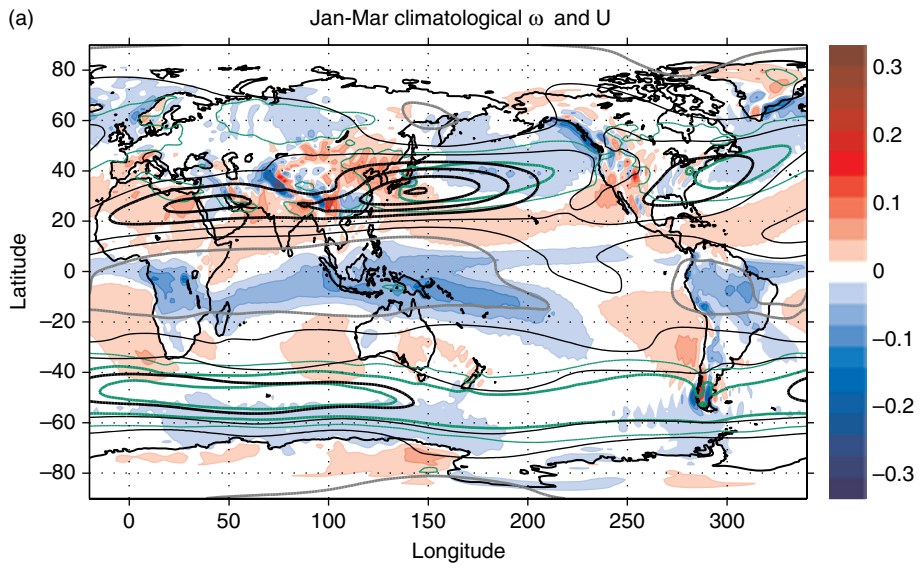


Fig. 6.2. Seasonal mean distribution of: 400–600 hPa  $\omega$  ( $\text{hPa s}^{-1}$ , shading), 300 hPa zonal wind (black contours, contour interval  $10 \text{ ms}^{-1}$ ,  $30 \text{ ms}^{-1}$  and above thick, zero contour gray, and negative values dashed) and 925–700 hPa zonal wind (green contours, contour interval  $5 \text{ ms}^{-1}$ ,  $10 \text{ ms}^{-1}$  and higher thick, only positive values are shown), for (a) Jan–Mar, (b) Jun–Aug.

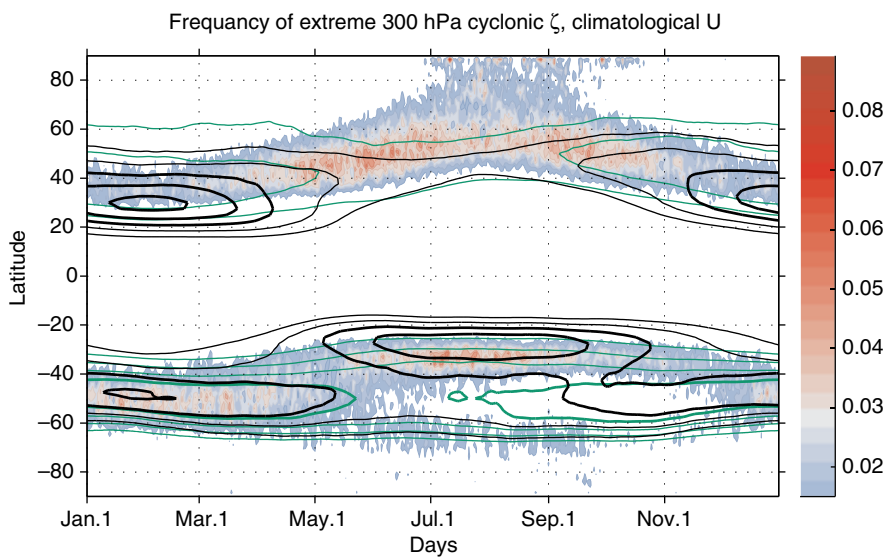
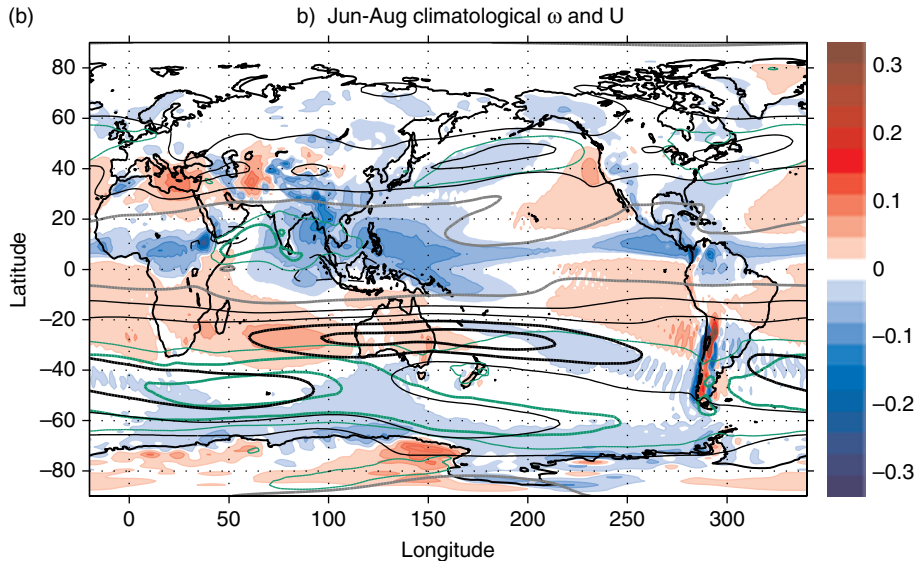
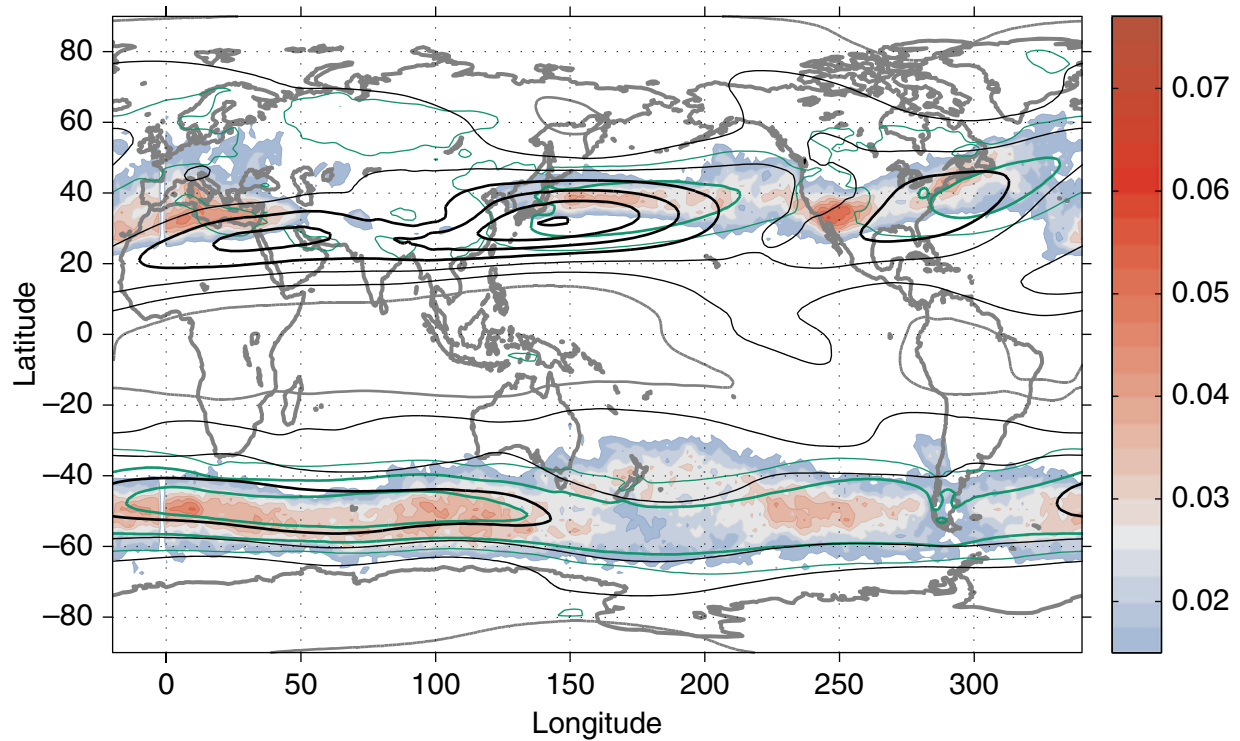


Fig. 6.3. Frequency of extremely strong cyclonic 300 hPa vorticity values on a given day and latitude, counting over all years and longitudes (color shading), with extreme cyclonic vorticity values defined as the lowest (highest) 1% for the Southern (Northern) hemisphere. Also shown in contours on all plots are the daily climatological zonal mean 300 hPa (black) and 925–700 hPa (green) zonal winds, with contour levels and line widths as in Fig. 6.6. The Southern Hemisphere results were presented in Harnik (2014).

Plate 12

(a)

Extreme Jan-Mar 300 hPa cyclonic  $\zeta$  and Climatological U



(b)

Extreme Jun-Aug 300 hPa cyclonic  $\zeta$  and Climatological U

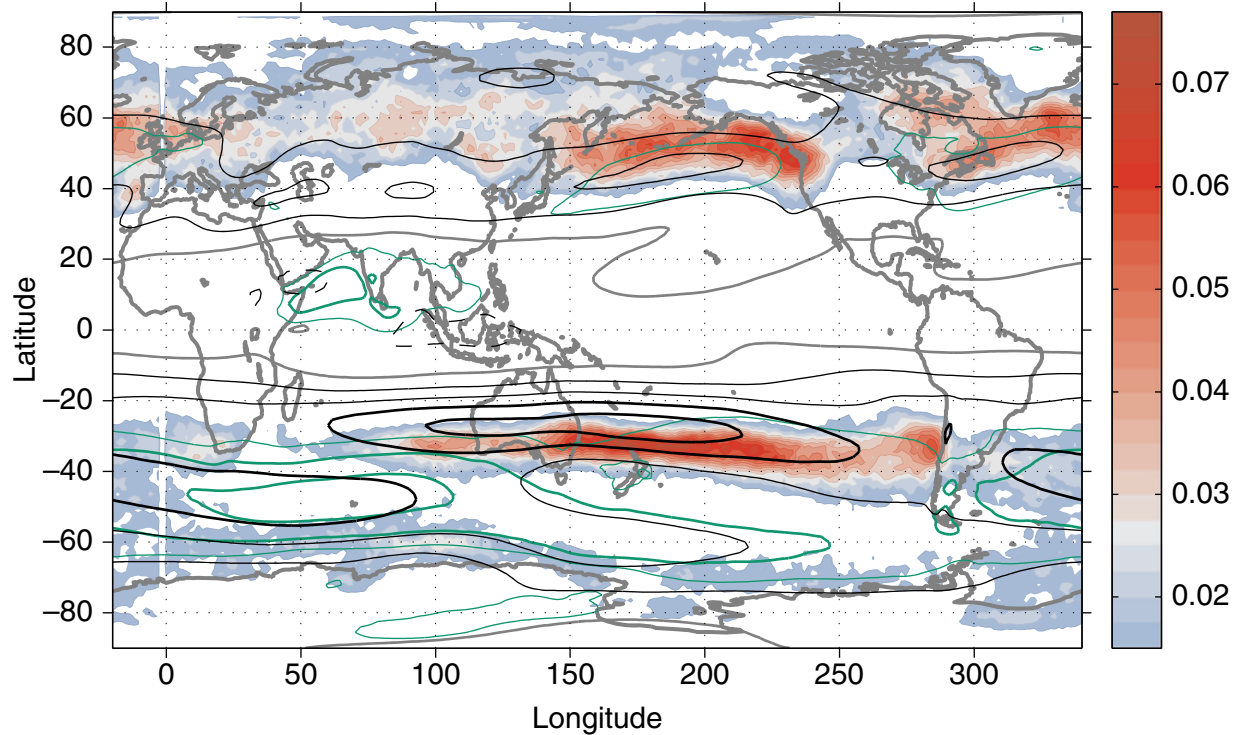


Fig. 6.4. Seasonal mean maps of the frequency of extreme 300 hPa cyclonic vorticity values at a given grid point (color shading) counting over all seasons for 1979–2012 for the periods: (a) Jan–Mar, (b) Jun–Aug. Also shown in contours on both graphs are the corresponding climatological seasonal mean zonal winds at 300 hPa and 925–700 hPa (black and green contours respectively, with values and line thicknesses as in Fig. 6.2. The Southern Hemisphere results were presented in Harnik (2014).

**Plate 13**

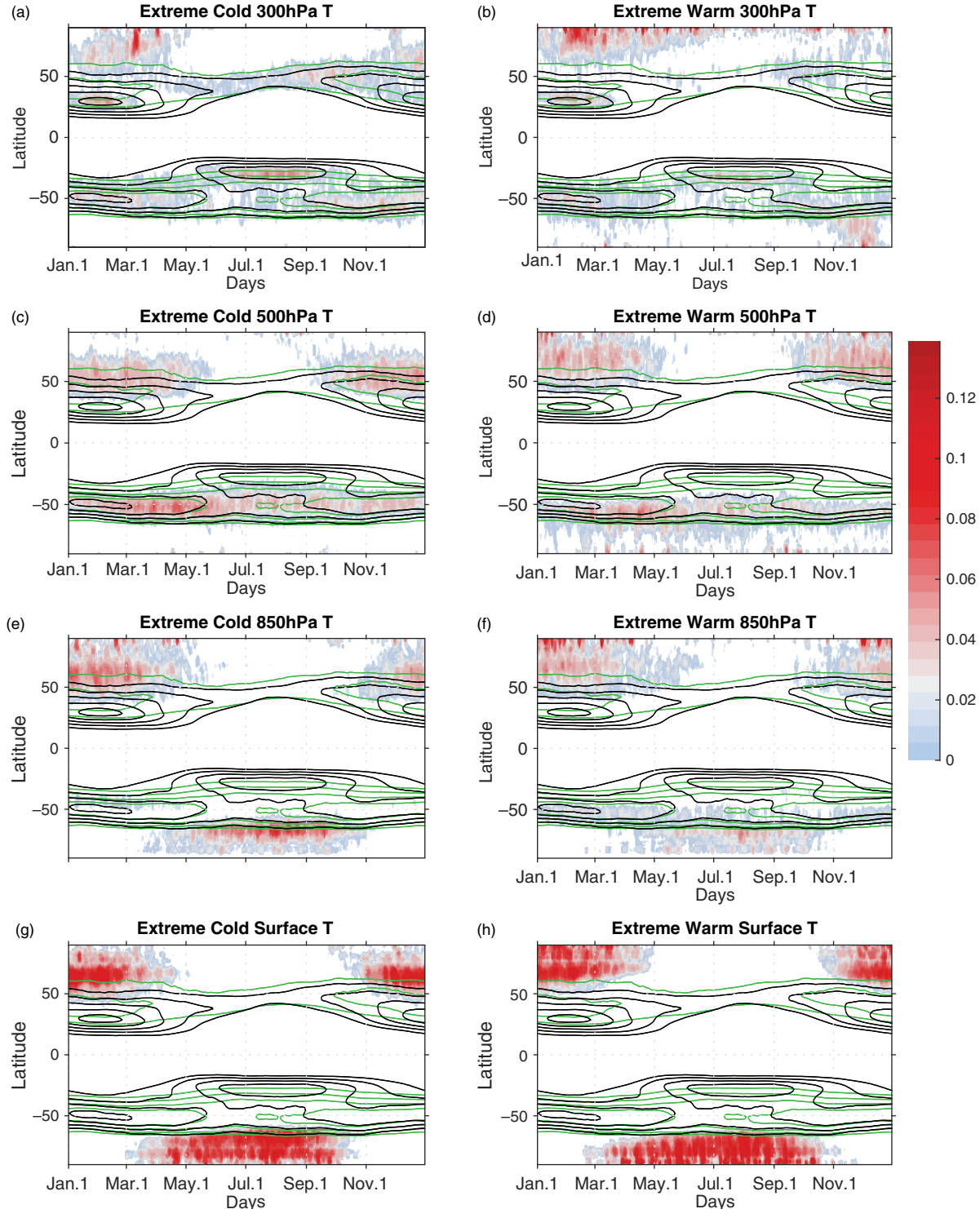


Fig. 6.9. As in Fig. 6.3, but for extreme temperature anomalies defined using the highest and lowest percentiles for each hemisphere. The left and right columns show extreme negative and positive anomalies respectively, at (a-b) the surface, (c,d) 850 hPa, (e,f) 500 hPa, (g,h) 300 hPa. The black and green contours show the upper and lower level jets as in Fig. 6.3.

## Plate 14

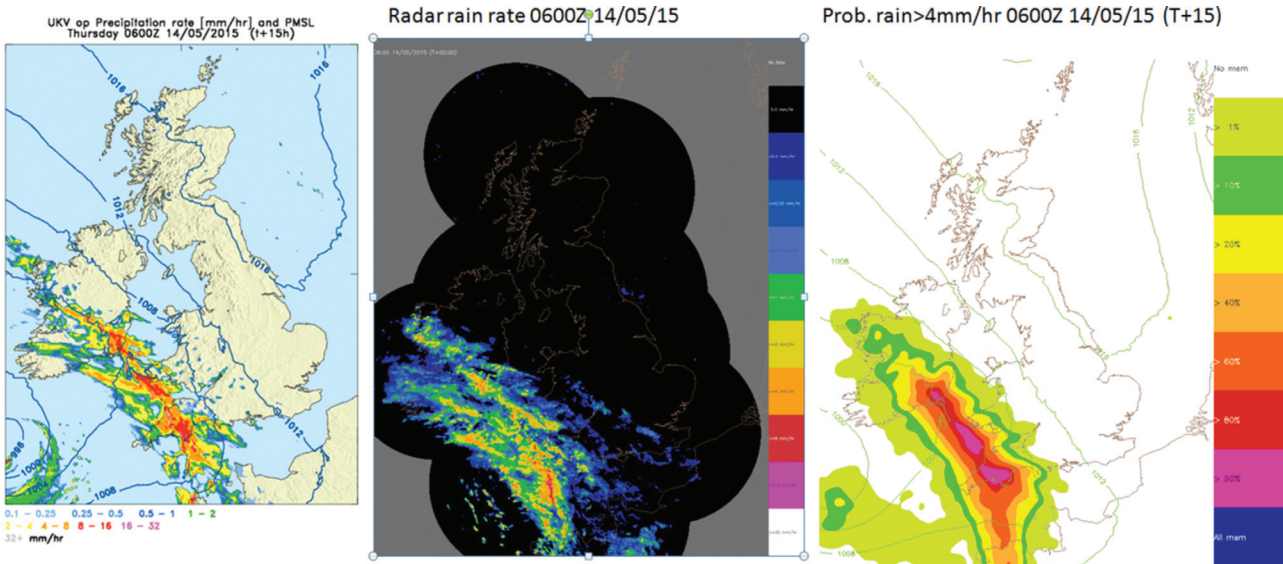


Fig. 7.7. Example of precipitation forecast products from the deterministic UKV model (left) and MOGREPS-UK ensemble (right), along with the verifying radar image (centre). The UKV and radar products show instantaneous rain rates, while the MOGREPS-UK chart illustrates the ‘Chance of Heavy Rain in the Hour’ which is defined as 4 mm/hr.

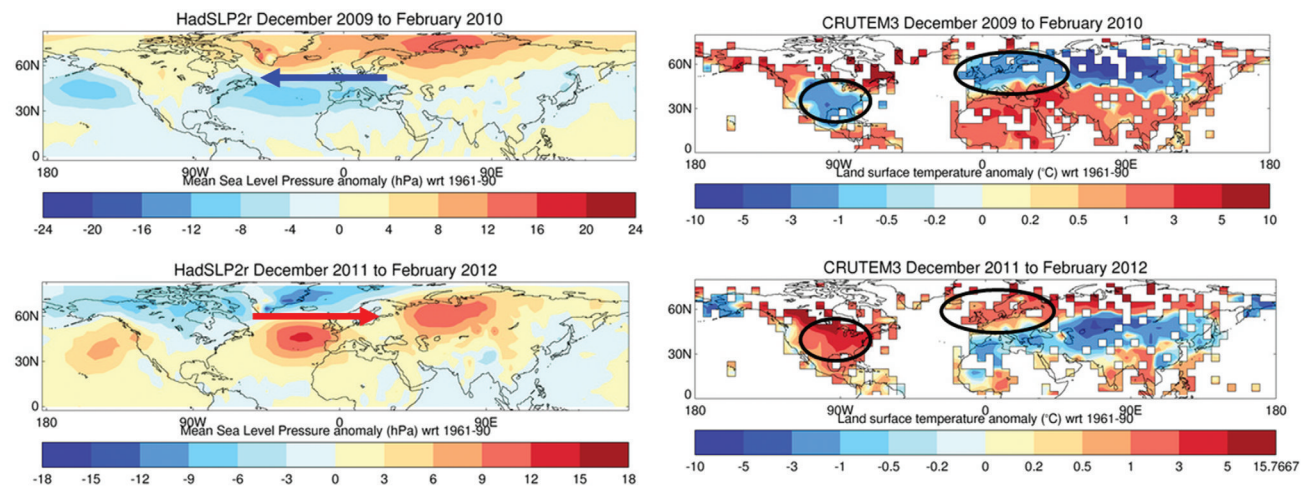


Fig. 9.1. Recent extreme phases of the winter North Atlantic and Arctic Oscillations. Winter mean sea level pressure anomalies (left) and winter mean land surface temperature anomalies (right) for the extreme negative NAO winter of 2009/10 (upper) and extreme positive NAO winter of 2011/12 (lower). Blue and red arrows show the sense of anomalous advection across the Atlantic due to anomalous mean winds. Data are from Hadley Centre observational analyses ([www.hadobs.org](http://www.hadobs.org)).

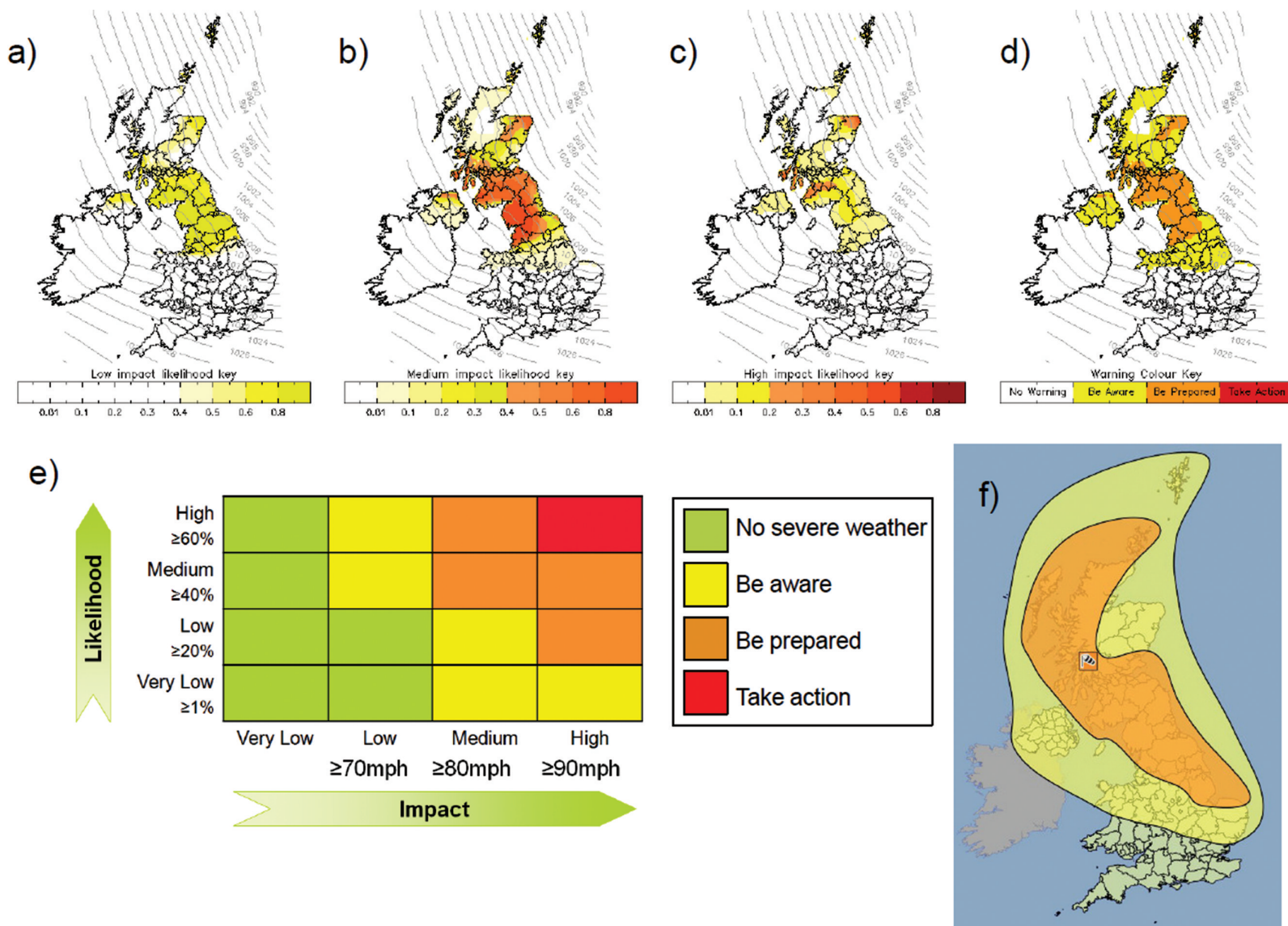


Fig. 7.13. Example of how the automatic probabilistic EPS-W system can be used to support the production of weather warnings, for a case of strong winds on 5 December 2013. (a), (b), and (c) show 24-hour forecasts (valid at 12 UTC on the 5th) of the probabilities of wind speed exceeding low, medium, and high impact thresholds, respectively. These data are combined to generate an overall warning colour (d), with impact taking precedence over likelihood. (e), the impact matrix, shows how the warning level depends on both likelihood and impact. Example wind speed impact thresholds are shown for the Scottish Highlands and Islands in winter; the thresholds for other regions will generally be different. (f) shows the warning map issued on 4 December.

**Plate 16**

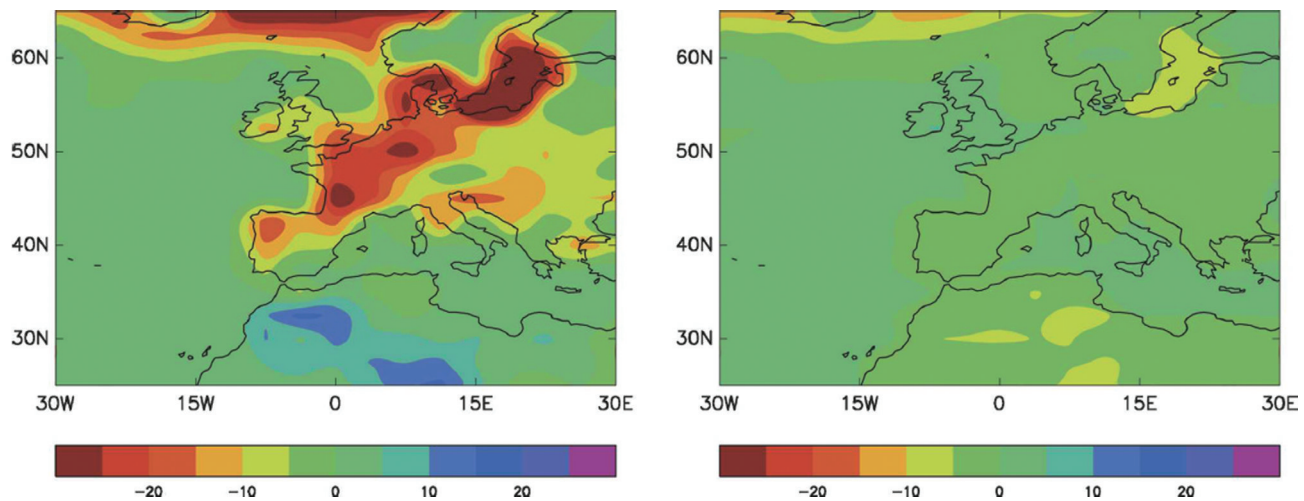


Fig. 9.2. Modelled changes in the frequency of winter frost days between 1960–65 and 1990–95. The left-hand panel shows a large reduction in the number of frosts per winter in a global climate model which includes known climate forcings, such as greenhouse gases and observed changes in sea surface conditions. The right-hand panel shows the change in the number of frosts in a similar climate model simulation but without the change in the North Atlantic Oscillation. Units are frost days per winter. Figure from Scaife *et al.* (2008).

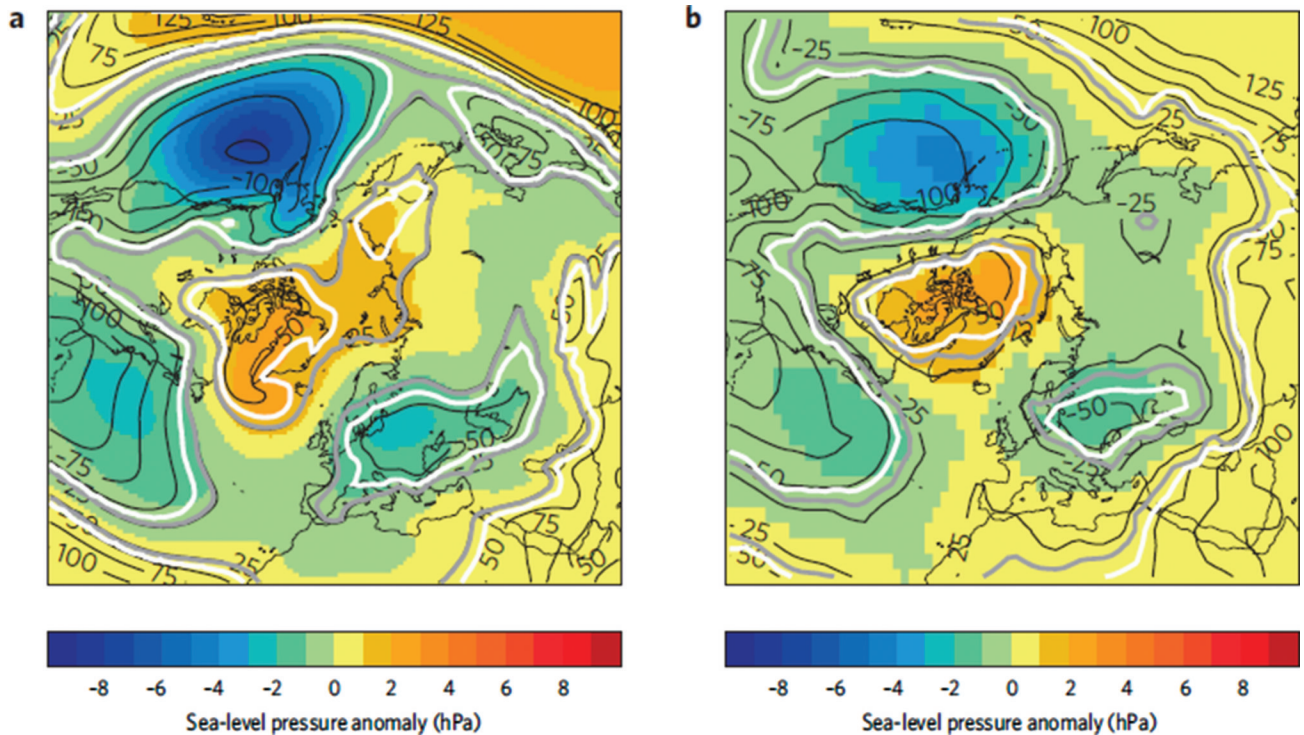


Fig. 9.3. The effect of El Niño on extratropical sea level pressure in late winter (Jan–Mar). Note the high pressure over the Arctic and low pressure in a surrounding annulus in both model simulation (left) and observations (right). Solid contours show the anomaly as a proportion of the year-to-year standard deviation. See Ineson and Scaife (2009) for further details.

Plate 17

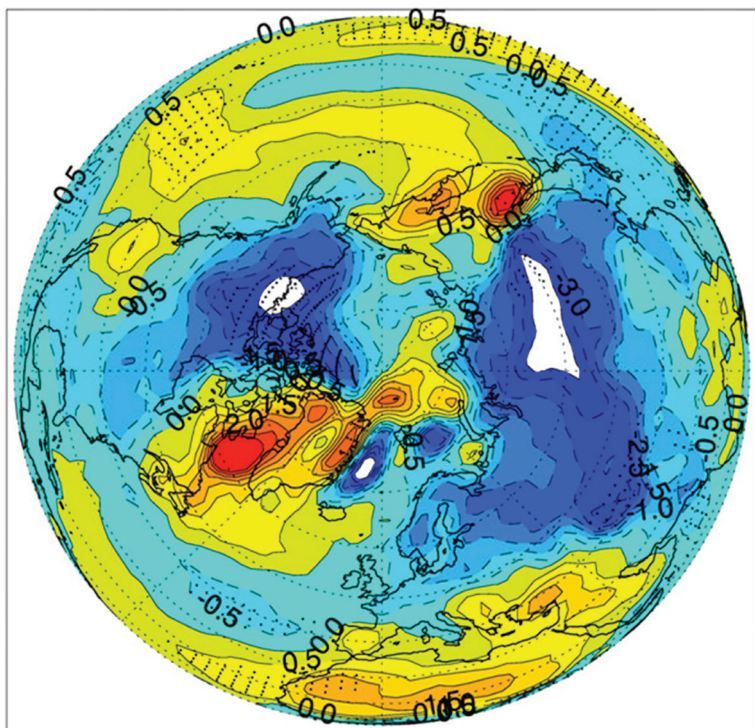


Fig. 9.4. Near surface temperature impact of the Quasi-Biennial Oscillation in winter. Note the characteristic quadrupole pattern of cold–warm–cold–warm across northern Europe, Mediterranean, eastern USA, and eastern Canada. This change results from a shift in the surface NAO towards negative phase during the easterly phase of the QBO.

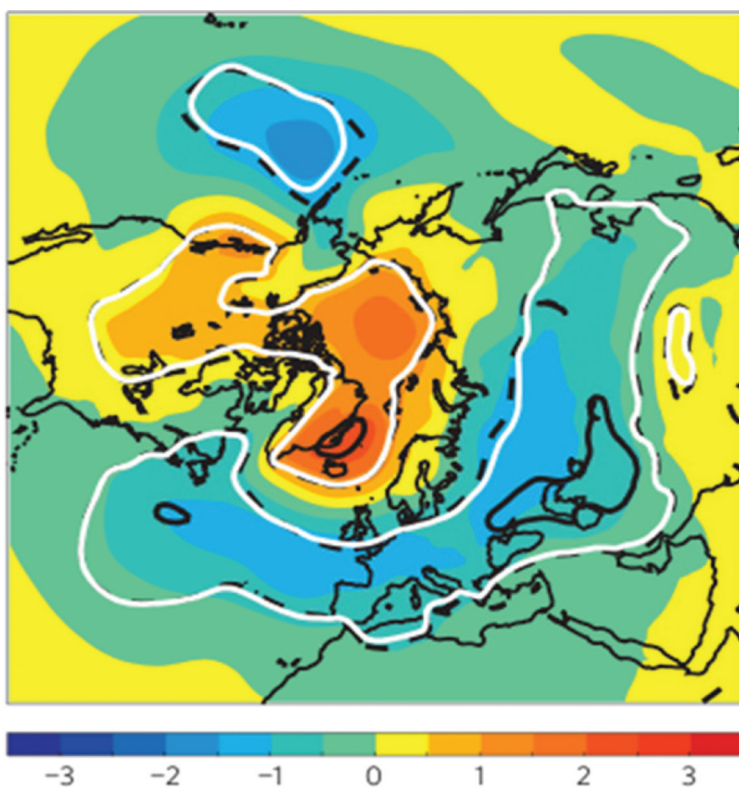


Fig. 9.5. Impact of low solar activity on winter sea level pressure in the Northern Hemisphere. Note the high pressure signal over the Arctic and the low pressure signal in a surrounding annulus. White contours show statistical significance at the 95% level using a t-test. Units are hPa. See Ineson *et al.* 2011 for further details.

### Plate 18

Ensemble mean anomaly : mean sea level pressure : Dec/Jan/Feb  
Issued November 2009

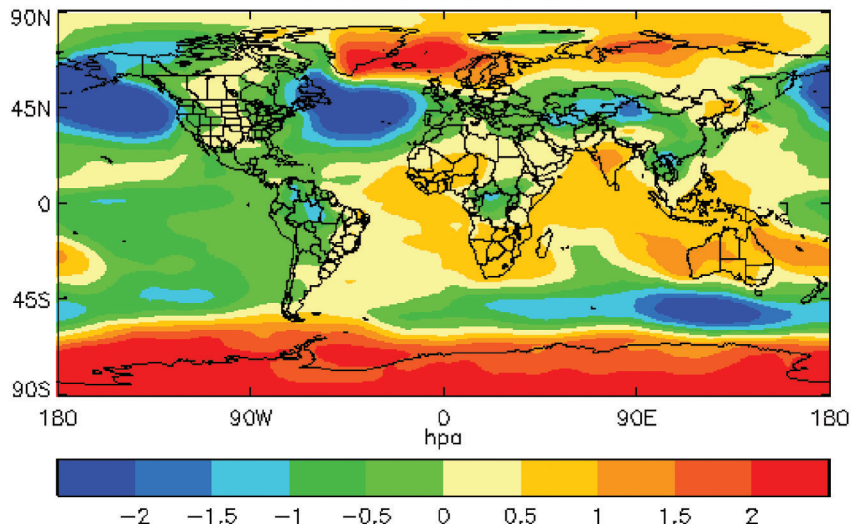


Fig. 9.7. Real time seasonal prediction of mean sea level pressure anomalies prior to the extreme negative NAO in the winter of 2009/10. Sea level pressure anomalies are plotted for the ensemble mean forecast for winter (December–February). Forecasts were issued in real time before the start of winter in November from the Met Office. Units are hPa. The observed sea level pressure anomalies for this extreme winter are shown in Fig. 9.1 (upper left panel).

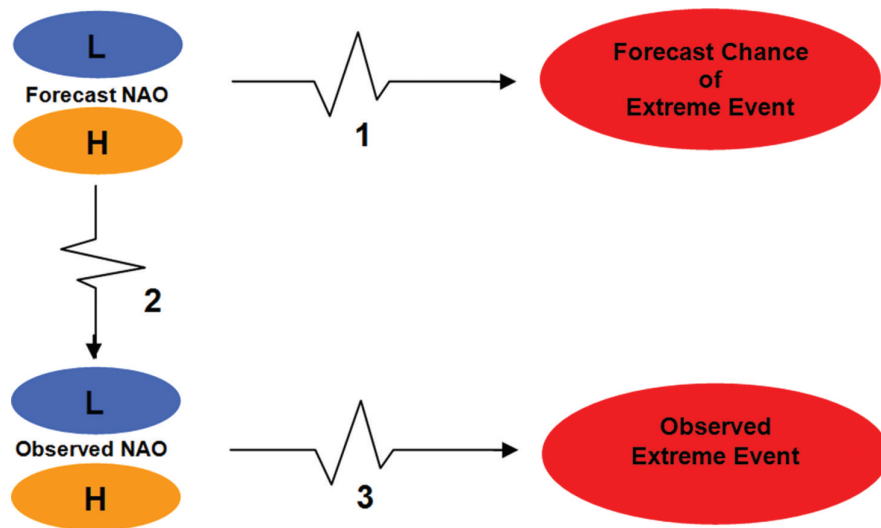


Fig. 9.8. Relationship between forecasts and observations of extreme events that are governed by the NAO. The relationship between the forecast chance of extreme events (upper right) and the observed occurrence of an event (lower right) is limited by imperfect links (broken arrows) between: (1) the forecast number of extreme events and the forecast NAO, (2) the forecast NAO and the observed NAO, and (3) the observed NAO and the observed occurrence of extreme events. Using the forecast NAO as a direct predictor of the observed events (an example of statistical downscaling) can therefore improve forecast skill by eliminating link 1 which is both noisy and imperfectly represented in global circulation models.

## Plate 19

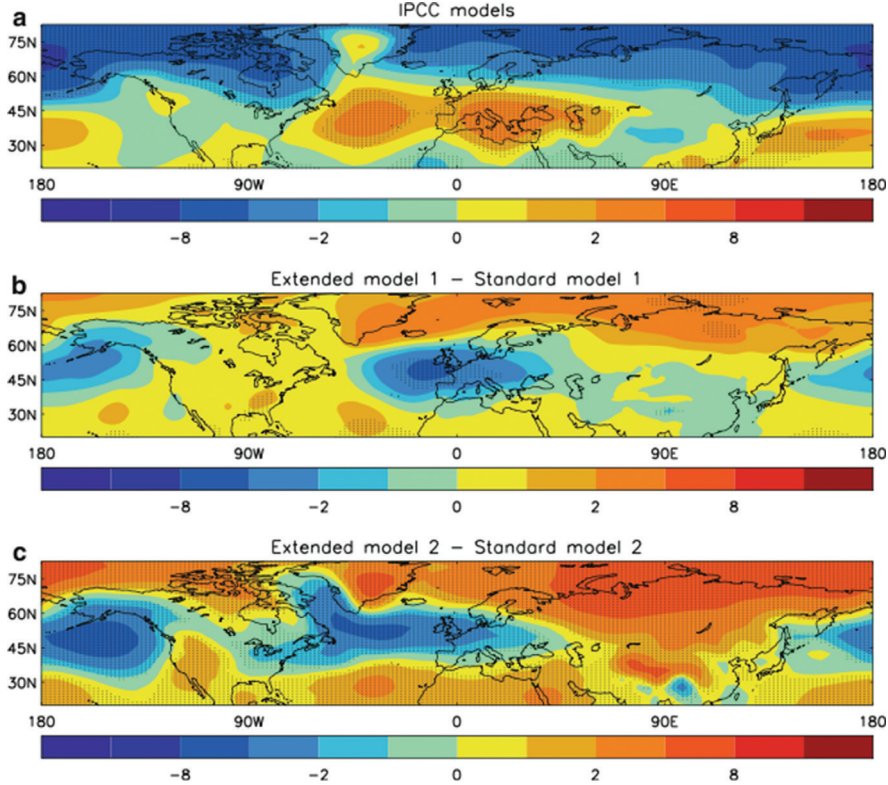


Fig. 9.6. Changes in winter sea level pressure under conditions of quadrupled CO<sub>2</sub>. The upper panel shows sea level pressure changes in standard climate model projections. The lower two panels show the additional change in two independent climate models when the representation of stratospheric circulation is improved. Note that the scales are the same in all cases so that the additional NAO/AO-like signal cancels much of the original change. Figure from Scaife *et al.*, 2012.

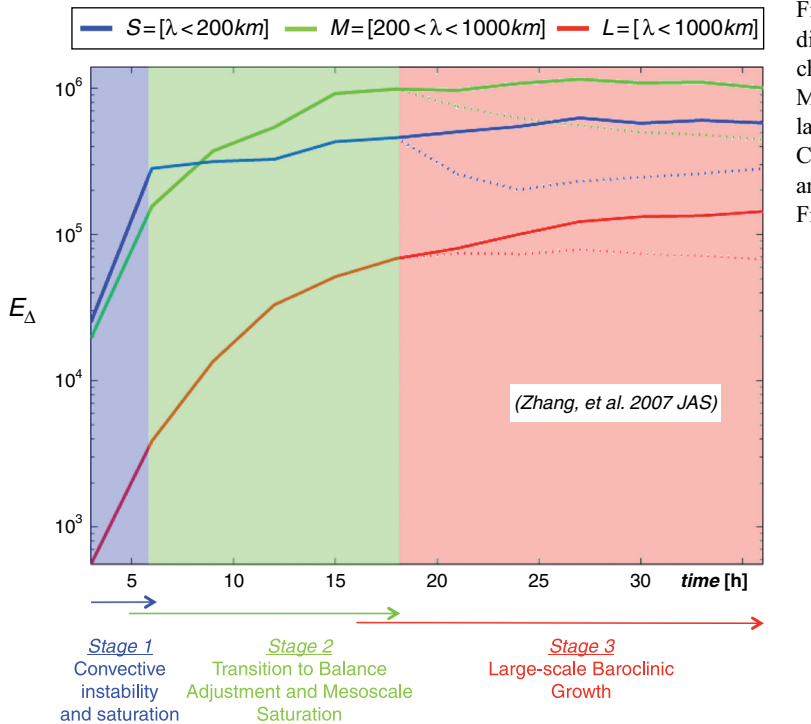


Fig. 11.3. Evolution of the domain-integrated difference total energy ( $E_{\Delta}$ ,  $m^2 s^{-2}$ ) at three different characteristics scales (S: smaller scale  $L < 200 \text{ km}$ ; M: intermediate scale  $200 < L < 1000 \text{ km}$ ; and L: larger scale  $L > 1000 \text{ km}$ ), between CNTL-D3 and CNTL-D3P (solid curves) and between CNTLfd-D3 and CNTLfd-D3P (dotted curves). Adapted from Figure 7 of Zhang *et al.* (2007).

Plate 20

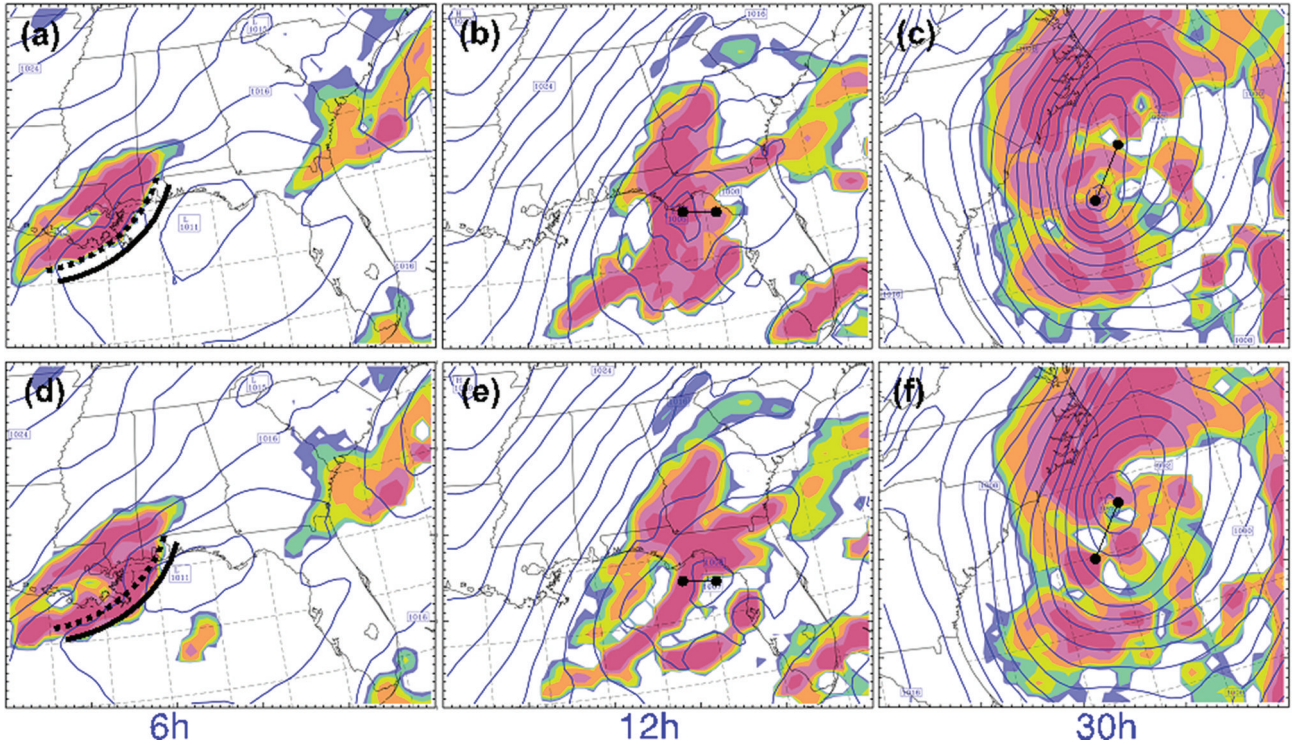


Fig. 11.1. Comparison of mean sea level pressure (contour interval 4 hPa) and simulated reflectivity (dBZ, coloured) on the 30 km grid for Cntl-3.3km and Pert-3.3km. Simulations are shown at (a), (d) 6 h, (b), (e) 12 h, and (c), (f) 30 h. Thick curves in (a) and (b) denote the relative locations of the convective outflow boundary in Cntl-3.3km (dashed) and Pert-3.3km (solid). The dots in (b), (c), (e), and (f) denote the locations of the primarily surface cyclone centres in Cntl-3.3km and Pert-3.3km. Adapted from Figure 12 of Zhang *et al.* (2003).

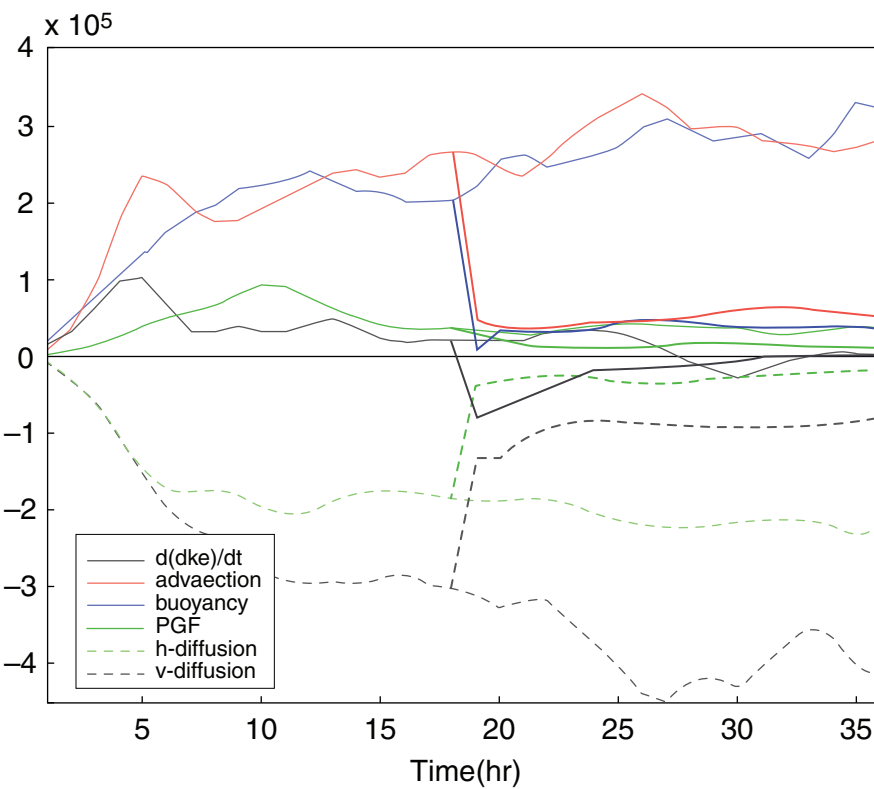


Fig. 11.4. Time evolution of the DKE tendency and each of the source/sink terms ( $Jm^{-2}s^{-1}$ ) estimated with the 10 km grid hourly outputs from CNTL-D3 and CNTL-D3P (solid) and from CNTLfd-D3 and CNTLfd-D3P (dashed). Adapted from Figure 14 of Zhang *et al.* (2007).

Plate 21

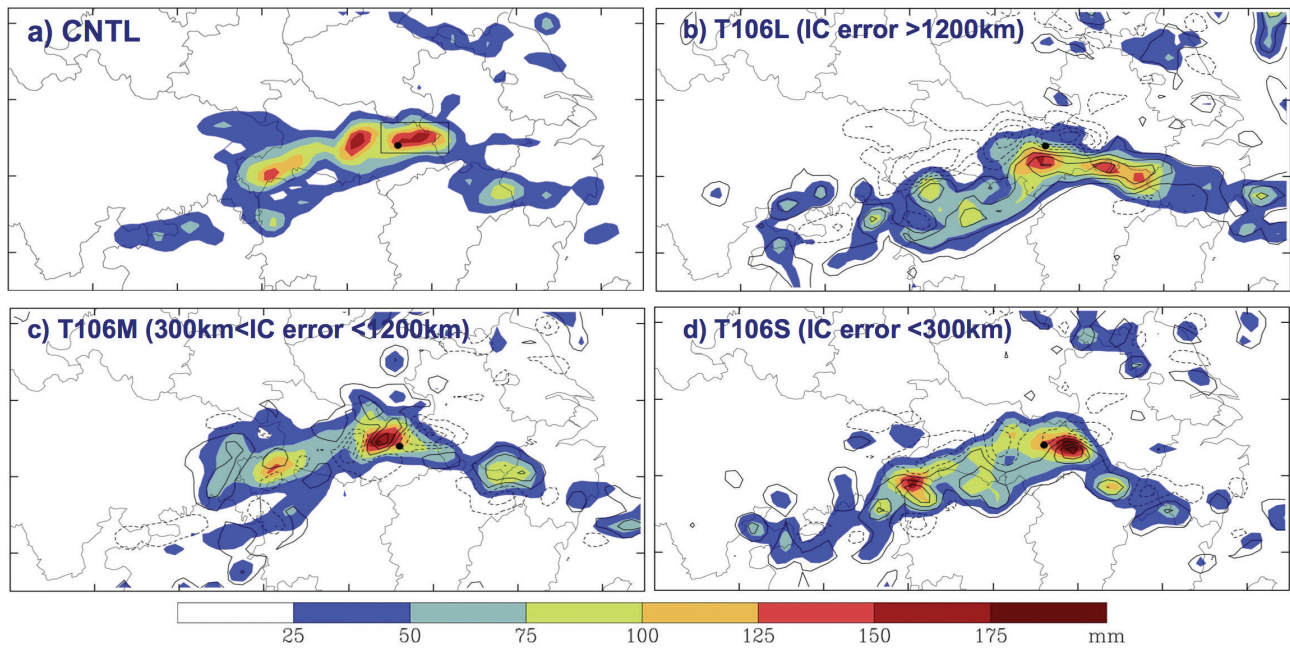


Fig. 11.5. The simulated 24 h accumulated precipitation (mm, shaded) from 12:00 UTC 20 to 12:00 UTC 21 July 1998 by experiments (a) control (CNTL), (b) large-scale error (T106L), (c) medium-scale error (T106M), and (d) small-scale error (T106S) plotted on the 30 km domain (D1) and the corresponding difference from CNTL (contoured every 30 mm). Adapted from Figure 5 of Bei and Zhang (2007).

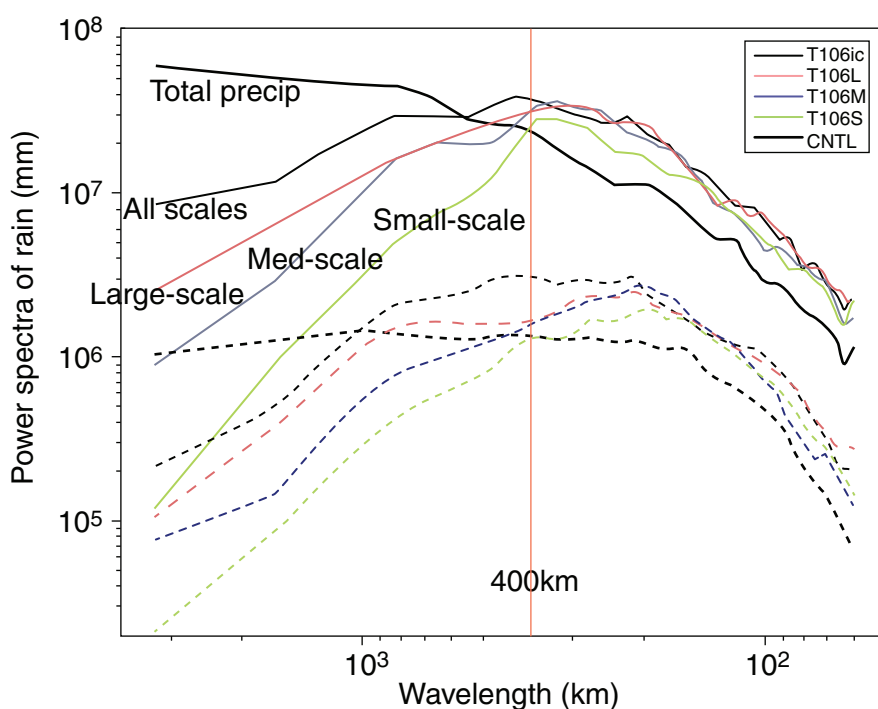


Fig. 11.6. Power spectra of the 3 h (dash) and 24 h (solid) accumulated precipitation difference ( $mm^2$ ) between control experiment (CNTL) and the four experiments of different initial data source (T106ic), large-scale error (T106L), medium-scale error (T106M), and small-scale error (T106S), valid at the 24 h and 36 h forecast times, respectively. Adapted from Figure 9(c) of Bei and Zhang (2007).

Plate 22

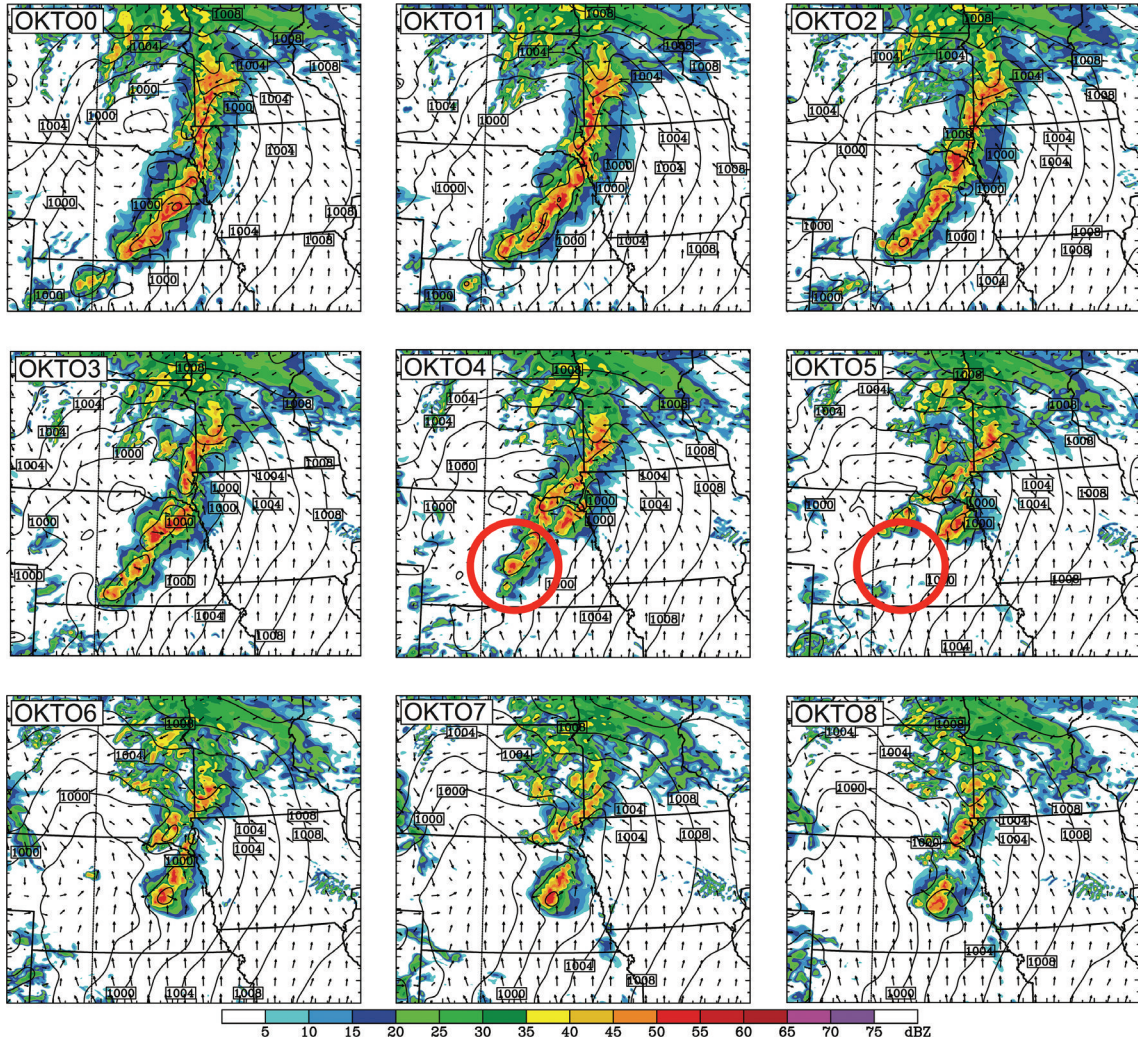


Fig. 11.7. Simulated radar reflectivity (shaded every 5 dBZ), sea level pressure (contoured every 2 hPa), and surface wind vectors for linearly averaged sensitivity forecasts (OKTO0 is the simulation with the developing initial condition, while OKTO8 is the simulation with the non-developing initial condition. OKTO1–OKTO7 are in between.) at 0400 UTC 10 Jun. The red circles denote the area of strong forecast divergence. Adapted from Figure 11 of Melhauser and Zhang (2012).

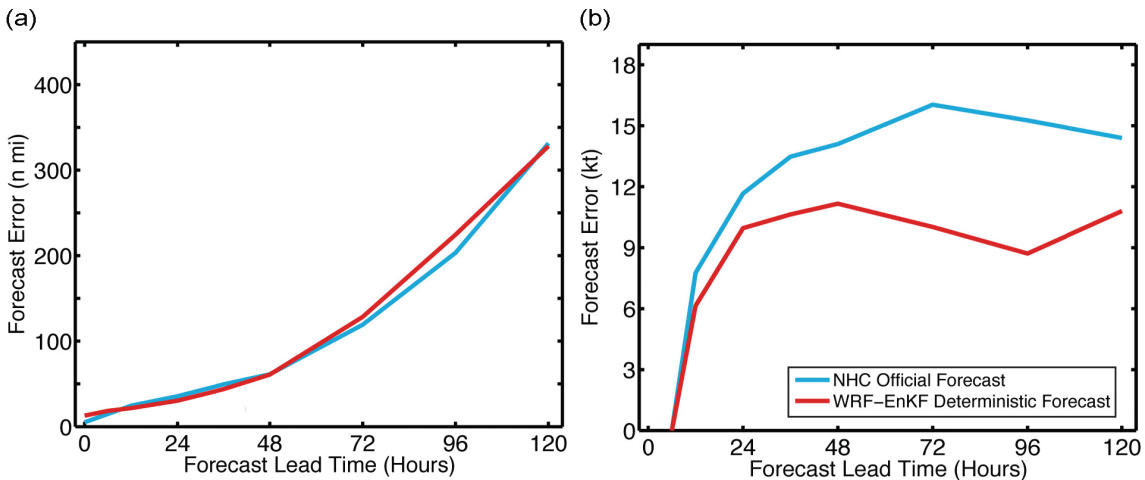


Fig. 11.11. The mean absolute forecast errors of (a) track and (b) intensity at different forecast lead times (verified 346 against post-storm best track observations estimated by NHC) for the PSU WRF-EnKF system (red) and the 347 NHC official forecasts (cyan), averaged over all applicable P3 Doppler missions during 2008–2012. Adapted from Figure 2a–b of Zhang and Weng (2015).

Plate 23

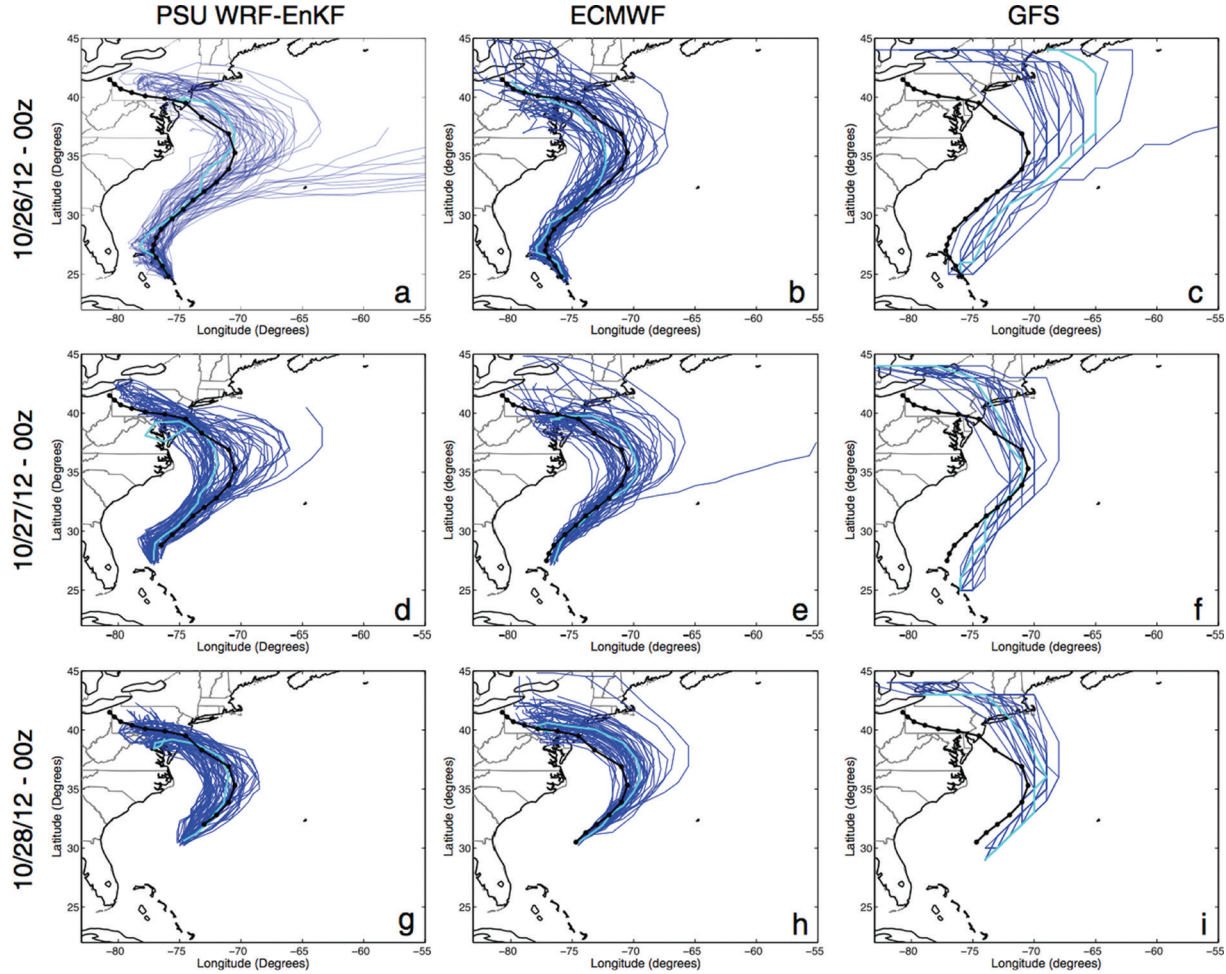


Fig. 11.9. Ensemble tracks (blue lines) for the PSU WRF-EnKF (first column), ECMWF (second column), and GFS (third column) forecasting systems for Hurricane Sandy initialized at (a–c) 0000 UTC 26 October 2012, (d–f) 0000 UTC 27 October 2012, and (g–i) 0000 UTC 28 October 2012. The three forecasting systems utilize 60, 50, and 20 ensemble members, respectively. The NHC best track for Hurricane Sandy is overlaid in black, with positions marked every 6 h and the deterministic runs are plotted in cyan. Adapted from Figure 1 of Munsell and Zhang (2014).

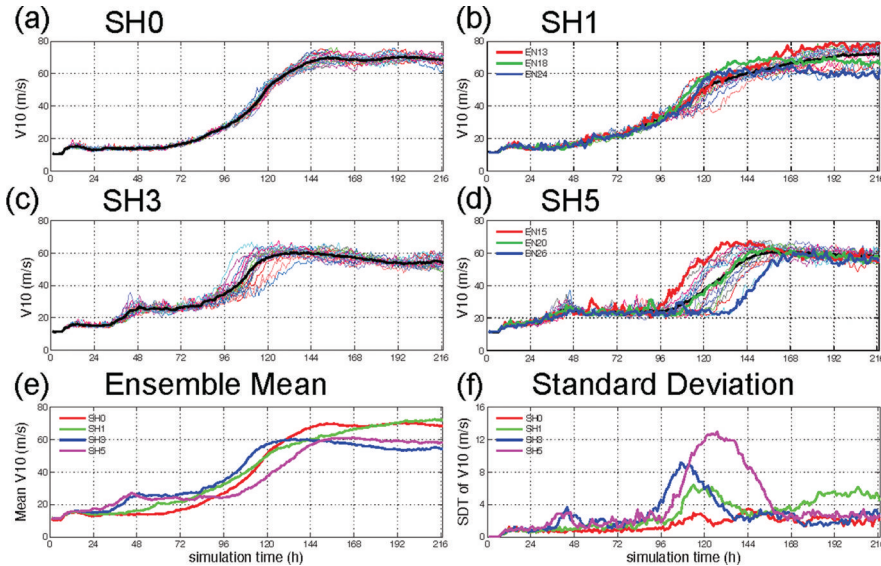


Fig. 11.10. Time evolution of the tropical cyclone intensity in terms of the 10 m maximum wind speed for all ensemble members of (a) SH0 (no background flow), (b) SH1 (1 m/s shear), (c) SH3 (3 m/s shear), (d) SH5 (5 m/s shear), along with (e) the ensemble mean and (f) the standard deviation (ensemble spread) from all ensemble experiments. The thick black lines in (a)–(d) denote the ensemble mean, while members EN13, EN18, and EN24 of SH1 in (b) and members EN15, EN20, and EN26 of SH5 in (d) are denoted as thick coloured lines. Adapted from Figure 2 of Zhang and Tao (2013).

**Plate 24**

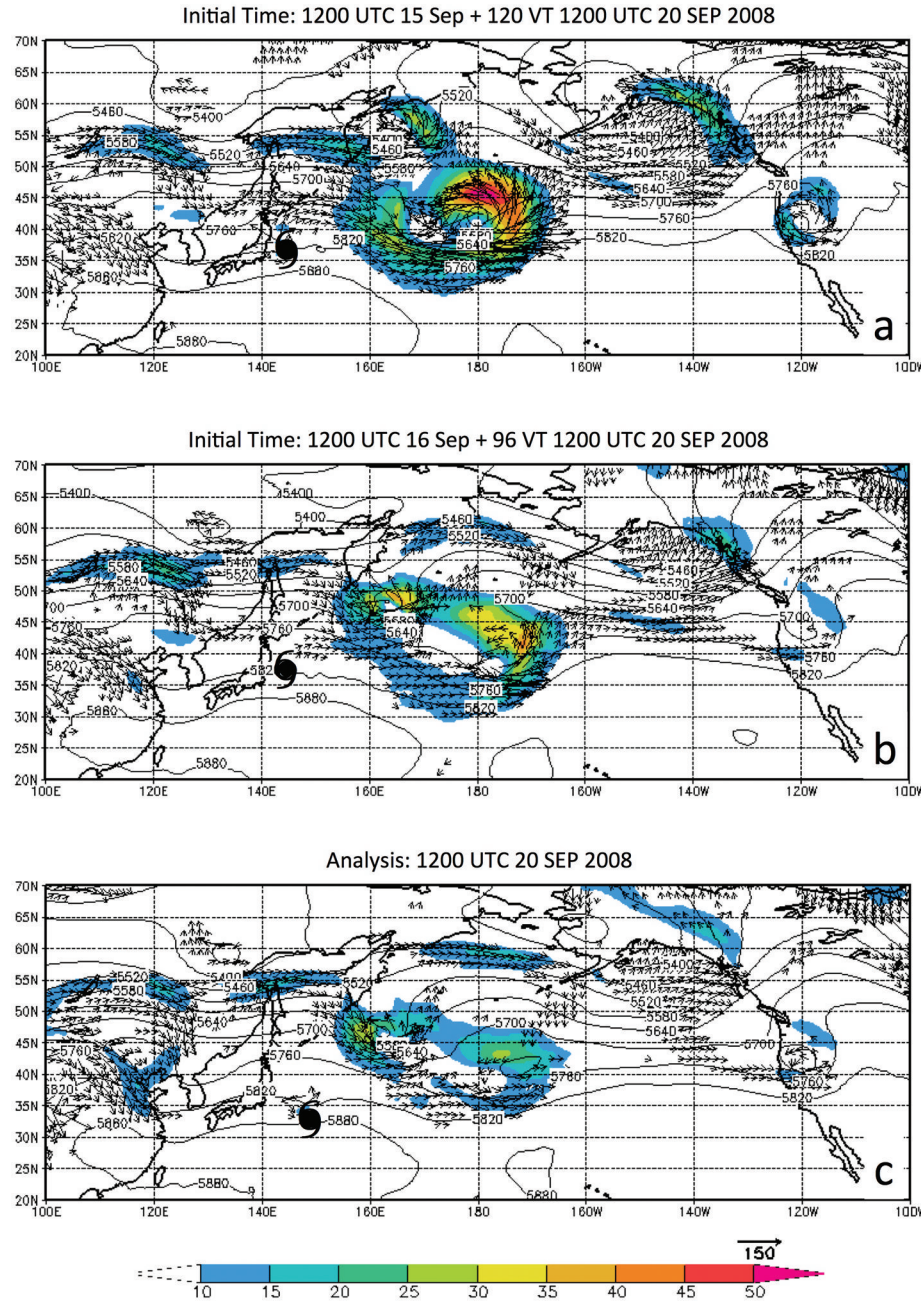


Fig. 12.6. Vertically averaged  $K_e$  (shaded,  $10^5 \text{ J m}^{-2}$ ) and total energy flux vectors (reference vector in lower right,  $10^5 \text{ W m}^{-2}$ ) from (a) five-day forecasts produced by the ECMWF global Integrated Forecast System with an initial time of 1200 UTC 15 September 2008, and (b) four-day forecasts initialized at 1200 UTC 16 September 2008, and analyzed at 1200 UTC 20 September 2008. The tropical cyclone symbol marks the location of TY Sinlaku at each forecast and analysis time.

**Plate 25**

Average Brier Skill Score LT1

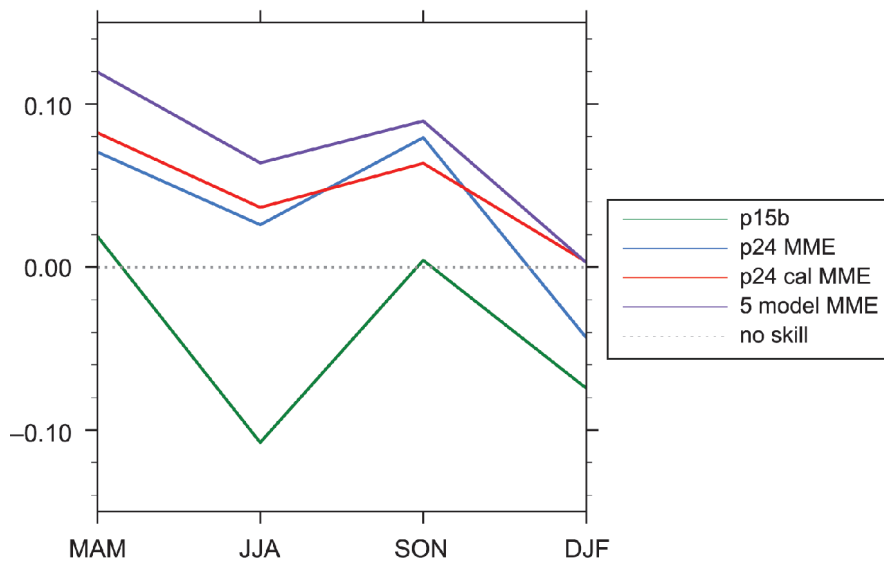


Fig. 14.1. Australian rainfall Brier skill score for POAMA1.5 (p15b), POAMA 2.4 (P24 MME), a re-calibrated version of POAMA2.4 (P24 cal MME), and a five member multi-model ensemble that incorporates POAMA 2.4a, POAMA 2.4b, POAMA 2.4c plus ECSys3 and the UKMO HadGEM2 seasonal forecast (5 model MME).

JJA climatological HWF across China

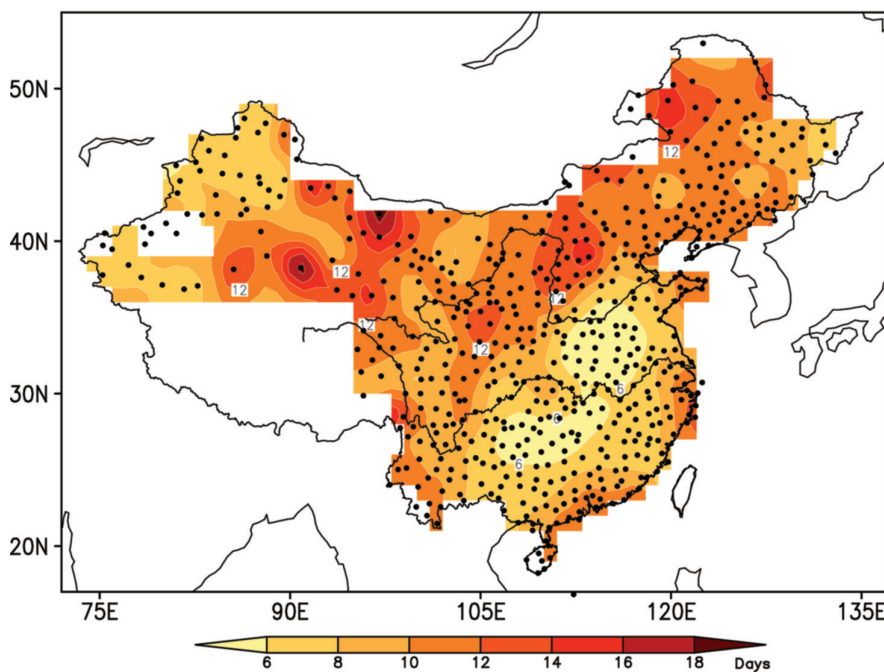


Fig. 17.1. The climatological heat wave frequency (HWF) across China for June–August (JJA) (color shadings in unit of day). Black dots denote 605 surface air temperature (SAT) gauge stations across China.

**Plate 26**

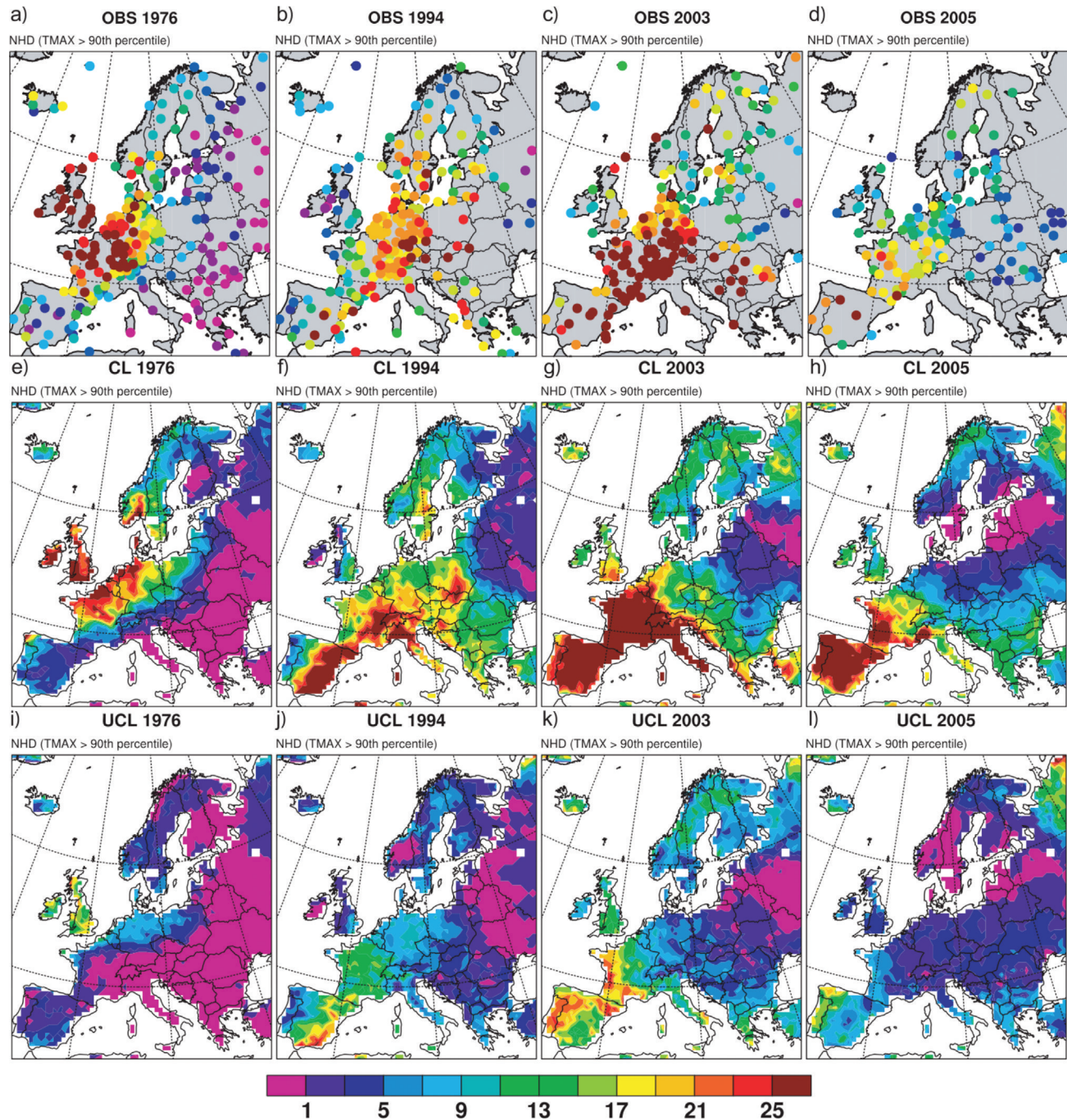


Fig. 15.4. Number of hot days (NHD) during the summers (JJA) of 1976, 1994, 2003, and 2005 derived from: (a–d) observed ECAD daily maximum temperature series, (e–h) simulations with (CL), and (i–l) without land–atmosphere coupling (UCL). From Fischer *et al.* (2007).

Plate 27

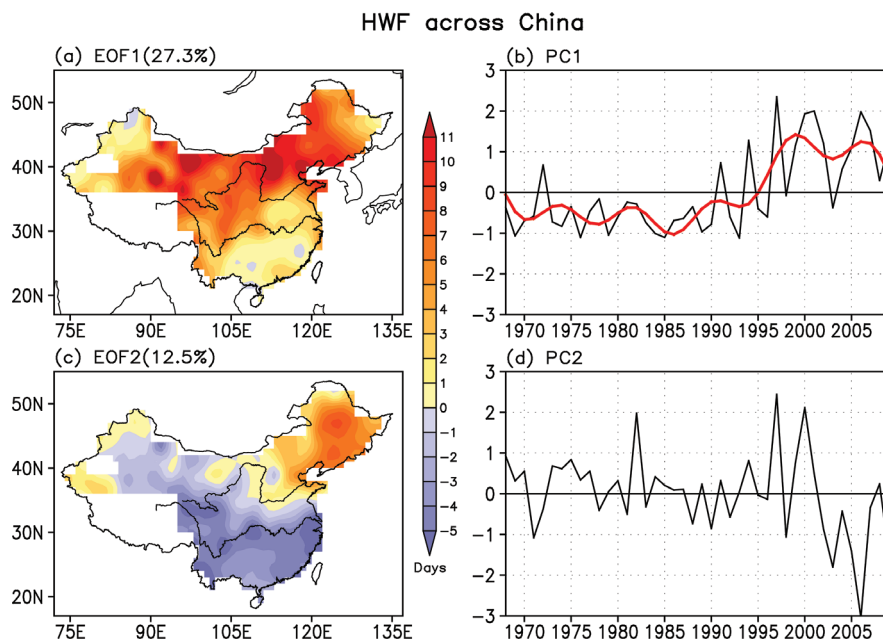


Fig. 17.2. Upper panels: (a) spatial pattern (color shadings in unit of day) and (b) the corresponding principal component (PC) of the first empirical orthogonal function (EOF) mode of the JJA HWF across China. Lower panels (c) and (d): same as in (a) and (b) but for the second mode. The numbers in the brackets indicate fractional variance of the EOF modes. The red curve in (b) is the decadal-to-interdecadal component (ID) of PC1, namely, PC1(ID).

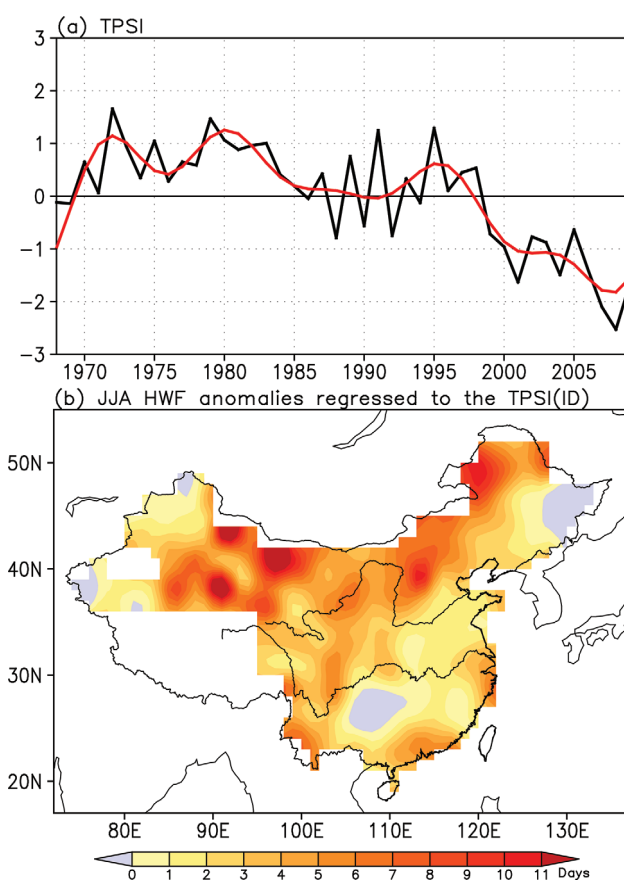


Fig. 17.3. (a) Time series of the normalized Tibetan Plateau (TP) snow cover index (TPSI) (black curve) and its decadal-to-interdecadal component TPSI(ID) (red curve) for the 1968–2009 summers (JJA); (b) The JJA HWF anomalies regressed to the TPSI(ID) (color shadings in unit of day). For comparison purposes, the sign of the TPSI(ID) time series has been reversed, hereafter.

**Plate 28**

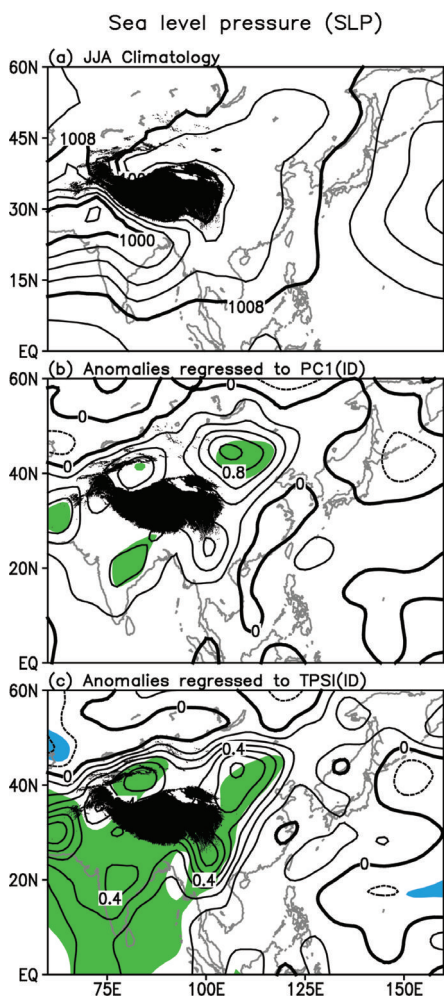


Fig. 17.4. (a) JJA climatology in sea level pressure (SLP; contours in units of hPa) and their anomalies regressed to the (b) PC1(ID) and (c) TPSI(ID). The black shadings denote TP, and the color shadings the 95% confidence level based on the Student's t-test.

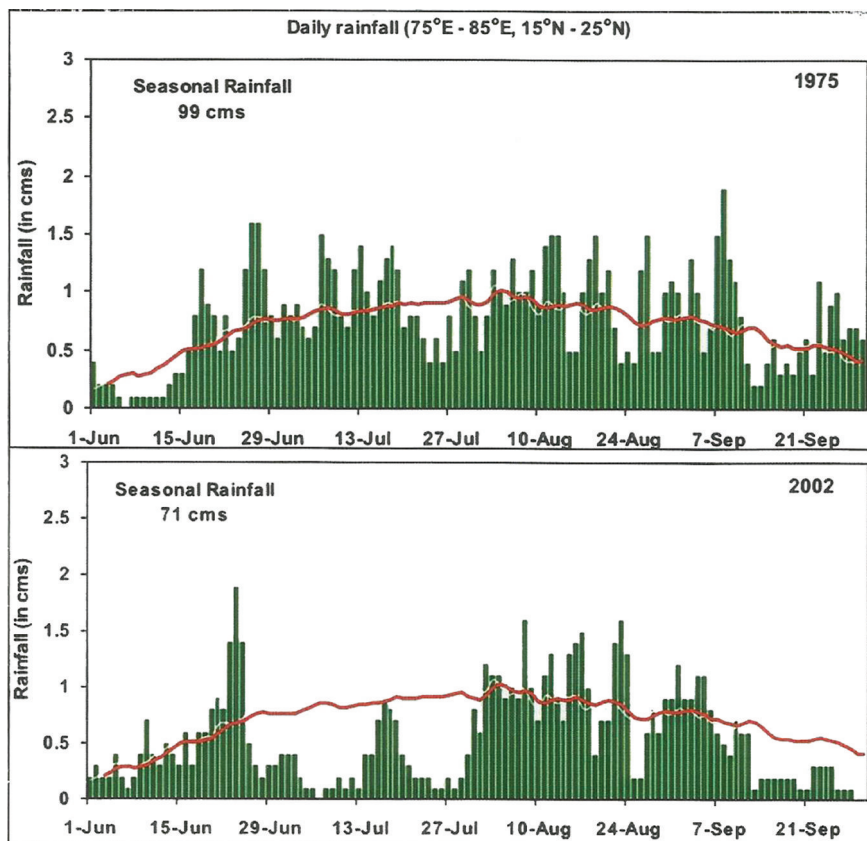


Fig. 25.2. Daily rainfall averaged over central India during two contrasting monsoon seasons 1975 (excess) (upper panel) and 2002 (drought)(lower panel). Red line indicates the climatological normal daily rainfall.

## Plate 29

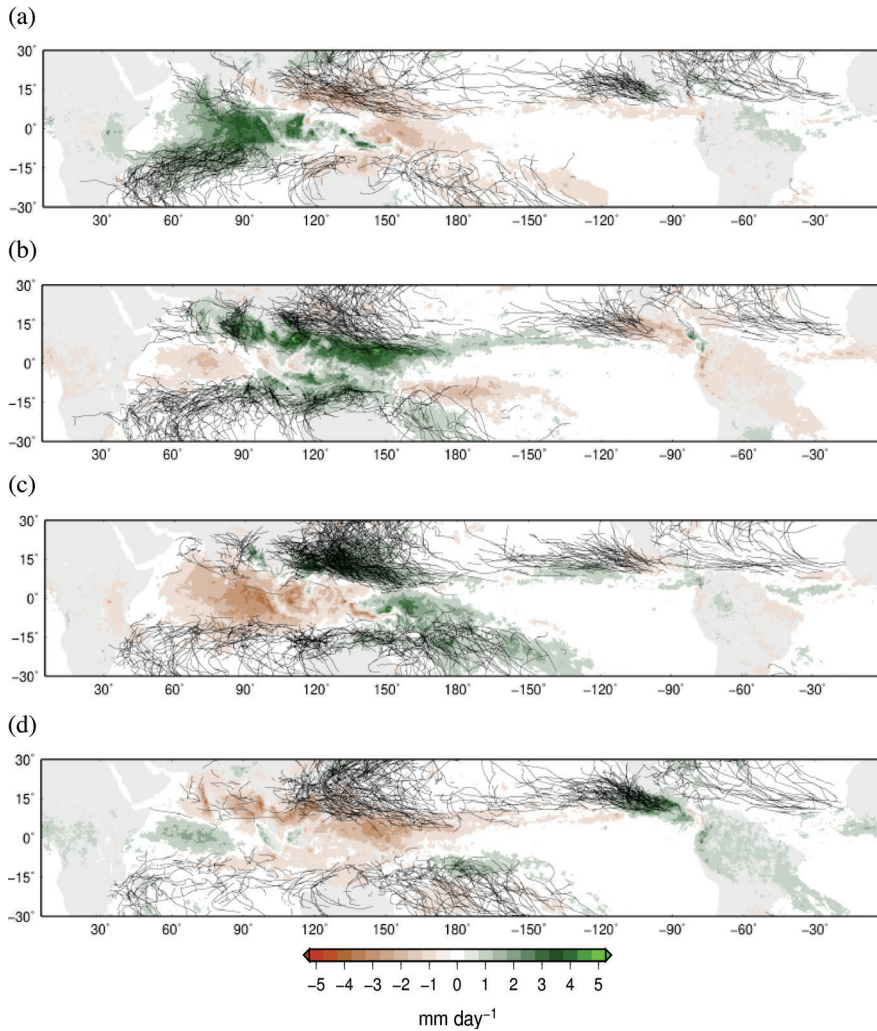


Fig. 24.1. TC tracks (1975–2011; black lines) and precipitation anomalies (1998–2011; color shading) when the MJO convection center is over the (a) Indian Ocean, (b) Maritime Continent, (c) western Pacific, and (d) Americas and Africa. Based on Zhang (2013).

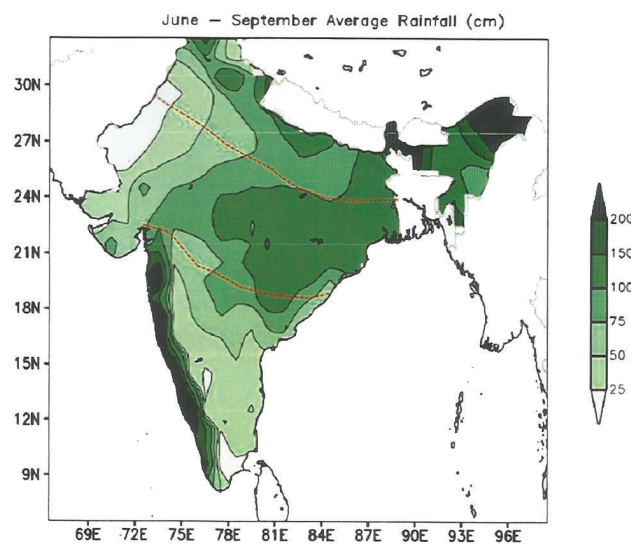


Fig. 25.1. Monsoon seasonal mean (June to September) rainfall for India. The yellow dashed lines show the position of the monsoon trough. Upper line is for 'break' monsoon and the lower line is for active monsoon conditions.

Plate 30

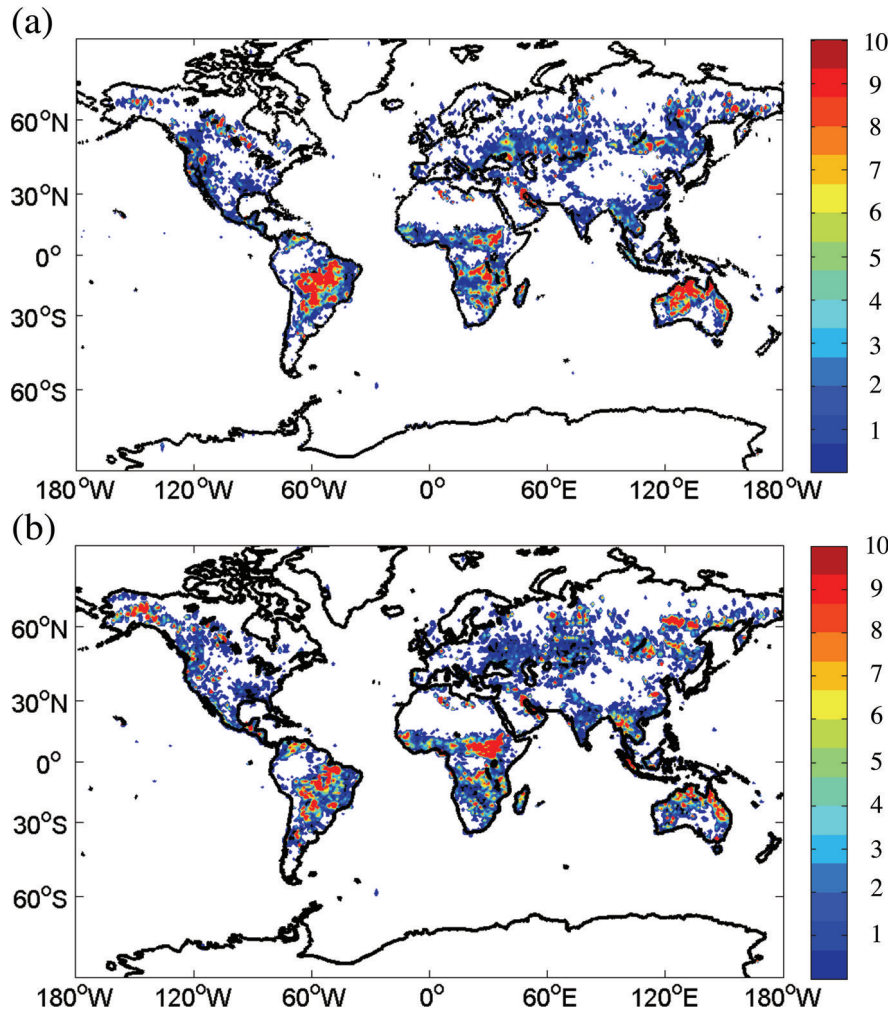


Fig. 24.3. Fire frequency (%), color shading) in each  $1^\circ \times 1^\circ$  grid box during the (a) MJO initiation stage (MJO convection center starts over the Indian Ocean), and (b) MJO WP stage (MJO convection center is over the western Pacific). The fire count data are ATSR World Fire Atlas (Arino *et al.* 2011. <http://due.esrin.esa.int/wfa/>).

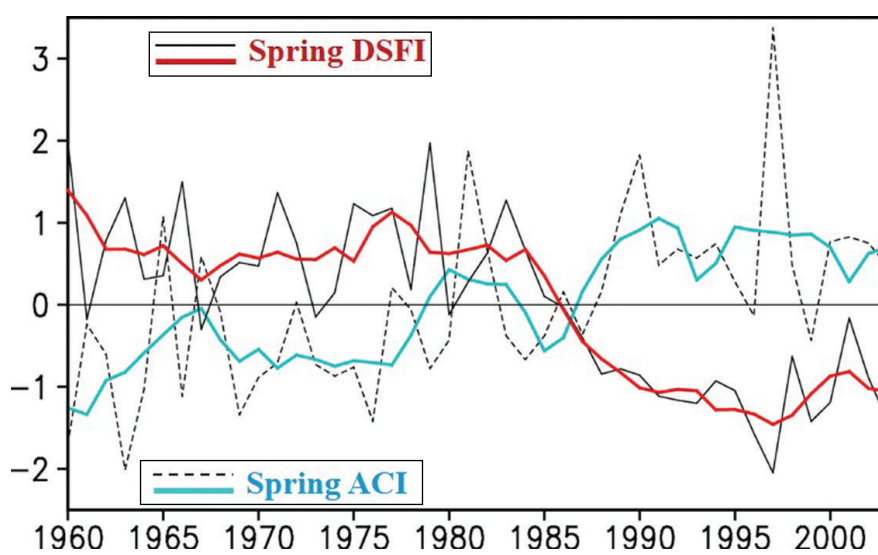


Fig. 27.2. Normalized spring DSFI (thin solid line) in NWC and ACI (thin dashed line) over MPMS. The thick solid lines are the corresponding 9-year running mean time series.

### Plate 31

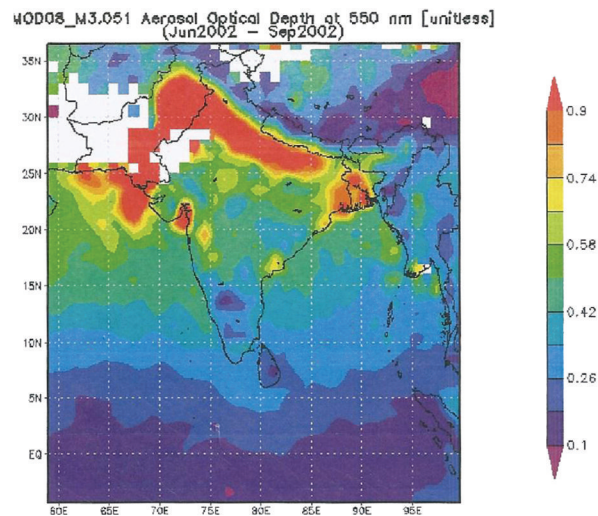


Fig. 25.8. Distribution of aerosol optical depth at 550 nm wavelength as observed by MODIS for the season of June to September; upper panel is for the year 2002 and lower panel for 2006.

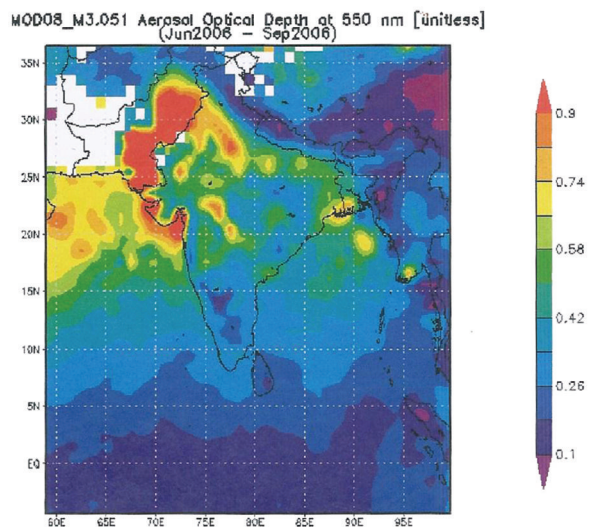


Fig. 27.6. Normalized time series of the winter NAOI (bars) and SWRI (open dotted line) for 1951–2011.

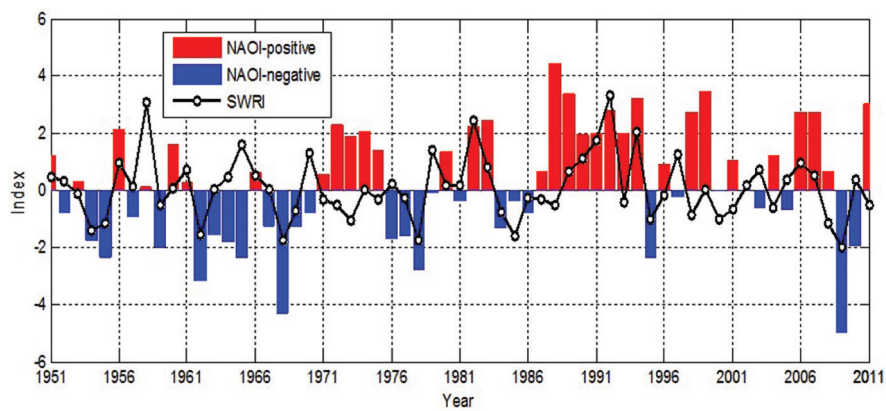


Plate 32

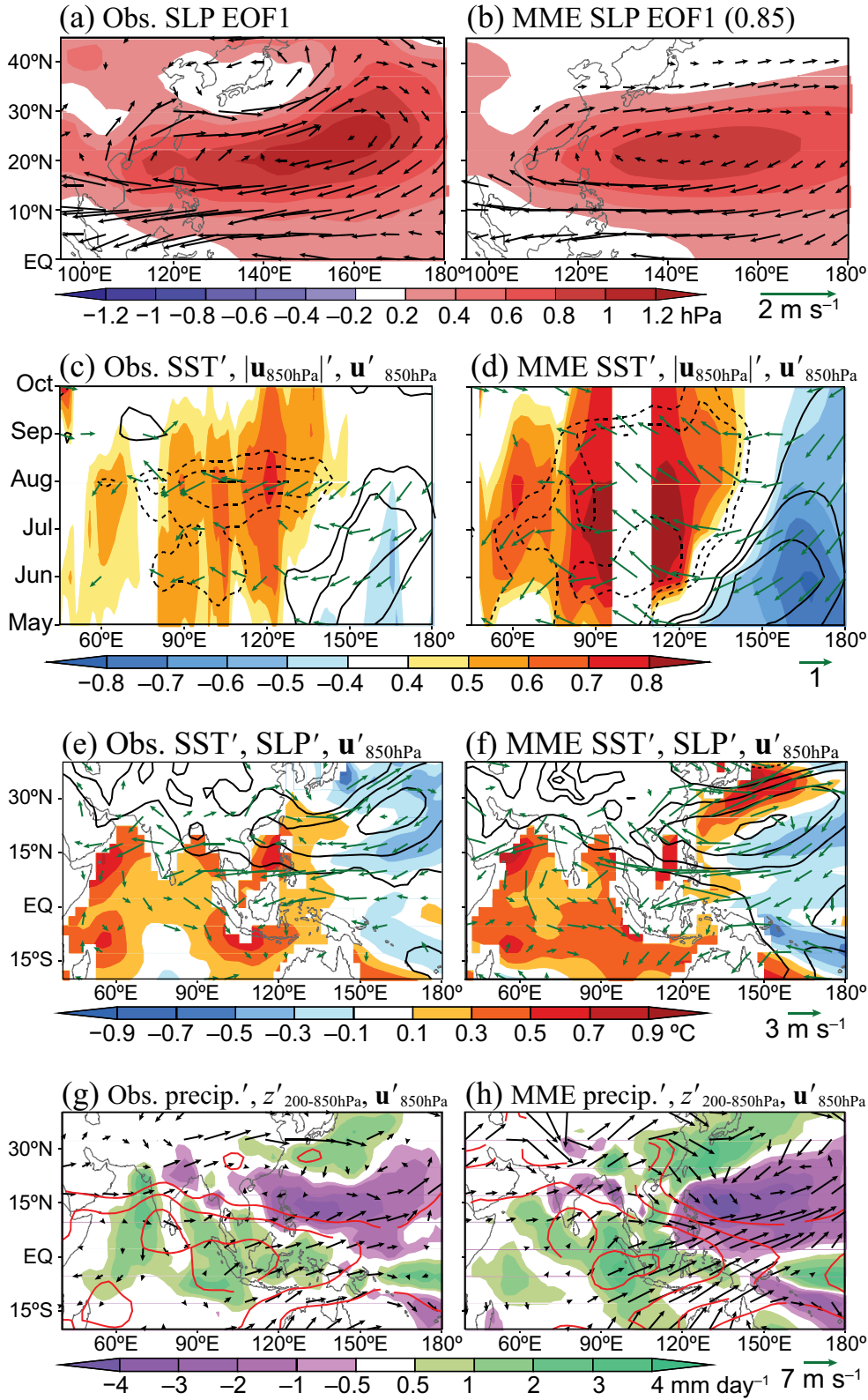


Fig. 26.4. (a,b) The leading EOF of JJA SLP (shading) and anomalies of 850 hPa wind velocity regressed against the corresponding PC. Pattern correlation coefficient between the two EOFs is 0.85. (c,d) Lag correlations of 5–20°N SST (shading), 850 hPa wind speed (contours; plotted for  $\pm 0.4$ ,  $\pm 0.6$ ,  $\pm 0.8$ ), and wind velocity (arrows) with respect to the PC. (e–h) Anomalies of (e,f) SST (shading), SLP (contours; plotted for 0.5, 1, 1.5, 2 hPa), and 850 hPa wind velocity (arrows), and (g,h) precipitation (shading), 850–200 hPa thickness (contours; plotted for 5, 10, 15, 20 gpm), and 200 hPa wind velocity (arrows) composited for JJA 1983, 1992, and 1998. (left) Observations and (right) MME for 11 seasonal hindcasts. HadISST, NCEP-DOE reanalysis (Kanamitsu *et al.*, 2002), and CMAP (Xie and Arkin, 1997) were used as observations. From Chowdary *et al.* (2010).

cover is located in the western and southern TP within large mountain ridges.

In this paper, we attempt to answer whether and how the TPSC is connected with the HWF variability across China. Section 17.2 describes the data sets, model, and methodology used in this study. Section 17.3 presents the observed relationship between the TPSC and the China HWF. In Section 17.4, numerical experiments are carried out with a simple general circulation model (SGCM) and the possible physical mechanism is explored. The last section summarizes major findings and some outstanding issues.

## 17.2 Data, model, and methodology

The major data sets used in this work include: (1) daily surface air temperature data at 605 gauge stations across China from China Meteorological Administration (see black dots in Fig. 17.1); (2) 1968–2009 monthly snow cover area extent data from the Global Snow Lab (Rutgers University) (<http://climate.rutgers.edu/snowcover/>); (3) the monthly circulation data, gridded at  $2.5^\circ \times 2.5^\circ$  resolution, taken from the European Centre for Medium-Range Weather Forecasts (ECMWF) 40-year reanalysis data set (ERA-40; Uppala *et al.*, 2005) and the ERA-interim data set; (4) the monthly total cloud cover (TCC) and surface solar radiation data (SSR) obtained from the ECMWF. Note that the ERA-40 data are extended from 2003 to 2009 by using ERA-interim data. To maintain temporal homogeneity, the

2003–2009 ERA-interim data are adjusted by removing the climatological difference between the ERA-40 and ERA-interim data (see the method in Wang *et al.*, 2010).

The numerical experiments are based on the SGCM, as described in detail in Hall (2000). The resolution used here is triangular 31, with ten equally spaced sigma levels, as in Wu *et al.* (2009). We used the National Centers for Environmental Prediction (NCEP) reanalysis version 1 (NCEP-1; Kalnay *et al.*, 1996) data to drive the numerical experiments. An important feature of this model is that it uses a time-averaged forcing calculated empirically from observed daily data. As shown in Hall (2000), this model is able to reproduce remarkably realistic stationary planetary waves, and the broad climatological characteristics of the transients are in general agreement with the observations.

According to the definition by Fischer and Schär (2010), a heat wave is defined as a spell of at least six consecutive days with maximum temperatures exceeding the local 90th percentile of the control period (1961–1990). To account for the seasonal cycle, the 90th percentile is calculated for each calendar day, and at each grid point using a centered 15-day-long time window. The HWF refers to the average frequency of days meeting the heat wave criterion. To derive the leading modes of the HWF, we performed an empirical orthogonal function (EOF) analysis by constructing an area-weighted covariance matrix.

The major snow cover areas in summer are basically located in the western and southern plateau regions (particularly the Himalaya Mountains), which have higher altitudes and therefore, are favorable for the snow cover persisting through summer. Most of the interior of the plateau with lower altitudes has relatively less snow cover persistence (Pu *et al.*, 2007; Wu *et al.*, 2012a,b). To quantitatively measure the TPSC variations, we used a TPSC index (TPSI) proposed by Wu *et al.* (2012a). This index is defined as the snow cover averaged within the domain ( $70^\circ$ – $80^\circ$ E,  $31^\circ$ – $41^\circ$ N) where the summer climatology center and the year-to-year variability maximum are located (see Figure 1 in Wu *et al.*, 2012a). Such notable snow cover changes yield significant low boundary forcing signals for the atmosphere (e.g. Wang *et al.*, 2008a; Wu *et al.*, 2012a,b).

## 17.3 The China HWF and TPSC

Figure 17.1 presents the climatology of the JJA HWF across China. A prominent feature is that the HWF values in northern China are generally larger than those in southern China, with the maximum in northwestern China, the desert region. Since most areas in northern China belong to dry or semi-dry regions, such a pattern indicates that heat waves more frequently occur in dry regions than in wet

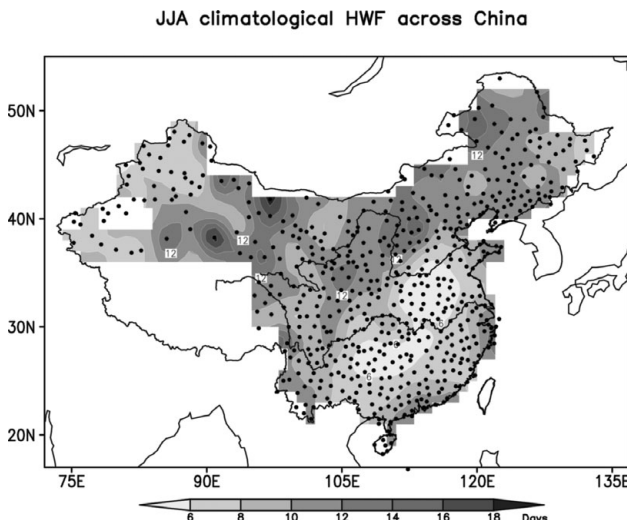


Fig. 17.1. The climatological heat wave frequency (HWF) across China for June–August (JJA) (color shadings in unit of day). Black dots denote 605 surface air temperature (SAT) gauge stations across China. A black and white version of this figure will appear in some formats. For the colour version, please refer to Plate 25.

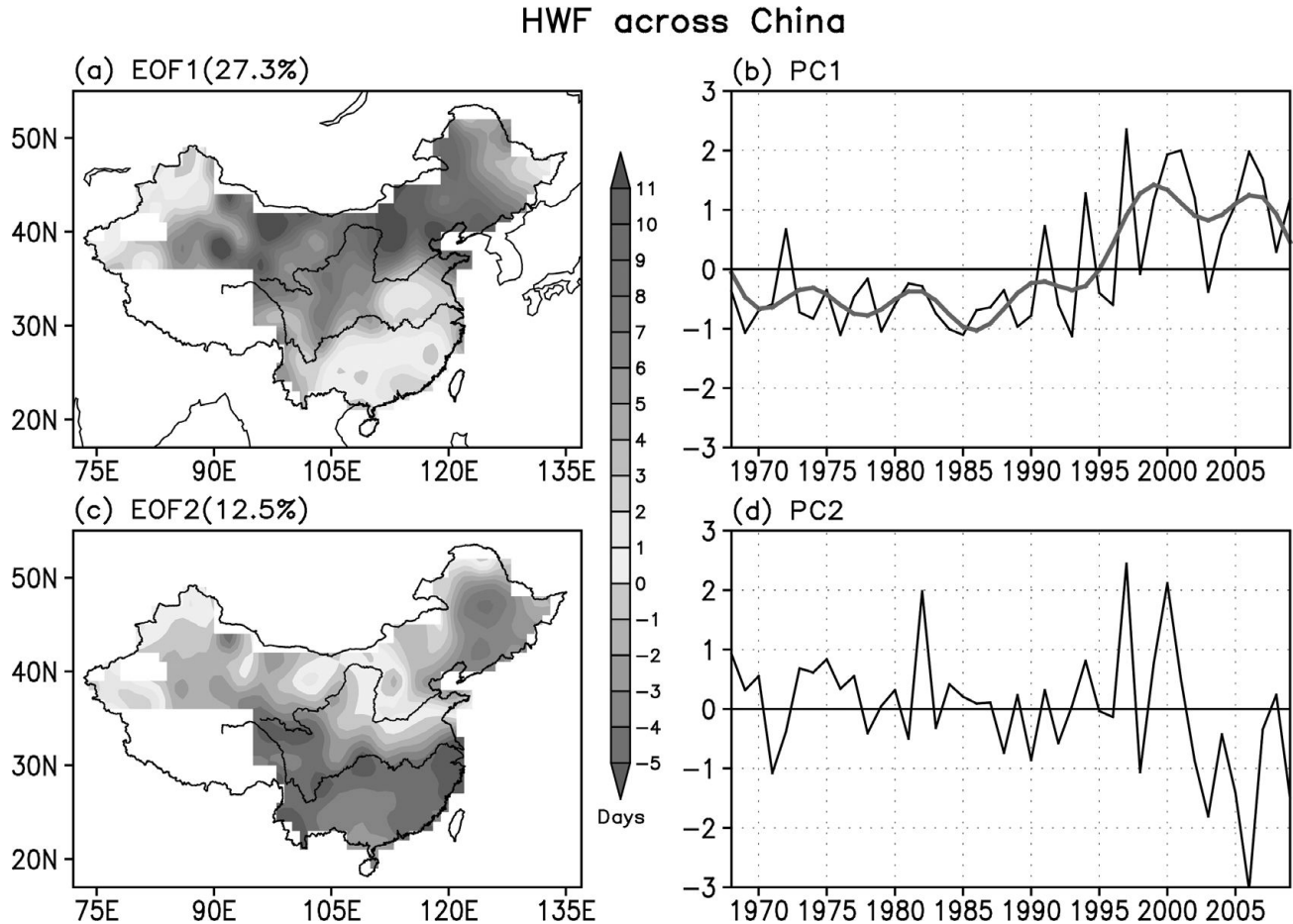


Fig. 17.2. Upper panels: (a) spatial pattern (color shadings in unit of day) and (b) the corresponding principal component (PC) of the first empirical orthogonal function (EOF) mode of the JJA HWF across China. Lower panels (c) and (d): same as in (a) and (b) but for the second mode. The numbers in the brackets indicate fractional variance of the EOF modes. The red curve in (b) is the decadal-to-interdecadal component (ID) of PC1, namely, PC1(ID). A black and white version of this figure will appear in some formats. [For the colour version, please refer to Plate 27.](#)

regions. This is consistent with the notion of extreme heat rooted in dry soils (e.g. Alexander, 2010; Hirschi *et al.*, 2010).

Figure 17.2 displays the two leading EOF modes of the HWF across China. The first mode accounts for 27.3% of the total variance, and the second mode, 12.5% (Figs. 17.2a and 17.2c). According to the rule given by North *et al.* (1982), the two leading modes are, statistically, distinguished from each other. They are also separable from the rest of the other high modes in terms of the sampling error bars (not shown). The EOF1 mode basically bears a monosign pattern with maximum loading located in northern China and is therefore labeled as the northern China mode, its amplitude decreasing southward (Fig. 17.2a). PC1 is primarily dominated by an interdecadal increasing trend with significant interannual variations superposed upon it (Fig. 17.2b). Most years before the mid 1990s have a

negative PC1, while those after the mid 1990s have a positive PC1. A positive PC1 refers to more heat waves over northern China, and vice versa. Therefore, the EOF1 mode reflects the interdecadal increase in the northern China HWF. This result is consistent with the observed fact that the most severe warming over eastern Asia takes place in northern China with the interdecadal shift of China summer climate in 1996–1998 (Hu, 1997, Trenberth *et al.*, 2007, Li *et al.*, 2010, R. Wu *et al.*, 2010).

The prominent feature of the EOF2 mode is a meridional dipole pattern with anomalies of opposite signs between northern and southern China (Fig. 17.2c). The extreme value center is located in northeastern China. A high PC2 year corresponds to a higher HWF in northern China and lower in southern China, and vice versa. The amplitude of PC2 has considerably amplified since the mid 1990s (Fig. 17.2d), suggesting that the EOF2 pattern became

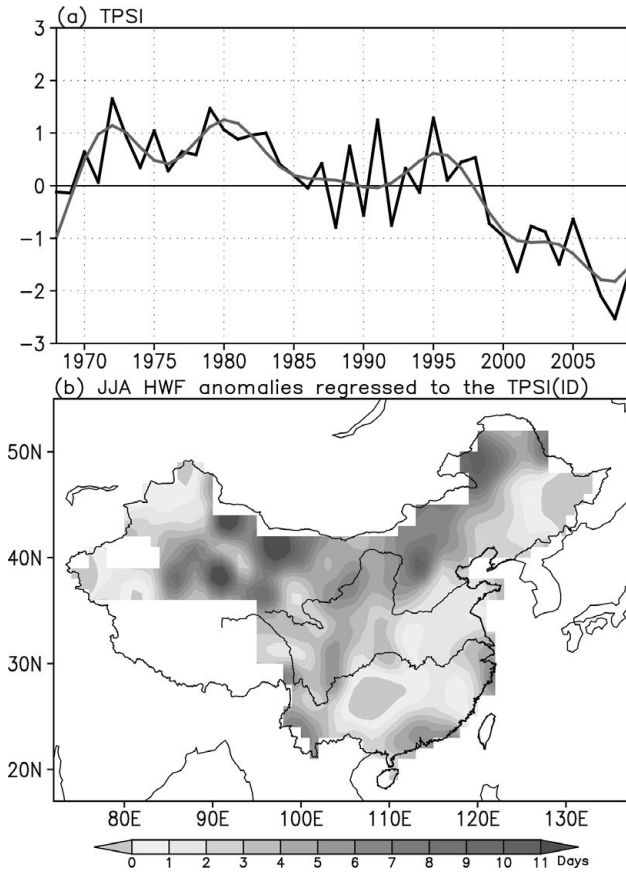


Fig. 17.3. (a) Time series of the normalized Tibetan Plateau (TP) snow cover index (TPSI) (black curve) and its decadal-to-interdecadal component TPSI(ID) (red curve) for the 1968–2009 summers (JJA); (b) The JJA HWF anomalies regressed to the TPSI(ID) (color shadings in unit of day). For comparison purposes, the sign of the TPSI(ID) time series has been reversed, hereafter. A black and white version of this figure will appear in some formats. [For the colour version, please refer to Plate 27.](#)

more obvious after the mid 1990s. Moreover, the EOF2 pattern highly resembles the anomalous summer precipitation pattern over China (e.g. Zhu *et al.*, 2007), indicating a coupled linkage between the HWF and the local rainfall.

It is interesting to notice that the TPSC exhibits an intimate linkage with the northern China mode (Fig. 17.3). In corresponding to the increasing tendency of PC1 (red curve in Fig. 17.2b), the TPSI displays a decreasing trend after the mid 1990s, indicating a reduced TPSC (Fig. 17.3a). To focus on the decadal-to-interdecadal (ID) time scales, PC1 and TSPI have been smoothed through keeping all Fourier harmonics that have periods longer than eight years and labeled as PC1(ID) and TPSI(ID), respectively (red curves in Fig. 17.2b and Fig. 17.3a). The HWF pattern that is projected as a result of the

decreasing TPSC resembles the EOF1 mode (Figs. 17.2b and 17.3b), namely, featuring an extreme center over northern China. Note that the ID components have persistence and the correlations computed using ID components have artificial skills due to data filtering. Therefore, when examining statistical significance of correlations between two ID components, the degrees of freedom must be reassessed using the method proposed by Chen (1982). For the 1968–2009 period, the degree of freedom is reduced to about 8. For a given confidence level of 95%, a significant correlation should be greater than 0.64.

In light of the close connection between the TPSC and northern China mode, this study will focus on how the TPSC decreasing more slowly modulates the northern China HWF.

Before investigating the physical mechanism, we need to clarify the planetary-scale three-dimensional circulation structure associated with the northern China mode and the anomalous TPSC, respectively. In general, the large-scale circulation anomalies regressed against PC1(ID) resemble a similar pattern to that with TPSI(ID) (Figs. 17.4–17.6). Near the surface (Figs. 17.4b and 17.4c), a large area of positive sea level pressure (SLP) anomalies occupies northern China with a major ridge extending southwestward towards TP. Comparing with the climatology, this pattern reflects the high pressure anomalies over Mongolia and the adjacent regions. This feature is more evident at the middle and upper troposphere (Figs. 17.5 and 17.6). The enhanced high accompanied by anti-cyclonic wind anomalies prevails over northern China, with the high ridge axis tilting toward TP (Figs. 17.5c and 17.6c). Such high ridge tilting implies its linkage with the TPSC, which is consistent with the results of Zhao *et al.* (2010). In addition, weak negative geopotential height anomalies (GHAs) and cyclonic wind anomalies prevail over South China.

To verify whether the above high pressure anomalies over Mongolia and the adjacent regions can also be observed in anomalous TPSC summers, we calculate the composite difference of circulations between the reduced and excessive TPSC decades (not shown). According to the evolution feature of TPSI(ID) (Fig. 17.3a) and some previous studies (Yu *et al.*, 2004, Sutton and Hodson, 2005, Zhao *et al.*, 2010), the 1972–1995 and 1996–2009 periods are defined as the reduced and excessive TPSC decades, respectively. The high pressure anomalies over Mongolia and the adjacent regions are evident over the mid and upper troposphere, 500 hPa in particular (not shown). A salient high pressure center controls northern China and expands towards TP. The vertical high ridge also tilts towards TP. A weak low anomaly covers South China. These high pressure anomalies over Mongolia and the adjacent regions are considerably similar to those accompanied by the northern China mode.

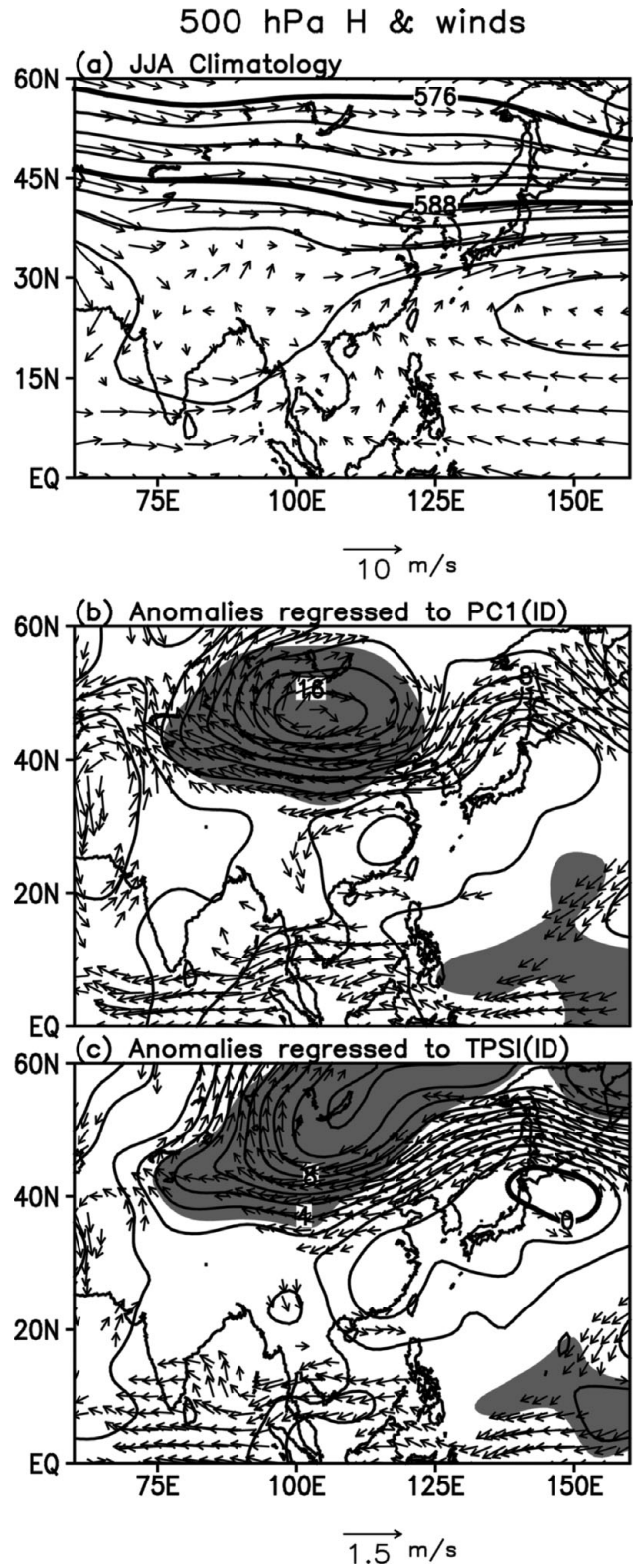
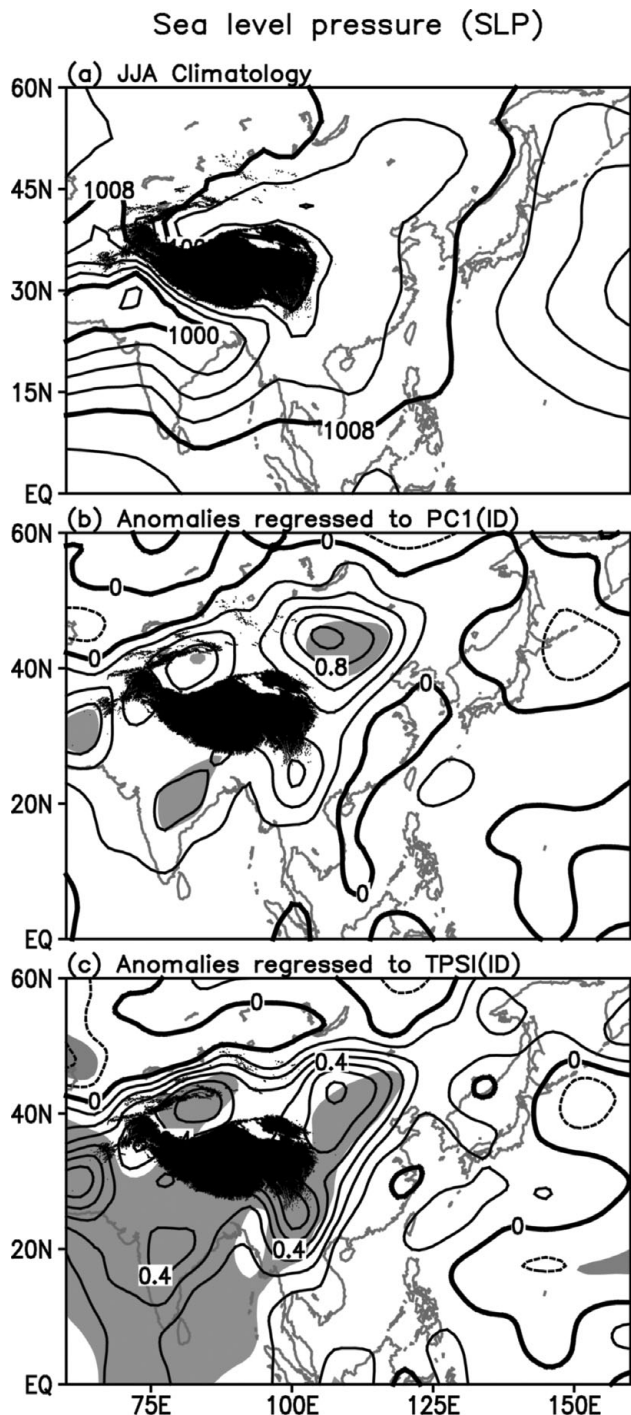


Fig. 17.4. (a) JJA climatology in sea level pressure (SLP; contours in units of hPa) and their anomalies regressed to the (b) PC1(ID) and (c) TPSI(ID). The black shadings denote TP, and the color shadings the 95% confidence level based on the Student's t-test. A black and white version of this figure will appear in some formats. For the colour version, please refer to Plate 28.

Fig. 17.5. Same as Fig. 17.4, but for the 500 hPa geopotential height (H500) and winds.

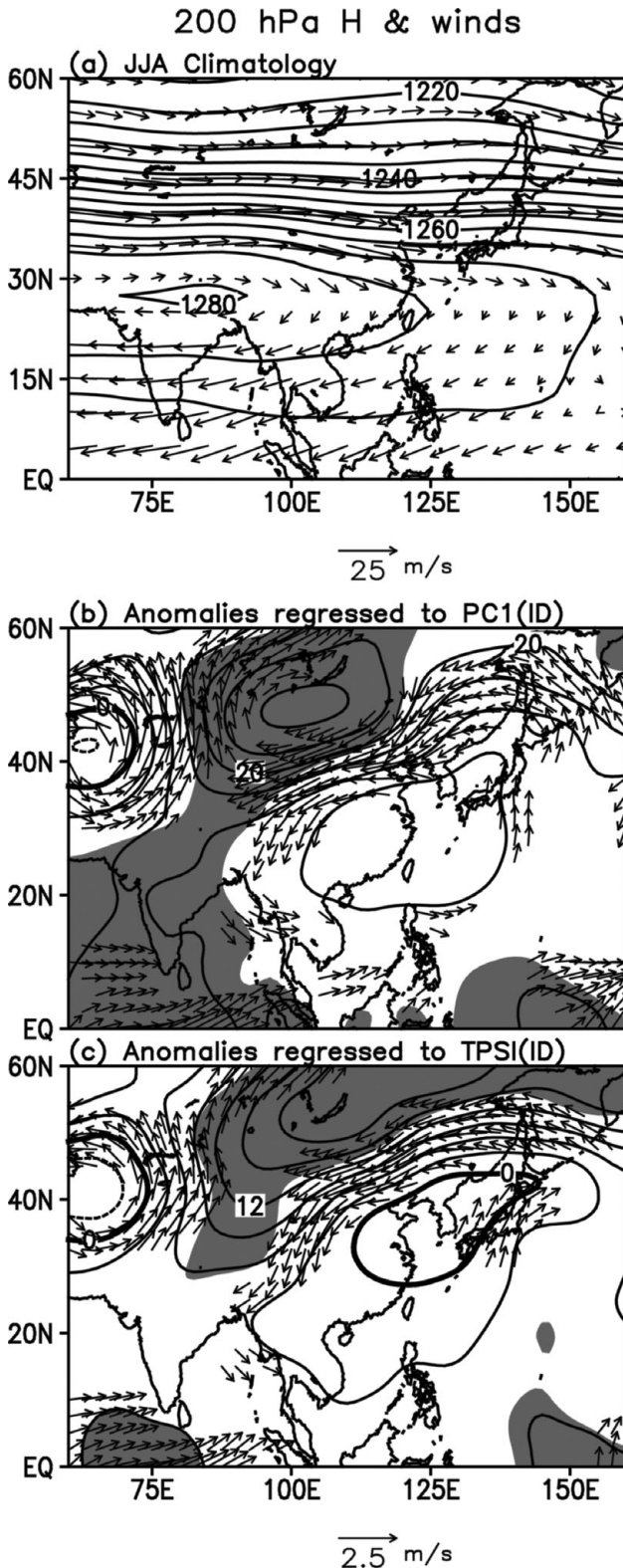


Fig. 17.6. The same as Fig. 17.4, but for the 200 hPa geopotential height (H<sub>200</sub>) and winds.

From the above statistical analysis, the linkage between the northern China HWF, the high pressure anomalies over Mongolia and adjacent regions, and the TPSC may be summarized as follows: the northern China HWF anomalies are usually associated with the GHAs over Mongolia and the adjacent regions, while the GHAs are significantly related to the TPSC variations. However, the correlations do not warrant any cause and effect.

#### 17.4 Physical mechanisms

How can the TPSC affect the HWF over northern China? To figure out this question, we need to understand how the atmospheric anomalies over Mongolia and the adjacent regions couple with the HWF anomalies over northern China. Then, it should be established whether and how the TPSC influences the atmospheric anomalies over Mongolia and the adjacent regions.

We take PC1(ID) as a reference and compute the lead-lag regression with 200 hPa geopotential height (H<sub>200</sub>) fields. The results are shown in Fig. 17.7. The absolute values of the regressed H<sub>200</sub> anomalies over northern China continuously increase from 1-month lead through 1-month lag. In 1-month lead (Fig. 17.7a), before more heat waves take place, positive H<sub>200</sub> anomalies emerge over northern China, favoring the high pressure anomalies over Mongolia and the adjacent regions. From 0-month lead through 1-month lag (Figs. 17.7b and 17.7c), the high pressure anomalies are enhanced, which indicates that the northern China mode has a positive feedback to the GHAs over Mongolia and the adjacent regions. Thus, the northern China mode of the HWF may be at least in part due to such positive feedback with the GHAs over Mongolia and the adjacent regions.

To further clarify the physical processes of the GHAs over Mongolia and adjacent regions impacting on heat waves, we computed the TCC and SSR anomalies lead-lag regressed to PC1(ID) (not shown). In corresponding to a positive phase of the northern China mode, the reduced TCC anomalies over northern China persist from 1-month lead through 1-month lag, reaching a maximum during the simultaneous period. Associated with a positive phase of the northern China mode, the increased net shortwave radiation at the surface can be observed over northern China and sustains from 1-month lead through 1-month lag.

In light of these, the possible physical processes might be summarized as follows. The reduced TPSC may induce high pressure anomalies at the mid and upper troposphere over Mongolia and adjacent regions. The subsidence associated with the high pressure anomalies tends to suppress the local cloud formation, which increases the net radiation

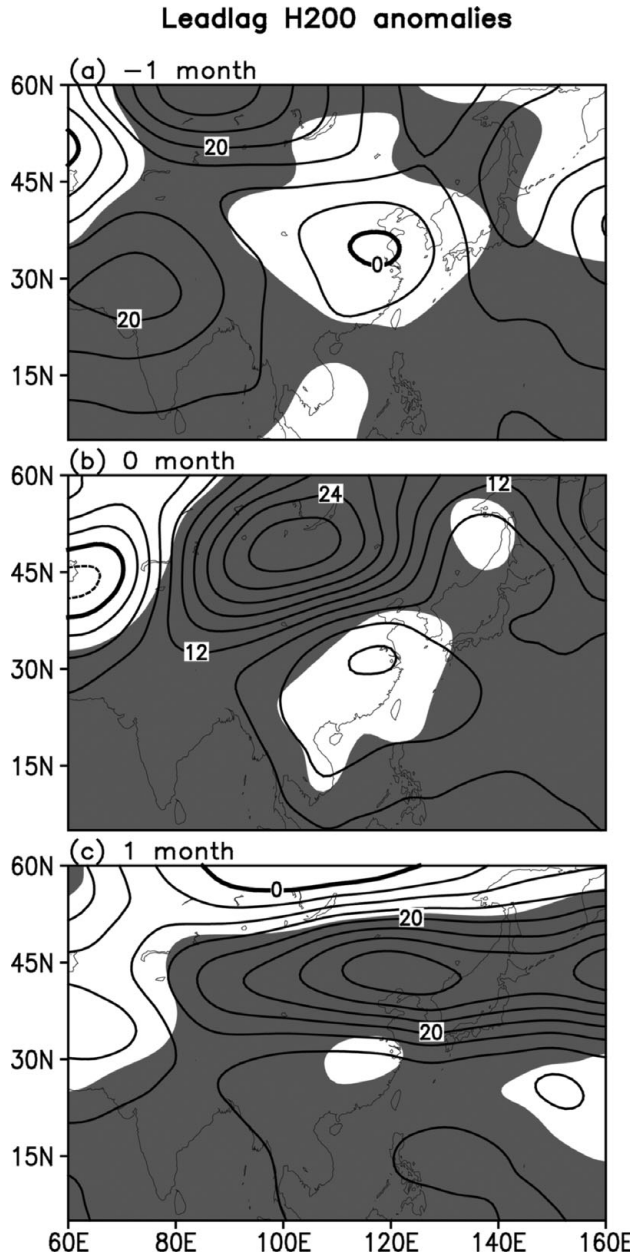


Fig. 17.7. The lead-lag H200 anomalies regressed to PC1(ID) (contours in units of gpm). PC1(ID) leads the H200 by (a)  $-1$ , (b)  $0$ , and (c)  $1$  month. Note that  $-1$ ,  $0$ , and  $1$  month correspond to May, JJA, and September, respectively. The shadings denote the 95% confidence level based on the Student's t-test.

budget, heats the surface, and favors more heat waves (see Figure 1 in Alexander, 2010). On the other hand, local surface heating can excite the high pressure anomalies at the mid and upper troposphere and further strengthen the local high pressure system. Through such a positive feedback effect, the TPSC anomaly is tied to the anomalous

HWF over northern China. Note that the reason why the TCC and the SSR are introduced to interpret the relevant physical process is based on the research results of Alexander (2010) and Hirschi *et al.* (2010). They found that cloud cover and net shortwave radiation near the surface play critical roles in heat wave formation in dry regions.

To elucidate the effects of an anomalous TPSC forcing on the GHAs at mid and upper levels over northern China, we performed a numerical experiment with the non-linearized SGCM to see what effects changing the TPSC would have on planetary-scale atmospheric circulations. The existence of anomalous snow cover works to cut the upward sensible heat flux, rather than evaporation over TP, because of its dry ground condition (Ose, 1996). To mimic the diabatic heating of the reduced TPSC, we imposed a warming anomaly centered at  $75^{\circ}\text{E}$ ,  $35^{\circ}\text{N}$  which has an elliptical squared cosine distribution in latitude and longitude, with a maximum heating of  $2.5\text{ K/day}$  near  $500\text{ hPa}$  (Wu *et al.*, 2012a,b). The vertical heating profile of the TPSC is  $\sigma^4 \sin(\pi\sigma)$ , peaking at around  $500\text{ hPa}$ . The perturbed experiments were integrated for 3700 days. The last 3600-day integrations were used to construct an ensemble (arithmetic) mean. Note that the result is not sensitive to the selection of initial condition, since the analysis is conducted for the period after climate equilibrium is reached.

The model responses of  $250\text{ hPa}$  geopotential height (H250) to the reduced TPSC forcing are shown in Fig. 17.8a. A high anomaly is induced at the upper troposphere and centered over northern China. The  $550\text{ hPa}$  geopotential height (H550) exhibits a similar pattern with H250 (Fig. 17.8b). At the lower level ( $950\text{ hPa}$ ), air temperatures respond with a warm center over northern China which extends eastward to the North Pacific and southwestward towards TP (Fig. 17.8c). The numerical experiment confirms that the anomalous TPSC forcing can excite high pressure anomalies at the middle and upper troposphere and warm anomalies at the lower level over northern China. Note that the simulation has some discrepancies in the middle latitudes, north of  $45^{\circ}\text{N}$  (the position of the geopotential height negative center in particular) or central Asia, if compared with Fig. 17.6b. It implies that the TPSC anomaly cannot satisfactorily interpret the circulation variations over these regions and some other factors may dominate the circulations there, i.e. an upstream effect or the importance of atmospheric internal dynamics (reviewed in Chapter 26 of this book by Xie and Kosaka).

To summarize, the primary response of the atmosphere to the reduced TPSC is a high pressure anomaly at the mid and upper troposphere over Mongolia and the adjacent regions, which tilts southwestward towards TP. Such high

### SGCM responses

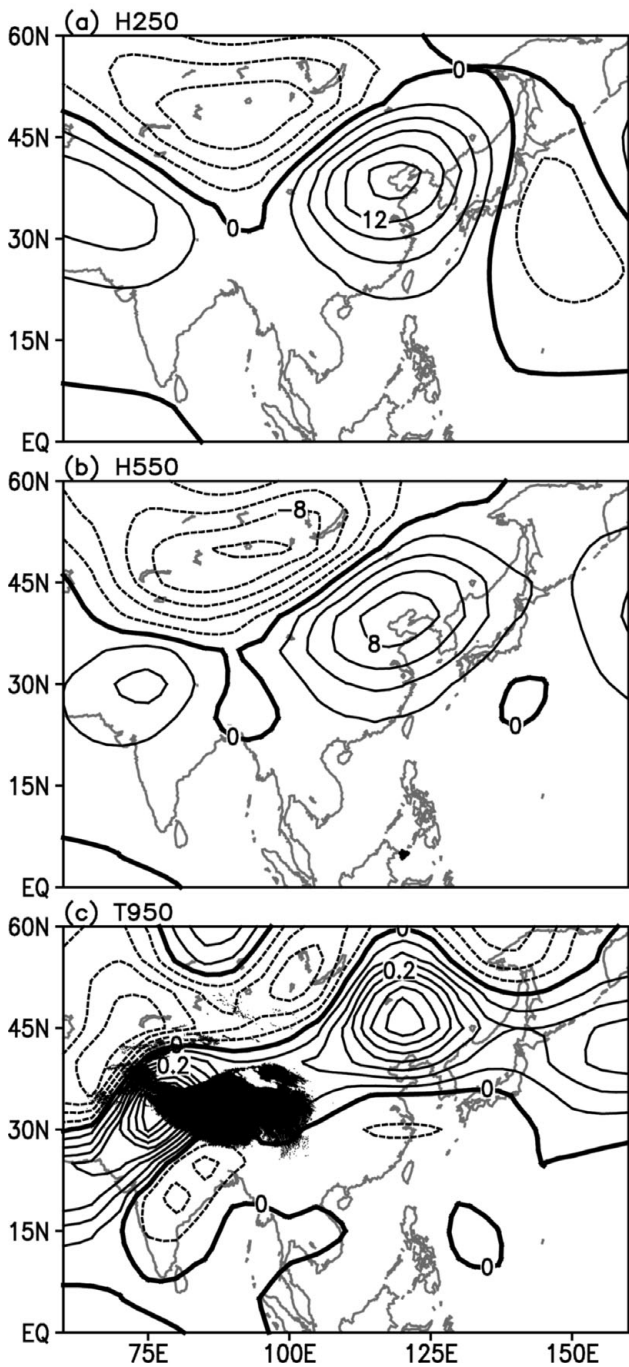


Fig. 17.8. JJA (a) 250 hPa geopotential height (H250), (b) 550 hPa geopotential height (H550) (in units of gpm), and 950 hPa temperature (T950) (in units of K) responses to the reduced TPSC forcing in the SGCM.

pressure anomalies favor more heat waves in northern China via triggering positive feedback among the H, TCC, and surface heating.

### 17.5 Conclusion and discussion

Climate change is expected to affect not only the means of climatic variables, but also their variabilities and extremes such as heat waves (e.g. Easterling *et al.*, 2000, Wu *et al.* 2006, 2010). In this study, we examined the observed relationship between the TPSC and the HWF across China and found that the decadal to interdecadal variations of northern China HWF are significantly connected with the TPSC. A reduced TPSC is often accompanied by more heat waves over northern China, and vice versa. Numerical experiments suggest that the anomalous TPSC can induce a high pressure anomaly over northern China, which in turn modifies the local cloud formation, the net radiation budget, and the HWF. On the other hand, the HWF responds with positive feedback to the anomalous geopotential height at the mid and upper troposphere over Mongolia and the adjacent regions. Through such physical processes, the TPSC is linked to the northern China HWF.

As a matter of fact, previous studies have proposed some explanations on the origin of high pressure anomalies over the Mongolian Plateau and the associated seasonal effect in triggering local subseasonal heat extremes (e.g. Hu *et al.* 2011, Wu *et al.* 2012b, Ito *et al.* 2013). The role of the TPSC, however, has seldom been noticed before. This is probably partly due to lack of high-quality, long-term climate data in investigating decadal to interdecadal changes in extreme weather and climate events such as heat waves (Easterling *et al.*, 2000). For instance, the TPSC data in this study is available only from 1968. Because of the limitation of data time length, it is difficult to obtain unequivocal evidence of climate change.

Besides the above positive feedback process, it should be pointed out that some negative feedbacks also modulate HWF decadal-to-interdecadal variability. For example, the EOF2 mode has considerably amplified since the mid 1990s, but with opposite polarity to the EOF1 mode (particularly over northeastern China) (Fig. 17.2). The resemblance between the EOF2 mode and the China summer precipitation anomaly pattern implies that intensified precipitation may reduce the local HWF (northeastern China in particular). As a matter of fact, Zhao *et al.* (2010) suggested that the thermal state of TP may alter the East Asian thermal contrast and summer monsoon rainfall.

In addition, other factors (including remote oceanic impacts and greenhouse gas concentrations) can also affect the northern China HWF (e.g. Hu *et al.*, 2003, Ding *et al.*, 2008, 2009, Meehl *et al.*, 2009, Alexander, 2010). Since the TPSC is expected to further decrease with increasing levels of greenhouse gases in the atmosphere in future (Meehl *et al.*, 2007), the results obtained in this study imply that the TPSC may play an increasingly important role in shaping northern China heat waves over future decades.

## 17.6 Acknowledgments

We appreciate the National Meteorological Information Center of China for providing gauge station data across China and the Global Snow Lab (Rutgers University) for snow cover extent area data. This is jointly supported by the National Natural Science Foundation of China (Grant No. 91437216) and the Ministry of Science and Technology of China (Grant Nos. 2015CB953904, 2015CB453201 and 2013CB430202).

## References

- Alexander, L. (2010). Extreme heat rooted in dry soils. *Nat. Geosci.*, **3**, 1–2.
- Chen, W. Y. (1982). Fluctuations in Northern Hemisphere 700 mb height field associated with southern oscillation. *Mon. Wea. Rev.*, **110**, 808–832.
- Ding, Y. H. (1992). Summer monsoon rainfalls in China. *J. Meteor. Soc. Japan*, **70**, 397–421.
- Ding, Y. H., Ren, G. Y., Zhao, Z. C., et al. (2007). Detection, causes and projection of climate change over China: An overview of recent progresses. *Adv. Atmos. Sci.*, **24**(6), 954–971.
- Ding, Y. H., Wang, Z. Y., and Sun, Y. (2008). Inter-decadal variation of the summer precipitation in East China and its association with decreasing Asian summer monsoon. Part I: Observed evidences. *Inter J Climatol*, **28**(9), 1139–1161.
- Ding, Y. H., Sun, Y., Wang, Z. Y., Zhu, Y. X., and Song, Y. F. (2009). Inter-decadal variation of the summer precipitation in East China and its association with decreasing Asian summer monsoon. II: Possible causes. *Inter. J. Climatol.*, **29**(13), 1926–1944.
- Duan, A. M., Li, F., Wang, M. R., and Wu, G.X. (2011). Persistent weakening trend in the spring sensible heat source over the Tibetan Plateau and its impact on the Asian summer monsoon. *J. Clim.*, **24**, 5671–5682.
- Easterling, D. R., Evans, J. L., Groisman, P. Y., et al. (2000). Observed variability and trends in extreme climate events: a brief review. *Bull. Amer. Meteor. Soc.*, **81**, 417–425.
- Fu, C. B. (2003). Potential impacts of human-induced land cover change on East Asia monsoon. *Global Planet Change*, **37**, 219–229.
- Fischer, E. M. and Schär, C. (2010). Consistent geographical patterns of changes in high-impact European heatwaves. *Nat. Geosci.*, **3**, 398–403.
- Garcia-Herrera, R., Diaz, J., Trigo, R. M., Luterbacher, J., and Fischer, E. M. (2010). A review of the European summer heatwave of 2003. *Crit. Rev. Environ. Sci. Technol.*, **40**, 267–306.
- Hall, N. M. J. (2000). A simple GCM based on dry dynamics and constant forcing. *J. Atmos. Sci.*, **57**, 1557–1572.
- Hirschi, M., Seneviratne, S. I., Alexandrov, V., et al. (2010). Observational evidence for soil-moisture impact on hot extremes in southeastern Europe. *Nat Geosci*, **3**, doi: 10.1038/NGEO1032.
- Hu, Z. Z. (1997). Interdecadal variability of summer climate over East Asia and its association with 500 hPa height and global sea surface temperature. *J. Geophys. Res.*, **102**(D16), 19403–19412.
- Hu, Z. Z., Yang, S., and Wu, R. (2003). Long-term climate variations in China and global warming signals. *J. Geophys. Res.*, **108**(19), 4614, doi: 10.1029/2003JD003651.
- Hu, K. M., Huang, G., and Huang, R. H. (2011). The impact of tropical Indian Ocean variability on summer surface air temperature in China. *J. Clim.*, **24**, 5365–5377.
- Ito, H., Johnson, N. C., and Xie, S. P. (2013). Subseasonal and interannual temperature variability in relation to extreme temperature occurrence over East Asia. *J. Clim.*, **26**, 9026–9042.
- Kalnay, E., Kanamitsu, M., and Kistler, R., et al. (1996). The NCEP/NCAR 40-year reanalysis project. *Bull. Amer. Meteor. Soc.*, **77**, 437–471.
- Li, J., Yu, R. C., Zhou, T. J., and Wang, B. (2005). Why is there an early spring cooling shift downstream of the Tibetan Plateau? *J. Clim.*, **18**, 4660–4668.
- Li, J. P., Wu, Z. W., Jiang, Z. H., and He, J. H. (2010). Can global warming strengthen the East Asian summer monsoon? *J. Clim.*, **23**, 6696–6705.
- Liu, J. and Chen, R. (2011). Studying the spatiotemporal variation of snow-covered days over China based on combined use of MODIS snow-covered days and in situ observations. *Theor. Appl. Climatol.*, doi: 10.1007/s00704-011-0441-9.
- Massimo, B. and Benedict, S. (2004). The role of the Himalayas and the Tibetan Plateau within the Asian monsoon system. *Bull. Amer. Meteor. Soc.*, **85**, 1001–1004.
- Meehl, G. A., et al. (2007). Global climate projections, in *Climate Change 2007: The Physical Science Basis: Fourth Assessment Report of the Intergovernmental Panel on Climate Change*, ed. S. Solomon, et al., Cambridge University Press, Cambridge, UK.
- Meehl, G. A., et al. (2009). Decadal prediction. *Bull. Amer. Meteor. Soc.*, **90**, 1467–1485.
- Nitta, T. and Hu, Z. Z. (1996). Summer climate variability in China and its association with 500 hPa height and tropical convection. *J. Meteor. Soc. Japan*, **74**(4), 425–445.
- North, G. R., Bell, T. L., Cahalan, R. F., and Moeng, F. J. (1982). Sampling errors in the estimation of empirical orthogonal functions. *Mon. Wea. Rev.*, **110**, 699–706.
- Ose, T. (1996). The comparison of the simulated response to the regional snow mass anomalies over Tibet, eastern Europe, and Siberia. *J. Meteor. Soc. Japan*, **74**, 845–866.
- Pu, Z. X., Xu, L., and Salomonson, V. V. (2007). MODIS/Terra observed seasonal variations of snow cover over the Tibetan Plateau. *Geophys. Res. Lett.*, **34**, L06706, doi: 10.1029/2007GL029262.
- Qian, Y. F., Zheng, Y. Q., Zhang, Y., and Miao, M. Q. (2003). Responses of China's summer monsoon climate to snow anomaly over the Tibetan Plateau. *Inter. J. Climatol.*, **23**, 593–613.
- Seol, K. H. and Hong, S. Y. (2009). Relationship between the Tibetan snow in spring and the East Asian summer monsoon in 2003: A global and regional modeling study. *J. Clim.*, **22**, 2095–2110.

- Sutton, R. T. and Hodson, D. (2005). Atlantic Ocean forcing of North American and European summer climate science. *Science*, **309**, 115–118.
- Trenberth, K. E., Jones, P. D., Ambenje, P., et al. (2007). Observations: Surface and Atmospheric Climate Change. In *Climate Change 2007: The Physical Science Basis. Contribution of Working Group I to the Fourth Assessment Report of the Intergovernmental Panel on Climate Change*, ed. S. Solomon, D. Qin, M. Manning, et al. Cambridge University Press, Cambridge, UK and New York, NY, USA.
- Uppala, S. M., Kallberg, P. W., Simmons, A. J., et al. (2005). The ERA-40 re-analysis. *Quart. J. Roy. Meteor. Soc.*, **131**, 2961–3012.
- Wang, B., Bao, Q., Hoskins, B., Wu, G., and Liu, Y. (2008a). Tibetan Plateau warming and precipitation change in East Asia. *Geophys. Res. Lett.*, **35**, L14702, doi:10.1029/2008GL034330.
- Wang, B. and Ding, Q. (2006). Changes in global monsoon precipitation over the past 56 years. *Geophys. Res. Lett.*, **33**, L06711, doi:10.1029/2005GL025347.
- Wang, B., Wu, Z. W., Li, J. P., et al. (2008b). How to measure the strength of the East Asian summer monsoon. *J. Clim.*, **17**, 4449–4462.
- Wang, B., Wu, Z. W., Chang, C. P., et al. (2010). Another look at interannual to interdecadal variations of the East Asian winter monsoon. *J. Clim.*, **23**, 1495–1512.
- Wu, G. X. and Coauthors. (2007). The influence of mechanical and thermal forcing by the Tibetan Plateau on Asian climate. *J. Hydrometeor.*, **8**, 770–789.
- Wu, R. and Kirtman, B. P. (2007). Observed relationship of spring and summer East Asian rainfall with winter and spring Eurasian snow. *J. Clim.*, **20**, 1285–1304.
- Wu, R., Wen, Z. P., Yang, S., and Li, Y. Q. (2010). An interdecadal change in southern China summer rainfall around 1992–93. *J. Clim.*, **23**, 2389–2403.
- Wu, Z. W., Li, J. P., He, J. H., and Jiang, Z. H. (2006). Occurrence of droughts and floods during the normal monsoons in the mid- and lower reaches of the Yangtze River. *Geophys. Res. Lett.*, **33**, L05813, doi:10.1029/2005GL024487.
- Wu, Z. W., Wang, B., Li, J. P., and Jin, F. F. (2009). An empirical seasonal prediction model of the East Asian summer monsoon using ENSO and NAO. *J. Geophys. Res.*, **114**, D18120, doi: 10.1029/2009JD011733.
- Wu, Z. W., Li, J. P., Jiang, Z. H., and Ma, T. T. (2012a). Modulation of the Tibetan Plateau snow cover on the ENSO teleconnections: From the East Asian summer monsoon perspective. *J. Clim.*, **25**, 2481–2489.
- Wu, Z. W., Jiang, Z. H., Li, J. P., Zhong, S. S., and Wang, L. J. (2012b). Possible association of the western Tibetan Plateau snow cover with the decadal to interdecadal variations of Northern China heatwave frequency. *Clim. Dyn.*, **39**, 2393–2402.
- Yu, R. C., Wang, B., and Zhou, T. J. (2004). Climate effects of the deep continental stratus clouds generated by the Tibetan Plateau. *J. Clim.*, **17**, 2702–2713.
- Zhai, P. M., Sun, A. J., Ren, F. M., et al. (1999). Changes of climate extremes in China. *Clim. Change*, **42**, 203–218.
- Zhang, Y., Li, T., and Wang, B. (2004). Decadal change of the spring snow depth over the Tibetan Plateau: the associated circulation and influence on the East Asian summer monsoon. *J. Clim.*, **17**, 2780–2793.
- Zhao, P., Zhou, Z. J., and Liu, J. P. (2007). Variability of Tibetan spring snow and its associations with the hemispheric extratropical circulation and East Asian summer monsoon rainfall: An observational investigation. *J. Clim.*, **20**, 3942–3955.
- Zhao, P., Yang, S., and Yu, R. C. (2010). Long-term changes in rainfall over eastern China and large-scale atmospheric circulation associated with recent global warming. *J. Clim.*, **23**, 1544–1562.
- Zhu, X. Y., He, J. H., and Wu, Z. W. (2007). Meridional seesaw-like distribution of the Meiyu rainfall over the Changjiang-Huaihe River Valley and characteristics in the anomalous climate years. *Chin. Sci. Bull.*, **52**(17), 2420–2428.

# 18

## Global warming targets and heat wave risk

Robin Clark

This chapter examines how extreme hot days and heat waves could change in a world warmed by 2 °C as a result of a doubling of the atmospheric concentration of CO<sub>2</sub>. The range in regional warming is quantified, as is the plausibility of the warming, by comparing model simulations with observations. The chapter also covers aspects of soil drying on variations in warming.

### 18.1 Introduction

In recent years, the issue of anthropogenic warming from increases in greenhouse gases emitted from fossil fuel burning has moved on from whether warming has been caused and whether it will continue, to one of how much the warming will be and its possible impacts. In the media and international discussions, however, targets have often been quoted in terms of globally averaged temperature increases. The European Union, for example, reiterated its longstanding commitment to a 2°C target above pre-industrial levels in January 2009 (EU/EC, 2009). However, for adaptation to climate change, such targets are unlikely to convey the risk of enhanced local changes. The continents, for example, are likely to warm faster than the oceans (Sutton *et al.*, 2007). Regional contrasts are also likely to depend on geographical variations in feedbacks from changes in atmospheric and oceanic circulation processes. Targets are also often quoted as multi-decadal means which hide year to year variability, seasonality, and extreme events. If these issues were likely to be confined to scientists alone the problem would probably not be particularly serious. Adaptation though, will likely be required of anyone at risk of being affected, even if they are not aware of it. As a result, there is a clear requirement for the wider community beyond scientists to be aware of and appreciate what the global targets could actually bring in terms of weather. Preparing for heat waves by assuming that a 2°C global rise will imply a 2°C local rise in someone's backyard, for example, is almost certainly going to

lead to a substantial ill-preparedness if the local warming ends up being much greater. There is thus a requirement to provide interpretations of global means on regional scales.

The ideal method for doing this would be to run a climate model with a specific equilibrium global target temperature. Unfortunately, the myriad of feedbacks and their interactions within a classical climate model make this impossible. Furthermore, consideration must be made of the fact that many differing configurations of regional patterns can also give the same global target.

A pragmatic approach instead is to sub-select from ensembles of simulations already produced, based on their globally averaged temperature responses. Multi-model ensembles, such as CMIP3 and 5 offer this possibility. Unfortunately, these are often too small in terms of ensemble members to offer accurate measures of uncertainty in regional changes. The desire to explore possible mechanisms behind changes is also difficult with this approach since the component models are often quite structurally different. An alternative method is to sub-select from larger ensembles based on a single model, such as those being compiled at climateprediction.net or the UK Met Office (Murphy *et al.*, 2004); designed to explore the effects of parameter uncertainties.

### 18.2 Data

Considered here is the version produced by the Met Office, based on an ensemble of simulations of the equilibrium response to doubled CO<sub>2</sub>, using perturbed variants of HadSM3, a coupled atmosphere/mixed-layer ocean configuration of the HadCM3 climate model. The ensemble explores the effects of perturbations to 31 parameters which control key parameterizations of large-scale cloud, convection, radiative transfer, sea ice, surface and boundary layer process, and dynamical transports (see Murphy *et al.*, 2004, Collins *et al.*, 2006, 2010, Rougier *et al.*, 2009). To compile the ensemble, pairs of simulations using

control (pre-industrial) and doubled CO<sub>2</sub> atmospheric concentrations were produced for 224 perturbation configurations (i.e. 448 simulations in total). Twenty years' of data from each simulation beyond the point of equilibrium provide results for analysis.

Quantifying regional changes and their uncertainty in extreme events for given global warming targets is therefore a simple case of identifying which of the 224 pairs give globally averaged mean changes within certain pre-specified intervals of global target, for example, between 1.5 and 2.5 °C. For a predefined interval, the relevant pairs of simulations can then be studied further to explore regional variations in temperature change consistent with the interval. By ranking the temperature changes at each gridpoint, for example, the regional range consistent with the global interval can also be deduced. This can be expressed as the full range or, to avoid outliers, part of the range.

### 18.3 Results

For the HadSM3 ensemble, 44, 110, and 49 of the 224 pairs gave globally averaged increases in the intervals 1.5 to 2.5, 2.5 to 3.5, and 3.5 to 4.5 °C respectively. The maps in

**Fig. 18.1** show some aspects from the 44 pairs in the 1.5 to 2.5 °C range. The top row shows changes in the surface temperature for extreme hot days corresponding to the 99th percentile. This roughly corresponds to the hottest day of each summer. The relevant day is identified separately in the control and double CO<sub>2</sub> components of each of the 44 pairs, with the change defined as the difference between the two components. The left and right panels show the lower and upper estimates encompassing the central 80% range of the 44 ranked changes, i.e. from the 4th and 40th ranked changes respectively. The ranking is done separately for each grid box. The second row of maps shows the equivalent changes but for the hottest 7-day period found in each of the simulations of the 44 pairs. Since 20 years of data are analysed, this corresponds to an empirical return period of 20 years.

The principal result shown by the maps in **Fig. 18.1** is the large difference in warming over land compared to the 1.5 to 2.5 °C globally averaged warming which the 44 runs give. Even in the lower estimate, warming in many regions exceeds the central 2 °C of the global temperature increase. The principal reason for this discrepancy is the reduced warming over oceans which, by covering 70% of the globe, exerts an overall lowering effect on the globally

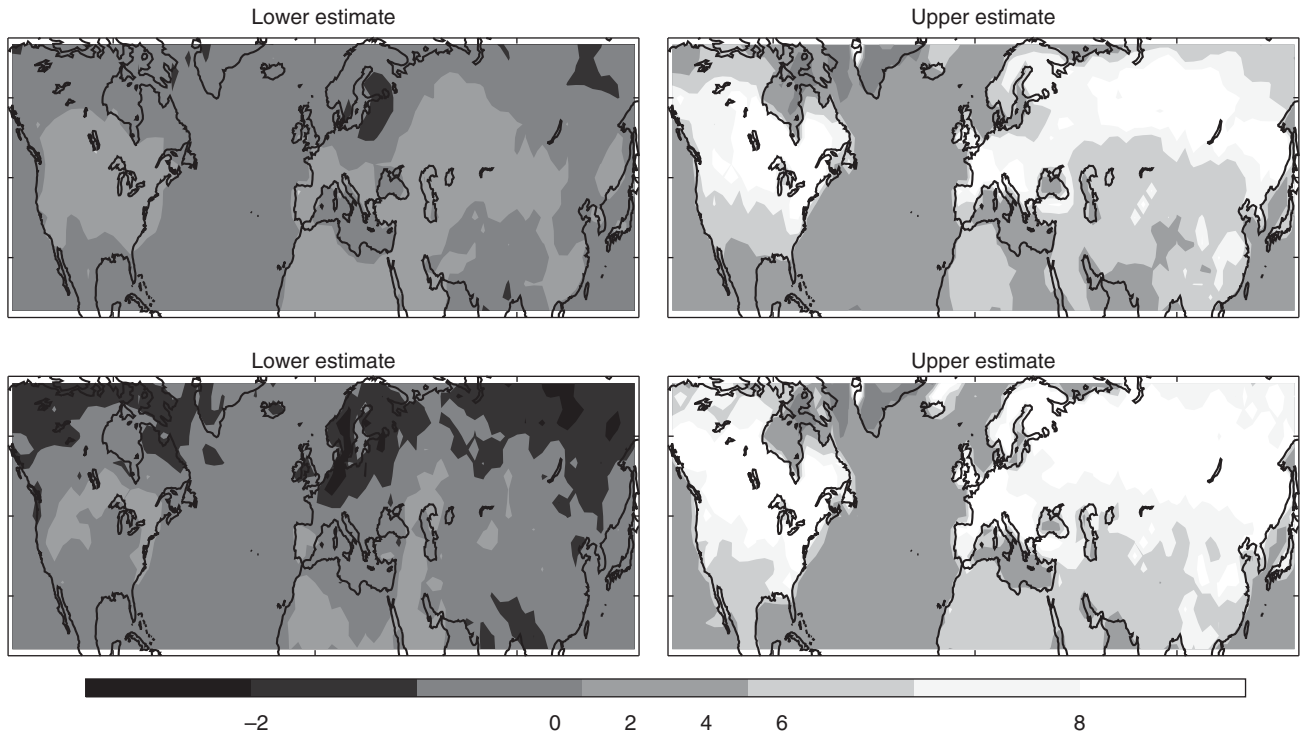


Fig. 18.1. Lower 10% and upper 90% estimates covering the central 80% range of temperature increases (°C) in the 99th percentile of daily maximum summer (June to August) temperature (top row), and heat waves lasting at least 7 days with a 20 year return period (bottom row), for the 44 ensemble members of globally averaged warming within the range 1.5–2.5 °C. The lower and upper estimates show the 4th and 40th of the 44 ranked relevant responses to CO<sub>2</sub> doubling respectively. (Figure from Clark *et al.*, 2010)

Table 18.1. Lower 10% and upper 90% estimates of area averaged changes in surface temperature from ensemble members simulating a globally averaged warming within the range 1.5 to 2.5 °C. Lower and upper estimates come from the 4th and 40th of the 44 ranked changes (ranked separately at each gridbox).

	Change (°C) in temperature during 99th percentile days (hottest day of year)		Change (°C) in average temperature during hottest 7-day period	
	Lower estimate	Upper estimate	Lower estimate	Upper estimate
W North America	2.3	6.2	1.3	7.5
E North America	3.1	8.1	2.1	9.8
N Europe	0.5	6.6	-1.1	9.2
S Europe	2.7	6.4	1.4	7.5
Eastern Asia	2.0	6.0	0.8	7.5

averaged temperature increase. Table 18.1 summarizes the findings of Fig. 18.1 by showing area averages of the lower and upper estimates of the temperature changes for five regions. A striking result in the table is the difference between the lower and upper estimates. While the globally averaged warming range of the 44 pairs is no greater than 1.0 °C (by their adherence to the 1.5 to 2.5 °C interval), the range in large parts of eastern Canada, western Europe, and northern Asia is of several degrees. Estimate ranges were approximately equally as large for the 110 and 49 pairs of HadSM3 simulations which gave globally averaged warming in the ranges of 2.5 to 3.5 and 3.5 to 4.5 °C (not shown). Regional changes (also not shown) of land for these 110 and 49 pairs were also considerably greater than their globally averaged warming values.

#### 18.4 Plausibility of the upper estimates

Estimates such as those shown in Fig. 18.1 give an illustration of what could happen with a 1.5 to 2.5 °C warming. However, they give no indication of their relative merit. Therein lies a possible danger for adaptation, from a possible assumption that the upper estimates come from simulations which are somehow less plausible and could be ignored because they look too large compared to the global target.

To address this issue, root mean squared errors (RMSE) were calculated between the control components of the 44 pairs (from which Fig. 18.1 was produced), and gridded observations for a set of 15 variables, including temperature, sea level pressure, precipitation, total cloud cover, as well as surface and atmosphere heat fluxes. These were normalized by corresponding RMSEs from 16 independent

Table 18.2. Simulation errors, normalized against IPCC (2007) models for HadSM3 members whose response to CO<sub>2</sub> doubling is between 1.5 and 2.5 °C. M\_Low and M\_High columns show scores averaged for the members where local responses were below and above the upper estimates shown in Fig. 18.1 for the regions in Table 18.1.

	W North America	E North America	N Europe	S Europe	E Asia
M_Low	1.29	1.30	1.31	1.30	1.30
M_High	1.38	1.36	1.29	1.30	1.30

models contributed to the IPCC AR4 (2007) and then averaged over the 15 variables to produce a global error metric M for each of the 44 control members. The approach has aspects similar to those used by Murphy *et al.*, 2004 and Reichler and Kim, 2008. For the regions in Table 18.1, Table 18.2 shows the average scores for those pairs giving increases in the 99th percentile of summer daily maximum temperature above and below (rows M\_HIGH and M\_LOW respectively) the upper estimates shown in Fig. 18.1. The scores in the table show that the HadSM3 ensemble has skill comparable to the IPCC ensemble despite the IPCC models each having fully coupled ocean–atmosphere systems, whereas the HadSM3 did not. More importantly though, the scores suggest that those members giving the largest estimates are no less plausible than the rest of the HadSM3 members.

#### 18.5 Role of soil drying on range of regional warming

Narrowing the range between the lower and upper estimates in Fig. 18.1 may, however, be possible by considering the inter-dependence of variables. The HadSM3 ensemble data can be used, for example, to examine the effect that soil moisture has on the air temperature. By evaporation, soil moisture acts to cool the air close to the surface (e.g. Brabson *et al.*, 2005). If the soil moisture in a particular region is small relative to elsewhere, with all other factors being equal, solar radiation will have a relatively greater propensity for warming the surface and the air close to it. Future changes in soil moisture could thus exert an influence on local temperature beyond that caused by the background, global warming. For regions with already dry soils in the present day, further drying is unlikely since moisture is already scarce. As a result, future temperature increases relative to the present day are unlikely to be enhanced due to changes in soil moisture. On the other hand, for regions with relatively damp soils in the present day, future reductions in soil moisture are possible and where this occurs, the reduction in

evaporative cooling by the reduced soil moisture is likely to enhance the temperature increases relative to the background global warming. The extent of this influence, however, depends on a critical threshold of soil moisture below which reductions act to restrain evaporation. For wet soils with a present day and future moisture greater than such a threshold, reductions in moisture may not be sufficient to constrain evaporation. In these situations, enough moisture remains present to maintain evaporation at present day values, giving little or no temperature enhancement.

Figure 18.2 demonstrates how the variations in drying are associated with regional temperature changes. Percentiles of soil moisture ( $P_{\text{soil}}$ ) are deduced for each HadSM3 grid box over land by ranking the daily soil moisture and taking 100 equally spaced values from the ranked series. This is done for both the control and doubled  $\text{CO}_2$  simulations of the 44 HadSM3 pairs which contributed to

Fig. 18.1. By comparing the two sets of  $P_{\text{soil}}$ , changes in the distribution of soil moisture from  $\text{CO}_2$  doubling can thus be deduced. By comparing temperature changes for the days of soil percentiles with large decreases in soil moisture with days of no decrease in moisture, the warming enhancement associated with drying can then be calculated. This is shown as the map in Fig. 18.2a. For Canada, Europe, and Russia, warming enhancement is large and corresponds roughly with the regions of greatest temperature increase in Fig. 18.1. For some regions, for example, over Africa, Mexico, and India however, the enhancement is different. There are also some areas where the enhancement does not match the patterns in Fig. 18.1.

For an explanation of pattern mismatches, and more importantly of the range in temperature between the estimates in Fig. 18.1, a closer examination is required. To do this, three example members from the HadSM3 ensemble

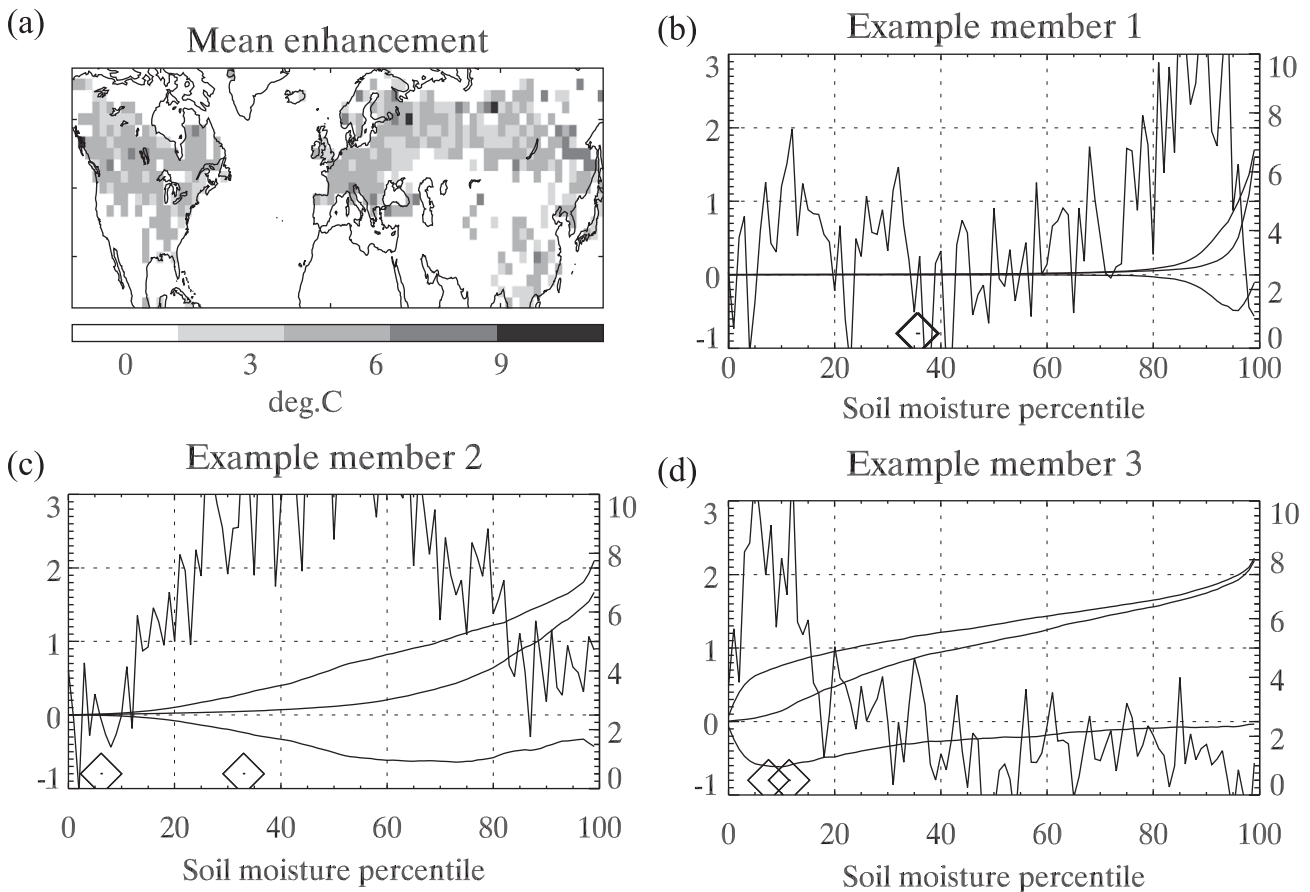


Fig. 18.2 (a) Ensemble mean average change in daily maximum temperature (Tmax) for percentiles of normalized soil moisture (SM) whose SM value decreases from above 0.5 to below 0.5 with a change exceeding 0.1, minus the average Tmax change for percentiles where SM remains above 0.5. (b-d) Relationships, for each SM percentile, between normalized SM and Tmax change for Northern Italy, from three examples. In each panel, the two uppermost smooth lines show simulated control and  $2 \times \text{CO}_2$  values of normalized SM respectively, and the lowest smooth line the difference. All three smooth lines use the left-hand scale. The noisy line in each panel shows the average Tmax change (right-hand scale) for the days corresponding to each SM percentile. The diamonds indicate the SM percentile corresponding to TX99 in the control and  $2 \times \text{CO}_2$  simulations respectively. SM percentiles 0 and 100 correspond to the driest and dampest days of summer respectively. (Figure from Clark *et al.*, 2010)

for an example grid box (in Northern Italy) have been chosen. Panels b, c, and d illustrate the relationship between temperature and soil moisture changes for these choices. The two uppermost smooth lines in the panels show the soil moisture for each soil moisture percentile in the control and doubled CO<sub>2</sub> simulations respectively. The difference between the two lines is shown by the third smooth line in each panel. The noisy line in each panel shows the temperature change (using the right-hand axis) between the control and doubled CO<sub>2</sub> simulations corresponding to each soil moisture percentile. Example member 1 thus presents a control CO<sub>2</sub> simulation in which soil moisture is extremely small for most summer days. With CO<sub>2</sub> doubling, no further drying is possible and corresponding temperature increases, for these days, beyond the global 2 °C background warming are negligible. For member 2, drying is possible and associated with enhanced warming. For member 3, although moderate drying occurs for most summer days, it is only in the driest days that drying has an enhancing effect on the future temperature increases. The implications of these patterns on extreme heat events thus depend on where these events sit in the spectrum of soil moisture. For the 99th temperature percentile events (of the type whose changes were presented earlier in Fig. 18.1), these are shown by the diamonds in Fig. 18.2. In the first example, the extreme temperature events are clearly associated with already dry conditions in the control and little drying and temperature increase with CO<sub>2</sub> doubling. This member is associated with the lower estimate panel in Fig. 18.1. Conversely, in example member 3, the extreme temperature events are associated with a part of the soil moisture distribution where drying with CO<sub>2</sub> doubling is large and temperature changes also large. This member is associated with the upper estimate in Fig. 18.1. Plots (not shown here) for other regions suggest this association between soil moisture and temperature applies more broadly. For already arid regions, such as North Africa and Mexico, hot days are already dry in all HadSM3 simulations so there is little possibility for future drying, with associated considerably smaller ranges in the temperature change compared to regions where soil moisture differs heavily between the HadSM3 simulations.

## 18.6 Conclusions

Using a large ensemble of climate model simulations, this chapter has shown a simple method for determining possible ranges in regional temperature changes for prescribed globally averaged temperature increases. The results clearly illustrate how globally averaged warming of between 1.5 and 2.5 °C could manifest itself on regional scales with a warming considerably greater than the overall

global mean. A wide range in regional warming within the simulations, considerably greater than the range of the global average from which the simulations were selected, has also emerged as a clear result. By examining the relative performance of the control parts of the simulations compared to observations, little evidence was found which would enable the largest regional changes to be ruled out.

Uncertainty in future soil moisture change was found to be strongly associated with the range in temperature changes. Reduction of this uncertainty thus appears key to reducing the overall range in temperature change.

## 18.7 Acknowledgments

The author would like to thank James Murphy and Simon Brown for their invaluable contributions to this chapter.

## References

- Brabson, B. B., D. H. Lister, P. D. Jones, and J. P. Palutikof (2005). Soil moisture and predicted spells of extreme temperatures in Britain, *J. Geophys. Res.*, **110**, D05104.
- Clark, R., T. Murphy, J. M., and Brown, S. J., (2010). Do global warming targets limit heat wave risk? *GRL*, **37**, L17703
- Collins, M., B. B. Booth, B. Bhaskaran, G. R. Harris, J. M. Murphy, D. M. H. Sexton, and M. J. Webb (2011). Climate model errors, feedbacks and forcings: a comparison of perturbed physics and multi-model ensembles. *Clim. Dyn.* **36**, 1737–1766.
- Collins, M., B. B. Booth, G. R. Harris, et al. (2006). Towards quantifying uncertainty in transient climate change *Clim. Dyn.* **27**, 127–147.
- EU/EC Communication (2009), available at <http://eur-lex.europa.eu/LexUriServ/LexUriServ.do?uri=COM:2009:0039:FIN:EN:HTML> (2009)
- IPCC, (2007): *Climate Change 2007: The Physical Science Basis. Contribution of Working Group I to the Fourth Assessment Report of the Intergovernmental Panel on Climate Change* [Solomon, S. et al (eds.)]. Cambridge University Press, Cambridge, UK and New York, NY, USA, 996 pp.
- Murphy, J.M., D. M. H. Sexton, D. N. Barnett, et al. (2004). Quantification of modelling uncertainties in a large ensemble of climate change simulations. *Nature* **430**, 768–772.
- Reichler, T. and J. Kim (2008). How well do coupled models simulate today's climate? *Bull. Am. Met. Soc.* **89**, 303–311.
- Rougier, J., D. M. H. Sexton, J. M. Murphy, and D. Stainforth (2009). Analysing the climate sensitivity of the HadSM3 climate model using ensembles from different but related experiments. *J. Clim.* **22**, 3540–3557.
- Sutton, R. T., B. Dong, and J. M. Gregory (2007). Land/sea warming ratio in response to climate change: IPCC AR4 model results and comparison with observations. *Geophys. Res. Lett.* **34**, L02701

# 19

## Cold-air outbreaks over East Asia associated with blocking highs: mechanisms and their interaction with the polar stratosphere

Hisashi Nakamura, Kazuaki Nishii, Lin Wang,  
Yvan J. Orsolini, and Koutarou Takaya

### 19.1 Introduction

The East Asian winter monsoon is one of the factors that dominate regional climate over the Far East and western North Pacific. Cold air is advected into the mid-latitude Far East by the prevailing monsoonal northerlies between the Siberian high (SH) and the Aleutian low (AL). At the same time, poleward heat transport is stronger than in any other region in the Northern Hemisphere (Higuchi *et al.*, 1991, Nakamura *et al.*, 2002). By sustaining a sharp meridional temperature gradient around Japan and abundant supply of heat and moisture from the warm ocean to the dry, cold, continental air mass, the winter monsoon can also influence storm track activity over the North Pacific (Blackmon *et al.*, 1977, Hoskins and Valdes, 1990, Nakamura, 1992, Nakamura *et al.*, 2002).

Sub-seasonal intensification of the winter monsoon accompanies a cold surge or a cold-air outbreak, giving rise to an abrupt temperature drop, severe frost, freezing rain, and heavy snowfalls over the Far East (Boyle and Chen, 1987, Jeong *et al.*, 2008). The influence of a cold surge often reaches as far south as southern China (Wu and Chan, 1997), and, rarely, it may even influence convective activity over the Maritime Continent (Ding and Krishnamurti, 1987). Many previous studies of cold-air outbreaks have focused on atmospheric circulation and lower-troposphere heat budgets (Boyle and Chen, 1987, Ding and Krishnamurti, 1987, Clark *et al.*, 1999). Nevertheless, it has been pointed out that sub-seasonal monsoon variability is closely linked to upper-tropospheric wave-like circulation anomalies (Suda, 1957, Joung and Hitchman, 1982, Lau and Lau, 1984, Hsu and Wallace, 1985, Wu and Chan, 1997, Takaya and Nakamura, 2005a). More recently, the influence of a blocking ridge that forms over the subpolar western North Pacific on sub-seasonal SH intensity has also been demonstrated (Takaya and Nakamura, 2005b).

The wave-like circulation anomalies over Eurasia may also be related to interannual SH variability via the Eurasian (EU) teleconnection pattern (Gong *et al.*, 2001) defined by Wallace and Gutzler (1981) or the Scandinavian pattern (Bueh and Nakamura, 2007), identified by Barnston and Livezey (1987). However, it has been pointed out that more zonally symmetric anomalies associated with the Arctic Oscillation or Northern Hemisphere annular mode (NAM; Thompson and Wallace, 1998, 2000, 2001) may influence interannual variability of the winter monsoon (Gong *et al.*, 2001, Wu and Wang, 2002, Gong and Ho, 2004, Jhun and Lee, 2004, Jeong and Ho, 2005). The winter monsoon is also known to exhibit multi-decadal variations (Nakamura *et al.*, 2002, Panagiotopoulos *et al.*, 2005, Wang *et al.*, 2009).

This chapter highlights recent progress in the study of the variability of the SH and East Asian winter monsoon. We focus on the interaction of the upper-level circulation anomalies with the surface air temperature (SAT) gradient, which is shown to be essential to the sub-seasonal amplification of the cold SH (Takaya and Nakamura, 2005a, 2005b). We also examine monsoon variability over interannual and decadal time scales, with particular attention given to the associated modulation of planetary waves. Because of their large upward group velocity, the planetary waves over the Far East can act as a vertical “connector” between the troposphere and the stratosphere (Nakamura *et al.*, 2010). As a surface manifestation of tropospheric planetary waves, the East Asian winter monsoon varies seasonally and interannually with modulated activity and structure of the planetary waves (Chen *et al.*, 2005, Wang *et al.*, 2009, Takaya and Nakamura, 2013), which can have specific impacts on the Arctic stratosphere. As revealed by (among others) Koldstad *et al.* (2010), the SH variability and associated cold-air outbreaks into East Asia are linked to the variability of the stratospheric polar vortex.

## 19.2 Upstream influence on winter monsoon variability

Cold-air outbreaks into the mid-latitude Far East are known to follow sub-seasonal SH amplification that occurs in conjunction with a Rossby wave train propagating from the North Atlantic along the subpolar westerly jet (Suda, 1957, Joung and Hitchman, 1982, Lau and Lau, 1984). Interestingly, for the first application of his wave theory, Rossby *et al.* (1939) looked to sub-seasonal SH fluctuations in relation to variations of zonal-mean westerlies (index cycle). Even earlier, Ficker (1911) found a large-scale wave-like SAT pattern over Russia, which can be interpreted today as a surface manifestation of a Rossby wave train propagating at the tropopause level in the course of sub-seasonal SH amplification.

Using the composite analysis and application of a wave-activity flux for stationary Rossby waves formulated by Takaya and Nakamura (2001), Takaya and Nakamura (2005a, 2005b) confirmed the primary importance of the Rossby wave train and an associated upper-level blocking ridge over the Ural Mountains for extreme SH amplification and subsequent cold-air outbreaks into East Asia (Fig. 19.1). They refer to this process as the Atlantic-origin

type or wave-train type of the SH amplification. This wave train resembles the Eurasian (EU) teleconnection pattern. Using a potential-vorticity (PV) inversion (Hoskins *et al.*, 1985), Takaya and Nakamura (2005a) elucidated how an equivalent barotropic anticyclonic anomaly associated with the Ural blocking can strengthen the cold surface SH (Fig. 19.1). The blocking develops to the west of the near-surface cold air mass, which accumulates climatologically over northeastern Siberia. To the southwest of the cold air mass a strong temperature gradient is located over Mongolia. Acting on this SAT gradient, which is equivalent to the equatorward PV gradient from PV thinking, anomalous northeasterlies induced at the surface by the blocking-associated tropopause-level PV anomalies yield anomalous cold air advection. The cold air mass thus pulled southward out of its core region contributes to the amplification of the surface SH. Once developed by the upper-level influence, the surface cold anomaly behaves as a surface thermal Rossby wave (Gill, 1982), acting to move itself eastward along the surface baroclinic zone collocated with a sharp meridional SAT gradient. As a surface thermal Rossby wave, the anomalous cold air thus generated forms an anticyclonic anomaly (Hoskins *et al.*, 1985), yielding anomalous cold advection to its east to

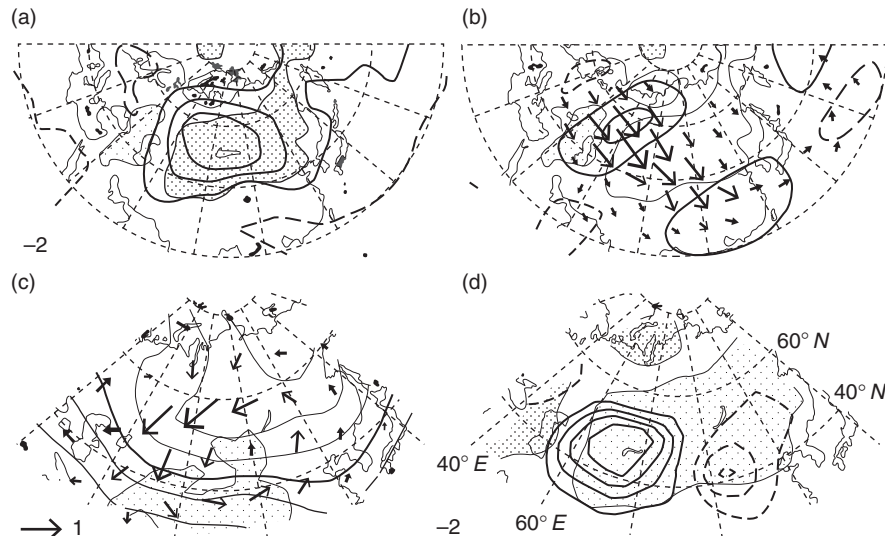


Fig. 19.1. Intra-seasonal intensification of the Siberian High (SH) composed for two days before the peak times of the 20 strongest sub-seasonal events observed around [47°N, 90°E] over 40 recent winters. (a) 250 hPa height anomaly ( $\pm 50, \pm 150, \pm 250, \dots$  m; dashed for negative) and associated wave-activity flux (arrows with scaling (units:  $m^2 s^{-2}$ ) at the lower right). (b) 1000 hPa height anomaly ( $\pm 20, \pm 60, \pm 100, \dots$  m; dashed for negative). In (a) and (b), SAT anomalies are superimposed (contoured for  $\pm 2, \pm 6, \pm 10, \dots$  °C; stippled heavily and lightly for cold and warm anomalies, respectively). (c) Anomalous 1000 hPa wind (arrows with scaling (units:  $ms^{-1}$ )) at the lower left, induced solely by composited 300 hPa PV anomalies, superimposed on total 1000 hPa temperature (contoured for every 8 °C and bold lines for 0 °C). (d) Anomalous tendency in 1000 hPa temperature (contoured for every  $2 ^\circ C day^{-1}$ ; dashed for warm advection) induced solely by the anomalous winds acting on the temperature field in (c). Observed warm and cold 1000 hPa temperature anomalies (stronger than 2 °C) are stippled lightly and heavily, respectively. The height anomalies and their tendencies are all rescaled with  $f(45^\circ N)/f(\text{lat.})$ , and the compositing was based on eight-day low-pass-filtered fields. After Takaya and Nakamura (2005a), Nakamura *et al.* (2010), and based on the NCEP/NCAR reanalysis data set.

shift the cold air itself eastward. Behind this eastward-moving cold anomaly, the upper-level blocking anticyclone continues to induce the anomalous cold advection, acting to retard the eastward migration of the cold anomaly and thereby retain its amplification. The anticyclonic anomaly thus built up has a baroclinic structure whose phase lines tilt northwestward with height, and it thereby transports heat poleward with a distinct upward component of Rossby wave-activity flux. More detailed discussions on the mechanisms through which the upper-level blocking anomaly intensifies the surface cold SH are given by Takaya and Nakamura (2005a) and by Nakamura *et al.* (2010).

Similar to this intra-seasonal connection, there is also a close connection between variations in the Ural blocking and SH at the interannual scale. In fact, Wang *et al.* (2010) found that the winter-mean Ural-blocking index exhibits a high positive correlation (+0.69) with the winter-mean SH intensity, which is significant at the 99% confidence level for the 44 winters since 1957. The winter-mean SH intensity, defined as sea-level pressure (SLP) averaged within [40–65°N, 80–120°E] as in Panagiotopoulos *et al.* (2005), is correlated with the Ural blocking more closely than with any other single teleconnection pattern investigated in previous studies. The Ural blocking typically accompanies an anticyclonic anomaly near the Kara Sea, and a pair of cyclonic anomalies, one over northern Europe and the other over East Asia. These wave-like anomalies are equivalent barotropic, and extend from the surface into the lower stratosphere. The blocking is associated with below normal and above normal lower-tropospheric temperatures over East Asia and northern Siberia, respectively, at the 99% confidence level, which result from the anomalous thermal advection around the blocking high.

### 19.3 Monsoon variability associated with the Western Pacific teleconnection pattern

In addition to the Rossby wave teleconnection from the Atlantic discussed above, intensification of the surface SH also follows a blocking formation over the subpolar western North Pacific (Takaya and Nakamura, 2005b), and the particular flow configuration resembles the positive phase of the western Pacific (WP) pattern (Pavan *et al.*, 2000, Rivière, 2010). As one of the major atmospheric teleconnection patterns over the wintertime Northern Hemisphere (Wallace and Gutzler, 1981), the WP pattern is characterized by north–south dipolar height anomalies over the western North Pacific. In this particular type of SH amplification, which may be called the Pacific-origin type (Takaya and Nakamura, 2005b), the SH centre is shifted to the northeast of its climatological mean position. Unlike the Atlantic-origin type, there is no indication of wave train

propagation to the amplifying blocking ridge from upstream (Fig. 19.2). Rather, the ridge develops as an anticyclonic anomaly and slowly retrogresses from the Aleutian region into eastern Siberia (Branstator, 1987, Kushnir, 1987). This process may be viewed as local inward (cyclonic) breaking of the polar vortex associated with the blocking formation (Swanson, 2000, 2001), because low-PV anomaly penetrates into the polar vortex and then becomes isolated within it, while high-PV air associated with the climatological trough over the Far East becomes elongated to the south of the blocking ridge. The development and maintenance of the blocking ridge occur under feedback forcing from synoptic-scale eddies migrating along the poleward-deflected Pacific storm track through their anomalous transport of vorticity (Takaya and Nakamura, 2005b). In contrast, the anomalous eddy heat transport acts to keep the blocking anomaly equivalent barotropic, especially during its amplification stage, even near the surface where the anticyclonic anomaly is accompanied by a warm anomaly. A distinct exception is observed to the northeast of the Tibetan Plateau, where a cold anticyclonic anomaly forms near the surface as the upper-level blocking anomaly is anchored to the north of the Sea of Okhotsk. It was revealed through a PV inversion diagnosis (Takaya and Nakamura, 2005b) that the upper-level blocking anomaly induces anomalous northeasterlies that advect an extremely cold air mass accumulated climatologically over eastern Siberia towards the northeast of the Plateau. After the peak time, the near-surface cold anticyclonic anomaly extends south into the mid-latitude Far East, where a cyclonic anomaly associated with the WP pattern still remains in the upper troposphere. Such baroclinic structure of the circulation anomalies over eastern China and Japan associated with the anomalous cold surface air is common to both the Atlantic-origin and Pacific-origin types of extreme SH amplification.

As one of the major factors that influence the East Asian winter monsoon (Takaya and Nakamura, 2005a, 2005b), the WP pattern significantly modifies the seasonal evolution of the tropospheric planetary waves (Takaya and Nakamura, 2013). In the upper troposphere the climatological seasonal progression from November to January over the extratropical Northern Hemisphere is characterized by an overall decline in geopotential height associated with tropospheric cooling (not shown). However, the height decline is not uniform over the extratropics. Over the Pacific, the decline is particularly enhanced in a zonally elongated mid-latitude domain from the Far East into the eastern North Pacific. In contrast, over the subpolar region between central Siberia and Alaska, the corresponding height decline is much reduced, and the climatological December–January tendency is even slightly positive around the Bering Strait (Figs. 19.2–19.3). These height

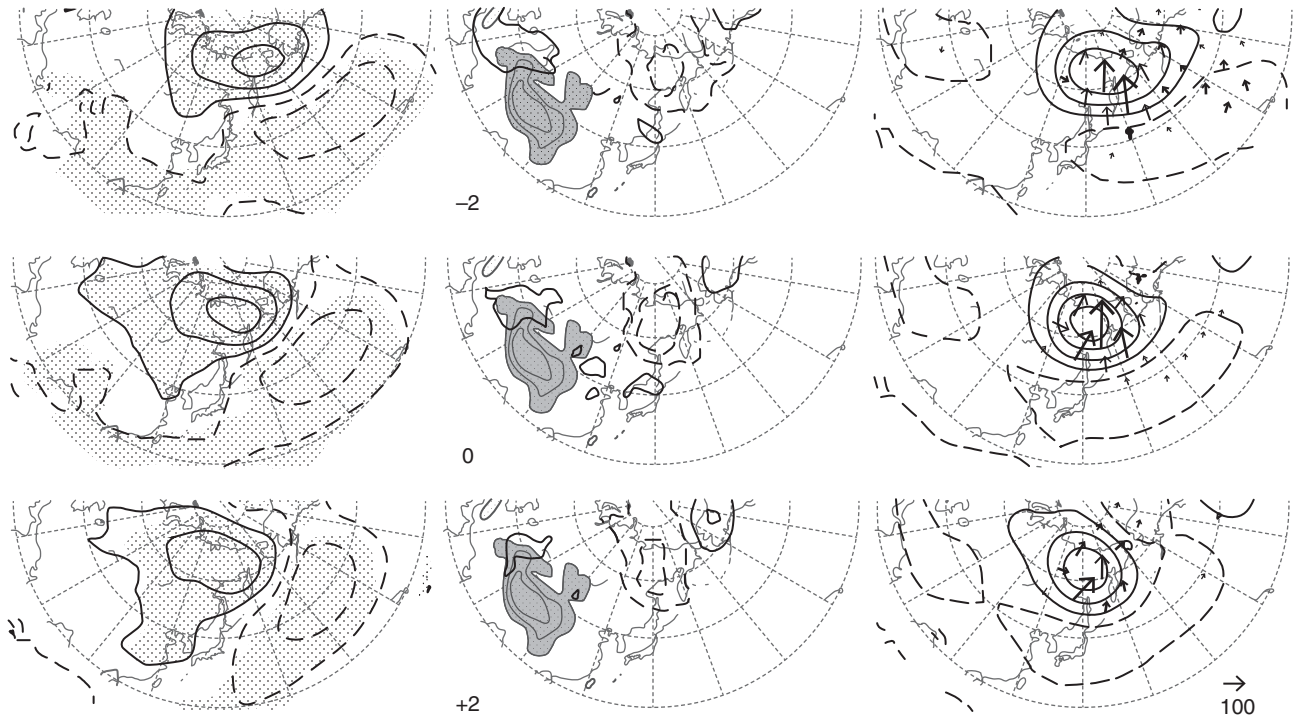


Fig. 19.2. Composite time evolution for the 20 strongest blocking events at the 250 hPa level observed around a target grid point [67°N, 140°E] over 40 recent winter seasons that induced the intra-seasonal SH intensification. The compositing was performed relative to the peak time (day 0) for each of the events. (left) 8-day low-pass-filtered 1000 hPa height anomalies normalized by a factor of  $\sin(45^\circ\text{N})/\sin(\text{lat.})$ , contoured every 40 m from  $\pm 20$  m (dashed for negative values). The anomalies significant at the 95% confidence level are stippled, (middle) 8-day low-pass-filtered temperature anomalies at the lowest model level ( $\sigma = 0.995$ ) (contoured every 4 °C from  $\pm 2$  °C; solid and dashed lines for cold and warm anomalies, respectively). Surface elevation over 1500 m is shaded. (right) 8-day low-pass-filtered 250 hPa height anomalies rescaled with  $f(45^\circ\text{N})/f(\text{lat.})$ , contoured every 100 m from  $\pm 50$  m (dashed for negative values). The horizontal component of wave-activity flux is superimposed with arrows whose scaling (units:  $\text{m}^2\text{s}^{-2}$ ) is given near the lower right panel. After Takaya and Nakamura (2005b) and based on the NCEP/NCAR reanalysis data set.

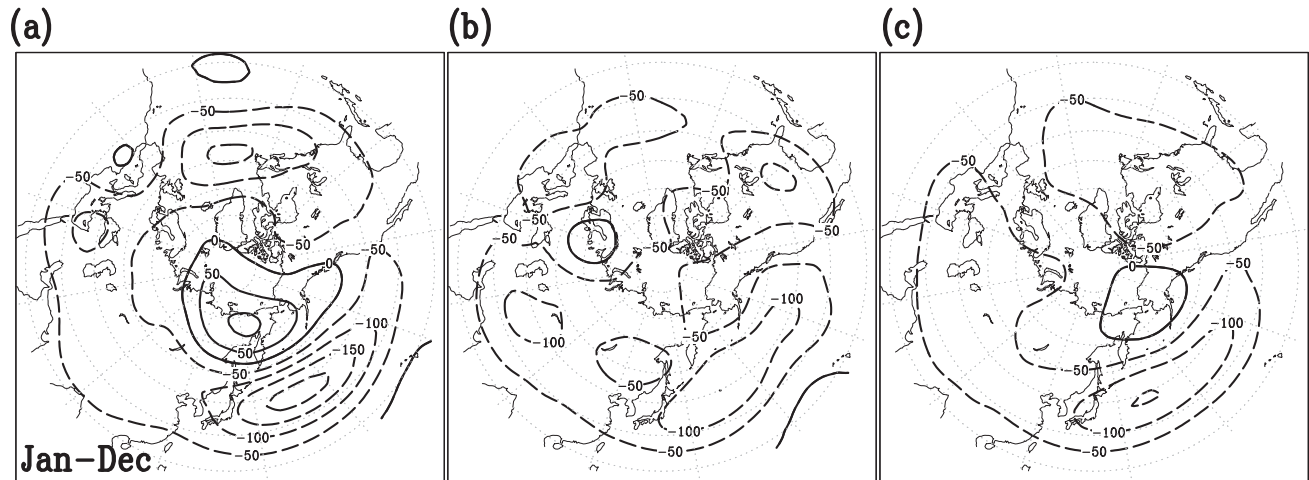


Fig. 19.3. Tendency in 250 hPa height (m) from November to January with colouring convention given below (c). Composed for 10 Januaries of (a) enhanced, and (b) weakened monsoon activity, and (c) climatological tendency. After Takaya and Nakamura (2013) and based on the NCEP/NCAR reanalysis data set

tendencies are a manifestation of the climatological development of the wintertime planetary waves, characterized by the southeastward development of the Far-Eastern pressure trough and the northwestward development of a pressure ridge over the Rockies. This climatological development of the planetary waves is enhanced substantially into extremely cold Januaries over the mid-latitude Far East associated with the positive WP pattern (Fig. 19.3a), including the enhancement of the northwestward development of the pressure ridge towards eastern Siberia, and the southeastward development of the Far Eastern upper-level trough extending into the mid-latitudes. These enhanced tendencies are consistent with the development of the dipolar height anomalies associated with the WP pattern.

However, the enhanced development of the planetary waves mentioned above does not necessarily manifest their amplification in a (quasi-) linear sense, but rather it leads to their enhanced breaking within the Pacific sector. The development of a blocking anticyclone associated with the positive WP pattern occurs near the Far Eastern pressure trough associated with the planetary waves (Fig. 19.4a), leading to the cyclonic breaking of the planetary-wave trough and subsequent reduction in magnitude. In other words, this is a destructive interference between climatological planetary waves and the dipolar height anomalies associated with the WP pattern (Nishii *et al.*, 2010, Woollings *et al.*, 2010). Consequently, the upward planetary-wave propagation is suppressed, resulting in the intensification of the polar vortex and the anomalous cooling of the Arctic stratosphere (Fig. 19.4b–d; Orsolini *et al.*, 2009). Generally, the blocking formation leads to the weakening and warming of the stratospheric polar vortex. Depending on their geographical locations relative to the pressure ridges and troughs of the planetary waves, some of the blocking events can nevertheless cause the strengthening and cooling of the Arctic stratospheric polar vortex by

reducing upward propagation of planetary waves, as is the case over the western North Pacific (Nishii *et al.*, 2011). In fact, brief episodes of polar stratospheric cooling observed during the 2009/10 winter were clearly linked to the development of the blocking high in association with the positive phase of the WP pattern (Dörnbrack *et al.*, 2012).

#### 19.4 Long-term modulation of the Siberian high and East Asian winter monsoon

The climate system over the Far East and North Pacific underwent a significant shift in the mid 1970s in association with the Pacific Decadal Oscillation (Nitta and Yamada, 1989, Trenberth and Hurrell, 1994, Schneider and Couruelle, 2005). A comparison between two periods, one before (1957–1976) and one after (1977–2000) this climatic shift, suggests possible modulations in seasonal impacts of the Ural blocking on the East Asian winter climate. During the earlier period, 850 hPa temperature anomalies over East Asia associated with the blocking were confined mainly to the north of 40°N (Fig. 19.5a), while the corresponding anomalies in the later period spread as far southeastward as about 25°N (Fig. 19.5b). Furthermore, the correlation coefficient between the winter-mean indices of the Ural blocking and SH intensity increased from +0.60 in the earlier period to +0.74 in the later period, exceeding the 99% confidence level in both periods. Correspondingly, the fraction of the interannual SH variance explained by the Ural blocking variability had increased from only 36% to 55%.

The aforementioned multi-decadal modulations were accompanied by enhanced downstream influence of the Ural blocking with a stronger cyclonic anomaly over East Asia in the mid-tropospheric wave-like anomalies associated with the blocking (Fig. 19.5c–d). This enhancement of

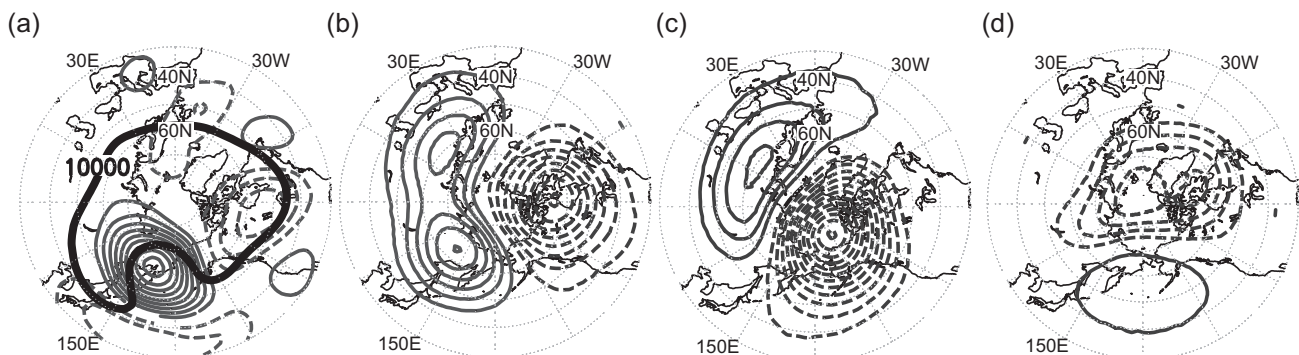


Fig. 19.4. Polar stereographic maps (poleward of 30°N) of (a) 250 hPa and (b) 30 hPa height anomalies (grey lines for every 50 m; dashed for negative; zero lines omitted) composed for the peak times of the 18 strongest positive events of the Western Pacific (WP) pattern. Based on the JRA-25 reanalysis. (c and d) As (b), but for (c) +5 and (d) +20 days, respectively, relative to the peak time. A black thick line in (a) indicates 250 hPa height of 10,000 m. See Nishii *et al.* (2010) for the corresponding detailed plots.

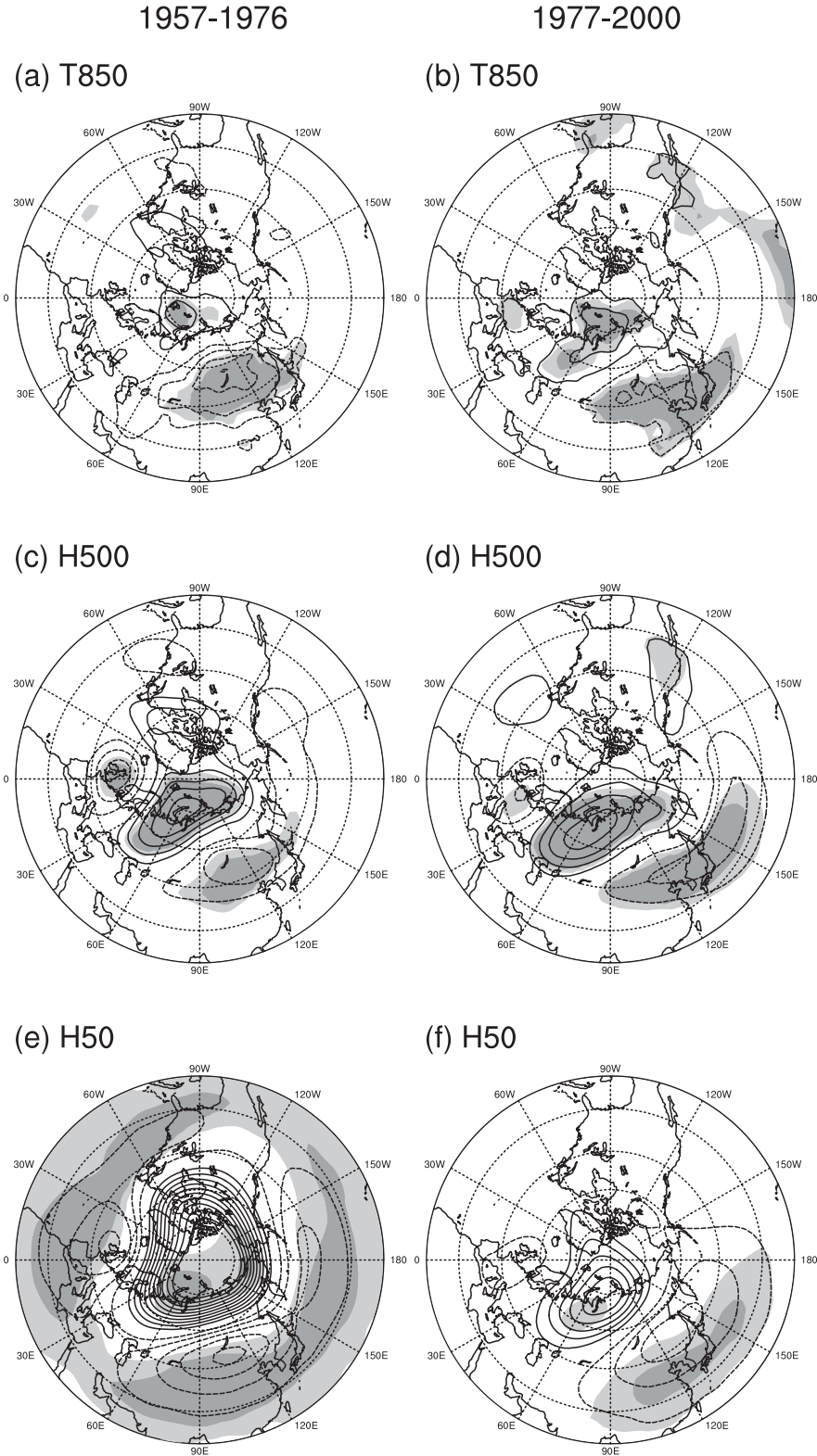


Fig. 19.5. Regression (contours) and correlation (shading) of detrended winter mean (a) 850 hPa air temperature, (c) 500 hPa geopotential height, and (e) 50 hPa geopotential height on detrended winter-mean index of the Ural blocking (UBI) for the period 1957–1976 based on the ERA40 data set. (b), (d), (f) are as (a), (c), (e), but for the period 1977–2000. Contour intervals are 0.5 °C in (a) and (b), and 10 gpm in (c)–(f). Dark and light shading indicates the 99% and 95% confidence levels, respectively. Modified from Wang *et al.* (2010).

the downstream extension may be explained partly from the viewpoint of stratosphere–troposphere dynamical coupling (Wang *et al.*, 2010). The Ural blocking accompanies a lower-stratospheric anticyclonic anomaly over the

Arctic region and cyclonic anomalies in mid latitudes, and this vertical coupling had weakened into the later period with a reduction in statistical significance (Fig. 19.5e–f). This feature is indicative of a compensatory tendency

between the upward influence of the Ural blocking into the stratosphere and its downstream influence into East Asia, which is suggested by the 3D propagation of stationary Rossby wave activity (Wang *et al.*, 2010). This compensatory tendency may be related to multi-decadal modulations of the stratospheric polar night jet (PNJ) and associated polar vortex. During the earlier period, the polar vortex was in its weak regime (Christiansen, 2003), which favoured the upward propagation of planetary waves, perhaps including the wave propagation from the Ural blocking ridge. In the later period, the PNJ and stratospheric polar vortex strengthened (Christiansen, 2003), and this suppressed the upward propagation of planetary waves. Consequently, the stationary Rossby wave activity emanating from the Ural blocking may become more confined to the troposphere, leading to a stronger downstream influence on SH intensity.

The intensity of the East Asian winter monsoon is known to show multi-decadal variations (Shi, 1996, Nakamura *et al.*, 2002, Panagiotopoulos *et al.*, 2005). An index defined by Wang and Chen (2014b) identifies three distinctive periods of monsoon intensity: two strong epochs, one from the mid 1970s to the mid 1980s and the other since the early 2000s, separated by a weak epoch. The multi-decadal variations of the winter monsoon were associated with modulations of the planetary waves and the intensity of the Pacific jet stream (Nakamura *et al.*, 2002). Compared with the strong epochs, the weak epoch was characterized by a weaker planetary-wave trough over the Far East and the Pacific jet, enhanced eddy activity along the Pacific storm track in midwinter (Nakamura *et al.*, 2002), and was accompanied by higher winter-mean SAT over East Asia (Wang and Chen, 2014a), a reduced likelihood of cold-air outbreaks into China (Wang *et al.*, 2009), enhanced precipitation over South China, and reduced precipitation over the mountainous regions of northern Taiwan (Hung and Kao, 2010, Wang and Feng, 2011).

In addition to these distinct climatic changes associated with multi-decadal variations of the winter monsoon, there are subtle but significant differences between the two strong epochs. During the earlier epoch (1976–1987), a significant negative SAT anomaly as strong as  $-1^{\circ}\text{C}$  was observed, mainly along the East Asian coast (Fig. 19.6a), but also in northwestern Europe, southeastern North America, and the central North Pacific, while no significant warming was observed in the extratropical Northern Hemisphere. In contrast, during the recent strong epoch (2004–2012) a significant negative SAT anomaly, which exceeds  $-3^{\circ}\text{C}$ , is extending zonally, but confined to the inland area of northern East Asia (Fig. 19.6d), while significant positive SAT anomalies are observed over the Arctic and the Tibetan Plateau. Circulation anomalies observed during the earlier epoch (Fig. 19.6b–c) resembled those associated with NAM, but those from the recent

epoch do not. While exerting some influence (Jhun and Lee, 2004, Jeong and Ho, 2005, Wang *et al.*, 2009), NAM may not necessarily be the controlling factor of the decadal variability in the winter monsoon. However, a common feature between the two epochs is a significant barotropic anticyclonic anomaly around the Ural Mountains (Fig. 19.6b, c, e, and f), suggestive of the crucial contribution of the Ural blocking to the multi-decadal variations of the winter monsoon. In fact, the Ural blocking frequency decreased in around 1985, and then increased again in around 2002 (Barriopedro *et al.*, 2006, Wang and Chen, 2014a).

## 19.5 Summary and discussion

This chapter has considered recent progress in the study of the variability of the SH and East Asian winter monsoon. The interaction between upper-level circulation anomalies and a blocking anticyclone with a SAT gradient, which induces anomalous cold advection to intensify the cold SH (Takaya and Nakamura, 2005a, 2005b), is the main focus of the chapter. This is the mechanism through which the cold surface anomaly is induced by a warm, equivalent barotropic anomaly associated with a blocking anticyclone developing either over the Ural Mountains in association with a Rossby wave train from the Atlantic, or over the subpolar western North Pacific associated with the positive phase of the WP pattern.

Consequently, we also considered monsoon variability at interannual and decadal time scales from the viewpoint of modulations of the planetary waves. We concentrated on the monsoon variability associated with the WP pattern, whose positive phase corresponds to a blocking flow configuration over the Far East and western North Pacific. The seasonal tendency towards the positive WP pattern into midwinter leads to intensification of the winter monsoon associated with the enhanced seasonal development of planetary waves over the mid-latitude Pacific sector. Conversely, the blocking flow configuration leads to breaking of the planetary wave trough over the Far East and its weakening at subpolar latitudes, resulting in the reduction in upward propagation of the planetary waves and thereby the strengthening/cooling of the stratospheric polar vortex. If superimposed on the cooling trend in the stratosphere associated with global warming, this dynamically forced stratospheric cooling may enhance ozone depletion in the Arctic stratosphere. However, as noted earlier, the influence of a blocking high on the stratosphere is sensitive to its geographical location relative to the geographical phase of the climatological planetary waves (Woollings *et al.*, 2010, Nishii *et al.*, 2011). Thus, a blocking high that develops in association with a wave train from the Atlantic for SH intensification acts to weaken the stratospheric

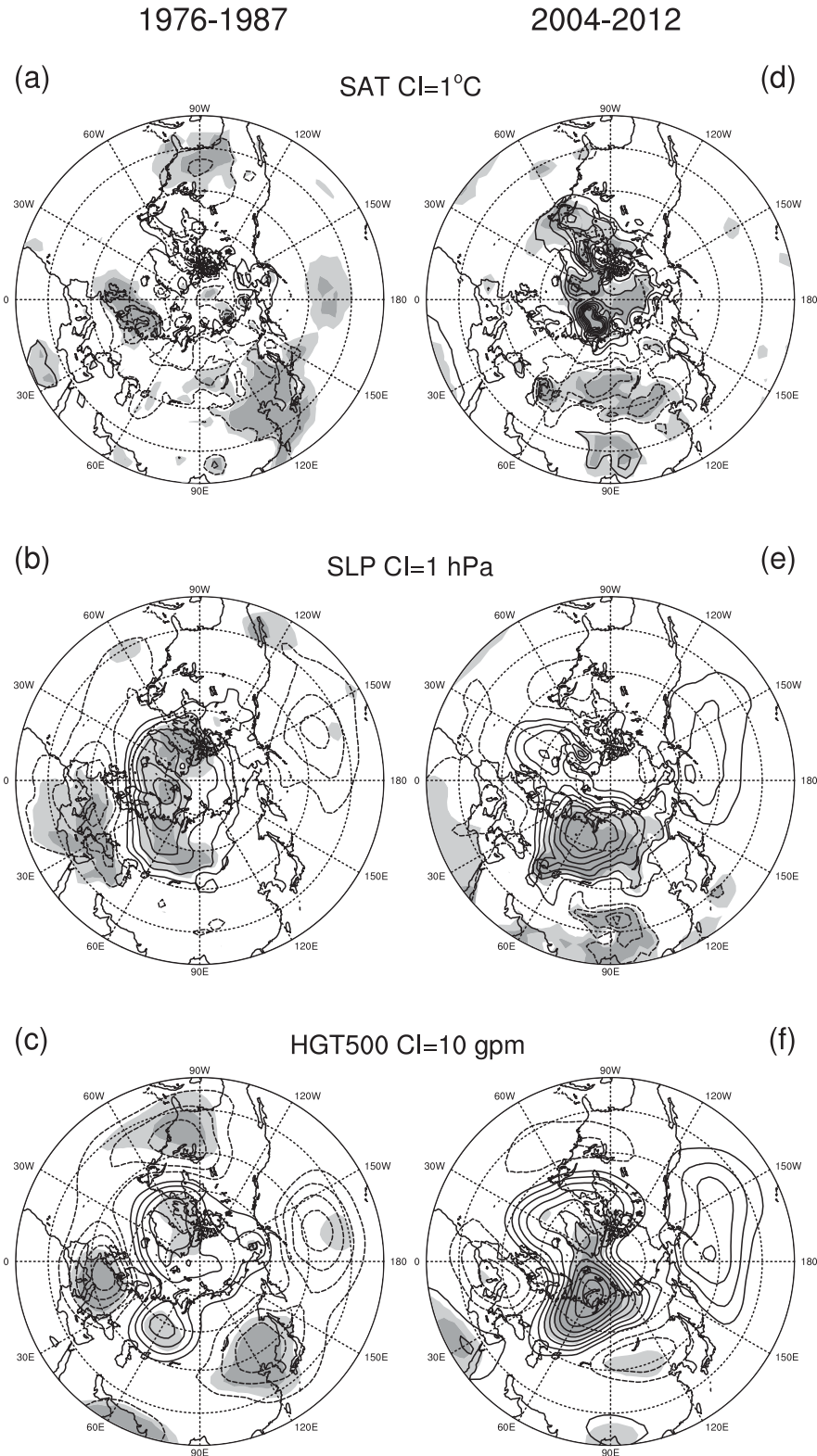


Fig. 19.6. Composited winter-mean anomalies in (a) surface air temperature (SAT; every 1 °C), (b) sea-level pressure (SLP; every 1 hPa), and (c) 500 hPa geopotential height (every 10 gpm) for the earlier epoch (1976–1987) of the strong East Asian winter monsoon based on the NCEP/NCAR reanalysis data set. The negative anomalies are defined as the deviations from the corresponding composites for the epoch (1988–2003) of the weak monsoon. Negative anomalies are indicated with dashed lines. Dark and light shading indicates the 99% and 95% confidence levels, respectively. (d)–(f) are as (a)–(c), but for the corresponding later epoch (2004–2012) of the strong monsoon. After Wang and Chen (2014a).

polar vortex (Nishii *et al.*, 2011). In fact, a significant anticyclonic anomaly has been identified around the Ural Mountains as a robust precursory signal in the troposphere for the NAM-related weakening of the stratospheric polar vortex (Takaya and Nakamura, 2008, Koldstad *et al.*, 2010).

It should be emphasized that the linkage between the winter monsoon variability and stratospheric variability is not necessarily a one-way process from the former to the latter. In fact, the weakening of the stratospheric polar vortex tends to be translated into the troposphere, acting to set up conditions favourable for cold-air outbreaks into mid latitudes (Thompson and Wallace, 2001, Koldstad *et al.*, 2010). The influence of the Ural blocking on a cold-air outbreak into East Asia may depend on the strength of the stratospheric PNA (Wang *et al.*, 2010). Furthermore, Kodera *et al.* (2013) argued that, in some cases, a blocking high over the western North Pacific can develop in association with a planetary wave packet that has been reflected back from the stratosphere. Further study is required to deepen our understanding of the two-way nature of the monsoon–stratosphere linkage and to assess whether this linkage can be used to improve predictions of monsoon variability.

One may wonder what forces a wave train over northern Eurasia or the positive WP pattern that induces the winter monsoon variability. As it tends to be observed during the cold phase (La Niña) of El Niño/Southern Oscillation (ENSO; Horel and Wallace, 1981), the positive WP pattern provides a linkage between the East Asian winter monsoon and ENSO. Likewise, decadal-scale anomalous coolness in sea surface temperature (SST) in the tropical Pacific may set a condition favourable for the formation of the positive WP pattern. In addition to these remote influences from the tropics, SST anomalies in the mid-latitude North Pacific may also force anomalies similar to the WP pattern that influences the polar stratosphere, as suggested by a recent numerical study (Hurwitz *et al.*, 2012). Although not discussed in detail here, Pacific SST anomalies either in the tropics or mid latitudes can also change the intensity of the Aleutian low (Horel and Wallace, 1981, Nitta and Yamada, 1989, Trenberth and Hurrell, 1994, Taguchi *et al.*, 2012), through which the winter monsoon may be modulated (Nakamura *et al.*, 2002). Recent studies have also suggested that rapidly declining ice cover in the Kara/Barents seas in late autumn may have resulted in the recent intensification of the winter monsoon and associated cold conditions prevailing over Eurasia (Honda *et al.*, 2009, Inoue *et al.*, 2012). A stationary Rossby wave train that acts to intensify the SH may be forced directly by enhanced sensible heat release from the ocean due to reduced ice cover, and indirectly through feedback forcing from synoptic-scale cyclones and anticyclones migrating along

a deflected storm track. Further study is necessary to clarify the mechanisms through which these boundary-forcing mechanisms can generate teleconnection to the winter monsoon, and this improved understanding could be used to increase the predictability of monsoon variability. In addition, further study is also required to establish how global warming will alter the winter monsoon. Global warming itself should ultimately weaken the winter monsoon, but in the course of its weakening, the monsoon may temporarily intensify, for example, under the influence of the decline in sea ice cover in the Arctic.

## 19.6 Acknowledgements

This work was supported in part by the Grant-in-Aid in Innovative Areas 2205 and 2409 of the Japan Society for Promotion of Science (JSPS) and the Global Environment Research Fund (A1201) of the Japanese Ministry of Environment. We thank an anonymous reviewer for giving us useful comments.

## References

- Barnston, A. G. and Livezey, R. E. (1987). Classification, seasonality and persistence of low-frequency atmospheric circulation patterns. *Monthly Weather Review*, **115**, 1083–1126.
- Barriopedro, D., García-Herrera, R., Lupo, A. R., and Hernández, E. (2006). A climatology of Northern Hemisphere blocking. *Journal of Climate*, **19**, 1042–1063.
- Blackmon, M. L., Wallace, J. M., Lau, N.-C., and Mullen, S. L. (1977). An observational study of the Northern Hemisphere wintertime circulation. *Journal of the Atmospheric Sciences*, **34**, 1040–1053.
- Boyle, J. S. and Chen, T.-J. (1987). Synoptic aspects of the wintertime East Asian monsoon. In *Monsoon Meteorology*, C.-P. Chang and T. N. Krishnamurti, Eds., Oxford University Press, 125–160.
- Branstator, G. (1987). A striking example of the atmosphere's leading traveling pattern. *Journal of the Atmospheric Sciences*, **44**, 2310–2323.
- Bueh, C. and H. Nakamura (2007). Scandinavian pattern and its climatic impact. *Q. Journal of the Royal Meteorological Society*, **133**, 2117–2131.
- Chen, W., Yang, S., and Huang, R.H. (2005). Relationship between stationary planetary wave activity and the East Asian winter monsoon. *Journal of Geophysical Research*, **110**, D14110, doi:10.1029/2004JD005669.
- Christiansen, B. (2003). Evidence for nonlinear climate change: Two stratospheric regimes and a regime shift. *J. Climate*, **16**, 3681–3690.
- Clark, M. P., Serreze, M. C., and Robinson, D. A. (1999). Atmospheric controls on Eurasian snow extent. *International Journal of Climatology*, **19**, 27–40.

- Ding, Y. and Krishnamurti, T. N. (1987). Heat budget of the Siberian high and the winter monsoon. *Mon. Weather Review*, **115**, 2428–2449.
- Dörnbrack, A., Pitts, M.C., Poole, L.R., et al. (2012). The 2009–2010 Arctic stratospheric winter – General evolution, mountain waves and predictability of an operational weather forecast model. *Atmospheric Chemistry and Physics*, **12**, 3659–3675.
- Ficker, H. V. (1911). Das Fortschreiten der Erwärmungen (der Wärmewellen) in Rußland und Nordasien, *Sitz. ber. Wiener Akad. Wiss., Abt. 2a*, **120**, 745–835.
- Gill, A. E. (1982). *Atmosphere–Ocean Dynamics*, 662 pp., Academic Press, London.
- Gong, D.-Y., Wang, S.-W., and Zhu, J.-H. (2001). East Asian winter monsoon and Arctic oscillation. *Geophysical Research Letters*, **28**, 2073–2076.
- Gong, D.-Y. and Ho, C.-H. (2004). Intra-seasonal variability of wintertime temperature over East Asia. *International Journal of Climatology*, **24**, 131–144.
- Higuchi, K., Lin, C. A., Shabbar, A., and Knox, J. L. (1991). Interannual variability of the January tropospheric meridional eddy sensible heat transport in the Northern Hemisphere. *Journal of the Meteorological Society of Japan*, **69**, 459–472.
- Honda, M., Inoue, J., and Yamane, S. (2009). Influence of low Arctic sea-ice minima on anomalously cold Eurasian winters. *Geophysical Research Letters*, **36**, L08707, doi:10.1029/2008GL037079.
- Horel, J. D. and Wallace, J. M. (1981). Planetary-scale atmospheric phenomena associated with the Southern Oscillation. *Monthly Weather Review*, **109**, 813–829.
- Hoskins, B. J. and Valdes, P. J. (1990). On the existence of storm tracks. *Journal of the Atmospheric Sciences*, **47**, 1854–1864.
- Hoskins, B. J., McIntyre, M. E., and Robertson, A. W. (1985). On the use and significance of isentropic potential vorticity maps. *Quarterly Journal of the Royal Meteorological Society*, **111**, 877–946.
- Hsu, H.-H. and Wallace, J. M. (1985). Vertical structure of wintertime teleconnection patterns, *Journal of the Atmospheric Sciences*, **42**, 1693–1710.
- Hung, C.-W. and Kao, P.-K. (2010). Weakening of the winter monsoon and abrupt increase of winter rainfalls over northern Taiwan and southern China in the early 1980s. *Journal of Climate*, **23**, 2357–2367.
- Hurwitz, M. M., Newman, P. A., and Garfinkel, C. I. (2012). On the influence of North Pacific sea surface temperature on the Arctic winter climate. *Journal of Geophysical Research*, **117**, D19110, doi:10.1029/2012JD017819.
- Inoue, J., Hori, M. E., and Takaya, K. (2012). The role of Barents Sea ice in the wintertime cyclone track and emergence of a warm-Arctic cold-Siberian anomaly. *Journal of Climate*, **25**, 2561–2568.
- Jeong, J.-H. and Ho, C.-H. (2005). Changes in occurrence of cold surges over East Asia in association with Arctic Oscillation. *Geophysical Research Letters*, **32**, L14704, doi:10.1029/2005GL023024.
- Jeong, J.-H., Kim, B. M., Ho, C. H., and Noh, Y. H. (2008). Systematic variation in wintertime precipitation in East Asia by MJO-induced extratropical vertical motion. *Journal of Climate*, **21**, 788–801.
- Jhun, J.-G. and Lee, E.-J. (2004). A new East Asian winter monsoon index and associated characteristics of the winter monsoon. *Journal of Climate*, **17**, 711–726.
- Joung, C.H. and Hitchman, M.H. (1982). On the role of successive downstream development in East Asian polar air outbreaks. *Monthly Weather Review*, **110**, 1224–1237.
- Lau, N.-C. and Lau, K.-M. (1984). The structure and energetics of midlatitude disturbances accompanying cold-air outbreaks over East Asia. *Monthly Weather Review*, **112**, 1309–1327.
- Kodera, K., Mukougawa, H., and Fujii, A. (2013). Influence of the vertical and zonal propagation of stratospheric planetary waves on tropospheric blockings. *Journal of Geophysical Research*, **118**, 8333–8345.
- Kolstad, E., Breiteig, T. and Scaife, A. A. (2010). The association between stratospheric weak polar vortex events and cold air outbreaks in the Northern Hemisphere. *Quarterly Journal of the Royal Meteorological Society*, **136**, 886–893.
- Kushnir, Y. (1987). Retrograding wintertime low-frequency disturbance over the North Pacific Ocean. *Journal of the Atmospheric Sciences*, **44**, 2727–2742.
- Nakamura, H. (1992). Midwinter suppression of baroclinic wave activity in the Pacific. *Journal of the Atmospheric Sciences*, **49**, 1629–1642.
- Nakamura, H., Izumi, T., and Sampe, T. (2002). Interannual and decadal modulations recently observed in the Pacific storm track activity and East Asian winter monsoon. *Journal of Climate*, **15**, 1855–1874.
- Nakamura, H., Miyasaka, T., Kosaka, Y., Takaya, K., and Honda, M. (2010). Northern Hemisphere extratropical tropospheric planetary waves and their low-frequency variability: Their vertical structure and interaction with transient eddies and surface thermal contrasts. *Climate Dynamics: Why Does Climate Vary?* D. Sun and F. Bryan, Eds., *Geophysical Monograph*, 189, American Geophysical Union, 149–179.
- Nishii, K., Nakamura, H., and Orsolini, Y.J. (2010). Cooling of the wintertime Arctic stratosphere induced by the Western Pacific teleconnection pattern. *Geophysical Research Letters*, **37**, L13805, doi:10.1029/2010GL043551.
- Nishii, K., Nakamura, H., and Orsolini, Y. J. (2011). Geographical dependence observed in blocking high influence on the stratospheric variability through enhancement and suppression of upward planetary-wave propagation. *Journal of Climate*, **24**, 6408–6423.
- Nitta, T. and Yamada, S. (1989). Recent warming of tropical sea surface temperature and its relationship to the Northern Hemisphere circulation. *Journal of the Meteorological Society of Japan*, **67**, 375–383.
- Orsolini, Y. J., Karpechko, A. Y., and Nikulin, G. (2009). Variability of the Northern Hemisphere polar stratospheric cloud potential: The role of North Pacific disturbances. *Quarterly Journal of the Royal Meteorological Society*, **135**, 1020–1029.
- Panagiotopoulos, F., Shahgedanova, M., Hannachi, A., and Stephenson, D. B. (2005). Observed trends and teleconnections of the Siberian High: A recently declining center of action. *Journal of Climate*, **18**, 1411–1422.

- Pavan, V., Tibaldi, S., and Brankovic, C. (2000). Seasonal prediction of blocking frequency: Results from winter ensemble experiments. *Quarterly Journal of the Royal Meteorological Society*, **126**, 2125–2142.
- Rivi  re, G. (2010). Role of Rossby wave breaking in the west Pacific teleconnection. *Geophysical Research Letters*, **37**, L11802.
- Rossby, C.-G. and collaborators, (1939). Relation between variations in the intensity of the zonal circulation of the atmosphere and the displacements of the semi-permanent centers of action. *Journal of Marine Research*, **2**, 38–55.
- Schneider, N. and Cournuelle, B.D. (2005). The forcing of the Pacific Decadal Oscillation. *Journal of Climate*, **18**, 4355–4373.
- Shi, N. (1996). Features of the East Asian winter monsoon intensity on multiple time scale in recent 40 years and their relation to climate. *Journal of Applied Meteorological and Climatology*, **7**, 175–182.
- Suda, K. (1957). The mean pressure field characteristic to persistent cold waves in the Far East. *Journal of the Meteorological Society of Japan*, **35**, 192–198.
- Swanson, K. L. (2000). Stationary wave accumulation and the generation of low-frequency variability of zonally varying flows. *Journal of the Atmospheric Sciences*, **57**, 2262–2280.
- Swanson, K. L. (2001). Blocking as a local instability to zonally varying flows. *Quarterly Journal of the Royal Meteorological Society*, **127**, 1341–1355.
- Taguchi, B., Nakamura, H., Nonaka, M., et al. (2012). Seasonal evolutions of atmospheric response to decadal SST anomalies in the North Pacific Subarctic Frontal Zone: Observations and a coupled model simulation. *Journal of Climate*, **25**, 111–139.
- Takaya, K. and Nakamura, H. (2001). A formulation of a phase-independent wave-activity flux of stationary and migratory quasi-geostrophic eddies on a zonally varying basic flow. *Journal of the Atmospheric Sciences*, **58**, 608–627.
- Takaya, K. and Nakamura, H. (2005a). Mechanisms of intraseasonal amplification of the cold Siberian High. *Journal of the Atmospheric Sciences*, **62**, 4423–4440.
- Takaya, K. and Nakamura, H. (2005b). Geographical dependence of upper-level blocking formation associated with intraseasonal amplification of the Siberian High. *Journal of the Atmospheric Sciences*, **62**, 4441–4449.
- Takaya, K. and Nakamura, H. (2008). Precursory changes in planetary wave activity for midwinter surface pressure anomalies over the Arctic. *Journal of the Meteorological Society of Japan*, **86**, 415–427.
- Takaya, K. and Nakamura, H. (2013). Interannual variability of the East Asian winter monsoon and related modulations of the planetary waves. *Journal of Climate*, **26**, 9445–9461.
- Thompson, D. W. J. and Wallace, J. M. (1998). The Arctic Oscillation signature in the wintertime geopotential height and temperature fields. *Geophysical Research Letters*, **25**, 1297–1300.
- Thompson, D. W. J. and Wallace, J. M. (2000). Annular modes in the extratropical circulation. Part I: Month-to-month variability. *Journal of Climate*, **13**, 1000–1016.
- Thompson, D. W. J. and Wallace, J. M. (2001). Regional climate impacts of the Northern Hemisphere annular mode. *Science*, **293**, 85–89.
- Trenberth, K. E. and Hurrell, J. W. (1994). Decadal atmosphere-ocean variations in the Pacific. *Climate Dynamics*, **9**, 303–319.
- Wallace, J. M. and Gutzler, D. S. (1981). Teleconnections in the geopotential height field during the Northern Hemisphere winter. *Monthly Weather Review*, **109**, 784–812.
- Wang, L., Chen, W., Zhou, W., et al. (2010). Effect of the climate shift around mid 1970s on the relationship between wintertime Ural blocking circulation and East Asian climate. *International Journal of Climatology*, **30**, 153–158.
- Wang, L. and Chen, W. (2014a). The East Asian winter monsoon: Re-amplification in the mid-2000s. *Chinese Science Bulletin*, **59**, 430–436.
- Wang, L. and Chen, W. (2014b). An intensity index for the East Asian winter monsoon. *Journal of Climate*, **27**, 2361–2374.
- Wang, L. and Feng, J. (2011). Two major modes of the wintertime precipitation over China. *Chinese Journal of the Atmospheric Sciences*, **35**, 1105–1116.
- Wang, L., Huang, R.H., Gu, L., Chen, W., and Kang, L.H. (2009). Interdecadal variations of the East Asian winter monsoon and their association with quasi-stationary planetary wave activity. *Journal of Climate*, **22**, 4860–4872.
- Woollings, T., Charlton-Perez, A. J., Ineson, S., Marshall, A. G., and Masato, G. (2010). Associations between stratospheric variability and tropospheric blocking. *Journal of Geophysical Research*, **115**, D06108, doi:10.1029/2009JD012742.
- Wu, B. and Wang, J. (2002). Winter Arctic Oscillation, Siberian high and East Asian winter. *Geophysical Research Letters*, **29**, doi:10.1029/2002GL015357.
- Wu, M. C. and Chan, J. C. L. (1997). Upper-level features associated with winter monsoon surges over south China. *Monthly Weather Review*, **125**, 317–340.



## PART V

### **Ocean connections**



# 20

## Response of the Atlantic Ocean Circulation to North Atlantic freshwater perturbations

Henk A. Dijkstra

### 20.1 Introduction and motivation

One of the main breakthroughs in climate research of the last 50 years is the reconstruction of past temperatures (and other properties) from sediment cores and ice cores. Isotope analyses from ice cores on Greenland, for example, provide information on the local temperatures over the last  $10^5$  years. The local temperature anomalies ( $\Delta T$ ) with respect to the mean temperature over the last century are plotted in Fig. 20.1. Slow variations are associated with the development of the last ice age, of which the maximum occurred around 25 kyr ago. What is fascinating in this plot are the relatively rapid transitions (for example between 50 kyr and 20 kyr) with a peak-to-peak amplitude of about  $10^\circ\text{C}$ . A typical period of these oscillations is 1500 years and these are called Dansgaard–Oeschger (DO) events. The DO events indicate that rapid temperature changes, which are not directly related to the (solar) forcing of the system, may occur in the climate system. Further research has indicated that the DO events are associated with changes in Atlantic Ocean circulation (Clement and Peterson, 2008).

The global ocean circulation is driven by momentum fluxes (by the wind), the tides, and affected by fluxes of heat and freshwater at the ocean–atmosphere interface. The buoyancy fluxes influence the surface density of the ocean water and through mixing and advection, density differences are propagated horizontally and vertically. A cartoon of the North Atlantic ocean circulation is provided in Fig. 20.2a. In the North Atlantic, the Gulf Stream transports relatively warm and saline waters northwards. In certain areas (the Greenland Sea and the Labrador Sea), when there is strong cooling in winter, the water column becomes unstably stratified resulting in strong convection. This affects the formation of a water mass called North Atlantic Deep Water (NADW), which overflows the various topographic ridges and enters the Atlantic basin.

This NADW is transported southwards at a depth of about 2–4 km, where it enters the Southern Ocean (Fig. 20.2b). Through upwelling in the Atlantic, Pacific,

and Indian Oceans, the water is brought back to the surface. To close the mass balance the water is eventually transported back to the sinking areas in the North Atlantic. In the Southern Ocean, bottom water is formed which has a higher density than NADW and therefore appears in the abyssal Atlantic (Fig. 20.2b). In the North Pacific no deep water is produced. Together, the deep water formation at high latitudes, the upwelling at lower latitudes, and the horizontal currents that feed these vertical movements are indicated as the three-dimensional global thermohaline (Wunsch, 2002) circulation (THC).

The part of the THC that can actually be measured is called the meridional overturning circulation (MOC), which is the zonally integrated (and hence two-dimensional) volume transport at each latitude and depth. The meridional overturning stream function  $\Psi$  is determined from the meridional velocity component  $v$  through

$$\Psi(\theta, z, t) = -r_0 \cos \theta \int_{\phi_W}^{\phi_E} \int_{-H}^z v(\phi, \theta, z', t) dz' d\phi, \quad (20.1)$$

where  $\phi$  is longitude,  $\theta$  latitude,  $z$  the height above mean sea level,  $t$  time, and  $r_0$  the radius of Earth. Furthermore,  $\phi_W$  and  $\phi_E$  are the (latitude dependent) longitude of the western and eastern boundary of the basin, respectively. Finally,  $H$  is the local bottom depth and  $v(\phi, \theta, z', t)$  the meridional velocity.

The strength and spatial pattern of the MOC are determined by the wind stress and density differences which set up pressure differences driving the flow. There are no observations available to reconstruct the pattern of the MOC, but its strength at  $26^\circ\text{N}$  in the Atlantic is now routinely monitored by the RAPID-MOCHA array (Cunningham *et al.*, 2007). The currently available time series of the MOC strength is shown in Fig. 20.2c, indicating a mean of about 19 Sv with a standard deviation of 5 Sv. At  $26^\circ\text{N}$  the heat transport associated with the Atlantic MOC is estimated to be 1.2 PW (Johns *et al.*, 2011). This heat is transferred to higher latitudes leading to a relatively mild

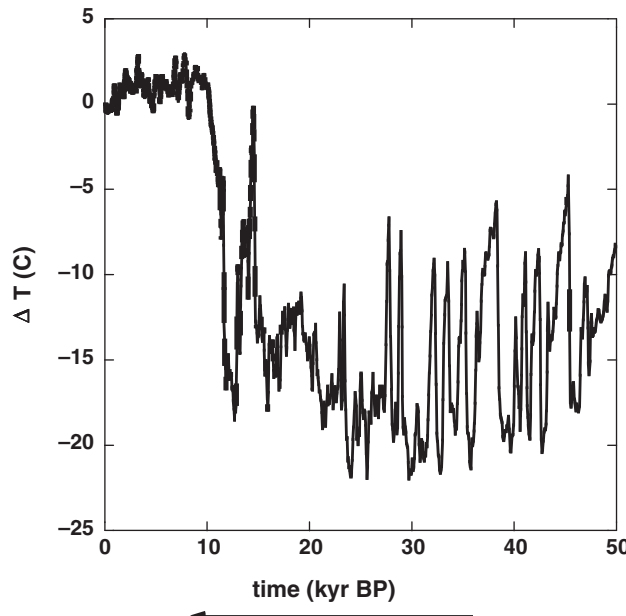


Fig. 20.1. Temperature anomaly (with respect to the mean over the last 100 years) at a location in central Greenland as reconstructed (Andersen and coauthors 2004) from oxygen isotope analysis (1 kyr = 1000 years).

climate over Western Europe, compared to similar latitudes on the eastern Pacific coast.

Changes in the MOC lead to changes in meridional heat transport and hence may induce temperature fluctuations in Greenland. One of the theories of the DO events is that rapid (relative to the changes in the external solar forcing) and large amplitude changes in the MOC occurred. This motivates the main questions addressed in this overview, i.e.

- (i) What are the physical mechanisms that can cause large changes in the MOC?
- (ii) Can such rapid changes occur again in the near future, in particular due to the increase of atmospheric greenhouse gas concentrations?

In Section 20.2, we will address issue (i) by looking at the results of a hierarchy of ocean–climate models, from conceptual models up to Global Climate Models (GCMs). The GCMs also form the basis for answering question (ii) and in Sections 20.3 and 20.4 we will consider whether these models are fit for this purpose. A summary and discussion is provided in Section 20.5.

## 20.2 Sensitivity of the MOC to fresh water perturbations

Henri Stommel was the first to realize that the Atlantic MOC is sensitive to freshwater anomalies in the North

Atlantic (Stommel, 1961). The theoretical model of Stommel is a so-called two-box model (Fig. 20.3a), with an equatorial reservoir (box e) and a polar reservoir (box p) which are connected at the surface and at depth. The circulation between the two boxes is driven by the density difference ( $\rho_p - \rho_e$ ) between the boxes, which in turn is determined by the exchange of heat and fresh water at the ocean–atmosphere surface. Its strength is indicated by  $\Psi$  and for  $\Psi > 0$  the surface circulation is directed from the equatorial to the polar reservoir, as in Fig. 20.3a. Here, the scalar  $\Psi$  mimics the strength of the upper branch of the MOC in the North Atlantic Ocean.

The different steady flow solutions of this model, for which the value of  $\Psi$ , versus the strength of the surface freshwater forcing (represented by a parameter  $\eta_2$ ) shows that there exists a range of freshwater forcing for which two stable states exist (Fig. 20.3b). One state (left panel in Fig. 20.3c usually referred to as the on state) is temperature driven and  $\Psi > 0$ , while for the other state (the off state with  $\Psi < 0$ ) the MOC is salinity driven. When the freshwater strength is increased (while being in the on state), the strength of the MOC decreases down to a point  $L_+$ . Just for values of  $\eta_2$  slightly larger than the value at  $L_+$ , the MOC will collapse and a situation without northern deepwater formation (the off state) will appear. When from the off state the freshwater forcing is decreased, this state will exist down to the value of  $\eta_2$  at the point  $L_-$ . For slightly smaller  $\eta_2$ , the MOC will restore to the on state which is the only state which exists for these values of  $\eta_2$ .

The existence of the regime of multiple equilibria in the Stommel model is due to a (salt advection) positive feedback (Fig. 20.4). If there is a freshwater perturbation in the northern North Atlantic (for example through melting of the Greenland Ice Sheet or additional rainfall), the water will become locally less dense. This leads to a decrease in deepwater formation and hence a weaker MOC. The MOC then transports less salt northward and hence the original freshwater perturbation is amplified. The MOC also transports less heat northward but this anomaly is quickly dissipated by atmospheric damping. The damping time scale of thermal anomalies is in the order of months, while salinity anomalies are effectively undamped by the atmosphere (Stommel 1961).

The 1961 paper by Stommel was neglected for a long time, probably because the two-box model was thought to be highly idealized. However, in 1986 Frank Bryan showed that multiple steady states could occur in a then state-of-the-art three-dimensional ocean model (Bryan, 1986). Although the bifurcation diagram as in Fig. 20.3b is obtained from a relatively simple model, it turns out that this diagram is found in bifurcation studies using a hierarchy of 2D and 3D ocean models. For example, the bifurcation diagram found in the global ocean model, with

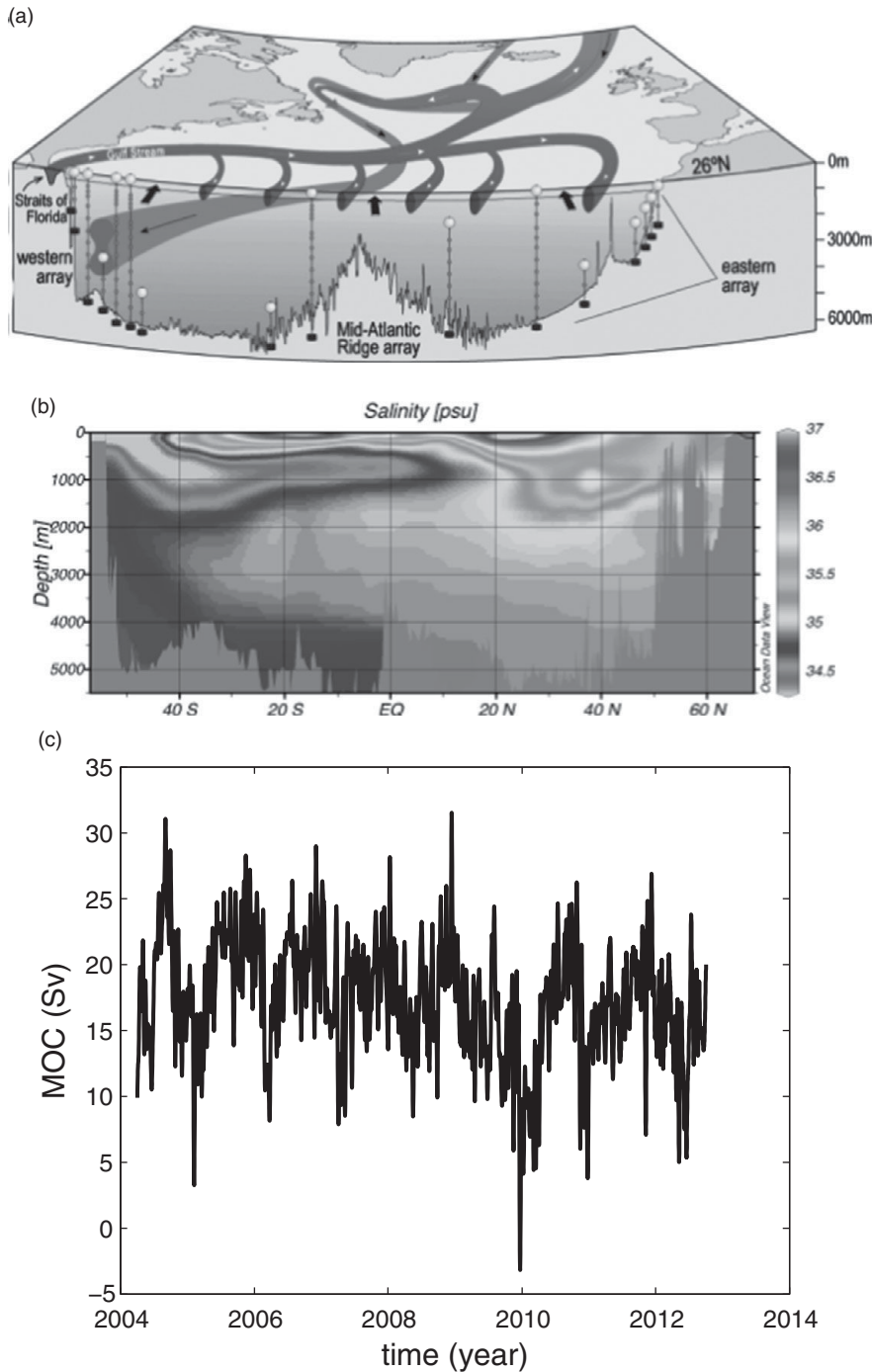
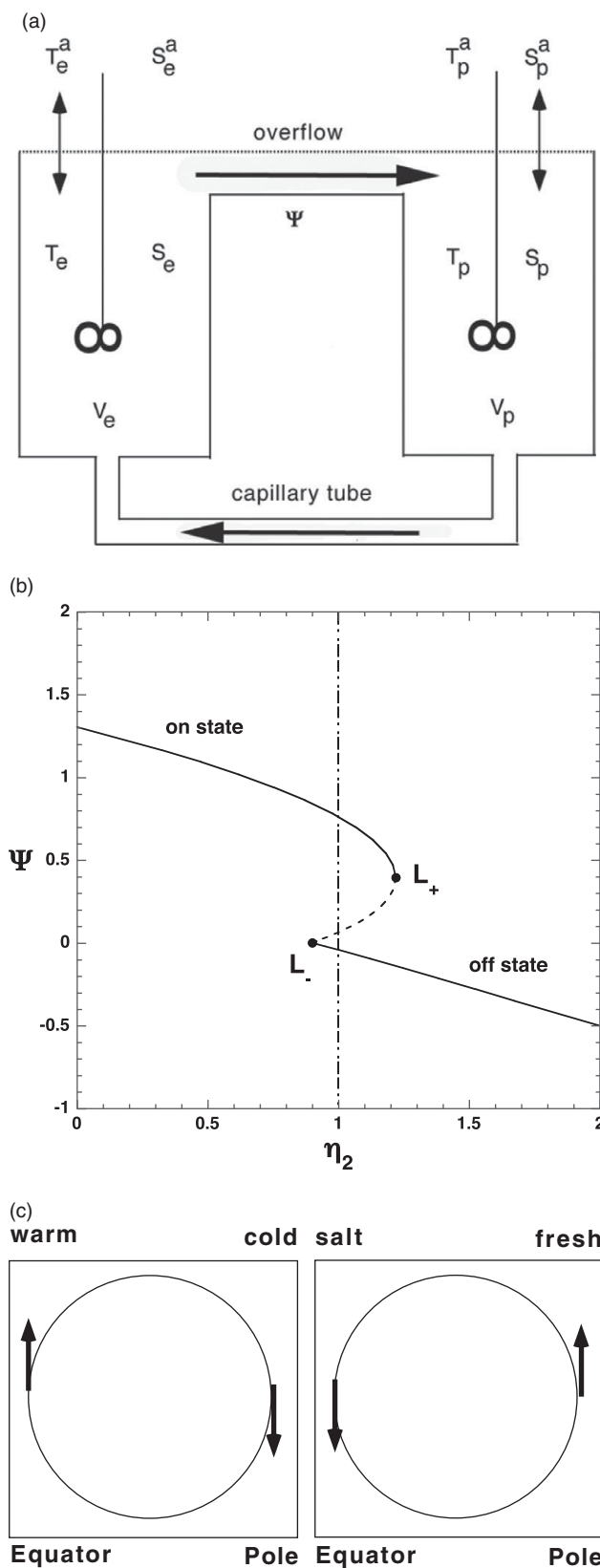


Fig. 20.2. (a) Strongly simplified sketch of the North Atlantic Ocean circulation. In the Atlantic, warm and saline waters flow northward into the deep water formation areas causing a return transport with a dominant component in the western boundary (figure from <http://www.noc.soton.ac.uk/rapidmoc/>). (b) Salinity climatology along the WOCE A16 (north–south) section in the Atlantic. The NADW is the water mass flowing southward at mid-depth. (c) Volume transports of the Atlantic MOC at 26°N as measured by the RAPID-MOCHA array (Cunningham *et al.*, 2007) over the years 2004–2012. (data from <http://www.noc.soton.ac.uk/rapidmoc/>).

a horizontal resolution of about 4°, of Dijkstra and Weijer (2005), is qualitatively similar to that in Fig. 20.3.

Results from a hierarchy of models are currently available to evaluate the response of MOC to freshwater anomalies. In the class of ocean-only models, these range from low-resolution models (such as the one used in Dijkstra and Weijer (2005)) to high-resolution models with a horizontal resolution of 0.1°, such as the Parallel Ocean Model

(POP), results of which will be discussed below. In the class of coupled ocean–atmosphere models, these range from Earth System Models of Intermediate Complexity (EMICs), with usually highly idealized ocean and atmosphere components, towards the GCMs used in CMIP3 and CMIP5 studies, with typical horizontal ocean component resolutions up to 1°. The FAMOUS model, results of which will also be discussed below, is a simplified version of the



UK Hadley Centre GCM, the HadCM3, and has a horizontal ocean-model component resolution of  $2.5^\circ \times 3.75^\circ$ .

For EMICs and GCMs, the bifurcation diagrams cannot be directly computed. In this case, so-called quasi-equilibrium transient simulations are carried out where a parameter  $\gamma_p$  measuring the freshwater anomaly is changed very slowly in time; such simulations are usually referred to as ‘hosing experiments’ (Fig. 20.5a). Here the freshwater anomaly is only applied on a relatively small area in the northern North Atlantic. Starting at the reference solution for  $\gamma_p = 0$ , the upper solution branch in Fig. 20.5a is then followed until  $L_+$  where the solution changes rapidly (‘collapse’ in Fig. 20.5a) to that on the lower branch and follows that branch with increasing  $\gamma_p$ . If from a large value of  $\gamma_p$  the solution is followed with decreasing  $\gamma_p$ , then the lower branch is followed down to  $\gamma_p$  at  $L_-$ , where a transition (‘recovery’ in Fig. 20.5a) occurs to the solution on the upper branch. Examples of such results for several EMICs are provided in Fig. 20.5b.

The most detailed GCM in which a multiple equilibrium regime of the MOC has been found so far is the FAMOUS model (Hawkins *et al.*, 2011). In more detailed models, for example those used in the CMIP3 archive (Drijfhout *et al.*, 2011), no indications for such multiple equilibrium regimes were found. It is fair to say, however, that the required quasi-equilibrium simulations have not yet been performed for these models. It has been suggested that for example ocean–atmosphere feedbacks could be responsible for the disappearance of the multiple equilibrium regimes. When the MOC changes, also the surface forcing fields of the ocean will change (such as the heat flux, the freshwater flux, and the wind stress) which lead in turn to MOC changes. Bifurcation analyses of models which capture these feedbacks, however, show that the effects of these feedbacks do not remove the multiple regime (Den Toom *et al.*, 2012). This is compatible with the results in the FAMOUS model in which also all of these ocean–atmosphere feedbacks are captured.

However, it has so far been difficult (if not impossible) to find off states of the MOC in CMIP3 models, even though large freshwater perturbations have been applied. For example, in the ESSENCE project (Sterl *et al.*, 2008), simulations were done with the ECHAM5-OM1 model (developed by the Max Planck Institute for Meteorology in Hamburg) over the period 2001–2100. The dashed curve in Fig. 20.6a shows the MOC decrease (a 16-member ensemble mean) due to the increase of  $\text{CO}_2$  according to

Fig. 20.3. (a) Sketch of the two-box model in Stommel (1961). (b) Bifurcation diagram of the dimensionless MOC strength  $\Psi$  versus the dimensionless freshwater forcing strength  $\eta_2$ . (c) Sketch of the two states of the Stommel (1961) model with the on state (left) and the off state (right).

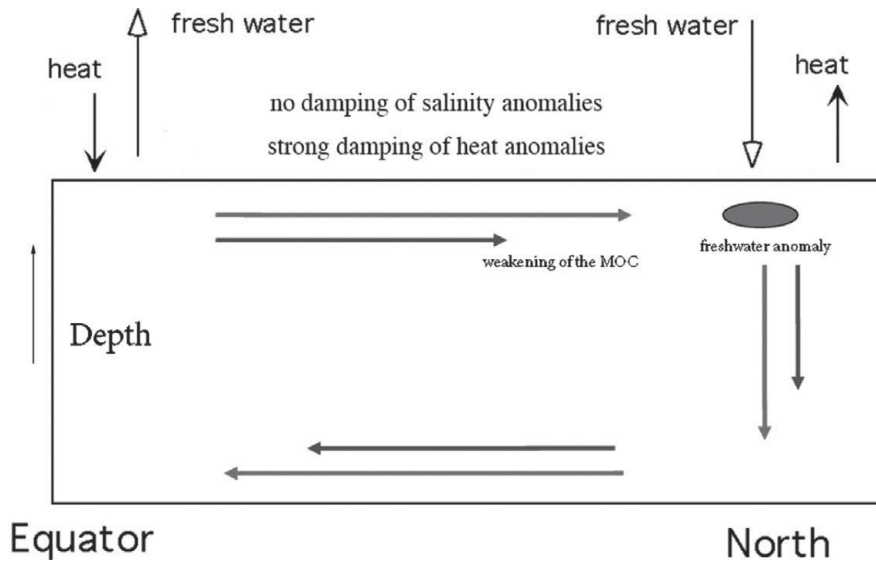


Fig. 20.4. Sketch to illustrate the salt-advection feedback. A freshwater anomaly in the northern part of the Atlantic causes a weakening of the MOC. As a consequence, less salt is transported northward from equatorial areas, which amplifies the original freshwater anomaly.

the SRES-A1B scenario, which is only a few Sv over 100 years. The drawn curve represents the response to an additional freshwater anomaly of 1 Sv (about the volume transport of all the rivers on Earth), and shows a MOC decrease of about 15 Sv over a period of 20 years (Fig. 20.6a). After 25 years, the difference in surface temperature (compared to the year 2000) indeed shows that (Fig. 20.6b) the annual mean surface temperature over a large area in the North Atlantic has decreased by about 10 °C. Although this transition is not one from an on state to an off state (only a weakened on state), the results provide an indication of the impact of the weakening of the MOC. Figure 20.6b also provides support for the theory that the DO events were associated with large changes in the MOC. During the last ice age, there were periods during which large quantities of icebergs were discharged into the North Atlantic. Because of salt-advection feedback, the strength of the MOC decreased rapidly and consequently it became colder on Greenland.

Other CMIP3 GCMs have similar responses to those in Fig. 20.6 and the issue remains of why there seem to be no collapsed MOC states in these GCMs. A related question is whether these models adequately represent the response of the Atlantic MOC to freshwater anomalies. In the next two sections, we will focus on representation issues in these GCMs and the consequences for modeling the future development of the MOC.

### 20.3 Biases in Global Climate Models

The first question when addressing the behavior of the GCMs is whether one can determine if the parameters in

these models are such that there are multiple equilibria. One direction of research has therefore been to develop indicators for the multiple equilibrium regime of the MOC. It is very beneficial in this regard that one can compute bifurcation diagrams of low resolution ocean-climate models explicitly (Dijkstra, 2000).

Using a simple box model, it has already been pointed out by Rahmstorf (1996) that the multiple equilibrium regime may be related to the net freshwater budget over the Atlantic basin. This issue was revisited by de Vries and Weber (2005) who showed (using an EMIC) that the sign of the net freshwater export by the Atlantic MOC, indicated by  $M_{ov}(\theta)$ , near the latitude  $\theta = 35^\circ$  S in the Atlantic may be controlling whether, in addition to the on state, a stable off state exists or not.

In Dijkstra (2007), it was shown that a measure of the divergence of the freshwater transport  $\Sigma$  of the Atlantic MOC over the Atlantic basin is a good indicator of the multiple equilibrium regime. When the freshwater transport at the northern boundary is neglected,  $\Sigma$  reduces to the indicator in de Vries and Weber (2005), since

$$\Sigma(\theta_s, \theta_n) = M_{ov}(\theta_s) - M_{ov}(\theta_n), \quad (20.2)$$

where  $\theta_n$  and  $\theta_s$  are the northern and southern latitudes of the Atlantic domain. To demonstrate the usefulness of  $\Sigma$  as an indicator for the multiple equilibrium regime, bifurcation diagrams were computed in Dijkstra (2007) using a fully implicit global ocean model. Starting from the steady-state solution determined under restoring conditions for the surface salinity field (Levitus 1994), steady states were calculated versus a parameter  $\gamma_p$  representing again a freshwater anomaly in the northern North Atlantic. The maximum of the Atlantic MOC ( $\psi_A$ ) is plotted versus  $\gamma_p$  in

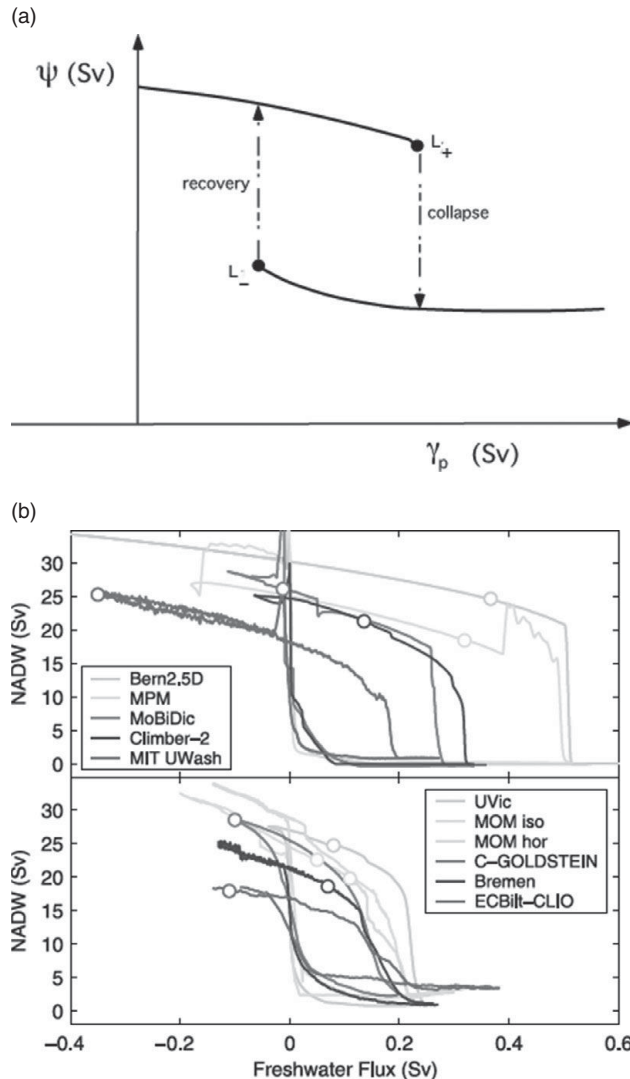


Fig. 20.5. (a) Sketch of the quasi-equilibrium simulations with  $\gamma_p$ . Near the saddle-node bifurcations in (a) the solution jumps from one stable steady state to another. The directions of these transient jumps are indicated with an arrow. (b) Typical hysteresis behavior as found in a set of EMICs (figure from Rahmstorf *et al.* (2005) with permission from AGU) when the freshwater flux is increased slowly in time from zero up to large values and back. On the vertical axis is a measure of the strength of the MOC. The curves are lined up with the recovery transition and the equilibrium solutions of the various models obtained with zero freshwater perturbation are shown as open circles.

Fig. 20.7a. The stable (drawn) branches are indicated with the on branch and with the off branch. The dashed branch represents unstable steady states. The saddle-node bifurcations  $L_-$  and  $L_+$  limit the multiple equilibria regime.

The indicator  $\Sigma(\theta_s, \theta_n)$  is already given in (20.2) where, following de Vries and Weber (2005),  $M_{ov}$  (the overturning component) and  $M_{az}$  (the azonal component) are defined as

$$\begin{aligned} M_{ov}(\theta) &= -\frac{\eta}{S_0} \int \langle v \rangle (\langle S \rangle - S_0) dz; M_{az}(\theta) \\ &= -\frac{\eta}{S_0} \int \langle v' S' \rangle dz. \end{aligned} \quad (20.3)$$

Here,  $\eta$  and  $\langle F \rangle$  (for a function  $F$ ) are given through

$$\eta = \int r_0 \cos \theta d\phi; \langle F \rangle = \frac{1}{\eta} \int F r_0 \cos \theta d\phi \quad (20.4)$$

with  $v' = v - \langle v \rangle$  and  $S' = S - \langle S \rangle$ . In addition,  $r_0$  is again the radius of the Earth and  $S_0$  is a reference salinity. The indicator  $\Sigma(\theta_s, \theta_n)$  is plotted along the on branch of Fig. 20.7a in Fig. 20.7b for  $\theta_n = 60^\circ$  N (in the sinking region) and  $\theta_s = 35^\circ$  S (at the southern tip of Africa).  $\Sigma$  changes sign (from positive to negative) just as the multiple equilibrium (ME) regime is approached (near the saddle-node bifurcation  $L_-$ ). Indeed in the single equilibrium (SE) regime, the Atlantic MOC exports salt ( $\Sigma(\theta_s, \theta_n) > 0$ ), while in the ME regime, it is exporting freshwater ( $\Sigma(\theta_s, \theta_n) < 0$ ).

It is remarkable that the indicator  $\Sigma$ , which is evaluated on the on branch, is able to detect the presence of the saddle-node bifurcation  $L_-$  which is located on the off branch. Certainly, the on states for  $\gamma_p > \gamma_{L_-}$  are linearly stable (i.e. very small perturbations on these states will decay), but they are susceptible to finite amplitude instabilities. As was shown in Dijkstra *et al.* (2004), the attraction domains of the on state and off state seem to be bounded by the unstable state and so it requires a finite amplitude perturbation, which crosses the unstable branch to make a transition from the on state to the off state. But how would  $\Sigma$  provide any information on the behavior of finite amplitude perturbations?

A more descriptive view of this connection is the following. When  $\Sigma < 0$ , the MOC transports freshwater out of the Atlantic basin (or imports salt into the basin). Hence when the MOC is weakened due to a freshwater perturbation, the salt import decreases and hence effectively the freshwater export decreases. Consequently, the Atlantic becomes fresher and hence this amplifies the original perturbation. In this way,  $\Sigma$  can be seen as an integral salt-advection feedback. In Huisman *et al.* (2010), it was shown that the sign of  $\Sigma$  can indeed be quantitatively connected to the finite amplitude stability of the MOC, if the perturbation MOC pattern (due to freshwater perturbations) has the same spatial structure (but opposite sign) as the mean MOC.

If a perturbation  $(\tilde{v}, \tilde{S})$  is assumed on a steady state  $(\bar{v}, \bar{S})$ , the development of the salinity perturbation is determined, (considering only meridional advective transport, and hence neglecting all other (zonal/vertical advection and diffusive) transports) by the equation

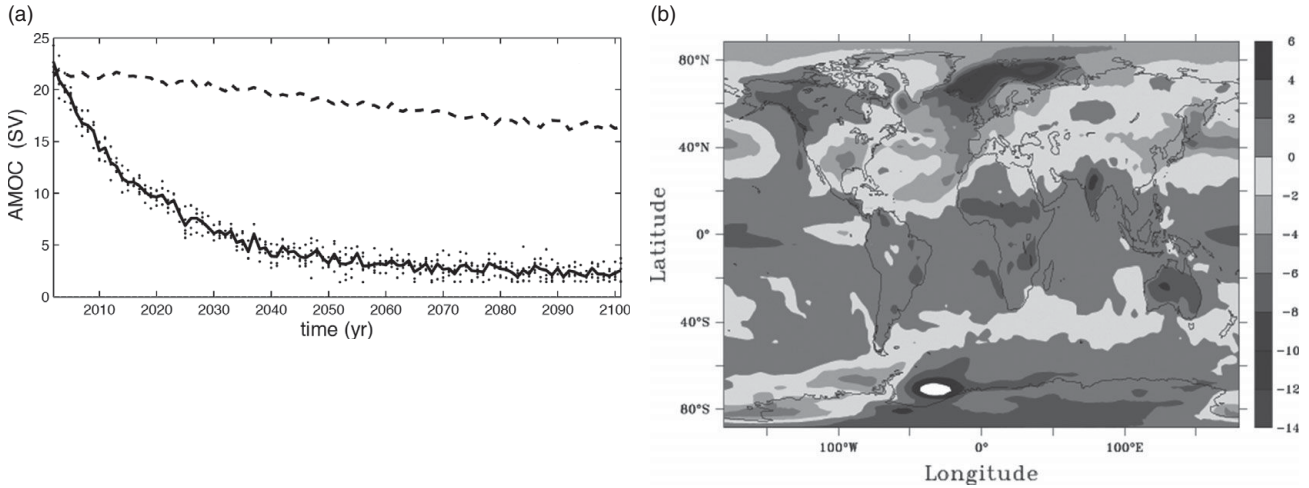


Fig. 20.6. (a) Drawn curve: time series of the MOC in the ECHAM-OM1 model, where 1 Sv of fresh water is added in the northern North Atlantic. The dots indicate the annual mean MOC values for five ensemble members. The dashed curve provides the MOC change due to an increase in CO<sub>2</sub> according to the SRES-A1B scenario. (b) The difference in annual mean surface (2 m) temperature between year 2025 and year 2001 (°C) due to the 1 Sv fresh water input (data are from the ESSENCE project (Sterl *et al.* 2008)).

$$\frac{\partial \tilde{S}}{\partial t} \approx -\frac{1}{r_0} \left[ \tilde{v} \frac{\partial \bar{S}}{\partial \theta} + \bar{v} \frac{\partial \tilde{S}}{\partial \theta} + \tilde{v} \frac{\partial \tilde{S}}{\partial \theta} \right]. \quad (20.5)$$

When we integrate (20.5) over the Atlantic basin (longitude  $\phi$  from coast to coast,  $z$  from bottom to surface and latitude  $\theta$  from  $\theta_s$  to  $\theta_n$ ), then the development of the Atlantic basin averaged salinity anomaly is governed by the equation

$$\frac{\partial}{\partial t} \left( \int_V \tilde{S} d^3x \right) \approx \int_z \int_\phi (\tilde{v} \bar{S} + \bar{S} \tilde{v} + \tilde{v} \tilde{S}) r_0 \cos \theta_s d\phi dz \quad (20.6)$$

where the fluxes through the northern boundary are neglected. This relation shows that the growth of the salinity anomaly in the Atlantic basin is related to the anomalous meridional salt transport terms integrated over the southern boundary.

The behavior of these terms for the case as in Fig. 20.7 was presented by Huisman *et al.* (2010) for an initial perturbation of  $\Delta \gamma_p = 0.02$  Sv. Note that because this value of  $\Delta \gamma_p$  is relatively small, both linear interaction terms in (20.6) are of larger magnitude than the nonlinear interaction term  $\tilde{v} \tilde{S}$ . The  $\bar{v} \bar{S}$  term is positive for both SE (light curves) and ME (dark curves) regimes and this transport is stabilizing the MOC (Fig. 20.8a), as they cause salt import into the basin. The nonlinear interaction term is negative (making the Atlantic fresher) and hence is destabilizing the MOC for both regimes. The central difference between the results for both regimes is that the  $\tilde{v} \bar{S}$  term is stabilizing in the SE regime, while it is destabilizing in the ME regime.

A link of the section integral over  $\tilde{v} \bar{S}$  and  $M_{ov}(\theta_s)$  can be made more explicit assuming that  $\langle \tilde{v} \rangle \approx -\varepsilon(t) \langle \bar{v} \rangle$ . Physically, this makes sense because the MOC decreases due to the imposed change in freshwater flux in the northern North Atlantic, and the overall spatial pattern of the MOC remains the same for small  $\Delta \gamma_p$ . In other words, there is a southward velocity perturbation in the upper layers and a northward velocity perturbation at depth. When we now decompose  $\tilde{v} = \langle \tilde{v} \rangle + \tilde{v}'$ ,  $\bar{S} = \langle \bar{S} \rangle + \bar{S}'$ , then the section integral of  $\tilde{v} \bar{S}$  in (20.6) can be written as

$$\int_z \int_\phi \tilde{v} \bar{S} r_0 \cos \theta d\phi dz = \eta \int_z \langle \tilde{v} \rangle \langle \bar{S} \rangle dz + \int_z \int_\phi \tilde{v}' \bar{S}' r_0 \cos \theta d\phi dz. \quad (20.7)$$

Using  $\langle \tilde{v} \rangle \approx -\varepsilon(t) \langle \bar{v} \rangle$ , the first term in the right-hand side is proportional to  $M_{ov}(\theta_s)$ . The second integral is dependent on the azonal components of  $\tilde{v}$  and  $\bar{S}$ . For both SE and ME cases in Fig. 20.8a, the three integrals in (20.7) are plotted in Fig. 20.8b. For the ME-regime (dark curves) the integral involving the  $\tilde{v}' \bar{S}'$  term is much smaller than that involving the  $\langle \tilde{v} \rangle \langle \bar{S} \rangle$  term. Hence, the sign of the section integral of  $\tilde{v} \bar{S}$  is the same as that of  $M_{ov}$  at 35°S.

When  $\Sigma \approx M_{ov}(\theta_s)$  is computed for the equilibrium solutions of typical CMIP3 GCMs (Drijfhout *et al.*, 2011), it is found that for nearly all models  $\Sigma > 0$  (Fig. 20.9). Based on the indicator, this would mean that the MOC in these models is not in a multiple equilibrium regime. This is consistent with the fact that it is difficult to determine an off state in these models. However, the reason that  $\Sigma > 0$  in

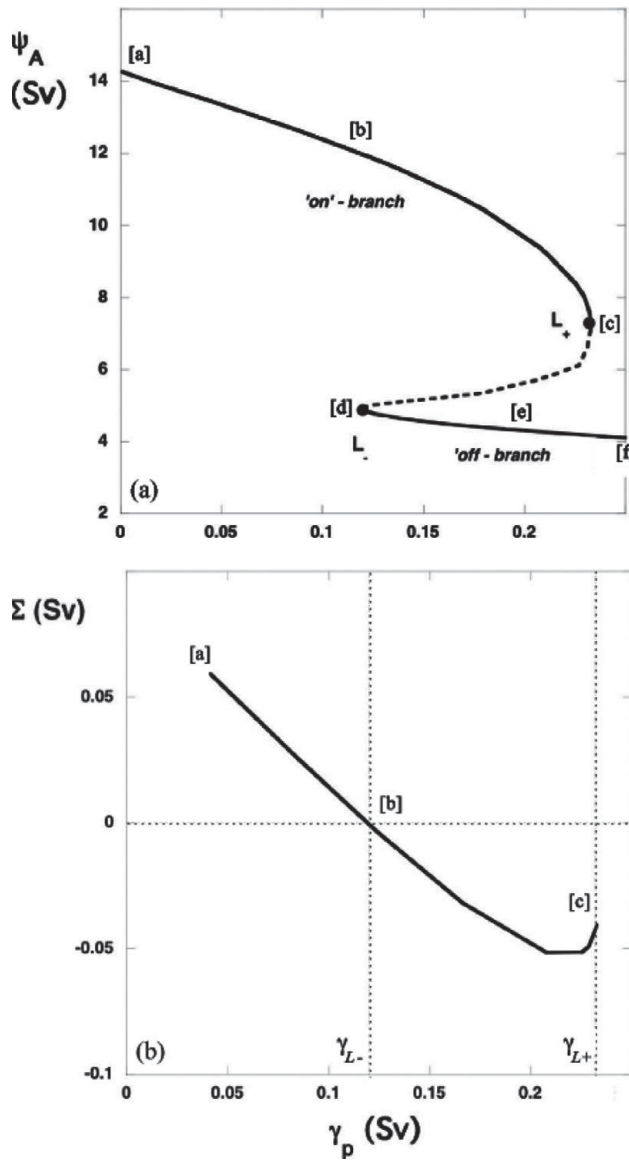


Fig. 20.7. (a) Bifurcation diagram where the strength of the Atlantic MOC ( $\psi_A$ ) is plotted versus the strength of the anomalous freshwater forcing ( $\gamma_p$ ). The labeling [a]–[f] along the branches refers to particular steady-state solutions. (b) Indicator function  $\Sigma(\theta_s, \theta_n)$  for  $\theta_n = 60^\circ$  N and  $\theta_s = 35^\circ$  S along the ‘on’ branch of the bifurcation diagram in (a). The vertical dotted lines indicate the positions of  $L_-$  and  $L_+$ . Figure is from Huisman *et al.* (2010) with permission from the AMS.

these models is that they have a large bias in the freshwater budget in the Atlantic, mainly related to too strong evaporation over the Atlantic. Hence the MOC has to import freshwater transport at its southern boundary to close the freshwater balance.

On the other hand, when  $\Sigma$  is determined from observations, all estimates so far (Hawkins *et al.*, 2011) provide

$\Sigma < 0$  (Fig. 20.10). The observational estimates of Weijer *et al.* (1999) follow from an inversion of WOCE data and provide the most negative value of  $\Sigma \approx -0.2$  Sv. The estimate from Huisman *et al.* (2010) is directly from one WOCE section and gives  $\Sigma \approx -0.1$  Sv. The one from Bryden *et al.* (2011) is at 24°S and gives a mean of  $\Sigma \approx -0.13$  Sv. The values from the different reanalysis projects give values between 0.0 and -0.2 Sv and hence are consistent with the observational estimates (Fig. 20.10).

What is learned from the results presented in this section is that GCMs (as used in CMIP3) have a bias in the freshwater budget in the Atlantic such that the MOCs in these models export salt. From observations and reanalysis products, however, all evidence points to the MOC exporting fresh water. The indicator  $\Sigma$ , although valid only under the specific assumption on the relation between the MOC perturbation pattern and the mean MOC pattern, then expresses that the MOC in these GCMs is in a different regime than the observations suggest. Hence these GCMs do not provide an adequate representation of the response of the MOC to freshwater anomalies.

## 20.4 Effects of subgrid-scale processes

In most of the CMIP3 (and also the CMIP5) GCMs, the internal Rossby deformation radius is not resolved and hence eddy processes are parameterized. When processes on this scale are explicitly represented, ocean eddies and their associated transport will be dominant in the ocean model flow and one may question whether this changes the sensitivity of the MOC to freshwater anomalies.

A systematic study was performed on this issue using two versions of the global Parallel Ocean Program (POP) with horizontal resolutions of 1 (the HR version), and 0.1 (the LR version). The atmospheric forcing is based on the repeat annual cycle (normal-year) Coordinated Ocean Reference Experiment (CORE<sup>1</sup>) forcing data set (Large and Yeager, 2004). The problem studied with these models is the response of the Atlantic MOC to freshwater input due to Greenland Ice Sheet (GrIS) melting. A realistic pattern of the fresh water input was prescribed (Mernild *et al.*, 2010), but its integral amplitude was taken as much larger (0.1 and 0.5 Sv,  $1\text{Sv} = 1 \times 10^6 \text{m}^3 \text{s}^{-1}$ ) compared to present-day estimates (at most 0.01 Sv, (Rignot *et al.*, 2011)).

In Weijer *et al.* (2012) it was shown that the transient response to the addition of 0.1 Sv of fresh water is significantly different between the two POP configurations. In the low-resolution version of the model, the Atlantic MOC (AMOC) strength levels off after a rapid initial decline,

<sup>1</sup> see <http://www.clivar.org/organization/wgmd/core/core.php>

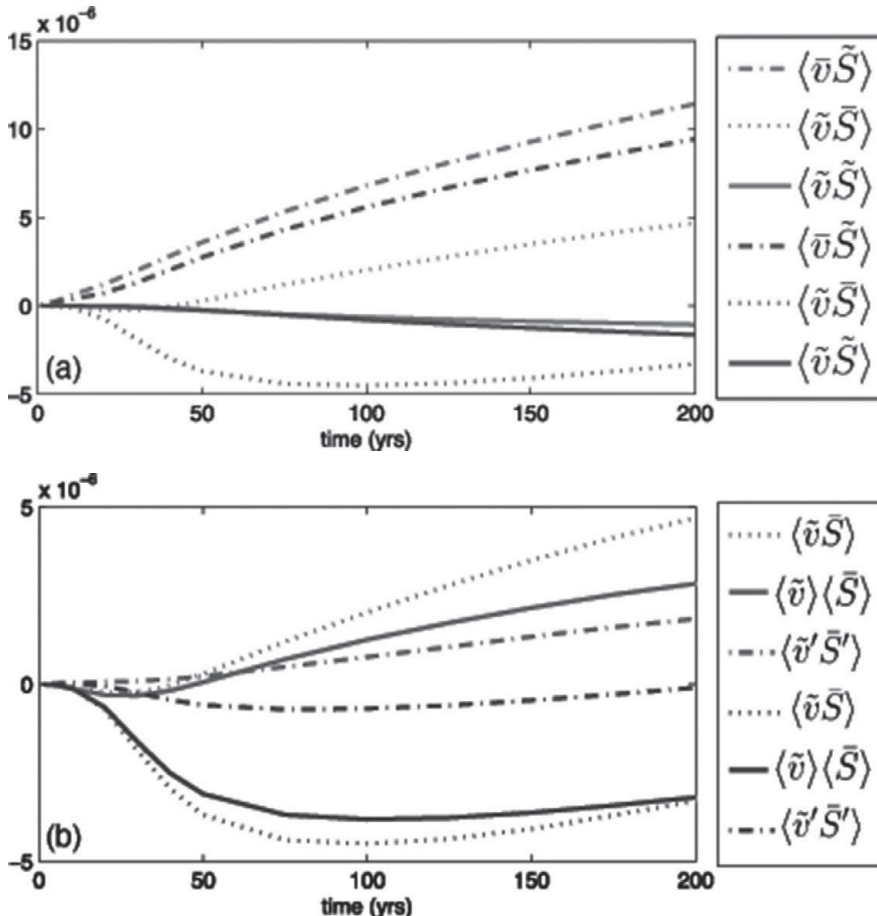


Fig. 20.8. (a) Time development of the three different terms in the right-hand side of (20.6) in response to a 0.2 Sv perturbation in  $\gamma_p$ . The light curves are for the SE regime and the dark ones for the ME regime; a similar line style indicates a similar term. (b) Integral terms in (20.7). The dotted curve is again the  $\bar{v} \bar{S}$  integral term similar to the one in (a). The drawn (dashed-dotted) curve is the first (second) term in the right-hand side of (20.7). Figure is from Huisman *et al.* (2010) with permission from the AMS.

while in the high-resolution configuration, the AMOC decline is more gradual and persistent. In addition, only in the high-resolution configuration is the response found to depend strongly on where the anomalous freshwater forcing is applied. The initial (first 20 years) decline of the AMOC in these simulations can be related to the behavior of convection, meaning that the efficiency of the anomalous freshwater transport to the sites of convection is an important factor in explaining the differences between the simulations.

In Den Toom *et al.* (2014), the detailed response of the two POP versions to an even larger GrIS discharge of 0.5 Sv was analyzed. For both configurations, results of two experiments were presented: an unperturbed reference simulation (REF) and the experiment with the enhanced runoff from the GrIS (PERT). The anomalous flux in the PERT simulations is applied throughout the duration of the experiments. The integrated flux varies seasonally around an annual mean amplitude of 0.5 Sv, reaching a maximum amplitude of 0.9 Sv in July. The two simulations were continued for 45 years and 100 years for the HR and LR configurations, respectively.

#### 20.4.1 AMOC response

For the LR simulations, Fig. 20.11a,b show the maximum value of  $\Psi$  at 26.5°N and 34°S, respectively. For the REF simulation, the mean at 26.5N is 21 Sv, which is somewhat stronger than the RAPID-MOCHA observations. The root mean square deviation is 1.7 Sv, which is clearly smaller than what is observed ( $\pm 5$  Sv). The transient response of the AMOC to the freshwater perturbation (PERT) is characterized by a rapid decline in the first eight years, followed by a slight resumption up to year 11, after which the decrease continues until the end of the simulation. After 45 years (the duration of the HR simulations), the AMOC has weakened by 8.5 Sv. Even 100 years after the onset of the perturbation, the AMOC strength is still decreasing. The decline of the AMOC strength is a meridionally coherent signal (Fig. 20.11c–d). As a result, it affects the basin-wide divergence of freshwater transport.

In the HR simulations, the strength of the  $\Psi$  at 26.5N and 34S is plotted in Fig. 20.12a and b, respectively. Comparison with Fig. 20.11 shows that the average strength of the AMOC in the REF case (22 Sv) is similar to that in the LR configuration. The typical 1 year root

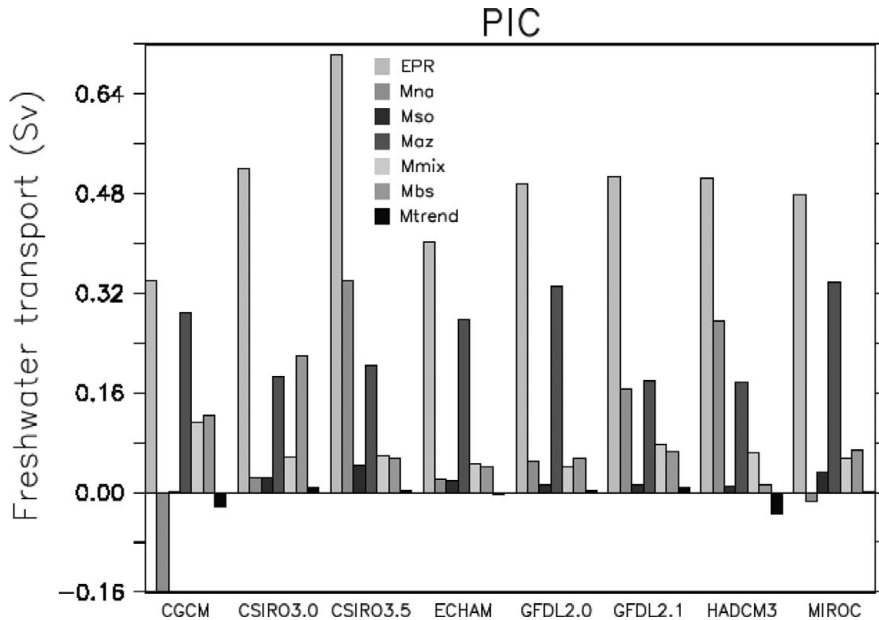


Fig. 20.9. Freshwater budget of several CMIP3 models (from Drijfhout *et al.* (2011) with permission from Springer Verlag). The freshwater transport induced by the MOC at 35°S is indicated by the green bar. The acronyms of the models are explained in Drijfhout *et al.* (2011).

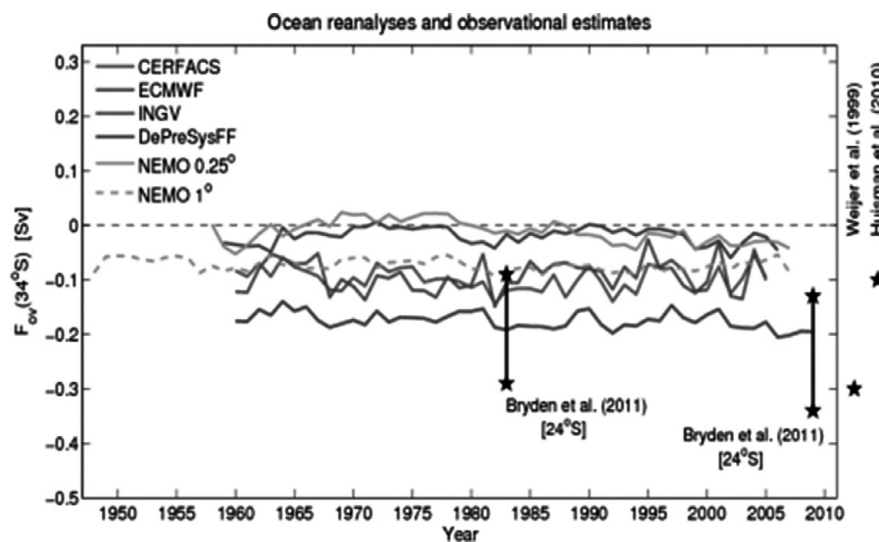


Fig. 20.10. Estimates of  $\Sigma \approx F_{ov}(\theta_s)$ ,  $\theta_s = 34^\circ\text{S}$  from observations and reanalysis project results, slightly modified from Hawkins *et al.* (2011) with permission from the AGU.

mean square deviation (about 1.5 Sv) is also comparable. Although a long-term adjustment to a quasi equilibrium situation may still be underway, most of the year to year variations must be attributed to intrinsic variability. In the PERT simulation, the AMOC strength shows a small decrease in the first three years after the onset of the freshwater perturbation, attaining an annual mean value below the weakest annual mean strength in REF in year 78. Only after about two decades, however, is there a persistent, gradual decline in overturning strength, resulting in an anomaly with respect to the REF experiment that clearly exceeds the intra-annual variations. The

year 120 anomaly of the annual mean strength equals  $-10.4$  Sv, exceeding the response in the LR configuration by about 2 Sv.

Comparison of Fig. 20.12c and Fig. 20.12d shows that there is no change in the depth of maximum overturning between year 76 and year 116 of the PERT experiment. This is also true for the minimum of the stream function at 4.5 km depth, representing northward bottom flow, although the strength of this negative cell increases by roughly 2 Sv between year 76 and year 116. For the LR simulation (Fig. 20.11c–d), the pattern also does not change. For both cases, the rate of overturning has changed

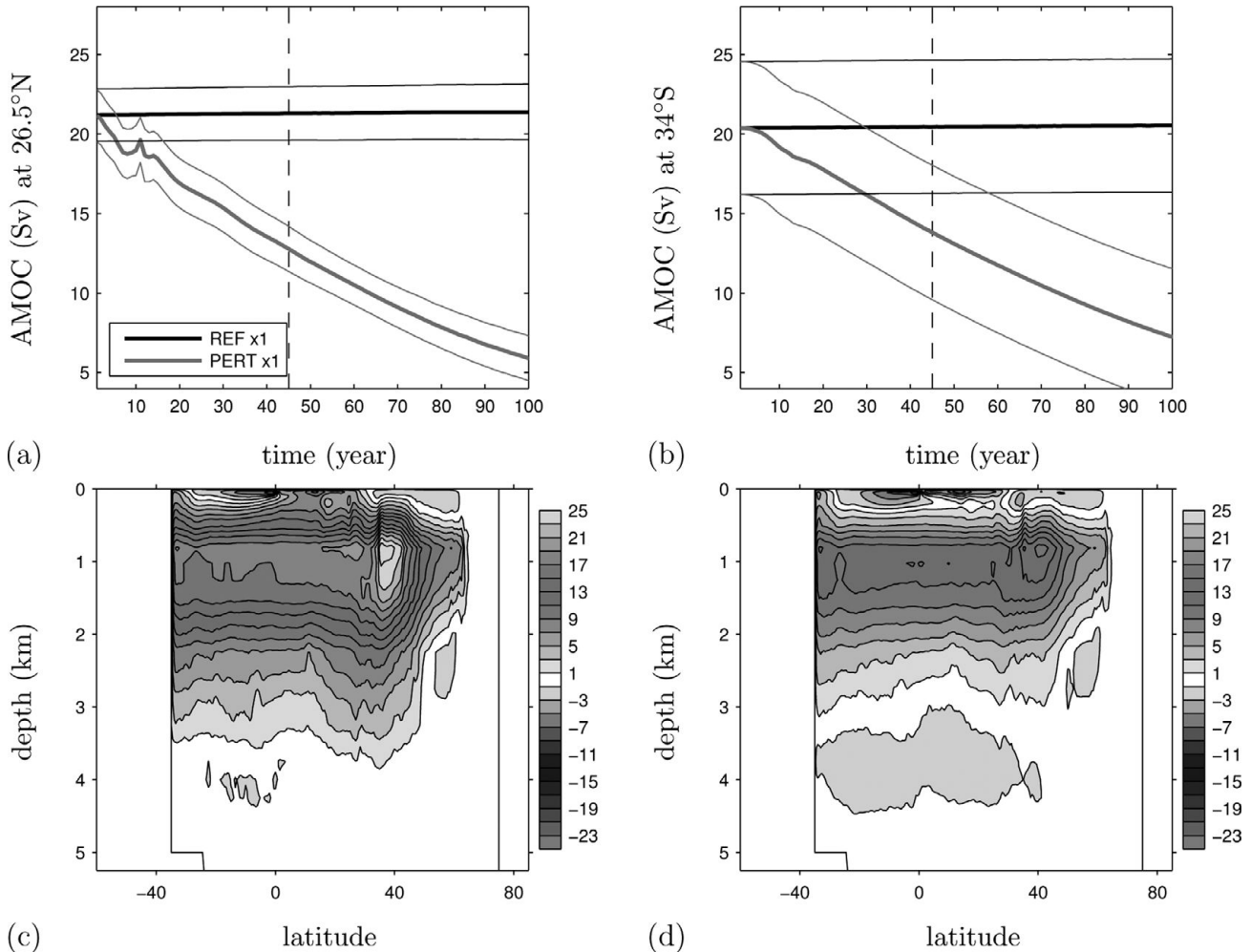


Fig. 20.11. The AMOC for the LR POP configuration. (a,b) AMOC strength at (a) 26.5°N and (b) 34°S, diagnosed as the maximum value of the meridional overturning streamfunction  $\Psi$ , which occurs at the depth of about 1 km. In this and subsequent time series plots, the thick lines are yearly mean values, while the thin lines represent the 1 year root mean square deviation. The dashed line drawn at 45 years indicates the duration of the corresponding HR simulations. (c,d) Stream functions (contour interval 2 Sv) of the annual mean AMOC in PERT for (c) year 1 and (d) year 41. Figure from Den Toom *et al.* (2014) with permission from the AMS.

but the pattern of  $\Psi$  is essentially not modified during the simulation, which suggests that the AMOC does not experience a transition (collapse) to a different state. The integration period is, however, quite short and it is possible that were the simulation to be continued, the AMOC would eventually collapse.

#### 20.4.2 Relation between AMOC and meridional density contrast

As reviewed by, for example, Rahmstorf (1996) and De Boer *et al.* (2010), theoretical scaling relations indicate that the AMOC is driven by a meridional density contrast. Although counterexamples are provided by De Boer *et al.* (2010), there are many model results that indeed

show a positive relation between the AMOC strength and meridional density contrast (Rahmstorf, 1996, Dijkstra, 2008), or meridional pressure difference (Griesel and Maqueda, 2006). Note that in the conceptual model of Stommel (1961), the dependence of the flow strength on the meridional density difference is expressed by a diagnostic relation.

In Den Toom *et al.* (2014), the meridional potential density contrast ( $\Delta\sigma_0$ , referenced to the surface) at a depth of 918 m, where the difference is taken between the latitudinal strips 50–55°N and 35–40°S, is determined for both POP LR and HR configurations. Figure 20.13a shows that  $\Delta\sigma_0$  reduces in response to the freshwater perturbation. When plotted against  $\Psi$  at 26°N, a positive correlation is evident (Fig. 20.13b), although the relation is clearly not

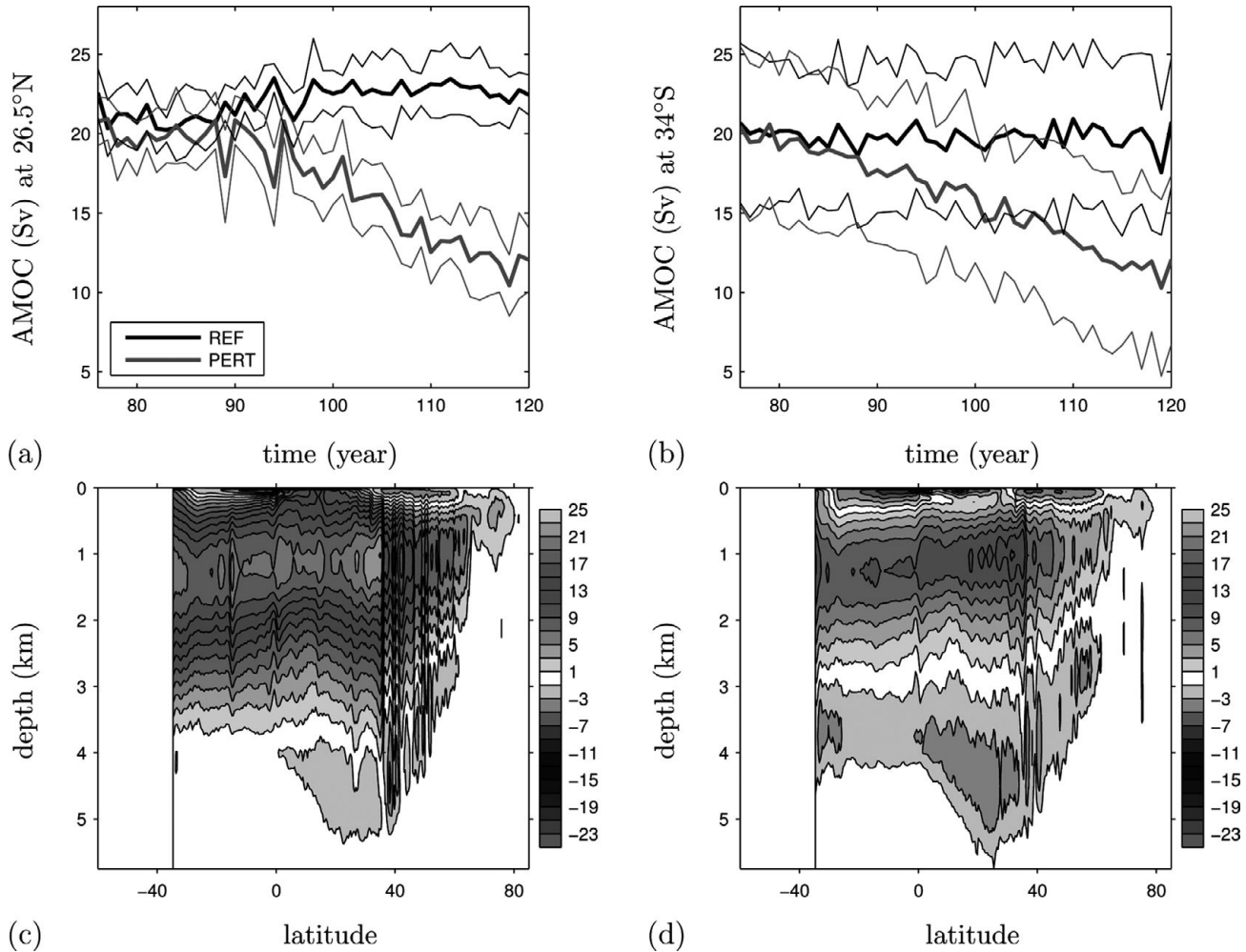


Fig. 20.12. The AMOC for the HR POP configuration simulations. (a,b) AMOC strength at (a)  $26.5^{\circ}\text{N}$  and (b)  $34^{\circ}\text{S}$ , diagnosed as the maximum value of the meridional overturning streamfunction  $\Psi$ , which occurs at the depth of about 1 km.(c,d) Stream functions (contour interval 2 Sv) of the annual mean AMOC in PERT for (c) year 76 and (d) year 116. Figure from Den Toom *et al.* (2014) with permission from the AMS.

linear. Obviously, the positive correlation does not imply causality, but the result is at least consistent with the flow law used in Stommel's (1961) model. This is, however, not the case for the HR POP model. In Fig. 20.13c, it is shown that in PERT the density difference  $\Delta\sigma_0$  even increases in time and becomes larger than that of REF. This may seem at odds with the fact that a freshwater perturbation is applied in the North Atlantic, which should lead to a density reduction. It is, however, caused by densities decreasing faster in the southern strip than in the northern strip. For PERT, a correlation holds between  $\Delta\sigma_0$  and the AMOC strength, but it is opposite to that found in the LR version of the model (Fig. 20.13d). A similar conclusion is reached based on the computation of meridional density differences at different depths and on meridional pressure differences, as in Griesel and Maqueda (2006).

#### 20.4.3 The AMOC and the Atlantic freshwater balance

For POP, the freshwater budget is obtained by multiplying the salinity equation by  $-1/S_0$ , where  $S_0 = 35$  is a reference salinity, and integrating the result over the Atlantic and Arctic basins. Written in short, the result is

$$\text{EPR} = Q_t + M + R. \quad (20.8)$$

The left-hand side of this equation is the total evaporation, minus precipitation and runoff and is calculated as the integral of the virtual salt flux (positive for a flux corresponding to evaporation) across the surface of the Atlantic and Arctic. The first term on the right-hand side of Eq. (20.8),  $Q_t$  represents the change in time of the freshwater content of the total basin. The second term on the right-hand side of Eq. (20.8) represents net advection of freshwater,

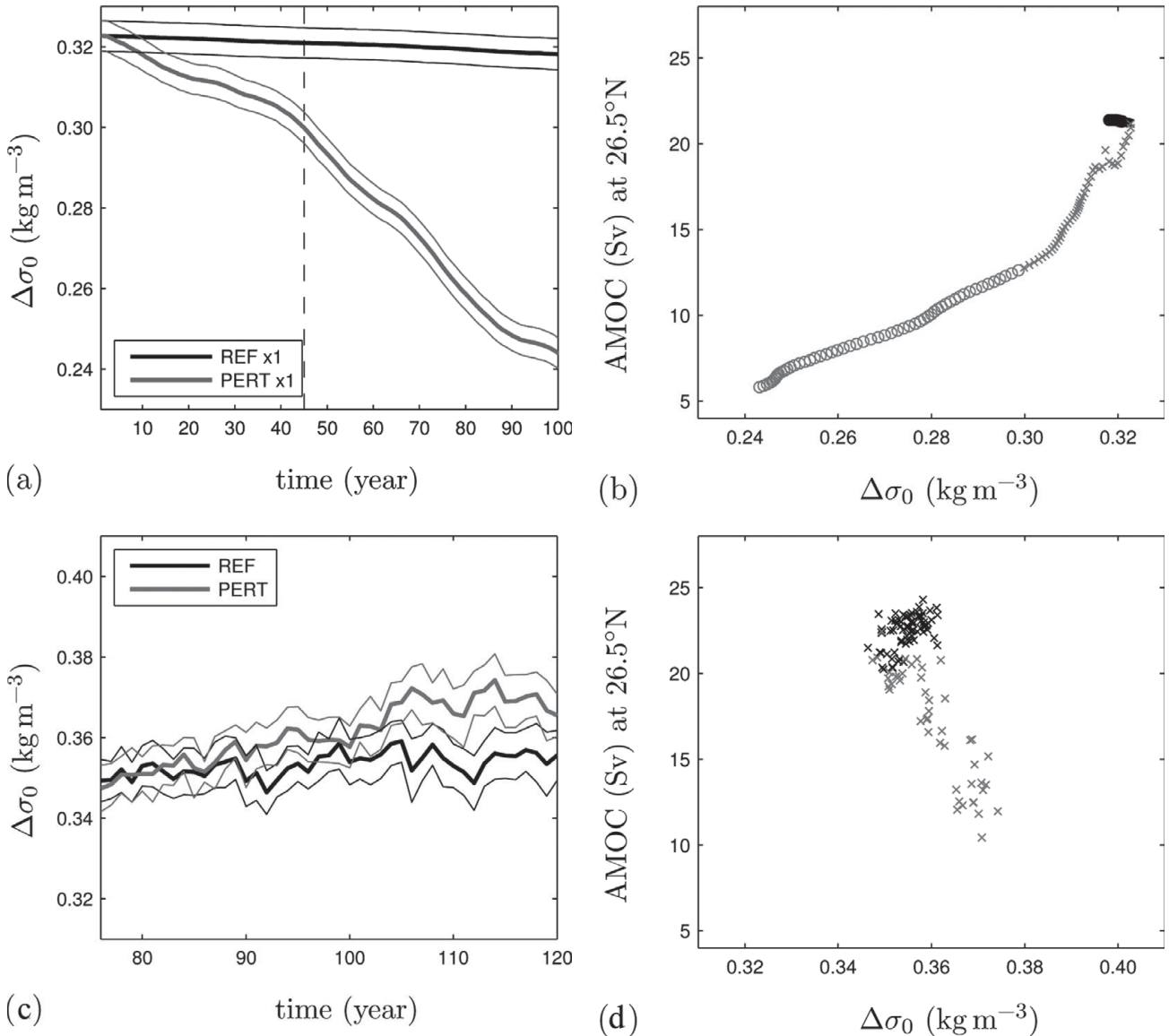


Fig. 20.13. (a) Changes in the density difference  $\Delta\sigma_0$  versus time for the LR model for both the REF and PERT simulation. (b) Relation between AMOC strength at  $26.5^\circ\text{N}$  and  $\Delta\sigma_0$ , based on yearly means in the LR configuration. Crosses indicate values from years 1–45, while circles indicate values from years 46–100. Similar relations hold for other latitudinal ranges and for other depths. (c) Same as (a) but for the HR configuration. (d) Same as (b) but for the HR configuration. Figure from Den Toom *et al.* (2014) with permission from the AMS.

$$M = \frac{-r_0}{S_0} \iint_{\text{BS}} vS \cos\theta \, dz \, d\varphi + \frac{-r_0}{S_0} \iint_{34^\circ\text{S}} vS \cos\theta \, dz \, d\varphi, \quad (20.9)$$

consisting of contributions due to advection across the Bering Strait (subscript BS) and the section between South America and South Africa at  $34^\circ\text{S}$ , respectively. Parameterized subgrid-scale transports are captured by the last term in Eq. (20.8), which is denoted by  $R$  because it is

not calculated explicitly, but diagnosed as the residual in the freshwater equation.

For the LR configuration, the mean value of EPR equals  $0.37 \text{ Sv}$  in REF, and is  $-0.13 \text{ Sv}$  in PERT, as expected. The mean value of  $Q_t$  in the REF simulation is about  $0.005 \text{ Sv}$ , indicating that the integrated freshwater budget is close to steady state. In the PERT experiment,  $Q_t > -0.5 \text{ Sv}$ , meaning that the overall freshening of the basin is smaller than what is expected solely from the freshwater perturbation. The main reason for this is that  $M$  decreases in time

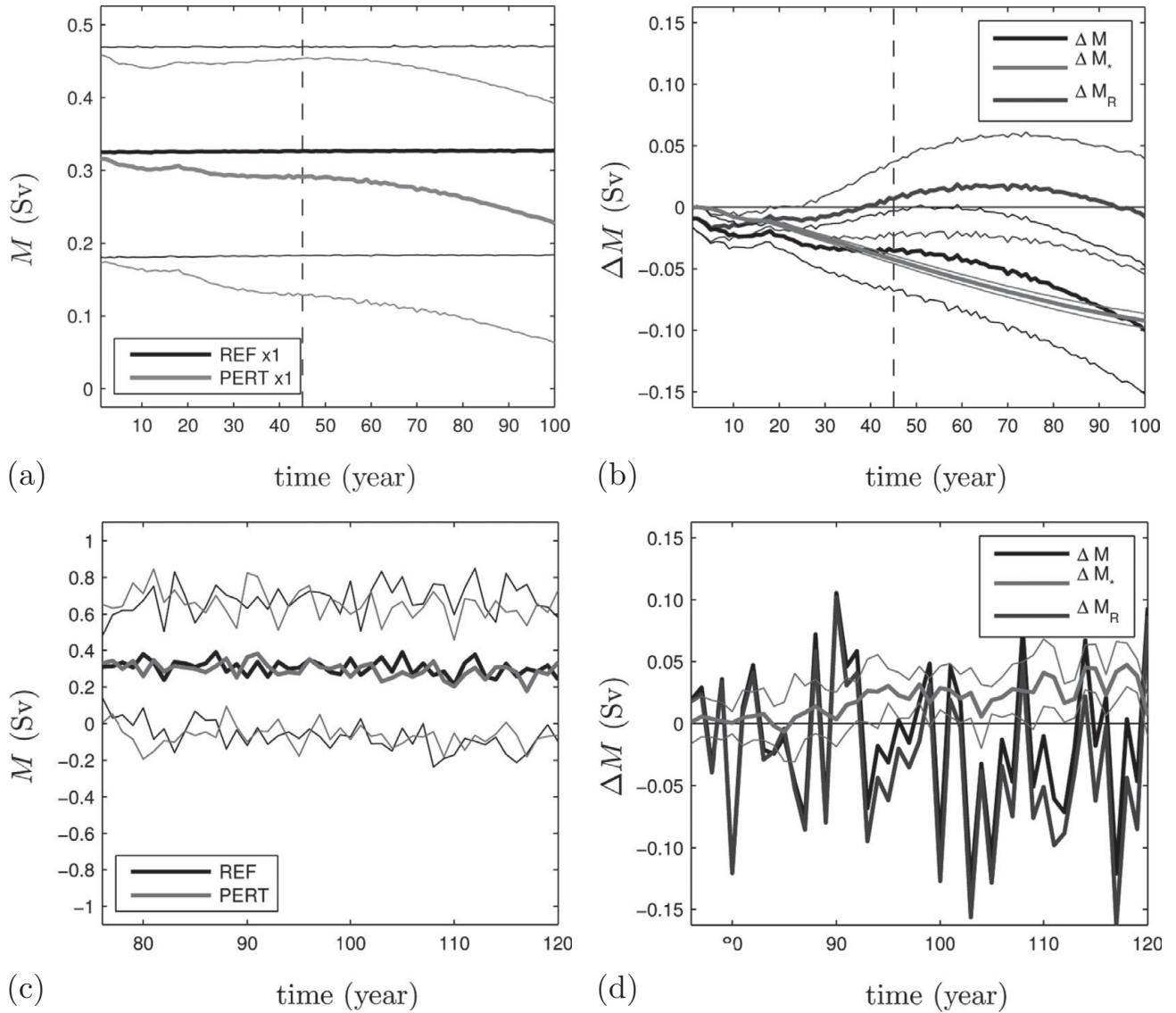


Fig. 20.14. (a) Net advective contribution to the freshwater budget  $M$  (Eq. 4.29) for the LR configuration. (b) Shown in black is  $\Delta M$ , the difference between REF and PERT of net advection of freshwater presented in panel a. This difference is decomposed into a contribution  $\Delta M_*$  due to the advection of the salinity of REF by the difference zonally integrated velocity, and a remainder  $\Delta M_R$ . (c-d) Same but for the HR model results. For the black and blue lines, the thin lines indicating the 1 year root mean square deviation are omitted to avoid overloading the figure.

(Fig. 20.14a). In REF, the mean value of  $M$  is 0.33 Sv, while in PERT its yearly mean values decrease to 0.29 Sv after 45 years and further to 0.23 Sv after 100 years. The implication is that the change in  $M$  in the PERT simulation partly offsets the original perturbation. The residual term is relatively small (the mean value of  $R$  in REF is 0.03 Sv), and is only modestly affected by the freshwater perturbation.

In Den Toom *et al.* (2014), the change in freshwater transport at 34°S due to the changes in the AMOC was determined and indicated by  $\Delta M_*$ . The remainder of the

total change  $\Delta M$ , where  $\Delta M = M^{\text{PERT}} - M^{\text{REF}}$  was indicated by  $\Delta M_R$  ( $\Delta M = \Delta M_* + \Delta M_R$ ). Based on this decomposition, it appears that the reduction of  $M$  in PERT can to a large degree be attributed to the change in AMOC strength, since the yearly mean values of  $\Delta M_R$  are relatively small (Fig. 20.14b). As suggested by Huisman *et al.* (2010), and discussed in Section 20.3,  $\Delta M_*$  can be related to a characteristic of the unperturbed reference simulation, i.e.  $\Delta M_* \approx -\zeta(t)M_{ov}^{\text{REF}}$ , where  $M_{ov}$  is the freshwater transport associated with the reference AMOC state. The mean value of  $M_{ov}$  in the REF simulation of the LR configuration

equals 0.14 Sv. The fact that it is positive is hence consistent with  $\Delta M_*$  being negative (Fig. 20.14b).

For the HR simulation,  $M$  is calculated from monthly averaged model output, which means that the contribution due to within month variations of  $v$  and  $S$  is neglected. The resulting errors are part of the residual  $R$ , but it was shown in Den Toom *et al.* (2014) that the mean value of  $R$  is small in both REF and PERT. Figure 20.14c hence shows that the extra freshwater input in PERT is totally compensated by storage within the Atlantic and Arctic basins, as the change in  $M$  between PERT and REF is near zero. To evaluate the significance of the AMOC reduction in PERT for the net advection of freshwater the same decomposition  $\Delta M = \Delta M_* + \Delta M_R$  was applied. The variability in  $\Delta M$  (Fig. 20.14d) is clearly dominated by the remainder  $\Delta M_R$ , and it has an amplitude that is significantly stronger than the mean of the AMOC contribution  $\Delta M_*$ . The latter is of comparable magnitude to that in the LR case, but of opposite sign during most of the simulation, despite the fact that the forcing is similar in the two configurations. This means that the effect of the AMOC, if any, is to enhance the original freshwater perturbation. According to the theory proposed by Huisman *et al.* (2010), the fact that  $\Delta M_*$  is positive during most of the simulation should be reflected in  $M_{ov}$  being negative for the REF simulation; however, it is slightly positive, i.e. 0.07 Sv, and hence the theory appears to fail for the HR configuration.

In summary, it appears that the freshwater transport anomaly due to GrIS meltwater perturbations at the southern boundary of the Atlantic associated with the changes in the MOC has an opposite sign in the LR and HR configurations. Apparently, the effect of ocean eddies on the freshwater budget of the Atlantic, which is not represented in CMIP3 GCMs, is crucial for the response of the MOC to freshwater anomalies.

## 20.5 Discussion and perspective

The Atlantic MOC is definitely sensitive to freshwater perturbations due to the existence of the salt-advection feedback. The advective transport of salt by the circulation, the density dependence on salinity, and the fact that the circulation is affected by density differences cause this to be a robust feedback in the Atlantic Ocean circulation. The following three conditions are important for the salt-advection feedback to operate: (1) the large-scale flow is proportional to a meridional density gradient; (2) the large-scale flow carries heat and fresh water, affecting that density gradient; and (3) the boundary conditions are such that temperature anomalies are damped out much quicker than salinity anomalies, so that the flow has a stronger control

over the salinity gradient than over the temperature gradient. In relatively simple ocean-only and ocean-climate models, this feedback causes the existence of a multiple equilibrium regime with the simultaneous existence of an on and off state of the MOC under the same atmospheric forcing conditions.

However, in GCMs as used in CMIP3 it is difficult to find off states and collapses of the MOC have not been calculated. There are two arguments to support the statement that the Atlantic MOC may be much more sensitive to freshwater anomalies than CMIP3 GCMs indicate. The first argument is based on the bias in the Atlantic freshwater budget of the GCMs, as was mentioned in Section 20.3. Because of this bias, the equilibrium MOC states appear to be in the unique regime and hence no transition to a collapsed state can occur. From observations (and also reanalysis results), the present-day MOC appears to export freshwater and hence an off state may exist (Fig. 20.10). The second argument is that when ocean eddies are explicitly represented, the response of the MOC to freshwater anomalies turns out to be stronger than in the lower resolution models, such as those used in CMIP3 GCMs (Weijer *et al.* 2012). In agreement with earlier studies and condition (1) above, a positive correlation between yearly mean values of the AMOC strength and the potential density contrast ( $\Delta\sigma_0$ ) was established for the LR POP configuration. However, in the HR version of the model, the correlation was found to be weak and of opposite sign. In addition, the response of the Atlantic Ocean circulation to freshwater perturbations (condition (2) above) differs in an important aspect. The transient net freshwater advection by the overturning at the southern boundary of the Atlantic, which forms a central element in the salt-advection feedback (Huisman *et al.*, 2010), has an opposite sign in the low- and high-resolution versions of the model.

The fact that CMIP3 GCMs (and likely also CMIP5 GCMs) do not adequately simulate the MOC response due to freshwater anomalies may have far reaching consequences regarding the value of stability indicators based on the Atlantic freshwater budget (de Vries and Weber, 2005, Huisman *et al.*, 2010, Drijfhout *et al.* 2011), the existence of a multiple equilibria regime of the AMOC (Rahmstorf, 1996), and the theories of rapid climate transitions in the past (Alley *et al.*, 2003). We may expect some surprises over the next decades in the behavior of the MOC.

## 20.6 Acknowledgements

The author thanks his colleagues Wilbert Weijer, Mat Maltrud, and Matthew Hecht (LANL, USA), Matthijs den Toom, Selma Huisman (IMAU, NL), Erik van Sebille

(UNSW, Australia), Andrea Cimatoribus, and Sybren Drijfhout (KNMI, NL) for the interesting, productive, and very pleasant collaboration over the years on this topic. Michael Kliphus (IMAU, UU) is thanked for carrying out the many POP simulations of which results were presented in this paper. The computations were done on the Huygens IBM Power6 at SURFsara in Amsterdam. Use of these computing facilities was sponsored by the Netherlands Organization for Scientific Research (NWO), through EW project SH-084-11.

## References

- Alley, R. B., Marotzke, J., Nordhaus, W. D., *et al.* (2003). Abrupt climate change, *Science* **29**, 2005–2010.
- Andersen, K. and coauthors (2004). High-resolution record of Northern Hemisphere climate extending into the last interglacial period, *Nature* **431**, 147–151.
- Bryan, F. O. (1986). High-latitude salinity effects and interhemispheric thermohaline circulations, *Nature* **323**, 301–304.
- Bryden, H. L., King, B. A., and McCarthy, G. D. (2011). South Atlantic overturning circulation at 24S, *Journal of Marine Research* **69**, 38–55.
- Clement, A. C. and Peterson, L. C. (2008). Mechanisms of abrupt climate change of the last glacial period, *Reviews Of Geophysics*, **46**: RG4002.
- Cunningham, S. A., Kanzow, T., Rayner, D., *et al.* (2007). Temporal variability of the Atlantic Meridional Overturning Circulation at 26.5 N, *Science* **317**(5840), 935–938.
- De Boer, A. M., Gnanadesikan, A., Edwards, N. R., and Watson, A. J. (2010). Meridional density gradients do not control the Atlantic Overturning Circulation, *Journal of Physical Oceanography* **40**(2), 368–380.
- de Vries, P. and Weber, S. L. (2005). The Atlantic freshwater budget as a diagnostic for the existence of a stable shut down of the meridional overturning circulation, *Geophys. Res. Letters* **32**, No. 9, L09606.
- Den Toom, M., Dijkstra, H. A., Cimatoribus, A. A., and Drijfhout, S. S. (2012). Effect of atmospheric feedbacks on the stability of the Atlantic Meridional Overturning Circulation, *Journal of Climate* **25**(12), 4081–4096.
- Den Toom, M., Dijkstra, H. A., Weijer, W., *et al.* (2014). Response of a strongly eddying Global Ocean to North Atlantic Freshwater Perturbations, *Journal of Physical Oceanography* **44**, 464–481.
- Dijkstra, H. A. (2000). *Nonlinear Physical Oceanography: A Dynamical Systems Approach to the Large Scale Ocean Circulation and El Niño*, Kluwer Academic Publishers, Dordrecht, the Netherlands.
- Dijkstra, H. A. (2007). Characterization of the multiple equilibria regime in a global ocean model, *Tellus* **59A**, 695–705.
- Dijkstra, H. A. (2008). Scaling of the Atlantic meridional overturning in a global ocean model, *Tellus A* **60**, 749–760.
- Dijkstra, H. A., Te Raa, L. A., and Weijer, W. (2004). A systematic approach to determine thresholds of the ocean's thermohaline circulation, *Tellus* **56A**, 362–370.
- Dijkstra, H. A. and Weijer, W. (2005). Stability of the global ocean circulation: basic bifurcation diagrams, *Journal of Physical Oceanography* **35**, 933–948.
- Drijfhout, S. S., Weber, S. L., and Swaluw, E. (2011). The stability of the MOC as diagnosed from model projections for pre-industrial, present and future climates, *Climate Dynamics* **37**(7–8), 1575–1586.
- Griesel, A. and Maqueda, M. (2006). The relation of meridional pressure gradients to North Atlantic deep water volume transport in an ocean general circulation model, *Climate Dynamics* **26**, 781–799.
- Hawkins, E., Smith, R. S., Allison, L. C., *et al.* (2011). Bistability of the Atlantic overturning circulation in a global climate model and links to ocean freshwater transport, *Geophysical Research Letters* **38**(10), L10605.
- Huisman, S. E., den Toom, M., Dijkstra, H. A., and Drijfhout, S. (2010). An indicator of the multiple equilibria regime of the Atlantic Meridional Overturning Circulation, *Journal Of Physical Oceanography* **40**(3), 551–567.
- Johns, W. E., Baringer, M. O., and Beal, L. M. (2011). Continuous, array-based estimates of Atlantic Ocean heat transport at 26.5 N, *Journal of Climate* **24**, 2429–2449.
- Large, W. G. and Yeager, S. (2004). Diurnal to decadal global forcing for ocean and sea-ice models: the data sets and flux climatologies, *Technical report*, National Center for Atmospheric Research, Boulder, CO, U.S.A.
- Levitus, S. (1994). *World Ocean Atlas 1994*, Volume 4: Temperature., NOAA/NESDIS E, US Department of Commerce, Washington DC OC21: 1–117.
- Mernild, S. H., Liston, G. E., Hiemstra, C. A., and Christensen, J. H. (2010). Green land Ice Sheet Surface Mass-Balance Modeling in a 131-Yr Perspective, 1950–2080, *Journal of Hydrometeorology* **11**(1) 3–25.
- Rahmstorf, S. (1996). On the freshwater forcing and transport of the Atlantic thermohaline circulation, *Clim. Dyn.* **12**, 799–811.
- Rahmstorf, S., Crucifix, M., Ganopolski, A., *et al.* (2005). Thermohaline circulation hysteresis: a model intercomparison, *Geophysical Research Letters* **L23605**, 1–5.
- Rignot, E., Velicogna, I., van den Broeke, M., Monaghan, A., and Lenaerts, J. (2011). Acceleration of the contribution of the Greenland and Antarctic ice sheets to sea level rise, *Geophysical Research Letters* **38**, doi:10.1029/2011GL046583.
- Sterl, A., Severijns, C., Dijkstra, H. A., *et al.* (2008). When can we expect extremely high surface temperatures?, *Geophysical Research Letters* **35**, L14703.
- Stommel, H. (1961). Thermohaline convection with two stable regimes of flow, *Tellus* **2**, 244–230.
- Weijer, W., De Ruijter, W. P. M., Dijkstra, H. A., and Van Leeuwen, P. J. (1999). Impact of interbasin exchange on the Atlantic overturning circulation, *Journal Of Physical Oceanography* **29**, 2266–2284.
- Weijer, W., Maltrud, M., Hecht, M., Dijkstra, H., and Kliphus, M. (2012). Atlantic Ocean Circulation to Greenland Ice Sheet Melting, *Geophysical Research Letters* **39**, L09606, doi:10.1029/2012GL051611.
- Wunsch, C. (2002). What is the thermohaline circulation?, *Science* **298**, 1179–1180.

# 21

## Key role of the Atlantic Multidecadal Oscillation in twentieth century drought and wet periods over the US Great Plains and the Sahel

Suman Nigam and Alfredo Ruiz-Barradas

### 21.1 Introduction

Sea surface temperatures (SST) exert a significant, and often predictable, influence on the climate of near and far away regions. Interannual SST variations related to El Niño Southern Oscillation (ENSO), for instance, impact the Indian summer monsoon to the west (Rasmusson and Carpenter, 1983) and the North American hydroclimate to the east (e.g. Ropelewski and Halpert, 1987, Joseph and Nigam, 2006). The link between SST and hydroclimate is also manifest on decadal time scales, as in the case of droughts over North America (Namias, 1966, Ting and Wang, 1997, Nigam *et al.*, 1999) and Africa (Hulme, 1992). Multi-year droughts such as the 1930s ‘Dust Bowl’<sup>2</sup> over the Great Plains, and the multi-decade ‘drying’ of Sahel (Folland *et al.*, 1986) mark notable excursions of regional hydroclimate, with devastating socioeconomic impacts. Such decadal-scale excursions, rooted in ocean–atmosphere–land interaction, are attractive targets for climate simulation and prediction for societal and scientific reasons.<sup>3</sup>

Multi-year, summertime droughts over North America have been observationally linked to decadal SST variability in the Pacific (Ting and Wang, 1997, Nigam *et al.*, 1999, Barlow *et al.*, 2001, McCabe *et al.*, 2004, White *et al.*, 2008, Nigam *et al.*, 2011) and the Atlantic (Namias, 1966, McCabe *et al.*, 2004, Ruiz-Barradas and Nigam, 2005, Wang *et al.*, 2006, Guan, 2008, McCabe *et al.*, 2008, Mo *et al.*, 2009, Nigam *et al.*, 2011) but the extent of the SST influence in major twentieth century droughts (including

basin contributions) remained unevaluated, observationally, until the attribution analysis of Nigam *et al.* (2011).

The drying of the Sahel has been attributed to local land-surface–atmosphere interaction – the overgrazing hypothesis (Charney, 1976, Charney and Stone, 1976) – and to tropical Atlantic and global SSTs (Folland *et al.*, 1986, Giannini *et al.*, 2003, Zhang and Delworth, 2006), global warming (Held *et al.* 2005) and recently to anthropogenic aerosols (Biasutti and Giannini, 2008).

Droughts are typically simulated using dynamical models of the atmosphere. The models are forced by observed SST which provides the temporal context, including drought links. The SST influence can be dynamically evaluated from a sufficiently large ensemble of drought simulations provided the atmospheric–land-surface model is realistic, at least, from the perspective of the hydroclimate variability structure (and mechanisms) of the target region. The currently deployed atmospheric models (Schubert *et al.*, 2004, Seager *et al.*, 2005, Sutton and Hodson, 2005, Cook *et al.*, 2009, Schubert *et al.*, 2009) simulate many aspects of the atmospheric general circulation, but the simulation of regional hydroclimate (precipitation, evaporation/evapotranspiration, soil moisture, surface air temperature, etc.) remains challenging. The problematic portrayal includes a distorted representation of the atmospheric and terrestrial water-cycles over the Great Plains (Ruiz-Barradas and Nigam, 2005, Nigam and Ruiz-Barradas, 2006, Ruiz-Barradas and Nigam, 2013), i.e. of regional processes relevant to droughts (Ruiz-Barradas and Nigam, 2010a,b).

In spite of such shortcomings, aspects of the notable Great Plains droughts have been simulated by SST-forced dynamical models. But the modeled drought core is often misplaced, e.g. to the southwest in the case of the Dust Bowl drought (Seager *et al.*, 2005, Cook *et al.*, 2009). The modeled drought is moreover characterized using *annual-mean* precipitation deficits in these studies, which downplays the hydroclimate simulation deficiencies of the warm season (late spring to fall) – the season of drought

<sup>2</sup> The intense decade-long (1931–39) drought got its name on 15 April 1935, the day after Black Sunday. Robert Geiger, a reporter for the Associated Press, travelled through the region and wrote the following: “Three little words achingly familiar on a Western farmer’s tongue, rule life in the *dust bowl* of the continent—if it rains.”

<sup>3</sup> Decadal prediction of regional hydroclimate, especially in the hind cast mode, provides unique opportunities for vetting climate system models used in projection of centennial-scale climate change.

occurrence over the Great Plains.<sup>4</sup> The modeled drought signal, as such, reflects more the La Niña footprint on winter–spring precipitation (Seager *et al.*, 2005) than the larger precipitation deficits observed in the warm season. Some notable North American droughts are, moreover, conspicuously absent while others fictitiously present in some of the simulations (Schubert *et al.*, 2004). Do the drought simulation discrepancies reflect the limited influence of SSTs in models or nature?

North American droughts are more strongly linked with the Pacific than Atlantic SST anomalies in dynamical model simulations (e.g. Figure 3 in Schubert *et al.*, 2004); the Pacific influence resulting, largely, from tropical SST anomalies (Schubert *et al.*, 2004, Seager *et al.*, 2005). The coordinated modeling experiments of the US CLIVAR Drought Working Group (Schubert *et al.*, 2009) reiterate the primacy of Pacific SSTs in generating North American droughts. The La Niña – US Drought paradigm – operative on interannual time scales in nature – was found most relevant in the context of decadal droughts by these modeling studies.

How does one define the simulation targets for the SST-based dynamical modeling of droughts? Clearly, the targets are not the full observed drought signal in view of the land-surface contribution: Are the models being judged too harshly above? Or are the present-day models not quite ready for scoping out the influence of Pacific and Atlantic SSTs on Great Plains and Sahel’s precipitation?

The goal of this observationally rooted analysis is to quantitatively characterize the full SST contribution in drought generation over North America and Africa, including the relative role of the Pacific and Atlantic basins. The characterization closely follows Nigam *et al.* (2011), where an evolution-centric spatiotemporal analysis of twentieth century SST variations (Guan and Nigam, 2008, 2009) and related hydroclimate links, and subsequent reconstruction of North American droughts yield the impact of Pacific and Atlantic SST variations on continental hydroclimate. The observationally based impacts immediately provide the sought after quantitative targets for the SST-forced dynamical modeling of droughts.

The observationally rooted statistical reconstruction of major hydroclimate episodes in Nigam *et al.* (2011) indicates a dominant role of Atlantic SSTs in the generation of multi-year droughts and wet episodes over North America – in contrast with the secondary role of this basin

in model-based assessments. The Atlantic Multidecadal Oscillation (AMO), in particular, had a singular influence on the twentieth century North American hydroclimate, especially during spring and fall, as discussed in subsequent sections. The AMO is a dominant contributor in the drying of the Sahel from the 1950s to the 1980s as well, and in the recovery of rainfall since.

Data sets are described in Section 21.2, and the notable hydroclimate episodes of the twentieth century in Section 21.3. The enabling SST analysis is briefly discussed in Section 21.4. The drought-period SST and precipitation signals are reconstructed from contemporaneous analysis in Section 21.5, while the Great Plains drought origin and predictability are investigated in Section 21.6. The drying of the Sahel is reconstructed in Section 21.7 to assess the influence of regional and remote SSTs. Discussions and conclusions follow in Section 21.8.

## 21.2 Data sets

The sea surface temperature data comes from the UK Met Office’s Hadley Centre Sea Ice and Sea Surface Temperature data set (HadISST 1.1, Rayner *et al.*, 2003), which is globally available on a 1° grid for the 1870-onward period. The long-term mean of each calendar month is first removed from the monthly data, yielding monthly anomalies. Seasonal anomalies are then constructed by averaging monthly anomalies over standard three-month periods (e.g., DJF, JJA). Seasonal anomalies are interpolated on to a 5° × 2.5° longitude–latitude grid for computational efficiency in extended-EOF analysis.

Precipitation data is from the University of East Anglia’s Climate Research Unit (CRU); the high resolution TS 3.0 analysis of station data (Mitchell and Jones, 2005). Monthly precipitation is available over land on a 0.5° grid for the 1901 onward period.

The Palmer Drought Severity Index, a nondimensional number that measures the severity of meteorological drought, is obtained from Dai *et al.*’s (2004) analysis. Monthly PDSI is available over land regions on a 2.5° grid for the 1870 onward period.

Evapotranspiration estimates are obtained from NOAA’s Climate Prediction Center, where they are generated using a one-layer hydrological model (Huang *et al.*, 1996, van den Dool *et al.*, 2003) that is driven by observed precipitation (and surface air temperature). Monthly evaporation is available on a 2.5° grid for the 1931 onward period.

Upper-air meteorological analysis for the full century was obtained from NOAA’s Twentieth Century Reanalysis (20CR; Compo *et al.*, 2011), which was developed from short-term forecasts generated from assimilation of synoptic surface/sea-level pressure and monthly SST and

<sup>4</sup> The downplay results from the comparatively superior simulation of winter hydroclimate variability which is dynamically controlled (through stormtrack modulation). Warm-season hydroclimate variability, in contrast, is more influenced by land-surface–atmosphere interactions which are robust (dormant) in summer (winter) but which remain poorly rendered in atmospheric and climate models.

sea-ice boundary conditions. The modern period upper-air data comes from NOAA's NCEP Reanalysis (Kalnay *et al.*, 1996).

### 21.3 Notable hydroclimate episodes of the twentieth century

The hydroclimate of the US Great Plains is marked by two notable dry periods in the twentieth century (Fig. 21.1a): one in the 1930s and the other in the 1950s. The 1930s drought was intense and prolonged (decade-long), and turned much of the Great Plains, the US breadbasket, into a ‘Dust Bowl’. The 1950s drought, while relatively short (4–5 years), was no less intense; its fall precipitation deficit was, in fact, larger than the peak seasonal deficit during the Dust Bowl drought (Fig. 21.1b–c). The 1950s drought was unrelenting as well, as is evident from the complete absence of positive precipitation anomalies (in any season) during the episode (Fig. 21.1a), in contrast with the distribution in Dust Bowl years. The ‘Dust Bowl’ winters, interestingly, had near-normal precipitation, on average; a feature, not evident in descriptions based on the Palmer Drought Severity Index (PDSI; Palmer, 1966). Droughts are commonly marked using the PDSI but this index is, seasonally, less discriminating than a precipitation based one (Fig. 21.1b–d), and thus not as insightful on drought mechanisms which are keyed to seasonal process.<sup>5</sup>

The Dust Bowl was largely a spring–summer drought while the 1950s one a summer–fall drought (Fig. 21.1b–c). The Great Plains precipitation record also includes wet periods, with a notable one in the mid 1980s that is focused on fall (Fig. 21.1d). Regional evapotranspiration anomalies (Fig. 21.1b–d) are largest in summer following the climatological rhythm, but never sufficient to account for even half the concurrent precipitation deficits, especially in the peak phase of the episodes – indicating, indirectly, a significant role for larger-scale circulation variations and attendant moisture transports in modulating the water cycle over the Great Plains (Ruiz-Barradas and Nigam, 2005).

Geographically, the Dust Bowl precipitation deficit is focused in the southern Plains and along the Gulf Coast in spring and in the central-northern Plains in summer (Fig. 21.1e–f). Drought severity can be assessed by comparing the precipitation deficit in the box outlined in Fig. 21.1f (~0.6 mm/day) with the regional summer climatology (~3.0 mm/day) (e.g. Nigam and Ruiz-Barradas, 2006)

and standard deviation (~0.9 mm/day) (e.g. Ruiz-Barradas and Nigam, 2005). The 1950s fall drought was more intense (~1.0 mm/day deficit against a fall climatology of ~2.7 mm/day and standard deviation of ~1.0 mm/day) and widespread, with the entire USA impacted (Fig. 21.1g). The drought core is located southward, extending into the southern Plains and the Gulf Coast states. The 1980s wet episode is essentially a mirror image of the 1950 drought, in both structure and amplitude; not surprising, given that both attain their peak-phase in the fall.

The Pacific SSTs during the Dust Bowl spring and summer were, on average, colder, especially in the extratropics, although not by much (~0.3 K) (Fig. 21.2a–b); the tropics, interestingly, were near normal. In contrast, robustly warm SSTs are found in the Atlantic, especially in summer when most of the mid-latitude basin has large SST anomalies (0.5–0.8 K); the tropical Atlantic is mildly warmer as well. The cold SST anomalies in the central-eastern equatorial Pacific during the 1950s fall drought (Fig. 21.2c) clearly resemble the La Niña signal [e.g. Fig. 3 (right panels) in Guan and Nigam (2008)], in the opposite phase. The Atlantic anomalies in the 1980s wet period (Fig. 21.2d) are broadly a mirror image of the drought ones, while the Pacific ones are more fragmented at this time.

### 21.4 The enabling SST analysis

The drought reconstruction reported here is rooted in the innovative analysis of natural variability and secular trend in the Pacific and Atlantic SSTs in the twentieth century (Guan and Nigam 2008, 2009; hereafter GN2008 and GN2009). By focusing on spatial *and* temporal recurrence but without imposition of any periodicity constraints, the extended empirical orthogonal function analysis (EEOF; Weare and Nasstrom, 1982) discriminates between biennial, interannual, and decadal variabilities, leading to refined evolutionary descriptions and, equally importantly, separation of natural variability and the secular trend – all without any advance filtering (and potential aliasing) of the SST record. The implicit accommodation of natural variability, in particular, leads to a nonstationary SST secular trend, one that includes mid-century cooling.

#### 21.4.1 Pacific analysis

Seasonal SST anomalies between 1900 and 2007 were analyzed in the Pan-Pacific domain ( $20^{\circ}\text{S}$ – $60^{\circ}\text{N}$ ,  $120^{\circ}\text{E}$ – $60^{\circ}\text{W}$ ) using the EEOF technique; five-season-long anomaly sequences were targeted in the primary analysis. The technique is equivalent to multichannel singular spectrum analysis (e.g. von Storch and Zwiers, 1999). The seven

<sup>5</sup> Smoothed versions of PDSI can moreover be synthesized from precipitation, indicating the latter’s adequacy in multi-year drought analysis; smoothed precipitation and PDSI indices are correlated at 0.91 in Fig. 21.1a.

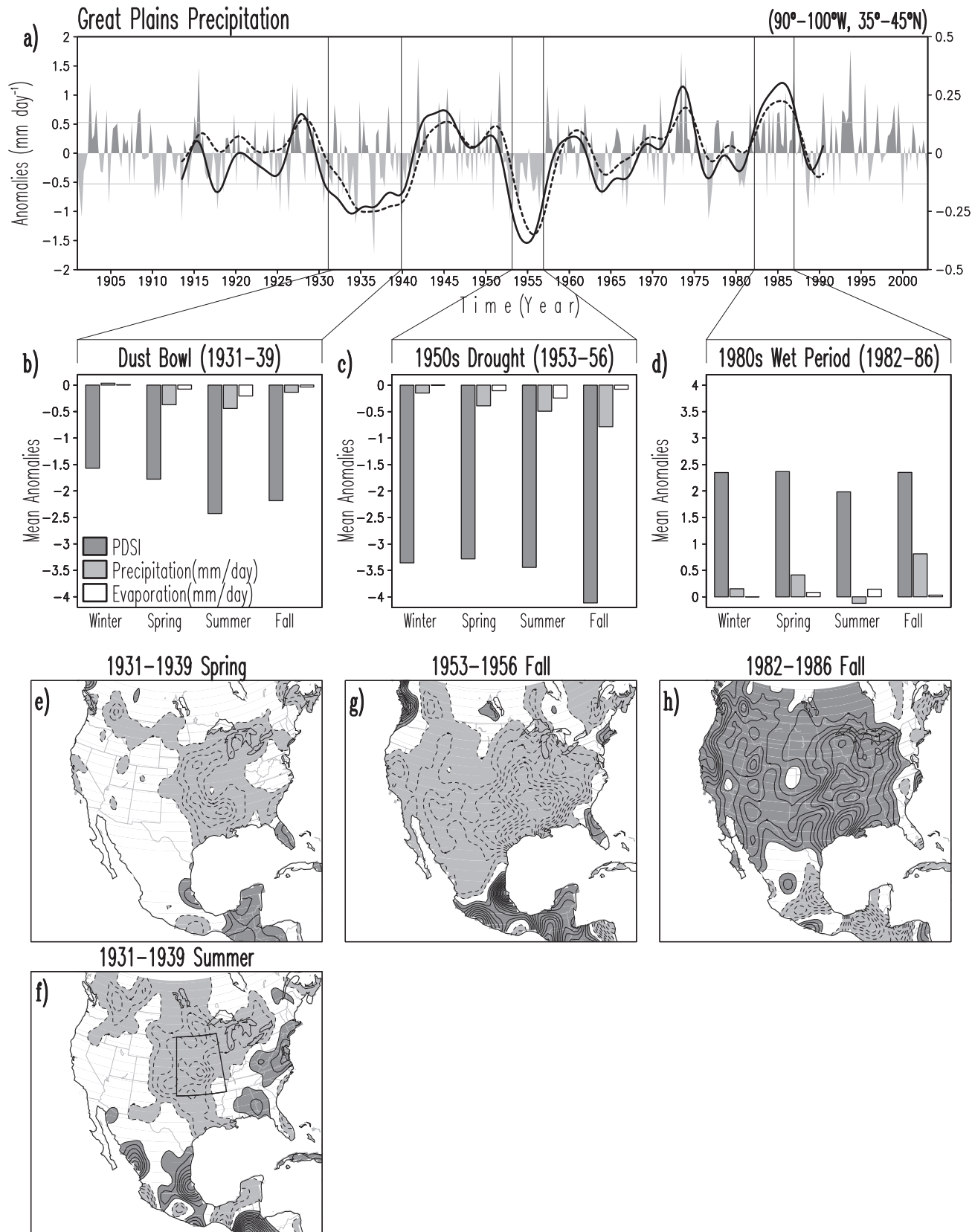


Fig. 21.1. North American drought and wet episodes: (A) Great Plains precipitation in the twentieth century, from Climate Research Unit's TS 3.01 data (University of East Anglia); averaging region ( $90^{\circ}\text{W}$ – $100^{\circ}\text{W}$ ,  $35^{\circ}\text{N}$ – $45^{\circ}\text{N}$ ) outlined in (F). Seasonal anomalies (mm/day, left scale) are in green/brown shades; solid black line shows a smooth version (from 50 applications of 1-2-1 averaging)

leading principal components (PCs) were rotated using the VARIMAX method. Canonical ENSO variability is captured as two modes: growth ( $\text{ENSO}^-$ ) and decay ( $\text{ENSO}^+$ ); departures from it are identified as the non-canonical mode ( $\text{ENSO}^{\text{NC}}$ ); see Figures 3–9 and related discussion in GN2008. Pacific decadal variability is resolved into two modes, Pan Pacific (PDV-PP) and North Pacific (PDV-NP): The first, with a horseshoe structure in the Pacific, exhibits connections to the tropical–subtropical Atlantic resembling the AMO footprint in this region (Figure 11 in GN2008). The second, capturing the 1976/77 climate shift, is closer to Pacific Decadal Oscillation in structure, but with interesting links to other basins (Figure 12 in GN2008). The nonstationary secular trend (SST-Trend) consists of widespread but nonuniform warming of all basins along with a sliver of cooling in the central equatorial Pacific (Figure 13 in GN2008). The physicality of decadal modes – of key interest given their multi-year drought links – was assessed via correlations with the fish recruitment records, following Hare and Mantua (2000); the correlations were found to be comparable, if not larger, than those obtained by these authors. Analog counts were also used in assessing the physicality of the modes (see Section 5 in GN2008).

#### 21.4.2 Atlantic analysis

The Atlantic SSTs were subject to similar spatiotemporal analysis, but after removal of the Pacific influence. The leading mode of Atlantic SST variability is a multidecadal oscillation focused in the extratropical basin (AMO-*Atl*; GN2009). It differs from its conventional description (Enfield *et al.*, 2001, Enfield and Cid-Serrano, 2010) in the western tropical basin where the amplitude is weaker due to the absence of the Pacific’s influence (see Figure 5b in GN2009). The seasonally resolved AMO-*Atl* PC is shown in Fig. 21.3a (thin red) along with other markers of this variability, including a recent one from Ting *et al.* (2009) based on observations and climate model simulations; note Fig. 21.3 is identical to Figure 1 in Nigam *et al.* (2011), and reproduced with permission. Negative decadal pulses reflecting massive discharge of sub-Arctic water

into the North Atlantic, as during the Great Salinity Anomaly of 1968–82 (e.g. Slonosky *et al.*, 1997), are evident in the AMO-*Atl* PC (and to an extent in the Ting index) but not in other AMO markers; AMO-*Atl* differs from others in the 1940s and 1950s too.

The AMO-*Atl*’s SST footprint (Fig. 21.3b) is focused in the northern basin, in the subpolar gyre. The same-sign extension into the Tropics develops a little after the northern lobe attains significant amplitude; AMO-*Atl* evolution is shown in GN2009. The fall-season regressions on land precipitation (Fig. 21.3b) show a general drying over the Americas (except southern Mexico and Central America), but wetter conditions to the east, notably, over Sahel. Given AMO-*Atl*’s decadal time scales, its warm phase can lead to multi-year droughts over central-eastern United States.

#### 21.4.3 AMO-*Atl*’s seasonal precipitation footprints

AMO-*Atl*’s impact on North American seasonal precipitation (Fig. 21.3c) is significant in the transitional and warm seasons, with the fall impact being largest (0.4–0.5 mm/day per unit PC amplitude). The AMO-*Atl*’s warm phase is associated with precipitation deficits in all three seasons; the absence of offsetting surpluses (or seasonal compensation) makes AMO-*Atl* even more relevant for North American droughts. The overlaid regressions of the 700 hPa geopotential and column stationary moisture flux (from a data set completely independent of CRU precipitation) indicate a strikingly consistent circulation context for the precipitation signal: low-level northerly flow across the central continent and related southward moisture transport. The flow opposes the seasonal southerly flow (including the Great Plains low-level jet in spring) which brings moisture from the Gulf of Mexico into the continental interior (e.g. Nigam and Ruiz-Barradas, 2006, Weaver and Nigam, 2008). The AMO-*Atl* circulation leads to a precipitation deficit both from reduced moisture transport and the low-level subsidence generated by northerly anomalies [assuming a Sverdrup vorticity balance, namely,  $\beta \cdot v \approx f (\partial w / \partial z)$ ].

---

Caption for Fig. 21.1 (*cont.*) using the right scale. Dashed line shows the Palmer Drought Severity Index anomalies (similarly smoothed but scaled by 0.1) using the same right scale. Horizontal lines mark the  $\pm 1.0$  SD of the smoothed precipitation index. Vertical lines identify periods when this index exceeds  $\pm 1.0$  SD. (B) Seasonal Palmer Drought Severity Index, precipitation, and evapotranspiration (from NOAA Climate Prediction Center, in mm/day) anomalies over the Great Plains in the Dust Bowl years (1931–39). (C) As in B except for the 1950s drought (1953–56). (D) As in B except for the 1980s wet period (1982–86). All anomalies in (B)–(D) are relative to the 1931–2002 seasonal climatology. Dust Bowl precipitation anomalies in Spring (E) and Summer (F). Fall precipitation anomalies in the 1950s drought (G) and 1980s wet period (H). Precipitation is smoothed by five applications of ‘smth9’ in the GrADS plotting software, and displayed using a 0.15 mm/day interval; zero-contour is suppressed. Green (brown) shades denote positive (negative) values.

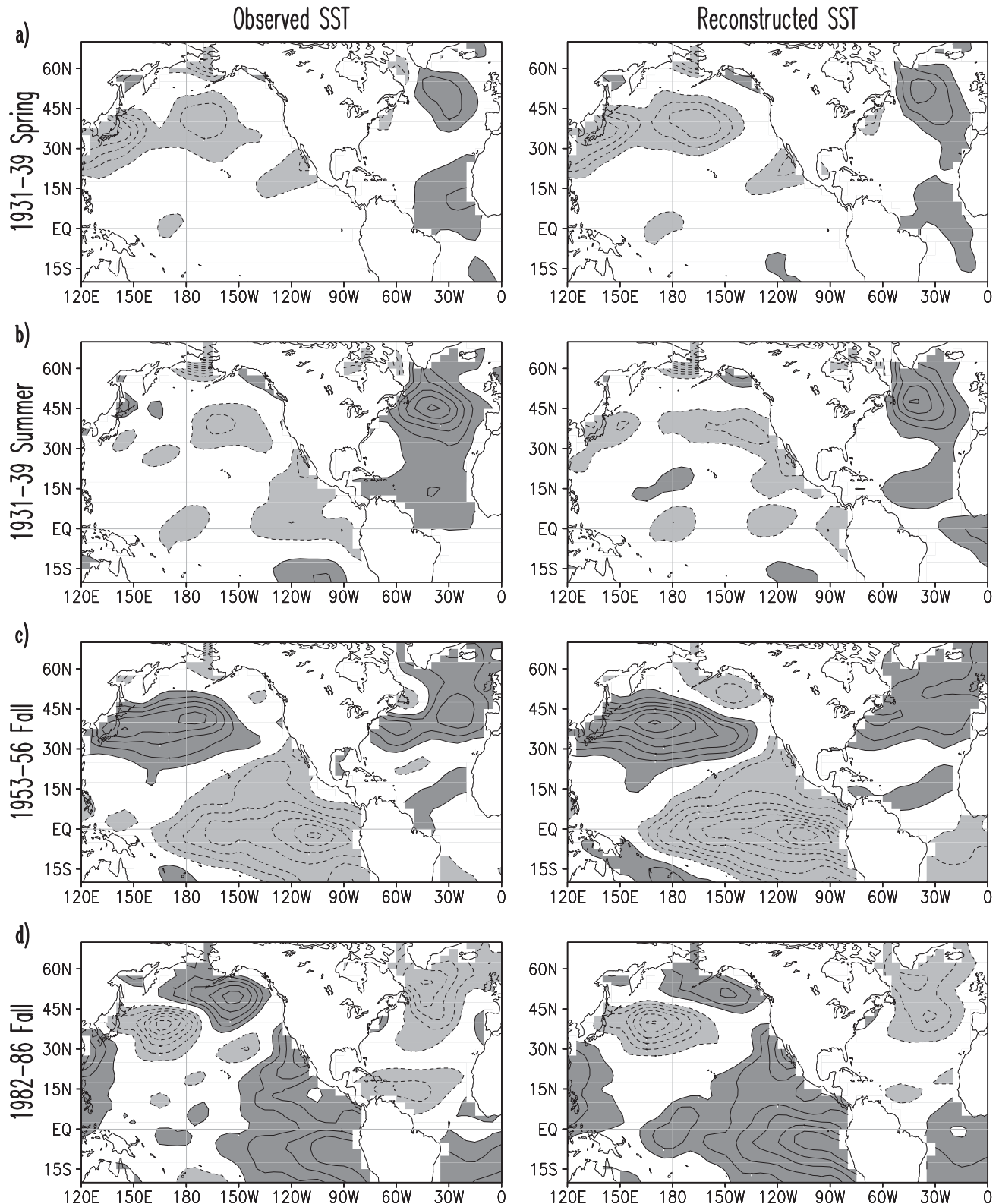


Fig. 21.2. Observed sea surface temperature anomalies during notable North American drought and wet episodes, from the Hadley Centre's HadISST 1.1 analysis (UK Meteorological Office); relative to the 1900–2002 period's seasonal climatology, and plotted on a  $5^{\circ}$  longitude by  $2.5^{\circ}$  latitude grid: (A) Dust Bowl (1931–39) spring, (B) Dust Bowl summer, (C) 1953–56 fall drought, and (D) the 1982–86 wet episode (fall). The SST anomalies reconstructed from seasonal regressions of the seven Pacific and four Atlantic SST principal components are shown in the right panels. Solid (dashed) contours denote positive (negative) values and the zero-contour is suppressed; contour interval is 0.15 K. Sea surface temperature is spatially smoothed by one application of 'smth9' in the GrADS plotting software. Red (blue) shades denote positive (negative) values.

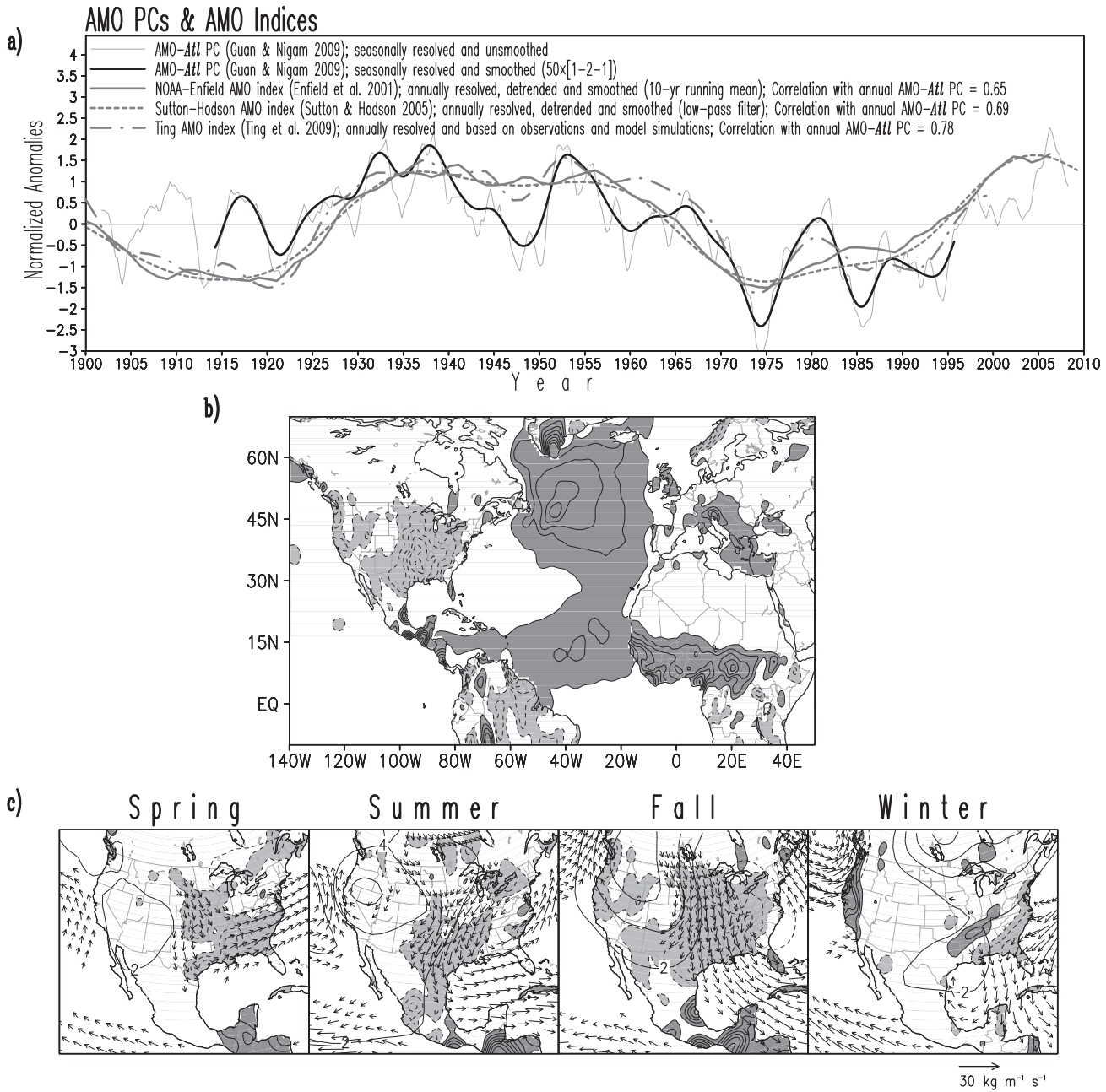


Fig. 21.3. (A) Atlantic Multidecadal Oscillation SST principal component (AMO-Atl PC, red) is compared with other AMO indices: NOAA-Enfield (black); Sutton-Hodson (green); and the Ting *et al.* index (purple-x). The notable 1970s decadal pulse in the AMO-Atl PC is coincident with the Great Salinity Anomaly (see text). The smoothed PC (thick red) is obtained from 50 applications of the 1-2-1 smoother on seasonally resolved values (thin red); all indices are normalized over the January 1900–April 2009 period. Smoothed index correlations: (Red, Black)=0.65; (Red, Green)=0.69; (Red, Purple)=0.78. (B) All-season regressions of the smoothed AMO-Atl PC on *residual* Atlantic SSTs (see text for definition) are shaded blue-to-red while its *fall*-season regressions on precipitation are shown in brown-to-green colors. SST is contoured at 0.1 C intervals and precipitation is shaded/contoured at 0.075 mm/day. (C) AMO's impact on North American *seasonal* hydroclimate: Regressions of smoothed AMO-Atl PC on precipitation, and NOAA-20CR's 700 hPa geopotential and surface-300 hPa column stationary moisture flux. Precipitation is plotted as above, height is contoured at 2 m, and the column moisture flux is in blue vectors with the indicated scale (in  $\text{kg m}^{-1} \text{s}^{-1}$ ), and with values less than 15% of the scale not plotted; zero contours are omitted in all panels. All regressions are for the April 1914–July 1995 period, the interval over which the thick red curve (panel a) is defined. To preclude aliasing of the nonstationary SST Secular Trend PC in the regressions, its signal in seasonal data was removed prior to regression analysis; smoothing of the AMO-Atl PC alters the orthonormal property of the SST PCs, necessitating this pre-emptive measure.

Statistical significance of the regressions is assessed via a two-tailed Student's t-test at the 5% level using an effective sample size  $N_e [=N/(1+2r_{x,1}r_{y,1}+2r_{x,2}r_{y,2}+\dots)]$ , where  $N$  is time-series length;  $r_{x,1}, r_{x,2}\dots$  are the first, second,  $\dots$ -order autocorrelations for time series  $x$ , and  $r_{y,1}, r_{y,2}\dots$  for time series  $y$ ; Quenouille, 1952] that accounts for serial autocorrelation; stable  $N_e$  (and thus t-test) values are obtained by summing up to the fourth-order. Figure 21.3b–c show regressions where t-values (obtained with  $N_e$ ) exceed the theoretical values at the 5% significance level.

## 21.5 Drought-period SST and precipitation reconstruction

The linear seasonal regressions of the SST principal components on contemporaneous SST and precipitation in the full record (October 1901–April 2006) constitute the building blocks in this reconstruction. Multiplication of each SST PC with its temporally fixed seasonal regression pattern, and summing the 11 contributions yields the reconstructed signal. The intra-basin PCs are temporally orthogonal (assured by the analysis method) while the inter-basin ones are nearly so (ensured by filtering of Pacific's influence from Atlantic SSTs prior to analysis); the largest inter-basin PC correlation is only 0.08, facilitating reconstruction of the SST and drought signals. A similar strategy was recently used to reconstruct the tropical cyclone counts in the Atlantic sector (Nigam and Guan, 2011).

### 21.5.1 SST reconstruction

The SST anomalies during drought and wet episodes are first reconstructed as a test of the reconstruction paradigm. The fidelity of the reconstruction (Fig. 21.2, right panels) attests to the efficacy of the SST analysis; although 11 basis functions are used in the reconstruction, only about half contribute significantly in any given period. The hydroclimate episodes are reconstructed next, relying on the SST–precipitation links operative in nature rather than in SST–forced dynamical models of the atmosphere.

### 21.5.2 Drought reconstruction

The SST-based precipitation reconstruction is remarkable, as is evident from the close correspondence of the observed and reconstructed structure at both regional and subcontinental scales in Fig. 21.4a (identical to Figure 2a in Nigam *et al.* 2011). The AMO-*Atl* is influential over large swaths of the eastern continent, while the Pacific's influence (not shown, but approximately, middle minus bottom row) is confined to the central longitudes.

### Dust Bowl

The Dust Bowl spring drought is remarkably reconstructed but the Dust Bowl summer drought proves challenging, with reconstruction over the Great Plains weaker in amplitude by as much as 50% (cf. Fig. 21.4a). The structural correspondence, including placement of focal points from the Gulf Coast to the Northern Plains, is however reasonable; the correspondence extends to precipitation surplus features.

The deficit in reconstruction of the Dust Bowl summer drought from SSTs is consistent with the potential contribution of other processes, notably, regional and upstream land-surface states and attendant interactions. It is also not inconsistent with arguments for additional inclusion of human land degradation in drought simulation (Cook *et al.*, 2009).

### 1950s drought

The shorter but more intense 1950s *fall* drought is apparently shaped by the Pacific's influence (~ middle minus bottom row) which accounts also for the wetness of the Pacific Northwest and Central America. The largely in-phase contribution of the Atlantic is important for drought severity over the southern Plains and the Gulf Coast, leading to nearly full accounting of the core precipitation deficit; the deficit feature over the southern tier states to the east of the Mississippi is however not fully recovered.

In contrast with the success in fall, the summer drought proves challenging – even more than the Dust Bowl summer drought (Guan, 2008). Drought reconstruction fails in the 1950s summer as this drought was generated, principally, by decadal SST variability in the Pacific and Atlantic basins, i.e. by modes having weak concurrent summer precipitation links. Canonical La Niña variability, which also contributes, has weak summer links as well (Guan, 2008). The summer precipitation deficit in the 1950s drought may thus have its origin in the unrelenting fall (and winter) precipitation deficits that were sequestered in the land surface until the following spring and summer, when they would find expression as reduced evaporation (and precipitation); a well-known moisture pathway in seasonal hydroclimate evolution (e.g., Nigam and Ruiz-Barradas, 2006).

### 1980s wet episode

The 1980s wet episode is quite reasonably reconstructed from the SST links, though not to the extent of the 1950s drought. The in-phase basin influences generate a realistic wet pattern, but the amplitude is recovered primarily over the Lower Mississippi.

### 21.5.3 Drought reconstruction: synopsis

The AMO-*Atl* contribution itself is shown in Fig. 21.4a (bottom row) and is sizeable in the spring and fall episodes.

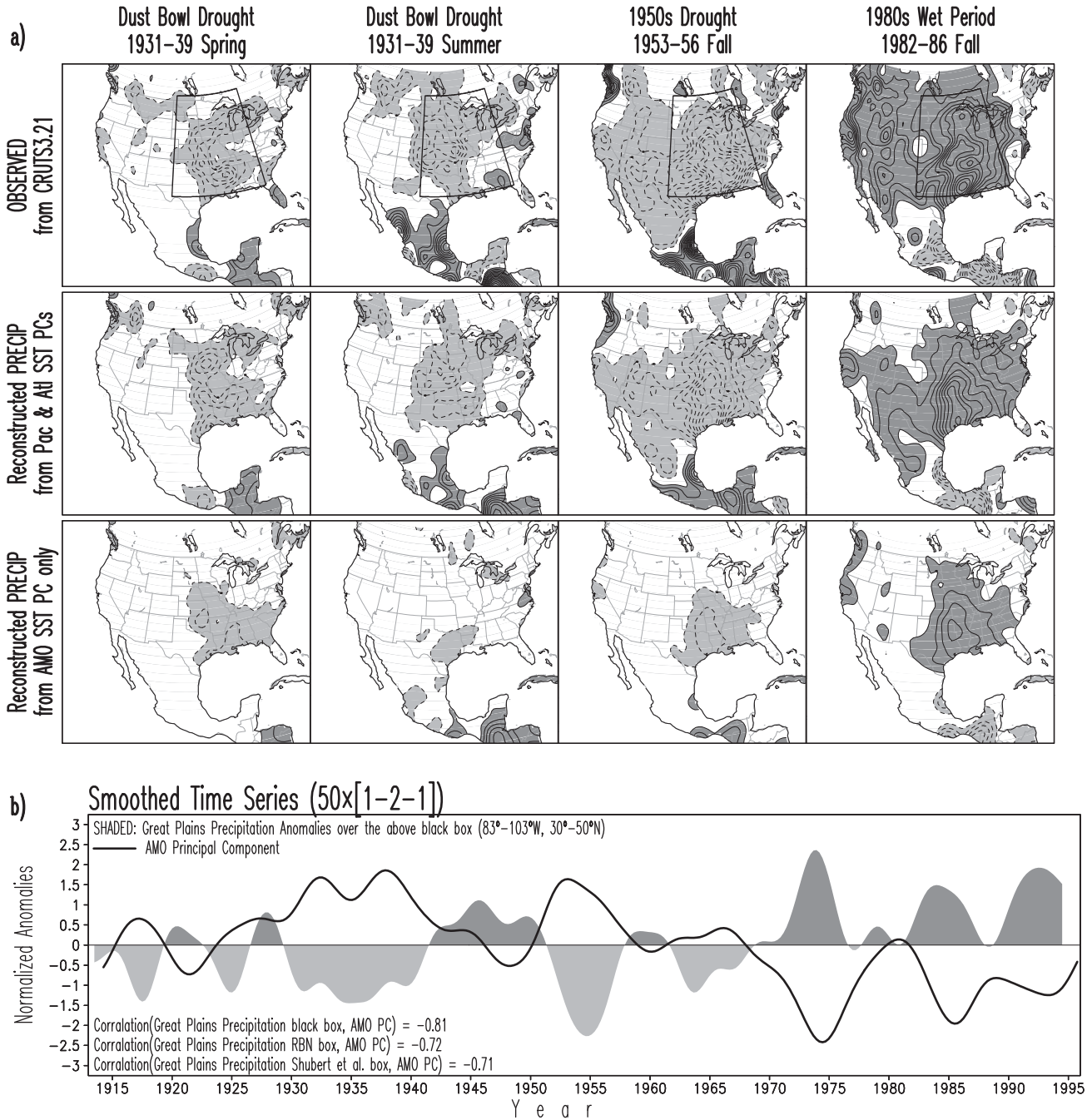


Fig. 21.4. (A) Observed (top row) and reconstructed (second row) twentieth century Great Plains droughts and wet episodes. Seasonal precipitation regressions of the seven Pacific and four Atlantic SST principal components over the October 1901–April 2006 period constitute the building blocks of the Dust Bowl (1931–39) spring and summer droughts (first and second column), 1953–56 fall drought (third column), and the 1982–86 fall wet episode (right column). The AMO-Atl contribution to the reconstruction is shown in the third row. Contouring, shading, and smoothing of precipitation as in Fig. 21.1e–h. The 20° wide latitude-longitude box marked in red in the top panels identifies a common impacted region; (B) Average precipitation in the marked red box is plotted along with the AMO-Atl SST principal component; both time series are smoothed by 50 applications of the 1-2-1 smoother on seasonal values, and normalized. The AMO-Atl curve is identical to that displayed in Fig. 21.3A, and is correlated with the precipitation curve at  $-0.78$ ; its correlation with other precipitation averages is noted in the legend. RBN box: 100–90W, 35–45N (Ruiz-Barradas and Nigam, 2005); Schubert *et al.* box: 105–95W, 30–50N (Schubert *et al.*, 2004).

Table 21.1. Percentage contribution of the Pacific and Atlantic SST principal components to Great Plains droughts and wet episodes; the principal components are defined and displayed in GN2008 and GN2009. The contributions are noted when the reconstructed signal is  $\geq 10\%$  of the observed precipitation anomaly in the  $20^\circ$  latitude-longitude box ( $103-83W$ ,  $30-50N$ ) covering  $\sim 4$  million  $km^2$  and outlined in red in the top panels of Fig. 21.4a.

Hydroclimate Episodes	Canonical ENSO (ENSO <sup>-</sup> + ENSO <sup>+</sup> )	ENSO Non-Canonical (ENSO <sup>NC</sup> )	North Pacific Decadal Var. (PDV-NP)	SST Secular Trend (Nonstationary)	Atlantic Multidecadal Oscillation (AMO-Atl)	Tropical Atlantic SST Variability (Niño <sup>-</sup> + Niño <sup>+</sup> )	TOTAL (from 11 modes)
<b>Dust Bowl Drought</b> (Spring 1931–1939) <b>Deficit:</b> 0.253 mm/day	8			26	<b>55</b>	12ñ	92
<b>Dust Bowl Drought</b> (Summer 1931–1939) <b>Deficit:</b> 0.291 mm/day		9		22	12	<b>31</b>	82
<b>1950s Drought</b> (Fall 1953–1956) <b>Deficit:</b> 0.626 mm/day	23		<b>29</b>		24		78
<b>1980s Wet Period</b> (Fall 1982–1986) <b>Surplus:</b> 0.687 mm/day	14		19		<b>37</b>		75

AMO-Atl is dominant in Dust Bowl spring and in the 1980s wetness in the central-eastern continent ( $\sim 4$  million  $km^2$  region outlined in red in the top panels of Fig. 21.4a). Interestingly, the tropical Atlantic SST modes contribute the most during Dust Bowl summer (cf. Table 21.1). The Atlantic SSTs are thus very influential in three of the four hydroclimate episodes, with the Pacific SST influence dominant only in the 1950s fall drought; a quantitative assessment of the basin contributions is given in Table 21.1 and discussed in Section 21.6.

A compelling view of AMO-Atl's influence on Great Plains' hydroclimate is provided by Fig. 21.4b, which shows the normalized AMO-Atl SST PC (red curve) and central-eastern US precipitation in the twentieth century. Their negative correlation ( $-0.78$ ) indicates an important role for the AMO in Great Plains hydroclimate variability; see also Kushnir *et al.* (2010). Together with the role of tropical Atlantic SSTs in Dust Bowl summer (noted above), this analysis suggests that, as a basin, the Atlantic is, perhaps, more influential than the Pacific for multi-year Great Plains drought and wetness.

## 21.6 Great Plains drought origin and predictability

A reasonable reconstruction of the major drought and wet episodes, and assessment of the Pacific and Atlantic SST

contributions are prerequisite for the investigation of drought and wetness origin. In this observational analysis, the origin is investigated by resolving the basin contributions into components attributed to that basin's SST variability modes. Modal contributions are noted in Table 21.1 when they typically exceed 10% of the precipitation deficit/surplus in the red outlined box marked in Fig. 21.4a. This condition is met by canonical ENSO, non-canonical ENSO, North Pacific decadal variability, SST Secular Trend, AMO-Atl, and the tropical Atlantic SST modes; some of these were briefly discussed in Section 21.4, and all are fully described in GN2008 and GN2009.

### 21.6.1 Modal contributions

Over 90% of the Dust Bowl spring drought is reconstructed, principally, from the in-phase impact of the SST Secular Trend ( $\sim 25\%$ ), AMO-Atl ( $55\%$ ), and tropical Atlantic SST modes ( $\sim 10\%$ ); note, the impact of low-frequency NAO is also significant but off-setting ( $-15\%$ ). The Atlantic basin (tropical and extratropical) is thus quite influential for the spring drought. The drought is reconstructed to a lesser extent in summer ( $\sim 80\%$ ), from non-canonical ENSO ( $\sim 10\%$ ), SST Secular Trend ( $\sim 20\%$ ), AMO-Atl ( $\sim 10\%$ ), and the tropical Atlantic ( $30\%$ ) contributions. The Dust Bowl summer drought is thus found to be linked with tropical SST variations in the adjoining basins.

The 1950s fall drought and the 1980s fall wetness are reconstructed to an even lesser extent (~75%). The former has >20% contributions from canonical ENSO (La Niña, ~25%), PDV-NP (~30%), and AMO-*Atl* variability (warm phase, ~25%). The latter – a wet episode – is significantly influenced by canonical ENSO (El Niño, 15%), PDV-NP (~20%), and AMO-*Atl* variability (cold phase, ~35%). Both the 1950s and 1980s fall-season hydroclimate episodes, each of multi-year duration, are nominally consistent with the La Niña – US Drought paradigm, which captures the interannual influence on winter–spring precipitation. While clearly relevant, it is however not the only key SST–drought link in the fall season: Table 21.1 shows that AMO-*Atl* exerts the strongest influence in two of the four episodes (with the tropical Atlantic modes being most influential in another), indicating an important role of Atlantic SSTs in generation of multi-year drought and wet episodes over North America.

### 21.6.2 Drought predictability

The above reported drought reconstruction was based on contemporaneous precipitation regressions of the SST PCs, and as such, does not allow for the inference that SST variations lead to drought and wet episodes. If North American droughts were primarily linked with tropical SST variability, the SST attribution would have been more straightforward, in view of the amassed observational and modeling evidence for the regional-to-hemispherical scale influence of tropical SST anomalies; the profound impact of El Niño SSTs, for example.

The SST–drought links articulated above however involve patterns with tropical *and* extratropical SST features, necessitating further analysis of causality. That tropical features remain the real instigators of droughts, with the mid-latitude ones (shaped, to an extent, by ensuing feedbacks) exerting more modest influence, is a distinct possibility, but one that cannot be confirmed or refuted by this observational analysis or even by modeling with present-day atmospheric models, which remain challenged in simulation, let alone prediction, of regional hydroclimate variability and change.

Regardless, some insight on the role of SST is provided from reconstructing droughts with antecedent SSTs. As the hydroclimate episodes of interest have durations of 4–10 years, the reconstruction is undertaken using decadal modes of SST variability. The droughts are reconstructed in Fig. 21.5 from the SST-leading regressions on continental precipitation. The reconstruction is obtained by multiplying the decadal SST PCs with their 1–6 year lagged precipitation regressions. The coherent nascent drought signals in the SST-leading reconstructions in Fig. 21.5 (and their absence in most SST-lagged reconstructions

shown in the far-right column of this figure) support the case for a causative role of SSTs in North American droughts. However, as the drought reconstruction reported in Fig. 21.5 is for periods not independent of the one used in generating the underlying building blocks (regressions), the drought/wetness reconstructed from antecedent SSTs in Fig. 21.5 cannot be considered SST-based hindcast prediction. This analysis nonetheless provides preliminary evidence for the potential predictability of droughts.

## 21.7 Drying of the Sahel

The declining precipitation over Sahel over a three-decade period (1950s to 1980s) remains enigmatic, as noted in the introduction. The multi-decade ‘drying’ is reconstructed in this section to gain insight into its causes. The drying signal is clearly manifest in the regionally averaged (20W–40E; 10N–20N) boreal summer (June–August) rainfall anomaly record (Fig. 21.6, solid black curve). The precipitous drop in precipitation from the mid 1950s to the mid 1980s (by over 1.5 mm/day) is idealized by the straight black line. The rainfall decline is very significant – leading to widespread use of the term ‘drying’ – as the seasonal summer rainfall over this continental strip (mostly its southern part) is 4.2 mm/day with an interannual standard deviation (SD) of 0.5 mm/day, i.e. the rainfall decline was almost 2 SD in the peak dry phase!

The Sahel rainfall record was reconstructed using Pacific and Atlantic SST PCs, just as over the Great Plains. The reconstructed rainfall (dashed black line in Fig. 21.6) tracks the observed rainfall closely (correlation 0.91), robustly capturing the drying of the Sahel and the rainfall recovery since. With the target in hand, partial rainfall reconstructions are undertaken to identify the influential modes of SST variability within the context of this analysis. Both the Atlantic and Pacific (green and blue curves respectively) are influential, albeit at different stages; Atlantic in the early and Pacific in the latter period, as indicated by the idealized green and blue straight-line drops. North Pacific decadal SST variability dominates the Pacific contribution and AMO-*Atl* the Atlantic one. Interestingly, the rainfall reconstructed from just these two modes of SST variability tracks the observed rainfall record almost as well as the full reconstruction (0.83 versus 0.91 correlation).

Statistical analysis and reconstruction often suffer from concerns related to causality and physicality in the case of analysis, and over-fitting in the case of reconstruction. The over-fitting is readily put to rest by noting that just two modes of SST variability can generate the Sahel rainfall record, including the multi-decade long drying episode and subsequent rainfall recovery. The first concern is more

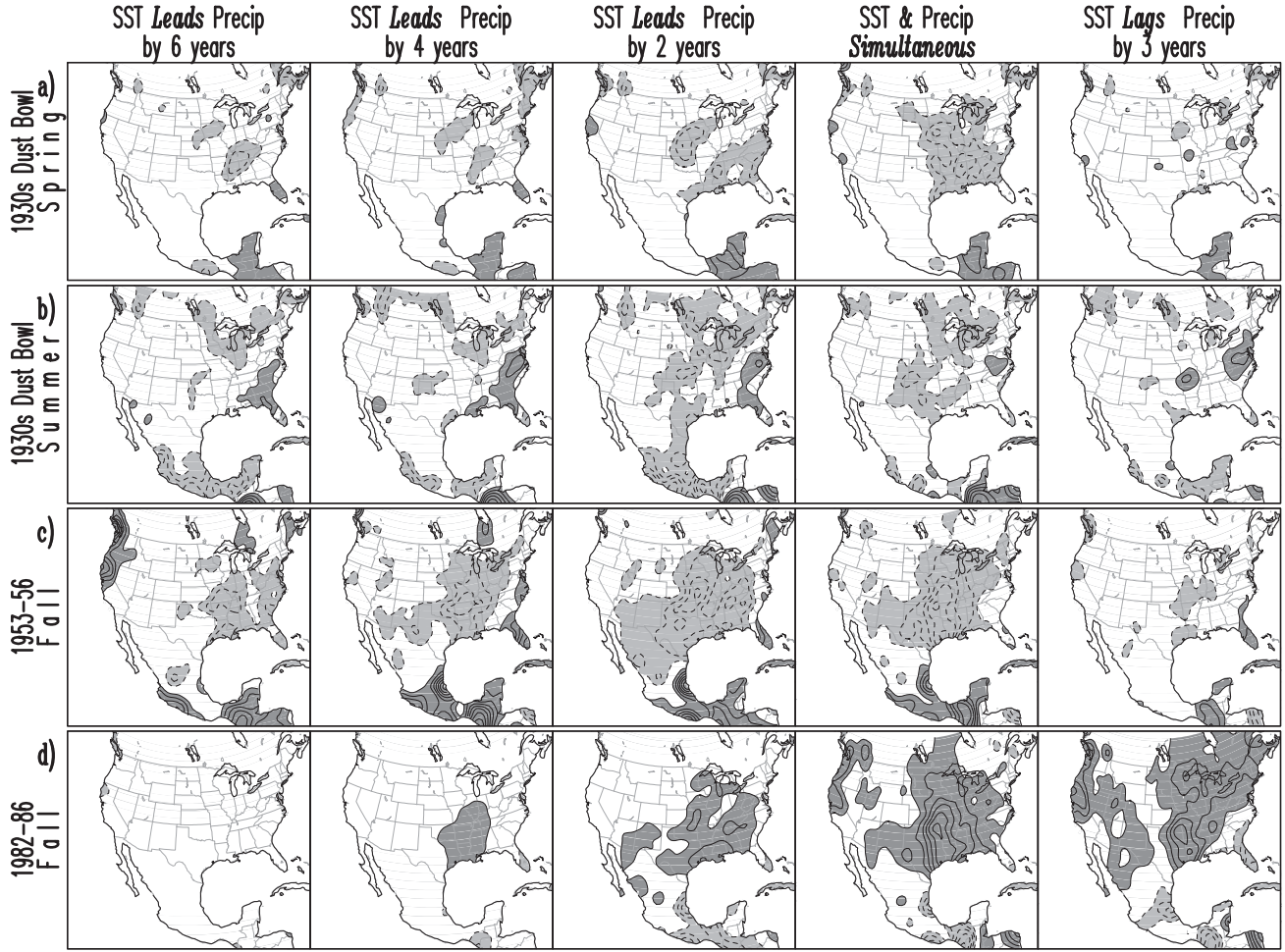


Fig. 21.5. Drought reconstruction based on SST-leading (and lagging) regressions of the decadal SST PCs (SST Secular Trend, PDV-North Pacific, ENSO-Non Canonical, AMO-*Atl*, and Low Frequency NAO): The SST-lead ranges from 6-to-0 years, and a 3-year SST-lag case (far right) is also shown. The drought build-up is evident with reduced SST-lead in each case. Rest as in Fig. 21.4a.

pertinent though as, unlike the Great Plains case, no follow-up analysis was presented to provide insight into the dynamical and thermodynamical processes causing the rainfall decline over the Sahel. This analysis, nonetheless, suggests that warm Atlantic SSTs (both in middle-high latitudes and the tropics-subtropics, cf. Fig. 21.3b) lead to a wetter Sahel, not a drier one; note Giannini *et al.* (2003) argue that warmer Atlantic SSTs lead to build-up of the oceanic ITCZ at the expense of the continental one, i.e. at odds with the AMO-*Atl* influence noted here.

A contemporaneous statistical link between North Pacific decadal SST variability (PDV-NP *a la* PDO) and Sahel rainfall seems more intriguing. Even if SSTs are assumed to be the cause, elaboration on the mechanism by which mid-latitude Pacific SST anomalies impact summer rainfall over northern tropical Africa would be challenging, as SST anomalies in only the Tropics are

generally considered causative. Interestingly, the PDV-NP is not without tropical links, notwithstanding its name. Guan and Nigam (2008) showed PDV-NP linked with the tropical Indian and Pacific basin SSTs; see also Deser *et al.* (2004). Figure 12 of Guan and Nigam shows SST regressions and correlations of the PDV-NP SST principal component. The correlation map readily reveals the tropical links, especially in the Indian Ocean and Western Pacific, where smaller amplitudes of SST variability create a detection challenge, but not for the correlation statistic.

The Indian Ocean SST links of the PDV-NP mode both impart plausibility and indicate a potential pathway by which this mode of Indo-Pacific SST variability can influence Sahel rainfall on decadal time scales. Note, the 1960s–1980s decline in Sahel rainfall is coincident with the phase-reversal of the PDV-NP mode (from positive to negative phase; cf. Figure 2 in GN2008), i.e. coincident

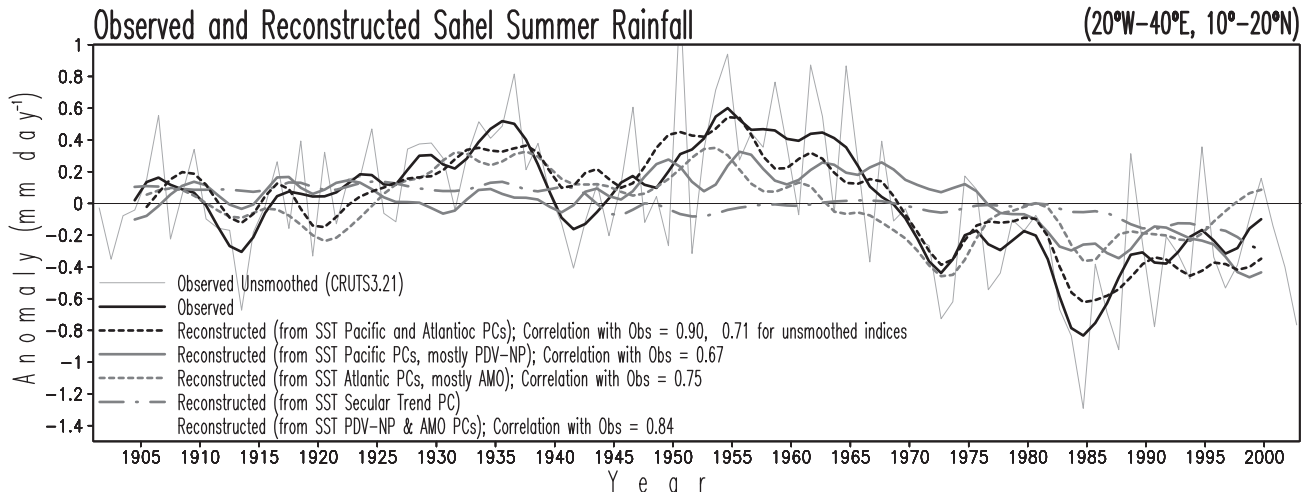


Fig. 21.6. Observed and reconstructed Sahel rainfall record. The 20W–40E and 10N–20N averaged rainfall anomaly in boreal summer (June–August) is shown during the twentieth century. Observed anomaly is depicted by the solid black line, while the Pacific and Atlantic SST based rainfall reconstruction is shown by the dashed black line (correlated at 0.91 with the observed record). The individual basin contributions to the reconstruction are in blue (Pacific) and green (Atlantic); the contribution of SST Secular Trend alone is in red. All curves have been smoothed from three applications of the 1-2-1 smoother on yearly summer data. That Sahel rainfall variations can be effectively reconstructed from just the AMO-*Atl* and PDV-NP rainfall regressions is evident from the 0.83 correlation of this reconstruction with observations, as noted in legend. Inclusion of the other nine SST principal component contributions improves the correlation only slightly, to 0.91; the correlation is 0.72 without any smoothing.

with the multidecadal warming of the tropical-subtropical Indian Ocean basin. The competition between continental (African and Indian) and oceanic (Indian basin) convection could be a mechanism underlying the statistical link between Sahel rainfall and North Pacific (and Indian Ocean) decadal SST variability.

## 21.8 Concluding remarks

Droughts (and wet episodes) over the Great Plains have been linked to SST variability in the Pacific and Atlantic basins. The basin influences have however yet to be fully evaluated, in part, because the SST-forced dynamical models of the atmosphere – a common investigative tool – remain challenged in simulation of regional hydroclimate variability; the specification of SST anomalies in the models' extratropics may be problematic as well (Kushnir *et al.*, 2002).

Here we adopt a statistical approach rooted in spatio-temporal (extended-EOF) analysis of twentieth century SST variations (GN2008, GN2009) and related drought links (Guan, 2008), which leads to impressive reconstruction of several (but not all) major droughts and wet episodes; attesting to the extent of the SST influence on Great Plains hydroclimate in nature. We find Atlantic SSTs, tropical, and extratropical, to be particularly

influential; often, more than the Pacific ones, and more than indicated in previous analyses (especially those based on SST-forced atmospheric models): AMO is the dominant contributor in the Dust Bowl spring drought and in the 1980s fall wetness (i.e. in two of the four episodes), while tropical Atlantic SST variability is in another (Dust Bowl summer). As a basin, the Atlantic is more influential than the Pacific in three of the four reconstructed episodes (cf. Table 21.1).

The AMO's influence on continental hydroclimate is provided circulation context from analysis of low-level flow and column stationary moisture flux, both obtained from NOAA's Twentieth Century Reanalysis. The modulation of moisture transport is important, especially in fall when AMO's impact on Great Plains precipitation is strongest. A hypothesis for how the AMO atmospheric circulation anomalies are generated from AMO SSTs was proposed by Nigam *et al.* (2011) to advance discussion of the influence pathways of the mid-to-high latitude SST anomalies.

The Atlantic SSTs evidently exert a profound influence on Great Plains hydroclimate on decadal time scales, especially in the transition seasons; an influence not represented in the SST-forced dynamical models of the atmosphere. For instance, Schubert *et al.* (2009) find a cold Pacific and neutral Atlantic to be significantly more influential for US droughts than a neutral Pacific and warm Atlantic

(PcAn>>PnAw in their drought modeling experiment nomenclature).

Our analysis suggests that the La Niña – US drought paradigm – operative on interannual time scales in nature – has been conferred excessive relevance on decadal time scales in the recent literature, in part, because dynamical models of the atmosphere are unable to represent the influence of Atlantic SSTs on Great Plains hydroclimate.

With respect to multidecadal rainfall variations over Sahel, including the drying of Sahel in the 1950s to 1980s, our statistical analysis indicates an important role for both AMO-*Atl* and Indo-Pacific decadal SST variability (PDV-NP). The dynamical and thermodynamical mechanisms underlying these links need elaboration, but a potential influence pathway is briefly discussed.

Regardless, the present analysis is encouraging for the investigation of the SST-based experimental statistical decadal prediction of North American and African droughts, complementing related dynamical predictions.

## 21.9 Acknowledgments

The reported analysis draws heavily – text and figures – on the authors’ prior publication: Nigam, S., B. Guan, and A. Ruiz-Barradas (2011): Key role of the Atlantic Multidecadal Oscillation in 20th century drought and wet periods over the Great Plains. *Geophys. Res. Lett.*, **38**, L16713, doi:10.1029/2011GL048650.

A.B. contributed to data set development and the preliminary analysis of Pacific SST variability. Bin Guan refined and extended the Pacific analysis, performed the Atlantic SST analysis, and extracted the SST-drought links, all as part of his doctoral dissertation to the University of Maryland (defended October 2008). S.N. formulated the research design, refined the analysis strategy, conducted the column moisture-flux analysis, and developed the manuscript.

## References

- Barlow, M., S. Nigam, and E. Berbery (2001). ENSO, Pacific decadal variability, and US summertime precipitation, drought, and stream flow. *Journal of Climate* **14**(9), 2105–2128.
- Biasutti, M., et al. (2008). SST forcings and Sahel rainfall variability in simulations of the twentieth and twenty-first centuries. *Journal of Climate* **21**(14), 3471–3486.
- Charney, J. (1976). Dynamics of deserts and drought in Sahel – Reply. *Quarterly Journal of the Royal Meteorological Society* **102**(432) 468–468.
- Charney, J. and P. Stone (1976). Drought in Sahara – Insufficient biogeophysical feedback. *Science* **191**(4222), 100–102.
- Compo, G., et al. (2011). The twentieth century reanalysis project. *Quarterly Journal of the Royal Meteorological Society* **137**(654), 1–28.
- Cook, B., R. Miller, and R. Seager (2009). Amplification of the North American “Dust Bowl” drought through human-induced land degradation. *Proceedings of the National Academy of Sciences of the United States of America* **106**(13), 4997–5001.
- Dai, A., K. Trenberth, and T. Qian (2004). A global dataset of Palmer Drought Severity Index for 1870–2002: Relationship with soil moisture and effects of surface warming. *Journal of Hydrometeorology* **5**(6), 1117–1130.
- Deser, C., A. Phillips, and J. Hurrell (2004). Pacific interdecadal climate variability: Linkages between the tropics and the North Pacific during boreal winter since 1900. *Journal of Climate* **17**(16), 3109–3124.
- Enfield, D. and L. Cid-Serrano (2010). Secular and multidecadal warmings in the North Atlantic and their relationships with major hurricane activity. *International Journal of Climatology* **30**(2), 174–184.
- Enfield, D., A. Mestas-Nunez, and P. Trimble (2001). The Atlantic multidecadal oscillation and its relation to rainfall and river flows in the continental US. *Geophysical Research Letters* **28**(10), 2077–2080.
- Folland, C., T. Palmer, and D. Parker (1986). Sahel rainfall and worldwide sea surface temperatures, 1901–85. *Nature* **320** (6063) 602–607.
- Giannini, A., R. Saravanan, and P. Chang (2003). Oceanic forcing of Sahel rainfall on interannual to interdecadal time scales. *Science* **302**(5647) 1027–1030.
- Guan, B. (2008). Pacific sea surface temperatures in the twentieth century: Variability, trend, and connections to long-term hydroclimate variations over the Great Plains, *Ph.D. thesis*, 116 pp., Univ. of Maryland, College Park.
- Guan, B. and S. Nigam (2008). Pacific sea surface temperatures in the twentieth century: An evolution-centric analysis of variability and trend. *Journal of Climate* **21**(12), 2790–2809.
- Guan, B. and S. Nigam (2009). Analysis of Atlantic SST variability factoring interbasin links and the secular trend: Clarified structure of the Atlantic Multidecadal Oscillation. *Journal of Climate* **22**(15), 4228–4240.
- Hare, S. and N. Mantua (2000). Empirical evidence for North Pacific regime shifts in 1977 and 1989. *Progress in Oceanography* **47**(2–4), 103–145.
- Held, I., et al. (2005). Simulation of Sahel drought in the 20th and 21st centuries. *Proceedings of the National Academy of Sciences of the United States of America* **102**(50), 17891–17896.
- Huang, J., H. vandenDool, and K. Georgakakos (1996). Analysis of model-calculated soil moisture over the United States (1931–1993) and applications to long-range temperature forecasts. *Journal of Climate* **9**(6), 1350–1362.
- Hulme, M. (1992). Rainfall changes in Africa – 1931–1960 to 1961–1990. *International Journal of Climatology* **12**(7) 685–699.
- Joseph, R. and S. Nigam (2006). ENSO evolution and teleconnections in IPCC’s twentieth-century climate simulations:

- Realistic representation? *Journal of Climate* **19**(17) 4360–4377.
- Kalnay, E., et al. (1996). The NCEP/NCAR 40-year reanalysis project. *Bulletin of the American Meteorological Society* **77**(3), 437–471.
- Kushnir, Y., et al. (2002). Atmospheric GCM response to extra-tropical SST anomalies: Synthesis and evaluation. *Journal of Climate* **15**(16), 2233–2256.
- Kushnir, Y., et al. (2010). Mechanisms of tropical Atlantic SST influence on North American precipitation variability. *Journal of Climate* **23**(21), 5610–5628.
- McCabe, G., et al. (2008). Associations of multi-decadal sea-surface temperature variability with US drought. *Quaternary International* **188** 31–40.
- McCabe, G., M. Palecki, and J. Betancourt (2004). Pacific and Atlantic Ocean influences on multidecadal drought frequency in the United States. *Proceedings of the National Academy of Sciences of the United States of America* **101**(12), 4136–4141.
- Mitchell, T. and P. Jones (2005). An improved method of constructing a database of monthly climate observations and associated high-resolution grids. *International Journal of Climatology* **25**(6), 693–712.
- Mo, K., J. Schemm, and S. Yoo (2009). Influence of ENSO and the Atlantic Multidecadal Oscillation on Drought over the United States. *Journal of Climate* **22**(22) 5962–5982.
- Namias, J. (1966). Nature and possible causes of northeastern United States drought during 1962–65. *Monthly Weather Review* **94**(9), 543–554.
- Nigam, S. and B. Guan (2011). Atlantic tropical cyclones in the twentieth century: natural variability and secular change in cyclone count. *Climate Dynamics* **36**(11–12), 2279–2293.
- Nigam, S., B. Guan, and A. Ruiz-Barradas (2011). Key role of the Atlantic Multidecadal Oscillation in 20th century drought and wet periods over the Great Plains. *Geophysical Research Letters* **38**.
- Nigam, S. and A. Ruiz-Barradas (2006). Seasonal hydroclimate variability over north America in global and regional reanalyses and AMIP simulations: Varied representation. *Journal of Climate* **19**(5), 815–837.
- Nigam, S., M. Barlow, and E. H. Berbery (1999). Analysis links Pacific decadal variability to drought and streamflow in United States, *Eos Trans. AGU*, **80**, 621–625, doi:10.1029/99EO00412.
- Quenouille, M. H. (1952). *Associated Measurements*, Academic, New York.
- Palmer, W. C. (1966). Meteorological drought. *U.S. Weather Bureau Tech. Paper 45*, 58 pp. Available from NOAA/National Weather Service, 1325 East-West Highway, Silver Spring, MD 20910.
- Rasmusson, E. and T. Carpenter (1983). The relationship between eastern equatorial Pacific sea-surface temperatures and rainfall over India and Sri-Lanka. *Monthly Weather Review* **111**(3) 517–528.
- Rayner, N., et al. (2003). Global analyses of sea surface temperature, sea ice, and night marine air temperature since the late nineteenth century. *Journal of Geophysical Research-Atmospheres* **108**(D14).
- Ropelewski, C. and M. Halpert (1987). Global and regional scale precipitation patterns associated with the El Niño Southern Oscillation. *Monthly Weather Review* **115**(8) 1606–1626.
- Ruiz-Barradas, A. and S. Nigam (2005). Warm season rainfall variability over the US great plains in observations, NCEP and ERA-40 reanalyses, and NCAR and NASA atmospheric model simulations. *Journal of Climate* **18**(11) 1808–1830.
- Ruiz-Barradas, A. and S. Nigam (2010a). Great Plains precipitation and its SST links in twentieth-century climate simulations, and twenty-first- and twenty-second-century climate projections. *Journal of Climate* **23**(23), 6409–6429.
- Ruiz-Barradas, A. and S. Nigam (2010b). SST-North American Hydroclimate Links in AMIP Simulations of the Drought Working Group Models: A Proxy for the Idealized Drought Modeling Experiments. *Journal of Climate* **23**(10), 2585–2598.
- Ruiz-Barradas, A. and S. Nigam (2013). Atmosphere-land surface interactions over the Southern Great Plains: Characterization from pentad analysis of DOE ARM field observations and NARR. *Journal of Climate* **26**(3), 875–886.
- Schubert, S., et al. (2009). A US CLIVAR project to assess and compare the responses of global climate models to drought-related SST forcing patterns: Overview and results. *Journal of Climate* **22**(19) 5251–5272.
- Schubert, S., et al. (2004). Causes of long-term drought in the US Great Plains. *Journal of Climate* **17**(3) 485–503.
- Seager, R., et al. (2005). Modeling of tropical forcing of persistent droughts and pluvials over western North America: 1856–2000. *Journal of Climate* **18**(19) 4065–4088.
- Slonosky, V., L. Mysak, and J. Derome (1997). Linking Arctic sea-ice and atmospheric circulation anomalies on interannual and decadal timescales. *Atmosphere-Ocean* **35**(3), 333–366.
- Sutton, R. and D. Hodson (2005). Atlantic Ocean forcing of North American and European summer climate. *Science* **309**(5731), 115–118.
- Ting, M., et al. (2009). Forced and internal twentieth-century SST trends in the North Atlantic. *Journal of Climate* **22**(6), 1469–1481.
- Ting, M. and H. Wang (1997). Summertime US precipitation variability and its relation to Pacific sea surface temperature. *Journal of Climate* **10**(8), 1853–1873.
- van den Dool, H., J. Huang, and Y. Fan (2003). Performance and analysis of the constructed analogue method applied to US soil moisture over 1981–2001. *Journal of Geophysical Research-Atmospheres* **108**(D16).
- von Storch H. and F. W. Zwiers (1999). *Statistical Analysis in Climate Research*. Cambridge University Press, 494 pp.
- Wang, C., et al. (2006). Influences of the Atlantic warm pool on western hemisphere summer rainfall and Atlantic hurricanes. *Journal of Climate* **19**(12), 3011–3028.

- Weare, B. and J. Nasstrom (1982). Examples of extended empirical orthogonal function analyses. *Monthly Weather Review* **110**(6), 481–485.
- Weaver, S. and S. Nigam (2008). Variability of the great plains low-level jet: Large-scale circulation context and hydroclimate impacts. *Journal of Climate* **21**(7), 1532–1551.
- White, W. B., A. Gershunov, and J. Annis (2008). Climatic influences on Midwest drought during the twentieth century, *Journal of Climate* **21**, 517–533.
- Zhang, R. and T. Delworth (2006). Impact of Atlantic multi-decadal oscillations on India/Sahel rainfall and Atlantic hurricanes. *Geophysical Research Letters* **33**(17).

# Floods and droughts along the Guinea Coast in connection with the South Atlantic Dipole

Hyacinth C. Nnamchi and Jianping Li

## 22.1 Introduction

Precipitation is arguably the most important climatic factor affecting the landscape and socio-economic activities in Africa. The socio-economic significance of precipitation derives partly from the preponderance of subsistence agriculture, often relying solely on precipitation, and on the influence of precipitation on the local hydrology and water resources. Africa is subject to frequent floods and droughts. In fact, it has been argued that the economic fortunes of the continent may be directly linked to variations in precipitation (Washington *et al.*, 2006, Sheffield *et al.*, 2014).

The Guinea Coast is bordered by the tropical Atlantic Ocean and includes the countries of West and Central Africa. These countries are among the most densely populated places on the continent, with the highest concentrations near the coasts, where the population is projected to rise by >30% more than the continent-wide increase by 2050 (Population Reference Bureau, 2013). This rapidly growing population translates into a significant and growing pressure on the precipitation-dependent resources available for use by agriculture, industries, energy production, etc.

Understanding precipitation variability across Africa has presented a considerable problem, and various lines of research have been followed in different areas. For instance, largely motivated by cycles of drought and flood in the Sahel, research has focused on the albedo–precipitation feedback caused by land cover changes (e.g. Xue and Shukla, 1993, Taylor *et al.*, 2002) and the impacts of sea surface temperature (SST) variability (e.g. Giannini *et al.*, 2003, Held *et al.*, 2005, Biasutti *et al.*, 2008, Rodríguez-Fonseca *et al.*, 2011).

For the Guinea Coast region, the Gulf of Guinea SST, or specifically the Atlantic Niño (the basin's equivalent of the equatorial Pacific El Niño), is usually implicated as the dominant driver of interannual variability (Wagner and Da Silva, 1994, Vizy and Cook, 2001, Losada *et al.*, 2010). However, recent observational and modeling studies show

that precipitation along the Guinea Coast is not only positively related to the Atlantic Niño sector, but also coherently negatively related to SST anomalies off the Brazil–Uruguay–Argentina coast (Nnamchi and Li, 2011, Nnamchi *et al.*, 2013). Indeed, the correlation map of Guinea Coast precipitation indices with SST clearly reproduces the opposite pattern characteristic of the South Atlantic Ocean Dipole (SAOD), and not merely the equatorial Atlantic Niño (Venegas *et al.*, 1996, 1997, Nnamchi *et al.*, 2011, Nnamchi, 2013).

In this chapter, we highlight the connection between this oceanic mode of variability and the occurrence of floods and droughts on the Guinea Coast. We draw from the recent studies mentioned above, and also present original analyses based on data sets of monthly total precipitation and wet day frequency obtained from the Climatic Research Unit of the University of East Anglia, Norwich, United Kingdom v3.21 available at  $0.5^\circ \times 0.5^\circ$  longitude–latitude grids (Harris *et al.*, 2014), as well as the month mean SST data set obtained from the Hadley Centre Sea Ice and Sea Surface Temperature v1 at  $1^\circ \times 1^\circ$  grids (Rayner *et al.*, 2003).

## 22.2 Gross features of annual precipitation on the Guinea Coast

Annual total precipitation shows well-defined spatial and temporal patterns over West and Central Africa (Fig. 22.1). Maximum annual total precipitation occurs around the western coastal extremity near the Guinea and Fouta Djalon highlands, with slightly lower amounts recorded from the Cameroon Mountain range and extending into much of southern Nigeria (Fig. 22.1a). The comparatively higher annual total precipitation in these areas reflects the combined roles of coastal and orographic influences. However, this coastal influence is not evident around the prime meridian south of latitude  $10^\circ\text{N}$ , which marks the ‘Ghana–Togo gap’ where the annual total precipitation is

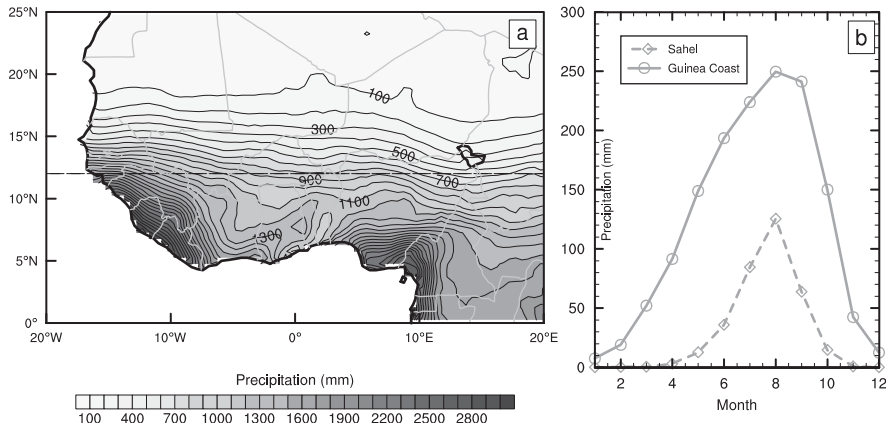


Fig. 22.1. Annual distribution of precipitation over West Africa. (a) Spatial distribution of total annual precipitation ( $\text{mm}^{-1}$  year). (b) Annual cycle of precipitation ( $\text{mm}^{-1}$  month) over the Sahel ( $20^{\circ}\text{E}$ – $20^{\circ}\text{W}$ ,  $12$ – $20^{\circ}\text{N}$ ) and the Guinea Coast ( $20^{\circ}\text{E}$ – $20^{\circ}\text{W}$ ,  $4$ – $12^{\circ}\text{N}$ ). The boundary between the two regions is shown at  $12^{\circ}\text{N}$  by the dashed line in Fig. 22.1a.

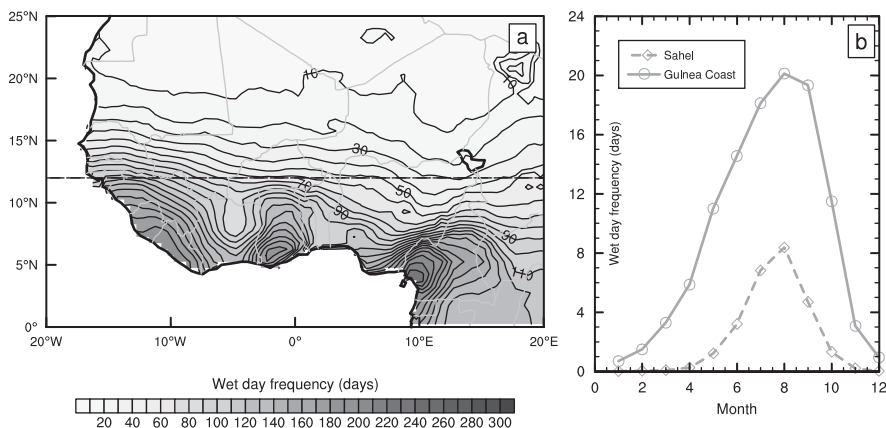


Fig. 22.2. As for Fig. 22.1, but for wet day frequency.

generally lower (Acheampong, 1982, Hayward and Oguntanyibo, 1987). North of latitude  $10^{\circ}\text{N}$ , the annual total precipitation is strongly dependent on latitude, and decreases steadily into the Sahel.

Two precipitation regions are commonly recognized in West Africa and are delineated here by the latitude  $12^{\circ}\text{N}$ . One is the Guinea Coast, which borders the Gulf of Guinea and lies south of latitude  $12^{\circ}\text{N}$ ; the other is the Sahel, which is farther north. The evolutions of monthly mean precipitation averaged over the Guinea Coast ( $20^{\circ}\text{W}$ – $20^{\circ}\text{E}$ ,  $4$ – $12^{\circ}\text{N}$ ) and Sahel ( $20^{\circ}\text{W}$ – $20^{\circ}\text{E}$ ,  $12$ – $20^{\circ}\text{N}$ ) are shown in Fig. 22.1b. Precipitation in both regions is characterized by a pronounced annual cycle. Precipitation amounts increase from the beginning of the year, peak in August, and then decline relatively rapidly. This quasi-symmetrical annual cycle of precipitation highlights the well-known influence of the West African monsoon. Consistent with the spatial pattern in the map of annual total precipitation (Fig. 22.1a), we see also in the line plot of the annual cycle that precipitation on the Guinea Coast exceeds the amount over the Sahel throughout the year (Fig. 22.1b).

As shown in Fig. 22.2a, the spatial distribution of annual total wet day frequency closely resembles that of annual

precipitation, especially over the Sahel. Over the Guinea Coast, however, the ‘Ghana–Togo gap’ is small in size, and is largely restricted to east of the prime meridian. The similarity of the annual precipitation and wet day frequency reflects the seasonal character of precipitation in the region. Thus, the annual cycle of wet day frequency (Fig. 22.2b) follows the cycle of total precipitation shown earlier in Fig. 22.1b.

The highest monthly precipitation amounts and frequencies are observed in July–August–September (JAS hereafter). These three months account for around 50% and 80% of the total annual precipitation for the Guinea Coast and Sahel, respectively (see Table 22.1). Interestingly, this peak season of precipitation over West Africa coincides with the peak phase of the SAOD (Nnamchi *et al.*, 2011) and the West African summer monsoon (WASM). The WASM constitutes a dominant influence on interannual precipitation variability in the Sahel. However, the WASM index (Li and Zeng, 2002, 2003) is not correlated with summer precipitation on the Guinea Coast. On the other hand, the SAOD is not correlated with precipitation over the Sahel, but is strongly correlated with precipitation over the Guinea Coast (Nnamchi and Li, 2011).

The remainder of this chapter describes the interannual variability of precipitation, floods, and droughts on the Guinea Coast, before examining the associated dominant SAOD SST-type and atmospheric mechanisms. Table 22.1 shows some basic statistical properties of Guinea Coast and Sahel precipitation based on JAS mean data from 1901 to 2012. The mean precipitation in these months exhibits marked variability with a range of 88.11 mm/month and a standard deviation of 17.88 mm/month on the Guinea Coast. However, Sahel precipitation shows much greater variability. For example, the coefficient of variability ( $CV = \sigma/\text{mean}$ , where  $\sigma$  is the standard deviation) of Sahel precipitation is more than two times greater than the CV of Guinea Coast precipitation.

All subsequent analyses are based on the anomaly time series of the parameter under consideration. The anomaly time series is calculated for every grid-point as follows:

$$x' = x - \bar{x}, \quad (22.1)$$

where  $x'$  is the monthly anomaly time series for the parameter (precipitation, wet day frequency, SST),  $x$  is the original monthly time series, and  $\bar{x}$  is the mean of  $x$  from 1901 to 2012.

**Table 22.1. Statistical analysis of Guinea Coast precipitation. Except the percentages, all other properties are JAS-mean in units of mm/month.**

Property	Guinea Coast	Sahel
Mean	238.29	91.30
% of annual total	49.90%	80.09%
Median	240.96	90.90
Lower quartile	225.46	80.04
Upper quartile	249.84	102.46
Standard deviation	17.88	15.41
Coefficient of variation	7.50%	16.89%
Range	88.11	86.78
Highest precipitation	279.00 (1963)	137.21 (1950)
Lowest precipitation	90.88 (1914)	50.43 (1984)

Figure 22.3 shows time evolution of the JAS interannual (that is, year to year) precipitation anomaly averaged over the Guinea Coast from 1901 to 2012, which has been normalized by its standard deviation. We now see that despite the earlier comparison of the CVs indicating far greater variability for the Sahel, the Guinea Coast precipitation really exhibited very strong inter-annual variability during the entire 112-year study period.

## 22.3 Floods and droughts on the Guinea Coast

Here, a flood is defined as an overflow of water that submerges locations normally dry. The inundation may come from rivers (lakes) overflowing their banks (basins), or as a direct result of surface runoff due to precipitation. Flooding can result from changes in atmospheric conditions (e.g. precipitation amount, type, and timing, as well as temperature), land use/land cover change related to agricultural practices, and urbanization or water management practices such as the construction of dams, levees, and river diversions (Peterson *et al.*, 2013). At particular locations, several combinations of these factors may occur together so that it becomes extremely difficult to determine the relative importance of each.

A drought is a period of unusually dry weather that persists long enough to cause water supply shortages with attendant environmental and socio-economic consequences. Roughly speaking, droughts may be regarded as the opposite of floods, except that dry conditions tend to develop more gradually than wet conditions. Like floods, droughts are a complex phenomenon, and exhibit varying characteristics in terms of their duration, intensity, areal extent, and environmental and socio-economic impacts. Both floods and droughts are widespread, naturally occurring phenomena that are often exacerbated by human activities.

Given the obvious importance of precipitation to the water cycle, a large-scale precipitation index for the Guinea Coast can be used to constrain the conditions

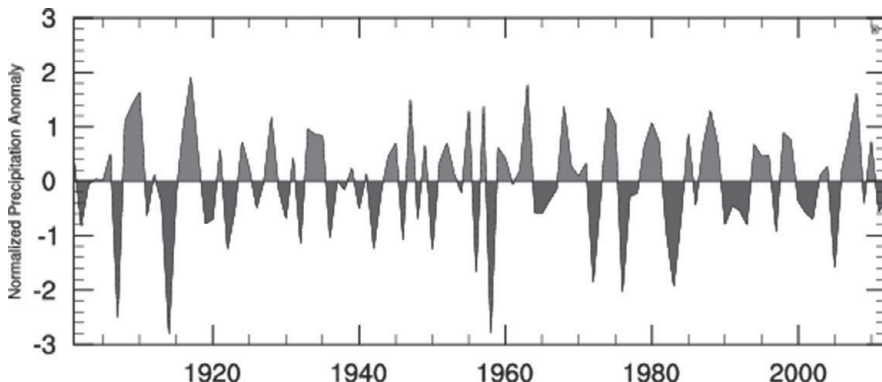


**Fig. 22.3.** Interannual fluctuations in JAS precipitation over the Guinea Coast for the period 1901–2012. The decadal variation, determined using an 11-year running mean, has been removed from the time series.

required to generate floods and droughts. Simply put, a large excess of precipitation on the Guinea Coast over any particular year leads to large-scale floods. On the other hand, a large precipitation deficit leads to widespread droughts. According to Saha (2010), a useful threshold for determining the large excess or deficit, and therefore the occurrence of floods and droughts, is  $\pm 1.28\sigma$ . Thus, we have:

$$\text{Flood if } [x_i - \bar{x}/\sigma_x] > +1.28,$$

$$\text{Drought if } [x_i - \bar{x}/\sigma_x] < -1.28,$$

where  $x_i$  denotes the Guinea Coast JAS precipitation for the  $i$ th year,  $\bar{x}$  represents the average precipitation for the 112 years from 1901 to 2012 inclusive, and  $\sigma_x$  represents the standard deviation of precipitation for the same period.

Based on the above definition, there were 11 flood years and eight drought years along the Guinea Coast between 1901 and 2012. These flood and drought years are listed in

**Table 22.2.** However, it is important to note that although floods may occur more frequently than droughts, the droughts tend to be more severe. For example, the precipitation anomaly is less than  $-1.5\sigma$  in all eight drought years, but exceeded  $+1.5\sigma$  only in five flood years (1910, 1917, 1947, 1963, and 2008).

Using the threshold of  $\pm 1.28\sigma$  for flood and drought years, we created composite maps of the JAS total precipitation over the Guinea Coast (Fig. 22.4). In flood years, precipitation over the Guinea Coast shows widespread above-average amounts. Maximum excesses occur from western Nigeria to Ghana, and over Liberia. In contrast, most locations recorded below-average precipitation during drought years. Again, the maximum deficits occurred in regions of excessive precipitation during flood years.

As would be expected, most locations on the Guinea Coast recorded an above-average number of wet days during the flood years, and a below-average number of wet days during the drought years (Fig. 22.5). The highest

Table 22.2. Flood and drought years on the Guinea Coast.

Event	Years of occurrence	Mean anomaly of precipitation (mm/month)
Flood	1909, 1910, 1917, 1947, 1955, 1957, 1963, 1968, 1974, 1988, 2008.	+83.92 mm
Drought	1907, 1914, 1956, 1958, 1972, 1976, 1983, 2005.	-112.45 mm

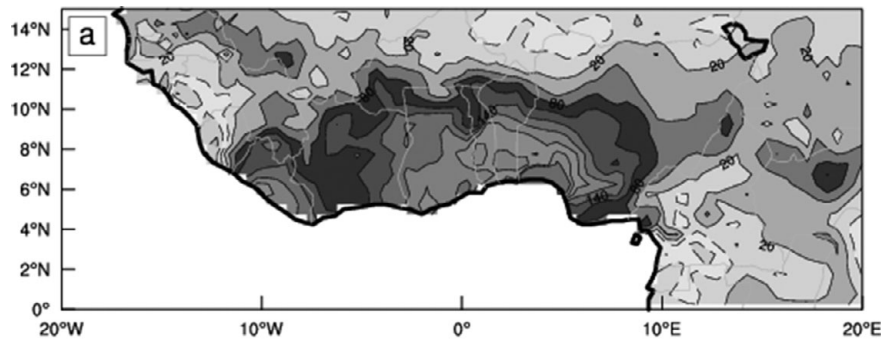
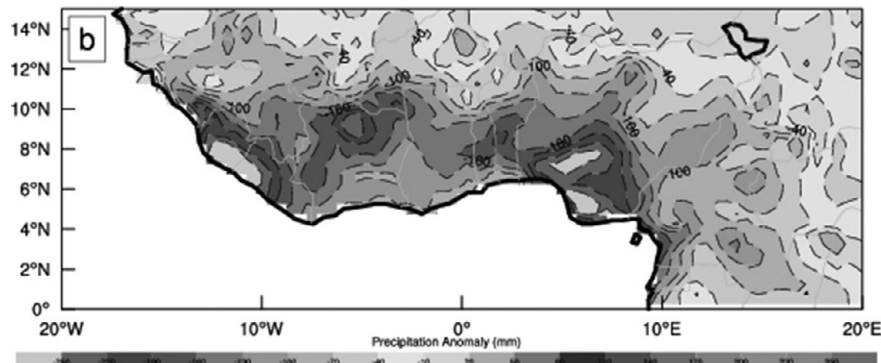


Fig. 22.4. Spatial distribution of the JAS total precipitation anomaly over the Guinea Coast in flood years.



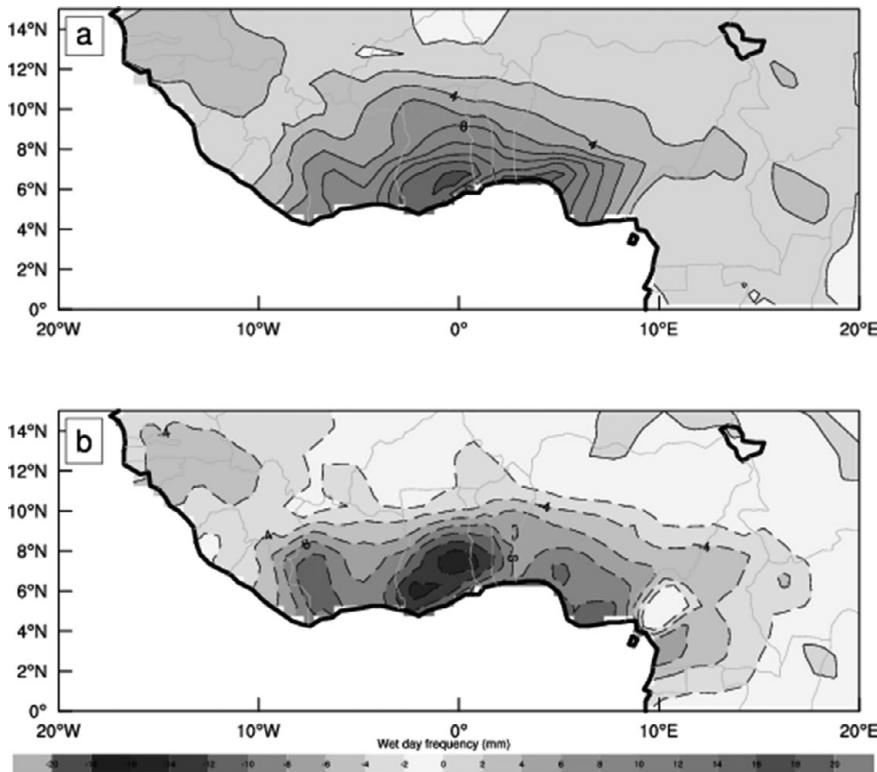


Fig. 22.5. Spatial distribution of the JAS total wet day frequency anomaly over the Guinea Coast in flood and drought years.

wet day anomalies occurred in the coastal central areas of the ‘Ghana–Togo gap’, where the annual total precipitation is comparatively low. In contrast, Fouta Djalon, Guinea, and the Cameroon highlands have the highest annual total precipitation amounts and experience low anomalies of wet day frequency in both flood and drought years. The frequent occurrence of wet day anomalies in the climatologically drier ‘Ghana–Togo gap’ suggests that the floods result mainly from the higher frequency (but lower magnitude) of precipitation there. However, during drought years in the ‘gap’, the number of rainy days declines drastically. The Fouta Djalon, Guinea, and Cameroon highlands areas are characterized by lower-frequency, higher-magnitude, precipitation events.

#### 22.4 Discussion: influence of the SAOD on regional precipitation

Recent studies have investigated the character and impacts of the SAOD on regional precipitation (Venegas *et al.*, 1996, 1997, Nnamchi *et al.*, 2011, 2013, Nnamchi and Li, 2011). The description in this chapter of the process through which the SAOD could influence the Guinea Coast is based on these research papers. Here, we again use the flood and drought years along the Guinea Coast to generate composite maps of SST anomaly patterns (Fig. 22.6). During the Guinea Coast flood years, the

equatorial Atlantic Ocean (i.e. the Atlantic Niño sector in the Gulf of Guinea bordering the coast) is characterized by a positive SST anomaly pattern. There is also a widespread negative SST anomaly in the southwestern part of the South Atlantic Ocean off the coasts of Brazil, Uruguay, and Argentina. This opposite polarity pattern in SST is referred to as the SAOD.

Strongly coupled to the SAOD-type SST patterns are the modelled fields of atmospheric motion (Fig. 22.7). Thus, during Guinea Coast flood years, the southeastern coast of South America is marked by anticyclonic circulation, while low-level cyclonic motion occurs over the Gulf of Guinea. Therefore, precipitation is greatly enhanced over the Gulf of Guinea and nearby coastal countries (and suppressed over the Brazil–Uruguay–Argentina complex due to the nearby anomalously cool ocean surface).

The opposite SST and atmospheric circulation polarities are associated with a horizontal gradient. Thus, the atmospheric mass subsiding off the Brazil–Uruguay–Argentina coast tends to boost the mass convergence, and then upward motion over the Gulf of Guinea through a modified Hadley circulation. This equatorial rising motion is consistent with the widespread increase in Guinea Coast precipitation in flood years. Furthermore, the Gulf of Guinea and equatorial Atlantic Ocean are the major moisture sources for floods on the Guinea Coast. As a result of the oceanic/coastal nature of the SAOD-related convergence, the continental convergence traditionally associated with

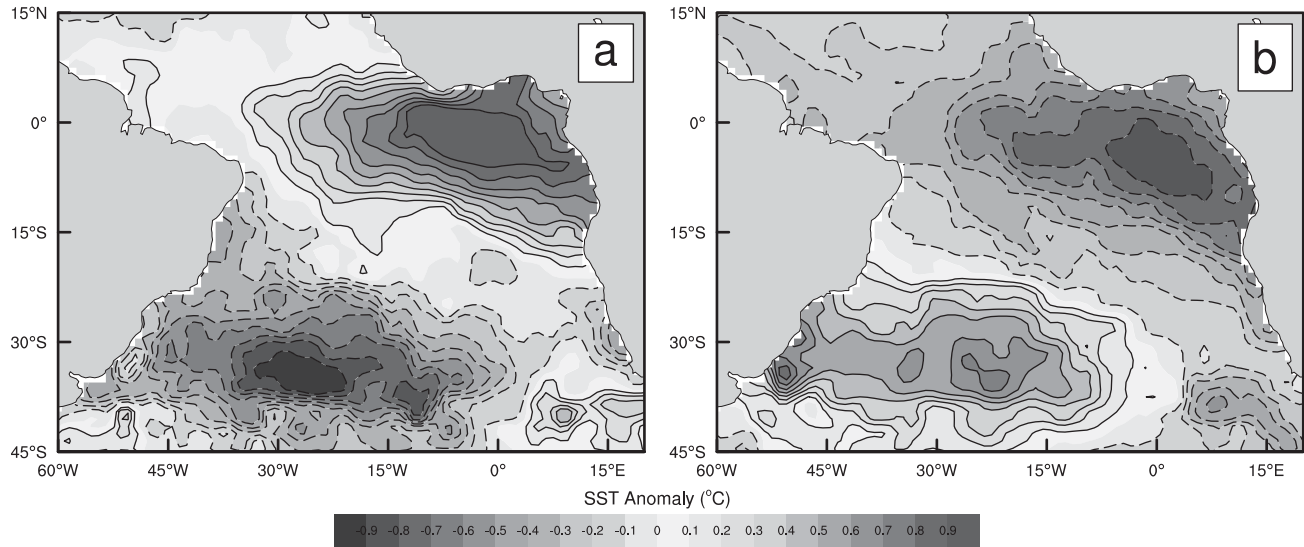


Fig. 22.6. Composite of Atlantic SST anomaly showing the SAOD in flood and drought years on the Guinea Coast.

the West African summer monsoon is weakened, and therefore precipitation is largely restricted to the coast.

The SST distribution in the South Atlantic Ocean is completely reversed in drought years over the Guinea Coast. Thus, the Atlantic Niño sector is characterized by widespread cool SST anomalies. On the other hand, warming anomalies occur off the coast of southeastern South America. As a result, the atmospheric circulation pattern is equally reversed (not shown here), with the result of a widespread decline in both precipitation amounts and the number of wet days over the Guinea Coast.

## 22.5 Summary and prospects

As a major monsoon region, precipitation in West Africa, and extending well into Central Africa, exhibits a strong annual cycle with the highest precipitation amounts occurring during the boreal summer monsoon season. The annual distribution is dominated by oceanic, orographic, and latitudinal dependencies, a pattern disrupted by the ‘Ghana–Togo gap’. However, in addition to these quasi-regular features of the mean annual total and cycle of precipitation, that are easily explained by the aforementioned factors, the region also experiences marked year to year variations. In particular, both floods and droughts are relatively common occurrences.

Understandably, several factors may lead to the occurrence of floods and droughts. These include atmospheric conditions; land use/land cover change related to agricultural practices; urbanization or water management practices, such as the construction of dams, levees, and river diversions; and socio-economic circumstances, such as the

level of infrastructural development. In reality, these factors are usually intertwined, and isolating them can prove difficult. However, atmospheric conditions are a primary driver of the occurrence of floods and droughts, and precipitation is perhaps the most important atmospheric indicator of both phenomena.

Over the seasonal and longer time scales, the ocean is a major driver of atmospheric and climate variability. In this chapter, we have focused on the connection between a recently described oceanic phenomenon (the SAOD) and the occurrence of floods and droughts along the Guinea Coast. The choice of the SAOD was largely motivated by our recent studies (Nnamchi *et al.*, 2011, 2013, Nnamchi and Li, 2011, Nnamchi, 2013) that demonstrate its strong impacts on the Guinea Coast precipitation. The question that arises is thus: Is the SAOD the only oceanic influence on Guinea Coast precipitation? And, if not: What other oceanic domain or phenomenon could be implicated?

To address these questions, we present a correlation map of the summer precipitation index over the Guinea Coast with the global SST anomaly (Nnamchi, 2013). As shown in Fig. 22.8, the SAOD represents the dominant, physically meaningful, SST pattern over the oceans. While a statistically significant correlation is found over the north-central tropical Pacific Ocean and the Arctic ice, physical interpretation is not yet made for these SST patterns and their connections with Guinea Coast precipitation. In fact, Nnamchi *et al.* (2013) compared two sets of numerical experiments: one forced by global SST anomaly in SAOD years, and the other forced by SAOD-type SST pattern in the South Atlantic Ocean basin only—while the climatological SST is prescribed elsewhere over the global oceans.

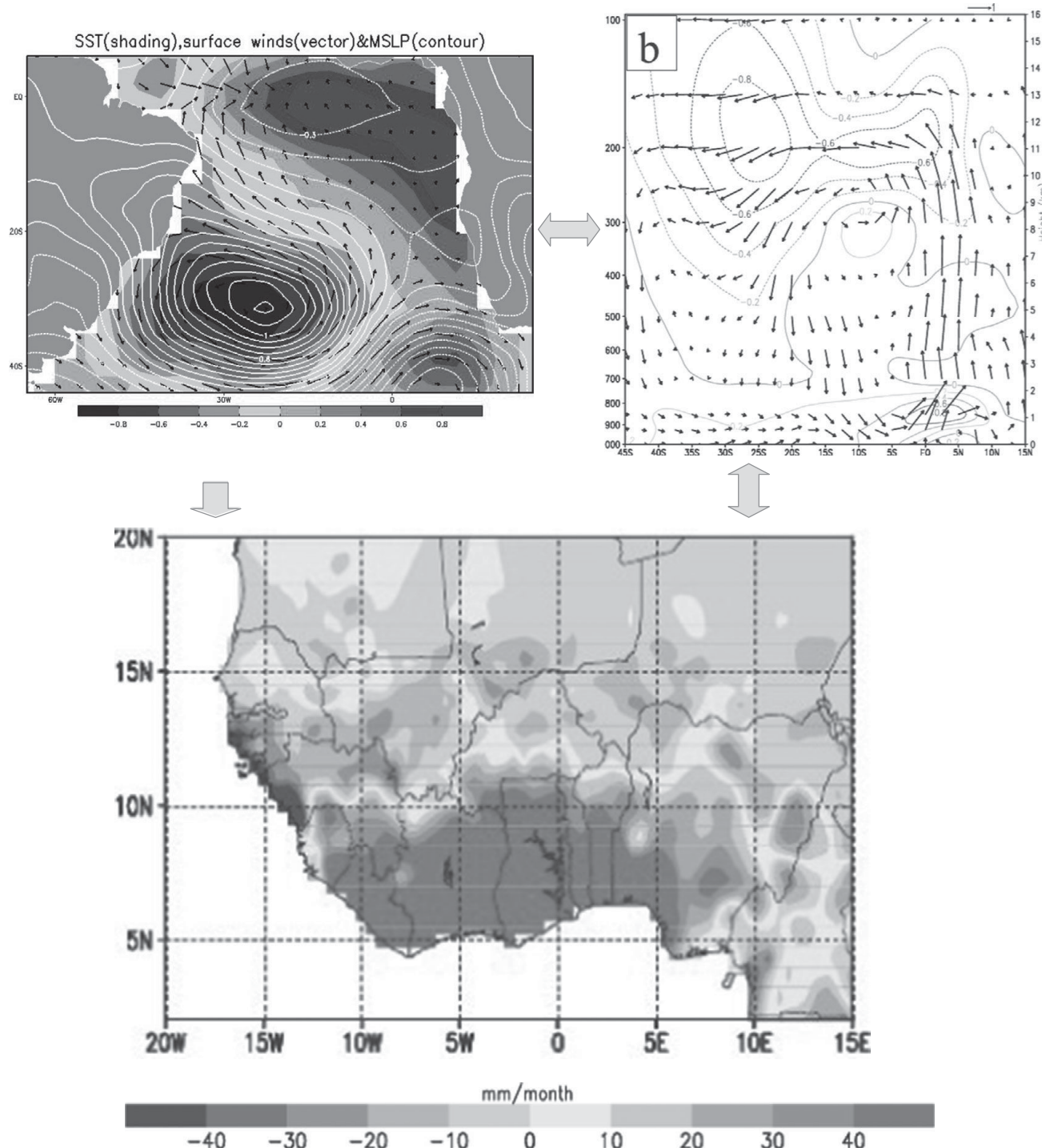


Fig. 22.7. Interaction of SST, surface and vertical circulation, and Guinea Coast precipitation during an SAOD year. (a) Atmospheric modelling result. (b) Observations and reanalysis. (Sources: a, Nnamchi, 2013; b–c, Nnamchi and Li, 2011).

They found that these two SST patterns have essentially the same effect on Guinea Coast precipitation. That is, the additional effect of the inclusion of the SST anomaly from other oceanic basins and regions is rather small.

Another question may arise regarding the possibility of improving the prediction of floods and droughts over the Guinea Coast based on the SAOD. To our knowledge, there has been little systematic work on this subject to

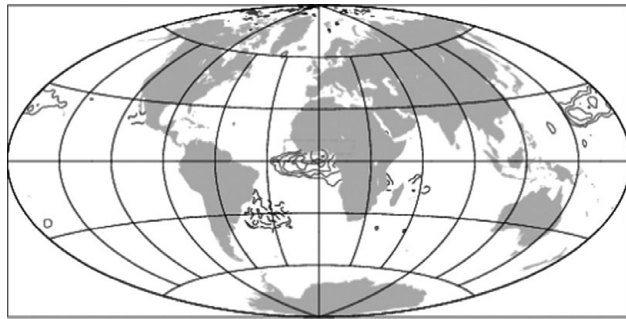


Fig. 22.8. Correlation map of Guinea Coast precipitation and global SST during June–July–August. The Guinea Coast precipitation is defined as the domain average over the dashed box ( $20^{\circ}\text{E}$ – $20^{\circ}\text{W}$ ,  $4$ – $12^{\circ}\text{N}$ ). Only statistically significant correlations at the 99.9% confidence level (two-tailed t-test) are shown. Positive (negative) correlations are represented by solid (dashed) curves. Modified from Nnamchi (2013).

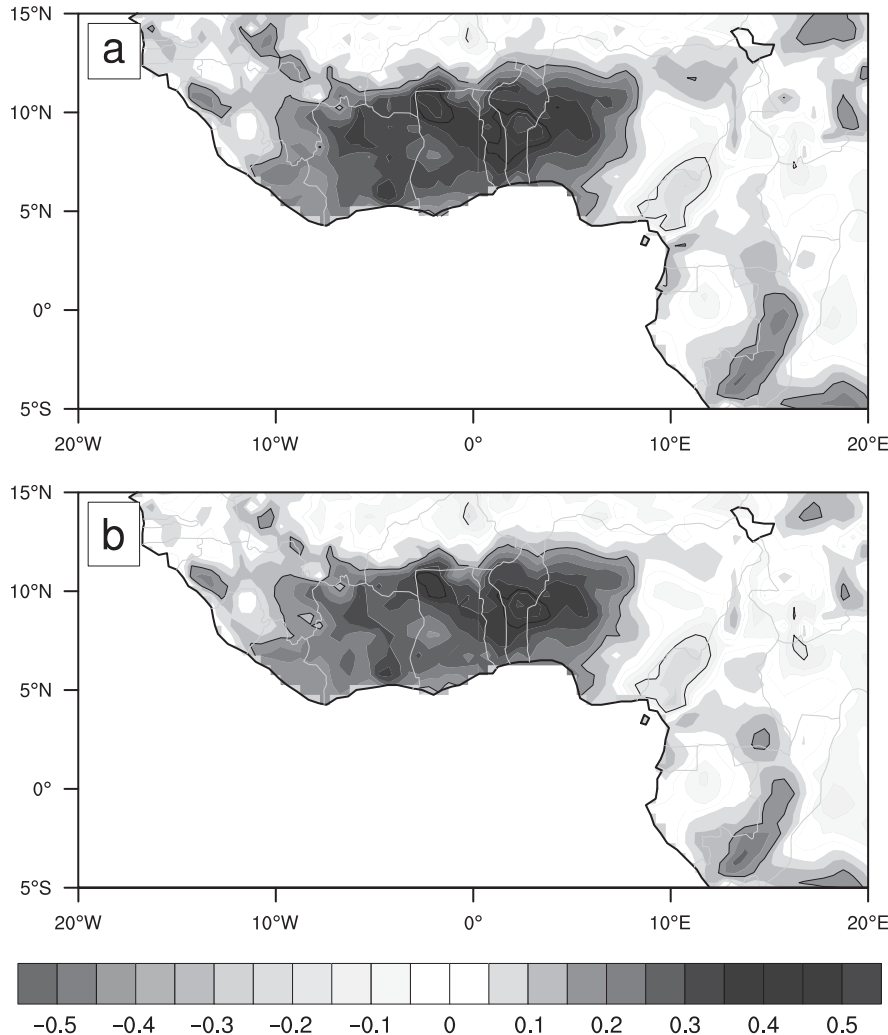


Fig. 22.9. Correlation of March–April–May averaged SAOD index with JAS averaged global tropical–subtropical precipitation. (a) Bivariate correlation map. (b) Partial correlation, with the El Niño influence removed. Statistically significant (at the 95% confidence level) correlation coefficients are contoured. (Source: Modified from Nnamchi, 2013).

date. Thus, we review an essentially preliminary analysis here. Nnamchi *et al.* (2011) defined the SAOD index (SAODI) by calculating the difference between the domain-averaged SST anomaly in the northeastern and southwestern parts of the South Atlantic Ocean. Thus, the SAODI is determined as follows:

$$\text{SAODI} = [\text{SSTA}]_{\text{NEP}} - [\text{SSTA}]_{\text{SWP}}, \quad (22.2)$$

where the square brackets indicate domain averages, and the subscripts show the area over which the SST anomaly averages are computed. These domains are the northeast pole (NEP:  $10^{\circ}\text{E}$ – $20^{\circ}\text{W}$ ,  $0$ – $15^{\circ}\text{S}$ ) and the southwest pole (SWP:  $10$ – $40^{\circ}\text{W}$ ,  $25$ – $40^{\circ}\text{S}$ ) of the South Atlantic Ocean.

Here, we show a correlation map of the SAODI for the boreal spring (that is, March–April–May, MAM) with the following summer (that is, JAS) precipitation on the Guinea Coast (Fig. 22.9). There are significant correlations

over large areas across the Guinea Coast in the bivariate correlation map (Fig. 22.9a). The equatorial Pacific El Niño is globally recognized as the largest inter-annual mode of climate variability with near-global impacts. We therefore, show an MAM SAODI versus JAS Guinea precipitation partial correlation map in which the influence of the Pacific El Niño has been removed. We see from Fig. 22.9b that the correlation map remains largely unchanged after accounting for the possible influence of El Niño. Given this promising lead-correlation, one hopes that future work could establish a prediction scheme for Guinea Coast precipitation, including floods and droughts, based on the SAOD.

## 22.6 Acknowledgements

This work was supported by the China 973 Program (2010CB950400), NSFC Key Project (41030961), and the EU FP7 Project (603521)—PREFACE.

## References

- Acheampong, P. K. (1982). Rainfall anomaly along the coast of Ghana—its nature and causes. *Geografiska Annaler*, **64**, 199–211.
- Biasutti, M., Held, I. M., Sobel, A. H., and Giannini, A. (2008). SST forcings and Sahel rainfall variability in simulations of the twentieth and twenty-first centuries. *J. Clim.*, **21**, 3471–3486.
- Giannini, A., Saravanan, R., and Chang, P. (2003). Oceanic forcing of Sahel rainfall on interannual to interdecadal time scales. *Science*, **302**, 1027–1030.
- Held, I. M., Delworth, T. L., Lu, J., Findell, K. L., and Knutson, T. R. (2005). Simulation of Sahel drought in the 20th and 21st centuries. *Proc. Natl. Acad. Sci.*, **102**, 17891–17896.
- Harris, I., Jones, P. D., Osborn, T. J., and Lister, D. H. (2014). Updated high-resolution grids of monthly climatic observations—the CRU TS3.10 dataset. *Int. J. Climatol.*, **34**, 623–642.
- Hayward, D. F. and Oguntoyinbo, J. S. (1987). *The Climatology of West Africa*. Hutchinson, London.
- Li, J. and Zeng, Q. (2002). A unified monsoon index. *Geophys. Res. Lett.*, **29**, 1274, doi:10.1029/2001GL013874.
- Li, J. and Zeng, Q. (2003). A new monsoon index and the geographical distribution of the global monsoons. *Adv. Atmos. Sci.*, **20**, 299–302.
- Losada, T., Rodriguez-Fonseca, B., Janicot, S., et al. (2010). A multi-model approach to the Atlantic Equatorial mode: Impact on the West African monsoon. *Clim. Dyn.*, **35**, 29–43.
- Nnamchi, H. C. (2013). *Diagnosis and Modelling of an Intrinsic Dipole Oscillation in the South Atlantic Ocean*. Unpublished Sc.D Thesis, Institute of Atmospheric Physics, Chinese Academy of Sciences.
- Nnamchi, H. C., Li, J., Kang, I-S., and Kurchaski, F. (2013). Simulated impacts of the South Atlantic Ocean Dipole on summer precipitation at the Guinea Coast. *Clim. Dyn.*, **41**, 677–694.
- Nnamchi, H. C., Li, J., and Anyadike, R. N. C. (2011). Does a dipole mode really exist in the South Atlantic Ocean? *J. Geophys. Res.*, **116**, D15104, doi:10.1029/2010JD015579.
- Nnamchi, H. C. and Li, J. P. (2011). Influence of the South Atlantic Ocean Dipole on West African summer precipitation. *J. Clim.*, **24**, 1184–1197.
- Peterson, T. C. and Coauthors. (2013). Monitoring and understanding changes in heat waves, cold waves, floods, and droughts in the United States: State of knowledge. *Bull. Amer. Meteor. Soc.*, **94**, 821–834.
- Population Reference Bureau (2013). *World population data sheet*. Population Reference Bureau, Washington DC (Available from:[http://www.prb.org/pdf13/2013-population-data-sheet\\_eng.pdf](http://www.prb.org/pdf13/2013-population-data-sheet_eng.pdf)).
- Rayner, N. A., Parker, D. E., Horton, E. B., et al. (2003). Global analyses of sea surface temperature, sea ice, and night marine air temperature since the late nineteenth century. *J. Geophys. Res.*, **108**, D14, 4407, doi: 10.1029/2002JD002670.
- Rodríguez-Fonseca, B., Janicot, S., Mohino, E., et al. (2011). Interannual and decadal SST-forced responses of the West African monsoon. *Atmos. Sci. Lett.*, **12**, 67–74.
- Saha, K. (2010). *Tropical Circulation Systems and Monsoons*. Berlin: Springer-Verlag.
- Sheffield, J., Wood, E. F., Chaney, N., et al. (2014). A drought monitoring and forecasting system for Sub-Saharan African water resources and food security. *Bull. Amer. Meteor. Soc.*, doi/abs/10.1175/BAMS-D-12-00124.1
- Taylor, C. M., Lambin, E. F., Stephenne, N., Harding, R. J., and Essery, R. L. H. (2002). The influence of land use change on climate in the Sahel. *J. Clim.*, **15**, 3615–3629.
- Vizy, E. K. and Cook, K. H. (2001). Mechanisms by which Gulf of Guinea and eastern North Atlantic sea surface temperature anomalies can influence African rainfall. *J. Clim.*, **14**, 795–821.
- Venegas, S. A., Mysak, L. A., and Straub, D. N. (1996). Evidence for interannual and interdecadal climate variability in the South Atlantic. *Geophys. Res. Lett.*, **23**, 2673–2676.
- Venegas, S. A., Mysak, L. A., and Straub, D. N. (1997). Atmosphere–ocean coupled variability in the South Atlantic. *J. Clim.*, **10**, 2904–2920.
- Wagner, R. G. and Da Silva, A. M. (1994). Surface conditions associated with anomalous rainfall in the Guinea coastal region. *Int. J. Climatol.*, **14**, 179–199.
- Washington, R., Harrison, M., Conway, D. et al. (2006). African climate change: taking the shorter route. *Bull. Amer. Meteor. Soc.*, **87**, 1355–1366.
- Xue, Y. and Shukla, J. (1993). The influence of land surface properties on Sahel climate. part 1: desertification. *J. Clim.*, **6**, 2232–2245.

## 23

# The effect of global dynamical factors on the interannual variability of land-based rainfall

Peter G. Baines and Benjamin J. Henley

### 23.1 Introduction

Australia is a reasonably compact region spanning both the tropics and mid latitudes, and hence may be used to provide examples of the effect of various global factors on seasonal rainfall on large length scales. A number of studies of Australian rainfall in recent years have shown that seasonal variability is dependent on various large-scale dynamical processes, notably the El Niño-Southern Oscillation (ENSO) (e.g. McBride and Nichols, 1983, Power *et al.*, 1999, Drosdowsky and Chambers, 2001, Risbey *et al.*, 2009), the Indian Ocean Dipole (IOD) (Ashok *et al.*, 2003, Risbey *et al.*, 2009), and the Southern Annular Mode (SAM) (Meneghini *et al.*, 2007). The effects of ENSO and IOD are now incorporated into climate and rainfall forecasts issued by the Australian Bureau of Meteorology (among others) for periods of up to several months ahead. The objective of the present study is to examine the evidence for the influence on Australian seasonal rainfall of these and a variety of other global dynamical factors, which are described in the next section. The same methodology can be applied to global rainfall, and Australian rainfall is taken here as a test case. This is because Australia is a reasonably compact part of the globe, its rainfall has been well recorded with good national coverage for the past 100 years or more, and it covers a range of latitudes from the tropics to mid latitudes with a variety of different rainfall processes. This study confirms ENSO and IOD as major influences on seasonal rainfall, but several other dynamical factors are found to have a significant impact in particular regions for certain seasons.

Rainfall is a notoriously noisy variable, and Australian rainfall is no exception. Any advance in understanding this variability is potentially valuable and useful. For much of the country there is high density of rain gauges (the exceptions being the centre and north). The  $0.5^\circ$  monthly rainfall data used in this study was generated by spatial and temporal averaging of  $0.05^\circ$  daily data (Jones *et al.*, 2009). The

seasonal means (i.e. averaging over December–February (DJF), March–May (MAM), June–August (JJA), and September–November (SON)) of rainfall are shown in Fig. 23.1 for the years 1900–2009, and the corresponding standard deviations are shown in Fig 23.2. These figures give a good picture of the resolution of the data, and the variability in the data set. Since variance is the square of standard deviation, the range of variances is very large, particularly in the tropics in DJF. The analysis was applied to two sets of data: firstly, the seasonal means ranging from 1950 to 2009, as just described (60 years for each season), and secondly, to the same seasonal means but from 1900 to 2009 (110 years for each). For the latter, the first 50 years of data are less reliable than the later 60, particularly for some of the factors as described below.

Ten dynamical factors are used, which include the overall trend in rainfall, ENSO (with two indices), the tropical Indian Ocean Dipole, the Atlantic meridional overturning circulation (AMOC), solar activity as represented by the sunspot number, the quasi-biennial oscillation (QBO) in the equatorial stratosphere, the atmospheric southern annular mode (SAM), the North Pacific ocean gyre oscillation (NPGO) and the volcanic dust in the atmosphere. Some of these factors are predictable, up to a year or more in advance. They are all described in more detail in the next section. Each of them is represented by a time series for each season, with one value per year, giving 40 time series in all. The mean of each time series is removed, and it is then normalized by its standard deviation. A cross-validated multiple regression analysis is then performed for each season, with each rainfall grid point treated as an independent calculation. This results in a spatial pattern of influence, for each factor, for each season, which is then assessed for significance.

The ten factors are described in Section 23.2, the regression analysis in Section 23.3, the results are presented and assessed in Section 23.4, and the conclusions are summarized in Section 23.5.

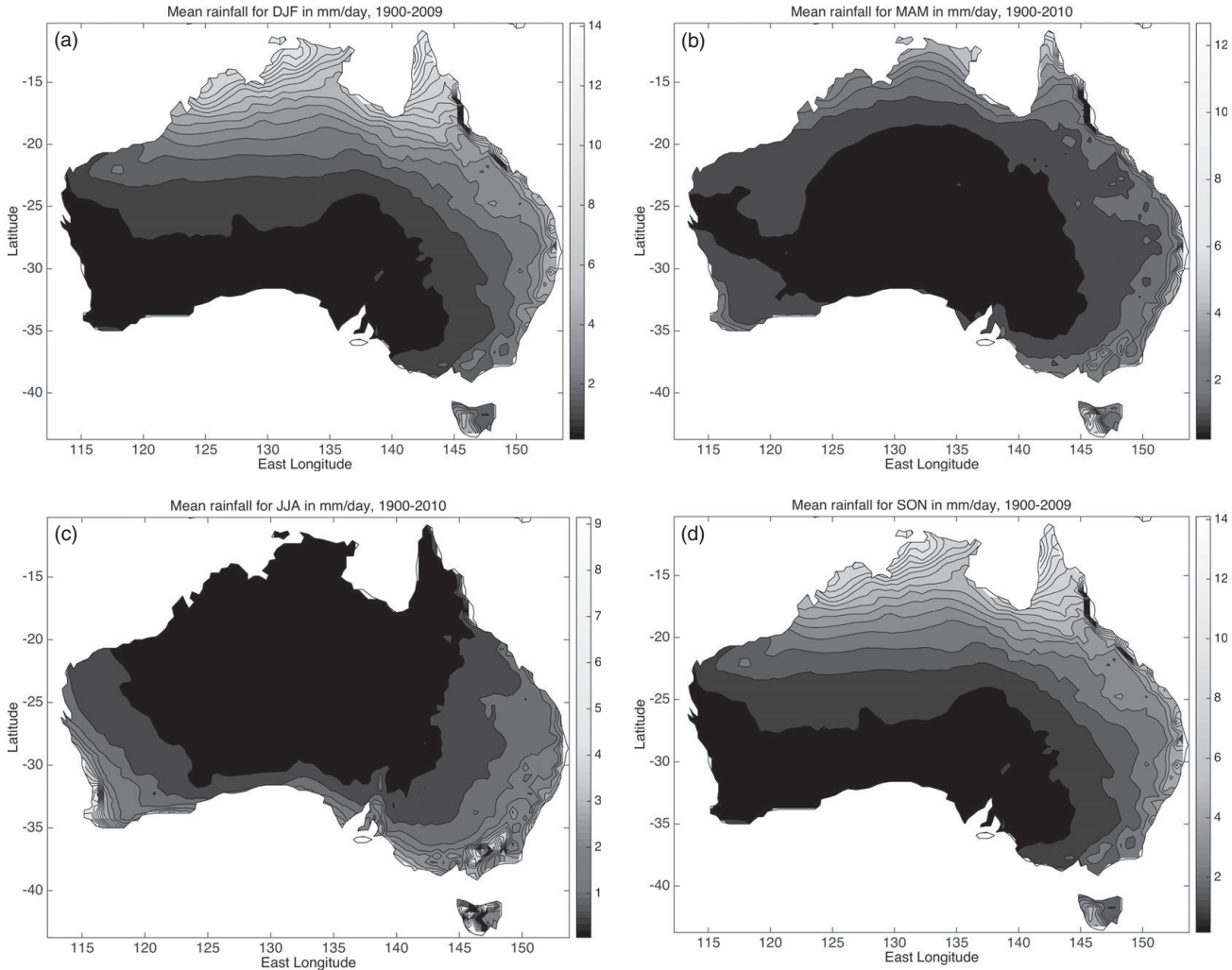


Fig. 23.1. Mean rainfall for the four seasons, taken over the years (of first month) from 1950–2009, for December–February (DJF), March–May (MAM), June–August (JJA) and September–November (SON). The data used was provided by Peter Briggs of CSIRO in gridded form with  $0.5 \times 0.5$  degree resolution, obtained from the Bureau of Meteorology (Jones *et al.* 2009).

### 23.2 The dynamical factors

Several of the dynamical factors are based on sea surface temperature (SST). To obtain time series for these, an empirical orthogonal function (EOF) analysis was performed on the global SST data set ERSST V3b (Smith *et al.*, 2008), for each season separately, from 1898 to 2011, and a five-year running mean was applied. The physical interpretation of the first three of these global EOFs is well known in general terms (e.g. Parker *et al.*, 2007, Baines, 2011 and Figure 2.10 of Prentice *et al.*, 2012), and are understood as follows. EOF1 describes the pattern of global trend in SST, and its time series shows a mostly monotonic increase that represents an increase in global temperature in most locations. This increase is larger in the last 60 years than in the first 50. EOF2 has

its main features in the Pacific with an ENSO-like spatial SST pattern, and is associated with a decadally varying form of ENSO known as the Pacific Decadal Oscillation (PDO) or Interdecadal Pacific Oscillation (IPO). EOF3 has strong features in the Atlantic, with opposite sign in the North and South Atlantic, and is conceptually associated with the notional ‘conveyor belt’ ocean circulation known as the Atlantic Meridional (or multi-decadal) Oscillation (AMO) (Parker *et al.*, 2007). With this background, we next discuss the ten dynamical forcing factors in turn. No particular significance is attached to the order, though important ones are generally early in the list.

The first factor is denoted GW, notionally for ‘global warming’, and is the time series for EOF1 of SST, with the five-year running mean, for each season separately, as

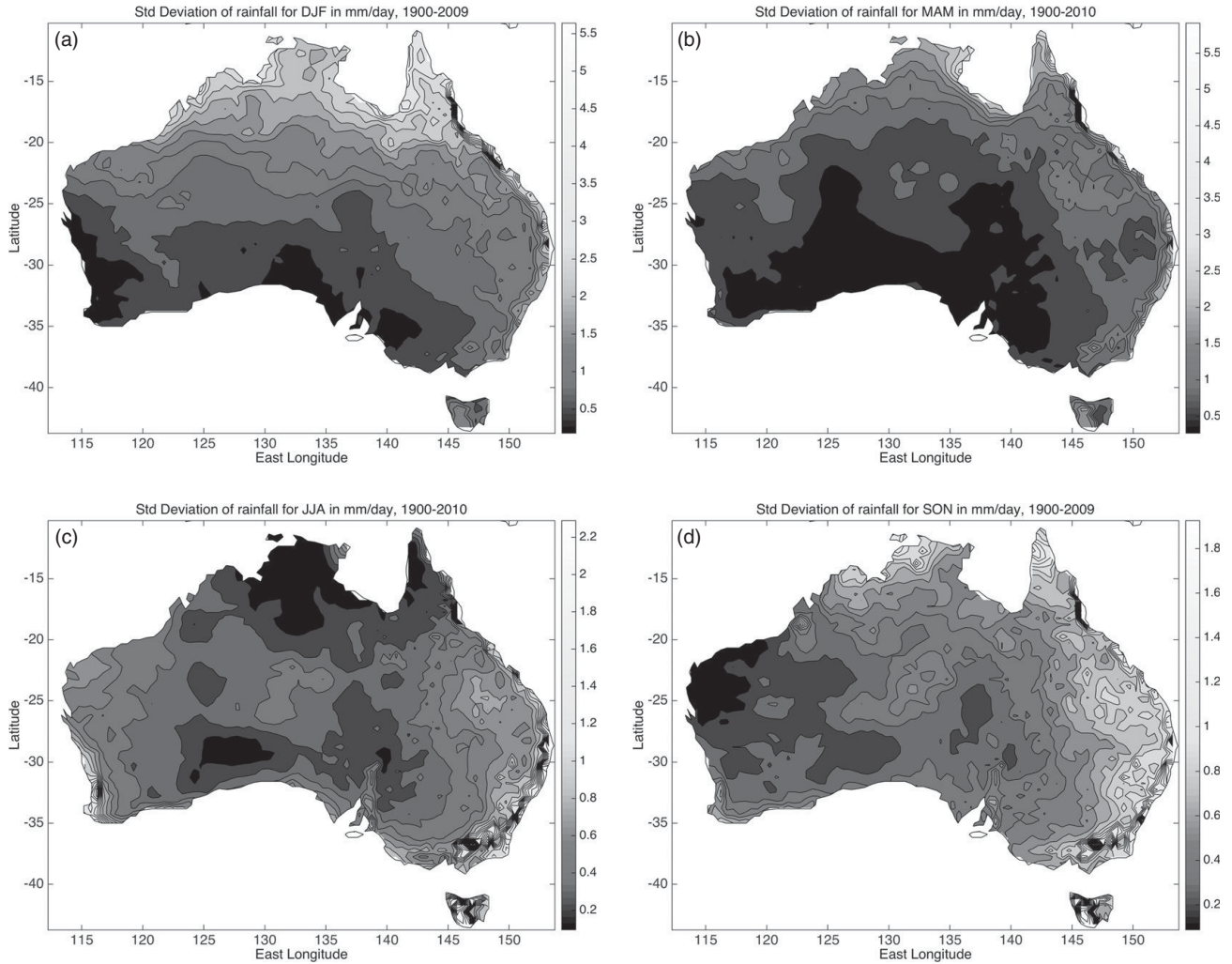


Fig. 23.2. The same as Fig. 23.1, but showing standard deviations.

described above, from central years 1900 to 2009. For each season, the time series is approximately linear, and hence GW represents the trend in the observations, without identifying any particular physical process that causes it. One could conceivably take the time series for EOF2 as the second factor, but since this represents a low frequency form of ENSO, and we wish to examine interannual variability, we have instead taken two commonly used indices of ENSO. The first of these is Niño3.4, which is the mean for each season for each year of SST in what is known as the ‘Niño3.4 region’ of the central Pacific: the box  $5^{\circ}\text{N}$ – $5^{\circ}\text{S}$ ,  $120^{\circ}$ – $170^{\circ}\text{W}$ . Monthly values are taken from the ERSST V3b data set, and used to compute seasonal means, but with a five-month running mean. The second index for ENSO is the Trans-Niño Index (TNI) defined by Trenberth and Stepaniak (2001). This index is given by the mean SST in regions Niño1 ( $10^{\circ}\text{S}$ – $5^{\circ}\text{S}$ ,  $80^{\circ}\text{W}$ – $90^{\circ}\text{W}$ ),

Niño2 ( $5^{\circ}\text{S}$ – $0^{\circ}$ ,  $80^{\circ}\text{W}$ – $90^{\circ}\text{W}$ ) and Niño4 ( $5^{\circ}\text{S}$ – $5^{\circ}\text{N}$ ,  $160^{\circ}\text{E}$ – $160^{\circ}\text{W}$ ), by the expression

$$\text{TNI} = \text{Niño1} + \text{Niño2} - \text{Niño4}, \quad (23.1)$$

where the mean SST in each region is implied. A five-month running mean is applied here also. The TNI involves differences in SST between the eastern and western extremes, and captures variations in the structure of ENSO events, which includes the ‘modoki’ pattern (Ashok *et al.*, 2007) and the warm pool–cold tongue variations (Kug *et al.*, 2009).

The Indian Ocean Dipole (IOD) is measured by the IOD Index, which is a measure of the anomalous zonal SST gradient across the equatorial Indian Ocean. It is here defined as the difference between the SST anomaly in a western ( $60^{\circ}\text{E}$ – $80^{\circ}\text{E}$ ,  $10^{\circ}\text{S}$ – $10^{\circ}\text{N}$ ) box and an eastern ( $90^{\circ}\text{E}$ – $110^{\circ}\text{E}$ ,  $10^{\circ}\text{S}$ – $0^{\circ}\text{S}$ ) box, i.e.

IOD Index = SST(West box)–SST(East box).

It has a significant impact on Australian weather (see Aust. Bureau of Met. web site [www.bom.gov.au/climate/enso](http://www.bom.gov.au/climate/enso)), particularly in spring (September–November). The SSTs used are taken from the ERSST V3b data set, averaged over each box for each season.

The AMO, also called the Atlantic Multidecadal Oscillation or the Atlantic Meridional Overturning Circulation (AMOC), is, for present purposes, represented by EOF3 of the global SST, with a five-year running mean (as for GW with EOF1). This represents the well-known ‘conveyor belt’ associated with sinking at the northern end of the North Atlantic (Broecker, 2010), but the circulation is believed to be global, and may include variations in the Indonesian throughflow, so that some influence on Australian rainfall is quite possible. A positive value of the index for the AMO implies anomalously warm SST in the North Atlantic and cold in the South Atlantic, which is associated with a northward transport anomaly in the overturning ocean circulation (Parker *et al.*, 2007).

The quasi-biennial oscillation (QBO) is an oscillation in the equatorial stratosphere in which the zonal winds alternate in sign with a period of approximately two years (Baldwin *et al.*, 2001). This phenomenon is due to absorption by the stratospheric shear flow of the energy of upward-propagating (Rossby-gravity) equatorial waves from the troposphere, so that the change in stratospheric wind direction moves downward with time. It is usually represented by the QBO index, which is the mean zonal velocity between 5°N and 5°S in the lower stratosphere, at the level 30 hPa. Averages are taken over individual seasons. The index has been extended back to the beginning of the twentieth century to the present day by Brönimann *et al.* (2007). Positive numbers imply eastward (westerly) winds at 30 mb.

The effect of the solar cycle on rainfall is represented by the Sunspot Number Index (SSN), which is effectively a count of sunspot numbers, obtained from the Solar Influences Data Analysis Centre (SIDC), which is the solar physics research department of the Royal Observatory of Belgium. The values given are averaged over each season. Positive SSN numbers imply a more active sun (Gray *et al.*, 2010), and stronger nett solar irradiance.

The southern annular mode (SAM) is a significant parameter in the dynamics of the southern reaches of the Southern Hemisphere. The SAM index is defined to be the zonal mean surface pressure at 40°S minus that at 65°S, here averaged over the respective season. This is clearly related to the strength of the surface winds, and hence also, in general terms, to the strength of the Antarctic Circumpolar Current. This index has been reconstructed by

Marshall (2003) and Jones *et al.* (2009), and values are given at [www.antarctic.ac.uk/met/gima/sam.html](http://www.antarctic.ac.uk/met/gima/sam.html) and the Ohio State University website: [http://polarmet.asu.edu/ACD/sam/sam\\_recon.html](http://polarmet.asu.edu/ACD/sam/sam_recon.html). Means are taken over each season.

Variations in the strength of the ocean circulation in the North and South Pacific may be expected to have some impact on climate and rainfall in regions bordering the Pacific, in a manner that is different from that of ENSO. Connections between the North Pacific circulation (as determined by sea surface height observations) and the chemistry and ecology of coastal regions have been described by di Lorenzo *et al.* (2008), and an index of the strength of the North Pacific gyre – the NPGO Index, back to 1950 has been determined by E. di Lorenzo, and an index provided at [www.o3d.org/npgi/](http://www.o3d.org/npgi/). Positive values imply stronger ocean circulation. SST and sea surface height fluctuations are known to be related on monthly time scales (Davis, 1976), and a proxy for the NPGO is EOF2 of the SST of the North Pacific. The time series for this quantity is taken to represent the NPGO for analysis over the longer period 1900–2010. Seasonal means are computed, but no other smoothing is applied. For the South Pacific, observations of sea surface height, and even of SST, are not sufficient to give a measure of the ocean circulation strength. However, it is plausible that the South Pacific circulation will vary in a similar manner to that of the North Pacific because the trade winds are a major driver of both. Hence, this index is here referred to as the PGO Index, but is more precisely the NPGO Index.

The final factor concerns the possible influence of volcanic eruptions on rainfall, due to the loading of volcanic dust in the stratosphere. This process is clearly episodic, but needs to be incorporated for the interpretation of effects from other factors such as the seasonal cycle. An index based on Vernier *et al.* (2011), has been produced and is denoted VI for Vernier Index. A monthly time series dated back to 1900 has been provided to the authors by C. Folland (pers. comm., 2014). Mean values are taken over each season.

The time series for all ten factors from 1900 to 2009 for the season December–February (DJF) are shown in Fig. 23.3. There are differences between the curves for other seasons (which are not shown), but their overall appearance is similar. The correlation coefficients between these curves are shown in Table 23.1, with values having magnitude greater than 0.2 shown as bold. Most of these correlations are small. The GW time series effectively represents the overall quasi-linear trend in the data, regardless of what might be causing it. An overall trend in any of the other factors will result in a significant correlation with GW, and this occurs with Niño3.4 for all seasons, and the SAM and PGO for DJF and MAM. There is also notable

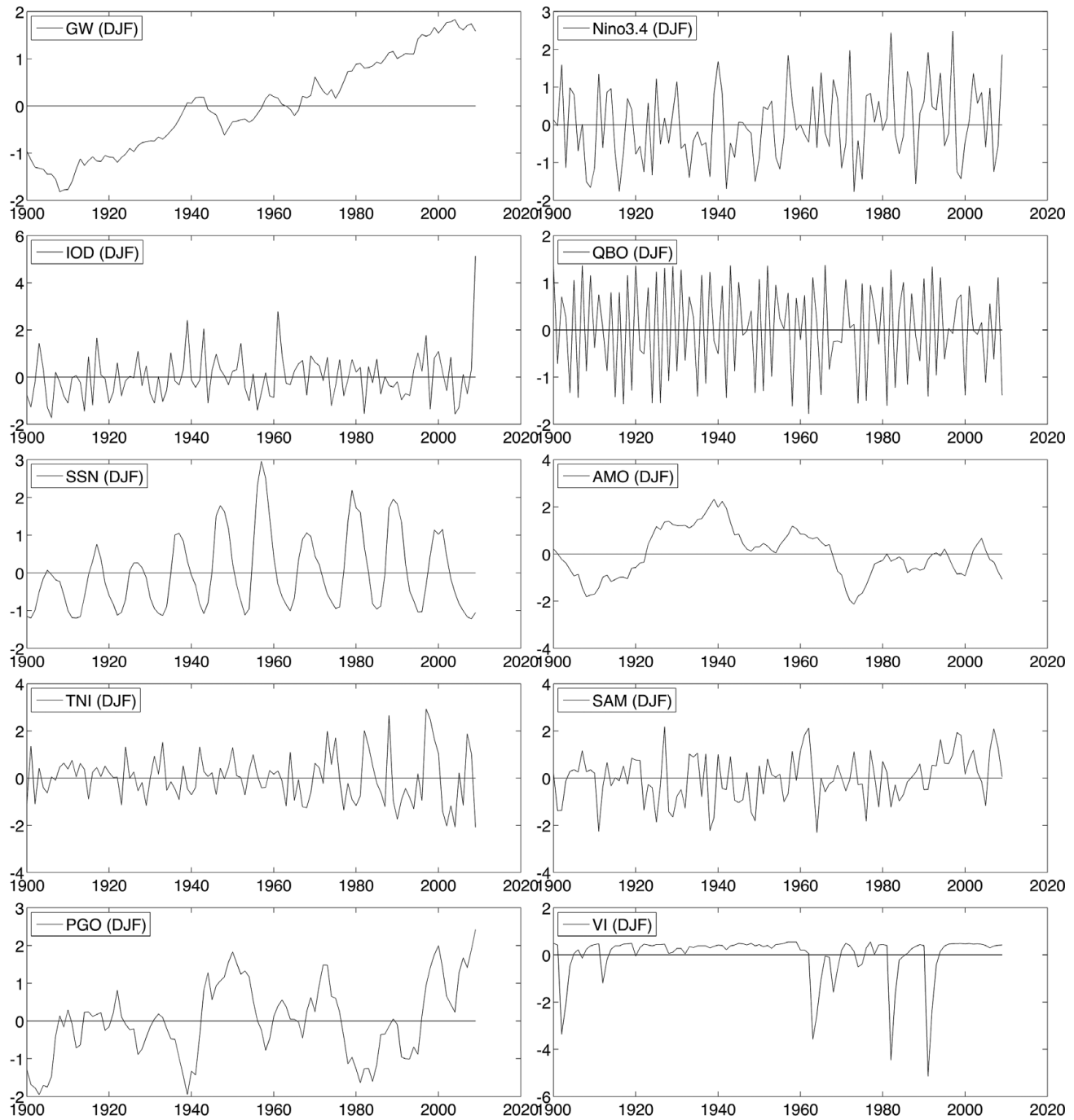


Fig. 23.3. Time series for the ten factors for the season December–February (DJF), with one point (i.e. season) per year from 1900 to 2009, with their titles above each figure.

correlation between Niño3.4 and the TNI, particularly in DJF, which is not surprising as they are both ENSO factors, with the TNI manifesting behaviour late in the cycle. Niño3.4 also shows modest correlation with the PGO. The volcano index VI shows some persistent correlation with the PGO, which is surprising but presumably

coincidental, and the only large correlation (0.495) is between Niño3.4 and the Indian Ocean Dipole in September–November.

For the period 1950–2009, the correlation coefficients (not shown) mostly show the same patterns of apparent connections with similar magnitudes. The time series for

Table 23.1. Correlation coefficients for the time series of the ten factors used, for seasons (a) December–February, (b) March–May, (c) June–August, (d) September–November, over the period 1900–2009. Values with magnitude greater than 0.2 are marked as bold.

(a)

DJF	GW	Niño3.4	IOD	QBO	SSN	AMO	TNI	SAM	PGO	VI
GW	1	0.19	0.163	-0.016	0.191	0	-0.087	<b>0.245</b>	<b>0.262</b>	-0.019
Niño3.4	0.19	1	0.074	0.038	0.069	0.049	<b>-0.472</b>	-0.068	-0.164	<b>-0.281</b>
IOD	0.163	0.074	1	-0.098	0.004	0.045	-0.094	0.113	0.184	0.138
QBO	-0.016	0.038	-0.098	1	-0.016	0.006	-0.004	0.021	-0.023	-0.025
SSN	0.191	0.069	0.004	-0.016	1	0.097	-0.122	-0.030	-0.087	0.055
AMO	0	0.049	0.045	0.006	0.097	1	-0.158	-0.147	<b>-0.251</b>	0.059
TNI	-0.087	<b>-0.472</b>	-0.094	-0.004	-0.122	-0.158	1	0.017	0.186	0.017
SAM	<b>0.245</b>	-0.068	0.113	0.021	-0.030	-0.147	0.017	1	0.185	0.184
PGO	<b>0.262</b>	-0.164	0.184	-0.023	-0.087	<b>-0.251</b>	0.186	0.185	1	<b>0.295</b>
VI	-0.019	<b>-0.281</b>	0.138	-0.025	0.055	0.059	0.017	0.184	<b>0.295</b>	1

(b)

MAM	GW	Niño3.4	IOD	QBO	SSN	AMO	TNI	SAM	PGO	VI
GW	1	<b>0.285</b>	-0.05	0.046	<b>0.215</b>	0	-0.038	<b>0.247</b>	<b>0.251</b>	-0.01
Niño3.4	<b>0.285</b>	1	-0.123	0.017	0.132	0.1	-0.197	-0.15	-0.206	<b>-0.265</b>
IOD	-0.05	-0.123	1	0.082	-0.09	0.121	-0.112	0.108	0.103	0.133
QBO	0.046	0.017	0.082	1	0.017	-0.054	0.018	0.104	0.045	0.011
SSN	<b>0.215</b>	0.132	-0.09	0.017	1	0.08	-0.04	-0.013	0.016	0.09
AMO	0	0.1	0.121	-0.054	0.08	1	-0.075	0.069	-0.069	0.087
TNI	-0.038	-0.197	-0.112	0.018	-0.04	-0.075	1	0.089	<b>0.219</b>	-0.06
SAM	<b>0.247</b>	-0.15	0.108	0.104	-0.013	0.069	0.089	1	-0.043	0.087
PGO	<b>0.251</b>	<b>-0.206</b>	0.103	0.045	0.016	-0.069	0.219	-0.043	1	<b>0.22</b>
VI	-0.01	<b>-0.265</b>	0.133	0.011	0.090	0.087	-0.06	0.087	<b>0.22</b>	1

(c)

JJA	GW	Niño3.4	IOD	QBO	SSN	AMO	TNI	SAM	PGO	VI
GW	1	<b>0.31</b>	0.158	0.012	0.197	0	-0.138	0.066	-0.048	-0.004
Niño3.4	<b>0.31</b>	1	<b>0.282</b>	0.014	0.011	0.158	0.015	0.109	<b>-0.231</b>	-0.132
IOD	0.158	<b>0.282</b>	1	0.111	-0.11	0.023	0.077	0.116	-0.011	-0.047
QBO	0.012	0.014	0.111	1	-0.001	-0.021	0.05	-0.074	0.026	-0.022
SSN	0.197	0.011	-0.11	-0.001	1	0.06	-0.056	0.024	-0.034	0.079
AMO	0	0.158	0.023	-0.021	0.06	1	<b>-0.208</b>	0.043	<b>-0.201</b>	0.015
TNI	-0.138	0.015	0.077	0.05	-0.056	<b>-0.208</b>	1	0.065	0.2	-0.08
SAM	0.066	0.109	0.116	-0.074	0.024	0.043	0.065	1	-0.111	0.138
PGO	-0.048	<b>-0.231</b>	-0.011	0.026	-0.034	<b>-0.201</b>	0.2	-0.111	1	<b>0.229</b>
VI	-0.004	-0.132	-0.047	-0.022	0.079	0.015	-0.08	0.138	<b>0.229</b>	1

(d)

SON	GW	Niño3.4	IOD	QBO	SSN	AMO	TNI	SAM	PGO	VI
GW	1	<b>0.269</b>	0.168	-0.014	0.179	0	<b>-0.206</b>	0.068	0.025	-0.041
Niño3.4	<b>0.269</b>	1	<b>0.492</b>	0.071	0.005	0.078	-0.148	0.024	<b>-0.217</b>	-0.167
IOD	0.168	<b>0.492</b>	1	0.179	-0.098	0.047	-0.05	-0.075	0.108	-0.119
QBO	-0.014	0.071	0.1791	1	-0.04	0.029	-0.029	0.12	-0.04	-0.061
SSN	0.179	0.005	-0.098	-0.04	1	-0.097	-0.097	0.033	-0.068	0.016
AMO	0	0.078	0.047	0.029	-0.097	1	<b>-0.253</b>	0.033	<b>-0.253</b>	0.027
TNI	<b>-0.206</b>	-0.148	-0.05	-0.029	-0.097	<b>-0.253</b>	1	0.05	0.174	-0.027
SAM	0.068	0.024	-0.075	0.119	0.033	0.033	0.05	1	-0.088	0.044
PGO	0.025	<b>-0.217</b>	0.108	-0.040	-0.068	<b>-0.253</b>	0.174	-0.088	1	<b>0.347</b>
VI	-0.041	-0.167	-0.119	-0.061	0.016	0.027	-0.027	0.044	<b>0.347</b>	1

this shorter period are part of the same time series for 1900–2009, except for the PGO, which is defined by sea surface height observations after 1949. One difference is that the AMO and GW show correlation over this range, whereas this correlation is zero by definition for 1900–2009.

### 23.3 Regression analysis of seasonal rainfall

We are interested in determining to what extent the above factors may influence the variability in Australian rainfall, as evidenced in particular in Fig. 23.2. We assume that any dependence on these factors is linear, in the first instance, and express the rainfall for each season  $S = 1:4$  in the form

$$\begin{aligned} R(r, S, \text{year}) &= R\text{mean}(r, S) \\ &+ \sum_{n=1}^{10} R\text{Coef}(r, n).Factor(n, S, \text{year}) \\ &+ Residual(r, S, \text{year}), \end{aligned} \quad (23.2)$$

where  $r$  denotes position,  $S = 1$  denotes DJF, 2 denotes MAM etc.,  $R\text{mean}(r, S)$  denotes the mean rainfall for season  $S$ ,  $Factor(n, S, \text{year})$  denotes the time series for factor  $n$  for season  $S$ ,  $R\text{Coef}(r, n)$  denotes the regression coefficients for each grid position for factor  $n$ , and  $Residual(r, S, \text{year})$  denotes the residual rainfall. The regression coefficients are determined by the customary process of least squares (e.g. von Storch and Zwiers, 2001). This procedure has been carried out for both time periods: 1900–2009, and 1950–2009, with each rainfall grid point treated as an independent calculation. Statistical significance was also calculated at each grid point, as described below.

For each time period, the results have been cross-validated (Davis, 1976, von Storch and Zwiers, 2001) on a leave-one-out basis. That is, the regression analysis for the rainfall from 1900 to 2009 has been carried out 110 times for each season, with each year in turn being removed. The resulting regression coefficients are then averaged over the 110 realizations to give  $R\text{Cv}(r, S, n)$ ,  $S = 1:4$ ,  $n = 1:10$ . This may be regarded as using all the other data to obtain an approximation to the (seasonal) rainfall on any particular year, and then averaging the result. For comparison purposes, single regression has also been performed for each factor alone, and then cross-validated in the same way. The regression patterns from the two processes are generally similar for every factor, i.e. treating each one individually produces similar results to treating them collectively (not shown).

A similar cross-validated analysis has been carried out for the 60-year period March 1950–February 2010. There are some differences, but for the most part the results are consistent. They are noted in the discussion, but again, space limitations prevent the details from being shown here.

### 23.4 Results and discussion

The regression patterns for the four seasons for the period March 1900–February 2010 for all ten variables are shown in Fig. 23.4, with 4(a) denoting the results for December–January, 4(b) March–May, 4(c) June–August, and 4(d) September–November. Since the time series of the ten factors have all been normalized in the same way, the magnitude of the regression coefficient denotes the relative magnitude of the effect of the relevant factor, in units of mm/season. These results are shown grouped in seasons for compactness, with the most negative regression coefficient represented as black, and the most positive represented as white. Statistical significance of these values has been calculated on a point-by-point basis, and the outlined stippled regions denote significance at the 90% level. In locations where the rain-gauge density is high, in stippled regions that extend for a distance of several hundred km in at least one direction, the results may be regarded as highly significant.

Since this is a statistical analysis, we cannot draw firm conclusions about the influence of the various factors, but we can infer that there are indications that they influence Australian rainfall in the following manner. The same analysis for the period March 1950–February 2010 shows some differences for some factors, and these are mentioned in the discussion. The various factors are discussed in turn. Only the salient points are mentioned, and Fig. 23.4 should be examined for more details.

The first factor (GW) describes the overall trend in rainfall (regardless of what causes it). This has been described by others, but this analysis indicates a significant increase in the northwest of the continent in DJF (summer), a decrease in the eastern part of the continent in all seasons except SON (spring), which shows an increase in the coastal regions. There is a significant decrease in rainfall in southwest Western Australia, particularly in winter, and Tasmania shows a decrease in all seasons.

The effects of the El Niño-Southern Oscillation (ENSO) are represented by Niño3.4 and the TNI, and are well known. Positive values of Niño3.4 imply a reduction in rainfall in northern Australia in SON, DJF, and MAM, through the annual cycle. The TNI (which may become prominent in the late stages of an ENSO event) provides a more complex picture, increasing the rainfall in some regions and decreasing it in others.

Positive values of the Indian Ocean dipole (the west box is warmer) show a decrease in rainfall in Southeast Australia in JJA and SON, but not (significantly) in DJF and MAM, consistent with previous studies (Ashok *et al.*, 2003). Instead, in the latter two seasons the results for 1900–2010 show a marginal increase in rainfall in the coastal regions of the North, but this is only weakly supported by the results for 1950–2010 (not shown). This suggests that the influence of the IOD on northern

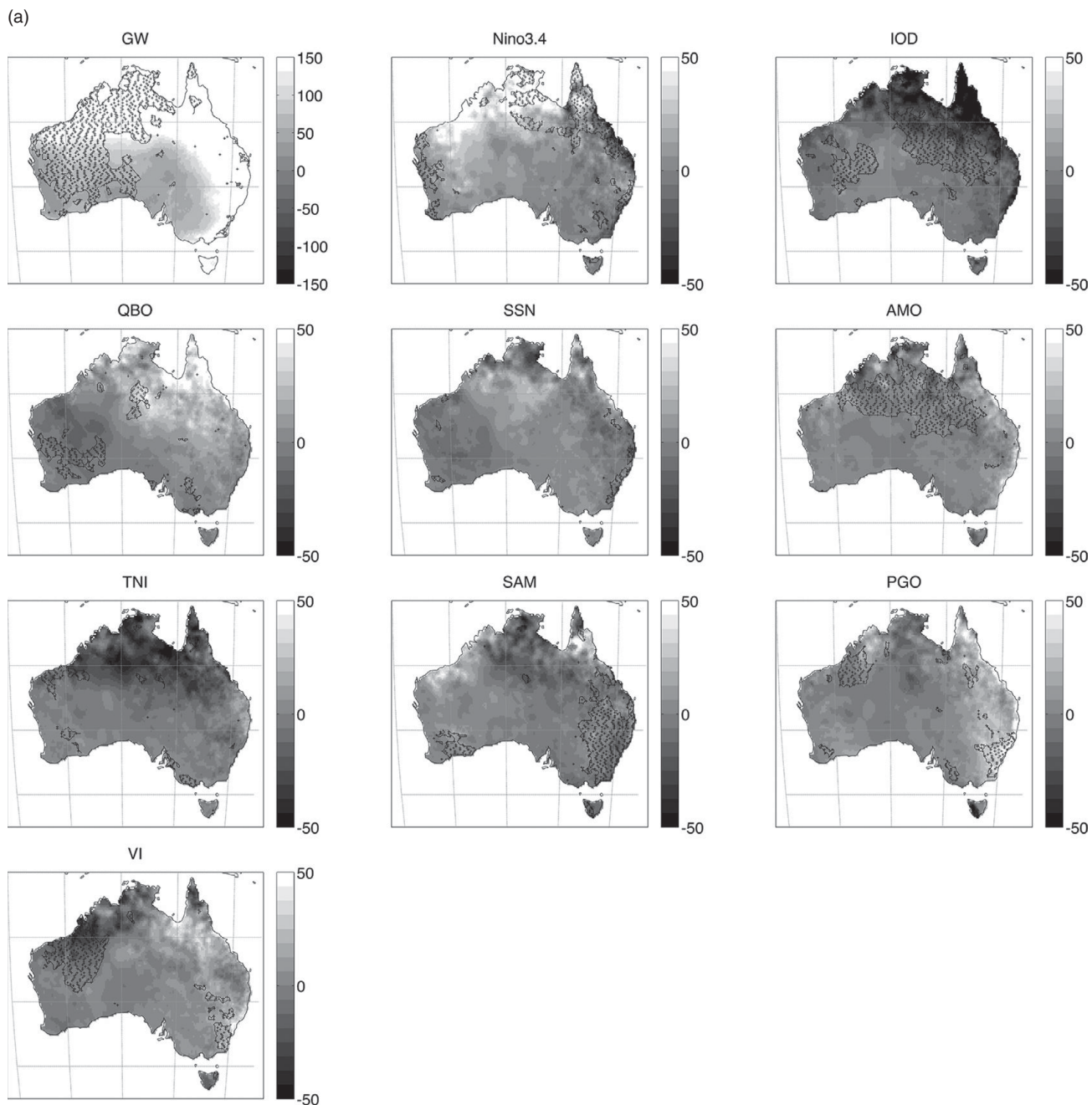


Fig. 23.4. Regression coefficients from the cross-validated multiple factor analysis for the four seasons (mm/season): (a) DJF, (b) MAM, (c) JJA, (d) SON. The most negative regression coefficient is represented with black; the most positive represented with white. The regions where the data are statistically significant at the 90% level are outlined with dark stippling.

Australian rainfall was different in the years 1900–1950 from the more recent years 1950–2010.

The QBO appears to have modest but significant influence on rainfall in the Northwest Pilbara region in DJF, and in the southeast coastal region in MAM and JJA.

The sunspot number (representing solar irradiance) appears to have a positive effect along the East Australian

coast in DJF, and to a lesser extent in MAM. There is also an indication that the eastern part of the continent is affected in the ‘off seasons’ – positively in MAM, and negatively in SON. This shows up more strongly in the 1950–2010 analysis. The results in Fig. 23.4 are consistent with the observations shown by Meehl *et al.* (2009) and Figure 16 of Gray *et al.* (2010).

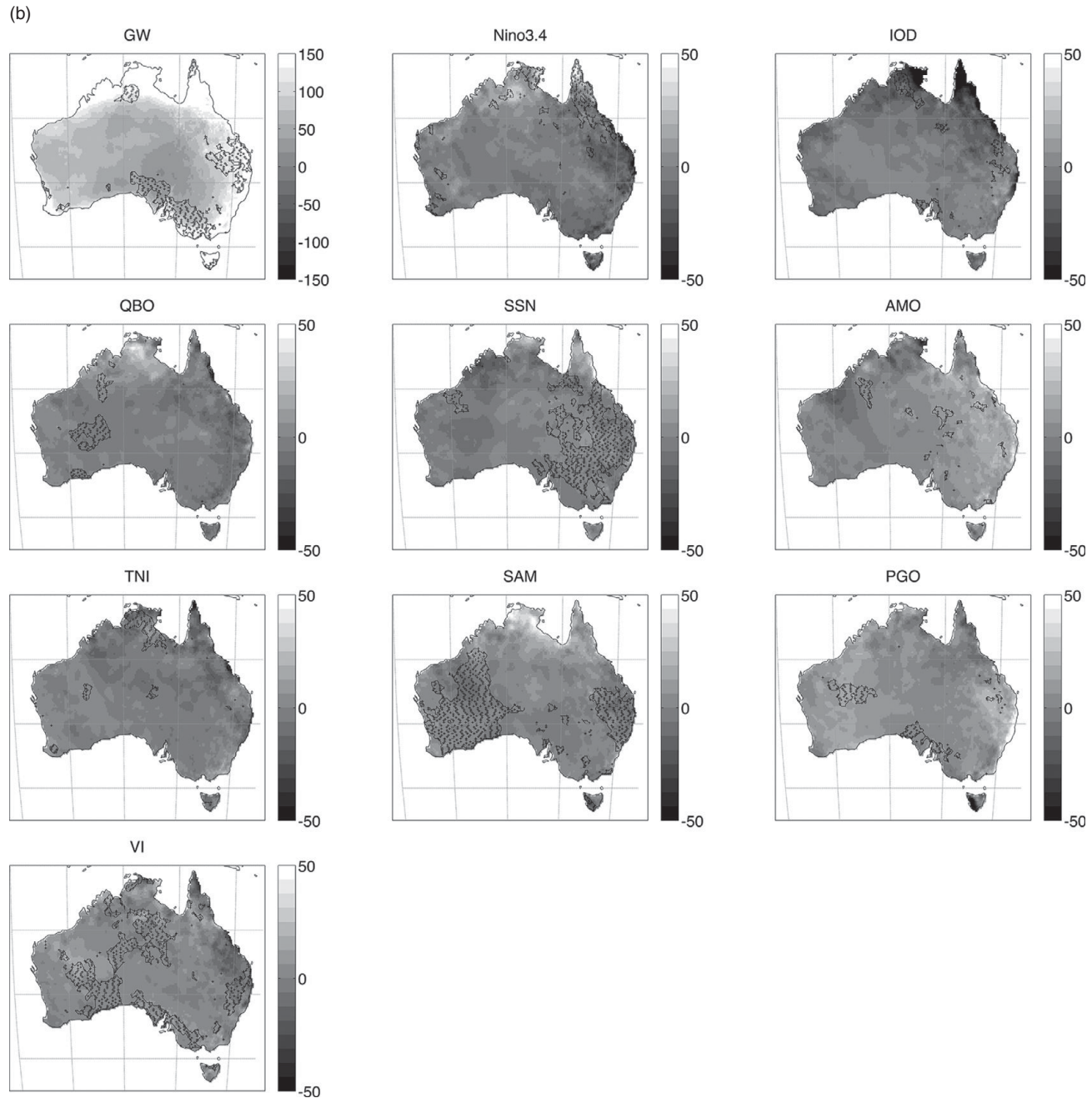


Fig. 23.4. (cont.)

The AMO has a negative effect on the rainfall in Northern Australia in DJF, and also to a lesser extent in MAM and SON. Since the positive phase of the AMO index (time series) implies a positive anomaly in the overturning ocean circulation, and presumably also in the Indonesian throughflow, this would appear to suggest that long-term stronger throughflow gives decreased northern Australian rainfall.

Positive values of the Southern Annular Mode (SAM) are associated with reduced rainfall in Tasmania in all seasons, and reduced rainfall in southwest WA in JJA. It is also associated with increased rainfall near the southern east coast, in all seasons.

The NPGO appears to be associated with a negative anomaly in the northwest and (less convincingly) a positive anomaly in the northeast in DJF.

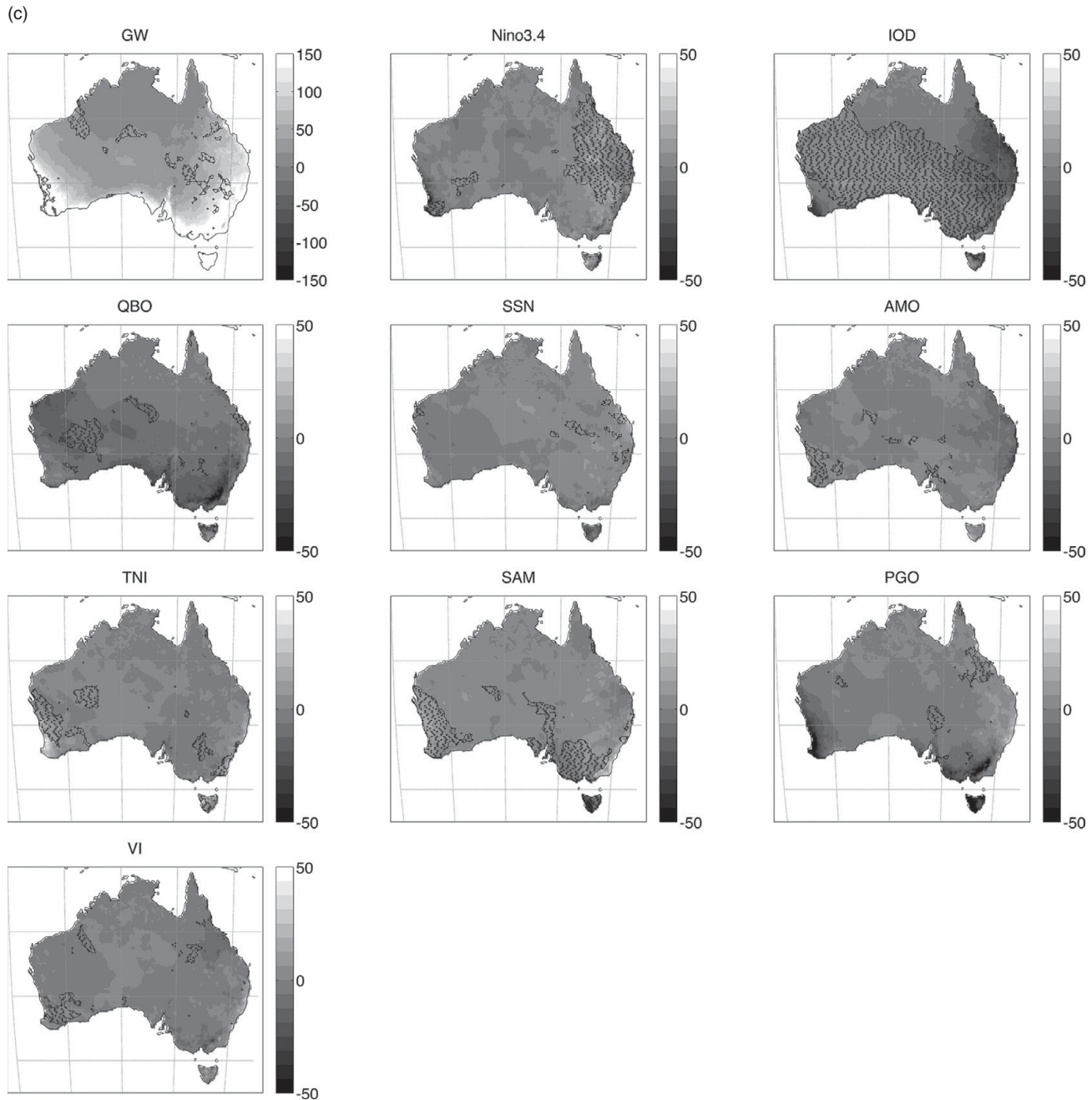


Fig. 23.4. (cont.)

The volcano index VI is associated with a negative rainfall anomaly in the southeast of the continent in SON. There is also a suggestion of a negative anomaly in the northern latitudes in DJF and MAM.

One may ask, given the identification of these dynamical spatial relationships, what fraction of the total variance remains unexplained by these regressed factors? The results are shown in Fig. 23.5. It is sobering to see that

the fraction unexplained is greater than 65% over the continent, and is over 90% in some areas. If one breaks down this residual rain with an empirical orthogonal function analysis (von Storch and Zwiers, 2001), one finds that, for each season, approximately 50% of this residual rainfall is described by the first three EOFs, the first containing approximately 30%. The spatial patterns of these EOFs is quite simple: EOF1 is mostly single-signed (i.e. + or -),



Fig. 23.4. (cont.)

EOF2 has wavenumber 1 form, and EOF3 has three ‘nodes’ (+ – +, or wavenumber 1.5). The time series of each of them has the form of white noise, as suggested by the high frequency oscillations in lagged auto-regression coefficients (not shown). If one calculates the same EOFs for the original rainfall data, superficially they appear similar, and one may ask, in what way are they different? If systematic effects, some of which have time scales of many

years, have been removed, one may expect this to be manifested in the time series of these EOFs. This may be investigated by computing the Hurst coefficient, or exponent (Hurst, 1951, Ghil *et al.*, 2011). For a time series of zero mean (which applies to these EOFs) and length  $n$ , the Hurst coefficient is obtained by first computing all the cumulative consecutive sums  $\text{Sum}(k)$  of terms in the sequence of length  $k$  (where  $0 < k < n$ ), and then the

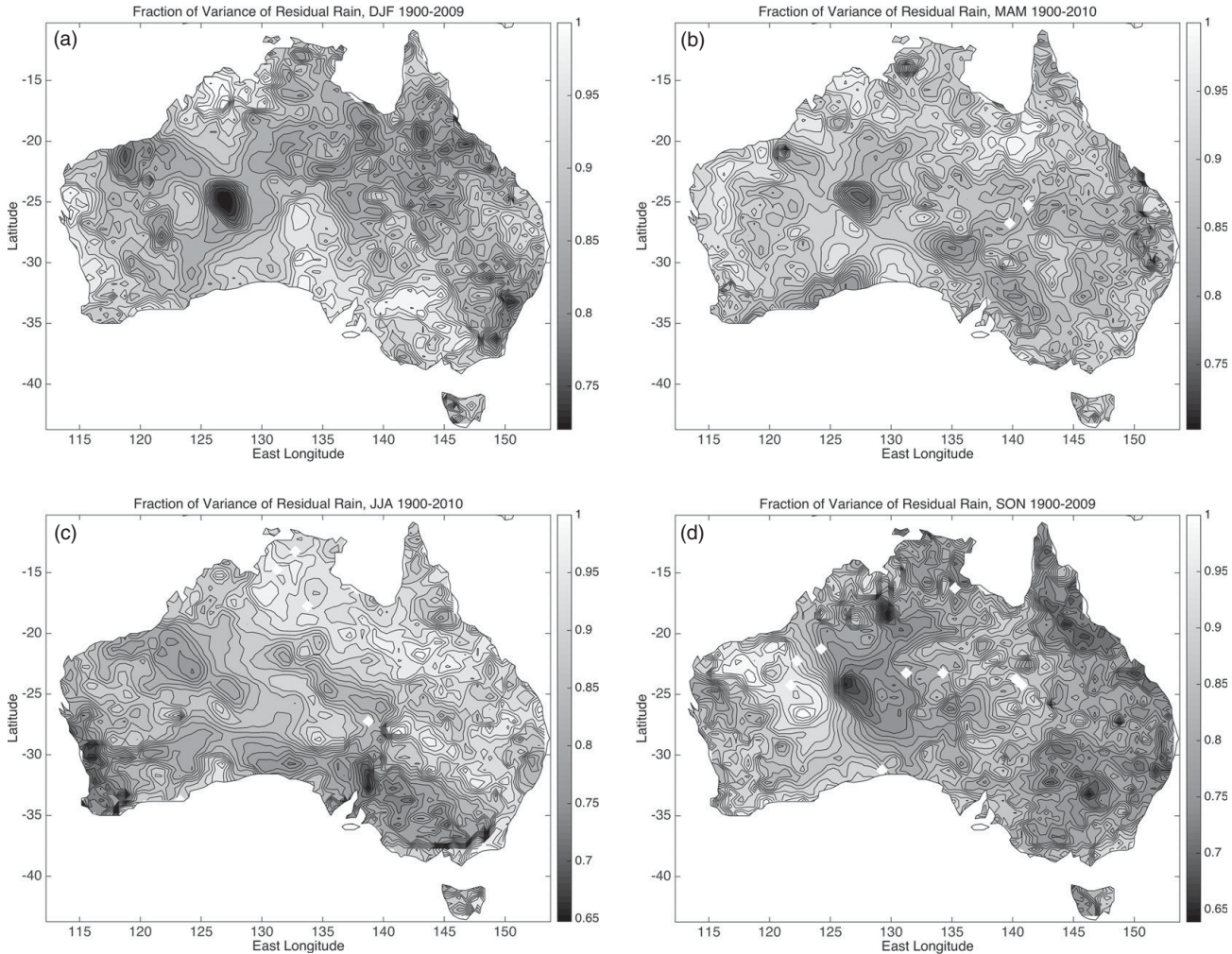


Fig. 23.5. The fraction of variance in seasonal rainfall that remains after the effects attributable to the ten factors considered via linear regression analysis have been removed. (a) December–February; (b) March–May; (c) June–August; (d) September–November.

difference between their maxima and minima. One may then compute the rescaled range parameter  $R(k)$ , defined by (e.g. Whiting *et al.*, 2003)

$$R(k) = [\text{maximum of all sums } \text{Sum}(k) - \text{minimum of all sums } \text{Sum}(k)]/\sigma, \quad (23.3)$$

where  $\sigma$  is the standard deviation of the time series. The Hurst exponent is then the mean slope of the curve  $\log(R(k))$  versus  $\log(k)$ , with  $k$  ranging from 2 to 30. The curves on these plots are not straight lines, but the mean slope has been (crudely) estimated, and the values for the first three EOFs, for each season, for the total rainfall and also for the residual rainfall, are given in Table 23.2. From Hurst's analysis, it is apparent that the larger the low frequency component in the time series, the larger is the value of the Hurst exponent. The main point depicted in Table 23.2 is that the value of the exponent is smaller (or at least, no

larger) in the residual time series than in the original one, implying that any low frequency component present in the observed rainfall has been reduced by removal of components correlated with the ten factors.

### 23.5 Conclusions

A multiple regression analysis has been performed on the seasonal means of Australian rainfall data, to investigate the spatial impact of ten globally significant dynamical processes on interannual rainfall variability. These processes are represented by their time series, and they are not completely independent (dynamically or statistically) of each other, but correlations between them are mostly small. The analysis can be applied to global rainfall data in the same manner. Two time periods have been considered,

Table 23.2. Estimated values of the Hurst exponent H for the time series of the first three empirical orthogonal functions of seasonal Australian rainfall, and similarly for the residual rainfall, after the effects of the ten factors have been removed. Estimated errors are +/-0.05.

	EOF number	Rainfall	Residual rainfall
MAM	1	0.34	0.34
	2	0.44	0.36
	3	0.33	0.16
JJA	1	0.39	0.25
	2	0	0
	3	0.58	0.25
SON	1	0.35	0.35
	2	0.43	0.35
	3	0.4	0.4
DJF	1	0.42	0.14
	2	0.71	0.56
	3	0.5	0.38

1900–2010 and 1950–2010, the first having the virtue of being a longer record, and the second with more recent, better quality data for both the factors and rainfall. The results for the longer period are shown here. There are statistical traps in this kind of analysis (e.g. Pittock, 1978), which we believe have been circumvented. However, a large part of the variance in rainfall at each location is not related to the factors considered, and the predictive power attributable to them can therefore only be regarded as influencing the probabilities of rainfall in any given location.

The first factor is the overall trend, which shows up as an increase in rainfall in the north and northwest in DJF, but no significant large-scale changes elsewhere or in other seasons. Other factors (Niño3.4 and the TNI) describe ENSO and the Indian Ocean dipole (IOD), the effects of which are reasonably well known and regularly monitored, but the analysis indicates that there are other factors that also have significant separate impact in various regions. These include the Atlantic Meridional Overturning circulation (AMO), which affects rainfall in northern Australia, particularly in DJF, and the Southern Annular mode (SAM), which affects the rainfall near the southeast coast, in all seasons. Variations in the solar constant, as measured by sunspot numbers (SSN) appear to have an influence along the Australian east coast in DJF, and a large-scale effect in the eastern part of the continent in the off-seasons (MAM and SON). One could make a long list of conclusions, but the best way to assess and compare the various influences is to inspect the plots in Fig. 23.4 where the stippled regions are formally statistically significant at the 90% level. In general, the results for ENSO and the IOD

are consistent with the results of previous studies, but the significance plots suggest that sunspot number, the AMO, and the SAM have notable contributions in certain regions in particular seasons.

## References

- Ashok, K., Behera, S. K., Rao, S.A., Weng, H., and Yamagata, T. (2007). El Niño Modoki and its possible teleconnection. *J. Geophys. Res.* **112**, doi:10.1029/2006JC003798, 2007.
- Ashok, K., Guan, Z., and Yamagata, T. (2003). Influence of the Indian Ocean Dipole on the Australian winter rainfall. *Geophys. Res. Lett.* **30**, 1821, doi:10.1029/2003GL017926, 15.
- Baines, P. G. (2011). Patterns of decadal climate variability and their impact on global rainfall. *Earth System Science 2010: Global Change, Climate and People*, Edinburgh; *Procedia Environmental Sciences* **6**, 70–87, S. Cornell, C. Downy and M. Rounsevell eds..
- Baldwin, M. P. and 14 others, (2001). The quasi-biennial oscillation, *Rev. Geophys.* **39**, 179–229.
- Broecker, W. S. (2010). *The Great Ocean Conveyor, Discovering the Trigger for Abrupt Climate Change*, Princeton University Press.
- Brönnimann, S., Annis, J. L., Vogler, C., and Jones, P. D. (2007). Reconstructing the quasi-biennial oscillation back to the early 1900s. *Geophys. Res. Lett.* **34**, L22805, doi: 10.1029/2007GL031354.
- Davis, R. E. (1976). Predictability of sea-surface temperature and sea-level pressure anomalies over North Pacific Ocean. *J. Phys. Oceanogr.* **6**, 249–266.
- Di Lorenzo, E. and 11 others, (2008). North Pacific Gyre Oscillation links ocean climate and ecosystem change. *Geophys. Res. Lett.* **35**, L08607, doi:10.1029/2007GL032838.
- Drosdowsky, W. and Chambers, L. E. (2001). Near-global sea surface temperature anomalies as predictors of Australian seasonal rainfall. *2001 J. Clim.* **14**, 1677–1687.
- Ghil, M. and 16 others, (2011). Extreme events: dynamics, statistics and prediction. *Nonlin. Processes Geophys.*, **18**, 295–350.
- Gray, L. J. and 14 others, (2010). Solar influences on climate, *Rev. Geophys.* **48**, doi: 10.1029/2009RG000282.
- Hurst, H. E. (1951). Long-term storage capacity of reservoirs, *Trans. Am. Soc. Civil Eng.*, **116**, 770–799.
- Jones, D. A., Wang, W., and Fawcett, R. (2009). High quality spatial climate data-sets for Australia, *Aust. Met. Oceanogr. J.* **59**, 233–249.
- Jones, D. A., Fogt, R. L., Widmann, M, et al. (2009). Historical SAM variability. Part I: Century-length seasonal reconstructions. *J. Clim.* **22**, 5319–5345.
- Kug J.-S., F.-F. Jin, and S.-I. An (2009). Two types of El Niño events: Cold Tongue El Niño and Warm Pool El Niño. *J. Climate* **22**, 1499–1515.
- Marshall, G. J. (2003). Trends in the Southern Annular Mode from observations and reanalyses. *J. Clim.*, **16**, 4134–4143.

- McBride, J. L. and Nichols, N. (1983). Seasonal relationships between Australian rainfall and the Southern Oscillation. *Mon. Wea. Rev.* **111**(10), 1998–2004.
- Meehl, G. A., J. M. Arblaster, K. Matthes, F. Sassi, and H. van Loon (2009). Amplifying the Pacific climate system response to a small 11 year solar cycle forcing, *Science*, **325**, 1114–1118, doi:10.1126/science.1172872.
- Meneghini, B., Simmonds, I., and Smith, I. N. (2007). Association between Australian rainfall and the Southern Annular Mode. *J. Climatol.* **27**, 100–121.
- Parker, D., Folland, C., Scaife, A., et al. (2007). Decadal to multidecadal variability and the climate change background. *J. Geophys. Res.*, **112**, D18115, doi:10.1029/2007JD008411.
- Pittock, A. B. (1978). A critical look at long-term Sun-weather relationships. *Rev. Geophys.* **16**, 400–420.
- Power, S., Casey, T., Folland, C., Colman, A., and Mehta, V. (1999). Inter-decadal modulation of the impact of ENSO on Australia. *Climate Dyn.* **15**, 319–324.
- Prentice, C., Baines, P. G., Scholze, M., and Wooster, M. J. (2012). Fundamentals of climate change science. Chapter 2 of *Understanding the Earth System – Global Change Science for Application*. S. E. Cornell, I. C. Prentice, J. I House and C. J. Downy eds., Cambridge University Press, 267 pp.
- Risbey, J. S., Pook, M. J., McIntosh, P. C., Wheeler, M. C., and Hendon, H. H. (2009). On the remote drivers of rainfall variability in Australia, *Mon. Wea. Rev.* **137**(10), 3233–3253.
- Smith, T. M., R. W. Reynolds, T. C. Peterson, and J. Lawrimore (2008). Improvements to NOAA's historical merged land-ocean surface temperature analysis (1880–2006). *Journal of Climate*, **21**, 2283–2296.
- Trenberth, K. E. and D. P. Stepaniak (2001). Indices of El Niño evolution. *J. Climate*, **14**, 1697–1701.
- Vernier, J.-P., et al., (2011). Major influence of tropical volcanic eruptions on the stratospheric aerosol layer during the last decade, *Geophys. Res. Lett.*, **38**, L12807, doi:10.1029/2011GL047563.
- von Storch, H. and Zwiers, F. W. (2001). *Statistical Analysis in Climate Research*, Cambridge University Press, 484 pp.
- Whiting, J. P., Lambert, M. F., and Metcalfe, A. V. (2003). Modelling persistence in annual Australian point rainfall, *Hydr. & Earth System Sci.* **7**, 197–211.

# 24

## MJO and extreme weather/ climate events

*Chidong Zhang*

### 24.1 Introduction

The Madden–Julian oscillation (MJO) affects global weather and climate via two main mechanisms. One is directly, through the enhanced or suppressed tropical convection and rainfall along its propagation pathway from the Indian Ocean to the Pacific Ocean. The other is by generating atmospheric or oceanic waves that propagate into regions that show little or no direct signals of the MJO itself. MJO influences on weather and climate are not separated from each other. The degree to which global weather is affected by the MJO often depends on the phases of certain climate modes. Climate phenomena under the influence of the MJO in turn modulate weather events in many regions of the world. In addition, the MJO also affects other important and interesting phenomena in the atmosphere and ocean that are not commonly categorized as either weather or climate. Because of the large number of weather, climate, and other phenomena in the Earth system that are influenced by the MJO, only very brief descriptions are possible here. More detailed discussion of the global impact of the MJO and the literatures that this chapter is based on can be found in Lau and Waliser (2011) and Zhang (2013).

rainfall anomalies in the global tropics at four stages of the MJO. The density of the tracks reflects TC frequency, which varies with the longitudinal location of the MJO convection center. Over the southern Indian Ocean, TC frequency is highest when the MJO convection center is over the Indian Ocean, but lowest when it is in the western hemisphere. Over the Bay of Bengal, TCs are most frequent when the MJO convection center is over the Maritime Continent, and least frequent when it is in the western hemisphere. Over both the northwestern and southwestern Pacific, as well as north of Australia, TCs are most (least) frequent when the MJO convection center is over the western Pacific (Indian) Ocean. TCs (or hurricanes) over the northeastern tropical Pacific occur most frequently when the MJO convection center is in the western hemisphere and least frequently when the MJO convection center is over the Maritime Continent. Atlantic hurricanes are most (least) frequent when the MJO convection center is over the Indian Ocean (western Pacific). The MJO may affect TCs by changing local vertical wind shear, low-level convergence, midlevel moisture, cyclonic relative vorticity, deep convection, small eddies, and synoptic disturbances serving as embryos for TCs.

### 24.2 Weather

Severe weather occurs around the world both with and without the influence of the MJO. However, the strength, frequency, and spatial and temporal distributions of severe weather can be affected by the MJO. More precisely, these characteristics of severe weather may change depending on periods with and without active MJO events, and the location of the MJO convection center.

#### 24.2.1 Tropical cyclones

The effects of the MJO on tropical cyclone (TC) frequency are illustrated in Fig. 24.1, which shows TC tracks and

#### 24.2.2 Tornadoes

In spring (March, April, and May), the contiguous USA is prone to tornadoes. Violent tornado outbreak days, with six or more strong tornadoes within a 24-hour period, are more than twice as frequent when the MJO convection center is over the Indian Ocean than at other locations. Combined intraseasonal anomalous patterns (an upper tropospheric trough extending east from the western USA, upper-tropospheric southwesterly wind anomalies, and low-level southerly wind anomalies over the southern Great Plains) and the seasonal circulation (a ridge over the southeastern USA) provide atmospheric conditions favorable for violent tornado formation.

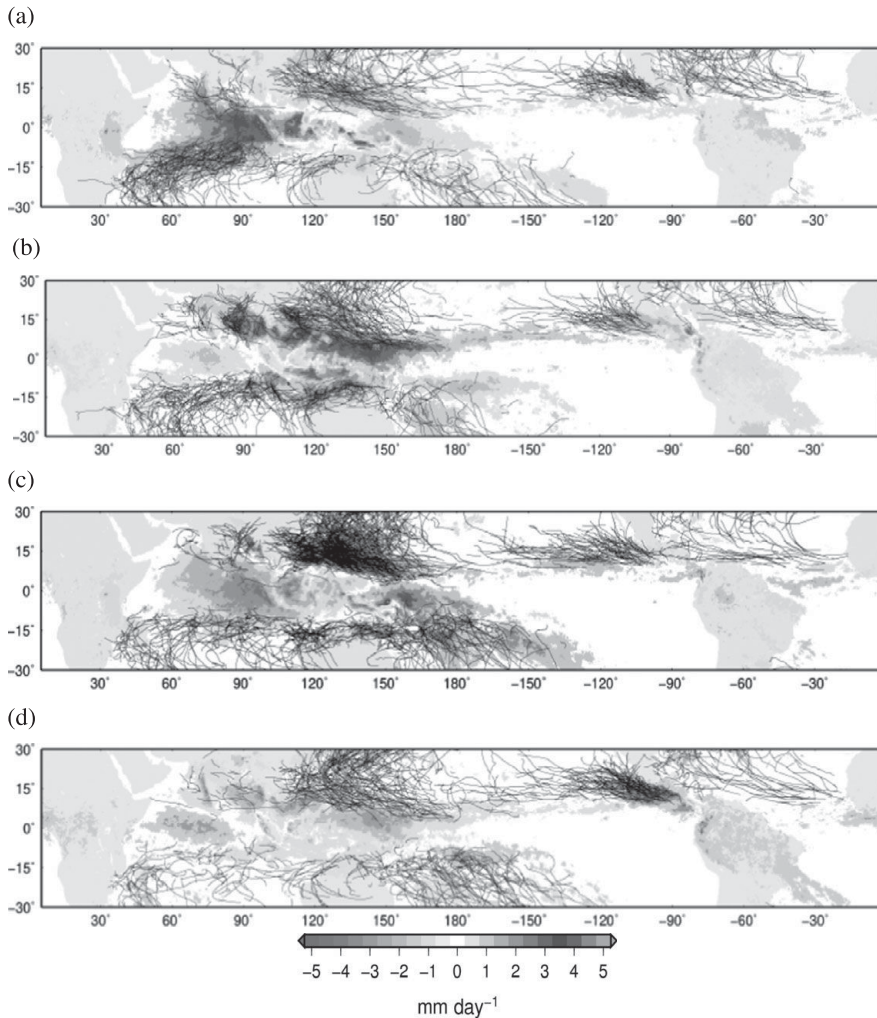


Fig. 24.1. TC tracks (1975–2011; black lines) and precipitation anomalies (1998–2011; color shading) when the MJO convection center is over the (a) Indian Ocean, (b) Maritime Continent, (c) western Pacific, and (d) Americas and Africa. Based on Zhang (2013). A black and white version of this figure will appear in some formats. For the colour version, please refer to Plate 29.

#### 24.2.3 Extreme rainfall

Extreme rainfall events are defined here as record-breaking rain events or total rain amounts within a given top percentile of the local rainfall probability distribution. While several such events, which caused tremendous damage, are suspected to have occurred partly because of the MJO, the most convincing evidence of MJO modulation of extreme rainfall is the change in extreme rainfall frequency as a function of the longitudinal location of the MJO convection center. For example, 62% of extreme rainfall events over the highland region of equatorial East Africa between March and May occur when the MJO convection center is over the Indian Ocean, while 72% of extreme rainfall near the equatorial East African coastal region occur when MJO convection is suppressed over the Indian Ocean and Maritime Continent. Extreme rainfall events in the semiarid north-central coastal area of Chile typically occur only 3–5 times during the fall and winter of rainy years, and about 80% of them happen when the MJO convection

center is in the central equatorial Pacific. During the boreal winter over the contiguous USA, extreme rainfall (exceeding the 90th percentile of the frequency distribution of intensity and spatial coverage) occurs twice as frequently during periods with strong MJO events than in those without, and is most frequent when the MJO convection center is over the Indian Ocean. Globally, the frequencies of extreme rainfall events during periods of strong MJO are about 40% higher than periods with weak, or no, MJOs.

#### 24.2.4 Flood

It has been suggested that some extreme flood events that caused large numbers of casualties were associated with particular MJO events. However, as for extreme rainfall events, the most evident effect of the MJO on flooding comes from fluctuations in the flood frequency through the life cycle of the MJO, or between periods with and without MJO events. Take large flood events as an example. They

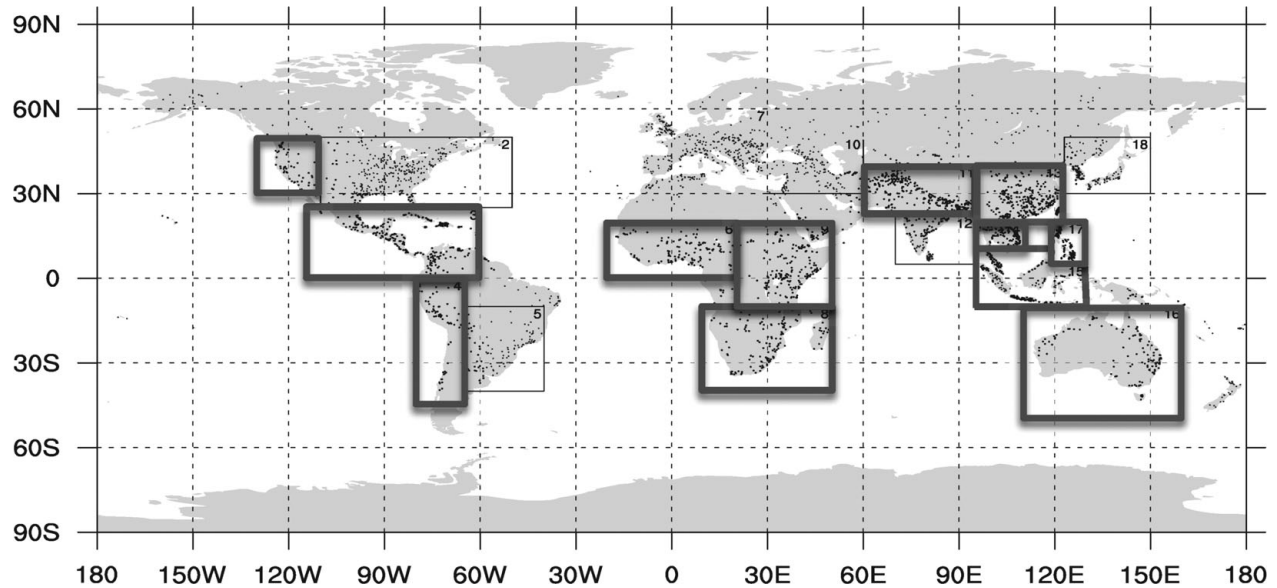


Fig. 24.2. Locations of large flood events for the period 1985–2010 based on the Dartmouth Flood Observatory Global Archive of Large Flood Events at the University of Colorado (Brakenridge 1996; <http://floodobservatory.colorado.edu/Archives/index.html>). Red boxes mark regions where the probability of total flood days and/or events is significantly affected by the MJO. Based on Zhang (2013).

are defined as extreme events that cause unusual damages, reported once per decade or a longer time. Their probability is measured by the total number of flood events or the total number of flood days in all flood events within a given period in a given region. The frequency of large flood events in many parts of the world is modulated by the MJO (Fig. 24.2). When the MJO convection center is over the western Pacific, large flood events are most frequent along the west coast of North America, in the Philippines, and in South Asia and West Africa. They are least frequent in these regions when the MJO convection center is over the Indian Ocean. In contrast, large flood events in Central America and East Africa are most (least) frequent when the MJO convection center is over the Indian Ocean (western Pacific). Over China, frequencies of large flood events tend to be reduced during periods of strong MJO activity in comparison with those without. Similar MJO effects on large flood events can be found in other regions (Australia, the Maritime Continent, the Middle East, southern Africa, and the Andes).

#### 24.2.5 Lightning

By affecting deep convection, the MJO also modulates global lightning frequency. In the main region of MJO activity, namely the tropical Indian and Pacific oceans, very deep ( $>10$  km) lightning-producing convective towers tend to occur immediately prior to the local onset

of MJO convective periods, yielding the highest lightning frequency. The MJO also affects lightning outside the tropics. For example, summertime lightning over the USA exhibits a migrating pattern as the MJO convection center moves from the Indian to the Pacific Ocean. The MJO effect on lightning is projected onto the Schumann resonances (SR), which are electromagnetic waves of zonal wavenumber one, that occur in the natural cavity between the Earth and the ionosphere. The intensity of the SR is mainly modulated by fluctuations in the number and intensity of global lightning. Intraseasonal perturbations in the SR have been detected and related to the MJO.

#### 24.2.6 Wildfire

Through its modulation of rainfall, and perhaps also wind, humidity, and temperature, the MJO affects the frequency of wildfire in many regions globally. Global monthly fire counts are always larger when there are active MJO events than otherwise. Figure 24.3 compares global fire frequencies at two stages of the MJO life cycle: the first when MJO convection has just begun over the Indian Ocean (initiation stage), and the second when MJO convection has propagated across the Maritime Continent and reached the western Pacific (WP stage). Fire frequencies are much higher during the MJO initiation stage than the WP stage over the Amazon and northern Australia, whereas they are lower over Alaska and north of Lake Victoria over equatorial

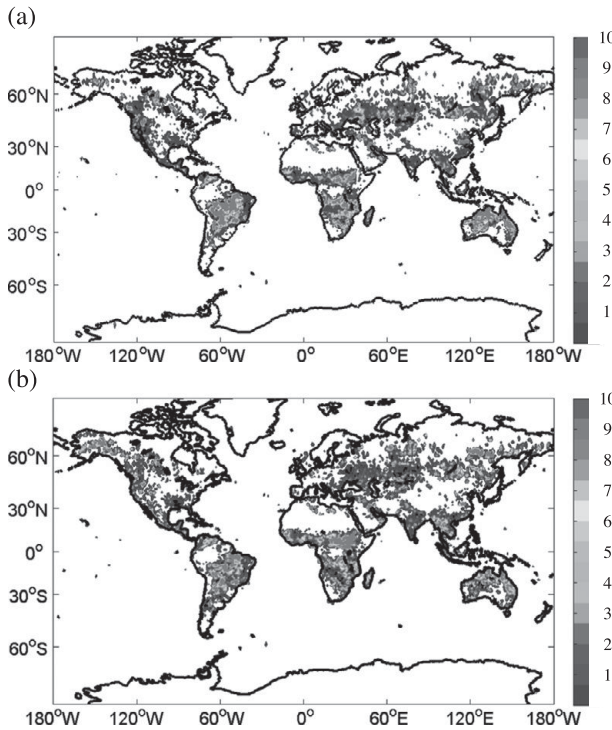


Fig. 24.3. Fire frequency (%), color shading) in each  $1^\circ \times 1^\circ$  grid box during the (a) MJO initiation stage (MJO convection center starts over the Indian Ocean), and (b) MJO WP stage (MJO convection center is over the western Pacific). The fire count data are ATSR World Fire Atlas (Arino *et al.* 2011. <http://due.esrin.esa.int/wfa/>). A black and white version of this figure will appear in some formats. [For the colour version, please refer to Plate 30.](#)

Africa. Over Eastern Europe and European Russia, fire is more concentrated to the south during the MJO initiation stage, but spreads to the north when the MJO matures. Other regions experience their fire maxima and minima at different MJO stages (phases). Over Siberia, fire is most frequent when MJO convection is most enhanced over the eastern Indian Ocean, and least frequent when MJO convection is most suppressed there.

#### 24.2.7 Cold surges

Two-thirds of extreme cold surges with temperature reductions greater than two standard deviations in East Asia occur when the MJO convection center is over the Indian Ocean. Although, in general, the MJO tends to prevent weak cold surges from penetrating southward into the subtropics and tropics, an MJO event with its convection center stalled over Sumatra resulted in an extreme cold event during a cold year of ENSO (February 2008) that broke the 50-year records for the minimum daily temperature and duration of large negative temperature anomalies over Southeast Asia.

An extreme cold surge with record-breaking snowfall in Korea during the winter of 2009–2010 might have resulted from the combined effects of the MJO and the Arctic Oscillation.

### 24.3 Climate

Climate phenomena subject to MJO influences include the monsoons and several climate modes, such as the El Niño–Southern Oscillation (ENSO), the North Atlantic Oscillation (NAO), the Arctic Oscillation (AO) and Antarctic Oscillation (AAO), the Pacific North American pattern (PNA), and the Indian Ocean Dipole (IOD). These climate phenomena occur because of their respective dynamics, not because of the MJO. But their strength, timing, and other characteristics can be affected by MJO activities.

#### 24.3.1 Monsoons

The MJO is the main source of intraseasonal fluctuations in many, if not all, monsoon systems. Between 33% and 80% of the intraseasonal variability of monsoon rainfall is related to the MJO. Summer monsoon onsets and breaks are often related to the MJO, especially for the Indian and Australian monsoons. Convectively active episodes of the MJO can enhance heavy rainfall events during summer monsoons. The northward propagation of the MJO during the boreal summer is as important as its eastward propagation to the Asian monsoon. The MJO affects the American monsoons through two mechanisms. One is eastward propagation of the MJO along the Pacific ITCZ (intertropical convergence zone). The other is the Rossby wave train, excited by MJO convection in the tropical Indo-Pacific region that enters South America via the extratropics. Equatorial Rossby waves excited by MJO convection over the Indian Ocean and propagating westward are considered to be the main mechanism by which the MJO affects the African monsoon.

#### 24.3.2 ENSO

Strong episodes of the MJO often occur prior to major ENSO warming events (El Niño). The peak of ENSO warming in the eastern Pacific during the boreal winter is usually preceded by enhanced MJO activity during the boreal spring. This leads to a significant correlation between ENSO sea surface temperature (SST) and MJO activities, with the former lagging the latter by six to ten months. Oceanic downwelling Kelvin waves forced by westerly wind anomalies of the MJO are the main mechanism by which the MJO influences ENSO. In an ENSO paradigm, the MJO acts as a main source of high frequency

stochastic forcing that drives ENSO. Meanwhile, feedback from ENSO SST to the MJO can be important to this MJO–ENSO connection, making the MJO a multiplicative stochastic forcing of ENSO.

#### 24.3.3 NAO

Enhanced (depressed) MJO convection over the central Pacific can considerably amplify the NAO in its negative (positive) phase. Northward momentum transport by Rossby wave dispersion from the tropical Pacific to the extratropical North Atlantic is thought to be the main mechanism of MJO influence on the NAO. The daily sign of the wintertime NAO can be predicted with a success rate of about 70% at a lead-time of 9–13 days using a statistical model based on the connection between the MJO and NAO.

#### 24.3.4 AO

During winter, the positive (negative) phase of the AO, also known as the Northern Annular Mode (NAM), is twice as likely to occur as the opposite phase when MJO convection is enhanced (suppressed) over the Indian Ocean. When MJO convection is enhanced (suppressed) in the eastern hemisphere, especially over the Maritime Continent, the number of days of positive (negative) AO phase becomes large. For the period November–March, between 18% and 21% of the variance in extratropical 1000 hPa geopotential height is related to the MJO. The MJO influences the AO also through Rossby wave trains, which are excited by MJO convection and then propagate from the tropical Pacific into the extratropics.

#### 24.3.5 AAO

The southern hemispheric counterparts of the NAM and AO are the Southern Annular Mode (SAM) and Antarctic Oscillation (AAO), and they are also influenced by the MJO. Negative (positive) phases of the AAO during the austral winter tend to occur when MJO convection is enhanced (suppressed) over the central Pacific. The SAM reaches its maximum positive phase immediately after MJO convection peaks over the equatorial Indian Ocean. The Antarctic circumpolar transport can be accelerated by the MJO-enhanced surface westerly wind associated with the SAM that covers almost the entire latitude circle at 60°S.

#### 24.3.6 PNA

The PNA teleconnection pattern undergoes both interannual and intraseasonal variations. Over intraseasonal time scales, about 30% of the emergence of the PNA pattern is related to the MJO. The positive (negative) phase of the

PNA pattern is most likely to occur when MJO convection is suppressed (active) over the region between the Bay of Bengal and the western Pacific. This MJO–PNA connection is caused by Rossby wave trains generated by the anomalous convection of the MJO and propagating into the extratropics.

#### 24.3.7 IOD

Anomalous upwelling Kelvin waves forced by anomalous easterlies associated with suppressed convection of the MJO over the equatorial Indian Ocean can lead to shoaling of the thermocline in the eastern Indian Ocean, and thereby promote the onset of positive phases of the IOD. After an IOD positive phase is initiated, downwelling oceanic Kelvin waves generated by the anomalous surface westerly wind associated with active convection of the MJO tend to deepen the thermocline and help to terminate a positive phase of the IOD. By the same token, an IOD mature phase can sustain itself only in the absence of strong MJO events.

### 24.4 Upper ocean

Through its anomalies in surface wind, cloudiness, and rainfall, the MJO strongly disturbs fluxes of momentum, heat, and freshwater at the ocean surface along its path from the Indian Ocean to the Pacific Ocean. The direct consequences are changes in the upper ocean structures of currents, temperature, and salinity, the generation of oceanic waves, and fluctuations in the upper ocean chemistry and biology. Some of them are briefly discussed in this subsection.

#### 24.4.1 Surface currents

Another consequence of the strong surface wind associated with the MJO, especially its westerly wind anomalies, is the acceleration of the surface currents beneath, of which the Wyrtki jet is the most striking example. The Wyrtki jet is a narrow ( $2^{\circ}\text{N}$ – $2^{\circ}\text{S}$ ), eastward flowing near-surface (0–100 m) ocean current along the equator across the Indian Ocean. It is generated by the seasonal mean surface westerly wind during the transition periods (April–May and October–November) between the two monsoon seasons. The surface westerly wind associated with the MJO can substantially enhance the Wyrtki jet over intra-seasonal time scales, with its amplitudes ( $0.5$ – $2 \text{ ms}^{-1}$ ) often greater than their seasonal means. An anomalous Wyrtki jet can also occur during other seasons as a result of strong westerly forcing by the MJO. The intraseasonal variability of the Wyrtki jet exhibits two spectral peaks. Direct MJO forcing results in a 30–60 day peak, while resonant

excitation of the second-baroclinic-mode waves by the low frequency MJO wind, accompanied by interference between directly forced and reflected ocean waves, generate a 90-day peak.

The MJO also causes intraseasonal fluctuations in the Indonesian Throughflow (ITF), which is the surface current passing through the Indonesian archipelago that acts as the main artery transporting heat and mass from the Pacific to the Indian Ocean. The intraseasonal spectral peaks of the ITF at 50–60 days are partly due to direct MJO wind forcing, and partly to MJO-forced oceanic waves. In addition, the MJO also induces intraseasonal fluctuations in other ocean currents, such as the Somali current, and the Indian Ocean south equatorial current.

#### 24.4.2 Waves

The strong surface westerly wind associated with the MJO often generates downwelling Kelvin waves that propagate eastwards, and equatorial Rossby waves that propagate westwards, along the equatorial wave guide. The downwelling Kelvin waves play an instrumental role in MJO impacts on ENSO, the IOD, and the ITF, among others. When these Kelvin waves reach the eastern boundary of an ocean basin (e.g. Sumatra), they lead to coastal waves that move along the coastlines towards higher latitudes where they have local impacts, such as large intraseasonal fluctuations in SST near the northwestern coast of Australia.

#### 24.4.3 Sea level

Sea level fluctuates intraseasonally with amplitudes of more than 10 cm in many areas of the Indian and Pacific oceans due to anomalies in MJO-related surface wind and MJO-forced equatorial Kelvin and Rossby waves and coastal waves. The greatest sea level fluctuations in response to the MJO are in the equatorial Pacific, the coastal region of Sumatra, the Bay of Bengal, and the Gulf of Carpentaria. Along the equator, sea level anomalies

propagate eastwards at the phase speed of the oceanic Kelvin wave. MJO-generated coastal waves originated in the tropics may propagate into the higher latitudes and lead to intraseasonal fluctuations in sea level there.

## 24.5 Concluding remarks

The broad global impacts of the MJO are strong testament to the unique role of the MJO in connecting weather and climate, and in affecting many aspects of the Earth system. There is hardly any other single atmospheric phenomenon that even comes close to the MJO with regard to its broad global impacts. As a result of this unique role, improvements in MJO prediction could potentially lead to advances in the prediction of many other phenomena within the Earth system. It has been demonstrated that numerical models that produce more realistic MJO signals are capable of predicting many other phenomena, such as tropical cyclones and extratropical circulation patterns, with a lead-time of 1–2 weeks. Clearly, improvements in Earth system prediction can be achieved only if we are able to better understand and predict the MJO.

## References

- Arino O., S. Casadio, and D. Serpe (2011). Global night-time fire season timing and fire count trends using the ATSR instrument series. *Remote Sensing of Environment*. doi:10.1016/j.rse.2011.05.025
- Brakenridge, G. R. (1996). The Dartmouth Flood Observatory: an electronic research tool and electronic archive for investigations of extreme flood events. *Geological Society of America Annual Meeting*.
- Lau, W.K.M. and D. E. Waliser, Eds. (2011). *Intraseasonal Variability of the Atmosphere-Ocean Climate System*, 2<sup>nd</sup> Ed. Springer, Heidelberg, Germany, 613 pp.
- Zhang, C. (2013). Madden-Julian Oscillation: Bridging Weather and Climate. *Bull. Amer. Met. Soc.*, **94**, 1849–1870.



## PART VI

### **Asian monsoons**



## 25

# Extreme weather and seasonal events during the Indian summer monsoon and prospects of improvement in their prediction skill under India's Monsoon Mission

D. R. Sikka

## 25.1 Introduction

India, being an ancient agricultural society, has been curious about the study of its weather and climate for over 5000 years. The tools have changed from looking at the heavens for control over weather phenomena in the distant past to the present scientific meteorology for weather and climate observations and prediction, aided by high technology for observations and computational purposes. There are historical records to suggest that rain was being measured by some sort of recording system in India even in the third century BC, and its marked spatial variability and inter-annual and intra-seasonal variability was broadly known for the main rainy season, "Varsha ritu", which is now commonly known as monsoon season (June–September). Underlying causes for the variability in rains were hotly debated by scholars and thinkers, both among themselves as well as with the visiting scholars who had accompanied Alexander the Great in his invasion of India. There are mentions in ancient Sanskrit literature which point to the statement that 'Even though the foreigners (Yavnas) are invaders of peace and tranquility of the country, yet there are scholars among them who are no less distinguished than our own scholars (Rishis) and hence they must be respected like our rishis'. This tradition of acknowledging the contributions of foreign scholars for their help in advancing the knowledge on understanding and prediction of weather and climate events has been passed on to Indians from generation to generation. The past few generations in the modern era of scientific meteorology in India have gained a lot from foreign scientists' participation in this common endeavour of improving the skill of forecasting weather and climate events. In the present, too, India has launched a major mission-mode scientific programme, known as the Monsoon Mission, to improve the skill of weather and climate predictions at all scales ranging from short-to-medium and to extended and seasonal scales. In the

Monsoon Mission, collaborative research between Indian atmospheric-ocean scientists and international scientific organizations / institutions / universities is to be vigorously promoted over the 2012–2017 period, to advance monsoon prediction on the above mentioned scales.

From the early years of the establishment of the India Meteorological Department (IMD) in 1875, prediction of extreme weather and climate events has been well emphasized and pursued with vigour. Historically, IMD was established within about a decade of the infamous drought of 1865 and the severe tropical cyclone which had struck the port of Calcutta (now Kolkatta) and had caused devastation to shipping and mercantile interests. Another drought sequence from 1876 to 1877, had led the then head of the IMD, Professor Henry Blanford (1884), to launch the Seasonal Monsoon Forecasting System, based on one precursor parameter, namely, the Himalayan snowfall in the previous winter and spring seasons. Monsoon droughts had become more frequent between 1896 and 1911 and Sir Gilbert Walker, who had taken over as the third head of the IMD in 1904, took it upon himself to find the global precursors for the performance of a sub-continental and four-month duration of the rainy season. He believed that deficit performance of summer monsoon over a large spatio-temporal scale of Indian rainfall must have some precursors on the global scale which could be used to foreshadow the seasonal monsoon rainfall over India.

Surface synoptic weather charts were introduced in India, towards the end of the nineteenth century. This made forecasting of heavy rainfall another important activity of the IMD. Thus by the beginning of the twentieth century IMD became involved in predicting extreme events, like the path and intensity of tropical cyclones, the monsoon seasonal rainfall (particularly the drought and excess summer rainfall season), and the heavy rainfall events over different parts of the country during the monsoon season.

Over the past 100 years or so, intensive research has taken place in India towards the diagnosis and forecasting of extreme weather and climatic events. The international atmospheric science community has become a vigorous partner in this pursuit since the International Indian Ocean Expedition (IIOE), 1963–65. Marvellous technological advances in the form of observational techniques on land, in the ocean, and in space, have also helped in accessing crucial observations through advanced communication technologies. Advances in remote sensing, computational techniques, and high speed computing have helped in maximizing efficiency of analysing the new data on atmospheric–ocean dynamics. Also advances with the introduction of dynamical models have enormously enabled atmosphere–ocean scientists in the diagnosis and prediction of weather and climatic events.

The present paper is an attempt to summarize the vast progress made in understanding and predictions of monsoon-linked weather and climatic events over India. [Section 25.2](#) is devoted to phenomenological advances in the monsoon meteorology of India. [Section 25.3](#) covers studies on the large scale tropospheric circulations and rainfall features of the monsoon system. [Section 25.4](#) deals with the features during onset and advanced phases of monsoon rainfall. [Section 25.5](#) deals with low frequency sub-seasonal and inter-annual monsoon variability, and even the multi-decadal signal of variability. [Section 25.6](#) covers the coupled system approach of the role of land-surface processes, aerosols, ocean (local and remote forcing of the Indian Ocean and the equatorial Pacific Ocean respectively) in monsoon processes. With this background of massive understanding on monsoon processes, [Section 25.7](#) focuses on assessing the prediction skill of a dynamical modeling system for monsoon. This sets the goals for the prospects for the Monsoon Mission research, which is discussed in [Section 25.8](#). Summary and conclusions are presented in [Section 25.9](#).

## 25.2 Phenomenological studies on the South Asian Monsoon

Observations are used to understand developments in weather and climatic events which are important, followed by theory and modelling. In the case of the South Asian Monsoon (SAM) too, observations and their interpretation became the key elements of research from the early days of scientific meteorology. Also in recent times, special campaigns have been carried out to understand key processes in the South Asian Monsoon system. We shall touch upon the major phenomenological advances in monsoon in two phases: Early Phase 1875–1950 and Recent Phase 1951–2010.

### 25.2.1 Phenomenological studies in the Early Phase – 1875–1950

With the establishment of IMD in 1875, a lot of effort was devoted between 1875 and 1900 to establish a regular network of surface observatories using standard equipment and observatory lay-outs. Thereafter, between 1902 and 1950 the network was expanded and an upper-air observing system using meteo-sonde, kite balloons, pilot balloons, and even a radiosonde network was progressively established. Observations from these networks were properly archived and data processed and analysed, to understand and document the phenomenological aspects of the monsoon. Blanford established a system of documenting the research in IMD through publication of the Memoirs of the IMD, and communicating research via some of the leading European journals of that time. When the strength of the IMD increased during the 1920s and 1930s through the induction of Indian scientists for meteorological work, IMD established a practice of publishing Scientific Notes and Technical Notes, and finally in 1950, the first Indian Head of the IMD, Dr. S. K. Banerjee, established publication of the quarterly *Indian Journal of Meteorology and Geophysics*. This journal has been renamed twice since, and is presently in its 63rd year of publication in the form of *Mausam*. Enormous amounts of important work on different weather and climatic phenomena have been published in the above mentioned media and it is extremely difficult to discuss all the advances made over this period. However, the following prominent aspects are noted:

- (a) Rainfall of India by Blanford (1886) – discussing in detail rainfall features over all seasons in India. Concerning the monsoon seasons, details of major phenomenological advances mentioned in this publication refer to the role of the Monsoon Trough (MT) in regulating rainfall.
- (b) The active–break cycle of a monsoon, the transient monsoon low pressure systems (LPSs) (lows and depressions), and their role in rainfall distribution.
- (c) The role of land-surface processes like forests, water bodies, orography, etc. on the distribution of monsoon rainfall.
- (d) The influence of Himalayan winter and spring season snow cover on seasonal monsoon rainfall, the influence of deforestation on local rainfall in India, and a detailed description of about 15 years' of annual rainfall etc. Blanford (1886), showed a great depth of understanding in depicting the processes in Indian weather and climate, with only 10–15 years' of surface weather records, and could intuitively figure out a possible structure for the monsoon circulation in the troposphere.

- (e) Blandford's successor, Sir John Eliot, was synoptic meteorologist par excellence, and between 1880 and 1903 he contributed to original research on monsoon depressions (Eliot 1884), the onset of the monsoon and the influence of cross-equatorial flow in the onset process, formation and intensification of tropical cyclones on the forward edge of the advancing / retreating monsoon, and the role of latent heat in their intensification and maintenance.
- (f) Sir Gilbert Walker's original work covers two decades (1904–1924) of his stay in India, detailing the statistical prediction of seasonal monsoon rainfall which led to the discovery of the North Pacific Oscillation (NPO), Southern Oscillation (SO), and the North Atlantic Oscillation (NAO); the last two oscillations are still today considered important in the global climate system.
- (g) Sir G. C. Simpson's (1921) work on the containment of moisture within box-like geographical features provided by the South Asian and Himalayan orography.
- (h) Normand's work between 1930 and 1945 on the thermo-dynamical processes in convective weather development over India.

Additionally, important research by Indian scientists such as K. R. Ramanathan, S. K. Banerjee, A. K. Roy, B. N. Desai, S. Mull, R. Ananthakrishnan, P. R. Pishorty, P. Koteswaram, and others on monsoon depressions, tropical cyclones, convective organizations, and atmospheric electricity in relation to the weather and climate of India etc. between 1930 and 1960, set the formulation of phenomenological meteorology in India on firm ground.

### **25.2.2 Phenomenological studies in the Recent Phase – 1950–2010**

Scientific literature on the South Asian Summer Monsoon (SASM) began to grow steadily from 1957 onwards, primarily due to stimulus from several international field campaigns under IGY (1957–58), IIOE (1963–65), Indo-Soviet Monsoon Experiment – ISMEX (1973), Monsoon – 77, Summer MONEX-1979, Tropical Ocean Global Atmosphere TOGA, followed by a series of field programs organized by the Indian atmosphere–ocean science community, like the Monsoon Tough Boundary Layer Experiment – MONTBEX (1989–90), Land Surface Processes Experiment – LASPEX (1995–96), Bay of Bengal Monsoon Experiment – BOBMEX (1998–99), Arabian Sea Monsoon Experiment – ARMEX (2002–05), and the ongoing Continent Tropical Convergence Zone CTCZ (2009–2014). SASM, as a challenging subject, has also attracted the attention of prominent atmospheric scientists from around the world,

from the USA, Europe, Japan, China, Australia, and other countries, whose enormous contributions have advanced phenomenological studies to cover several crucial aspects, of which the following are very important:

- Air-sea interactions in monsoon,
- Lower tropospheric inversions in monsoon flow,
- Satellite studies on monsoon,
- Role of tropical easterly jet and sub-tropical westerly jet streams in monsoon modulations,
- East–west circulation and monsoon regional and planetary scales divergent circulation and monsoon,
- Monsoon onset and advance,
- Monsoon transient disturbances, like the trough off the west coast of India, monsoon depressions, mid-tropospheric cyclones,
- Intra-seasonal, inter-annual, and decadal variability of monsoon,
- Inter-regional influence on SAM such as Western Pacific circulation and monsoon, Southern Hemisphere (SH) and monsoon, Northern Hemisphere (NH) and monsoon etc.,
- Land-surface process and monsoon, including the role of aerosols, oceans and monsoon (ENSO and Indian Ocean Dipole (IOD) and local air–sea interactions), cryosphere and monsoon, and predictability and prediction of monsoon on different scales: short, medium, extended, and seasonal (short-term climate scale) of monsoon.

Scientific literature has grown enormously and particularly in the past four decades. Several good books have been published, such as Ramage (1971), Rao (1976), Das (1986), Fein and Stephens (1987), Chang and Krishnamurti (1987), Keshavamurty and Shankar Rao (1992), Pant and Rupakumar (1997), Wang *et al.* (2007), Asnani (1993, 2005), Chang *et al.* (2011), etc. Also several authoritative articles are available (Gadgil, 2003, Goswami *et al.*, 2006, Ding and Sikka, 2006). IMD published several Monographs under its Forecasting Manual Series during the 1970s. The latest Monsoon Monograph by IMD (2011, 2012) has recently been published in two volumes and its soft version is available from IMD, Pune.

### **25.3 Large-scale features of tropospheric circulation and rainfall during the South Asian Summer Monsoon**

#### **25.3.1 Tropospheric circulation**

Near-surface reversals of the winds over the tropical oceans on an annual basis have been known for over three centuries. Webster (1987) has discussed the fundamental conceptual framework of the driving mechanisms of tropical summer monsoon and they are:

- (a) The variation in space and time of the solar heating of the Earth system that results from the annual cycle of the sun and the character of the Earth's surface at a particular location (continents versus oceans) or in other words, the annual cycle of radiative heating which creates land-sea contrasts.
- (b) Creation of pressure gradients between warm continents and cooler oceans in summer and the response of winds to this body force.
- (c) The swirl of the rotating Earth (Coriolis force) which turns the winds on crossing the equator to south-westerlies in the Northern Hemisphere (NH) and north-westerlies in the Southern Hemisphere (SH).
- (d) Moist processes which fire the monsoon with latent heat release and result in maintenance of the monsoon during the summer season.
- (e) The hydrology of the wet land surface.

SASM, besides being a planetary scale phenomenon, has regional dimensions, such as the South Asian Monsoon, the East Asian Monsoon, the West African Monsoon, the North American Monsoon in the NH and the Australian Monsoon and the South American Monsoon in the SH. SASM, due to the geographical setting of South Asia, is the most active of all the regional monsoons and has been extensively studied over the past 150 years. As a result of the work of several researchers in India and the world over, the following prominent large-scale circulation features characterize the SASM:

- (i) The sub-continental scale NW / SE oriented monsoon trough (MT), which is anchored to the west by the seasonal low pressure area over Pakistan and passing through the Indo-Gangetic plain lies over the warm waters of the north Bay of Bengal. From here the MT bifurcates into two branches. One branch passes over NE India and thence merges with the trough over the Yangtze valley of central China and even towards Korea and Japan in July, feeding into the Meiyu, Changma, and Baiu rainfall of the respective countries. The second branch passes over South-East Asian countries and thence to the South China Sea and the Phillipine Sea, as the traditional extension of the MT in the form of the South China Sea monsoon. Thus, MT is both sub-regional over India and extends north-east and south-east over neighbouring east Asia and South East Asia. The low-level flow is eastward to the south of the MT, and being convergent in character and moist, it ascends in the vertical and produces copious precipitation, aided by the local land surface, including orographic processes, over the entire Indo-Pacific monsoon region.
- (ii) The Tibetan High or anti-cyclone in the upper troposphere (Flohn, 1960, Koteswaran, 1958a,b, Yanai and Song, 1992, Wu and Zhang, 1998).

- (iii) The divergent winds emanating from the Tibetan High give rise to the Tropical Easterly Jet Stream (TEJ) (Koteswaram, 1958b) which is accelerating downstream from the South China Sea to South Peninsular India and then decelerates toward West Africa. TEJ is responsible for maintaining the updraft of the large-scale SAM.
- (iv) Low Level Jet (LLJ) off the Somalia coast (Findlatter, 1969, 1977) and its extension over Peninsular India (Joseph and Raman, 1966) which is the main artery for supply of moisture for the monsoon in the lower troposphere.
- (v) Mascarene High (Krishnamurti and Bhalme, 1976) in the South Indian Ocean, which feeds into the SE trade and the cross-equatorial flow across 40–50° E.
- (vi) Subsidence inversions in temperature over the upwelled waters of the west and central Arabian Sea, which suppress convection over these waters. (Colon, 1964, Bhat, 2006, Rao and Sikka, 2005). Maintenance of the MT over India (Keshvamurti, 1968, Keshvamurti and Awade, 1970) heat and moisture budget of the MT (Anjaneylu, 1969, Bhide *et al.*, 1997) and dynamics of the tropospheric circulation during contrasting monsoon seasons (Kanamitsu and Krishnamurti, 1978, Awade *et al.*, 1984, Mohanty *et al.*, 1983, 2003, 2005, Mohanty and Ramesh, 1994, Datta *et al.*, 2011). Besides these regional large-scale components of the SAM, planetary scale control is exercised by the east-west divergent circulation in the upper troposphere (Krishnamurti, 1971) and the coupled ocean-atmosphere processes through ENSO-Monsoon connections (Sikka, 1980, Pant and Parthasarathy, 1981, Rasmusson and Carpenter, 1983). Rao *et al.* (1999) and others have examined the mean dynamical characteristics of monsoon as simulated by the global analysis forecast system.

Fluctuation of the above mentioned large-scale circulation features occurs on intra-seasonal (IS) and inter-annual (IA) scales, which are as a result of the complex multi-scalar interactions between the large scale, synoptic, and meso-scale weather systems.

### 25.3.2 Monsoon rainfall

Monsoon rainfall, since the first work by Blanford (1886), has been studied most extensively. There are three important long-term series of the Indian Summer Monsoon rainfall (ISMР): (i) IITM, Pune Series (Parthasarathy *et al.*, 1994) for the period 1871 to the present, based on a fixed number of stations; (ii) IMD Series for the period 1901 to the present, based on a variable number of stations; and

Table 25.1. Climatological aspects of the rainfall over different countries of South Asia for the SASM season (June to September)

Country	Approx area (km <sup>2</sup> )	Monsoon rainfall (cm)	Percentage of SAM season rainfall to annual rain	Coefficient of variability (percent of normal)
Bangladesh	148390	175	70	12
Bhutan	690	157	75	10
India	1287260	88	78	10
Maldives	300	71	60	10
Nepal	147180	137	75	10
Pakistan	796100	16	60	40
SriLanka	65610	45	40	14
South Asia area weighted	444530	78	74	14

(iii)  $1^\circ \times 1^\circ$  gridded rainfall series by Rajeevan *et al.*, (2006), for the period 1950–2010, which has recently been extended to beginning from 1901, and even on a  $0.25^\circ \times 0.25^\circ$  basis, and is based on a variable number of stations for grid-averaging. The IITM series excludes the hilly and island meteorological sub-divisions of India, whereas the IMD series includes these areas also. The good points of these series are that the coefficient of variability is about 10% for the whole of India and the years of drought ( $<10\%$  of the normal) and excess rainfall ( $>10\%$  of the normal) are the same for the three series. Table 25.1, after Sikka (2011), shows the climatological aspects of SASM rainfall for different countries of the region.

There is a seasonally sustained component of SAM rainfall and a fluctuating component on a year to year basis. On the extreme seasonal scale, the seasonal monsoon rainfall of India has fluctuated between 22% to about –30% of the long-term average in nearly 155 years of instrumental records. Average daily rainfall varies from month to month of the season, but for the season as whole, for India it is about 7.4 mm per day.

Figure 25.1 shows the average June to September rainfall for the Indian region, with an approximate boundary of the ‘core monsoon region’ whose seasonal rainfall is highly correlated with all India rainfall (Rajeevan *et al.* 2008a)

Figure 25.2 gives the average daily rainfall over central India for a good monsoon year (1975) and a deficient monsoon year (2002). It shows that for India as a whole, the rainfall begins to increase from 01 June, from 2.5 mm / day to about 10 mm / day, between about 10 July and 10 August and then it begins to fall rapidly from the third week of August to the end of September. On the inter-annual scale there could be substantial variations from the

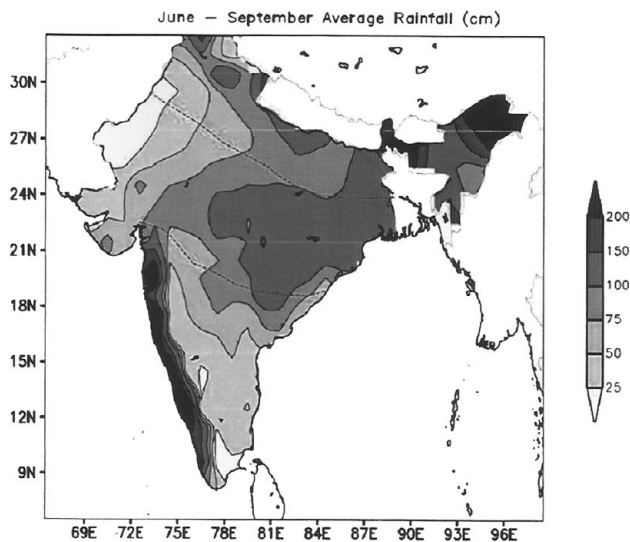


Fig. 25.1. Monsoon seasonal mean (June to September) rainfall for India. The yellow dashed lines show the position of the monsoon trough. Upper line is for ‘break’ monsoon and the lower line is for active monsoon conditions. A black and white version of this figure will appear in some formats. For the colour version, please refer to Plate 29.

normal over different parts of India, which are accompanied by synoptic and meso-scale disturbances, which are described in a subsequent section (Section 25.5).

IMD classifies daily rainfall over a station exceeding 64 mm / day as a heavy rainfall day, and exceeding 124 mm / day as a very heavy rainfall day. The number of heavy and very heavy rainfall days within the monsoon season varies a lot from sub-division to sub-division, depending on the situation of the sub-division with regard to orography and location, with regard to the position of the MT, distance from the sea, and the normal tracks of the monsoon transients in the season. Three heavy rain belts are (i) all along the west coast of India, (ii) the NE Indian states and the sub-Himalayan belt, and (iii) over central India along the tracks of monsoon LPSs. The high rainfall along the first two belts is mainly controlled by the orographic features. Satellite-based rainfall estimates by IR, microwave, and TRMM precipitation radar are available for varying periods. A comparison of these estimates with observed rain-gauge measurements broadly agree over all three heavy rainfall belts, and also for the dry zones on the lee side of the Western Ghats and over extreme western India. However, the satellite derived estimates are somewhat lower than the observed estimates (Durai *et al.*, 2010, Pokhrel and Sikka, 2012). Satellite based rainfall also shows that the most intense rainfall occurs on a monthly and seasonal basis over the north Bay of Bengal adjoining the Myanmar and Bangladesh coasts, and exceeds 20 mm / day.

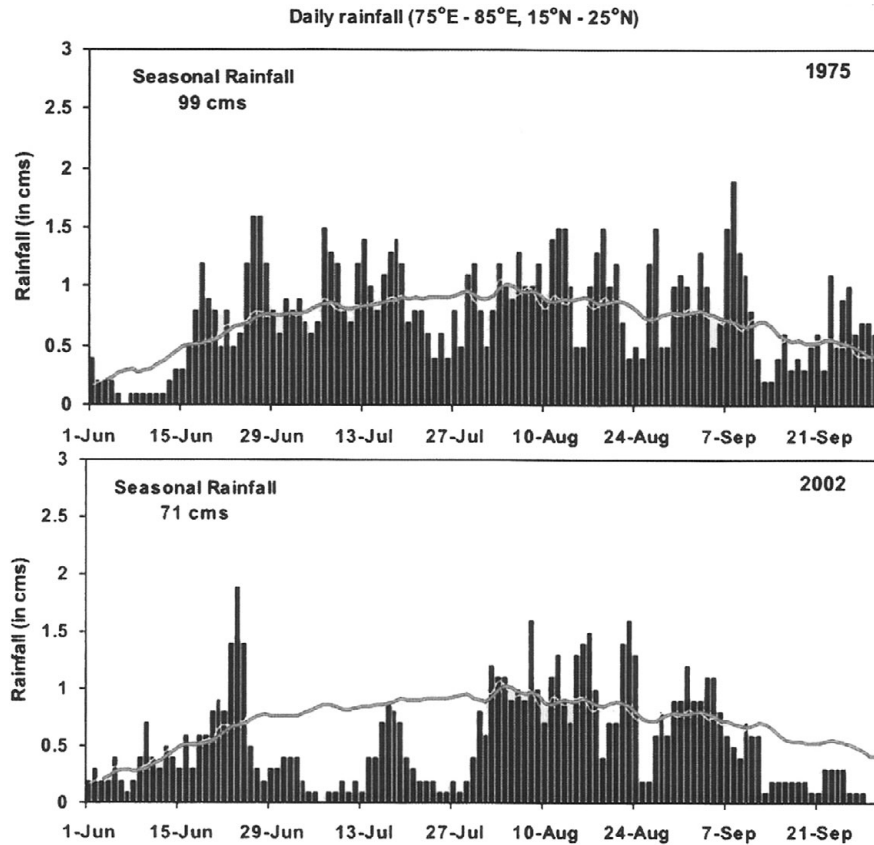


Fig. 25.2. Daily rainfall averaged over central India during two contrasting monsoon seasons 1975 (excess) (upper panel) and 2002 (drought)(lower panel). Red line indicates the climatological normal daily rainfall. A black and white version of this figure will appear in some formats. For the colour version, please refer to Plate 28.

Pokhrel and Sikka (2012) have also discussed various aspects of the TRMM-PR rainfall over the Indian region. According to their estimates, stratified and convective rainfall occurs in almost equal proportions of the total rainfall over central India, which is situated along the tracks of monsoon LPSs and falls within the ‘core region of monsoon’. These authors have also discussed the dipole nature of rainfall over the north Bay of Bengal and the eastern equatorial Indian Ocean, which has implications on the IS scale of monsoon fluctuations. They have also speculated about a sort of compensation taking place in rainfall on a seasonal scale between the Bay of Bengal and central India, as well as north Bay of Bengal and the eastern equatorial Indian Ocean on a IA basis. There is scope to further quantify this internal compensation of rainfall in different regions of the SASM system to understand the mechanism responsible for such internal compensation on monthly and seasonal scales. TRMM satellite data have been used extensively by Romatsechke *et al.* (2010) and Romatsechke and Houze (2011) for investigations on the precipitating systems during the monsoon season. SST fluctuations over the North Bay of Bengal (Sengupta and Ravichandran, 2001) play an important role in modulation of convection over the region, brought about through processes in the formation of a

barrier layer near the ocean surface due to freshwater discharge (Vinayachandran *et al.*, 2002).

### 25.3.3 Heavy rainfall events over India on the daily scale

Heavy rainfall occurs over some parts of India during the monsoon season almost daily. The incidence of such events and the number of stations depend on the stage of the monsoon in the season, synoptic forcing coupled with orographic forcing, and the meso-scale convective systems embedded within precipitating synoptic systems. As an example, we have collected the daily count of stations reporting 6.5 cm of rain over each of the 36 sub-divisions of India, as given in the Weekly Weather Reports of IMD, based (covering nearly 2200 rain gauges and automatic rain-gauge stations) for the monsoon season of 2012. Figure 25.3 presents this data.

The following are noted:

- Numbers of stations are less and confined to Kerala and Karnataka coasts at the time of onset of the monsoon. As the monsoon progresses, This is followed by an increase in number over north-eastern

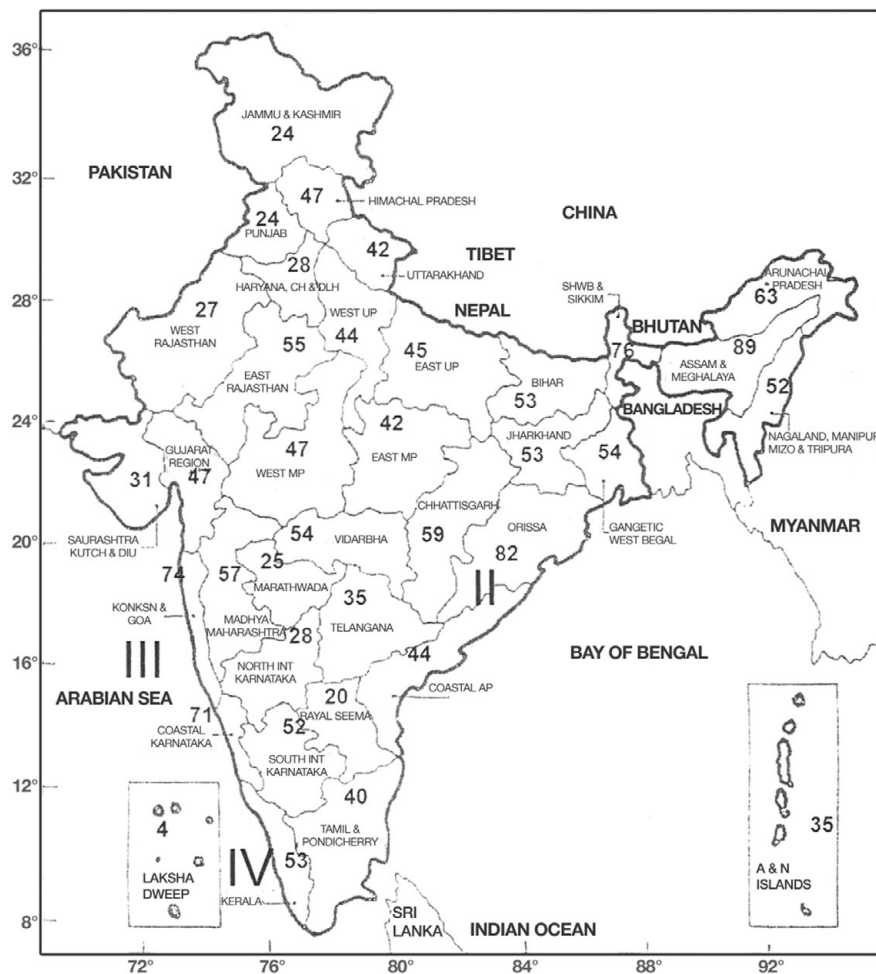


Fig. 25.3. The number of days in June to September 2012 for each meteorological sub-division of India, when heavy rainfall ( $> 6.5 \text{ cm/day}$ ) was recorded for at least one station. Four clusters are identified. Cluster I: Assam and Meghalaya, Arunachal Pradesh, Nagaland, Manipur, Mizoram and Tripura, Sub Himalayan West Bengal; Cluster II: Orissa, Jharkhand, Bihar, Chattisgarh, Vidarbha and West Bengal; Cluster III: Konkan and Goa; Cluster IV: Coastal Karnataka, South Interior Karnataka and Kerala.

India and the adjoining eastern sub-Himalayan range, mainly confined to the sub-divisions of Arunachal Pradesh, Assam, Meghalaya, and sub-Himalayan West Bengal.

- (ii) A further increase is noted by mid June over the Orissa State of India bordering north Bay of Bengal and the Konkan and Goa region along the west coast. Finally, from the beginning of July to mid September, the central parts of the country also begin to receive heavy rainfall with the passage of LPSs across the area.
- (iii) The number of stations in India receiving heavy rainfall on average for four months of the monsoon – 2012 and their ranges are as follows:

June – 43 stations varying between 6 to 160 stations on a daily basis during the month,  
 July – 84 stations varying between 24 to 146 stations on a daily basis during the month,  
 August – 400 stations varying between 26 to 200 stations on a daily basis during the month,

September – 66 stations varying between 6 to 215 stations on a daily basis during the month.  
 Season (June–September) 75 stations on the daily average basis.

These figures are based on real-time operational records. The figures change slightly when late data are considered. There are days when the monsoon is vigorous to active or weak simultaneously over several sub-divisions. Thus the number of stations reporting heavy rainfall varies significantly on a day to day basis depending upon monsoon activity. However, there is not a day in the season when a few stations over India would not receive heavy rainfall.

The monsoon-2012 underperformed with seasonal departure from normal being  $-8\%$ . A noteworthy feature of monsoon-2012 was that the frequency of such stations during the season with rainfall amounting to 6.5 cm or more on a daily basis was confined to three or four clusters (with a frequency of 50 days or more), comprising (I) NE India, (II) Orissa and adjoining states, (III) Konkan and Goa coast, and (IV) coastal Karnataka, South Interior

Karnataka and Kerala, as shown in Fig. 25.3. The orographically controlled clusters over north-east India and across the west coast have dimensions of about 500–700 km across. Similarly the cluster around Orissa and central India also covers around 500–700 km in the horizontal. This shows that the scale of a heavily raining system is at best about 1000–1500 km and the heavy rainfall lasts generally for about two days at a time (very occasionally three days at a time), showing the synoptic scale control over heavy rainfall. Within each of these clusters there is a meso-scale organization of about 50–100 km in horizontal extent where the rainfall even exceeds 25 cm / day. There has been considerable debate in recent years over trends for increase in heavy rainfall events, or otherwise (Goswami *et al.*, 2006, Guhathakurta and Rajeevan, 2008, Guhathakurta *et al.*, 2011, and others). However, there is a consensus that heavy to very heavy rainfall events have increased along the central and northern parts of the west coast of India (say Mumbai), even though the low-level monsoon flow has shown a slight weakening.

The rainfall for a 50 km x 50 km area exceeds 25 cm / day. Maximum daily rainfall for the severe-most rainstorms over different parts of India even exceed 50 cm / day locally

(the record maximum has even touched 90 cm / day). Such heavy rainfall is associated with active to vigorous monsoon conditions, which are accompanied by a strong westerly monsoon along the west coast over the Assam hills and close to the position of transient monsoon disturbances (lows and depressions) along central India and the Indo-Gangetic plain. The presence of the off-shore trough along the west coast and the incidence of a sub-tropical cyclone (Miller and Keshavamurty, 1968) off the north Konkan / Gujarat coast also leads to heavy to very heavy rainfall. Dhar and Nandargi (1999) have shown three preferred zones of tracks for the transients (LPSs), as given in Fig. 25.4, which resulted in daily rainfall of 7.20 cm or more for one day's duration.

Heavy to very heavy rainfall occurs in the southwest sector of LPSs and at a distance of about 200 to 400 km south-west of the center of the LPS. Thus the correct forecast of the center of the LPS is very crucial for predicting the cluster of heavy rainfall. If the predicted position is incorrect by 200 km (which is often the case) the penalty for an incorrect forecast becomes very high as the heavy rain does not occur where predicted, but is situated 200–400 km away. Complexity in the meso-scale behaviour of

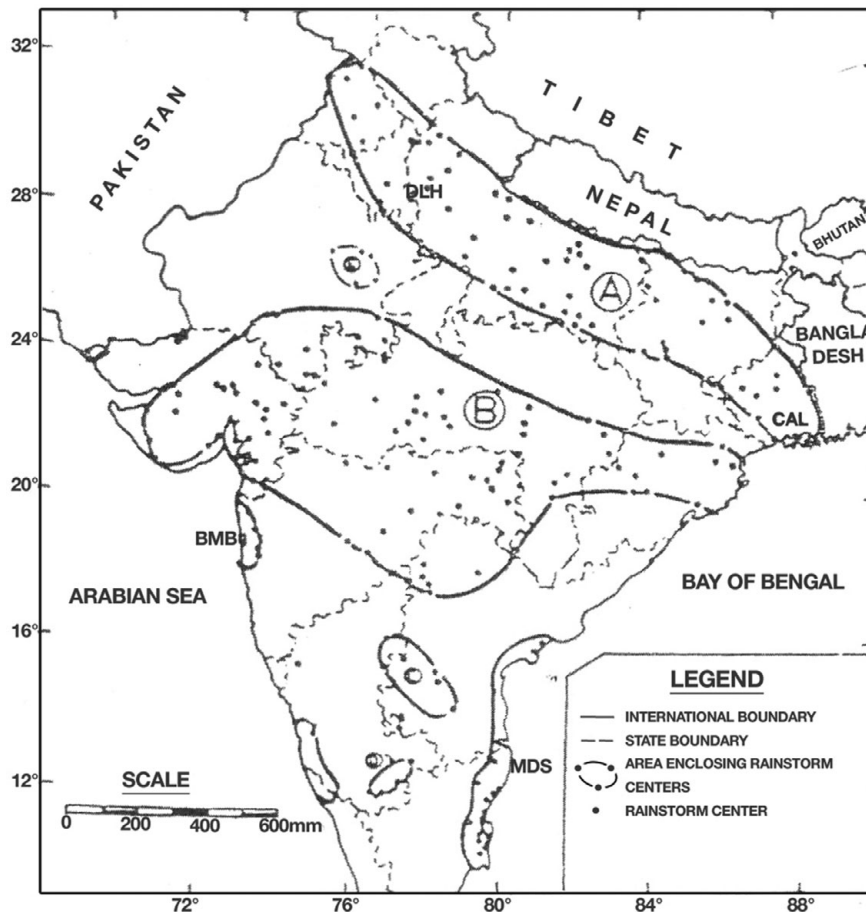


Fig. 25.4. Distribution of severe rainstorm centres ( $> 20 \text{ cm/day}$ ) in different zones for 1 day's duration (1880–1990) (Dhar and Nandargi, 1999).

extreme rainfall events is recognized and their forecasting can improve only if the forecasting models are able to resolve multi-scalar phenomena well and the parameterized physics is good at capturing nonlinearity in the interacting components of the multi-scalar phenomena. Such extreme rainfall events in which the 24 hour rain rate exceeds 25 cm/day are rare and occur rather suddenly, often without clear warning and on scales much smaller compared to the synoptic scale in which they are embedded. The predictability limit for such a meso-scale cluster is only a few hours and hence nowcasting with radar coverage can only provide skilful prediction to a certain degree. Heavy rainfall events lasting two days or more often lead to floods in the river basins of India. Climatologically it is observed that for almost all river basins in India, 10% of wet periods occur in July/August with an average duration of one to three days and rainfall intensity varying from 44 mm to 89 mm / day, which is 50 to 100% higher than the average intensity (Deshpande and Singh, 2010). Such wet periods occur for more than 40–60 days in the monsoon season over the Ganges, Mahanadi, Narbada, and Kaveri river basins and even for 80 days in the Brahmaputra basin.

Goswami *et al.* (2006), using gridpoint rainfall data from 1950 onward showed an increasing trend of heavy rainfall events over central India, which they ascribed to a warming environment resulting from anthropogenic causes. However, later studies by Rajeevan *et al.* (2008a) using 104 years of gridded data and by Guhathakurta *et al.* (2011) using station rain gauge data do not support the analysis of Goswami *et al.* (2006). The difference could be due to multi-decadal variability in extreme rainfall events. Further studies in this regard are needed to clarify the position regarding trends in extreme rainfall events in the monsoon season over India.

#### **25.4 Transition from spring to monsoon season over South Asia and onset and advance of the SAM**

**March of convective organizations from pre-monsoon season to onset and advance of monsoon over India:** The onset of the monsoon over mainland India is the most important singularity in the monsoon calendar and hence has been a greatly investigated event. During the pre-monsoon season (April–May), surface temperatures over most of India during the day are high and heat wave conditions occur when maximum temperatures exceed 42 °C at many places. The sub-tropical middle and upper level westerly flows over north India begin to weaken in April and convective thunderstorms, developing over north-west India / eastern India and Peninsular India, are the dominant weather phenomena. SSTs over the Arabian Sea and Bay

of Bengal, particularly in the near-equatorial region begin to increase, with the spring transition occurring in mid March. The centre of organized convection in the ITCZ at that time lies close to the equator and it shifts to about 5° N by mid April. Ananthakrishnan (1977) discussed the build-up of the seasonal reversal of atmospheric circulation features from the pre-monsoon season to the monsoon season. On the eastern part of the Indo-Pacific tropical belt, the ITCZ shifts from the near equatorial Indonesian region to the tropical north Pacific along 10–15° N by mid April. Convection gets organized over Thailand and the adjoining South China Sea by the beginning of May and shifts to South Bay of Bengal and the Andaman Sea by the middle of May. Thus, the onset of the rainy season begins first over South-East Asia and South Bay of Bengal by mid May. The Arabian Sea is still under the influence of an anti-cyclonic circulation and the weak cross-equatorial flow is restricted off the Somali coast only and would not penetrate to over the central Arabian Sea. Rapid changes begin to take place from mid May over the Indian region, accompanied by the disappearance of the near-surface Arabian Sea anticyclone, peaking of SST warming in the south-east Arabian Sea (mini warm pool) and South Bay of Bengal, strengthening of the cross-equatorial flow towards the central Arabian Sea, northward shift of the anticyclone over western India at 700 hPa, weakening and even disappearance of the sub-tropical jet stream (STJ) south of the Himalayas, and adjustment of the mid-tropospheric westerly regime under the influence of the weakening meridional temperature gradients. These changes set the stage for the onset of the monsoon over mainland India across the Kerala coast, known as the Monsoon Onset over Kerala (MOK) (Ananthakrishnan *et al.* 1967, Ananthakrishnan and Soman, 1988, Joseph *et al.*, 1994, Joseph *et al.*, 2006, Simon *et al.*, 2006 have investigated the climatology of MOK and its IA variability). There are years when the onset is a regular one step process, accompanied in several years by the formation of a cyclonic vortex known as the Monsoon Onset Vortex, after Krishnamurti *et al.* (1981) in the Arabian Sea or in the Bay of Bengal. In other years the monsoon is heralded by the formation of an active east–west shear line in the lower-mid troposphere from 70° E to 90° E, in which a cyclonic vortex may be embedded. The vortex slowly moves northward, thus advancing the monsoon along the west and east coasts of India. Krishnamurti and Ramanathan (1982) investigated the monsoon onset using a dynamical model and found differential heat sources over North-East India and the Indo-Pacific region crucial to the MOK. The onset is accompanied by a sudden drop in SST over the central Arabian Sea, depending upon the mixed layer (Rao, 1986a,b, 1987). Rao and Shrivkumar (1999) have linked the formation of the warm pool over the south-east Arabian Sea with the monsoon onset and

formation of onset vortex. Mishra *et al.* (1985) investigated the barotropic dynamic instability process associated with MOK. Pearce and Mohanty (1984) showed the major precursor for monsoon onset is the build-up of moisture up to mid troposphere about two weeks in advance of MOK. Besides the synoptic studies atmospheric generation circulation models have been also used to simulate MOK and its variability (Ratnam *et al.*, 2007, Goswami and Gauda, 2010, Nagaraju *et al.*, 2012). In some years during the MOK, the rain spell over Kerala has been short-lived and occurs too early (by mid May). This leads to a rather long period of cessation of rainfall soon after MOK. This is known as temporary or false onset of monsoon and is followed by regular onset after about two to three weeks of a much reduced rainfall epoch (Fasullo and Webster, 2003). Because of the importance of MOK and the variability of precursors, which herald it, the IMD have for operational purposes laid down objective criteria for the purpose, based on duration of sustained rainfall over rain gauges of Kerala, outgoing long-wave radiation (OLR) field, strength of the low-level westerlies etc. Goswami and Xavier (2005) have emphasized the change in mid / upper tropospheric meridional temperature gradient as an important parameter for defining MOK. Pasch (1983) introduced global onset of monsoon and Zhang and Lu (2004) have also advocated for the globally unified monsoon onset index. There are several other objective indices proposed by different authors to define MOK. The dates of MOK defined in different ways, agree among them to within about three to four days, and the MOK event is important as a major singularity. According to the IMD the normal date of MOK is 1 June with a standard deviation of seven days.

After the MOK the monsoon begins to advance over India and on average it takes nearly 45 days to cover the entire country up to the western desert (Thar Desert) of India with the inter-annual range of 30 to 70 days (Ananthakrishnan and Soman, 1980, Soman and Krishna Kumar, 1993, Li and Yanai, 1996). The advance process is not regular, as shown by the IMD normal dates, but in many years it is punctuated by one to three hiatuses. Each hiatus may be of seven to ten days' duration. Biswas *et al.* (1998) have found that the hiatuses or temporary cessations in advance of the monsoon occurred due to increased activity of the sub-tropical westerlies trough along 65 to 80° E. This is accompanied by temporary cessation of the formation of synoptic scale disturbances over the Bay of Bengal. It is the passage of these disturbances which helps inland penetration of the rainfall over India. Recently Krishnamurti *et al.* (2012) have investigated the advance of monsoon isochrones over India using an WRF model. They have tried to show that the stratified rainfall in advance of the monsoon helps in enriching soil moisture,

which in turn promotes advance of monsoon isochrones. The hiatuses in monsoon advance emphasize the role of monsoon transients in retarding the advance process. As shown by Dhar *et al.* (1980), the performance of seasonal monsoon rains over India does not depend on the MOK. However, the period taken from the date of MOK to the date of establishment of monsoon over the whole of India is in some way related to the overall seasonal performance of monsoon rains in a season. It is also worthwhile examining the IA variability of this period based on multi-decadal runs of atmospheric or coupled general circulation models. Goswami *et al.* (2010) have reported on secular trends in the onset phase of monsoon and ascribed it to changes in the ENSO phenomena and the resultant vertical spears in the troposphere.

## 25.5 Monsoon variability on synoptic, intra-seasonal, inter-annual, and decadal scales

From surface weather data alone, Blanford (1886) had recognized that monsoon rainfall performance over India fluctuated day to day, week to week, and on the basis of extended periods of wet spells and dry spells, and from one monsoon season to another. He could explain the day to day fluctuations based on the existence of precipitating weather systems (synoptic variability), break and active cycle of the rains within a season for extended-range scale variability, and the deficient (drought) or excess performance of the rains on an inter-annual basis. He found that the low frequency intra-seasonal and the inter-annual fluctuations of the rains are very complex phenomena. For want of explaining their underlying causes, Blanford termed these fluctuations as the 'vicissitudes of monsoon' which uses a beautiful word meaning 'charming fickleness'. Translated into local dialect in India it can be referred to as the charming 'Nakhras' of the monsoon. Later on in the Indian monsoon literature, the word vicissitudes was changed to 'vagaries' of the monsoon. In the modern literature, with our improved understanding, such rainfall fluctuations are broadly referred to as monsoon variability.

### 25.5.1 Synoptic and meso-scale precipitating system

Rao (1976), Ding and Sikka (2006), Sikka (2011), and several others have discussed the synoptic and meso-scale precipitating systems of the SASM. These systems include the following:

- (i) Monsoon Low Pressure Systems (LPSs): These are rather frequently forming weaker low pressure areas (L) and depressions (D), occasionally developing into

- intense vortices such as tropical cyclones (T) and severe tropical cyclones (ST). Climatology of LPSs and their tracks are available for the period 1888–2003 (Mooley and Shukla, 1989, Sikka, 2006, Jadhav and Munot, 2004, Krishnamurthy, 2011). These systems are indicative of the dominant daily rainfall patterns and contribute substantially to the seasonal monsoon rainfall over India on their own scale (1000–2000 km). As mentioned earlier, high impact rainfall is confined to about 50–100 km of the south-west of their daily position and they distribute rainfall along their WNW/NW tracks. They form more frequently over the north and central Bay of Bengal and occasionally over the land part of the MT, as well as over the north Arabian Sea. Data on LPSs have also shown that while their frequency has not shown a long-term decreasing trend, there is a marked decreasing trend in the numbers of D, T, and ST, while the number of L has increased (Singh, 2003, Dash *et al.*, 2004, Sikka, 2006, and others). There have also been some studies explaining this decrease in D, T, and ST based on the overall weakening of the strength of the 850 hpa zonal wind flow over Indian seas from the NCAR-NCEP Reanalysis. L and D contribute nearly 97% of the LPSs and T and ST only 3% and hence L and D are the major precipitating systems. Their tracks terminate after a travel of 500 to 1500 km across the Indo-Pakistan belt. Overlapping systems form under active monsoon conditions and travel more WNWward. The frequency of their clustering formation is much reduced under break monsoon conditions, overlapping formation of LPSs is reduced, and their tracks are predominantly short during weak monsoon (Sikka *et al.*, 1987, Goswami *et al.*, 2003b). Various aspects of monsoon depressions have been studied extensively (Daggupathy and Sikka, 1974, Godbole, 1977, Sikka, 1977, Rajamani and Sikdar, 1989, Dhar and Nandargi, 1999, Rajeevan *et al.*, 2002). Romatsechke *et al.* (2010) and Romatsechke and Houze (2011) have extensively used TRMM satellite data to investigate the characteristics of synoptic scale precipitating systems over the Indo-Pakistan region. Zuluago *et al.* (2010) have studied the distribution of latent heating based on TRMM data.
- (ii) Mid-Tropospheric Cyclone: MTC (Miller and Keshavamurti, 1968, Grossman and Durran, 1981) is another synoptic entity which forms over the north Arabian Sea, exists for three to five days in a quasi-stationary location, and results in copious rainfall over the Konkan and Gujarat coastal and inland areas. It forms predominantly from mid June to mid August in the advancing and peak phases of the monsoon with a

frequency of two or three systems within a season. There are monsoon seasons when a WNW / NW moving LPS and a MTC coexist. When such a synoptic situation develops, the SAM is in its grand organization with heavy rainfall occurring at several places between 18–24° N across India. Carr (1977) and Brode and Mak (1978) have also studied the role of MTC in monsoon fluctuations.

- (iii) Monsoon Trough Activity, without any circulation embedded in it. These occasions result in widespread rainfall accompanied by very heavy rainfall about 50–100 km south of the MT. The scale of this well organized activity is about 2000–4000 km. Once or twice in an active monsoon situation there is a grand organization of MT from 70–75° E extending up to 120° E. An example of such an organization is in the satellite cloud imagery on 30 July 2012 (Fig. 25.5). Mega-scale multiple cloud clusters exist in such a situation. Each cluster is about 1000 km in length with embedded very low cloud top temperatures ( $-50^{\circ}$  C or lower) where high impact rainfall occurs on the meso-scale. Feeble cyclonic circulations in the lower and middle troposphere (850–600 hpa) within the MT region on some days form with a horizontal extent of 500–1000 km. Although the relative vorticity is small ( $2\text{--}4 \times 10^{-5} \text{ sec}^{-1}$ ), yet such vortices are accompanied by a large amount of moisture convergence, resulting in heavy to very heavy rainfall in their vicinity.
- (iv) Monsoon Off Shore Trough with embedded meso-scale cyclonic vortices off the west coast of India: This system was first analysed by George (1956) and later investigated by Mukherjee *et al.* (1984) and Francis and Gadgil (2006). There are occasions when two feeble cyclonic whirls may coexist each associated with its own cluster of heavy rainfall structures. A special campaign called ARMEX was carried out in India during the 2002 monsoon season to understand this precipitating system, which has now become a characteristic system in the monsoon season. Mohanty *et al.* (2003) have examined the structure of these vortices with the data collected during ARMEX.
- (v) Western disturbances (WDs): These are southward penetrating and eastward moving troughs in mid-latitude westerlies which produce rainfall over north Pakistan, NW India, and even Nepal (Pisharoty and Desai, 1956, and others since then). Their nature is complex and occasionally they lead to the recurvature of a monsoon LPS and an increase in rain over N / NE of their recurring track. Their approach to 70–75° E and 30–35° N leads to the setting up of the ‘break monsoon’ condition (Ramaswamy, 1962), as well as

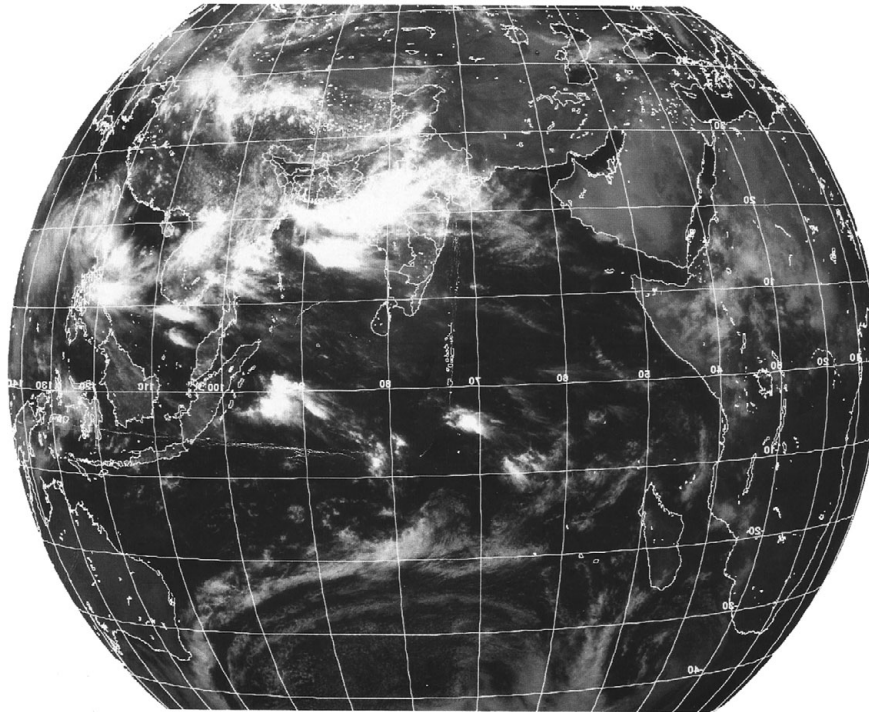


Fig. 25.5. Indian National Satellite System (INSAT) Kalpana-1 image (visible channel) showing grand cloud organization over the Indian region at 0600Z on 30 July 2012.

results in vigorous monsoon rains under recurvature of LPSs, depending upon the state of the monsoon over south Asia on the intra-seasonal scale. If the monsoon is in its weakening (intensifying) stage, approach of a WD may lead to ‘break’ (active) monsoon.

### 25.5.2 Active-break cycle of monsoon, low-frequency intra-seasonal variability, and northward propagating convective episodes and their links with the MJO

In the active phase of the monsoon, extensive and copious rainfall occurs over most of India, particularly over central India. In this situation MT is situated 2–3° latitude south of its mean position. In contrast, the ‘break’ monsoon is characterized by the MT lying close to the foothills or north of the Himalayas and the rains sharply decreasing over central India. Also rains at first increase near the foothills of the Himalayas and if the break monsoon becomes longer than four days, rainfall activity even disappears from the Himalayan belt too. There are shorter (two to three days) and longer breaks (six to twelve days). Several studies have been carried out on the break monsoon since the seminal work of Ramamoorthy (1969), who first documented details of the ‘break’ phenomenon. The phenomenon has engaged the attention of several researchers. (Raghavan, 1973, Pant, 1983), Rao, 1988), Rodwell,

1997, Rao *et al.*, 2004, Prasad and Hayashi, 2007). In recent years too, great interest has been shown by researchers (Krishnan and Sundaram, 2005, Krishnan *et al.*, 2006, De and Mukhopadhyay, 2002, Gadgil and Joseph, 2003, Annamalai and Slingo, 2001, Annamalai and Sperber, 2005, Prasad and Hayashi, 2007, Rajeevan *et al.*, 2008a, Joseph and Sabin, 2008). Some of these studies have examined the dynamics of the break (Rodwell, 1997, Ferranti *et al.*, 1997, Annamalai and Slingo, 2001, Wang *et al.*, 2005, and others). Rameshkumar *et al.* (2009) have even reported on the increasing trend in break monsoon episodes and attributed it to SST warming of the equatorial Indian Ocean. Prolonged break spells are rather rare, as the majority of breaks are of three to five days’ duration. During prolonged breaks not only does rainfall cease over central India and the Gangetic plain, but surface temperatures also rise and even dusty north-west winds blow persistently for several days adding to the discomfort and desiccation of the moisture over the cropland. Subsidence inversions in the lower troposphere prevail during break monsoon (Rao and Sikka, 2005, Bhat, 2006).

Figure 25.6 shows the satellite cloud imagery on 16 July 2012, during the early phase of the break / weak monsoon. Notice the sub-Himalayan cloud band is linked to cloud band (Meiyu) over central China, and the link of the monsoon cloud zone over India with the South-East Asian cloud system has broken down. This type of large-scale cloud organization raises question about the connection of organized convection over China with the

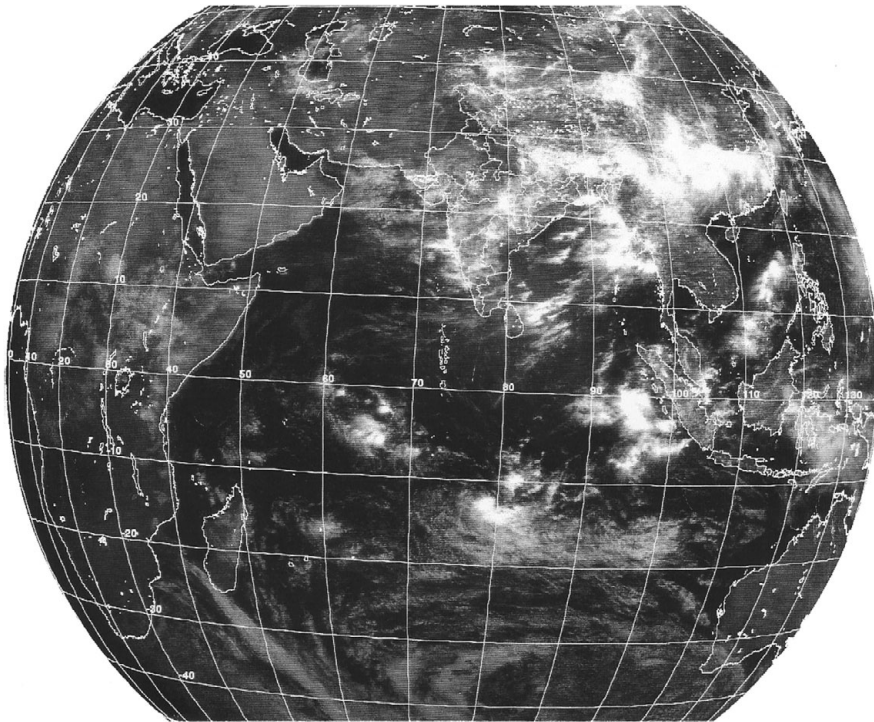


Fig. 25.6. INSAT Kalpana-1 image (visible channel) of cloud organization over the Indian region at 0600Z on 16 July 2012.

weakening of the monsoon over India, and could be a subject of further studies.

The active-break cycle of the monsoon has been linked to monsoon intra-seasonal oscillation (MISO) with the migration of the monsoon cloud band (MCZ), first studied by Yasunari (1980, 1981), Sikka and Gadgil (1980), and since then by many other authors. Recently, Ajay Mohan and Goswami (2007) examined the also poleward moving IS mode of the monsoon in relation to the mean monsoon simulation in models. Ajay Mohan *et al.* (2011) examined the poleward propagating IS mode in a coupled model, but improvement over the atmospheric stand-alone model was not very remarkable. Nanjundiah *et al.* (1992), Nanjundiah and Krishnamurti (2007), and others have also examined theoretical aspects of the IS mode of the monsoon. Chattopadhyay *et al.* (2009) have proposed the role of stratified rain in northward propagation. Northward migration of the MCZ occurs at a rate of about  $1^{\circ}$  latitude per day from the near-equatorial north Indian Ocean to about  $25^{\circ}$  N in the monsoon core zone, and its disappearance over the Himalayan region. It is a low-frequency sub-seasonal oscillation of the monsoon on a 30–50-day scale. Suhas and Goswami (2008) have speculated on the regime shift in climatological IS oscillation for the 1951–75 to 1979–2004 periods, due to changes in vertical shear and meridional gradients in relative humidity. The period of the oscillation may change between 25 and 60 days in different years of the monsoon season, which has significant influence on the performance

of the seasonal rains (Singh *et al.*, 1994, Lawrence and Webster, 2001, Suhas *et al.*, 2010, 2012a,b). If the period is 25–35 days there would be three cycles within a season and if it is 50–60 days only two cycles would result. The dynamics of change in the period is still not well understood and the atmospheric and coupled general circulation models differ in simulating the period, rate of migration, and amplitudes of this oscillation. This low frequency IS oscillation has been recognized as a convectively coupled oscillation with strong coherence in fluctuations of circulation and rainfall. Chattopadhyay *et al.* (2008) have proposed objective identification of the ISO of monsoon and its implications for predictions. Suhas *et al.* (2012a) have suggested an index, based on extended EOF (EEOF) analysis of rainfall data, to monitor the progress of MISO on a bi-weekly scale. Chattopadhyay *et al.* (2013) have used this technique for real-time monitoring, based on merged rain gauge and satellite rainfall data for monitoring. This index is similar to the index of the MJO, after Wheeler and Hendon (2004). MJO is a low-frequency intra-seasonal global mode of the Earth's near-equatorial climate which organizes convection on the low-frequency (30–60 day) scale. It is initiated over the Indian Ocean region and travels eastward in the equatorial region. When its upward branch is over the south-east Arabian Sea and the Bay of Bengal, the MJO may excite a low-frequency northward propagating convective episode resulting in revival of the monsoon with overlapping formation (clustering) of LPSs on a

low-frequency intra-seasonal scale. Hence it is eagerly awaited during a break or weak monsoon condition over India. Joseph *et al.* (2008) have associated the dry phase of the MJO over the Indian Ocean with lows / break monsoon conditions. Pai *et al.* (2009) have examined the links of MJO with monsoon droughts over India. A method after Wheeler and Hendon (2004) is currently used operationally for global tracking of the MJO. Zhang (2005) has provided an exhaustive review of investigation in the global scale MJO and its links with weather over different regions.

There are occasions when the northward propagating mode of the monsoon is generated without the MJO episode passing over the equatorial Indian Ocean. The phenomenon has attracted the attention of many researchers over the last 30 years and through observations and modelling. In several of these studies, the role of coupling between the ocean and the atmosphere has been emphasized, as moist dynamics lies at the core of the oscillation. Some of the important recent references on such studies are papers by Srinivasan *et al.* (1993), Annamalai and Slingo (2001), Waliser *et al.* (2003a,b), Veechi and Harrison (2002), Krishnan *et al.* (2006), Goswami *et al.* (2006), Pai *et al.* (2009), Annamalai (2010), and Prasanna and Annamalai (2012). Krishnamurti *et al.* (2003) have proposed a mechanism of the MJO based on interactions in the frequency domain. Currently Krishnamurti *et al.* (2013) are revisiting this problem based on scale interactions between synoptic and low-frequency modes of MJO. Several prediction models are used to predict the state of the atmosphere out to a couple of weeks. These models, although imperfect, include sufficient physics of the MJO but are constrained by the inherent limit of predictability of some aspects of the atmosphere, and other factors. Thus, model predictions phases of MJO, and its structure are not perfect. Hence MJO phases are tracked by satellite observations on the organized convection in the equatorial region, which are empirically extrapolated.

### 25.5.3 Inter-annual monsoon variability

Even though the coefficient of variability of All India Summer Monsoon Rainfall (AISM) is only 10%, which is smaller than IA variability of all other regional monsoon systems, its societal impacts of monsoon IA variability on the Indian economy is immense. As such, the study of IA fluctuations in Indian Summer Monsoon rainfall has attracted the attention of many generations of monsoon researchers. Historically, interest in investigating monsoon rainfall began with the statement of Varahamihra, a sixth century AD scholar in India, who stated

If food is the elixir of life  
And food comes from rains  
Let us investigate the rains

However, nearly 12 centuries later, Blanford began to seriously investigate the IA variability of monsoon. The study was followed in detail by Sir Gilbert Walker, who even attempted to foreshadow it with global precursors. Although tools and data sources have been enhanced since the 1970s, the subject of IA remains as one of the greatest challenges of modern monsoon meteorology. Extensive work has been done over the past four decades on the IAV of the monsoon and even its evolution has been examined based on the ECMWF and NCEP re-analysis data sets (Annamalai *et al.*, 1999). Recently, Suhas *et al.* (2012b) have advocated that monsoon IAV arises from interactions between seasonal mean and MISO. The subject will continue to receive attention in the future. IA variability of the monsoon controls the incidence of deficient (<10% of the normal) and excess (>10% of the normal) monsoon rainfall for the season, which depends on the sub-seasonal variability of the monsoon (Shukla, 1987, Krishnamurthy and Shukla, 2000, 2007, 2008). Modelling has also been used to diagnose and even predict IA variability by atmospheric and coupled global models. Internal feedbacks from mid-latitude interactions may also help in causing monsoon droughts (Krishnan *et al.*, 2009). Complete success in predicting IA variability is yet to be achieved, even though the basic paradigm was defined by Charney and Shukla (1981) three decades ago. The paradigm is that the slow varying boundary conditions of tropical land and ocean largely control the statistical evolution of the seasonal climate over the tropics. Sikka (1999) and Sikka (2001) have examined the incidence of the Indian monsoon droughts and excess monsoon seasons over India and the meteorological sub-divisions of India.

### 25.5.4 Decadal monsoon variability and trends in monsoon rainfall

The incidence of all India monsoon droughts and excess years on a decadal basis are given Table 25.2. Although multi-decadal variations in the incidence of drought and excess monsoon years have been recognized, the cause of

Table 25.2. Multi-decadal (three decades) monsoon drought and excess years.

Decade	No. of all India monsoon drought years	No. of all India monsoon excess years
1871–1900	4	6
1901–1920	6	3
1921–1950	2	3
1951–1980	7	5
1981–2010	7	3

this is not well understood. Perhaps it lies in the interactions between ocean and atmosphere, such as ENSO, IOD, and Pacific decadal variability.

The year of lowest rainfall was 1877 (recently 2009) and highest rainfall was 1961 (recently 1988). Also, rainfall has shown a decreasing trend since 1951 for all India, west-central India, and for the north-east India sub regions. Monsoon rainfall for Peninsular India has been the most stable. Table 25.3 shows trends in monsoon rainfall over different regions.

Figure 25.7 shows the trend for all India rainfall. Negative trends in land monsoon rainfall has been noted globally by

Zhang and Zhou (2011), who have also noted a rising trend between 1901 and 1955, as is found in the Indian rainfall. The negative trend in Indian rainfall in recent decades, in agreement with the trend in global monsoon rainfall, has raised concerns. Frequent occurrence of droughts in the last two to three decades (period of mega-droughts) has slowed down the economic growth in the drought years over India (Gadgil *et al.*, 2004). Studies have indicated several factors leading to a monsoon drought over India, such as Himalayan / Eurasian snow-cover (Blanford, 1884, Hahn and Shukla, 1976), El Nino–Southern Oscillation phenomena (Sikka, 1980, Ramusson and Carpenter, 1983, Pant and

Table 25.3(a). All India monsoon drought ( $AISM\leq 10\%$  of normal) with month-wise and seasonal rainfall departures (%) from normal – Period 1901–2012.

S.No	Year	Jun	Jul	Aug	Sep	Season	Remarks
1	1901	-30	-17	+11	-28	-13	Non-ElNino
2	1904	+3	-8	-17	-24	-12	ElNino
3	1905	-44	-12	-21	+3	-17	ElNino
4	1911	+22	-46	-16	-17	-15	ElNino
5	1913	+38	-6	-26	-37	-10	ENSO-ElNino
6	1918	+13	-47	-11	-42	-25	ENSO-ElNino
7	1920	-6	+1	-33	-33	-17	Non-ElNino
8	1941	-3	-20	-11	-16	-13	ElNino
9	1951	-14	-19	-12	-33	-19	ElNino
10	1965	-33	-5	-23	-21	-18	ElNino
11	1966	+4	-16	-19	-12	-13	ElNino
12	1968	-13	+5	-17	-25	-10	Non-ElNino
13	1972	-27	-31	-14	-24	-24	ElNino
14	1974	-26	-4	-5	-22	-12	Non-ElNino
15	1979	-15	-16	-19	-28	-19	Non-ElNino
16	1982	-17	-23	+9	-32	-15	ElNino
17	1986	+11	-14	-13	-31	-13	ElNino
18	1987	-22	-29	-4	+25	-19	ElNino
19	2002	+9	-54	-2	-13	-19	ElNino
20	2004	-1	-20	-4	-30	-14	ElNino
21	2009	-47	-4	-27	-20	-22	ElNino

Table 25.3(b). El Nino but no drought of AISMR.

S.No	Year	Jun	Jul	Aug	Sep	Season
1	1902	-34	-14	+2	+20	-9
2	1915	-1	-21	-9	+2	-9
3	1925	+25	+4	-11	-31	-3
4	1930	+7	+3	-23	-2	-5
5	1939	-8	-9	-7	-12	-9
6	1957	-11	+1	+13	-22	-2
7	1963	-12	-15	+22	-6	-2
8	1992	-22	-19	+15	-3	-7
9	1997	+6	-2	+9	-6	+2
10	2012	-34	-14	+2	+16	-9

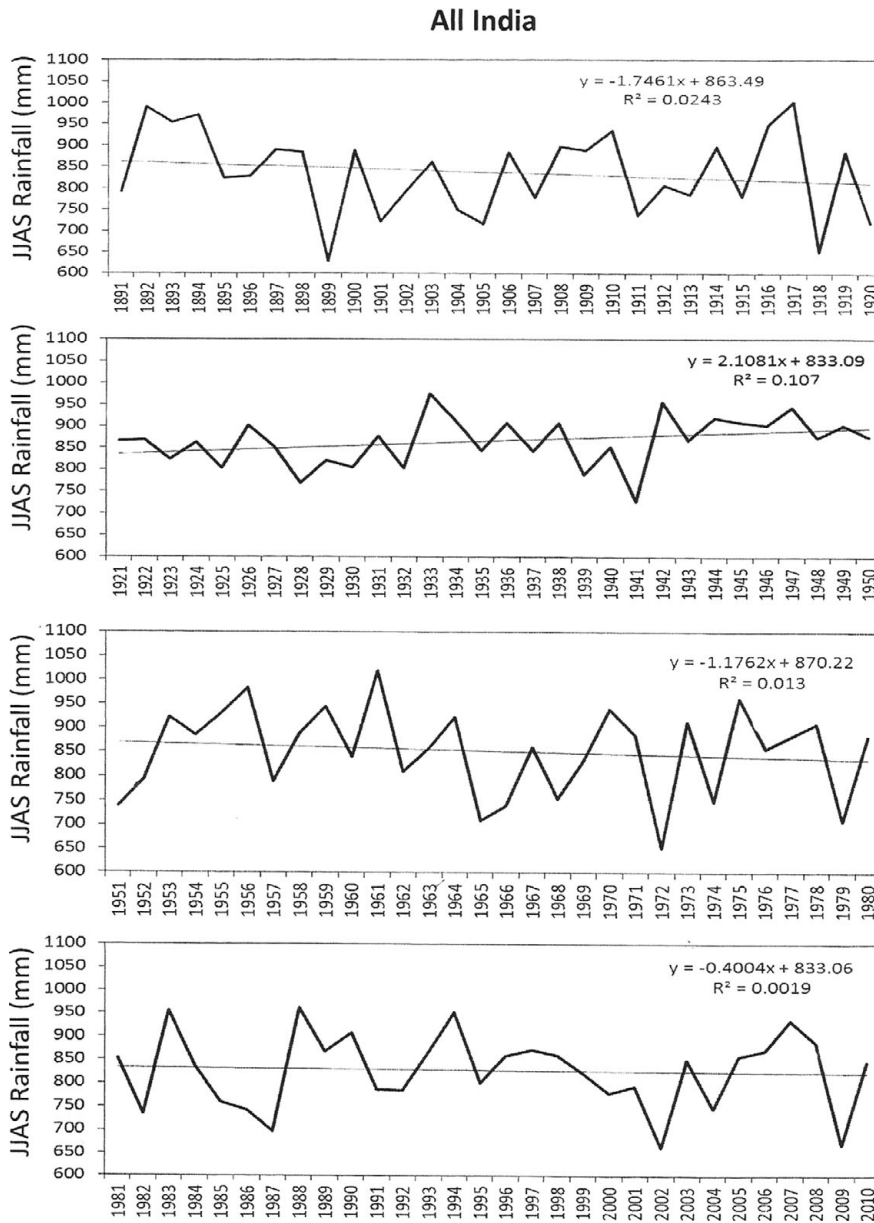


Fig. 25.7. Trend for all India monsoon rainfall over four 30-year periods.

Parthasarathy, 1981, and several others since then), and even the Indian Ocean Dipole (Saji *et al.* and Webster *et al.*), the Equatorial Indian Ocean Oscillation (EQUINO) (Gadgil *et al.*, 2004), and others. In recent decades, notable advances have been made in understanding monsoon droughts over India and the causes of droughts. Both ENSO and the IOD-EQUINO phenomena have secular variations at decadal scale which could be linked with the decadal oscillation of the monsoon rainfall. However, the connections are not very robust. Kucharski *et al.* (2006) have even linked the decadal variability of Indian rainfall to SST forcing rainfall and Kug and Kang (2006) have examined the interactive feedback between the Indian Ocean and ENSO.

**Table 25.3(a)** shows the years of drought in the monsoon season rainfall over India with month-wise and season-wise departure of rainfall from normal during the period 1901–2012 and the incidence of El Nino or Non-El Nino in the respective years. **Table 25.3(b)** shows the incidence of El Nino years which were not accompanied by monsoon drought. Note that there have been 16 droughts which can be associated with the incidence of El Nino years, but five of the droughts have also occurred with non-El Nino years. There have been ten El Nino years (**Table 25.3b**) in which monsoon rainfall over India was near-normal but of these, seven years (1902, 1915, 1925, 1930, 1939, 1992, and 2012) received rainfall between -5 and -9% of the normal

(below normal category). Excepting the year 1997, which received rainfall of +2% of the normal, in all other nine years the rainfall was on the negative side of the normal. Slingo and Annamalai (2000) have discussed in detail the possible reasons for the warmest ENSO year of 1997 being associated with rainfall on the positive side of the normal (+2%). Thus 112 years of records (1901–2012) show that there have been 25 El Nino years. Of these, monsoon drought over India occurred on 16 occasions. Thus, 64% of the El Nino years are associated with drought and on 88% of the El Nino years, Indian monsoon rainfall is below normal ( $\leq 5\%$  of the normal). The El Nino–monsoon relationship, first pointed to by Sikka (1980), is quite robust and there does not appear to be any slackening in it, though there may be weakening of the correlation coefficient between monsoon rainfall over India and SST over Niño 3.4, as suggested by Krishna Kumar *et al.* (2005, 2006). During Monsoon droughts accompanied by El Nino, deficient rains ( $\leq 10\%$  of normal) occur in all combinations on monthly scales, early season (June and July), mid season (July and August), and late season (August and September). However, during two years, 1951 and 1972, the deficiency was in all four months of the season. Deficiency in rainfall had lasted for three months on 12 occasions and for only two months on seven occasions. Table 25.4 shows the long-term trends of rainfall for all India and five homogeneous regions on the basis of IITM monsoon rainfall series. On the all India scale, period 1891–1950 shows a positive trend and the period 1951–2010 shows a negative trend. However, on a decade to decade basis too, the two decades of 1901–1910 and 2001 to 2010 showed rainfall below the long-term average by –6% and the decade of 1951–1960 showed above normal rainfall by +6%. Thus the decadal average of all India monsoon rainfall may fluctuate between  $\pm 6\%$  of the long-term average, but it is stable on a long-term basis.

There is a possibility that anthropogenic forcing of the aerosols may also influence the decadal variability of monsoon rains (Ramanathan *et al.*, 2005). There is also a

possibility that the decadal variability of the monsoon rains over India may be caused by the intrinsic decadal mode of the coupled global ocean–atmosphere system. However, the quasi-persistence of droughts or mega-droughts over India for the last two periods of 30 years each, and the decreasing trend of the monsoon rains, raise concerns about causes of the decreasing trend as the double CO<sub>2</sub> runs of the global models have a consensus for an increase in the all India monsoon rains, in contrast with the observed decreasing tendency.

Over the Indo-Pacific monsoon region, atmosphere and ocean interact with each other on a variety of spatio-temporal scales, which may modulate the synoptic, intra-seasonal, inter-annual, and even decadal scale variability in monsoon rainfall over India. It has been found by several investigators (Sperber and Palmer, 1994, Webster *et al.*, 1998, Goswami and Ajaymohan, 2000, and others) that the dominant modes of IS and IA of monsoon variability have similar structures. In some years the two modes are controlled by remote and local SST variability over the equatorial central Pacific (ENSO), and in other years by the SST over the east equatorial Indian Ocean (IOD mode). In some years the two modes amplify each other, whereas in other years they act in opposition and annul each other. The internal dynamics of the MT and the intra-seasonal modes may even reverse the influence of the ENSO and IOD on the monsoon, as is evident from the performance in some past years, such as 1992, 1997, and 2012 monsoons. IOD seems to have multi-year variability like ENSO, but it also has intra-seasonal variability. In some years the intra-seasonal variability of IOD may become dominant and even upset the multi-year mode projected before the beginning of a monsoon season. Investigation of the relative roles of the ENSO and IOD multi-year modes and their impacts on each other, as well as the multi-year IOD and sub-seasonal IOD modes for the performance of the SAM system is currently a challenging area for research. (Ashok *et al.*, 2001, 2004, Allan *et al.*, 2003, Pascal *et al.*, 2012, Pokhrel *et al.*, 2012). Wu and Kirtman (2003, 2004) have investigated the biennial oscillation of the monsoon ENSO system within the modelling framework and even pointed out the role of the Indian Ocean in ENSO variability in a coupled model.

Table 25.4. Monsoon season (JJAS) rainfall trend (mm / season) over India for two 60-year periods.

Region	Period (1891–1950)	Period (1951–2010)
All India	0.78 *	–0.83 *
Central North East India	0.65	0.10
NE India	1.10 *	–1.20 *
NW India	0.67	–0.53
Peninsular India	0.01	–0.11
West Central India	1.19 *	–1.80 *

\*Statistically significant at 90% using one-tailed test.

## 25.6 Monsoon and ocean – atmospheric processes on regional and global tropical scales, regional cryosphere and monsoon, and monsoon and aerosol connections

*Monsoon and ocean-atmosphere processes:* Monsoon is a complex interacting system in which the atmospheric, oceanic, and land-surface processes (including cryospheric

processes and aerosol processes) are highly coupled on different spatio-temporal scales (Webster, 2006). Some process occur through remote tele-connections.

### 25.6.1 Local oceanic processes and monsoon

Air-sea interactions over the Bay of Bengal are involved in modulating monsoon activity on diurnal, synoptic, and low frequency sub-seasonal scales. Over the south-eastern Arabian Sea and equatorial Bay of Bengal, the spring and early solar warming results in generation of a mini-warm pole over the south-eastern Arabian Sea (Hareesh Kumar *et al.*, 2009), which helps in the monsoon onset over Kerala, brought about in several years by the formation of a cyclonic vortex in the lower troposphere by mid May. The warming of the north Bay of Bengal in May generates north-south gradients in SST (as the clouding over the equatorial bay leads to lowering of SST from April to May), which promotes the onset and advance of monsoon over the bay. The cooling of the west and central Arabian Sea, after the burst of strong winds with the establishment of LLJ, suppresses convection up to the central Arabian Sea, and the convergent monsoon wind stream along with warmer SST over the east Arabian Sea promote organized convection off the west coast of India. The freshwater flux over the north Bay of Bengal from heavy rains and river water discharge from Brahmaputra-Ganges and Mahanadi-Irrawadi river systems generate a barrier layer over the region which maintains the warm SSTs of the Bay of Bengal for convective organizations. Durand *et al.* (2011) have found significant inter-annual variations in river water discharge over the Bay of Bengal and related it to salinity and SST variability over the bay. The sub-seasonal variability of the SST in the Bay of Bengal can reach up to 2 °C in some monsoon seasons (Sengupta and Ravichandran, 2001). Similarly, over the eastern equatorial Indian Ocean excessive / less cooling across Malaysia due to higher / lower upwelling also causes IA variability in the east-west gradients in SST over the equatorial Bay of Bengal. Warmer SSTs over the eastern equatorial Indian Ocean would promote sustained organized convection over the region that competes with the convection over the north Bay of Bengal, thus disturbing the intensity of the local Hadley cell. Several of the above mentioned aspects have been already discussed and appropriate references provided.

### 25.6.2 Remote SST forcing, ENSO and monsoon, and IOD and monsoon

Warming / cooling of the equatorial central Pacific resulting from the El Nino / La Nina phenomenon plays a vital role in seasonal scale monsoon performance. In warm El Nino years, Indian monsoon under-performs and

on about 64% of the El Nino years, a drought accompanies when El Nino is in its rising phase. Several authors (Sikka, 1980, Webster and Yang, 1992) have suggested that monsoon and ENSO are selectively interacting systems, and Webster *et al.* (1998) and Slingo and Annamalai (2000) have even proposed a tirade type of interaction which involves east-west Walker circulation, north-south Haddley type circulation, and transverse circulation over the Indo-Pacific region. Monsoon-ENSO interactions have been a dominant topic for monsoon research since 1980. However, its use in the long-range prediction of monsoon through boundary forcing of SSTs still remains a challenge for coupled models to realize the potential predictability of monsoon. (Wang *et al.*, 2005). The ENSO-monsoon relationship is a tantalizing one and is largely valid, though not on a year to year basis, and some authors (Goswami and Xavier, 2005) have even proposed that the ENSO controls the length of the monsoon season. Torrence and Webster (1999) have suggested inter-decadal changes in ENSO-monsoon connections. Connections between the equatorial Indian Ocean SST and monsoon have been sought through Monsoon IOD-EQUINO connections, already referred to earlier (Ashok *et al.*, 2001, 2004, Gadgil *et al.*, 2004, and others). Roxy *et al.* (2011) have observed seasonality between ENSO and IOD modes. Krishnan and Swapna (2009) have even suggested that frequent occurrence of IOD events might have caused under-normal performance of the monsoon in the last two decades. Sundaram *et al.* (2010) have examined the dynamics of the intensification of monsoon during positive IOD events. Gadgil *et al.* (2004) make the point that warm El Nino and IOD-EQUINO either enforce or oppose each other and the phase-locked influence of both determines the performance of extreme seasonal monsoon episodes. There is a need to set-up a special field campaign to understand the growth of IOD with the evolution of monsoon season, to determine whether IOD is forced by monsoon evolution or vice versa. The monsoon season of 2012 occurred when a warm El Nino and a negative IOD were developing, and it was expected (which was supported by dynamical seasonal prediction models) that a monsoon drought would occur. Until July 2012, the Indian rainfall was much below normal (~ -19%). However, the monsoon made a dramatic recovery in August and September under active MT through internal feedbacks of circulation and convection. Finally the season ended with -8% of the normal rainfall and it was not a drought season. It is curious to note that the ongoing amplifying El Nino was arrested and the ongoing negative IOD phase abruptly changed into a positive IOD phase from mid August 2012 to the end of September 2012 within the monsoon season. The important aspect which emerges from recent research (central equatorial Pacific SSTs) ENSO-IOD variability and its

impact on the climate variability of monsoon, is that the Indian Ocean SST variability is equally as important as the equatorial Pacific SST variability for IA variability of monsoon rainfall over India. Behra and Yamagata (2003) have even examined the role of IOD on the ENSO. Krishnamurthy and Goswami (2000) have examined ENSO–monsoon connections on a decadal scale, and Kinter *et al.* (2002) have noted some changes in ENSO–monsoon connections over Asia. Krishnan *et al.* (2009) have described monsoon droughts influencing mid-latitude circulation, like Ramaswamy (1962). Again Kumara *et al.* (2007) have provided a methodology for estimating the unpredictable component of seasonal variability.

### 25.6.3 Himalayan Eurasian cryosphere and monsoon

In the early years of IMD, Blanford (1884) had suggested that winter and spring snow cover over the Himalayas may modulate the performance of the ensuing monsoon. This was also supported by Walker (1910–1928) and Walker and Bliss (1932) through their empirical approach. Since the work of Hahn and Shukla (1976) several observational studies have been performed to support the role of Himalayan, Tibetan, Eurasian snow cover and even snow depth in modulating seasonal monsoon (Parthasarathy and Yang, 1995, Yang 1996, Kriplani *et al.*, 1996, Kriplani and Kulkarni, 1999, Bamzai and Shukla, 1998, Sikka, 1999). Several modelling studies have been done to support the role of the regional cryosphere on the performance of monsoon (Barnett *et al.*, 1989, Yasunari *et al.*, 1991, Kitoh, 1994, Vernekar *et al.*, 1995, Ose, 1996, Shankar Rao *et al.*, 1996, Douville and Royer, 1996). The robustness of the results in all these experiments shows the influence of the regional cryosphere on IA variability of the monsoon.

### 25.6.4 Monsoon and aerosols

Since the implementation of the INDOEX-1999 campaign in the Indian Ocean for the study of aerosols on the regional climate system, study of linkages of aerosol and monsoon has become a favourite subject of research. Several authors have examined the role of radiative heating of the aerosol in different layers of the atmosphere column on the monsoon climate. (Menon *et al.*, 2002, Chakraborty *et al.*, 2004, Ramanathan *et al.*, 2005, Chung and Ramanthan, 2006, Meehl *et al.*, 2008, Lau and Kim, 2006, Lau *et al.*, 2008a,b, Bolastina *et al.*, 2011). These studies suggest that aerosol load may impact on the performance of the monsoon in such a way that monsoon rainfall may decrease under high aerosol load. On the sub-seasonal scale, too high an aerosol load may prolong a monsoon break. However, aerosol load observations using MODIS of the seasonal-load on a year to year basis

(like 2002 and 2009) have shown that the aerosol load over the Indo-Gangetic plains is high under prolonged break monsoon conditions, during which desert origin air-mass frequently prevails over the Indo-Gangetic plain. Contrary to this, in the years (say 2006, 2012) when the MT is south of the normal position, the cleaner easterly marine air-mass of the Bay of Bengal prevails over the Indo-Gangetic plain.

Figure 25.8 illustrates the contrast in the aerosol optical depth (AOD) over the Indian region, as obtained from MODIS data for two extreme years, 2002 and 2006.

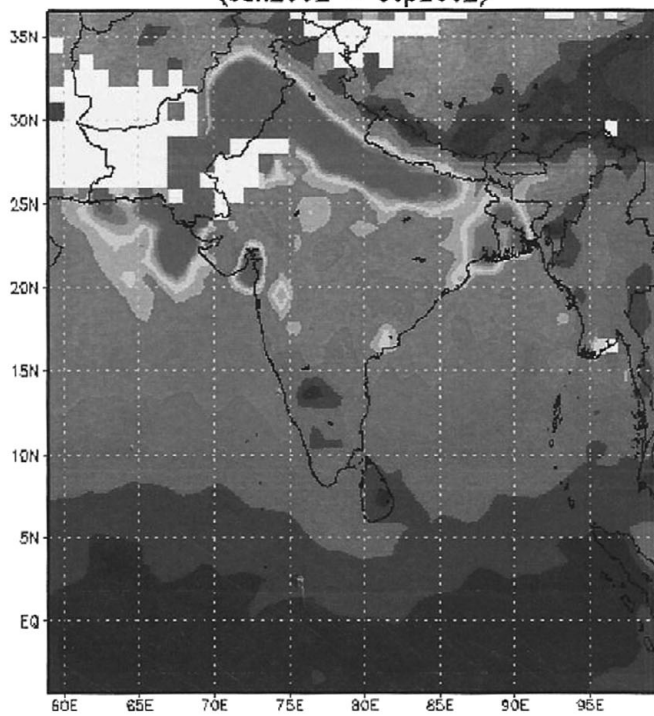
## 25.7 Monsoon predictability and operational dynamical prediction on different scales

### 25.7.1 Monsoon predictability

Weather forecasting began in India towards the end of the nineteenth century, using an empirical synoptic-climatological approach. Numerical weather prediction (NWP) was introduced rather late in India. Application of NWP models in India began only in early 1970 and such techniques based on PE models were introduced for operational purpose in IMD from the early 1980s. However, the success of the global system, in Europe at the ECMWF, for medium-range weather prediction, after the completion of the FGGE in 1980, also helped India to seriously consider using global models for predicting weather three to five days in advance. India established NCMRWF at New Delhi with adequate infrastructures and with help from COLA and NCEP USA; NCMRWF introduced an operational prediction system at a coarse resolution of T-80 in 1992. The system was upgraded to T-278 and T-378 resolution subsequently and currently, since 2010, a high resolution model of NCEP origin, T-574, is under operational use at NCMRWF and IMD. NCMRWF is also experimentally using the UK Met Office unified weather prediction model. Thus, high resolution dynamical models are now being used in India for the short to medium-range scale (1–7 days). No detailed systematic study on the predictability of tropical weather, particularly weather in highly moist monsoon circulation regime, has been carried out for India.

Shukla (1985) has surveyed the work done on predictability of deterministic weather prediction and has also discussed the conceptual difficulties in arriving at an upper limit for deterministic predictability. According to him, if the differences between two predictions made with identical models but slightly different initial conditions become equal to the difference between two randomly chosen weather maps for the same time of the year, then the upper limit of prediction has been reached. Applying such a criterion for monsoon prediction over the Indian region suggests that at present, even with a high resolution model, the predictability limit is less than one week (Taraphdar

MOD08\_M3.051 Aerosol Optical Depth at 550 nm [unitless]  
(Jun2002 – Sep2002)



MOD08\_M3.051 Aerosol Optical Depth at 550 nm [unitless]  
(Jun2006 – Sep2006)

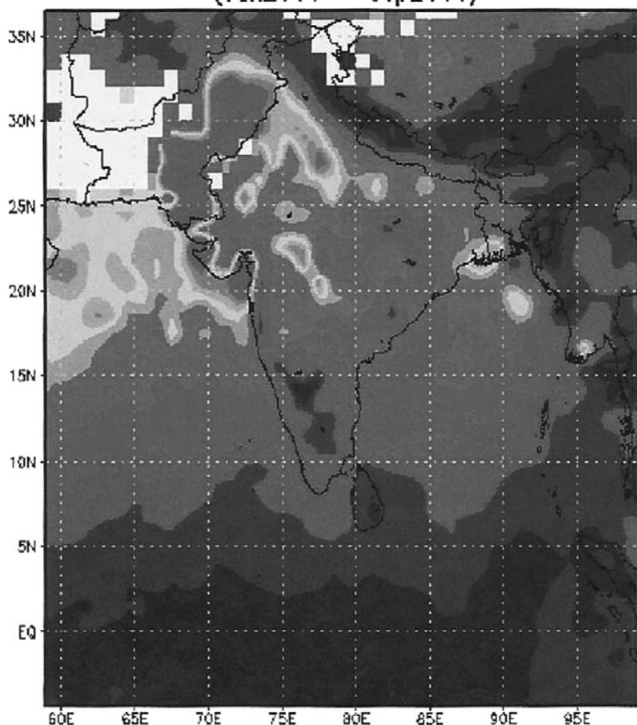


Fig. 25.8. Distribution of aerosol optical depth at 550 nm wavelength as observed by MODIS for the season of June to September; upper panel is for the year 2002 and lower panel for 2006. A black and white version of this figure will appear in some formats. For the colour version, please refer to Plate 31.

*et al.*, 2010), in contrast with the accepted limit for mid-latitudes weather of two weeks. However, within this one-week predictability estimate for the monsoon region, there could be weather regimes during which the predictability

limit may be higher or lower. In India such studies have yet to be taken up. For the prediction of the active-break cycle of the monsoon some estimates have been suggested and studies indicate that the transition from active to break or

break to active may vary among themselves (Suhas *et al.*, 2012b). However, once a break monsoon has been established, its persistence over five days in advance is well predicted by the models on the extended range of a few weeks. At present, techniques based on analogues or extrapolation of the MJO cycle are being employed (Xavier and Goswami, 2007, and others). However, the skill varies from poor to highly satisfactory depending upon the weather regime of the monsoon. Waliser *et al.* (2003a,b,c,d) have discussed the dynamical predictability of monsoon related features and potential predictability of monsoon. Palmer and Anderson (1999) and Palmer and Williams (2008) have written about the prospects for seasonal forecasting and the role of stochastic processes on climate dynamics respectively. Ajay Mohan and Goswami (2003) have discussed the potential predictability of monsoon. Also initial conditions of the ocean and even the time interval used for ocean–atmosphere coupling could be crucial (Pascal *et al.*, 2012) for the monthly and seasonal dynamical prediction, using prescribed SST with the Atmospheric General Circulation Model or with coupled models. The success of predictions so far on extended and seasonal scales has been mixed. It is very rare that there is consensus among models, even for an emerging El Niño year. Delsole and Shukla (2012) have expressed hope on improving skill for seasonal prediction based on dynamical models, which has been contested by Gadgil and Srinivasan (2012). The present status is that the potential predictability for seasonal prediction for the land-locked region of India is hard to achieve, as the present models show only low skill. However, monsoon seasonal prediction using coupled models has shown improvement in the last two decades. It has been noted that further improvement in seasonal prediction may be related to model performance on mean state and annual cycle (Lee *et al.*, 2010). Tabaldi and Knutti *et al.* (2010) have advocated use of multi-model ensembles in a probabilistic manner.

### **25.7.2 Operational dynamical monsoon prediction on the short to medium-range scale**

In India, some efforts have been made to use multi-model ensembles for short to medium-range monsoon rainfall prediction using NCMRWF, UK Met Office, NCEP, ECMWF, and JMA models (Mitra *et al.*, 2011, Roy Bhownik and Durai, 2008). The results are not very encouraging as the success for moderate rainfall prediction (1 to 3 cm/day) does not extend more than one to three days and the heavy rainfall predictions are not even nearly correct. IMD also operationally uses multi-models for predicting the track of tropical cyclones, but the doubling time of error in the position of the track is one to two days, even though forecasts are becoming slightly more successful than in the past (Mahapatra *et al.*, 2012). India also uses meso-scale models

of 3 to 27 km resolution (MM5, RAMS, WRF etc.) for short-range weather prediction. Research has shown the efficacy of various parameterizations for high impact rainfall prediction (Vaidya and Kulkarni, 2006, Das *et al.*, 2002, 2008, Sikka and Rao, 2008, and others). No consensus is available as to which scheme would work better under all conditions. Radar data assimilation is also being used in research mode and it promises better results for high impact weather prediction. Professor T. N. Krishnamurti's (Personal communication) recent work has shown improvement in high impact rainfall (rainfall exceeding 7.4 mm/hour) prediction up to 1 day by using dense network or radar data in the assimilation mode, using a physical initialization scheme. There is the prospect for improved high impact weather prediction in years to come up to 2 days or so.

High resolution global models, such as T-384 L64 (about 50 km resolution) and T-574 L64 (22 km resolution) of NCEP have been introduced for operational weather prediction since 2010, but it is too early to provide statistics of their verification. NCMRWF has produced a technical report in which they have validated their high resolution T-574 model for medium-range prediction of the monsoon over India for monsoon 2011. Overall, their T-574 model is observed to perform better than the T-382 model. The performance of a model, besides its resolution and physics, also depends upon the availability of observations to be fed into the model. Since there has been a deterioration in the quality and quantity of observatories in India over the last three to four years, it is possible that the T-574 forecast system may even provide better forecasting when the observations over India improve.

IMD also receives detailed forecasts during the monsoon season from the ECMWF, JMA, and UK Met Office models run from their respective centres. A cursory comparison of forecasts from these high resolution models have shown that there is fidelity in the models for generating new LPSs in three to seven days in advance, which at times agree with observations, but there are also significant false signals. The models appear to over-predict events of cyclogenesis. They also over-predict the frequency of heavy to very heavy rainfall events over orographic regions, such as the west coast, NE India, and sub-Himalayan range. Roy Bhownik and Durai (2008) and Mitra *et al.* (2011) have examined the use of multi-model ensembles on short to medium-range weather prediction. However, their results showed that the technique did not improve rainfall prediction for more than two days and the falls with higher than 3 cm daily rainfall were not predicted well. All of the above leads us to conclude that short-range monsoon prediction, though a very difficult problem, could be achieved on a grid scale of 100 km x 100 km up to a maximum of three days at present. Medium range, extended range, and seasonal monsoon predictions could be improved by adopting probability rather than deterministic estimates by using an ensemble

model or multi-model ensembles (Krishnamurti *et al.*, 2001, 2006, 2007). Great effort is needed to systematically evaluate these estimates. There is a hope in using TIGGE data for the purpose. A special programme is needed to do focused research by using TIGGE ensembles for the purpose of short to medium-range prediction.

## 25.8 Prospects for improved prediction skill under the Monsoon Mission

India has launched a challenging research programme entitled Monsoon Mission, aimed at improving the skill of weather predictions across the scales from short–medium to extended–seasonal scale. The Mission invites the international scientific community to participate in this collaborative research with provision of research funds from India. It is hoped that the intellectual resources of leading universities and institutes around the world would enable India to produce state of the art forecasting on monsoons on day to day, week to week, and even seasonal scales. Most of the emphasis for this research would be focused on improving the skills of operational systems such as NCEP GFS-574, the UK Met Office unified system for short to medium-range scale, and the NCEP–CFS for monthly to seasonal scale. IITM is coordinating this project for which funds are provided by the Ministry of Earth Sciences, Government of India. The collaborating agencies in India are the IMD, New Delhi, the NCMRWF, NOIDA, the INCOIS, Hyderabad and the IITM, Pune. Already the first batch of about 20 projects from USA, Europe, Japan, and India have been provided funds for the next three years (2013–2015). It is expected that more projects would be undertaken using these research funds and well-focused efforts would enhance the prospects for improved skill in monsoon forecasting to satisfy societal demands.

## 25.9 Summary and concluding remarks

Enormous understanding of the phenomenology of SAM has been achieved since scientific methodology began in India in 1875. The progress has been rather vigorous since the 1960s as observational tools, computational infrastructures, and exchange of data among countries have increased. Monsoon studies on all aspects have attracted the attention of scientists in the USA, Europe, Japan, China, Australia, as well as other countries in Asia. The subject is very vast and in this review we have only briefly touched on various aspects of the coupled atmosphere–land–ocean system, which impacts on the predictability and prediction of monsoon rainfall and circulation on short, medium, seasonal, and climate scales. We have purposely not touched on

monsoon climate change, as in itself research on this subject has become very extensive over the past two decades, and expert opinions even differ with regard to certainty in regional climate change. Variations and irregularities in monsoon rainfall, which in any given monsoon season modulate the normal or ideal system, were recognized at the beginning of scientific meteorology. More knowledge of the causes of factors that influence monsoon rainfall has remained the paramount objective of IMD since its very inception and understanding monsoon variability on all scales has remained a challenging problem for over a century. Its connection with remote and local forcing of ocean–land surface processes, as well as with the internal dynamics of the MT have been explored in very many studies. Because a monsoon drought implies prolonged rainfall and moisture deficit, ocean–atmosphere and land surface coupling modulates their interactions with the atmosphere and causes monsoon variability. Recent research has shown that for seasonal monsoon prediction, variability of the equatorial Indian Ocean on IA and IS scales, in the form of low and high frequency changes in the state of the Indian Ocean through IOD mode is quite important, like the monsoon connections with ENSO phenomena of the equatorial Pacific. Land-surface boundary conditions of snow and soil moisture have also memory on a monthly scale and hence can influence the build-up of the summer monsoon system of Asia. The global climate science community is now focused on climate and even Earth system prediction (Shukla *et al.*, 2009). It is important and necessary that India marches ahead hand in hand with the global community, otherwise India would miss the climate prediction revolution as it missed the scientific revolution over 15 to 17 centuries and the NWP revolution in the 1950s.

This chapter has also emphasized the need for enhancement of the skill of monsoon weather and climate prediction using dynamical models. These aspects are now receiving focused attention in India's Monsoon Mission programme. Under this programme, India is forging sustainable links with experts in advanced countries to pursue monsoon studies for improving the skill of prediction models. The Mission requires the availability of a sufficiently large number of trained atmosphere–ocean scientists in India to address different issues. Observations from space on various interacting components of the complex coupled system are contributing enormously to the monitoring of the coupled system. The role played by sustained conventional upper air and ocean observations still remains crucial for preparing the initial conditions for dynamical models. Highly reliable initial conditions are not only important for short and medium-range NWP, but recent research has shown their impact even on seasonal predictions. Realizing that no amount of data assimilation would provide the best initial conditions, scientists have devised an ensemble

prediction technique to reduce the uncertainty in the forecasting on all spatio-temporal scales. Multi-model prediction takes care of the performance of models on different areas by assigning weights to each model (Krishnamurti *et al.*, 2001, 2006, 2007, and others). In the multi-model approach, the uncertainties in individual model predictions are combined in a probabilistic manner to arrive at the final prediction (Tabaldi and Knutti, 2011). The international community has established a storehouse of ensemble model data on short to medium-range predictions under the TIGGE programme. These data sets have yet to be used for determining the uncertainty in the SAM forecast with the purpose of reducing its uncertainty. Indian researchers are currently moving forward, leaving the restrictive traditional regional and synoptic approaches and adopting the inter-regional and global approaches based on dynamical models. Reliable weather prediction, particularly on the incidence and position of occurrence of high impact weather events (like rainfall exceeding 10 cm/day or tropical cyclone track and intensity) has become crucial. Society is putting ever increasing demands on meteorologists, some of which are within the reach of realization, while others are even beyond the present state of knowledge about processes related to predictability of weather and climate. The public needs to be made aware about the prospects for a science-based prediction system and its uncertainties or limitations. Nations, including India, are putting in enormous financial resources to meet the genuine requirements of the weather and climate sciences. These resources need to be sustained. Establishment of sophisticated systems of observation and high speed computing within the technological advances are very cost intensive and sustaining them is equally difficult. However they are needed, as without them there would be no possible warning on impending disastrous high impact hydro-climatological events. The international research community has set for themselves a new horizon on seamless weather and climate predictions in which a seamless model would serve the purpose of prediction encompassing all scales. The day is not far away when Earth system models may ultimately be introduced for global prediction on an operational basis. To meet these challenges, India is engaged in strengthening its capacity of research by inter-institutional collaboration within India, as well as enhancing collaborative research with the international scientific community through its Monsoon Mission programme. The next decade may show great promise for advancing the skill of the prediction of extreme weather and climate events.

## 25.10 Acknowledgements

The author expresses his thanks to Professor Jian Ping Li of the Institute of Atmospheric Physics, Chinese Academy

of Sciences for inviting him to write this review. He also thanks Professor J. Shukla of COLA / IGES for encouragement of the author to keep him engaged in South Asian monsoon studies. He also thanks Mrs Shanthi Natarajan for typesetting the manuscript.

## References

- Ajay Mohan, R. S. and B. N. Goswami (2003). Potential predictability of the Asian Summer Monsoon on monthly and seasonal time scales, *Met Atmos. Phys.*, **84**, 83–100.
- Ajay Mohan, R. S. and B. N. Goswami (2007). Dependence of boreal summer tropical intra-seasonal oscillations on the simulation of seasonal mean. *J. Atmos. Sci.* **64**, 460–478.
- Ajay Mohan, R. S., M. Annamalai, J. J. Iho, J. Hafner, and T. Yamagata (2011). Poleward propagation of boreal summer intra-seasonal oscillations in a coupled model: role of internal processes, *Clim. Dyn.*, **37**, 851–867.
- Allan, R. J., C. J. C. Reason, J. A. Lindesay, and T. J. Ansell (2003). Protracted ENSO episodes and their impacts in the Indian Ocean region, *Deep Sea Research, II*, **50**, 2331–2347.
- Ananthakrishnan, R., U. R. Acharya, and A. R. Ramakrishnan (1967). On the criteria for declaring the onset of South-West monsoon over Kerala. *Forecasting Manual, FMU Ref. No. IV, 18.1. IMD*, Pune, 52 pp.
- Ananthakrishnan, R. (1977). Some aspects of monsoon circulation and rainfall, *Pure and Appld. Geophys.* **115**, 1209–1249.
- Ananthakrishnan, R. and M. K. Soman (1988). The onset of SW monsoon over Kerala, *J. Climatol.* **8**, 283–296.
- Anjaneyulu, T. S. S. (1969). On the estimates of heat and moisture budgets over the Indian monsoon trough zone, *Tellus*, **21**, 64–74.
- Annamalai, H., J. M. Slingo, K. R. Sperber, and K. Hodges (1999). The mean evolution and variability of the Asian Summer Monsoon: Comparison of ECMWF and NCEP NCAR analyses, *Mon. Wea. Rev.*, **127**, 1157–1186.
- Annamalai, M. and J. M. Slingo (2001). Active – break cycle, diagnosis of the intra-seasonal variability of the Asian Summer Monsoon, *Climate Dynamics*, **18**, 85–102.
- Annamalai, M. and K. R. Sperber (2005). Regional heat sources and active and break phases of intra-seasonal boreal summer (30–50 day) variability *J. Atmos. Sci.* **62**, 2726–2748.
- Annamalai, M. (2010). Moist dynamical linkages between the equatorial Indian Ocean and the South Asian Monsoon trough, *J. Atmos. Sci.*, **67**, 589–610.
- Ashok, K., Z. Guan, N. H. Saji, and T. Yamagata (2004). Individual and combined influences of ENSO and Indian Ocean Dipole on the Indian Summer Monsoon. *J. Climate* **17**, 3141–3155.
- Ashok, K., Z. Guan, and T. Yamagata (2001). Impact of the Indian Ocean Dipole on relationship between the Indian Monsoon rainfall and ENSO. *J. Meteorol. Soc. Japan* **81**(1), 41–56.
- Asnani, G. C. (1993) (2005 revised edition): *Tropical Meteorology Vol. I, II, and III*, Praveen Printing Press, Pune, India.
- Awade, S. T., M. Y. Totagi, S. M. Bawiskar, and D. R. Sikka (1984). Dynamics of the large scale tropospheric circulation

- during summer monsoon and tropical droughts, *Mausam*, **35**, 315–322.
- Bamzai, A. S. and J. Shukla (1999). Relation between Eurasian snow cover, snow depth and the Indian summer monsoon: an observational study, *J. Climate*, **12**, 3117–3132.
- Barnett, T., L. Dummel, G. Senkse, E. Roeckner, and M. Latif (1989). *J. Atmos. Sci.* **46**, 661–685.
- Behra, S. K. and T. Yamagata (2003). Influence of the Indian Ocean dipole on the Southern Oscillation, *J. Climate* **6**, 450–469.
- Bhat, G. S. (2006). The Indian drought of 2002: a sub-seasonal phenomenon. *Q. J. Roy. Meteor. Soc.*, **32**, 2583–2602.
- Bhide, U. V., Muzamar, S. P., Ghanekar, O. K. et al. (1997). A diagnostic study on heat sources and moisture sinks in the monsoon trough area during active-break phase of the Indian monsoon of 1979, *Tellus*, **49A**, 455–473.
- Blanford, H. F. (1884). On the connection of the Himalayan snowfall and seasons of drought In India, *Proc. Roy Soc., London*, **32**, 3–22.
- Blanford, H. F. (1886). Rainfall of India, *Memoir No. 4, Ind. Met. Dept*, **2**, 668 pp.
- Bolastina, R. A., Y. Ming, and R. Ramaswamy (2011). Anthropogenic aerosols and the weakening of the south Asian summer monsoon, *Science*, **334**, 502–505.
- Brode, R. W. and M. K. Mak (1978). On the mechanics of the monsoonal mid-troposphere cyclone formation. *J. Atmos. Sci.*, **35**, 1473–1484.
- Carr, F. H. (1977). Mid-tropospheric cyclones and the summer monsoon. *Pure and Appld. Geophys.*, **115**, 85–1412.
- Chakraborty, A. S., S. K. Sateesh, R. S. Nenjundiah, and J. Srinivasan (2004). Impact of absorbing aerosols on the simulation of climate over the Indian region in an atmosphere general circulation model. *Annales Geophysical*, **22**, 1421–1434.
- Chang, C. P. and T. N. Krishnamurti (Eds) (1987). *Monsoon Meteorology Oxford Monographs on Geology of Geophys*, N07 Oxford University Press.
- Chang, C. P., Y. Ding, N. C. Lau, et al. (Eds.) (2011). *The Global Monsoon System*, World Scientific, Singapore.
- Charney, J. G. and J. Shukla (1981). Predictability of monsoon in *Monsoon Dynamics*, Ed. J. Lighthill and R. P. Pearce, 99–110, Cambridge University Press.
- Chatopadhyay, R., A. K. Sahai, and B. N. Goswami (2008). Objective identification of non-linear coupled phases of monsoon intra seasonal oscillation: Complications for prediction 2008: *J. Atmos. Sci.*, **65**, 1549–1569.
- Chatopadhyay, R., B. N. Goswami, A. K. Sahai, and K. Fraedrich (2009). Role of stratiform rainfall in modifying the northward propagation of monsoon intra-seasonal oscillation, *J. Geophys. Res.* **114**, D191141 doi 10.1029/2009/D011869
- Chung E. and V. Ramanathan (2006). Weakening of northern Indian Ocean SST gradients and the meteorological rainfall in India and the Sahel, *J. Geophys. Res.* **110**:011102:10,10129 / 2004 J 0005441
- Colon, J. A. (1964). On interaction between the South West monsoon and the sea surface over the Arabian Sea, *Ind. J. Meteor. Geophys.*, **45**, 183–200.
- Daggupathy, S. M. and D. R. Sikka (1974). On the vorticity and vertical velocity distribution associated with a life cycle of monsoon depression. *J. Atmos. Sci.* **33**, 773–792.
- Das Gupta, M., P. K. Pradhan, S. Das, and U. C. Mohanty (2007). Simulation of rain-bearing summer monsoon systems during the west coast of India by use of ARMEX re-analysis *Natural Hazards*, **42**, 379–390.
- Das, P. K. (1986). Monsoon, 5<sup>th</sup> WMO Lecture, WMO No. 613, 155 pp.
- Das, S., A. K. Mitra, G. Iyengar, and J. V. Singh (2002). Skill of medium range forecasts over the Indian monsoon region using different parameterization of deep convection, *Weather and Forecasting*, **17**, 1194–1210.
- Das, S., R. Ashrit, G. R. Iyengar, et al. (2008). Performance of mesoscale models over India during monsoon season, NCMRWF Tech. Rept. NCMRWF, NOIDA, India, 144 pp.
- Dash, S. K., J. R. Kumar, and H. S. Shekhar (2004). On the decreasing frequency of monsoon depressions over the Indian region, *Curr. Sci.*, **86**, 1404–1411.
- Dash, S. K., G. P. Singh, M. S. Shekhar, and A. D. Vernekar (2005). Response of the Indian summer monsoon circulation and rainfall to seasonal snow depth anomaly over Eurasia. *Climate Dyn.*, **24**, 1–10.
- Dash, S. K., P. Sarthi, and S. K. Panda (2006). A study on the effect of Eurasian snow in the summer monsoon circulation and rainfall using a spectral GCM. *Int. J. Climatol.*, **26**, 1017–1025.
- Datta, S., S. G. Narkhedkar, D. R. Sikka, and S. Devi (2011). A dynamical comparison between two recent drought southwest monsoon seasons 2002 and 2009 over India, *Mausam*, **62**, 133–144.
- De, U. S. and R. K. Mukhopadhyay (2002). Breaks in monsoon and related precursors, *Mausam*, **53**, 205–212.
- Deshpande, N. R. and N. Singh (2010). Spatial and temporal variations in the occurrence of wet periods over river basins of India, *J. Earth Sys. Sci.*, **199**, 561–570.
- Delsole, T. and J. Shukla (2012). *Geophys. Res. Lett.* **39**, doi 10.1029/2012 GL 05 1279
- Dhar, O. N., P. R. Rakhecha, and B. N. Mandal (1980). Does the early or late onset of monsoon provide any clue to subsequent rainfall during the monsoon season, *Mon. Wea. Rev.* **108**, 1069–1072.
- Dhar, O. N. and S. Nandargi (1999). Role of low pressure areas in the absence of tropical disturbances during the monsoon months in India. *Int. J. Climatol.*, **19**, 1153–1159.
- Dickson, R. R. (1984). Eurasian snow cover versus Indian monsoon rainfall, *J. Clim. Appl. Meteor.*, **24**, 171–173.
- Ding, Y. and D. R. Sikka (2006). *Synoptic Systems and Weather in the Asian Monsoon* (Ed. B. Wang) Praxis, Chichester, UK, 131–202.
- Douville, H. and J. F. Royer (1996). Sensitivity of the Asian summer monsoon with the Meteo-France GCM, *Climate Dyn.*, **12**, 440–466.
- Durai, V. R., S. K. Roy Bhowmik, and B. Mukhopadhyay (2010). Evaluation of Indian summer monsoon rainfall features using TRMM and Kalpana satellite derived precipitation and raingauge observation, *Mausam*, **61**, 317–336.

- Durand, F., F. Papa, A. Rahman, and S. K. Bala (2011). Impact of Ganges – Brahmaputra Inter-annual Discharge Variations on Bay of Bengal Salinity and Temperature during 1992–1999 Period, *J. Earth Sp. Sci.*, **120**, 859–872.
- Eliot, J. (1884). Accounts of south-west monsoon storms generated in the Bay of Bengal during 1877–1881: *Mem. Ind Met. Dept.* **2**, 217–448.
- Fasullo, J. and P. J. Webster (2003). A hydrological definition of Indian monsoon onset and withdrawal. *J. Climate*, **16**, 3200–3211.
- Fein, J. S. and P. L. Stephens (Eds) (1987). *Monsoons*, John Wiley and Sons, 632 pp.
- Ferranti, L., J M. Slingo, T. N. Palmer, and B. J. Hoskins (1997). Relations between inter-annual and intra-seasonal monsoon variability as diagnosed from AMPI investigations. *Q. J. Roy. Meteor. Soc.* **123**, 1323–1357.
- Findlatter, J. (1969). A major air current near the west Indian Ocean during the northern summer, *Quart. J. Roy. Meteorol. Soc.*, **95**, 1251–1262.
- Findlatter, J. (1977). Observational aspects of the low-level cross-equatorial jet stream of the western Indian Ocean, *PAGEOPH*, **115**, 1251–1259.
- Flohn, H. (1960). Recent investigations on the mechanism of the summer monsoon over southern and eastern Asia. In *Monsoons of the World*, Ind. Met. Dept., pp. 75–88.
- Francis, R. A. and S. Gadgil (2006). Intense rainfall events over the west coast of India, *Met. Atmos. Phys.* Doi 10.1007/S0073-005-0167-2.
- Gadgil, S. (2000). Monsoon-Ocean coupling, *Curr. Sci.*, **78**, 309–323.
- Gadgil, S. and P. V. Joseph (2003). On the breaks of the Indian Monsoon. *Proc. Ind. Acad. Sci. 25 (E and P. Sci)* **112**, 529–558.
- Gadgil, S. (2003). The Indian monsoon and its variability. *Ann. Rev. Earth and Planetary Sci.*, **31**, 429–467.
- Gadgil, S., P. N. Vinaychandran, and P. A. Francis (2003). Droughts of the Indian summer monsoon, Role of clouds over the Indian Ocean, *Current Sci.*, **88**, 1713–1719.
- Gadgil, S., P. N. Vinaychandran, P. A. Francis, and S. Gadgil (2004). Extremes of Indian summer monsoon rainfall, ENSO and equatorial Indian Ocean oscillation *Geophys. Res. Lett.* **31**, doi. 10. 1029/2004 GL 019733.
- Gadgil, S., R. Rajeevan, and P. A. Francis (2007). Monsoon variability: Links to major oscillations over the equatorial Pacific and Indian Oceans *Curr. Sci.*, **98**, 182–194.
- Gadgil, S and J. Srinivasan (2012). Monsoon prediction: are dynamical models getting better than statistical models? *Current Sci.*, **103**, 257–259.
- George, P. A. (1956). Effect of off shore vortices on rainfall along with west coast of India, *Ind. J. Met. Geophys* **7**, 235–240.
- Godbole, R. V. (1977). The composite structure of monsoon depression over India, *Pure and Appld. Geophys.*, **24**, 1–14.
- Goswami, B. N and R. S. Ajaymohan (2000). Intra seasonal oscillation and inter-annual variability of the Indian summer monsoon, **14**, 1180–1198.
- Goswami, B. N. and P. K. Xavier (2003a). Potential predictability and extended range prediction Indian summer monsoon breaks. *Geophys. Res.Lett.*, **32**, doi.10. 1029/2003, GL 017810.
- Goswami, B. N., R. S. Ajaymohan, P. K. Xavier, and D. Sengupta (2003b). Clustering of low pressure systems during the Indian summer monsoon by intra-seasonal oscillations, *Geophys. Res. Lett.* **80**(8), doi. L0, 1 029/2002/GLO 16734
- Goswami, B. N and P. K. Xavier (2005). ENSO central to the South Asian monsoon and length of the rainy season, *Geo Phys. Res. Lett.* **32**, 18717
- Goswami, B. N., G. Wu, and T. Yasunuri (2006). Annual cycle, intra-seasonal oscillation, and road block to seasonal predictability of the Asian summer monsoon. *J. Climate*, **19**, 5078–5099.
- Goswami, B. N., J. R. Kulkarni, V. R. Mujumdar, and R. Chatopadhyay (2010). On factors responsible for recent secular trend in the onset phase of monsoon intra seasonal oscillations, *Int. J. Climatol.* **30**, 2240–2246.
- Goswami P. and K. C. Gauda (2010). Evaluation of a dynamical basis for advance forecasting of the date of onset of monsoon rainfall over India, *Mon. Wea. Rev.*, **138**, 3120–3141.
- Grossman, R. L. and D. R. Durran (1981). Interaction of low level flow with the western ghat mountains and off-shore convection in the summer monsoon, *Mon. Wea. Rev.*, **112**, 652–672.
- Guhathakurta, P. and M. Rajeevan (2008). Trends in the rainfall patterns over India, *Int. J. Climatol.* **28**, 1453–1469.
- Guhathakurta, P., O. P. Sreejith, and P. A. Menon (2011). Impact of climate change on extreme rainfall events and flood risks of India, *J. Earth Syst. Sci.*, **120**, 359–373.
- Hahn, D. G. and J. Shukla (1976). An apparent relation between Eurasian snow cover and Indian monsoon rainfall *J. Atmos. Sci.* **33**, 2461–2462.
- Hareesh Kumar, P. V., M. Joshi, K. V. Sanil kumar, A. D. Rao, and others (2009). Growth and decay of the Arabian Sea mini warm pool during May 2000: Observations and simulations. *Deep Sea Res.*, doi. 10. 1016/j.dsr.2008, 12.004.
- India Met. Dept (IMD) (2011, 2012). *Monsoon Monograph I & II, IMD*, Pune.
- Jadhav, S. K. and A. A. Munot (2004). Statistical study of the low pressure systems during summer monsoon season over the Indian region. *Mausam*, **55**, 15–30.
- Johnson, R. B. (2006). *Mesoscale processes*. In *The Asian Monsoon* (Ed. B. Wang) Paraxizs/Springer Pub., pp. 331–356.
- Joseph S., A. K. Sahai, and B. N. Goswami (2008). Eastward propagating MJO during Boreal Summer and Indian Monsoon Droughts, *Clim. Dyn.* Doi 10.10071 00382 – 088.0412–8
- Joseph, P. V. and P. L. Raman (1966). Existence of low level westerly jet stream over Peninsular India during July. *Ind. J. Met. Geophys.*, **17**, 407–410.
- Joseph, P. V., J. K. Eischeid, and R. J. Phyle (1994). Inter annual variability of the onset of summer monsoon and its associations with atmospheric features, El Nino and sea surface temperature anomalies, *J. Climate*, **7**, 81–105.
- Joseph, P. V., K. P. Suraj, and C. K. Rajan (2006). The summer monsoon onset process over South Asia and an objective method for the date of monsoon onset over Kerala. *Int. J. Climatol.*, **26**, 1871–1893.

- Joseph, P. V. and T. P. Sabin (2008). Ocean-atmosphere interaction mechanism for the active-break cycle of the Asian summer monsoon, *Clim. Dyn.* **30**, 553–566.
- Joseph, S., A. K. Sahai, and B. N. Goswami (2009). Eastward propagating MJO during boreal and Indian monsoon droughts, *Clim. Dyn.* **32**, 1139–1153.
- Ju, J. and J. M. Slingo (1995). The Asian summer monsoon and ENSO, *Quart. J. Roy. Meteor. Soc.* **77**, 437–471.
- Kakade, S. B. and S. S. Dugam (2008). Impact of cross-equatorial flow on intra-seasonal variability of Indian summer monsoon rainfall, *Geophys. Res. Lett.* **35**, L 1–2805
- Kanamitsu, M. and T. N. Krishnamurti (1978). Northern summer circulation during drought and normal rainfall months, *Mon. Wea. Rev.*, **106**, 331–347.
- Kar, S. C., M. Sugi, and N. Sato (2001). Inter-annual variability of the Indian summer monsoon and internal oscillations in the JMA global model simulations. *J. Meteor. Soc., Japan,* **9**, 607–623.
- Keshavamurty, R. N. (1968). On the maintenance of the mean zonal motion in the Indian summer monsoon, *Mon. Wea. Rev.*, **96**, 23–31.
- Keshavamurty, R. N. and S. T. Awade (1970). On the maintenance of the mean monsoon trough over north India, *Mon. Wea. Rev.* **98**, 315–320.
- Keshavamurty, R. N. (1982). Response of the atmosphere to sea surface temperature anomalies in the equatorial Pacific teleconnection of the Southern Oscillation. *J. Atmos. Sci.*, **39**, 1241–1259.
- Keshavamurty, R. N. and M. Shankar Rao (1992). *The Physics of Monsoon*, Allied Pub.
- Kinter J. L. III, H. Miyakoda, and S. Yang (2002). Recent changes in the connection from the Asian Monsoon to ENSO, *J. Climate*, **15**, 1203–1215.
- Kitoh, A. (1994). AGCM Experiment on Tibetan snow and monsoon, *Proc. Int. Conf. on Meteorological Variability & Prediction, WHO, Trieste*, pp. 661–665.
- Koteswaran, P. (1958a). Easterly jet stream in the tropics, *Tellus*, **10**, 43–57.
- Koteswaran, P. (1958b). *Monsoons of the World* pp. 105–110, *Ind. Met. Dept.*, New Delhi.
- Kriplani, R. H., S. V. Singh, A. D. Vernekar, and V. Thapaliyal (1996). Empirical study on Nimbus-7 snow mass and Indian summer monsoon rainfall, *Int. J. Climatol.* **16**, 23–34.
- Kriplani, R. H and A. Kulkarni (1999). Climatology and variability of Soviet snow depth: Some new perspectives in snow Indian monsoon teleconnection. *J. Atmos. Sciences* **15**, 475–489.
- Krishnan, R. and S. Sundaram (2005). On the dynamical extended range predictability of active / break spells of the Indian Summer Monsoon: Sensitivity to initial conditions, *Int. J. Ecology and Development*, **505**, 1–23.
- Krishnan, R., K. V. Ramesh, R. K. Samda, et al. (2006). Indian ocean-monsoon coupled interactions and impending monsoon droughts, *I Geophys. Res. Lett.*, **31**, L08711
- Krishnan R., V. Kumar, M. Sugi, and J. Vishimura (2009). Internal feedbacks from mid-latitude interactions during droughts in the Indian monsoon, *J. Atmos. Sci.*, **660**, 553–578.
- Krishna Kumar, K., M. Hoerling, and B. Rajagopalan (2005). Advancing dynamical prediction of Indian monsoon rainfall, *Geophys. Res. Lett.* **82**, 1–4.
- Krishna Kumar, K., B. Rajagopalan, M. Hoerling, G. Batesal, and M. Care (2006). Unraveling the mystery of Indian monsoon failure during El Niño, *Science*, **314**, 115–119.
- Krishnamurti, T. N. (1971). Tropical east-west circulation of the tropical upper troposphere motion field during the northern hemisphere summer, *J. Atmos. Sci.* **28**, 1342, 1347.
- Krishnamurti, T. N. and H. N. Bhalme (1976). Oscillations of monsoon system, Pt. I., observational aspects, *J. Atmos. Sci.*, **45**, 1937–1954.
- Krishnamurti, T. N., P. Ardanay, Y. Ramanathan, and R. Pasch (1981). On the onset vortex of the summer monsoon, *Mon. Wea. Rev.*, **109**, 341–363.
- Krishnamurti, T. N. and Y. Ramanathan (1982). Sensitivity of monsoon onset to differential heating, *J. Atmos. Sci.*, **39**, 1290–1306.
- Krishnamurti, T. N., M. Subramaniam, D. Oosterhofaud, and G. Daughenbang (1990). On the predictability of low frequency modes, *J. Meterol. Atmos. Phys.*, **42**, 19–37.
- Krishnamurti, T. N., S. Sajani, D.W. Shin, et al. (2001). Real time multi-analysis – multimodel super ensemble forecasts of precipitation using TRMM and SSM/L products. *Mon. Wea. Rev.*, **120**, 2861–2883.
- Krishnamurti, T. N., D. R. Chakraborty, N. Cubuke, L. Stefnova, and T. S. V. Vijayakumar (2003). A mechanism of the Madden Julian Oscillation based on interactions in the frequency domain, *Quart. J. Roy. Meteor. Soc.*, **129**, 2559–2590.
- Krishnamurti, T. N., J. Sanjay, A. K. Mitra, and T. S. V. Vijay Kumar (2004). Determination of forecast errors arising from different components of model physics and dynamics. *Mon. Wea. Rev.*, **132**, 2570–2594.
- Krishnamurti, T. N., A. K. Mitra, T. S. V. Vijay Kumar, W.T. Yun, and W. K. Devar (2006). Seasonal climate forecasters of the Asian Summer monsoon using multiple coupled models, *Tellus (A)*, **58**, 487–507.
- Krishnamurti, T. N., Simon A., Thomas A., Mishra A., Sikka D., Niyogi D., Chakraborty A. and Li-Li (2012a). Modeling of forecast sensitivity on the march of monsoon isochrones from Kerala to New Delhi: The First 25 Days, *J. Atmos. Sci.*, **69**, 2465–2487.
- Krishnamurti T. N., R. Krishnamurti, A. Simon, A. Thomas, and V. Kumar (2012b). A mechanism of the MJO, Special Issue, *Yanai AMS Monograph*
- Krishnamurti, T. N. (2013). Personal discussions.
- Krishnamurthy, V. and B. N. Goswami (2000). Indian monsoon – ENSO relationship on inter-decadal time scale. *J. Climate*, **13**, 579–595.
- Krishnamurthy, V. and J. Shukla (2000). Intra-seasonal and inter-annual variation of rainfall over India, *J. Climate*, **13**, 4366–4375.
- Krishnamurthy, V. and J. Shukla (2007). Intra-seasonally and seasonally persisting patterns over the Indian monsoon region. *J. Climate*, **20**, 3–20.

- Krishnamurthy, V. and J. Shukla (2008). Seasonal persistence and propagation of intraseasonal patterns over the Indian Summer monsoon region. *Climate Dynamics*, **30**, 353–367.
- Krishnamurthy, V. (2011). Extreme Events and Trends in the Indian Summer Monsoon, COLA Tech. Rept., 314, COLA / IGES, 4041, Powder Mill Road, Suite, 302, Calverton, Hd. 20705, USA.
- Krishnan, R., V. Kumar, M. Sugi, and J. Yosimura (2009). Internal feedbacks from monsoon – mid-latitude interactions during droughts in the Indian summer monsoon. *J. Atmos. Sci.* (under publication)
- Krishnan, R. and P. Swapna (2009). Significant influence of the Boreal summer monsoon flow on the Indian Ocean response during dipole events., *J. Climate*, **22**, 5611–5634.
- Kucharski, F., F. Molteni, and J. H. Yoo (2006). SST forcing of decadal Indian monsoon rainfall variability. *Geophys. Res. Lett.*, **83**, L037709.
- Kug, J. S. and I. S. Kang (2006). Interactive feedback between the Indian Ocean and ENSO, *J. Climate*, **19**, 1784–1801.
- Kumara A, B. Jha, Q. Zhangal, and L. Bounoua (2007). A methodology for estimating the unpredictable component of seasonal atmospheric variability, *J. Climate*, **20**, 3888–3901.
- Lau, K. M. and K. M. Kim (2006). Observational relationship between aerosol and Asian monsoon rainfall and circulation, *Geophys. Res. Lett.*, **33**, 121810: doi:10.1029/2006GL027546
- Lau, K. M., M. K. Kim, and K. M. Kim (2008a). Asian summer monsoon anomalies induced by aerosol direct radiative forcing – the role of Tibetan high. *Climate Dyn.*, **28**.
- Lau, K. M., V. Ramanathan, G.X. Wu, et al. (2008b). The joint aerosol-hydrological cycle interaction – a new challenge to monsoon climate research. *Bull. Am. Meteorol. Soc.*, **89** (3), 369–383.
- Lawrence, D. M and P. J. Webster (2001). Inter annual variations of the intra-seasonal oscillation in the South Asian summer monsoon region. *J. Climate*, **14**, 2910–2922.
- Lee, J. F. et al. (2010). How are seasonal prediction skills related to model performance on mean state and annual cycle, *Clim. Dyn.*, **35**, 267–283.
- Li, C. and M. Yanai (1996). The onset and inter-annual variability of Asian summer monsoon in relation to land-sea thermal contrast. *J. Climate*, **9**, 358–375.
- Meehl, G. A., J. M. Arblaster, and W. D. Coolins (2008). Effects of black carbon aerosols on the Indian monsoon, *J. Climate*, **21**, 23–34.
- Menon, S., J. Hansen, Z. Nazarenko, and Y. Luo (2002). Climate effects of black carbon aerosols in China and India, *Science*, **297**, 2250–2253.
- Miller, F. R. and R. N. Keshavamurti (1968). *IIOE Meteorological Monograph*, East-West Centre Press, Hawaii, USA.
- Mishra, S. K., M. D. Patwardhan, and L. George (1985). A primitive equation barotropic instability study of the monsoon onset vortex, 1979. *Q.J.R. Meteor.* **111**, 427–444.
- Mitra, A. K., G. R. Iyenger, V. R. Durai, et al. (2011). Experimental real time multi model ensemble (MME) of rainfall during monsoon 2008, large scale medium range aspects, *J. Earth Sys. Sci.*, **120**, 27–52.
- Mohanty, U. C., S. K. Dube, and M. P. Singh (1983). A study of heat and moisture budgets over the Arabian Sea and their role in the onset and maintenance of summer monsoon. *J. Met. Soc. Japan*, **61**, 208–221.
- Mohanty, U. C. and K. J. Ramesh (1994). A study on the dynamics and energetics of the Indian summer monsoon. *Proc. Ind. Acad. Sci. (E&Psci)* **60A**, 23–55.
- Mohanty, U. C., N. V. Sam, and S. Basu (2003). A study on the structure of convective atmosphere over the west coast of India during ARMEX-1 2005, *Mausam*, **56**, 49–58.
- Mohanty, U. C., P. V. S. Rao, and R. Bhatia (2005). A study on the climatological features of the Asian Summer monsoon, dynamics, energetic and variability, *Pure Appld. Geophys.*
- Mooley, D. A. and J. Shukla (1989). Main features of the westward moving low pressure systems which form over the Indian region during the monsoon season and their relationship with the monsoon rainfall, *Mausam*, **40**, 137–152.
- Mukherjee, A. K., S. Kumar, and G. Krishnamurthy (1984). The dynamics of the offshore vortex in east Arabian Sea and its associated rainfall, *Ind. J. Met. Hydrol. Geophys.*, **35**, 233–234.
- National Centre for Medium Range Weather Forecasting (NCMRWF) (2009).
- Nanjundiah R. and T. N. Krishnamurti (2007). Intra-seasonal oscillations of tropical convergence zones: Theory and prediction, *Curr. Sci.*, **93**, 173–181.
- Nanjundiah, R. S., J. Srinivasan, and S. Gadgil (1992). Intra-seasonal variation of the Indian summer monsoon: Theoretical aspects. *J. Meteor. Soc. Japan*, **70**, 529–550.
- Nagaraju, C., D. R. Sikka, and S. Basantha Kumar (2012). *The ability of a high resolution atmospheric general circulation model for the march of monsoon isochromes from Cochin to Jodhpur: Paper presented at the Int. Conf. on opportunities and challenges in monsoon prediction in a changing climate and predictability of monsoon*, IITM, Pune, 21–25, Feb., 2012.
- Normand, C. (1953). Monsoon seasonal forecasting, *Q. J. Roy. Meteor. Soc.*, **79**, 463–473.
- Ose, T. (1996). The comparison of the simulated response to the regional snow mass anomalies over Tibet, Eastern Europe and Siberia, *J. Meteor. Soc. Japan*, **74**, 845–866.
- Pai, D. S., Bhate, J., Sreejith, O. P., Hatwar, H. R. (2009). Impact of MJO on the intraseasonal variation of summer monsoon rainfall over India, *Clim. Dyn.* doi:10.1007/s00382-009-0634-4.
- Pai, D. S., J. Bhate, O. P. Sreejith, and H. R. Hatwar (2011). Impact of MJO on intra-seasonal variation of summer monsoon rainfall over India, *Clim. Dyn.* **36**, 41–55.
- Palmer, T. N. and P. Williams (2008). Stochastic physics and climate dynamical *Phil. Trans. Roy. Soc.*, July issue.
- Pant, G. B. and B. Parthasarathy (1981). Some aspects of an association between the Southern Oscillation and Indian summer monsoon, *Arch. Meteor. Geophys. Biokl.*, **B29**, 245–252.
- Pant, P. S. (1983). A physical basis for changes in the phases of the summer monsoon over India. *Mon. Wea. Rev.*, **106**, 771–781.

- Pant, G. B. and K. Rupakumar (1997). *Climate of South Asia*, John Wiley and Sons, Chichester, USA.
- Parthasarathy, B., A. A. Munot, and D. R. Kothawale (1994). All India monthly and seasonal rainfall series 1871–1993. *Tehor. Appl. Climatol.*, **49**, 217–224.
- Parthasarathy, B. and S. Yang (1995). Relationship between regional summer monsoon rainfall and Eurasian snowcover, *Adv. Atmos. Sci.*, **12**, 143–150.
- Pascal, T., K. Kamala, S. Masson, and others (2012). The role of intra-daily SST variability in the Indian monsoon variability and monsoon – ENSO – IOD relationship in a global coupled model, *Clim. Dyn.*, **30**, 729–754.
- Pasch, R. J. (1983). On the onset of the planetary scale monsoon, Report NO.83–9, Dept. Met., F.S.U. Tallahassee, Fla.
- Pearce, R. P. and U. C. Mohanty (1984). Onsets of the Asian Summer Monsoons 1979–82. *J. Atmos. Sci.*, **41**, 1620–1639.
- Pisharoty, P. R. and B. N. Desai (1956). Western disturbances and Indian Weather, *Ind. J. Meteor Geophys.*, **8**, 333–338.
- Pisharoty, P. R. and G. C. Asnani (1957). Rainfall around monsoon depression southwest monsoon in India, *Ind. J. Met. Geophys.*, **7**, 333–338.
- Pokhrel, S. and D. R. Sikka (2013). Variability of the TRMM-PR total, Convective and Statiform Rain Fractions over the Indian Region during the Summer Monsoon, *Clim. Dyn.*, **41**, 21–44.
- Prasad, V. S. and T. Hayashi (2007). Active, weak and break spells in the Indian summer monsoon, *Meteor. Atmos. Phys.*, **95**, 53–61.
- Prasanna V. and H. Annamalai (2012). Moist dynamics of extended monsoon breaks over South Asia, *J. Climate*, **25**, 3810–3831.
- Raghavan, K. (1973). Break monsoon over India. *Mon. Wea. Rev.* **101**, 33–43.
- Rajamani, S. and D. N. Sikdar (1989). Some dynamical characteristics and thermal structure of monsoon depressions over the Bay of Bengal. *Tellus*, **41** A, 255–269.
- Rajeevan, M., D. S. Pal, and M. R. Das (2002). Asymmetric thermodynamic structure of monsoon depression revealed in microwave satellite data, *Current Sci.*, **81**, 448–450.
- Rajeevan M., J. Bhate, J. D. Kale, and B. Lal (2006). High resolution daily gridded rainfall data for the Indian region. Analysis of break and active monsoon spells. *Curr. Sci.*, **91**, 296–306.
- Rajeevan M., J. Bhate, and A. K. Jaiswal (2008a). Analysis of variability and trends of extreme rainfall events over India using 104 years of gridded daily rainfall data, *Geophys. Res. Lett.*, **35** L 18707 doi: 10.1029/2008 GL 035143
- Ramage, C. S. (1971). Monsoon Meteorology, *Int. Geophys. Ser.* 15, Academic Press, San Diego, USA.
- Ramamoorthy, K. (1969). *Monsoon of India – Some aspects of break in the Indian South West monsoon during July and August*. Forecasting manual 1–57, No.IV, 183, Ind. Met. Dept., Poona, India, Roy Bhowmik
- Ramanathan, V., C. Chung, D. Kunm, et al. (2005). Atmospheric brown clouds: Impact on South Asian climate and hydrological cycle, *Proc. Nat. Acad. Sci (USA)*, **102**, 5326–5333.
- Ramaswamy, C. (1962). Break in the Indian summer monsoon as a phenomenon of interaction between the easterly and westerly jet streams, *Tellus* **14**, 337–349.
- Rameshkumar, M. R., R. Krishnan, and others (2009). Increasing trend of break monsoon condition over India – role of ocean-atmosphere processes in the Indian Ocean, *IEE Geosci. And Remote Sensing Let.*, **6**, 332–336.
- Rao, K. G. (1988). Diagnosis of dominant forcing factors for large scale vertical velocities during active and break phases of the monsoon. *Pure Appld. Geophys.*, **127**, 669–693.
- Rao, K. G., M. Desbois, R. Rocca, and K. Nakamura (2004). Upper tropospheric drying and the transition to break in the Indian summer monsoon during 1999: *Geophys. Res. Lett.*, **Dir 10**. 1029/2003, GLO18269.
- Rao, P. L. S., U. C. Mohanty, and K. J. Ramesh (1999). Mean dynamical characteristics of the Asian summer monsoon with a global analysis forecast system, *Met. Atmos. Phys.*, **68**, 57–77.
- Rao, P. S. and D. R. Sikka (2005). Intra-seasonal variability of the summer monsoon over north Indian Ocean as revealed by the BOBME and ARMEX field programs. *Pure and Appld. Geophys.*, **162**, 1481–1510.
- Rao, R. R. (1986a). The observed thermal response of the upper north eastern Arabian Sea to the onset of summer monsoon during ISMEX-73, *Mausam*, **37**, 429–434.
- Rao R. R. (1986b). Cooling and deepening of the mixed layer on the central Arabian Sea during monsoon-77: Observations and Simulations, *Deepsea Res.*, **32**, 1413–1424.
- Rao, R. R. (1987). The observed variability of the cooling and deepening of mixed layer in the Central Arabian Sea during Monsoon – 77, *Mausam*, **38**, 43–48.
- Rao, R. R. and R. Shivkumar (1999). On the possible mechanisms of the evolution of a mini warm pool during the pre-monsoon season and the onset vortex in the South Eastern Arabian Sea, *Q. J. R. Meteorol. Soc.*: **125**, 787–809.
- Rao, Y. P. (1976). *Southwest Monsoon, Met. Monography, Synoptic Meteorology*, India Met. Dept., Pune, 367 pp.
- Rasmusson, E. M. and T. H. Carpenter (1983). Relationship between eastern equatorial Pacific sea surface temperature and rainfall over India and Sri Lanka *Mon. Wea. Rev.* **111**, 517–528.
- Ratnam, J. V., D. R. Sikka, A. Sudipta, and others (2007). Dynamical prediction of monsoon rainfall over India, using NCEP T-171 model, *Pure and Appld. Geophys.*, **164**.
- Rodwell, M. J. (1997). Breaks in the Indian Monsoon: The influence of southern hemisphere weather systems, *J. Atmos. Sci.*, **54**, 2597–2611.
- Romatsechke, U., S. Medina, and R. Houze (2010), Regional seasonal and diurnal variation of convection in the South Asian region, *J. Clim.*, **23**, 419–439.
- Romatsechke, U. and R. Houze (2011). Characteristics of precipitating convective system in the South Asian monsoon, *J. Hydromet.*, **12**, 3–26.
- Roxy, M., S. Guladi, H. K. L. Drobhlar, and A. Navarra (2011). Seasonality in the relationship between El Nino and Indian Ocean dipole, *Clim. Dyn.*, **37**, 221–236.

- Roy Bhownik, S. K. and U. R. Durai (2008). Multimodel ensemble forecasting of rainfall over Indian monsoon region, *Atmosfera*, **21**, 225–239.
- Sengupta, D. and M. Ravichandran (2001). Oscillation of the Bay of Bengal, SST during the 1998 summer monsoon, *Geophys. Res. Lett.*, **28**, 2033–2036.
- Shankar Rao, M. L. Lau, and S. Yang (1996). On the relationship between Eurasian snow cover and the Asian summer monsoon, *Int. J. Climatol.*, **16**, 605–616.
- Shukla, J. (1985). Predictability, *Adv. Geophys.*, **283**, 87–122.
- Shukla, J. (1987). Inter-annual variability of monsoon. In *Monsoons* (eds. J. S. Fein and P. L. Stephens) Wiley, New York, 399–464.
- Shukla, J. (1998). Predictability in the midst of chaos: A scientific basis for climate forecasting, *Science*, **282**, 726–773.
- Shukla, J., R. Hagelorn, B. Hoskins, *et al.* (2009). Revolution in climate prediction is both necessary and possible. *Bull. Amer. Meteor. Soc* (unclear publication).
- Sikka, D. R. (1977). Some aspects of the life history, structure and movement of monsoon depressions *Pure & Appld. Geophys.*, **115**, 1501–1526.
- Sikka, D. R. (1980). Some aspects of the large scale fluctuations of summer monsoon rainfall over India in relationship to fluctuations in the planetary and regional scale 2 parameters. *Proc. Ind. Acad Sci.*, **89**, 179–195.
- Sikka, D. R. and S. Gadgil (1980). On the maximum cloud zone and the ITCZ over the Indian longitudes during the southwest monsoon, *Mon. Wea. Rev.*, **108**, 1840–1853.
- Sikka, D. R., D. K. Paul, V. R. Deshpande, R. Mujumdar, and P. V. Puranik (1987). Sub-seasonal scale fluctuations of the ITC over the Indo-Pacific region during summer monsoon features over the Indian region, *Proc. Ind. Acad. Sci., E & P Sci.*, **95**, 47–74.
- Sikka, D. R. (1999b). *Monsoon Droughts*, Joint COLA/CARE ARE Rept. No.2, Available at COLA, 4041, Powder Mill Road Calverton MD, USA.
- Sikka, D. R. (2001). *Monsoon Floods*, Joint COLA/CARE Report No.4, Available at COLA, 4041, Powder Mill Road, Calverton, MD, USA.
- Sikka, D. R. (2006). *A study in the monsoon low pressure systems over the Indian region and their relationship with drought and excess monsoon seasonal rainfall*. COLA Tech. Rept. 217, Available at COLA, 4041, Powder Mill Road, Calverton, Md. USA.
- Sikka, D. R. and P. S. Rao (2008). The use and performance of mesoscale models over the Indian region for two high impact events. *Natural Hazards*, **44**, 353–372.
- Sikka D. R. (2011). Synoptic and meso-scale weather disturbances over South Asia during the Southwest Summer monsoon season, *In The Global Monsoon System* Ed. C.P. Chang *et al.*, World Scientific Forum, Singapore.
- Slingo, J. M. and N. Annamalai (2000). 1997: The El Nino of the century and the response of the Indian monsoon *Mon. Wea. Rev.*, **128**, 1778, 1797.
- Simon B., S. H. Rehman, and P. C. Joshi (2006). Conditions leading to onset of Indian monsoon: A satellite perspective, *Met. Atmos. Phys.*, DOI 10. 1007/B00703-005-0155–6.
- Simpson, G. (1921). The SW Monsoon, *Quart. J. Roy. Met. Society*.
- Singh, N., (1994). Optimizing a network of raingauges over India to monitor summer monsoon rainfall variations, *International J. Climatol.*, **14**, 61–70.
- Singh, O. P. (2003). Long term trends in the frequency of monsoonal cyclonic disturbances over the north Indian Ocean, *Mausam*, **52**, 655–658.
- Soman, M. K. and K. Krishna Kumar (1993). Space-time evolution of meteorological features associated with the onset of the Indian summer monsoon, *Mon. Wea. Rev.*, **121**, 1177–1194.
- Sperber, K. and T. N. Palmer (1994). Atmospheric Model Inter-companion Project. Monsoon Simulations. Prof. Int. Conf. on Monsoon variability and Prediction Trieste, WMD/TD-619, 601–608.
- Srinivasan, J., S. Gadgil, and P. J. Webster (1993). Meridional propagation of large scale convective zone, *Meteor. Atmos. Phys.*, **52**, 15–35.
- Suhas, E., J. M. Neena, and B. N. Goswami (2012a). Regime shift in Indian summer monsoon climatological intraseasonal oscillations. *Geophys. Res. Lett.*, **35**, L20703, doi:10.1029/2008GL035511
- Suhas, E. and B. N. Goswami (2008). An Indian monsoon intra-seasonal oscillation (MISO) index for real time monitoring and forecast verification, *Clim. Dyn.*, doi: 10.1007/s 00383-012-1462–3.
- Suhas, E., J. M. Neena, and B. N. Goswami (2012b). Inter-annual variability of Indian summer monsoon arising from interactions between seasonal mean and intra-seasonal oscillations, *J. Atmos. Sci.*, **69**, 1761–1774.
- Sundaram, S., R. Krishnan, A. Dey, and P. Swapna (2010). Dynamics of intensification of the boreal summer monsoon flow during IOD events, *Meteorol. Atmos. Phys.*, **107**, 17–31.
- Tabaldi, C. and R. Knutti (2010). The use of multi-model ensembles in probabilistic climatic projections, *Philos. Trans. Roy. Soc.*, **365**, 2053–2075.
- Taraphdar, S., P. Mukhopadhyay, and B. N. Goswami (2010). Predictability of Indian Summer Monsoon weather during active and break phases using a high resolution regional model, *Geophys. Res. Let.*, **37**, L21812, doi: 10229 / 2010 G L 044967
- Torrence, C. and P. J. Webster (1999). Interdecadal changes in the ENSO-monsoon system, *J. Climate*, **12**, 2679–2690.
- Vaidya, S. S. and J. R. Kulkarni (2006). Simulation of heavy precipitation over Santacruz, Mumbai on 26 July 2005 using meso-scale model, *Meteorol. Atmos. Phys.*, **98**, 55–66.
- Veechi, G. A. and D. E. Harrison (2002). Monsoon breaks and sub-seasonal temperature variability in the Bay of Bengal, *J. Clim.*, **15**, 1485–1493.
- Vernekar A. D., J. Zhou, and J. Shukla (1995). The effect of Eurasian snow cover on the Indian meteorological, *J. Climate*, **8**, 248–266.
- Vinayachandran, P. N., V. S. N. Murty, and V. Ramesh Babu (2002). Observations of barrier layer formation in the Bay of Bengal during summer monsoon. *J. Geophys. Res.*, **107**, 10291, JC000831.
- Waliser, D. E., K. M. Lau, W. Stern, and J. H. Kim (2003a). Potential predictability of the Madde Julian Oscillation. *Bull. Amer. Meteor. Soc.*, **84**, 33–50.

- Waliser, D. R., W. Stern, S. Schubert, and K. M. Lau (2003b). Dynamic predictability of intra-seasonal variability associated with the Asian summer monsoon, *Q.J.R. Meteorol. Soc.*, **129**, 2897–2925.
- Waliser, D. E., *et al.* (2003c). AGCM simulations of intra-seasonal variability associated with the Asian Monsoon, *Clim. Dyn.*, **21**, 423–446.
- Waliser, D. E., W. Stern, S. Schubert, and K. M. Lau (2003d). Dynamic predictability of intra-seasonal variability associated with the Asian Summer Monsoon, *J. Roy Met. Soc.*, **129**, 2897–2925.
- Walker, G. T. (1910 to 1924). Several papers on correlation in seasonal variation in weather *Mem. Ind. Met. Dept.*, **21**, 23 and 24.
- Walker, G. T. (1910). On the meteorological evidence for supposed changes of climate in India. *Mem. Ind. Met. Dept.*, **21**, 1–21.
- Walker, G. T. (1928). World weather, *Q. J. Roy. Meteor. Soc.*, **54**, 79–87.
- Walker, G. T. and E. W. Bliss (1932). World Weather V, Mem. *Roy. Meteor. Soc.* **4** (36), 53–84.
- Wang, B., P. J. Webster, and H. Teng (2005). Antecedents and self-induction of active-break south Asian monsoon modelling by satellites, *Geophys. Res. Lett.* **32**, L04704 der: 10.1029/2004GLO20996.
- Webster, P. J. (1987). The elementary monsoon, In *Monsoons* eds J. S. Fein and P. L. Stephens, *Wiley Int. Publ, John Wiley and sons*, New York, pp. 3–32.
- Webster, P. J., V. Magaña, T. Palmer, *et al.* (1998). Monsoon processes, predictability and the prospects for prediction. *J. Geophys. Res.*, **103**, 14451–14510.
- Webster, P. J. and S. Yang (1992). Monsoon and ENSO: Selectively interactive system, *Quart J. Roy Meteor. Soc.* **118**, 877–926.
- Wheeler, M. and H. H. Hendon (2004). An all-season real-time multivariate MJO Index Development of an index for monitoring and prediction, *Mon. Wea. Rev.*, **132**, 1917–1932.
- Wu, R. and B. Kirtman (2003). Biennial oscillation of the Monsoon – ENSO system in an interactive ensemble coupled GCM, *J. Climate*, **17**, 1623–1640.
- Wu, A. and B. Kirtman (2004). Understanding the impact of the Indian Ocean on ENSO variability in a coupled GCM. *J. Climate*, **17**, 4019–4031.
- Wu, G. and Y. Zhang (1998). Tibetan Plateau forcing and the timing of the monsoon onset over South Asia and the South China Sea, *Mon. Wea. Rev.*, **126**, 913–927.
- Xavier, P. K. and B. N. Goswami (2007). An analog method for real-time forecasting of summer monsoon sub-seasonal variability. *Mon. Wea. Rev.* **135**, 4149–4160.
- Yanai, M. and Z. Song (1992). Seasonal heating of the Tibetan Plateau and its effects on the evolution of the Asian Summer Monsoon. *J. Meteor. Soc. Japan*, **70**, 319–351.
- Yang, S. (1996). ENSO-snow – monsoon associations and seasonal inter-annual predictions, *Int. J. Climatol.*, **16**, 125–134.
- Yasunari, T. (1980). A quasi-stationary appearance of 30–40 day period in the cloudiness fluctuations during the summer monsoon over India. *J. Meteor. Soc. Japan*, **58**, 225–229.
- Yasunari, T. (1981). Structure of the Indian monsoon system with around 40-day-period. *J. Meteor. Soc. Japan*, **59**, 225–229.
- Yasunari, T., A. Kitoh, and T. Tokioka (1991). Local and remote responses to excessive snow mass over Eurasia appearing in the northern spring and summer climate – a study with MRT-GCM, *J. Meteor. Soc. Japan*, **67**, 473–487.
- Zhang, L. and T. Zhou (2011). An assessment of monsoon precipitation changes during 1901–2011, *Clim. Dyn.*, **37**, 279–296.
- Zhang, X. and E. Lu (2004). Globally unified monsoon onset and retreat indices. *J. Climate*, **17**, 2241–2248.
- Zhang C. (2005). Madden Julian Oscillation, *Rev. Geophysics*, **43**, RQ 2003 / 2005
- Zuluago M. D., C. D. Hoyos, and P. J. Webster (2010). Spatial and temporal distribution of latent heating in the South Asian monsoon region, *J. Clim.*, **23**, 2010–2029.

# 26

## Interannual variability and predictability of summer climate over the Northwest Pacific and East Asia

Shang-Ping Xie and Yu Kosaka

### 26.1 Introduction

Over monsoon Asia, from India to China, summer is the rainy season, and June–August (JJA) rainfall accounts for 50% or more of the annual total. In particular, over East Asia during June and July, a rainband oriented from the southwest towards northeast, known as the Meiyu in China, Changma in Korea, and Baiu in Japan, extends from the eastern flank of the Tibet Plateau, through Japan, to the Northeast Pacific. In late July, this rainband moves north and diffuses (Ueda *et al.*, 1995), bringing much needed rainfall to the usually dry area of northern China. With more than 1 billion people living in the region, summer climate variability has important socio-economic impacts; e.g. the 1993 rice harvest failure in Japan caused by excessive rainfall and insufficient sunlight, the great Yangtze flood of 1998, and the record heat waves of 2010 in Japan and 2013 in southeastern China.

The leading empirical orthogonal function (EOF) mode of interannual rainfall variability in the Northwest (NW) Pacific region for June and July features a band of increased precipitation from eastern China through southern Japan, which represents an intensification of the climatological rainband (Fig. 26.1a). This mode of Meiyu–Baiu variability is correlated with a decrease of rainfall in the tropics, over and east of the Philippines. This meridional dipole of rainfall anomalies is called the Pacific–Japan (PJ) pattern, and was first detected from satellite high-cloud observations (Nitta, 1987). The PJ pattern also features a meridional dipole of low-level circulation anomalies, which, in the polarity of Fig. 26.1, represents a southwestward shift of the NW Pacific subtropical high (PASH). The mode of NW Pacific rainfall variability is correlated with the El Niño/Southern Oscillation (ENSO), not concurrently, but peculiarly with the ENSO events that peak in the preceding winter (November–January; NDJ) and have dissipated by summer (Fig. 26.1b). Climate anomalies over East Asia during post-ENSO summers are well known (Huang *et al.*, 2004), but their causes and mechanisms remain poorly understood.

Rapid progress has been made in characterizing and understanding interannual variability over the NW Pacific and East Asia, and this paper reviews recent scientific advances in climate variability and predictability in this region. One important advance is the recognition of tropical Indian Ocean (IO) effects on summer anomalies of NW Pacific climate, including the PJ pattern. Sections 26.2 and 26.3 discuss the dynamics and predictability, respectively, of the tropical Indo-NW Pacific climate in summer. Section 26.4 outlines the challenges associated with predicting summer climate anomalies over East Asia, and Section 26.5 presents a summary.

### 26.2 Tropical Indo-NW Pacific variability

A typical El Niño event, as measured by sea surface temperature (SST) in the Niño3.4 region, begins to develop during summer, peaks in winter, and decays rapidly in the following spring (Fig. 26.2). Via an atmospheric bridge, El Niño causes SST to increase over the tropical IO with a time lag of one season (Klein *et al.*, 1999), and this IO warming persists through the summer (Fig. 26.2). By the summer, Niño3.4 SST anomalies have dissipated, and the most robust SST anomalies are found over the tropical IO, while the most pronounced surface atmospheric anomalies are over the NW Pacific as the PJ pattern. These ocean–atmosphere anomalies are the last echo of El Niño, and include reduced rainfall east of the Philippines (Fig. 26.1) and an anomalous anticyclone with easterly anomalies on its south flank that extend from the NW Pacific to the northern IO (Fig. 26.3).

From an atmospheric viewpoint, the persistent IO warming induces the atmospheric anomalies in the post-El Niño summer through the so-called capacitor effect (Yang *et al.*, 2007, Xie *et al.*, 2009). The IO warming excites a warm atmospheric Kelvin wave that propagates into the Pacific, as seen in tropospheric temperatures in

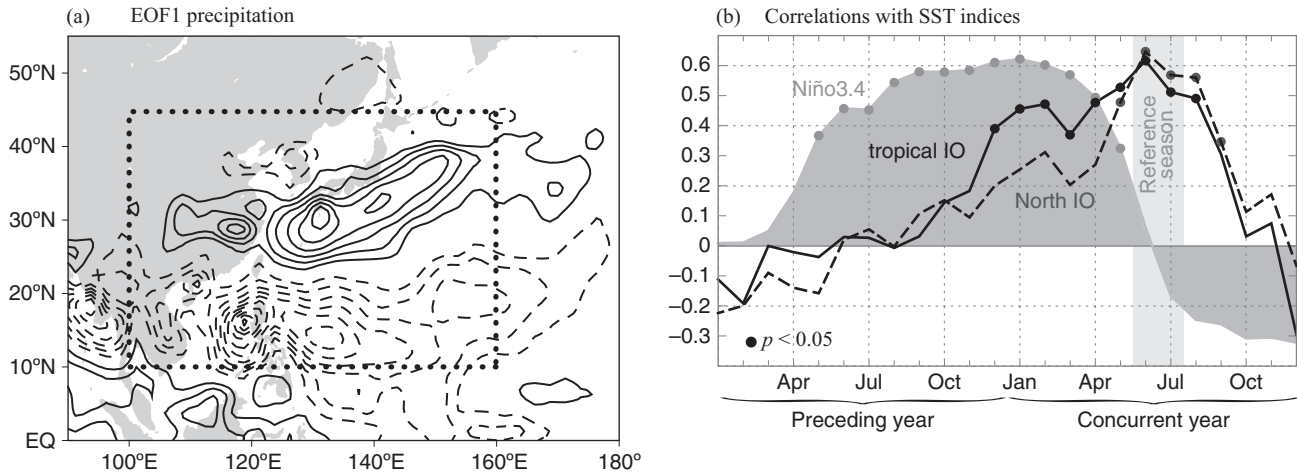


Fig. 26.1. (a) Precipitation anomalies (contour interval:  $0.3 \text{ mm day}^{-1}$ , with the zero contour removed) regressed onto the leading PC of June–July precipitation over  $[10\text{--}45^\circ\text{N}, 100\text{--}160^\circ\text{E}]$  (dotted box). (b) Lagged correlations of the PC with Niño3.4 (dark shading) and tropical ( $20^\circ\text{S}\text{--}20^\circ\text{N}, 40\text{--}100^\circ\text{E}$ ; solid curve) and northern ( $5\text{--}25^\circ\text{N}, 40\text{--}100^\circ\text{E}$ ; dashed curve) IO SST. Dots indicate statistical confidence  $>95\%$ . Based on detrended GPCP (Adler *et al.*, 2003) and HadISST (Rayner *et al.*, 2003) with 1979–2012 reference period.

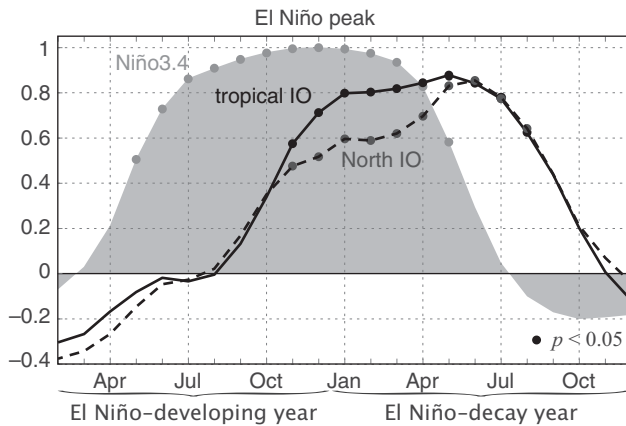


Fig. 26.2. Lagged correlations of monthly SST anomalies over the Niño3.4 region (shading) and the tropical ( $20^\circ\text{S}\text{--}20^\circ\text{N}, 40\text{--}100^\circ\text{E}$ ; solid curve) and northern ( $5\text{--}25^\circ\text{N}, 40\text{--}100^\circ\text{E}$ ; dashed curve) IO with respect to NDJ Niño3.4 SST. Dots indicate statistical confidence  $>95\%$ . Based on detrended HadISST with 1978/79–2011/12 reference period.

Fig. 26.3b, with easterly anomalies trapped on the equator in the free troposphere. In the planetary boundary layer, surface friction forces surface wind towards the low pressure trough on the equator and induces divergence on the northern flank of the Kelvin wave (Fig. 26.3b). In the tropical NW Pacific, the surface wind divergence suppresses convection (Fig. 26.1a), and the convection–circulation feedback amplifies the anomalies of reduced rainfall and the surface anticyclone (Fig. 26.3a). The convection–circulation feedback is strong in the summer hemisphere due to abundant climatological precipitation,

and explains why surface atmospheric anomalies are not as pronounced south of the equator, despite the symmetric Kelvin wave. The NW Pacific surface anticyclone extends westward to the northern IO as a high-pressure Rossby wave (Fig. 26.3a).

From an oceanic viewpoint, the northern IO warming is partially a response to the anomalous anticyclonic circulation that extends from the northern IO to the NW Pacific (Fig. 26.3a). Specifically, the easterly anomalies on the southern flank of the anticyclone weaken the prevailing southwesterly monsoonal winds, reduce surface evaporation, and contribute to ocean warming over the northern IO and South China Sea (SCS; Fig. 26.3a; Du *et al.*, 2009). The importance of the southwesterly mean flow in driving this mechanism is apparent in the development of a summer peak in the northern IO warming during June and July following the onset of the southwest summer monsoon (Fig. 26.2a).

The circular argument outlined above suggests a positive feedback between the IO warming and atmospheric anticyclone: the IO warming excites the anticyclonic circulation, which in turn amplifies the warming over the northern IO and SCS (Kosaka *et al.*, 2013). The tropical precipitation anomalies over the NW Pacific trigger the PJ pattern that affects East Asia. While the PJ pattern can arise as an atmospheric internal mode (Kosaka and Nakamura, 2010), a large part of the PJ variance (estimated as 64% by Kosaka *et al.*, 2013) is associated with this IO–PJ coupled mode. The conditions necessary for this coupled mode include the southwesterly mean winds over the northern IO–SCS, and strong convective feedback over the tropical NW Pacific. These conditions are met during the summer

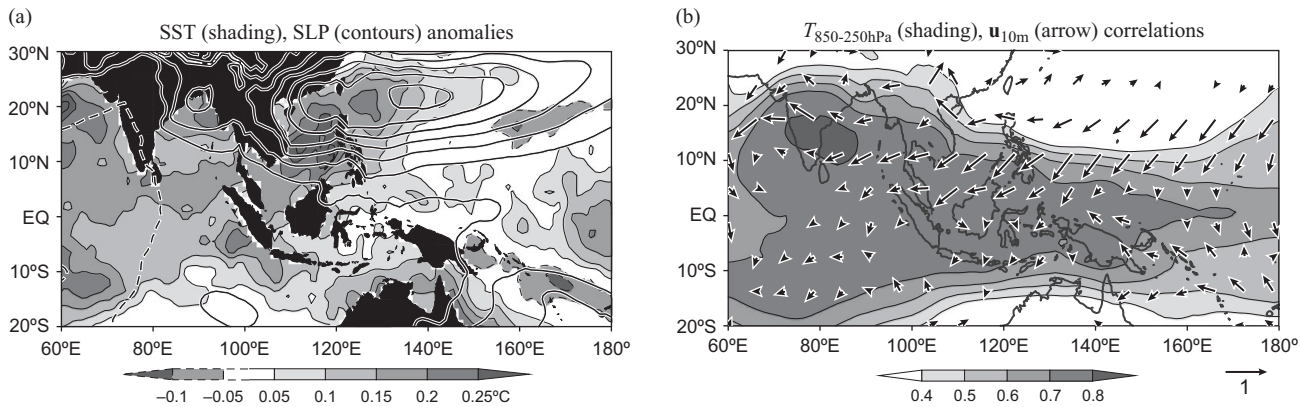


Fig. 26.3. (a) Regressed anomalies of SST (shading) and SLP (contours with an interval of 0.1 hPa; the zero contour removed), and (b) correlations of 850–250 hPa temperature (shading) and surface wind velocity (arrows) in JJA with respect to Niño3.4 SST in preceding NDJ. Based on detrended HadISST and JRA55 (Ebita *et al.*, 2011) with the 1978/79–2011/12 reference period.

season. The coupled IO–PJ mode can exist without ENSO, but El Niño-induced pre-summer IO warming sets this mode in motion, explaining why the last echo of El Niño is most pronounced over the Indo-NW Pacific during post-El Niño summers.

The IO–PJ mode affects the counts and tracks of tropical cyclones (TCs) over the NW Pacific. While summer TC counts do not correlate with ENSO during the ENSO-developing year, they tend to decrease during post-El Niño summers due to atmospheric circulation anomalies (Du *et al.*, 2011). For example, TC counts were very low for 1998 and 2010, both summers following El Niño. In addition, the southwestward extension of the NW PASH during post-El Niño summers prevents TCs moving northward. As a result, TC occurrence over the East China and Yellow seas, and landfall in coastal central and northern China, are reduced (Choi *et al.*, 2010, Wang *et al.*, 2013).

### 26.3 Tropical predictability

The leading EOF mode (EOF1) of summer (JJA) sea level pressure (SLP) variability over the NW Pacific features the anomalous anticyclone, which in association with a cyclone to the north, forms the PJ pattern (Fig. 26.4a). Chowdary *et al.* (2010) examined the seasonal reforecast from an ensemble of 11 coupled ocean–atmosphere general circulation models (GCMs), each for at least 22 years. Each model makes 9–15 member forecasts each year, initialized on 1 May. The models capture the EOF1 of SLP (Fig. 26.4b). The correlations between the predicted and observed principal components (PC1s) range from 0.5 to 0.7, with that for the multi-model ensemble (MME) mean forecast being 0.7.

The SLP pattern is anchored by SST warming over the northern IO/SCS. The two have a correlation coefficient of 0.6 in observations, and the correlation is much higher for the MME. Figure 26.4c and d illustrate the coupling between wind and SST anomalies during summer, which is especially well defined in the MME, in support of the coupled IO–PJ mode. The weakening of the southwesterly mean flow helps to warm the northern IO/SCS, while the ocean warming excites the circulation pattern of which the easterly wind anomalies are a part. Overall, the MME wind and SST coupling seems more robust than in the observations, with coupled wind and SST anomalies persisting well through September, possibly due to the heavy averaging that suppresses noise.

While the anticyclone covers a broad area from the northern IO through the international dateline, the easterly anomalies cause a zonal dipole of scalar wind speed, which is negative in the prevailing westerly and positive in the mean easterly regime (Fig. 26.4c and d). The scalar wind increases in the mean easterly regime cool SST, helping to drive the anticyclone by forcing atmospheric Rossby waves (Wang *et al.*, 2000). The apparent eastward propagation of the nodal line for the SST/scalar wind dipole is due to the eastward expansion of the mean monsoon westerlies over time. The SST cooling in the mean easterly regime seems excessive in the MME when compared with the observational data.

The MME forecast at a one-month lead (i.e. initialized on 1 May) is remarkably successful in producing many features of Indo-NW Pacific climate anomalies in post-El Niño summers (Fig. 26.4e–h). They include the IO-SCS warming, anomalous anticyclonic circulation with easterly anomalies on the south flank, the Kelvin wave wedge in tropospheric temperature that penetrates from the IO to the Pacific, reduced rainfall over the tropical NW Pacific, and

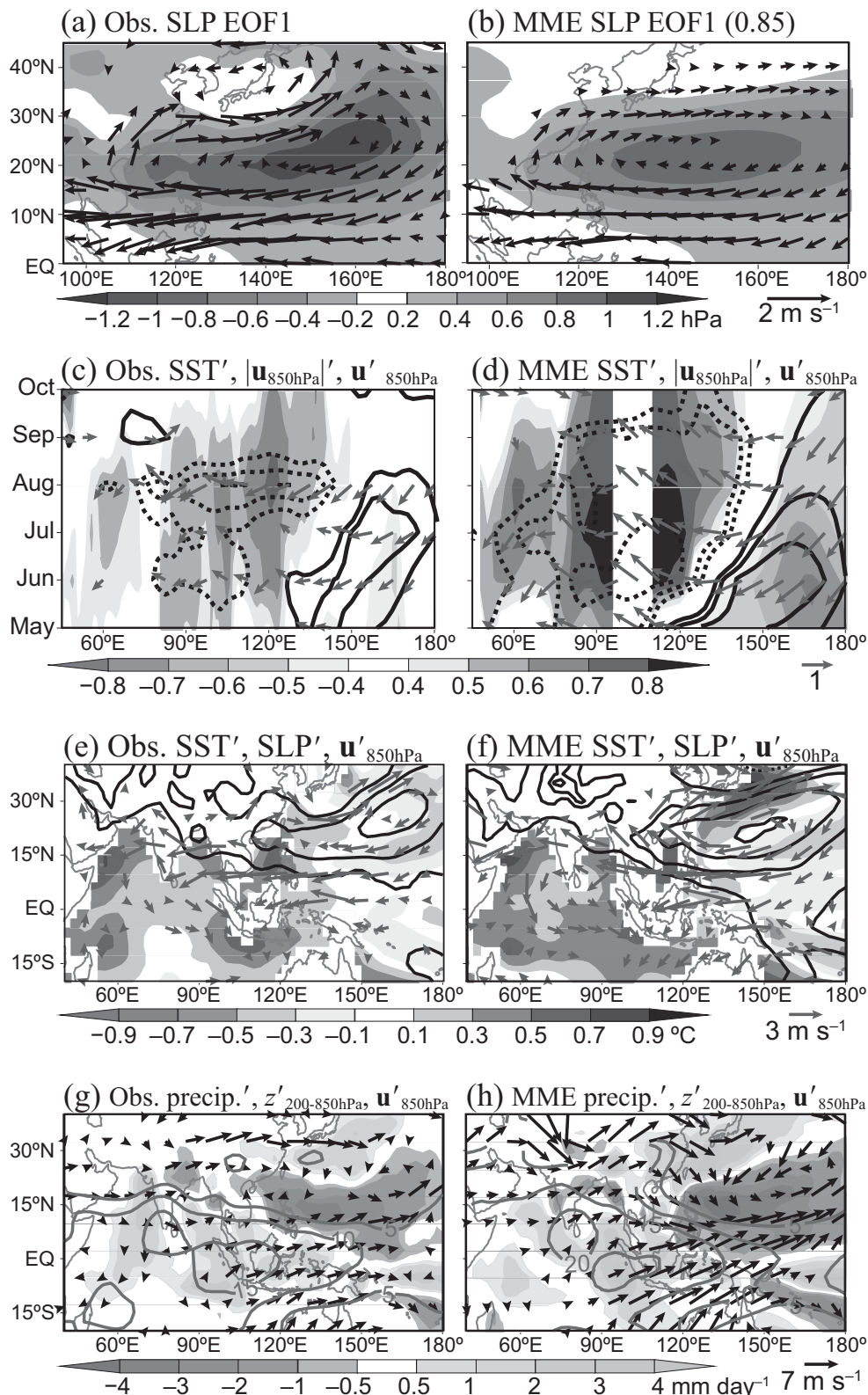


Fig. 26.4. (a,b) The leading EOF of JJA SLP (shading) and anomalies of 850 hPa wind velocity regressed against the corresponding PC. Pattern correlation coefficient between the two EOFs is 0.85. (c,d) Lag correlations of 5–20°N SST (shading), 850 hPa wind speed (contours; plotted for  $\pm 0.4$ ,  $\pm 0.6$ ,  $\pm 0.8$ ), and wind velocity (arrows) with respect to the PC. (e–h) Anomalies of (e,f) SST (shading), SLP (contours; plotted for 0.5, 1, 1.5, 2 hPa), and 850 hPa wind velocity (arrows), and (g,h) precipitation (shading), 850–200 hPa thickness (contours; plotted for 5, 10, 15, 20 gpm), and 200 hPa wind velocity (arrows) composited for JJA 1983, 1992, and 1998. (left) Observations and (right) MME for 11 seasonal hindcasts. HADISST, NCEP-DOE reanalysis (Kanamitsu *et al.*, 2002), and CMAP (Xie and Arkin, 1997) were used as observations. From Chowdary *et al.* (2010). A black and white version of this figure will appear in some formats. For the colour version, please refer to Plate 32.

increased precipitation to the north over East Asia. Thus, the coupled IO–PJ mode, when properly initialized, enables the prediction of atmospheric anomalies over the NW Pacific and East Asia during post-ENSO summers.

## 26.4 East Asian predictability

Whereas the PJ pattern is seasonally predictable to a large extent due to tropical ocean–atmosphere coupling, recent studies have revealed zonal wave-like teleconnections in the extratropics that perturb the East Asian summer climate. Figure 26.5a features two Rossby wave guides over the Eurasian sector, each associated with a large meridional gradient of mean potential vorticity. One corresponds to the Asian jet (ca. 40°N), a subtropical jet blowing on the northern periphery of the Tibetan (Asian) High. The other forms along the polar front jet (PFJ), anchored by the meridional temperature gradient between the Eurasian continent and the Arctic Ocean. Along these wave guides, there is large interannual variability in the meridional wind at 40°N and around 60°N (Fig. 26.5b). Figure 26.6 shows such wave trains that developed in 2003 and 2010, which coincided with extremely cold and hot summers, respectively, in Japan. Cyclonic (anticyclonic) circulation anomalies are

evident over northern China and Japan in 2003 (2010). These wave trains are rather unpredictable at monthly to seasonal leads, as discussed below.

### 26.4.1 The Silk Road pattern along the Asian jet

The wave train along the subtropical Asian jet is known as the Silk Road pattern (Enomoto, 2004; Fig. 26.7), affecting the NW PASH and summer East Asian climate. Recent Silk Road events include record hot summers in Japan in 2004 and 2010 (Fig. 26.6b), and the record cold summer in 2003 (Fig. 26.6a). The Silk Road pattern is often represented by the first and second EOF modes of meridional wind variability along the Asian jet, with a quarter-wavelength zonal phase difference between them (Fig. 26.7). The PCs, in any linear combinations (i.e. any zonal phases) are not correlated with ENSO in the preceding or following winter at the 90% significance level (Kosaka *et al.*, 2012). The absence of effective ENSO forcing sets serious limitations on the seasonal predictability of the Silk Road pattern.

Indeed, seasonal prediction models do not reliably reproduce the observed temporal phase of the Silk Road pattern (Kosaka *et al.*, 2012). Individual seasonal hindcasts by coupled GCMs initialized on 1 May feature the realistic spatial structure of the Silk Road pattern as internal modes,

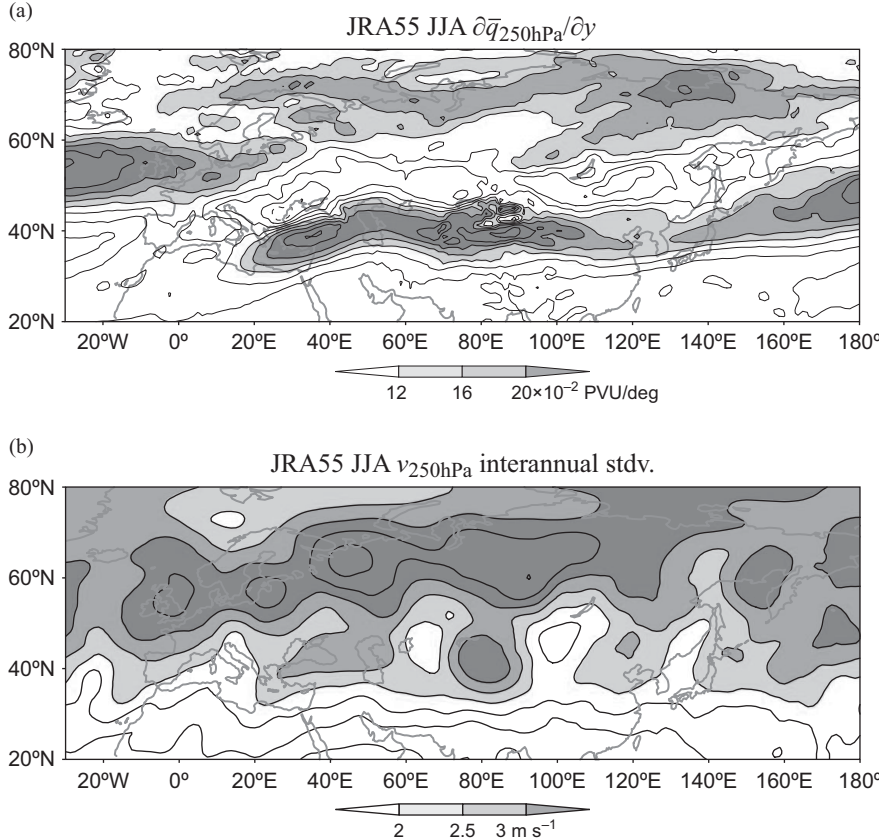


Fig. 26.5. (a) Meridional gradient of climatological potential vorticity at 250 hPa in JJA. (b) Interannual standard deviation of 250 hPa meridional wind velocity in JJA. Contour interval is (a)  $4 \times 10^{-2}$  PVU deg $^{-1}$ , and (b)  $0.5 \text{ ms}^{-1}$ , with shading for values larger than (a)  $12 \times 10^{-2}$  PVU deg $^{-1}$ , and (b)  $2 \text{ ms}^{-1}$ . Based on JRA55 for 1979–2012.

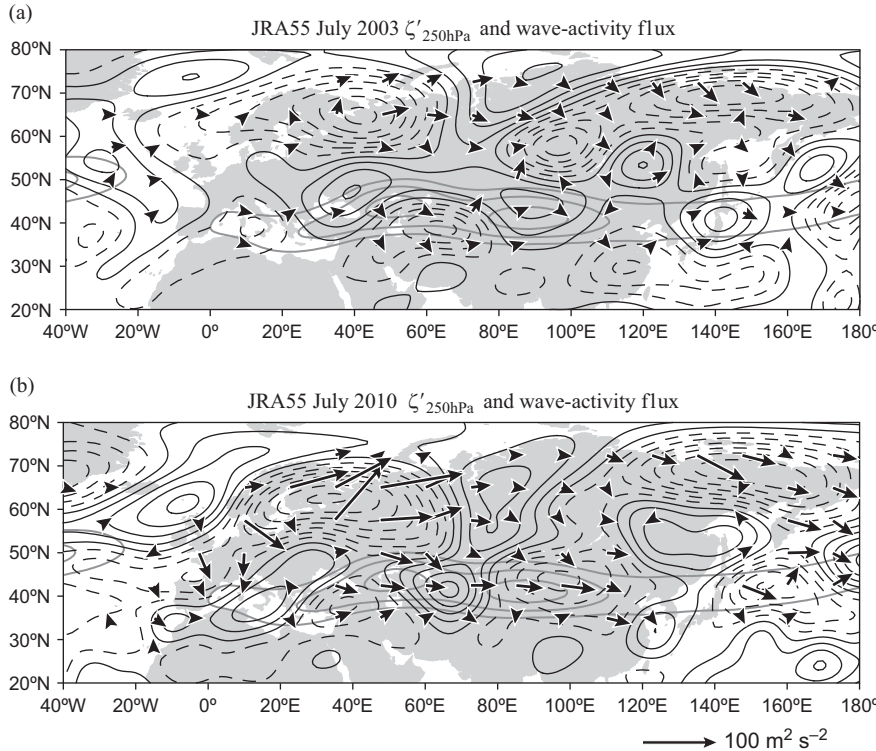


Fig. 26.6. Observed anomalies of 250 hPa vorticity (thin contours; plotted with an interval of  $6 \times 10^{-6} \text{ s}^{-1}$  from  $-39$  to  $+27 \times 10^{-6} \text{ s}^{-1}$ ) in (a) July 2003 and (b) July 2010 based on 1979–2012 climatology. Arrows indicate the associated wave-activity flux (Takaya and Nakamura, 2001). Thick lines show 20, 25, and 30  $\text{ms}^{-1}$  contours of climatological zonal wind velocity at 200 hPa. Based on JRA55.

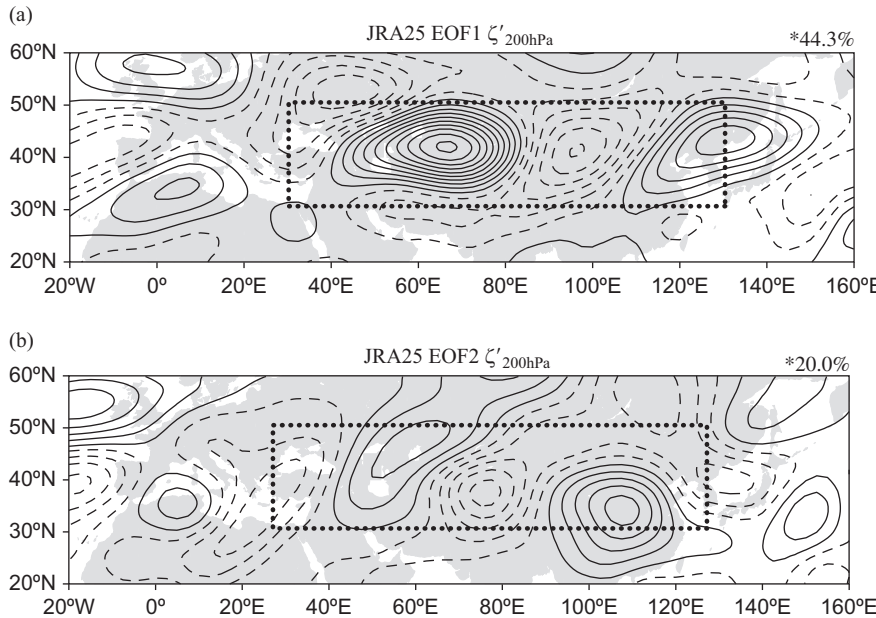


Fig. 26.7. The 200 hPa vorticity anomalies (plotted with an interval of  $1 \times 10^{-6} \text{ s}^{-1}$  from  $-5.5$  to  $+9.5 \times 10^{-6} \text{ s}^{-1}$ ) regressed onto the (a) leading and (b) second PCs of 200 hPa meridional wind over  $[30\text{--}50^\circ\text{N}, 30\text{--}130^\circ\text{E}]$  (dotted boxes) in JJA. Corresponding variance fractions are shown in the upper right corner of each panel, with asterisks indicating that the two EOF modes are significantly isolated based on the criteria of North *et al.* (1982). Based on JRA25 (Onogi *et al.*, 2007) for 1979–2009.

as shown in high pattern correlations for the EOF modes (Table 26.1). In spite of the skill in simulating the spatial pattern of the internal modes, the signal-to-noise ratio (defined as the variance of the ensemble-mean PC divided by the inter-member variance of the PC) is typically 0.1–0.3 (Table 26.1), indicating that the temporal phase of the pattern is unpredictable.

The summer circumglobal teleconnection (CGT) pattern is defined as the second EOF mode of 200 hPa geopotential height variability over the Northern Hemisphere (Ding and Wang, 2005). It correlates with the developing ENSO. The CGT contains a zonal-mean component, while, by design, the Silk Road pattern emphasizes zonal-wavy variability. The zonal phase of the Silk Road pattern is

Table 26.1. Summary of the Silk Road pattern in seasonal prediction models examined in Section 26.4.1, showing hindcast period, ensemble sizes, pattern correlations with observational counterparts, and the signal-to-noise (S/N) ratios measured as the variance of the ensemble-mean PC divided by the inter-member variance of the PC. The S/N ratio is shown in boldface (and with an asterisk or a dagger) if the ensemble can be significantly distinguished from white noise at a confidence level of 90% (or 95% or 99%, respectively), based on the Monte-Carlo method. From Kosaka et al. (2012).

Model	Hindcast period	Ensemble size	Pattern correlation with JRA25 EOFs		Var(ensemble-mean PC) / Var(inter-member PC)		
			EOF1	EOF2	PC1	PC2	PC1+PC2
NCEP CFS	1981–2003	15	0.73	0.62	0.08	0.05	0.07
BMRC POAMA1.5	1980–2002	10	0.90	0.79	<b>0.22†</b>	<b>0.18*</b>	<b>0.20*</b>
FRCGC SINTEX-F	1982–2004	9	0.96	0.89	0.07	<b>0.20</b>	0.11
SNU	1980–2001	6	0.38	0.28	0.13	<b>0.34*</b>	0.22
JMA	1979–2008	5	0.42	0.53	<b>0.42*</b>	0.35	<b>0.39</b>

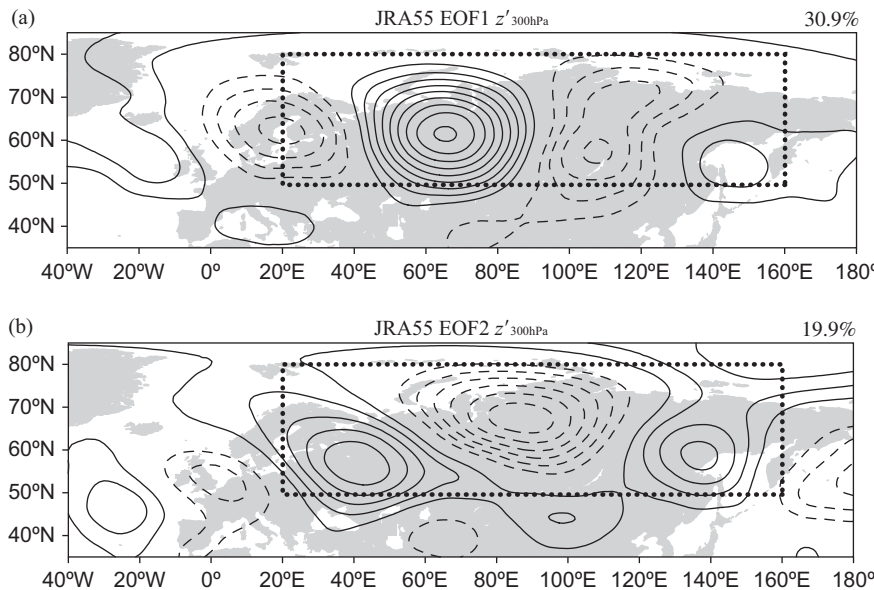


Fig. 26.8. Anomalies associated with the (a,c,d) leading and (b,e,f) second PCs of 300 hPa meridional wind over [50–80°N, 20–160°E] (dotted boxes) in JJA. (a,b) Regressed anomalies of 300 hPa geopotential height (contour interval: 5 gpm). Corresponding variance fractions are shown in the upper right corner of each panel. The two EOF modes are not significantly isolated based on the criteria of North et al. (1982). (c–f) Regressed anomalies of (c,e) SLP (contours with an interval of 0.1 hPa) and surface wind (arrows), and (d,f) surface air temperature (contour interval: 0.1 °C). The zero contours are suppressed in all panels. Based on JRA55 for 1979–2012.

anchored by zonal variations in the climatological Asian jet (Kosaka et al., 2009), as evident in Figs. 26.5 and 26.6. The wavy component of the CGT pattern is zonally in phase with the Silk Road EOF1 pattern over the Eurasian sector. It appears that the long zonal wave component of the CGT is correlated with ENSO (Seager et al., 2003) and hence predictable, whereas the wavy component is not (Lee et al., 2011).

The Silk Road pattern may be viewed as the least damped mode of the dry atmosphere (Kosaka et al., 2009) and is excited by a blocking formation upstream,

as in the 2010 Russian blocking event. Otomi et al. (2013) suggest a potential contribution from North Atlantic SST anomalies to the Russian blocking. While this connection to SST offers hopes for improved seasonal predictions (Yasui and Watanabe, 2010), predicting blocking development remains challenging.

#### 26.4.2 The PFJ wave train pattern

Anomalous development of the surface Okhotsk high is another source of variability in the East Asian summer

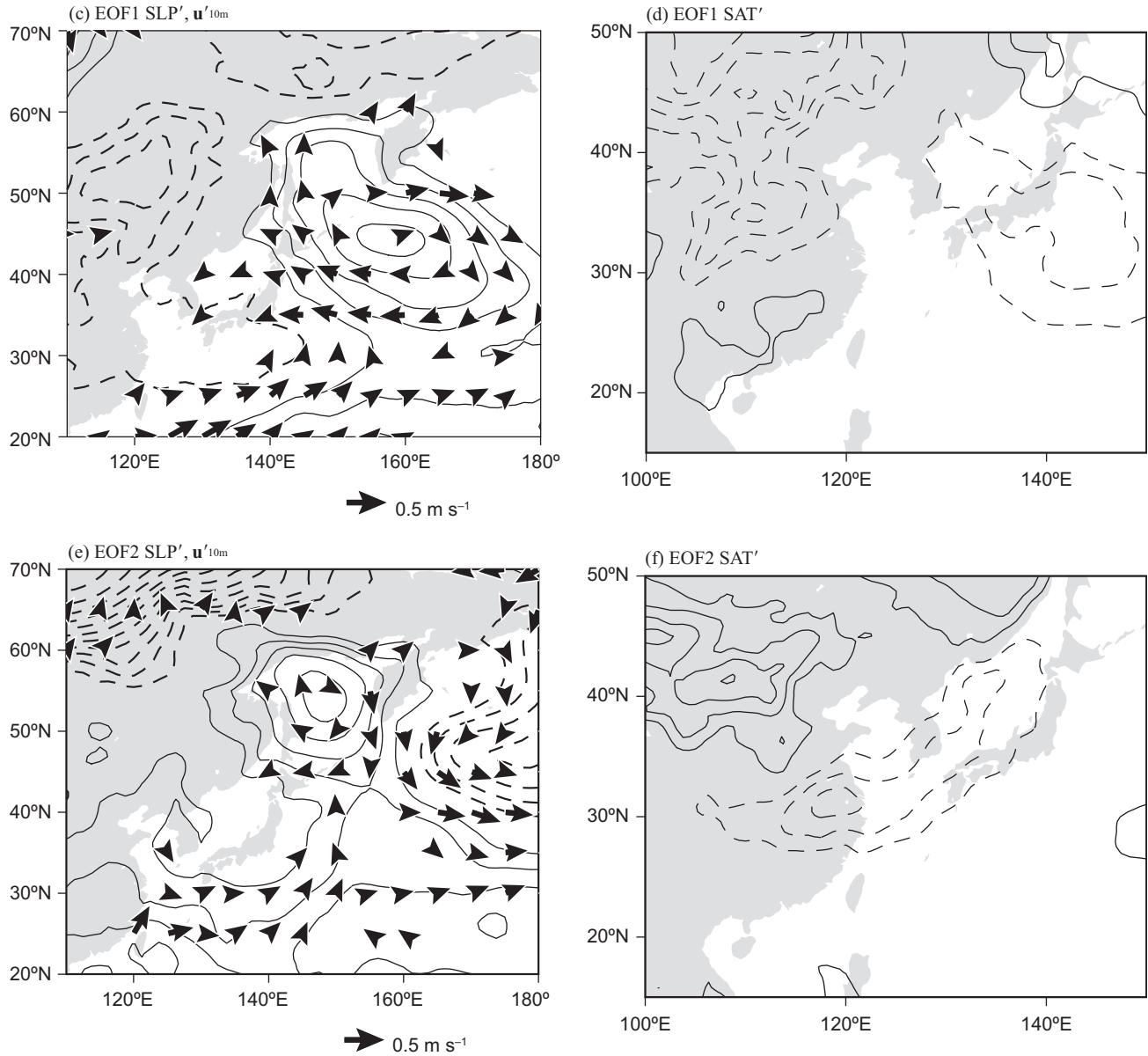


Fig. 26.8. (cont.)

climate. An intensified Okhotsk high prevents the northward seasonal shift of the Meiyu–Baiu rainband, and the resultant insolation deficit, combined with surface cold advection by the northeasterlies, brings cold and wet summers to Japan, Korea, and eastern China (Fig. 26.8e and f). The surface Okhotsk high accompanies an upper-level blocking anticyclone. This East Siberian blocking is in turn associated with a wave-like teleconnection along the PFJ (Nakamura and Fukamachi, 2004). The cold summers of 1993 and 2003 in Japan were caused by an anomalously strong Okhotsk high (negative vorticity anomalies in Fig. 26.6a).

Figure 26.8 shows the PFJ wave train patterns. The second EOF (EOF2) is associated with the development of the Okhotsk high (Fig. 26.8e), and EOF1 has some projection onto the climatological high at the surface (Fig. 26.8c). (The two EOFs are not well separated statistically.) In any combination, the PCs are not correlated significantly with ENSO in either the preceding or subsequent winter, and the correlation with SST is globally low (figure not shown). These results suggest that seasonal predictability of the PFJ wave train pattern is limited. There are patches of moderate SST correlations over the North Atlantic (Kimoto, 2005) and Barents Sea (Ogi *et al.*,

2004). Complicating the matter even more is the tenuous relationship between the PFJ wave train and the surface Okhotsk high. The zonal phase of the PFJ wave train is similar between 2003 and 2010 across the Eurasian Continent (Fig. 26.6), but the Okhotsk high intensified at the surface only in 2003. Further studies are needed for the PFJ wave trains.

## 26.5 Summary

ENSO is a mode of Pacific ocean–atmosphere interaction and naturally has the centre of action over the Pacific during the developing to peak phase. During post-ENSO summers, equatorial Pacific SST anomalies have largely dissipated, but ocean–atmosphere anomalies linger in the Indo-NW Pacific, and are manifested specifically as IO warming and an anomalous anticyclone over the NW Pacific. While the IO warming is traditionally viewed as a passive response to El Niño, recent studies show that it is coupled with the PJ pattern, and the coupled feedback allows the ocean–atmospheric anomalies to persist through the summer, explaining why the last echo of El Niño is found displaced into the Indo-NW Pacific. The summer IO–PJ mode is highly predictable at a lead time of one to three months in coupled models that are initialized properly.

While the IO–PJ mode offers predictability for the tropical Indo-NW Pacific region, serious challenges remain for climate prediction over mid-latitude East Asia because of perturbations from the west along the wave guides of the Asian jet and PFJ. The analysis of a large MME forecast shows that the temporal phase of the Silk Road pattern along the subtropical jet is not predictable. Low seasonal predictability is similarly suggested for the PFJ wave train pattern. These zonal wave-like teleconnections are dominated by atmospheric internal variability, highlighting the importance of uncertainty assessment in predictions. European blocking, sometimes triggering the Silk Road and PFJ wave train patterns, is predictable a week in advance (Matsueda, 2009), and persists for a few weeks. It takes a few more days for perturbation energy to propagate along the jets from Europe to East Asia. These mechanisms can be exploited for extended weather prediction.

Models perform poorly in simulating the climatology and variability of the Meiyu–Baiu rainband (Ninomiya, 2009). Rainfall and latent heating anomalies in the Meiyu–Baiu region are important to form the full meridional dipole of the PJ pattern (Lu and Lin, 2009). Improved understanding and simulation of the Meiyu–Baiu may help to exploit the tropical predictability more fully via the PJ pattern.

The amplitude of ENSO displays a pronounced variance cycle on interdecadal to centennial time scales (Li *et al.*,

2013, Ogata *et al.*, 2013). The correlation between summer IO SST and the preceding ENSO shows substantial interdecadal modulations (Chowdary *et al.*, 2012), apparently following the ENSO variance cycle. The correlation was high at the turn of the twentieth century and after the 1970s, both periods with high ENSO variance. There is evidence that the correlation between the PJ pattern and preceding ENSO was also high during these periods, but low during the rest of the twentieth century (Kubota *et al.*, 2015) when ENSO variance was low. This indicates the importance of non-ENSO related noise, which can overwhelm ENSO's last echo over the Indo-NW Pacific region when the ENSO amplitude is low.

## References

- Adler, R. F., Huffman, G. J., Chang, A., *et al.* (2003). The version-2 global precipitation climatology project (GPCP) monthly precipitation analysis (1979–present). *Journal of Hydrometeorology*, **4**, 1147–1167.
- Choi, K.-S., Wu, C.-C., and Cha, E.-J. (2010). Change of tropical cyclone activity by Pacific-Japan teleconnection pattern in the western North Pacific. *Journal of Geophysical Research*, **115**, D19114.
- Chowdary, J. S., Xie, S.-P., Lee, J.-Y., Kosaka, Y., and Wang, B. (2010). Predictability of summer Northwest Pacific climate in 11 coupled model hindcasts: Local and remote forcing. *Journal of Geophysical Research*, **115**, D22121, doi:10.1029/2010JD014595.
- Chowdary, J. S., Xie, S.-P., Tokinaga, H., *et al.* (2012). Interdecadal variations in ENSO teleconnection to the Indo-western Pacific for 1870–2007. *Journal of Climate*, **25**, 1722–1744.
- Ding, Q. and Wang, B. (2005). Circumglobal teleconnection in the Northern Hemisphere summer. *Journal of Climate*, **18**, 3483–3505.
- Du, Y., Xie, S.-P., Huang, G., and Hu, K. (2009). Role of air–sea interaction in the long persistence of El Niño-induced north Indian Ocean warming. *Journal of Climate*, **22**, 2023–2038.
- Du, Y., Yang, L., and Xie, S.-P. (2011). Tropical Indian Ocean influence on Northwest Pacific tropical cyclones in summer following El Niño. *Journal of Climate*, **24**, 315–322.
- Ebita, A., Kobayashi, S., Ota, Y., *et al.* (2011). The Japanese 55-year Reanalysis “JRA-55”: An interim report. *Scientific Online Letters on the Atmosphere*, **7**, 149–152.
- Enomoto, T. (2004). Interannual variability of the Bonin high associated with the propagation of Rossby waves along the Asian jet. *Journal of the Meteorological Society of Japan*, **82**, 1019–1034.
- Huang, R., Chen, W., Yang, B., and Zhang, R. (2004). Recent advances in studies of the interaction between the East Asian winter and summer monsoons and ENSO cycle. *Advances in Atmospheric Sciences*, **21**, 407–424.
- Kanamitsu, M., Ebisuzaki, W., Woollen, J., *et al.* (2002). NCEP–DOE AMIP-II Reanalysis (R-2), *Bulletin of the American Meteorological Society*, **83**, 1631–1643.

- Kimoto, M. (2005). European heat wave and cool summer in Japan in 2003. *Tenki (Bulletin journal of the Meteorological Society of Japan)*, **52**, 608–612 (in Japanese).
- Klein, S. A., Soden, B. J., and Lau, N.-C. (1999). Remote sea surface temperature variations during ENSO: Evidence for a tropical atmospheric bridge. *Journal of Climate*, **12**, 917–932.
- Kosaka Y. and Nakamura, H. (2010). Mechanisms of meridional teleconnection observed between a summer monsoon system and a subtropical anticyclone. Part I: The Pacific-Japan pattern. *Journal of Climate*, **23**, 5085–5108.
- Kosaka, Y., Chowdary, J. S., Xie, S.-P., Min, Y.-M., and Lee, J.-Y. (2012). Limitations of seasonal predictability for summer climate over East Asia and the Northwestern Pacific. *Journal of Climate*, **25**, 7574–7589.
- Kosaka, Y., Nakamura, H., Watanabe, M., and Kimoto, M. (2009). Analysis on the dynamics of a wave-like teleconnection pattern along the summertime Asian jet based on a reanalysis dataset and climate model simulations. *Journal of the Meteorological Society of Japan*, **87**, 561–580.
- Kosaka, Y., Xie, S.-P., Lau, N.-C., and Vecchi, G. A. (2013). Origin of seasonal predictability for summer climate over the Northwestern Pacific. *Proceedings of the National Academy of Sciences of the United States of America*, **110**, 7574–7579.
- Kubota, H., Y. Kosaka, and S. -P. Xie (2015). A 117-year long index of the Pacific-Japan pattern with application to interdecadal variability. *International Journal of Climatology*, in press, doi:10.1002/joc.4441.
- Lee, J.-Y., Wang, B., Ding, Q., et al. (2011). How predictable is the northern hemisphere summer upper-tropospheric circulation? *Climate Dynamics*, **37**, 1189–1203.
- Li, J., Xie, S.-P., Cook, E. R., et al. (2013). El Niño modulations over the past seven centuries. *Nature Climate Change*, **3**, 822–826.
- Lu, R. and Lin, Z. (2009). Role of subtropical precipitation anomalies in maintaining the summertime meridional teleconnection over the western North Pacific and East Asia. *Journal of Climate*, **22**, 2058–2072.
- Matsueda, M. (2009). Blocking predictability in operational medium-range ensemble forecasts. *Scientific Online Letters on the Atmosphere*, **5**, 113–116, doi:10.2151/sola.2009-029.
- Nakamura, H. and Fukamachi, T. (2004). Evolution and dynamics of summertime blocking over the Far East and the associated surface Okhotsk high. *Quarterly Journal of the Royal Meteorological Society*, **130**, 1213–1233.
- Ninomiya, K. (2009). Characteristics of precipitation in the Meiyu-Baiu season in the CMIP3 20th century climate simulations. *Journal of the Meteorological Society of Japan*, **87**, 829–843.
- Nitta, T. (1987). Convective activities in the tropical western Pacific and their impact on the Northern Hemisphere summer circulation. *Journal of the Meteorological Society of Japan*, **65**, 373–390.
- North, G. R., Bell, T. L., Cahalan, R. F., and Moeng, F. J. (1982). Sampling errors in the estimation of empirical orthogonal functions. *Monthly Weather Review*, **110**, 699–706.
- Ogata, T., Xie, S.-P., Wittenberg, A., and Sun, D.-Z. (2013). Interdecadal amplitude modulation of El Niño/Southern Oscillation and its impacts on tropical Pacific decadal variability. *Journal of Climate*, **26**, 7280–7297.
- Ogi, M., Tachibana, Y., and Yamazaki, K. (2004). The connectivity of the winter North Atlantic Oscillation (NAO) and the summer Okhotsk high. *Journal of the Meteorological Society of Japan*, **82**, 905–913.
- Onogi, K., Tsutsui, J., Koide, H., et al. (2007). The JRA-25 Reanalysis. *Journal of the Meteorological Society of Japan*, **85**, 369–432.
- Otomi, Y., Tachibana, Y., and Nakamura, T. (2013). A possible cause of the AO polarity reversal from winter to summer in 2010 and its relation to hemispheric extreme summer weather. *Climate Dynamics*, **40**, 1939–1947.
- Rayner, N. A., Parker, D. E., Horton, E. B., et al. (2003). Global analyses of sea surface temperature, sea ice, and night marine air temperature since the late nineteenth century. *Journal of Geophysical Research*, **108**, 4407, doi:10.1029/2002JD002670.
- Seager, R., Harnik, N., Kushnir, Y., Robinson, W., and Miller, J. (2003). Mechanisms of hemispherically symmetric climate variability. *Journal of Climate*, **16**, 2960–2978.
- Takaya, K. and Nakamura, H. (2001). A formulation of a phase-independent wave activity flux for stationary and migratory quasigeostrophic eddies on a zonally varying basic flow. *Journal of the Atmospheric Sciences*, **58**, 608–627.
- Ueda, H., Yasunari, T., and Kawamura, R. (1995). Abrupt seasonal change of large-scale convective activity over the western Pacific in the northern summer. *Journal of the Meteorological Society of Japan*, **73**, 795–809.
- Wang, B., Wu, R., and Fu, X. (2000). Pacific-East Asian teleconnection: How does ENSO affect East Asian climate? *Journal of Climate*, **13**, 1517–1536.
- Wang, B., Xiang, B., and Lee, J.-Y. (2013). Subtropical High predictability establishes a promising way for monsoon and tropical storm predictions. *Proceedings of the National Academy of Sciences of the United States of America*, **110**, 2718–2722.
- Xie, P. and Arkin, P. A. (1997). Global precipitation: A 17-year monthly analysis based on gauge observations, satellite estimates, and numerical model outputs. *Bulletin of the American Meteorological Society*, **78**, 2539–2558.
- Xie, S.-P., Hu, K., Hafner, J., et al. (2009). Indian Ocean capacitor effect on Indo-Western Pacific climate during the summer following El Niño. *Journal of Climate*, **22**, 730–747.
- Yang, J., Liu, Q., Xie, S.-P., Liu, Z., and Wu, L. (2007). Impact of the Indian Ocean SST basin mode on the Asian summer monsoon. *Geophysical Research Letters*, **34**, L02708, doi:10.1029/2006GL028571.
- Yasui, S. and Watanabe, M. (2010). Forcing processes of the summertime circumglobal teleconnection pattern in a dry AGCM. *Journal of Climate*, **23**, 2093–2114.

# Impacts of annular modes on extreme climate events over the East Asian monsoon region

Jianping Li

## 27.1 Introduction

Low-frequency circulation patterns in the middle and high latitudes of the Southern Hemisphere (SH) and the Northern Hemisphere (NH) may provide important contributions to the total variability of the atmosphere. For instance, the SH Annular Mode (SAM) (Gong and Wang, 1998, 1999, Thompson and Wallace, 2000, Nan and Li, 2003) and NH Annular Mode (NAM) (Thompson and Wallace, 1998, 2000, Li and Wang, 2003) are the dominant modes of atmospheric variability in the SH and NH extra-tropical regions, respectively. The SAM and NAM are also known as the Antarctic Oscillation (AAO) and the Arctic Oscillation (AO). Additionally, the Northern Atlantic Oscillation (NAO) can be regarded as the regional manifestation of the NAM (Wallace, 2000). The annular modes have a strong association with the Ferrel cell (Li and Wang, 2003, Li, 2005). Many studies have investigated the broad impacts of these low-frequency circulation patterns on regional and global climate (Thompson and Wallace, 2001, Gillett *et al.*, 2006, Scaife *et al.* 2008, Li *et al.*, 2013a). For example, Scaife *et al.* (2008) pointed out that extreme winter weather events over Europe are linked to changes in the NAO. Chapter 9 in this book, by Scaife (2015), discusses some drivers of the NAO and associated predictability of the AO, and this chapter discusses Asian impacts of the annular modes and relevant feedbacks.

East Asian monsoon variability and related weather and climate events (e.g. flood or drought) are challenging and difficult scientific issues that also impact societal concerns such as property security and economic development. A better understanding of the East Asian monsoon system and its variability depends on improved knowledge of the factors that control or contribute to the variability of the East Asian monsoon. Existing research suggests that the El Niño–Southern Oscillation (ENSO) is an important driver of East Asian monsoon variability (Li *et al.*, 2010, 2013a).

Many studies have already demonstrated that both the SAM and NAM have important influences on the variability

of the East Asian monsoon. For example, the boreal spring SAM can influence summer precipitation over the middle and lower reaches of the Yangtze River valley (Nan and Li, 2003, Nan *et al.*, 2009, Li *et al.*, 2013b). The boreal winter SAM may impact rainfall in the following spring over South China (Zheng and Li, 2012, Li *et al.*, 2013b), and the preceding boreal autumn SAM is associated with the East Asian winter monsoon (EAWM) (Wu *et al.* 2009). In addition to these cross-seasonal relationships between the SAM and the East Asian monsoon, there are also some cross-seasonal relationships between the NAM and East Asian monsoon. For instance, the winter NAM is related to the following spring dust storms in Northwest China (NWC) (Liu and Ding, 2007). The spring NAO/NAM may strongly modulate the East Asian summer monsoon (EASM) (Wu *et al.*, 2009, 2012), and the preceding winter NAM can influence spring temperature extremes in Northeast China (NEC) (Yin *et al.*, 2013).

The ‘coupled oceanic–atmospheric bridge’ or ‘coupled land–atmospheric bridge’ plays a key role in understanding the cross-seasonal relationships previously mentioned (Fig. 27.1). Oceanic or land anomalies caused by preceding atmospheric anomalies act as an oceanic or land bridge that stores the preceding large-scale atmospheric signal for the following season. The atmospheric response (e.g. teleconnection) to ocean or land anomalies in the following season is an atmospheric bridge that links the remote or local climate to oceanic or land anomalies. There is much evidence that the annular modes also have important contemporaneous and cross-seasonal impacts on extreme climate events over the East Asian monsoon region. The mechanism responsible for cross-seasonal effects of the annular modes on extreme climate events is also mainly related to the ‘coupled oceanic–atmospheric bridge’ or ‘coupled land–atmospheric bridge’. This chapter will review some studies of the impacts of the NAM and SAM on extreme climate events over the East Asian monsoon region.

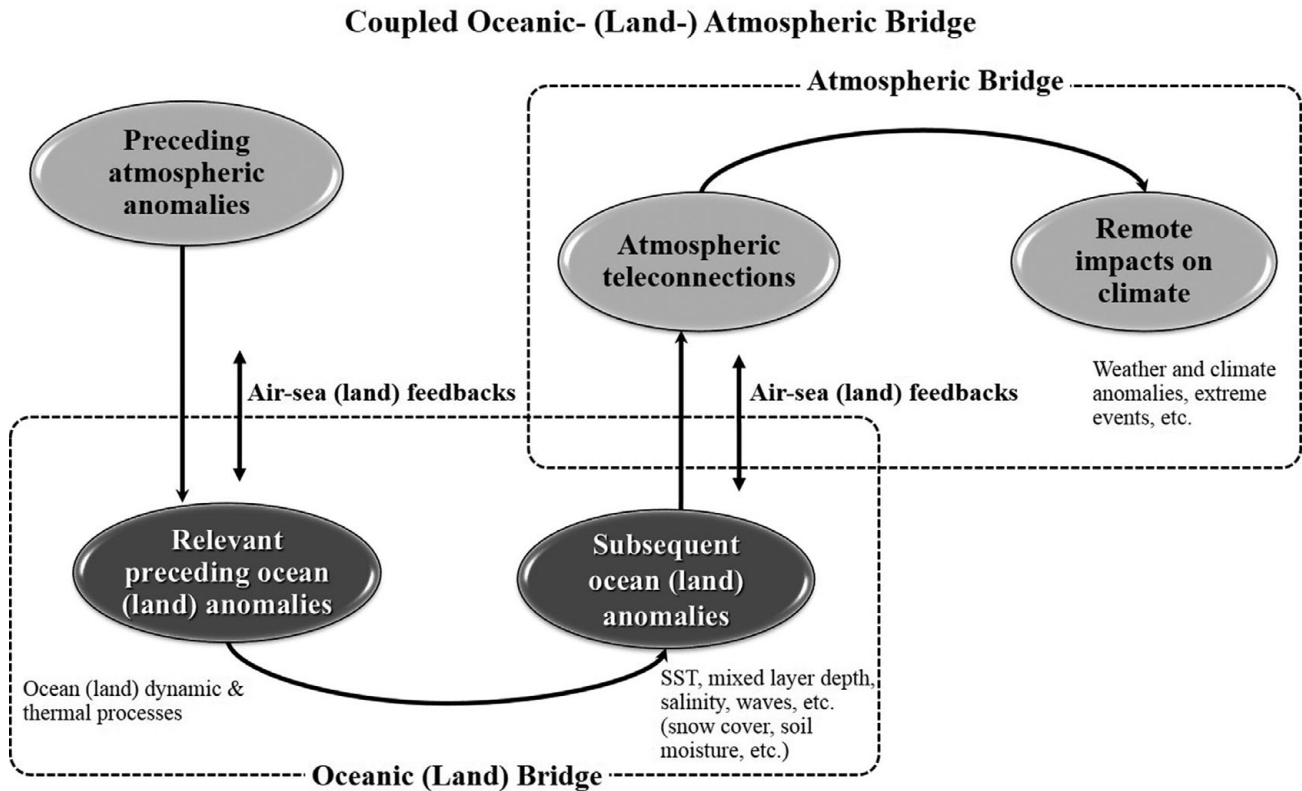


Fig. 27.1. Schematic diagram of the ‘coupled oceanic–atmospheric bridge’ or ‘land–atmospheric bridge’ for the cross-seasonal relationship between preceding atmospheric anomalies and subsequent remote climate response.

This chapter is organized as follows. In Section 27.2 we provide a brief review of the data and methodology used in this analysis. In Section 27.3 we discuss the cross-seasonal relationship between the preceding winter NAM and spring dust storms in NWC. In Section 27.4 we study the cross-seasonal relationship between the preceding winter NAM and extreme low temperature events in spring in NEC. Section 27.5 explores the relation between the winter NAM and East Asian snowstorms. Section 27.6 discusses the asymmetric impact of winter NAO on winter precipitation (including extreme drought in winter) in Southwest China (SWC). Section 27.7 reveals the cross-seasonal influences of the preceding boreal winter SAM on spring precipitation over South China. Section 27.8 provides a summary of the key results.

## 27.2 Data and methodology

The main data sets employed in this study include: the  $2.5^\circ \times 2.5^\circ$  reanalysis data (1958–2011) from the National Centers for Environmental Prediction/National Center for Atmospheric Research (NCEP/NCAR); monthly precipitation and temperature (1951–2011) from China’s 160

stations; daily minimum and maximum temperature and frost days from 160 stations in China (1959–2007); daily dust storm occurrence from 48 meteorological observing stations located in NWC (1960–2003); continental snow cover area from the Rutgers University Climate Lab (1967–2008); and the Met Office Hadley Centre’s sea surface temperature (SST) data set (HadSST3) (1850–2011) (Kennedy *et al.*, 2011).

The various indices used include, for example, the NAM index (NAMI) for 1873–2011 (Li and Wang, 2003, Li *et al.*, 2013b), the NAO index (NAOI) for 1873–2011 (Li and Wang, 2003), and the SAM index (SAMI) for 1948–2011 (Nan and Li, 2003). A dust storm frequency index (DSFI) over NWC is defined by averaging the 48-station observations of total dusty days for spring (Ding *et al.*, 2005). The domain-averaged 500 hPa geopotential height (GHT) over the Mongolian Plateau and Middle Siberia (MPMS) region ( $85^\circ\text{--}110^\circ\text{E}$ ,  $40^\circ\text{--}65^\circ\text{N}$ ) is defined as an atmospheric circulation index (ACI) over the region. Positive ACI denotes a positive 500 hPa GHT anomaly over MPMS, and vice versa. The SWC rainfall index (SWRI) is defined as the average precipitation of 12 stations in SWC for 1951–2011. To show the relationship between the previous winter NAM and the spring surface

horizontal wind in NWC, the domain-average 700 hPa horizontal wind field over NWC ( $75^{\circ}$ – $110^{\circ}$ E,  $35^{\circ}$ – $45^{\circ}$ N) is defined as a wind index (WI) in this region. The autumn Arctic sea ice area (DSIA) is obtained from the National Snow and Ice Data Center (Fetterer *et al.*, 2002).

We use five extreme low temperature indices based on the definitions from the Expert Team on Climate Change Detection and Indices (Klein Tank *et al.*, 2009). These indices include cold nights (TN10p), or the count of days where daily minimum temperature (TN) is less than the 10th percentile, and cold days (TX10p), or the count of days where daily maximum temperature (TX) is less than the 10th percentile. The minimum TN (TNn) is the monthly minimum value of daily TN, and the minimum TX (TXn) is the monthly minimum value of daily TX. Frost days (FD) is the count of days where TN (daily minimum temperature) is less than  $0^{\circ}\text{C}$ .

The season in this chapter refers to the boreal season (i.e. winter (DJF), spring (MAM), summer (JJA), and autumn (SON)). For a certain index, its ‘high index years’ refers to variability greater than one standard deviation above the mean, and its ‘low index years’ refers to variability less than one standard deviation below the mean. The statistical significance of the correlation between two auto-correlated time series is determined via a two-tailed Student’s t-test using the effective number of degrees of freedom ( $N_{\text{eff}}$ ; Bretherton *et al.*, 1999; Li *et al.*, 2012, 2013b) as follows:

$$\frac{1}{N_{\text{eff}}} \approx \frac{1}{N} + \frac{2}{N} \sum_{j=1}^N \frac{N-j}{N} \rho_{XX}(j) \rho_{YY}(j),$$

where  $N$  is the sample size, and  $\rho_{XX}$  and  $\rho_{YY}$  are the auto-correlations of two time series  $X$  and  $Y$  at time lag  $j$ , respectively.

The ‘coupled oceanic-atmospheric bridge’ or ‘coupled land-atmospheric bridge’ (Fig. 27.1) is mainly employed to understand relevant physical processes of cross-seasonal relationships between preceding NAM/SAM anomalies and succeeding climate anomalies over East Asia.

### 27.3 Cross-seasonal relationship between the preceding winter NAM and spring dust storms in NWC

In spring, dust storms frequently occur over NWC (Ding *et al.*, 2005). Severe dust events and sand transport cause desertification and considerable damage to agriculture and health in the surrounding area.

As shown in Fig. 27.2, the DSFI in NWC exhibits decadal variability with a sharp decadal decrease after 1985. Ding *et al.* (2005) found that the variability of DSFI is associated with the 500 hPa GHT over MPMS

(Table 27.1). When the spring 500 hPa GHT over MPMS is anomalously positive (i.e. an anomalous anticyclone over MPMS), in the western region of NWC the spring northwest surface wind intensity weakens and precipitation increases. As a result, spring dust storms decrease; the opposite conditions occur when the 500 hPa GHT is anomalously negative over MPMS in spring (Ding *et al.*, 2005). The spring ACI over MPMS experienced a decadal increase after the mid 1980s, and this contributed to the decadal decrease in spring dust storms in NWC.

Further analysis shows that the preceding winter NAM may be an important climatic factor that influences the occurrence of, and changes in, spring dust storms in NWC (Liu and Ding, 2007). There exists a significant negative correlation between the preceding winter NAM and the spring DSFI in NWC, and a significant positive correlation between the preceding winter NAM and the spring ACI over MPMS (Table 27.1). The ‘land-atmospheric bridge’ may play a key role in this cross-seasonal relationship. The Eurasian snow cover (ESC)

Table 27.1. Correlation coefficients between the winter NAMI and the following spring ACI over MPMS and WI in NWC.

	Spring DSFI	Spring ACI	Spring WI
Winter NAMI	<b>-0.47</b> ( <b>-0.63</b> )	<b>0.42</b> ( <b>0.68</b> )	<b>-0.40</b> ( <b>-0.55</b> )
Spring DSFI		<b>-0.63</b> ( <b>-0.83</b> )	<b>0.52</b> ( <b>0.64</b> )
Spring ACI			<b>-0.80</b> ( <b>-0.87</b> )

The period of the indices is 1954–2003, except DSFI (1960–2003). Bold values are significant at 95% confidence level. The values in brackets are for Gaussian 9-yr low-pass time series.

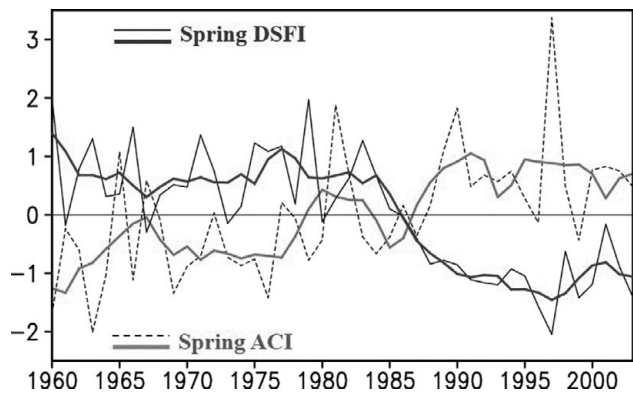


Fig. 27.2. Normalized spring DSFI (thin solid line) in NWC and ACI (thin dashed line) over MPMS. The thick solid lines are the corresponding 9-year running mean time series. A black and white version of this figure will appear in some formats. For the colour version, please refer to Plate 30.

may play an important role as a bridge that links the preceding winter NAM to the following spring dust storms in NWC, because the ESC anomaly has a close relationship with NAM and persists for a long time (Bamzai, 2003, Saito and Cohen, 2003, Saito *et al.*, 2004). Yin *et al.* (2013) also indicated that there is a significant negative correlation between the wintertime NAMI and the winter and spring ESC area. When there is a strong NAM in the preceding winter, surface air temperatures over the mid–high latitudes of Eurasia are higher than normal. As a result, the ESC area is smaller than normal in winter. This reduced ESC area tends also to be reduced in the following spring, and this situation corresponds to positive 500 hPa GHT anomalies over MPMS in the spring. These 500 hPa GHT anomalies contribute to the springtime anomaly in surface southeast winds in NWC and the increase in precipitation in the western region of NWC. These drier conditions favor the decrease in spring dust storm frequency in NWC. The decadal strengthening of the winter NAM in the mid 1980s has thus resulted in the decadal decline in spring dust storms in NWC.

#### 27.4 Influence of the preceding winter NAM on the spring extreme low temperature events in NEC

The preceding boreal winter NAM may exert important influences on the following spring's extreme low temperature events in NEC ( $30^{\circ}$ – $50^{\circ}$ N,  $110^{\circ}$ – $130^{\circ}$ E). As a result, it may have significant impacts on the growth of the crops in this region.

It can be seen from Fig. 27.3 that the preceding boreal winter NAMI is negatively correlated with spring cold nights, cold days, and the number of FD in NEC. This index is positively correlated with the minimum value of daily TN and TX in NEC. This indicates that extreme cold events in the following spring are weaker in intensity and less frequent over NEC when the NAMI in the preceding winter is high, and vice versa. High MAMI conditions in the preceding winter are followed in the spring by negative GHT anomalies in the upper troposphere, positive GHT anomalies in the lower troposphere, and an anomalous sinking flow and weak northeast cold vortex over NEC. These conditions favor atmospheric circulation patterns associated with fewer and weaker springtime extreme low temperature events in NEC (Yin *et al.*, 2013). In contrast, low MAMI conditions in the preceding winter suggest the opposite springtime patterns over NEC.

The physical mechanism of this cross-seasonal relationship between the preceding winter NAM and spring extreme low temperature events is related to the ‘land–

atmospheric bridge’ mentioned in the previous section. Yin *et al.* (2013) suggested that the strong NAM in winter causes a smaller ESC area during the following spring. This results in a weakened spring cold vortex and increased spring time average temperatures over NEC. These conditions offer a favorable seasonal-scale mean background for fewer and weaker spring extreme low temperature events in NEC. For a weak NAM, the opposite is true. Therefore, the preceding winter NAM may potentially be a valuable signal for predicting springtime extreme low temperature events in NEC. A schematic diagram of the relevant mechanism of this cross-seasonal relationship is shown in Fig. 27.4.

Besides, temperature changes in other regions in the NH are also associated with changes in the NAM and NAO (e.g. Kolstad *et al.*, 2010).

#### 27.5 Winter NAM and East Asian snowstorms

During January and February 2008, East Asia experienced a record-breaking and long-lasting snowstorm that led to huge losses of property and hundreds of deaths. This snowstorm was particularly strong in China, and was one of the most severe in many decades (Tao and Wei, 2008). Examining the physical mechanisms that may be responsible for such cold extremes could benefit the seasonal prediction of high-impact weather associated with an abnormal EAWM.

Wu *et al.* (2011) found that East Asian winter snowstorms such as the one in 2007/08 winter were significantly connected to anomalies in the central Siberian High, which are in turn accompanied by the third principal mode of the EAWM variability. They used a simplified general circulation model to show that reduced Arctic sea ice forcing induces high anomalies over northern Eurasia (positive abnormal Siberian High) and favors the development and maintenance of blocking highs over Siberia. As a matter of fact, such a circulation anomaly may be a regional indicator of anomalous NAM. Using partial regression analysis, they suggested that this pattern was linked to a reduction in autumn sea ice that is associated with the classical winter NAM pattern (Fig. 27.4); this highlights the importance of autumn Arctic sea ice in modulating the NAM variability and snowstorms, as also reported by Li and Wu (2012).

Based on the above results, we summarize the physical mechanism by which autumn Arctic sea ice influences the East Asian winter snowstorms as follows. Anomalous Arctic sea ice persists from autumn through the following winter and has been suggested to influence the NAM variability. The resulting abnormal NAM deforms the central Siberian High, and this has impacts on the outbreak of

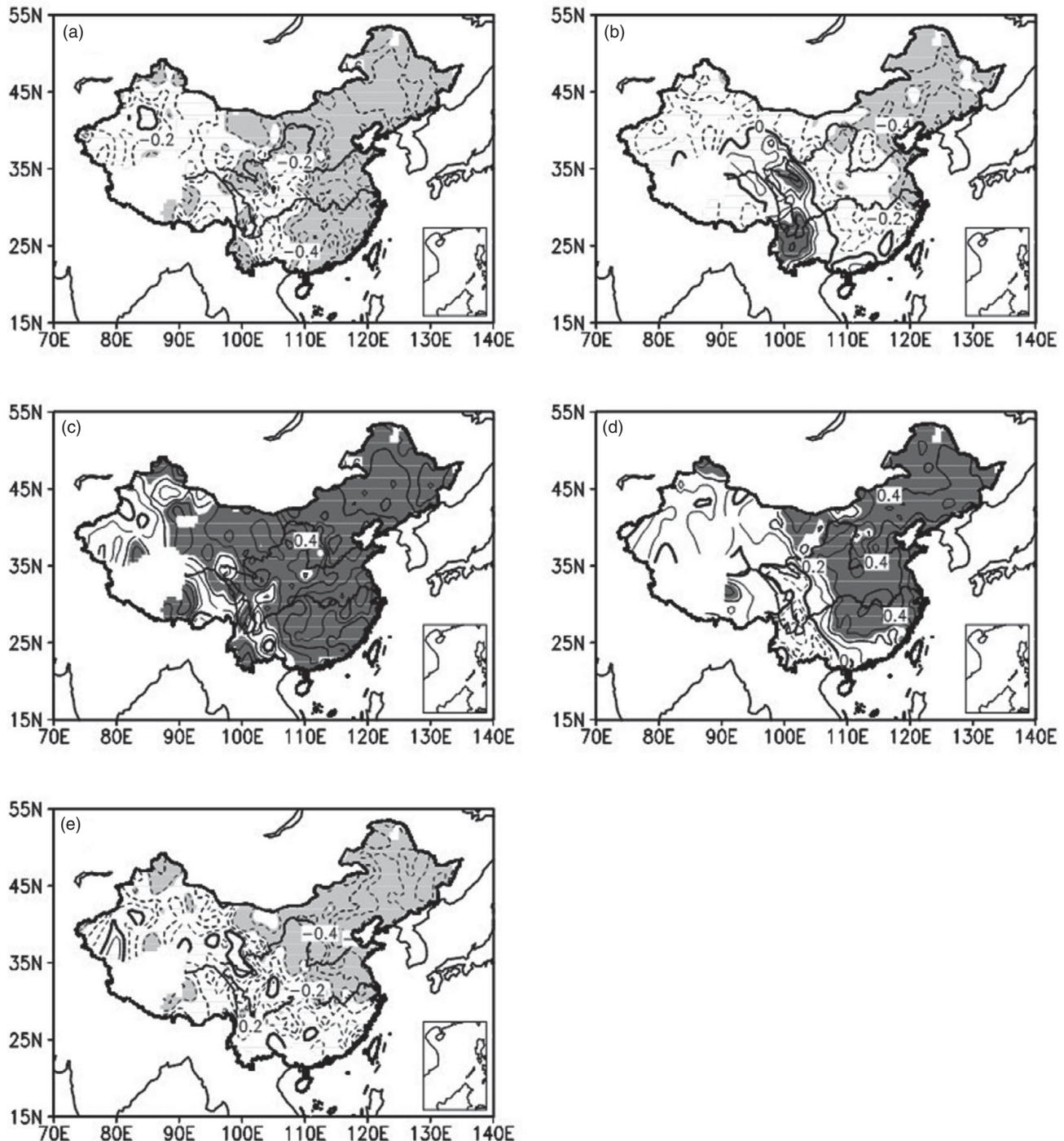


Fig. 27.3. Correlation coefficients between the preceding boreal winter NAMI and spring extreme low temperature indices in China for the period 1960–2008: (a) TN10p. (b) TX10p. (c) TNn. (d) TXn. (e) FD. Contour interval is 0.1. Shaded areas are significant at the 95% confidence level.

cold waves that then affect the occurrence of snowstorms over East Asia. Influences of Arctic sea ice depletion on atmospheric mid-latitude circulation in the NH can also be seen in Screen and Simmonds (2013).

## 27.6 Impact of winter NAO on winter precipitation in SWC

In the 2009/10 winter, SWC suffered a severe drought of a magnitude not experienced in a century. The NAO during

this winter was in its extreme negative phase (Sun and Li, 2012, Fereday *et al.*, 2012), and there was a significant positive correlation between the winter NAOI and rainfall in SWC (not shown). However, the relationship between the winter NAOI and rainfall index SWRI is asymmetric between NAO phases (Table 27.2). In other words, the significant correlation between the winter NAOI and SWRI happens during the negative NAO phase.

Further analysis shows that the main circulation pattern associated with winter precipitation in SWC is the so-called Southern Eurasian (SEA) teleconnection pattern (Xu *et al.*, 2013). The SEA has four anomaly centers in the Southern Eurasian region: Southwest Europe, the Middle East, the Arabian Sea, and the Tibetan Plateau (Fig. 27.5). Precipitation below (above) normal winter precipitation in SWC corresponds to the negative (positive) SEA pattern. An anticyclonic anomaly over the Tibetan Plateau during a negative SEA resists warm and moist airflow from the Bay of Bengal to SWC, creating conditions unfavorable to winter precipitation in SWC. Similar to winter precipitation over SWC, the winter SEA pattern also shows an asymmetric relationship with the winter NAO (Table 27.2).

Table 27.2. Correlation coefficients between the NAOI and SWRI and the NOI and SEAI for 1951–2011.

	NAOI(61 years)	NAOI at negative phase(30 years)	NAOI at positive phase(29 years)
SWRI	0.57**	0.63**	0.14
SEAI	0.50**	0.52*	0.21

Values with \*\* and \* are significant at the 99.9% and 99% confidence levels, respectively.

Previous studies suggest that the Rossby wave train along the subtropical westerly jet has an important impact on the NAO/NAM and the climate of East Asia (Watanabe, 2004, Hong *et al.*, 2008). Xu *et al.* (2013) indicated that the SEA pattern is linked to the asymmetric relationship between the winter NAO and precipitation over SWC. In winter, a negative NAO could lead to significant divergence anomalies over Southwest Europe and the Mediterranean at high levels in the troposphere upstream region of the SEA. The related Rossby waves triggered by the NAO could propagate along the subtropical westerly jet (Watanabe, 2004), favoring a strengthening of the negative phase of the SEA pattern (Xu *et al.*, 2013). As a result, the winter precipitation in SWC would be less than normal (Fig. 27.5). When the winter NAO is in its much stronger, negative phase, SWC may suffer severe drought in winter. However, when the winter NAO is positive, the convergence anomaly over Southwest Europe and the Mediterranean at high levels in the troposphere is weak. Consequently, there is no obvious impact of the NAO on the positive SEA pattern, and there is thus no evident influence of the positive NAO on the winter precipitation over SWC.

## 27.7 Cross-seasonal influence of the preceding boreal winter SAM on spring precipitation over South China

South China is an important economic region, with approximately 55% of the total population of China. The occurrence of flooding or drought in South China results in large economic costs every year. There are two peaks in the annual cycle of rainfall over South China, one in spring and one in summer. These peaks are called the first rainy

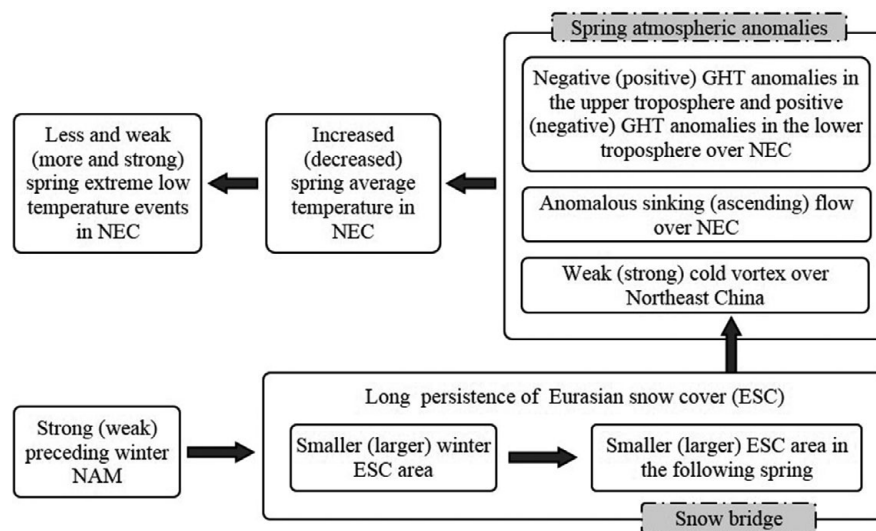


Fig. 27.4. Schematic diagram of the 'land-atmospheric bridge' showing processes of the cross-seasonal influence of the preceding boreal winter NAM on the following spring extreme low temperature events in NEC.

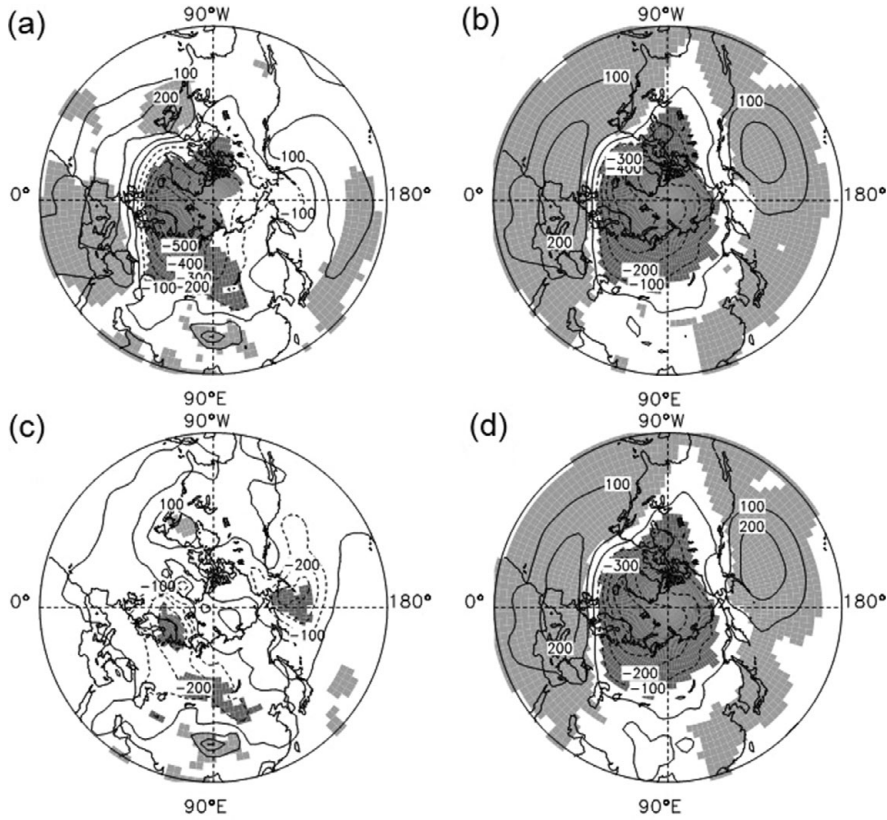


Fig. 27.5. Linear regression of winter SLP (Pa) on the (a) detrended autumn Arctic sea ice area (DSIA) anomaly and (b) winter NAMI. (c) Same as (a) but for the partial linear regression after removing the effect of the NAMI. (d) Same as (b) but for the partial linear regression after removing the effect of the DSIA. The areas above the 95% confidence level are shaded.

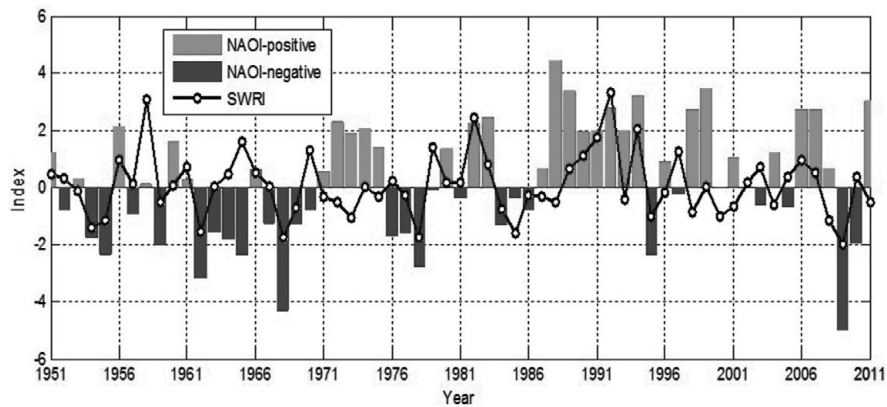


Fig. 27.6. Normalized time series of the winter NAOI (bars) and SWRI (open dotted line) for 1951–2011. A black and white version of this figure will appear in some formats. [For the colour version, please refer to Plate 31.](#)

season and the Meiyu season, respectively. Studies of spring rainfall variation over South China, as well as its causes are important both as a scientific endeavor and for use in disaster mitigation.

Zheng and Li (2012) found that there is a significant negative correlation between the preceding boreal winter SAMI and spring rainfall over South China (Fig. 27.6a). In other words, less (more) spring rainfall over South China follows strong (weak) boreal winter SAM events. Since the correlation pattern between the preceding boreal winter

SAMI and spring rainfall over South China becomes even stronger after removing the winter El Niño–Southern Oscillation (ENSO) signal, this cross-seasonal relationship does not rely on ENSO, an important, well-known forcing of interannual global and regional climate variability (Fig. 27.6b).

We employ the ‘oceanic–atmospheric bridge’ concept to understand the physical mechanism by which the boreal winter SAM has a cross-seasonal influence on spring rainfall over South China. As indicated by Zheng and Li

(2012), when the boreal winter SAMI is positive, westerlies are stronger in the SH high latitudes ( $70^{\circ}$ – $45^{\circ}$ S) and weaker in the SH middle latitudes ( $45^{\circ}$ – $30^{\circ}$ S) (Fig. 27.7a). This helps to increase evaporation and latent heat release from the ocean in the SH high latitudes; the opposite conditions occur in the SH middle latitudes. These differences result in a SH Ocean Dipole (SOD) in SST that has cooler SST in the SH high latitudes and warmer SST in the SH middle latitudes (Fig. 27.7b). Because of the large heat capacity of the ocean, this SOD maintains a similar dipole structure in the following spring, and the spring SOD in

turn modulates springtime atmospheric circulations in East Asia by impacting meridional circulations from the SH to NH (Fig. 27.7c). In other words, the positive SAM usually leads to a weakening and westward shift of the Western North Pacific subtropical high and an abnormal cyclonic circulation over the Western North Pacific that causes abnormal north easterlies and divergence over South China. All of these conditions favor decreased water vapor transport to South China and reduced spring rainfall over South China. When the boreal winter SAMI is negative, the opposite SOD and spring atmospheric conditions

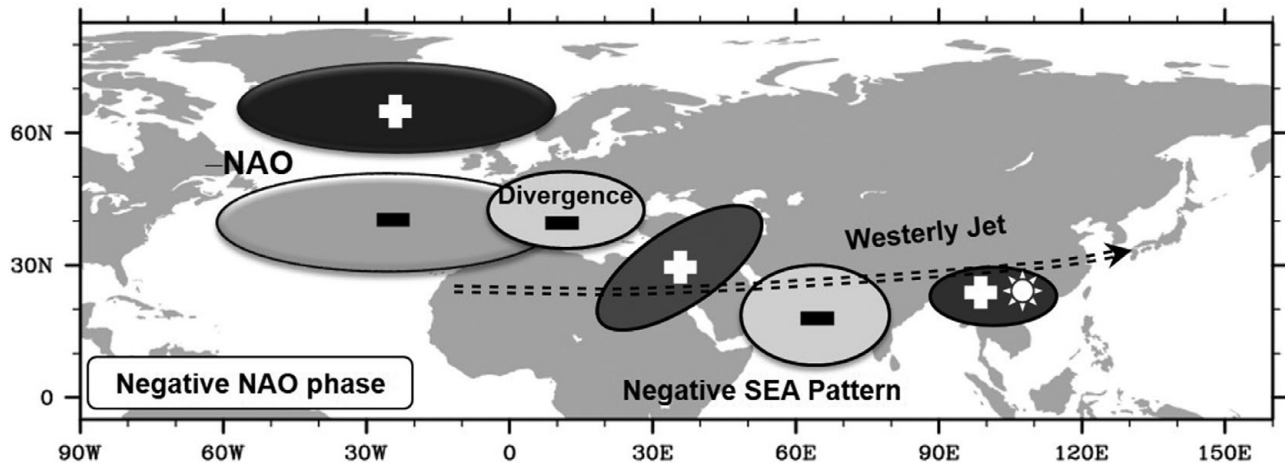


Fig. 27.7. Schematic diagram of the physical mechanism underlying the impact of the winter negative NAO phase on winter precipitation in SWC. The symbols “+” and “-” represent positive and negative GHT anomalies. The Southern Eurasian (SEA) teleconnection pattern consists of four anomaly centers in the Southern Eurasian region located in Southwest Europe, the Middle East, the Arabian Sea, and the Tibetan Plateau. The dashed arrow denotes the westerly jet.

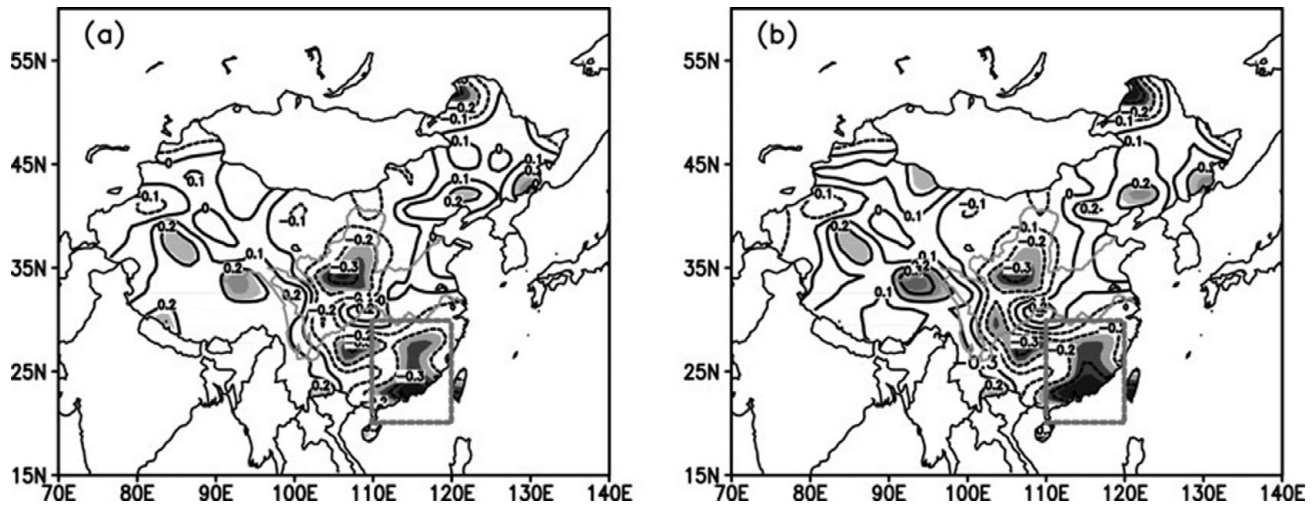


Fig. 27.8. (a) Correlation coefficients (contours and shading) between the preceding boreal winter SAMI and spring precipitation over China. (b) Same as (a) after removing the boreal winter ENSO signal. The dashed box shows the domain of South China in this study.

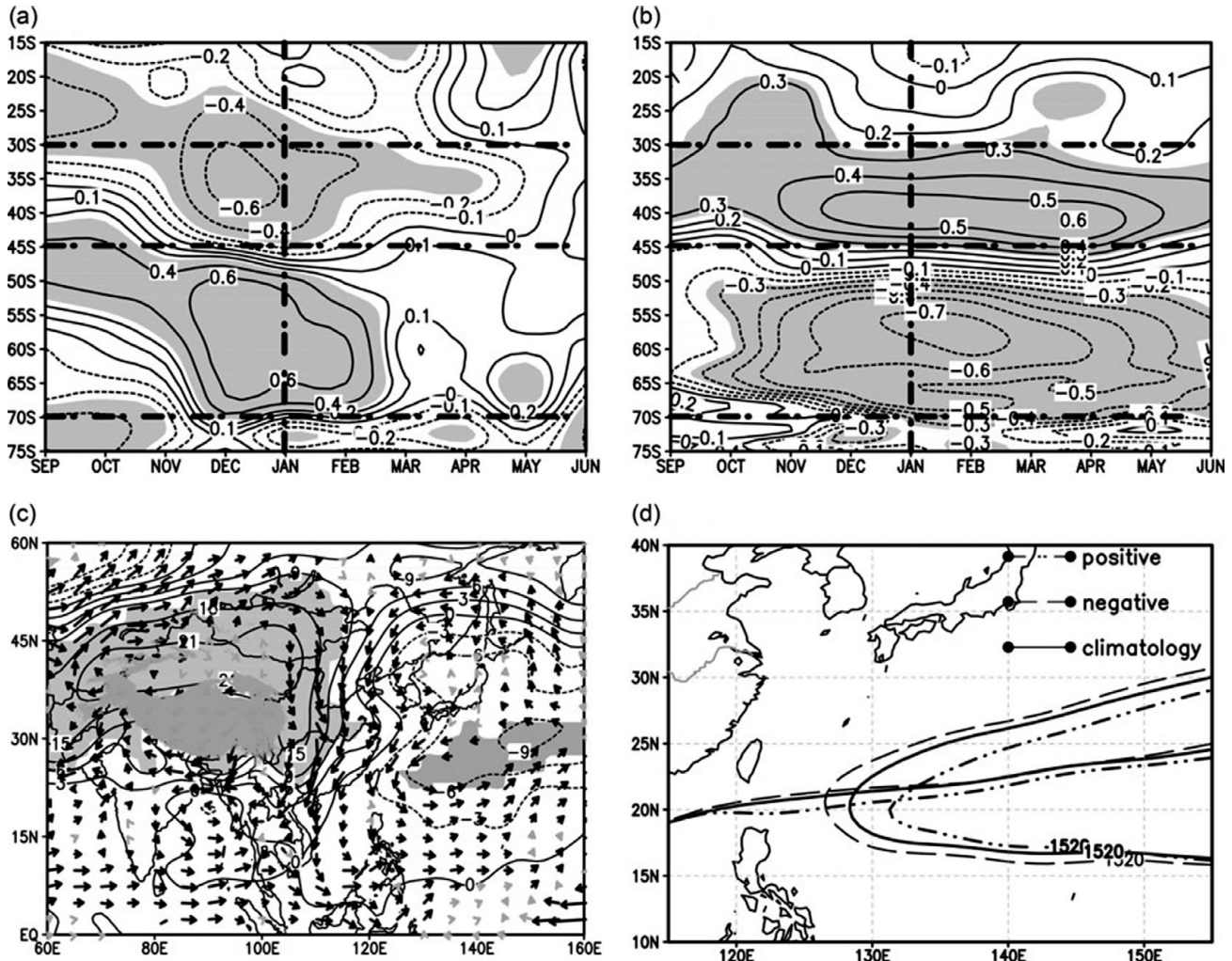


Fig. 27.9. Lead-lag correlation coefficients between the boreal winter SAMI and (a) the zonal-mean wind, and (b) the zonal-mean SST. The vertical dot-dashed lines in (a) and (b) indicate Jan(0) where the simultaneous correlations are shown. (c) Composite differences in spring GHT (gpm; contour) and horizontal wind ( $\text{ms}^{-1}$ ; vector) at 850 hPa between high and low boreal winter SAMI years. The shaded areas in (a)–(c) denote significance at the 95% confidence level. (d) Same as (c) but for the position of the main body of the Western North Pacific subtropical high at 850 hPa (indicated by the contour 1520 gpm). The solid, dot-dashed, and dashed lines indicate climatological conditions, positive SAM phases, and negative SAM phases, respectively.

occur. A negative boreal winter SAMI leads to increased spring rainfall over South China. This mechanism of the ‘coupled oceanic–atmospheric bridge’ can also be simulated by numerical experiments (Zheng and Li, 2012). The result here suggests that the boreal winter SAM could provide an important source of predictability for springtime rainfall over South China. Further, the boreal winter SAM is valuable in order to statistically downscale seasonal rainfall prediction over South China.

Besides, it would be worth mentioning that rainfall extremes in the SH are associated with Antarctic ozone depletion (e.g. Kang *et al.*, 2013), which shows a modulation on the SAM (Thompson *et al.*, 2011).

## 27.8 Conclusions

This chapter reviews the contemporaneous and cross-seasonal impacts of the NAM and SAM on extreme climate events over the East Asian monsoon region. The results show that, excluding the effects of ENSO, both the NAM and SAM are important drivers of East Asian monsoon variability and extreme events over East Asia. The preceding winter NAM can modulate the following spring’s dust storms in NWC, and springtime extreme low temperature events in NEC. The winter NAM may contribute to East Asian snowstorms, and the NAO may have an asymmetric impact on winter extreme drought in SWC. The preceding boreal winter SAM may exert important

influences on springtime precipitation over South China. The ‘coupled oceanic–atmospheric bridge’ and ‘coupled land–atmospheric bridge’ play important roles in understanding the underlying mechanisms of the cross-seasonal effects of the annular modes on extreme climate events over East Asia. Further study is needed to understand how to use these cross-seasonal relationships between the annular modes and the East Asian monsoon to make seasonal predictions of the East Asian monsoon and extreme weather events.

### 27.9 Acknowledgments

The author thanks Drs. Ruiqiang Ding, Zhiwei Wu, Fei Zheng, Shan Yin, Hanlie Xu, and Cheng Sun for their help during the preparation of this chapter. This work was jointly sponsored by the National Basic Research Program of China (2010CB950400) and the National Natural Science Foundation of China (41030961).

### References

- Alexander, L. V., Zhang X., Peterson T. C., *et al.* (2006). Global observed changes in daily climate extremes of temperature and precipitation. *Journal of Geophysical Research*, **111**, D05109, doi:05110.01029/02005JD006290.
- Bamzai, A. S. (2003). Relationship between snow cover variability and Arctic Oscillation Index on a hierarchy of time scales. *Int. J. Climatol.*, **23**, 129–142.
- Bretherton, C. S., M. Widmann, V. P. Dymnikov, J. M. Wallace, and I. Bladé (1999). The effective number of spatial degrees of freedom of a time-varying field. *J. Climate*, **12**, 1990–2009.
- Ding, R. Q., J. P. Li, S. Wang, and F. Ren (2005). Decadal change of the spring dust storm in northwest China and the associated atmospheric circulation. *Geophys. Res. Lett.*, **32**, L02808, doi:10.1029/2004GL021561.
- Fereday, D. R., A. Maidens, A. Arribas, A. A. Scaife, and J. R. Knight (2012). Seasonal forecasts of northern hemisphere winter 2009/10. *Env. Res. Lett.*, **7**, 034031.
- Fetterer, F., K. Knowles, W. Meier, and M. Savoie (2002). *Sea Ice Index (updated 2009)*. National Snow and Ice Data Center, Boulder, CO.
- Gillett, N. P., T. D. Kell, and P. D. Jones (2006). Regional climate impacts of the Southern Annular Mode. *Geophys. Res. Lett.*, **33**, L23704, doi:10.1029/2006GL027721.
- Gong, D. Y. and S. W. Wang (1999). Definition of Antarctic Oscillation index. *Geophys. Res. Lett.*, **26**, 459–462.
- Gong, D. Y. and S. W. Wang (1998). Antarctic Oscillation: Concept and applications. *Chinese Sci. Bull.*, **43**(9), 734–738.
- Hong, C. C., H. H. Hsu, H. H. Chia, and C. Y. Wu (2008). Decadal relationship between the North Atlantic Oscillation and cold surge frequency in Taiwan. *Geophys. Res. Lett.*, **35**, L24707.
- Kang, S. M., L. M. Polvani, J. C. Fyfe, *et al.* (2013). Modeling evidence that ozone depletion has impacted extreme precipitation in the austral summer. *Geophys. Res. Lett.*, **40**, 4054–4059.
- Kennedy, J. J., N. A. Rayner, R. O. Smith, D. E. Parker, and M. Saunby (2011). Reassessing biases and other uncertainties in sea surface temperature observations measured in situ since 1850: 1. Measurement and sampling uncertainties. *J. Geophys. Res.*, **116**, D14103, doi:10.1029/2010JD015218.
- Klein Tank, A. M. G., F. W. Zwiers, and X. Zhang (2009). Guidelines on analysis of extremes in a changing climate in support of informed decisions for adaptation. WMO-TD No. 1500, 56 pp.
- Kolstad, E. W., T. Breiteig, and A. A. Scaife (2010). The association between stratospheric weak polar vortex events and cold air outbreaks in the Northern Hemisphere. *Quart. J. Roy. Met. Soc.*, **136**, 886–893.
- Li, J. P. (2005). Physical nature of the Arctic Oscillation and its relationship with East Asian atmospheric circulation. In Q. Yu, W. Chen, *et al.* (Eds.), *Air-Sea Interaction and its impacts on China Climate*. Beijing: China Meteorological Press, pp.169–176.
- Li, J. P. and J. X. L. Wang (2003). A modified zonal index and its physical sense. *Geophys. Res. Lett.*, **30**(12), 1632, doi:10.1029/2003GL017441.
- Li, J. P., Wu Z. W., Jiang Z. H., and He J. H. (2010). Can global warming strengthen the East Asian summer monsoon? *J. Climate*, **23**, 6696–6705.
- Li, J. P., R. Ren, Y. Qi, *et al.* (2013a). Progress in air–land–sea interactions in Asia and their role in global and Asian climate change. *Chinese J. Atmos. Sci.*, **37**(2), 518–538. (in Chinese)
- Li, J. P., C. Sun, and F.-F. Jin (2013b). NAO implicated as a predictor of Northern Hemisphere mean temperature multi-decadal variability. *Geophys. Res. Lett.*, **40**, 5497–5502, doi:10.1002/2013GL057877.
- Li, J. P. and Z. W. Wu (2012). Importance of autumn Arctic sea ice to northern winter snowfall. *Proc. Natl. Acad. Sci. USA*, **109**, 10.1073/pnas.1205075109.
- Li, Y., J. P. Li, and J. Feng (2012). A teleconnection between the reduction of rainfall in Southwest Western Australia and North China. *J. Climate*, **25**, 8444–8461.
- Liu, X. H. and R. Q. Ding (2007). The relationship between the Spring Asian Atmospheric circulation and the previous winter Northern Hemisphere annular mode. *Theor. Appl. Climatol.*, **88**, 71–81.
- Nan, S. L. and J. P. Li (2003). The relationship between the summer precipitation in the Yangtze River valley and the boreal spring Southern Hemisphere Annular Mode. *Geophys. Res. Lett.*, **30**(24), 2266, doi:10.1029/2003GL018381.
- Nan, S. L., J. P. Li, X. Yuan, and P. Zhao (2009). Boreal spring Southern Hemisphere Annular Mode, Indian Ocean sea surface temperature, and East Asian summer monsoon. *J. Geophys. Res.*, **114**, D02103, doi:10.1029/2008JD010045.
- Saito, K. and J. Cohen (2003). The potential role of snow cover in forcing interannual variability of the major Northern Hemisphere mode. *Geophys. Res. Lett.*, **30**, 1302, doi:10.1029/2002GL016341

- Saito, K., T. Yasunari, and J. Cohen (2004). Changes in the sub-decadal covariability between Northern Hemisphere snow cover and the general circulation of the atmosphere. *Int. J. Climatol.*, **24**, 33–44.
- Scaife, A. A., C. K. Folland, L. V. Alexander, A. Moberg, and J. R. Knight (2008). European climate extremes and the North Atlantic Oscillation. *J. Climate*, **21**, 72–83.
- Screen, J. A. and I. Simmonds (2013). Exploring links between Arctic amplification and mid-latitude weather. *Geophys. Res. Lett.*, **40**, 959–964.
- Scaife, A. A. (2015). The North Atlantic and Arctic Oscillations: Climate variability, extremes and stratosphere troposphere interaction. In J. P. Li, R. Swinbank, H. Volkert and R. Grotjahn (Eds), *Dynamics and Predictability of Large-Scale High-Impact Weather and Climate Events*. Cambridge University Press..
- Sun, C. and J. P. Li (2012). Analysis of anomalously low surface air temperature in the Northern Hemisphere during 2009/2010 winter. *Climatic and Environmental Research*, **17**, 259–273. (in Chinese)
- Tao, S. Y., and J. Wei (2008). Severe snow and freezing rain in January 2008 in the southern China. *Climatic Enviro. Res.*, **13**, 337–350. (in Chinese)
- Thompson, D. W. J and J. M. Wallace (1998). The Arctic Oscillation signature in the wintertime geopotential height and temperature fields. *Geophys. Res. Lett.*, **25**, 1297–1300.
- Thompson, D. W. J and J. M. Wallace (2001). Regional climate impacts of the Northern Hemisphere Annular Mode. *Science*, **293**(5527), 85–89, DOI:10.1126/science.1058958.
- Thompson, D. W. J. and J. M. Wallace (2000). Annular modes in the extratropical circulation, Part I: Month-to-month variability. *J. Climate*, **13**(5), 1000–1016.
- Thompson, D. W. J., S. Solomon, P. J. Kushner, et al. (2011). Signatures of the Antarctic ozone hole in Southern Hemisphere surface climate change. *Nat. Geosci.*, **4**, 741–749.
- Wallace, J. M. (2000). North Atlantic Oscillation/annular mode: Two paradigms-one phenomenon. *Quart. J. Roy. Meteor. Soc.*, **126**, 791–805.
- Watanabe, M. (2004). Asian jet waveguide and a downstream extension of the North Atlantic Oscillation. *J. Climate*, **17**, 4674–4691.
- Wu, Z. W., J. P. Li, Z. H. Jiang, and J. H. He (2011). Predictable climate dynamics of abnormal East Asian winter monsoon: once-in-a-century snowstorms in 2007/2008 winter. *Clim. Dyn.*, **37**, 1661–1669.
- Wu, Z. W., J. P. Li, B. Wang, and X. H. Liu (2009). Can the Southern Hemisphere annular mode affect China winter monsoon? *J. Geophys. Res.*, **114**, D11107, doi:10.1029/2008JD011501.
- Wu, Z. W., J. P. Li, Z. Jiang, J. He, and X. Zhu (2012). Possible effects of the North Atlantic Oscillation on the strengthening relationship between the East Asian summer monsoon and ENSO. *Int. J. Climatol.*, **32**, 794–800, doi: 10.1002/joc.2309.
- Xu, H. L., J. P. Li, J. Feng, and J. Y. Mao (2013). The asymmetric relationship between the winter NAO and the precipitation in southwest China. *Acta Meteorol. Sin.*, **70**, 1276–1291.
- Yin, S., J. Feng, and J. P. Li (2013). Influences of the preceding winter Northern Hemisphere annular mode on spring extreme low temperature events in the north of eastern China. *Acta Meteorol. Sin.*, **71**(1), 96–108. (in Chinese)
- Zheng, F. and Li, J. P. (2012). Impact of preceding boreal winter southern hemisphere annular mode on spring precipitation over south China and related mechanism. *Chinese J. Geophys.*, **55**(11), 3542–3557.

# Index

- 2 °C target, 220
- absolute angular momentum, 170
- active monsoon, 313
- adiabatic process, 16
- aerosols, 304–5, 319
- Africa (covering Lake Victoria), 295–7
- African Easterly Wave (AEW), 138
- African systems, 136
- air-sea interaction, 305, 320
- AL, 225, *See Aleutian low*
- Aleutian low, 225, 233
- annular mode, 343, 352
- Antarctic circumpolar transport, 298
- Antarctic Oscillation (AAO), 297–8, 343
- Arctic, 115, 117–18
- Arctic Oscillation (AO), 122, 297, 343
- Arctic sea ice area, 345
- Asia (including China, Australia, Middle East, Siberia, Korea, Bay of Bengal, Gulf of Carpentaria), 296–7
- Asian jet, 337, 339, 341
- Asian Monsoon, 139, 304, 343, *See monsoon*
- Atlantic Meridional (or multi-decadal) Oscillation (AMO), 281, 283
- Atlantic meridional overturning circulation (AMOC), 280, 283, 292, *See meridional overturning circulation*
- Atlantic Multidecadal Oscillation (AMO), 256, *See Atlantic Meridional Oscillation*
- Atlantic, 122–4, 127
- Atlantic SST variability, 267
- atmospheric circulation index (ACI), 344
- Australian rainfall, 280, 283, 286–8, 291
- axisymmetrization, 168–71, 173
- baroclinic instability, 141–4
- barotropic energy conversion, 202
- Beijing floods of 21 July 2012, 177
- beta-skirt axisymmetrization (BSA), 169–70
- binary vortex interaction, 170
- blocking, 74, 76, 114–15, 117–18, 202, 339–41
- blocking high, 346
- bootstrap resampling, 201
- boundary layer, 170
- boundary layer dynamics, 168–72
- boundary layer inflow, 170–1
- TC boundary layer, 169
- unbalanced boundary layer flow, 171
- break monsoon, 313–14, 316, 321, 323
- Brier score (BS), 103
- Bulletin of the American Meteorological Society's State of the Climate Report, 38
- calibration, 97, 104–6
- CCSM4, 203–7
- bias, 204–5, 207–8
- future hot spells, 206
- Central America, 296
- chaotic, 141, 146, 150–1
- circumglobal teleconnection (CGT) pattern, 338
- climate change, 113–15, 118, 125
- climate extremes, 50
- climate model, 202–4, 208
- bias correction, 204
- LSMP, 198–9, 201–2, 204–5
- climate models, 114–15, 117–18
- CMIP5, 114, 116–18
- CO<sub>2</sub>, 220–1, 223–4
- CO<sub>2</sub> doubling, 223–4
- cold days, 54–5, 345–6
- cold nights, 54–5, 345–6
- cold surges, 297
- cold vortex, 346
- consensus forecast, 133
- convection permitting, 142, 145–8, 150
- convective instability, 143–4, 146
- convergence, 170–1
- correct negatives, 134
- COSMO (Consortium for Small Scale Modelling), 99–100, 102–3, 105, 107
- coupled land-atmospheric bridge, 343, 345, 352
- land bridge, 343
- coupled oceanic-atmospheric bridge, 343, 345, 351–2
- cross-equatorial flow, 305–6, 311
- cross-seasonal effect, 343, 352
- cross-seasonal relationship, 343–6, 349, 352
- CRPS (continuous ranked probability score), 103–5, 107
- cyclogenesis, 146
- cyclone, 113–18
- Cyclone Yasi, 176, 179, 181
- cyclonic vorticity, 79, 83–8, 90, 92–3
- cyclonic wave breaking, 156, 162
- Dansgaard-Oeschger (DO) events, 239
- data assimilation, 4–6, 12–14, 96–7, 99, 106
- decadal variability, 345
- degeneracy, 125
- detection and attribution, 37, 41–2, 47, 49, 52, 60, *See optimal fingerprinting*
- diabatic heating, 16, 19–20, 23, 27, 31–5, 170, 172–3
- divergent outflow, 156, 160–2
- downscaling, 180–1, 203, 208, *See LSMP*
- downstream development, 155–6, 158–9, 164–5
- drought, 255–7, 259, 262, 265, 267–8, 271, 273–7, 279, 343–4, 347–8, 351
- dry air intrusion, 148
- Dust Bowl, 255, 257, 262, 264, 267
- dust storm, 343–6, 351
- dust storm frequency index (DSFI), 344
- dynamics, 142, 144–5, 148, 150–1
- axisymmetric dynamics, 173
- balanced dynamics, 170, 172–3
- boundary layer dynamics, 168–72
- internal dynamics, 172
- unbalanced dynamics, 170–1
- vortex dynamics, 173
- E vector, 202
- Earth System Models of Intermediate Complexity (EMICs), 241
- East Asian monsoon, 343, 351–2
- East Asian summer monsoon (EASM), 343
- East Asian winter monsoon (EAWM), 343
- East Asian winter monsoon, 225, 227, 231, 233
- eddy kinetic energy (K<sub>e</sub>), 156
- eddy-driven jet, 71–2, *See extratropical jet*
- effective number of degrees of freedom, 345
- Ekman, 171
- El Niño, 176, 180, 280, 286
- El Niño/Southern Oscillation (ENSO), 72, 163, 297–9, 305–6, 312, 317–21, 324, 333, 343, 349, *See low frequency variability*
- ensemble, 95–110
- ensemble forecasting system, 13, *See ensemble prediction system*
- ensemble forecasts, 158, 160
- ensemble Kalman filter (EnKF), 147, 170
- ensemble of data assimilations, 13
- ensemble prediction system (EPS), 95–7, 108, 110
- error growth, 141–5, 150–1
- Ertel potential vorticity, 16–18, 21
- Eurasian (EU) teleconnection pattern, 225–6
- Eurasian snow cover (ESC), 345
- Europe (covering Russia), 297
- European Centre for Medium-range Weather Forecasts (ECMWF), 133–4, 136–40
- ensemble, 32-day, 133–4, 136–40
- extended-range forecasts (5–30 days), 134, 136
- extratropical jet, 70, 72–3, *See Asian jet, jet stream*
- extratropical transition (ET), 153, 164
- extreme, 95, 98, 102–4, 107–8, 110
- extreme events, 185
- extreme low temperature, 76, 344–6, 351
- extreme precipitation, 50–1, 59–63, 75
- extreme rainfall, 295
- extreme temperature, 50, 52–3, 55–6, 59, 62, 76
- extreme value theory (EVT), 48–9, 52, 55, 62, 107
- extreme weather, 75, 122, 127–8, 303–4, 325, *See extreme events*
- extreme weather-related events, attribution of, 37
- floods, 37, 41, 43–5
- heat waves, 38, 45
- human-induced climate change, 37, 39–40
- selection bias, 42, 44
- eyewall, 168–71, 173
- double eyewall, 168, 171, 173
- eyewall replacement cycle, 168, 172–3
- inner eyewall, 168–9
- outer eyewall, 168
- secondary eyewall formation (SEF), 168
- false alarms, 134–5
- ferrel cell, 343
- flood, 295–6, 343

- floods, 122, 176, 271, 273–7, 279  
 forecast, 125, 127–8  
 forecast error, 142, 145, 150  
 forecast model, 141–2  
 forecast sensitivity, 146  
 forecastability, 136–7  
 forecastable, 136–7  
 forecasting, 95–7, 102–3, 105, 108–10  
 formations, 134, 137–40
  - baroclinically influenced, 138
 fraction of attributable risk, 39  
 freshwater flux, 242, 244–5  
 freshwater perturbation (PERT), 240, 242, 244, 247–53  
 frontogenesis, 162, 165  
 frost days, 344–5  
 frosts, 122
- generalized extreme value 49, 52, 55, 59  
 geopotential height (GHT), 344  
 geostrophic balance, 17, 33  
 geostrophic wind, 17  
 GIFS (Global Interactive Forecast System), 97  
 global warming, 221–3  
 gradient wind, 170, 172
  - gradient wind balance approximation, 171
 greenhouse gases, 122  
 Guinea Coast, 271–9
- hazard, 110  
 heat flux, 202
  - by transients, 202
 heat wave, 118, 185–6, 189–94, 210–11, 215–17, 220, *See hot spells and drought, synoptic description*  
 high-impact weather, 69, 75–6, 97, 108–10, *See extreme weather*  
 hits, 134, 138  
 hot spells, 198–9, 201–5, 208
  - LSMP, 198, 201
  - synoptic description, 198
  - target ensemble mean, 201, 208
 Hovmöller diagram, 202  
 Hurricane, 146–8, 150
  - intensity, 146, 150
 Hurst coefficient, 290  
 hydroclimate variability, 255, 264–5  
 hydrostatic balance, 17
- idealized toy model, 141  
 Impact of Typhoons on the Ocean in the Pacific (ITOP), 136  
 inaccuracy, 141  
 Indian Ocean (IO), 294–9, 333  
 Indian Ocean Dipole (IOD), 176, 280, 282, 284, 286, 292, 305  
 Indian Summer Monsoon, 306, 316  
 Indonesian Throughflow (ITF), 299  
 initial conditions (IC), 141–2, 144–6, 148, 150–1  
 initial tendencies, 6–7  
 instability, 141–2, 150–1  
 interannual variability, 333, 337  
 Interdecadal Pacific Oscillation (IPO), 281  
 interdecadal variability, 217, *See interdecadal variation*  
 interdecadal variation, 205  
 intrinsic predictability, 141–2, 146, 151  
 isentropic surface, 16–17, 20–2, 32–3, 35  
 ITCZ (intertropical convergence zone), 297
- jet meandering, 88  
 jet pulsing, 84  
 jet stream, 79–85, 87, 90, 92–3, 113, 122, 124, 127, 202, *See eddy-driven jet, extratropical jet*  
 Joint Typhoon Warning Center (JTWC), 134
- Kelvin wave, 297–9
- La Niña, 176–9, 181  
 Lagrangian perspective, 19, 21–2, 33  
 land cover change, 194  
 land surface processes, 304–5, 319, 324  
 LC1, 69–74, *See life cycle of baroclinic*  
 LC2, 69–74, 76, *See life cycle of baroclinic*  
*life cycle of baroclinic* 69–70  
 lightning, 296  
 likelihood value (LHV), 134  
 low-frequency variability, 70, 74  
 low pressure systems (LPSs), 304, 312  
 LSMP (large scale meteorological pattern), 198, 208
  - in CCSM4 data, 205
  - in reanalysis data, 205
  - is useful, 208
  - model hot spells, 204
  - useful for downscaling extreme events, 203
 LSMP index, 199, 201–3, 205–6, 208
  - value, 199, 202, 205–6, 208
  - distribution, 203, 205, 208
 Madden-Julian Oscillation (MJO), 72, 125, 139, 163, 294, *See low frequency variability*  
 Maritime Continent (covering Philippines, Sumatra), 178, 295–6, 298  
 maximum temperature, 344–5  
 Meiyu–Baiu, 333, 340–1  
 merged jet, 80–1, 84, 88, 90, 92–3  
 meridional overturning circulation (MOC), 239, *See Atlantic meridional overturning circulation*  
 mesoscale convective system, 141  
 mesoscale convective vortex, 145  
 mid latitude, 141, 144, 148  
 minimum temperature, 345  
 misses, 134  
 model error, 96, 97, 142, 145, 150  
 model resolution, 3–4  
 modified quasi-geostrophic (MQG) model, 83, 92  
 MOGREPS (Met Office Global and Regional Ensemble Prediction System), 100–2, 108  
 moist convection, 142, 144, 146, 148, 150–1  
 moisture transports, 257  
 monsoon Asia, 333, *See Asian monsoon*  
 Monsoon Trough (MT), 304, 306, 313  
 monsoons, 297  
 multiple equilibrium, 242–5, 253
- NAM, 225, 231, 233, 298, 343–6, 348, 351, *See Northern Annular Mode, Northern Hemisphere Annular Mode*  
 NAO, 297–8, *See North Atlantic Oscillation*  
 NASA Hurricane and Severe Storm Sentinel (HS3), 136  
 National Centers for Environmental Prediction / Department of Energy reanalysis, 201  
 National Hurricane Center (NHC), 136  
 NCEP/NCAR reanalysis, 205, 207  
 negative log-likelihood, 53
- nonlinear life cycle, 88, 93  
 North America (covering USA, Alaska), 296–7  
 North Atlantic Deep Water (NADW), 239  
 North Atlantic Oscillation (NAO), 73, 122, 343–4, 346–7, *See low frequency variability*  
 Northern Annular Mode (NAM), 298, *See Northern Hemisphere Annular Mode*  
 Northern Hemisphere Annular Mode, 225, 343  
 numerical weather prediction (NWP), 3–4, 95–6, 98
- observation, 96, 101–8, 141, 148, 150–1  
 ocean–atmosphere interaction, 341  
 optimal fingerprinting, 37, 41, 43
- Pacific Decadal Oscillation (PDO), 50–1, 229, 281
  - modulation of, 225
  - planetary wave, 225, 227, 229, 231, 233
 Pacific North American pattern (PNA), 297  
 Pacific Ocean, 294, 296, 298–9  
 Pacific–Japan (PJ) pattern, 333  
 Parallel Ocean Model (POP), 241  
 parameterization, 97, 99  
 Petterssen–Smebye Type-B cyclogenesis, 153  
 PIT (probability integrated transform), 103  
 POAMA, 176–8, 181, *See predictive ocean–atmosphere model*  
 polar front jet (PFJ), 337  
 postprocessing, 107  
 potential vorticity, 69, 226  
 practical predictability, 141–2, 151  
 precession, 148–9  
 precipitation, 113, 116  
 predictability, 126–7, 133, 136–42, 153, 156, 158–9, 163–4, 333, 337, 340–1
  - limit of, 133
 prediction, 3–4, 10–11, 13, 95–9, 102, 105–10
  - probabilistic, 95, 97, 100, 102–3, 106–8, 110
  - deterministic, 95–9, 101, 103, 108–10
 predictive ocean–atmosphere model (POAMA), 176  
 probabilistic forecast, 14  
 process tendencies, 7  
 PV streamer, 79, 87, 92–3
- quality measure, 134, 136  
 quantile, 100, 102–7  
 quantile score (QS), 103  
 quasi-biennial oscillation (QBO), 124, 127, 280, 283  
 quasi-geostrophic, 83, 92
- rainfall, 176–81, 343–4, 348–51  
 rank histogram, 102–3  
 rapid intensification (RI), 146, 148  
 re-forecast, 3, 14  
 reliability diagram, 11  
 representative concentration pathways, 205  
 risk ratio, 39, 41–4, *See fraction of attributable risk*  
 Rossby wave, 226–7, 231, 233, 297–9, 348
  - thermal, 226–7
  - train, 226–7, 231, 233, *See wave train*
 Rossby wave breaking, 69, *See wave breaking*  
 Rossby wave packet, 153, 155–6, *See wave packet*
- salt advection feedback, 243, 253  
 SAM, 178–9, 298, 343–5, 348–51, *See Southern Annular Mode*

Sawyer–Eliassen, 172  
 Sawyer–Eliassen equation, 172  
 Sawyer–Eliassen model, 172  
 Schumann resonances (SR), 296  
 sea breeze, 198, 203, 205  
 sea level, 299  
 sea surface temperature (SST), 149, 176, 178, 297, 344  
 seasonal cycle, 81, 83  
 seasonal forecast, 177, 181  
 seasonal forecasting, 176  
 seasonal prediction, 138  
 severe weather, 141, 144, 151  
 SH, *See* Siberian high  
 Siberian high, 225  
 Atlantic-origin type, 226–7  
 Pacific-origin type, 227  
 sub-seasonal amplification of, 225  
 sign count, 201  
 Silk Road pattern, 337–9, 341  
 slantwise vorticity development, 16–17, 19–22, 33  
 snow cover, 125, 304, 317, 321, 344  
 snow cover area, 344  
 snowstorm, 344, 346–7, 351  
 soil moisture, 189, 191–4, 222–4  
 South America (covering Chile, Andes, Amazon), 297  
 South Asian Monsoon, 304, 306, 325  
 Southern Annular Mode (SAM), 280, 283, 288, 292  
 Southern Eurasian (SEA) teleconnection pattern, 348  
 Southern Hemisphere Annular Mode (SAM), 343, *See* Southern Annular Mode  
 Southern Hemisphere Ocean Dipole (SOD), 350  
 Southern Oscillation (SO), 280, 286, 305, 317  
 spin-up mechanism, 171  
 static stability, 16–19, 22, 26–7, 34–5  
 statistical, 208  
 20-year return value, 206, 208  
 bootstrap resampling, 201  
 consistency tests, 201  
 target ensemble mean, 201  
 storm track, 113–18, 122, 127  
 stratosphere, 124–5, 127  
 subsidence inversion, 97, 199  
 subtropical high, 350

subtropical jet, 71, 73, 80–1, 83, 85–6, 88, 92–3  
 sunspot number, 280, 283, 287, 292  
 supergradient force, 171  
 supergradient wind, 171, 173  
 surface currents, 298  
 SWFDP (Severe Weather Forecast Demonstration Project), 98  
 teleconnection, 343, 348  
 teleconnection pattern, 225–7  
 Arctic Oscillation (AO), 225  
 Eurasian (EU) teleconnection pattern, 225  
 Northern Hemisphere Annular Mode (NAM), 225  
 Scandinavian pattern, 225  
 Western Pacific (WP) teleconnection pattern, 227  
 temperature extremes, 84, 92–3  
 the C20C+ project, 44  
 The Weather Risk Attribution Forecast, 44  
 The weather@home, 44  
 thermal low, 198  
 thermal wind, 17  
 thermohaline circulation (THC), 239  
 THORPEX (The Observing System Research and Predictability Experiment), 97  
 THORPEX-Pacific Asian Regional Campaign (T-PARC), 133  
 Tibetan Plateau (TP) snow cover, 210  
 TIGGE (THORPEX Interactive Grand Global Ensemble), 97–8  
 tornadoes, 294  
 track, 148, 150  
 Trans-Niño, 282  
 tropical cyclone (TC), 76, 97–8, 110, 133–4, 136–41, 146, 148, 150, 153–62, 164–5, 168, 176, 179–81, 294, 299, *See* typhoon, hurricane  
 Atlantic, 133, 136–40  
 event, 133–4, 136–40  
 forecast, 133–40  
 intensity, 133, 136  
 motion, 133, 139  
 rainfall, 136  
 track forecast, 133–4  
 tropical cyclone structure (TCS-08), 133  
 tropical storm, 147  
 warnings, 133  
 western North Pacific, 133–4, 136–40  
 tropopause, 85, 88  
 typhoon, 134, 136, 139  
 uncertainty, 95–7, 102–4, 106, 108, 142, 146–9  
 upscale energy cascade, 170  
 Ural blocking, 226–7, 229–31, 233  
 vegetation, 185, 191–4  
 verification, 102–3, 105, 107, 110, 134, 138  
 track analog, 134  
 vertical vorticity, 16–17, 19–24, 26–7, 31–5  
 vertical wind shear, 148–9  
 volcanic dust, 280, 283  
 volcanic eruptions, 125  
 vortex Rossby waves (VRWs), 169  
 vortex tilt, 148  
 vorticity, 16–24, 26–7, 31–5, 169–70  
 vorticity gradient, 169–70  
 vorticity ring, 169–70  
 vorticity skirt, 169  
 vorticity extremes, 85, 90, 93  
 vorticity tongue, 87–8, 90, 93  
 warm air advection, 162  
 warm conveyor belt (WCB), 154  
 warm season precipitation, 144–5  
 warning, 95, 108–9  
 wave breaking, 122, *See* Rossby wave breaking  
 wave packets, 80, 88, *See* Rossby wave packet  
 wave train, 337, 340–1, *See* Rossby wave train  
 wave-activity flux, 226–7  
 weather versus climate, 38  
 weighted-mean vector motion, 133  
 weighting factor, 133–4  
 westerly ducts, 72, 75  
 wildfire, 296  
 wind index (WI), 345  
 wind storm, 76, 98  
 wind-induced surface heat exchange (WISHE) mechanism, 146–7  
 winter, 122–7  
 WMO (World Meteorological Organization), 97–8, 110  
 Wyrtki jet, 298